TMS2016

145th Annual Meeting & Exhibition

FEBRUARY 14-18 DOWNTOWN NASHVILLE, TENNESSEE MUSIC CITY CENTER

Connecting the Global Minerals, Metals, and Materials Community

SUPPLEMENTAL PROCEEDINGS

TMS

Springer

TMS2016

145th Annual Meeting & Exhibition

SUPPLEMENTAL

PROCEEDINGS

TMS2016

145th Annual Meeting & Exhibition

FEBRUARY 14-18 DOWNTOWN NASHVILLE, TENNESSEE MUSIC CITY CENTER

New proceedings volumes from the TMS2016 Annual Meeting:

- 7th International Symposium on High-Temperature Metallurgical Processing
- CFD Modeling and Simulation in Materials Processing 2016
- Characterization of Minerals, Metals, and Materials 2016
- Energy Technology 2016: Carbon Dioxide Management and Other Technologies
- EPD Congress 2016
- Light Metals 2016
- Magnesium Technology 2016
- Rare Metal Technology 2016
- REWAS 2016
- Shape Casting: 6th International Symposium
- TMS 2016 Supplemental Proceedings

TMS2016

145th Annual Meeting & Exhibition

SUPPLEMENTAL

PROCEEDINGS

Editor
The Minerals, Metals & Materials Society

ISBN 978-3-319-48624-6 ISBN 978-3-319-48254-5 (eBook)
DOI 10.1007/978-3-319-48254-5

Chemistry and Materials Science: Professional

Published by Springer International Publishers, Switzerland, 2016
Reprint of the original edition published by John Wiley & Sons, Inc., 2016, 978-1-119-22583-6

Printed on acid-free paper

This Springer imprint is published by Springer Nature
The registered company is Springer International Publishing AG
The registered company address is: Gewerbestrasse 11, 6330 Cham, Switzerland

TABLE OF CONTENTS
TMS 2016 Supplemental Proceedings

Edited Proceedings

Additive Forming of Components - Tailoring Specific Material Properties in Low Volume Production

Materials Research in Reduced Gravity

Metal and Polymer Matrix Composites II

Unedited Proceedings

Additive Manufacturing: Building the Pathway towards Process and Material Qualification

Computational Materials Engineering for Nuclear Reactor Applications

Computational Methods for Uncertainty Quantification, Model Validation, and Stochastic Predictions

Computational Thermodynamics and Kinetics

General Poster Session

ICME Infrastructure Development for Accelerated Materials Design: Data Repositories, Informatics, and Computational Tools

Material Behavior Characterization via Multi-Directional Deformation of Sheet Metal

Material Design Approaches and Experiences IV

Materials and Fuels for the Current and Advanced Nuclear Reactors V

Mechanical Behavior at the Nanoscale III

Nanostructured Materials for Nuclear Applications

Phase Transformations and Microstructural Evolution

Phase Transformations in Multi-component Systems: An MPMD Symposium Honoring Gary R. Purdy

Powder Metallurgy of Light Metals

Recent Developments in Biological, Structural and Functional Thin Films and Coatings

Refractory Metals 2016

TMS2016

145th Annual Meeting & Exhibition

SUPPLEMENTAL
PROCEEDINGS

EDITED
PROCEEDINGS

TMS2016
145th Annual Meeting & Exhibition

SUPPLEMENTAL PROCEEDINGS

Additive Forming of Components - Tailoring Specific Material Properties in Low Volume Production

Judith Ann Schneider
University of Alabama at Huntsville

Mark Stoudt
National Institute of Standards and Technology

Kester Clark
Los Alamos National Laboratory

Lee Semiatin
US Air Force Research Laboratory

Mohsen Asle Zaeem
Missouri University of Science and Technology

ANISOTROPIC MECHANICAL PROPERTIES IN A BIG-SIZED Ti-6Al-4V PLATE FABRICATED BY ELECTRON BEAM MELTING

Pan Wang[1], Mui Ling Sharon Nai[1], Xipeng Tan[2], Wai Jack Sin[1], Shu Beng Tor[2], Jun Wei[1]

[1]Singapore Institute of Manufacturing Technology, 71 Nanyang Drive, 638075, Singapore
[2]Singapore Centre for 3D Printing, School of Mechanical & Aerospace Engineering, Nanyang Technological University, HW1-01-05, 2A Nanyang Link, 637372 Singapore

Keywords: Additive manufacturing; Electron beam melting; Titanium alloy; Anisotropy; Mechanical properties

Abstract

In this study, in order to realize the application of the electron beam melting (EBM) technology for the printing of large components, the microstructure and mechanical properties of a big-sized Ti-6Al-4V plate (6 mm×180 mm×372 mm) additively manufactured by EBM were investigated. The paper focused on the graded microstructure and anisotropic mechanical properties by using x-ray diffraction, optical microscope, scanning electron microscope, microhardness and tensile test. A gradual change in microstructure with an increase in build height was observed. The formation of a graded microstructure was observed and discussed based on the thermal history experienced during printing. The mechanical properties were influenced accordingly by the graded microstructure. Moreover, the specimens which were printed parallel and perpendicular to the printing directions exhibited high elongation of ~18% and ~14%, respectively. The anisotropy in ductility was also observed and discussed according to the columnar prior β structure and grain boundary α phases present.

Introduction

Additive manufacturing (AM) technologies shorten the design to product time and reduce the process steps involved [1-3] thus overcoming some limitations of the traditional manufacturing methods like casting [4], forging [5, 6] and rolling [7]. In particular, AM technologies have exhibited promising applications in high value added industries [1, 8, 9]. Electron beam melting (EBM) is one of the layer-by-layer AM techniques, which has the capability of producing near-net shaped parts with complex geometries. Furthermore, due to its vacuum controlled process and high energy electron beam, it can be used to process high melting point and reactive metallic materials. Therefore, it is suitable for fabricating Ti alloy parts for the aerospace and biomedical applications [10, 11].

Layer-by-layer fusion step in EBM introduces rapid thermal cycles, which results in a different microstructure as compared to their cast or wrought counterparts. Moreover, the previous layers experience a thermal history during printing and this further introduces a different thermal history for each subsequent layer. In order to ensure the use of these printed parts in structural applications, their mechanical properties must be characterized. Therefore, many researchers have focused on understanding the microstructure and mechanical properties of Co-Cr-based alloys [12], Ti alloys [11, 13, 14] and Ni-based alloys [15] fabricated by EBM technology. Although these results exhibited excellent mechanical properties, the previous

investigations only focused on small build samples and/or parts with short build heights. However, for industry applications, in particular, aerospace applications, a big-sized part with complex shape is of actual industrial need. Recently, graded microstructure and mechanical properties were reported by Tan *et al.* in a 10 mm×100 mm× 30 mm block [16]. However, there is still lack of understanding with regards to the microstructure and mechanical properties of big-sized parts. Moreover, anisotropic tensile behavior of directed energy deposition additive manufactured Ti-6Al-4V was reported [17]. It is suggested that the presence of grain boundary α phase plays a critical role on the anisotropic ductility. Therefore, it is reasonable to predict that anisotropic mechanical properties may also appear in the EBM-built parts. Accordingly, in the present study, the effects of build height on the microstructure and mechanical properties of a big-sized plate were investigated. The anisotropic mechanical properties were also discussed.

Experimental procedures

An Arcam A2X EBM system with a build envelope of 200mm×200mm×380mm was used (software version 3.2, accelerating voltage 60,000 V, layer thickness 50 μm, Arcam AB standard build theme for Ti-6Al-4V alloy) to print four plates (6 mm×180 mm×372 mm in thickness, length and height, respectively) centered on a 210 mm×210 mm stainless steel start plate. Fig. 1 (a) shows an as-built plate. The pre-alloyed Ti–6Al–4V (Grade 5) virgin powder with a nominal composition of Ti-6Al-4V-0.03C-0.1Fe-0.15O-0.01N-0.003H supplied by Arcam AB, was used in the present study. After ~1 hour vacuum, the 10 mm thick start plate was heated when both a chamber pressure and an electron beam column pressure reached to below 5×10^{-4} mbar and 5×10^{-6} mbar, respectively. The four big-sized Ti-6Al-4V plates were directly built on the preheated start plate once the bottom temperature that was measured by a thermal couple placed beneath the start plate reached 730 ℃. High-purity helium was applied to regulate a vacuum of $\sim2\times10^{-3}$ mbar during the building process.

In order to examine the microstructure and mechanical properties of the printed plate, tensile specimens were wire-cut from the plate in two orientations (parallel and perpendicular to build direction). In each orientation, they were divided into three groups of specimens that were taken from the bottom, middle and top sections, respectively (Fig. 1 b). The dimensions of tensile specimens were illustrated in Fig. 1 (c). The surface of all the tensile specimens was smoothened by plunge grinding. The tensile test was conducted at room temperature in air, at an initial strain rate of 3.3×10^{-4} s^{-1}, using the Instron 4505 universal tensile testing machine with a load cell capability of 100 kN. In addition, an extensometer was applied to measure the strain. Microhardness tests were conducted on the polished specimens by using a micro hardness tester (Mitutoyo MVK-G350AT) with a load of 300 gf and a dwell time of 15 seconds. The specimens for microhardness tests were cut at a build height of ~13 mm (Fig. 1 b).

Phase identification was carried out using the X-ray diffraction (XRD), at room temperature with Cu K_α radiation operated at 40 kV and 40 mA. Microstructural observation was conducted using an optical microscope (OM) after etching by the Kroll's reagent. Scanning electron microscopy (SEM) was also used for microstructural analysis.

Results

Some small spherical pores (Fig. 2 a) with an average diameter of ~12 μm and irregular pores (Fig. 2 b) were occasionally observed. This is a common phenomenon in AM Ti-6Al-4Vparts

[17-19] due to the eargon during the production of gas atomized Ti-6Al-4V powder and the lack of fusion during layerwise melting [10, 18]. It is also worth noting that any spherical or irregular pores are supposed to be detrimental to fatigue properties while those small spherical pores in Fig. 2a may not significantly affect the tensile properties.

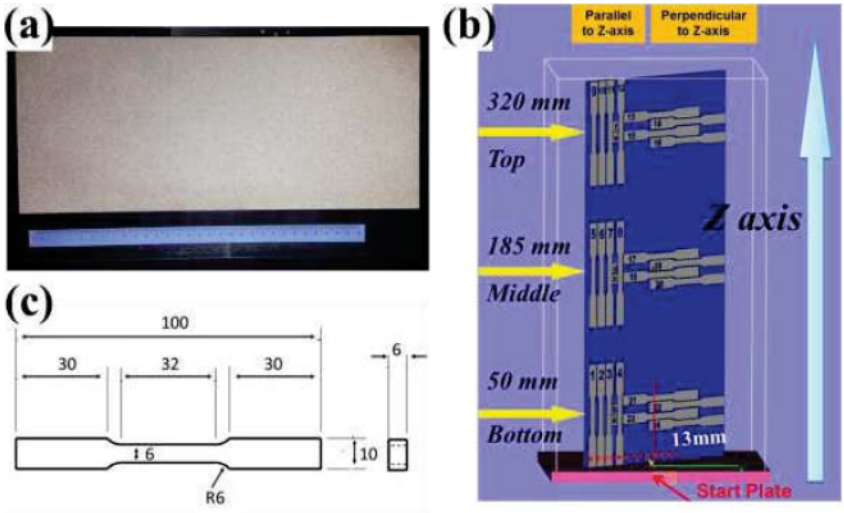

Fig. 1 (a) Picture of plate fabricated by EBM, (b) schematic illustration of locations of tensile specimens and microhardness specimens cut from plate, and (c) dimensions of tensile specimens in mm. The tensile specimens was divided into two groups, parallel to Z axis and perpendicular to Z axis. The microhardness was measured along the red round dot lines, which was ~13 mm high. It is noted that the microhardness specimens were cut from another plate as continuous microhardness values across the plate (from the left edge) were desired.

The microstructures at the bottom (Fig. 3 a and d), middle (Fig. 3 b and e) and top (Fig. 3 c and f) regions in the Ti-6Al-4V plate were shown in Fig. 3. Regardless of the build height (Fig. 3 a-c), columnar grain structures were clearly observed in all the three specimens. The columnar prior β grain is a typical feature of EBM-built Ti-6Al-4V part because of the high thermal gradient along Z axis, which has been reported eleswhere [13, 16]. The microstructure contained grain boundary α and transformed α + β microstructure within the columnar prior β grains. Only ~8 layers were shown in Fig. 3 (a) because the build layer thickness is 50 μm. However, the columnar prior β grains obviously grow across many layers, which differs from that manufactured by selective laser melting and laser aided additive manufacturing.

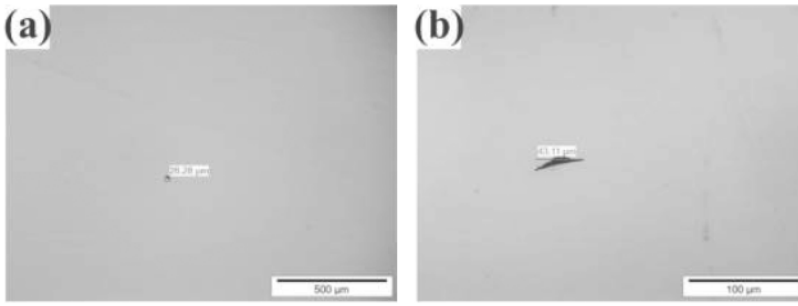

Fig. 2 Optical microscopy images of (a) the typical pore and (b) lack of fusion pore observed in Ti-6Al-4V plate fabricated by EBM.

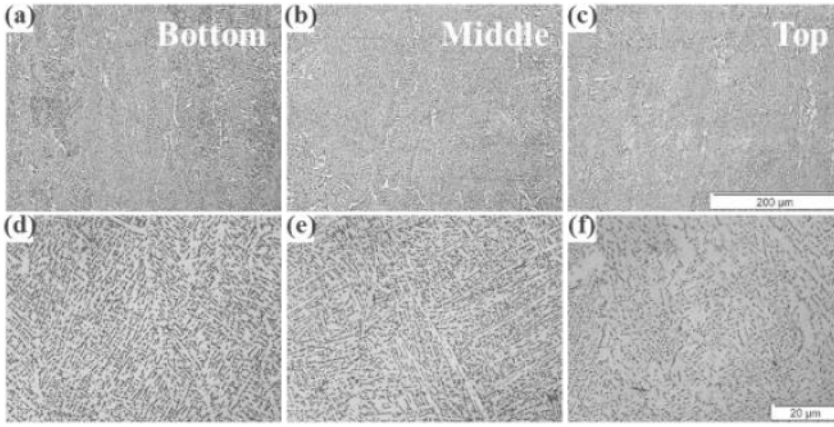

Fig. 3 Optical microscopy images of (a, d) bottom, (b, e) middle (c, f) top regions in the Ti-6Al-4V plate fabricated by EBM. (a-c) show columnar structure by using low magnification and (d-f) show α + β microstructure by using high magnification.

Fig. 3 (d-f) show the high magnification optical micrographs from the bottom region to the top region. Only α phase and β phase were observed, regardless of the build height. Because phase constitution and their distribution strongly influenced the mechanical properties [4, 13, 20] and α′ martensitic phase may exist in the EBM-built Ti-6Al-4V [11, 21], XRD measurements [22] and SEM analysis were carried out. It is confirmed that only α phase and a relatively small fraction of β phase exist in the present plate. However, the α lath width increased with an increase in build height. In particular, the α lath width was observed to increase from the middle region (Fig. 3. e) to the top region (Fig. 3 f). The graded microstructure was also observed in Co-Cr alloy fabricated by EBM [12]. This is caused by the effect of different thermal histories on different build heights. The increase of α lath width is attributed to the slower cooling rate in the top region. Since the bottom build directly connects to the stainless steel start plate, the heat

inside the bottom region is easily transferred to the start plate and then spread out. However, with the increase in build height, it becomes challenging to transfer the heat to the bottom region as quickly as compared to the stainless steel start plate due to the low thermal conductivity of Ti-6Al-4V solid, which is even worse for the case of Ti-6Al-4V powder [23]. A long exposure at higher temperatures on the top region resulted in the coarser α phase lath widths.

Fig. 4 shows the microhardness values measured from left edge to center at a build height of ~13 mm. All the measured values were around 340 HV and no significant difference was observed at the same build height. These results indicated that the tensile specimens wire-cut from the plate (Fig. 1 b) will yield the same tensile properties because those designated layers underwent the same thermal history in the present study.

Fig. 5 shows the Young's modulus at different build heights and orientations. It was observed that their Young's modulus values in the present study were almost constant, which is consistent with the finding of the previous report [10].

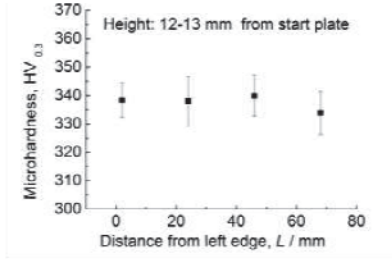

Fig. 4 Trend of microhardness values across the EBM printed Ti-6Al-4V plate (from the left edge), at a height of ~ 13mm from the start plate.

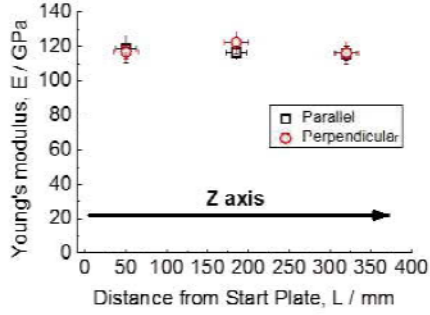

Fig. 5 Trend of Young's modulus values of the EBM printed Ti-6Al-4V plate (from the base of the start plate).

Fig. 6 shows the stress-strain tensile curves at room temperature. Similar to the commercial wrought Ti-6Al-4V, only a weak work hardening phenomenon was observed. Both the yield

strength and ultimate tensile strength were found to be dependent on the build height and orientation. These strength values were comparable to the results reported by S.S. Al-Bermani *et al.* [13] and that of the wrought Ti-6Al-4V according to ASTM 1472-14 [24]. Moreover, the yield strength and ultimate tensile strength were observed to decrease with an increase in build height. This is attributed to the finer α + β microstructure. It has been reported that the yield strength decreased with the increase of α lath width in Ti-6Al-4V alloys [13].

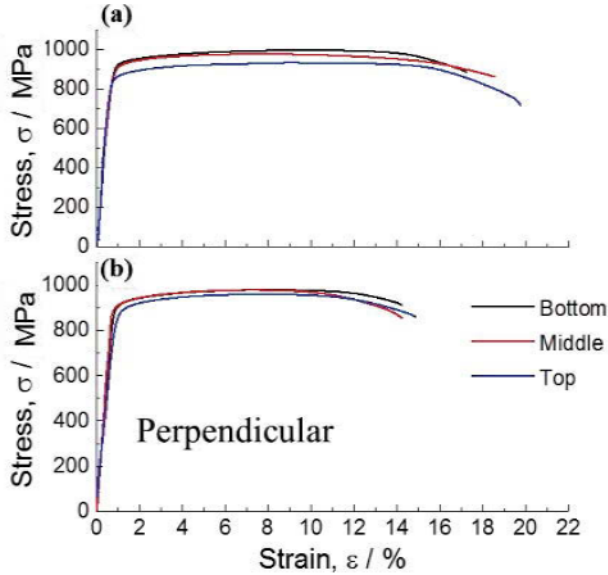

Fig. 6 Stress-strain curve of (a) parallel and (b) perpendicular to Z-axis specimens cut from Ti-6Al-4V plate fabricated by EBM.

On the other hand, more than 14% deformation strains were obtained in all the EBM printed specimens, regardless of their build height and orientation. These values were higher than that of the wrought form (ASTM 1472-14, 10%) [24]. It should be noted that the plastic strain in parallel orientation (~18%) was higher than that of perpendicular orientation (~14%). It is suggested that the anisotropy in ductility is mainly attributed to the appearance of the grain boundary α phase. The grain boundary α phase (Fig. 3 a-c) provides a preferential path for damage accumulation along the grain boundary. When a load is applied to the orientation perpendicular to the prior β grain boundary, a tensile opening mode is subjected to accelerated damage [17]. Therefore, a low plastic strain was observed in the perpendicular orientation (Fig. 6).

Conclusions

The graded microstructure as well as the anisotropic mechanical properties of a big-sized Ti-6Al-4V plate (6mm×180mm×372mm) were investigated. The following conclusions can be drawn.

(1) Columnar grain structure containing grain boundary α phase and transformed α + β microstructure within the prior β grain were observed, regardless of the build height.
(2) Only α phase and a relatively small fraction of β phase were detected in the microstructure of the as-built Ti-6Al-4V specimens. The α phase lath width increased with an increase in build height.
(3) With the increase in build height, the yield strength and ultimate tensile strength of the specimens were found to decrease. This is attributed to the increase of α lath width due to the different thermal histories along the build height.
(4) Anistropic mechanical properties was observed because of the presence of grain boundary α. A low deformation strain (~14%) was obtained in the perpendicular orientation and a high deformation strain (~18%) was obtained in the parallel orientation.
(5) The yield strengh and ultimate tensile strength of all the examined specimens were comparable to that of the wrought material and their elongations were even higher (ASTM 1472-14).

References

[1] Zhai Y, Lados DA, LaGoy JL. Additive manufacturing: making imagination the major limitation. JOM. 2014;66:808-16.
[2] Gong X, Anderson T, Chou K. Review on powder-based electron beam additive manufacturing technology. Manufacturing Review. 2014;1:2.
[3] Frazier WE. Metal additive manufacturing: A review. Journal of Materials Engineering and Performance. 2014;23:1917-28.
[4] Wang P, Feng Y, Liu F, Wu L, Guan S. Microstructure and mechanical properties of Ti–Zr–Cr biomedical alloys. Materials Science and Engineering: C. 2015;51:148-52.
[5] Guan S, Wu L, Wang P. Hot forgeability and die-forging forming of semi-continuously cast AZ70 magnesium alloy. Materials Science and Engineering: A. 2009;499:187-91.
[6] Wang P, Zhu S, Wang L, Wu L, Guan S. A two-step superplastic forging forming of semi-continuously cast AZ70 magnesium alloy. Journal of Magnesium and Alloys. 2015;3:70-5.
[7] Yi C, Guan S, Lu G, Zhao H, Wang P. Influence of annealing process on microstructure and properties of twin-roll cast 5052 aluminium alloy [J]. Transactions of Materials and Heat Treatment. 2011;4:013.
[8] Greenemeier L. To Print the Impossible. Scientific American. 2013;308:44-7.
[9] Lipson H, Kurman M. Fabricated: The new world of 3D printing: John Wiley & Sons; 2013.
[10] Murr L, Esquivel E, Quinones S, Gaytan S, Lopez M, Martinez E, et al. Microstructures and mechanical properties of electron beam-rapid manufactured Ti–6Al–4V biomedical prototypes compared to wrought Ti–6Al–4V. Materials Characterization. 2009;60:96-105.
[11] Ikeo N, Ishimoto T, Nakano T. Novel powder/solid composites possessing low Young's modulus and tunable energy absorption capacity, fabricated by electron beam melting, for biomedical applications. Journal of Alloys and Compounds. 2015;639:336-40.
[12] Sun S-H, Koizumi Y, Kurosu S, Li Y-P, Chiba A. Phase and grain size inhomogeneity and their influences on creep behavior of Co–Cr–Mo alloy additive manufactured by electron beam melting. Acta Materialia. 2015;86:305-18.
[13] Al-Bermani S, Blackmore M, Zhang W, Todd I. The origin of microstructural diversity, texture, and mechanical properties in electron beam melted Ti-6Al-4V. Metallurgical and Materials Transactions A. 2010;41:3422-34.

[14] Kok Y, Tan X, Tor SB, Chua CK. Fabrication and microstructural characterisation of additive manufactured Ti-6Al-4V parts by electron beam melting. Virtual and Physical Prototyping. 2015;10:13-21.
[15] Prabhakar P, Sames W, Dehoff R, Babu S. Computational modeling of residual stress formation during the electron beam melting process for Inconel 718. Additive Manufacturing. 2015.
[16] Tan X, Kok Y, Tan YJ, Descoins M, Mangelinck D, Tor SB, et al. Graded microstructure and mechanical properties of additive manufactured Ti–6Al–4V via electron beam melting. Acta Materialia. 2015;97:1-16.
[17] Carroll BE, Palmer TA, Beese AM. Anisotropic tensile behavior of Ti–6Al–4V components fabricated with directed energy deposition additive manufacturing. Acta Materialia. 2015;87:309-20.
[18] Tammas-Williams S, Zhao H, Léonard F, Derguti F, Todd I, Prangnell P. XCT analysis of the influence of melt strategies on defect population in Ti–6Al–4V components manufactured by Selective Electron Beam Melting. Materials Characterization. 2015;102:47-61.
[19] Mok SH, Bi G, Folkes J, Pashby I. Deposition of Ti-6Al-4V using a high power diode laser and wire, Part I: Investigation on the process characteristics. Surf Coat Technol. 2008;202:3933-9.
[20] Pan W, Todai M, Nakano T. β-Phase Instability in Binary Ti-xNb Biomaterial Single Crystals. Materials Transactions. 2013;54:156-60.
[21] Tan X, Kok Y, Tan YJ, Vastola G, Pei QX, Zhang G, et al. An experimental and simulation study on build thickness dependent microstructure for electron beam melted Ti–6Al–4V. Journal of Alloys and Compounds. 2015;646:303-9.
[22] Wang P, Nai MLS, Sin WJ, Wei J. Effect of building height on microstructure and mechanical properties of big-sized Ti-6Al-4V plate fabricated by electron beam melting. Advanced Materials Research: Trans Tech Publ; 2015.
[23] Lütjering G, Williams JC. Titanium: Springer; 2003.
[24] International A. Standard Specification for Wrought Titanium-6Aluminum-4Vanadium Alloy for Surgical Implant Applications (UNS R56400). West Conshohocken, PA: ASTM International; 2014.

CHARACTERIZATION OF MICROSTRUCTURE AND MECHANICAL PROPERTIES OF DIRECT METAL LASER SINTERED 15-5 PH1 STAINLESS STEEL POWDERS AND COMPONENTS

Jing Zhang[1], Yi Zhang[1], Xingye Guo[1], Weng Hoh Lee[1], Bin Hu[2], Zhe Lu[3], Yeon-Gil Jung[3], Je-Hyun Lee[3]
1. Indiana University – Purdue University Indianapolis, Indianapolis, IN 46202, USA
2. Dartmouth College, Hanover, NH 03755, USA
3. Changwon National University, Changwon, Gyeongnam 641-773, Republic of Korea

Corresponding author: jz29@iupui.edu

Keywords: 15-5 PH1 stainless steel; powder characteristic; direct metal laser sintering.

Abstract

15-5 PH1 stainless steel powder is one of the common materials used for the DMLS process. In this study, both the powder and parts fabricated via DMLS have been characterized. The microstructure and elemental composition have been examined. The microhardness and surface roughness have also been measured. The results show that most powder particle are in spherical with a particle size of 5 ~ 60 μm. Chemical compositions of the powder compare well with the literature data. The thickness of rough surface is about 1 μm. The measured Rockwell hardness is HRC 42.9±0.3, which is also in good agreement with literature.

Introduction

Direct metal laser sintering is an additive manufacturing technique that uses a laser as the power source to sinter powdered metal material, aiming the laser automatically at points in space defined by a 3D model, binding the material together through sintering process to create a solid structure [1]. An important group of metals using DMLS technique is stainless steel [2], which has a broad applications in medical and structural fields [3].

This study is focus on powder characterizations of the 15-5 PH1 stainless steel powders and parts through a variety of techniques to provide fundamental data for processing improvements. The characterization techniques include scanning electron microscopy (SEM), energy dispersive X-ray spectroscopy (EDS), atomic force microscope (AFM), and Rockwell microhardness.

Experimental

Particle size and particle shape/morphology are the most important characteristics for powders. Microstructural images of the powder have been taken by using a field emission scanning electron microscope (FESEM, JEOL 7800F), using an acceleration voltage of 5 kV, with

electron beam current of 18 nA. The magnification of the SEM images is in the range of from 200 to 5000. In order to get the composition information of 15-5 stainless steel powder, an energy-dispersive X-ray spectroscopy (EDS) analysis was conducted. Additionally, atomic force microscopy (AFM) was used to measure the surface roughness of the printed parts.

Results and discussion

15-5 stainless steel powders

The SEM images of the EOS 15-5 PH1 stainless steel powders are shown in Figures 1 and 2. As shown in Figure 1, the powders are mostly spherical. Some of the powders (< 30%) are ellipsoid, and very few (< 5%) are in irregular shapes. Particle sizes are in a range of 5 - 60 μm, which indicates that there is a powder particle size distribution. Several bonded powder pairs are visible, with neck between them, which is commonly observed in powder atomization or sintering process. Another cause may be due to some of the powders are partially recycled during previous DMLS process. In Figure 2, high magnification image reveals the surface texture of the particle. Poly-grain structure is visible in the right side of the particle.

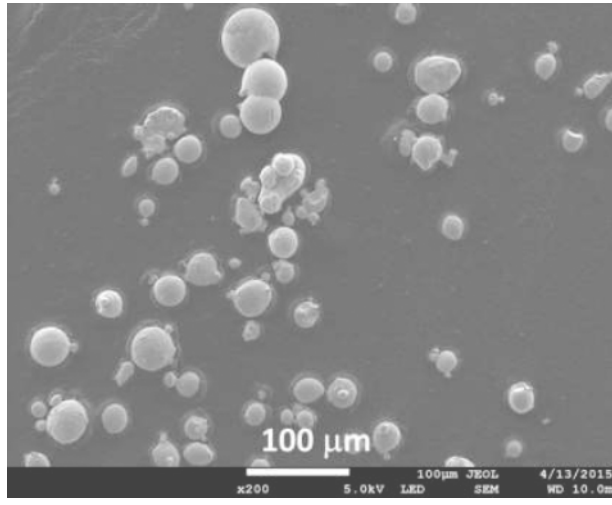

Figure 1: SEM image of the 15-5 PH1 powders

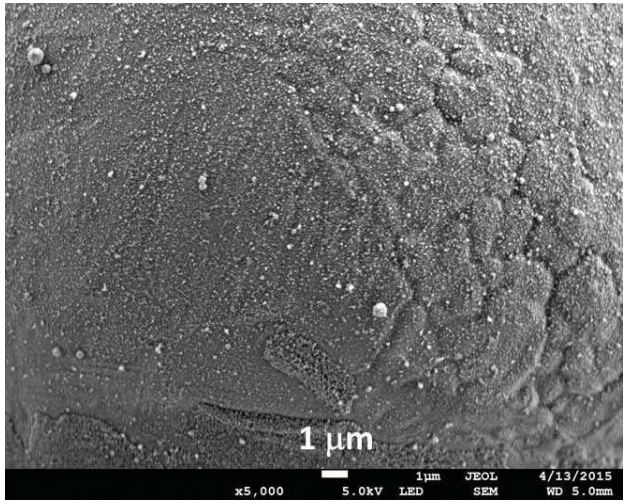

Figure 2: SEM image showing surface texture of the powder

Compositional analysis was conducted by using energy-dispersive X-ray spectroscopy (EDS) at powder surfaces, as shown in Figure 3. The resulting element compositions of selected area 1 (in Figure 3) are shown in Figure 4.

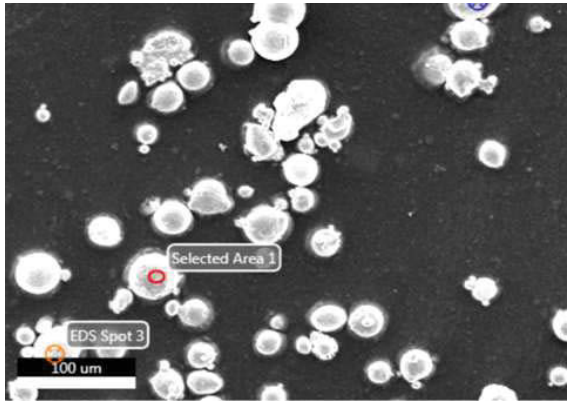

Figure 3: Locations of EDS sampling

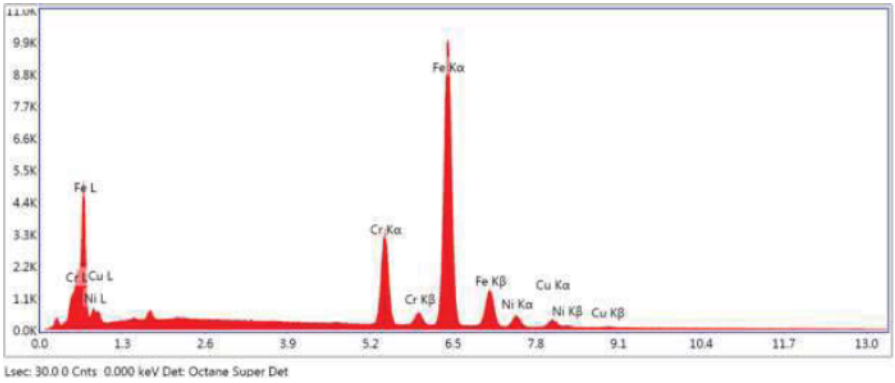

Figure 4: EDS for elements in selected area 1 (in Figure 3).

The detailed concentrations of each element are listed in Table 1. Fe, Cr, Ni and Cu are the four major elements. The compositional data are in good agreement with the EOS powder datasheet [3].

Table 1: Elemental composition of 15-5 stainless steel powder

Element	Weight %	Atomic %	Atomic % from reference [3]
CrK	13.33	14.27	14 ~15.5
FeK	78.27	78.03	balance
NiK	4.73	4.48	3.5-5.5
CuK	3.67	3.22	2.5-4.5

DMLS printed 15-5 stainless steel components

A DMLS printed part using the PH-1 powder was analyzed, as shown in Figure 5. Detailed regions, such as the curved surface, were imaged by using SEM.

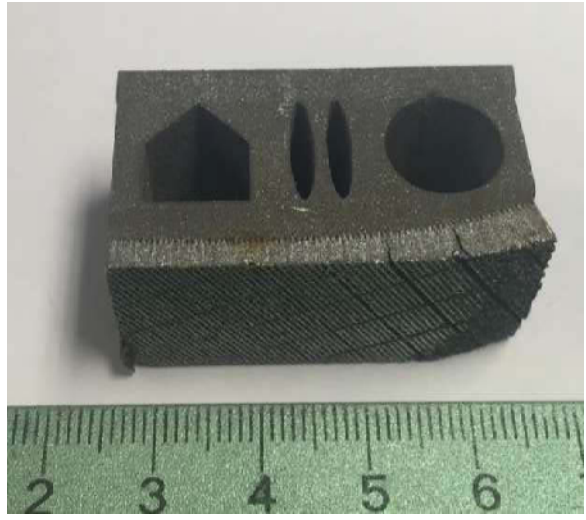

Figure 5: DMLS printed sample for microstructure analysis. Ruler unit is cm.

Figure 6 shows the SEM image shows the edge of the elliptical-shaped hole in Figure 5. Rough surface can be observed around the printed part since the residual metal powders adhered on the surface. More powders can be found on the curved surface than the flat surface.

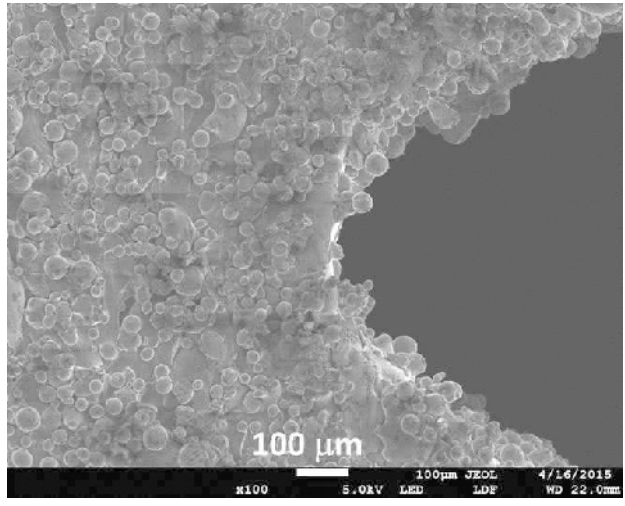

Figure 6: SEM image of DMLS printed part

The surface roughness of another 15-5 stainless steel printed part was studied by atomic force microscopy, as shown in Figure 7. The three-dimensional surface roughness map is shown in Figure 8. The maximum surface roughness in the measured are (20×20 μm^2) of this sample is about 0.93 μm.

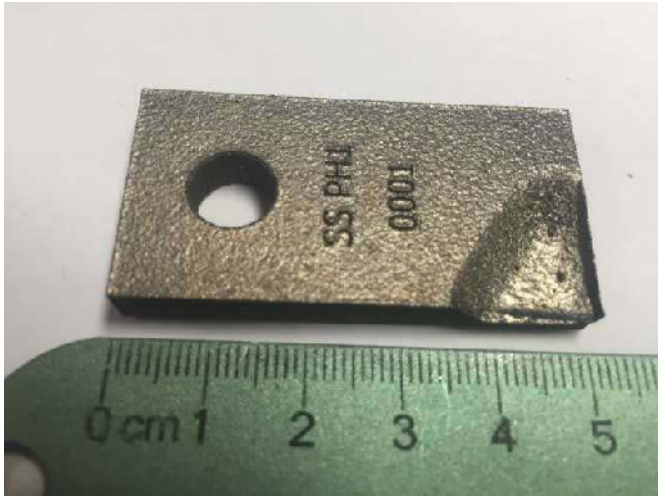

Figure 7: DMLS printed part for AFM analysis

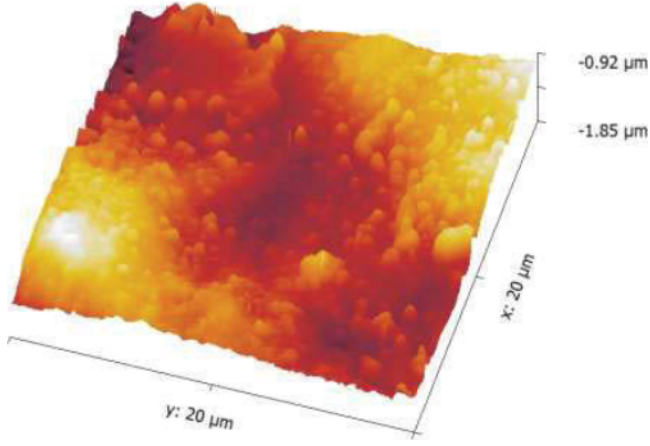

Figure 8: AFM measured surface roughness of 15-5 stainless steel printed part

The measured Rockwell microhardness according to ASTM 18E-15 is HRC 42.9±0.3 (load 150 kgf). The result is in good agreement with EOS datasheet [3], which is ~40, after age hardening. The indentation mark of the HRC is given in Figure 9.

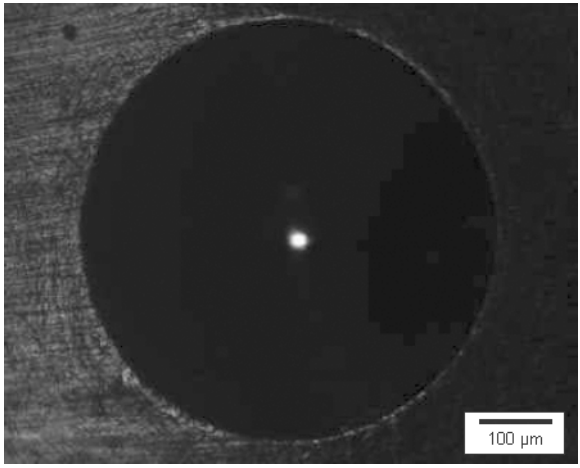

Figure 9: HRC indentation mark

Summary

15-5 PH1 stainless steel metal powders and printed parts have been characterized. Most powder particle are in spherical with a particle size of 5 ~ 60 µm. Chemical compositions of the powder were also measured by EDS and compared well with the literature data. Surface roughness was measured by AFM, the thickness of rough surface is about 1 µm. The measured Rockwell hardness is HRC 42.9±0.3, which is also in good agreement with literature.

Acknowledgements

JZ and YZ acknowledge the financial support provided by Walmart Foundation (project title: Optimal Plastic Injection Molding Tooling Design and Production through Advanced Additive Manufacturing). JZ also thanks the DMLS powders and parts provided by Kim Brand at 3D Parts.

References

1. Wikipedia. *Direct metal laser sintering*. Available from: http://en.wikipedia.org/wiki/Direct_metal_laser_sintering.
2. Wikipedia. *Inconel*. Available from: http://en.wikipedia.org/wiki/Inconel.
3. *EOSINT M Materials for Direct Metal Laser Sintering (DMLS).* 2009.

TMS2016
145th Annual Meeting & Exhibition

SUPPLEMENTAL
PROCEEDINGS

Materials Research in Reduced Gravity

Douglas M. Matson
Tufts University

EFFECT OF THERMAL DRIFT ON THE INITIAL TRANSIENT BEHAVIOR IN DIRECTIONAL SOLIDIFICATION OF A BULK TRANSPARENT MODEL ALLOY

F.L. Mota[1*], N. Bergeon[1], D. Tourret[2], A. Karma[2], R. Trivedi[3], B. Billia[1]

[1]IM2NP, Aix Marseille Université, CNRS UMR 7334, Marseille - France
[2]Physics Department, Northeastern University Boston, USA
[3]Department of Materials Science & Engineering, Iowa State University, USA

Keywords: Directional solidification, *in situ* observation, transparent systems, interface dynamics, initial transient

Abstract

In situ monitoring of directional solidification experiments on a transparent model alloy was carried out under low gravity in the Directional Solidification Insert of the Device for the Study of Critical Liquids and Crystallization (DECLIC-DSI) on-board the International Space Station. The present work is focused on the analysis of the interface recoil and its macroscopic shape evolution. Theoretically the interface movement is due to the formation of a solute boundary layer in front of the interface. However, the bulk configuration and the thermal specificities of transparent systems induce thermal effects, which are usually not observed in the classical thin sample configuration. Numerical thermal modeling highlights two thermal contributions to the interface recoil, both increasing with pulling rate. The Warren and Langer model is modified to take into account these contributions that modify the interface dynamics, and a good agreement is obtained between the experiments and the modified model.

Introduction

In order to design and process new materials, the study of solidification microstructures formation is crucial, as the interface patterns formed by solidification largely govern its mechanical and physical properties. One of the main techniques used to precisely study the fundamental aspects is the directional solidification, where the vertical Bridgman method is one of the most widely used since it has the advantage of steady temperature fields and a controllable temperature gradient.

The wide use of transparent organic analogs that behave like metallic alloys regarding solidification is related to their transparency to visible light, so that *in situ* and real time observation of the interface can be done by classical optical techniques [1, 2]. Many experiments on transparent systems have been conducted in thin samples [3-6], which led to significant progress in understanding the dynamics of solidification. However, these configurations are not representative of three-dimensional (3D) samples and quantitative data extracted from thin samples cannot be extrapolated to 3D configuration. Bulk experiments are therefore required and essential. However, in 3D samples there is a complex coupling between fluid flow and morphological instability: ground-based studies, in both metallic and organic alloys, clearly

showed that the fluid convection on Earth modifies the structure of the solute boundary layer, causing non-uniform morphological instability along the interface [7, 8]. Fluid flow elimination in 3D samples requires the reduced gravity environment of space.
The present study was conducted on board the International Space Station (ISS) in the framework of the French Space Agency (Centre National d'études Spatiales, CNES) project MISOL3D (Microstructures de Solidification 3D) and National Aeronautics and Space Administration (NASA) project DSIP (Dynamical Selection of 3D Interface Patterns). Experiments were realized using the directional solidification insert (DSI) of the Device for the study of Critical Liquids and Crystallization (DECLIC) developed by CNES, which is dedicated to *in situ* and real time characterization of the dynamical selection of the solid-liquid interface morphology on bulk samples of transparent materials [9-11].
A transient period is always present as the first stage of the evolution of the solid-liquid interface from rest to a steady state characterized by a growth velocity equal to the applied pulling rate. Theoretical models assume that, at rest, initially the smooth interface is located on the *liquidus* isotherm, at a fixed position determined by the thermal profile in the adiabatic area. The motion from the initial interface position (*liquidus* isotherm) to its steady state one (*solidus* isotherm in case of planar front growth) is called front recoil, the duration of which also defines the initial transient [12, 13]. One important point to note is that the growth microstructure usually develops during the initial solidification transient. Analyzing the dynamics of this initial transient is thus critical for the understanding of the final steady state microstructure. In this work, experiments will be analyzed in terms of their solidification front recoil.

Experimental procedure

The DECLIC-DSI mainly contains two elements: the Bridgman furnace and the experimental cartridge. Complete description of the device and its inserts may be found elsewhere [10, 11]. The experimental cartridge includes a quartz crucible and a system of volume compensation. The cylindrical crucible has an inner diameter of 10 mm and a length that allows ~10 cm of solidification. In this study, we used a succinonitrile (SCN) – 0.24wt% camphor alloy. In order to fill the crucible, SCN purified by NASA by both distillation and zone melting was used. The alloy was then prepared by adding the solute. All procedures for sample preparation were carefully realized under vacuum to avoid humidity contamination. Once sealed, the cartridge was inserted inside the Bridgman furnace. The thermal gradient G is imposed by regulating hot and cold zones, located above and below the adiabatic area where the interface is positioned. After the thermal regulation, partial melting is performed (a solid seed of ~20mm is always kept to preserve the oriented single crystal) and the sample is then homogenized for at least 24h before performing solidification. Directional solidification is carried out by pulling the crucible into the cold zone at a constant rate for a length of 60 mm. Experiments with pulling rates V_p ranging from 0.5 to 8μm/s and G=12K/cm will be considered in this work.
The crucible is equipped with a flat glass window at the bottom and an immersed lens at the top. The axial observation is the main observation mode and it takes advantage from the complete axial transparency of the cartridge. This observation mode is used to study the pattern dynamics and characteristics. However in this work the results were obtained from the side view observation, which allows imaging the interface motion as well as its macroscopic shape.

Results

The interface recoil was investigated by measuring the motion of the interface in the adiabatic area using the transverse observation. Fig.1(a) shows a step-by-step evolution of the whole experiment starting from rest for 4 µm/s (G=12K/cm) and Fig.1(b) shows the interface position as a function of the solidified length L (namely the pulled length : $L = V_p\, t$, with t: solidification time) for a set of different pulling rates and a fixed thermal gradient.

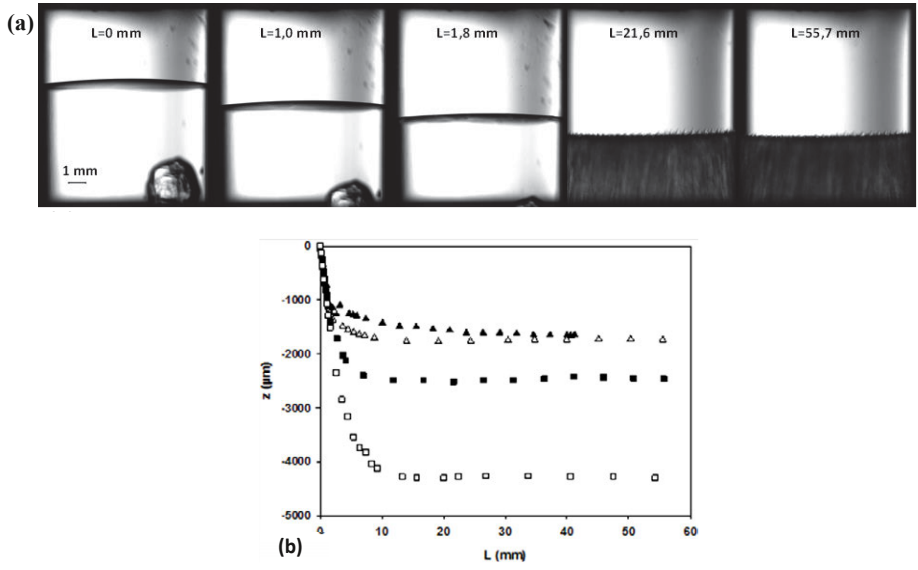

Figure 1 – (a) Interface evolution from rest to steady state under microgravity at G=12K/cm and V_p= 4µm/s; (b) Interface position (z) as a function of solidified length (L) at G=12K/cm for different pulling rates (▲, 1; Δ, 2; ■, 4; □, 8 µm/s).

The build-up of a solute boundary layer ahead of the interface during growth leads to a change of the interface temperature (or interface position) that, for a planar front growth, should reach the *solidus* temperature for the nominal concentration C_0; the recoil associated is named "solutal recoil" with an amplitude of $\frac{m_L C_0}{G}\frac{k-1}{k}$ corresponding to the thermal length l_T (*liquidus* slope m_L=-1.365K/wt%; C_0=0.24wt%; partition coefficient k=0.138 at the *solidus*). For G=12K/cm, this displacement is 1.71mm and is independent of the pulling rate. In all experiments treated, the pulling rate is higher than the critical velocity V_c corresponding to the transition from planar front growth to cellular growth so that a microstructure develops. The cells or dendrites tips grow in the undercooled area towards the liquidus isotherm. Measurements were performed as much as possible at the tips level, as the *solidus* position is unknown. At steady state, tips are located at a distance Δ_t of the *solidus* estimated by the Bower, Brody and Flemings (BBF) expression [14]:

$$\Delta_{t,BBF} = \frac{D_L}{V_p}\left(\frac{V_p}{V_c} - 1\right) = l_T - \frac{D_L}{V_p} \text{ with } V_c = \frac{kGD_L}{(k-1)m_L C_0}$$

where D_L is the solute diffusion coefficient in the liquid (270 µm²/s). Theoretically, the higher the pulling rate, the closer the tips will be from the *liquidus*, and the lower the front recoil will be. However, as can be seen in Fig.1(b), the experimental front recoil increases with pulling rate. This disagreement comes from the theoretical assumption of a frozen thermal field, meaning that the thermal field is neither shifted nor disturbed by pulling. The tip advance as well as the experimental recoil values can be found elsewhere [15].

To analyze the thermal field in the furnace and the interface recoil induced by pulling, the software packages CrysVUn® and CrysMAS® which are designed for the global modeling of solidification processes in complex furnaces with axial or translational symmetry are used. Calculations are based on a method of finite volumes on unstructured grids that enables tackling the entire growth setup on the basis of a geometrical model of the furnace, crucible and sample. It is worth noticing that in these purely thermal simulations, the microstructure is not taken into account: interface recoil therefore corresponds to the motion from the liquidus isotherm to the solidus one, as in a planar front growth. To analyze the different contributions to recoil, additional simulations are performed fixing the latent heat of fusion ΔH to zero. An example of the results for G=12K/cm and V_p=4µm/s is given in Fig.2 (a).

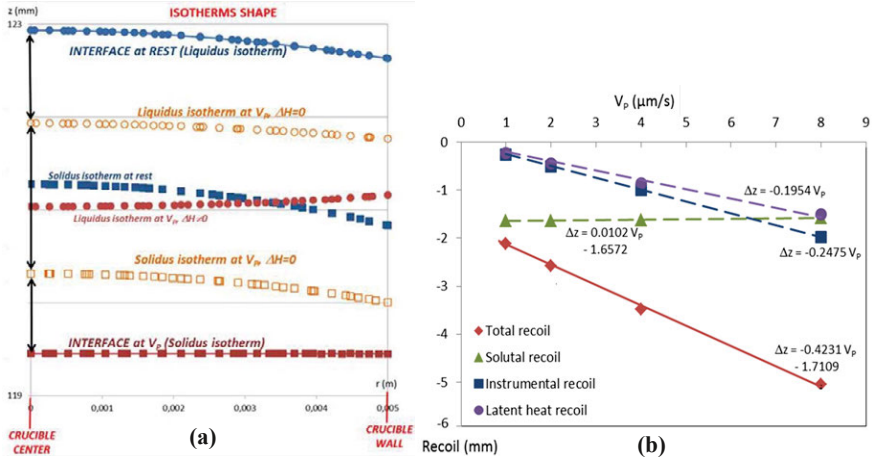

Figure 2 – (a) Position of the *liquidus* and *solidus* isotherms at G=12K/cm. In blue: at rest (V_p=0). In orange: at V_p=4µm/s with a latent heat ΔH=0. In red: at V_p=4µm/s with ΔH ≠ 0; (b) Analysis of the interface recoil with pulling rate (G=12K/cm).

Three different contributions to the recoil are therefore highlighted:

- Instrumental recoil: isotherm shift due to the thermal exchanges induced by pulling deduced from the comparison between *liquidus* isotherm positions at rest and during pulling with ΔH=0;

- Solutal recoil: corresponds to the interface temperature change from the *liquidus* to *solidus* (ΔH=0);
- Latent heat recoil: isotherm shift due to latent heat release measured from the comparison between *solidus* isotherms positions during pulling for ΔH=0 and the normal value of ΔH (3.7kJ/mol).

CrysMAS was then used to determine the sensitivity of the different contributions to recoil to pulling rate (Fig.2(b)). Numerically, the solutal contribution to recoil is roughly insensitive to pulling rate, whereas instrumental and latent heat contributions increase linearly with pulling rate. The total numerical and experimental recoils display the same variation with pulling rate, thus explaining the relative positions of the interface for different pulling rates (Fig.1(b)).

Warren and Langer (WL) [13] developed an approach to describe the acceleration of the interface and the simultaneous build-up of the solutal boundary layer during the initial transient based on the assumption of an exponential transient concentration profile in the liquid, similar to the one obtained in the steady state but with some time-dependent solutal length and solute concentration at the interface. As a result, their model predicts the instantaneous solutal length, interface velocity, solute concentration at the interface and interface position. One assumption behind this model is that the thermal field is frozen so that the recoil is only of solutal origin. We have previously demonstrated that we are not in such a configuration. Thus, the WL model cannot be directly used but it has to be modified to include the thermal effects previously identified. Numerical studies to evaluate the transient interface velocity for purely thermal effects after a velocity jump in a Bridgman furnace [16, 17] concluded that the interface position asymptotically approach its steady state position with a time dependent thermal shift Δz_T [1 - exp(-t/τ)], where t is the time, Δz_T is the total isotherm shift at the steady state resulting from both latent heat release and instrumental recoil, and τ is a delay time dependent of the physical parameters of the alloy, the geometry of the furnace and crucible, the thermal gradient and the pulling rate.

Warren and Langer (WL) [13] formulated the problem in terms of two time-dependent variables: the solute boundary layer thickness l and the interface position z_0 in a reference frame that is moving with a constant velocity V_p, whose origin is taken at the isotherm corresponding to the melting point of the pure solvent (SCN, T_m=58.08°C). A modified WL model was then developed which includes thermal drift by writing the temperature field in a frame translating at velocity V_p in the form:

$$T(z) = T_m + Gz + G\Delta z_T\left(1 - e^{-t/\tau}\right)$$

The interface equilibrium condition is then given by:

$$C_0 = \frac{T_m - T(z_0)}{|m_L|} = -\frac{G}{|m_L|}\left[z_0 + \Delta z_T\left(1 - e^{-t/\tau}\right)\right]$$

where z_0 is the position of the solid-liquid interface in the moving frame and C_0 is the solute concentration on the liquid side of the interface. The dynamical equations of the modified WL model including the thermal drift are the same as the original ones used jointly with the modified interface equilibrium condition:

$$(V_P + \dot{z}_0) = \frac{2D_L}{l}\left[\frac{z_0 + \Delta z_T\left(1 - e^{-t/\tau}\right) - z_\infty}{(1-k)\left(z_0 + \Delta z_T\left(1 - e^{-t/\tau}\right)\right)}\right]$$

$$\dot{l} = \frac{4D_L}{l}\left[\frac{z_\infty - k\left(z_0 + \Delta z_T\left(1 - e^{-t/\tau}\right)\right)}{(1-k)\left(z_0 + \Delta z_T\left(1 - e^{-t/\tau}\right)\right)}\right] - l\left[\frac{\dot{z}_0 + \Delta z_T e^{-t/\tau}/\tau}{z_0 + \Delta z_T\left(1 - e^{-t/\tau}\right) - z_\infty}\right]$$

where l is the instantaneous boundary layer thickness, C_∞ is the fixed nominal concentration of the alloy that is not affected by the thermal drift, z_∞ is the initial position of the interface at rest ($z_\infty = -\frac{|m_L|}{G} C_\infty$), and $\dot{l}$ and $\dot{z}_0$ denote first order time derivatives.

We applied this modified model to analyze our results, treating τ as an adjustable parameter. Δz_T was used as input into the model for each pulling rate and it was deduced from experiments taking into account the theoretical solutal recoil and the tip advance. The best fit results are presented in Fig.3. The predictions result from a least squares fit with τ against the experimental data at early time ($L \leq 2$mm) while the solid-liquid interface is still planar before morphological destabilization.

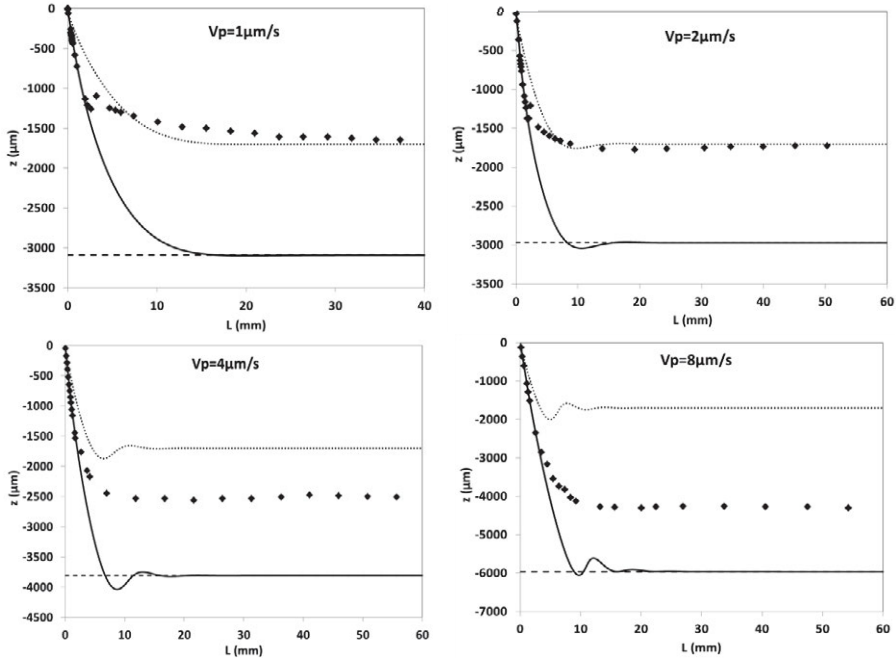

Figure 3 – Interface position ($z = z_0 - z_\infty$) as a function of solidified length (L) for different pulling rates: experimental points are superimposed with the modeling results using Warren and Langer [13] model modified to take into account the isotherm shift (full line) and the original model (dotted line), for G=12K/cm. The dashed line corresponds to the estimated *solidus* line.

The results presented in Fig.3 illustrate the good agreement obtained between the experimental and modeling results during early microstructure development (initial transient). The dashed line

corresponds to the estimated *solidus* position using BBF model and it can be seen that the model results converge to this value once the steady-state is attained. The fitted values of τ, as well as the values of Δz_T, are presented in Table 1. It can be seen that τ decreases with V_p. The dotted line in Fig.3 corresponding to the predictions of the original WL model (i.e. Δz_T=0) highlights the importance of the thermal drift contribution to accurately reproduce the experimental measurements. Additional results can be found elsewhere [15].

Table 1 – Δz_T values and fitted values of the delay time τ(s) used in the modified WL model considering a BBF tip undercooling for G=12K/cm.

V_p (μm/s)	Δz_T (mm)	τ(s)
1	1.39	1998
2	1.60	837
4	2.44	563
8	4.26	487

Conclusion

This work was realized in the framework of the DECLIC-DSI project, dedicated to *in situ* and real time observation of the solid-liquid interface during directional solidification of bulk transparent alloys. DECLIC was installed on board the ISS, under microgravity, thus avoiding fluid flow influence. Even if the main observation mode of this device is the axial observation, the data presented here come from the side view observation, which enables the study of the interface motion during the whole experiment. The experiments analyzed have been carried out on a transparent organic alloy (succinonitrile-0.24wt% camphor).

Thermal analyses were performed revealing two contributions to interface motion during pulling. These contributions add to the standard physical recoil that corresponds to the interface temperature change from the *liquidus* to the *solidus*. These contributions justify the qualification of a not frozen thermal field, and they increase linearly with pulling rate.

Experimentally, the evolution of the interface position as a function of the solidification length was measured for different pulling rates. The global interface recoil increase with pulling rate is compatible with a not frozen thermal field condition. The WL model was modified to take into account the isotherm shift contribution and a good agreement was obtained between experiments and the modified model.

The present work gave a better understanding of the general front behavior for geometrical configurations not associated to a frozen thermal field, and it clearly appeared that the thermal transients have to be taken into account for a complete understanding of front dynamics for such bulk samples.

References

1. B. Billia and R. Trivedi, *Pattern formation in crystal growth*, in D. Hurle (Eds.), Handbook of Crystal Growth (Bristol, UK: North-Holland, 1993), 899-1074.
2. K.A. Jackson and J.D. Hunt, "Transparent compounds that freeze like metals", *Acta Metallurgica,* 13 (1965), 1212-1215.

3. S. Akamatsu, et al., "Symmetry-broken double fingers and seaweed patterns in thin-film directional solidification of a nonfaceted cubic-crystal", *Physical Review E,* 51 (1995), 4751-4773.
4. J. Deschamps, et al., "Growth directions of microstructures in directional solidification of crystalline materials", *Physical Review E,* 78 (2008), 1605.
5. K. Somboonsuk, et al., "Interdendritic spacing .1. Experimental studies", *Metallurgical Transactions a-Physical Metallurgy and Materials Science,* 15 (1984), 967-975.
6. R. Trivedi and K. Somboonsuk, "Pattern-formation during the directional solidification of binary-systems", *Acta Metallurgica,* 33 (1985), 1061-1068.
7. H. Jamgotchian, et al., "Localized microstructures induced by fluid flow in directional solidification", *Physical Review Letters,* 87 (2001), 6105.
8. T. Schenk, et al., "Application of synchrotron X-ray imaging to the study of directional solidification of aluminium-based alloys", *Journal of Crystal Growth,* 275 (2005), 201-208.
9. N. Bergeon, et al., "Necessity of investigating microstructure formation during directional solidification of transparent alloys in 3D", *Advances in Space Research,* 36 (2005), 80-85.
10. R. Marcout, et al. *DECLIC: a facility to investigate fluids and transparent materials in microgravity conditions in ISS*. in *57th International Astronautical Congress*. 2006. Valencia, Spain.
11. G. Pont, et al. *DECLIC: a facility to study crystallization and critical fluids*. in *60th International Astronautical Congress*. 2009. Daejeon, Republic of Korea.
12. W. Losert, et al., "Evolution of dendritic patterns during alloy solidification: Onset of the initial instability", *Proceedings of the National Academy of Sciences of the United States of America,* 95 (1998), 431-438.
13. J.A. Warren and J.S. Langer, "Prediction of dendritic spacings in a directional-solidification experiment", *Physical Review E,* 47 (1993), 2702-2712.
14. T.F. Bower, et al., "Measurements of solute redistribution in dendritic solidification", *Transactions of the mettalurgical society of AIME,* 236 (1966), 624.
15. F.L. Mota, et al., "Initial transient behavior in directional solidification of a bulk transparent model alloy in a cylinder", *Acta Materialia,* 85 (2015), 362-377.
16. T.W. Fu and W.R. Wilcox, "Rate change transients in bridgman-stockbarger growth", *Journal of Crystal Growth,* 51 (1981), 557-567.
17. M. Saitou and A. Hirata, "Numerical-calculation of 2-dimensional unsteady solidification problem", *Journal of Crystal Growth,* 113 (1991), 147-156.

Acknowledgments

The authors express their gratitude to CNES and NASA for the support received in the scientific projects MISOL3D and DSIP. A.K. and D.T. were supported by NASA awards NNX07AK69G and NNX11AC09G.

RAPID QUENCH IN AN ELECTROSTATIC LEVITATOR

Michael P. SanSoucie[1], Jan R. Rogers[1], and Douglas M. Matson[2]

[1]NASA Marshall Space Flight Center
Mail Code: EM50, MSFC, AL, 35812, USA
[2]Tufts University, Medford, MA, 02155, USA

Keywords: electrostatic levitation, rapid quench, metastable states, solidification

Abstract

The Electrostatic Levitation (ESL) Laboratory at the NASA Marshall Space Flight Center (MSFC) is a unique facility for investigators studying high-temperature materials. The ESL laboratory's main chamber has been upgraded with the addition of a rapid quench system. This system allows samples to be dropped into a quench vessel that can be filled with a low melting point material, such as a gallium or indium alloy, as a quench medium. Thereby allowing rapid quenching of undercooled liquid metals. Up to eight quench vessels can be loaded into a wheel inside the chamber that is indexed with control software. The system has been tested successfully with samples of zirconium, iron-cobalt alloys, iron-chromium-nickel, titanium-zirconium-nickel alloys, and a silicon-cobalt alloy. This new rapid quench system will allow materials science studies of undercooled materials and new materials development. The system is described and some initial results are presented.

Introduction

The NASA Marshall Space Flight Center (MSFC) Electrostatic Levitation (ESL) Laboratory is a unique facility for investigators studying high-temperature materials. The laboratory has two levitators in which samples can be levitated, heated, melted, undercooled, and resolidified, all without the interference of a container or data-gathering instrument [1].

The ESL laboratory's main levitation chamber has been upgraded with the addition of a rapid quench system. This system allows samples to be dropped into a quench vessel that can be filled with a low melting point material, such as a gallium-indium alloy, as a quench medium. Thereby allowing rapid quenching of undercooled liquid metals.

It has been established that rapid solidification can be achieved by increasing the cooling rate (rapid quenching) or by increasing the undercooling before nucleation [2]. By using a containerless processing technique, such as electrostatic levitation, deep undercooling can be attained. With the rapid quench system added to the MSFC electrostatic levitator, both rapid solidification methods can be done simultaneously.

Quenching in an electromagnetic levitator (EML) has been performed; however, this has involved dropping the sample onto a copper substrate [3]. Similarly, quenching in an electrostatic levitator has also been performed, and in this case, the sample was dropped onto a copper sample launch stem [4].

Quenching on a substrate is less desirable because the cooling occurs from only the contacted surface. It was observed that when the liquid drops onto the copper stem, the heat extraction rates are different at the top and bottom of the sample, which produces different undercooling for the two regions, which causes microstructural transition across different parts of the sample [4].

By submersion quenching into a liquid, the quenching occurs at all surfaces. Quenching with liquid indium-gallium was pioneered by Koseki on steel alloys [5] and surface cooling rates greater than 10^6 W/m^{2}sec were demonstrated. The difference between EML and ESL quenching is that in EML induced fluid flow from the levitation field is both significant and variable across the surface while in ESL the sample is quiescent and the quench conditions are more readily controlled.

Hardware Description

The system is designed so that quench vessels can be raised or lowered using the same stem that is used to launch the samples. Up to 8 quench vessels can be loaded into the quench wheel. An exploded view of the system can be seen in Figure 1, along with the inside of the levitation chamber and the quench hardware.

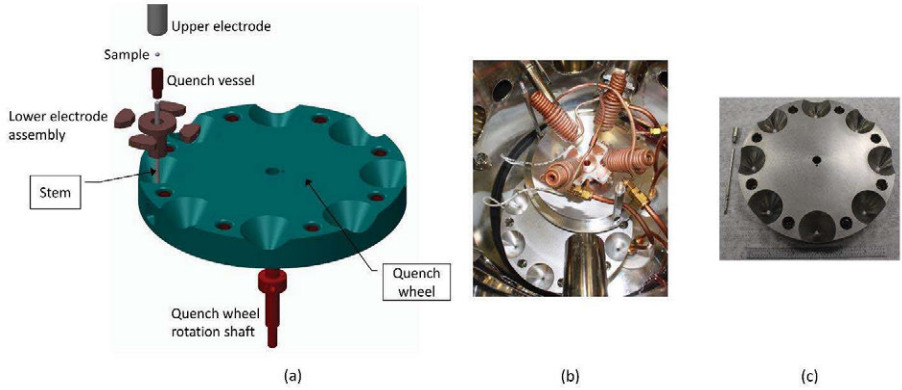

Figure 1. (a) Exploded view schematic of the quench system, (b) inside of the levitation chamber showing the quench wheel, and (c) quench wheel, stem, and quench vessel outside of the chamber.

The wheel is indexed with servo motors that are controlled with LabVIEW software. This allows up to 8 samples to be quenched before having to break vacuum and open the chamber.

The system has been tested successfully on several zirconium, iron-chromium-nickel, and iron-cobalt samples. Future work will be done with other materials and/or different quench mediums.

High-speed video allows observance of the solidification front in sample recalescence. Three high-speed video cameras and two CCD cameras were installed in front of port windows. Two of the high speed cameras and one of the CCD cameras were positioned in front of upper points that have views of the sample from the top. The high-speed cameras available include a Vision Research Phantom V7, an Integrated Design Tools (IDT) Y7, and an IDT Y4.

Results

One of the first rapidly quenched materials in the MSFC ESL lab was an iron-cobalt alloy, Fe50Co50. The sample was melted, and then undercooled to about 30°C under the melting temperature. The quench vessel was then brought up to the quench position and the electrostatic field was removed, causing the sample to fall. Figure 2 shows a still image from the high-speed video taken by the Phantom V7 high-speed camera.

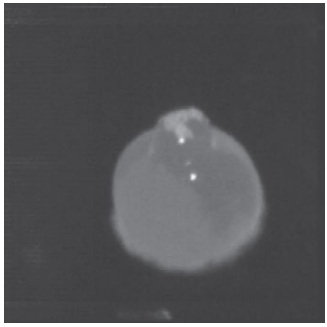

Figure 2. Quench of a Fe50Co50 sample. The video captured the recalescence of the sample as can be seen by the lighter gray region that will eventually engulf the entire sample. The lighter portion at the top of the sample is an oxide.

Sometimes the sample splits into multiple pieces, as can be seen in Figure 3, which shows still images from the high-speed video taken by the IDT Y3 high-speed camera.

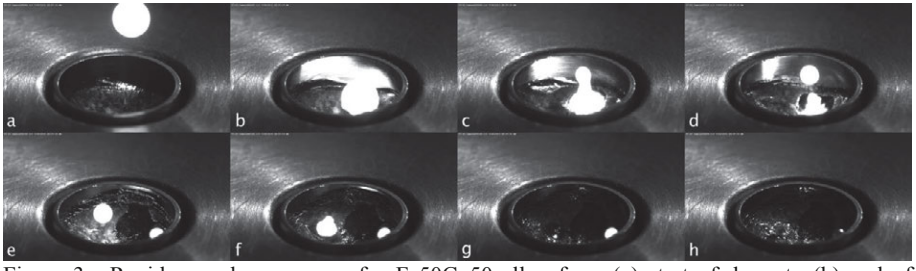

Figure 3. Rapid quench sequence of a Fe50Co50 alloy from (a) start of drop, to (h) end of quench.

The samples were dropped into a gallium-indium alloy (61Ga 25In 13Sn 1Zn), and a post-quench vessel is shown in Figure 4.

Figure 4. Quench vessel filled with a gallium-indium alloy (61Ga 25In 13Sn 1Zn).

Conclusions

Samples of pure zirconium, an iron-cobalt alloy, an iron-chromium-nickel alloy, a titanium-zirconium-nickel alloy, and a silicon-cobalt alloy have been quenched in this facility.

The MSFC electrostatic levitation (ESL) laboratory rapid quench system allows for studies of solidification of a variety of materials. Studies of double recalescence are planned. The quench of a sample during second recalescence will be attempted in order to retain the primary metastable structure.

References

1. J.R. Rogers and M.P. SanSoucie, "Containerless Processing Studies in the MSFC Electrostatic Levitator" (Paper presented at the 50th AIAA Aerospace Sciences Meeting, Nashville, TN, 2012).
2. M.C. Flemings and Y. Shiohara, "Solidification of Undercooled Metals," *Materials Science and Engineering*, 65 (1984), 157-170.
3. R. Herman et. al., "Metastable phase formation in undercooled Fe-Co melts," *Materials Science and Engineering: A*, 375-377 (2004), 507-511.
4. G.W. Lee, A.K. Gangopadhyay, and K.F. Kelton, "Phase diagram studies of Ti–Zr–Ni alloys containing less than 40 at.% Ni and estimated critical cooling rate for icosahedral quasicrystal formation from the liquid," *Acta Materialia*, 59 (2011), 4964-4973.
5. T. Koseki, M.C. Flemings, "Solidification of Undercooled Fe-Cr-Ni Alloys III: Phase Selection in Chilling", *Metallurgical and Materials Transactions A*, 28A (11) (1997), 2385-2395.

Simulation of shrinkage-induced macrosegregation in a multicomponent alloy during reduced-gravity solidification

Ali Saad[1], Charles-André Gandin[2], Michel Bellet[2], Thomas Volkmann[3], Dieter Herlach[3]

[1]TRANSVALOR S.A., Parc de Haute Technologie, 06255 Mougins, France
[2]MINES ParisTech, Centre de Mise en Forme des Matériaux, UMR CNRS 7635, CS10207, 06904 Sophia Antipolis, France
[3]Institut für Materialphysik im Weltraum, Deutsches Zentrum für Luft- und Raumfahrt (DLR), 51147 Köln, Germany

Keywords: solidification, segregation, shrinkage, reduced-gravity, modeling

Abstract

Segregation is a key phenomenon responsible for altering alloys' properties during solidification. The factors that lead to solute partitioning at the scale of the solidified parts are related to movements of liquid and solid phases. However, when considering a reduced gravitational field, convection forces become less significant compared to other factors. Consequently, predicting segregation in this context requires considering other prevailing driving forces, namely solidification shrinkage that arises from the density difference between the liquid and solid phases. We propose a numerical model that accounts for energy conservation via a thermodynamic database, together with fluid momentum conservation and species conservation to predict segregation driven by solidification shrinkage in a multicomponent alloy. We apply it on a specific steel grade for which reduced-gravity experiments were performed via parabolic flights.

Introduction

Containerless solidification has drawn the attention of many researchers for over two decades [1] and is still an active research area. It allows reaching high degrees of undercooling, which was not possible in classical solidification setups. In the past, many simulations attempts [2, 3] were made to understand the hydrodynamics during electromagnetic levitation. However, these attempts considered only the liquid state, hence solidification and segregation were not simulated. In the current project, Chill Cooling for the ElectroMagnetic Levitator in Continuous Casting of steel (CCEMLCC), we aim at studying the effect of directional solidification triggered by a chill contact. In this European Space Agency (ESA) project, we are mainly interested in the formation of reduced-gravity flow by density differences between the liquid phase and the solid phases, created during solidification and the subsequent effects on the segregation behaviour in a steel droplet. The objective is then providing a test case for numerical simulation.

Numerical model

Interface tracking

The level set method [4] is employed in the current work to capture the dynamic interface separating the liquid metal and the argon gas. Its advantage lies in the way the interface

between two domains, F_1 and F_2 is implicitly captured, unlike other methods where the exact interface position is needed. By taking $d_\Gamma(\boldsymbol{x})$ as the minimum distance separating a point x from an interface Γ, we can define the distance function, denoted α, as: $\alpha = d_\Gamma(\boldsymbol{x})$ if the point belongs to F_1, $\alpha = -d_\Gamma(\boldsymbol{x})$ if the point belongs to F_2, and $\alpha = 0$ if the point belongs to the interface Γ. The definition of a signed distance function leads to the smoothed Heaviside function, denoted H. The latter gives the presence of one domain with respect to the interface position. It is given by:

$$H = \begin{cases} 0 & \text{if } \alpha(\boldsymbol{x}) < -\varepsilon \\ 1 & \text{if } \alpha(\boldsymbol{x}) > \varepsilon \\ \frac{1}{2}\left(1 + \frac{\alpha(\boldsymbol{x})}{\varepsilon} + \frac{1}{\pi}\sin\left(\frac{\pi\alpha(\boldsymbol{x})}{\varepsilon}\right)\right) & \text{if } -\varepsilon \leq \alpha(\boldsymbol{x}) \leq \varepsilon \end{cases} \tag{1}$$

where the interval $[-\varepsilon; +\varepsilon]$ is an artificial interface thickness around the zero distance. Eq. (1) is used to perform an *arithmetic mixing* of the variables. Therefore, a physical quantity $\langle\psi\rangle$ is mixed between by: $\widehat{\langle\psi\rangle} = H^M \langle\psi^M\rangle + H^A \langle\psi^A\rangle$, where capital superscripts M and A respectively refer to metal and argon domains. Within each domain, the properties are averaged among phases by considering a representative volume element, hence no direct interface tracking between the phases. For instance, a metal-related property is averaged using: $\langle\psi^M\rangle = \sum_{\phi\in M} g^\phi \langle\psi\rangle^\phi$, where ϕ is a phase referring to liquid (l) or solids (s) in the metal, while in the argon domain, the only phase is the argon gas (a) itself, so that $g^a = 1$, resulting in the equality $\langle\psi^A\rangle = \langle\psi\rangle^a$.

Monolithic conservation equations

The monolithic model combines all conservation equations derived for metal and gas in a unique set of equations, to be solved on a fixed Eulerian mesh by the finite element method. The model couples averaged conservation equation for mass, liquid momentum, energy and chemical species, in a weak fashion.

Mass and momentum conservation An arithmetic mixing between the molten metal's average velocity, $\langle\boldsymbol{v^l}\rangle$, and the argon's average velocity, $\langle\boldsymbol{v^a}\rangle$, gives the system's fluid velocity, $\langle\boldsymbol{v^F}\rangle$. The metal domain thus consists of a single fluid phase, i.e. the liquid plus the solid phases. We further assume that the latter phase forms in fixed and rigid structures, $\boldsymbol{v^s} = 0$ (assuming that solidification results in an undeformable columnar dendritic, peritectic and eutectic structures, without any freely moving equiaxed dendritic structure), while the domain surrounding the metal entirely consists of argon gas. Finally, the monolithic mass balance writes:

$$\boldsymbol{\nabla}\cdot\langle\boldsymbol{v^F}\rangle = H^M\left(-\frac{1}{\langle\rho\rangle^l}\left(\frac{\partial\langle\rho\rangle^M}{\partial t} + \langle\boldsymbol{v^l}\rangle\cdot\boldsymbol{\nabla}\langle\rho\rangle^l\right)\right) \tag{2}$$

The momentum balance is transformed into averaged Navier-Stokes-Darcy equations as follows:

$$\begin{cases} \widehat{\rho}\left(\dfrac{\partial\left\langle \boldsymbol{v}^{\boldsymbol{F}}\right\rangle}{\partial t}+\dfrac{1}{g^{F}}\boldsymbol{\nabla}\cdot\left(\left\langle \boldsymbol{v}^{\boldsymbol{F}}\right\rangle\times\left\langle \boldsymbol{v}^{\boldsymbol{F}}\right\rangle\right)\right)= \\ -g^{F}\boldsymbol{\nabla}p-2\widehat{\mu}\boldsymbol{\nabla}\cdot\left(\overline{\overline{\boldsymbol{\nabla}}}\left\langle \boldsymbol{v}^{\boldsymbol{F}}\right\rangle+\overline{\overline{\boldsymbol{\nabla}^{\mathrm{t}}}}\left\langle \boldsymbol{v}^{\boldsymbol{F}}\right\rangle\right)-g^{F}\widehat{\mu}\widetilde{\mathbb{K}}^{-1}\left\langle \boldsymbol{v}^{\boldsymbol{F}}\right\rangle+\widehat{\rho g}\mathbf{g} \\ \\ \boldsymbol{\nabla}\cdot\left\langle \boldsymbol{v}^{\boldsymbol{F}}\right\rangle=H^{M}\left(-\dfrac{1}{\left\langle \rho\right\rangle^{l}}\left(\dfrac{\partial\left\langle \rho\right\rangle^{M}}{\partial t}+\left\langle \boldsymbol{v}^{\boldsymbol{l}}\right\rangle\cdot\boldsymbol{\nabla}\left\langle \rho\right\rangle^{l}\right)\right) \end{cases} \tag{3}$$

The mechanical properties used in eq. (3) are mixed as follows:

$$\text{Fluid fraction}: g^{F}=H^{M}g^{l}+H^{A}g^{a}=H^{M}g^{l}+H^{A} \tag{4}$$

$$\text{Density}: \widehat{\rho}=H^{M}\left\langle \rho\right\rangle^{l}+H^{A}\left\langle \rho\right\rangle^{a} \tag{5}$$

$$\text{Dynamic viscosity}: \widehat{\mu}=H^{M}\mu^{l}+H^{A}\mu^{a} \tag{6}$$

$$\text{Weight force}: \widehat{\rho g}\mathbf{g}=H^{M}g^{l}\left\langle \rho\right\rangle^{l}\mathbf{g}+H^{A}g^{a}\left\langle \rho\right\rangle^{a}\mathbf{g}=H^{M}g^{l}\left\langle \rho\right\rangle^{l}\mathbf{g}+H^{A}\left\langle \rho\right\rangle^{a}\mathbf{g} \tag{7}$$

The Darcy term depends on the fluid fraction, g^{F}, and the secondary dendrite arm spacing, λ_{2}, through a modified permeability model:

$$\widetilde{\mathbb{K}}=\frac{\lambda_{2}^{2}{g^{F}}^{3}}{180\left(1-g^{F}\right)^{2}} \tag{8}$$

As for the weight force in both domains, it is taken into account via eq. (7). The phase densities may vary as functions of other parameters such as temperature or phase composition, creating buoyancy forces inside the fluid. In our approach, $\left\langle \rho\right\rangle^{l}$ is a tabulated function of temperature and phase intrinsic composition (w_{i}^{l} is the liquid composition of the i^{th} species), given by a suitable thermodynamic database [5, 6]. We keep however the argon phase density $\left\langle \rho\right\rangle^{a}$ constant, so as to prevent a mixture of convection forces around the interface between domains, which helps stabilise the fluid flow resolution.

Energy conservation We model the heat transfer and the phase change using a temperature-based resolution [7] The method relies on predefined thermodynamic mappings [5] computed at full equilibium. The gouverning equation is given by:

$$\frac{\partial\widehat{\left\langle \rho h\right\rangle}}{\partial t}+\left\langle \boldsymbol{v}^{\boldsymbol{F}}\right\rangle\cdot\boldsymbol{\nabla}\widehat{\left(\rho h\right)^{F}}=\boldsymbol{\nabla}\cdot\left(\widehat{\left\langle \kappa\right\rangle}\boldsymbol{\nabla}T\right)+\widehat{\Phi} \tag{9}$$

The solution of eq. (9) is $\widehat{\left\langle \rho h\right\rangle}$, a mixed field between both domains average volumetric enthalpies. The other parameters are $\widehat{\left(\rho h\right)^{F}}$ and $\widehat{\left\langle \kappa\right\rangle}$ which denote respectively the fluids' mixture volume enthalpy and the mixture of average thermal conductivities. The last term, $\widehat{\Phi}$, is an average heat source accounting for energy change caused by the alloy's shrinking volume [8]. As no volume change was considered for the argon, $\widehat{\Phi}$ is present only in the metal's energy balance.

Species conservation The conservation of species mass is gouverned by the following equation using the macroscopic solute diffusion coefficient in the liquid, D^l:

$$\begin{aligned}
&\langle\rho\rangle^M \frac{\partial\widehat{\langle w\rangle}}{\partial t} + \langle\rho\rangle^l \langle \boldsymbol{v^l}\rangle \cdot \boldsymbol{\nabla}\widehat{\langle w\rangle} - \boldsymbol{\nabla}\cdot\left(g^l \langle\rho\rangle^l D^l \boldsymbol{\nabla}\widehat{\langle w\rangle}\right) = \\
&- \frac{\partial \langle\rho\rangle^M}{\partial t}\left[\left(\langle w\rangle^M\right)^t - \left(\langle w\rangle^l\right)^t\right] \\
&+ \langle\rho\rangle^l \langle \boldsymbol{v^l}\rangle \cdot \boldsymbol{\nabla}\left(\left(\langle w\rangle^M\right)^t - \left(\langle w\rangle^l\right)^t\right) - \boldsymbol{\nabla}\cdot\left[g^l \langle\rho\rangle^l D^l \boldsymbol{\nabla}\left(\left(\langle w\rangle^M\right)^t - \left(\langle w\rangle^l\right)^t\right)\right]
\end{aligned} \tag{10}$$

The right-hand side terms emerge from a variable splitting.

Computational configuration

Geometry and boundary conditions

The simulation considers only 1/4 of the droplet-gas system, given the axial symmetry of the problem. The steel sample is not perfectly spherical initially as surface oscillations perturb the equilibrium shape. The droplet is hence an ellipsoid having a vertical minor axis of 5.68 mm and a horizontal major axis of 6.6 mm, as shown in fig. 1. The bottom is a planar surface (diameter of 2 mm, where the contact is initiated). Also in fig. 1, the alloy is immersed in a gas medium (argon), such that both subdomains form together 1/4 of a cylinder having 8 mm in radius and 8 mm in height. The mesh is automatically adapted to the moving interface using anisotropic elements to reduce the computational cost while maintaining sufficient numerical accuracy. The time step is 0.01 s. For the velocity-pressure boundary conditions, fig. 2 shows the no-slip condition imposed on the droplet-substrate surface, since this area solidifies in the first place without further fluid motion. The only thermal boundary condition is a convection flux with constant heat transfer coefficient, h_{ext} ($6 \times 10^4\,\text{W m}^{-2}\,\text{K}^{-1}$), and constant external temperature, T_{ext} (25 °C), that replaces the ceramic chill. We consider that the heat flux dissipated by the chill is dominant with respect to other heat transfer mechanisms (e.g. radiation). The gravitational acceleration magnitude is assumed to be in order of $5 \times 10^{-5}\,\text{m s}^{-2}$, hence designated by $\mu\mathbf{g}$, as typically measured in under reduced-gravity conditions.

Choice of alloy

Various steel grades were considered in the CCEMLCC project. Each grade was assigned to a specific experiment. We limit our study to the steel assigned for TEXUS sounding rocket missions, the grade is designated as "*b1*" alloy. Its nominal composition is given in table 1. The current approach relies on thermodynamic tabulations to determine density and composition for all phases as functions of the evolving average alloy composition. By considering three solute species, a quaternary Fe-C-Si-Mn alloy referred to as *b1Quat* alloy, is used to predict segregation.

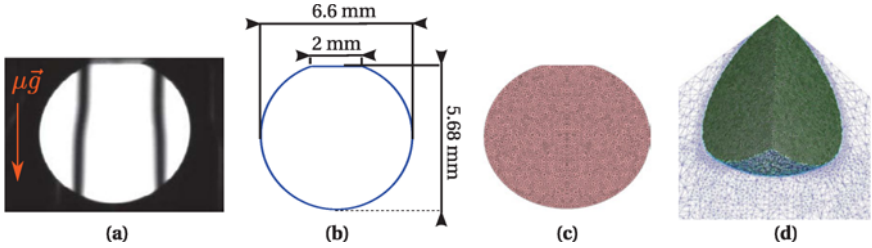

Figure 1 – The camera frame (a) before the onset of solidification gives the essential information [9] to (b) rebuild the 2D droplet geometry then (c) a standalone 2D mesh used to obtain (d) the final immersed axisymmetrical 3D mesh, including the argon reservoir surrouding the droplet.

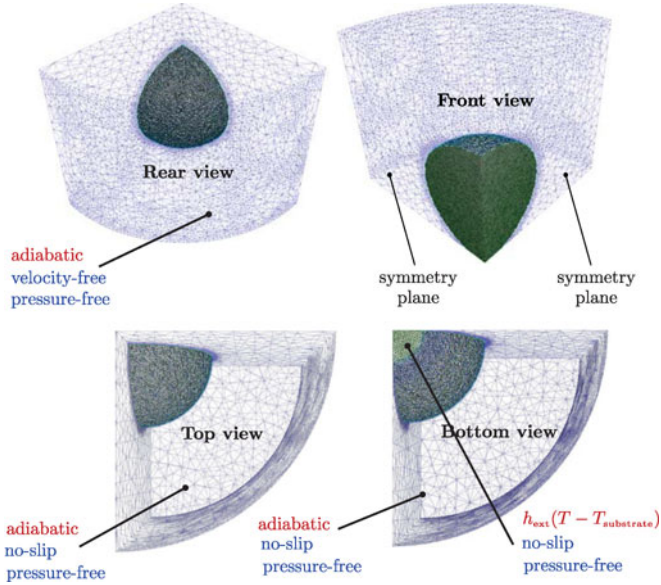

Figure 2 – 3D views showing the thermal (red) and mechanical (blue) boundary conditions used in reduced-gravity simulations.

Table 1 – Nominal composition (wt.%) of the experimental *b1* steel and its simulation quaternary equivalent alloy, *b1Quat*.

Alloy	C	Si	Mn	Al	S	P
b1	0.105	0.268	0.636	0.0067	0.009	0.0189
b1Quat	0.105	0.268	0.636	-	-	-

Results and discussion

Shrinkage-induced flow

The flow pattern shown in fig. 3 reveals distinct regions at 0.25 s and 1 s: upward flow driven by solidification shrinkage contributes to a slight enrichment by inverse segregation, while a downward flow driven by gravity, redistributes species in the containerless melt. At 8 sec, the mushy zone reaches the droplet vertex marking a flow pattern change. Upon completely solidifying, the droplet forms a rigid and static solid, surrounded by natural argon flow, seen at 20 s in fig. 3.

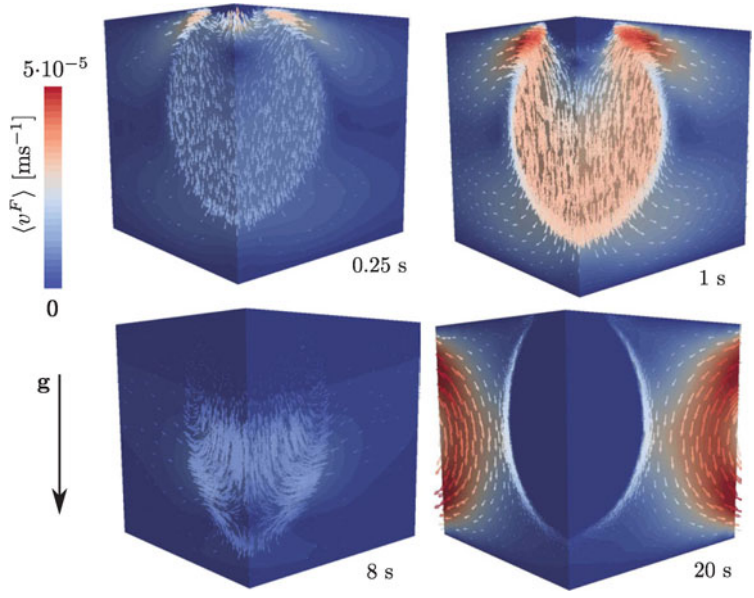

Figure 3 – Flow patterns in reduced-gravity solidification with shrinkage.

Segregation

The shrinkage-induced fluid flow is behind the reduced-gravity segregation shown at different stages in fig. 4. A restricted region of positive segregation settles at the contact area with the substrate, from the first second after the contact. Later, between 2 s and 8 s, the solid front advances in the melt, creating a noticeable negatively segregated area, about 4% less than the nominal composition, just below the positive segregation zone. This is not the expected inverse segregation profile obtained by directional solidification. Usually, we would expect that the composition decreases gradually once the solid front advances in time. To interpret this unusual observation, we refer to the fluid flow shown earlier in fig. 3. At 0.25 s, a no-velocity isovolume (i.e. depicting a volume with null velocity magnitude) forms between the two distinct regions of upward and downward flow.

The strong negative divergence that settles in this area results in solute depletion in the two directions and due to the various driving forces. However, at 1 s, the no-velocity isovolume clearly shrinks in a matter of only 0.75 s. That is because the initial temperature gradient is the highest during the process, then it decreases gradually. Since a higher temperature gradient produces a greater cooling flux according to the Fourier model, solidification is faster in the beginning and the volume shrinkage is greater, hence the shrinkage flow coexists with the gravity flow. As the transformation progresses, shrinkage flow becomes insignificant compared to the latter, therefore the negative segregation intensity decreases gradually from 2.2 mm to 4.3 mm from the chill, corresponding to the first seconds of contact. This result is also shown in fig. 5 for carbon, where we plot the relative segregation profile along the vertical rotation axis of the droplet. At 8 s, fig. 3 shows the zero-velocity isovolume moved down the vertical revolution axis by following the solidification front, then vanishing at about 10 s. It means that from this point in time, the flow is dissipated by the mushy zone's low permeability, hence the low-magnitude shrinkage flow dominates again.

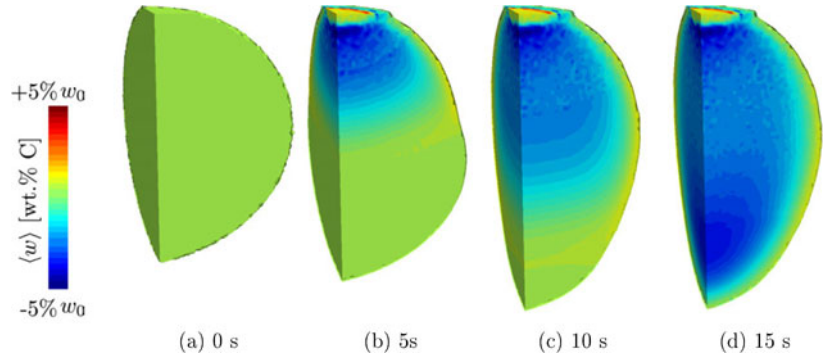

Figure 4 – Evolution of the carbon average composition with solidification time, showing evidence of mesosegregation and shape deformation between 0 s and 15 s.

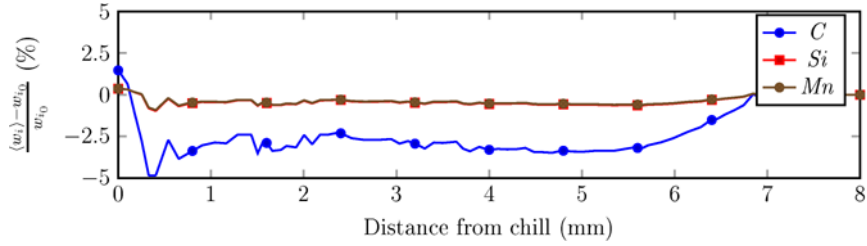

Figure 5 – Relative segregation profiles for each chemical species as function of the distance from the chill, plotted along the vertical revolution axis of the solidified sample.

Conclusion

A multicomponent alloy solidification has been studied in a reduced-gravity environment. Segregation due to shrinkage-feeding flow and gravitational flow is studied for each chemical species, carbon, silicon and manganese. The simulation results show a flow competition in reduced-gravity solidification, which affects the final solidified shape, and the segregation intensity.

Acknowledgments

This work was conducted as a part of the Microgravity Applications Promotion (MAP) program, funded by the European Space Agency - ESTEC (Noordwijk, NL) under the CCEMLCC project (grant AO-2004-017).

References

[1] R. Willnecker, D. M. Herlach, and B. Feuerbacher. "Containerless undercooling of bulk Fe-Ni melts". *Applied Physics Letters* 49 (20) (11/1986), pp. 1339–1341.

[2] J. Lee et al. "Magnetohydrodynamic Modeling and Experimental Validation of Convection Inside Electromagnetically Levitated Co-Cu Droplets". *Metallurgical and Materials Transactions B* 45 (3) (12/2013), pp. 1018–1023.

[3] J. Lee, X. Xiao, D. M. Matson, and R. W. Hyers. "Numerical Prediction of the Accessible Convection Range for an Electromagnetically Levitated Fe50Co50 Droplet in Space". *Metallurgical and Materials Transactions B* 46 (1) (09/2014), pp. 199–207.

[4] S. Osher and J. A. Sethian. "Fronts propagating with curvature-dependent speed: Algorithms based on Hamilton-Jacobi formulations". *Journal of Computational Physics* 79 (1) (11/1988), pp. 12–49.

[5] J.-O. Andersson, T. Helander, L. Höglund, P. Shi, and B. Sundman. "Thermo-Calc & DICTRA, computational tools for materials science". *Calphad* 26 (2) (06/2002), pp. 273–312.

[6] TCFE6. *TCFE6: a thermodynamic database for different kinds of steels and Fe-based alloys.* Stockholm, SE, 2010.

[7] A. Saad, C.-A. Gandin, and M. Bellet. "Temperature-based energy solver coupled with tabulated thermodynamic properties – Application to the prediction of macrosegregation in multicomponent alloys". *Computational Materials Science* 99 (03/2015), pp. 221–231.

[8] A. Saad. "Numerical modelling of macrosegregation formed during solidification with shrinkage using a level set approach". PhD Thesis. MINES ParisTech, 2016.

[9] C.-A. Gandin. *Project ESA-MAP CCEMLCC phase #2 – Final Report.* 2014.

IN SITU INVESTIGATION OF THE EFFECTS OF GRAVITY LEVEL VARIATIONS ON THE DIRECTIONAL SOLIDIFICATION MICROSTRUCTURES DURING PARABOLIC FLIGHTS

L. Abou-Khalil [1], G. Salloum-Abou-Jaoude[2], G. Reinhart[1], C. Pickmann[3], G. Zimmermann[3], Y. Houltz[4], J. Li[4], O. Janson[4], H. Nguyen-Thi [1]

[1]Aix Marseille University, CNRS, IM2NP UMR 7334, 13397, Marseille, France
[2]BCAST, Brunel University, Uxbridge, Middlesex UB8 3PH, UK
[3]ACCESS e.V., Intzestrasse 5, 52072 Aachen, Germany
[4]Swedish Space Corporation, P.O. Box 4207, SE-171 04 Solna, Sweden

Keywords: directional solidification, microstructures, gravity level variation, CET

Abstract

In the framework of an ESA-MAP project entitled XRMON, directional solidification experiments of Al – 20 wt% Cu with in situ and real-time X-ray radiography were carried out during Parabolic Flight campaigns. Parabolic flights offer successions of periods with different gravity levels, allowing the investigation of the impact of gravity level variations on the solidification microstructure formation. Directional solidifications of refined Al – 20 wt% Cu alloy were investigated in a dedicated apparatus for a wide range of cooling rates and a constant temperature gradient. X-ray radiography was successfully used to observe the microstructure evolution following the variations of gravity level. During the columnar growth of the refined alloy a sharp increase of gravity level provoked the sudden nucleation of numerous grains ahead of the front. The most potent explanation of this effect is the variation of the liquid undercooling ahead of solid/liquid interface due to the changes of hydrostatic pressure in the melt.

Introduction

Metals properties are strongly related to solidification microstructures and to the accompanying segregation, which are both very sensitive to gravity [1]. Indeed, gravity induces natural convection in the melt due to density variations following the local temperature and concentration [2]. The coupling between fluid flow and solidification has been the subject of a great deal of experimental, theoretical and numerical works. The main conclusion of these studies is that the convection has a significant impact on the solidification process, such as the macroscopic deformation of the solid/liquid interface, macro-segregation in the sample, and the modification of the primary arm spacing. In addition, due to solute rejection during the liquid to solid transition, growing grains and surrounding liquid have generally different densities. Consequently, buoyancy force can act on the solid grains, which lead to their sedimentation or floatation in the liquid phase. Therefore, equiaxed microstructures on Earth and in microgravity are dramatically different. Furthermore, gravity is at the origin of mechanical effects, which can induce the bending of secondary arms when the latter are long enough. In some cases, the bending phenomenon can precede the dendrite fragmentation [3, 4]. Finally, a less common issue

related to gravity is the hydrostatic pressure in the melt. It is well known that hydrostatic pressure applied during solidification significantly reduces the formation of porosities. On the contrary, under microgravity conditions, hydrostatic pressure vanishes and the liquid shape is only determined by the surface tension and the wetting behavior of the melt on solid surfaces. Hence, the loss of hydrostatic pressure in the melt can cause shrinkages or the formation of voids along the sample during microgravity experiments [5]. Therefore, a deeper understanding of gravity effects in solidification microstructure is of great importance for scientists and industrialists alike.

It has long been realized that solidification under microgravity conditions is an efficient way to eliminate most of the buoyancy-related phenomena, providing valuable benchmark data in near-diffusive conditions for the validation of analytical models and numerical simulations. In addition, a comparative study of solidification experiments carried out on Earth and in space can also enlighten the effects of gravity. In this paper, we report experimental results obtained during the 60th ESA-PF (Parabolic Flights) campaign in April 2014. To investigate the impact of gravity level variations on the dynamic of the solidification microstructure formation, it is crucial to achieve in situ and real-time characterization during the solidification experiment. It is now well recognized that X-ray radiography is the method of choice for investigating the solidification front evolution of metallic alloys grown from the melt [6]. In the framework of the ESA-MAP (Microgravity Application Promotion) entitled XRMON (X-ray MONitoring of advanced metallurgical processes under microgravity and terrestrial conditions), a dedicated apparatus named XRMON-GF (Gradient Furnace) was developed to perform directional solidification experiments on Al-based alloys, with in situ X-ray radiography. This facility was successfully used in microgravity conditions onboard MASER-12 sounding rocket in 2012 [7]. In a second step, the XRMON-GF facility was slightly modified to be utilized during parabolic flights. This new facility, entitled XRMON-PFF (Parabolic Flight Facility), was used onboard the Airbus A300 operated by Novespace (www.novespace.fr) to study equiaxed growth of Al – 20 wt% Cu in nearly isothermal conditions [7, 8].

Experiments

Contrary to ISS (International Space Station), satellite and sounding rockets, parabolic flights offer only very short reduced-gravity periods (about 20 seconds) in comparison with typical solidification experiments (several hours). For this reason, the main interest to perform solidification during parabolic flights is to focus on the influence of g-level variations on the growth process. During the 60th ESA-PF campaign, a series of directional solidification experiments on Al – 20 wt% Cu sample was carried out in the XRMON-PFF facility.

XRMON-PFF facility

The XRMON-PFF is shown in Figure 1a in the Airbus A300 Zero-G, with the experimental and control racks. The experimental rack figures three essential components (Figure 1b): the X-ray source, the X-ray detector and the solidification furnace. The furnace is of Bridgman type. A temperature gradient along the sample is imposed by two heaters separated by a gap. The gradient furnace enables directional solidification with thermal gradients within a range of 5-15 K/mm. The heater gap has a “hole” of 5 mm x 5 mm for the X-ray transmission. Solidification is

induced by the power-down method, which consists of applying the same cooling rate *R* on both heater elements to keep a constant temperature gradient during the process.
A sketch of the X-ray radiography system is presented in Figure 1c. The microfocus X-ray source is a transmission type X-ray tube with a molybdenum target and a 3 µm focal spot. It provides a sufficient photon flux with two peaks of energy at 17.4 keV and 19.6 keV that ensure a good image contrast to study Al-Cu based alloys. The camera system is made of a digital camera with a CCD-sensor adapted for X-ray usage by the integration of a 50 mm thick fiber optical plate that protects the sensor from radiation. A scintillator plate placed in front of the optical fiber converts X-ray radiation to visible spectrum light. As a result of the X-ray beam divergence, a geometric magnification of the object is observed at the detector, which is the ratio of the source-detector to source-object distances; the object in this case being the sample. In this work a magnification of ~5 was obtained, for a FOV of about 5 x 5 mm^2 and an effective pixel size of ~4 µm. The acquisition rate is typically 3 frames/s.

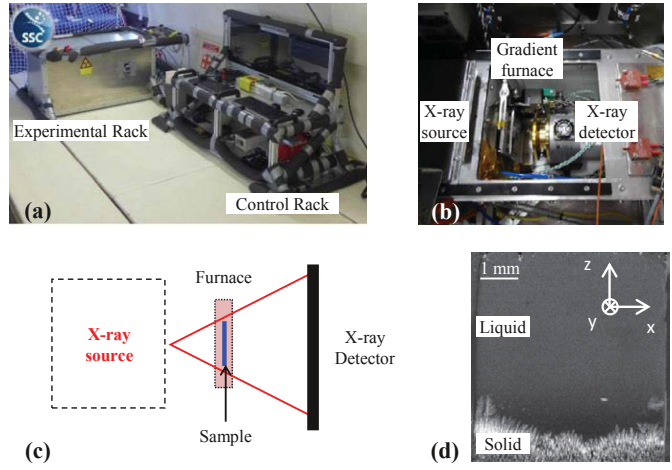

Figure 1. (a) XRMON-Parabolic Flight Facility in Novespace Airbus A300 Zero-G, (b) picture of the solidification furnace and X-ray systems in the experimental rack, (c) sketch of the X-ray radiography system, (d) example of radiograph after image processing.

Variations of grey levels in the radiographs are related to the difference in X-ray absorption of the different parts of the sample, which depends mainly on the local density and composition of the sample. In Al-Cu alloys, copper provides a greater attenuation of the incident X-ray beam than aluminum. Image quality was enhanced by applying an image processing consisting in dividing each frames by a reference picture before cooling starts [9]. After the image processing, radiographs like Figure 1d are obtained, showing the solid-liquid interface during the solidification of Al – 20 wt% Cu. Regions of high copper concentration show up as dark regions in the images, while α-Al dendrites with low copper concentration are discernible as bright regions in the field of view.

Sample preparation

During the 60th ESA-PF campaign, an Al – 20 wt% Cu alloy inoculated with 0.1 wt% AlTiB refiners was investigated in order to determine the solidification conditions that can give rise to a Columnar-to-Equiaxed Transition (CET) [10, 11]. CET is a transition that occurs when equiaxed grains nucleate in the undercooled liquid region ahead of an advancing columnar front. If the number of grains is large enough, they can grow and stop the columnar growth and there is formation of an equiaxed microstructure. AlTiB refiners are used to act as preferential sites for heterogeneous nucleation, and thus to promote the Columnar-to-Equiaxed Transition [12].
The sample dimensions were 50 mm in length, 5 mm in width and 200 to 250 μm in thickness. The sample was placed between stainless steel spacers sandwiched by two glassy carbon sheets sewn together with a silica thread (Figure 2). The crucible was enclosed inside the heaters, having a contact with both sides to achieve the same thermal behavior in microgravity environment as on ground-based experiments.

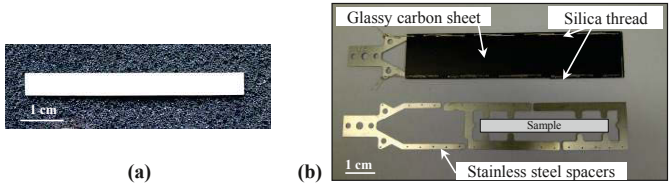

Figure 2. (a) Al – 20 wt% Cu sample and (b) glassy carbon crucible with stainless steel frame, sewn together with a silica thread.

Parabolic flight timeline

According to the parabolic flight trajectory, the gravity level changes during each parabola (Figure 3a) from $1g_0 \rightarrow \sim 1.8g_0 \rightarrow \sim 0g_0 \rightarrow \sim 1.8g_0 \rightarrow 1g_0$, with approximately 24s and 22s at $\sim 1.8g_0$ and $\sim 0g_0$ respectively. During the course of the flight, the parabola is repeated a total of 31 times: a first series of six parabolas, followed by five series of five parabolas with a time interval between two series of 5-8 minutes (Figure 3b).

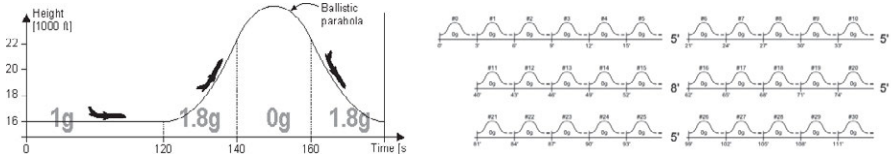

Figure 3. (a) Parabola profile showing the gravity level variation with time, (b) sequence of 31 parabolas during the course of the flight.

Accelerations were recorded for all experiments on three accelerometers on mutually orthogonal axes mounted to the experimental rack. Figure 4 gives typical accelerometer data for five parabolic maneuvers. For a typical maneuver, during low gravity the acceleration on all axes was below ~0.05g_0. During pullout and climb, the high gravity acceleration parallel to the longitudinal axis of the sample reached ~1.8g_0 while the accelerations on the two other axes are less than 0.15g_0. Therefore, we can assume that the gravity vector is always parallel to the sample longitudinal growth axis.

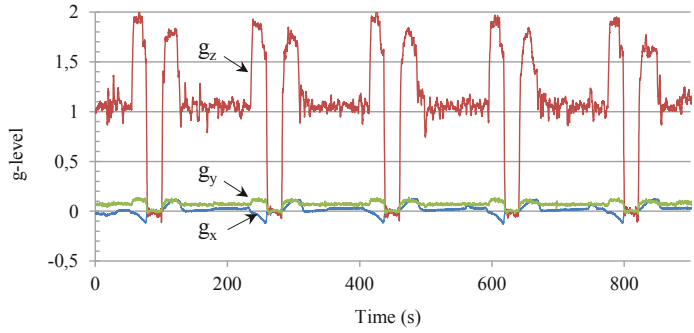

Figure 4. Typical acceleration data during five parabolic maneuvers. The g_z curve is the acceleration parallel to the longitudinal axis of the sample and directed from the top to the bottom of the sample, g_x and g_y curves are the accelerations parallel to the transverse direction of the sample and perpendicular to the main surface of the sample respectively.

Before the beginning of the series of parabolas, the heater temperatures were adjusted to have the solid-liquid interface visible at the bottom in the Field-of-View of the camera, and then kept constant at these temperatures. The cooling of the sample was then triggered a few seconds before the beginning of the first parabola (during the 1g_0 period), and extended over the whole series of five parabolas (Figure 4). The origin of time (t = 0s) was chosen at the beginning of the cooling down. In this paper, we focus on the solidification experiment, at a very slow cooling rate (R = -0.05 K/s) and for a temperature gradient (G = 15 K/mm).

Results

CET triggering by variation of gravity level

Figure 5 displays a sequence of radiographs recorded during a part of the solidification experiment under varying gravity level. During the 1g_0 period, the development of a columnar microstructure was observed at the bottom of the Field-of-View (FOV) (white microstructure in Figure 5a). Due to solute rejection during solidification, the liquid just ahead of the columnar front was copper-enriched and appeared darker than the liquid far from the columnar front. Fragmentation phenomena occurred along the solid/liquid interface and the dendrite fragments floated from the bottom to the top due to buoyancy force. Indeed, for this alloy composition (Al – 20 wt% Cu), the dendrite fragments are lighter than the surrounding liquid [7]. During their motion toward the hot region of the sample, the dendrite fragments rapidly melted until their

complete disappearance. Moreover, a few grains nucleated on the crucible wall. Most of them floated toward the top of the sample and melted, but one remained stuck on the crucible wall on the right-hand side of the sample (Figure 5b).

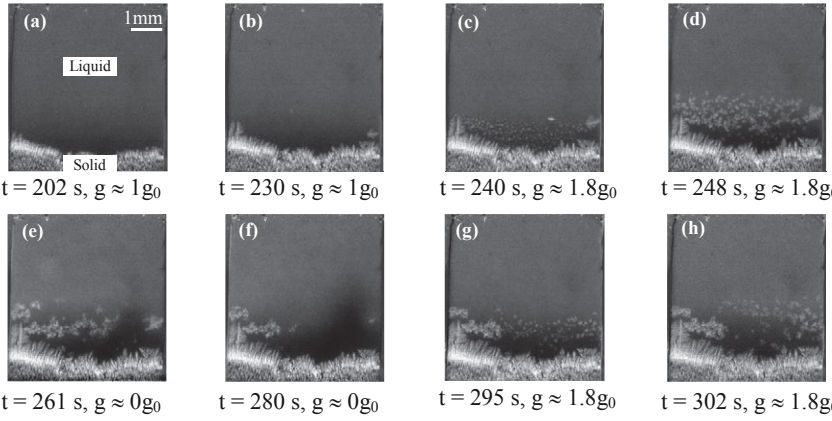

Figure 5. Sequence of radiographs recorded during the solidification of refined Al – 20 wt% Cu, for a cooling rate (R = -0.05 K/s), and temperature gradient (G = 15 K/mm) during a parabola. The gravity vector is directed vertically downwards relative to the FOV.

When the gravity level suddenly increased from $1g_0$ to ~$1.8g_0$ at the beginning of the parabola, a sudden nucleation of a large number of equiaxed grains ahead of the columnar front was observed (Figure 5c). The nucleation rate is about 100 grains/second, which is of the same order of the nucleation rate measured by Murphy for equiaxed growth of a refined Al - 20wt% Cu sample in near-isothermal experiment [8].

This explosive nucleation phase is obviously provoked by the sharp increase of the gravity level. Actually, the grain nucleation event ahead of the columnar front was triggered by an increase of the liquid undercooling ahead of the columnar front. The liquid undercooling at an altitude z is defined as the difference between the liquidus temperature $T_{eq}(z)$ and the real temperature imposed by the temperature gradient $T_L(z)$. If the liquid undercooling reaches the value of the nucleation undercooling of the refining particles, nucleation can occur. The question that rises is: why the liquid undercooling increases when the gravity level augments?

The most potent explanation of this increase of the undercooling is a decrease of the liquid composition ahead of the columnar structure. This composition decrease is attributed to the increase of the hydrostatic pressure of the melt when the gravity level changed from $1g_0$ to ~$1.8g_0$. As the two thin glassy carbon sheets are flexible, the hydrostatic pressure rise caused a larger bulging of the sample at the solid-liquid interface, as mentioned by A. Murphy [7]. As a consequence, this bulging increase induced a downward flow of poorer fluid toward the columnar front. Because of the decrease of liquid composition ahead of the columnar front, the local equilibrium temperature augments as well as the constitutional undercooling.

After their nucleation, like dendrite fragments, the new grains started to float and then melted when they reached the hot region of the liquid (Figure 5d and 5e). Some grains remained stuck in the thickness of the sample when their size was too large compared to the sample thickness (Figure 5f). As soon as the gravity level reached ~$0g_0$ (Figure 5e), the equiaxed grains stopped moving upward because buoyancy force vanished. During the $0g_0$ period (Figure 5e to Figure 5f), the grains remelted due to an upward copper-enriched fluid flow, which is visible in Figure 4f as a dark region in the liquid ahead of the microstructures. Once again, the origin of this upward fluid flow is related to the vanishing of the hydrostatic pressure and thus the contraction of the crucible during the microgravity period. During the subsequent ~$1.8g_0$ period, the explosive nucleation phenomenon occurred again (Figure 5g and 5h). All these phenomena were repeated in the following parabolas. It is worth noting that these observations were also observed in other experiments, with different cooling rates.

Conclusion

X-ray radiography was successfully used during solidification experiments carried out during parabolic flights. It was observed that gravity level variations can have a significant impact on the microstructure formation. The variation of g-level induces a variation of the liquid composition ahead of the solid/liquid interface which affects the constitutional undercooling. In a refined alloy, this undercooling increase can provoke an explosive nucleation of equiaxed grains. Further solidification experiments with different alloy composition are scheduled during future parabolic flight campaigns in the framework of the XRMON project.

Acknowledgments

This study was partly supported by the XRMON project (AO-2004-046) of the MAP program of the European Space Agency (ESA) and by the French National Space Agency (CNES).

References

1. H. Nguyen-Thi, A. Bogno, G. Reinhart, B. Billia, R. H. Mathiesen, G. Zimmermann, Y. Houltz, K. Löth, D. Voss, A. Verga and F. d. Pascale. Investigation of gravity effects on solidification of binary alloys with in situ X-ray radiography on earth and in microgravity environment. *Journal of Physics: Conference Series* 2011;327:012012

2. D. T. J. Hurle. Interactive Dynamics of Convection and Solidification 1992

3. G. Reinhart, H. Nguyen-Thi, N. Mangelinck-Noel, J. Baruchel and B. Billia. In Situ Investigation of Dendrite Deformation During Upward Solidification of Al-7wt.%Si. *JOM* 2014;66:1408-1414

4. G. Reinhart, A. Buffet, H. Nguyen-Thi, B. Billia, H. Jung, N. Mangelinck-Noel, N. Bergeon, T. Schenk, J. Hartwig and J. Baruchel. In-Situ and real-time analysis of the formation of strains and microstructure defects during solidification of Al-3.5 wt pct Ni alloys. *Metallurgical and Materials Transactions a-Physical Metallurgy and Materials Science* 2008;39A:865-874

5. B. Drevet, D. Camel, C. Malmejac, J. J. Favier, H. Nguyen Thi, Q. Li and B. Billia. Cellular and Dendritic Solidification of Al-Li Alloys during the D2-Mission. *Adv. In Space Res.* 1995;16:173-176

6. H. Nguyen-Thi, L. Salvo, R. H. Mathiesen, L. Arnberg, B. Billia, M. Suery and G. Reinhart. On the interest of synchrotron X-ray imaging for the study of solidification in metallic alloys. *Comptes Rendus Physique* 2012;13:237-245

7. H. Nguyen-Thi, G. Reinhart, G. Salloum-Abou-Jaoude, D. J. Browne, A. G. Murphy, Y. Houltz, J. Li, D. Voss, A. Verga, R. H. Mathiesen and G. Zimmermann. XRMON-GF Experiments Devoted to the in Situ X-ray Radiographic Observation of Growth Process in Microgravity Conditions. *Microgravity Science and Technology* 2014;26:37-50

8. A. G. Murphy, J. Li, O. Janson, A. Verga and D. J. Browne. Microgravity and Hypergravity Observations of Equiaxed Solidification of Al-Cu Alloys using In-situ X-radiography recorded in Real-time on board a Parabolic Flight. *Materials Science Forum* 2014;790-791:52-58

9. H. Nguyen-Thi, G. Reinhart, G. S. Abou Jaoude, R. H. Mathiesen, G. Zimmermann, Y. Houltz, D. Voss, A. Verga, D. J. Browne and A. G. Murphy. XRMON-GF: A novel facility for solidification of metallic alloys with in situ and time-resolved X-ray radiographic characterization in microgravity conditions. *Journal of Crystal Growth* 2013;374:23-30

10. H. Nguyen Thi, G. Reinhart, N. Mangelinck-Noël, H. Jung, B. Billia, T. Schenk, J. Gastaldi, J. Härtwig and J. Baruchel. In-Situ and Real-Time Investigation of Columnar to Equiaxed Transition in Metallic Alloy. *Metall. Mater. Trans. A* 2007;38-7:1458-1464

11. G. Reinhart, N. Mangelinck-Noël, H. Nguyen Thi, T. Schenk, J. Gastaldi, B. Billia, P. Pino, J. Härtwig and J. Baruchel. Investigation of Columnar-Equiaxed Transition and Equiaxed growth of Aluminium Based Alloys by X-Ray Radiography. *Materials Science and Engineering A* 2005;413-414:384-388

12. G. Reinhart, H. Nguyen-Thi, N. Mangelinck-Noël, T. Schenk, B. Billia, J. Gastaldi, J. Härtwig and J. Baruchel. In-situ observation of transition from columnar to equiaxed growth in Al-3.5 wt% Ni alloys by synchrotron radiography. *Modeling of Casting, Welding and Advanced Solidification Processes* 2006;XI:359-366

MICROSTRUCTURAL EVOLUTION IN UNDERCOOLED Al–8wt%Fe MELTS

J. Valloton[1], A. A. Bogno[1], J. Chen[2], R. Lengsdorf[3], H. Henein[1],
D. M. Herlach[3], U. Dahlborg[4], and M. Calvo-Dahlborg[4]

[1] Chemical and Materials Engineering, University of Alberta, Edmonton, Canada
[2] NINT, NRC, Edmonton, Canada
[3] Institut für Materialphysik im Weltraum, Deutsches Zentrum für Luft- und Raumfahrt, Köln, Germany
[4]GPM, CNRS-UMR 6634, University of Rouen, France

Keywords: Non-equilibrium solidification, electromagnetic levitation, impulse atomization, Al-8Fe, reduced gravity

Abstract

Containerless rapid solidification of hypereutectic Al–8wt%Fe is investigated experimentally using the Impulse Atomization technique (IA), as well as ElectroMagnetic Levitation (EML) under terrestrial and reduced gravity conditions. The samples were analyzed using scanning and transmission electron microscopy, X-ray and neutron diffraction, as well as electron backscattered diffraction. In both EML and IA, the samples experience some undercooling for the solidification of the primary intermetallic phase, which is likely metastable Al_mFe (m = 4.0–4.4). After recalescence, the solidification path then continues with the nucleation and growth of stable $Al_{13}Fe_4$. While $Al_{13}Fe_4$ dominates in EML samples, it becomes minor in favor of Al_mFe in IA droplets. The morphology differences of the primary intermetallics growing under terrestrial and microgravity conditions in EML are clear with acicular morphology for the former and a star-like morphology for the latter. The α–Al has a strong texture in microgravity EML and in IA samples while a weak one is observed on terrestrial EML. This difference is attributed to the weaker fluid flow occurring under reduced gravity conditions and in IA droplets.

Introduction

Al–based alloys are of high importance for aerospace and automotive industry. Al–Fe basis alloys in particular have long been of interest for high temperature applications such as compressor sections of gas turbine engines and low temperature fan [1–2]. Recent research found new Al–Fe alloy competing with titanium up to 573 K in aerospace structure [3–4]. However, by forming intermetallics such as $Al_{13}Fe_4$ (θ phase), iron can be deleterious to the mechanical properties of aluminum alloy. Thus, strategies have to be developed to modify the negative effect of iron. One of them is by using physical processing such as rapid solidification processing (RSP) to increase the solubility of Fe or obtain finer dissemination of Al–Fe precipitates. The presence of non-equilibrium phases produced by RSP allows greater flexibility and control of the final microstructure to combine good high temperature strength with sufficient ductility, high elastic moduli and excellent thermal stability, superior to those obtained by conventional ingot metallurgy and casting techniques. In this study, containerless rapid solidification of

hypereutectic Al–8wt%Fe is investigated experimentally using the Impulse Atomization technique (IA), as well as ElectroMagnetic Levitation (EML) under terrestrial and reduced gravity conditions.

Experimental

Electromagnetic levitation (EML) is a powerful containerless solidification technique for processing of electrically conducting samples such as metals and semiconductors. By avoiding contact with any container walls and operating under high purity environment, heterogeneous nucleation is strongly reduced and a large range of undercoolings can be achieved. In EML, the sample is placed within a conical levitation coil typically consisting of five to seven water-cooled copper windings with one or two counterwindings at its top (Figure 1, left). Eddy currents are induced in the sample by the electromagnetic field generated by the levitation coils. The sample is heated and molten by ohmic losses, whereas the interaction of these eddy currents with the electromagnetic field leads to a displacement force on the sample that is opposite to the gravitational force. The temperature of the sample is monitored continuously with a contactless pyrometer. To cool the sample below its liquidus temperature and induce solidification, a jet of high purity helium is then used. Detailed information on the EML technique can be found in [5].

Impulse atomization (IA) is the other containerless solidification technique used in this study (Figure 1, right). It consists in the transformation of a bulk liquid into a spray of liquid droplets that solidify rapidly during free fall by losing heat to a surrounding gas of choice (N_2, Ar, or He are commonly used). The bulk liquid is produced by heating a material above its melting point and the atomization is achieved by the application of a pressure (impulse) to the melt, to push it through a nozzle plate with one or several orifices of known size and geometry so that a liquid ligament emanates from each orifice and breaks up into droplets. Cooling rate is both a function of droplet size and the gas used to atomize the molten metal. The solidified powders are then collected in a beaker at the bottom of the atomization tower, washed, and sieved into different particle size ranges for analysis. Detailed information on the IA technique can be found in [6].

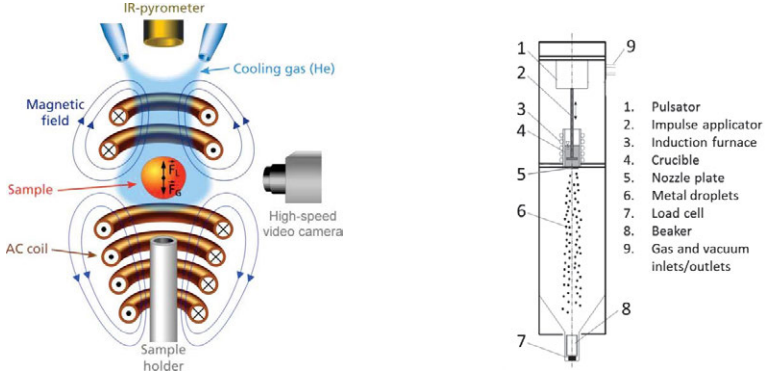

Figure 1. Schematic views of electromagnetic levitation (EML, left) and impulse atomization (IA, right).

Results and Discussion

According to the phase diagram, solidification of Al–8wt%Fe alloy should start with the crystallization of $Al_{13}Fe_4$ intermetallic followed by the eutectic decomposition of the remaining liquid into α–Al and $Al_{13}Fe_4$. Figure 2 shows the microstructure of Al–8wt%Fe EML samples processed under terrestrial (referred as 1g Al–8Fe) and reduced gravity condition (referred as PFC Al–8Fe), (A) and (B) respectively. Temperature measurements show that both samples experienced some undercooling before the solidification of the primary intermetallic phase (ΔT_p = 155 K for 1g and 116 K for PFC) and of the eutectic structure (ΔT_e = 23 K for 1g and 28 K for PFC). The microstructures obtained under those two conditions are different. The primary phase in 1g Al–8Fe is a very acicular-dendritic like morphology, while it has a star-like morphology in PFC Al–8Fe. Some small acicular phase can also be found within the observed area. The existence of star-like morphology suggests PFC Al–8Fe experienced higher cooling rate compared with 1g Al–8Fe. In both samples, α–Al surrounds the primary phase, and the eutectic appears to have formed on the dendrite boundaries between the α–Al matrix.

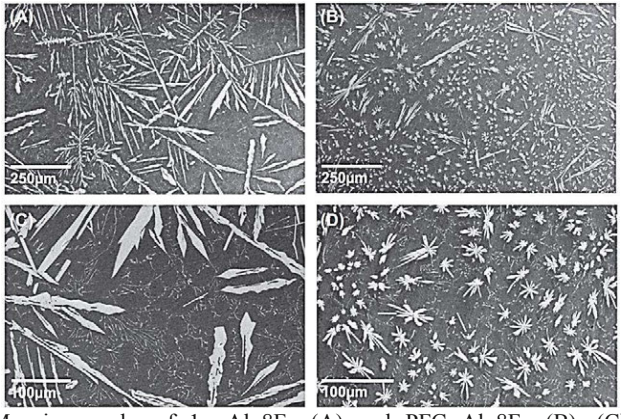

Figure 2. SEM micrographs of 1g Al–8Fe (A) and PFC Al–8Fe (B). (C) and (D) are enlargements of (A) and (B), respectively.

Prior to metallography, neutron diffraction was used for phase identification in the bulk of both samples, together with texture determination. Figure 3 displays the diffraction patterns from 2.6 to 3.2 $Å^{-1}$ (A) and from 1.2 to 2.0 $Å^{-1}$ along with the computed peaks from Rietveld refinement (B). Besides α–Al, the diffraction patterns suggest the existence of $Al_{13}Fe_4$ as well as metastable Al_mFe (m = 4.0–4.4) in the structure for both samples. To corroborate those results, TEM observation was carried out [7]. Selected area electron diffraction pattern simulations (not shown here) confirm unambiguously that the primary intermetallic phase is indeed $Al_{13}Fe_4$ in both 1g and PFC samples. TEM analysis also indicates that the intermetallic within the eutectic is $Al_{13}Fe_4$ as well. Note that in the extensive TEM observation, no Al_mFe was found. However, since the information TEM supplied is from small lamellae taken from the spheres (~6 mm in diameter), it is quite possible that Al_mFe is not in the area investigated. This shows that neutron diffraction and TEM are complementary techniques in the microstructure analysis.

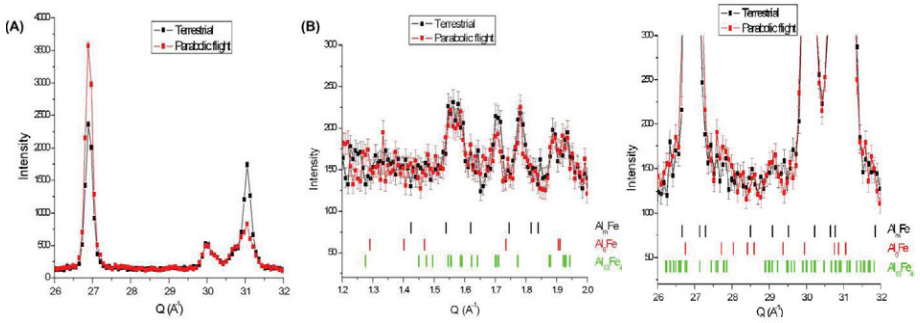

Figure 3. Neutron diffraction spectra of 1g Al–8Fe and PFC Al–8Fe together with Rietveld refinement calculated peaks in (B).

Neutron diffraction also shows a difference in intensity of the α–Al diffraction peaks at about 2.7 and 3.1 Å^{-1} between both samples (Figure 3 (A)). This indicates a difference in texture arising from the difference in solidification of the two samples. However, it seems there are no texture effects neither for Al_mFe nor $Al_{13}Fe_4$; the intermetallic crystals are small and randomly oriented and there is no orientation relationship between α–Al and Al_mFe or $Al_{13}Fe_4$ phases for both samples. Texture of the α–Al phase is also visible on the X-ray diffraction patterns shown in Figure 4 left. The relative intensity of the α–Al peaks in 1g Al–8Fe is almost identical to that of standard JCPDS data, meaning that the microstructure is randomly oriented. On the other hand, the spectrum of PFC Al–8Fe shows an opposite intensity sequence, highlighting a preferred orientation. This is confirmed by electron backscattered diffraction (EBSD, Figure 4 right). From the {110} pole figures it can be seen that the 1g Al–8Fe has a weak texture (C) while texture in sample PFC Al–8Fe is strong (D). This shows the effect of reduced fluid flow in microgravity experiments in this system.

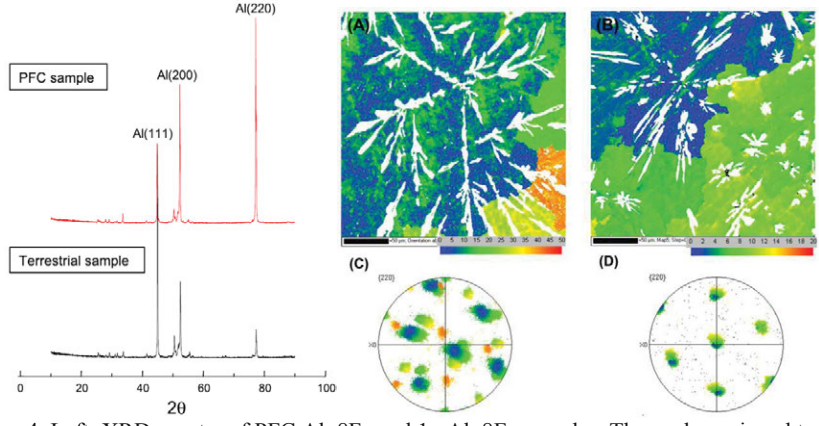

Figure 4. Left: XRD spectra of PFC Al–8Fe and 1g Al–8Fe samples. The peaks assigned to α–Al are marked. The unmarked peaks belong to $Al_{13}Fe_4$. Right: EBSD map of 1 g Al–8Fe (A) and PFC Al–8Fe (B) and their corresponding pole figure ((C) and (D)).

The images shown in Figure 5 are SEM micrographs of a 355 µm Al–8Fe droplet atomized in nitrogen. The microstructure looks somewhat similar to the PFC Al–8Fe sample. The primary intermetallic phase also has a star-like morphology but seems to be blockier. A lamellar α–Al/intermetallic eutectic can also be observed (B), as well as blade-shaped intermetallics in the α–Al matrix (as indicated by arrows in (C)). However, TEM investigation of this sample revealed that the star-shaped primary intermetallic in this case is the metastable Al_mFe, while the blade-shaped intermetallic is the stable $Al_{13}Fe_4$. Furthermore, the simulation of the selected area electron diffraction pattern suggests the intermetallic in the eutectic structure is Al_6Fe. The fact that Al_mFe becomes the major intermetallic phase over $Al_{13}Fe_4$ is confirmed by neutron diffraction (Figure 6). Indeed, the peaks at about 1.42, 1.55, and 1.81 $Å^{-1}$ can be attributed to Al_mFe and are much more pronounced than in the EML samples (Figure 3).

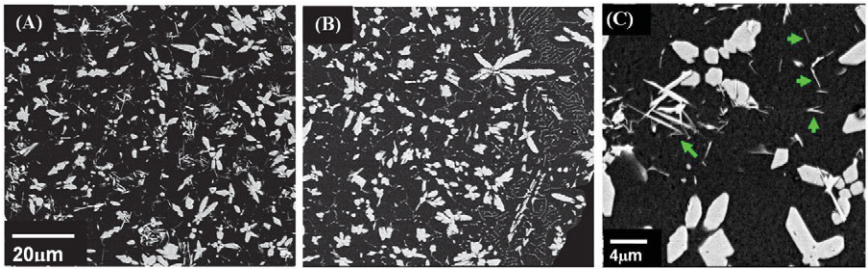

Figure 5. SEM micrographs of a 355 µm Al–8Fe droplet atomized in nitrogen.

According to the aluminum-rich end of the Al-Fe equilibrium phase diagram with metastable extensions, as calculated by Murray [8], we might expect the formation of primary $Al_{13}F_4$, metastable primary Al_6Fe, eutectic α–Al/$Al_{13}Fe_4$, metastable eutectic α–Al/Al_6Fe, or α–Al, depending on the melt undercooling at solidification. Although there is no metastable extension of Al_mFe in Murray's calculation, both differential scanning calorimetry and phase diagram calculation show that Al_mFe has lower metastable eutectic temperature than Al_6Fe [9]. Other research demonstrated that Al_mFe formed at higher cooling rate compared to that of Al_6Fe [10–11]. The existence of primary metastable Al_mFe and stable $Al_{13}Fe_4$ in both 1g and PFC Al–8Fe, as well as in the IA powders, indicates that the primary undercoolings achieved exceed the critical undercooling necessary to form Al_mFe. Otherwise, only stable $Al_{13}Fe_4$ would be present. After nucleation and growth of metastable Al_mFe during recalescence, the rest of the liquid solidifies under quasi-equilibrium conditions with the formation of the stable $Al_{13}Fe_4$ intermetallic. EML samples being much larger than IA droplets, it is expected that for a same undercooling and recalescence event, the proportion of metastable phase in the droplet volume would be larger in IA than in EML. The reason $Al_{13}Fe_4$ dominates the structure in both 1g and PFC Al–8Fe is thus assumed to be the long period of time it has for growth relative to Al_mFe in EML samples. The presence of a metastable α–Al/Al_6Fe eutectic in the IA experiments suggests that the falling droplets either experienced a larger eutectic undercooling than the EML samples or the phase is easier to detect in IA droplets because of the smaller sample volume and higher cooling rate they experience. This higher cooling rate would help retain any metastable structure formed during eutectic nucleation and recalescence.

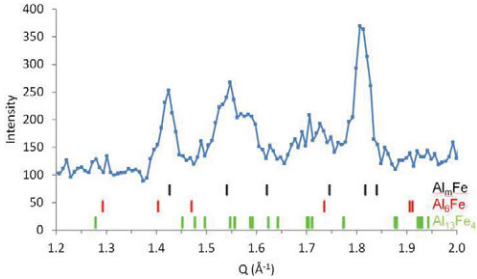

Figure 6. Neutron diffraction spectra of 355 µm Al–8Fe droplets atomized in nitrogen together with Rietveld refinement calculated peaks.

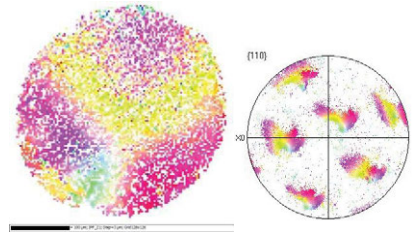

Figure 7. EBSD map and corresponding pole figure of a 355 µm Al–8Fe droplet atomized in nitrogen.

Figure 7 shows the EBSD map and corresponding pole figure of a 355 µm Al–8Fe droplet atomized in nitrogen. Similarly to the the PFC Al–8Fe sample, it can be seen that IA droplets have a strong texture. The pole figure suggests that the α–Al phase in the entire analyzed droplet is made up of one single grain. This again shows the effect of low convection and the similarity of IA experiments to reduced gravity experiments. The smearing of the pole most likely originates from a deformation of the lattice. This can be due to internal stresses occurring during rapid solidification as well as to stresses induced during the mechanical polishing of the sample.

Conclusions

The microstructures of Al–8wt%Fe samples solidified containerless using electromagnetic levitation under different gravity conditions as well as impulse atomization have been studied. The microstructures in EML samples feature primary star-like $Al_{13}Fe_4$ with α–Al/$Al_{13}Fe_4$ eutectic for the droplet experiencing microgravity while the droplet solidified under terrestrial condition is dominated by $Al_{13}Fe_4$ dendrites with α–Al/$Al_{13}Fe_4$ eutectic. Neutron diffraction analysis indicates that, besides the primary $Al_{13}Fe_4$, there is minor metastable Al_mFe (m = 4.0–4.4) in both samples. In the IA droplets, Al_mFe is the major primary intermetallic while $Al_{13}Fe_4$ becomes minor. The eutectic is comprised of α-Al and metastable Al_6Fe, indicating a possibly larger eutectic undercooling than in EML samples. In all cases, metastable Al_mFe is likely the first primary phase to form followed by $Al_{13}Fe_4$ after recalescence. Al_mFe is the dominant intermetallic in the IA droplets due to their small size. $Al_{13}Fe_4$ dominates the structure in both 1g and PFC Al–8Fe because of the long period of time it has for growth relative to Al_mFe in EML samples. This study also demonstrates and contrasts two containerless solidification methods. While it is possible to measure undercooling temperatures in EML, the large sample volume and low cooling rate make it difficult to retain or find the metastable phases in the sample. By contrast with IA, the small droplet sizes and thus their high cooling rate retain the metastable phases formed during undercooling and recalescence. Finally, this study shows that due to their small volume, limited convection occurs in IA droplets during solidification similarly to PFC–EML samples. This is seen in the similar strong texture of α–Al observed in IA and PFC–EML samples but not in the 1g–EML samples.

Acknowledgments

Financial support from the Canadian Space Agency FAST program and the European Space Agency within the NEQUISOL project under contract #4200015236 is acknowledged. Funding form the Natural Sciences and Engineering Research Council of Canada is also acknowledged.

References

[1] D.J. Skinner and K. Okazaki, Rapidly Solidified Powder Aluminum Alloys, ed. M.E. Fine and E.A. Starke Jr (Philadelphia: ASTM, 1986), 211
[2] C.M. Adam, J.W. Simon, and S. Langerbeck, Third Conference on Rapid Solidification Processing: Principles and Technologies, ed. R. Mehrabien (Washington, DC: National Bureau of Standards, 1983), 629
[3] E. Solis-Ramos, H. Jones, and W.M. Rainforth, Mater. Sci. Technol. 22 (2006) 1369
[4] Y. Barbaux and G. Pons, J. Phys. IV 3 (1993), 191
[5] D. M. Herlach, Solidification of Containerless Undercooled Melts, ed. D. M. Herlach and D. M. Matson (Weinheim: Wiley-VCH, 2012), 9–16
[6] H. Henein, Mat. Sci. Eng. A 326 (2002), 92–100
[7] J. Chen, R. Lengsdorf, H. Henein, D. M. Herlach, U. Dahlborg, and M. Calvo-Dahlborg, J. Alloys Compd. 556 (2013), 243–251
[8] J. L. Murray, MRS Symp. Proc. 19 (1983), 249
[9] C. A. Ahravci and M. O. Pekguleryuz, Calphad 22 (1998), 147–155
[10] R. M. K. Young and T. W. Clyne, Script. Metall. 15 (1981), 1211–1216
[11] A. Griger and V. Stefaniay, J. Mat. Sci. 31 (1996), 6645–6652

TMS2016

145th Annual Meeting & Exhibition

SUPPLEMENTAL PROCEEDINGS

Metal and Polymer Matrix Composites II

Nikhil Gupta
New York University

DEGRADATION STUDY OF HIGH MELT STRENGTH POLYPROPYLENE/CLAY NANOCOMPOSITES IN ENVIRONMENTAL AND ACCELERATED CONDITIONS

[1]Luiz Gustavo Hiroki Komatsu, [1]Duclerc Fernandes Parra, [1]Washington Luiz Oliani, [1]Ademar Benevolo Lugao, [2]Vijaya Kumar Rangari

[1]Nuclear and Energy Research Institute, IPEN-CNEN/SP
Av. Prof. LineuPrestes, 2242 – Cidade Universitária
CEP 05508-000, São Paulo – SP, Brazil
**dfparra@ipen.br*

[2]Center for Advanced Materials Science and Engineering Tuskegee University, AL 36088, USA

Keywords: Nanocomposites, Clay, Environmental Ageing, Thermal ageing

Abstract

The Polypropylene (PP) was initially modified by γ radiation or high melt strength PP. HMS-PP/ Cloisite 20 nanocomposites processed by melt mixing in twin-screw extruder derived samples to evaluate under environmental and thermal degradation conditions. PP-g-MA was the compatibilizing agent. The tests were conducted on dumbbell shaped samples under two different ageing conditions of degradation: environmental exposition and accelerated exposition. The morphology of aged samples was evaluated by XRD. TEM microscopy showed intercalation and exfoliation. Thermal degradation was studied by TGA. The DSC and the results showed decrease of melting point and increased crystallization under ageing conditions. The FTIR results showed the increase of carbonyl index related to the surface oxidation of the nanocomposites.

Introduction

Polypropylene is a polymer widely used in many applications, and their thermal, rheological, mechanical, and gas permeation properties need to be improved. A large number of studies have been focused in the promotion of a range of capabilities for automotive industries and with great potential for use in the aeronautical field [1].

The Toyota group reported formation of Polypropylene (PP) nanocomposites by direct melt mixing of organoclays based on montmorillonite (MMT) and PP grafted with maleic anhydride (PP-g-MA) [1].

The ageing process of the PP nanocomposites under environmental conditions has been studied by diverse researchers. Through those studies it was found that incorporation of nanoclays does not change the ageing mechanism of the composite, but rather decreases its induction time, meaning that MMT can accelerates the oxidation process. In other hand, the thermo-oxidation is induced by temperature. Concerning the ageing kinetics of nanofilled PP there are only a small number of studies in the literature [2].

In the present work the synthesis of nanocomposite used the High Melt Strength Polypropylene (HMSPP), obtained by gamma irradiation under acetylene atmosphere

[3]. The HMSPP/ nanocomposites were prepared by melt-blending in order to solve the lack of compatibility between the HMSPP and the MMT [4].
The samples were submitted to environmental and accelerated assay. The UV – radiation would cause a serious degradation in the nanocomposites and consequently weaken the strength of the material. It leads to the formation of free radicals that react by scission, causing brittleness. Consequently, it lowers the molecular mass of chains [5, 6]. As a result, physical changes can be seen on the degraded specimens or products such as change of color to yellowish or brown and formation of cracks.

Experimental

Materials and methods

The iPP pellets were manufactured by Braskem and added of compatibilizer agent, propylene maleic anhydride graft copolymer (PP-g-MA) supplied by Addivant (Polybond 3200). The clay filler was Cloisite 20 by BYK Additives Company, a montmorillonite clay modified with quaternary ammonium salt (95meq/100g). The iPP was placed in plastic bags with acetylene and irradiated in ^{60}Co gamma source at dose of 12.5 kGy in order to obtain the HMSPP. Two different formulations containing the clay were prepared and are represented in Table 1. The samples were prepared in molten state using a twin-screw extruder (Thermo Haake Polymer Laboratory) to incorporate the clay in the polypropylene. The operation temperatures were 170–200 ºC and speed ranging from 30 to 60 rpm. The dumbbell samples for testing were obtained from thermal molding pressure (80 bar and 190 ºC), for type IV dimensions according to ASTM D638-2014 [7]. After molding, the dumbbell samples were mounted in appropriated device for environmental and thermal ageing, as illustrated in Figure.1.

Table 1. Content of clay and compatibilizer used in the samples

Samples	Matrix	PP-g-MA / %	Cloisite 20 / %
H1	HMSPP	-	-
NC1	HMSPP	3	1
NC2	HMSPP	3	10

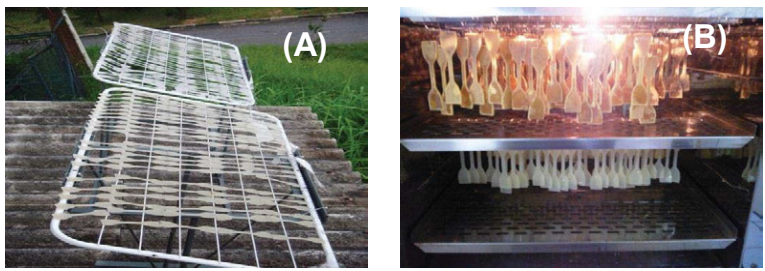

Figure 1. Exposition conditions:**(A)** Device with dumbbell samples for environmental ageing exposed outside at the IPEN/CQMA, and **(B)** nanocomposite samples in air circulation stove at the temperature of 110 ºC

X-ray diffraction (XRD)

X-ray diffraction measurements were carried out in the reflection mode on a Rigaku diffractometer Mini Flex II (Tokyo, Japan) operated at 30 kV voltage and a current of 15 mA with CuKα radiation (λ = 1,541841 Å).

Transmition Eletronic Microscopy – TEM
Samples prepared by crioultramicrotomy using a diamond knife cooled at -60°C used Leica Ultra Crio Microtomo - Reichert Ultracuts FC S. The transmission electron microscopy (TEM) image was obtained at 80 kV with a JEOL JEM-2100 in samples of 50nm.

Differential scanning calorimetry (DSC)
Thermal properties of specimens were analyzed using a differential scanning calorimeter (DSC) 822, Mettler Toledo. The thermal behavior of the films was obtained by the following program: heating from 25 to 280 ºC at a heating rate of 10 ºC min^{-1} under nitrogen atmosphere, according to ASTM D 3418-2015 [8]. The cristallinity was calculated according to the equation (1):

$$Xc = \mathrm{P} \times \frac{\Delta H_f \times 100}{\Delta H_0} \qquad (1)$$

Where: ΔH_f is melting enthalpy of the sample, P is the polymer fraction, ΔH_0 is melting enthalpy of the 100% crystalline PP which is assumed to be 209 kJ kg^{-1} [9, 10].

Thermogravimetric Analysis (TGA)
The TGA analysis was carried out in Mettler-Toledo TGA/SDTA 851 thermobalance under oxygen atmosphere of 50 mL min^{-1}, in the range from 25 up to 650 °C at a heating rate of 10 °C min^{-1}.

Fourier transformed Infrared spectroscopy (FTIR)
Infrared spectroscopy was performed at Thermo Scientific (Nicolet 6700) with ATR accessory Smart Orbit Diamond, in the range from 400 to 4000 cm^{-1}.

X-ray fluorescence (XRF)
The sample of Cloisite 20 was placed in a crucible in a muffle furnace at 900 °C to eliminate volatile components. One pastille, by pressing under one layer of boric acid was analyzed in spectrometer Rigaku Fluorescence X-ray, model RIX.

Results

In the X-ray Fluorescence was evidenced the composition of clay mainly as: SiO_2 (43%), Al_2O_3 (16. 8%) and Fe_2O_3 (3.6%). Those metallic ions act as pro-oxidant agents [11, 12].
The extrusion of PP and clay in presence of compatibilizer promoted the intercalation and exfoliation of the clay, according to the microscopy result, Figure 1.

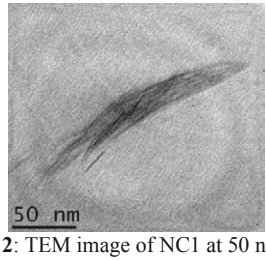

Figure 2: TEM image of NC1 at 50 nm scale.

The melting temperature (T_m), and the crystallinity (X_c) of the aged samples are presented in the Table 2 and Table 3, respectively, after environmental and thermal ageing. Two effects of the clay are operative on the nanocomposites ageing: one is the barrier effect; and the second is the catalytic effect of the clay on the oxidation process.

Table 2: DSC of samples aged in environment for 6 months

Months	T_m / °C				X_c / %			
	zero	1	2	6	Zero	1	2	6
H1	160.1±0.11	161.2±0.14	160.5±0.13	153.4±0.11	46.1±0.1	45.2±0.6	45.1±0.4	45.0±0.5
NC1	159.4±0.12	152.1±0.13	146.2±0.13	145.8±0.13	44.1±0.4	47.6±0.7	39.9±0.6	45.5±0.6
NC2	162.8±0.13	161.5±0.15	163.7±0.15	156.1±0.14	48.2±0.5	45.0±0.5	46.2±0.7	43.1±0.6

T_m = melt temperature; X_C = degree of crystallinity, as average of three samples.

Table 3: DSC of samples aged in stove with air circulation

Days	T_m / °C					X_c / %				
	Zero	7	14	49	56	zero	7	14	49	56
H1	160.0±0.15	162.0±0.14	162.0±0.11	159.5±0.15	-	46.0±0.4	47.7±0.6	47.8 ±0.6	49.8±0.8	-
NC1	159.4±0.13	159.1±0.15	141.0±0.10	-	-	44.1±0.5	49.8±0.5	46.8±0.7	-	-
NC2	162.8±0.15	162.4±0.16	163.2±0.10	161.2±0.16	140.5±0.14	48.0±0.5	45.5±0.7	44.4±0.5	43.8±0.6	41.0±0.4

T_m = melt temperature; X_C = degree of crystallinity, as average of three samples.

The catalytic effect of the clay, with chain scission and decrease of melt temperature, was more evident in the NC1, in both conditions. The cristallinity decreased mainly in the NC2 after 2 months of assay, as effect of dispersion of the clay in the matrix that difficult the chain segments to move from amorphous phase to crystallize. Also this result can be explained by formation of imperfects molecules; due to oxidation degradation and that defects difficult the crystallization.

Under these conditions the H1 was more stable compared to NC1, on attempt to catalytic effect of the ions in the clay. On the other hand the NC2 had more stability than NC1, in thermal degradation, owing to the barrier effect.

On TGA analysis, these two effects are observed by T_{onset}, represented in Table 4.

Table 4: Values of initial temperature of decomposition (T_{onset}) in samples aged under environmental or thermal conditions.

Environment Assay/Months	**H1**	**NC1**	**NC2**
	T_{onset} / ºC		
Zero	251.9	234.3	297.6
1	238.9	207.4	232.0
2	229.1	214.4	224.3
6	225.2	213.2	215.0
Thermal Assay/Days	T_{onset} / ºC		
7	238.4	218.0	222.0
14	235.8	205.9	220.5
49	228.6	-	224.0
56	-	-	213.3

Considering that the main difference between NC1 and NC2 is the clay content and that thermal ageing is one drastic condition, in comparison with environmental condition,

the observed effects on DSC results corroborated with that of TGA analysis. In the environmental ageing, the barrier effect was more intense at 2 months in NC2 than in NC1. In NC1, the decrease of T_{onset}, is due to the catalytic effect of the clay overlapping the barrier effect, according to Table 4.
In the thermal assay, the catalytic effect is more intense due to constant temperature and air circulation. In NC1, the assay stopped after 14 days, due to samples had disrupted in the stove. In the sample NC2, the catalytic effect of degradation occurs, however, the barrier effect was more intense. In fact, the higher content of clay can catalyze the oxidation on the polymer matrix. One explanation for this fact is that the sample has more exfoliated species than clusters [13].
On the H1 the T_{onset} decreases as effect of the chain scission caused by environment condition (UV, rain, etc) and also by temperature effects (air circulation and constant temperature in the stove).
With degradation of the polymer matrix, the formation of carbonyl species occurs. It is usually measured by FT-IR in which carbonyl index is calculated by the ratio of the absorbance area of carbonyl stretching at 1720 cm^{-1} and absorbance area at 2720 cm^{-1} [14]. The calculated values are showed in the Table 5.

Table 5: Carbonyl index of the samples calculated in FT-IR spectra

Environmental assay/Months	**H1**	**NC1**	**NC2**
1	0.7	0.5	1.9
2	0.6	6.9	1.8
6	18.7	4.9	9.7
Thermal Assay/Days			
7	0	8.3	1.7
14	0	4.2	1.9
49	2.1	-	2.1
56	-	-	2.9

Comparing the nanocomposites NC1 and NC2 with the polypropylene H1 is observed that barrier effect of the clay protect against oxidation. On other hand, under thermal ageing, in NC1 the higher carbonyl index can be justified due to the effect of the clay ions while the barrier effect inhibits the formation of oxidative groups in NC2.

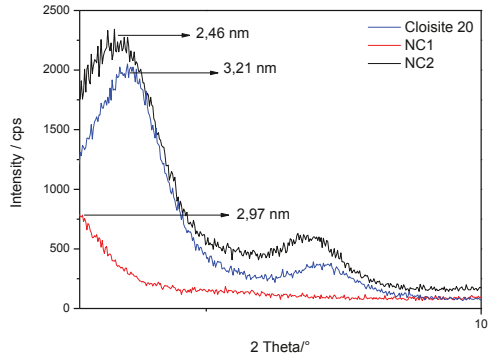

Figure 3- XRD spectra of the samples H1, NC1 and NC2.

The spectra of XRD of the samples, Figure 3, showed the comparison of NC1 and NC2 clay dispersion. In both occurred intercalation of polymer in the clay and exfoliation in the case of NC1 that corroborated with the TEM result (Figure 2).

Conclusion

In the thermal properties the nanocomposites has showed the competition of the effects of the clay as barrier and oxidation promoter. In terms of dispersion, the NC1 has showed better dispersion, as observed in the TEM image. The effects of this better dispersion can be observed on DSC results, but on other hand, this lower content of clay, promoted the acceleration of the oxidation process in thermal assay by insufficient barrier effect.

Acknowledgements

The authors thank CAPES/PROEX, FAPESP (2014/26393-1) and Capes for grants in SWB program, Centre of Science and Technology of Materials, the technicians Mr. Eleosmar Gasparin and Nelson R. Bueno, for technical support; Dr. Lidiane Costa from Sao Carlos University, for TEM samples preparation; BYK Additives Company; Braskem; Centre Lasers and Applications, CLA/IPEN for X-ray fluorescence analysis and CTR/IPEN for multipurpose gamma irradiation facilities.

References

[1] M. A. Perez, B. L. Rivas, S. M. Rodríguez, A. Maldonado, C. Venegas, "Polypropylene/Clay nanocomposites. Synthesis and Characterization," *Journal of the Chilean Chemical Society*, 55(2010), 440 - 444.

[2] G. Gutiérrez, B. Fayolle, G. Régnier, J. Medina, "Thermal oxidation of clay-nano reinforced polypropylene," *Polymer Degradation and Stability*, 95 (2010), 1708-1715.

[3] L. G. H. Komatsu, W. L. Oliani, A. B. Lugao, D. F. Parra, "Environmental ageing of irradiated polypropylene/montmorillonite nanocomposites obtained in molten state," *Radiation Physics and Chemistry*, 97(2014), 233-238.

[4] D. D. J. Rousseaux, N. Sallem-Idrissi, A. C. Baudouin, J. Devaux, P. Godard, J. Marchand-Brynaert, M. Sclavons, "Water-assisted extrusion of polypropylene/clay nanocomposites: A comprehensive study," *Polymer*, 52 (2011), 443-451.

[5] M. K. A. Sofiah, O. H. Lin, H. M. Akil, A. R. Villagracia, "Effect of compatibilizer on the accelerated weathering performance of polypropylene – silica nanocomposites," *Materials Research Innovations*, 18 (2014), 433-438.

[6] W. L. Oliani, D. M. Fermino, L. F. C. P. Lima, A. B. Lugao, D. F. Parra, "Effects of accelerated thermal aging on polypropylene modified by irradiation process," *TMS (Characterization of Minerals, Metals, and Materials)*, 2015, 651-658, DOI:10.1002/9781119093404.ch82.

[7] ASTM D638 (2014) – Standard test method for tensile properties of plastics.

[8] ASTM D3418 (2015) - Standard test method for transition temperatures and enthalpies of fusion and crystallization of polymers by differential scanning calorimetry.

[9] J. Brandrup; E. H. Immergut; E. A. Grulke. *Polymer Handbook.* Wiley Interscience; 1999.

[10] J. E. Mark, *Crystallization kinetics of polymer in Physical Properties of Polymers Handbook*, Springer, Cincinnati - USA, 639, 2007.

[11] J. K. Pandey, R. Reddy, A. P. Kumar, R. P. Singh, "An Overview on the degradability of polymer nanocomposites," *Polymer Degradation and Stability*, 88 (2005), 234-250.

[12] S. Molart, B. Mailhot, D. Gonzales, J. L. Gardette, "Photo-oxidation of polypropylene/montmorillonite nanocomposites. 1. Influence of nanoclay and compatibilizing agent," *Chemistry of Materials*, 16 (2004), 377-383.

[13] C. Zhao, H. Qin, F. Gong, M. Feng, S. Zhang, M. Yang, "Mechanical, thermal and flammability properties of polyethylene/clay nanocomposites," *Polymer Degradation and Stability*, 87 (2005), 183 -189.

[14] V. Camontagne, P. Dumas, V. Mouillet, J. Kister. "Comparison by fourier transform infrared spectroscopy (FTIR) of different ageing techniques: application to road itumen's," *Fuel*, 80(2001), 483-488.

Nanotube Sheet - Graphite Hybrid Nanocomposite for Damage Detection

Jiukun Li[1] and Sirish Namilae[2]
Aerospace Engineering Department
Embry-Riddle Aeronautical University
600 S. Clyde Morris Blvd., Daytona Beach, FL 32114, USA

Keywords: Nanocomposites, Peizoresistivity, Damage sensing

Abstract

In this study, we fabricate carbon nanotube (CNT) sheet – graphite powder hybrid nanocomposites and determine their strain dependent electrical resistivity for applications in damage sensing of aerospace composites. CNT sheet – graphite powder nanocomposites are prepared by epoxy resin infiltration under vacuum followed by oven curing. The electrical resistivity of the composites is measured while simultaneously subjecting it to tensile loading. The resistivity of the nanocomposite films without load reduces from about $34.7 \times 10^{-5} \Omega \cdot m$ to $8.1 \times 10^{-5} \Omega \cdot m$ by the addition of varying quantities of graphite powder. Additionally, the change in resistivity with tensile strain shows a significant improvement from $0.85 \times 10^{-5} \Omega \cdot m$ to $8.9 \times 10^{-5} \Omega \cdot m$ when epoxy resin is modified with 5 wt% graphite powder. There is an associated particle size effect. The improvements are observed only when the second phase is graphitic particles (300 -1000 μm) and not for fine graphene flakes (0.5 - 3 μm). We propose the application of these nanocomposites in damage sensing of aerospace carbon-fiber composites.

Introduction

Carbon nanotubes (CNTs), with their remarkable electrical and mechanical properties have attracted research interest since the landmark publication in 1991 by Iijima [1]. Commercial availability of large nanotube sheets (a few square meters in size) in recent times [2] has generated a renewed interest in the use of carbon nanotubes (CNTs) for bulk applications such as in aerospace composites. CNTs have been employed as fillers in a wide range of polymer matrices such as polyethylene [3] polypropylene [4], PEEK [5], PET [6] with the objective of improving mechanical properties and for functional applications based on electrical conductivity.

The discovery of the dramatic and convertible correlation between mechanical deformation and electrical resistance of individual carbon nanotubes [7] has led to the application of CNTs as actuators and strain sensing devices. Several publications discuss utilizing CNTs for strain sensing in the form of nanocomposites [e.g. 8]. Researchers have observed both linear and nonlinear variation of electrical resistance with the application of mechanical load for various matrix materials [8-11]. This piezo-resistive property of CNT composites has been utilized for applications such as gas identification [10] and cardiac and neurophysiological recording [11]. In these studies carbon nanotubes are directly dispersed in the matrix.

Because of the mass production of carbon nanotubes it is now possible to make carbon nanotube sheets in large sizes (few meters square) [2]. These CNT sheets or buckypaper consist of entangled carbon nanotube networks forming into a thin macroscopic membrane with the assistance of van der Waals interactions at the junction of nanotubes [12]. They have been fabricated using single-walled and multi-walled nanotubes both aligned and with random orientations and have been used to make composites with various polymeric matrices [e.g. 13, 14]. Researchers have demonstrated many applications of nanotube sheet composites including actuators [13], sensors [15] and artificial muscles [16].

[1] Graduate student, [2] Assistant Professor and corresponding author (namilaes@erau.edu)

Carbon fiber reinforced composites with epoxy matrix are the current materials of choice for the aerospace industry. While the reliability of composite products has increased significantly in the last decade, many manufacturing defects and in-service defects are commonly encountered such as wrinkles and delamination. The piezo-resistive property of CNT sheet composites can be utilized to detect damage in these structures. In this paper, we fabricate epoxy - CNT sheet - graphite powder and epoxy - CNT sheet - graphene composites and test their mechanical behavior and electrical conductivity. The second filler is added in an effort to increase the piezo-resistive response of the composite films. Epoxy matrix is used so that the nanocomposite films can be compatible with aerospace composite structures for damage sensing. The next section describes the experimental procedures followed by results and discussion.

Experimental Procedure

The multiwall carbon nanotube sheet (Buckypaper) consisting of 100% free standing nanotubes was procured form Nano Tech Labs. The product specifications mention area density of 21.7 g/m^2 and surface electrical resistivity of 1.5 Ω/ m^2. The electrical resistivity was independently verified in our experiments. The graphite particles used as the additional filler were prepared by finely chopping low resistance (2.8×10^{-2} Ω/ m^2) graphene sheet supplied by Graphene Supermarket. The suppliers report that this sheet (6 inch x 6 inch) is made out of multiple layers of nanoscale graphene flakes adhesively bonded together. The size of the chopped powder varied between 300 -1000 μm. The fine graphene flakes used in the experiments are carboxyl-Functionalized graphene nanoplatelets, also supplied by Graphene Supermarket. Scanning electron microscope micrographs indicate that these graphene flakes are much smaller than graphite powder and typical size of a flake is in the range of 0.5 - 3 μm. The epoxy resin used in this study is West System # 105 Epoxy Resin combined with West System # 206 Slow Hardener with a 20 minute working time and a resin to hardener ratio of 5:1. Silver-epoxy paste supplied by MG chemicals is used as a conducting adhesive.

The CNT sheet is cut into $6.35 \times 1.27 \times 10^{-2}$ m strip samples using a laser blade. Copper plates gauging 32 with dimension of $1.27 \times 1.27 \times 10^{-2}$ m are attached to both sides of the CNT sheet using by conductive silver- epoxy paste. The copper plates are used for conductivity measurement. These CNT sheets are placed on a peel-ply on a flat aluminum mold. The second filler particles (coarse graphene particles or graphene flakes) are mixed into the epoxy. Several of these epoxy mixtures are prepared with varying quantities of the second filler. Separate mixtures are made with resin and hardener in 1:5 volume ratio with (a) 5 wt% , (b) 10 wt % and (c) 15 wt% coarse graphene powder as well as (d) 5 wt% , (e) 10 wt % and (f)15 wt% graphene flakes. The evenly mixed resin-filler mix is then applied to both surfaces of the samples. It is then covered with another piece of peel-ply and breather film to remove the excess matrix. This setup is sealed under vacuum and a pressure of 88.05 KPa is provided by the vacuum system to assist the breathing film to absorb the extra epoxy. The samples are peeled after curing the resin for 12 hours at room temperature. Copper wires are soldered to the plates on either side to facilitate stable resistance measurement.

The resistance of nanocomposites samples with and without application of mechanical load is obtained by four point probe testing method according to IEEE and ASTM standard test methods [17-19]. This method works by forcing a current and measuring voltage (FCMV) using a four-wire Kelvin-connection scheme. The resistance of the sample is calculated using ohm's law by a passing controlled current (I) of 0.5A and recording a voltage drop (ΔV).

The tensile test for nanocomposite samples is performed using the CS-225 Digital Force Tester. A constant head speed of 0.16 mm/search is applied to the samples and the resistance

change is recorded as the sample is subject to loading is recorded simultaneously. Insulating pads are used between the copper plate and grips to isolate the sample for tensile loading.

Results and Discussion

1. Composite resistivity without load application

The electrical resistivity of the nanocomposite strips is obtained as:

$$\rho = R\ (w \times t)/l \quad (1)$$

Where R is the calculated resistance by ohm's law, w and t are the width and thickness of composite strips. l is the length of the composite strip. The thickness of the samples is obtained using SEM micrographs of cross sections as shown in Figure 1 (a). There is no significant variation in cross-section thickness between samples with different quantities of graphite powder and graphene flake fillers. An average thickness of 100 μm is used in the resistivity calculation. Figure 2 shows the resistivity of the clean buckypaper nanocomposite and buckypaper composite with different quantities of graphene flakes and graphite powder without any application of loading. The values reported are averaged from tests on three identical samples. Table 1 compares the resistivity values for neat buckypaper composite obtained in the current investigation with those from the literature. The resistivity of composites is comparable to similar values in literature, particularly there is a good correlation between values obtained in this study and that by Wang [19] and Chapartegui [20] with Epon862 and benzoxazine matrix materials. The resistivity of the neat CNT sheet without any matrix [19-21] and that with aligned nanotubes [22] is understandably lower than that of the composite in the current study.

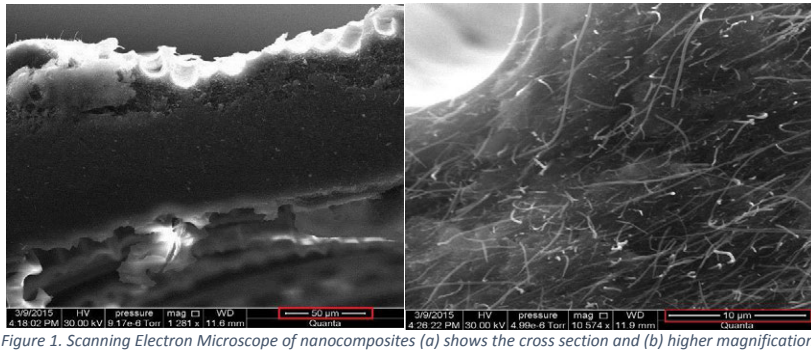

Figure 1. Scanning Electron Microscope of nanocomposites (a) shows the cross section and (b) higher magnifications showing nanotubes.

When the second conductive filler is added to the nanocomposite system the resistivity decreases, but there is a pronounced particle size effect. When the second phase filler is coarse graphite particles there is a significant decrease from 34.7×10^{-5} Ω·m to 13.4×10^{-5} Ω·m using the 5 % graphite powder- epoxy as the matrix. This further decreases as the content of filler is increased to 10 % and 15 %. Though there is a decrease in resistivity using graphene flakes to modify epoxy, the change in resistivity is an order of magnitude lower in comparison.

There are several theoretical models for e.g. by Kirkpatrick [23], McLachlan [24], Mamunya [25] that have been proposed to explain the resistivity (or conductivity) of composites with conductive fillers like carbon nanotubes. Kirkpatrick's model is based on contact between filler particles in a matrix and is given by

$$\sigma_m = \frac{1}{\rho_m} = A(\phi - V_{bc})^b \quad (2)$$

Where σ_m is the conductivity and ρ_m is the resistivity of the composite, A is the conductivity of the fillers, ϕ is volume fraction of the fillers, V_{bc} is the percolation threshold of filler, and b is an experimentally determined constant exponent and depends on the particle shape. This phenomological model has successfully explained conductivity of many particulate and fiber composites including carbon nanotube – polymer composites [26]. There is a significant increase in conductivity when the volume fraction of the filler particles is higher than the percolation threshold (V_{bc}) which represents the minimum quantity of filler to form a continuous network. The percolation threshold as well as the critical exponent have been known to vary depending on particle size [27]. Larger particle typically lowers the percolation threshold as smaller quantities of filler particles can result in a continuous network.

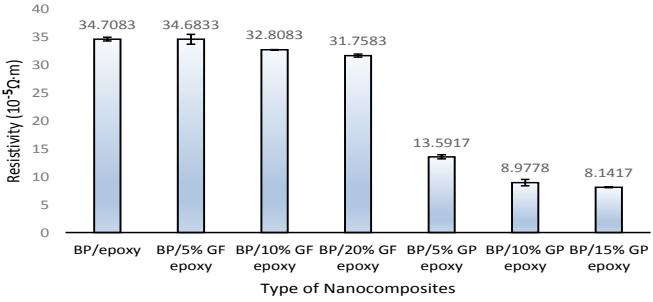

Figure 2. The resistivity of CNT sheet nanocomposites studied

Table 1. The resistivity of buckypaper composites from literature

Reference	Material	Resistivity (10^{-5} Ω·m)
Wang et al [29]	Magnetic aligned MWCNT buckypaper	1.13
Chapartegui et al[30]	Neat buckypaper	22.7
Chang et al [31]	Neat buckypaper	20.8
Wang et al [29]	MWCNT buckypaper/Epon862	39.2
Chapartegui et al[30]	MWCNT buckypaper / Benzoxazine	34.5
Chang et al [31]	MWCNT bucky paper /Parmax	10
Li et al [32]	Aligned MWCNT buckypaper/pCBT [46]	1.9

In the current study, the neat CNT sheet is a connected network therefore has low resistivity. Infiltrating the nonconductive epoxy into the CNT sheet results in reduced connectivity, therefore, increases the resistivity of the composite. Addition, of second conductive filler can reduce the conductivity by (a) increasing the volume fraction of conductive fillers ϕ and (b) reducing the percolation threshold V_{bc} . There is an increase in the content of conductive fillers with both coarse graphite powder and fine graphene flake addition to epoxy resin. In the case of larger graphite powder addition, there is a significant decrease in resistivity, potentially because the percolation threshold for the composite is also reduced. It is known that percolation threshold is lower when the filler particles are larger [27]. The larger size of graphite powder (300 -1000

μm) potentially modifies the percolation threshold in CNT sheet – graphite powder – Epoxy composite while this effect is not present in CNT sheet – graphene flake – Epoxy composite with fine graphene particles (1-3 μm). Results indicate that the coarse graphite powder bridges CNT network more effectively than the graphene flakes.

2. Piezo-resistivity of two-filler composite

Figure 3 shows the stress-strain and resistivity strain response of the graphite powder modified CNT-sheet-epoxy composites. Each dataset corresponds to an average of three samples as shown in Figure 4 for 5% graphite powder reinforced epoxy- buckypaper composite. The neat CNT sheet-epoxy composite shows a linear stress strain response followed by clean fracture at 5% strain. Addition of graphite powder to epoxy and CNT sheet increases the stiffness and strength of the composites. The improvement in stiffness reduces as the graphite powder content is increased. Also the strain at failure is lower (4.1%) when the graphite powder content is increased to 10 and 15 wt %. There is a corresponding increase in tensile strength to 16.12 MPa from 7.28 MPa for neat CNT sheet composite for 15% graphite powder modification. Even with a 5% modification of epoxy matrix the tensile strength increases to 10.28 MPa.

The resistivity of the composites without load application reduces as the quantity of graphite powder in epoxy resin increases. There is a clear increase in resistance with load application in neat CNT-sheet composites from 35.2×10^{-5} Ω·m to 36.03×10^{-5} Ω·m. This effect is increased by an order of magnitude when the epoxy resin is modified by 5 wt% graphite powder addition. The resistivity increases from 18.1×10^{-5} Ω·m to 26.8×10^{-5} Ω·m. There is a similar increase for 10 wt % and 15 wt % graphite powder modified epoxy resin composites, however the change in resistance is highest for 5 wt% graphite powder.

Figure 5 shows the stress-strain and resistivity-strain response of nanotube sheet –epoxy resin composite modified with fine graphene flakes. There is a small increase in stiffness with the addition of graphene flakes, but not as big an increase as that observed with course graphite powder. The strain to failure decreases from 5 % to 4.6 %. Unlike with coarse graphite powder there is no appreciable increase in tensile strength, in fact, tensile strength decreases marginally from 7.28 MPa to 6.59 MPa and 6.404 MPa to 5% and 10% graphene flake modifies resin mixtures.

There is an increase in piezo-resistive response with the graphene flake addition, for example with 5% addition of graphene flakes in resin, the resistivity changes from 32.9×10^{-5} Ω·m to 34.16×10^{-5} Ω·m. The comparable numbers for neat CNT sheet composite are 35.2×10^{-5} Ω·m to 36.03×10^{-5} Ω·m. Though there is a marginal increase, this is not on the same scale as that observed for coarse graphite particles.

There has been a significant research effort over the past decade in using carbon nanotubes as fibers for structural composites. While the carbon nanotubes by themselves have excellent strength, stiffness, the predicted mechanical properties have not yet been realized in nanotube composites. This is because of microstructural problems related to fiber–matrix interfacial strength, dispersion of nanotubes within composite and alignment of the nanotubes in the loading direction. There have been efforts to improve all three aspects, by approaches like functionalization [28], use of surfactants [29] and magnetic or mechanical alignment [19]. Present effort represents another way to improve the mechanical properties by addition of second filler.

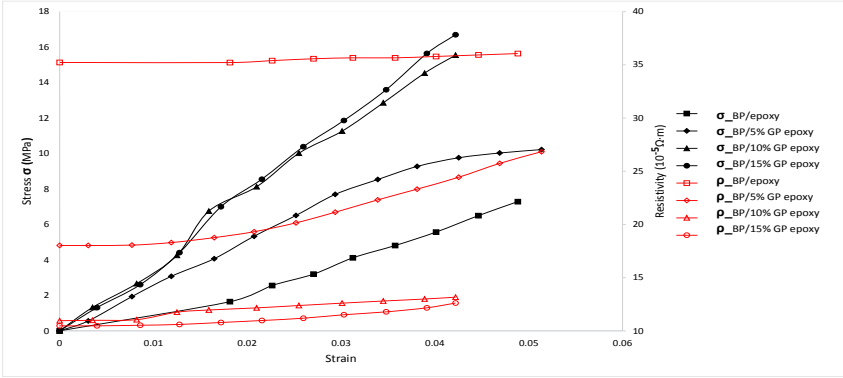

Figure 3. Stress & resistivity for various content of Graphene powder epoxy mixture impregnated Buckypaper

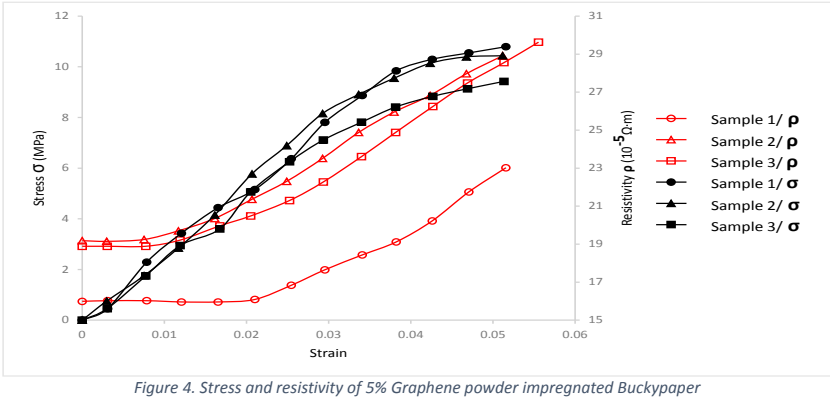

Figure 4. Stress and resistivity of 5% Graphene powder impregnated Buckypaper

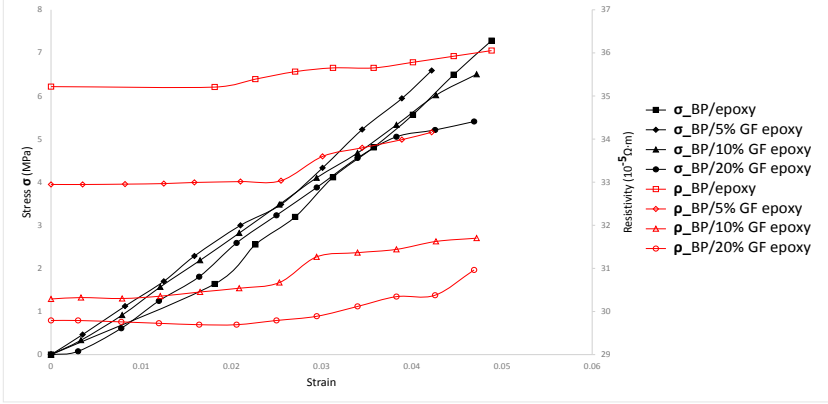

Figure 5. Stress & resistivity for various content of Graphene flakes epoxy compounds prepared Buckypaper

The changes in electrical resistivity with the application of load presents opportunities for many applications in structural health monitoring of aerospace composites. Specifically the order of magnitude increase in resistivity change under tensile loading with the addition of 5 wt% graphene powder to the composite reduces the strain level required to measure resistivity changes for these applications. Though CNTs exhibit intrinsic peizoresistivity [7] researchers have often attributed the change in resistance to modifications of interactions between carbon nanotubes in the network [30]. The addition of second phase particles enhances this effect, therefore an increase in resistivity change is observed for the two fillers considered in this study. There is however much more pronounced change with coarse graphite powder. The breakup of contacts between a large particle and CNT network under loading can affect a larger area of the composite, therefore the piezoresistivity is more pronounced with the addition of coarse particles.

Conclusion

Addition of coarse graphitic particles as a second filler to CNT sheet- epoxy composites results in strength increase and reduction in the resistivity. Further, the change in resistivity with tensile strain shows a significant improvement from 0.85 $x10^{-5}\Omega\cdot m$ to $8.9x10^{-5}\Omega\cdot m$ with 5 wt% graphite powder addition. This has potential applications in composite damage detection.

References

1. S. Iijima, “Helical microtubules of graphitic carbon,” Nature, 354 (1991), 56–58.
2. De Volder, M. F., Tawfick, S. H., Baughman, R. H., & Hart, A. J. (2013). Carbon nanotubes: present and future commercial applications. Science, 339(6119), 535-539.
3. Y. Bin, M. Kitanaka, D. Zhu, and M. Matsuo, “Development of Highly Oriented Polyethylene Filled with Aligned Carbon Nanotubes by Gelation/Crystallization from Solutions,” Macromolecules, 36 (2003), 6213–6219.
4. Z.-J. Wang, D.-J. Kwon, G.-Y. Gu, H.-S. Kim, D.-S. Kim, C.-S. Lee, K. L. DeVries, and J.- M. Park, “Mechanical and interfacial evaluation of CNT/polypropylene composites and monitoring of damage using electrical resistance measurements,” 81 (2013),69–75.
5. M. Mohiuddin and S. Van Hoa, “Electrical resistance of CNT-PEEK composites under compression at different temperatures,” Nanoscale Res. Lett., 6 (2011), 419–419.
6. S. Yesil and G. Bayram, “Poly(ethylene terephthalate)/carbon nanotube composites prepared with chemically treated carbon nanotubes,” Polym. Eng. Sci., 51 (2011), 1286.
7. T. W. Tombler, C. Zhou, L. Alexseyev, J. Kong, H. Dai, L. Liu, C. S. Jayanthi, M. Tang, and S.-Y. Wu, “Reversible electromechanical characteristics of carbon nanotubes under local-probe manipulation,” Nature, 405 (2000), 769–772.
8. Y.-T. Huang, S.-C. Huang, C.-C. Hsu, R.-M. Chao, and T. K. Vu, “Design and Fabrication of Single-Walled Carbon Nanonet Flexible Strain Sensors,” Sensors, 12 (2012), 3269.
9. C. Li, E. T. Thostenson, and T.-W. Chou, “Sensors and actuators based on carbon nanotubes and their composites: A review,” Compos. Sci. Technol., 68 (2008), 1227.
10. S. Kim, “CNT Sensors for Detecting Gases with Low Adsorption Energy by Ionization,” Sensors, 6 (2006), 503–513.
11. R. Gerwig, K. Fuchsberger, B. Schroeppel, G. S. Link, G. Heusel, U. Kraushaar, W. Schuhmann, A. Stett, and M. Stelzle, “PEDOT-CNT Composite Microelectrodes for Recording and Electrostimulation Applications:” Front. Neuroengineering, 5 (2012), 8.
12. M. Chapartegui, J. Barcena, X. Irastorza, C. Elizetxea, M. Fernandez, and A. Santamaria, “Analysis of the conditions to manufacture a MWCNT buckypaper/benzoxazine nanocomposite,” Compos. Sci. Technol., 72 (2012), 489–497.

13. C.-Y. Chang, E. M. Phillips, R. Liang, S. W. Tozer, B. Wang, C. Zhang, and H.-T. Chiu, "Alignment and properties of carbon nanotube buckypaper/liquid crystalline polymer composites," J. Appl. Polym. Sci., 128 (2013), 1360–1368.
14. Q. Wu, C. Zhang, R. Liang, and B. Wang, "Fire retardancy of a buckypaper membrane," Carbon, 46 (2008), 1164–1165.
15. H. Papa, M. Gaillard, L. Gonzalez, and J. Chatterjee, "Fabrication of Functionalized Carbon Nanotube Buckypaper Electrodes for Application in Glucose Biosensors," Biosensors, 4 (2014), 449.
16. U. Vohrer, I. Kolaric, M. Haque, S. Roth, and U. Detlaff-Weglikowska, "Carbon nanotube sheets for the use as artificial muscles," Eur. Mater. Res. Soc. 2003 Symp. B Adv. Multifunct. Nanocarbon Mater. Nanosyst., 42 (2004), 1159–1164.
17. "IEEE Standard Test Methods for Measurement of Electrical Porperties of Carbon Nanotubes," *IEEE*, 2005.
18. "Standard Test Method for D-C Resistance or Conductance of Moderately Conductive Materials," *ASTM*, 2004.
19. S. Wang, "Characterization and Analysis of Electrical Conductivity Properties of Nanotube Composites," Florida State University, 2015.
20. M. Chapartegui, J. Barcena, X. Irastorza, C. Elizetxea, M. Fernandez, and A. Santamaria, "Analysis of the conditions to manufacture a MWCNT buckypaper/benzoxazine nanocomposite," *Compos. Sci. Technol.*, 72 (2012), 489–497.
21. C.-Y. Chang, E. M. Phillips, R. Liang, S. W. Tozer, B. Wang, C. Zhang, and H.-T. Chiu, "Alignment and properties of carbon nanotube buckypaper/liquid crystalline polymer composites," *J. Appl. Polym. Sci.*, 128 (2013), 1360–1368.
22. Z. Li, R. Downes, and Z. Liang, "In Situ Polymerized pCBT Composites with Aligned Carbon Nanotube Buckypaper: Structure and Properties," *Macromol. Chem. Phys.*, 216 (2015), 292–300.
23. S. Kirkpatrick, "Percolation and Conduction," Rev Mod Phys, 45 (1973), 574–588.
24. D. S. McLachlan, M. Blaszkiewicz, and R. E. Newnham, "Electrical Resistivity of Composites," J. Am. Ceram. Soc., 73 (1990), 2187–2203.
25. Y. P. Mamunya, V. V. Davydenko, P. Pissis, and E. V. Lebedev, "Electrical and thermal conductivity of polymers filled with metal powders," European Polymer Journal, 38 (2002), 1887–1897.
26. R. Vargas-Bernal, G. Herrera-Pérez, M. E. Calixto-Olalde, and M. Tecpoyotl-Torres, Analysis of DC Electrical Conductivity Models of Carbon Nanotube-Polymer Composites with Potential Application to Nanometric Electronic Devices. 2013.
27. G. P. Moriarty, J. H. Whittemore, K. A. Sun, J. W. Rawlins, and J. C. Grunlan, "Influence of polymer particle size on the percolation threshold of electrically conductive latex-based composites," J. Polym. Sci. Part B Polym. Phys., 49 (2011), 1547–1554.
28. Namilae, S., & Chandra, N. (2005). Multiscale model to study the effect of interfaces in carbon nanotube-based composites. Journal of Engineering materials and technology, 127(2), 222-232.
29. Kim, S. W., Kim, T., Kim, Y. S., Choi, H. S., Lim, H. J., Yang, S. J., & Park, C. R. (2012). Surface modifications for the effective dispersion of carbon nanotubes in solvents and polymers. *Carbon*, *50*(1), 3-33.
30. M. D. Rein, O. Breuer, and H. D. Wagner, "Sensors and sensitivity: Carbon nanotube buckypaper films as strain sensing devices," Compos. Sci. Technol., 71 (2011), 373–381.

EFFECT OF NANO-PARTICLE ADDITION ON GRAIN STRUCTURE EVOLUTION OF FRICTION STIR PROCESSED Al 6061 DURING POST-WELD ANNEALING

Guo Junfeng[1], Lee Bing Yang[1], Du Zhenglin[2], Bi Guijun[1], Tan Ming Jen[2], Wei Jun[1]

[1]Singapore Institute of Manufacturing Technology
71 Nanyang Drive, Singapore 638075

[2]Nanyang Technological University, 50 Nanyang Avenue, Singapore 639798

Keywords: Friction stir processing; Nano-composites; Grain structure; Abnormal grain growth

Abstract

The fabrication of nano-composites is quite challenging because uniform dispersion of nano-sized reinforcements in metallic substrate is difficult to achieve using powder metallurgy or liquid processing methods. In the present study, Al-based nano-composites reinforced with Al_2O_3 particles have been successfully fabricated using friction stir processing. The effects of nano-Al_2O_3 particle addition on grain structure evolution of friction stir processed Al matrix during post-weld annealing were investigated. It was revealed that the pinning effect of Al_2O_3 particles retarded grain growth and completely prevented abnormal grain growth during post weld annealing at 470 °C. However, abnormal grain growth can still occur when the composite material was annealed at 530 °C. The mechanism involved in the grain structure evolution was discussed therein.

1. Introduction

It has been reported that abnormal grain growth (AGG) could occur during the post weld heat treatment (PWHT) of friction stir welds. Abnormal grain growth alternatively known as secondary recrystallization, takes place in recrystallized materials at high temperatures during annealing. This process may lead to the formation of large grains of even greater than several millimeters [1], which causes negative effects for mechanical property, especially the formability of material. A review of this phenomenon in friction stir welded joints could be found in the work of Y.S. Sato et al. [2]. Kh.A.A. Hassan et al. [3] studied the stability of friction stir welded AA7010 alloy during solution treatment. It was concluded that the abnormal grain growth might be promoted by the fine grain structure in nugget zone and the partial dissolution of second phase particles during solution treatment. It was also revealed that the rotation speed and the welding speed can be used as a tool to control abnormal grain growth during subsequent heat treatment [4]. According to Humphreys [5], an obvious and effective solution to prevent abnormal grain growth would be to increase the particle pinning pressure by increasing the density of stable second phase particles (increase the ratio of F_v/d, where F_v is the volume fraction of second phase particle and d is the particle diameter). However, addition of such fine particles into metal

matrix is quite challenging because uniform dispersion of nano-sized reinforcements in metallic substrate is difficult to achieve by using conventional powder metallurgy or liquid processing methods [6, 7]. Over past few years, friction stir processing (FSP) method has attracted much attention since the first attempt on fabrication of nano-particles reinforced metal matrix composites (MMC) [8].

Friction stir processing, a relatively new processing technique, was developed for microstructural modification based on the basic principles of friction stir welding (FSW) [9, 10]. Similar to friction stir welding, FSP is carried out by using a rotating non-consumable tool plunging into the workpiece. The heat generated by the friction between welding tool and workpiece will plasticize the material, but the workpiece never melts. A volume of material can then be processed as the tool travels forwards. The concept of fabricating MMCs by FSP is considered to be beneficial as undesirable intermetallics formation between reinforcement and matrix can be avoided [11, 12]. Our previous work showed that multi-pass FSP could uniformly disperse nano-sized particles into aluminum matrix. More pronounced grain refinement and significant increases in microhardness and tensile strengths were observed in comparison with the Al matrix in the same condition. Nonetheless, the effects of nano-particles addition on grain structure evolution of friction stir processed Al matrix during post-weld annealing has yet been reported. The present study aims to investigate the pinning behavior of Al_2O_3 particles during post-weld annealing of friction stir processed Al matrix. The grain structures of the friction stir processed Al without/with particle addition were compared before/after annealing.

2. Experimental Procedures

Rolled plates of AA6061 alloy and nano-sized Al_2O_3 particles (nominal diameter: 320 nm) were used as base materials. The Al plates were cut into dimensions measuring 300 mm long and 100 mm wide (rolling direction). An array of 960 cylindrical holes measuring 1 mm in diameter, 2 mm in depth was machined in an area of 240 mm x 50 mm as reservoir to hold the Al_2O_3 particles for FSP. All plates were then carefully degreased with acetone and dried in air. Alumina slurry with a concentration of 50 vol.% was prepared by step-wise addition of alumina nano-powder (Sumitomo-AKP30, Japan) to deionized water during ball milling. 0.5wt% Dolapix CE64 (Zschimmer & Schwarz, Germany) was added as a dispersant. The prepared slurry was squeezed into the holes in aluminum plates and dried in a convection oven at 110 °C for 2 h. The density of the dried slurry in the holes was estimated to be 2.189 g/cm^3. The nominal volume fraction of the reinforcement in the composite produced by FSP is around 14%. However, the actual particle concentration could be slightly lower than this value because of the particle loss during FSP ($F_V = 0.12$ will be used for later calculations).

Friction stir processing is carried out using a robotic friction stir welding machine (Friction Stir Link, ABB IRB7600 Robot) which is capable of generating up to 12 kN downward force. The welding tool has a shoulder with 12.5 mm diameter and a threaded conical probe with three flats (2 mm probe length and 5 mm diameter at probe base). In order to uniformly disperse nano-particles in the matrix, four passes FSP tests were conducted at a rotation speed of 1200 rpm,

travel speed of 3 mm/s, tilt angle of 2.5° and downward force of 3.6-4.2 kN. The friction stir processed specimens were then annealed at 470 °C and 530 °C respectively for one hour.
Metallographic samples were transversely sectioned from the specimens and polished using conventional mechanical polishing method. Microstructural characterization was performed using a scanning electron microscope (EVO-50 & ULTRA plus, Carl Zeiss) equipped with electron backscattered diffraction (EBSD). For EBSD analysis, a further electro-polishing after mechanical polishing was carried out using a mixture of 80% alcoholic and 20% $HClO_4$ for 5-20 s at ambient temperature. The voltage during electro-polishing was fixed at 15 V while the current was not controlled. Step size between 0.2-1 μm was used during data acquisition.

3. Results & Discussion

3.1 Microstructures before annealing

Fig. 1 shows the SEM images of the base metal and the friction stir processed Al without/with Al_2O_3 particle addition. Some Al-Fe containing intermetallics scatter in the base metal (Fig. 1a). Invisible change is observed after FSP though it is believed that FSP might have redistributed these intermetallics. As seen in Fig. 1c, uniform dispersion of Al_2O_3 particle (white color) was obtained through multi-pass FSP.

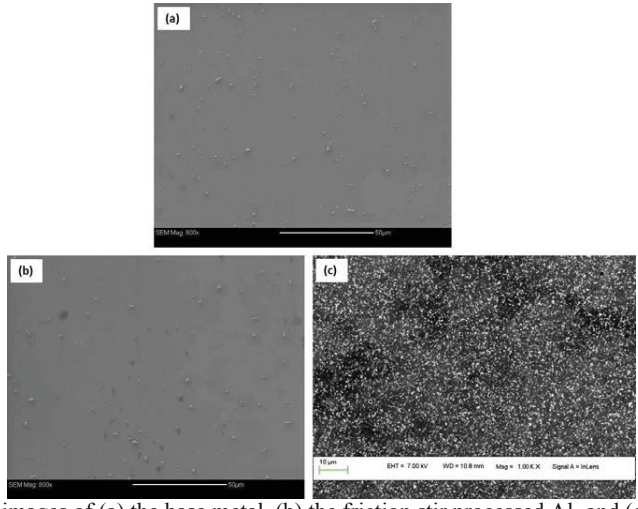

Fig. 1 SEM images of (a) the base metal, (b) the friction stir processed Al, and (c) friction stir processed Al with Al_2O_3 particle addition.

The grain structure of the base metal and the friction stir processed Al without/with Al_2O_3 particle addition is shown in Fig. 2. Significant grain refinement was observed in the friction stir processed specimens as compared to that of base metal. The equivalent grain size diameters were

obtained through EBSD analysis over around 1000 grains with grain boundary angle larger than 15 °. The average grain size in the base metal and the friction stir processed Al without/with Al_2O_3 particle addition are 70±3 μm, 5.9±0.2 μm, 2.5±0.1 μm respectively. This grain refinement can be attributed to continuous dynamic recrystallization in which a continuous introduction of strain is coupled with rapid recovery and migration of subgrain/grain boundaries. It is worth noting that more pronounced reduction in grain size was characterized in the specimen with Al_2O_3 particle addition. The large amount of nano-sized Al_2O_3 particles acted as nucleation sites during dynamic recrystallization and thus promoted formation of new grains. In addition, some of these Al_2O_3 particles might also exert strong pinning pressure to the grain boundaries and limit grain growth. The grain boundary misorientation distribution for the friction stir processed Al without/with Al_2O_3 particle addition is shown in Fig. 3. The specimen with particle addition contains much higher fraction of low angle grain boundaries. It was suggested by Tweed et al. [13] that the interaction between the pinning particles and grain boundaries is very complicated. In their study, a relatively high fraction of high angle boundaries were found to be unpinned, all the low angle boundaries analyzed were found to exhibit pinning interactions. This is probably the reason why in the present study, the number of low-angle boundaries (<= 15 °) increased significantly with the addition of alumina particles. For high angle grain boundaries, the high energy of such type grain boundary could curve the boundary plane when it touches a second phase inclusion, which allows bypassing long before the boundary as a whole is bent into a half circle. In contrast, the lower energy and higher flexibility of a low angle grain boundary leads to a more perturbed boundary plane. The process of migration of a low angle grain boundary is a cooperative process relying on the sequential movement of the constituent dislocations.

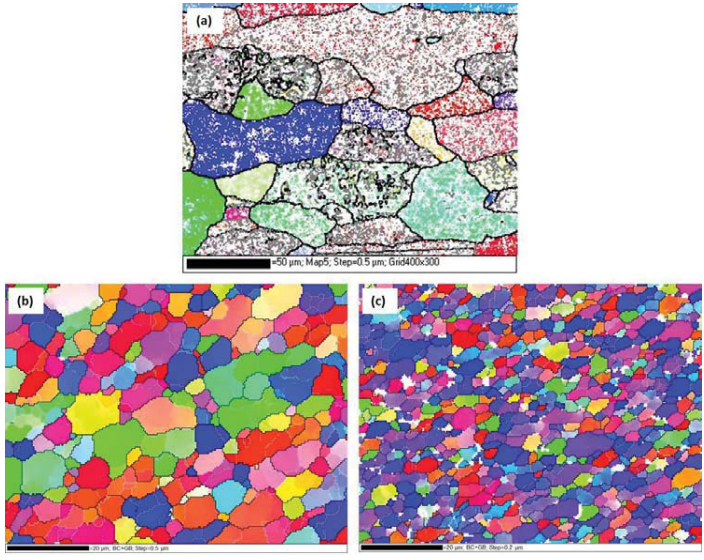

Fig. 2 Grain structure of (a) the base metal, (b) the friction stir processed Al, and (c) friction stir processed Al with Al_2O_3 particles addition.

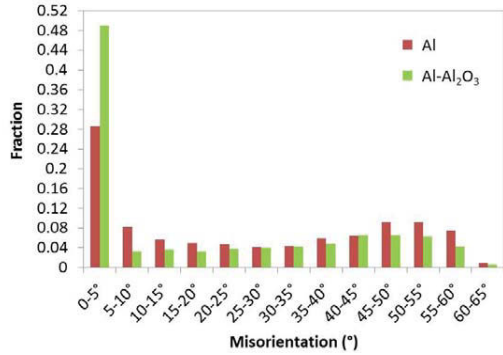

Fig. 3 Grain boundary misorientation distribution for the friction stir processed Al without/with Al_2O_3 particle addition

3.2 Microstructures after annealing

The friction stir processed Al specimens without/with Al_2O_3 particle addition were then annealed at 470 °C and 530 °C using an air furnace. Both specimens showed similar morphology under SEM compared to those of specimens before annealing (Fig. 1b & c). The grain structures however changed drastically, as shown in Fig. 4. For specimens annealed at 470 °C, the friction stir processed Al specimen without Al_2O_3 particle exhibited abnormal grain growth, as shown in Fig. 4a. Large grains with equivalent diameter up to 1 mm can be observed. Such abnormal grain growth is mainly driven by the stored energy in the drastically deformed fine grain boundaries. It is interesting to note that the friction stir processed Al specimen with Al_2O_3 particles only showed slight growth to around 3-4 μm although their initial grains were actually finer than the specimen without particle (Fig. 4b). This is mainly attributed to the pinning pressure of large amount of Al_2O_3 particles has stopped grain boundary migration although the driving force of the initial grains is higher than the specimen without Al_2O_3 particles. In contrast, for specimens annealed at 530 °C, both specimens without/with Al_2O_3 particles showed abnormal grain growth in the friction stir processed zone as shown in Figs. 4c & 4d. At high annealing temperatures, the energy of grains boundaries increased tremendously. Thus the grains boundaries could pass the pinning particles very easily as the effectiveness of particle pinning have decreased substantially.

According to Humphreys [1,5], stable second phase particles may exert a pinning effect during grain boundary migration and thus prevent the occurrence of abnormal grain growth. In a cellular microstructure containing second phase particles, abnormal grain growth will occur if an individual cell grows faster than the surrounding matrix of average cells, which can be described as

$$\bar{R}\frac{dR}{dt} - R\frac{d\bar{R}}{dt} > 0 \qquad (1)$$

Where R, $\bar{R}$, dR/dt and $d\bar{R}/dt$ are the cell radius and the growth rates of the cell and the surrounding average cells.

$$\frac{dR}{dt} = M\left(\frac{\bar{\gamma}}{\bar{R}} - \frac{\gamma}{R} - \frac{3F_v\gamma}{d}\right) \qquad (2)$$

$$\frac{d\bar{R}}{dt} = \bar{M}\bar{\gamma}\left(\frac{1}{4\bar{R}} - \frac{3F_v}{d}\right) \qquad (3)$$

Where γ and $\bar{\gamma}$ are the boundary energies of the individual and average matrix cells. In a friction stir processed zone, $\gamma = \bar{\gamma}$, normal grain growth of the matrix will stagnate when $d\bar{R}/dt = 0$. Under such conditions, abnormal grain growth of an individual grain can still occur provided it has a sufficient size differential ($X = R/\bar{R}$) over its surrounding neighbors, which gives

$$\bar{R}\frac{dR}{dt} > 0 \qquad (4)$$

Rearrangement of (2) and (4) gives

$$\bar{R} < \frac{d}{3F_v}\left(1 - \frac{1}{X}\right) \qquad (5)$$

Where d is the equivalent particle size diameter. In the present study, d = 0.32, F_v = 0.12, the maximum X = 5 (as measured by EBSD analysis), abnormal grain growth will easily occur as long as $\bar{R} < 0.7$ μm. Obviously, the Al_2O_3 particles added in the matrix can provide sufficient pinning pressure to stop abnormal grain growth under relatively low annealing temperatures. However, at high annealing temperatures, the effectiveness of particle pinning has decreased substantially, which increases the critical $\bar{R}$ tremendously and makes abnormal grain growth possible.

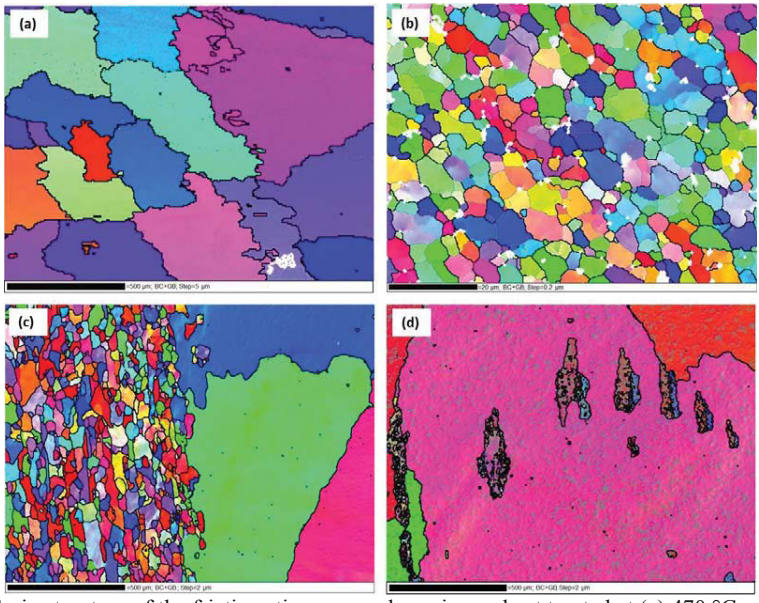

Fig. 4 Grain structure of the friction stir processed specimens heat treated at (a) 470 °C without particle, (b) 470 °C with Al_2O_3 particle, (c) 530 °C without particle, (d) 530 °C with Al_2O_3 particle addition.

4. Conclusions

In the present study, the effects of nano-Al_2O_3 particle addition on grain structure evolution of friction stir processed Al matrix during post-weld annealing were investigated. The following conclusions can be drawn based on the above results and discussion.

a. Uniform dispersion of Al_2O_3 particles (white color) was obtained through multi-pass FSP;
b. Addition of Al_2O_3 particles exerted strong pinning pressure to the grain boundary and thus led to more pronounced grain size reduction;
c. The pinning effect of Al_2O_3 particles completely prevented abnormal grain growth during post weld annealing at 470 °C. However, the effectiveness of the pinning decreased substantially and abnormal grain growth can still occur at 530 °C.

5. References

[1] F.J. Humphreys and M. Hatherly, “Recrystallization and related annealing phenomena”, 2nd edition, Elsevier Ltd., 2004.

[2] Y.S. Sato, H. Watanabe and H. Kokawa, “Grain growth phenomena in friction stir welded 1100 Al during post-weld heat treatment”, Science and Technology of Welding and Joining, Vol. 12, No. 4, 2007, pp. 318-323.
[3] Kh. A.A. Hassan, A.F. Norman, D.A. Price and P.B. Prangnell, “Stability of nugget zone grain structures in high strength Al alloy friction stir welds during solution treatment”, Acta Materialia, Vol. 51, No. 7, 2003, pp. 1923–1936.
[4] M.M. Attallah and H.G. Salem, “Friction stir welding parameters: a tool for controlling abnormal grain growth during subsequent heat treatment”, Materials Science and Engineering A, Vol. 391, No. 1-2, 2005, pp. 51–59.
[5] F.J. Humphreys, “A united theory of recovery, recrystallization and grain growth, based on the stability and growth of cellular microstructures - II. the effect of second-phase particles”, Acta materialia. Vol. 45, No. 12, 1997, pp. 5031-5039.
[6] N. Chawla, K.K. Chawla, Metal Matrix Composites, Springer, New York, 2006.
[7] S.R. Bakshi, D. Lahiri, A. Agarwal, International Materials Reviews, 55 (2011) 41-64.
[8] R.S. Mishra, Z.Y. Ma, I. Charit, Materials Science and Engineering A, A341 (2003) 307-310.
[9] R.S. Mishra, Z.Y. Ma, Materials Science and Engineering R, 50 (2005) 1-78.
[10] Z.Y. MA, Metallurgical and Materials Transactions A, 39A (2008) 642-658.
[11] J. Guo, P. Gougeon, X.-G. Chen, Materials Science & Engineering A, 553 (2012) 149-156.
[12] E.R.I. Mahmoud, M. Takahashi, T. Shibayanagi, K. Ikeuchi, Wear, 268 (2010) 1111-1121.
[13] C.J. Tweed, B. Ralph, N. Hansen, Acta Metallurgica, 32 (1984) 1407-1414.

ENHANCED DUCTILITY WITH SIGNIFICANT INCREASE IN STRENGTH OF AS-CAST CNTs/AZ91D NANOCOMPOSITES

Rongyu Feng[1], Lin Zhu[2], Wenzhen Li[1]

[1]School of Materials Science and Engineering (Tsinghua University, Beijing100084, China)
[2]Tsinghua-Foxconn Nanotechnology Research Center (Tsinghua University, Beijing 100084, China)

Keywords: Magnesium matrix nanocomposite, Carbon nanotubes, Heat treatment, Microstructure, Mechanical properties

Abstract

This paper was focused on significantly increasing the ductility and strength of as-cast CNTs/AZ91D nanocomposites by solid solution (T4) and aging treatment (T6). The CNTs/AZ91D nanocomposite fabricated by permanent gravity casting assisted with ultrasonic processing was subject to as-cast, T4 and T6 treatment and the mechanical properties were tested. The results showed that the ductility and the tensile strength of the nanocomposites after T4 treatment were increased by 23.8 percent and 82.8 percent compared with the as-cast properties. After T6 treatment, the tensile strength and especially the yield strength of the nanocomposites was increased by 26.2 and 17.6 percent, while its ductility was still increased by 20.7 percent. The strengthening and toughing mechanisms of the nanocomposites were discussed based on the microstructure characterization results.

Introduction

Stir casting is an effective way for batch production of magnesium matrix nanocomposites. However the as-cast strength and toughness of magnesium matrix nanocomposites produced using this method are usually unsatisfactory. Though better performance can be achieved by subjecting the cast magnesium matrix nanocomposite to heavy plastic deformation [1], this method only applies to those parts having simple shapes. The existed studies have given little attention to whether heat treatment can be used to strengthen and toughen the magnesium matrix nanocomposites. In this paper, the stirring casting and high-energy ultrasonic dispersion method were used to prepare the as-cast AZ91D composite reinforced with CNTs and the research was focused on increasing the ductility and strength of as-cast CNTs/AZ91D nanocomposites by solid solution (T4) and aging treatment (T6). The strengthening and toughing mechanisms were analyzed through microstructure characterization.

Experimental Procedures

Preparation and Heat Treatment of CNTs/AZ91D Composites

AZ91D magnesium alloy was selected as matrix alloy with composition of 8.0-9.0wt.%Al, 0.50-0.90wt.%Zn, 0.15-0.40wt.%Mn and balanced Mg. The 1.5wt%CNTs with the mean diameter of 40 nm was used as reinforcing filler. The CNTs/AZ91D composites were prepared using semi-solid mechanical stirring and high intensity ultrasonic composite dispersion method as the processing

described in other work [2].

The box-type resistance furnace with temperature control was used for heat treatment. For solid solution treatment (T4), the composite samples were heated to 688K and held for 24 hours, and then quenched in 343K hot water. For artificial aging (T6), the T4 treated composite samples were heated to 473K and held for 16 hours, then air-cooled to room temperature. The sample for heat treatment was 4 mm-thick rectangular tensile test specimen machined in accordance with GB/T228-2002, and the heat treatment was conducted with the protection of CO_2 gas.

Mechanical Property Test and Microstructure Characterization

The tensile tests were done on the SANS 4105 electronic universal testing machine. The gage length, width and thickness of rectangular specimen are 25 mm, 6 mm and 4 mm respectively. The tensile speed was set at 0.5 mm/min. Each group of data was obtained by testing five pieces of tensile test specimen and then averaged the measured values.

Metallographic specimen was ground and polished on the Buehler automatic grinding and polishing machine, and then eroded with 1vol.% nital. The Zeiss-Axio Imager.A 1m optical microscope (OM) was used to observe the microstructure at the different processing conditions. The FEI-Siron200 field emission scanning electron microscopy (FESEM) with energy disperse spectroscopy (EDS) was used to show the effects of CNTs on the morphology of precipitates after heat treatment. The TECNAI G2 F20 transmission electron microscopy (TEM) was used to characterize the interface and distribution of CNTs and the deformation mechanism of the nanocomposites.

Results and Discussions

Mechanical Properties of CNTs/AZ91D Composites after Heat Treatment

After the solid solution treatment (T4), the tensile strength and elongation after fracture of CNTs/AZ91D were improved by 23.8% and 82.8% to 260MPa and 10.6%, respectively, compared with the composites in their as-cast condition. After the aging treatment (T6), the yield strength and tensile strength of composites were further improved. In contrast to the solid solution state (T4), the elongation after fracture decreased, but remained greater than that in the as-cast condition. After the aging treatment (T6), the yield strength, tensile strength and elongation after fracture of CNTs/AZ91D were improved by 17.6%, 26.2% and 20.7% to 140MPa, 265MPa and 7.0%, respectively, compared with those in the as-cast condition (see Figure 1).

Microstructure of CNTs/AZ91D Composites after Heat Treatment

The XRD results shows that the structure of composites in the as-cast condition was mainly composed of two phases - α-Mg and β-$Mg_{17}Al_{12}$; after the solid solution treatment (T4) of composites, the eutectic phase β-$Mg_{17}Al_{12}$ in the gravity casting condition was almost dissolved into α-Mg completely and the single supersaturated α-Mg solid solution phase was then formed; after the aging treatment (T6), the β-$Mg_{17}Al_{12}$ which had been dissolved in solid solution during T4 treatment was precipitated again to form the precipitated phase (see Figure 2).

The grain images of AZ91D and CNTs/AZ91D composite after solid solution treatment (T4) were obtained through OM under polarized light. The grains of composites with CNTs after T4 treatment was significantly decreased (see Figure3). The MIAPS software attached to Zeiss

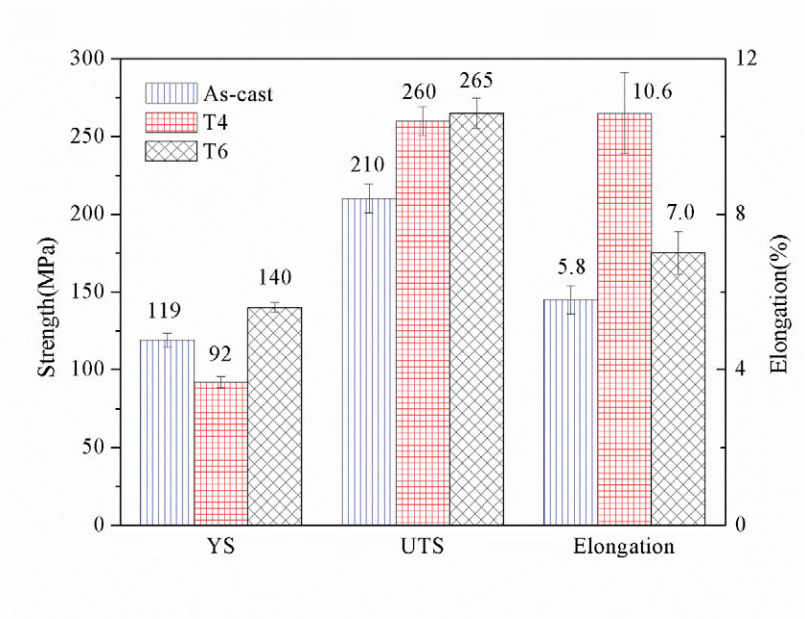

Figure 1. Mechanical properties of CNTs/AZ91D composite at different heat treatment conditions

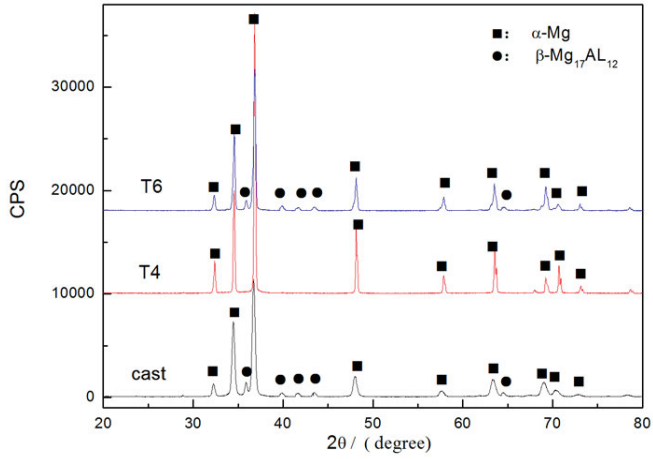

Figure 2. XRD patterns of CNTs/AZ91D composites at different heat treatment conditions.

microscope was applied to measure the grain size. The results showed that the grain size of AZ91D was 205μm (see Figure 3 (a)) while that of CNTs/AZ91D was 75μm (see Figure 3 (b)).

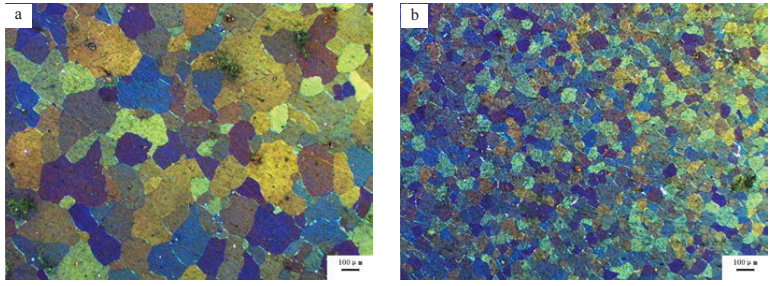

Figure 3. OM images of AZ91D-T4 (a) and CNTs/AZ91D-T4 (b)

The microstructures of CNTs/AZ91D composites after the aging treatment (T6) were analyzed with SEM (see Figure 4). The discontinuous lamellar or cellular β-$Mg_{17}Al_{12}$ was precipitated near the grain boundary, and the continuous precipitation of β-$Mg_{17}Al_{12}$ phase occurred inside the grain (see Figure 4 (a)). The initial stage of aging was dominated by discontinuous precipitation. Lamellar β-$Mg_{17}Al_{12}$ phase was first precipitated and grew at grain boundary. In the later stage of aging, the precipitation mainly occurred inside the grain, and the β-$Mg_{17}Al_{12}$ phase was continuously precipitated. In the areas with fewer secondary-precipitated phase of β-$Mg_{17}Al_{12}$, some slender, white and strip-shaped substances were found in the α-Mg matrix, as indicated by the arrow in Figure 4(b). Principal component analysis of EDS showed that besides the peak of Mg, Al and Zn elements, the peak of C element also appeared at the arrowed place and was identified as CNTs.

The distribution of CNTs and the morphology of precipitated phase inside the grain were analyzed. The precipitated β-$Mg_{17}Al_{12}$ was mainly the dispersed cellular structure with the size of 100-200 nm. CNTs were also uniformly distributed around the precipitated phase of cellular β-$Mg_{17}Al_{12}$, the diameter of the CNTs was about 50nm and their length was 200nm-500nm, as indicated by the arrow in Figure 4 (c). A contrast experiment was conducted to show the morphology and distribution of the precipitated phase of β-$Mg_{17}Al_{12}$ inside the grain of mono AZ91D alloy after the same heat treatment process (see Figure 4 (d)). It clearly indicates that the CNTs/AZ91D composites had precipitated fewer phase of β-$Mg_{17}Al_{12}$ than the mono AZ91D alloy without CNTs.

The discontinuous precipitation of β-$Mg_{17}Al_{12}$ occurred near the grain boundary and the morphology of the precipitated phase of β-$Mg_{17}Al_{12}$ was mostly lamellar. The thickness of lamella was 100-150 nm and the length was 5-10 μm (see Figure 4 (e)). The majority of lamellas were distributed in some order and in parallel in a certain direction. A small amount of cellular precipitated phase with the size of 100nm-150nm was also distributed between lamellar β-$Mg_{17}Al_{12}$ phases. Besides, some white and strip-shaped CNTs were dispersed between lamellar precipitated phases, as indicated by the arrow in Figure 4 (e).

The precipitation of secondary phase near the grain boundary of AZ91D alloy was also found after the same heat treatment process (see Figure 4(f)). By comparing Figure 4(e) and Figure 4(f), it was found that the precipitated phase of the composites with CNTs at grain boundary was mainly lamellar β-$Mg_{17}Al_{12}$ after the aging treatment (T6), together with very few cellular β-$Mg_{17}Al_{12}$, and the distance between lamellar precipitated phases was relatively large; in contrast, lamellar and cellular precipitated phase of β-$Mg_{17}Al_{12}$ coexisted near the grain boundary of AZ91D matrix, and the precipitated phase had a relatively large size and was densely distributed. The above analysis indicates that in the composites with CNTs after T6 heat treatment, CNTs has an influence on the morphology of precipitated phase of β-$Mg_{17}Al_{12}$. When CNTs were uniformly distributed in AZ91D, a coherent or semi-coherent relation was developed between CNTs and α-Mg interfaces. CNTs generated a very strong stress field which can inhibit the nucleation of β-phase effectively and hinder the growth of grain. As a result, the precipitated phase was more diffusely distributed and its size was finer, thus contributing to the precipitation strengthening effect of precipitated phase.

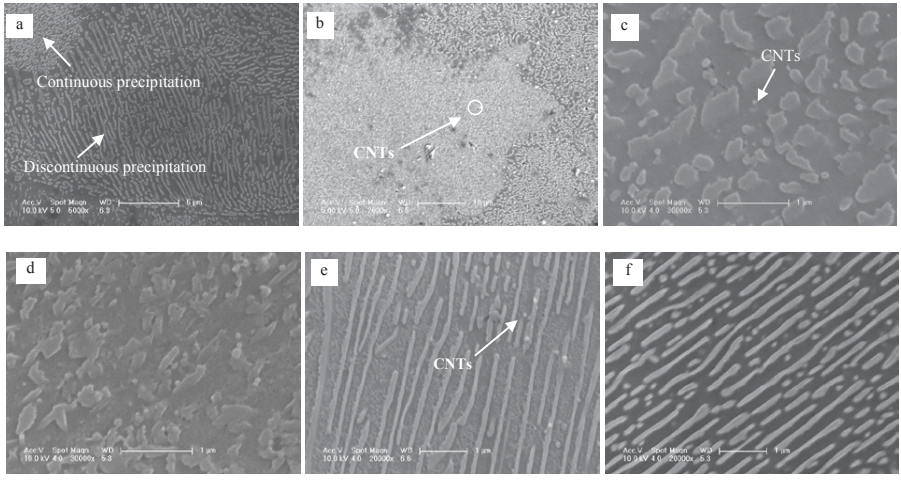

Figure 4. Morphology of β-$Mg_{17}Al_{12}$ secondary precipitation and distribution of CNTs in the composite matrix after T6 treatment. (a) Morphology of secondary precipitation in the grain and at the grain boundary, (b) CNTs nanoparticles distributed at grain boundary, (c) CNTs nanoparticles distributed in grain, (d) no CNTs nanoparticles distributed in grain for AZ91D alloys, (e) CNTs nanoparticles distributed between the lamellar β-$Mg_{17}Al_{12}$, (f) no CNTs nanoparticles distributed between the lamellar β-$Mg_{17}Al_{12}$ for AZ91D alloys.

The distribution of CNTs in the composite and the interface between the CNTs and the matrix alloy were analyzed with TEM (see Figure 5). The results showed that CNTs were tightly combined with matrix in the as-cast composites and no significant gaps were found, but there were obvious boundaries at joints (see Figure 5 (a)). After T4 and T6 treatment, CNTs were well combined with matrix all the time and the interfaces between CNTs and matrix were relatively

fuzzy (see Figure 5 (b) and (c)), which may suggest that the combination between CNTs and matrix be further improved after heat treatment.

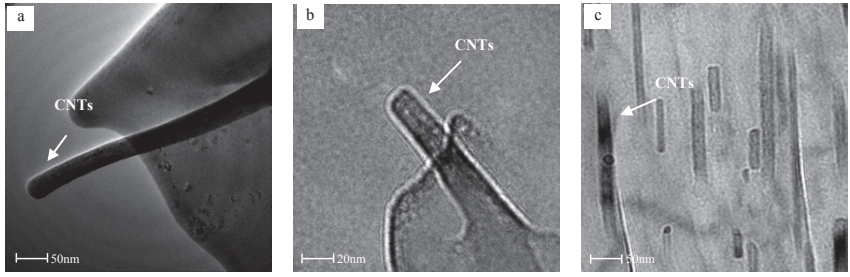

Figure 5. TEM images of CNTs in composites at different heat treatment conditions: (a) As-Cast, (b) T4, (c) T6.

Analysis of Strengthening and Toughing Mechanism

Strengthening Mechanism of Grain Refinement. According to the results of the grain size analysis, the grain size of AZ91D was 205μm while that of CNTs/AZ91D was 75μm. It suggests that the alloy grain was significantly refined after the addition of CNTs. Based on the classic Hall-Petch formula [3]:

$$\sigma_y = \sigma_0 + k_y d^{-\frac{1}{2}} \tag{1}$$

Where σ_y is the yield strength, σ_0 and k_y are material-related constants, and d is the average grain diameter. Finer grain indicates higher yield strength. The refinement of grain improves both the strength and the plasticity of composites. In this work the grain size of AZ91D was 205μm while that of CNTs/AZ91D was 75μm (see Figure 3). Therefore the grain refinement due to CNT addition significantly enhance the strength and ductility of the composites.

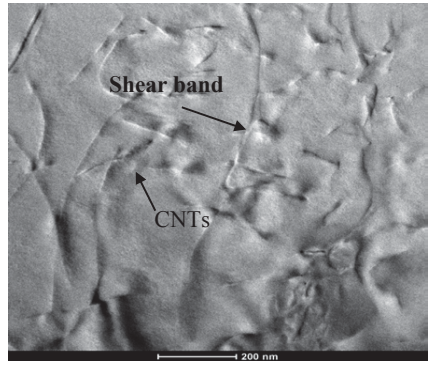

Figure 6. The effect of load transfer of the CNTs in composite materials

Strengthening Mechanism of Load Transfer. CNTs have excellent mechanical properties. The tensile strength and axial elasticity modulus of CNTs are up to 800GPa and 1TPa, respectively, and the elastic strain is up to 12% [4]. In the magnesium matrix composite reinforced by CNTs, the CNTs can bear partial deformation under load in matrix. As shown in Figure 6, CNTs were distributed in composites after the solid solution treatment (T4). They all had a complete shape, no fracture of CNTs was found, and a large number of shear bands arranged in a certain direction were identified in the matrix, suggesting that CNTs bore the shearing force on materials. Therefore, the strengthening of load transfer is one of the important strengthening mechanisms of CNTs/AZ91D composites.

Mechanism of Ductility Enhancement. Magnesium alloy can be deformed by means of slippage. Slippage occurs usually along a certain slip plane and the direction in the close-packed plane, which is related to crystal structure. When a crystal material starts to slip, there must be a critical shear stress. In the deformation of magnesium the critical shear stress for basal slip at room temperature should be much lower than that for the slip plane of prism. Therefore, the slip system of magnesium in close-packed hexagonal crystal structure at room temperature is $\{0001\}\langle 11\bar{2}0\rangle$ [5-6].

After the T4 treatment of CNTs/AZ91D composites, TEM analysis was used to observe the slipping deformation plane in the tensile test sample of composites, as shown in Figure 7 (a). It can be seen that many groups of parallel lines appeared in the composites with CNTs after the T4 treatment, showing obvious slip traces. They should be considered as (0001) basal slip line. Figure 7 (b) shows the high definition image of slip line at 50 nm scale. Moreover, the TEM images also show that a lot of dislocations lines were produced at the two ends of the slip lines. It suggests that in the composites with CNTs after the T4 treatment, obvious slippage occurred, and a lot of dislocations were generated and the plasticity was improved. The more detailed analysis will be done in the future research.

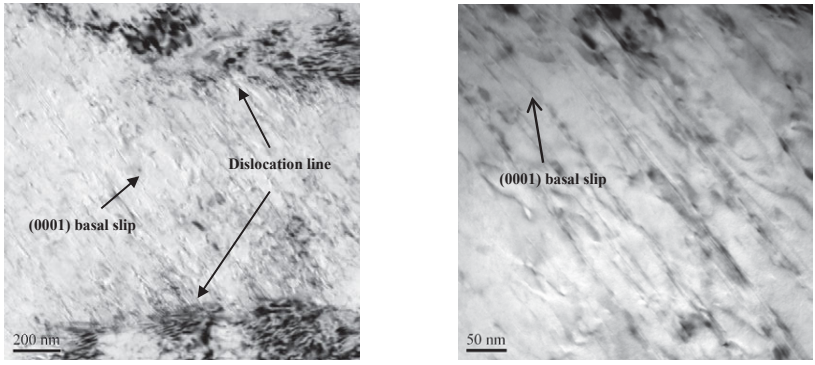

Figure 7. Dislocation and slip lines of CNTs/AZ91D-T4 after tensile test
(a)(0001) slip line; (b) high magnification image of slip line

Conclusions

The stirring casting and high-energy ultrasonic dispersion method were used to prepare the as-cast AZ91D composite reinforced with 1.5wt% CNTs and the solid solution and aging treatment were used to improve the ductility and strength of as-cast CNTs/AZ91D nanocomposites.

- The ductility and the tensile strength of the T4-treated nanocomposites were increased by 82.8 percent and 23.8 percent compared with the as-cast ones, which were 10.6 percent and 260MPa respectively. After T6 treatment, the tensile strength and especially the yield strength of the nanocomposites was increased by 26.2 and 17.6 percent to 265MPa and 140MPa respectively, while its ductility was still increased by 20.7 percent.
- The addition of CNTs to the matrix had an obvious effect on grain refinement and resulted in significant improvement of the strength and ductility of CNTs/AZ91D nanocomposites. The load transfer is another important strengthening mechanism.
- During the tensile deformation process of the T4-treated nanocomposites CNTs contributes to the increase of dislocation lines and slip lines. This might be the reason of the strengthening and toughening CNTs/AZ91D nanocomposites.

Acknowledgement

This work was partially financially supported by University Initiative Scientific Research Program of Tsinghua University (Grant No. 20111080980) and National High-Tech Research and Development Program (Grant No. 2013AA031201).

References

1. X. J. Wang et al., "Influences of Extrusion Parameters on Microstructure and Mechanical Properties of Particulate Reinforced Magnesium Matrix Composites," *Materials Science and Engineering A*, 528 (2011), 6387-6392.
2. Shiying Liu et al., "Fabrication of Carbon Nanotubes Reinforced AZ91D Composites by Ultrasonic Processing," Transactions of Nonferrous Metals Society of China, 20 (2010), 1222-1227
3. Congyang Zhang, Rongyu Feng, Wenzhen Li, "Effect of Heat Treatment on Microstructure and Mechanical Properties of Squeeze Cast n-SiCp/AZ91D Magnesium Matrix Composites," Rare Metal Mateirals and Engineering, 44 (2) (2015), 463-468.
4. E. T. Thostenson, Z. F. Ren and T. W. Chou, "Advances in the science and technology of carbon nanotubes and their composites: a review," *Composites Science and Technology*, 61 (13) (2001), 1899-1912.
5. B. L. Mordike, "Magnesium and Magnesium Alloys," *Journal of Japanese Institute of Light Metal*, 51 (1) (2001), 2-13.
6. Y. Zojima, "Platform Science and Technology for Advanced Magnesium Alloys," *Materials Science Forum*, 350-351 (2000), 3-18.

The Synthesis and Processing Self-Healing Structural Al/Mg Lamellar Composite Materials

Yasser Fouad[1]
Bakr Mohamed Rabeeh[2]
[1] Associate Professor, Engineering and Materials Science,
German University in Cairo, GUC.
[2] Professor, Engineering and Materials Science,
German University in Cairo, GUC.

Keywords: Diffusion couples, Spinel, HIPing, Hybrid, Composite; interface, interphase, micro-laminated, Nano composite.

Abstract

Self-healing alloy composites have been designed to address the need for self-repairable high-strength materials. However, delamination and cracking is a major limitation, stitching, and healing is established via the synergetic effect of low melting phase, Zn, and alloying element segregation. Under the controlled parameters, polycrystalline double layers are grown experimentally at the interfacial contacts between Al-Mg foils. The growth behavior of the interphase layers characterizing interface motion and long-range diffusion is established. The kinetic of controlled interphase with stitching/bridging and healing mechanism is introduced with microstructural and mechanical characterization. Chemical and mechanical bonding via inter diffusion processing with alloy segregation are dominant for interphase kinetics. SEM, EDX and tensile testing with interfacial shear strength are introduced. The interphase kinetic established through localized micro plasticity, metal flow, alloy segregation and delocalized Al oxide and Mg oxide. The kinetic of interface/interphase introduce new nontraditional self-healing composite with new bridging and shielding mechanisms.

Introduction

Mg alloy along with Aluminum alloy is being introduced for a lamellar composite structure processing that recommended for many applications. Mg alloys are being increasingly employed in the aerospace, automobile and 3C (Computer, Communication, Consumer electrics products) industries as important structural materials because of their low density, high strength-to-weight ratio, good damping characteristics and low casting costs, etc.[1]. One of the major drawbacks of magnesium alloys in many applications is their low corrosion resistance [2,3] reported that introducing an outer ply of aluminum alloy could improve the corrosion resistance of the magnesium substrate effectively, while maintaining the low density and high specific strength of the assembly. Al/Mg/Al foils are symmetrically hot isostatic pressed, HIPed at different parametric study. Temperature, pressure as well as holding time are being controlled and studied for lamellar metal matrix composite processing. The Al/Mg-based laminated composites can be comprised to meet a wide variety of demands. Temperature ranges are selected from 450^{o}C to 560^{o}C for different holding times 10, 20 and 30 minutes in a working chamber of 30 Ton capacity hydraulic press. However, the bonding processes mentioned above require special facilities, such as vacuum system, complex equipment or high-cost instrument, etc. The present work introduced with new emerged facility that induce metal flow, air bleeding as well as diffusion processing [4-10]. The kinetic of interphase is also introduced with scanning electron microscopy along with energy dispersive X-ray spectroscopy and mechanical characterization.

Hot Isostatic Pressing is now being applied to fabricate Al (6082)/Mg–3Al–1Zn (AZ31) laminated composites as an emerging method for bonding of dissimilar materials in a solid state processing. In particular, Bakr et al. demonstrated the feasibility to produce a lamellar MMC with controlled interphase/interface by hipping method [11]. The kinetic of interface/interphase at varying experimental settings (load, temperature and experiment duration) is established. Interfacial twining and Microstructural and textural evolution of magnesio-aluminate spinel reaction are formed. Deformation fracturing and twinning of constituent interface, low melting phase segregation, along with oxidation induce the formation of localized magnesio-aluminate structure. This internal deformation of constituent interface disturbed the reaction interphase and introduced localized zones of concentrated stress and directional solidification in a semisolid state [12-13].

Experimental Procedures

The extrinsically modified Al/Mg alloys are introduced via HIPing at different parametric study. Chemical compositions of the intrinsically alloyed monolithic materials; Al 6082 and Mg Az31 are presented in table 1.

Table 1. Chemical Composition of Al 6082 and AZ31 Magnesium Alloy.

Alloys	Cu	**Zn**	Mn	Si	Mg	Cr	Fe	Al
Al 6082	0.04	0.02	0.05	1.92	0.79	0.15	0.24	Bal.
						Ca	**Ni**	**Al**
AZ31	< 0.05	1.05	0.20	< 0.15	Bal.	< 0.04	< 0.005	3.10

Al and Mg alloy are prepared as thin foil/sheet of 3 mm thickness and different dimensions of 100X50 mm (lengths x width). A hydraulic press with hot working chamber is applied with special fixture that promotes metal flow and inters diffusion kinetics. Al/Mg foil/foil technique symmetrically HIPed at different parametric study of temperature 450^{o}C to 640^{o}C, and press of 30 Ton, with holding time varied from 10 to 60 minutes. Different HIPed samples are tested for microstructural observation to investigate bonding characteristics, interphase kinetics as well as delamination behavior. Scanning electron microscopy and energy dispersive X-ray spectroscopy is applied for microstructural characterization and chemical analysis. The best results of parametric study are applied for tensile test samples. Mechanical characterization is applied for both composite and its constituents. Al alloy, Mg alloy as well as Al/Mg metal matrix composite (MMC) samples are separately tested using servo hydraulic tensile testing machine. The kinetic of interface/interphase is established monitoring its micro constituents.

Results and Discussion

Interfacial bonding of laminated composite materials is an interesting point of study. Al/Mg/Al lamellar structure is introduced by Hot Isostatic Pressing, HIPing, in three symmetrically applied plies for structural applications. A new emerging solid state processing is introduced to study the kinetic of interface / interphase under HIPing conditions. Temperature, pressure and holding time are controlled with microstructural analysis and EDX to introduce interfacial behavior and mechanical characterization. The kinetic of interphase in a lamellar composite structure introduces in steps of formulation with microstructural observations along with alloying elements effect that induce either micro-laminated structure or delocalized oxides that induce toughening mechanisms. However, delamination is a major limitation in a lamellar composite structure; this work introduces a mitigation behavior of delamination along with new introduced toughening mechanisms along interphase/interface. Extremities are captured along with the

commencement of delocalized liquid phase in a semisolid reaction. Compared with other bonding methods, the bonding strength of the experimental laminates prepared by hipping bonding was medium due to delamination. For diffusion bonding, the maximum bonding strength of pure Al/pure Mg laminate with or without interlayer was 86.1 MPa[4] and 22.7 MPa[6], respectively; and that of 2024 Al alloy/AZ31B Mg alloy and 6061 Al alloy/AZ31BMg alloy was 56 MPa[8] and 41.3 MPa[4], respectively. The maximum bonding strength of 7075 Al alloy/AZ31B Mg alloy fabricated by explosive welding was 70 MPa [10]. The maximum bonding strength of Al 6082/AZ31/ Al 6082 laminated composite fabricated by hipping in this work was 95.4MPa. The bonding strength depends on the thermo mechanical processing conditions of the laminated composite. Mechanical bonding occurs instantaneously or over a very short time period and depends on the forces of attraction between the atoms. It is believed that not only mechanical bond played a major role in the bonding strength in this research but also kinetic of interphase/interface. As interfacial bonding started at a HIPing temperature, elemental concentration gradients played a role in driving certain elements from the internal layers to the interfaces. Metal flow, along with micro-laminated interface is induced by diffusion mechanism.

Microstructural Analysis

During HIPing, Al/Mg/Al 3-ply introduced at different parametric study of temperature, pressure and holding time. Aluminum ply reveal more ductility compared with Mg ply that produced transverse micro cracking along interface in Mg ply and presented in Figure 1. Figure 1 presents Al/Mg metal matrix composite with clear interfacial bonding and transverse micro cracking HIPed at 530^{o}C for 30 minutes and high press 30Ton. This represents the upper bound of press that induces transverse cracking along interface. Figure 2 presents Al/Mg MMC with lateral micro cracking, that HIPed at 620^{o}C for 60 minutes and high press 30Ton. The increase in HIPing temperature and pressure induce localized interfacial melting and complete consumption of Mg with lateral cracking as upper bound of temperature and pressure. Figure 1 and Figure 2 represent the two extremities of parametric study (pressure and temperature). Figure 3 presents Al/Mg metal matrix composite with clear bonding interface at 500^{o}C for 30 minutes and high press 20Ton. The commencement of interfacial bonding with no delamination or micro voids established at 20 minute with 20Ton press along Al/Mg interface. The upper bound of interfacial growth that produces a clear interphase with delocalized zone of interests established in Figure 4. This specimen is HIPed at 600^{o}C for 20 minutes and high press 20Ton and presents growth kinetic, delamination with lateral cracking along interface. The kinetic of interface/interphase is detected and presented in Figure 5 to 9. Figure 5 presents Al/Mg metal matrix composite with clear interfacial bonding but with a minor transverse cracking of a specimen HIPed at 540^{o}C for 20 minutes and high press 15Ton. Interfacial control introduced with micro-laminated interface and micro voids in aluminum (Figure 6). Figure 6 presents Al/Mg metal matrix composite with micro laminated interphase but no evidence of interphase at 540^{o}C for 20 minutes and low press 10Ton. Slight increase in temperature and pressure at the same holding time induces interfacial growth. Figure 7 introduces Al/Mg metal matrix composite with micro laminated interphase, bulk interfacial growth and bulk metal flow that induces interphase at 620^{o}C for 20 minutes and high press 15Ton. However, interphase is introduced, minor voids are captured along laminated interface may due to the depletion of diffused elements. Interface/interphase growth kinetics established with more delocalized zone of interests and bulk delocalized eutectic melts (Figure 8 and Figure 9). Micro laminated interface and delocalized Nano particulate/whiskers interphase established at 620^{o}C for 30 minutes and high press 10Ton (Figure 8). High magnification of the interphase established with delocalized whiskers enriched with alumina as well as magnesia in bulk aluminum enriched interphase (Figure 9). Solid state processing with HIPing produces a

semi-solid eutectic reaction with delocalized melts and directional solidification whiskers. The hipping temperature ranges from 500°C to 620°C to control interface with no delamination to interphase with localized melting phases. In the case of deformation twinning, the decreased load along with increase holding time indicates later commencement of interfacial growth. Next to twins, the reaction interface is characterized by tight physical contact on the Mg side and less tight contact on the other side of Al. However, cracks formed in the initial stages of an experiment, deformation and twining, spinel formed along these interface segments at high temperature, high holding time and low press.

Energy dispersive X-ray spectroscopy EDX

Energy dispersive X-ray spectroscopy EDX is applied on a specimen (Figure 9) to study micro constituents of composite and the semi-solid eutectic reaction with delocalized melts and interfacial front. Fig. 10 presents elemental distributions across Al 6082/AZ31/Al 6082 interface of the laminated composite: (1) bulk Mg ply (Figure 10a), interphase (Figure 10 b, and c), and bulk Al ply (Figure 10d). The diffusion characteristics of aluminum through interface and magnesium induce delocalized interphase with magnesium oxide and aluminum oxide. Alloy segregation induces delocalized zones with different composition, bulk zones with 80% Mg, 16% Al and 4 % O_2 (Figure 10 b), and branched frontal interphase with Mg 56%, 40% Al and 4% O_2 (Figure 10 c). Oxygen content induces the formation of alumina, and magnesia with different weight percent. Magnesium aluminate spinel is delocalized along interphase. Interphase growth indicates aluminum diffuse along Mg interface with less Al % at frontal interface.

Mechanical testing

Mechanical characterization established for both micro-constituents and bulk composite at different conditions. Stress-strain diagram applied for both Al-6082 and Mg-AZ31ply separately and presented in Fig. 11a and b for both Al and Mg respectively. Fig.12 presents typical stress–strain diagram of the Al 6082/AZ31/Al 6082 laminated composite that HIPed at 620°C for 30 minutes and high press 10Ton. The modification established at interphase induces stress-strain diagram that presented in Figure 13. Nonlinear stress-strain diagram (Fig. 13) reveal hardening exponent and minor delamination established at sample HIPed at 620°C for 30 minutes and low press 10Ton. Crack mitigation, toughening mechanisms and more ductility established for the new sample that presented in Figure 9. The maximum bonding strength of Al 6082/AZ31/ Al 6082 laminated composite fabricated by hipping was 95.4MPa. The bonding strength depends on the thermo mechanical processing conditions of the laminated composite. The application of Al/Mg/Al lamellar composite reveals more toughening with modified interface/interphase (Figure 13). Crack mitigation introduced with an increase of both strength and toughness in stress-strain diagram. The enhancement of interfacial shear stress established with nonlinear stress-strain diagram induced more toughening behavior. Magnesium aluminate spinel is that delocalized along interphase induce toughening mechanism.

Conclusions

Al/Mg/Al lamellar structure is established by Hot Isostatic Pressing, hipping, in three plies for structural applications. Parametric study with a new emerging solid state processing is introduced to study the kinetic of interphase/interface under HIPing conditions. The hipping temperature ranges from 500°C to 620°C to control interface with no delamination to interphase

with localized melting phases. The extremities are controlled for the optimal conditions. The localized liquid phases are delocalized along interface induce directional solidification and branching with oriented shape. High press (30 ton) induces the formation of cracks in Mg ply. In the case of deformation twinning, the decreased load along with increase holding time indicates later commencement of interfacial growth. Next to twins, the reaction interface is characterized by tight physical contact on the Mg side and less tight contact on the other side of Al. The interphase variations are less pronounced in high load (30 Ton). In contrast, low load (20 ton) experiments with low temperature and high holding time show large lateral cracking and tearing in the Aluminum interface, however no spinel formed along these interface segments. The spinel commencement increase with increasing temperature and time and they show delocalized zone manifested by deviation from low melting phase, oxidation, and directional solidification. Delocalized nucleation and directional growth were identified as the main mechanism of texture formation of self-healing structural composite materials.

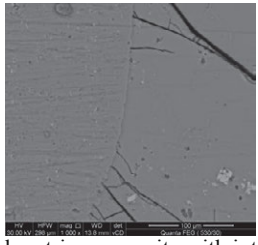

Figure 1: Al/Mg metal matrix composite with interface micro cracking at 530oC for 30 minutes and high press 30Ton.

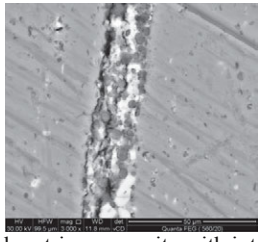

Figure 2: Al/Mg metal matrix composite with interface lateral cracking at 620^{o}C for 60 minutes and high press 30Ton

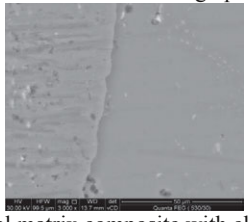

Figure 3: Al/Mg metal matrix composite with clear bonding interface at 500^{o}C for 30 minutes and high press 20Ton.

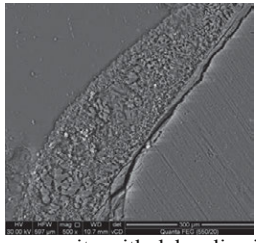

Figure 4: Al/Mg metal matrix composite with delocalize interphase and lateral cracking at 600oC for 20 minutes and high press 20Ton

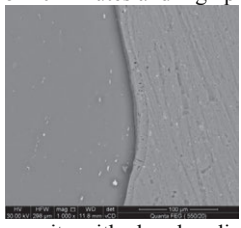

Figure 5: Al/Mg metal matrix composite with clear bonding interface with minor transverse cracking 540^{o}C for 20 minutes and high press 15Ton

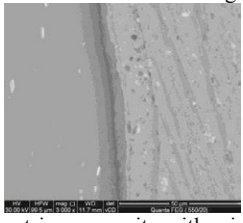

Figure 6: Al/Mg metal matrix composite with micro laminated interphase and bulk flow interface at 540^{o}C for 20 minutes and high press 10Ton.

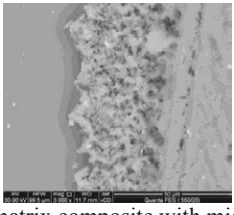

Figure 7: Al/Mg metal matrix composite with micro laminated interphase and bulk material flow interphase at 620^{o}C for 20 minutes and high press 15Ton

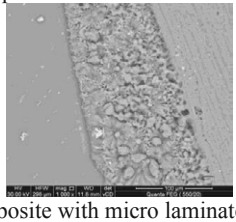

Figure 8: Al/Mg metal matrix composite with micro laminated interphase and delocalized Nano particulate/whiskers interphase at 620^{o}C for 30 minutes and high press 10Ton.

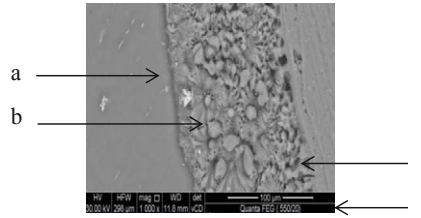

Figure 9: Al/Mg metal matrix composite with micro laminated interphase and delocalized alumina and magnesia interphase at 620^{o}C for 30 minutes and high press 10Ton.

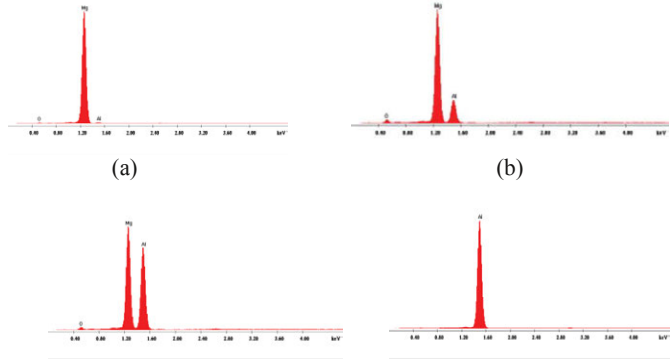

(a) (b)

(c) (d)

Fig. 10: Elemental distributions across Al 6082/AZ31/Al 6082 interface of the laminated composite: (a) bulk Mg ply, b, and c interphase, and d- bulk Al ply.

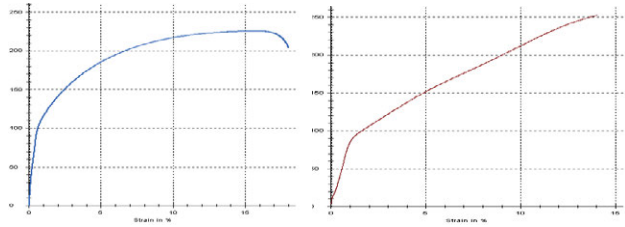

(a) (b)

Fig. 11: Typical stress–strain curve of (a) Al 6082 (b) AZ31 before hipping

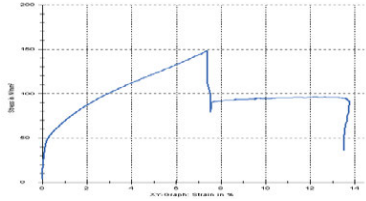

Fig.12: Typical stress–strain curve of the Al 6082/AZ31/Al 6082 laminated composite after the shear strength test:

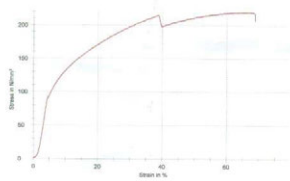

Fig.13: Typical stress–strain curve of the Al /Mg/Al laminated composite after the modified interphase.

References

1. Hidetoshi Somekawa, Hiroyuki Watanabe, Toshiji Mukai, Kenji Higashi, "Low temperature diffusion bonding in a superplastic" Scripta Materialia 48 (2003) 1249–1254.
2. Zhang XP, Zhao ZP, Wu FM, et al. "Corrosion and wear resistance of AZ91D magnesium alloy with and without micro arc oxidation coating in Hank's solution", J Mater Sci. 2007;42:8523–8.
3. Zhao LM, Zhang ZD. "Effect of Zn alloy interlayer on interface microstructure and strength of diffusion-bonded Mg–Al joints", Scripta Mater 2008; 58:283–6.
4. Li YJ, Liu P, Wang J, et al. "XRD and SEM analysis near the diffusion bonding interface of Mg/Al dissimilar materials Vacuum", 2008;82:15–9.
5. Liu FC, Liang W, Li XR, "Improvement of corrosion resistance of pure magnesium via vacuum pack treatment", J Alloys Comp. 2008; 461:399–403.
6. Liu LM, Tan JH, Zhao LM, et al. "The relationship between microstructure and properties of Mg/Al brazed joints using Zn filler metal", Mater Charact2008;59:479–83.
7. Mahendran G, Balasubramanian V, Senthilvelan T. "Developing diffusion bonding windows for joining AZ31B magnesium–AA2024 aluminum alloys", Mater Des 2009;30:1240–4.
8. Liu XB, Chen RS, Han EH. "Preliminary investigations on the Mg–Al–Zn/Al laminated composite fabricated by equal channel angular extrusion", J Mater Process Technol 2009; 209:4675–81.
9. Del Valle, J.A., Pérez-Prado, M.T., Ruano, O.A., 2005. Accumulative roll bonding of a Mg-based AZ61 alloy, Mater. Sci. Eng. A 410–411, 353–357.
10. Yan YB, Zhang ZW, Shen W, et al. "Microstructure and properties of magnesium AZ31B–aluminum 7075 explosively welded composite plate", Materials Sci. Eng. A 2010; 527:2241–5.
11. Bakr M. Rabeeh, Mona M. El Batanouny, Ali E. El Ashram "Microstructural Characterization And Solid State Processing Of Cu-Zn-Al Shape Memory Alloy In A Metal Matrix Composite" Canadian Journal on Mechanical Sciences and Engineering Vol. 2, No. 2 February 2011, P.P. 11-17.
12. Götze, L. C.; Abart, R.; Milke, R.; Schorr, S.; Zizak, I.; Dohmen, R.; Wirth, R.," Growth of magnesio-aluminate spinel in thin-film geometry: in situ monitoring using synchrotron X-ray diffraction and thermodynamic model", Physics and Chemistry of Minerals, Springer, Verlag Berlin Heidelberg , 5-2014.
13. Jerabek, Petr; Abart, Rainer; Rybacki, Erik; Habler, Gerlinde," The effects of stress concentrations on reaction progress: an example from experimental growth of magnesio-aluminate spinel at corundum - periclase interfaces under uniaxial load", EGU General Assembly 2014, held 27 April - 2 May, 2014 in Vienna, Austria, id.11155.

FILLER SURFACE NATURE, BEAD, SOLUTION VISCOSITY AND FIBRE DIAMETER OF ELECTROSPUN PARTICLE-REINFORCED POLYLACTIDE

[1]S.O. Adeosun, [2]E. I. Akpan, [1]O.P. Gbenebor, [1]A. A. Peter and [3]S. A. Olaleye

[1]Department of Metallurgical and Materials Engineering, University of Lagos, Nigeria
[2]Department of Materials and Production Engineering, Ambrose Alli University, Nigeria
[3]Department of Mechanical Engineering, University of Lagos, Nigeria

Keywords: solution viscosity, electrospinning, fibre and bead diameter, morphology

Abstract

The effect of viscosity of agro particle reinforced polylactide (PLA) solution on the electrospun fibre diameter and bead size produced is examined. Solutions of agro waste particle reinforced PLA were made at varying filler weight fraction and these electrospun into fibres. A scanning electron microscope was used to examine the morphologies of fibres while the fibre diameters were determined using ImageJ software. Results show that solution viscosity does not affect fibre diameter when agro particle fillers are processed by a combination of mechanical, thermal and chemical treatments prior to been used as reinforcement. At lower concentration of reinforcement, beads generated from treated particles were of smaller diameter. High solution viscosity gave rise to large bead diameters for treated and untreated reinforcements. Thus, the effect of solution viscosity on fibre and bead diameters depends largely on surface nature of the agro filler.

Introduction

Electrospinning has recently become the most used method to produce nanofibers from polymer solutions [1 – 4]. These electrospun fibres are widely used as scaffolds in tissue engineering, drug delivery, wound dressings, filtration, enzyme immobilization and biosensors [5]. Studies in this area include electrically conductive nanofibers [6] nanofibrous membranes for the development of high performance batteries [7], piezoelectric nanofibrous devices [8], nanofibers alignment [9], nanofiber crossbars [10], nanotubes [11], fabrication of tubular products to serve as blood vessel prosthesis [12], nanofiber composites [13], electrospun mats for fine filtration [14] and nanofibres for wound dressing [15]. The need for structural fibres prompt studies on electrospinning method of composites production using nano materials in polymer solutions and creating fibres with diameters in the nano to micro scale [16 – 18]. This led to the formation of reinforced fibres with high porosity due to high surface area to volume ratio which is very advantageous in the production of scaffolds for tissue engineering. These are functionalized material with interconnected pores and large surface area that mimics extra-cellular matrix [19, 20]. To satisfy biomedical needs of biocompatible and biodegradable scaffolds, most research in this area has been focused on the use of electrospun polylactic acid (PLA) for tissue scaffold [20]. However, such studies in the use of electrospun PLA focused on the use of carbon and halloysite nanotubes as reinforcing fillers [20, 21 – 23]. Recent works has shown that natural fillers in PLA results in increased crystallinity of electrospun PLA nanocomposite fibres with improved strength and decreased fibre diameter [24]. These nanofibres have qualities that make

them useful as scaffolds in tissue engineering. In the production of electrospun fibres there are key parameters that determine the needed properties of the electrospun fibres. Thus, properties such as fibre morphology, average fibre diameter, bead formation are directly linked to solution viscosity, surface tension, concentration, molecular weight and machine parameters [23, 26-33]. Therefore, for the development of useful applications, thorough knowledge of the interconnection between electrospinning parameters and the final product properties is required.

Most works focused on solving the problem of machine parameters such as voltage, distance between plate and tip of the needle, vertical and horizontal setups, inclination of collector plates, flow rate and pressure. However, very limited studies have been targeted on creating a linkage between the surface property of reinforcing filler, solution viscosity, bead formation, surface morphology and average fibre diameter. The objective of this research is, to create a synergy between surface property of reinforcing filler, solution viscosity, bead formation, surface morphology and average fibre diameter of agro- fibre reinforced PLA electrospun fibres. Preliminary electrospinning parameters for optimum mechanical properties of the fibres have earlier been determined [34].

Experimental Methodology

Preparation of Agro-Wastes Fibres

Rice husk, coconut husk and groundnut shells were collected, washed, sun dried for two weeks and then cut into small pieces. The cut agro-wastes materials were ground to pass 10 mm screen in a mechanical crusher. They were then divided into two parts. One part was used in untreated form and thus termed 'untreated' throughout the presentation. The other part was subjected to mechanical, thermal and chemical treatment as in Akpan et al. [35].

Electrospinning Solution Preparation

Mixtures of PLA and selected agro-wastes particles (treated and untreated) were dissolved in DCM at a constant composition of 12.50% (w/v). The solutions were left in the sealed bottles at room temperature (310C) for 24 hours in order to dissolve the PLA and the particles.

Process Setup and Electrospinning

The electrospinning process was conducted as in Adeosun et al. [34]. Electrospinning process was repeated by varying the weight fractions of reinforcements in the mixture from 0 – 8 wt. %.

Viscosity of the Composite Fibres

Solution viscosity was analytically determined using the relationship in Mituppatham et al. [36].

$$\mu = (1/0.00137)\ln((d - 88.7)/0.804) \quad (2)$$

Scanning Electron Microscopy (SEM)

Morphological features of the electrospun composite fibres were acquired using a scanning electron microscope (Model: ASPEX 3020) located at the Materials Science and Engineering

Laboratory of Kwara State University, Nigeria. It was operated at 15kV to determine the fibre morphology of the electrospun samples. The electrospun samples were coated with conducting carbon tape. The Digital SEM images of the samples were captured at 100x and 250x magnifications. The average diameters of fibres and beads were determined using ImageJ software.

Results and Discussion

PLA Reinforced Coconut Particles Electrospun Fibres

Table 1 and Figures 1 – 2 show the characteristics of composite fibres with coconut filler particles. Table 1 shows the variation in average fibre diameter for the composite fibres. Composites with treated fillers show higher average fibre diameters compared to that with untreated filler. Similarly, the viscosities of composites fibres with treated fillers are higher than that with untreated filler. This is an indication that the higher the viscosity the higher the fibre diameter. This phenomenon had earlier been observed by Chien and Wang [23] that decrease in solution viscosity of fibres facilitates reduction in fibre diameter. Figure 1a compared to 1b shows that the fibre surfaces of the untreated fillers look smooth than those with treated filler particles. It is also apparent from Table 1 that increase in filler weight fraction promotes increase in fibre viscosity and diameter. The SEM images show that composites with treated filler particles have more beads than that with untreated filler. It is suggested that the treated filler particle forms a good surface adhesion to the matrix leading to increased viscosity and consequently increased fibre diameter and number of beads. It has been stated in an earlier study that using treated fibre fillers led to increase in viscosity of the composite [35]. It is noted that the average fibre diameter and viscosity of composites with 4 wt. % of untreated filler are lower than that of virgin PLA and other composite fibres.

Table 1: Average fibre diameter and solution viscosity of composite fibres (fourteen readings)

	Rice Husk			Groundnut shell		
Weight fraction (wt. %)	4	5	8	4	5	8
Fibre diameter (untreated filler) µm	9.85±4.1	10.08±5.2	10.89±4.2	9.26±3.4	10.96±4.8	12.46±5.9
Viscosity (untreated filler) cP	6864±351	6881±509	6938±388	6818±275	6943±471	7037±490
Fibre diameter (Treated filler) µm	15.65±5.86	13.89±4.0	12.28±4.8	12.61±5.9	11.59±5.8	10.06±4.1
Viscosity (Treated filler) cP	7204±318	7117±219	7026±346	7046±584	6984±491	6880±468
	Coconut husk					
Weight fraction (wt. %)	Control	4	5	8		
Fibre diameter (untreated filler) µm	10.11±1.34	9.46±2.3	10.41±3.8	11.23±3.9		
Viscosity (untreated filler) cP	6883±317	6834±196	6905±317	6961±304		
Fibre diameter (untreated filler) µm		11.52±3.5	13.01±5.7	11.25±4.8		
Viscosity (untreated filler) cP		6979±224	7069±336	6962±367		

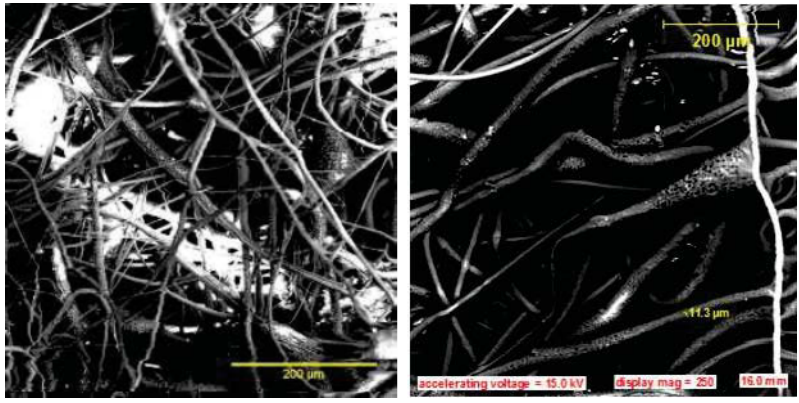

Figure 1. SEM of electrospun composite with 4 wt. % (a) untreated (b) treated coconut fibres

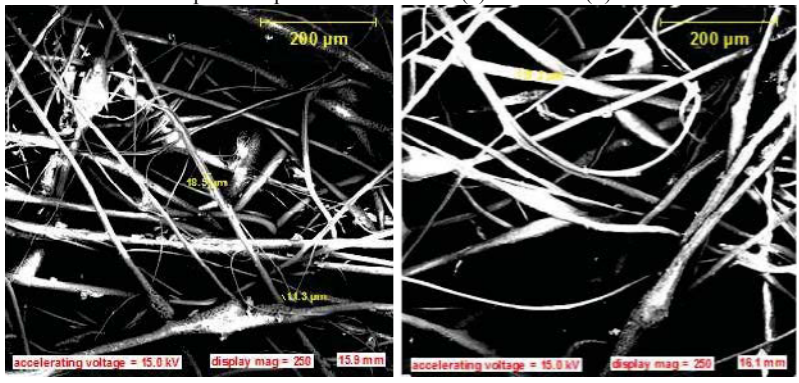

Figure 2. SEM of electrospun composite with 8 wt. % (a) untreated (b) treated coconut fibres

PLA Reinforced Groundnut Particles Electrospun Fibres

The average fibre diameter of composite fibres with groundnut shell filler is shown in Table 1. Here increase in fibre diameter occurred with increase in weight fraction of the filler with the lowest (9.26 µm) recorded at 4 wt. % untreated filler. Average fibre diameter for treated filler filled PLA decrease with increasing weight fraction of fillers. This trend is repeated for fibre viscosity as displayed in Table 1, showing that increase in viscosity of the solution leads to increase in the fibre diameter of electrospun fibres. Contrary to that obtained in composites with coconut shell filler particles, the fibres with treated groundnut shell particles show smooth surface with similar fibre diameters compared to the untreated filler (see Figures 3 and 4). However, higher fibre diameter and viscosity are shown except at 8 wt. % filler where fibre diameter and viscosity are better in untreated filler PLA fibre. In Figures 3 and 4 there are more beads formed with untreated filler-PLA than with treated filler composites. Increase in weight fraction of filler is also found to lead to growth in bead and fibre diameter. Pillay et al. [32] had shown that increase in viscosity leads to increase in fibre diameter and it is also known that

beads are formed as a result of agglomeration of fibres [23] as 1 wt. % of carbon nanotubes in PLA yielded uniform fibre size with fewer beads. However, addition of up to 5 wt. % increased the number of beads. Studies have shown that beads are undesirable in electrospun fibres as these act as defects resulting to inferior mechanical properties of composite fibres [34, 37]. In this study it is noted that untreated filler catalyzes the formation of beads. Thus, bead formation is dependent on surface quality of reinforcement and solution viscosity.

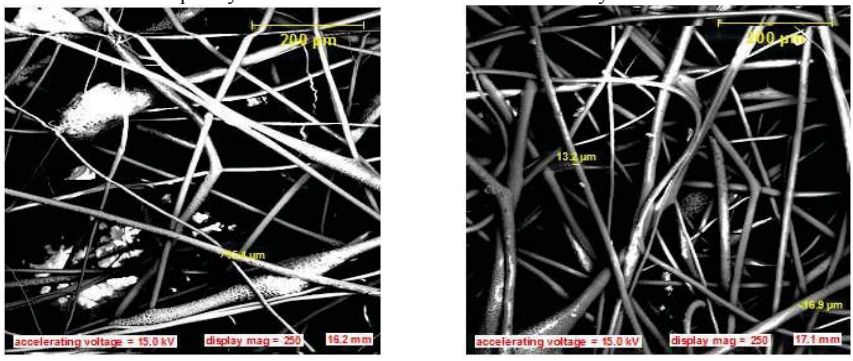

Figure 3. SEM of composite fibres with 4 wt. % (a) untreated (b) treated groundnut shell fibres

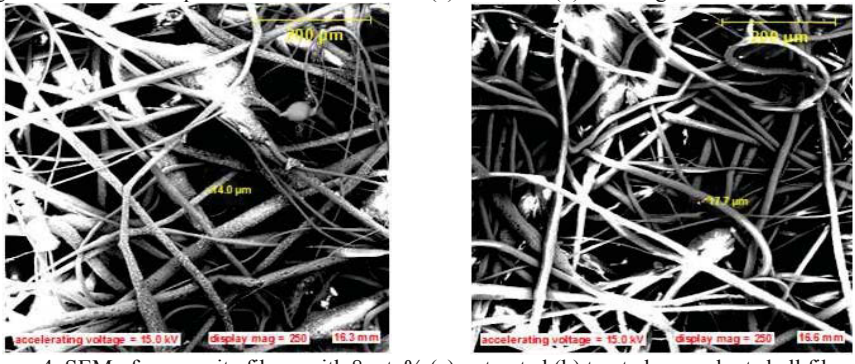

Figure 4. SEM of composite fibres with 8 wt. % (a) untreated (b) treated groundnut shell fibres

PLA Reinforced Rice Husk Particles Electrospun Fibres

Fibre diameter, viscosity and SEM images of rice husk filled electrospun PLA composite fibres are shown in Table 1 and Figures 5 – 6. Table 1 shows increase in fibre diameter with increase in weight fraction of the filler particles. All composites with treated filler show higher average fibre diameter compared to that with untreated filler. However, it is observed that the composite with 4 wt. % untreated filler has the smallest fibre diameter. This indicates that lower composition of the filler results into lower fibre diameter. This is in contrast to the response of composites with treated filler showing decrease in fibre diameter as the weight fraction increases. Viscosity of the composite fibres displays similar trend (see Table 1). All composites with treated filler have higher viscosities than those with untreated filler. Increase in weight fraction of untreated filler in

PLA composite also leads to increase in viscosity except at 4 wt. % filler. In composites with treated filler the viscosities decrease with increase in fibre weight fraction. The SEM images show that composites with treated filler have larger beads compared to those with untreated filler. The beads are observed to increase as filler weight fraction increases. Pores are found mostly on the surface of composites with treated filler (see Figure 5b). It is generally observed that increase in viscosity leads to increase in fibre diameter and bead size. In an earlier study [38] it was observed that treatment of filler before use promoted increase in melt viscosity of compounded PLA – rice husk composites. This was attributed to good surface adhesion of the treated filler resulting in the development of cohesive, plastic and sticky dough during compounding.

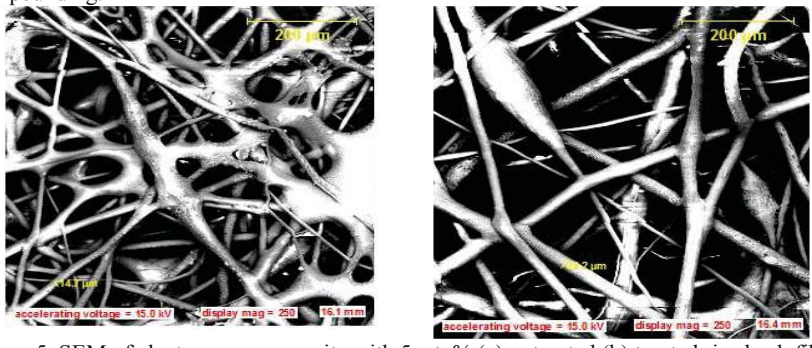

Figure 5. SEM of electrospun composite with 5 wt. % (a) untreated (b) treated rice husk fibres

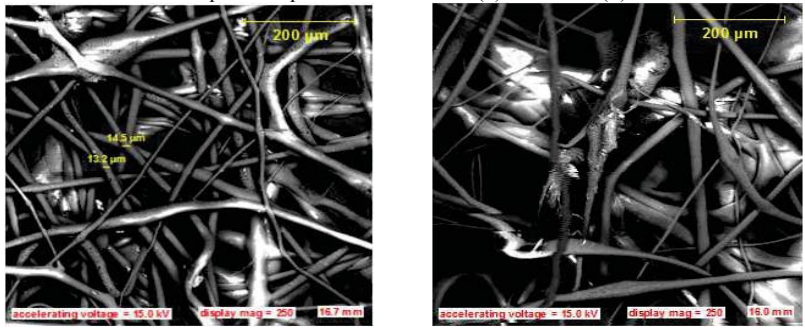

Figure 6. SEM of electrospun fibres with 8 wt. % (a) untreated (b) treated rice husk fibres

Conclusion

From this investigation, it is observed that electrospun fibre properties such as average fibre diameter, fibre morphology and bead formation are related to solution viscosity and surface quality of the reinforcing filler. Poor surface quality of reinforcing filler is found to cause beads formation, which is detrimental to mechanical properties of the composite fibres. Average solution viscosity with improved filler surface quality is desired for small fibre diameter and good fibre morphology. Agro-fillers can be used to develop electrospun fibres for tissue engineering with the correct combination of surface quality and solution viscosity.

References

1. D. H. Reneker et al. “Bending instability of electrically charged liquid jets of polymer solutions in electrospinning,” J Appl Phys, 87(2000), 4531–47.
2. A. L. Yarin, Koombhongse S., Reneker D. H. “On bending instability in electrospinning of nanofibers,” J Appl Phys,89(2001), 3018–26.
3. A. Theron, E. Zussman, A. L. Yarin, “Electrostatic field-assisted alignment of electrospun fibers,” Nanotechnology 12(2001), 384–90.
4. M. Bognitzki et al. “Nanostructured fibers via electrospinning,” Adv Mater 13 (2001),70–72.
5. K. S. Athira, S. Pallab, C. Kaushik “Fabrication of Poly(Caprolactone) Nanofibers by Electrospinning,” Journal of Polymer and Biopolymer Physics Chemistry, 2(4) (2014), 62-66
6. A. C. MacDiarmid et al. “Electrostatically generated nanofibers of electronic polymers” Synth Met, 119 (2001), 27–30.
7. I. D. Norris et al. “Electrostatic fabrication of ultrafine conducting fibres: polyaniline/polyethylene oxide blends,” J Synth Metals 114 (2000), 109–14.
8. A. G. Scopelianos “Piezoelectric biomedical device,” US patent 5522879, 1996.
9. E. D. Boland et al. “Tailoring tissue engineering scaffolds using electrostatic processing techniques: a study of poly(glycolic acid) electrospinning,” *J Macromol Sci-Pure Appl Chem*, A38(12) (2002), 1231–1243.
10. E. Zussman, A. Theron, A. L. Yarin “Formation of nanofiber crossbars in electrospinning,” Appl Phys Lett, 82(6)(2003), 973–5.
11. M. Bognitzki et al. “Polymer, metal, and hybrid nano and mesotubes by coating degradable polymer template fibres (TUFT process),” Adv Mater, 12(9) (2000), 636–40.
12. A. Bornat “A production of electrostatically spun products,” US patent 4689186, 1987.
13. D. H. Reneker et al. “Electrospinning and nanofibers,” Book of abstracts. New frontiers in fiber science, spring meeting 2001. Available from: http://www.tx.ncsu.edu/jtatm/volume1specialissue/presentations/pres_part1.doc.
14. P. W. Gibson, H. L. Schreuder-Gibson, D. Riven “Electrospun fiber mats: transport properties”, AIChE J, 45(1)(1999),190–195.
15. H. J. Jin, S. Fridrikh, G. C. Rutledge, D. Kaplan, “Electrospinning Bombyx mori silk with poly(ethylene oxide),” *Abstr Pap Am Chem Soc*, 224(1–2) (2002), 408 -
16. K. M. Sawicka, P. J. Gouma, “Electrospun composite nanofibers for functional applications” Nanoparticle Res, 8 (2006), 769-781
17. J. J. Mack et al. “Graphite nanoplatelet reinforcement of electrospun polyacrylonitrile nanofibers,” Adv Mater, 17 (2005), 77.
18. K.. Saeed et al. “Preparation of electro-spun nanofibres of carbon nanotube/polycaprolactone nanocomposite,” Polymer, 47 (2006), 8019 - 8025.
19. C. Li et al. “Electrospun silk-BMP-2 scaffolds for bone tissue engineering,” Biomaterials, 27(16) (2006), 3115-3124.
20. S. D. McCullen et al. “Characterization of electrospun nanocomposite scaffolds and biocompatibility with adipose derived human mesenchymal stem cells,” International Journal of Nanomedicine, 2(2) (2007), 253–263

21. H. T. Ahmed et al. “Effect of electrospinning parameters on the characterization of PLA/HNT nanocomposite fibers,” Journal of Materials Research, 25 (2010), 857-865.
22. S. Ramaswamy, “Study of Morphological, Mechanical and Electrical properties of Electrospun Poly (lactic acid) Nanofibers incorporated with Multiwalled Carbon Nanotubes as a Function of Thermal Bonding,” (M.Sc. thesis, North Carolina State University, 2009),
23. H-S. Chien, C. Wang, “Effects of Temperature and Carbon Nanocapsules (CNCs) on the Production of Poly(D,L-lactic acid) (PLA) Nonwoven Nanofibre Mat.” Fibres and Textiles in Eastern Europe, 21 (97) (2013), 72-77.
24. C. Xiang, Joo Y. L., Frey, “Cellulose Based Composites: Cellulose Based Composites,” Journal of Biobased Materials and Bioenergy, 3(2) (2014), 147-155
26. D. Rodoplu, M. Mutlu, “Effects of Electrospinning Setup and Process Parameters on Nanofiber Morphology Intended for the Modification of Quartz Crystal Microbalance Surfaces,” Journal of Engineered Fibers and Fabrics, 7 (2) (2012), 118 - 123.
27. C. Henriques et al. “A Systematic Study of Solution and Processing Parameters on Nanofiber Morphology Using a New Electrospinning Apparatus,” Journal of Nanoscience and Nanotechnology, 8 (1–11) (2008), 1 - 11
28. A. Koski, K..Yim, S. Shivkumar, “Effect of molecular weight on fibrous PVA produced by electrospinning,” Materials Letters, 58 (2004), 493– 497.
29. Z. M. Huang et al. “A review on polymer nanofibers by electrospinning and their applications in nanocomposites,” Composite Science and Tech. 63(2003), 2223-2253.
30. S. Ramakrishna et al. “An Introduction to Electrospinning and Nanofibers,” World Scientific Publishing Co. Pte. Ltd., 2005.
31. M. Chowdhury, G. Stylios, “Effect of Experimental Parameters on the Morphology of Electrospun Nylon 6 fibres,” International Journal of Basic and Applied Sciences, 10(6) (2010), 70 - 78
32. V. Pillay et al. “A Review of the Effect of Processing Variables on the Fabrication of Electrospun Nanofibers for Drug Delivery Applications,” Journal of Nanomaterials, (2013), http://dx.doi.org/10.1155/2013/789289
33. F. Abdel-Hady, A. Alzahrany, M. Hamed, “Experimental Validation of Upward Electrospinning Process,” ISRN Nanotechnology, (2011), http://dx.doi:10.5402/2011/851317
34. S. O. Adeosun et al. “Mechanical Behaviour of Electrospun Palmfruit Bunch Reinforced Polylactide Composite Fibres,” Journal of the Minerals, Metals and Materials Society (TMS), DOI: 10.1007/s11837-015-1565-7
35. E. I. Akpan et al., “Structural Characteristics of Batch Processed Agro-Waste Fibres', World Academy of Science, Engineering and Technology,” International Journal of Chemical, Molecular, Nuclear, Materials and Metallurgical Engineering, 8(3) (2014), 247 - 254.
36. C. Mit-uppatham, M. Nithitanakul, P. Supaphol, “Effects of Solution Concentration, Emitting Electrode Polarity, Solvent Type, and Salt Addition on Electrospun Polyamide-6 Fibers: A Preliminary Report,” Macromol. Symp., 216 (2004) 293 - 300.
37. G. Ahmet, “Electrospinning of Polystyrene/Butyl Rubber Blends: A Parametric Study “(M.Sc. Middle East Technical University, 2008).
38. E. I. Akpan “Processing and Characterisation of Selected Biodegradable Fibre-PLA Composites,” (Ph.D. Thesis, University of Lagos, Nigeria, 2004)

EVALUATION OF INTERMETALLIC REACTION LAYER FORMATION WITHIN STEEL ENCAPSULATED METAL MATRIX COMPOSITES

Sean Fudger [1, 2], Eric Klier [2], Prashant Karandikar [3], Chaoying Ni [1]
[1]Department of Materials Science and Engineering, University of Delaware, 201 Du Pont Hall, Newark, DE 19716-1501, USA
[2]Army Research Laboratory Building 4600, Aberdeen Proving Ground, MD 21005, USA
[3]M Cubed Technologies, Inc., 1 Tralee Industrial park, Newark, DE 19711, USA

Keywords: Encapsulation, Metal Matrix Composite, Intermetallic, Reaction Layer

Abstract

Macro hybridized systems consisting of steel encapsulated light metal matrix composites (MMCs) deliver a low cost/light weight composite with enhanced mechanical properties. By exploiting the high strength, modulus, and damage tolerance of steels and the high stiffness and low density of MMCs the resultant macro hybridized systems alleviates the high density of steel and the poor ductility of MMCs. The resultant system, when properly designed, offers higher specific properties and a more structurally efficient system can be attained. However, the combination of these dissimilar materials, specifically iron and aluminum, often results in the formation of intermetallic compounds. In certain loading situations, these typically brittle intermetallic layers can result in degraded performance. In this research, X-ray Diffraction (XRD), X-ray Energy Dispersive Spectroscopy (EDS), and Electron Backscatter Diffraction (EBSD) are utilized to characterize the intermetallic reaction layer formed between an aluminum or magnesium MMCs reinforced with Al_2O_3, SiC, or B_4C particles and encapsulated by A36 steel, 304 stainless steel, or Nitronic® 50 stainless steel.

Introduction

A high demand exists in the aerospace, marine, and automotive industries for components which are light weight but maintain their structural integrity. Recent interest includes materials such as high strength composites, magnesium, aluminum, steel, and combinations in the form of metal matrix composites and hybrid structures [1]. Metal matrix composites have a wide range of applicability for automotive and structural applications due to the tailorability of their mechanical and physical properties [2,3]. Moreover, particulate reinforced aluminum or magnesium based MMCs with a high volume fraction of the ceramic phase provide for very high stiffness, low CTE, and low density observed in ceramics while maintaining the damage tolerance and processing advantages of cast light metals. These mechanical and physical properties can be fine-tuned by adjusting the size, distribution, or volume fraction of the reinforcement phase, utilizing different reinforcement phases, matrix alloy selection, or adjusting the processing parameters used in fabricating the MMCs [4-6]. Since cost has limited the implementation of aluminum into many automotive applications, hybrid components consisting of both aluminum and steel have drawn much attention. Joining of dissimilar metals can be performed via arc welding, spot welding, diffusion bonding, ultrasonic welding, friction stir welding, laser brazing, etc. Mechanical assembly of these materials can also be performed by using rivets [7-12]. Each process exhibits

its own limitations such as the requirement for specific filler materials, the ability to join only plate or simple geometric configurations, high cost, and/or the formation of intermetallic phases.

The steel encapsulated metal matrix composites produced for this work are formed by casting or infiltration of a molten MMC into a steel shell. The casting/infiltration processes require no additional filler material, can be incorporated into complex geometries, and are produced at a relatively low cost [13]. Inherent to the processing temperatures, hold times, and the specific steel/MMC system utilized, intermetallic regions form between the steel and MMC. These intermetallic regions can exhibit poor mechanical properties, specifically ductility, compared with the parent alloys. The Iron-Aluminum phase diagram is shown in Figure 1 with the steel/MMC encapsulation processing temperature conditions superimposed. As shown in Figure 1, the formation of each of the following intermetallic phases is possible: FeAl, $FeAl_2$, Fe_2Al_5, $FeAl_3$ (or Fe_4Al_{13}). A literature review was performed and preliminary Thermo-Calc Gibbs Free Energy predictions calculated to determine which intermetallics were most probable under these conditions.

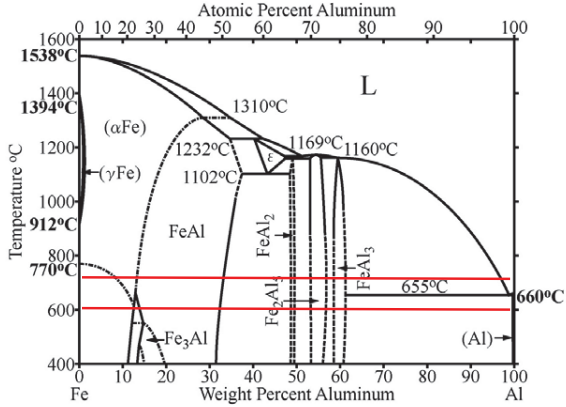

Figure 1. Iron-Aluminum Phase diagram illustrating steel/MMC encapsulation processing temperature range [13].

The formation of the intermetallic phases is driven by interdiffusion which has a direct relationship with the time and temperature history, where thicker reaction layers at the interface occur with longer time and/or higher temperature. Considerable hold times, on the order of several hours, were necessary during fabrication to guarantee the volume within the steel shell was filled completely.

Experimental Procedure

The evaluation of intermetallic reaction layers between Steel/MMC macro hybridized samples represents the main focus of this work. Steel (A36, 304, and Nitronic ® 50) bar with a diameter of greater than 0.5" was bored to produce a tube with an inside diameter of 0.188". The steel tubes were then processed to fill the internal void with various compositions of particulate MMCs,

Al-SiC, Al-Al_2O_3, and Mg-B_4C using a cast or infiltration approach. Finally, the gauge section of the steel/MMC bars were turned to a diameter of 0.300", 0.400" or 0.500" creating cylindrical dog-bone tensile samples as per ASTM B557-10. The various MMC cores therefore remained constant at 0.188" but with 3 different thicknesses of steel to provide for 3 different residual stress conditions. [14-19].

Table I. List of macro hybridized materials systems with resulting average reaction layer thickness.

Steel Encapsulant	**Matrix Material**	**Reinforcement**	**Reinforcement percentage**	**Average Reaction Layer Thickness (in µm)**
A36	Al-10Si	SiC	30 vol%	Max 3.5
A36	Al-10Si	SiC	55 vol%	Max 15
A36	Al-4Mg	Al_2O_3	46 vol%	250
304SS	Al-10Si	SiC	30 vol%	30
304SS	Al-10Si	SiC	55 vol%	140
304SS	Al-4Mg	Al_2O_3	55 vol%	160
Nitronic® 50	Al-10Si	SiC	55 vol%	190
Nitronic® 50	Mg AZ91E	B_4C	45 vol%	10

Table I presents the hybridized tensile bars produced by M-Cubed Technologies Inc. Newark DE. Two different aluminum alloys were used for the matrix material of the particulate reinforced aluminum MMCs, Al-10Si and Al-4Mg. The matrix alloys were chosen specifically for the reinforcement type in order to avoid certain thermodynamic instabilities. Since SiC tends to form Al_4C_3 when it reacts with aluminum, Al-10Si was chosen to inhibit formation of Al_4C_3 and subsequent degradation of the reinforcement particles which can drastically diminish mechanical properties [5]. An Al-4Mg alloy was selected for use with the Al_2O_3 reinforcement as this alloy provides better ductility than Al-10Si. Aluminum matrix composites were produced with SiC and Al_2O_3 particles as reinforcement at 30 and 55 vol%. An Mg AZ91E alloy was infiltrated into a bed of B_4C particles packed into the hollowed steel tube resulting in 45 vol% reinforcement.

Extensive characterization was performed on the tensile specimens in the form of X-ray Diffraction (XRD) and Scanning Electron Microscopy (SEM) paired with X-ray Energy Dispersive Spectroscopy (EDS) and Electron Backscatter Diffraction (EBSD). Cross sections transverse to the direction of testing, see Figure 2, were taken at multiple locations thoughout the gage section to investigate the reaction layers both within and away from the necked region after fracture. Specimens were cross sectioned using a wet diamond cut-off saw with a feed speed of 0.05 mm/s to minimize deformation. The resulting cross-sections were mounted in Bakelite and ground with silicon carbide paper from 320 to 800 grit. Subsequently, they were polished using 3, 1, and 0.3 micron diamond slurries and final polished with 0.05 colloidal silica in a Buhler VibroMet2 vibratory polisher. This resulted in a mirror like finish which allowed for microscopic inspection of the surface.

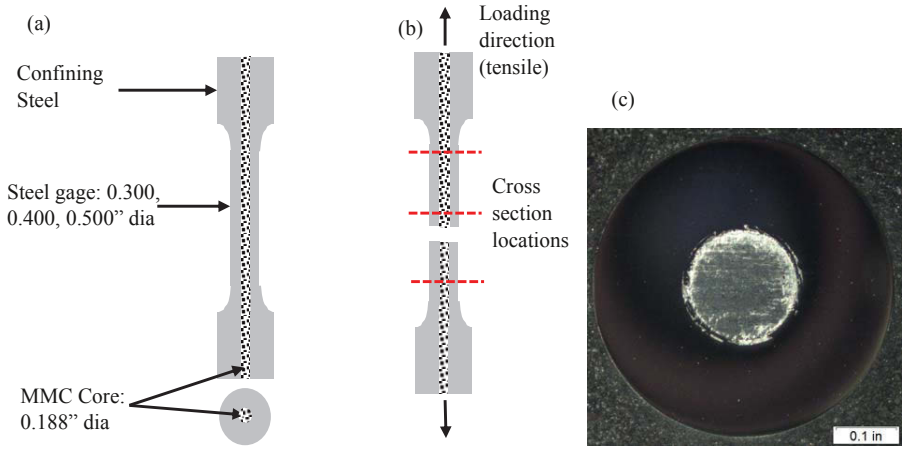

Figure 2. Design of composite tensile test sample. Illustrating (a) dimensions and material schematic (b) loading direction and typical cross section locations (c) mounted and polished cross section from 0.500" A36/Al-Al_2O_3 specimen.

XRD was performed on a Bruker D8 X-ray diffraction system in conjunction with the DIFFRAC.SUITE software. The target X-ray material was Cu with a 1.5418 angstrom wavelength operating at 40 kV and 40mA. The monochromatic Cu $K_{\alpha 1}$ line is isolated by the Vario monochromater at the X-Ray tube. A LynxEye position sensitive detector is included which permits up to 4 ° 2θ of diffracted beam to be measured continuously while scanning. A continuous 2θ scan mode was applied from 20-120° 2θ with an increment of 0.05°.

SEM analysis was performed using a Zeiss Auriga 60 Crossbeam™ FIB-SEM to study reaction zones, particle size, and distribution. Furthermore EDS and EBSD were performed utilizing the Oxford Aztec software. Line, area, and map scans were created covering the reaction layers of each hybrid material. Quantitative results were obtained and cross referenced with measured XRD peaks to aid in properly identifying intermetallic formation. Electron Backscatter Diffraction was utilized for phase identification at the interface.

Results and discussion

XRD was performed on the interface between each of the hybridized materials systems. Each system consists of a unique combination of steel and MMC resulting in considerably different reaction layers based on the interaction of the constituents. Table II shows the elemental composition of the steels and MMC matrix alloys used in this work. As evident from table II, significant amounts of alloying elements are present, specifically Chromium, Nickel, and Manganese, within the stainless steels. Although the focus of this paper is on the formation of Fe-Al intermetallics, future effort will include identifying and characterizing all intermetallic phases present in the hybridized materials systems.

Table II. Steel and matrix alloys utilized within the steel encapsulated metal matrix systems.

Element	A36	304	Nitronic® 50	AZ91E	Al-4Mg	Al-10Si
Carbon	0.25 -0.29	0.08 max	0.06 max	-	-	-
Copper	0.20 max	-	-	0.003	-	0.2
Chromium	-	18.0 - 20.0	20.5 - 23.5	-	-	-
Manganese	1.03 max	2.00 max	4.0 - 6.0	0.22	-	0.1
Molybdenum	-	-	1.5 - 3.0	-	-	-
Nickel	-	8.0 12.0	11.5 - 13.5	-	-	-
Nitrogen	-	0.1 max	0.3 max	-	-	-
Phosphorus	0.04 max	0.045 max	-	-	-	-
Silicon	0.28 max	0.75 max	1.00 max	0.035	-	8.5-9.5
Sulfur	0.05 max	0.03 max	-	-	-	-
Titanium	-	-	-	-	-	0.2
Vanadium	-	-	0.10 - 0.30	-	-	-
Zinc	-	-	-	0.63	-	0.05
Aluminum	-	-	-	8.25	Balance	Balance
Iron	Balance	Balance	Balance	0.014	-	0.2
Magnesium	-	-	-	Balance	4	0.45 -0.60

Due to the variation in the reaction layer thicknesses, XRD was only able to index intermetallic phases in the hybridized materials systems which exhibit a sufficiently thick reaction layer. Figures 3 and 4 show the X-ray diffraction peaks, plotting counts vs. 2θ position, collected from the A36/Al-Al_2O_3 and Nitronic/Al-SiC systems respectively.

The X-ray tests were setup to maximize the amount of intermetallic layer area measured as compared with the surrounding materials. However, some of the adjacent material was also bombarded with x-rays and thus their peaks are present in the scans. Figure 4 shows the presence of Fe_4Al_{13} and Fe_2Al_5 at the A36/Al-Al_2O_3 interface. Some minor peaks also identify Al_2O_3 which is consistent with the reinforcement particles in the MMC. Similarly, Figure 4 shows the resultant x-ray diffraction peaks from the Nitronic-AlSiC interface, in which Fe_4Al_{13} appears to be the only intermetallic compound formed in this system.

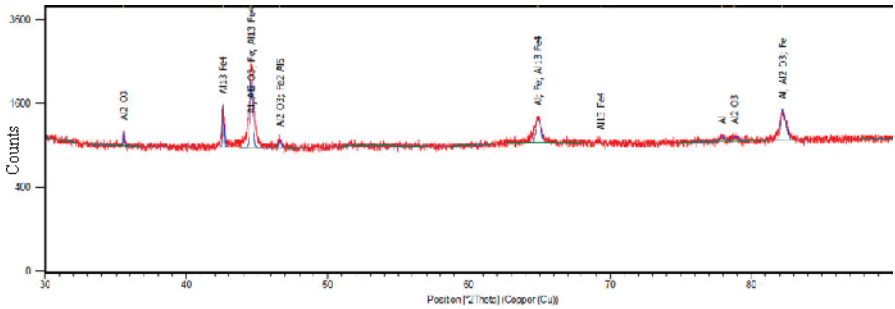

Figure 3. X-ray diffractogram A36/Al-Al_2O_3 interface.

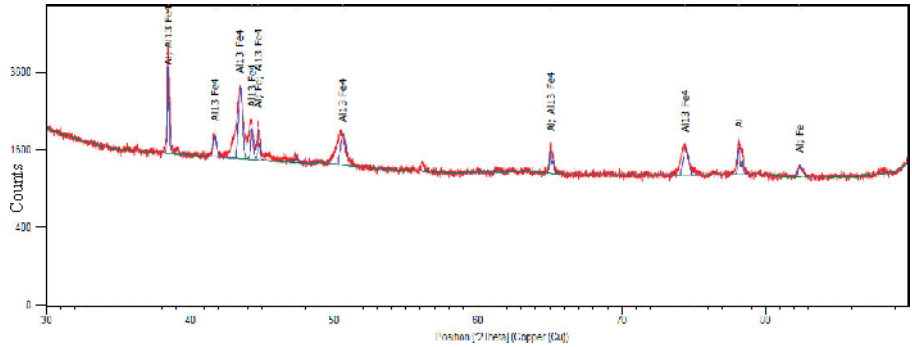

Figure 4. X-ray diffractogram of Nitronic/Al-SiC interface.

The structure of the aluminum rich phase Fe_4Al_{13}, as determined by X-ray diffraction is monoclinic, space group B2/m and with lattice parameters a= 1.5489 nm, b=0.8083 nm, c=1.2476 nm. The Fe_2Al_5 is orthorhombic, with lattice parameters a=0.7675 nm, b= 0.64030 nm, c= 0.4203 nm. The identified Fe-Al intermetallics formed, Fe_4Al_{13} and Fe_2Al_5, are consistent with previous literature [1, 20], where Al rich phases are typically observed below processing temperatures of 1200°C and Fe rich phases above.

As evident from Figure 5, the reaction layer between the materials not only varies by thickness but also its shape. The top darker region is the MMC, the intermediate brighter region the reaction layer, and the bottom brightest region the steel in each case. The reaction layer seen in 5(a), A36 steel/Al-Al_20_3 46P, exhibits irregular dendritic like structure with an average thickness of about 250µm. Figure 5(b), 304 stainless steel/Al-SiC 55P, shows a much more uniform reaction layer with average thickness of about 170µm. This reaction layer appears to be much more brittle as compared with (a). Figures 5c and 5d show the Nitronic/Mg-B_4C 45P interface. The images illustrate a reaction layer thickness of about 10µm.

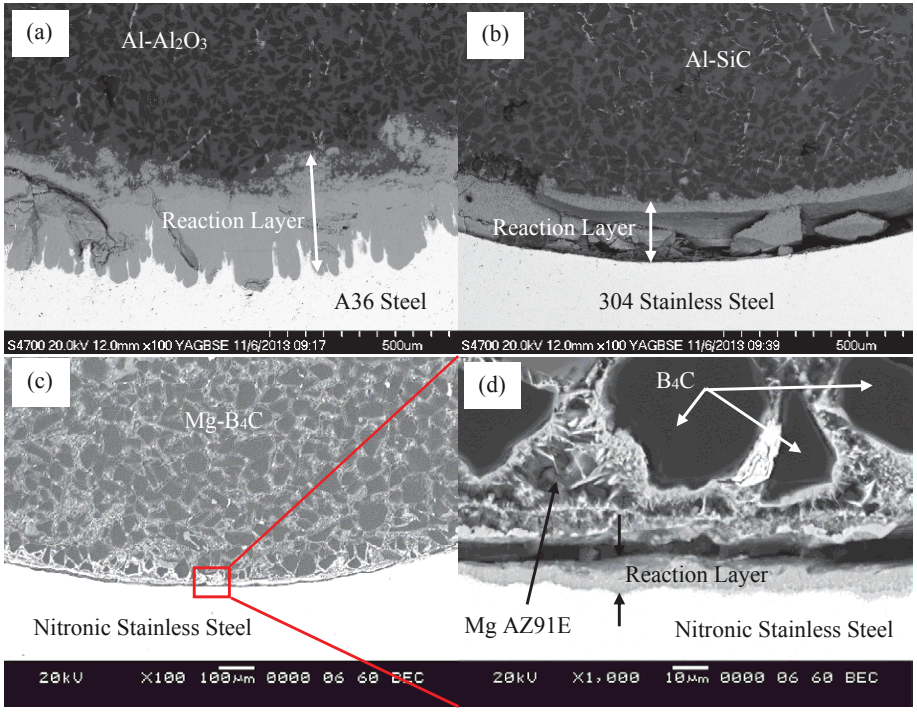

Figure 5. Backscatter electron micrographs of the interface between steel and MMC. (a) 100x magnification of A36/Al-Al_2O_3 (b) 100x magnification of 304/Al-SiC (c) 100x magnification of Nitronic/Mg-B_4C (d) 1000x magnification of Nitronic/Mg-B_4C.

The interfaces in the A36/Al-SiC 30P, A36/Al-SiC 55P, 304/Al-SiC 30P, and Nitronic/Mg-B_4C 45P samples varied from having no SEM detectible reaction layer to having some thin discontinuous areas of reaction thus no XRD intermetallic peaks were observed on these samples. The thinner reaction layers are likely due to the substantially shorter processing times associated with the 30P process and the fact that Mg does not react with Fe. Future efforts will make use of transmission electron microscopy (TEM) to adequately identify these minute reaction zones.

EDS and EBSD were then performed to more accurately map the intermetallic regions within the reaction layer. Due to the significant hardness difference between the multiple phases: steel, intermetallics, aluminum, and ceramic materials, substantially different material removal rates are experienced during polishing resulting in some topographical artifacts. Figure 6 shows the A36/Al-Al_2O_3 interface as imaged from an EBSD phase map. The red color on the left represents ferrite, the green section Fe_2Al_5, the yellow section Fe_4Al_{13}, and a small blue area on the right the alumina reinforcement.

Figure 6. EBSD phase map of the A36/Al-Al_2O_3 interface.

Differentiated intermetallic layers were only observed on the A36/Al-Al_2O_3 sample as the other materials only exhibit one intermetallic phase rather than the two observed here. It will be important to analyze the interfaces between the phases; steel-intermetallic interface and intermetallic-matrix interface to fully understand the macro composite properties. In addition for the A36/Al-Al_2O_3 system, the Fe_2Al_5 - Fe_4Al_{13} interface will need to be evaluated. Future work will include quantifying the mechanical properties of these intermetallics, specifically efforts on hardness and ductility of the Fe-Al phases.

Conclusions

The intermetallic reaction layer formation of several steel encapsulated metal matrix composites was studied and characterized in this work. Specific conclusions from this research include:

1. XRD analysis and microstructural characterization suggest Fe_2Al_5 and Fe_4Al_{13} are present in the reaction layer in the A36/Al-Al_20_3 system. Whereas only Fe_2Al_5 are observed in the Nitronic/Al-SiC and 304/Al-SiC systems.
2. The reaction layer thickness observed in the A36/Al-Al_20_3 system exhibits irregular dendritic like structure with an average thickness of about 250 μm.
3. The 304/Al-SiC and 304/Al-Al_2O_3 systems displays a uniform reaction layer with average thickness of about 140 μm and 160 μm respectively.
4. The A36/Al-SiC 30P, A36/Al-SiC 55P, 304/Al-SiC 30P, and Nitronic/Mg-B_4C 45P systems all exhibit comparatively thin, discontinuous reaction layers up to ~30 μm thick.
5. EDS and EBSD confirm the A36/Al-Al_2O_3 interface exhibits a two phase intermetallic region with a relatively smooth boundary layer between the two.

This research was supported in part by an appointment to the Postgraduate Research Participation Program at the U.S. Army Research Laboratory administered by the Oak Ridge Institute for Science and Education through an interagency agreement between the U.S. Department of Energy and USARL.

References

1. E. Taban et al. “Characterization of 6061-T6 aluminum alloy to AISI 1018 steel interfaces during joining and thermo-mechanical conditioning” Materials Science and Engineering A 527 (2010) 1704–1708.
2. A. Mazahery and M. Ostadshabani, “Investigation on mechanical properties of nano-Al_2O_3 reinforced aluminum matrix composites”, Journal of Composite Materials, 45 (2011), pp. 2579-2585.
3. V. Kumar GB, Rao CSP, Selvaraj N, Bhagyashekar MS. “Studies on Al6061-SiC and Al 7075-Al_2O_3 metal matrix composites. J Miner Mater Charact Eng 2010;99(1):43-55.
4. McDaneals DL. “Analysis of stress, strain, fracture and ductility behavior of Al matrix composite containing discontinuous SiC reinforcement”. Metall Trans A 1985; 16A: 1105–1115.
5. Ibrahim IA, Mohammed FA and Lavernia EJ. “Particulate reinforced metal matrix composites: a Review”. J Mater Sci 1991; 26: 1137–1156.
6. Lloyd DJ. “Particle reinforced aluminum and magnesium matrix composites”. Int Mater Rev 1994; 39: 1–21.
7. M. Yılmaz et al. “Interface properties of aluminum/steel friction-welded components” Materials Characterization 49 (2003) 421– 429.
8. G. Schrader et al. “Manufacturing Processes & Materials Society” Manufacturing Engineers 2000.
9. T Sakiyama et al. “Dissimilar Metal Joining Technologies for Steel Sheet and Aluminum Alloy Sheet in Auto Body” Nippon Steel Technical Report 103 May 2013.
10. A. Mathieu et al. “Laser brazing of a steel/aluminum assembly with hot filler wire (88% Al, 12% Si)” Materials Science and Engineering: A Vols 435–436, 5 November 2006, Pages 19–28.
11. O. Pasic et al. “Welding dissimilar metals – Status, requirements and trends of development” Welding in the World, 51, Pages 377-384.
12. S. Lazarevic et al. “Formation and Structure of Work Material in the Friction Stir Forming Process” Journal of Manufacturing Science and Engineering.
13. T. B. Massalski, 1986 Binary Alloy Phase Diagrams 1 ASM, 148 0-87170-261-4
14. M. Aghajanian, et al., “Processing of Hybrid structures consisting of Al-based metal matrix composites (MMCs) with metallic reinforcement of steel or titanium”, TMS2013 Annual Meeting Supplemental Proceedings, John Wiley & Sons, Inc., Hoboken, NJ, (2013), 629-638.
15 P. G. Karandikar et al., “Al/Al_2O_3 MMCs and macrocomposites for armor applications,” Ceramic Engineering and Science Proceedings 34 (5) (2013), 63-74.
16. P. G. Karandikar et al., “Net shape Al/B_4C metal matrix composites (MMCs) for high specific stiffness and neutron absorption applications**,”** TMS 2013 Annual Meeting Supplemental Proceedings, John Wiley & Sons, Inc., Hoboken, NJ, (2013), 683-689.
17. B. Givens, et al., “Effect of particle loading on the properties of Al/SiC metal matrix composites,” in Aluminum Alloys: Fabrication, Characterization and Applications II, Yin et al. editors, TMS, Warrendale, PA (2009) 197-202.
18. P. Karandikar et al. “Metal Encapsulated MMC Macrocomposites” Materials Science & Technology 2014 Conference Proceedings.
19. S. Fudger et al. "Mechanical Properties of Steel Encapsulated Metal Matrix Composites." *Advanced Composites for Aerospace*. New York: John Wiley & Sons, 2015. 121-36. Print.
20. S. Fukumoto, et al. “Evaluation of friction weld interface of aluminum to austenitic stainless steel joint,” Materials Science and Technology Volume 13, Issue 8 (01 August 1997), pp. 679-686

EFFECT OF LOAD AND GRIT SIZE ON HIGH STRESS ABRASIVE WEAR OF Al-Mg-Si HYBRID COMPOSITES

Kaushik N Ch[1,*], Narasimha Rao R[1]

[1]Department of Mechanical Engineering, National Institute of Technology-Warangal, Telangana-506004, India

Abstract

In the present investigation, the two body abrasive wear behavior of Al-6082 alloy, Al 6082-10% SiC (Al-SiC) composites & Al 6082-5%SiC-5%Gr (Al-SiC-Gr) hybrid composites was studied at load of 5-15N, 75m sliding distance and abrasive grit size of 100-200µm by using pin-on-disc equipment. The composites were synthesized by stir casting technique, a liquid metallurgy route. It was observed that load and type of emery paper used would have profound influence on the abrasive wear characteristics in the present set of experiments. The results show that graphitic composites yielded better wear resistance compared to alloy and SiC alone reinforced composites. At higher load and abrasive grit size, 16.4% and 11.6% improvement was observed for Al-SiC-Gr and Al-SiC composites respectively when compared to unreinforced alloy. Worn surface analysis of tested samples and tested grit papers were observed by using scanning electron microscope (SEM).

Keywords— Two body abrasive wear, hybrid composites, wear resistance, worn surface analysis.

1. Introduction

Wear of the critical components like brake drums, cylinder blocks, cylinder liners, drive shafts etc was one of the serious concerns that affect the overall operational efficiency in automotive applications. In this regard, several experimental investigations have been made in adding individual reinforcements such as SiC, Al_2O_3, graphite etc to aluminium matrix metal. This lead to improvement in not only mechanical properties but also tribological properties of the materials. The aluminum metal matrix composites (Al-MMCs) have been successfully introduced in automobile, aircraft, space equipment and structural components [1-6]. Automobile companies like Honda, Nissan, Toyota, and General Motors etc have successfully implemented these Al-MMCs in different engine applications by using various particle and fiber type reinforcements [6].

Recent investigation studies show that attention has been given in reinforcing multiple reinforcements i.e. graphite and SiCp to aluminium matrix which produced by different techniques. This was done to know the synergistic effects of hard type and soft type of reinforcements in the sliding wear behaviour on the matrix material. It was proven that wear behavior of Al MMCs with multiple reinforcements was found to be superior compared to alloy and single reinforcement [7-11]. It was reported that the graphite addition was found to be advantageous in tribolayer formation, subsurface deformation and machining of Al-SiC composites [9]. However, it was observed that the abrasive wear behavior of single particle

reinforced composites was well understood and investigation is required to study on abrasive wear behavior of Al-SiC-Gr hybrid composites.

2. Materials & Methods

2.1 Composite Preparation

An Al-Mg-Si (6082) alloy and Al 6082-10%SiC and Al 6082-5%SiC-5%Gr composites were used for present investigation. The chemical composition of alloy has Cu-0.06%, Mg-0.77%, Si- 0.95%, Fe-0.32%, Mn-0.532%, Zn-0.016%, Ti-0.037%, Cr-0.038% and Al-balance. The composites were synthesized by stir casting technique i.e. liquid metallurgy route using SiC and graphite particles of size 20-40µm. The process involves melting of alloy, adding of preheated SiC and graphite particles in the melt through mechanical stirring and pouring of composite melt into stainless steel mould of size: 170 mm length & Ø40 mm. Similarly the alloy melt and SiC reinforced composites were synthesized. The wear testing samples of 27mm length & Ø 8mm were prepared from casted ones by machining process.

2.2. Microscopy

The morphology of fresh emery papers before abrasive testing was observed under scanning electron microscopy (SEM) (Model: TESCAN, Vega LMU 3) shown in Fig 1. The worn surfaces of specimens and emery papers were also observed which were discussed later in this work.

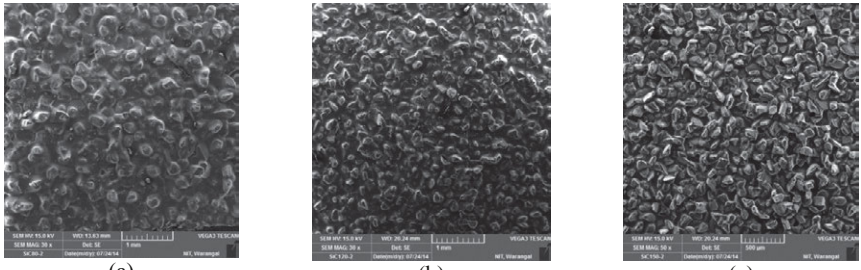

(a) (b) (c)

Fig. 1: Morphology of emery papers used in the abrasion tests (a) 200µm abrasive grit size (b) 125µm abrasive grit size (c) 100µm abrasive grit size

2.3 Wear Testing

The two body abrasive wear tests were conducted on a pin-on-disc machine (Magnum make, model: TE-165-SPOD, Bangalore). The parameters such as load of 5N, 10N & 15N and constant 75m sliding distance on different 100µm, 125µm, 200µm abrasive grit size silicon carbide emery papers. The desired grit paper was cut to size and fixed on a wheel diameter: 50 mm, thickness: 12 mm to serve as an abrasive medium. The specimens were cleaned before and after the wear tests using acetone. The each test was conducted for three times and average weight loss was noted. The wear rates (mm^3/m) were calculated from the weight loss measured.

3. Results & Discussions

The two body abrasive wear rate (mm^3/m) of the materials was plotted as a function of grit size at different loads and constant sliding distance of 75m. This was shown in Fig. 2(a)-(c). The wear characteristics were found to be having profound influence by load and type of emery paper used.

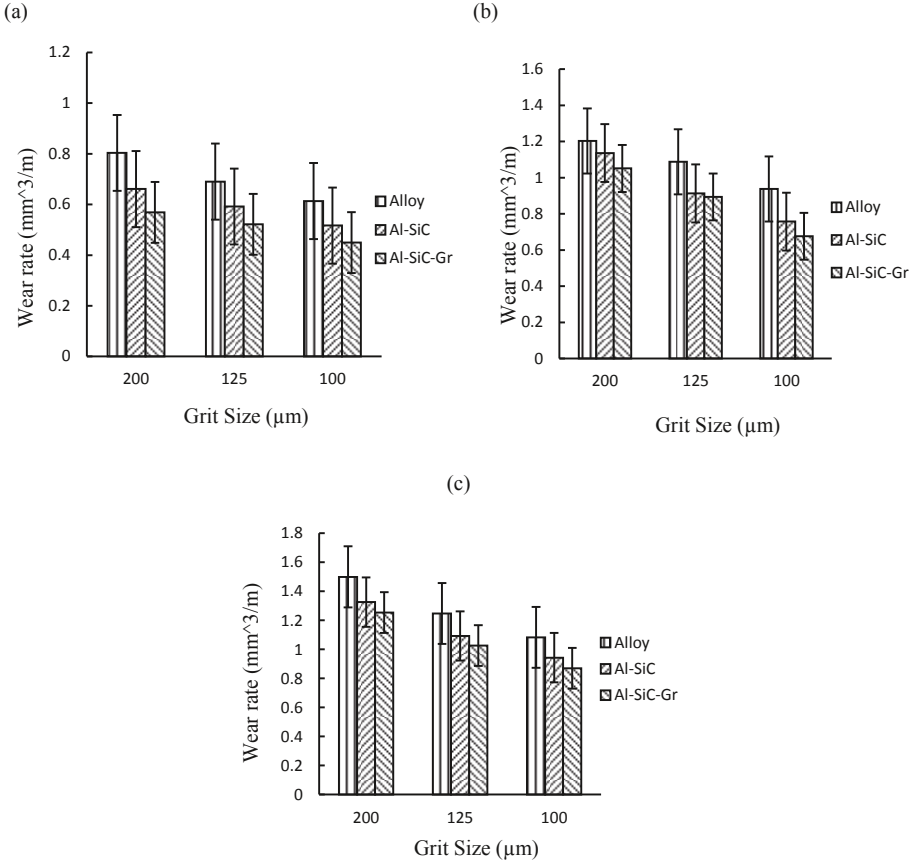

Fig. 2: Variation of wear rate of alloy and its composites at load (a) 5N (b) 10N and (c) 15N on abrasive grit size 100μm to 200μm at 75m sliding distance.

At 5N load and 200μm grit size, the wear rate of Al 6082 alloy, Al 6082-SiC composite and Al 6082-SiC-Gr composite was found to be 0.8036, 0.6608 and 0.5684 respectively. This

indicates the percentage improvement of wear rate is around 17.7 and 29.3 for Al-SiC and Al-SiC-Gr respectively. But on 100µm grit size, the wear rate of Al 6082 alloy, Al 6082-SiC composite and Al 6082-SiC-Gr composite was found to be 0.6133, 0.5166 and 0.4496 respectively. This indicates the percentage improvement of wear rate is around 15.8 and 26.7 for Al-SiC and Al-SiC-Gr respectively. At 10N load and 200µm grit size, the wear rate of Al 6082 alloy, Al 6082-SiC composite and Al 6082-SiC-Gr composite was found to be 1.2025, 1.1359 and 1.0511 respectively. This indicates the percentage improvement of wear rate is around 5.5 and 12.6 for Al-SiC and Al-SiC-Gr respectively. But on 100µm grit size, the wear rate of Al 6082 alloy, Al 6082-SiC composite and Al 6082-SiC-Gr composite was found to be 0.9378, 0.7570 and 0.6759 respectively. This indicates the percentage improvement of wear rate is around 19.3 and 27.9 for Al-SiC and Al-SiC-Gr respectively. At 15N load and 200µm grit size, the wear rate of Al 6082 alloy, Al 6082-SiC composite and Al 6082-SiC-Gr composite was found to be 1.4998, 1.3257 and 1.2539 respectively. This indicates the percentage improvement of wear rate is around 11.6 and 16.4 for Al-SiC and Al-SiC-Gr respectively. But on 100µm grit size, the wear rate of Al 6082 alloy, Al 6082-SiC composite and Al 6082-SiC-Gr composite was found to be 1.0825, 0.9429 and 0.8696 respectively. This indicates the percentage improvement of wear rate is around 12.9 and 19.6 for Al-SiC and Al-SiC-Gr respectively.

The worn surface analysis was done on tested pin sample surfaces as well as grit papers. Fig. 3 (a) and (b) shows the abraded surfaces of alloy pin at load of 5N and 15N respectively at 200µm grit size whereas Fig. 3 (c) and (d) shows the abraded surfaces of alloy pin at load of 5N and 15N respectively at 100µm grit size. Fig. 3 (e) and (f) shows the abraded surfaces of Al-SiC-Gr hybrid composite pin at load of 5N and 15N respectively at 200µm grit size whereas Fig. 3 (g) and (h) shows the abraded surfaces of Al-SiC-Gr hybrid composite pin at load of 5N and 15N respectively at 100µm grit size.

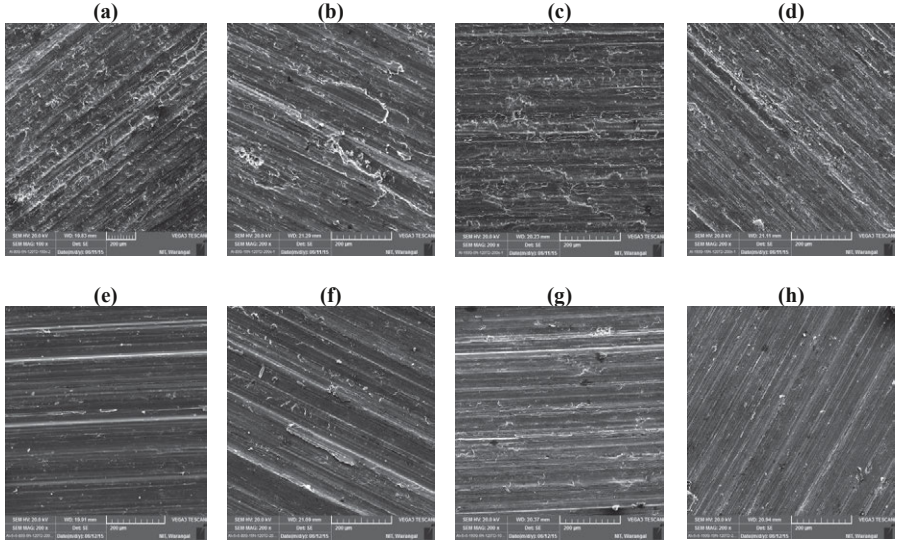

Fig. 3: Worn surface analysis of samples (a)Al 6082 alloy at load 5N and 200µm grit size (b)Al 6082 alloy at load 15N and 200µm grit size (c) Al 6082 alloy at load 5N and 100µm grit size (d)Al 6082 alloy at load 15N and 100µm grit size (e)Al 6082-SiC- Gr composite at load 5N and 200µm grit size (f)Al 6082-SiC- Gr composite at load 15N and 200µm grit size (g)Al 6082-SiC-Gr composite at load 5N and 100µm grit size (h)Al 6082-SiC- Gr composite at load 15N and 100µm grit size

Fig. 4 (a) and (b) shows the abraded surfaces of 200µm grit size paper tested on Al 6082 alloy at load of 5N and 15N respectively whereas Fig. 4 (c) and (d) shows the abraded surfaces of 100µm grit size paper tested at load of 5N and 15N respectively. Fig. 4 (e) and (f) shows the abraded surfaces of 200µm grit size paper tested on Al-SiC-Gr hybrid composite pin at load of 5N and 15N respectively whereas Fig. 4 (g) and (h) shows the abraded surfaces of 100µm grit size paper tested on Al-SiC-Gr hybrid composite pin at load of 5N and 15N respectively.

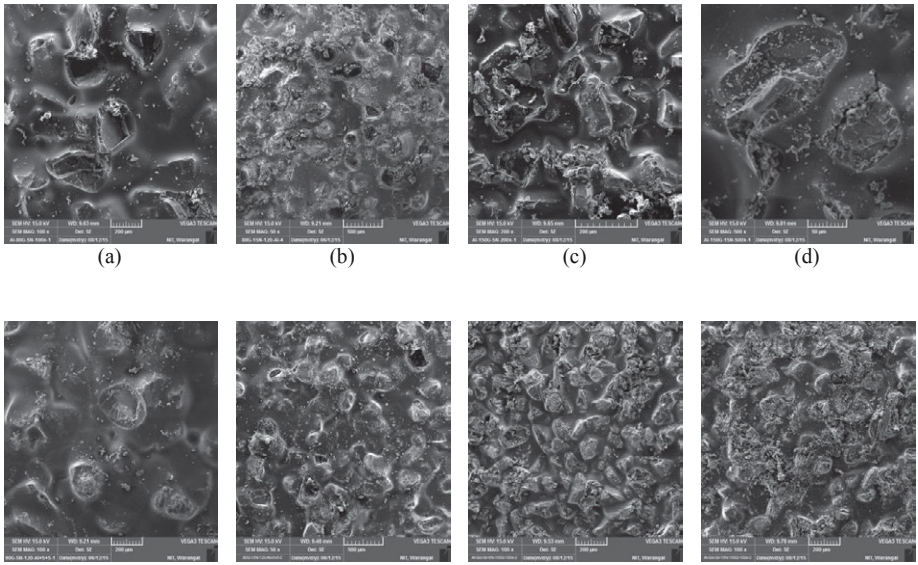

(a) (b) (c) (d)

(e) (f) (g) (h)

Fig. 4: Worn surface analysis of grit papers (a)Al 6082 alloy at load 5N and 200µm grit size (b)Al 6082 alloy at load 15N and 200µm grit size (c) Al 6082 alloy at load 5N and 100µm grit size (d)Al 6082 alloy at load 15N and 100µm grit size (e)Al 6082-SiC- Gr composite at load 5N and 200µm grit size (f)Al 6082-SiC- Gr composite at load 15N and 200µm grit size (g)Al 6082-SiC- Gr composite at load 5N and 100µm grit size (h)Al 6082-SiC- Gr composite at load 15N and 100µm grit size

The composite material typically will wear away by ploughing or cutting action of abrasive particles or asperities on the hard counter face. This will expose the protrusions of second phase particles present in the composite material. The further abrasion process will be hindered by the hard phased protrusions rather than soft one. The importance of the matrix material lies in the level of support given to the second phase particles. The more the capacities of the upholding capacity, the better wear resistance of the composite material.

The SEM characterization of abraded surface revealed that long continuous grooves have been formed. It was similar to that abraded surfaces during preparation of the metallographic specimens. The abrasive particles plough across the surface by displacing the material into ridges along groove sides. The worn surfaces of the composites show the shallow scratches when compared to alloy material. The wear tracks of the composite specimens exhibited a worn surface which is relatively smoother. This could be due to the tendency of microploughing is less on the surface of composite material. For the Al-SiC-Gr composites graphitic film would be formed and it would act as a lubricating layer [12,13,16]. During this eventual process of the abrasive wear, this layer could be removed first and after that hard SiC reinforcement particles takes role in further reduction of wear process. This indicates that the graphitic films tend to behave as a sacrificial layer in the initial wear process. Hence it was observed that the wear resistance was improved in the case of graphitized Al-SiC composites.

4. Conclusions

Based on the experimental investigation carried on materials the following conclusions were drawn:

- The composites were prepared using liquid metallurgy route.
- Two body abrasive wear tests were carried at load 5-15N and sliding distance 50-75m on 200μm grit size emery paper.
- As the load increases to 15N, the improvement of wear rate of Al-SiC and Al-SiC-Gr was 11.6% and 16.4% respectively when compared to alloy at 75m sliding distance.
- The Al-SiC-Gr composites yielded better abrasive wear resistance properties when compared with single SiC reinforced composite and alloy materials. The combination of SiC (hard) and graphite (soft) reinforcements found to beneficial due to formation of graphitic film which acts as an self-lubricant in Al-SiC-Gr composites.
- SEM analysis of worn surfaces revealed that shallower grooves were observed in graphitized composites when compared to alloy and un-graphitized composites.
- Lesser fragmentation of matrix material was observed on the surface of pin in case hybrid composites compared to alloy material.

References

[1] P.K. Rohatgi, Cast aluminum matrix composites for automotive applications, Journal of The Minerals, Metals & Materials Society, 1991, pp. 10–15.

[2] D.J. Lloyd, Particle reinforced aluminium and magnesium matrix composites, International Material Review, Vol. 39 (1) 1994, pp. 1–23.

[3] A.E. Nitsham, New application for Al based MMC, Light Metal Age, 53 1997, pp.53-54.

[4] R.S. Rawal, Metal matrix composites for space applications, Journal of The Minerals, Metals & Materials Society 2001, pp. 14-17.
[5] S. Das, Development of aluminium alloy composites for engineering applications, Transactions of Indian Institute of Metals, Vol. 57 2004, pp. 325–334.
[6] S.V. Prasad, R. Asthana, Aluminium metal-matrix composites for automotive applications: tribology considerations, Tribology Letters, Vol. 17(3) 2004: pp. 445-453.
[7] M.L.Ted Guo, C.Y.A. Tsao, Tribological behavior of self-lubricating aluminium - SiC - graphite hybrid composites synthesized by the semi-solid powder densification method, Composites Science and Technology Vol. 60 (1) 2000: pp. 65–74.
[8] S.Basavarajappa, G Chandramohan, Dry sliding wear behavior of hybrid metal matrix composites, Material Science, Vol.11 (3) 2005: pp. 253-257.
[9] S. Suresha, B.K. Sridhara, Wear characteristics of hybrid aluminium matrix composites reinforced with graphite and silicon carbide particulates, Composites Science and Technology, Vol. 70 2010: pp 1652–1659.
[10] M. Vamsi Krishna, A. M. Xavior, An Investigation on the Mechanical Properties of Hybrid Metal Matrix Composites. Procedia Engineering, Vol. 97, 2014: pp. 918–924.
[11] G. Elango, B.K. Raghunath Tribological behavior of hybrid (LM25Al-SiC-TiO2) metal matrix composites, Procedia Engineering, Vol. 64, 2015: pp. 671-680.
[12] K.S. Al-Rubaie, H.N. Yoshimura, J. D. B de Mello, Two body abrasive wear of Al-SiC composites, Wear, 233-235, 1999: pp. 444-454.

THE CORROSION OF 30% Mo-ZrO_2 CERMET IN MOLTEN SLAG OF CaO-MgO-Al_2O_3

Xiaopeng Li, Ziming Wang,Yang Yang, Yanling Guo*, Jieyu Zhang, Wende Dan
(State Key Laboratory of Advanced Special Steel, School of Materials Science and Engineering, Shanghai University, Shanghai 200072, China)

Keyword: Mo-ZrO_2 cermet, corrosion, molten slag

Abstract

Mo-ZrO_2 cermet is a potential material for application as electrode in steel purifying process with addition of electrical field because of its high electrical conductivity and good corrosion resistance to molten slag and steel at high temperature. This paper describes the static corrosion test of Mo-ZrO_2 cermet sample with Mo content 30 vol.% in CaO-MgO-Al_2O_3 molten at 1550℃. The results showed that a dense $CaZrO_3$ layer was formed during test and it will prevent the further corrosion of cermet by slag.

Introduction

Cermet with some of the advantages of both metals and ceramics is widely discussied by international scholars' [1][2]. With the development of metallurgical technology and the requirement of environmental protection, scholars raised a new clean deoxidizing method "controlled oxygen flow metallurgy"[3], namely in the slag-metal interface. A certain direction of the electric field is applied in the slag-metal interface, by controlling the oxygen ion transport in the slag to achieve pollution-deoxy metal melt[4] [5]. Deng [6] found that adding 10% alumina zirconia ceramic thermal shock resistance is the best. Lei Tang [7] studied its resistivity, thermal shock resistance, and found that the electric conductivity is good. Yanling Guo[8] found that Mo-ZrO_2 cermet in molten steel and slag corrosion is associated with the composition of the ceramic substrate .The cermet without adding stabilizer of pure monoclinic zirconia matrix m-ZrO_2/Mo cermet anti-corrosion steel is best, while adding 3Y-PSZ/Mo of 3% (mol) Y_2O_3 cermet slag corrosion resistance is best. Chang [9] studied the influence of the Mo content on the Mo-ZrO_2 cermet liquid steel and slag corrosion resistance. The influence showed that with the increase of Mo content, cermet corrosion resistance to molten steel weaken and slag corrosion resistance increased.

In this paper,we use powder metallurgy method to prepare the Mo-ZrO_2 cermet which Mo volume fraction was 30% and the relative density is greater than 95% . The corrosion medium was the slag CaO-MgO-Al_2O_3 which the CaO, MgO, Al_2O_3 mixed uniformly by melting.

The experiment

materials

Experimental material are Mo powder (99.00% purity), ZrO2 powder (99.00% analysis purity), polyvinyl alcohol (99.00% purity), alcohol (national medicine group chemical reagent co.LTD.) and argon (the Shanghai five steel gas company). The composition of slag as follows.

Table 1. Synthetic slag composition

ingredient	CaO	Al_2O_3	MgO
Content	44.16%	51.14%	4.7%

The preparation of metal ceramic

In this experiment ,we weighed powder Mo with 36.1% and ZrO_2 with 63.9% according to the stoichiometric ratio and put the mix into the ball mill tank of PTFE material with the ball material ratio approximately 6:1[10].Wet grinding ball mill tank was put a certain amount of alcohol. Raw material was mixed in the planetary ball mill with speed 500 r/min for 12 h. The slurry was put into the oven till the paste is completely dry. The dried block material was put into the mortar with adding PVA binder of about 5% then grinded. The particle size was selected about in the range of 60~100 mesh [11]. The mold diameter is 20mm and forming pressure is 12 Mpa. Then the green bodies were sintered in horizontal furnace at 1600℃ in argon for 2 h [12] .

Corrosion experiment

In this experiment, we used static corrosion method. We put the pre-melting alkaline slag CaO-MgO-Al_2O_3 into the bottom of corundum crucible and then put cermet sample into the tubular furnace heating to 1550 ℃ at a speed of about 3 ℃ /min. Choosing temperature 1550 ℃ was that the alkaline slag melting point is at about 1500 ℃. The sample was heated for 1h and 2h then cooled.

Results and Discussion

Metal ceramic sample morphology corrosion before

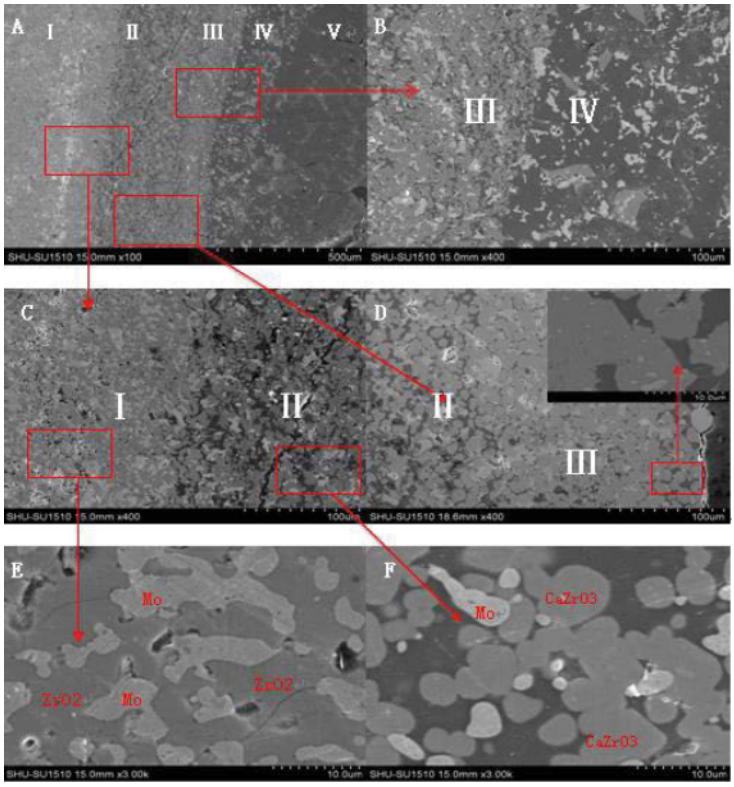

Fig 1.SEM of sample after corrosion in CaO-MgO-Al_2O_3 slag at 1550℃ for 1h

Figure 1 shows the details of cermet sample after corrosion. There are five distinct layers formd in the sample after corrosion and they are marked as layer I to layer V from the side of ceramic to slag. Layer I is uncorroded cermet and Layer II and III are corrosion layer at cermet side. The thickness of layer Ⅱ and Ⅲare 0.45 mm. Its internal slag is much more than of Ⅲ layer from the morphology of Ⅱ with corrosion which is far from slag. Layer Ⅲ with the thickness of 0.16 mm is densed corrosion layer, which is identified by EDS and XRD as $CaZrO_3$.Ⅳwas the excessive layer of slag corrosion diffusing into cermets, Ⅴis the layer of slag without corrosion. Fig. 1B is the border morphology of the layer Ⅱ and Ⅲ. C is the border morphology of the layer Ⅰ and Ⅱ . D is the border morphology of the layer Ⅱ and Ⅲ, The Mo and ZrO_2 of Ⅲ disappeared entirely and was replaced by a new generation of

$CaZrO_3$ and slag which diffused. E is the amplification of layer and the layer is the cermet raw ingredients without corrosion. Light grey part is the metal Mo and dark gray parts is ZrO_2. F is the cermet sample Ⅱ with corrosion. Former ZrO_2 disappeared and a new phase of $CaZrO_3$ appeared.$CaZrO_3$ of this layer is smaller than of Ⅲ because layer Ⅲ is near the slag and more fully contacted with the ZrO_2 and continuously generated $CaZrO_3$ which generated by the CaO of invasion in the sample. so the slag with diffusion was constantly digested and $CaZrO_3$ grain grew gradually.

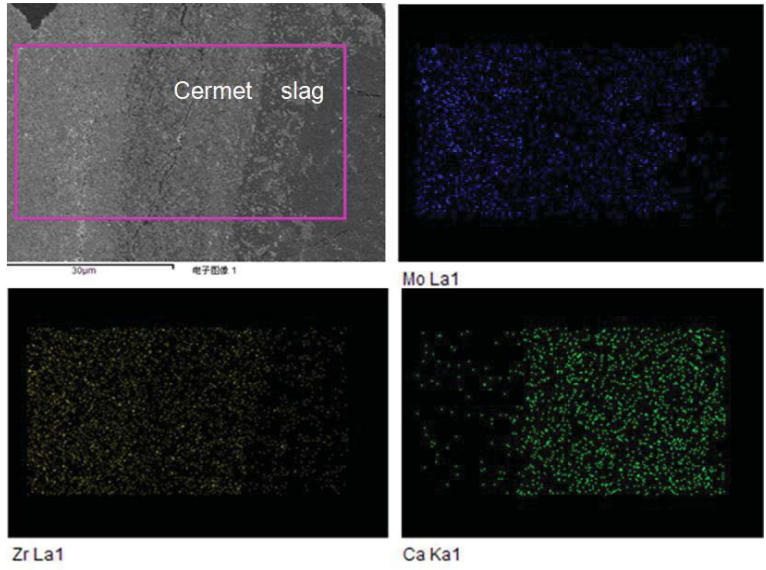

Fig 2. SEM - DES of sample after corrosion in CaO-MgO-Al_2O_3 slag at 1550℃ for 1h

Figure 2 shows that after corrosion of cermet samples the depth of cermet sample corrosion about Ca was overlapped with the depth of $CaZrO_3$ which generated. From the picture, the amount of Zr element in the cermet in the boundary of the cermet and slag began to significantly reduce also proving the point of view. The Mo would significantly reduce when Ca appeared in the corresponding area in the sample.

The corrosion mechanism

From the cermet XRD analysis after corrosion, the boundary layer of sample after corrosion appeared a new phase $CaZrO_3$.

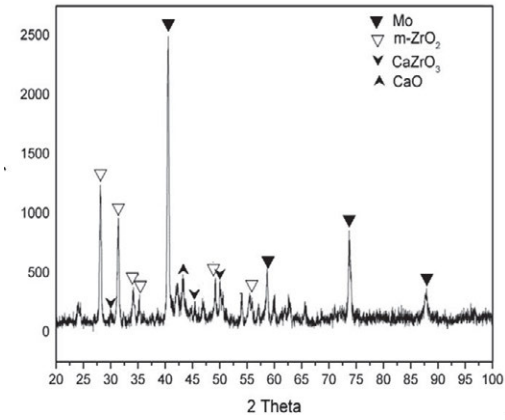

Fig 3 XRD of sample after corrosion in CaO-MgO-Al_2O_3 slag at 1550℃ for 1h

From the corrosion of cermet sample, the Ca element diffusing into the cermet sample from slag, it is not a gradient distribution. But it gathered in the excessive layer corrosion in the ceramic sample. This fully proves the existence of the $CaZrO_3$ in layers of excessive corrosion and the block of slag composition further diffusing into cermet sample. The stratification from Zr of the edge of sample and slag in the sample is obvious. There is the same reason because the ZrO_2 in the cermet and CaO in slag generated $CaZrO_3$ to prevent the loss of ZrO_2. Metal element Mo gradually reduced in the sample from the cermet to the slag. The loss of Mo in the sample prepared the blank for CaO which diffused from slag to sample.

The experiment gets enough data to obtain the result that corrosion process can be summed up in three steps from the XRD spectrum, SEM and SEM EDS. First, cermet sample was surrounded by alkaline molten slag. Second, the elements diffused each other, which are in slag and cermet. The invasion compound in this paper is Mo, ZrO_2 in the cermet and CaO in the slag. The Mo in the cermet gradually diffused into slag and the CaO of slag gradually diffused into cermet to form excessive layer. Finally, when temperature rose to 1180 ℃,CaO and ZrO_2 generated $CaZrO_3$ which CaO diffused into the cermet to generate $CaZrO_3$ with ZrO_2.

The relationship between degree of corrosion and corrosion time

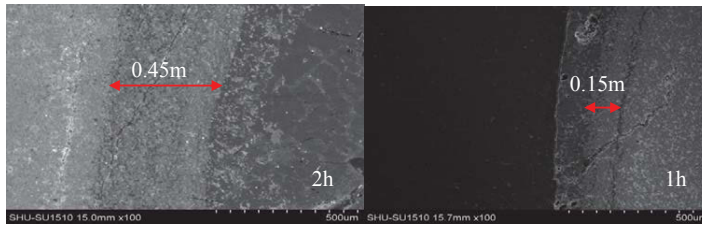

Fig 4 SEM of sample after corrosion in CaO-MgO-Al_2O_3 slag at 1550℃ for 2h and 1h

Figure 4 shows that the thickness under 2h is deeped than that under 1h. The degree of erosion increases with time becomes dark.

Conclusion

The static corrosion test of Mo-ZrO_2 cermet was conducted in CaO-MgO-Al_2O_3 at 1550 ℃ for 1 h and 2 h, respectively and the conclusions are obtained as follows.

The corrosion resistance of Mo-ZrO_2 cermet in CaO-MgO-Al_2O_3 slag is mainly due to that the outflow of Mo in the cermet provided CaO with space reacting with ZrO_2 to generate $CaZrO_3$ dense layer to prevent further corrosion

The more time of corrosion is, the worse corrosion resistance is, the more slag diffusing into the cermet is, the deeper thickness of corrosion is.

Acknowledgement

The authors gratefully acknowledge the support from the National Natural Science Foundation of China (51304131), and the Innovative Foundation of Shanghai University, China (sdcx2012003).

References

1. Rongjiu Li， “Ceramic-metal composite materials,” Beijing: Metallurgical industry press, 23 (2004), 105-109.

2. Kuihan Wang and Chuanmeng Cui, “Molybdenum fund of ceramic thermocouple protection tube study,” Journal of northeast institute of technology, 13 (4) (1992), 348-352.

3. Chou K C. et al., “Metallurgy with Controlled Oxygen Flow,” The Iron and Steel Institute of Japan, 14 (2004), 162−167.

4. kuo-chih Chou. et al., “The exploration of new directions - metallurgical process controlled oxygen flow metallurgy,” Beijing: science press, 16 (2006).

5. Xionggang Lu and kuo-chih Chou, “medium. Charged particles control technology application and prospect in metallurgical process,”. Journal of college of iron and steel research journal, 15 (5) (2003), 10.

6. Xuemeng Deng. et al., “equality additives on the influence of zirconia ceramics reting resistance,” Rare metal materials and engineering 12(2007).8

7. Lei Tang. et al., “Mo-ZrO_2 ceramic preparation and conductive performance study,”. Shanghai: shanghai University, 2013.

8. Yanling Guo. et al., “Zirconia - molybdenum metal ceramic molten steel and slag corrosion resistance”. Journal of process engineering of 2014.06.

9. Chang Jie. et al., “Mo-ZrO_2 ceramic metal corrosion resistant performance and the relationship between composition,”. Journal of process engineering of 2014.06,1206-1211.

10. Panxin Wang. “Powder metallurgy,”. Beijing: metallurgical industry press, 19 (1997).145-162

11. Peiyun Huang. et al. “Powder metallurgy principle,”. Metallurgical industry press, (1982).

12. Jifang Xu. “Plus oxygen transfer mechanism in the process of slag deoxidation dc field research,” Shanghai University, (2012). 25.

STUDY ON MECHANICAL PROPERTY OF POROUS TITANIUM BY ADDING POWDER CARBON

Guibao Qiu*[1]， Hao Cui[1], Tengfei Lu[1], Yilong Liao[2], Yang Yang[1]
(1, College of Materials Science & Engineering, Chongqing University, Chongqing 400044, China
2, China zhenhua group wing electric appliance co., LTD, Guizhou, China)

Keywords: porous titanium; powder carbon; initial yield strength

Abstract

Titanium alloys have a wide variety of applications in the aerospace, automotive and biomedical industries. Furthermore, titanium carbide (TiC) has been used for reinforcement of titanium alloy matrices due to its compatibility.
In this paper, under the experimental condition of 0.1 Pa, the sintering temperature of 1250℃ and sintering time of 2h, the porous titanium is fabricated by powder metallurgy blend element method. The conclusions manifest that porosity has a decreasing trend with increasing the addition of carbon; however, apparent increase of porosity appears when the addition of carbon increases to 2.5 wt%. The TiC is generated in the matrix manifested from the detection results of XRD. When the carbon content achieves 1.5 wt% and 2.0wt%, the initial yield strength reaches the highest with 339.8±15MPa and 331.1±10MPa separately. When the content of carbon powder achieves 2.5 wt%, the initial yield strength decreases to 195.1± 15MPa.

Introduction

In recent years, titanium (Ti) and its alloys have been applied in a variety of fields including aerospace, automobile and biomedical industrial as a result of their strength-to-weight ratio, favorable mechanical properties and admirable biocompatibility[1]. Moreover, porous titanium becomes one of the most promising biomaterials for orthopedic implants owing to its excellent corrosion resistance and unique nontoxicity[2]. However, porous titanium often suffers from inadequate hardness and initial yield strength, which hindered the further application. Titanium matrix composites, short for TMC, are composited with Ti metal and the other material, in which Ti is acted as matrix and another element named reinforcement. Compared with conventional Ti alloys, the specific strength, fatigue resistance performance along with high-temperature behavior and corrosion resistance of titanium matrix composites apparently increase[3]. With the underlying assumption that these novel materials that improve the properties of Ti alloys could be applied in more fields and especially be used as structural material under complex environment. The commonly used reinforcements in Ti matrix composites are TiC, SiC, Al_2O_3 and B_4C.[4, 5].
Titanium carbide (TiC) ceramic materials have the advantages of high elasticity

modulus and melting points, and moreover excellent compatibility and wettability with titanium metal that avoids separating from the matrixes. The use of titanium carbide for reinforcement have attracted much attention in recent years with the aim of improving their mechanical performance due to their density, elastic modulus, chemical and thermal stability being similar to those of titanium metal[6]. The possibility of reinforcement in metal matrix composites can change the properties of the composites so that their applications can be broadened[7]. The powder metallurgy (P/M) technique has been utilized to produce titanium alloys and their composites, offering advantages such as low cost, near net-shape fabrication, increase in material yield with same shape, and variation of composition[8]. As the most vital process during the powder metallurgical technique, the sintering needs to be performed in either a protective gas atmosphere or in vacuum. The in situ formation technique offers the advantages of better control of size and level of reinforcement so that the properties of the composites can be modified[8]. The yield strength and compressive strength of titanium matrix composites that contains 10% volume fraction of TiC are about 651MPa and 697MPa, much higher than those of pure Ti metal[4].
In this study, titanium matrix composites were fabricated by the in situ formation of TiC from the reaction between Ti powder and carbon powder. Then, the mechanical properties, phase constituents and pore characteristics of materials are studied.

Experimental procedures

Raw materials and preparation procedure

Ti powder metal (Beijing Red New Material Technology Co. Ltd.) and carbon powder are used as raw materials. The spacer holder has great impact on the pore structure and property of materials by adding different content or choosing different shapes during the process. As a result of apparent advantages such as low cost and environmental friendly, carbamide is chosen as spacer holder in the experiment. Under 400℃, the carbamide could be rapidly and thoroughly removed, the thermal decomposition equation is as follows:

$$CO(NH_2)_2 \rightarrow C_3H_6N_6 + 6NH_3 + 3CO_2 \quad (1)$$

Ti powders have particle sizes of ~40μm(with purity≥99.5%), carbon powders have particle sizes of < 30μm(with purity > 99.5%). The compositions of Ti powder are showed in Table 1.

Table 1 Chemical compositions of titanium powder

Ti powder	Ti	Fe	Si	Cl	C	N	O	H
Content (%)	99.5	0.05	0.03	0.03	0.02	0.01	0.6	0

In the study, the porosity is designed as 40%, which is closed to those of human bones. The content of carbon to form reinforcement is showed in Table 2. In this table, 1#～5# are green samples that are pressed with powders without pretreatment and, on the contrary, 6#～10# are green samples compressed with powders grinded in the ball mill machine. In spite of pretreatment is accepted or not, the contents of carbon are 0 wt%, 1 wt%, 1.5 wt%, 2 wt%, 2.5 wt% apparently in each group. The metal powders are blended homogenous with carbamide in proportion. During the

mixing process, a little alcohol and zinc stearate (about 0.5g) are used to ensure the fluidity of powders. To ensure the repeatability, five group experiments of each composite are tested.

Table 2 Compositions of porous titanium alloys

No.	Content of composites（60vol%）		Content of carbamide
	Ti	C	
1#	100wt%	0wt%	40vol%
2#	99wt%	1wt%	
3#	98.5wt%	1.5wt%	
4#	98wt%	2wt%	
5#	97.5wt%	2.5wt%	
6#	100wt%	0wt%	
7#	99wt%	1wt%	
8#	98.5wt%	1.5wt%	
9#	98wt%	2wt%	
10#	97.5wt%	2.5wt%	

The raw powders are blended and pretreated in ball-milling machine for 1 hour at a speed of 300 rpm to become homogeneous and moreover improve the interface energy of powders. The mixed powders were pressed into a rigid die by applying a uniaxial pressure of 200MPa for 1min to form a cylindrical green compact (16 mm diameter and 10 mm height).

The sintering process including four parts: moisture removal stage, carbamide removal stage, sintering stage and cooling stage. The heat treatment curve is showed in Fig. 1.

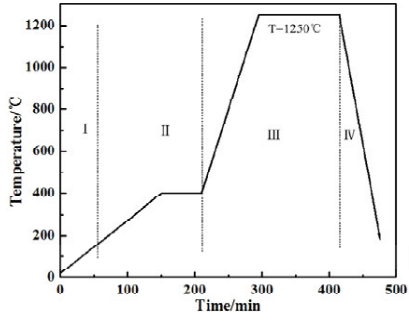

Fig. 1 Temperature curve during heat-treatment process

The moisture removal stage could be finished under 160℃. To ensure the spacer holder could be removed clearly, the carbamide removal stage will last 1hour under 400℃ and temperature increases slowly to prevent cracks and collapse. As the most significant process during preparation, sintering stage directly affect the mechanical property and organization structure of the samples, mainly manifested in the

confirmation of sintering temperature and holding time. In this study, the sintering temperature is defined at 1250℃[9] and the holding time lasts 2 hours[10].

Characterization

The green samples are sintered in the Vacuum tubes furnace. Images of the TiC porous composites are captured and observed by optical microscopy. The phase composition of the TiC composites is identified by X-ray diffraction (XRD). The pore distribution is characterized using scanning electron microscopy (SEM). SEM is also used to observe the powders after being blended in the planetary ball mill. The porosity of samples is calculated by Image-J. Finally, the compression property is examined by Material Testing Machine (CMT-5150) to obtain the stress-strain curve of samples and then analyze the initial yield strength of materials.

Results and Discussion

High-energy ball mill pretreatment

In order to refine the particle size, improve the reactivity and even improve the homogeneity and density of raw material, these powders are blended in a planetary ball mill for 1hour at the speed of 300r/min. The powders are examined by Laser particle Size analyzer to observe the pore distribution. The different particle ratio of Ti powders before and after ball mill process are revealed in Fig. 2. Fig. 3 shows the SEM images of Ti powder before and after pretreatment. It could be concluded from these pictures that the particle size of Ti powder mainly gathers among 50 and 150μm, which could be attributed to the agglomeration during pretreatment. Fig. 4 shows the SEM image of mixing raw materials after pretreatment with carbon content of 2.5%. Fig. 5 shows us the particle size distribution of mixed powders after pretreatment with the carbon content of 2.5wt%. Particle size of mixed powder reached about 100μm, which similarly on account of the agglomeration owing to the increasing surface energy of mixing powders after grinding.

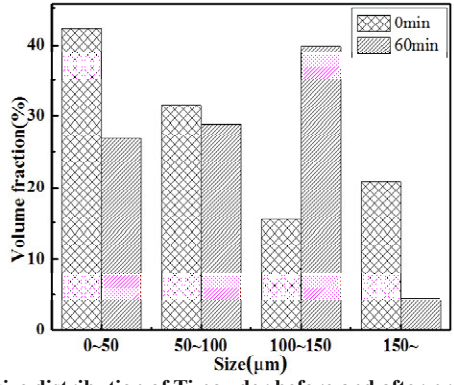

Fig. 2 Particle size distribution of Ti powder before and after pretreatment

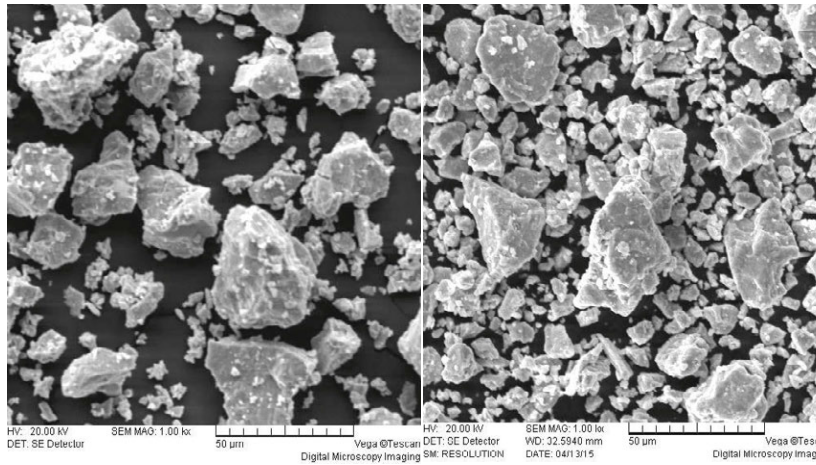

Fig. 3 SEM images of Ti powder before and after grinding (×1000)

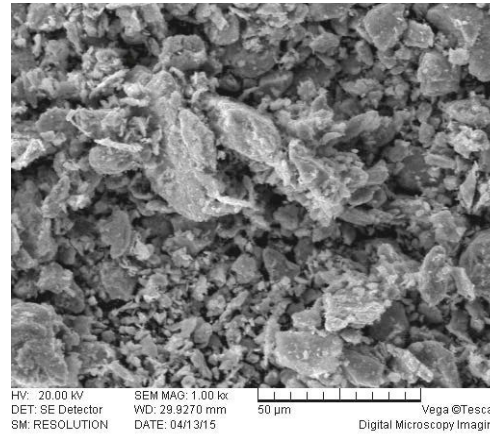

Fig. 4 SEM image of mixing raw materials after pretreatment with carbon content of 2.5%

Fig. 6 shows the XRD pattern of mixing raw powders after grinding. The mixing powders are Ti powder and carbon powder, which does not have any differences before and after grinding in term of ingredient. However, ball-milling process do has the advantage of improving the surface energy of powders, i.e. mechanical activation. Thus, this process could effectively and efficiently improve the properties of final products.

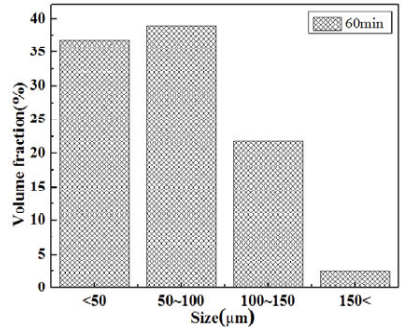

Fig. 5 Particle size distribution of mixing powders after pretreatment

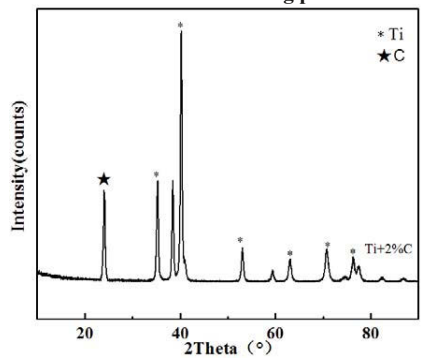

Fig. 6 XRD patterns of mixing raw material after grinding

Porosity

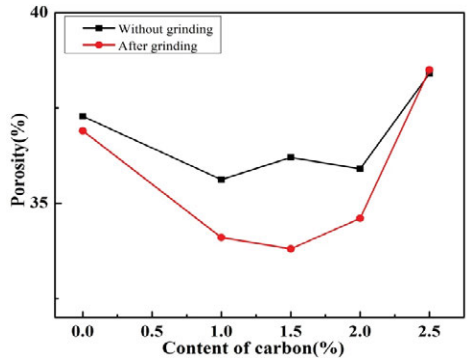

Fig. 7 Effect of different content of carbon on porosity

The tendency curve of porosity by adding different content of carbon is depicted in Fig. 7. It is easy to conclude that the porosity decreases as the content of carbon increases. When the content of carbon reaches 2.5%, the porosity increases

obviously. It should be note that appropriate carbon content could effectively improve the density and the fluency of samples. However, when the content of carbon reaches much higher, i.e. too much non-metallic inclusions added into metal powder, amount of cracks appear as a result of the fluidity of powders is deteriorated and then increases the porosity of the samples.

Compressive resistance property

Fig. 8 shows the stress-strain curves of materials by adding different content of carbon that is blended with Ti powder in the ball mill machine. These curves have similar tendency with three different deformation stages. It also shows the initial yield strength tendency of samples by adding different content of carbon, from which it could be concluded that the initial yield strength achieves the highest with 339.83±15MPa and 331.77±10MPa when the content of carbon achieve 1.5% and 2.0%. As the content of carbon further increases, the compressive strength of the sample sharply decreases as a result of the appearance of many cracks. Furthermore, we could also easily find in Fig. 9 that the pretreatment of the raw powders could obviously improve the mechanical property of the porous Ti composites.

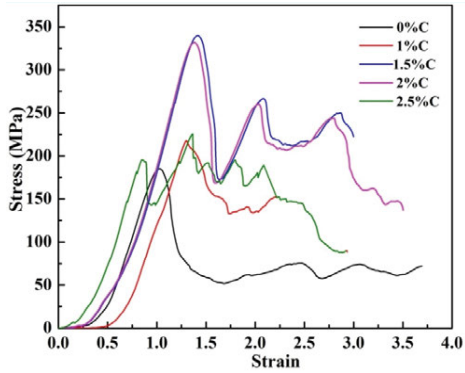

Fig. 8 Stress-strain curves with different content of carbon

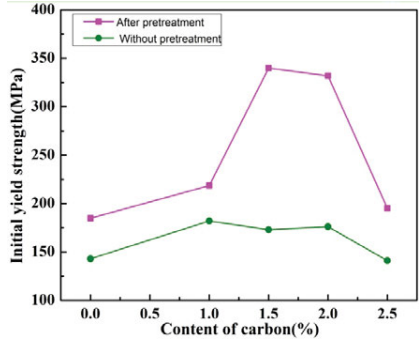

Fig. 9 Effect of pretreatment on initial yield strength by adding different content of carbon

Conclusions

Porous Ti matrix composites can be fabricated by powder metallurgy technique using Ti and carbon powders and the use of carbamide as spacer holder. The initial yield strength of materials could be 339.8±15MPa and 331.1±10MPa separately when the carbon content achieves 1.5 wt% and 2.0wt%. Moreover, the adding of carbon powder and the ball mill technique could effectively and obviously improve the mechanical property and microstructure of samples.

Acknowledgments

This study was supported by the National Natural Science Foundation (51174243) and the Fundamental Research Funds for the Central Universities (106112015CDJZR135502).

References

1. Oh, K.T., H.M. Shim, and K.N. Kim, *Properties of titanium-silver alloys for dental application.* J Biomed Mater Res B Appl Biomater, 2005. **74**(1): p. 649-58.
2. Tang, C.Y., et al., *Fabrication and characteristics of porous NiTi shape memory alloy synthesized by microwave sintering.* Materials Science and Engineering: A, 2011. **528**(18): p. 6006-6011.
3. Tong, X.C. and H.S. Fang, *Al-TiC composites In Situ -processed by ingot metallurgy and rapid solidification technology: Part I. Microstructural evolution.* Metallurgical and Materials Transactions A, 1998(NO.3): p. 875-891.
4. Pingwei, L.W.Z.X.Z.D.W.R.B.Y.F., *Growth Mechanism of In Situ Synthesis of TiC/Ti Composite Reinforcing.* Acta Metallurgica Sinica, 1999(5): p. 536-541.
5. Radhakrishna Bhat, B.V., J. Subramanyam, and V.V. Bhanu Prasad, *Preparation of Ti-TiB-TiC & Ti-TiB composites by in-situ reaction hot pressing.* Materials Science and Engineering, 2002(No.1): p. 126-130.
6. Jiang, J.-Q., et al., *In situ formation of TiC-(Ti-6Al-4V) composites.* Materials Science and Technology, 1996(No.4): p. 362-365.
7. Roy, R., et al., *Full sintering of powdered-metal bodies in a microwave field.* Nature, 1999. **399**(6737): p. 668.
8. Tang, C.Y., et al., *In situ formation of Ti alloy/TiC porous composites by rapid microwave sintering of Ti6Al4V/MWCNTs powder.* Journal of Alloys and Compounds, 2013. **557**(0): p. 67-72.
9. Lubing, C., *Study of microstructure and properties of porous titanium by powder sintering technique*, 2007.
10. Yan, Z., *The preparation and compression performance research of titanium foams*, 2010.

FABRICATION OF GAMMA-IRRADIATED POLYPROPYLENE AND AgNPs NANOCOMPOSITE FILMS AND THEIR ANTIMICROBIAL ACTIVITY

[1]Isabelle Oliveira Berenguer, [1]Washington Luiz Oliani, [1]Duclerc Fernandes Parra, [1]Luiz Gustavo Hiroki Komatsu, [1]Vinicius Juvino dos Santos, [2,3]Nilton Lincopan, , [1]Ademar Benevolo Lugao, [4]Vijaya Kumar Rangari

[1]Nuclear and Energy Research Institute, IPEN-CNEN/SP, Av. Prof. Lineu Prestes, 2242, Cidade Universitária, CEP 05508-000, São Paulo – SP, Brazil
**isa_berenguer@hotmail.com*
[2]Department of Microbiology, Institute of Biomedical Sciences, University of Sao Paulo, CEP 05508-000, São Paulo, Brazil
[3]Department of Clinical Analysis, School of Pharmacy, University of Sao Paulo, Brazil, São Paulo
[4]Center for Advanced Materials Science and Engineering Tuskegee University, AL 36088, USA

Keywords: polypropylene, nanocomposites, silver nanoparticles, silicon dioxide, sonochemical

Abstract

Polymer nanocomposite films of polypropylene and AgNPs were prepared by melt extrusion using twin-screw extruder. These polymer nanocomposites were further modified by γ-irradiation in acetylene at dose of 12.5 kGy. The AgNPs (silver nanoparticles) used in this study were synthetized using sonochemical method from silver nitrate precursor. The polymer nanocomposites were evaluated using differential scanning calorimetry (DSC), X-Ray diffraction (XRD), FTIR spectroscopy and Scanning electron microscopy (SEM). We have also studied the antibacterial activity of these polymer nanocomposite films against two different groups of bacteria-*Staphylococcus aureus* (*S. aureus*; gram-positive bacteria) and *Escherichia coli* (*E. coli*; gram-negative bacteria).

1. Introduction

Polypropylene as a commodity represents a versatile material with continuous increasing of applications [1,2]. Radiation modified polypropylene resins (PP) induces degradation, grafting and radiation-induces LCB (long chain branched). It can be taken advantage to the improvement of polymer material quality owing to physical properties. The most significant improvement from radiation induced LCB is on the rheological properties in the polymer processability, especially for the high melt-strength-polypropylene (HMSPP) [3,4]. PP films performing bactericidal effect is an application that is only beginning to be investigated.

Recent survey [5] has been developed in silver nanoparticles deposited on the surface of an extruded film of linear low density polyethylene/cyclo olefin copolymer (LLDPE/COC) blend by ultrasound method. The ultrasound method on the silver deposition on the film surface and the fungicidal effect on the films were evaluated. The author suggested a method for antimicrobial packaging films through AgNPs deposition.

An important aspect of the nanosilver is that the use as is less toxic to human cells compared to other metals, against infections [6]. Therefore, silver nanoparticles possess excellent antimicrobial activity against a broad spectrum of microbes [7]. The silver nanoparticles biocide effect is related to particle size and shape and it is highly dependent on particle dispersion. The presence of macro aggregates can lead to a decrease in antibacterial activity; therefore, good particle dispersion of appropriate dimensions is needed [8].

Sonochemical, among different methods to produce silver nanoparticle composites is one of the most interesting ways. The sonochemical method enables the synthesis of nanoparticles and their deposition on various substrates in a one-step procedure [9]. The irradiation has proven to be an effective aid for the synthesis of nanosized materials [10].

In this project it was used sonochemical method from silver nitrate precursor. To synthesize the silver nanoparticles it was utilized a growth process based on the reduction of silver ion to zerovalent metal atom acting as nucleation sites and Ag nanoparticles on decorated silica sphere core grew using formaldehyde as a reducing agent by N,N-Dimethylformamide (DMF) with the addition of poly(N-vinyl-2-pyrrolidone) (PVP), a protective agent under ultrasound irradiation method. It can be noticed a growth of silver shell on the basis of silver seed dispersed on the surface of silica spheres [11].

One of the effective approaches to improve melt strength and extensibility is to promote chain branches onto polypropylene backbone using gamma radiation and acetylene. Branching and grafting result from the radical combinations during irradiation process [12]. The strain hardening effect of the HMSPP represents an important role in many processing operations like film blowing, blow molding, foam expansion, fiber spinning and thermoforming [13].

The IPEN developed the production of branched PP, based on the grafting of long-chain-branches on PP backbone using acetylene as a crosslink promoter under gamma radiation process. The focus of the present work was the synthesis of silver nanoparticles on silica carrier using sonochemical method for polypropylene nanocomposite films with and evaluation of biocide action versus *Escherichia coli* and *Staphylococcus aureus*.

2.1. Materials

The isotactic Polypropylene (iPP) was supplied by Braskem – Brazil in pellets with MFI= 2.1 dg min^{-1}, M*w*= 470,000 g mol^{-1} and density= 0.905 g cm^{-3}. The acetylene 99.8% supplied by White Martins S/A, of Brazil, was used to synthesis of modified polypropylene. It was used N,N Dimethylformamide (DMF) analytical grade with molecular weight 73.09 g Mol^{-1}. Silica was purchased by Merck. AgNPs were synthesized with silver nitrate in presence of silica, which and the Irganox was provided by Ciba.

The samples evaluated, in Table 1, were PP1 = Polypropylene and PP2 = Polypropylene SiO_2 @ Ag nanocomposite.

Table 1: Composition of constituents of polypropylene nanocomposites (wt%)

Samples	Matrix	Dose/kGy	Irganox	AgNPs	Si
PP1	HMSPP	12.5	2	-	-
PP2	HMSPP	12.5	2	0.1	1.0

2.2. Methods

2.2.1. Radiation process

The irradiation of the PP pellets was performed under acetylene atmosphere in a ^{60}Co gamma source at dose rate of 5 kGy h^{-1}. The polypropylene irradiation was performed at 12.5 kGy dose monitored by a Harwell Red Perspex 4034 dosimeter. After irradiation, the samples were heated for 1h at 90 ºC to promote the recombination and annihilation of residual radicals [14, 15].

2.2.2. Synthesis of SiO_2@Ag-NPs by sonochemical method from silver nitrate precursor

To synthesize the AgNPs with silica, it was used 50 mL of water and 50 mL of the DMF in a 300 mL beaker then added approximately 1000 mg of silica (SiO_2), 200 mg of PVP and 400 mg of silver nitrate ($AgNO_3$). The becker with the solution was putted in another larger recipient with cold water for cooling. It was used a Unique ultrasound equipment model DES 500, with a working frequency of 20 kHz and maximum intensity output of 500 Watts. The process was divided in three steps, each one with 30 minutes. Between the steps, it was changed the cooling water to maintain the room temperature. In the final process, the precipitated was washed with distilled water. After washings, it was putted in the stove and dried for 2 hours and stored in a dark container. The synthesis of the silver is presented on Figure 1.

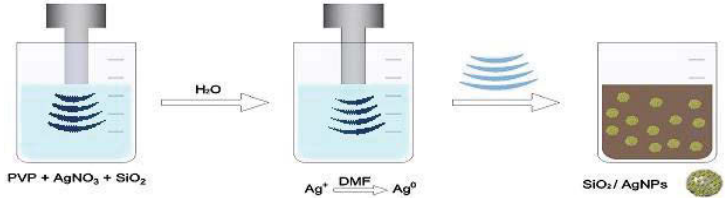

Figure 1. Schematic diagram illustrating the synthesis process of the silver decorated silica (SiO_2 / Ag)

2.2.3. Preparations of SiO_2 @ Ag-NPs/PP Nanocomposites Films

The HMSPP 12.5 kGy in pellet was mixed with Irganox B 215 ED in a rotary mixer and maintained under this condition for 2 hours. Then the mixture was processed with the addition of silver nanoparticles (AgNPs 0.1% by weight) with silica in a twin-screw extruder Haake co-rotating, model Rheomex PTW 16/25, with the following processing conditions: the temperature profile (feed to die) was 175-230 °C, with a speed of 100 rpm. After processed, the nanocomposites were granulated in a granulator Primotécnica W-702-3. The PPSiO_2@Ag-NPs films were produced in blow extruder and the material was placed directly into the hopper of the extruder with a temperature profile (feed to die) of 175-220 ºC, screw speed of 20 rpm and torque of 70-80 Nm. The films were produced with a thickness of ~ 0.08 mm.

2.3. Characterization Films

2.3.1 Scanning electron microscopy and dispersive spectroscopy

Scanning electron microscopy was done using an EDAX PHILIPS XL 30. In this project, thin coat of carbon was sputtered onto the samples.

2.3.2. Fourier transformed infrared spectroscopy

The analyses were performed using attenuation total reflectance accessory (ATR) transmittance in the Thermo Nicolet spectrophotometer, model 380 FT-IR.

2.3.3. Differential scanning calorimetry

Thermal properties of specimens were analyzed using a differential scanning calorimeter DSC 822, Mettler Toledo. The thermal behavior of films was obtained by (1) heating from -50 to 280 ºC at a heating rate of 10 ºC min^{-1} under nitrogen atmosphere; (2) holding for 5 min at 280 ºC; and (3) then cooling to -50 ºC and reheating to 280 ºC at 10 ºC min^{-1}.

2.3.4. X-ray diffraction

X-ray diffraction measurements were carried out in the reflection mode on a Rigaku diffractometer Mini Flex II (Tokyo, Japan) operated at 30 kV voltage and current of 15 mA with CuKα radiation (λ = 1,541841 Å).

2.3.5. Determination of antibacterial activity

An aliquot (400 µL) of a cell suspension of either *Staphylococcus aureus* ATCC 27853 (10^6 cells mL^{-1}) or *Escherichia coli* ATCC 25922 (10^6 cells mL^{-1}) prepared using the method described in JIS Z 2801 [16] were held in intimate contact with each of the 2 replicates of the test surfaces supplied using a 45 x 45 mm^2 polypropylene film for 24 hours at 37 °C under humid conditions. The size of the surviving population was determined using a method based on JIS Z 2801. The viable cells in the suspension were enumerated by viable cell counts on MacConkey Agar after incubation at 37 °C for 24 hours using a 100 µL sample taken from the test surfaces.

3. Results and discussion

3.1. Scanning electron microscopy and dispersive spectroscopy

The SEM-EDX results are shown in Figure 2.

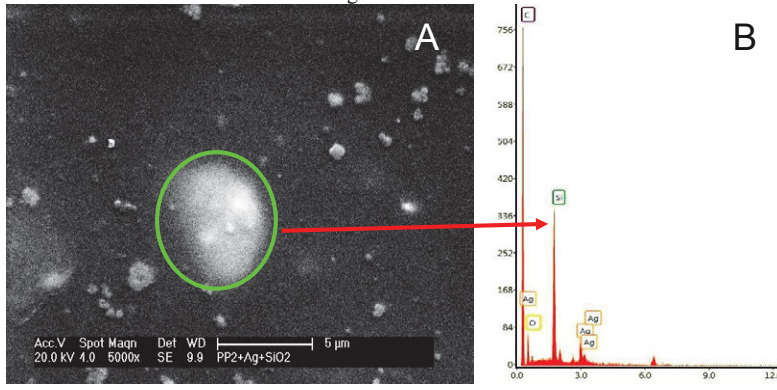

Figure 2. SEM micrograph (A), and EDX of nanocomposite PP2 film (B)

The micrograph of polypropylene nanocomposite film, Figure 2, shows the of SiO_2 particle in which, by sonification, the nanosilver particles grown, as characterized by EDX. Encircled the particle observed is the SiO_2 carrier of nanosilver particles in PP matrix.

3.2. Fourier transformed infrared spectroscopy

Figure 3 shows the infrared spectrum of the samples PP1 and PP2.

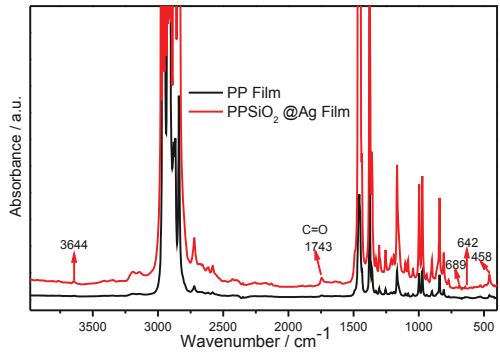

Figure 3. Illustration of the FTIR spectra of polypropylene films

The weak band at around 1743 cm^{-1} is attributed to stretching of the carboxylic group C=O, as presented in the Figure 3. Furthermore, there is a band at around 3644 cm^{-1} characteristic of the O–H related to Si-OH [17]. However two peaks in the IR spectrum of modified PP were observed at around 458 cm^{-1} and 642 cm^{-1}. According to the literature [18-21], in the low wavenumber range typical bands of silica are clearly detected at about 460 cm^{-1} and 640 cm^{-1} that refers to peak attributed to vibration of cyclic Si-O-Si.

3.3. Differential scanning calorimetry

The DSC results for PP1 and PP2 are presented in Table 2 and Figure 4.

Table 2. Sample values of melting peak temperature, melt-crystallization temperature and degree of crystallinity

Samples	Melting peak temperature, Tm_1 / °C	Crystallization peak temperature, T_c / °C	Melting peak temperature, Tm_2 / °C	Crystallinity 1st melting, X_C / %
PP1	169.7 ± 0.12	115.5 ± 0.14	162.0 ± 0.11	39.2± 0.9
PP2	169.4 ± 0.13	115.4 ± 0.13	164.0 ± 0.14	38.6± 0.5

T_m = melt temperature; T_C = crystallization temperature; X_C = degree of crystallinity, as average of three samples

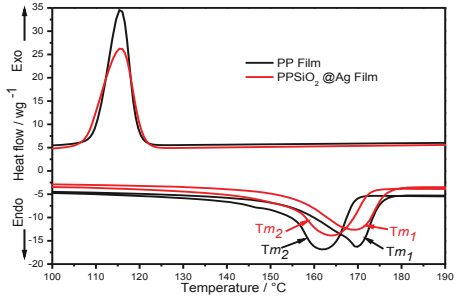

Figure 4. DSC curves in the melting of PP and PP SiO_2@Ag-NPs films

Crystallization was not affected by SiO_2@Ag-NPs addition in the same sense as usually occurs with nucleating agents. As shown in Table 2 the value of the crystallinity of the PP film is similar to that of PPSiO_2@Ag-NPs film.

3.4. X-Ray diffraction

The X-Ray diffraction patterns of the samples are shown in Table 3 and Figure 5.

Table 3. DRX data of PP and SiO_2@Ag-NPs PP nanocomposites

Samples configurations	Crystal plane	Diffraction angle 2θ /°	Interplanar distance d / nm	Crystallites size / nm
PP	(110)α	14.72	0.600	12.4
	(300)β	16.74	0.529	19.3
	(040)α	17.52	0.506	17.3
	(130)α	19.19	0.462	14.4
	(131)+(041)β	22.30	0.398	10.7
	(150)+(060)α	26.14	0.341	14.8
	(220)α	29.32	0.304	5.5
PPSiO_2@Ag-NPs	(110)α	14.17	0.625	8.8
	(040)α	16.83	0.526	11.1
	(130)α	18.50	0.479	9.5
	(131)+(041)β	21.99	0.404	5.2
	(150)+(060)α	25.50	0.349	11.6
	(220)α	28.75	0.310	7.6

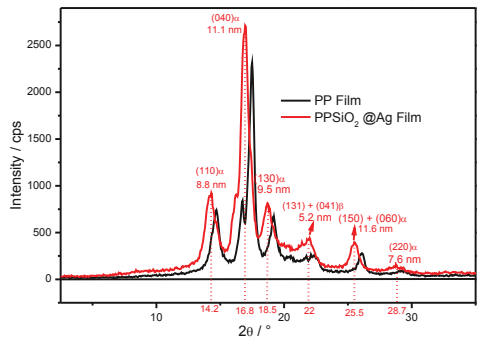

Figure 5. X-ray diffraction pattern of PP and SiO_2@Ag-NPsPP films

It can be noticed two interesting peaks for PP SiO_2@Ag-NPs in Figure 5. The crystal plane (131)+(041)β and (150)+(060)α showed a peak at 2θ=21.99º and 2θ= 25.50º, respectively. The first one presented a crystallite size 5.2 nm and the second one 11.6 nm. In terms of interplanar distance, the β form showed a 0.404 nm and the α form showed a 0.349 nm. According to crystallinity determination by XRD, in which the integral of halo amorphous phase is related to the integral area of the diffraction pattern, the values calculated were: 31.9 $\pm$ 1.0 for PP film and 33.6 $\pm$ 0.9 for PPSiO_2 @Ag film.

The formation of the β-phase, among other factors, is dependent of the shear level imposed to the polymer during the processing [22].

3.5. Antibacterial Activity

The antibacterial effects of the nanocomposites films at different concentrations of silver and silica against *Staphylococcus aureus* and *Escherichia coli*, as determined by the JIS Z 2801 technique, showed negative efficiency results versus bacteria. The result is attributed to the dimension of the carriers in which has grown the silver nanoparticle during sonification.

Conclusion

The silver nanoparticles synthesized in SiO_2 carrier showed distinct results on the bactericide performance of PP@ SiO_2AgNPs films. The scanning electron microscopy and dispersive spectroscopy images have shown the large dimension of silicon (5 microns) supporting nanoparticles of silver. The FTIR spectra of PPSiO_2@Ag films also showed intense bands of silicon, while DSC results revealed that the crystallinity of PP film was affected by presence of SiO_2@Ag. The PPSiO2 @Ag film did not show efficiency to combat the bacteria *Staphylococcus aureus* and *Escherichia coli*, probable owing to the hindrance represented for the silica to nanosilver attack into the bacteria cell, our challenge for future work.

Acknowledgements

This article was supported by CAPES PROJECT and FAPESP project n° 2014-26393-1. The authors are thankful to the Centre of science and technology of materials-CCTM/IPEN, for microscopy analysis (SEM), the technicians Mr. Eleosmar Gasparin and Nelson R. Bueno, for technical support and multipurpose gamma irradiation facility at the CTR/IPEN.

References

[1] C. D. Castel, M. A. S. Oviedo, S. A. Liberman, R. V. B. Oliveira, R. S. Mauler, "Solvent-assisted extrusion of polypropylene/clay nanocomposites," *Journal of Applied Polymer Science*, 121(2011), 389-394.

[2] A. Bouaziz, M. Jaziri, F. Dalmas, V. Massardier, "Nanocomposites of silica reinforced polypropylene: Correlation between morphology and properties," *Polymer Engineering and Science*, 54(2014), 2187-2196.

[3] M. Keijo, C. Song, *Radiation Processing of Polymer Materials and Its Industrial Applications*, John Wiley & Sons, Inc., Hoboken & New Jersey (2012).

[4] W. L. Oliani, D. F. Parra, L. F. C. P. Lima, A. B. Lugao, "Morphological characterization of branched PP under stretching," *Polymer Bulletin*, 68(2012), 2121–2130.

[5] S. Sanchez-Valdes, "Sonochemical deposition of silver nanoparticles on linear low density polyethylene/cyclo olefin copolymer blend films," *Polymer Bulletin*, 71(2014) 1611-1624.

[6] F. Furno, K. S. Morley, B. Wong, B. K. Sharp, P. L. Arnold, S. M. Howdle, R. Bayston, P. D. Brown, P. D. Winship, H. J. Reid, "Silver nanoparticles and polymeric medical devices: A new approach to prevention of infection?," *Journal of Antimicrobial Chemotherapy*, 54(2004), 1019-1024.

[7] J. R. Morones, J. L. Elechiguerra, A. Camacho, K. Holt, J. B. Kouri, J. T. Ramírez, M. J. Yacaman, "The bactericidal effect of silver nanoparticles," *Nanotechnology*, 16(2005), 2346-2353.

[8] E. Fages, J. Pascual, O. Fenollar, D. Garcia-Sanoguera, R. Balart, **"**Study of Antibacterial Properties of Polypropylene Filled With Surfactant-Coated Silver Nanoparticles**,"** *Polymer Engineering and Science*, 51(2011), 804-811.
[9] A. Gedanken, "Using sonochemistry for the fabrication of nanomaterials," *Ultrassonics sonochemistry*, 11(2004), 47-55.
[10] A. Matsumoto, T. Ishikawa, T. Odani, H. Oikawa, S. Okada, H. Nakanitshi, "An organic/inorganic nanocomposite consisting of polymuconate and silver nanoparticles," *Macromolecular chemistry and physics*, 207 (2006), 361-369.
[11] X. Ye, Y. Zhou, J. Chen, Y. Sun, "Deposition of silver nanoparticles on silica spheres via ultrasound irradiation", *Applied Surface Science*, 253(2007), 6264-6267.
[12] A. B. Lugao, B. W. H. Artel, A. Yoshiga, L. F. C. P. Lima, D. F. Parra, J. R. Bueno, S. Liberman, M. Farrah, W. R. Terçariol, H. Otaguro, "Production of high melt strength polypropylene by gamma irradiation," *Radiation Physics and Chemistry* , 76 (2007), 1691–1695.
[13] A. B. Lugao, H. Otaguro, D. F. Parra, A. Yoshiga, L. F. C. P. Lima, B. W. H. Artel, S. Liberman, "Review on the production process and uses of controlled rheology polypropylene gamma radiation versus electron beam processing," *Radiation Physic Chemistry*, 76(2007), 1688-1690.
[14] W. L. Oliani, D. F. Parra, A. B. Lugao, "UV stability of HMS-PP (high melt strength polypropylene) obtained by radiation process," *Radiation Physics and Chemistry,* 79(2010), 383-387.
[15] D. M. Fermino, D. F. Parra, W. L. Oliani, A. B. Lugao, F. R. V. Díaz, "HMSPP nanocomposite and Brazilian bentonite properties after gamma radiation exposure," *Radiation Physics and Chemistry,* 84(2013), 176–184.
[16] JIS Z 2801:2010 (adapted). Japanese Industrial Standard. Antimicrobial Products - Test for antimicrobial activity and efficacy.
[17] J. G. Martınez-Colunga, S. Sanchez-Valdes, L. F. Ramos-de-Valle, L. Munoz-Jimenez, E. Ramırez-Vargas, M. C. Ibarra-Alonso, T. Lozano-Ramirez, P. G. Lafleur, "Simultaneous Polypropylene Functionalization and Nanoclay Dispersion in PP/Clay Nanocomposites using Ultrasound," *Journal of Applied Polymer Science***,** (2014), 40631 (1 of 8).
[18] N. Primeau, C. Vautey, M. Langlet, "The effect of thermal annealing on aerosol-gel deposited SiO_2 films: a FTIR deconvolution study", *Thin Solid Films*, 310(1997), 47-56.
[19] J. G. M. Colunga, S. S. Valdes, L. F. R.Valle, L. M. Jimenez, E. R. Vargas, M. C. I. Alonso, T. L. Ramirez, P. G. Lafleur, "Simultaneous Polypropylene Functionalization and Nanoclay Dispersion in PP/Clay Nanocomposites using Ultrasound," *Journal of Applied Polymer Science*, 131(2014), 40631.
[20] T. Li, S. Xiang, P. Ma, H. Bai, W. Dong, M. Chen, "Nanocomposite Hydrogel Consisting of Na-montmorillonite with Enhanced Mechanical Properties," *Journal of Polymer Science Part B: Polymer Physics*, 53(2015), 1020-1026.
[21] E. V. D. G. Líbano, L. L. Y. Visconte, E. B. A. V. Pacheco, "Propriedades térmicas de compósitos de polipropileno e bentonita organofílica," *Polímeros*, 22(2012), 430-435.
[22] M. M. Favaro, M. C. Branciforti, R. E. S. Bretas, "A X-ray Study of β-Phase and Molecular Orientation in Nucleated and Non-Nucleated Injection Molded Polypropylene Resins," *Materials Research*, 12, 4, (2009), 455-464.

NATURAL AGING EFFECTS IN HMS-POLYPROPYLENE SYNTHESIZED BY GAMMA RADIATION IN ACETYLENE ATMOSPHERE

[1] Washington Luiz Oliani, [1] Luiz Gustavo Hiroki Komatsu, [1] Ademar Benevolo Lugao, [2] Vijaya Kumar Rangari, [1] Duclerc Fernandes Parra

[1] Nuclear Energy Research Institute – IPEN-CNEN/SP, Av. Prof. Lineu Prestes, 2242, 05508-900, São Paulo, Brazil

washoliani@usp.br

[2] Center for Advanced Materials Science and Engineering Tuskegee University, AL 36088, USA.

Keywords: polypropylene, gamma radiation, chain scissions, environmental aging

Abstract

High melt strength polypropylene (HMSPP) is produced by γ-radiation process to improve the melt viscosity suitable for melt blow film process. The melt strength (MS) properties of a polymer increases with molecular weight and with long chain branching due to the increase chain entanglement levels in the polymer. The main scope of this study is to evaluate the stability of HMSPP prepared by gamma radiation with doses of 5, 12.5 and 20 kGy in comparison with virgin PP. The samples were subjected to the natural aging for a period of one year. These polymers were characterized by: Thermogravimetry analysis (TGA), Differential scanning calorimetry (DSC), Infrared spectroscopy (FTIR) and Scanning electron microscopy (SEM). These results show predominantly chain scissions degradation mechanism, owing to the reactivity of the tertiary carbon of macro chains. The chemi-crystallization caused by degradation processes (thermal and photodegradation) was detected in HMSPP.

Introduction

Radiation processing of polymers received great interest because it can be a way to modify the molecular structure of polymers as an alternative to traditional chemical methods. Several basic studies of gamma-radiation induced modifications of polymers are reported. It is well known that the main effect of the interaction of ionizing radiation caused is chain scissoning and crosslinking of the polymer chain of PP, while crosslinking is predominant in the case of PE [1-4]. Physically, the success achieved by the irradiation of plastics is based on the fact that, currently, energy into the material generates favorable changes provided as used in the proper doses. On the other hand, it represents an economic advantage, because it reduces the uses of additives in the formula [2].

A number of factors affect the sensitivity of polymers during photooxidation: a) The nature, concentration, and absorptivity of impurity chromophores; b) The quantum yield of photolysis; c) The rate of subsequent photochemical and photophysical processes and d) The intensity of incident radiation and the extention of spectrum of light sources from that of natural sunlight at normal latitudes. The effects of temperature, humidity and other environmental factors can further complicate a proper evaluation of a photooxidation process [5,6].

In the natural aging process of photooxidative degradation is predominant. Decomposition of the material by the action of light, which is considered as one of the

primary sources of damage exerted upon polymeric substrates occurs at ambient conditions. The polypropylene is susceptible to degradation initiated by UV and visible light, normally the UV damaging at 370 nm wavelengths. The mechanisms of the degradation and oxidation reactions are determined by the extraneous groups and/or impurities in the polymer, which absorb light quanta and form excited states. The initially short-lived singlet state is transformed to long live triplet state. Excited triplet states may cleave the polymer chains and form radical pairs or pairs (Norrish Type I reaction) of saturated and unsaturated chain ends by hydrogen transfer (Norrish Type II reaction). Thus polymeric radicals formed may add molecular oxygen (in triplet ground state) to peroxy radicals, which absorb UV light or become excited by energy transfer, the weak O-O bonds break. The hydroperoxide binding energy is very low causing the disruption of this connection by forming thermolysis and pairs of alkoxy and hydroxyl radicals are formed which may react in various ways, e.g. by hydrogen abstraction, chain scission, rearrangement and accelerate photodegradation [7-9]. The polypropylene undergoes faster photooxidation compared with polyethylene because of the tertiary hydrogen atoms and the concerned mechanism of peroxide formation [8].

When iPP sample was exposed to UV radiation, oxidation reactions occur, resulting in chain scissions. The strained or entangled sections of the molecules can then be released, and further crystallization occurs by the rearrangement of these free molecule segments. The chemi-crystallization is connected with the reduction in molecular size and involves segments released by scission from entanglements or tethering to crystals. Evidence for this is given by the correlation between the increase in degree of crystallinity and the decrease in molecular weight. The melting peaks highly degraded specimens containing a higher amount of β-phase, double peaks were obtained in this research [10,11].

Our Institute developed the production of branched PP, based on the grafting of long chain branches on PP backbone using acetylene as a crosslink promoter under gamma radiation process. The aim of the present paper is to investigate the fundamental aspects of the environmental aging on the morphology of the radiation modified polypropylene (HMSPPs) and durability of these materials.

Materials and Methods

The HMSPP samples were obtained from iPP pellets (MFI = 1.5 dg min^{-1} from Braskem, Brazil). The iPP pellets were conditioned into nylon bags in which were fluxed with nitrogen in order to reduce as much as possible the internal oxygen concentration. The bags were submitted to the irradiation process in a ^{60}Co γ-source, at a dose rate of 5 kGy h^{-1} monitored with Harwell Red Perspex 4034. Dose levels ranged from 5, 12.5 up to 20 kGy in presence of acetylene [12,13]. After irradiation, the samples were heat treated at 90 °C for 1 hour with the aim of promoting recombination and termination reactions and also eliminate residual radicals [14,15]. The dumbbell samples were prepared with mold pressure at temperature of 190°C in type IV according to ASTM D 638 (2014) [16]. For completion of the experimental aging tests of the iPP and HMSPP samples, was assembled in apparatus for environmental aging according to Figure 1.

Figure 1. Device for environmental aging with polypropylene samples at IPEN

The disposal of the samples for natural exposition were placed 45° north, according to ASTM D 1435 (2013) [17]. Natural weathering was conducted for 12 months at the São Paulo exposure site of the Nuclear Energy Research Institute, IPEN, (São Paulo, Brasil), located at latitude 23°33`South, longitude 46°44` West and altitude 750 meters in São Paulo, IPEN-USP. After disposal of the samples for natural aging, three specimens of each sample were conditioned in air at 23.0 ± 1.0 ºC, light absent and tested.

Thermogravimetry analysis

Thermogravimetry curves were obtained with an SDTA 851 thermobalance (Mettler-Toledo), using samples of about 10 mg in alumina pans, under nitrogen atmosphere of 50 mL min^{-1}, in range from 25 up to 600 ºC, at a heating rate of 10 °C min^{-1}, according to ASTM D 6370-99 (2014) [18].

Differential scanning calorimetry

Thermal properties of specimens were analyzed using a differential scanning calorimeter (DSC) 822e, Mettler-Toledo. The thermal behavior of the samples (10-15 mg) were obtained by: (1) heating from 25 to 280 ºC at a heating rate of 10 ºC min^{-1} under nitrogen atmosphere, (2) holding for 5 min at 280 ºC, and (3) then cooling to 25 ºC and reheating to 280 at 10 ºC min^{-1}, according to ASTM D 3418 (2015) [19]. The crystallinity was calculated according to the equation (1):

$$X_C(\%) = \frac{\Delta H_f \times 100}{\Delta H_0} \quad (1)$$

Where ΔH_f is melting enthalpy of the sample, ΔH_0 is melting enthalpy of the 100% crystalline PP which is assumed to be 209 kJ kg^{-1} [20, 21].

Infrared spectroscopy

The FTIR was carried out with a Thermo Nicolet 6700 FTIR spectrometer with a Smart Orbit accessory, in the wavelength range 4000 to 400 cm^{-1}. In order to ensure satisfactory contact between the ATR diamond crystal and the sample, three or more FTIR spectra were recorded at various locations on the sample.

Scanning electron microscopy

Specimens were coated with gold in a sputter coater prior to examination to avoid charging. A Philips XL30 SEM was used for collect secondary electron images from the samples.

Results and discussion

Thermogravimetry

The TG results indicated decomposition of the samples, Figure 2 and 3.

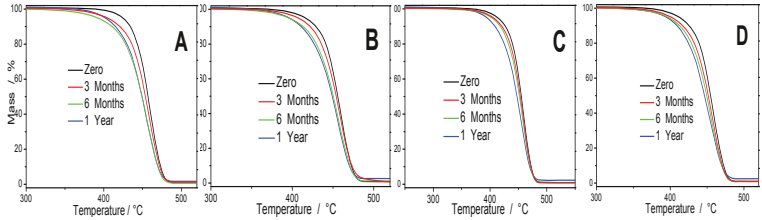

Figure 2. TGA decomposition curves of samples: iPP (A), HMSPP 5 kGy (B), HMSPP 12.5 kGy (C) and HMSPP 20 kGy (D), under environmental aging for 1year

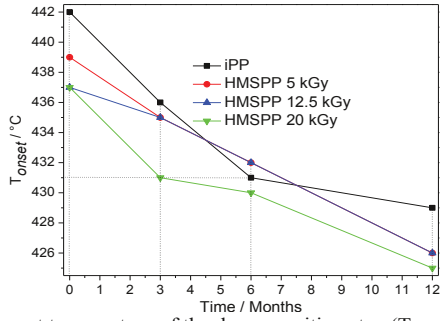

Figure 3. Values onset temperature of the decomposition step (T_{onset}) obtained from the TGA curves for iPP and HMSPPs.

As observed in the curves, Figure 2 presents significant variation of onset decomposition temperature (T*onset*) when decomposition starts, with decrease of stability under aging. According to Figure 3 the T*onset* decomposition of the iPP sample displaced from 442 to 429 °C after environmental aging of 1year. The HMSPP 5 kGy sample displaced from 439 to 426 ºC, as well as, values the HMSPP 12.5 kGy displaced from 437 to 426 ºC and HMSPP 20 kGy displaced from 437 to 425 ºC after 1 year of the aging. T*onset* decreases in all samples with increase of aging time. After 6 months iPP represents the higher decrease of T*onset* reflecting the lower stability. In the final (1 year) the samples are in similar degradation state.

Differential scanning calorimetry

Figure 4 shows the DSC event of melting in the second heating run of the iPP, as well as the HMSPPs.

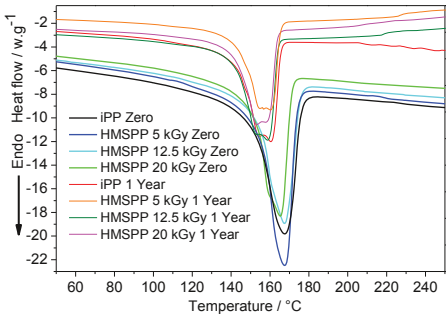

Figure 4. DSC 2nd heating curves of the iPP and HMSPP (5, 12.5 and 20 kGy)

The crystallinity is increased due to chain scission, with the consequence segregation of entangled molecule segments and crosslinks in the amorphous regions that were not able to crystallize during the original crystallization process. These free segments can reorganize themselves in a crystalline phase, with an appreciable mobility leading to an increase of crystallinity degree [22,23]. A progressive increase in crystallinity with UV exposure was observed in sample HMSPP 12.5 kGy. This behaviour can be attributed to the scission of tie chain molecules in the amorphous phase that are released and hence may crystallize onto pre-existing crystals, a process called chemi-crystallization [24]. The crystallinity starts to increase when a sharp decrease in molecular weight occurs but the continuous increase is limited by chemical irregularities (like carbonyl and hydroperoxide groups) that appear after prolonged exposures and hence the molecules become too defective to continue chemi-crystallization [24].
The DSC concerning the T_{m2} and X_C results are presented in Table 1.

Table 1. DSC data of the iPP and HMSPPs during the second run of melting

Time / Samples	T_{m2} / °C		X_C / %	
	Zero	1 Year	Zero	1 Year
iPP	167.0 ± 0.10	160.2 ± 0.12	49.2 ± 0.51	48.0 ± 0.53
HMSPP 5 kGy	168.1 ± 0.11	160.1 ± 0.11	47.1 ± 0.60	45.1 ± 0.54
HMSPP 12.5 kGy	167.0 ± 0.10	158.3 ± 0.13	44.3 ± 0.45	53.3 ± 0.55
HMSPP 20 kGy	165.1 ± 0.10	153.1 ± 0.11	51.4 ± 0.52	49.0 ± 0.49

T_{m2}: melt temperature; X_C: degree of crystallinity, as average of three specimens of each sample.

In the iPP sample was observed melting temperature displacement ΔT_{m2} = 7 ºC, HMSPP 5 kGy sample ΔT_{m2} = 8 ºC, HMSPP 12.5 kGy sample ΔT_{m2} = 9 ºC and HMSPP 20 kGy ΔT_{m2} = 12 ºC, indicating morphology modifications of the samples crystalline phase. Melting temperature decrease demonstrates that chain scission is the main mechanism of the degradation. This can be attributed to modification in crystal structure of iPP which resulted in the mobility of the iPP molecules that increases with the radiation dose. More prolonged exposure of the PP plates decreased the crystallinity and the samples of 1 year (iPP, HMSPP 5 kGy and HMSPP 20 kGy) showed a minimum in degree of crystallinity. This may be attributed to the further increase of photooxidation products such as the carbonyls and hydroperoxides that act as chemical irregularities and limit the crystallinity [11, 25]. The decrease in crystallinity can be explained by the reduced size of the crystallites of the samples due to the degradation process occurring

during the long time exposure, which results in the increase of the amorphous region [26].

Infrared spectroscopy

In order to study the chemical and morphological modifications induced during the outdoor exposure on the PP plates, absorption infrared analysis on samples exposed for zero, 2 months, 6 months and 1 year have been carried out. The photo-oxidation of PP plates was investigated by ATR experiments in order to detect oxidant species at the beginning of the exposure, Figure 5.

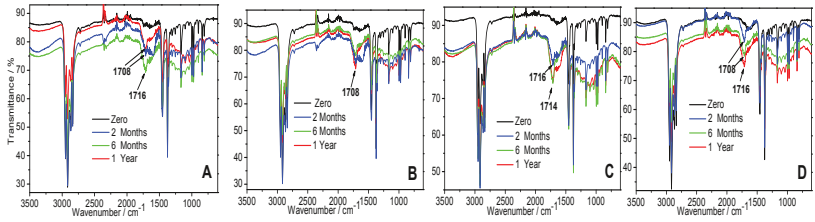

Figure 5. Illustration of the ATR infrared spectrum of the: iPP (A), HMSPP 5 kGy (B), HMSPP 12.5 kGy (C) and HMSPP 20 kGy (D), under environmental aging for 1year

The iPP and HMSPP (5, 12.5 and 20 kGy) samples natural aged for 1 year show typical absorption bands of carbonyl stretching in the region 1708-1716 cm^{-1}, Figure 5, with a substantial content of oxidation products. During thermal and photodegradation processes, carboxylic and carbonyl groups are present as end products of the oxidation.

Scanning electron microscopy

The surface and section morphology of PP plates exposed for 1 year were observed by means of scanning electron microscopy, Figure 6.

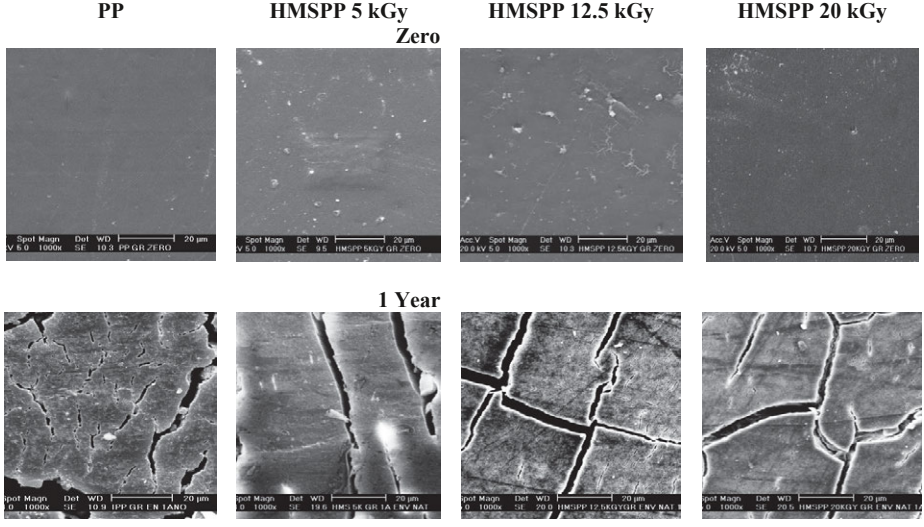

Figure 6. SEM images of the surface with development of samples cracks, 20 μm, aged by 1 year

In the similar work [27], the SEM of iPP plates were investigated with 5 months, 6 months and 16 months of exposure at Messina (Italy) after natural aging. The material close to the surface directly exposed to the sunlight shows several micro-fractures. SEM images of 1 year exposed samples, at magnification 20 μm of the surface, Figure 6, show a dense net of micro-fractures on the flat surface. At high time (1 year) of exposure, also the inner material is involved and the surface morphology is heavily affected.

Conclusions

The effects of thermal and photodegradation on iPP and HMSPPs were of the intense cracks formation on the surfaces. The thermo and photo oxidation acceleration at period of 6 months were more evident in samples of the iPP, according the results of decomposition temperature variation. However the thermal stability decreased with increase of exposition time. In addition, it was found a progressive increase of crystallinity degree in sample HMSPP 12.5 kGy of 1 year of environmental aging test attributed to the scission of tie chain molecules that may crystallize onto pre-existing crystals as effect of chemi-crystallization process.

Acknowledgements

The authors acknowledge financial support for this work from CAPES, FAPESP-2014/26393-1 process. Centre of Science and Technology of Materials – CCTM/IPEN, for microscopy analysis (SEM), the technician Mr. Eleosmar Gasparin for technical support and multipurpose gamma irradiation facility at the CTR/IPEN.

References

[1] G. Spadaro, A. Valenza, "Influence of the irradiation parameters on the molecular modifications of an isotactic polypropylene gamma-irradiated under vacuum," *Polymer Degradation and Stability*, 67 (2000), 449-454.

[2] J. Reyes, C. Albano, E. Davidson, R. Poleo, J. Gonzáles, M. Ichazo, M, Chipara, "Effects of gamma irradiation on polypropylene, polypropylene + high density polyethylene and polypropylene + high density polyethylene + wood flom," *Material Research Innovations*, 4 (2001), 294-300.

[3] P. Dahal, Y. C. Kim, "Preparation and characterization of modified polypropylene by using electron beam irradiation," *Journal of Industrial and Engineering chemistry*, 19 (2013), 1879-1883.

[4] W. Brostow, S. Deshpande, K. Fan, S. Mahendrakar, D. Pietkiewicz, S. R. Wisner, "Gamma-irradiation effects on polypropylene based composites with and without an internal lubricant," *Polymer Engineering and Science*, 49(2009), 1035-1041.

[5] Degradation and Stabilisation of Polyolefins, Chapter 7 – *Photostabilisation of Polyolefins*. Al-Malaika and Scott, G. (Edited by Norman S. Allen, Applied Science Publishers, London and New York, 1983), 283- 332.

[6] Comprehensive Polymer Science, *Photodegradation of Polymer Materials*. Ranby, B. and Rabek, J.F. (Pergamon Press, Oxford, 1992), 259.

[7] B. Singh, N. Sharma, "Mechanistic implications of plastic degradation," *Polymer Degradation and Stability*, 93(2008), 561-584.

[8] H. Zweifel, *Stabilization of Polymeric Materials,* (Berlin, Springer-Verlag, 1998), 1-40.

[9] M. A. De-Paoli, *Degradação e Estabilização de Polímeros*, Capítulo 2 – Tipos de reações de degradação, (Artliber, São Paulo, 2009), 43-68.
[10] M. S. Rabello, J. R. White, "Crystallization and melting behaviour of photodegraded polypropylene-I," *Polymer,* 38(1997), 6379-6387.
[11] M. S. Rabello, J. R. White, "Crystallization and melting behaviour of photodegraded polypropylene-II," *Polymer,* 38(1997), 6389-6399.
[12] W. L. Oliani, D. F. Parra, A. B. Lugao, "UV stability of HMS-PP (high melt strength polypropylene) obtained by radiation process," *Radiation Physics and Chemistry*, 79 (2010), 383–387.
[13] W. L. Oliani, L. F. C. P. Lima, D. F. Parra, D. B. Dias, A. B. Lugao, "Study of the morphology, thermal and mechanical properties of irradiated isotactic polypropylene films," *Radiation Physics and Chemistry*, 79 (2010), 325–328.
[14] W. L. Oliani, D. F. Parra, L. F. C. P. Lima, A. B. Lugao, "Morphological characterization of branched PP under stretching," *Polymer Bulletin*, 68(2012), 2121–2130.
[15] W. L. Oliani, D. F. Parra, H. G. Riella, L. F. C. P. Lima, A. B. Lugao, "Polypropylene nanogel: ''Myth or reality'','' *Radiation Physics and Chemistry*, 81 (2012), 1460–1464.
[16] ASTM D638 (2014) – Standard test method for tensile properties of plastics.
[17] ASTM D1435 (2013) - Standard practice for outdoor weathering of plastics.
[18] ASTM D6370-99 (2014) - Standard test method for rubber – Compositional analysis by thermogravimetry (TGA).
[19] ASTM D3418 (2015) - Standard test method for transition temperatures and enthalpies of fusion and crystallization of polymers by differential scanning calorimetry.
[20] J. Brandrup, E. H. Immergut and E. A. Grulke, eds., *Polymer Handbook,* (New York, NY, Wiley Interscience, 1999), 1, 445-450.
[21] J. E. Mark, *Physical properties of polymers handbook,* (New York, NY, Springer, 2007), 639.
[22] S. Mouffok, M. Kaci, "Artificial weathering effect on the structure and properties of polypropylene/polyamide-6 blends compatibilized with PP-g-MA," *Journal of Applied Polymer Science*, 132, 13, (2015), 41722, 1-9.
[23] A. Larena, S. Jimenez de Ochoa, F. Domınguez, "Dynamic-mechanical analysis of the photodegradation of long glass fibre reinforced polypropylene: Mechanical properties' changes," *Polymer Degradation and Stability*, 91 (2006) 940-946.
[24] R. F. Navarro, J. R. M. Almeida, M. S. Rabello, "Elastic properties of degraded polypropylene," *Journal of Material Science*, 42(2007), 2167-2174.
[25] E. L. Bedia, M. A. Paglicawan, C. V. Bernas, S. T. Bernardo, M. Tosaka, S. Kohjiya, "Natural weathering of polypropylene in a tropical zone," *Journal of Applied Polymer Science*, 87(2003), 931-938.
[26] E. Parparita, T. Zaharescu, R. N. Darie, C. Vasile, "Biomass effect on γ-irradiation behavior of some polypropylene biocomposites," *Industrial & Engineering Chemistry Research*, 54(2015), 2404-2413.
[27] R. Gallo, L. Branbilla, C. Castiglioni, F. Severini, "Characterization of naturally weathered polypropylene plates," *Journal of Macromolecular Science*, 43(2006), 535-554.

SUPERALIGNED CARBON NANOTUBES REINFORCED COPPER NANOCOMPOSITES WITH ENHANCED STRENGTH AND ELECTRICAL CONDUCTIVITY

Jing SHUAI[1], Yu JIN[1], Lin ZHU[2], Wenzhen LI[1]

[1]School of Materials Science & Engineering (Tsinghua University, Beijing 100084, China)
[2]Tsinghua-Foxconn Nanotechnology Research Center (Tsinghua University, Beijing 100084, China)

Keywords: Copper, Superaligned carbon nanotubes, Metal matrix nanocomposite, Electroplating

Abstract

A new kind of laminar metal matrix nanocomposite was fabricated by an electroplating process with copper and superaligned film of carbon nanotubes (SACNT film). We put the SACNT film on a titanium plate and then electroplated a layer of copper on it. By repeating the above process, we could get the laminar Cu/SACNT composite which contains dozens or hundreds layers of copper and SACNT films. The thickness of a single layer could be controlled by the electroplating parameter easily. Microscopic observation showed that the directional alignment structure of SACNT has been retained in the composite perfectly. Mechanical and electrical properties testing results showed that tensile and yield strengths of composites improve obviously compared to pure copper and retain the high conductivity. This technology is a potential method to make applicable MMC which characterizes directional alignment of carbon nanotubes.

Introduction

Pure copper has been widely used in manufacturing of electric equipment and heat conductors because of its high electrical and thermal conductivity. The use of pure copper, however, is limited by its low strength and high density. Traditional methods to improve the mechanical properties of pure copper have to bear the cost of decreased performance in electrical and thermal conductivity. Previous studies have made various attempts to solve this problem [1-5]. Nevertheless, materials they prepared, which show excellent performances in mechanical and electrical properties, cannot be applied in practical application because of their small size and complex processes. Nowadays, "composite method" allow us to add various enforcement materials specifically to improve properties. Carbon nanotube is an ideal reinforcement material because of its excellent mechanical, electrical, and thermal properties [6]. Most of previous studies on Cu/CNT composites, focused on how to improve the mechanical properties of copper matrix, do not address the conductive performance of the copper matrix [7-12]. Furthermore, the CNTs in these composites are dispersed in all directions randomly.

SACNT film [13] is a uniform CNT film processed from superaligned CNT arrays. Compared with traditional CNT films, carbon nanotubes in SACNT film are all lined up in the same direction. This endows the SACNT film with particular advantages to improve concerned properties of materials in one direction. SACNT has been used to prepare CNT/PVA composite

yarns [14] and CNT/epoxy composites [15, 16], and to our best knowledge, it has never been used to prepare metal matrix composites.

In this paper, we prepared laminar Cu/SACNT composite by a process of electroplating, since SACNT films and copper layers could be accumulated endlessly, this composite could be expanded to any size theoretically.

Experimental Procedures

Figure 1 schematically depicts the steps of the preparation of Cu/SACNT composite. SACNT films were provided by Tsinghua-Foxconn Nanotechnology Research Center. Electroplating was performed in an electrolyte of $CuSO_4 \cdot 5H_2O$ (300g/L), H_2SO_4 (50g/L), and glucose (5g/L) at room temperature. The electric current density ($3A/dm^2$) and the time (2min, 4min, or 8min per layer) would determine the thickness of copper coating to cover the SACNT film. The number of copper and SACNT film layers can be controlled by repeating the processes b, c, and d.

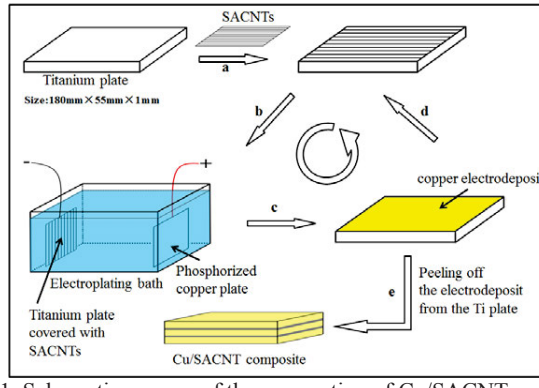

Figure 1. Schematic process of the preparation of Cu/SACNT composite

In order to explore the impact of different volume fractions of SACNT film on the composites' mechanical and electrical properties, we prepared composites with three different volume fractions of SACNT film (0.26%, 0.52% and 1.04%) and a sample without SACNT film (0%) under the same experimental conditions. The as-prepared composites were cut into specific sizes for performance test. Mechanical testing was accomplished in an Instron5848 tensile tester, and each tensile specimen was 70mm long and 5mm wide. Electrical testing was accomplished in a SB2230 precision digital resistor while each specimen was 120-150 mm long and 10-14mm wide. Electrical resistivity and conductivity were calculated with the resistance and size of the sample. All the specimens for mechanical testing and electrical testing were parallel to the direction of CNTs in their lengthwise direction (longitudinal direction). The samples for microscopic observation were prepared in a resin mounted and polished. They were first polished and then subject to mild corrosion, the corrosion was performed in an ethanol solution of HCl (10g/L) and $FeCl_3$ (30g/L) within 3 seconds.

Results and Discussion

Mechanical and Electrical Properties

The mechanical and electrical values presented in Figure 2 are an average of five measurements. As Figure 2 shows, both the average tensile and yield strengths (0.2% offset stain) increase as the volume fraction of SACNT increases. The result of electrical conductivity test shows that the presence of SACNT films has a much less effect on conductivities than on the strengths. When the volume fraction of CNTs is low, the Cu/SACNT composite has the same conductivity with pure copper. Two reasons lay behind the fact that higher volume fraction of CNTs leads to slight degradation in conductivity. First, the conductivity of CNTs is not as good as pure copper; and second, small gaps around the CNTs as shown in Figure 4(a) have adverse effects on conductivity.

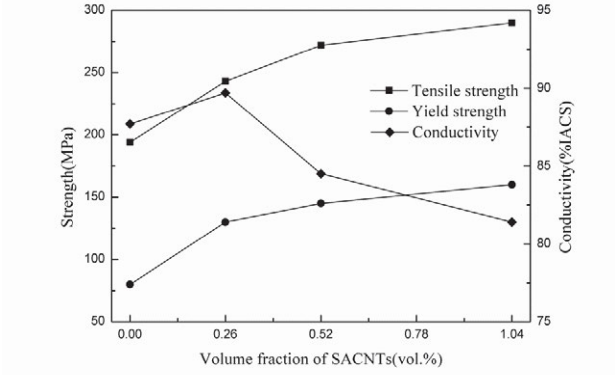

Figure 2. Mechanical and electrical properties of Cu and Cu/SACNT composites in longitudinal direction

Microstructural Observations

Figure 3 shows the metallographic graphs of Cu-0.26vol%SACNT composite, the graphs of other composites shows the same features. Before the corrosion processing, the metallographic graph of the polished cross-section shows no internal structures. After the corrosion, the copper on the SACNT films was removed, as Figures 3(a) and (b) show, the bright areas in the figures are actually copper layers and dark lines are SACNT films. Comparing Figures 3(a) and (b), one can spot differences between perpendicular cross-section and parallel cross-section. Black lines in the perpendicular cross-section are wave-shaped and discrete, which indicates CNTs in the SACNT films are not strictly aligned in a straight line. Furthermore, each waved line has a shape to those of the adjacent lines. Unlike the perpendicular cross-section, black lines in the parallel cross-section are straighter and longer. This is due to the fact that SACNT films maintain straight-line shape with the tension along the length of CNTs; the tension comes from the process of pulling out SACNT film from the SACNT array.

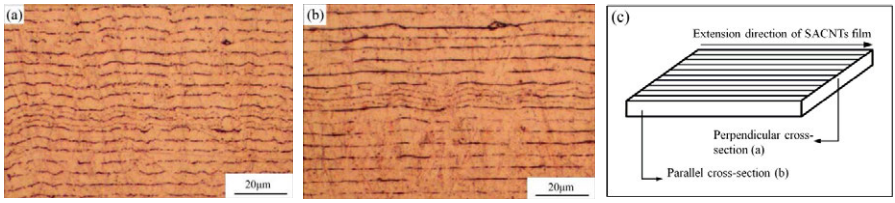

Figure 3. Metallographic graphs of the polished and corroded cross-section respectively of (a) and (b) Cu-0.26vol%SACNT. (c) Schematic of parallel cross-section and perpendicular cross-section.

Figures 4(a-c) provide more details of the shape, distribution and directionality of CNTs and the interface between the CNTs and copper. We can also spot some small gaps around the CNTs, which imply the gaps in SACNT films cannot be filled with copper completely by this traditional copper sulfate electroplating process. This is a problem that needs to be solved in future.

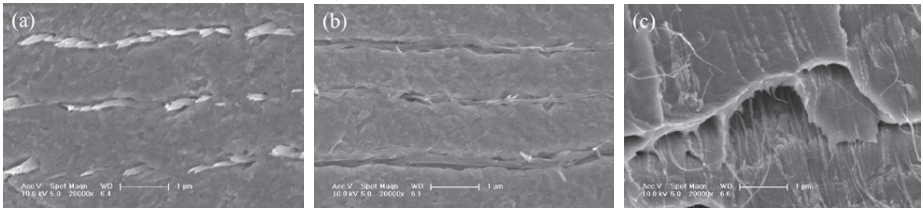

Figure 4. SEM images of Cu-0.52vol%SACNT composite respectively of (a) perpendicular cross-section, (b) parallel cross-section and (c) fracture of the tensile test sample

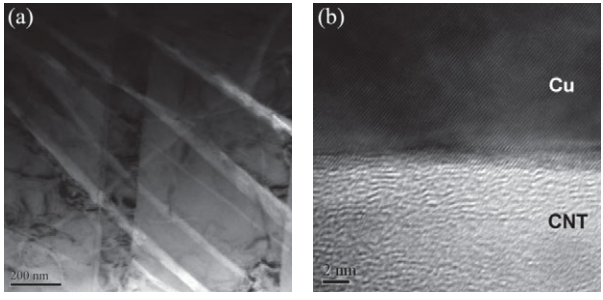

Figure 5. TEM images of Cu-2.6vol% SACNT composite

In order to explore the interface between CNTs and copper in atomic scale, TEM images were taken. Figure 5(a) shows several independent CNTs in the copper matrix. Figure 6(b) is a high resolution TEM image. The upper half of this figure shows the typical hexagonal structure of copper. The bottom half of the figure shows the irregular wavy stripes which represent the structure of multi-walled carbon nanotube. The bonding at the interface between CNT and

copper is well, which will help improve the mechanical properties of matrix by way of load transfer.

Theoretical Calculations for the Performance of Cu/SACNT Composites

Theoretical Calculation of the Mechanical Property

In order to predict the highest performance of Cu/SACNT composites under ideal conditions, the following assumptions are made:

- Carbon nanotubes are arranged completely in the same direction, which is consistent with the direction of the performance testing;
- Carbon nanotubes are dispersed in the matrix homogeneously, with no agglomeration or segregation;
- The interface bonding between the carbon nanotubes and the matrix is perfect.

Based on the above assumptions, we can directly use the rule of mixture (ROM) of composite to calculate the maximum tensile strength of our Cu/SACNT composite under ideal conditions.

$$\sigma_c = \sigma_{Cu} f_{Cu} + \sigma_{CNT} f_{CNT} \tag{1}$$

Where σ_c stands for the ideal tensile strength of the composites; σ_{Cu} andσ_{CNT} are the tensile strengths of pure copper and individual CNT, respectively; f_{Cu} and f_{CNT} signifies the volume fraction of pure copper and SACNT.

For calculation, we take the experimental value 194MPa as the tensile strength of pure copper, 63GPa and 20GPa as the strength of individual CNT for the calculation [17]. The result is shown in Table I. Difference exists in the calculated and experimental values, and it became greater with the increasing of the volume fraction of SACNT. The dispersion and the interface bonding with matrix of CNTs can never be ideal in practice, which results in limited enhanced effect. This indicates the mechanical property of Cu/SACNT composites would have a large rise if appropriate measures were taken to improve the interface bonding.

Table I. The calculated and experimental values of the tensile strength of composites

Volume fraction of SACNT		0%	0.26%	0.52%	1.04%
Tensile strength/MPa (calculated value)	CNT 63GPa	194	357	521	847
	CNT 20GPa	194	245	297	400
Tensile strength/MPa (experimental value)		194	244	272	290

Theoretical Calculation of the Electrical Property

Similar to the calculation of the mechanical property, under the same assumptions, the electrical property of Cu/SACNT composites also can be calculated by the ROM,

$$K_c = K_{Cu} f_{Cu} + K_{CNT} f_{CNT} \tag{2}$$

Where K_c stands for the ideal electrical conductivity of the composites; K_{Cu} and K_{CNT} are the electrical conductivity of pure copper and individual CNT, respectively; f_{Cu} and f_{CNT} are the same as in Equation (1).

Besides, Gao et al [18] use the Bruggeman effective medium theory (EMT) to investigate the effective electrical conductivity of carbon nanotube composites when CNTs distribute randomly and homogeneously. According to this method, the electrical conductivity of Cu/SACNT composites can be calculated by the following equation:

$$9 f_{Cu} \frac{K_e - K_{Cu}}{2K_e + K_{Cu}} + f_{CNT} \left(\frac{K_e - K_{CNT}}{K_e} + 4 \frac{K_e - K_{CNT}}{K_e + K_{CNT}} \right) = 0 \quad (3)$$

Where K_e stands for the effective electrical conductivity of the composites; K_{Cu}, K_{CNT}, f_{Cu} and f_{CNT} are the same as (2).

Table II. The calculated and experimental values of the electrical conductivity of composites

Volume fraction of SACNT		0%	0.26%	0.52%	1.04%
electrical conductivity/ MS/m	calculated by the rule of mixture	50.8	50.7	50.6	50.5
	calculated by EMT	50.8	50.9	50.8	50.6
	experimental value	50.8	52.5	49.0	47.2

For calculation, we take the experimental value 50.8MS/m as the electrical conductivity of pure copper, and the electrical conductivity of individual CNTs can be selected as 20.0MS/m [19]. The calculation result is shown in Table II. Because the electrical conductivities of CNTs and pure copper are of the same order of magnitude, and the volume fraction of SACNT is not high, so the calculated values of the composites, neither by the ROM nor by EMT show a significant difference to the pure copper. And the difference between the calculated values and experimental results is less than 7%, this is reasonable considering the actual dispersion and interface bonding with matrix of CNTs is not exactly the same as the assumptions.

Conclusions

The laminar metal matrix nanocomposite of copper and SACNT film was fabricated by an electroplating process.

- Electroplating is a simple and effective process to prepare large-size laminar Cu/SACNT composites. The directional alignment structure of SACNT is retained in the composite perfectly. This characteristic allows CNTs to play a role in reinforcing tensile strengths and conductivities in the aligned direction of CNTs;
- Compared to pure copper, the mechanical properties of laminar Cu/SACNT composites are significantly improved. With the increase of the volume fraction of SACNT films, the mechanical properties of composites are improved more and more. In the meanwhile, the presence of SACNT films has little impact on the conductivities;
- The calculated results by the ROM and EMT show the potential maximum tensile strength and electrical conductivity of the as-prepared Cu/SACNT composites. Theoretically, the mechanical property of the composites would have a further

improvement if appropriate measures were taken to improve the interface bonding when the composites can obtain conductivities as high as pure copper matrix.

Acknowledgement

This work was partially financially supported by University Initiative Scientific Research Program of Tsinghua University (Grant No. 20111080980).

References

1. D. P. Lu et al., "Study on High-strength and High-conductivity Cu-Fe-P Alloys," *Materials Science and Engineering A*, 421 (1-2) (2006), 254-259.
2. F. L. Wang et al., "Cu–Ti–C Alloy with High Strength and High Electrical Conductivity Prepared by Two-step Ball-milling Processes," *Materials and Design*, 61 (2014), 70-74.
3. D. V. Shangina et al., "Improvement of strength and conductivity in Cu-alloys with the application of high pressure torsion and subsequent heat-treatments," J*ournal of Materials Science*, 49 (19) (2014), 6674-6681.
4. L. Lu et al., "Ultrahigh strength and high electrical conductivity in copper," *Science*, 304 (5669) (2004), 422-426.
5. K. X. Wei et al., "Microstructure, mechanical properties and electrical conductivity of industrial Cu-0.5% Cr alloy processed by severe plastic deformation," *Materials Science and Engineering A*, 528 (3) (2011), 1478-1484.
6. E. T. Thostenson, Z. F. Ren and T. W. Chou, "Advances in the science and technology of carbon nanotubes and their composites: a review," *Composites Science and Technology*, 61 (13) (2001), 1899-1912.
7. Z. Q. Niu et al., "High-Strength Laminated Copper Matrix Nanocomposites Developed from a Single-Walled Carbon Nanotube Film with Continuous Reticulate Architecture," *Advanced Functional Materials*, 22 (24) (2012), 5209-5215.
8. J. H. Nie et al., "Friction and wear properties of copper matrix composites reinforced by tungsten-coated carbon nanotubes," *Rare Metals*, 30 (6) (2011), 657-663.
9. A. K. Shukla et al., "Processing of copper-carbon nanotube composites by vacuum hot pressing technique," *Materials Science & Engineering A*, 11 (2012), 365-371.
10. G. Y. Chai et al., "Mechanical properties of carbon nanotube-copper nanocomposites," *Journal of Micromechanics and Microengineering*, 18 (3) (2008), 035013-1-4.
11. Y. H. Li et al., "Cu/single-walled carbon nanotube laminate composites fabricated by cold rolling and annealing," *Nanotechnology*, 18 (20) (2007), 205607-1-6.
12. W. M. Daoush et al., "Electrical and mechanical properties of carbon nanotube reinforced copper nanocomposites fabricated by electroless deposition process," *Materials Science and Engineering A*, 513-514 (2009), 247-253.
13. C. Feng et al., "Flexible, Stretchable, Transparent Conducting Films Made from Superaligned Carbon Nanotubes," *Advanced Functional Materials*, 20 (6) (2010), 885-891.
14. K. Liu et al., "Scratch-resistant, highly conductive, and high-strength carbon nanotube-based composite yarns," *ACS Nano*, 4 (10) (2010), 5827-5834.
15. Q. F. Cheng et al., "Fabrication and properties of aligned multiwalled carbon nanotube-reinforced epoxy composites," *Journal of Materials Research*, 23 (11) (2008), 2975-2983.

16. Q. F. Cheng et al., “Carbon nanotube/epoxy composites fabricated by resin transfer molding,” *Carbon*, 48 (1) (2010), 260-266.
17. M. F. Yu et al., “Strength and breaking mechanism of multiwalled carbon nanotubes under tensile load,” *Science*, 287 (5453) (2000), 637-640.
18. G. Lei, X. F. Zhou, and Y. L. Ding, “Effective thermal and electrical conductivity of carbon nanotube composites,” *Chemical Physics Letters*, 434 (4-6) (2007), 297-300.
19. T. W. Ebbesen et al., “Electrical conductivity of individual carbon nanotubes,” *Nature*, 382 (6586) (1996), 54-56.

TMS2016

145th Annual Meeting & Exhibition

SUPPLEMENTAL
PROCEEDINGS

UNEDITED
PROCEEDINGS

TMS2016

145th Annual Meeting & Exhibition

SUPPLEMENTAL
PROCEEDINGS

Additive Manufacturing:
Building the Pathway towards Process and Material Qualification

SELECTIVE LASER MELTING OF TiB_2/H13 STEEL BULK NANOCOMPOSITES: INFLUENCE OF NANOSCALE REINFORCMENT

B. Almangour[1], Dariusz Grzesiak[2], J. M.Yang[1]

[1] Department of Materials Science and Engineering, University of California Los Angeles, Los Angeles, CA 90095, USA

[2] Department of Mechanical Engineering and Mechatronics, West Pomeranian University of Technology, Szczecin, Poland

Keywords: Nanocomposite, Metal matrix composite (MMC), Mechanical alloying, Selective laser melting

Abstract

Additive Manufacturing (AM) holds strong potential for the formation of a new class of multifunctional nanocomposites. Selective laser melting, as a promising AM fabrication route, was applied to produce nanocrystalline TiB_2-reinforced H13 steel matrix nanocomposites. Uniformly dispersed TiB_2 particles were obtained and fine homogenous needle-shaped martensitic microstructures were observed. The microstructural and hardness of SLM-processed nanocomposites were sensitive to the TiB_2 addition. Relative to the unreinforced H13 steel part, the TiB_2/ H13 steel nanocomposites parts with the novel architecture exhibited much higher hardness due to the combined effects of grain refinements and grain boundary strengthening.

Introduction

Additive Manufacturing (AM), as an inspiring advanced manufacturing technology, enables the quick production of three-dimensional metallic, ceramic, or metal matrix composite (MMC) parts with any complicated shapes directly from powder materials. Normally, these complex components/configurations are difficult or even impossible to be obtained through conventional processing methods [1, 2]. Selective laser melting (SLM), as a powder-bed-based AM process, creates bulk-form parts from the starting loose powder in a layer-by-layer manner, according to the Computer Aided Design (CAD) data of the desired components [3, 4].

As the development of modern industries has a higher requirement for the engineering materials, the relatively low hardness and tribological/wear performance of steel alloys have limited their broader applications. To this end, the steel matrix composites (SMC), with the combined favorable properties of steel matrix phase and reinforcing phases, have received considerable research interest [5]. One potential reinforcement for steel matrix is TiB_2 which has thermodynamic and mechanical stability for structural applications [5].

In the present study, the TiB_2/H13 composite powder systems with different starting TiB_2 particle volume were fabricated by SLM process. The variations of densification level, constitution phases, microstructural features, and hardness of the SLM-processed SMC parts

were studied. The underlying role of powder features in the improvement of laser processing ability and attendant microstructural and mechanical properties of SMC parts was disclosed.

Experimental procedures

The raw powder materials used in this study consisted of the 99.7% purity H13 tool steel powder with a spherical shape and a mean particle size of 35 μm (Fig. 1a), and the 99.5% purity TiB_2 powder with a poly-angular structure and a mean particle size of 2-12 μm (Fig. 1b). Four different TiB_2/H13 nanocomposites systems containing 2.5, 5, 10, and 15 vol.% TiB_2 particles were prepared by mixing the component powders. The mixing process was performed in a Fritsch Pulverisette 4 vario-planetary mill, using a ball-to-powder weight ratio of 5:1, a rotation speed of the main disk of 200 rpm, and a mixing time of 2, 4, 6, 8 h.

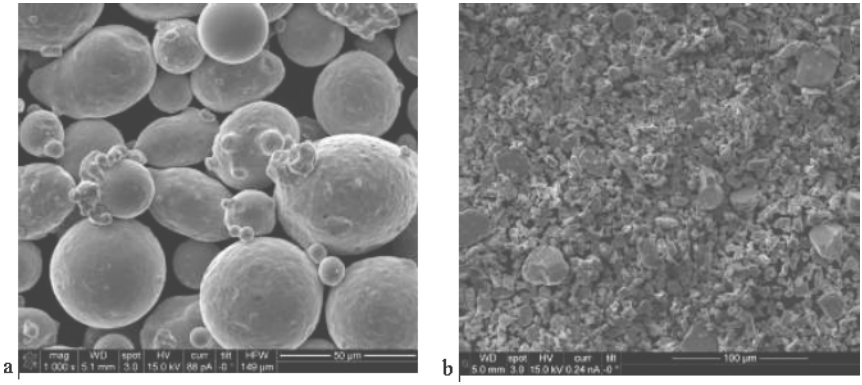

Figure 1: SEM images showing initial starting powders (a) H13; (b) TiB_2.

The processing parameters were optimized, with the laser power of 100 W and the scan speed of 100 mm/s, exhibited the relatively high densification level, higher microhardness than the parts processed at other laser parameters. The bulk-form samples with three-dimensions of 8 mm × 8 mm × 6 mm were fabricated by SLM in a layer-by-layer method.

Phase identification of SLM-processed samples was performed by a PANalytical X'Pert PRO X-ray Powder Diffractometer with Cu K_α radiation at 45 kV and 40 mA, using a continuous scan mode at 4°/min. The densification behaviors of parts were estimated using Archimedes' principle. The Vickers hardness of SLM-processed samples was measured using a (Leco, LM800AT) microhardness tester at a load of 200 g and an indentation time of 10 s.

Results and discussion

Microstructural characterizations

Figure 2 illustrates the XRD spectrums of the milled TiB_2/ H13 powders at different milling times. On increasing milling time from 2 to 8 h, the diffraction peaks for H13 phase became

apparently broadened and the intensity showed a significant decrease, which indicated the formation of considerably small-sized crystallites in the milled powders. Besides peak broadening, the H13 peaks generally shifted to lower angles as the milling time prolonged from 2 to 8 h as a result of compressive stresses. Generally, the decrease in crystallite size of milled particles with milling time is attributed to the generation of crystal defects such as point defects and dislocations induced by severe plastic deformation of soft powders. The defects enhance lattice strain and its internal energy, and therefore the milling system becomes unstable. To reach a steady state, the dislocations rearrange themselves to a lower energy state, which results in the formation of low angle sub-boundaries.

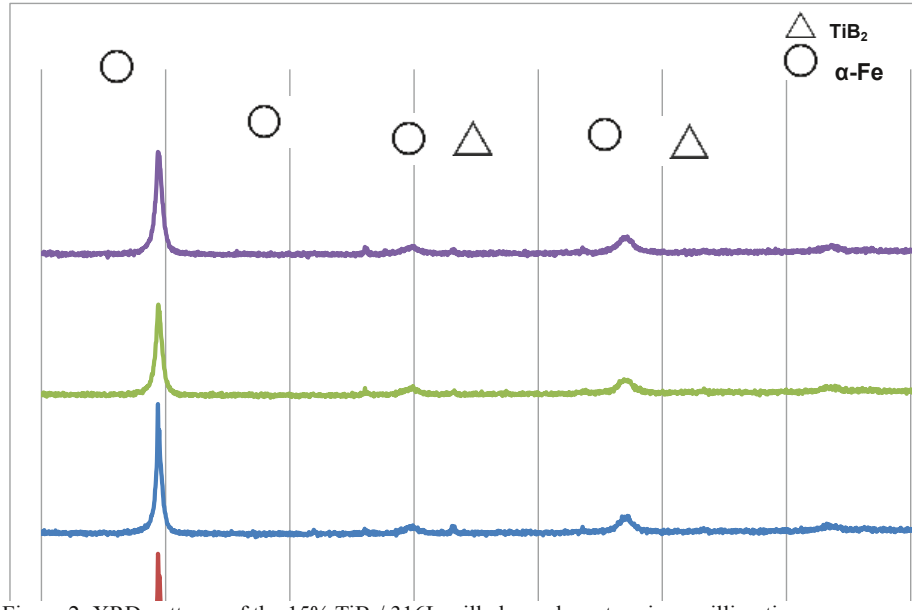

Figure 2: XRD patterns of the 15% TiB_2/ 316L milled powders at various milling times.

Figure 3 illustrate the typical XRD patterns of SLM-processed composites at various volume reinforcements. The three strong diffraction peaks detected for the H13-containing phase were generally located at $2\theta = 44.10°$, 64.93° and 78.79°, which exactly correspond to the 2θ locations of standard peaks for α-Fe.

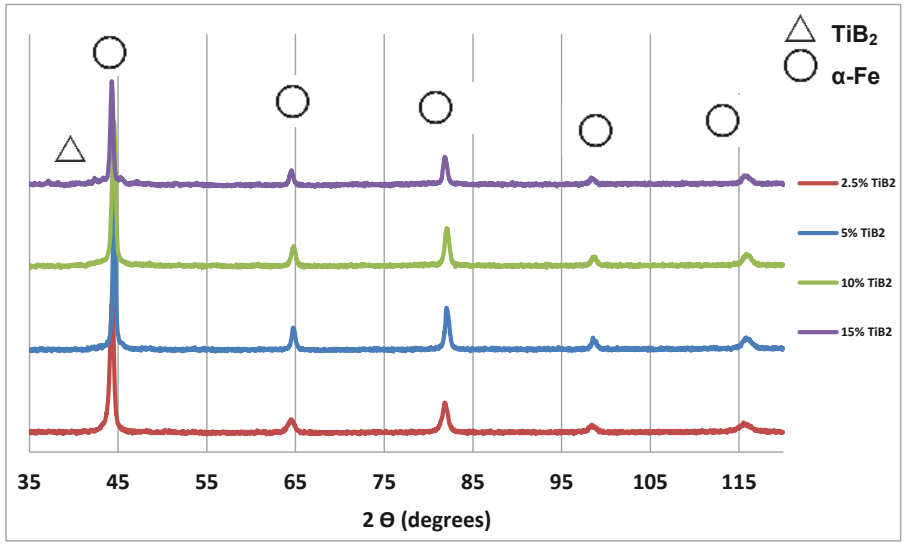

Figure 3: XRD spectrum of SLM processed SLM parts.

Figure 4 shows the effect of TiB_2 addition on the densification behavior of SLM-processed parts. The corresponding as-built of pure H13 consisted of coherently bonded scan tracks and the obtained densification rates were around 96% theoretical density (TD). The cross-sections of SLM parts containing low amount of TiB_2 shows homogeneous microstructures with relatively low interlayer pores. As the TiB_2 addition increased to 10 vol.%, the cross-section showed a decrease in density to 89% TD. A large number of balls with diameters of 20–140 µm were formed on the surface. It was accordingly inferred that a "balling" effect, which is a metallurgical defect typically associated with SLM had initiated in this instance. When 15 vol.% TiB_2 was added, interlayer pores 100 µm in size were present on the cross-section and, at the same time, clusters of balls and inter-ball porosity formed on the surface, resulting in an apparent decrease in densification. The high melt viscosity and limited wetting characteristics caused by an insufficient laser energy input are the key factor in producing balling effect and interlayer pores, hence weakening the densification activity of SLM-processed TiB_2/H13 nanocomposites parts.

Figure 5 shows the SEM microstructures for the nanocomposites parts produced by SLM. With the increase in the vol.% of the TiB_2 reinforcement, a series of TiB_2 nanoparticles was formed along the grain boundaries of the H13 matrix in a highly homogenous manner. As well, the dispersion/ TiB_2 concentration becomes higher. During the SLM process, which involves complete liquid formation, the TiB_2 reinforcing phase is formed via a dissolution mechanism by means of the heterogeneous nucleation of TiB_2 nuclei and subsequent grain growth. The solidification rate induced by high-energy laser melting can reach values as high as $10^6 – 10^8$ K/ s [7]. Therefore, the effective crystal development of TiB_2 nuclei is significantly restricted, due to insufficient time for grain growth to occur, and hence the favorable nanoscale structure of the TiB_2 reinforcing phase is retained.

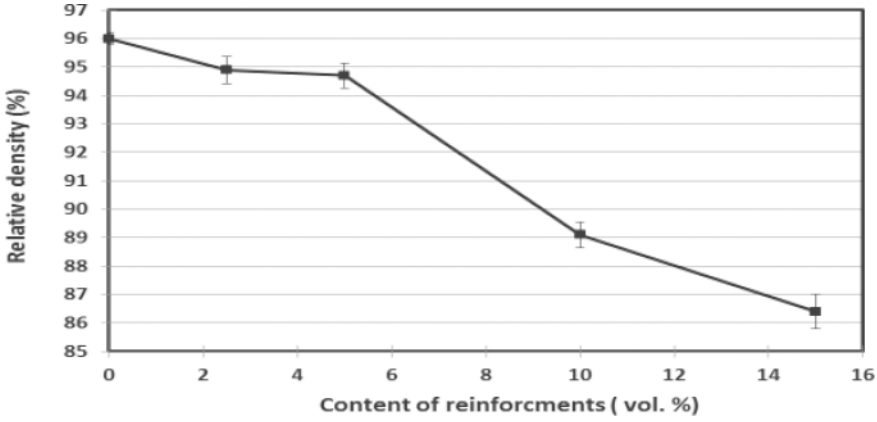

Figure 4: Densification levels of SLM-processed parts.

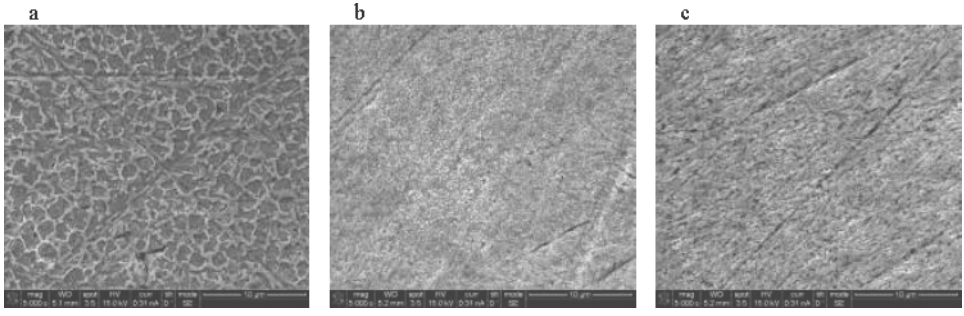

Figure 5: SEM images showing characteristics of etched morphologies of SLM-processed parts at various volume reinforcements: (b) 2.5%, (c) 5%, (d) 10%.

Mechanical Behavior

Figure 6 depicts the average microhardness measured on top and side views of pure H13 and 15% TiB_2 /H13 parts. A maximum microhardness of ~ $850HV_{0.2}$ was obtained when 15 vol.% TiB_2 nanoparticles were added. Nano sized grains significantly contribute to the strength and hardness of alloys due to the "Hall-Petch" strengthening effect. Nevertheless, with the 15 vol.% TiB_2/ H13, the microhardness, showing a relatively large data fluctuation (i.e. high standard deviation). The insufficient densification due to the pore formation at 15 vol.% TiB_2 (Fig. 4) was responsible for the high variation in hardness.

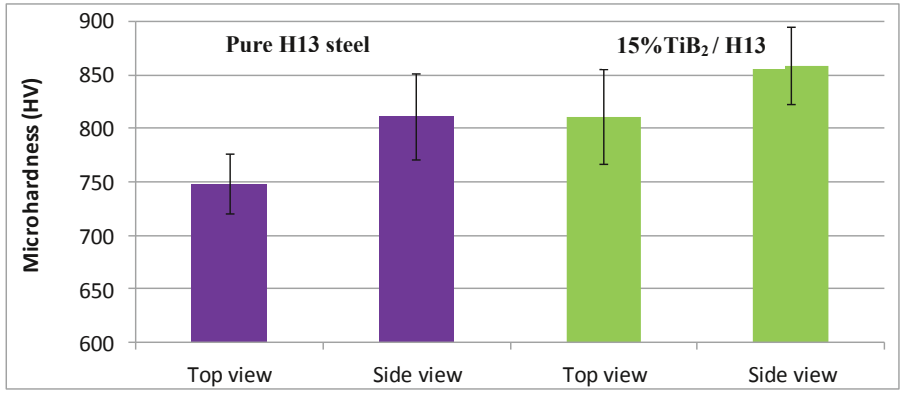

Figure 6: Influence of TiB_2 reinforcement on the microhardness of SLM-processed parts.

Conclusions

Selective laser melting (SLM), as a powder-bed-based additive manufacturing technology, was applied to process the TiB_2/H13 nanocomposite powder systems with different sizes of starting TiB_2 particles. The insufficient densification and disappearance of nanostructured TiB_2 reinforcement at a high TiB_2 content at 15 vol.% limits the hardness.

Acknowledgments

One of the authors, B. AlMangour, gratefully appreciates the financial support from Saudi Arabia Basic Industries Corporation (SABIC).

References

[1] Gibson I, Rosen DW, Stucker B. Additive manufacturing technologies: Springer; 2010.
[2] Wong KV, Hernandez A. A review of additive manufacturing. ISRN Mechanical Engineering 2012;2012.
[3] Bremen S, Meiners W, Diatlov A. Selective Laser Melting. Laser Technik Journal 2012;9:33-8.
[4] Campanelli SL, Angelastro A, Ludovico AD, Contuzzi N. Capabilities and performances of the selective laser melting process: INTECH Open Access Publisher; 2010.
[5] Tjong S, Lau K. Sliding wear of stainless steel matrix composite reinforced with TiB 2 particles. Materials Letters 1999;41:153-8.
[6] Suryanarayana C, Norton MG. X-ray diffraction: a practical approach: Springer Science & Business Media; 2013.
[7] Zhong M, Liu W. Laser surface cladding: the state of the art and challenges. Proceedings of the Institution of Mechanical Engineers, Part C: Journal of Mechanical Engineering Science 2010;224:1041-60.

IN-SPACE MANUFACTURING BASELINE PROPERTY DEVELOPMENT

Tom Stockman[1], Judith Schneider[1], Tracie Prater[2], Quincy Bean[2], Nicki Werkheiser[2]

[1] University of Alabama in Huntsville;
301 Sparkman Drive NW, Huntsville, AL 35899, USA

[2] NASA-Marshall Space Flight Center;
Redstone Arsenal, Huntsville, AL 35812, USA

Abstract

The In-Space Manufacturing (ISM) project at NASA Marshall Space Flight Center currently operates a 3D FDM (fused deposition modeling) printer onboard the International Space Station. In order to enable utilization of this capability by designer, the project needs to establish characteristic material properties for materials produced using the process. This is difficult for additive manufacturing since standards and specifications do not yet exist for these technologies. Due to availability of crew time, there are limitations to the sample size which in turn limits the application of the traditional design allowables approaches to develop a materials property database for designers. In this study, various approaches to development of material databases were evaluated for use by designers of space systems who wish to leverage in-space manufacturing capabilities. This study focuses on alternative statistical techniques for baseline property development to support in-space manufacturing.

Introduction

The 3D Printing in Zero G technology demonstration mission, is responsible for providing fast, local solutions to hardware needs during spaceflight operations. The capability to produce parts in flight could vastly improve sustainability for long duration missions and reduce launch costs. As part of the technology demonstration mission, a fused deposition modeling (FDM) 3D printer ~~on the ISS~~ was installed on the International Space Station in fall 2014. The initial set of builds consisted of 20 parts, which ranged from mechanical test coupons to functional tools such as a hex head socket and ratchet.

In order for ISM to progress and develop further manufacturing capabilities, baseline material properties must be established. The development of material properties is a familiar challenge to the additive manufacturing (AM) community as a whole. In parallel with the FDM processing for ISM, NASA is also developing specifications for metal based AM processing and looking for transferable concepts, procedures, methodologies, and standards. NASA's current approach involves the development of a probability reference distribution which is capable of evolving to reflect changes/improvements in the AM process.

Limitations on astronaut crew time impart a unique challenge by significantly limiting the number of test coupons that can be produced to quantify material properties and verify the materials produced by the process are of sufficient quality. In addition to the time limitations, developing a design allowables database for AM in general must account for the complex relationship between the build parameters and the resulting properties. Thus the goal of materials characterization for AM is to provide an engineering understanding of material behavior under a range of conditions. Statistical techniques must be utilized to effectively analyze limited data, especially with regard to properties of ISS printed components.

Design Allowables Approach

There are processes where traditional approaches to allowables development are appropriate, but these processes have characteristics that are not generally associated with AM at this point in time and include:

1) Well established material and manufacturing method, product form, and product thickness.
2) Governing of the production process/manufacturing technique by an industry or government-quality specification.
3) Utilization of a closed loop and control feedback/*in situ* process which incorporate identified quality indicators.
4) Failure modes for materials are well-understood.
NASA's standard materials and processes requirements for spacecraft components combine the various standards individually developed for different material families into NASA-STD-6016 [1]. Common to all material families is the establishment of design allowables (or tolerance band).

Typically design allowables are created by systematically testing a set number of samples from various lots. These lots can be defined on the basis of material processing such as temperature, build direction, cross sectional areas, etc. The results of these tests are statistically analyzed to define a baseline property referred to as an allowable. The highest level or most stringent on the number of specimens and their interpretation is the A-basis, or A-value. The A-basis design allowables are defined on the basis of a 95% lower confidence level bound applied to the 1st percentile of a specified population of measurements [2, 3]. This provides a tolerance band for the acceptable materials properties.

B-basis, or B-value design allowables are generally applied to the design of non-structural or redundant materials. B-basis allowables are defined using a 95% lower confidence level bound applied to the 10th percentile of a specified population of measurements [2, 3].

An S-basis allowable, which is simply a minimum design value specified by a governing industry or government specification, does not have an associated tolerance bound. If neither an A-basis nor B-basis database has been developed for a material, a statistically based S-basis allowable for a material can be used. Per NASA-STD-6016 [1], S-basis allowables are not typically used in primary structures or fracture-critical hardware without justification and documentation.

Per NASA-STD-6016, NASA can create a material usage agreement (MUA), to provide technical rationale for use of the materials which do not have A-basis or B-basis allowables such as those with an S-basis allowable. In these instances, the hardware developer must provide a plan describing the material property development philosophy and provide detailed insight into how the material design properties will be determined. This plan must also include information on statistical approaches.

Allowables cataloged in or derived using the procedures in NASA-STD-6016 are widely accepted among the aerospace design community. The number of test specimens required for A-basis and B-basis allowables varies among the various families of materials. Metallic materials require a minimum sample size of 100 obtained from 10 lots with 10 samples each [3]. If the distribution is non-parametric (i.e. does not fit a normal distribution), at least 300 samples are required. In contrast, polymeric composites only require 30 samples for an A-basis allowable. Thus materials made using FDM have the additional complication of not having standards to guide the generation of an A-basis or B-basis design allowables database.

Components manufactured using AM processes, either for metals or polymers, are highly process dependent. Composites are in many ways similar to AM produced materials. In both cases the properties are highly process dependent, often anisotropic, and very sensitive to test specimen geometry and test technique. Thus MIL-HDBK-17 details standardized and validated methods for establishing composite allowables that are slightly different from those established by MIL-HDBK for metals in terms of number of samples, number of lots, and other constraints and rules. MIL-HDBK-17 also specifies design allowables for the constituents of the polymeric composite which may have applicability to the FDM polymeric materials.

Another limitation of NASA-STD-6016 type methodologies for AM is that once material property development activities are complete, little opportunity exists to revisit the established allowables database. The risk inherent in using this approach for an evolving process, such as AM, is that once the established design allowables no longer reflect the process or the materials produced, the development work needs to be repeated. Without methods to update the allowables as the AM process matures, designers will continue to use values that do not represent the materials being produced.

AM broadly challenges the established allowables development philosophy. Traditional allowables approaches are not suitable for in-space manufacturing and specifically development of material design values for materials produced using the 3DP FDM hardware currently on the ISS. The ISM team is limited in the scope of a fully executed allowables development program based on the guidelines of the design handbooks [2, 3]. Considering the variability and evolving nature of the AM process, the data derived from such an effort may not retain meaningfulness in the long-term.

At this time, the parts selected for fabrication using the 3DP FDM process on the ISS have low consequences of failure. To help develop the procedures and methodology, a complementary

effort is focused on structural modeling at the macroscale. Given these constraints and considerations, an alternative approach using statistical techniques for baseline property development to support in-space manufacturing may provide a better solution for confidence in establishing a design allowables database.

Modified Approach

A two phase study is proposed to statistically establish material properties for 3DP using FDM. Phase I of this work seeks to understand the sensitivity of parts produced using the process to manufacturing process variables. This can be accomplished by carefully crafting a set of screening experiments that will assess whether and to what degree, the first-tier material properties are a function of feedstock material, build orientation, filament layup, test temperature, and printer. The study seeks to broadly answer the following questions:

1) How do build orientation and layup impact material properties?
2) What degradation or improvement in properties can be expected based on the test temperature, and, by extrapolation, the use temperature of the component?
3) What amount of variability in material properties can be expected when two parts with the same feedstock, build orientation, and layup are printed on different printers?
4) Does feedstock manufacturer impact material properties of the as-built part in an engineering significant way?

The Phase 1 study is an exploratory test that includes: 35 sets of tensile, compression, and shear specimens. 3 temperatures, 5 combinations of build orientation and filament layup, and 3 feedstock materials, printed on 2 printers. The primary goal of the first phase is to closely examine specimens printed in space and compare them both quantitatively and qualitatively to the same specimens printed on the ground. Each of the ISM specimens has a twin built on a twin machine on the ground. These specimens will go through mechanical testing (tensile, compression, etc) along with measurements for mass, volume, and tolerancing. The specimens will also be subject to x-ray radiography to give a visual inspection of the internal structure. If the specimens printed in space are found to have very little difference from specimens printed on the ground, then further material characterization can be performed on the ground where crew time and transportation to and from ISS are not needed. The sensitivity analysis/screening experiment will indicate which factors have a statistically significant impact on material quality and the ISM team will use this data to develop a Phase II Design of Experiments (DOE) protocol/experimental matrix.

Data from the Phase II DOE will be modeled using regression techniques. The response surface generated by the regression models will be used to define a statistical tolerance region which bounds characteristic material properties for a given combination of temperature, build orientation/layup, printer, and feedstock. While nontraditional, this approach represents the best

fit for the current needs thereby allowing the execution of a material property development program that will:

1) Enable the development of an efficient test plan that will minimize the number of test articles yet still provide validated information about material behavior that can be used for design and analysis.
2) Generate analyzable data.
3) Calculate basis values for a combination of material and processing characteristics that will reduce reliance on engineering judgment.

The approach will leverage DOE techniques to optimize the value of information and allow material property development and materials characterization activities to occur simultaneously. Subsequent investigations such as assessing machine variability, lot to lot variability, the effect of feedstock, etc., can be performed as needed through additional/follow-on DOEs. Because DOE enables variation of several factors at a time, the technique is more cost-effective and less experimentally intensive than the "one piece at a time" approach.

Summary

ISM is a significant advancement to in space capabilities. However, certification and development of material properties is made difficult by the newness of the technology, the high process dependency of the technology, and a limited capability to produce large numbers of samples. Using a phased approach a database baseline can be established to develop usable properties. These properties will not necessarily be representative of traditional A-basis/B-basis allowables but will still be sufficient for the design and production of 3D printed parts in space.

References

[1] "Standard materials and processes requirements for spacecraft," *NASA-STD-6016*, July 11, 2008.

[2] Composite Materials Handbook: Vol. 1 Polymer matrix composites guidelines for characterization of structural materials, Pub. Department of Defense, *MIL-HDBK-17-1F*, June 17, 2002. Now published as the Composites Materials Handbook (CMH)-17.

[3] Metallic materials and elements for aerospace vehicle structures, Pub. Department of Defense, MIL-HDBK-5J, January 31, 2003. Now published as the "Materials Properties Development and Standardization (MMPDS)."

USING POWDER CORED TUBULAR WIRE TECHNOLOGY TO ENHANCE ELECTRON BEAM FREEFORM FABRICATED STRUCTURES

Devon Gonzales[1], Stephen Liu[1], Marcia Domack[2], Robert Hafley[2]

[1]Colorado School of Mines; 1500 Illinois St.; Golden, CO 80401, USA
[2]NASA-Langley Research Center, AMPB; 8 W. Taylor St.; Hampton, VA 23681-2199, USA

Keywords: EBF^3, Additive Manufacturing, Powder Cored Wire, Ti-6Al-4V, Al 6061, Composite Builds, Grain Refinement, Epitaxy

Abstract

Electron Beam Freeform Fabrication (EBF^3) is an additive manufacturing technique, developed at NASA Langley Research Center, capable of fabricating large scale aerospace parts. Advantages of using EBF^3 as opposed to conventional manufacturing methods include, decreased design-to-product time, decreased wasted material, and the ability to adapt controls to produce geometrically complex parts with properties comparable to wrought products. However, to fully exploit the potential of the EBF^3 process development of materials tailored for the process is required. Powder cored tubular wire (PCTW) technology was used to modify Ti-6Al-4V and Al 6061 feedstock to enhance alloy content, refine grain size, and create a metal matrix composite in the as-solidified structures, respectively.

Introduction

Electron Beam Freeform Fabrication is a layer-additive manufacturing process that uses a CNC controlled electron beam welder coupled with wire feedstock to methodically build parts from a base substrate [1]. The vacuum environment and the high energy density beam create favorable conditions for vaporization loss of alloying elements with higher vapor pressures than the bulk material being melted. Aluminum loss from Ti-6Al-4V and magnesium loss from Al 6061 alloys were recorded in deposits made using monolithic wires. The alloy loss was significant to the effect that deposits were no longer within industrial compositional specification. Alloying enhancements of aluminum and magnesium, respectively, made to powder cored tubular wires can be used as a cost effective way to commercialize the EBF^3 process for each of the two alloy systems. Experiments were conducted to determine the necessary enrichment required from PCTWs to create as-solidified builds of Ti-6Al-4Vand Al 6061 alloys. Partial re-melting of the previous layers during additive processes creates thermal cycles and gradients throughout the build. Consequently, certain alloy systems such as Ti-6Al-4V, are susceptible to epitaxial growth [2]. Epitaxy is directional grain growth across the fusion line which leads to elongated grains in the build direction. Potential problems include decreased fatigue strength, ductility, and anisotropic mechanical properties [3]. Additions of iron-boron powder were implemented in Ti-6Al-4V builds using PCTWs to mitigate epitaxial grain growth. Although not discussed in this paper, beam modulation and focal height were studied as viable processing modifications to improve the microstructure.

High strength, lightweight materials are highly sought after in the aerospace industry. A feasibility study was conducted to determine if 6061/SiC_p metal matrix composite structures can be produced using EBF^3. Commercially produced metal matrix composites are produced through casting or sintering. Further processing of this material is difficult due to the wear resistance and hardness of the material. Laser-additive manufacturing processes are not feasible for producing 6061/SiC_p structures. The thermal and optical properties of the aluminum and silicon carbide lead to decomposition of the silicon carbide particles and the development of detrimental phases in the melt pool [4]. Coated and uncoated silicon carbide particulates and alloying additions were incorporated in powder cored tubular wires to produce 6061/SiC_p composite structures using EBF^3.

Discussion

Modified Ti-6Al-4V powder cored tubular wire was manufactured using mass balance calculations and deposited in the EBF^3 system. Solid monolithic alloy Ti-6Al-4V and Ti-7Al-4V composition wires were deposited using the same parameters as the PCTW. The chemical compositions of these monolithic builds were compared with that of the PCTW. Figure 1 shows the compositions of the EBF^3 builds made using Ti-6Al-4V and Ti-7Al-4V monolithic wires, and the PCTW build composition with the expected alloy loss of 0.5 wt. pct. during the EBF^3 process [5]. The target composition was achieved using both the Ti-7Al-4V and PCTWs, however the standard deviation was greater for the PCTW. It is expected that optimization of the PCTW fabrication process and EBF^3 build parameters should result in standard deviations comparable to the alloy Ti-7Al-4V wires at a lower cost of production. Thus, this comparison shows PCTWs are a viable substitution for alloy Ti-6Al-4V and Ti-7Al-4V monolithic wires with regards to composition [5].

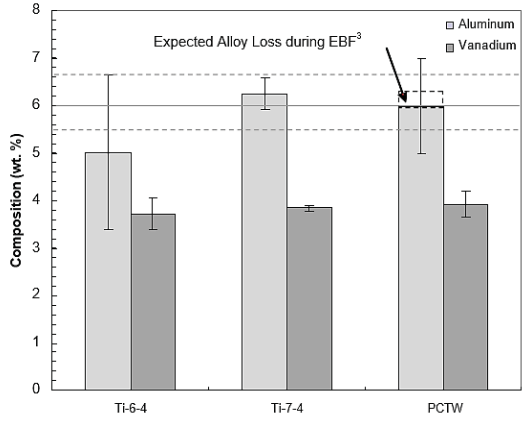

Figure 1. Comparison of post-deposition composition between monolithic and PCTWs. Solid and dashed lines are included to show the target and upper and lower chemistry tolerances, respectively, of the alloy Ti-6Al-4V [5].

Macrostructural analysis was performed comparing the PCTW build with that made using Ti-7Al-4V monolithic wire. Figure 2 shows typical short transverse cross-sections of EBF^3 builds

made using PCTW and the monolithic Ti-7Al-4V wire. Both builds were composed of two preheat passes and ten deposited layers and were deposited under identical parameters of current, voltage, travel speed, and wire feed rate. The characteristic epitaxial growth of prior β grains originating from the HAZ and extending through all layers is present in each build, as is the Widmanstätten morphology of α phase within the prior β grain boundaries. Banding can also be observed from the macrographs of Figure 2, more so in the PCTW build than the monolithic wire build. Microstructures in the banding show a refinement of α Widmanstätten structure. Banding can also indicate the degree to which the previously deposited layer was re-melted during a pass. It is speculated that the close proximity of the banding indicates a high degree of re-melt is occurring, supporting the claim that compositional homogeneity of the EBF^3 deposits is being achieved through melting and mixing of the deposited layers. Near the top of the builds, a coarser alpha structure exists, and in the heat affected zone coarse β grains have grown from the original base plate microstructure. In addition, Vickers microhardness tests taken at the top of each deposit revealed the PCTW and monolithic builds to be of similar hardness, 314 and 312 VHN, respectively [5].

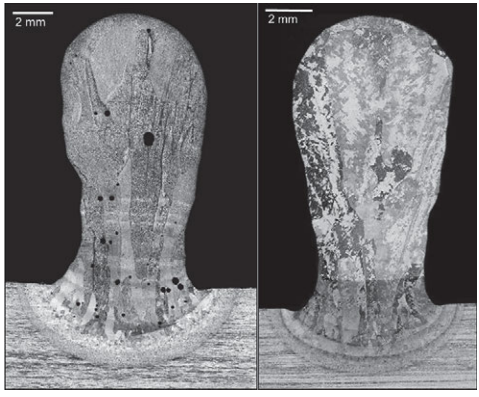

Figure 2. Short transverse cross-sections of ten-layer EBF^3 deposits of (a) PCTWs, (b) Ti-7Al-4V monolithic wires [5].

Differences between the monolithic and PCTW builds arise in the high degree of porosity and both β and α grain refinement in the PCTWs. The aspect ratios of α laths at the top of each sample were determined, as shown in Figure 3a and b. The average length of α laths are comparable between the PCTW and monolithic samples, yet the width of the laths in monolithic builds are much larger than PCTW builds, resulting in aspect ratios of 20:1 in PCTW and 5:1 in monolithic builds [5]. The size of the β grains, determined by observing the long transverse orientation of the builds, of the PCTW builds were nearly half the width of the monolithic wire builds, 500 μm as opposed to 950 μm [5].

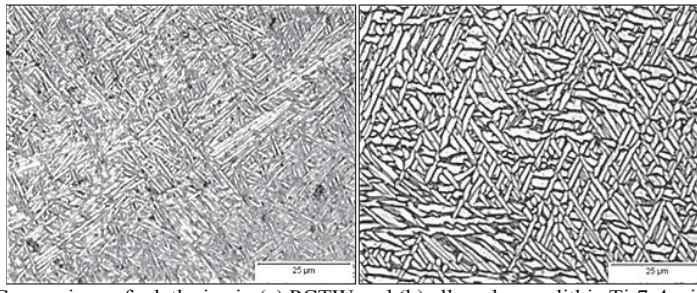

Figure 3. Comparison of α lath size in (a) PCTW and (b) alloyed monolithic Ti-7-4 wires showing a much finer α structure in PCTWs than monolithic builds [5].

Stricter procedures for the wire manufacturing process as well as optimized baking times to remove entrapped wire drawing lubricant were implemented for subsequent PCTW iterations. The PCTWs made using these modifications produced EBF^3 deposits with minimal to no porosity in the as-solidified structure. However, epitaxial growth of the prior β grains continued resulting in microstructural anisotropy in the as solidified builds. New iterations of wires were produced with the addition of the iron-boron inside a Ti-6Al-4V alloy PCTW. Cross-section macrographs of the Ti-6Al-4V and Ti-6Al-4V+FeB PCTW builds are compared in Figure 4. Large β grain refinement due to the iron-boron addition was observed. Traditional Ti-6Al-4V alloy builds had an average β grain size of 1450 µm in Figure 4a, compared to 290 µm with the iron-boron modified chemical composition in Figure 4b [3].

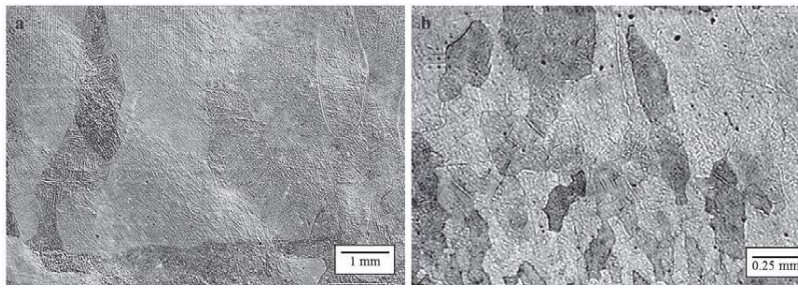

Figure 4. β grain refinement due to iron-boron addition: (a) Traditional build macrostructure; (b) Ti-6Al-4V+FeB PCTW macrograph [3].

The formation of very fine basketweave Widmanstätten α laths in intermittent areas of the steady-state regions was an unexpected effect of the boron modification. The two types of α lath morphologies are shown in Figure 5 and reflect a refinement of α colony intercept length from 3.1 to 2.0 µm. The α width decreased from 0.75 µm, in a traditional Ti-6Al-4V build, to 0.44 µm in the boron modified build [3]. Improved nucleation on intragranular boride particles is thought to be the reason for the large α phase refinement observed, as the increased nucleation sites caused a more competitive lath growing environment. The addition of the FeB powder refined the overall microstructure. Iron additions stabilized the β phase while boron additions created TiB precipitates which acted as pinning points at the grain boundaries and created nucleation

sites for new β grains, interrupting epitaxial growth [3]. The versatility of the PCTW technology allowed for chemical and microstructural improvements to be made to Ti-6Al-4V builds using the EBF^3 system.

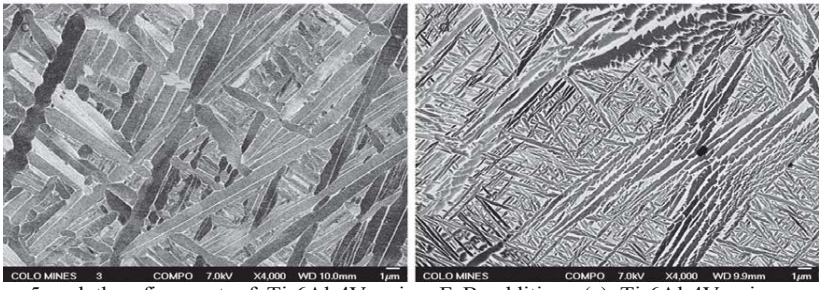

Figure 5. α-lath refinement of Ti-6Al-4V using FeB addition. (a) Ti-6Al-4V micrograph at magnification 4000x (b) Ti-6Al-4V+FeB micrograph at magnification 4000x [3].

Principles used to create modified Ti-6Al-4V powder cored tubular wires for the EBF^3 system were also applied to other alloy systems. For example, magnesium loss when depositing Al 6061 poses similar issues seen from aluminum loss in Ti-6Al-4V deposits. Modified Al 6061 PCTWs were developed to accommodate this loss. Studies were then conducted to determine the feasibility of creating a metal matrix composite as-solidified structure using PCTWs in the EBF^3 system. Al 6061 alloy was used as the matrix and SiC particulates, uncoated or coated with varying thicknesses of copper and nickel, were used as reinforcements. Coatings were used to compare the degree of protection from aluminum carbide formation, a detrimental reaction that occurs between aluminum and SiC, as well as promote particle dispersion in the matrix. It was observed that deposits containing nickel coated SiC formed less, in some cases no, aluminum carbide. Deposits exhibited clustering of the particulates, shown in Figure 6.

Figure 6. Macroscopic image of a ten layer deposit with low nickel coated SiC made using EBF^3.

The degree of clustering was measured and plotted in Figure 7. The cluster size (area) and mean free path (MFP) measurements were normalized by volume fraction of silicon carbide in the deposit since this can vary between different builds. Values residing in Quadrant I indicate that deposits have relatively small cluster size, a sign of increased dispersion, but a high mean free path which indicates a low volume percent of silicon carbide. The more favorable values follow the direction of the arrow in Quadrant III. These values indicate a high volume fraction of dispersed particles. Values in Quadrants II and IV indicate large amounts of agglomeration and are highly unfavorable. The data in Figure 7 indicates that low copper content (LCC), and low nickel content (LNC) coated conditions provided the highest amount of dispersion in the matrix. Agglomeration of silicon carbide particles with high copper and nickel content may occur because the coating re-solidifies too rapidly after deposition trapping the particles in large clusters. This may be exacerbated by thermal gradients generated by transitions from conductive to semi-conductive material. The electrical and thermal properties of SiC and other ceramic reinforcements make it difficult to process using additive manufacturing, however, modifications to the matrix and the use of metallic coatings on the reinforcement particles can lead to successful deposition of metal matrix composites using EBF^3.

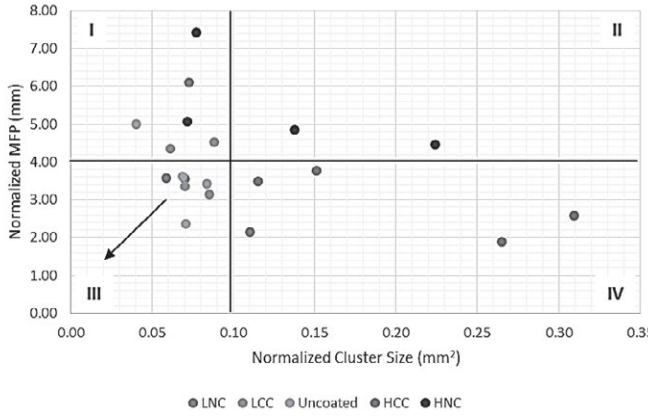

Figure 7. Plot comparing normalized mean free path and cluster size values for the five coating conditions. Highest favorability of dispersion in the direction of the arrow.

Conclusions

Powder cored tubular wire technology was used to modify the composition to produce as-solidified Ti-6Al-4V deposits using the EBF^3 additive manufacturing process. Powder cored tubular wires successfully replenished aluminum loss in EBF^3 deposits. The deposits made using PCTWs were comparable in size and hardness to that of deposits made using commercially produced monolithic wire at a lower cost of production. Strict quality control implemented during the wire manufacturing process minimized porosity previously observed in deposits made using PCTWs. Iron-boron enhancements to the powder core significantly refined the α-lath structure and broke up epitaxial growth of the prior β grains in multiple layer EBF^3 deposits of Ti-6Al-4V alloy. PCTW principles were applied to the Al 6061 alloy to replenish magnesium

vaporization loss in EBF^3 deposits. Further steps were taken to develop metal matrix composite powder cored tubular wires for use in the EBF^3 system. It was determined that nickel coating on the silicon carbide, in optimal thicknesses, can protect the particles during deposition and enhance particle dispersion in the matrix. Results found were used as first steps for developing a commercial metal matrix composite using the Electron Beam Freeform Fabrication system.

References

1. K.M.B. Taminger and R. A. Hafley, "Electron beam freeform fabrication: a rapid metal deposition process," Proceedings of the 3rd Annual Automotive Composites Conference, Society of Plastics Engineers, Sept. 9-10, Troy, Michigan, 2003.

2. M. Karen and M. T. Robert, "Electron Beam Freeform Fabrication for Cost Effective Near-Net Shape Manufacturing." (NATO Unclassified Report).

3. Mitzner, S. V., "Grain Refinement and Epitaxial Interruption of Freeform Fabricated Ti-6Al-4V Alloy" (M.S. thesis, Colorado School of Mines, 2012).

4. T.J. Lienert, E.D. Brandon, J.C. Lippold, "Laser and Electron Beam Welding of SiC_p Reinforced Aluminum A-356 Metal Matrix Composite," *Scripta Metallurgica*, 28 (1993), 1341-1346.

5. Hillier, C. K., "Powder-cored Tubular Wire Development for Electron Beam Freeform Fabrication" (M.S. thesis Colorado School of Mines, 2010).

MICROSTRUCTURE EVOLUTION OF MARTENSITIC STAINLESS STEEL IN LASER HOT WIRE CLADDING WITH MULTIPLE HEATING PASSES

Shaopeng Wei[1], Gang Wang[1], Zhenguo Nie[1], Zilin Huang[2], Yiming Rong[1,3]

[1]Beijing Key Lab of Precision/Ultra-precision Manufacturing Equipments and Control, Tsinghua University, Beijing, 100084, China
[2]School of Mechanical, Electronic and Control of Engineering, Beijing Jiaotong University, Beijing, 100044, China
[3]Department of Mechanical Engineering, Worcester Polytechnic Institute, Worcester, 01609, USA

Keywords: Laser hot wire cladding, Wire transfer behavior, Microstructure characterization, Grain structure, Precipitation hardening.

Abstract

Laser cladding is one of attractive and cost effective means for repairing or remanufacturing high value engineering components. The microstructure and property in laser cladding process with multiple heating passes were investigated by using experimental method. Single-pass cladding experiments were conducted to investigate the wire transfer behavior and further optimize the laser hot wire cladding process. Multiple layers were cladded on the surface of martensite stainless steel by using fiber laser. The microstructure of clad layer and heat affected zone was characterized using an optical microscope, SEM and EDS. The orientation imaging microscopy of grain structure was obtained by the electron backscatter diffraction technique. The gradient microhardness from the clad layer to the substrate was tested. The uneven temperature distribution and high cooling rate led to the forming of gradient microstructure, and further affect the mechanical property of the remanufacturing parts.

Introduction

Martensitic precipitation hardening stainless steel has been widely used for producing load-bearing parts due to its comprehensive properties of high strength and toughness, as well as good corrosion resistance [1]. As a core component, the service life of the load-bearing part directly affects the overall performance of the equipment. Subjected to severe working conditions, such parts usually failed prematurely because of abrasion, erosion and fracture failure, accompanied with the material loss. From an economical point of view, repairing the damaged parts instead of producing new ones is the better choice [2]. Laser cladding is regarded as an appropriate technology for repairing such parts, due to its low heat input, which generates less distortion and minor damage to the substrate [3].

In the laser hot wire cladding process, the wire is preheated by the resistance heat before entering the molten pool. It shows that the deposition rate in laser hot wire cladding was four times higher than the laser powder cladding and laser cold wire cladding process [4]. Various studies have investigated the cladding process and its mechanism. Researchers focused on process optimization [2, 5], microstructural characterization and the evaluation of mechanical properties [6-7], and the interaction mechanism based on real-time monitor technique [8-10].

The essence of the laser cladding is the interaction among the laser, filler material and substrate material. The laser beam is the main heat source that will melt the filler and base metal creating the mixed metallurgy. The material experiences a rapid heating and cooling process under multiple laser heating (heating rate: 10^4 -10^9 K/s; cooling rate: 10^6 K/s). The material is repeatedly heated to a temperature beyond the phase transition temperature. The melting and solidification occurs in the fusion zone while the material in the heat affected zone experiences a non-equilibrium phase transformation.

In this paper, single-pass cladding experiments were carried out to optimize the laser cladding process. Then multiple layers were cladded on the surface of martensite stainless steel by using the optimum process parameters. The microstructure of as-cladded layer was characterized using the optical microscope and SEM. The orientation imaging microscopy of grain structure was obtained by the electron backscatter diffraction technique. The gradient microhardness from the cladding layer to the substrate was measured.

Experimental procedure

1. Material preparation

The substrate metal was martensite precipitation hardening stainless steel FV520B. It had been normalized by heating up to 1050℃, followed by solution treatment at 850℃, and finally ageing at 470℃. The original microstructure was composed of martensite laths and dispersed precipitation phases. FV520B steel plates of dimension 90×60×10 mm were prepared by electrical discharge machining. The working surface was cleaned with ethyl alcohol before cladding. The filler wire was FeCrNi steel with 1.2 mm diameter. The chemical compositions of FeCrNi wire and FV520B steel substrate are shown in Table 1.

Table.1 Chemical composition of FV520B steel substrate and FeCrNi wire (wt%)

	C	Cr	Ni	Mn	Si	Cu	Mo	P	S	Nb	Fe
FV520B	0.034	13.34	5.7	0.55	0.21	1.42	1.49	0.024	<0.025	0.25-0.45	Bal
FeCrNi	0.029	14.02	6.2	0.54	0.32	0.33	1.15	0.014	0.009	0.33	Bal

2. Experimental method

The experimental setup is shown in Fig.1. A 2KW IPG fiber laser with the wave length of 1.07 μm was applied for the cladding process. The associated components are: (1) CNC control system; (2) laser head; (3) wire feeder; (4) power source for wire preheating; (5) a chiller for cooling the laser head. Fig.1b shows the schematic of laser hot wire cladding. Two independent heat sources are used. The laser power is applied as the main heat source to melt the substrate while the filler wire is preheated by a Panasonic YC-400TX power source. During the cladding process, the wire is transported by the lateral feed torch and injected into the molten pool at an angle of 30° normal to the surface. Argon gas is used to protect the molten pool from oxidation.

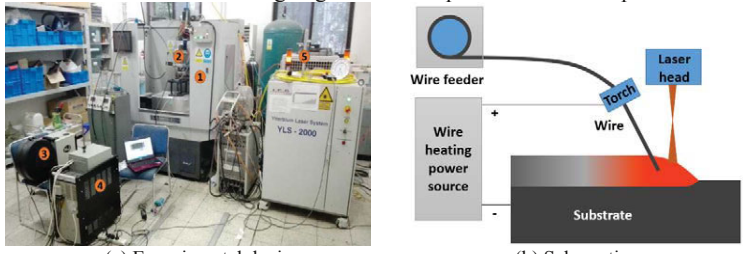

(a) Experimental device (b) Schematic

Fig. 1. Experimental setup of laser hot wire cladding process

Single-pass cladding experiments were carried out to optimize the cladding parameters until a good clad formation was achieved. The main optimized process parameters are listed in Table 2. A three layers cladding material was obtained by using the optimized parameters. The clad samples were characterized by analyzing the surface topography. Then the samples were cross-sectioned using electrical discharge machining. The cross section was polished and then etched with a solution mixture of 5ml hydrochloric acid, 1g picric acid and 100ml ethanol. The optical microscope and SEM were used to observe the microstructure. The orientation imaging microscopy was obtained by the electron backscatter diffraction system. The microhardness profile was measured by Vickers Hardness Tester under a load of 0.1kgf with an indentation time of 10s.

Table.2 Cladding process parameters

Parameter	Value	Unit
Laser power	1810	W
Scanning speed	0.5	m/min
Wire feed rate	1.5	m/min
Overlap ratio	33	%
Wire current	55	A
Shielding Gas	20	L/min

Results and discussion

1. Surface morphology and wire transfer behavior

Fig.2 shows the three typical surface morphology of single-pass clad formation under different wire heating currents. The wire behavior in laser hot wire cladding is divided into three typical transfer modes: fusing transfer, continuous transfer and scratch transfer. A good and stable clad formation was obtained when the wire melted continuously in the molten pool, as shown in Fig.2b. With the increase of heating current, the wire fused outside the molten pool, which resulted in a discontinuous clad formation, as shown in Fig.2a. When the heating current increased to 50A, the solid wire scratched in the molten pool with the moving of laser head. Fig.2c shows the surface scratch in the middle of the deposited metal.

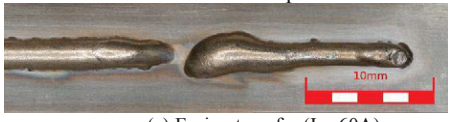

(a) Fusing transfer (I = 60A)

(b) Continuous transfer (I = 55A)

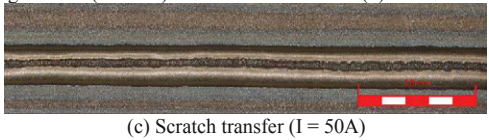

(c) Scratch transfer (I = 50A)

Fig. 2. Typical cladding formation under different wire transfer modes

The wire transfer behavior depends on the wire tip temperature when the wire arrived at the molten pool [8]. Fig.3 shows that schematic of wire transfer behavior in the laser hot wire cladding process. For the stable deposition process, the optimum temperature of the wire tip is within the semi-solid state. It means that the temperature of position A (T_A) should be lower than the solidus point while the temperature of position B (T_B) should be higher than the liquidus point of material. If T_A is beyond the liquidus point, the wire will be fused before arriving at the molten pool; if T_B is lower than the solidus point, the unfused wire will hit the base metal and destroy the cladding formation.

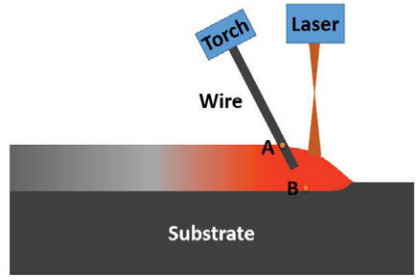

Fig. 3. Schematic of wire transfer behavior

It is necessary to develop a thorough understanding of the wire temperature field during the laser cladding process. The wire is preheated by the resistance heat, which can be described as follows:

$$\mathrm{dQ} = \varepsilon \cdot I^2 \cdot dR \cdot dt = c(T) \cdot dm \cdot dT,\ dm = \rho \cdot dl \cdot \pi r^2,\ dR = \rho_l \cdot \frac{dl}{\pi r^2} \tag{1}$$

$$\mathrm{dT} = \frac{\varepsilon \cdot I^2 \cdot \rho_l}{c(T) \cdot \pi^2 \cdot r^4 \cdot v \cdot \rho} \cdot dl \tag{2}$$

$$\mathrm{T} = T_0 + \int_0^L \frac{\varepsilon \cdot I^2 \cdot \rho_l}{c(T) \cdot \pi^2 \cdot d^4 \cdot v \cdot \rho} \cdot dl \tag{3}$$

where ε is the efficiency, I the heating current, $c(T)$ the heat capacity, ρ the mass density, r the wire radius, ρ_l the electrical resistivity, v the wire feed rate, L the heating length and T the temperature of wire tip. The wire temperature is mainly determined by wire feed rate, wire current and wire heating length.

A three layers cladding material was deposited on the substrate by the optimized process parameters. The dimensions of the cladding material is 80×50×4.5 mm. There are 22 passes in each layer. Fig.4 shows the surface morphology of the clad layer. A smooth and flat surface was obtained, and no defects were found on the surface.

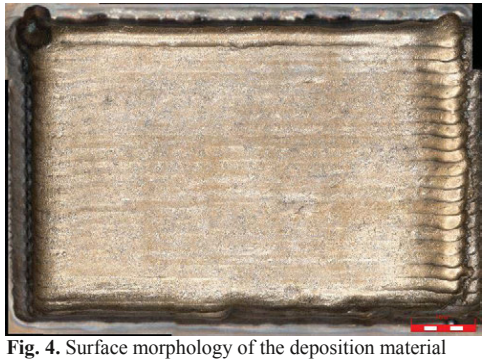

Fig. 4. Surface morphology of the deposition material

2. Microstructure of as-cladded layer

Fig.5 shows the optical micrograph of cross section of the clad layer. The microhardness indentations were marked by a red dash-dotted box. It shows a good metallurgical bonding in the interface. As shown in Fig.5a, the optical micrograph of the cross section was divided into three regions: cladding zone, heat affected zone and the substrate. The low heat input lead to the low dilution ratio. The microstructure in the heat affected zone was refined. Fig.5b shows the good

formation quality in the multi-pass clad material with three layers. The boundary between passes and layers can be distinguished clearly. No defects and cracks were found in the deposition layer.

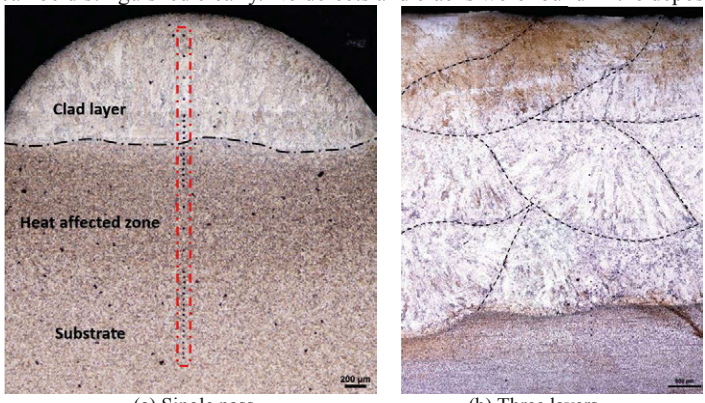

(a) Single pass (b) Three layers

Fig. 5. Microstructure of as-cladded layer

As shown in Fig.6, the microstructure of clad layer, heat affected zone and substrate were observed by scanning electron microscopy. Fig.6a shows a coarse as-cast dendritic microstructure in the cladding layer. It is a martensite microstructure due to the rapid cooling rate. Because of the good hardenability of FV520B steel, the microstructure of the heat affected zone and substrate was consisted of martensite laths. Fig.6c reveals a large number of precipitation particles (white dots) in the substrate. Compared with the substrate, the quantity of particles in the heat affected zone declines sharply, which may resulted from the dissolution of the precipitation particles. The precipitation particle located in position A was confirmed as NbC carbide by the EDS analysis, as shown in Fig.7.

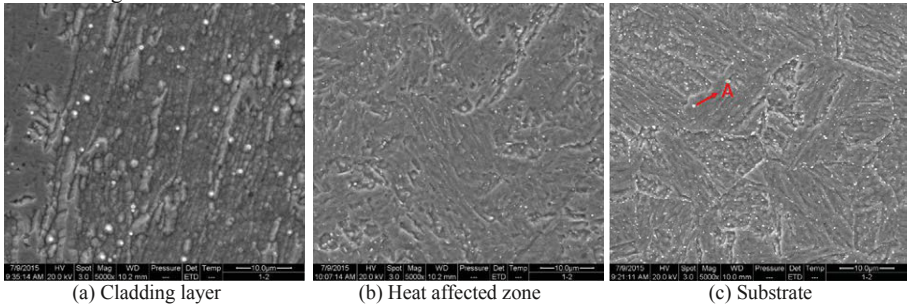

(a) Cladding layer (b) Heat affected zone (c) Substrate

Fig. 6. Microstructure of as-cladded layer

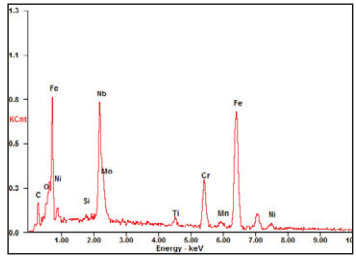

Fig. 7. EDS analysis of the precipitation particle

3. Grain structure

Fig.8 shows a typical cross-section orientation image of a single laser track. The grain growth of cladding material is controlled by the maximum temperature gradient. The grain grows rapidly towards the direction of material deposition, and the columnar crystal zone is formed. The grain located in the heat affected zone was refined. Due to the local high temperature, the heat affected zone experienced a recrystallization process. The rapid heating process increased the degree of superheat so that the nucleation increased. Also, the grain growth was restrained by the high cooling rate, which resulted in the fine microstructure in the heat affected zone.

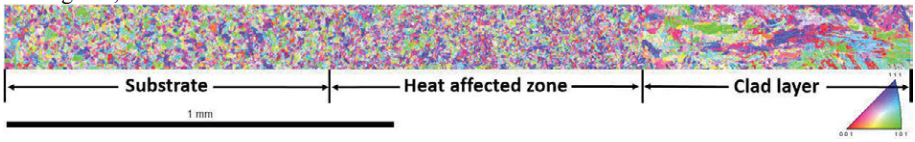

Fig. 8. Typical inverse pole figure of a transverse cut across a single laser track

The grain image of the heat affected zone and substrate were detected by the EBSD technique in Fig.9a and 9b. The size and shape of the grains could be statistically investigated due to the digital character of orientation imaging maps. The average grain size diameter calculated from the data in Fig.9b and 9c were respectively 4.35 μm and 9.77μm.

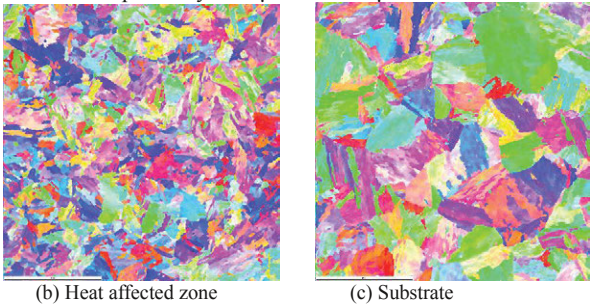

(b) Heat affected zone (c) Substrate

Fig. 9. Inverse pole figure of different areas

4. Microhardness

Fig.10 summarizes the vertical microhardness profile measured from the clad layer to the substrate. The distance between two adjacent positions ranges from 0.05mm to 0.2mm. High cooling rate lead to the formation of martensite, resulting in the great hardness. The gradient microstructure distribution has a great influence to the mechanical property. The boundary of different areas can be distinguished clearly from Fig.10. The hardness of the clad layer was

substantially lower than the hardness of the substrate. The coating-substrate interface was probably enhanced by the finer grains. Due to dissolution of the precipitation hardening phase, the microhardness decreases in the heat affected zone. With the distance increases, the hardness increases and gradually tends to be steady, which correspond respectively to the heat affect zone and substrate. Although the grains located in the heat affected zone were refined, the hardness is still lower than the substrate. It shows that the precipitation hardening plays the dominant role in the strengthening effect of the material.

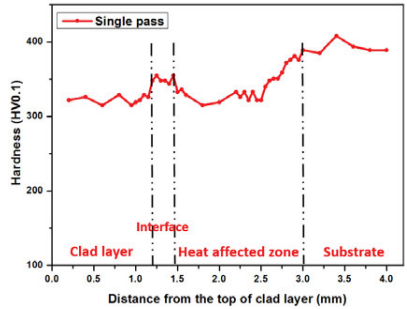

Fig. 10. The vertical microhardness profile

Conclusions

Single-pass cladding experiments were carried out to optimize the laser hot wire cladding process. A high quality cladding material of three layers was obtained by using the optimized process parameters. The microstructure and grain structure of the as-cladded layer were characterized. The gradient microhardness from the clad layer to the substrate was tested. The following conclusions can be drawn from the experimental results:

(1) The wire behavior can be described as three transfer modes: fusing transfer, continuous transfer and scratch transfer. The wire transfer behavior depends on the temperature when the wire arrived at the molten pool. A good and stable clad formation was obtained when the wire melted continuously into the molten pool.

(2) The microstructure of as-cladded layer was consisted of martensite laths. The heat affected zone experienced a recrystallization process, resulting in the refined grains and the dissolution of the precipitation phase. The precipitation phases were mainly NbC carbides. The average grain size diameter of the heat affected zone and substrate were respectively 4.35 μm and 9.77 μm.

(3) The hardness of the heat affected zone was lower than the substrate due to the dissolution of the precipitation phase. The precipitation hardening plays the dominant role in the strengthening effect of FV520B steel.

Acknowledgement

This work was financially supported by the National Basic Research Program of China (973 Program) (No. 2011CB013404). The authors are grateful to State Key Laboratory of Tribology and Dr. Peng Wen for facility support.

References

[1] Ping D H, Ohnuma M, Hirakawa Y, et al. Microstructural evolution in 13Cr–8Ni–2.5 Mo–2Al martensitic precipitation-hardened stainless steel[J]. Materials Science and Engineering: A, 2005,

394(1): 285-295.
[2] Wilson J M, Piya C, Shin Y C, et al. Remanufacturing of turbine blades by laser direct deposition with its energy and environmental impact analysis[J]. Journal of Cleaner Production, 2014, 80: 170-178.
[3] Wen P, Feng Z, Zheng S. Formation quality optimization of laser hot wire cladding for repairing martensite precipitation hardening stainless steel[J]. Optics & Laser Technology, 2015, 65: 180-188.
[4] Nurminen J, Riihimäki J, Näkki J, et al. Comparison of laser cladding with powder and hot and cold wire techniques[C]//ICALEO 2006, 25th International Congress on Applications of Lasers & Electro-optics, 30 October-2 November, 2006, Doubletree Paradise Valley Resort, Scottsdale, USA. 2006.
[5] Abioye T E, Folkes J, Clare A T. A parametric study of Inconel 625 wire laser deposition[J]. Journal of Materials Processing Technology, 2013, 213(12): 2145-2151.
[6] Wen P, Cai Z, Feng Z, et al. Microstructure and mechanical properties of hot wire laser clad layers for repairing precipitation hardening martensitic stainless steel[J]. Optics & Laser Technology, 2015, 75: 207-213.
[7] Fang C, Song Y, Wu W, et al. The laser welding with hot wire of 316LN thick plate applied on ITER correction coil case[J]. Journal of Fusion Energy, 2014, 33(6): 752-758.
[8] Zheng S Q, Wen P, Shan J G, et al. Numerical simulation of wire temperature field for prediction of wire transfer stability in laser hot wire welding[C]//ICALEO Congress Proceedings; 2013 Oct 6-10. Laser Institute of America Miami USA, 2013: 947-952.
[9] Liu S, Liu W, Harooni M, et al. Real-time monitoring of laser hot-wire cladding of Inconel 625[J]. Optics & Laser Technology, 2014, 62: 124-134.
[10] Tao W, Yang Z, Chen Y, et al. Double-sided fiber laser beam welding process of T-joints for aluminum aircraft fuselage panels: Filler wire melting behavior, process stability, and their effects on porosity defects[J]. Optics & Laser Technology, 2013, 52: 1-9.

EFFECT OF PRINTING ORIENTATION ON STRENGTH OF 3D PRINTED ABS PLASTICS

Linlin Cai[1], Philip Byrd[1], Hanyin Zhang[1], Kate Schlarman[2], Yi Zhang[1], Michael Golub[1], Jing Zhang[1]

[1]Department of Mechanical Engineering, Indiana University- Purdue University Indianapolis, Indianapolis, IN 46202
[2]Decatur County Community Schools, Greensburg, IN 47240

Keywords: 3D Printing, Additive Manufacturing, ABS, Mechanical Property

Abstract

The mechanical strengths of ABS (Acrylonitrile Butadiene Styrene) components fabricated by fused deposition modeling (FDM) technique have been studied, with the focus on the effect of printing orientations on the strength. Using the properties derived from stress-strain curves of the samples, the 0-degree printed sample has the strongest mechanical properties, which is likely due to preferred orientations in individual slice.

Introduction

Fused deposition modeling (FDM) is a type of three-dimensional (3D) printing that constructs physical models from computer aided design (CAD) data. Plastic filament is partially melted then systematically deposited to create one thin layer of the desired object. This process continues, one layer being printed on top of the previous, until the object is complete. The process starts when a 3D model is supplied to the printer's software. The software produces a plan for creating the object by slicing the model into thin horizontal sections. Each section is assigned a tool path that will guide the print head when creating that layer. The tool path consists of a perimeter and a fill. The perimeter, or outline of that slice, is created first. Next the inside is filled with long sweeps, or roads, going back and forth all of which are parallel to each other. The nozzle moves along its tool path and the newly extruded filament bonds with the previously laid down strips. The tool path for each layer is not identical. The parallel long sweeps that make up the fill are rotated slightly with each new layer. Research has been done to study the effects of altering process parameters on the physical properties of the printed object, and process parameters effect on dimensional accuracy and surface finish (Kumar, Ahuja, & Singh, 2012), and improving the compressive strength (Sood, Ohdar, & Mahapatra, 2012). In this study, the research is focused on the effect of printing orientation on the tensile strength of 3D printed specimens.

Methodology

The specimens used in this study are designed in accordance with the ASTM standard test method for tensile properties of plastics. The printer used is a Dimension SST 3D printer in conjunction with CatalystEx software, both products of Stratasys Inc. The 3D printed specimen material used is ABS, also a product of Stratasys Inc.

The tensile testing is done using a MTS Systems universal testing machine according to ASTM standards for tensile properties of plastics. The model number of extensometer used in the test is 634.12E-54.

Before the tensile tests, the width and thickness of the center section of each of the specimens are measured then entered into the testing program. As shown in Figure 1, the tensile specimen is loaded into the testing machine by attaching the clamps to both ends and the distance between the clamps is measured and entered into the program. Next the extensometer is attached to the center of the specimen. The extensometer will precisely measure the length of that section of the specimen as the tensile testing machine is pulling. The tensile strain rate applied is 0.2 in/min (0.0847 mm/s). The program will use the measurements to calculate strain (relative change in length) and stress (force over area). The program then compiles the raw data from the two components. Exporting the data in a .txt format allows us to view the data in Microsoft Excel.

Figure 1: Tensile specimen tested in the MTS testing machine

Specimens were printed at three orientations: 0, 45, and 90° (Figure 2). Printing orientation refers to where in the virtual x, y, z coordinate system of the 3D printer's software the model is placed (Stratasys, 2015a). When an STL file is opened it is placed in a default position.

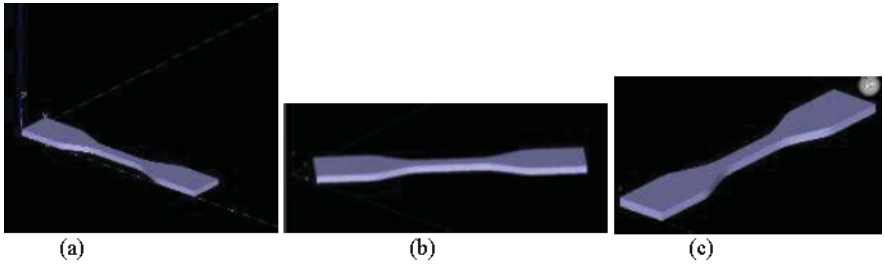

Figure 2: Printing orientations of the tensile specimens (a) 0°, (b) 45°, and (c) 90°

The 3D printer's software allows manipulation of that position by rotating the model around the x, y or z axis. The specimens were created with their broad side flush with the x-y plane at 45° increments around the z axis starting with the default position (Figure 3).

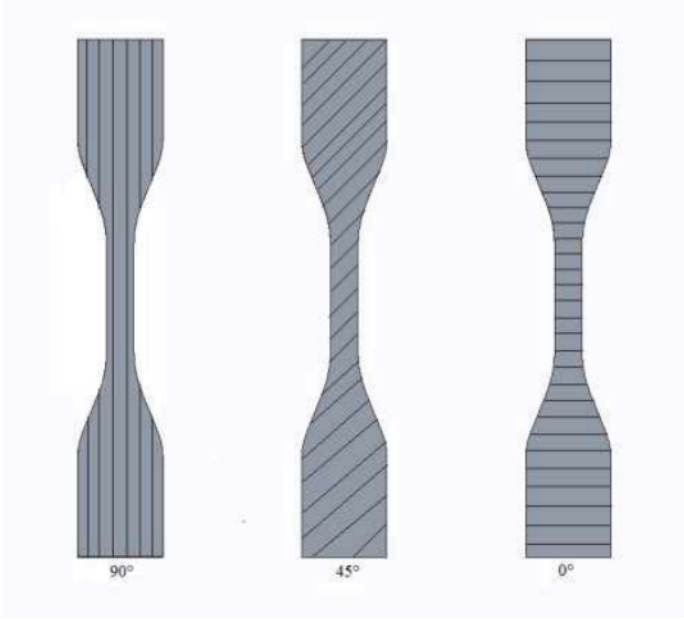

Figure 3: Illustration of fiber printed orientation in each slice

Results and discussion

As an example, figure 4 shows the 0° tensile bar sample before and after the tensile test. The broken point deviates from the middle of the bar a little bit but they still in the extended part of the bar, which verifies the correctness of the testing method.

(a) (b)

Figure 4: Optical images of the 0° tensile bar (a) before and (b) after the tensile test

The detailed cross sectional view of the fracture surface is given in Figure 5. The smeared surface suggests a ductile fracture. The 10 slices are visible from the left side of the fracture surface. Among these 10 slices, their orientations vary, resulting different facture patterns. The orientation of each slice is increased with a finite angle, so the fibers partially overlap each other in order to achieve maximum contact surface strengths.

Figure 5: Optical image of cross-section area of the 0° tensile bar fracture surface

The stress-strain curves of tensile bars in different printing orientations are plotted in Figure 6. It is suggested that the 0 degree orientation, which has the highest peak load and shortest

elongation, is the strongest one, followed by the 45 degree, and 90 degree orientations respectively. As shown in Table 1, the Young's moduli for the 0 degree, 45 degree, and 90 degree orientations respectively are 1.81 GPa, 1.80 GPa, and 1.78 GPa, respectively.

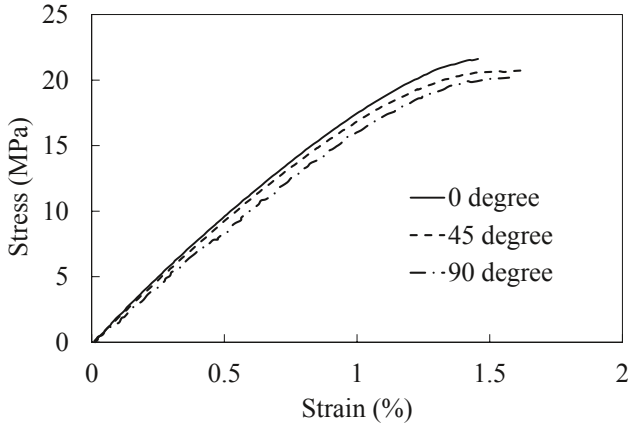

Figure 6. Stress-strain curve of ABS tensile bars in different printing orientations

Table 1: Averaged mechanical strength as a function of printing orientation

Printing orientation	0°	45°	90°
Young's modulus(GPa)	1.81+/-0.10	1.80+/-0.11	1.78+/-0.13
Ultimate strength (MPa)	22.4+/- 0.1	20.7+/-0.1	19.0+/- 0.2

The reason why the 0° orientation has the highest mechanical properties is that its printing orientation makes the original filament in the individual slice align with the loading force direction. This determines connected point between filaments by fused deposition modeling, to which attention should be paid when designing and application of various printed components.

Summary

In summary, the 0 degree orientation as it was defined has the highest mechanical properties, as shown with largest Young's modulus and ultimate strength. This result provides information about selecting printing direction during fused deposition modeling for ABS and its characteristic for application. To further understand the mechanics of fused deposition modeling, a detailed analysis of individual slice orientation and their characteristics is needed.

Acknowledgements

Linlin Cai and Philip Byrd thank the support provided by the CTEE (Commitment to Engineering Excellence Research Fund) research program and MURI (Multidisciplinary Undergraduate Research Institute) program at Indiana University- Purdue University Indianapolis. Kate Schlarman is supported by NSF (award number: EEC 1406995).

References

Kumar, P., et al. (2012). "Application of fusion deposition modelling for rapid investment casting–a review." International Journal of Materials Engineering Innovation 3(3-4): 204-227.

MTS (2015). "mts.com." from http://www.mts.com/en/products/producttype/test-components/grips-fixtures-accessories/extensometers/index.htm.

MTS (2015). "mts.com." from http://www.mts.com/en/products/producttype/test-systems/load-frames-uniaxial/servohydraulic/standard/index.htm.

Sood, A. K., et al. (2012). "Experimental investigation and empirical modelling of FDM process for compressive strength improvement." Journal of Advanced Research 3(1): 81-90.

Standard, A. (2003). "Standard test method for tensile properties of plastics." ASTM International. Designation: D 638.

Stratasys (2015). CatalystEx, Stratasys.

Stratasys (2015). "stratasys.com." from http://www.stratasys.com/.

VERIFICATION OF NUMERICALLY CALCULATED COOLING RATES OF POWDER BED ADDITIVE MANUFACTURING

H.-W. Mindt[1], M. Megahed[1], N.P. Lavery[2], A. Giordimaina[2], S.G.R. Brown[2]

[1]ESI Group, Kruppstr. 90, 45145 Essen, Germany
[2]Swansea University, Bay Campus, College of Engineering, Fabian Way, Crymlyn Burrows, Swansea, SA1 8EN United Kingdom

Keywords: Additive Manufacturing, Powder Bed, Direct Metal Laser Melting, Modelling, Verification

Abstract

In order to increase the powder bed production rates, the laser power and diameter are increased enabling faster scanning, thicker powder layers and wider hatches. These parameters however interact in a very complex manner: For example increasing the laser power may lead to significant evaporation of the molten metal. Increasing the scan speed may lead to reduced melting and lack of fusion of the powder particles. Combining higher scanning speeds with increased layer thickness enhances lack of fusion even more. Larger beam diameters reduce the energy density and hence impose limitations to scan speeds. Physics based modelling has the potential to shed light into how these competing phenomena interact and can accelerate fine tuning build parameters to achieve design goals. Models resolving the heat source powder interaction and describing the melt pool and solidification processes could not be formally validated using experimental data due to the extreme severity of the processing environment. In an effort to verify models describing melt pool behavior the results of two different algorithms are compared: Lattice Boltzmann and Finite Volume Computational Fluid Dynamics. Both codes were developed separately by two different and independent teams. A reference benchmark is defined with corresponding operation conditions. The physical assumptions are aligned as far as possible. The melt pool characteristics and the thermal cycles are compared.

Introduction

Multiple parameters affect powder bed additive manufacturing processes. Once a set of parameters is found for a certain powder, it is not guaranteed that they will perform in the same manner when a new powder batch is processed. There is therefore a need to better understand and quantify the influence of process inputs on final product quality. Physics based models have the potential to provide the required insight. Powder bed modelling is subdivided into two categories: In the first the powder layer is replaced by a material with equivalent properties mimicking powder behavior [1, 2, 3, 4]. N'Dri et al. performed an uncertainty quantification study to determine the influence of equivalent properties variations on the final results. They concluded that in spite of the numerical efficiency of such models, they are sensitive to the properties specified [5]. The second category of micro-models is based on resolving the powder particles eliminating the need for correlations describing the powder behavior [6, 7, 5, 8]. A preliminary validation effort was performed by comparing the measured track widths with those predicted numerically [5] and by comparing the level of porosity obtained for different conditions [9]. In an attempt to approach further code verification the authors purse the specification of a reference benchmark for DMLM/SLM.

Modelling Algorithms

Micro-models are pursued to resolve the melt pool physics including laser radiative interaction with the powder, heat transfer, phase change and surface tension forces and Marangoni forces. They are based on computational fluid dynamics algorithms to solve the Navier-Stokes equations [10, 11, 12, 13]. The momentum equations are extended using source terms to account for gravitational forces, recoil pressure and surface tension. The energy equation is complemented with source terms accounting for latent heat of fusion and evaporation as well as radiation. The laser is modelled as a Gaussian heat source. Two codes are used to solve the conservation equations, one based on the Finite Volume [14, 15, 16] and the other on Lattice Boltzmann [17, 18]: The Finite Volume code utilized is CFD-ACE+, ESI Group [20], which has been recently extended towards modelling additive manufacturing processes including blown powder [19] and powder bed processes [5, 9]. The Lattice Boltzmann method (LBM) simulates flow using imaginary particles which undergo propagation and collision events in a discrete lattice mesh rather than the conventional approach of solving conservation equations for macroscopic quantities such as mass, energy and momentum [21]. In this paper a 3-dimensional D3Q19 LBM model (based on the 2-dimensional numerical formulation of Attar [22]) is used. The model distinguishes between obstacles, solid, molten metal (surface or interior) and gas regions and uses a VOF algorithm to deal with convection of fluid. A Gaussian distributed laser heat source is included but heat radiation and gas flow are not. The LBM simulations are carried out on a 46×67×67 mesh with constant thermo-physical properties.

Experimental Comparisons

In order to enable a direct comparison of numerical results obtained via different codes, a set of operation conditions are extracted from experiments. A series of three experiments were done on a Renishaw AM250 to isolate and examine the melting tracks, as given in Table 1. For all the experiments a laser focus diameter of 70µm was used. Two powder metals both from LPW technologies were used for these experiments, a 316L steel and Ti-6Al-4V, both gas atomized under argon, with powder size distributions as shown in Figure 1 (a).

Experiment	Material	PD (µm)	HS (µm)	ET (µs)	Power (W)
(E1) Single layer onto base plate	316L	65	124	75, 150	100, 150, 200
(E2) Multilayer onto base plate	316L	65	124	75, 150	100, 150, 200
(E3) Single line onto powder	Ti-6Al-4V	75	N/A	138	200

Table 1: Experiments undertaken to isolate the melt pool

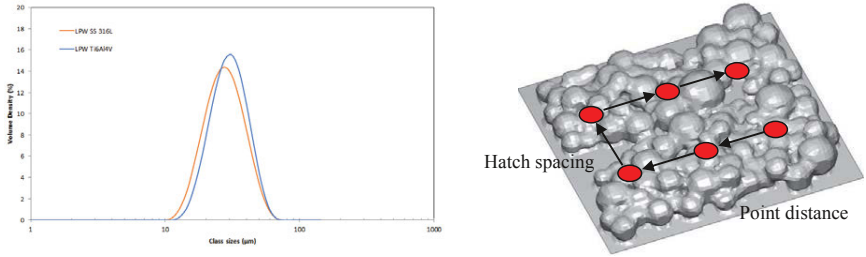

Figure 1: (a) LPW 316L and Ti-6Al-4V powder size distributions and (b) the meandre laser track build strategy

Experiment 1 (Single layer 316L)

In experiment (E1) a single layer of 316L was melted onto the base plate in a meander pattern using the point distance (PD=65 µm) and hatch spacing (HS= 124 µm). Various exposure times and laser powers were used, and micrographs were taken from the top and at cross-sections through the laser tracks (Figure 2) for a laser power of 200W and an exposure time of 150 µs. The measurements of the 316L melt bead onto the base plate give typical widths of about 100µm (30 µm wider than the laser beam) and heights of about 40-50µm. There is typically a shallow (elliptical shaped) heat affected zone below the bead into the base plate (Figure 2 (b)). The bead cross section is etched and there is a clear difference between the larger grain structures in the underlying base plate, also made from 316L steel and there is evidence of pitting in the heat affected zone below the bead. The gap between beads is less than or equal to 24µm, with in many cases the gap between alternative paths being closed in a weaving pattern.

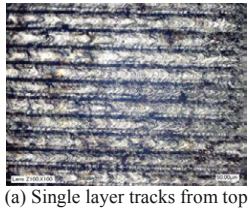

(a) Single layer tracks from top

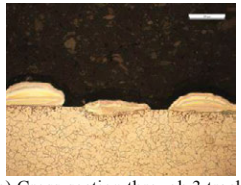

(b) Cross-section through 3 tracks

Figure 2: Results from single layer experiment (E1)

Experiment 2 (Multi-layer 316L)

The second experiment also used LPW 316L powder, and kept the same point distance and hatch spacing used in the first experiment. The laser power and exposure times were varied as given in Table 1. Multiple layers were built up on the base plate using 2, 4, 6, 8, 12, 24 and 36 layers. Some micrographs of this experiment with a power of 150W and exposure time of 150 µs are shown in Figure 3. It should be noted that at each subsequent layer the same hatch pattern is used, but is rotated randomly through 67°. Comparing results from the single layer experiment (Figure 2 a) with the double layer experiment (Figure 3 a & c) shows that the relatively small gaps between laser lines have now been filled with the second layer melt and the melt pool cross-section appears less domed. The re-melted/heat affected zone appears to be deeper, but still retaining a wide semi-elliptical form. This filling is continued in subsequent layer (24 and 36 layers are shown in Figure 3 b &d).

Experiment 3 (Single line Ti-6Al-4V)

The third experiment consisted in running the laser along a line directly onto various depths of Ti-6Al-4V powder using a laser power of 200W, an exposure time of 138µs and a point distance of 75µm (hatch spacing does not apply here as the laser was run in a single line, but a typical value used for Ti-6Al-4V is of 150µm). As can be seen from the results in Figure 4, as the powder depth is increased, the melt track becomes unstable and this is thought to be due to Rayleigh-Plateau instabilities. Measurements would indicate a laser track width of about 82µm which is only marginally higher than the laser diameter, however, it should be pointed out that this was done directly onto the powder, with less heat transmitted vertically it would be expected that the bead would have a higher dome than if melted onto the base plate, where it would run off closing the gaps between tracks slightly more. In normal builds using the same laser settings,

relative densities have been measured in the 97-99% range with low porosity identified by micrographs. This would suggest that the re-melting during a multi-layer deposition works in much the same way as seen in experiment 2, and any holes in the underlying layer are filled by subsequent melt liquid and smoothed by re-melting.

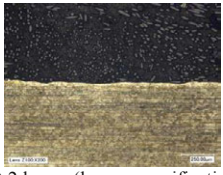

(a) 2 layers (lower magnification)

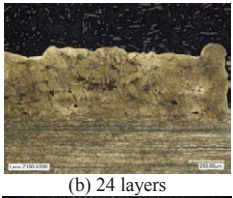

(b) 24 layers

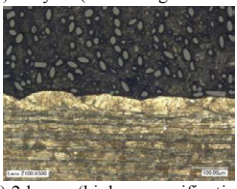

(c) 2 layers (higher magnification)

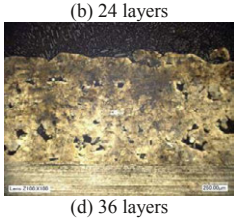

(d) 36 layers

Figure 3: Results from the multilayer experiment (E2)

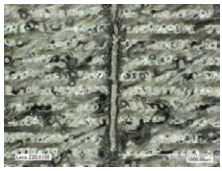

(a) Single line onto 50 µm of powder depth

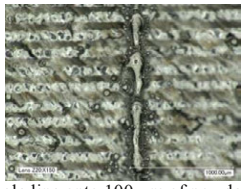

(b) Single line onto 100 µm of powder depth

Figure 4: Results from single line experiment (E3)

Numerical Simulations

The coating process of a Renishaw AM250 was modelled to obtain a numerical representation of the powder bed. The power layer thickness is 50 µm; the horizontal powder bed dimensions are 360 x 360 µm^2 (Figure 1 b). Material properties, operating conditions and probe co-ordinates are listed in Table 2.

	Ti-6Al-4V		
Property	**Solid**	**Liquid**	**Reference**
Density (kg/m3)	4200	3900	[23, 24, 25]
Viscosity (mPa s)	-	3.8	[23]
Specific heat (J/kg K)	0.65	0.83	[23, 24]
Thermal conductivity (W/m K)	18	34.5	[23, 24, 26]
Solidus (K)	1868.15		[23]
Liquidus (K)	1923.15		[23]
Latent heat of fusion (J/kg)	286000		[23]
Surface tension (N m)	-	1.3	[25]
Wetting angle (deg)	-	30	[24]
Emissivity	0.6	0.4	[24]
Absorption	0.6	0.4	[24]

	Ti-6Al-4V
Laser power (W)	200
Laser diameter on processed surface (□m)	70
Power distribution	Gaussian
Exposure time (□s)	125
Jump time (□s)	Instantaneous, max. 6
Point distance (□m)	75
Hatch spacing (□m)	150
Preheat temperature (K)	413

Point	X [m]	Y [m]	Z [m]
Melt pool surface	0.00215	+5.0e-5	0.000417
Melt pool center	0.00215	0	0.000417
Deep in melt pool	0.00215	-5.0e-5	0.000417

Table 2: Ti-6Al-4V Properties Operation Condition and Probe co-ordinates used for benchmark

Results & Discussion

Results presented here are those obtained for Ti-Al6-V4. Figure 1(b) shows the reference powder bed utilized for all calculations and the corresponding laser track. The particles representation is shown as resolved by the computational model. This particular specimen of the powder bed was chosen because it offers an interesting combination of smaller particles packed densely close to one another as well as some large particles that were pushed ahead of the coater causing some areas to be free of powder. Figure 5 shows a comparison of the melt pool shape as predicted by both codes. The colors show the temperature distribution. The finite volume results are shown using a temperature legend range covering all obtained values with a peak temperature is 3200 K - around the boiling temperature. The LBM results are shown using a legend that was limited at 2200 K just above the liquidus temperature. The unique processing strategy used in this machine leads to separate melt pools, each growing during the exposure time until it joins the melt pool created before. The chosen process parameters including the chosen point distance and hatch spacing lead to good joining of the deposited material as can be seen in Figure 6.

The Finite Volume and LBM predictions of the overall process behavior are very similar. In regions where the powder particles are densely packed continuous melt pools are created, the sizes predicted by both codes are very similar. Both codes show a large depression of the melt pool in the region denuded of particles on the left of the studied specimen. As the laser travels further to the right, surface tension retains the melt from filling into the depression as can be seen in the last snap shots of Figure 5. The difference in point distance and hatch spacing settings cause a difference in the joining characteristics of melt pools arranged along a line or adjacent to one another (Figure 6). The difference in joint depths correlates well with the experimentally observed weaving of the deposited beads (Figure 2 and Figure 6). Figure 7 shows the normalized thermal history at the point coordinates provided in Table 2. The probes are placed at different depths at the second exposure point. The temperature of the probes increases during the first exposure by conduction. Once the laser arrives to the second exposure point the temperature increases instantly well above the liquidus temperature. The increase rate is reduced temporarily when melting starts and then continues to a peak of about 2600 K when the laser is switched off and translated to the next exposure point. The different probes show the same heating behavior; the upper most point (closest to melt pool surface) is the quickest in response to laser changes and the point deepest in the build is the slowest. Once the laser moves away from the second exposure point the surface shows slower cooling than points further below (closer to thermal sink below the powder bed).

Summary & Conclusions

A benchmark for verification of micro models was designed based on the functionality of a commercial DMLM machine. The models do not include any machine specific details that would limit their use to model other machines, powders or materials. The result show good correlation with micrographs showing a weaving structure as the laser moves along lines and hatches with different point distances and hatch spacing.

Due to the lack of quantitative measurements validation of numerical algorithms is pursued by comparing two codes that were developed separately at ESI Group and University of Swansea. The qualitative results are comparable showing similar melt pools sizes and capturing solidified surface irregularities. The cooling rate is in the order of 1e6 $^{K}/_{s}$.

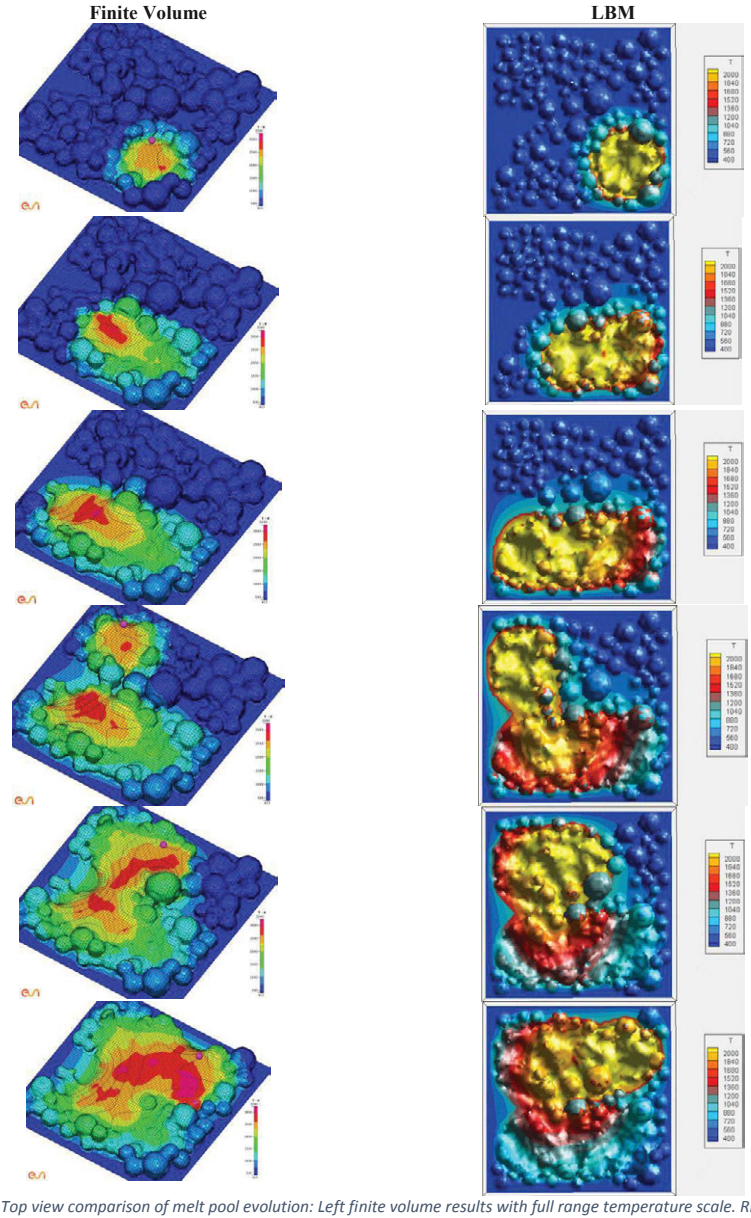

Figure 5: Top view comparison of melt pool evolution: Left finite volume results with full range temperature scale. Right LBM results with limited legend range showing more details of the particle melting

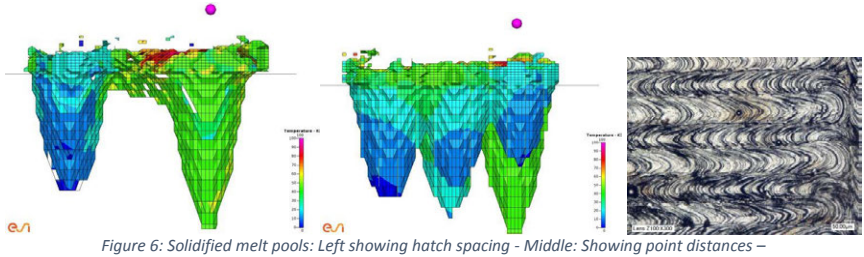

Figure 6: Solidified melt pools: Left showing hatch spacing - Middle: Showing point distances – Right: Micrograph showing top view of melt pools and corresponding weaving structure

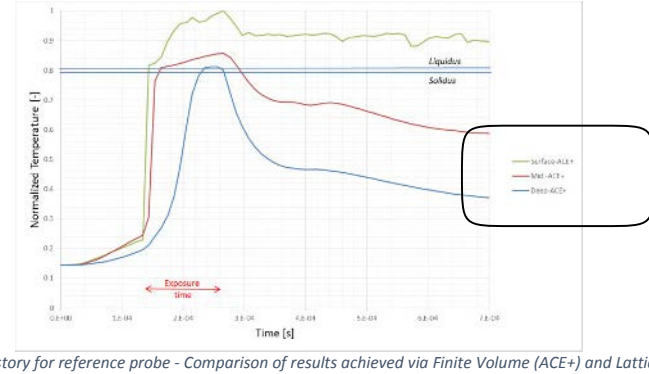

Figure 7: Thermal history for reference probe - Comparison of results achieved via Finite Volume (ACE+) and Lattice Boltzmann codes

Acknowledgement

The authors acknowledge the financial support of the European Commission 7th Framework Program AMAZE. The authors would like to also thank project partners and collaborators for the ongoing discussions, support and motivation. The authors would also like to thank the Welsh Government for the funds which made the MACH1 centre possible and where thermo-physical property measurements and validation was performed.

References

1. *Measurement and Prediction of the Thermal Conductivity of Powders at High Temperature.* S.S. Sih, J.W. Barlow, D.L. Bourell, R. Crowford. 1994. 5th Annual SFF Symposium Austin: The University of Texas, p.321-329.
2. *Sintering of Commercially Pure Titanium Powder with a Nd:YAG Laser Source.* P. Fischer, V. Romano, H.P. Weber, N.P. Karapatis, E. Boillat, R. Glardon. 2003, Acta Materialia, Vols. 51: pp. 1651-1662.
3. *Thermal and Mechanical Finite Element Modeling of Laser Forming from Metal and Ceramic Powders.* K. Dai, L. Shaw. [ed.] Elsevier Ltd. 2004, Acta Materialia, Vols. 52: 69-80.
4. *A Three Dimensional Finite Element Analysis of the Temperature Field During Laser Melting of Metal Powders in Additive Layer Manufacturing.* I.A. Robert, C.J. Wang, R. Esterlein, M. Stanford, D.J. Mynors. s.l. : Elsevier Ltd., 2009, International Journal f Machine Tools & Manufacture, Vols. 49: pp. 916-923.

5. *DMLS Process Modelling & Validation.* N. N'Dri, H.-W. Mindt, B. Shula, M. Megahed, A. Peralta, P. Kantzos, J. Neumann. Orlando : Wiley, TMS 2015 144th Annual Meeting & Exhibition, 2015. 978-1-119-08241-5.
6. *Mesoscopic Simulation of Selective Beam Melting Processes.* C. Körner, E. Attar, P. Heinl. s.l. : Elsevier B.V., 2011, Journal of Materials Processing Technology, Vols. 211: pp. 978-987.
7. W. King, A. Anderson, R. Ferencz, N. Hodge, C. Kamath and S. Khairallah. *Additive Manufacturing Challenges and Opportunities: 3D Modeling and Simulation.* s.l. : Lawrence Livermore National Laboratory, 2013.
8. *On the Role of Melt Flow into the Surface Structure and Porosity Development during Selective Laser Melting.* C. Qiu, C. Panwisawas,M. Ward, H.C. Basoalto, J.W. Brooks and M.M. Attallah. s.l. : Elsevier Ltd., 2015, Acta Materialia, Vol. 96, pp. 72-79.
9. *DMLM Models - Numerical Assessment of Porosity.* H.-W. Mindt, M. Megahed, A.D. Peralta, J. Neumann. Phoenix, AZ., USA. : s.n., 2015. 22nd ISABE Conference, Oct. 25-30.
10. R.B. Bird, W.E. Stewart, E.N. Lightfoot. *Transport Phenomena.* s.l. : John Wiley & Sons, 1960.
11. R. Ansorge, T. Sonar. *Mathematical Models of Fluid Mechanics.* s.l. : Wiley-VCH Verlag GmbH & Co KGaA, 1998. 978-3-527-40774-3.
12. P.W. Fuerschbach, J.T. Norris, X. He, T. DebRoy. *Understanding Metal Vaporization from Laser Welding.* s.l. : Sandia National Laboratories, 2003. SAND2003-3490.
13. Bäuerle, D. *Laser Processing and Chemistry.* s.l. : Springer Verlag, 2011. 978-3-642-17612-8.
14. Patankar, S.V. *Numerical Heat Transfer and Fluid Flow.* New York : McGraw-Hill, 1980.
15. J.H. Ferziger, M. Peric. *Numerische Strömungsmechanik* . s.l. : Springer-Verlag, 2008. 978-3-540-67586-0.
16. *Comparison of Finite-Volume Numerical Methods with Staggered and Collocated Grids.* M. Peric, R. Kessler, G. Scheuerer. 1988, Computers and Fluids, Vols. 16 (4): 389-403.
17. *A priori Derivation of the Lattice Boltzmann Equation.* He, X. and Luo, L.S. s.l. : Physical Review E, 1997. Vols. 55, No. 6: R6333-6336.
18. *Lattice Boltzmann Method for Fluid Flows.* S. Chen, D.G. Doolen. s.l. : Annu. Rev.: Fluid Mech., 1998. Vols. 30:329-364.
19. *A Coupled Approach to Weld Pool, Phase and Residual Stress Modelling of Laser Direct Metal Deposition (LDMD) Processes.* M. Vogel, M. Khan, J. Ibarra-Medina, A.J. Pinkerton, N. N'Dri and M. Megahed. Salt Lake City : s.n., 2013. 978-1-11876-689-7.
20. ESI Group. *CFD-ACE+ Theory & User Manuals.* 2014.
21. Succi, S. *The Lattice Boltzmann Equation for Fluid Dynamics and Beyond.* Oxford : Clarendon Press, 2001.
22. E. Attar. *Simulation der selektiven Elektronenstrahlschmelzprozesse.* Erlangen : Ph.D. Thesis, 2011.
23. Mills, K. C. Recommended values of thermophysical properties for selected commercial alloys. s.l. : Woodhead Publishing Limited, 2002.
24. Arce, Alderson Neira. Thermal Modeling and Simulation of Electron Beam Melting for Rapid Prototyping of Ti6Al4V Alloys. s.l. : North Carolina State University, 2012. Vol. PhD Thesis.
25. Thermophysical properties of liquid AlTi-based alloys. Egry, I., et al., et al. 4-5, s.l. : International Journal of Thermophysics, 2010, International Journal of Thermophysics, Vol. 31, pp. 949-965.
26. In-house measurements of Ti-Al6-V4 properties. MACH1. 2015.
27. Volume of Fluid (VOF) Method for the Dynamics of Free Boundaries. C.W. Hirt, B.D. Nichols. 1981, Journal of Computational Physics, Vols. 39, pp. 201-225.
28. The ThermoLab Project: Thermophysical Property Measurements in Space for Industrial High Temperature Alloys. Fecht, H.J. and Wunderlich, R. 4, 2005, J. Jpn. Soc . Microgravity Appl., Vol. 27, pp. 190-198.

TMS2016

145th Annual Meeting & Exhibition

SUPPLEMENTAL PROCEEDINGS

Advanced Materials in Dental and Orthopedic Applications

BETA-TYPE TITANIUM ALLOYS FOR USE AS RODS IN SPINAL FIXATION DEVICES

Mitsuo Niinomi[1], Masaaki Nakai[1], Huihong Liu[1] and Kengo Narita[2]

[1]Institute for Materials Research, Tohoku University, 2-1-1, Katahira, Aoba-ku, Sendai 980-8577, Japan
[2]Maruem Works Co., Ltd., 4-7-12, Nozaki, Daitou, Osaka 574-0015, Japan

Keywords: Beta-type titanium alloys, Ti-12Cr, Spinal fixation devices, Fatigue strength

Abstract

Ti-12Cr has been developed for use in various biomedical applications, in particular; it is expected to be used for the rods of the spinal fixation devices. When Ti-12Cr is deformed, its Young's modulus increases because of deformation-induced ω phase transformation. If a spinal rod made of Ti-12Cr is bent during operation, only the Young's modulus of the bent region will increase; this phenomenon decreases the springback of the rod so that the bent shape is maintained. The compression fatigue strength of Ti-12Cr obtained from compression fatigue tests performed according to ASTM F1717 can be significantly improved by cavitation peening. Details of the development of this Ti-Cr alloy for use as spinal rods are discussed.

Introduction

A substantial number of titanium (Ti) alloys with low Young's moduli have been developed for use as orthopedic implants because low Young's modulus is necessary to inhibit stress shielding between the implant and the surrounding bone, thereby inhibiting bone resorption [1]. However, during the course of surgery, rods, which are components of spinal fixation devices, are bent according to the shape of the spine in the body space, and their bent shape should be maintained. A high Young's modulus is advantageous for retaining the bent shape because it suppresses springback. Unfortunately, to date, none of the titanium alloys that have been developed for use in biomedical applications has met the requirements of both surgeons and patients when used for spinal fixation. The metallic rods used in spinal fixation devices are required to have a low Young's modulus, good biocompatibility and low springback. Accordingly, it is necessary to develop novel Ti alloys with good biocompatibility and an adjustable Young's modulus. To obtain these features, it should be possible to increase the local Young's modulus in certain parts of a device through deformation, while allowing the low Young's modulus of the rest of the device to remain unchanged [2].

Metastable β-type Ti alloys (hereafter referred to as β-type Ti alloys) have a low Young's modulus [3] in addition to good mechanical properties and excellent corrosion resistance. Furthermore, deformation-induced transformation, which can change the Young's modulus, can occur in β-type titanium alloys. Additionally, the ω phase, which can be introduced in β−type Ti alloys by deformation-induced transformation, has a significant effect on the mechanical

properties of the material [4]. However, deformation-induced phase transformation is dependent on the type of alloy and the stability of the β phase. Hanada et al. reported the formation of the ω phase during cold working of as-quenched Ti–Cr alloys containing 8–11.5 mass% Cr [5].

Recently, new Ti alloys with changeable Young's moduli have been developed by optimizing the Cr content of binary Ti-Cr alloys to allow deformation-induced ω phase transformation, and the Young's moduli and tensile properties of the developed alloys were systematically examined [6]. Furthermore, the springback and cytotoxicity of the optimized alloys were also investigated to determine their potential for use in spinal fixation applications [6]. The compressive fatigue strength of rods used in spinal fixation devices must be evaluated according to ASTM F1717 [7] to clear the materials for clinical study; therefore, the compressive fatigue strength of these Ti-Cr alloys has been reported. In addition, the compressive fatigue strength of Ti-Cr alloys has been shown to be improved by surface treatment,

In this paper, the above mentioned studies of Ti-Cr alloys developed for the use as rods in spinal fixation devices will be discussed.

Ti-Cr alloys with changeable Young's moduli

Ti-12Cr was the first titanium alloy with a changeable Young's modulus developed for use as rods in spinal fixation devices. To determine the optimal Cr content, Ti-Cr alloys were fabricated with Cr content ranging from 11 to 14 mass%. Then, Ti-(11-14)Cr composed of the metastable single β phase was subjected to solution treatment (ST) and cold rolled by a reduction ratio of 10 % (CR), which simulated the bending deformation of a spinal fixation rod. Figure 1 [6] shows the relationship between the Young's modulus and the Cr content in the Ti-Cr alloys before and after deformation through CR. The Young's modulus value of the Ti-Cr alloys before deformation is the lowest at a Cr content of 12 mass%. However, the Young's modulus of the Ti-Cr alloys after deformation decrease with increasing Cr content. Ultimately, Ti-12Cr exhibits the largest increase in Young's modulus by deformation. Ti-12Cr exhibits a low Young's modulus of approximately 68 GPa before deformation (i.e., under ST conditions) and a high Young's modulus of approximately 85 GPa after deformation (i.e., under CR conditions).

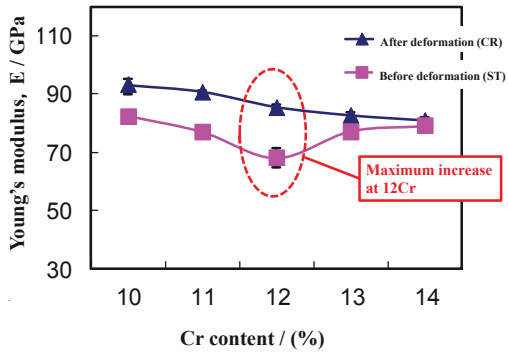

Figure 1. Relationship between Young's modulus and Cr content in Ti-Cr alloy subjected to solution treatment (before deformation (ST)) and after deformation through CR by a reduction of 10 % (after deformation (CR).

Figure 2 [6] shows the transmission electron microscopy (TEM) diffraction patterns of Ti-12Cr before and after deformation. Circular streaks related to an athermal ω phase are present in the diffraction pattern of Ti-12Cr before deformation (i.e., after ST). The amount of the athermal ω phase decreases because of an increase in β stability, that is, an increase in the Cr content. After deformation,

deflection from the ω phase is strengthened. Therefore, the deformation- induced ω phase is clearly observed in Ti-12Cr after deformation.

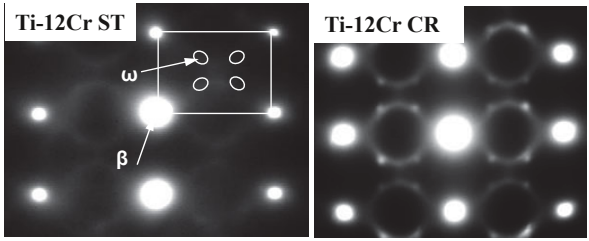

(a) Before deformation **(b) After deformation**

Figure 2. TEM diffraction patterns of Ti-12Cr (a) before deformation (Ti-12Cr ST) and (b) after deformation (Ti-12Cr CR).

The springback (i.e., the ratio of the springback per a unit load) of Ti-12Cr, TNTZ (Ti-29Nb-13Ta-4.6Zr), a low Young's modulus β-type titanium alloy for use in biomedical applications, and Ti64 ELI (Ti-6Al-4V ELI), the (α + β)-type titanium alloy most widely used in biomedical applications, is shown in Fig. 3 [6]. The springback of Ti-12Cr is much smaller than that of TNTZ, and nearly equal to That of Ti64 ELI.

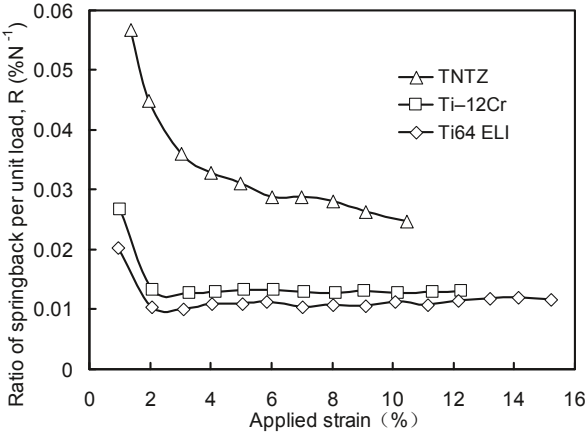

Figure 3. Ratio of springback per unit load as a function of applied strain for Ti-12Cr, Ti-6Al-4V ELI (Ti64 ELI), and Ti-29Nb-13Ta-4.6Zr (TNTZ), and strains for calculation of the springback ratio.

Cyto-toxicity of Ti-12Cr

The cyto-toxicity of Ti-12Cr subjected to ST, SUS 316L stainless steel (SUS 316L), and TNTZ (i.e., the cell number of MC3T3 cells cultured for 24h per 1 mm^2 of each material (cell density)) is shown in Figure 4 [6]. The highest cell density is observed on Ti-12Cr; the cell density is considerably higher than that on SUS 316L and Ti64 ELI, and similar to that on TNTZ. Therefore, the biocompatibility of Ti-12Cr can be considered to be high.

Further increasing the Young's modulus of Ti-Cr alloys

The amount of the athermal ω phase increases with decreasing Cr content in Ti-Cr alloys, thus increasing the Young's modulus. Therefore, if formation of the athermal ω phase in Ti-Cr alloys with low Cr contents could be suppressed, not only would the alloy have a low Young's modulus, but also an overall enhancement of the deformation-induced ω phase transformation could be expected. It is well known that the presence of oxygen (O) can suppress the formation of the athermal ω phase. Therefore, a small amount of O (2 mass% O) was added to Ti-(10-12)Cr to suppress the formation of the athermal ω phase, and the change in the Young's modulus of each

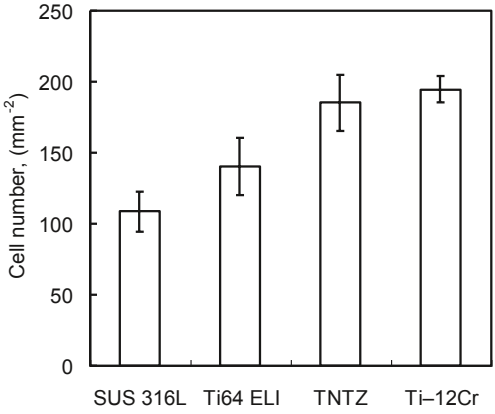

Figure 4. Density (cell number per one mm^2) of MC3T3-E1 cells cultured for 24 h in Ti-12Cr, SUS 316 L stainless steel (SUS 316L), Ti-6Al-4V ELI (Ti64 ELI), and Ti-29Nb-13Ta-4.6Zr (TNTZ)

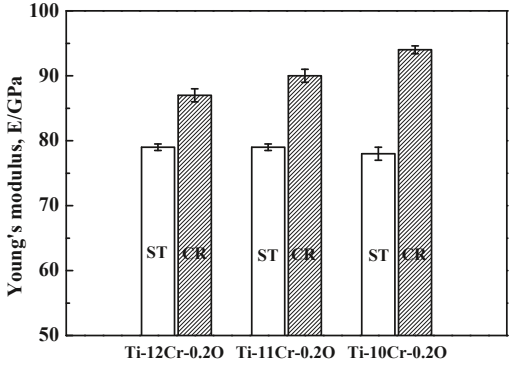

Figure 5. Young's moduli of Ti-(12, 11, 10)Cr-0.2O alloys subjected to solution treatment (ST) and cold rolling (CR) by a reduction ratio of 10 %.

alloy was investigated before and after deformation. Figure 5 [8] shows the Young's moduli of Ti-(12, 11, 10)Cr-0.2O alloys subjected to ST and CR. The Young's moduli are nearly the same (approximately 78 GPa) for all alloys subjected to ST. After the alloys are subjected to CR, all of the Young's moduli increase. Ti-10Cr-0.2O exhibits the greatest increase in Young's modulus after deformation.

The effect of O content on the Young' modulus of Ti-10Cr has been reported as shown in Fig. 6 [9]. The Young's modulus of Ti-10Cr subjected to ST first decreases with increasing O content from 0.06 to 0.2 mass%, then gradually increases with increasing O content up to 0.6 mass %. After CR, all of the alloys exhibit higher Young's moduli than those of all of the alloys before deformation; however, Ti-10Cr-0.2O exhibits the greatest increase in Young's modulus after deformation.

Enhancement of the balance of strength and ductility by twinning induced plasticity

β-Ti-Cr alloys have been reported to show {332}<113> mechanical twinning during deformation. Recently, twinning-induced plasticity (TWIP) has been used to improve the mechanical properties of steels and titanium alloys. Moreover, several studies have reported [6] that activating {332}<113> twinning in titanium alloys can significantly increase the work-hardening rate. Therefore, Ti-Cr alloys are likely to exhibit good plasticity thorough high deformation-twinning-induced work hardening.

Figure 7 [10] shows tensile true stress-strain curves for Ti-9Cr-0.2O and Ti-10Cr-0.06O subjected to ST (Ti-9Cr-0.2O and Ti-10Cr-0.06O) and the corresponding work-hardening rates. Both alloys exhibit significant work hardening in the tensile true stress-strain curves. Ti-10Cr-0.06O exhibits a true pre-necking stress of approximately 1150 MPa and a uniform elongation of approximately 30 %, whereas Ti-9Cr-

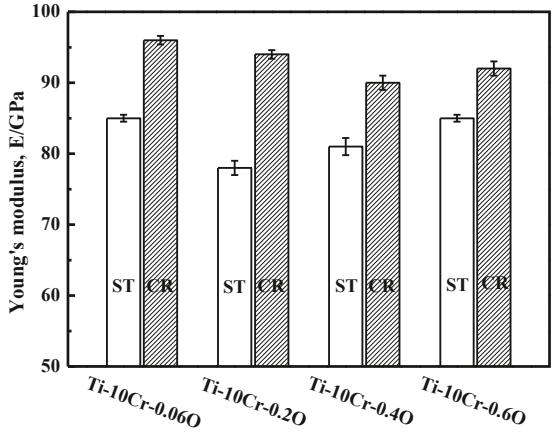

Figure 6. Young's moduli of Ti-10Cr-(0.06-0.6)O alloys subjected to solution treatment (ST) and cold rolling by a reduction ration of 10 % (CR).

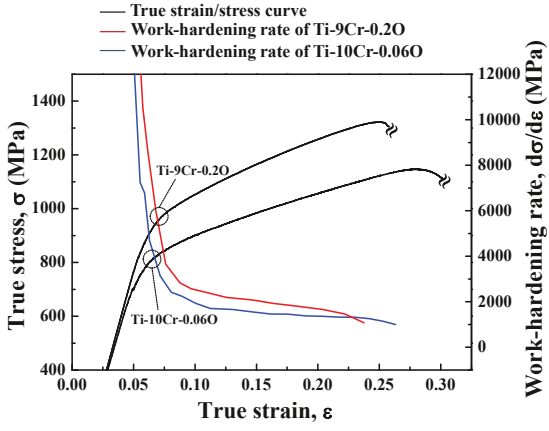

Figure 7. True tensile stress-strain curves for Ti-9Cr-0.2O and Ti-10Cr-0.06O subjected to solution treatment and corresponding work-hardening rates.

0.2O exhibits a true pre-necking stress of approximately 1300 MPa and a uniform elongation of more than 20 %. Both alloys exhibit an excellent balance of strength and elongation. The elongation and strength of Ti-Cr alloys can be controlled by controlling the contents of Cr and O within a narrow range. It has been reported that the remarkable work-hardening of Ti-10Cr-0.06O leads to balanced and significantly enhanced strength and ductility. This phenomenon could be attributed to significant dynamic second-phase strengthening caused by deformation-induced ω-phase transformation and to dynamic microstructure refinement, the so-called "dynamic Hall-Petch effect" caused by twin formation and twin-twin intersection, as well as dislocation/second phase, dislocation/twin, and dislocation/dislocation interactions. The remarkable work hardening that is occurred in Ti-9Cr-0.2O is also considered to have been caused by the same factors as those described above for Ti-10Cr-0.06O.

Compressive fatigue strength of Ti-12Cr

In spinal fixation devices, fatigue issues are generally investigated in the laboratory according to ASTM F1717, which describes a testing method used to evaluate the compressive fatigue strength of spinal fixation rods via a simulated spinal fixation model. The spinal fixation rod model used for performing compressive fatigue strength tests according to ASTM F1717 is schematically shown in Fig. 8 [7]. The spinal fixation device comprises a rod, screw and plug. In this case, the screw and plug are composed of Ti64 ELI, and the rod is composed of Ti-12Cr. A Ti64 ELI rod is also used for comparison. Bone is simulated using an ultrahigh

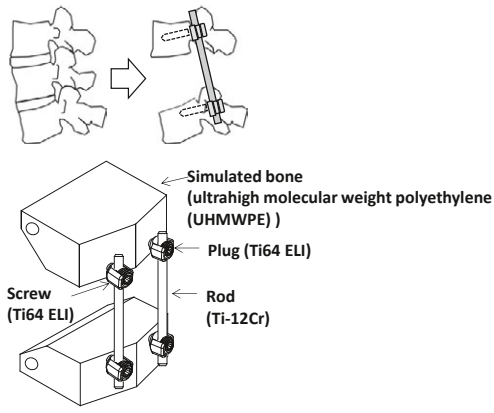

Figure 8. Schematic drawing of compressive fatigue strength test method according to ASTM F1717.

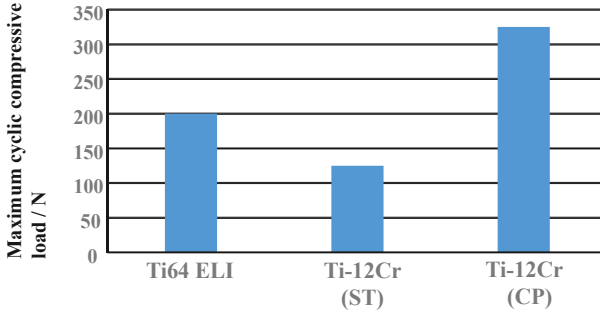

Figure 9. Compressive fatigue limit of Ti-6Al-4V ELI (Ti64 ELI), and Ti-12Cr subjected to solution treatment (ST) and cavitation peening after solution treatment (CP) evaluated according to ASTM F 1717.

molecular weight polyethylene (UHMWPE). The compressive fatigue limit of Ti-12Cr subjected to ST is less than that of Ti64 ELI, as shown in Fig. 9. In the ASTM F1717 compressive fatigue test, the rod is typically failed at the contact area between the rod and the plug. Therefore, fretting that is occurred between the rod and the plug is thought to have reduced the compressive fatigue strength of the rod. An effective solution to such a problem is improving the mechanical properties and tribology characteristics of the rod. To this end, the introduction of a hardened layer via compressive residual stress on the surface of the rod effectively prevents fretting fatigue. Peening techniques can introduce these hardened layers through plastic deformation, i.e., work hardening, by delivering a large impact to the material's surface. Among the major peening techniques, cavitation peening, which is schematically shown in Fig, 10 appears to be a highly promising method for improving the compressive fatigue strength of rods used in spinal fixation devices because it produces less surface damage than other peening techniques. Therefore, cavitation peening was performed on Ti-12Cr rods to improve their compression fatigue strength as evaluated by ASTM F1717; the technique significantly increases the compressive fatigue strength of the rods, as shown in Fig. 9.

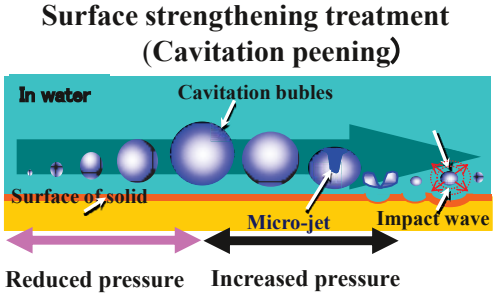

Figure 10. Schematic drawing of cavitation peening showing development and collapse of cavitation.

Summary

A titanium alloy with changeable Young's modulus, Ti-12Cr was developed for use as rods in spinal fixation devices; this alloy can meet the needs of both patients and surgeons. To enhance the changeability of the Young's modulus, the composition of Ti-12Cr was modified to Ti-10Cr-0.2O. To obtain Ti-Cr alloys with a changeable Young's modulus as well as high strength and high ductility, Ti-10Cr-0.06O and Ti-9Cr-0.2O were developed. Cavitation peening was shown to be a highly effective method for improving the compressive fatigue strength of Ti-12Cr as evaluated by ASTM F1717.

References

1. M. Niinomi, M, Nakai, and J, Hieda, "Development of New Metallic Alloys for Biomedical Applications", *Acta Biomaterialia*, 8(2012), 3888-3903.
2. M. Nakai et al., "Self-adjustment of Young's Modulus in Biomedical Titanium Alloys during Orthopaedic Operation", *Mater. Lett.,* 65(2011), 688–90.
3. L. Zardiackas, D. W. Mitchell, and J. A. Disegi, *Medical Applications of Titanium and Its Alloys: The Material and Biological Issues*, *ASTM STP*, *Vol. 1272*, (West Conshohocken, PA, USA: ASTM, 1996), 60–74.
4. T. Akahori et al., "Improvement in Fatigue Characteristics of Newly Developed Beta Type Titanium Alloy for Biomedical Applications by Thermo-mechanical Treatments", *Mater. Sci. Eng. C*, 25(2005), 248–54.
5. S. Hanada S and O. Izumi, "Deformation Behaviour of Retained β Phase in β-eutectoid Ti-Cr Alloys", *J. Mater. Sci.*, 21(1986), 4131–39.
6. X. F. Zhao et al., "Optimization of Cr Content of Metastable β-type Ti-Cr Alloys with Changeable Young's Modulus for Spinal Fixation Applications", *Acta. Biomaterialia*, 8(2012), 2392-2400.
7. Designation: F1717-13, *Annual Book of ASTM Standards, Section 13, Medical Devices and Services: Standard Test Methods for Spinal Implant Constructs in a Vertebrectomy Model*, (West Conshohocken, PA, USA: ASTM, 2013), 667-688.
8. H. H. Liu, PhD Thesis, Tohoku University, 2014.
9. H. H. Liu et al., "Mechanical Properties and Cytocompatibility of Oxygen-modified β-type Ti-Cr for Spinal Fixation Devices, *Acta Biomaterialia*, 12(2015), 352-361.
10. H. H. Liu et al., "Changeable Young's Modulus with Large Elongation-to-failure in β-type Titanium Alloys for Spinal Fixation Applications", *Scripta Materialia*, 82(2014), 29-32.

EFFECT OF MMT NANOPARTICLE CLAY ON FLEXURAL PROPERTIES OF POLYMER BASED BisGMA/TEGDMA RESIN

Duclerc Parra[1], Luiza Campos[1], Letícia Boaro[2], Henrique Ferreira[1], Ademar Lugão[1], Vijaya Rangari[3]

[1] Institute of Nuclear and Energy Research, University of São Paulo (IPEN/USP). Av. Lineu Prestes, 2242 - Cidade Universitária - 05508-000. São Paulo – SP. Brazil.

[2] University of Santo Amaro. Rua Isabel Schmidt, 349 - Santo Amaro - 04743-030- São Paulo- SP. Brazil.

[3]Center of Advanced Materials Science and Engineering. Tuskegee University. Tuskegee University, Tuskegee, AL 36088. USA.

Keywords: Flexural Properties, Nano Composites, Dental Composites.

Abstract

The objective of this study is to evaluate the (strength and modulus) and degree of conversion of dimethacrylate resin containing different amounts of Montomorillonite (MMT) Cloisite 20A nanoclay as filler. Eight formulations of polymer based BisGMA/TEGDMA (four with MMT and another four with barium glass (BG) as filler) at concentration of 20, 30, 40 and 50% by weight were studied. As control, a series of composites containing BG particles were also tested. The flexural strength data was analyzed using Kruskal-Wallis and Tukey's tests. The addition of MMT nanoparticles in a BisGMA / TEGDMA resin matrix resulted in similar degree of conversion and higher elastic modulus values compared to the groups filled with BG. The decrease in the resistance value with increasing concentration of MMT may be due to the formation of agglomerates (clusters) that decreases the reinforcement efficiency.

Introduction

Dental reparation based in composite resin replaced metal amalgams due to its advantages, as the possibility of performing conservative cavity preparation and superior aesthetics results [1]. However, this material suffers a volume contraction during polymerization, leading to residual stresses, postoperative soreness, microcracks formation between the tooth and the restoration, resin detachment from the remaining tooth and even cusp deflection may occur [2-3].

Structural changes caused by multifunctional methacrylate monomers introduction and higher inorganic filler additions produce more wear-resistant materials with higher elastic modulus. Up to 75-85 wt% of filler particles (such as quartz, silica and barium glass) may be added to the resin matrix to improve mechanical properties and reduce polymerization shrinkage to less than 3.0 % [4-5].

Polymers reinforced with different amounts of mineral clays have been studied, with enticing results in the plastic industry, due to the improvement of optical, thermal and mechanical properties [6-7]. Clays are formed by lamellar structure in which their layers present thickness of approximately 1nm, but length and breadth ranging between 100 and 1000 nm [7].

Many types of clay (such as Montmorillonite - MMT) have the capacity to absorb organic molecules in-between their layers. This level of interaction hinders in polymer-clay composites shrinkage due to changes in overall free volume, since clay lamellae can grow apart and disperse throughout the polymeric matrix. Some authors claim there was a polymerization shrinkage reduction of a BisGMA/TEGDMA based composite after the introduction of layered silicate [8-9]. The introduction of these mineral clays in the composite expected to reduce polymerization shrinkage and residual stresses [10-12].

Therefore, the aim of this study was to evaluate the degree of conversion and flexural properties (strength and modulus) of dimethylacrylate resin composites containing different amounts of MMT nanoparticles. Composites containing similar quantities of silanized barium glass particles (BG) were produced and tested as control groups. The null hypothesis was that the evaluated properties were not affected by the amount of MMT nanoparticles and were similar for both types of filler.

Materials

Two series of experimental composites were formulated, both with the same resin matrix (BisGMA:TEGDMA) and 20, 30, 40 or 50 wt % of filler. The photo initiator and tertiary amine corresponded to 0.2 wt% of all formulations tested. The first series used MMT nanoparticles, while in the second group the reinforcing phase was constituted by silanized barium glass particles (2μm).

The following materials were used in the polymeric matrix preparation: BisGMA: (Bisphenol A bis(2-hydroxy-3-methacryloxypropyl)ether) manufactured by Esstech (Essington, USA); TEGDMA: (Triethyleneglycol Dimethacrylate) produced by Esstech (Essington, USA); Camphorquinone: (camphorquinone, 97%) provided by Sigma-Aldrich (Germany); DMAEMA: (2-(Dimethylamino)ethyl methacrylate), 98% purchased form Sigma-Aldrich (Germany). As inorganic filler, the following materials were used: natural Cloisite® 20A MMT, manufactured by Southern Clay Products, USA; Silanized Barium Glass, provided by FGM, BRA. Table 1 show the materials used in composite formulation.

Mineral clay Cloisite® 20A MMT used in this study, according to the manufacturer, was previously organophilised through surface modification by dimethyl dehydrogenated tallow (2M2HT) quaternary ammonium chlorine, with a concentration of 95 meq per $100g^{-1}$ of clay. Tallow refers to a mixture of alkyl compounds with approximately 65% in weight of C_{18}, 30% of C_{16} and 5% of C_{14}. Cloisite® 20A MMT has d_{001} = 24.2 Å as the main X-Ray diffraction initial peak, which also indicates its interlamellar spacing.

Table 1: Formulations of experimental composites groups.

	Mass (mg)							
	Group1	**Group 2**	**Group 3**	**Group 4**	**Group 5**	**Group 6**	**Group 7**	**Group 8**
BisGMA	398	348	298	248	398	348	298	248
TEGDMA	398	348	298	248	398	348	298	248
Camphor.	2	2	2	2	2	2	2	2
DMAEMA	2	2	2	2	2	2	2	2
MMT 20A	200	300	400	500	-	-	-	-
BG	-	-	-	-	200	300	400	500
Total Mass	1000	1000	1000	1000	1000	1000	1000	1000

Methods

Degree of Conversion (DC)

Degree of conversion (DC) (n=5) was determined using near-IR spectroscopy (Vertex 70, Bruker Optik, Germany). Disc-shaped specimens were made using a silicon frame (h=0.8mm, Ø=7.0mm) between two glass slides. FTIR spectra were recorded before and 10 minutes after photo activation, using two scans per spectrum at a resolution of 6 cm^{-1}. The composite was photo-cured for 40 seconds, using a LED curing light (Kondorteck's Aigh-7A LED, at 470 nm wavelength, commonly used to the dental composite cure). Degree of conversion was determined by assessing the change in area of the absorbance peak at 1665 cm^{-1}, corresponding to the first overtone of the methacrylate vinyl stretch in relation to the uncured material [13].

Flexural Modulus and Flexural Strength

Specimens 10x2x1 mm (n=10) were built using a split steel mold. Ten minutes after photo activation using the same parameters described for degree of conversion, the specimen was removed from the mold and subjected to three-point bending in a universal testing machine (Instron 5565 Canton, MA, USA), with 8 mm distance between the supports and at a cross-head speed of 0.5 mm/min. Based on the linear portion of the load x displacement curve, flexural modulus was calculated according to the equation 1 [13]:

$$E = \frac{L \times D^3}{4 \times w \times h^3 \times d} x\,10^{-3} \qquad \text{(equation 1)}$$

where: E is the flexural modulus (GPa), L is the load recorded (N), D is the span between the supports, w is the width of the specimen, h is the height of the specimen and d is the deflection corresponding to L (all in mm).

Flexural strength was calculated according to the equation 2 [13]:

$$\sigma = \frac{3 \times F \times L}{2 \times b \times h^2} \qquad \text{(equation 2)}$$

where: σ is the flexural strength (MPa), F is the maximum load recorded before fracture (N), L is the span between the supports (mm), b is the width of the specimen (mm), h is the height of the specimen (mm).

X-Ray Diffraction (XRD)

The interaction between the polymer matrix and the clay nanoparticles was evaluated by XRD in all the groups containing MMT. The interlamellar spacing "d001" peak is characteristic for the nanoclay. MMT Cloisite® 20A has "d_{001}" = 2.42 nm. Changes in the interlamellar spaces refer to the intercalation effect associated to interaction clay with polymer, in the case of the composites. XRD diffratograms were obtained using a PAN analytical brand, model X'Pert PRO with X'Celerator detector, Rigaku D with Cu Kα radiation (λ=1.54186 A, 45 kV, 40A) at room temperature, the diffraction were scanned from 1.17° to 40° in 2θ range with 0.03° step at step/time 100s. The interlamellar spacing was calculated according to Bragg's equation: $\mathbf{n\,\lambda = 2dhkl \sin \theta}$ (equation 3), in which n is an integer, λ is the incident wavelength, d is the spacing between the planes of same {hkl} (Miller index) in the crystal lattice, and θ is the angle between the incident ray and the crystal plane.

Statistical Analysis

Data for degree of conversion and elastic modulus were analyzed using two way ANOVA/ Tukey's test. Data for flexural strength were analyzed using Kruskal-Wallis/ Tukey's test. For all tests, the global significance level was 5%.

Results and Discussion

Means and standard deviations for degree of conversion (DC) shown in Table 2. Composites containing silanized barium glass and MMT nanoparticles showed no statistically significant among filler contents. For a similar filler level, DC was statistically similar for both types of filler, except for the concentration of 40 wt% that resulted in higher DC for the MMT composite. According to the results obtained in this study (Table 2) it was observed similar degree of conversion for all concentrations in composites with BG.

The absence of statistical difference among different filler content has been reported in a previous study [5]. At concentrations of 20, 30 and 40% in weight, the composites added with MMT were statistically similar. The only exception corresponded to the group containing 50 wt% MMT that had a lower degree of conversion when compared to the other groups added with the same filler type. This may be related to the size, filler concentration and refractive index that may interfere in the dispersion of light and thus in the depth of cure and degree of conversion [14].

For given filler level, the degree of conversion of the groups using BG and MMT (Table 2) was statistically similar, except at a concentration of 40 wt%. These results suggest that the degree of conversion of experimental composites was not affected by the type of interaction between the MMT nanoparticle and a polymer matrix. In other words, there was no interference in the scission of carbon double bonds responsible for the

monomer conversion. Other studies reported no alterations in the monomer conversion in matrix-based BisGMA/TEGDMA filled with MMT nanoparticle [8-9].

Table 2: Means (with standard deviation in parentheses) for degree of conversion (%). For each variable, in the same line, means followed by the same lowercase letter are statistically similar. In the same column, means followed by the same uppercase letter are statistically similar.

Filler content (wt%)	**Degree of Conversion (%)**	
	MMT 20A	**Barium Glass**
20	69.9 (1.9) Aa	65.0 (6.7) Aa
30	71.2 (4.6) Aa	65.6 (6.0) Aa
40	71.9 (3.2) Aa	63.1 (6.3) Ab
50	65.6 (4.8)Ba	63.4 (4.9) Aa

Regarding flexural properties (Table 3), the interaction between filler type and content was significant for both strength and modulus (p=0.018). Flexural modulus decreased with filler content for the composites containing MMT nanoparticles. Among composites containing BG an increase in modulus was observed between 30 and 50 wt%. Regarding filler types, the groups with MMT nanoparticles showed higher flexural modulus, except at 50 wt% where both fillers displayed similar modulus.

Composites containing BG as filler showed an increase in the elastic modulus as the filler concentration increased (Table 3), in accordance with previous studies [15]. The increase in elastic modulus values due to an increase in filler generally follows the rule of mixture [16]. Composites filled with BG showed elastic modulus values similar to those reported in other studies [5]. Meanwhile the experimental composites filled with MMT had higher elastic modulus than the BG groups, except for the materials with 50 wt%, which were statistically similar. This higher elastic modulus found with the MTT composites values may be related to high stiffness and high modulus of the lamellar silicate particles [17]. In addition, the nanoparticles have greater contact surface with the organic phase, which can result in increased mechanical properties [6].

The composite containing 50 wt% MMT showed the lowest elastic modulus values compared to the others MTT-filled materials. The agglomeration of MMT nanoparticles in the polymer matrix, may have contributed to this result. These results match previous studies in which the authors observed the formation of a great number of tactoids in experimental dental composites containing above 16 wt% MMT [8]. After reached the optimum maximum level, the nanoparticles loading led to an induced aggregation state of nanoclay particles and reduced nanoparticles dispersion in the polymeric matrix [18-19].

Among the groups filled with MMT, the flexural strength results (Table 3) were similar at 20% and 30% (v/v). However, lower value was achieved at 40 and 50 wt%. With regard to the addition of BG, a relevant difference was observed for the group containing 20 wt%. By comparing the two types of filler, the groups filled with MMT

nanoparticle showed a value statistically higher in relation to the groups added with BG at a concentration of 20 and 30 wt%, while are observed lower values at concentrations of 40 and 50 wt%.

Table 3: Means (with standard deviation in parentheses) for elastic modulus (GPa) and flexural strength (MPa). For each variable, in the same line, means followed by the same lowercase letter are statistically similar. In the same column, means followed by the same uppercase letter are statistically similar.

Filler content (wt%)	Flexural modulus (GPa)		Flexural strength (MPa)	
	MMT	BG	MMT	BG
20	3.09 (0.48) Aa	0.35 (0.26)Bb	69.1 (8.1)Aa	32.0 (13.1)Bb
30	2.47 (0.51) Aa	0.49 (0.18)Bb	73.07(9.2) Aa	55.9 (18.1)Aba
40	1.81 (0.65) Ba	1.02 (0.5)ABb	38.4 (5.2) Bb	66.7 (25.5)Aa
50	1.68 (0.74) Ba	1.47 (0.55)Ab	23.9 (6.1) Bb	65.2 (18.0)Aa

Regarding flexural strength, the composites filled with MMT nanoparticle and BG showed different behaviors (Table 3). It was observed that for the MMT groups that strength decreased as filler concentration increased, while for the BG groups the opposite behavior was found, in accordance with previous studies [5]. At high MMT levels, the formation of agglomerates (clusters) decreases the reinforcement efficiency. According to Hussain (et al. 2007) [17], the particle agglomeration (MMT) is the primary reason for a decrease in the strength of the material, even if the agglomerate is strong enough to significantly increase the elastic. Flexural strength decreased because functionalization of MTT was not sufficient to form adherent strong interface between filler and polymeric matrix. Thereby, they act as defects within the composites that may act as a crack initiation sites. The increase in MMT's content also increases the risk of crack initiation. This could be related to the need of concentration optimization of MMT for each type of polymer matrix in order to adjust or improve mechanical properties [18].

Diffratograms of the MMT powder, as well as the MMT nanoparticles added to the resin matrix are shown in Figure 1. The diffraction peak interlamellar spacing of the "pure" MMT was calculated as d_{001}= 3.48 nm. The "d" values for the MMT filled on the polymeric matrix were: d= 3.77 nm for the composites containing 20 wt% MMT; d= 3.68 nm for the composites containing 30 wt% MMT; d= 3.58 nm for the composites containing 40 wt% MMT and d= 3.57 nm for the composites containing 50 wt% MMT. The displacement of 2θ peak related to the interlamellar spacing "d_{001}" for smaller angles was observed. That displacement of the inicial "d_{001}" peak for smaller angles for both groups characterized the entry of the polymer into the clay layers in intercalation form. XRD patterns (Figure 1) showed predominantly intercalation effect of MMT nanoparticle in relation to polymeric matrix for all groups, as previously observed in other studies [8-9]. An intercalated structure is defined when a single or more extended polymer chains are intercalated between the silicate layers resulting in a well ordered multilayer morphology built up with alternated polymeric and inorganic layers [7]. This type of interaction filler/matrix being stronger and more stable than the interaction that

occurs with BG, can result in an increase in properties as evidenced in the results of the flexural modulus analysis. All MMT groups' concentration, the flexural modulus values were statistically higher than the composites added with BG.

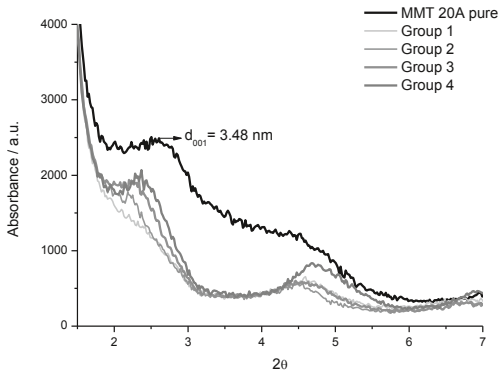

Figure 1: XRD patterns of MMT 20A pure and experimental composites groups.

Conclusion

Based on the results obtained in this study, it can be concluded: despite fillers MMT and BG interact with polymer matrix based BisGMA/ TEGDMA in a distinct manner, both cases showed a degree of conversion statistically similar; the experimental composites filled with MMT presented flexural modulus higher at all concentrations tested and it could be related to the high modulus of the MMT nanoparticles and the intercalation effect of nanoparticles in relation to polymeric matrix, as observed in XRD analysis; regarding flexural strength, only MMT group's with low concentration showed the highest value if compared to composites added with BG. The decrease in the resistance value with increasing concentration of MMT may be due to the formation of agglomerates (clusters) that decreases the reinforcement efficiency.

Acknowledgments

The authors thank to ESSETECH, SOUTHERN CLAY PRODUCTS and FGM for donating the materials; FAPESP (**process 2013/07229-3)** for the financial support.

References

[1] Min SH, Ferracane JL, Lee IB. "Effect of shrinkage strain, modulus, and instrument compliance on polymerization shrinkage stress of light-cured composites during the initial curing stage". Dental Materials, 26 (2010), 1024–1033.

[2] Davidson CL, Davidson-Kaban SS., "Handling of mechanical stresses in composite restorations". Dental Update, 25 (1998), 274-279.

[3] Ferracane JL. "Developing a more complete understanding of stress produced in dental composites during polymerization". Dental Materials, 21 (2005), 36-42.

[4] Mucci V, Pérez J, Vallo CI. (2010), “Preparation and characterization of light-cured methacrylate/ montmorillonite nanocomposites”. Polym Intern., 60, 247-254.

[5] Gonçalvez F, Azevedo CLN, Ferracane JL, Braga R.R. “BisGMA/TEGDMA ratio and filler content effects on shrinkage stress”. Dental Materials, 27 (2010), 520-526.

[6] Fournaris KG, Boukos N, Petridis D. “Aqueous polymerization of protonated 4-vinylpyridine in montimorillonite”. Appled Clay Science, 19 (2001),77-88.

[7] Alexandre M, Dubois P. “Polymer-layered silicate nanocomposites: preparation, properties and uses of a new class of materials. Materials Science and Engineering, 28 (2000), 61-63.

[8] Discacciati JAC, Oréfice RL. “Structural analysis on photopolymerized dental resins containing nanocomponents”. Journal of Materials Science, 42 (2007), 3883-3893.

[9] Campos LMP, Lugão AB, Vasconcelos MR, Parra DF. “Polymerization Shrinkage Evaluation on Nanoscale-Layered Silicates: BisGMA/TEGMA Nanocomposites, in Photo-Activated Polymeric Matrices”. Journal of Applied Polymer Science, 131 (2014), 413-418.

[10] Liu L, Qi Z, Zhu X. Studies on nylon-6-nanoclay nanocomposites by melt intercalation process. J Appl Polym Sci,1999; 71: 1133-1138.

[11] Salahudin N, Shehata M. (2001), “Polymethylmethacrilate-montmorillonite composites: preparation, characterization and properties”. Polymer., 42, 8379-8385.

[12] Discacciati JAC, Neves AD, Oréfice RL, Pimenta FJGS, Sander HH. “Effect of ligth intensy and irradiation time on the polymerization process of a dental composite resin”. Materials Research, 2, (2004), 313-318.

[13] Boaro LC, Gonçalves F, Guimarães TC, Ferracane JL, Pfeifer CS, Braga RR. “Sorption, solubility, shrinkage and mechanical properties of “low-shrinkage” commercial resin composites”. Dental Materials, 29, (2013), 398-404.

[14] Campbell PM, Johnston WN, O’brien WJ. “Light scattering gloss of an experimental quartz-filled composite”. Journal of Dental Research, 65 (1986), 892-894.

[15] Gonçalves F, Boaro LC, Ferracane JL,Braga RR. A comparative evaluation of polymerization stress data obtained with four different mechanical testing systems. Dental Materials, 28 (2012), 680-686.

[16] Massouras K, Silikas N, Watts DC. Correlation of filler content and elastics properties of resin-composites. Dental Materials, 24 (2008), 932-939.

[17] Hussain F, Chen J, Hojjati M. Epoxy-silicate nanocomposites: cure monitoring and characterization. Materials Science and Engineering, (2007), 467–476.

[18] Fournaris K G, Boukos N, Petridis D. Aqueous polymerization of protonated 4-vinylpyridine in montimorillonite. Applied Clay Science,19 (2001), 77-88.

FATIGUE PERFORMANCE OF NEW DEVELOPED BIOMEDICAL Ti-15Mo ALLOY WITH SURFACE MODIFIED BY TiO_2 NANOTUBES FORMATION

Nilson T. C. Oliveira, Leonardo C. Campanelli, Carolina C. Bortolan, Claudemiro Bolfarini

Department of Materials Engineering – DEMa, Federal University of São Carlos – UFSCar, São Carlos - SP, Brazil.

Keywords: TiO_2 nanotubes, Ti-15Mo alloy, surface modification, fatigue behavior

Abstract

In recent years, it was demonstrated that Ti-Mo alloys are promising to be use as orthopedic implants. The presence of TiO_2 nanotubes can increase the bioactivity and improve the osseointegration of Ti and its alloys implants, although this modification could lead to a reduction in the dynamic mechanical properties. In this context, the purpose of the present study was to obtain self-organized nanotubes on the surface of biomedical Ti-15Mo alloy and verify whether the fatigue performance was significantly changed. Organized nanotubes were obtained by anodic oxidation using ethylene glycol + NH_4F solution. The axial fatigue behavior was characterized by stepwise increases of the applied load in air and in physiological media at 37°C. The results was compared with the as-polished samples in order to compare if the Ti-15Mo alloy fatigue behavior was affected by the surface modification, and it was found that the mechanical performance of the Ti-15Mo alloy was affected by the surface modification, in that specific experimental conditions used to obtain the nanotubes.

Introduction

During the last decades a large and growing number of biomedical implants has been proposed for continuous use in the human body [1]. Titanium and some of its alloys become interesting material for research in the biomedical area, presenting adequate mechanical properties, corrosion resistance; and local and systemic biocompatibility [2-8]. Therefore, it has been developed β type Ti alloys, with lower elasticity modulus, and also composed of non-toxic and not allergenic elements such as Mo, Nb, Ta, Zr, and Sn [2, 4, 5, 9, 10].

Biomedical implants made of titanium-based materials must have certain basic features, including high bone-implant contact and good osseointegration, which are often influenced by the physical-chemical properties and the topography of titanium surface [8]. The surface modification of titanium and its biocompatible alloys is necessary to improve its biological activity and increase or accelerate the bone formation [8, 11-13].

Recently, it was found that nanosized pores or nanotubular oxide layers on the Ti alloys surface can increase the bioactivity and the osseointegration of an implant [7, 14-17]. However, some care must be taken since several processes of surface modification are known to strongly decrease the fatigue life of the implant material.

Therefore, the goal of the present study was to obtain self-organized nanotubes on the surface of β type biomedical Ti-15Mo alloy and investigate its fatigue behavior.

Materials and Methods

Nanotubes were obtained on the commercially β type Ti-15Mo alloy (ASTM F2066-08) samples by anodic oxidation, using a two electrode system, with a 304 stainless steel plate as the counter electrode, and an Agilent 6575A-J07DC Power Supply. Prior to anodization, the samples were polished with 1200 grade emery paper, and rinsed with distilled and deionized (Milli-Q®) water and Isopropyl alcohol. The electrochemical anodization was performed applying 40V for 6h, using as working electrolyte 0.25 M NH_4F in ethylene glycol solution at room temperature [17]. The morphology of the nanostructured surfaces was evaluated by Scanning Electron Microscopy (SEM), using FEI Magellan 400 L.
Axial fatigue tests were performed in a MTS Bionix servo-hydraulic testing machine at a frequency of 10 Hz and a stress ratio of R = 0.1. The fatigue behavior was investigated using a stepwise load increase method, in which the maximum stress started at 150 MPa and was increased by 50 MPa each 50,000 cycles until the complete specimen failure. Three replicates were tested for each surface condition; all tests were conducted in the atmosphere as well as in simulated physiological media at 37°C.

Results and Discussion

In the Figure 1 are presented the top-view and a cross sectional view of a mechanically fractured region of the respective sample of the nanostructured layer obtained on the Ti-15Mo alloy after anodization at 40V for 6h in NH_4F / ethylene glycol solution. As can be seen, it was obtained very organized nanotubes with geometry almost perfectly circular, presenting respectively average diameter and length of 90 nm and 5μm, which was consistent with previous work [17].
The formation of nanotubes on this alloy significantly decreased the maximum stress that the specimens resisted under fatigue loading, Fig. 2. The mean fatigue strength by the employed method was found to be slightly above 700 MPa for the as-polished condition, whereas the surface modification led to a mean strength of approximately 370 MPa (reduction of 47%). This fact is critical since one of the requirements for use in orthopedic or dental implant of a particular surface modification is that it cannot deteriorate the fatigue strength of the implant. Noting that the Ti-15Mo alloy recently developed for use in orthopedic implants, has shown very promising results in its mechanical and electrochemical properties [4, 5], and so it is important to understand the reason for this deterioration and / or find new conditions of anodization where it is possible to obtain nanotubes on this alloy without affecting its fatigue properties. Probably it is due the harder experimental conditions necessary to obtain TiO_2 nanotubes on this alloy when compared to the ones necessary to pure Ti, i.e, electrolytic solution completely without water, high potential as 40V and also long anodization time, 6h, instead of 20V for 1h for Ti in aqueous electrolyte solution.

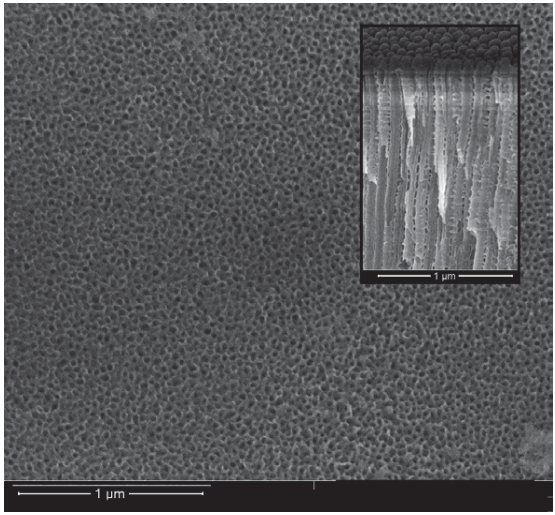

Figure 1: SEM micrograph (top-view) of Ti-15Mo alloy anodized at 40V for 6 h. Inset: cross sectional view.

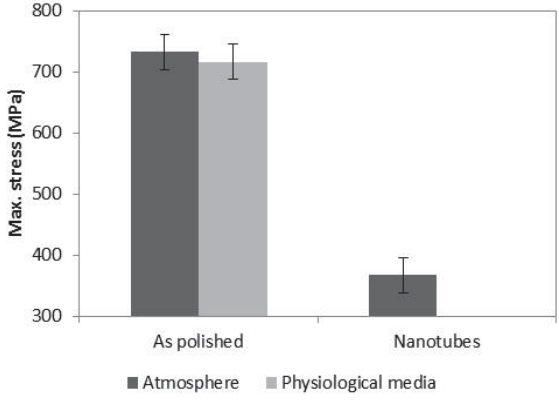

Figure 2: Max stress of the fatigue tests for Ti-15Mo alloy with as-polished surface and after TiO_2 nanotubes formation. Tests performed in air and also in Chloride solution.

Conclusions

The fatigue behavior of Ti-6Al-4V was not affected by nanotubes formation mainly because Highly organized nanotubes, with circular and well-defined geometry could be obtained on Ti-15Mo alloy by anodic oxidation using NH_4F / ethylene glycol solution.

A comparison with the as-polished samples revealed that the mechanical performance of the Ti-15Mo alloy was affected by the surface modification, in that specific experimental conditions used to obtain the nanotubes.

Therefore, these results suggest that it is possible to obtain TiO_2 nanotubes on the studied alloy, however it is important to find new anodizing conditions where it is possible to obtain nanotubes on this alloy, but without affecting its fatigue properties.

Acknowledgments: To FAPESP for scholarships (proc. 2012/11350-0, 2013/04423-3) and grants (proc. 2012/01652-9) that make this work possible.

References

1. S. Bauer, P. Schmuki, K. Von Der Mark, J.Park, "Engineering biocompatible implant surfaces Part I: Materials and surfaces." *Progress in Materials Science*, 58 (2013), 261–326.

2. M. Niinomi, D. Kuroda, K. Fukunaga, M. Morinaga, Y. Kato, T. Yashiro, A. Suzuki, "Corrosion wear fracture of new β type biomedical titanium alloys" *Journal of Materials Science and Engineering A*, 263 (1999), 193-199.

3. Y. Okazaki, S. Rao, T. Tateishi, Y. Ito, "Cytocompatibility of various metals and desenvelopment of new titanium alloys for medical implants" *Journal of Materials Science and Engineering A*, 243 (1998), 250-256.

4. N.T.C. Oliveira, G. Aleixo, R. Caram, A.C. Guastaldi, "Development of Ti-Mo alloys for biomedical applications: microstructure and electrochemical characterization" *J Journal of Materials Science and Engineering A*, 452/3 (2007), 727-731.

5. N.T.C. Oliveira, A.C. Guastaldi, "Electrochemical stability and corrosion resistance of Ti-Mo alloys for biomedical applications" *Acta Biomaterialia*, 5 (2009), 399-405.

6. H. Huang, C. Wu, Y. Sun, W. Yang, T. Lee, "Surface nanotopography of an anodized Ti–6Al–7Nb alloy enhances cell growth" *Journal of Alloys and Compounds*, 615 (2014), S648–S654.

7. B. Li, J. Hao, Y. Min, S. Xin, L. Guo, F. He, C. Liang, H. Wang, H. Li, "Biological properties of nanostructured Ti incorporated with Ca, P and Ag by electrochemical method" *Materials Science and Engineering C*, 51 (2015), 80–86.

8. M. Kulkarni, A. Mazare, E. Gongadze, Š. Perutkova, V. Kralj-Iglič, I . Milošev, P. Schmuki, A. Iglič, M. Mozetič, "Titanium nanostructures for biomedical Applications". *Nanotechnology*, 26 (062002) (2015), 1-18.

9. S.B. Gabriel, C.A. Nunes, G.A. Soares, "Production, Microstructural Characterization and Mechanical Properties of As-Cast Ti-10Mo-xNb Alloys" *Artificial Organs,* 32 (4) (2008), 299-304.

10. L.J. Xu, Y.Y. Chen, Z.H.G. Liu, F.T. Kong, "The microstructure and properties of Ti–Mo–Nb alloys for biomedical application" *Journal of Alloys and Compounds*, 453 (2008), 320–324.

11. J.M. Hernández-López, A. Conde, J. De Damborenea, M.A. Arenas, "Correlation of the nanostructure of the anodic layers fabricated on Ti13Nb13Zr with the electrochemical impedance response." *Corrosion Science*, 94 (2015), 61–69.

12. S. Minagar, C.C. Berndt, J. Wang, E. Ivanova, C. Wen, "A review of the application of anodization for the fabrication of nanotubes on metal implant surfaces". *Acta Biomaterialia*, 8 (2012), 2875–2888.

13. H. Huang, C. Wu, Y. Sun, T. Lee, "Improvements in the corrosion resistance and biocompatibility of biomedical Ti–6Al–7Nb alloy using an electrochemical anodization treatment" *Thin Solid Films*, 528 (2013), 157–162.

14. V.S. Saji, H.C. Choe, W.A. Brantley, "Nanotubular oxide layer formation on Ti–13Nb–13Zr alloy as a function of applied potential" *Materials Science*, 44 (2009), 3975–3982.

15. V.S. Saji, H.C. Choe, "Electrochemical corrosion behaviour of nanotubular Ti–13Nb–13Zr alloy in Ringer's solution" *Corrosion Science*, 51 (2009), 1658–1663.

16. V.S. Saji, H.C. Choe, W.A. Brantley, "An electrochemical study on self-ordered nanoporous and nanotubular oxide on Ti–35Nb–5Ta–7Zr alloy for biomedical applications". *Acta Biomaterialia*, 5 (2009), 2303–2310.

17. N.T.C Oliveira, J.F. Verderio, C. Bolfarini, "Obtaining self-organized nanotubes on biomedical Ti–Mo alloys" *Electrochemistry Communications*, 35 (2013), 139–141.

TMS2016

145th Annual Meeting & Exhibition

SUPPLEMENTAL PROCEEDINGS

Computational Materials Discovery and Optimization: From 2D to Bulk Materials

FIRST PRINCIPLES INVESTIGATION ON $TiAl_3$ ALLOYS SUBSTITUTIVELY DOPED WITH Si

Qing Du, WeiDong Hu, WangJun Peng , GuangXin Wu*, WenDe Dan, JieYu Zhang
State Key Laboratory of Advanced Special Steel, School of Materials Science and Engineering, Shanghai University, Shanghai 200072, China

Keywords: First principles, $TiAl_3$, Si doping, Antioxidant properties.

Abstract

The site preference of Si in $TiAl_3$ is calculated using first principles method based on Density Functional Theory. Through the analyses and comparison of the binding energy of systems with different substitution behaviors, it is shown that Si prefers to occupy the site of Al(2) and the limited solubility of Si in $TiAl_3$ is around 12.5%. Then this article made a research on the antioxidant properties of different doped concentration of Si in $TiAl_3$, and the result showed that the Si doping enhanced the oxidation resistance of the Ti-Al alloy.

Introduction

Ti-Al-based intermetallic compounds mainly contain Ti_3Al, TiAl, $TiAl_3$ alloys. The density of $D0_{22}$-$TiAl_3$ is lowest (3.36g/cm3) in aluminum alloys, and it has a high specific modulus and specific strength. In addition, the melting point of $TiAl_3$ is up to 1340 ℃ and the diffusion rate of Ti through Al is very low, The degree of lattice matching between$(200)_{TiAl3}$ and$(200)_{Al}$ is little misfit (<2.0%). Better property of $TiAl_3$ than other alloys makes it become a potential low-density high-temperature structural material[1-2]. However, the high temperature oxidation of alloys has been a problem to be solved. Although the increasing amounts of Al enhance the oxidation resistance of the $TiAl_3$, The surface of $TiAl_3$ still cannot form continuous and dense Al_2O_3[2-3].

In order to improve the antioxidant capacity of Ti-Al-based intermetallic compound, many works have been done focusing on the process of adding alloy elements. The studies have explored that adding Si, Mo, W, etc alloying elements into $TiAl_3$ crystal is beneficial to its oxidation resistance and Si doping will achieve relatively good results[3-4]. However, there are no clear explanations on the substitution behavior of Si in $TiAl_3$ and the internal mechanism of the oxidation resistance that Si doped in $TiAl_3$ crystal. In order to explain the question from atomic scale, the aritical investigated the substitution behavior of Si in $TiAl_3$ and the effect which doping different

*Corresponding Author：GuangXin Wu, email: gxwu@shu.edu.cn

concentration of Si on oxidation resistance of $TiAl_3$ by using a first principles method based on density functional theory.

Computational details

Method

In this study the calculations were based on density functional theory software package. The exchange interactions and correlation effects were treated using PBE of the generalized gradient approximation (GGA) [5]. The corresponding kinetic energy cutoff of plane waves was set as 380 eV. The calculations of total energy and electronic structure were followed by cell optimization with self consistent field (SCF) tolerance of 2×10^{-6}eV/atom, stress deviation was less than 0.05GP. Brillouin zone sampling was performed by the Monkhorst Pack scheme with 4×7×4 k-points mesh(a supercell contains 16 atom) and 3×4×3 k-points mesh(a supercell contains 32 atom)[6].

Model

$D0_{22}$-$TiAl_3$ crystal contains 2 Ti atoms and 6 Al atoms such as figure 1. Each atomic coordinates are as follows: Ti(0,0,0), Al(1)(0,0,0.5), Al(2)(0,0.5,0.25)[6-7]. In order to determine the accuracy of the selected pseudopotential and the reliability of calculation method, we calculated the basic properties of $D0_{22}$-$TiAl_3$, Si and O_2. The cell parameters of $D0_{22}$-$TiAl_3$ are a=b=3.8516Å, c=8.6366Å. The bond length of O_2 is 0.125nm. This conclusion and the experimental results reported in literature can be validated with each other[7]. It will confirm the reliability of our calculations. The article used the optimized structural crystal of $TiAl_3$ to build 1×2×1 and1×2×2 Supercell. The latter is used to build the crystal that Si doping concentration is 3.125%.

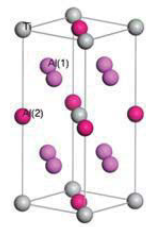

Figure 1 $TiAl_3$ (D022) crystal

The article investigated the situation that different doped concentration of Si occupied the Al site and the Ti site , the effect of the different doped concentration of Si on interstitial oxygen diffusion. When Si occupy Al site, we consider Si occupy two different Al sites in loose distributions. Si occupy Al (1) site, Al (2) site, and Ti site which doping concentration was 12.5% in a loose distribution was shown in figure 2.

As shown in figure (3) is the possible site occupancy of interstitial oxygen in $TiAl_3$. Considering the three different possible sites occupancy, the octahedral center of a Ti and five Al atoms (octahedral (1)), the octahedral center of two Ti and four Al atoms (octahedral (2)), the tetrahedron center of a Ti and three Al atoms (tetrahedron (1)).

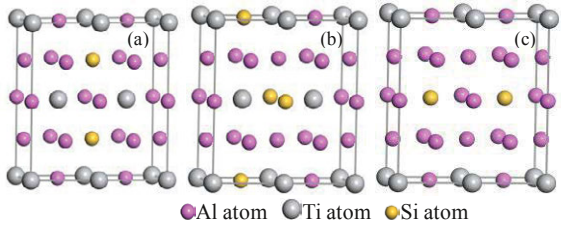

Figure 2 The supercell of Ti_4Al_{12} containing 12.5at% Si , (a) Si atom substitute Al (1) in lattice loose distribution, (b) Si atom substitute Al (2) lattice in loose distribution, (c) Si atom substitute Ti lattice

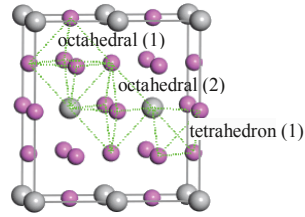

Figure 3 The possible site occupancy of interstitial oxygen in $TiAl_3$

Results and discussions

Si site preference in $TiAl_3$

Binding energy refers to the release energy during elemental forming a compound, it can be used for evaluating the difficult of compounds formed, when the Binding energy is negative, its absolute value was greater, it means the intermetallic compounds formed more easily. The Binding energy after Si atom replaced the site of Al and Ti in $TiAl_3$ was defined as follow:

$$E_b = (E_{tot} - xE_{atom}^{Al} - yE_{atom}^{Si} - zE_{atom}^{Ti})/(x+y+z) \qquad (1)$$

Where x, y, z represented the number of Al, Si, Ti atom in the cell of compound respectively, E_{tot} meant the total energy after structure optimization of compound, and xE_{solid}^{Al} ,yE_{solid}^{Si} ,zE_{solid}^{Ti} represented the energy when a single Al, Si, Ti were in atom state. In order to determine the Binding energy of doped system, the energy of

single Al, Si, and Ti atom was calculated and they were -52.4740eV, -1603.0552eV, -107.2644eV respectively. On this basis, the total energy which different doping concentration of Si (3.125%-25%) occupying the Al (1), Al (2), and Ti site in loose distribution (as shown in table I) was further calculated. In the process of calculation, these supercells contain different number of atom. The data in table I show the energy of supercell that contains 16 atoms.

Table I Total energy of different Si doping concentration occupying Al (1) site, Al (2) site, and Ti site in $TiAl_3$

Concentration	E Al(1)/eV	E Al(2)/eV	E Ti/eV
3.125%	-7121.7721	-7212.8087	-6347.0796
6.25%	-7147.2662	-7147.3119	-5597.9163
12.5%	-7198.1127	-7198.3696	-4100.1448
18.75%	-7249.0102	-7249.0553	-2602.2337
25%	-7299.6817	-7299.7582	-1104.9086

Table II Binding energy that 3.125%-25% doped concentration Si occupy the Al (1) site, Al (2) site, and Ti site

Concentration	E_b Al(1)/eV	E_b Al(2)/eV	E_b Ti/eV
3.125%	-0.4042	-0.4065	-0.3166
6.25%	-0.4104	-0.4132	-0.2374
12.5%	-0.4139	-0.4300	-0.1136
18.75%	-0.4206	-0.4234	-0.0189
25%	-0.4132	-0.4179	-0.1148

Table II shows the binding energy of system which different doping concentration of Si (3.125%-25%) occupy the Al(1), Al(2), and Ti site in $TiAl_3$ in a loose distribution. From the table, it is found that under the different Si doping concentration the binding energy that Si atoms occupy the Al site in $TiAl_3$ are far less than the Ti site. This shows that Si atoms tend to occupy the Al sites in $TiAl_3$ and the possibility of Si occupying Ti site is low. The reason may be that Al atomic radius is more close to the Si atoms radius than the atoms radius of Ti. When Si atoms occupy two different Al sites, the binding energy that Si atoms occupy the Al(2) site is smaller than the Al(1) site in $TiAl_3$. And with the increase of the Si doping concentration, the binding energy that Si atoms occupy the Al(2) site decreased first and then increased. When Si doping concentration is 12.5%, the binding energy that Si atoms occupy Al(2) site is 0.43ev which is minimum, the system is the most stable structure at this time. It could predict the largest solid solubility of Si atoms in $TiAl_3$ should be around 12.5%, this conclusion and the experimental results that the largest solid solubility of Si atoms in $TiAl_3$ should be 15 % can be validated with each other.

The diffusion of oxygen

At normal state, the small atomic radius atom dissolves in interstitial position of the

crystal. When the atom dissolves in different positions, the heat of formation will be different. There are three different possible interstitial positions (As shown in figure 3) in $TiAl_3$ crystal. The Heat of formation can determine the stability of structure, while oxygen enter three different interstitial sites of $TiAl_3$. The heat of formation of doped oxygen can be achieved using the following formula:

$$H(O) = E_{tot}(O) - E_{TiAl_3}^{bulk} - E_{atom}^{O} \qquad (2)$$

In the formula (2),$E_{tot}(O)$ meant the total energy of oxygen occupying possible interstitial position, $E_{TiAl_3}^{bulk}$ represented the total energy of $TiAl_3$, andE_{atom}^{O} represented the total energy of oxygen atom. The table Ⅲ shows the heat of formation that oxygen atoms enter three different interstitial sites of $TiAl_3$. From the results, it was found that the heat of formation which the oxygen atoms entered the octahedral center is lower than the tetrahedron center. The oxygen atoms entered the octahedral center of two Ti and four Al atoms (octahedral (2)) is the most stable. In order to reduce the amount of calculation, we only consider oxygen atoms occupy the octahedral center of two Ti and four Al atoms (octahedral (2)).

Table Ⅲ The heat of formation that oxygen atoms enter three different interstitial sites

Position	octahedral (1)	octahedral (2)	tetrahedron (1)
H(eV)	-7.03	-7.13	-6.76

The oxidation of material starts from the surface, but the surface oxygen spread to the inside of material may cause material further oxidation, so control the spread of oxygen in the material can inhibit the oxidation of material. At present there is no experimental method to directly measure the diffusion ability of oxygen in the material. In order to study the effect of doped Si on the diffusion ability of oxygen. This work calculated the heat of formation in the system that oxygen atoms occupied the crystal of Si doping $TiAl_3$ in the octahedral(2) center. The heat of formation will be achieved by the following formula:

$$H(O) = E_{Ti-Al-Si}(O) - E_{Ti-Al-Si}^{bulk} - E_{atom}^{O} \qquad (3)$$

In the Formula(3) $E_{Ti-Al-Si}(O)$ meant the total energy of oxygen atoms occupying interstitial position in the Si doping $TiAl_3$ crystal, $E_{Ti-Al-Si}^{bulk}$ meant the total energy of the Si doping $TiAl_3$ crystal , and the E_{atom}^{O} represented the total energy of oxygen atom. The calculated results were listed in table Ⅳ. It shows that with the increase of concentration of Si in $TiAl_3$ crystal, the heat of formation of oxygen doping will increase, and when the concentration of Si is 12.5%, the heat of formation of oxygen

doping is -6.552eV which is the largest. This suggested that the doped Si atoms in $TiAl_3$ crystal will hinder the diffusion ability of oxygen atom in the crystal. The increase of Si doping concentration will enhance $TiAl_3$ oxidation resistance ability. XiaoWei Hao etc experiment has showed that Si doping in Ti-Al alloy has a positive impact on the oxidation resistance. It is in accordance with the calculation results of this article.

Table Ⅳ The heat of formation of oxygen doping in different Ti-Al-Si

Concentration of Si	3.125%	6.25%	12.5%	18.75%	25%
H(O)/eV	-7.3858	-7.2501	-6.552	-7.2013	-7.2318

Conclusions

In order to study the substitution behaviour of Si in $TiAl_3$， and the effect of different doping concentration of Si in $TiAl_3$ crystal on its antioxidant properties. The article calculated the binding energy that different doping concentration of Si (3.125%-25%) occupied the Al (1) site, Al (2) site, and Ti site in $TiAl_3$ crystal. The calculated results indicate that Si prefers to occupy the site of Al (2), and the largest solid solubility of Si atoms in $TiAl_3$ should be around 12.5% which is validated with the experimental results. Meanwhile, the comparison of the heat of formation that oxygen atoms enter three different interstitial sites of $TiAl_3$ shows that the oxygen entering the octahedral center of two Ti and four Al atoms (octahedral (2)) is the most stable. This article also calculated the heat of formation of the system that oxygen atom occupied the octahedral (2) center of Si doped in $TiAl_3$ crystal. The results show that the diffusion ability of oxygen atom in $TiAl_3$ decreased after Si atom doping in $TiAl_3$. Therefore, increasing doping concentration of Si will enhance oxidation resistance ability of $TiAl_3$.

Acknowledgement

The author Wu would like to thank the support from National Natural Science Foundation of China (Grant No. 51104098) and Science and Technology Committee of Shanghai under No. 14521100603. Thanks for Analysis and Test Center of Shanghai University for the support of instrument.

References

[1]. Wang H Y, Li C Y, GAO J, Hu Q k. First-principles studies of the structural and thermodynamic properties of $TiAl_3$ under high pressure[J]. Acta Phys. Sin. 62(2012) 068105.

[2]. Li S H, Zuo D X, Zhang J. Development and research of Ti-Al intermetallic compounds [J]. Journal of Iron and Steel Research,1999(S):389-394.

[3]. Li H, Wang S Q, Ye H Q. Influence of Nb doping on oxidation resistance of TiAl: A first principles study[J]. Acta Phys. Sin. 58(2009) S224.

[4]. Liu N, Song R B, Sun H Y, Du D W. The electronic structure and thermodynamic properties of Mg2Sn from first principles calculations[J]. Acta Phys,Sin, 57(2008) 7145.
[5]. Zhu G L, Shu D, Dai Y B, Wang J, Sun B D. First principles study on substitution behaviour of Si in $TiAl_3$ [J]. Acta Phys. Sin. 58(2009) S210.
[6]. Shu D, Zhu G L, Wang J, Sun B D. 2007 Chinese Patent CN101086042.
[7]. Zhu G L, Dai Y B, Shu D, Xiao Y P. First-principles study of point defects and Si site preference in A13Ti[J]. Comput Mater. Sci. 50(2011) 2636.

EFFECT OF STRAIN ON THE PHYSICAL PROPERTIES OF LANTHANUM NICKELATE

D. Misra[1], T. K. Kundu[1], Ankit[1]
[1]Department of Metallurgical and Materials Engineering,
Indian Institute of Technology Kharagpur, Kharagpur, India, 721302

Keywords: Strain, Density of states, Resistivity, Optical conductivity

Abstract

Lanthanum nickelate ($LaNiO_3$) is a promising material for stable fuel-cell electrode, opto-electronic and magneto-electronic devices. Density functional theory (DFT) based calculations were carried out to investigate the effect of strain on the physical properties of the correlated metal $LaNiO_3$. Electronic structure, optical conductivity and temperature variation of resistivity have been studied in detail using GGA+U approach. It has been observed that $LaNiO_3$ under strain is more metallic compared to the unstrained system. However $LaNiO_3$ under compressive strain is found to be more metallic than that under tensile strain. Electron localization function calculation revealed that $LaNiO_3$ under tensile strain has more covalent bonding than that under compressive strain, which results in an increase in resistivity for the system under tensile strain. The theoretical understanding of the alternation of physical properties of the system, caused by misfit strain may help in the application of the system in different device purposes using strain engineering.

Introduction

Lanthanum nickelates ($LaNiO_3$), a member of the rare-earth nikelates series, has recently brought considerable attention due to its potential application in the field of thin film oxide electronics and fuel cell technology as a conducting electrode [1]. The popularity of $LaNiO_3$ as an electrode material lies in its metallic nature, which remains unaffected by any change in temperature. Apart from electrodes, $LaNiO_3$ is also a potential candidate for various opto-electronic and magneto-electronic devices [2]. Device application of this material in various fields demands a precise control over its physical properties and recently, strain engineering has emerged as a very popular tool which can adjust the electronic and structural properties of complex oxides according to the device requirements [3]. Recent experiments on $LaNiO_3$ have indicated that strain engineering can be extremely useful in finding new emergent phenomena in this compound as well [4]. Despite intense research efforts, very less has been explored in the theoretical front, regarding the effect of misfit strain on the physical properties of $LaNiO_3$ and its effect on the strong electronic correlation that the system possesses. This paper intends to give a clear insight of strain based control over the physical properties of $LaNiO_3$ within the framework of density functional theory (DFT). The theoretical understanding of the alternation of physical properties of the system, caused by misfit strain may help in the application of the system in different device purposes using strain engineering.

Computational Details

$LaNiO_3$ is known to have a rhombohedral crystal structure with $R\bar{3}c$ symmetry [5]. Density functional calculations were performed using VASP (Vienna ab initio simulation package) [6]. To incorporate the effect of electronic correlation within $LaNiO_3$, the local spin density + Hubbard *U* (LSDA+U) approach using GGA-PBE functional was adopted. The energy functional in GGA+U calculation is expanded to include the onsite Hubbard *U* term as well as the Hund's coupling term *J*. This method treats the effective electron interaction U_{eff} to be *U-J* and reproduces the correct ground states [7]. In case of our calculation, an effective *U* value of 3 eV was used. The atoms were fully optimized in all the cases and a 600 eV plane wave cut off with a 2x2x2 k-mesh, centered at the gamma (Γ) point, was used to optimize the unit cell using Gaussian integration scheme of width 0.1 eV. A force convergence of 0.01 eV/Å was obtained and the self-consistency was achieved within 10^{-5} eV. Different in-plane strains, both tensile and compressive in nature, were applied on $LaNiO_3$ within the DFT framework. For both unstrained and strained $LaNiO_3$ we calculated all the transport properties using the Boltz-Trap code [8] within the relaxation time approximation.

Results and discussion

Various in-plane tensile and compressive strains were applied within DFT, to study how the physical properties of $LaNiO_3$ can be tuned by applying external strain. While tensile strains are denoted by a '+' sign as they increase the lattice parameters, compressive strains are denoted by '-' sign as it reduces the same. The total and partial density of states (DOS) for unstrained rhombohedral $LaNiO_3$ is shown in Figure 1(a). While the La 4f and 5d states constitute mostly the unoccupied state above the Fermi level, the states at the Fermi level comes from the hybridization between Ni 3d and O 2p orbitals which puts the system into the category of conducting materials. The variation of resistivity with temperature for the unstrained $LaNiO_3$ compound is shown in Figure 1(b). $LaNiO_3$ exhibits a positive temperature coefficient of resistivity like a metal for the whole range observed, and has a room temperature resistivity (ρ) of 1.5 mΩ-cm which matches well with earlier studies [5]. While the linear variation of resistivity with temperature above 200 K is indicative of electron-phonon scattering, the quadratic behavior of resistivity below 200 K indicates that the low temperature transport is governed mostly by electron-electron scattering [9].

As various in-plane tensile and compressive strains are applied on the system, a drastic change in the conductivity is observed. To examine the effect of strain on $LaNiO_3$, optical conductivity calculations were carried out within density functional theory, for various tensile and compressive strains (-2% to 2%). Changes in the real part of the optical conductivity for $LaNiO_3$ under different magnitudes of strain are shown in Figure 2(a). For $LaNiO_3$ without strain, a Drude peak, a typical feature of a metal, is present. Additionally, there are certain peaks appearing in the optical spectra, which bear the signature of inter-orbital electronic transitions. From the density of states it is clear that, in the unstrained case, the population at Fermi level is governed by overlap between Ni 3d and O 2p orbitals and the peak arising at 4.2 eV is coming from the electronic transition between Ni 3d to La 4f and La 5d orbitals.

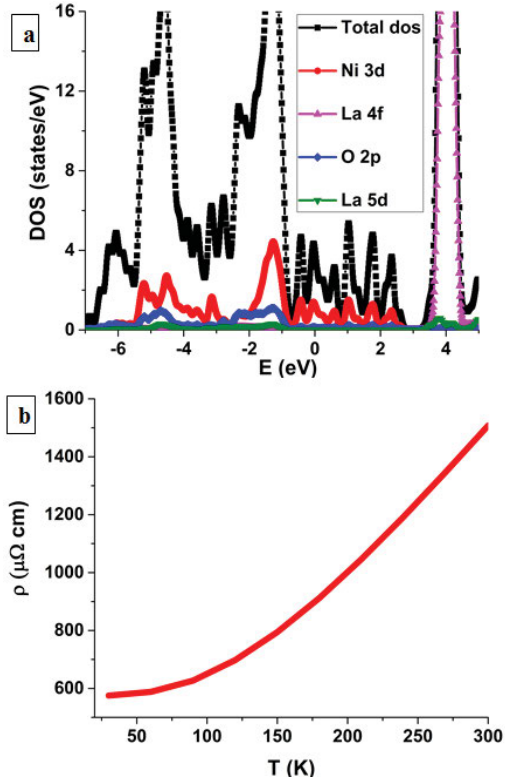

Figure 1: (a) Density of states and **(b)** ρ vs T plot for unstrained $LaNiO_3$.

Similarly the features appearing at relatively higher energies at 6 eV, 8.5 eV and 11 eV owe their origins to the transitions between O 2p to La 4f and La 5d orbitals. It is evident from Figure 2(a) that, as tensile strain is applied to the system; the peaks are getting shifted towards the lower energy region, trying to suppress the inter-band transition compared to the system under compressive strain. Compressive strain appears to enhance the inter-band transitions, shifting the peaks towards the higher energy region.

Variations of resistivity with temperature for tensile and compressive strains of same magnitude were also analyzed to examine the effect of sign of strain on $LaNiO_3$ in more details. ρ vs T plots for 1% tensile and compressive strains are shown in Figure 3(a). For both tensile and compressive strains we observed that the system becomes more conducting under strain, compared to the unstrained case. The variation profiles remain the same as the unstrained case but the magnitudes reduce by a factor of 10^3. Strikingly, $LaNiO_3$ under compressive strain becomes more metallic than that under tensile strain. Our findings match well with some earlier experimental studies [3].

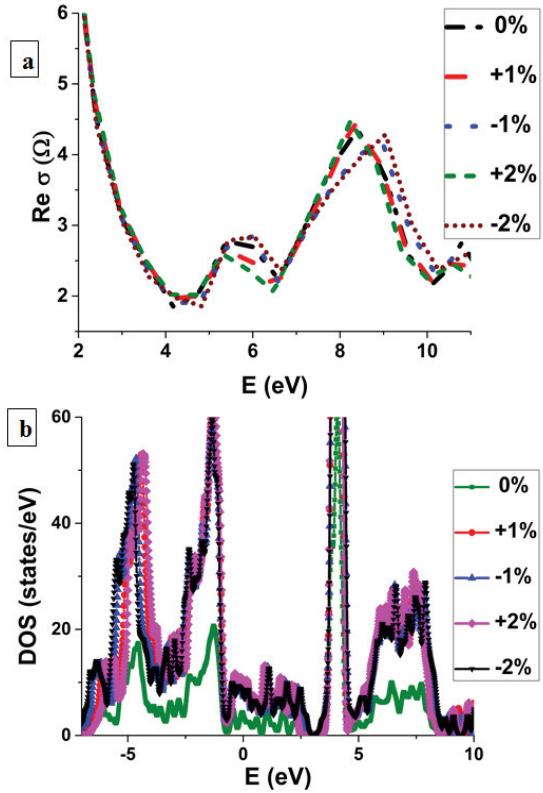

Figure 2: Changes in **(a)** optical conductivity and **(b)** total DOS of $LaNiO_3$ under various strains.

To see if the sign of strain alters the chemical bonding in the system, we calculated the electron localization function (ELF) and ELF plots for (012) planes containing Ni—O bonds in $LaNiO_3$ under 1% compressive and tensile strains respectively, are shown in Figure 3(b). Unstrained $LaNiO_3$ is known to have a mixture of both ionic and covalent bonding. Ionic bonding promotes metallic nature, whereas covalent bonding is responsible for insulating nature of a system. While high ELF value ('1') indicates localization, low ELF ('0') value reflects delocalization of electrons. It can be clearly seen that as strain evolves from -1% to +1%, electron localization in the system increases which in turn increases the covalent parts of the chemical bonding. The increased localization due to tensile strain hinders the itinerary of free electron and hence there is an increase in resistivity due to tensile strain compared to compressive strain.

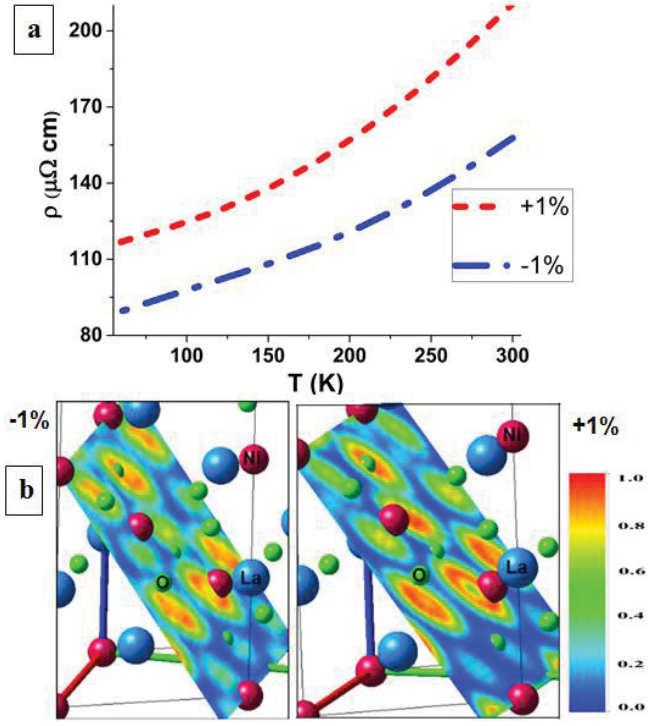

Figure 3: (a) Resistivity under strain and **(b)** ELF plots for $LaNiO_3$ under -1% and +1% strain respectively.

Summary

The electronic structure and transport properties of $LaNiO_3$ are highly sensitive to the magnitude and sign of external strain. Effect of strain on rhombohedral $LaNiO_3$ was investigated using first-principle calculations. $LaNiO_3$ without strain is characterized by a quadratic variation of resistivity below 200 K and a linear variation with temperature above 200 K. The optical conductivity spectra show a distinct Drude peak, typical of metal, and several inter-band transitions. Applying various in-plane tensile and compressive strains on the system, it was observed that strain enhances the conductivity of the system compared to the unstrained case. While tensile strain has a tendency of suppressing the inter-band electronic transition compared to compressive strain, compressive strain seems to enhance the conductivity more. The ELF calculation revealed that compared to compressive strain, system under tensile strain has more covalent bonding which corroborates the increase in resistivity under tensile strain.

References

[1] R. Scherwitzl, P. Zubko, C. Lichtensteiger, and J.M. Triscone, "Electric-field tuning of the metal-insulator transition in ultrathin films of $LaNiO_3$," *Appl. Phys. Lett.*, 95 (2009), 222114-1-222114-3.

[2] J.J. Zhu, W.W. Li , Y.W. Li , Y.D. Shen, Z.G. Hu, and J.H. Chu, "Effects of applied electrical field on electronic structures in $LaNiO_3$ conductive metallic oxide film: An optical spectroscopic study," *Appl. Phys. Lett*., 97 (2010), 211904-1-211904-3.

[3] M.K. Stewart, C.H. Yee, J. Liu, M. Kareev, R.K. Smith, B.C. Chapler, M. Varela, P.J. Ryan, K. Haule, J. Chakhalian, and D. N. Basov, "Optical study of strained ultrathin films of strongly correlated $LaNiO_3$," *Phys. Rev. B*, 83 (2011), 075125-1-075125-8.

[4] S. J. May, J.W. Kim, J.M. Rondinelli, E. Karapetrova, N.A. Spaldin, A. Bhattacharya, and P.J. Ryan, "Quantifying octahedral rotations in strained perovskite oxide films," *Phys. Rev. B*, 82 (2010), 014110-1-014110-7.

[5] N. Gayathri, A.K. Raychaudhuri, X.Q. Xu, J.L. Peng and R.L. Greene, "Electronic conduction in $LaNiO_{3-\delta}$: the dependence on the oxygen stoichiometry δ," *J. Phys.:Condens. Matter*, 10 (1998), 1323-1338.

[6] G. Kresse, and J. Furthmuller, "Efficient iterative schemes for ab initio total-energy calculations using a plane-wave basis set," *Phys. Rev. B*, 54 (1996), 11169-11186.

[7] G. Gou, I. Grinberg, A.M. Rappe, and J.M. Rondinelli, "Lattice normal modes and electronic properties of the correlated metal $LaNiO_3$," *Phys. Rev. B*, 84 (2011), 144101-1-144101-13.

[8] G.K.H. Madsen, D.J. Singh, "BoltzTraP. A code for calculating band-structure dependent quantities," *Computer Physics Communications*, 175 (2006), 67-71.

[9] M. Zhu, P. Komissinskiy, A. Radetinac, M. Vafaee, Z. Wang, and L. Alff, "Effect of composition and strain on the electrical properties of $LaNiO_3$ thin films," *Appl. Phys. Lett.*, 103 (2013),141902-1-141902-5.

HYDROGEN-INDUCED CORE STRUCTURES CHANGE OF SCREW AND EDGE DISLOCATIONS IN TUNGSTEN

Yinan Wang[1], Chengliang Li[2], Ben Xu[1,*], Wei Liu[1]

[1]Key Laboratory of Advanced Materials (MOE), School of Material Science and Engineering, Tsinghua University, Beijing 100084, PR China
[2]China Nuclear Power Engineering Co.,Ltd, Shenzhen 518172, China

[*]Corresponding author: xuben@mail.tsinghua.edu.cn

Keywords: screw dislocation, edge dislocation, QM/MM method

Abstract

A Quantum Mechanic/ molecular mechanical (QM/MM) method is employed in studying the screw and edge dislocation core structure of Tungsten. When absence of H, the widely used MEAM potential can successfully provide the core structure for both types of dislocations. However, no suitable W-H potential can describe the right structure when H is introduced. The coupling of the molecular dynamics and Ab initio calculation predicts a six-fold nondegenerate structure with a H atom added in screw dislocation, while in edge dislocation a partial dislocation appeared in the dislocation core.

Introduction

Recently, the increasing demand of energy calls for new energy sources which are more sufficient and environment-friendly. The thermonuclear fusion is considered to be a good candidate, but an appropriate plasma facing material (PFM) is one of the main issues for its implementation, since it is hard to maintain the mechanical properties when exposed to both plasma of He and H isotopes and other extreme conditions. Tungsten is chosen as one of the most promising PFM because of its high melting point and good thermal properties, etc [2]. However, hydrogen degrades the fracture behavior and causes hydrogen embrittlement, leading to the deformation and failure of the tungsten. The deformation and the fracture of the material is accompanied with the generation, growth and the motion of dislocation, while after hydrogen irradiation, the mobility of the dislocations may increase because the energy barrier of its movement will decrease, resulting in the microcracking and final instability of the material. So it is necessary to investigate the dislocations properties in tungsten and its deformation mechanisms with the presence of the hydrogen, in order to design better materials. Previous results show that bcc W screw dislocation will expand to three planes and form the asymmetric structure. After H irradiation, the core energy and Peierls potential in bcc metals both decreased when the hydrogen concentration increased, making the movement of dislocations easier [3].
In this paper, we first introduced the methods applied in our simulation, including the principle QM/MM relaxation steps, the molecular dynamic (MD) method and the density functional theory (DFT). Also we clarified the models we employed and visualization methods for both screw and edge dislocations. Then we presented our results and discussion of both screw and edge dislocation, in the cases with and without a hydrogen. Finally came the conclusion of our simulation.

Method

DFT and MD methods

The DFT calculations were performed within the spin-polarized generalized gradient approximation (GGA) [4], via the Vienna Ab-initio Simulation Package (VASP) [5-7] together with the projector augmented wave method and ultrasoft pseudopotentials were employed to realize the following simulations. We used the Blöchl's projector augmented wave (PAW) method [8] to describe the interactions between the ions and electrons. Brillouin zone sampling was carried out by using the Monkhorst-Pack scheme [9]. As for the MD simulations, a semi-empirical embedded atom method (EAM) potential based on a potential developed by X. W. Zhou *et al*. [10]. The original potential exhibited a different lattice constant and bulk modulus as the VASP results, making it unsuitable to deal with the coupling between the two methods. The embedded-atom method has a form like:

$$\mathrm{E}[R_i] = \sum_i F[\sum_{i\neq j} \rho^{EAM}(|R_{ij}|)] + \frac{1}{2}\sum_{i\neq j} \phi\left(\left|R_{ij}\right|\right) \quad (1)$$

We modified the potential by scaling both in r and in energy [11]:

$$\mathrm{F}[\rho] \rightarrow \alpha \mathrm{F}[\rho] \quad (2)$$

$$\rho^{EAM}(R) \rightarrow \rho^{EAM}(\beta R) \quad (3)$$

$$\phi(R) \rightarrow \alpha\phi(\beta R) \quad (4)$$

In this way the EAM potential function predicted a similar properties of tungsten system as the DFT one, which made it possible to do the QM/MM relaxation steps.
LAMMPS code was employed to carry out the MD simulations by integrating the Newton`s equations of motion. The time step was set to be 1 fs and a canonical NVT ensemble was used.

QM/MM method

In the study of dislocations, we employed a quantum mechanical (QM) and molecular mechanical (MM) coupling method [12], which divided the system into two regions: the core of the dislocation(I) and the surrounding area (Ⅱ). By this way we can predict the configuration of the dislocations properly because the inner defects could be described by the precise DFT method while the MD method could give the structures of the large influenced parts. Correctly dealing with the coupling part of the two methods, which we distinguished as part B, guaranteed the accuracy of our simulations. Here gives the following relaxation algorithm. (1) Minimize the total energy using MD method while holding I and b atoms fixed. (2) Perform one step of a conjugate-gradient minimization on the I and b atoms with the B atoms fixed. (3) Calculate the minimum energy of the I and B atoms with the I atoms fixed using MD method. (4) Repeat the process until the whole system is relaxed. In this way, the number of DFT calculations is greatly reduced, which made the process much quicker.

Dislocation models

As for the models employed in the calculations, the dislocations were set in the core of a cylinder. Considering an isolated 1/2<111>{-110} screw dislocation, we set the three dimensions as 28[112], 32[1-10], 2[11-1] along the X, Y, Z axes, and the whole system contains 13304 atoms. By the similar method, an isolated edge dislocation with Burgers vector 1/2[111] was built, and the other two dimensions were 72[-110] and 2[-1-12], leading to 78106 atoms as whole. Periodic boundary conditions are available in the Z direction which is along the dislocation line, while in X and Y directions the vacuum layers were applied outside of the simulation region during the simulation. To introduce the dislocations, we displaced the atoms according to the isotropic linear elastic fields [1]. H atom was added to the nearest tetrahedral interstitial to the dislocation core, which is the most stable position [13]. In the case of an edge dislocation, the space just below the extra half-plane of atoms acts as a trap for interstitial atoms, so we directly set the H atom there.

Visualization method

To illustrate the core structure of the screw dislocation, we used the differential displacement map (DD map) [14], as shown in figure 1, where the small vectors displays the relative displacement of neighboring W atoms introduced by the dislocation. The atoms are shown in [111] projection, which is the direction of the Burgers vector. The arrows are parallel to the line joining the two atoms, while the direction represents the sign, meaning that the atoms got smaller displacement after the dislocation added points to the larger one. In this case the length of the arrows is normalized by |a/6[111]|, one-third if the entire Burgers vector a/2[111]. A different tool was employed to represent the edge dislocation, called Nye tensor [15]. Specifically, a method based on the singular values and singular vectors of the Nye tensor was applied [16]. As shown in Figure 2, we distinguish the different Σ_i, the ratio between the norm of local Burgers vector and an ideal Burgers vector, by different colors. The red region represents a large ratio indicates the core structure of the edge dislocation. It is clear to see the structure of the dislocation core is localized.

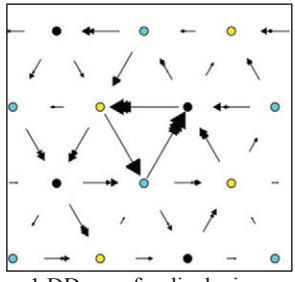

Figure 1 DD map for displaying screw dislocation. The Burgers vector is a/2[111], and different colors represents the different layers of atoms. The length of the arrows is proportional to the magnitude of displacement.

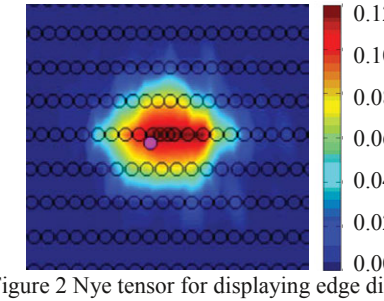

Figure 2 Nye tensor for displaying edge dislocation. The Burgers vector is a/2[111], and the black circles stand for the atoms. With the color changed from blue to red, the ratio the ratio between the norm of local Burgers vector and an ideal Burgers vector became larger.

Results

Configurations of screw dislocation cores

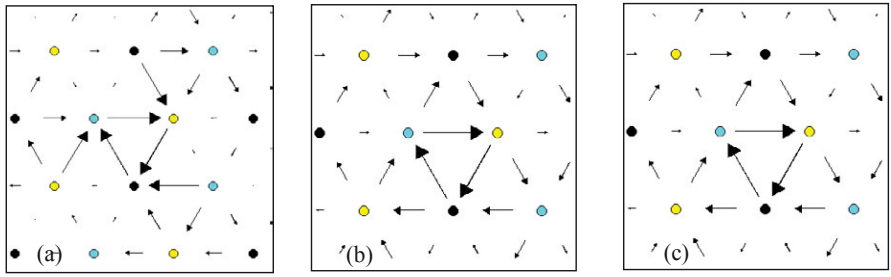

Figure 3 Screw dislocation predicted by EAM [10] (a), MEAM [21] (b) and QM/MM(c) methods. Meanings of the colors, arrows and its length are the same as figure 1.

Before we employed the QM/MM method to both screw and edge dislocations, a molecular dynamics (MD) method was tested using EAM [10], MEAM [21] and WCH-tersoff [17, 18] functions. Comparing the distinct results we found that the dislocation core structures predicted by various potential functions could be really diverse. Figure3 (a) revealed that for the EAM potential, the screw dislocation core is spread asymmetrically, basically into three {110} planes. We regard this phenomenon as a splitting into three adjacent {211} planes [19]. While the MEAM one is non-degenerate, expanding equally along the six <112> directions [20]. This is called the easy-core configuration, which is a typical non-polarized core, stands for the stable situation. Similarly, QM/MM presents a non-degenerate core structure like the MEAM result, implying that these two results are more reliable. Inserting a hydrogen atom did not disturbed the core structure, as shown in figure 4, because the volume of the hydrogen atom is not large enough to distort the lattice of tungsten and the compensation of local density leads to the strong binding in the present position. Instead the WCH-tersoff potential implied a split-core structure, which failed to give the reasonable configuration.

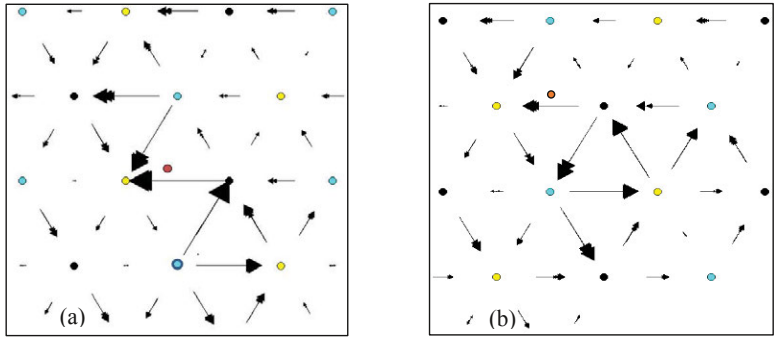

Figure 4 H (orange atom) added screw dislocation predicted by WCH-tersoff [17,18] (a)and QM/MM method(b). Meanings of the colors, arrows and length are the same as figure 1.

Configurations of edge dislocation cores

For edge dislocation, still we got different structures from different potentials. Figure 5 presents the EAM, MEAM and QM/MM results, revealing that all the method predicted a perfect dislocation, in spite the fact that EAM gave a wider core region than the MEAM and QM/MM ones. Up to here, the WCH-tersoff MEAM potential can still provide us satisfying information as the QM/MM methods. However, seeing from figure 6, after added a hydrogen atom to the

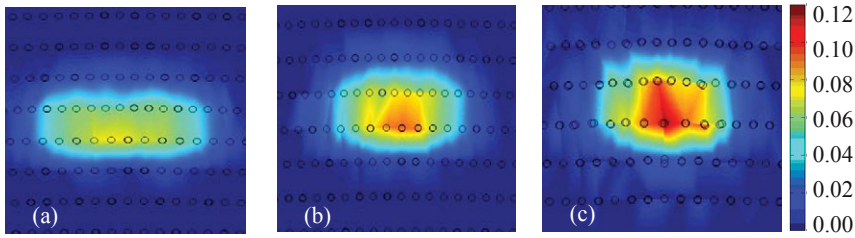

Figure 5 Edge dislocations predicted by EAM [10](a), MEAM [21](b) and QM/MM(c). Meanings of colors, circles and Burgers vector are the same as figure 2.

dislocation core, the WCH-tersoff potential predicted a paired partial dislocations structure instead of a perfect one, obviously different to the QM/MM result. In BCC metals, the stacking fault energy is too high, although little reduction can introduced by adjacent hydrogen atom, to observe the partial dislocations in edge dislocation. The influence of hydrogen atoms on the stacking fault energy will be discussed in our future work. Thus the configuration presented by the WCH-tersoff potential may considered to be unreliable, and the core structure of the edge dislocation became wider and show the tendency to split resulting from the adding hydrogen atom.

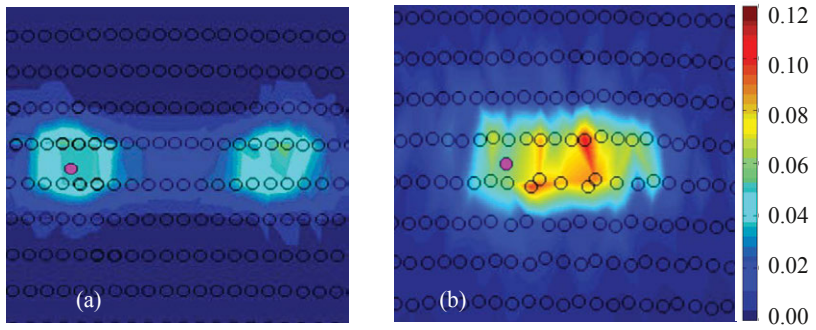

Figure 6 H (pink atom) added edge dislocations predicted by WCH-tersoff [17, 18] (a) and QM/MM method (b). Meanings of colors, circles and Burgers vector are the same as figure 2.

Conclusions

The QM/MM model derived a reasonable prediction of the screw and edge dislocation structures in bcc W. For screw dislocation, a non-degenerate and symmetric core structure was predicted which preserved its configuration after one hydrogen atom added. As for edge dislocation, no partial dislocations were found due to the high stacking fault energy, and one hydrogen atom could hardly influence the structure of the dislocation core. Compared with the MD method which differs a lot when selecting different potential functions, the QM/MM method presented a strong ability in predicting not only dislocation configurations but also other defects such as cracks and fracture.

Acknowledgment

This work was supported by the NSF of China 51301094 and by the Tsinghua National Laboratory for Information Science and Technology. The calculations were also conducted at the National Supercomputer center in Tianjin, and the calculations were performed on TianHe~1(A).

References

BOOK

1. Hirth, J. P., and J. Lothe. "*Theory of Dislocations, 2nd.*" Ed.: John Willey & Sons (1982).

JOURNAL

2. Zhou H B, Liu Y L, Jin S, et al. “Investigating behaviours of hydrogen in a tungsten grain boundary by first principles: from dissolution and diffusion to a trapping mechanism”, *Nuclear Fusion*, 2010, 50(2): 025016.

3. Baskes, M. I. "Modified embedded-atom potentials for cubic materials and impurities." *Physical Review B* 46.5 (1992): 2727.

4. Fuchs, Martin, and Matthias Scheffler. "Ab initio pseudopotentials for electronic structure calculations of poly-atomic systems using density-functional theory." *Computer Physics Communications* 119.1 (1999): 67-98.

5. Kresse, G., and J. Hafner. "Ab initio molecular dynamics for open-shell transition metals." *Physical Review B* 48.17 (1993): 13115.

6. Fuchs, Martin, and Matthias Scheffler. "Ab initio pseudopotentials for electronic structure calculations of poly-atomic systems using density-functional theory." *Computer Physics Communications* 119.1 (1999): 67-98.

7. Kresse, Georg, and Jürgen Furthmüller. "Efficiency of ab-initio total energy calculations for metals and semiconductors using a plane-wave basis set." *Computational Materials Science* 6.1 (1996): 15-50.

8. Blöchl, Peter E. "Projector augmented-wave method." *Physical Review B*50.24 (1994): 17953.

9. Monkhorst, Hendrik J., and James D. Pack. "Special points for Brillouin-zone integrations." *Physical Review B* 13.12 (1976): 5188.

10. Zhou, X. W., et al. "Atomic scale structure of sputtered metal multilayers."*Acta materialia* 49.19 (2001): 4005-4015.

11. Choly, Nicholas, et al. "Multiscale simulations in simple metals: A density-functional-based methodology." *Physical Review B* 71.9 (2005): 094101.

12. Liu, Yi, et al. "An improved QM/MM approach for metals." *Modelling and Simulation in Materials Science and Engineering* 15.3 (2007): 275.

13. Ramasubramaniam, Ashwin, Mitsuhiro Itakura, and Emily A. Carter. "Interatomic potentials for hydrogen in α–iron based on density functional theory." *Physical Review B* 79.17 (2009): 174101.

14. Vitek, V., R. C. Perrin, and D. K. Bowen. "The core structure of ½ (111) screw dislocations in bcc crystals." *Philosophical Magazine* 21.173 (1970): 1049-1073.

15. Hartley C S, Mishin Y. "Representation of dislocation cores using Nye tensor distributions."*Materials Science & Engineering A*, 2005, 400(8):18–21.

16. Dai, Fuzhi, and Wenzheng Zhang. "Identification of Secondary Dislocations by Singular Value Decomposition of the Nye Tensor." *Acta Metallurgica Sinica (English Letters)* 27.6 (2014): 1078-1082.

17. Yang, Xue, and Ahmed Hassanein. "Molecular dynamics simulation of deuterium trapping and bubble formation in tungsten." *Journal of Nuclear Materials* 434.1 (2013): 1-6.

18. Yang, Xue, and Ahmed Hassanein. "Molecular dynamics simulation of erosion and surface evolution of tungsten due to bombardment with deuterium and carbon in Tokamak fusion environments." *Nuclear Instruments and Methods in Physics Research Section B: Beam Interactions with Materials and Atoms* 308 (2013): 80-87.

19. Duesbery, M. and-S., and V. Vitek. "Plastic anisotropy in bcc transition metals." *Acta Materialia* 46.5 (1998): 1481-1492.

20. Samolyuk, German D., Y. N. Osetsky, and R. E. Stoller. "The influence of transition metal solutes on the dislocation core structure and values of the Peierls stress and barrier in tungsten." *Journal of Physics: Condensed Matter*25.2 (2013): 025403..

21. Park, Hyoungki, et al. "Ab initio based empirical potential used to study the mechanical properties of molybdenum." *Physical Review B* 85.21 (2012): 214121.

TMS2016

145th Annual Meeting & Exhibition

SUPPLEMENTAL
PROCEEDINGS

Computational Materials Engineering
for Nuclear Reactor Applications

Validation of BISON Calculation of Hydrogen Distribution by Comparison to Experiment

Evrard Lacroix[1] and Arthur Motta[1]

[1]Department of Mechanical and Nuclear Engineering,
The Pennsylvania State University, Pennsylvania, USA

Keywords: hydrogen, hydrides, BISON, transport, Soret effect, Fick's law

Abstract

During normal operation in nuclear reactors, the nuclear fuel cladding corrodes as a result of exposure to high temperature cooling water. During this process, hydrogen can enter the zirconium-alloy of the fuel cladding, and under proper conditions, precipitate as brittle hydride platelets which can severely impact cladding ductility and fracture toughness. Hydrogen tends to migrate to and precipitate at colder spots. Because high local hydride concentrations increase the risk of cladding failure, it is important to predict the local hydrogen distribution. To that end, a hydrogen transport model has been implemented in the 3D fuel performance code BISON. In this study, we present an initial attempt of using this model for benchmarking the BISON code as applied to a case of the hydrogen distribution measured in a nuclear fuel rod, which had undergone a five cycles exposure. The prediction of hydrogen distribution show good agreement with the post irradiation measurement, indicating the promise of this benchmarking method.

Introduction

In the core of a Light Water Reactor (LWR), the fuel pellets (UO_2) are contained in fuel rods. The nuclear fuel cladding tube prevents fission products from reaching the primary loop water. This tube is made of Zr-based alloys, because of their low neutron absorption cross-section (only 0.185 barns for thermal neutrons), superior resistance to high temperature corrosion and good mechanical properties [6]. However different phenomena can put the clad integrity into jeopardy. One of the main limiting factors to cladding performance is the ingress of hydrogen and consequent hydride embrittlement.

During corrosion, zirconium reacts with the oxygen present in the water. A fraction of the hydrogen generated by the corrosion reaction (i.e. the hydrogen pickup fraction) is absorbed by the cladding. Once in the cladding, the hydrogen either dissolves in solid solution in the interstitial sites of the $\alpha-$Zr matrix or precipitates in the form of zirconium hydrides (ZrH_x).During mechanical deformation of the cladding tube, those hydrides can fail at low strain thus decreasing cladding ductility [7]. Hydrogen in solid solution is mobile in the zirconium matrix and responds to concentration gradients (following Fick's Law) and temperature gradient (Soret Effect) as described in [1].

During normal operation, temperature gradients may exist in the cladding in the three directions (radial, axial and azimuthal). Radial gradients exist during operation

because of the heat flux passing through the cladding. Axial temperature gradients occur not only due to the gradual heating of the coolant along the axis such that at the higher grid spans corrosion is higher but also at the inter-pellet gaps where a local decrease of temperature is observed, which causes a higher hydrogen concentration. Finally, azimuthal variations can also be observed for various reasons such as: (i) a power gradient, caused for example by a pin having a control rod on one side and a highly enriched pin on the other [2] or (ii) oxide spallation causing a differential cooling around the cladding circumference. The resulting temperature gradients may create an inhomogeneous repartition of the hydrogen in the cladding.

Because the terminal solid solubilities for hydride dissolution increases with temperature, hydrogen tends to precipitate at the cooler spots near the outer rim. Therefore, a higher concentration of hydrogen at the cladding rim is observed at high burnup (the hydride rim). The hydride rim is located at the outer edge of the cladding and shows a very high hydrogen concentration, going up to 6,000 wt.ppm, as observed by Zhang [3].

The previous discussion has illustrated the importance of a tool that can predict hydrogen transport and precipitation, and that is benchmarked to reactor data. This study is an initial attempt to perform such a benchmarking study.

Experimental Data

Gravelines' Fuel Pin Data

The data used in this article was used in a previous study by J.-H. Zhang [3] and comes from the rods irradiated at the Gravelines nuclear power and which were and subjected to post irradiation examination. The characteristics of the pin studied are shown in Table I.

The interest of studying this pin was that it has reached a high burnup (about 60 GWd/tU) and was very well characterized in terms of hydrogen content. This study also included a hot vacuum extraction analysis to obtain the overall hydrogen content.

Table I: Studied fuel pin characteristics

Clad Material	Zircaloy-4	Number of cycles	5
Fuel	UO_2	Enrichment ($\%^5U$)	4.5
Z position (mm)	3250	Burnup (MWd/tU)	58 230
Outside diameter (mm)	9.49	Inside diameter (mm)	8.36
Pressure (bars)	155	Mass Flux ($g\,cm^{-2}\,s^{-1}$)	314
Inlet Enthalpy ($J\,g^{-1}$)	1 264	Inlet Temperature (°C)	286
Outlet Temperature (°C)	323		

Measurements

Measurements of the hydrogen content were performed using image analysis of micrographs taken from a cross-section of the fuel cladding, which had been etched to reveal

the hydrides. This analysis allowed to have a radial and azimuthal experimental distribution of the hydrogen in the cladding. The experimental data consists of four radial data points in four different azimuthal zones, defined by a rotation of 90° on the tube, which makes a total of sixteen data points for this pin. After abrasion of 9 µm off the outer cladding surface, it was possible to determine that the hydrogen content in that part of the cladding was 6 000 wt.ppm, which gives one more data point.

Data from the reactor operating conditions were also given. With these parameters, it is straightforward to compute the cladding outside temperature at the given z coordinate (given in Table I.) This allowed to calculate the hydrogen distribution with BISON and to compare it to the experimental data (Table II).

Table II: *Hydrogen experimental distribution determined by Image Analysis, quantities are given in wt.ppm*

Radial position µm	left	top	right	bottom	Average [H] per layer
499	685	713	726	745	717 ± 80
356	430	469	537	490	482 ± 80
214	195	142	244	296	219 ± 80
71	206	173	169	129	169 ± 80
Average	379	374	419	415	392 ± 40

The hydrogen distribution measurements made by J.-H. Zhang [3] have an accuracy of ± 80 wt.ppm, which creates a significant difference in overall hydrogen content: 392 wt.ppm is found by image analysis when 541 wt.ppm is found by hot vacuum extraction (HVE). A difference between Image analysis and the HVE measurements should be observed because the hydrogen content in this sample is very high and the software see overlapping hydrides and therefore calculates a hydrogen concentration below the real one. To address this issue, it is assumed that the missing hydrogen content is not seen in the first layer (position 499 µm). Therefore, since the hydrogen content found by HVE is 541 wt. ppm. and since Zhang found a hydrogen rim of 6000 wt. ppm. on a 9 µm thickness, it is possible to calculate the hydrogen content that is actually present in this layer. The value found is 861 wt.ppm.

BISON Simulations And Results

Assumptions And Introduction To The Subject

A few parameters are missing from the data set used in this work. For example, the environmental conditions or cladding outside temperature distribution were not given, and it was not possible to retrieve the position of the fuel pin in the assembly, and thus, it was difficult to determine the temperature gradient experienced by this pin. As a first

approach it was decided not to implement an azimuthal temperature gradient, and ton only focus on the radial hydrogen distribution: the experimental data was averaged over the azimuth (average per layer) which thus gave an average radial distribution over the whole azimuth.

In the study, no data of the neighboring fuel pins was provided, it was hence assumed that those pins do not influence the pin studied other than providing neutrons and heating the coolant. Furthermore, it has been considered that the influence of the stress gradient in the cladding on hydrogen migration is negligible compared to the influence of a temperature gradient by the Soret effect and a concentration gradient described by Fick's law, as shown by Puls in 2002 [9].

Problem Description, And Input Parameters

The hydrogen concentration in solid solution gradually increases in the cladding during reactor exposure due to hydrogen pickup until reaching the terminal solid solubility for precipitation (TSS_p) in colder spots. This leads to a complex picture of hydrogen migration, hydride dissolution and precipitation, which can be predicted by the hydrogen model in BISON. In this study, the operating conditions used are those used in the calculations made by J.-H. Zhang [3] based on the data given in Table I.

For Zircaloy-4, it has been reported that 10-20% of the hydrogen produced during the corrosion reaction is picked up by the cladding [5]. The value of 15% has been chosen here as an average value while noting that recent studies have shown the hydrogen pickup fraction to be variable over the exposure time. A reactor shutdown schedule needs to be included in the simulation since the observations were made at room temperature, and most hydrides precipitate during shutdown and the specific cooling rate should affect the hydride distribution seen at low temperature [1].

It is also considered that after the beginning of the shutdown, the fuel pin delivers 7% of the power it was delivering during its cycle at Hot Full Power, and slowly decreases following the equation (1):

$$\frac{P}{P_0} = 0.066 \left((t - t_0)^{-0.2} - t^{-0.2} \right) \tag{1}$$

Where P_0 is the reactor power before shutdown, t the time elapsed since reactor startup, t_0 the time of reactor shutdown and P the power at the considered time t as shown by A.R. Knief [8]. During the same time, the bulk temperature slowly cools down by steps, according to the reactor shutdown procedure given by J.-H. Zhang [3]. The power distribution and average clad outside temperature distribution are shown in figure 1 while figure 2 shows the outside clad temperature of the pin as a function of time during shutdown. With these input parameters it is possible to calculate the hydrogen content absorbed by the cladding and its distribution within the cladding, and compare it to the experimental data, as shown in figure 2 (right graph).

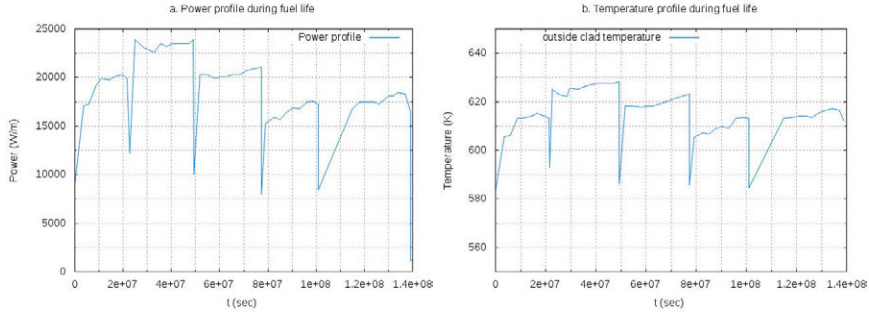

Figure 1: *linear power at the axial location (a.) and outside clad Temperature (b.) variation of the pin 1079 with respect to time*

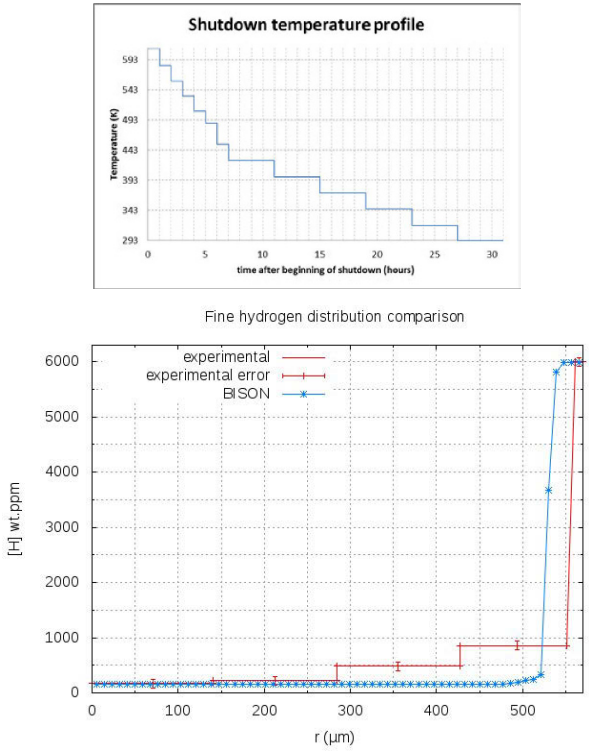

Figure 2: *Shutdown temperature profile of the pin 1079 (left) BISON caluclation results (right)*

As seen in fig. 2, the hydrogen distribution given here is not very accurate. Even though the total hydrogen content closely corresponds to the experimental measurement (542.5 versus 541), all of the hydrogen is calculated to precipitate near the metal/coolant interface. This can be explained by a numerical feature of BISON: there is no nucleation, germination and growth model of the zirconium hydrides implemented in the hydrogen model used in BISON. Therefore, the hydrogen follows the Soret effect and precipitates as soon as it enters the cladding, if the hydrogen content is higher than the TSS_p. This suggests that a nucleation model is needed to better describe hydride precipitation, but a work around is described in the next section.

Fine Mesh Description of Hydrogen Distribution

Experimental data consisted of only five points, i.e. the regular four image analysis points and the hydrogen content in the hydride rim. In this section, results obtained using BISON are compared to the experimental data in fig. 2 and 3. For this purpose, a mesh with sixty-four radial nodes and one hundred and forty four azimuthal nodes in order to have a 8.9 µm radial precision on the hydrogen distribution and thus have a node size comparable to the rim size found experimentally.

It has been observed that in the BISON calculation, when hydrogen is initially homogeneously distributed at $t_0 = 0s$, the final distribution matches the experimental data. In order to have a simulation that both simulates the hydrogen ingress and computes its distribution, a script has been made to counteract the nucleation problem. This script runs BISON a first time on a coarse mesh to obtain the hydrogen ingress, then reads the total hydrogen content in the cladding at the end of the simulation, and then performs another BISON run with no hydrogen pickup, and with the previously obtained hydrogen content homogeneously distributed in the cladding initially. The last run is made on the fine mesh described above, to calculate the hydrogen distribution on a fine mesh.

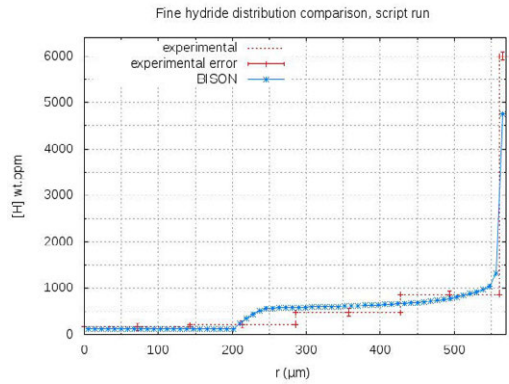

Figure 3: *Hydrogen distribution comparison between experimental data and BISON calculations on a 64 layer mesh*

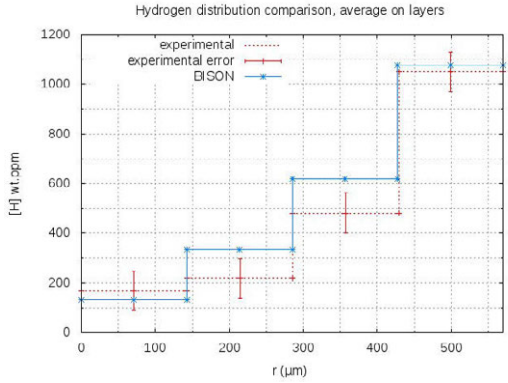

Figure 4: *Hydrogen distribution comparison between experimental data averaged on the 4 experimental layers*

It is important to keep in mind that the numerical model cannot compute the maximum hydrogen content in the metallic matrix at operating conditions. A "clamp parameter" has been put in place in BISON and has been set so that the maximal total hydrogen content (hydride + solid solution) is 6,000 wt.ppm, to match the experimental hydrogen content in the rim. The resulting radial hydride distribution is given by figures 3 and 4, and the previous experimental results have been added (with the extra data point provided by the zirconium hydride rim) for comparison. We can see that the hydrogen distribution calculated by BISON is very close to that observed experimentally.

The plot in figure 3 shows that the hydride rim thickness is well estimated by BISON although its hydrogen content is not the same, Zhang [3] showed that the hydrogen content in those samples was 6,000 wt. ppm. whereas BISON calculates it to be 4,750 wt.ppm. and the overall hydrogen distribution matches the experimental results reasonably well. It is considered that the results obtained are satisfying, given the paucity of data on operation conditions. However, when just looking at the hydrogen content in all four layers, we see that the hydride distribution given by the graph on figure 4, shows very good agreement with the experimental results.

Figures 3 and 4 also show a high concentration of zirconium hydrides in the cold regions (near the cladding/coolant interface), and a lower concentration of these species in the hot regions (near the cladding/gap or cladding/pellet interface), as predicted by the Soret effect, showing that hydrogen migrates from hot regions to cold regions. When the TSS_p is reached, hydrogen starts precipitating as zirconium hydrides and forms a rim. This rim can be observed in figure 3. As hydrogen migrates to the cold zones, hydrogen continues to precipitate until it can no longer do so, either because of mobility issues or because no more precipitation sites are accessible.

Discussion

As can be seen in the previous figures, the hydrogen distribution calculated by BISON is very close to that found experimentally. This difference in hydride content in the rim may come from the fact that this distribution is made without any model of nucleation, germination and growth of the zirconium hydrides. If the physics of that were to be implemented in the model, a difference in the distribution may be seen. Also, even though the stress gradient induced migration is negligible with respect to the Soret effect, this phenomenon coupled to the nucleation model described may be enough to make up for the slight mismatch in the hydride rim content observed in this study.

Even though this study shows promising results on the model's capability to predict zirconium hydride distribution, it is important to perform further benchmarking. To that effect a series of experiments will be held by the authors, that will allow to test the model with different kind of temperature gradients.

Conclusion

This study documents the benchmarking of the model implemented in BISON for hydrogen transport and precipitation. It is also the first comparison between the model calculations and in-reactor experimental data. Thus allowed to have a better understanding of the physics put in place during reactor shutdown, such as the precipitation kinetics that are dependent on the temperature of the clad [3,4].

Overall, the model showed a very good match with experimental results even though a mismatch can be observed in the rim's hydrogen content. The most important part of this type of simulation is to accurately predict the hydrogen content in the weakest point and thus, near the colder part of the cladding where the hydride rim forms. The size of the hydride rim is the same as that observed experimentally but the hydride content differs by about 20% from the experimental data.

In conclusion, the hydrogen distribution shows very good agreement between the experimental and numerical data. It can also be seen that the hydrogen model shows good agreement with the TSS_p and the TSS_d values and a slight over saturation can be observed in the kinetics during shutdown. In order to continue benchmarking the model, it has been decided to create an experiment which will consist of putting a ZIRLO tube under a controlled temperature gradient, this way, a very well defined environment will be established and the benchmarking of the 3D finite element code BISON will be possible. Once this task will be done, BISON will be used coupled with other high fidelity codes, such as DeCART and Cobra TF to compute the hydrogen distribution in more complex areas of the reactor such as near the mixing vanes.

Acknowledgments

This research was funded by DOE NEUP project 13-5180 of the US Department of Energy. This work is the result of collaborative project between Penn State University and the Idaho National Laboratory, which includes Maria Avramova (PSU), Kostadin Ivanov (PSU) and Richard Williamson (INL). We would like to thank Mike Mankosa and the BISON users' list for all the help in configuring, installing and troubleshooting BISON.

References

1. O. Courty, A.T Motta and J.D. Hales, "Modeling and simulation of hydrogen behavior in Zircaloy-4 fuel cladding", *Journal of Nuclear Materials*, 452 (2014), p.311-320.

2. C. Dances et. al. "Anisotropic Azimuthal Pozer and Temperature Distribution Impact on Hydride Distribution", (Paper presented at the 2014 ANS Winter Meeting and Nuclear Technology Expo, November 9-13, 2014, Anaheim, CA).

3. J.-H. Zhang "Hydruration du Zircaloy-4 et étude de la distribution de l'hydrogène dans une gaine de combustible REP", (Ph.D. Thesis, Commissariat à l'Énergie Atomique, France, 1992).

4. B.F. Kammenzind, D.G. Franklin, H.R. Peters, W.J. Duffin, *11th International Symposium on Zr in the Nuclear Industry*, 1996, ASTM STP 1245, p. 338-370.

5. A. Couet, A. T. Motta, Robert J. Comstock "Hydrogen pickup measurements in zirconium alloys: Relation to oxidation kinetics", *Journal of Nuclear Materials*, 451 (2014) 1-13.

6. Allen, T.R., R.J.L. Konings, A. T. Motta and J.M.K. Rudy, Editor-in-Chief, "5.03 - Corrosion of Zirconium Alloys", in *Comprehensive Nuclear Materials*, Oxford: Elsevier (2012) 49-68.

7. Daum, R. S., D. W. Bates, D.A. Koss and A.T. Motta, "The influence of a hydrided layer on the fracture of Zircaloy-4 cladding tubes", *International Conference on Hydrogen Effects on Material Behavior and Corrosion Deformation Interactions*, sep 22-26, 2002, Moran, WY, United States (2003) Minerals, Metals and Materials Society, Warrendale, PA 15086, United States, 249-258.

8. R. A. Knief, "Nuclear Engineering. Theory and technology of commercial nuclear power". American Nuclear Society, Inc 555 North Kensington Ave, La Grange Park, Illinois 60526 USA. ISBN-10:0-89448-458-3.

9. Plus, M.P., C. Leitch and S. Shi, "The Effect of Applied Stress on the Accommodation Energy and Solvi for the Formation and Dissolution of Zirconium Hydride", *In Proc. Int. Conference on Hydrogen Effects on material Behavior* (2002). Moran, WY: TMS.

TMS2016

145th Annual Meeting & Exhibition

SUPPLEMENTAL
PROCEEDINGS

Computational Methods for Uncertainty Quantification, Model Validation, and Stochastic Predictions

TMS2016 Annual Meeting Supplemental Proceedings
TMS (The Minerals, Metals & Materials Society), 2016

EFFECT OF K-POINT CONVERGENCE ON DERIVED PROPERTIES FOR PURE CRYSTALS

Thomas C. Allison[1]

[1]Material Measurement Laboratory, National Institute of Standards and Technology, 100 Bureau Drive, Gaithersburg, Maryland, 20899

Keywords: planewave DFT, material properties

Abstract

In planewave DFT calculations, a number of parameters have an effect on the overall accuracy of the calculation. Typically, a few of these parameters are under user control and have a significant effect. In this proceeding paper, these effects are explored through calculations of an fcc Al model system. The convergence of the total energy and several derived properties (e.g. unit cell volume and bulk modulus) is assessed with respect to the number of k points used to sample the Brillouin zone and the magnitude of the smearing parameter. Results are compared to those computed using the tetrahedron method. It is seen that some properties converge quickly with respect to the varied parameters, while others are more sensitive.

Introduction

Planewave density functional theory (DFT) calculations are routinely applied to compute properties of crystalline materials. Though the DFT method and pseudopotential may be carefully chosen, it is common to use "typical" values for other critical convergence parameters such as the planewave cutoff energies. In many cases, particularly in geometry optimizations, this approach gives good qualitative or semiquantitative results. However, the typical convergence parameters are rarely optimal, and the effect of this lack of convergence on a number of quantities derived from the computed results is not well understood. The motivations for using unconverged input parameters are clear: validation of the input parameter set is time consuming and the use of converged input parameters can increase the expense of a calculation considerably. These concerns are often more important than an understanding of the uncertainty in the computed results that arises from the compromises made in the input parameter values.

Understanding the sources and effect of error and uncertainty in DFT calculations is receiving more attention in the literature lately. A few illustrative references are cited here, and the interested reader is encouraged to consult these for additional information. Moruzzi et al. [1] compared calculated thermal properties of 14 cubic metals to experiment. Kurth et al. [2] studied several DFT approximations for molecular and solid-state systems. Staroverov et al. [3] tested a number of DFT functionals on bulk solids and surfaces. The calculation of lattice constants of solids was considered by Haas et al. [4]. Hautier et al. [5] explored the effect of the accuracy of DFT on phase stability for ternary oxides. A comprehensive treatment of pure atomic solid crystals has been performed by Lejaeghere et al. [6]. This study comprises the largest and most comprehensive study of its kind to

date, considering different codes and DFT methods, comparing results to experimental values. Finally, Palumbo and coworkers [7, 8] have considered a number of factors affecting the accuracy and uncertainty of calculations on thermodynamic properties.

In this article, the effect of varying two commonly used input parameters, the number of k points used to sample the Brillouin zone and the value of the smearing parameter used with the Methfessel-Paxton first-order spreading method [9], will be assessed by comparison with values given by the tetrahedron method [10] for several derived properties. In particular, the total energy, optimal unit cell volume, and bulk modulus (and its pressure derivative) will be examined. Derived properties are obtained through fitting the Birch-Murnaghan equation of state [11, 12]. The effects will be illustrated via calculations of fcc Al.

Computational Methods

Density Functional Theory Calculations

All calculations were performed using Quantum ESPRESSO (version 5.0.2) [13]. The calculations presented below were made for fcc Al using the Perdew-Burke-Ernzerhof (PBE) exchange-correlation functional with a scalar relativistic Vanderbilt ultrasoft pseudopotential due to Tambe et al. [14]. A kinetic energy cutoff of 100 Ry was used for the wavefunction and a cutoff of 1200 Ry was used for the charge density and potential. The self consistent energy was converged such that the error estimate was less than 1×10^{-10} Ry. Monkhorst-Pack grids were used to sample the Brillouin zone with the same number of k points used in each direction. A displacement of half of a grid step was found to lower the total energy and was used in all calculations.

Calculations were made for 5, 10, 15, 20, 25, 30 k points (in the x, y, and z directions). Results were obtained using the Methfessel-Paxton [9] smearing technique, and the tetrahedron method [10]. Smearing parameters of (0.025, 0.050, 0.100, 0.200, 0.300, 0.400, 0.500, 0.600, 0.700, 0.800, 0.900, 1.000) Ry were used.

Property Estimation

Each evaluation consisted of a 1d optimization (using the Brent method) of the lattice constant by minimizing the total energy as a function of lattice constant. This optimization was carried out with a tolerance of $1 \times 10^{-4} a_0$. Once the optimal lattice constant was found, calculations of the total energy were made at a set of eight displacements from the optimal point in increments of 0.02 a_0, with four points on either side of the optimal lattice constant value. This set of nine points was used to fit the parameters of the Birch-Murnaghan equation of state [11, 12].

$$E(\eta) = E_0 + \frac{9B_0V_0}{16}(\eta^2 - 1)^2 \left[6 + B_0'(\eta^2 - 1) - 4\eta^2\right] \tag{1}$$

where $\eta = (V/V_0)^{1/3}$, B_0 is the bulk modulus, B_0' is the derivative of the bulk modulus with respect to pressure, and V_0 is the equilibrium volume (from which the lattice constant may be obtained). The fitting was performed using a least-squares algorithm.

Results and Discussion

Convergence of Initial Parameters

Before the convergence due to smearing parameters and the number of k points used to sample the Brillouin zone is considered, the issue of convergence of the derived properties with respect to other critical parameters is addressed. Convergence in the total energy as a function of the wavefunction cutoff energy and the number of k points is presented in Table 1. It may be observed that the total energy converges very slowly with respect to the cutoff energy. It is clear, however, that the changes in energy are small (<0.01 eV/atom) at the larger cutoff energies. At this point, there is not a clear choice for the value for the cutoff energy. It was found that convergence with respect to the kinetic energy cutoff for charge density and potential was attained using a value of 12 times the kinetic energy cutoff for the wavefunction (as is recommended for ultrasoft pseudopotentials in Quantum ESPRESSO). Increasing this ratio did not significantly affect the results. Similarly, convergence with respect to the sizes of the FFT grids (the "hard" and "smooth" grids) was attained using the default values in Quantum ESPRESSO that are determined by the kinetic energy cutoff for the charge density and potential.

E_{cut} [Ry]	Total Energy [Ry]			
	$k = 5$	$k = 10$	$k = 15$	$k = 20$
20	−159.80673929	−159.80031514	−159.80245812	−159.80256838
30	−159.90546412	−159.90288753	−159.90291946	−159.90289834
50	−159.90985387	−159.90727722	−149.90730857	−159.90728719
100	−159.91355935	−159.91098317	−159.91101399	−159.91099251
200	−159.91745458	−159.91487951	−159.91490984	−159.91488821
400	−159.91951271	−159.91693762	−159.91696764	−159.91694594
800	−159.91976333	−159.91718825	−159.91721827	−159.91719656
1600	−159.92010866	−159.91753400	−159.91756485	−159.91754329

Table 1: Convergence of the total energy with respect to the value of the kinetic energy cutoff for the wave function (E_{cut}).

Convergence of the total energy to a particular tolerance may or may not be necessary to obtain converged values of derived properties. Values of the derived properties are presented in Table 2 for a range of wavefunction cutoff energies. It is seen that the property values rapidly converge by 50 Ry. For the purposes of the present study, a wavefunction cutoff energy of 100 Ry was used, which is more than sufficient to converge the properties of interest.

Limits on Smearing Parameter

A practical limit on the value of the smearing parameter used in the calculations on fcc Al was quickly found. This limit manifested itself in an increasing value of the optimal lattice constant as the smearing parameter was increased, with the value of the optimal lattice constant quickly growing too large (compared to the experimental value). This

E_{cut}	Energy [Ry]	B_0 [GPa]	B_0'	V [a_0^3]	a0 [a_0]
20	−159.80270089	126.75	17.01	111.26	7.6348
30	−159.90296626	75.90	3.48	111.72	7.6454
50	−159.90734297	76.81	4.78	111.60	7.6425
100	−159.91104571	76.89	4.69	111.53	7.6410
200	−159.91494120	77.00	4.77	111.52	7.6407

Table 2: Convergence of the total energy with respect to the value of the kinetic energy cutoff for the wave function (E_{cut}).

behavior is demonstrated in Figure 1. This behavior persisted for all k-point grid sizes studied, as well as for another choice of DFT method and pseudopotential.

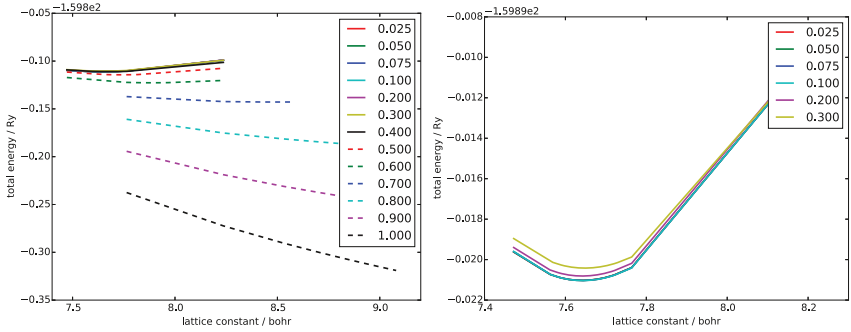

Figure 1: Plots of scans of total energy versus lattice constant for varying values of the smearing parameter.

Convergence of Smearing Parameter and k-point grid

Results on the simultaneous convergence of the smearing parameter and the size of the k-point grid that comprise the main contribution of this study are now presented.

Total energy A contour plot of the total energy as a function of the number of k points and the smearing parameter is given in Figure 2. It is seen that the surface is relatively flat with the notable exception the case where the number of k points and the smearing parameter are simultaneously small. The plot clearly shows that the value of the total energy is relatively insensitive to the number of k points used in the calculation, but that there is more variation due to the value of the smearing parameter. The colored contour regions coincide with the results obtained using the tetrahedron method in two places corresponding to smearing parameter values of approximately 0.4 Ry and less than 0.1 Ry.

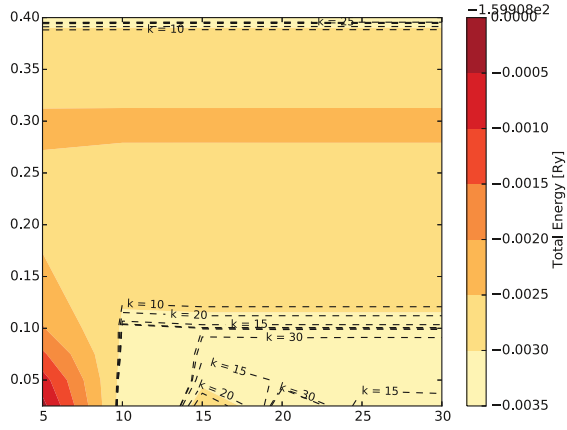

Figure 2: Plot of the total energy. The black lines denote contours where the Methfessel-Paxton results have the same value as the tetrahedron method for the number of k points shown.

Bulk Modulus The variation in the predicted values of the bulk modulus is shown in Figure 3. As with the total energy, the predicted value of the bulk modulus is not particularly sensitive to the number of k points used in the calculation, but is somewhat sensitive to the value of the smearing parameter. Smaller values of the smearing parameter tend to yield results that are in the best agreement with the tetrahedron method results (black lines on the contour plot). Two contour lines for $k = 30$ are shown on the plot for values of the smearing parameter of 0.075 Ry and 0.15 Ry. The contour lines for $k = 30$ are clearly bounded by the contour lines for $k = 20$ and $k = 25$ on either side, giving a limiting estimate of the uncertainty in the bulk modulus due to the number of k points used.

Pressure Derivative of the Bulk Modulus The behavior of the pressure derivative of the bulk modulus, presented in Figure 4, is markedly different from that of the bulk modulus. The contour plot is characterized by small values of the pressure derivative of the bulk modulus at small numbers of k points, but is relatively insensitive to the value of the smearing parameter. At 10 k points (per dimension) and above, the value of the pressure derivative of the bulk modulus remains relatively constant. Contour lines for $k = 20$ appear in this region, however, contour lines for larger number of k points are not shown as the predicted values for this property, 4.80 ($k = 25$) and 4.87 ($k = 30$), do not appear on the contour plot. This is thus a case where there is rapid convergence to a value that is not consistent with the results from the tetrahedron method (black contour lines).

Volume The optimal volume of the unit cell with respect to the change in smearing parameter and number of k points is shown in Figure 5. As has been seen previously, the

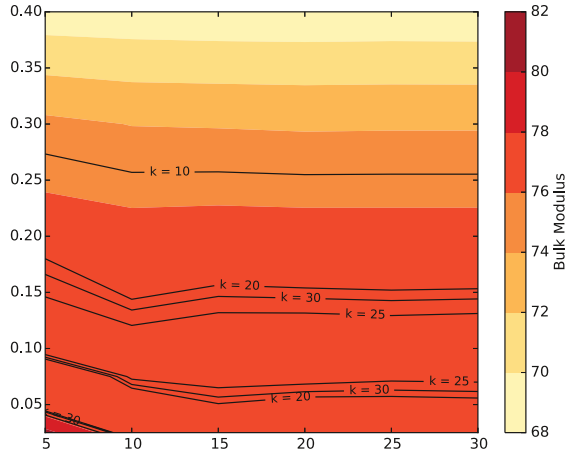

Figure 3: Plot of the bulk modulus.

convergence in the predicted value of the volume does not vary significantly with changes in the number of k points, and even at the smallest values of the smearing parameter and number of k points (the lower left of the plot), the variation is small. The values tend to agree best at smaller values of the smearing parameter (around 0.05 Ry). Increasing the value of the smearing parameter causes the volume to rise, albeit slowly, showing that this parameter is easily converged within 1–2% of it's limiting value (as compared to the tetrahedron results) with a wide range of parameters.

Conclusion

In this article, initial results for property predictions of the fcc crystal structure of Al are shown. A future study will expand on the results presented here by considering more elements and crystal structures, different codes, and different smearing methodologies to give a fuller picture of the effect of parameter convergence on derived properties. When computing derived properties such as those studied in this article, it is important to understand the effect that unconverged parameters can have on the resulting quantities.

The present results show that results for various derived properties can vary significantly with differing numbers of k points and smearing parameter values. It is shown that large numbers of k points and intermediate values of the smearing parameter tend to yield the best results, whereas other results may not be as well converged. For example, the geometric properties (unit cell volume, and the lattice constant) converged quite rapidly with little sensitivity to the k-point convergence, whereas the total energy was very sensitive to the wavefunction cutoff energy, but only somewhat sensitive to the smearing parameter. Rapid convergence in geometric properties is also seen in the value of the wavefunction cutoff energy (see Table 2), with slower convergence in the bulk modulus

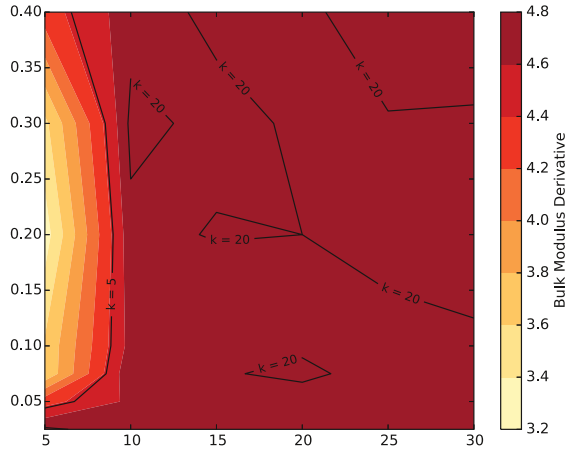

Figure 4: Plot of the pressure derivative of the bulk modulus.

and its derivative. The bulk modulus was most sensitive to the smearing parameter, whereas its pressure derivative was sensitive to the smearing parameter only at small numbers of k points.

References

[1] V. L. Moruzzi, J. F. Janak, and K. Schwarz. Calculated thermal properties of metals. *Phys. Rev. B*, 37:790–799, 1988.

[2] S. Kurth, J. P. Perdew, and P. Blaha. Molecular and solid-state tests of density functional approximations: LSD, GGAs and meta-GGAs. *Int. J. Quantum Chem.*, 75:889–909, 1999.

[3] V. N. Staroverov, G. E. Scuseria, J. Tao, and J. P. Perdew. Tests of a ladder of density functionals for bulk solids and surfaces. *Phys. Rev. B*, 69:075102, 2004.

[4] P. Haas, F. Tran, and P. Blaha. Calculation of the lattice constant of solids with semilocal functionals. *Phys. Rev. B*, 79:085104, 2009.

[5] G. Hautier, S. P. Ong, A. Jain, C. J. Moore, and G. Ceder. Accuracy of density functional theory in predicting formation energies of ternary oxides from binary oxides and its implication on phase stability. *Phys. Rev. B*, 85:155208, 2012.

[6] K. Lejaeghere, V. Van Speybroeck, G. Van Oost, and S. Cottenier. Error estimates for solid-state density-functional theory predictions: an overview by means of the ground-state elemental crystals. *Crit. Rev. Solid State Mater. Sci.*, 39:1–24, 2014.

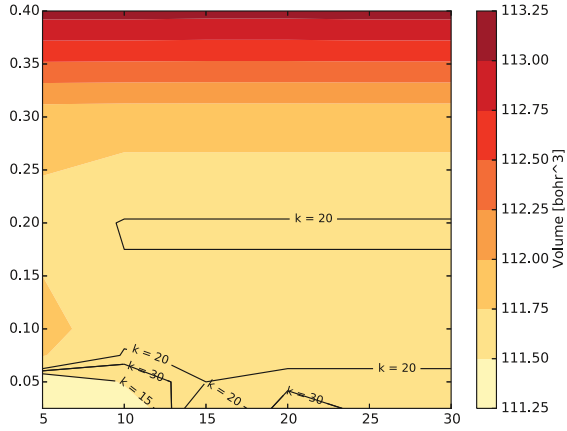

Figure 5: Plot of the unit cell volume.

[7] M. Palumbo, S. G. Fries, A. Dal Corso, F. Kürmann, T. Hickel, and J. Neugebauer. Reliability evaluation of thermophysical properties from first-principles calculations. *J. Phys.: Condens. Matter*, 26:335401, 2014.

[8] M. Palumbo, S. G. Fries, T. Hammerschmidt, T. Abe, J.-C. Crivello, A. A. H. Breidi, J.-M. Joubert, and R. Drautz. First-principles-based phase diagrams and thermodynamic properties of TCP phases in ReX systems (X = Ta, V, W). *Comp. Mat. Sci.*, 81:433–445, 2014.

[9] M. Methfessel and A. T. Paxton. High-precision sampling for Brillouin-zone integration in metals. *Phys. Rev. B*, 40:3616–3621, 1989.

[10] P. E. Blöchl, O. Jepsen, and O. K. Andersen. Improved tetrahedron method for Brillouin-zone integrations. *Phys. Rev. B*, 49(23):16223–16233, 1994.

[11] F. D. Murnaghan. The compressibility of media under extreme pressures. *Proc. Natl. Acad. Sci. U.S.A.*, 30(9):244–247, 1944.

[12] F. Birch. Finite elastic strain of cubic crystals. *Phys. Rev.*, 71(11):809–824, 1947.

[13] P. Giannozzi et al. QUANTUM ESPRESSO: a modular and open-source software project for quantum simulations of materials. *J. Phys.: Condens. Matter*, 21(39):395502 (19pp), 2009.

[14] M. J. Tambe, N. Bonini, and N. Marzari. Bulk aluminum at high pressure: A first-principles study. *Phys. Rev. B*, 77:177102–4, 2008.

QUANTIFYING MODEL-FORM UNCERTAINTY IN MOLECULAR DYNAMICS SIMULATION

Anh V. Tran and Yan Wang

Woodruff School of Mechanical Engineering
Georgia Institute of Technology, Atlanta, GA 30332, U.S.A.

Keywords: Molecular dynamics, Uncertainty quantification, Interval analysis

Abstract

The accuracy of the interatomic potential models plays a vital role toward the reliability of molecular dynamics (MD) simulation prediction. These interatomic potentials, which are the main source of model-form uncertainty in MD, are inherently imprecise due to errors in experimental measurement or first-principles calculation. Existing studies of uncertainty effect in MD simulation use non-intrusive uncertainty quantification (UQ) methods. In this work, a reliable MD (R-MD) mechanism as an intrusive UQ approach is developed. In R-MD, the locations and velocities of particles are not assumed to be precisely known, as a result of imprecise interatomic potentials. They have interval values. Kaucher arithmetic is applied for propagating uncertainty. Sensitivity can be efficiently analyzed with the calculated lower and upper bounds. The new simulation mechanism for isothermal-isobaric ensemble is implemented for demonstrations. The advantage of this approach is that uncertainty effect can be assessed on-the-fly with only one run of simulation.

Introduction

Modeling and simulation tools are essential for engineers to design and develop new materials. The accuracy and reliability of simulation predictions directly affect the effectiveness of the computational tools. The sources of uncertainty associated with simulation tools need to be identified, and uncertainty needs to be quantified to improve the robustness of predictions. In molecular dynamics (MD), the most popular atomistic simulation tool, model-form uncertainty mostly comes from the interatomic potentials. Variations exist among different interatomic potentials, even for the same material system. This is largely due to the choices of their forms and parameters. Furthermore, errors and approximations are introduced by either experiments or first principles calculation during their derivation process. Therefore, the interatomic potentials are inherently imprecise, and quantification of model-form uncertainty in MD simulations is necessary.

Generally speaking, there are two main approaches for uncertainty quantification (UQ), non-intrusive and intrusive methods. Non-intrusive methods such as Monte Carlo simulation, global sensitivity analysis, surrogate model, polynomial chaos, and stochastic collocation treat simulation models as black boxes and rely on statistical techniques to characterize the correlation between the assumed probability density functions (PDF) of the input parameters and the observable outputs. In contrast, intrusive methods such as local sensitivity analysis and interval-based approaches require the modification of the original simulation tools so that uncertainty is represented internally.

Non-intrusive UQ methods have been applied to multiscale simulation [1]. For MD simulation, Frederiksen et al. [2] applied Bayesian update with experimental data sets to construct better interatomic potentials. Jacobson et al. [3] constructed response surfaces with Lagrange interpolation to study the sensitivity of macroscopic properties with respect to interatomic potential parameters. Cailliez and Pernot [4] as well as Rizzi et al. [5] applied Bayesian model calibration to calibrate interatomic potentials parameters. Angelikopoulos et al. [6] showed the applicability of Bayesian model calibration with water molecule models. Rizzi et al. [7] applied polynomial chaos expansion to study the effect of input uncertainty in MD. Cailliez et al. [8] applied Kriging in water molecule MD model calibration.

As an intrusive approach, we recently proposed an interval based reliable MD (R-MD) mechanism [9] where Kaucher interval arithmetic [10] to assess uncertainty effect. Kaucher interval is a generalization and extension of classical interval [11] with simplified algebraic properties. It forms a group as opposed to semi-group formed by classical interval. Therefore, calculation in Kaucher interval arithmetic is simpler than that in classical interval. Most importantly, the overestimation of variation ranges in classical interval is avoided. In R-MD, the input uncertainty associated with interatomic potentials is represented with interval functions. As a result of arithmetic, each atom's position and velocity are intervals, as illustrated in Figure 1. In other words, the precise locations and momenta of atoms are unknown. Only the ranges can be estimated. In this work, the R-MD scheme is implemented in the framework of LAMMPS [12]. The details of how Kaucher interval arithmetic is applied in simulation including force calculation and configuration update are described next.

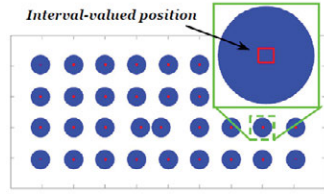

Figure 1: Schematic illustration of R-MD

Kaucher interval arithmetic

The generalized interval space formed by Kaucher intervals is denoted as $\mathbb{KR}$, which is a collection of interval $\boldsymbol{x} := [\underline{x}, \overline{x}]$, where the constraint of upper bound being greater than lower bound ($\underline{x} \leq \overline{x}$) is no longer necessary. The basic operation on $\mathbb{KR}$ is denoted with a circumscribed operator in order to differentiate from the classical interval arithmetic, defined as follows. $[\underline{x}, \overline{x}] \oplus [\underline{y}, \overline{y}] = [\underline{x} + \underline{y}, \overline{x} + \overline{y}]$. $[\underline{x}, \overline{x}] \ominus [\underline{y}, \overline{y}] = [\underline{x} - \underline{y}, \overline{x} - \overline{y}]$. $[\underline{x}, \overline{x}] \otimes [\underline{y}, \overline{y}]$ is defined in Table 1 . $[\underline{x}, \overline{x}] \oslash [\underline{y}, \overline{y}] = [\underline{x}, \overline{x}] \otimes [1/\overline{y}, 1/\underline{y}]$. In Table 1, the generalized interval space $\mathbb{KR}$ is decomposed into four subspaces: $\mathcal{P} := \{\boldsymbol{x} \in \mathbb{KR} \mid (\underline{\boldsymbol{x}} \geq 0), (\overline{\boldsymbol{x}} \geq 0)\}$ contains positive intervals, $\mathcal{Z} := \{\boldsymbol{x} \in \mathbb{KR} \mid (\underline{\boldsymbol{x}} \leq 0 \leq \overline{\boldsymbol{x}}\}$ contains zero, $-\mathcal{P} := \{\boldsymbol{x} \in \mathbb{KR} \mid -\boldsymbol{x} \in \mathbb{P}\}$ contains negative intervals, and

dual $\mathcal{Z} := \{\boldsymbol{x} \in \mathbb{KR} \mid \text{dual } \boldsymbol{x} \in \mathcal{Z}\}$ contains intervals that are contained in zero, where $\text{dual}[\underline{x}, \overline{x}] := [\overline{x}, \underline{x}]$.

	$\boldsymbol{y} \in \mathcal{P}$	$\boldsymbol{y} \in \mathcal{Z}$	$\boldsymbol{y} \in -\mathcal{P}$	$\boldsymbol{y} \in \text{dual } \mathcal{Z}$
$\boldsymbol{x} \in \mathcal{P}$	$[\underline{x}\underline{y}, \overline{x}\overline{y}]$	$[\overline{x}\underline{y}, \overline{x}\overline{y}]$	$[\overline{x}\underline{y}, \underline{x}\overline{y}]$	$[\underline{x}\underline{y}, \underline{x}\overline{y}]$
$\boldsymbol{x} \in \mathcal{Z}$	$[\underline{x}\overline{y}, \overline{x}\overline{y}]$	$[\min\{\underline{x}\overline{y}, \overline{x}\underline{y}\}, \max\{\underline{x}\underline{y}, \overline{x}\overline{y}\}]$	$[\overline{x}\underline{y}, \underline{x}\underline{y}]$	0
$\boldsymbol{x} \in -\mathcal{P}$	$[\underline{x}\overline{y}, \overline{x}\underline{y}]$	$[\underline{x}\overline{y}, \underline{x}\underline{y}]$	$[\overline{x}\overline{y}, \underline{x}\underline{y}]$	$[\overline{x}\overline{y}, \overline{x}\underline{y}]$
$\boldsymbol{x} \in \text{dual}\mathcal{Z}$	$[\underline{x}\underline{y}, \overline{x}\underline{y}]$	0	$[\overline{x}\overline{y}, \underline{x}\overline{y}]$	$[\max\{\underline{x}\underline{y}, \overline{x}\overline{y}\}, \min\{\underline{x}\overline{y}, \overline{x}\underline{y}\}]$

Table 1: Kaucher multiplication table

In order to compare intervals, a norm on $\mathbb{KR}$ is defined as $\|\boldsymbol{x}\| := \max\{|\underline{x}|, |\overline{x}|\}$ with the following properties: $\|\boldsymbol{x}\| = 0$ if and only if $\boldsymbol{x} = 0$. $\|\boldsymbol{x} + \boldsymbol{y}\| \leq \|\boldsymbol{x}\| + \|\boldsymbol{y}\|$. $\|\alpha\boldsymbol{x}\| = |\alpha|\|\boldsymbol{x}\|$ with $\alpha \in \mathbb{R}$. $\|\boldsymbol{x} - \boldsymbol{y}\| \leq \|\boldsymbol{x}\| + \|\boldsymbol{y}\|$. The distance metric on $\mathbb{KR}$ is then defined as $d(\boldsymbol{x}, \boldsymbol{y}) := \max\{|\underline{x} - \underline{y}|, |\overline{x} - \overline{y}|\}$ which is associated with the norm by $d(\boldsymbol{x}, 0) = \|\boldsymbol{x}\|$ and $d(\boldsymbol{x}, \boldsymbol{y}) = \|\boldsymbol{x} \ominus \boldsymbol{y}\|$. As shown in Ref. [10], $\mathbb{KR}$ is a complete metric space under the defined metrics. Interval $\boldsymbol{x}$ is called *proper* if $\underline{x} \leq \overline{x}$, and called *improper* if $\underline{x} \geq \overline{x}$. If $\underline{x} = \overline{x}$, then $\boldsymbol{x}$ is a *degenerated* or *pointwise* interval, or a precise value.

Reliable Molecular Dynamics (R-MD)

Error generating functions

In R-MD, the uncertainty associated with the interatomic potential is characterized error functions. For embedded atomic method (EAM) potentials, two types of error generating functions $e_1(r_{ij})$ and $e_2(\rho)$ with respect to distance and electron density are defined. They are associated with electron density function $f(r_{ij})$, pairwise potential function $\phi(r_{ij})$, and embedding energy function $F(\rho)$ respectively, where r_{ij} is the distance between atoms i and j, and the local electron density $\rho_i = \sum_{j \neq i} f_j(r_{ij})$ is the sum of electron density contributions from other neighboring atoms. The functional forms of the error generating functions are chosen in such a way that they capture the errors in the three original functions in the EAM potential model as well as their first derivatives. Figure 2 show examples of error generating functions associated with pairwise potential, local electron density, and embedding energy functions respectively, where the lower and upper bounds denoted by dash lines enclose the original functions. Table 2 tabulates these functions and their associated parameters used in this study. The principles to select the forms of error generating functions are [9]: (1) both the functions and their first derivatives should be continuous, and (2) the functions diminish to zeros when the original potential functions become infinities or zeros . The interval-valued potential functions will be the nominal function plus and minus the corresponding error function. For instance, the interval-valued embedding energy function is $F(\rho) \pm e_2^{(F)}(\rho)$.

Force calculation

In Kaucher interval arithmetic, $[\underline{x}, \overline{x}] \ominus [\underline{x}, \overline{x}] = 0$. The Newton's third law characterizing the interaction between atoms can then be generalized into $\mathbb{KR}$. As shown in Figure 3,

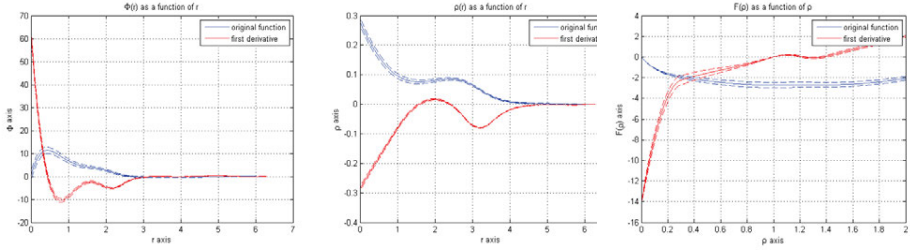

(a) pairwise potential $\phi(r)$ (b) electron density $\rho(r)$ (c) embedding energy $F(\rho)$

Figure 2: examples of error generating functions to model uncertainty in the interatomic EAM potentials

Function	Form of error generating function	First derivative of error
$\phi(r)$	$e_1^{(\phi)}(r) = ae^{-br}$	$\dfrac{\partial e_1^{(\phi)}(r)}{\partial r} = -ab\ e^{-br}$
$\rho(r)$	$e_1^{(\rho)}(r) = ae^{-br}$	$\dfrac{\partial e_1^{(\rho)}(r)}{\partial r} = -ab\ e^{-br}$
$F(\rho)$	$e_2^{(F)}(\rho) = a\Big(\dfrac{\rho}{\rho_0}\Big)^{b\rho_0} e^{-b(\rho-\rho_0)}$	$\dfrac{\partial e_2^{(F)}(\rho)}{\partial \rho} = ab\Big(\dfrac{\rho}{\rho_0}\Big)^{b\rho_0-1} e^{-b(\rho-\rho_0)}\Big(1-\dfrac{\rho}{\rho_0}\Big)$

Table 2: The forms of error generating functions and their derivatives

the lower and upper bound reaction forces between atoms i and j satisfy the constraint $\big[\underline{F}_{ij}, \overline{F}_{ij}\big] = -\big[\underline{F}_{ji}, \overline{F}_{ji}\big]$, which is called Newton's third law in Kaucher interval form.

Figure 3: Newton's third law in Kaucher interval form

The lower and upper bounds of force interval are calculated according to the extended Equations 1 and 2 respectively.

$$\begin{aligned}\underline{\vec{F}}_i \quad = -\sum_{j\neq i}\Bigg[\ & \Big(\frac{\partial F_i(\rho)}{\partial \rho}\Big|_{\rho=\rho_i} - \operatorname{sgn}\Big(\frac{\partial F_i(\rho)}{\partial \rho}\Big|_{\rho=\rho_i}\Big)\Big|\frac{\partial\ e_2^{(F)}(\rho)}{\partial \rho}\Big|_{\rho=\rho_i}\Big)\cdot\Big(\frac{\partial \rho_j(r)}{\partial r}\Big|_{r=r_{ij}} - \operatorname{sgn}\Big(\frac{\partial \rho_j(r)}{\partial r}\Big|_{r=r_{ij}}\Big)\Big|\frac{\partial\ e_1^{(\rho)}(r)}{\partial r}\Big|_{r=r_{ij}}\Big) \\ & +\Big(\frac{\partial F_j(\rho)}{\partial \rho}\Big|_{\rho=\rho_j} - \operatorname{sgn}\Big(\frac{\partial F_j(\rho)}{\partial \rho}\Big|_{\rho=\rho_j}\Big)\Big|\frac{\partial\ e_2^{(F)}(\rho)}{\partial \rho}\Big|_{\rho=\rho_j}\Big)\cdot\Big(\frac{\partial \rho_i(r)}{\partial r}\Big|_{r=r_{ij}} - \operatorname{sgn}\Big(\frac{\partial \rho_i(r)}{\partial r}\Big|_{r=r_{ij}}\Big)\Big|\frac{\partial\ e_1^{(\rho)}(r)}{\partial r}\Big|_{r=r_{ij}}\Big) \\ & +\Big(\frac{\partial \phi(r)}{\partial r}\Big|_{r=r_{ij}} - \operatorname{sgn}\Big(\frac{\partial \phi(r)}{\partial r}\Big|_{r=r_{ij}}\Big)\Big|\frac{\partial\ e_1^{(\phi)}(r)}{\partial r}\Big|_{r=r_{ij}}\Big)\Bigg]\cdot\frac{(\vec{r_i}-\vec{r_j})}{r_{ij}}\end{aligned} \tag{1}$$

$$\vec{\overline{F}}_i = -\sum_{j\neq i}\Bigg[\Big(\frac{\partial F_i(\rho)}{\partial \rho}\Big|_{\rho=\rho_i} + \mathrm{sgn}\Big(\frac{\partial F_i(\rho)}{\partial \rho}\Big|_{\rho=\rho_i}\Big)\Big|\frac{\partial\, e_2^{(F)}(\rho)}{\partial \rho}\Big|_{\rho=\rho_i}\Big) \cdot \Big(\frac{\partial \rho_j(r)}{\partial r}\Big|_{r=r_{ij}} + \mathrm{sgn}\Big(\frac{\partial \rho_j(r)}{\partial r}\Big|_{r=r_{ij}}\Big)\Big|\frac{\partial\, e_1^{(\rho)}(r)}{\partial r}\Big|_{r=r_{ij}}\Big)$$
$$\Big(\frac{\partial F_j(\rho)}{\partial \rho}\Big|_{\rho=\rho_j} + \mathrm{sgn}\Big(\frac{\partial F_j(\rho)}{\partial \rho}\Big|_{\rho=\rho_j}\Big)\Big|\frac{\partial\, e_2^{(F)}(\rho)}{\partial \rho}\Big|_{\rho=\rho_j}\Big) \cdot \Big(\frac{\partial \rho_i(r)}{\partial r}\Big|_{r=r_{ij}} + \mathrm{sgn}\Big(\frac{\partial \rho_i(r)}{\partial r}\Big|_{r=r_{ij}}\Big)\Big|\frac{\partial\, e_1^{(\rho)}(r)}{\partial r}\Big|_{r=r_{ij}}\Big)$$
$$+\Big(\frac{\partial \phi(r)}{\partial r}\Big|_{r=r_{ij}} + \mathrm{sgn}\Big(\frac{\partial \phi(r)}{\partial r}\Big|_{r=r_{ij}}\Big)\Big|\frac{\partial\, e_1^{(\phi)}(r)}{\partial r}\Big|_{r=r_{ij}}\Big)\Bigg] \cdot \frac{(\vec{r_i} - \vec{r_j})}{r_{ij}} \tag{2}$$

where sgn denotes the signum function. The interval forces calculated based in Equations 1 and 2 show that the atomic interactions can vary within some ranges and become slightly stronger or weaker based on the prescribed interval EAM functions, as illustrated in Figure 4. The assumption is that variations of forces from different atoms are not completely independent. When the variations are strongly correlated positively and they become stronger or weaker proportionally at the same time, the variation of the resulting total force is in the same direction but with different magnitudes. However, if the variations among the individual forces are not strongly positively correlated, the total force may vary in different directions.

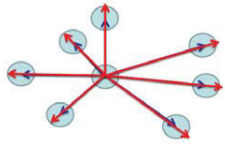

(a) stronger or weaker interaction between atoms can result in different force vectors

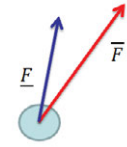

(b) resulting lower and upper bounds of total force $[\underline{F}, \overline{F}]$

Figure 4: Illustration for quantifying uncertainty in total force from imprecise interatomic potential

Midpoint-radius representation of intervals

An interval can be represented either by its lower and upper bounds, or by its midpoint and radius. In the implementation of R-MD, midpoint-radius representation is used. The radius of interval $\boldsymbol{x}$ is defined as $\mathrm{rad}\,[\underline{x}, \overline{x}] := (\overline{x} - \underline{x})/2$. Thus a proper interval has a positive radius, whereas an improper interval has a negative radius. From the computational point of view, the lower-upper representation has a slight advantage of shorter computational time for interval arithmetic. However, it requires to completely reconfigure the LAMMPS package for R-MD simulation. On the other hand, the midpoint-radius representation is easier to implement the dynamics.

The midpoints of position $\boldsymbol{r}$, velocity $\boldsymbol{v}$, and force $\boldsymbol{f}$ can be conveniently set as the values from traditional Verlet integrals. The lower and upper bounds then are calculated from radii, as illustrated in Figure 5a. To support the asymmetrical radius with respect to the midpoint in an interval, inner radius and outer radius are differentiated. The inner radius of a force is defined as the minimum distance from the traditionally calculated to one of the endpoints, whereas the outer radius is defined as the maximum distance from the traditionally calculated force to both of the endpoints. The radius is negative if the interval is improper and positive if the interval is proper. This is mathematically

expressed as

$$\mathrm{rad}_{\mathrm{inner}}\left[\underline{f},\overline{f}\right] = \begin{cases} \min\{\overline{f}-f^*, f^*-\underline{f}\}, & \text{if } \left[\underline{f},\overline{f}\right] \text{ is proper} \\ \max\{\overline{f}-f^*, f^*-\underline{f}\}, & \text{if } \left[\underline{f},\overline{f}\right] \text{ is improper} \end{cases} \tag{3}$$

$$\mathrm{rad}_{\mathrm{outer}}\left[\underline{f},\overline{f}\right] = \begin{cases} \max\{\overline{f}-f^*, f^*-\underline{f}\}, & \text{if } \left[\underline{f},\overline{f}\right] \text{ is proper} \\ \min\{\overline{f}-f^*, f^*-\underline{f}\}, & \text{if } \left[\underline{f},\overline{f}\right] \text{ is improper} \end{cases} \tag{4}$$

where f^* denotes the force calculated from traditional Verlet integrals. Those for position and velocity are defined similarly. During the simulation, the calculations of midpoints and radii are uncoupled, as illustrated in Figure 5b. At each step, the midpoints are estimated and updated through classical Verlet integrals, whereas the inner and outer radii are calculated separately and the uncertainty level thus is estimated. The updates of radii of velocity and position are based on $\mathrm{rad}\,[\underline{v},\overline{v}] = \mathrm{rad}\left[\underline{F},\overline{F}\right]/m$ and $\mathrm{rad}\,[\underline{r},\overline{r}] = \mathrm{rad}\,[\underline{v},\overline{v}]\Delta t$ respectively.

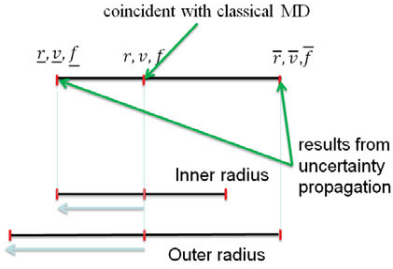

(a) inner/outer radius approximation

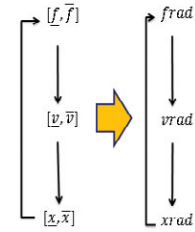

(b) uncoupled radius variable from the midpoint variable of atoms' positions, velocities, and forces in MD simulation

Figure 5: Update of system configuration from imprecise interatomic potentials

Two types of uncertainty are analyzed during simulation. Local uncertainty analysis assesses the effect of uncertainty from the potential functions at each time step without accumulating the error with respect to time, whereas global uncertainty analysis considers the accumulation effect along time.

Local uncertainty analysis is be done by first estimating the midpoint values according to the traditional Verlet integrals, then expanding the boxes according to lower and upper bounds of interval forces, and finally propagating the uncertainty from force to velocity and position respectively. The lower and upper bounds of velocity and position are updated from the respective midpoints calculated from traditional Verlet integration. That is, $\underline{v} = v + \underline{F}/m\Delta t$, $\overline{v} = v + \overline{F}/m\Delta t$, $\underline{r} = r + \underline{v}\Delta t$, and $\overline{r} = r + \overline{v}\Delta t$.

Global uncertainty analysis is done by incorporating Kaucher interval arithmetic into intergration to propagate the uncertainty of positions and velocities with respect to time. The on-going effort is to implement global uncertainty analysis in LAMMPS. The details will be reported in the future.

Numerical Results

To illustrate the effect of error generating functions, a R-MD simulation of stress-strain relation for aluminum single crystal with the load in the <100> direction is run on LAMMPS. The simulation cell size is 10 lattice units in x, y, and z directions, which has a total of 4000 atoms. The aluminum interatomic potential used here is developed by Mishin et al. [13], which was derived from both experiments and *ab initio* calculations. The simulation cell is initially equilibrated, and the lattice is allowed to expand at each simulation cell boundary to a temperature of 300K and a pressure of 0 bar. Next, the simulation cell is deformed in x direction at a strain rate of 10^{-10}s^{-1} under the isothermal-isobaric ensemble. The stress and strain values are output into a separate file, which later is post-processed in MATLAB.

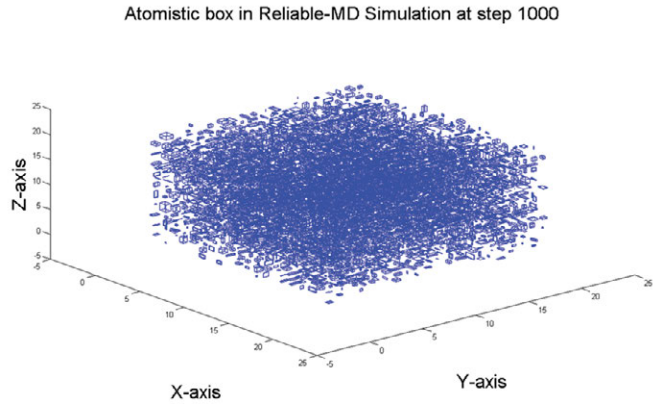

Figure 6: Visual simulation cell where atoms are presented as prisms according to their interval centers and radii

Function	Parameters of error generating function
$\phi(r)$	$a = 4.0000E{-}2, \quad b = 1.1513E0$
$\rho(r)$	$a = 2.7860E{-}4, \quad b = 9.2024E{-}1$
$F(\rho)$	$a = 2.7000E{-}3, \quad b = 2.0000E0$

Table 3: Parameters of error generating functions in EAM

Figure 6 shows the interval positions of atoms as prisms at the time $t = 1ps$ within the simulation cell where the center of intervals are from the Verlet integrals, where the parameters from Table 3 were used. Figure 7 shows the histogram of the radius variable $\text{rad}\,[\underline{x}, \overline{x}]$ described in Figure 6 with the mean $\mu = 0$, due to the constraint of Newton's third law in Kaucher interval form as shown in Figure 3. The range of the $\text{rad}\,[\underline{x}, \overline{x}]$ in Figure 7 are $[-1.4295, 1.6095]$.

Figure 8 shows the results of the stress-strain simulation curve with the quantified uncertainty under the assumption that the interval radius of atoms' velocities $\text{rad}\,[\underline{v}, \overline{v}]$

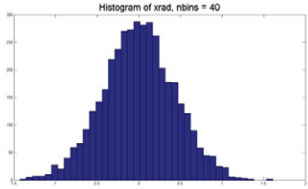

Figure 7: Histogram plot of the interval radius variable of atoms' positions

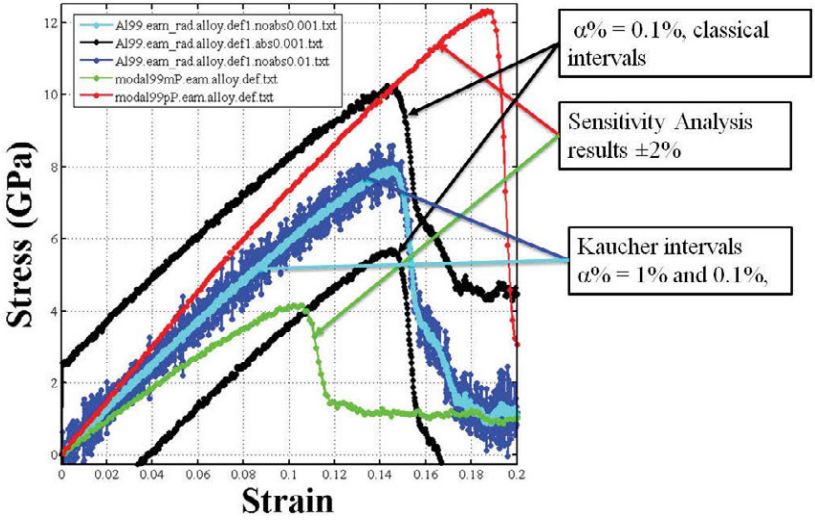

Figure 8: Numerical results of UQ in stress-strain simulation based on R-MD mechanism

is proportional to the atoms' Verlet integral velocities, by either $\text{rad}\,[\underline{v}, \overline{v}] = \alpha\% \cdot v^*$ or $\text{rad}\,[\underline{v}, \overline{v}] = \alpha\% \cdot |v^*|$. The former case is referred to as the Kaucher interval in the figure because the radius can be either positive or negative, whereas the later case is referred to as the classical interval because the radius is strictly positive. This coupling between velocity and uncertainty is conceptually equivalent to the temperature scaling process in isothermal-isobaric ensemble where a thermostat is applied. Given that the measurement device is consistent with systematic error, the uncertainty level of velocity should be proportional to the velocity itself. As shown in Figure 8, the classical interval case yields a considerably higher uncertainty level than the Kaucher interval case. Furthermore, the upper and lower bounds of stress in the Kaucher interval method swap across the traditional MD stress value frequently. In constrast, two distinct curves are obtained in the classical interval method.

Concluding remarks

One of the main sources of model form uncertainty in MD simulation is the interatomic potential. By choosing some closed-form error generating functions of the EAM potential components, the uncertainty of simulation outputs is quantified by interval analysis. In EAM, the force calculation is sensitive to the electron density function $f(r_{ij})$ and the pairwise potential function $\phi(r_{ij})$ and insensitive to the embedding energy function $F(\rho)$ under the effective pair scheme condition. The advantage of intrusive UQ techniques is the computational efficiency. However they require the modification and customization of simulation tools based on the problem settings. In order to quantify the uncertainty of the outputs, one needs to keep track of all the formulas and steps that have been used to derive the output quanitities. In the future, we will continue to incorporate interval arithmetic libraries such as C-XSC [14] into LAMMPS with Kaucher interval formalism.

Acknowledgement

The project is supported in part by NSF under grant number CMMI-1306996.

References

[1] Yan Wang. Uncertainty in materials modeling, simulation, and development for icme. In *Proc. 2015 Materials Science and Technology*, 2015.

[2] Søren L Frederiksen, Karsten W Jacobsen, Kevin S Brown, and James P Sethna. Bayesian ensemble approach to error estimation of interatomic potentials. *Physical review letters*, 93(16):165501, 2004.

[3] Liam C Jacobson, Robert M Kirby, and Valeria Molinero. How short is too short for the interactions of a water potential? exploring the parameter space of a coarse-grained water model using uncertainty quantification. *The Journal of Physical Chemistry B*, 118(28):8190–8202, 2014.

[4] Fabien Cailliez and Pascal Pernot. Statistical approaches to forcefield calibration and prediction uncertainty in molecular simulation. *The Journal of chemical physics*, 134(5):054124, 2011.

[5] F Rizzi, HN Najm, BJ Debusschere, K Sargsyan, M Salloum, H Adalsteinsson, and OM Knio. Uncertainty quantification in md simulations. part ii: Bayesian inference of force-field parameters. *Multiscale Modeling & Simulation*, 10(4):1460, 2012.

[6] Panagiotis Angelikopoulos, Costas Papadimitriou, and Petros Koumoutsakos. Data driven, predictive molecular dynamics for nanoscale flow simulations under uncertainty. *The Journal of Physical Chemistry B*, 117(47):14808–14816, 2013.

[7] F Rizzi, HN Najm, BJ Debusschere, K Sargsyan, M Salloum, H Adalsteinsson, and OM Knio. Uncertainty quantification in md simulations. part i: Forward propagation. *Multiscale Modeling & Simulation*, 10(4):1428, 2012.

[8] Fabien Cailliez, Arnaud Bourasseau, and Pascal Pernot. Calibration of forcefields for molecular simulation: Sequential design of computer experiments for building cost-efficient kriging metamodels. *Journal of computational chemistry*, 35(2):130–149, 2014.

[9] Anh V Tran and Yan Wang. A molecular dynamics simulation mechanism with imprecise interatomic potentials. In *Proceedings of the 3rd World Congress on Integrated Computational Materials Engineering (ICME)*, page 131. John Wiley & Sons, 2015.

[10] Edgar Kaucher. Interval analysis in the extended interval space $\mathbb{IR}$. In *Fundamentals of Numerical Computation (Computer-Oriented Numerical Analysis)*, pages 33–49. Springer, 1980.

[11] Ramon E Moore, R Baker Kearfott, and Michael J Cloud. *Introduction to Interval Analysis*. SIAM, 2009.

[12] Steve Plimpton. Fast parallel algorithms for short-range molecular dynamics. *Journal of computational physics*, 117(1):1–19, 1995.

[13] Y. Mishin, D. Farkas, M. J. Mehl, and D. A. Papaconstantopoulos. Interatomic potentials for monoatomic metals from experimental data and ab initio calculations. *Phys. Rev. B*, 59:3393–3407, Feb 1999.

[14] Rudi Klatte, Ulrich Kulisch, Andreas Wiethoff, and Michael Rauch. *C-XSC: a C++ class library for extended scientific computing*. Springer Science & Business Media, 2012.

ATOMISTIC STUDY OF CARBON NANOTUBES: EFFECT OF CUT-OFF DISTANCE

S. Thamaraikannan[1], S.C. Pradhan[2]

[1]Research Scholar, [2]Associate Professor
Department of Aerospace Engineering, Indian Institute of Technology Kharagpur, India

Keywords: Molecular Dynamics, Carbon nanotube, Cut-off function, AIREBO.

Abstract

Carbon nanotubes (CNTs) superiority have been proved by many experiments and studies. Molecular Dynamics was vastly used by many researchers to analyze properties of CNTs in atomistic scale with various interaction potentials (Force fields). Most of the carbon based interaction potentials were parameterized with cut-off function used to truncate potential energy between certain inner and outer cut-off interatomic distance. These values are having major effects on the mechanical properties. Improper cut-off values may leads to under or over coordination in interaction between two atoms which will exhibits the non-physical behaviours in properties. Most of the researchers have attempted to change outer cut-off value to avoid the non-physical behavior arises during uniaxial tensile studies, those approaches were end up with under coordination between atoms. This paper mainly deals about effect of cut-off distance used in Molecular Dynamics study for analyzing the mechanical properties of CNTs based on AIREBO potential.

Introduction

Nanostructural materials are expected to play an important role in future structural materials including components on aircraft and spacecraft. Enormous efforts have been made to study the mechanical properties of CNTs(1) and graphene. The usage of high resolution microscopes and development of nanomanipulation techniques has enabled the investigation of individual CNTs and graphene (2). However, the small dimension of CNTs and graphene has brought tremendous difficulties for experimental studies, such as picking and positioning of CNTs and graphene, loading and measuring mechanical deformations. So numerical simulations have become a powerful tool in the study of CNTs and graphene. A number of continuum models have been proposed (3; 4; 5), mostly based on the classical continuum theory such as elastic beam and shell theories. However, continuum models bear two obvious drawbacks: first, in continuum models, phenomenological parameter inputs such as the thickness of graphene which has prompted long debates have to be introduced. Second, continuum models cannot simulate defect motion and migration of atoms on the CNTs and graphene at an atomistic level.

The existence of single carbon formed chain structures were encountered by Yakson et al., (6), Molecular Dynamics (MD) study of carbon nanotube fracture at high strain rate using many body interaction (Tersoff) potential. Fracture behavior at grain boundaries for various loading conditions was studied by Shenderova and Brenner (7) using Reactive Empirical Bond order (REBO) multibody bond order based potential. They encountered arbitrary behavior of forces because of the influence of switching function, to avoid the problem they changed the cut-off value to 2.0Åas such far beyond the inflection point for C-C bonds of diamond. Belytschko et al., (8) reported the non-physical behavior arises because of

switching function used in REBO potential through Force Vs Strian curve. Fracture of carbon nanotube was studied with modified Morse potential and compared with Brenner's REBO potential. Steven et al., (9) were explored the mechanical properties of defected carbon nanotubes was under estimated by empirical bond-order potentials by conducted study using Density Functional Theory (DFT), semi empirical based Quantum mechanical methods, and empirical based Tersoff-Brenner potential. Jin and Yuan (10) investigated the macroscopic fracture parameters of 2D graphene using atomistic simulation with Tersoff-Brenner potential and they limited the cut-off values to 1.7Å. Markus (11) developed Mesoscopic model of Single wall Carbon Nanotubes (SWCNTs) and Bundles were generated based on atomistic study of SWCNTs using Tersoff potential with the cut-off vales of 2.1Å. Duan et al., (12) envisaged Fracture behavior of perfect CNTs using modified Morse potential, REBO and COMPASS potential. They set the bond breaking length for modified Morse and REBO potential as 1.776Åand 1.784Åby make changes to cut-off values. They compared fracture strain, Tensile strength and fracture angle values for above potentials. Jeong et al., (13) examined the tensile strength of single and double walled carbon nanotube as hollow and filled by butane like materials under tensile and tensile-torsion combined loading conditions using MD. The over estimation of bond breaking force by second generation REBO potential was eliminated by making covalent interaction inner cut-off distance from 1.7Åto 1.95Å.

Size and chiral dependency against mechanical strength and properties of graphene nano ribbon was investigated by Zhao et al., (14) using orthogonal tight-binding method and molecular simulation with Adaptive Intermolecular Reactive Bond Order (AIREBO) potential under uniaxial tensile test. To avoid the non-physical arises of bond breaking forces the cut-off value was changed to 2.0Å(14). Uniaxial tensile test of monolayer grpahene was investigated using molecular dynamics with AIREBO potential for various temperature, strain rate and defects to predict its effect on the mechanical properties graphene.Xiao et al., (15) analyzed fracture behavior of graphene and single wall carbon nanotube using atomistic based finite element model with molecular mechanics parameters were obtained from modified Morse potential. Three different cut-off values were choosen to examine the fracture progress. Dewapriya and Rajapakse, (16) reported the fracture strength of defected graphene through MD simulation using AIREBO potential with cut-off value of 2.0Å. Jhon et al., (17) tested with MD simualtion of graphene sheet using AIREBO potential with cut-off value of 2.0Åfor various tensile load angles to exhibit orientation dependency as similar to famous CNT types of armchair, zigzag and chiral. Zhang et al., (18) were studied Fracture toughness of pre-cracked graphene through experimnets, MD simulation and theory. MD simulations were carried out using REBO potential with cut-off distance of 1.92Åto avoid the non-physical behavior under large strain.

Interaction potentials

The larger interest in carbon nanotubes and difficulties in experimental measurements of their properties in nanoscale leads to use MD (soft experiment) to predict their mechanical, thermal and electrical properties. It also help as to understand mechanisms between atoms from pair to many-body interactions. In every MD simulations the interactions are controlled by Interaction potential (or) Forcefields. These Interaction potentials are mainly come under two categories Reactive and Non-Reactive, defined by potential functions with analytical or Empirical forms. Reactive bond order potentials are capable of bond breaking and making.

Most of the researchers used Morse potential (19) for bonded systems to predict the fracture behavior by considering the inflection point of tensile force as bond breaking force

and respective bond length as bond breaking distance between pair of atoms. But this was not not inclusive of local environment effects on the pair.

$$V(r) = D_e \left(\left(1 - e^{-\beta(r_{ij} - r_e)}\right)^2 - 1 \right) \tag{1}$$

The first forcefield which depends on bond order and bond length was introduced by Abell (20). The coordination effects on the bond order and bond length was implemented by Tersoff (21; 22; 23; 24). Since bond order (or) bond strength mainly depends on near neighbors which was close enough to make bond. The bonding energy sum over bonds as,

$$E = \sum_i \sum_{j(>i)} \left[V_R(r_{ij}) - \overline{B}_{ij} V_A(r_{ij}) \right] \tag{2}$$

Where V_R, V_A are repulsive and attractive pair energy terms,B_{ij} is bond dependent parameter which weighs the bond order, r_{ij} is the distance between atoms i and j, r_e equilibrium distance.

$$V_R(r_{ij}) = f_c(r_{ij}) \frac{D_e}{S-1} e^{-\sqrt{2S}\beta(r_{ij} - r_e)} \tag{3}$$

$$V_A(r_{ij}) = f_c(r_{ij}) \frac{D_e S}{S-1} e^{-\sqrt{2/S}\beta(r_{ij} - r_e)} \tag{4}$$

The following function (f_c)controls the nearest neighbors of pairs to smoothen potential energy to zero.

$$f_c(r_{ij}) = \begin{cases} 1 & r_{ij} < r_1 \\ \frac{1}{2}\left[1 + cos\left(\frac{\pi(r_{ij} - r_1)}{(r_2 - r_1)}\right)\right] & r_1 \le r_{ij} \le r_2 \\ 0 & r_{ij} > r_2 \end{cases} \tag{5}$$

r_1 and $r_2$are inner and outer cut-off distance for pairs.

$$\overline{B}_{ij} = \frac{1}{2}\left(B_{ij} + B_{ji}\right)$$

The original Tersoff potential was designed for Si and C and was able to describe single, double, and triple bond configurations. It was not able to describe radicals and conjugate versus non-conjugate structures, Lead to the development of Reactive Empirical Bond-Order (REBO) potential by Brenner (25; 26) as follows

$$\overline{B}_{ij} = \frac{1}{2}\left(B_{ij} + B_{ji}\right) + F_{ij}\left(N_i^t, N_j^t, N_{ij}^{conj}\right) \tag{6}$$

$N_i^{(t)}$is total number of neighbor atoms, $N_i^{(H)}, N_i^{(C)}$are number of Hydrogen and Carbon neighbor atoms respectively.

The REBO potential not deals about non-bonded or intermolecular interactions and torsional behaviors of many-body systems. So by considering deficiencies in previous potentials Sturat et al.,(27) introduces Adaptive Intermolecular REBO (AIREBO) potential, which was formed by adding nonbonded and torsional terms of REBO potential.

$$E = \frac{1}{2} \sum_i \sum_{j \neq i} \left[E_{ij}^{REBO} + E_{ij}^{LJ} + \sum_{k \neq i,j} \sum_{l \neq i,j,k} E_{ij}^{tors} \right] \tag{7}$$

$$E_{ij}^{REBO} = V_{ij}^{R} + b_{ij} V_{ij}^{A}$$

Nonbonded energy contribution to the *iandj* pair is given by Lennard-Jones potential form, mathematical expression for the LJ interaction between atoms i and j is given by

$$E_{ij}^{LJ} = S\left(t_r(r_{ij})\right) S\left(t_b(b_{ij}^{*})\right) C_{ij} V_{ij}^{LJ}(r_{ij}) + \left[1 - S\left(t_r(r_{ij})\right)\right] C_{ij} V_{ij}^{LJ}(r_{ij}) \tag{8}$$

$$V_{ij}^{LJ} = 4\epsilon_{ij}\left[\left(\frac{\sigma_{ij}}{r_{ij}}\right)^{12} - \left(\frac{\sigma_{ij}}{r_{ij}}\right)^{6}\right] \tag{9}$$

The Torsional potential terms are

$$E_{ij}^{tors} = w_{ki}(r_{ki}) w_{ij}(r_{ij}) w_{jl}(r_{jl}) V_{ij}^{tors}(\omega_{kijl}) \tag{10}$$

The use of bond weights ensures that associated given dihedral angle will be removed smoothly as any of the consituent bonds are broken.

Where

$$V_{ij}^{tors}(\omega_{kijl}) = \frac{256}{405}\epsilon_{kijl} cos^{10}\left(\omega_{kijl}/2\right) - \frac{1}{10}\epsilon_{kijl} \tag{11}$$

Making of E_{ij}^{LJ} (LJ interaction) to zero gives as Second generation REBO potential (28) which is an addition of torsional interaction terms to REBO potentail.

Carbon Nanotube

The atomic structure of nanotubes is described in terms of the tube chirality, or helicity, defined by the chiral vector C, and the chiral angle θ. Carbon Nanotube helicity can be modeled by cutting the graphene along the dotted lines as shown in Figure 1 and rolling the remaining so that the tip and the tail of the vector C match, where a1 and a2 are the unit vectors of graphite, and n and m are integers. Three special cases of Single-Walled Carbon Nanotubes (SWCNTs) are Zigzag $(n, 0)$, Armchair (n, n) and Chiral (n, m). The diameters of an (n, m) nanotube can be calculated by D, where a_{c-c} is the $C - C$ bond length. When the combination of individual SWCNTs are arranged about concentric center is called Multi-Walled carbon Nanotube (MWCNT). A Double-Walled Carbon Nanotube (DWCNT) can be specified by indexing each of the walls starting from inner layer, for example, (5, 5)@(10, 10).

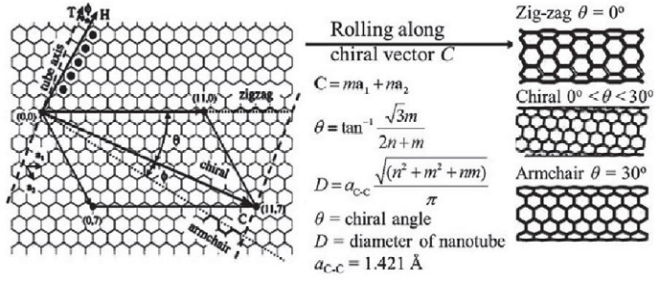

Figure 1: Schematic view of carbon nanotube rolling(29)

Modeling Aspects

The atomistic simulation was carried out using LAMMPS(Large-scale Atomic/Molecular Massively Parallel Simulator)(30) with AIREBO potential. This potential was widely used in the atomistic analysis of carbon nanotubes to calculate their distinctive properties. While particularly considering the structural applications of CNTs, we should have so much concern about strength and failure criteria of the material. This could be achieved by experiments like tensile test whereas in the case of CNTs due to their nanoscale dimension most of the researchers have performed an atomistic simulations. From the literature we could make out the discrepancies in mechanical properties of CNTs, there are so many factor which affects the CNTs MD simulation(31) are time-step, temperature, load-step,topology, scale and interaction potential. This work mainly concentrates about the discrepancy arises because of interaction potential (AIREBO). By having close observation to the previous literature, the researchers have taken various cut-off values to avoid the uncertain behavior of sp2 carbon network based materials.

The profound information gathered from literature was helpful to decide various cut-off ranges to conduct the fracture simulations of CNTs. There are 12 different pair of cut-off values were chosen to observe the significance of cut-off values used in switching function. In aspect of topology concern we have taken two different diameter of CNTs with some tolerance and explored the possiblities of various topology existance.We found 26 Carbon nanotubes which has different chiral indices with diameters of $\simeq$11.2Åand $\simeq$15Å. All the tube lengths are considered as 50Å. Details are presented in Table 1

Table 1: Simulation Model details and Parameters

Dia.$\simeq$11.2Å				
n	m	Dia. (Å)	Chiral angle	No. of atoms
14	0	10.97	0	658
8	8	10.86	30	640
13	2	11.05	7.05	664
12	3	10.77	10.89	642
13	3	11.54	10.16	692
12	4	11.3	13.9	676
11	5	11.11	17.78	668
10	6	10.97	21.79	658
11	6	11.7	20.36	702
9	7	10.88	25.87	653
10	7	11.59	24.18	694
9	8	11.54	28.05	693

Dia.$\simeq$15Å				
n	m	Dia. (Å)	Chiral angle	No. of atoms
19	0	14.89	0	893
11	11	14.93	30	880
18	2	14.95	5.21	896
17	3	14.64	7.99	879
18	3	15.41	7.59	924
17	4	15.13	10.33	908
16	5	14.89	13.17	892
15	6	14.68	16.1	882
16	6	15.43	15.3	928
14	7	14.51	19.11	875
15	7	15.25	18.14	915
14	8	15.11	21.05	908
13	9	15.01	24.01	901
12	10	14.95	27	898

Cut-off Ranges (Å)	
Inner	Outer
1.7	1.7
1.771	1.771
1.8	1.8
1.9	1.9
2.0	2.0
1.7	1.8
1.7	1.9
1.7	2.0
1.8	1.9
1.8	2.0
1.9	2.0
1.54	2.46

Initially the system was equilibriated through NVT ensemble (thermostat) by rescaling the system temperature. Then the system was under gone main production stage by applying incremental displacement in one end and other end was fixed for any movements. The potential energy variation of system monitored through out the production stage until the interatomic distance become more than outer cut-off value.

Results & Discussions

In AIREBO potential near neighboring interaction smoothing function (or) cut-off function plays main role, when the model subjected to large strain (i.e. Bond stretch beyond the

inner cut-off distance).The main purpose of this smoothing function is to adjust the potential energy to smoothly approach to zero after certain interatomic distance. This function causes over estimation of forces as the interatomic distance approaches inner cut-off value. Mainly this over estimation of forces effects the characteristic behaviors of fracture simulations or large strain simulations. In AIREBO inner cut-off and outer cut-off were taken as 1.7Åand 2.0Årespectively it results in nonphysical behavior in atomistic fracture simulations. In preliminary simulations the influence of a switching function results very high strength and strains for fracture. To avoid this circumstances researchers have changed the cut-off ranges according to their system. In some cases inner and outer cut-off values were made identical in such a way that value after the inflection point, this might totally disables the switching function and behaves like truncation scheme.

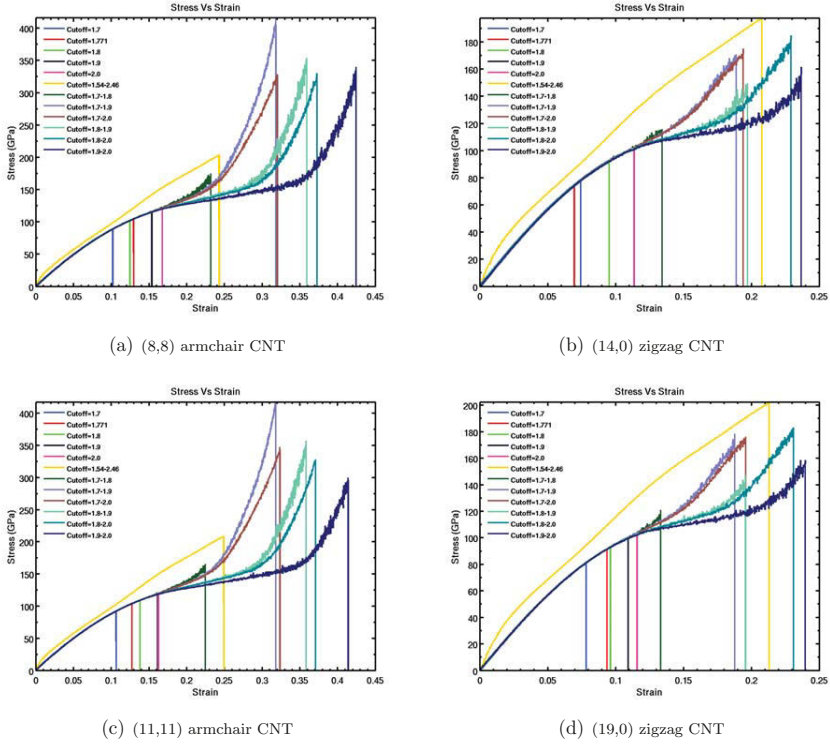

(a) (8,8) armchair CNT

(b) (14,0) zigzag CNT

(c) (11,11) armchair CNT

(d) (19,0) zigzag CNT

Figure 2: Stress-Strain behaviour various cut-off

We have tested with various pairs of cut-off values such as identical inner and outer cut-off values and different inner and outer cut-off values. The uniaxial tensile simulations have been carried out for 26 different topological CNTs with various cut-off values. while we considered identical inner and outer cut-off values the nonphysical behavior arises becuase of over estimation of forces after certain interatomic distance were avoided. We also explored the various aspects related to cut-off ranges as such changes in cut-off ranges leads to various stiffness characters in CNTs. Particularly the over estimation of forces decreases

when the difference between inner and outer cut-off values increases. In the case of inner cut-off was 1.54Åand outer cut-off was 2.46Å, we attained the stress-strain curve without any nonphysical behavior.The effects of CNT topology on various cut-off values were shown in Figure 2 .We have calculated the Youngs modulus and reported in Table 2 from various cases of fracture simulations and validated.

Table 2: Validation for tensile strength

Dia. (nm)	Ultimate strength (GPa)	Method
1.1∼1.4	≥45±7	AFM bending test on SWNT ropes (32)
1.6	65∼93	AS using modified Morse model, tensile loading(8)
0.68	62.9	Atomistic simulation and ab-initio calculation, w/o defects(33)
0.4∼2.2	40∼50	Theoretical analysis based on AS. Modulus(34)
1.36	4.92	Tight-binding simulation(35)
1.12	**54.97∼89.25**	**MD simulation with AIREBO cut-off-1.7Å**
1.12	**65.38∼104.91**	**MD simulation with AIREBO cut-off-1.771Å**
1.12	**75.56∼120.49**	**MD simulation with AIREBO cut-off-2.0Å**
1.5	**44∼80.86**	**MD simulation with AIREBO cut-off-1.7 Å**
1.5	**47.56∼91.62**	**MD simulation with AIREBO cut-off-1.771Å**
1.5	**56.39∼119.14**	**MD simulation with AIREBO cut-off-2.0Å**

References

[1] Iijima S. Helical microtubules of graphitic carbon. nature. 1991;Vol:354,pp:56–58.

[2] Yu M, Lourie O, Dyer M, Moloni K, Kelly T, Ruoff R. Strength and breaking mechanism of multiwalled carbon nanotubes under tensile load. Science (New York, NY). 2000;Vol:287(5453),pp:637–40.

[3] Ray M, de Villoria RG, Wardle B. Load transfer analysis in short carbon fibers with radially-aligned carbon nanotubes embedded in a polymer matrix. Journal of Advanced Materials. 2009;Vol:41,pp:82–94.

[4] Kundalwal SI, Ray MC. Effective properties of a novel composite reinforced with short carbon fibers and radially aligned carbon nanotubes. Mechanics of Materials. 2012;Vol:53,pp:47–60.

[5] Pradhan SC. Nonlocal finite element analysis and small scale effects of CNTs with Timoshenko beam theory. Finite Elements in Analysis and Design. 2012;Vol:50,pp:8–20.

[6] Yakobson BI, Campbell MP, Brabec CJ, Bernholc J. High strain rate fracture and C-chain unraveling in carbon nanotubes. Computational Materials Science. 1997;Vol:8(4),pp:341–348.

[7] Shenderova O, Brenner D, Omeltchenko a, Su X, Yang L. Atomistic modeling of the fracture of polycrystalline diamond. Physical Review B. 2000;Vol:61(6),pp:3877–3888.

[8] Belytschko T, Xiao S, Schatz G, Ruoff R. Atomistic simulations of nanotube fracture. Physical Review B. 2002;Vol:65(23),pp:235430.

[9] Mielke SL, Troya D, Zhang S, Li JL, Xiao S, Car R, et al. The role of vacancy defects and holes in the fracture of carbon nanotubes. Chemical Physics Letters. 2004;Vol:390(4-6),pp:413–420.

[10] Jin Y, Yuan FG. Nanoscopic Modeling of Fracture of 2D Graphene Systems. Journal of Nanoscience and Nanotechnology. 2005;Vol:5(4),pp:601–608.

[11] Buehler MJ. Mesoscale modeling of mechanics of carbon nanotubes: Self-assembly, self-folding, and fracture. Journal of Materials Research. 2006;Vol:21(11),pp:2855–2869.

[12] Duan WH, Wang Q, Liew KM, He XQ. Molecular mechanics modeling of carbon nanotube fracture. Carbon. 2007;Vol:45(9),pp:1769–1776.

[13] Jeong BW, Lim JK, Sinnott SB. Tensile mechanical behavior of hollow and filled carbon nanotubes under tension or combined tension-torsion. Applied Physics Letters. 2007;Vol:90(2),pp:023102.

[14] Zhao H, Min K, Aluru NR. Size and chirality dependent elastic properties of graphene nanoribbons under uniaxial tension. Nano letters. 2009;Vol:9(8),pp:3012–3015.
[15] Xiao JR, Staniszewski J, Gillespie JW. Fracture and progressive failure of defective graphene sheets and carbon nanotubes. Composite Structures. 2009;Vol:88(4),pp:602–609.
[16] Dewapriya MaN, Rajapakse RKND. Molecular Dynamics Simulations and Continuum Modeling of Temperature and Strain Rate Dependent Fracture Strength of Graphene With Vacancy Defects. ;Vol:.
[17] Jhon YI, Jhon YM, Yeom GY, Jhon MS. Orientation dependence of the fracture behavior of graphene. Carbon. 2014;Vol:66,pp:619–628.
[18] Zhang P, Ma L, Fan F, Zeng Z, Peng C, Loya PE, et al. Fracture toughness of graphene. Nature communications. 2014;Vol:5,pp:3782.
[19] Morse P. Diatomic Molecules According to the Wave Mechanics. II. Vibrational Levels. Physical Review. 1929;Vol:34(1),pp:57–64.
[20] Abell G. Empirical chemical pseudopotential theory of molecular and metallic bonding. Physical Review B. 1985;Vol:31(10),pp:6184–6196.
[21] Tersoff J. New empirical approach for the structure and energy of covalent systems. Physical Review B. 1988;Vol:37(12),pp:6991–7000.
[22] Tersoff J. Empirical Interatomic Potential for Carbon, with Applications to Amorphous Carbon. Physical Review Letters. 1988;Vol:61(25),pp:2879–2882.
[23] Tersoff J. Modeling solid-state chemistry: Interatomic potentials for multicomponent systems. Physical Review B. 1989;Vol:39(8),pp:5566–5568.
[24] Tersoff J. Erratum: Modeling solid-state chemistry: Interatomic potentials for multicomponent systems. Physical Review B. 1990;Vol:41(5),pp:3248–3248.
[25] Brenner D. Empirical potential for hydrocarbons for use in simulating the chemical vapor deposition of diamond films. Physical Review B. 1990;Vol:42(15),pp:9458–9471.
[26] Brenner D. Erratum: Empirical potential for hydrocarbons for use in simulating the chemical vapor deposition of diamond films. Physical Review B. 1992;Vol:46(3),pp:1948–1948.
[27] Stuart SJ, Tutein AB, Harrison Ja. A reactive potential for hydrocarbons with intermolecular interactions. The Journal of Chemical Physics. 2000;Vol:112(14),pp:6472.
[28] Brenner DW, Shenderova OA, Harrison JA, Stuart SJ, Ni B, Sinnott SB. A second-generation reactive empirical bond order (REBO) potential energy expression for hydrocarbons. Journal of Physics: Condensed Matter. 2002;Vol:14(4),pp:783–802.
[29] Dresselhaus MS, Saito R, Dresselhaus G. Physics of carbon nanotubes. Carbon. 1995;Vol:33(7),pp:883–891.
[30] Plimpton S. Fast parallel algorithms for short-range molecular dynamics. Journal of Computational Physics. 1995;Vol:117(1),pp:1–19.
[31] Mylvaganam K, Zhang LC. Important issues in a molecular dynamics simulation for characterising the mechanical properties of carbon nanotubes. Carbon. 2004;Vol:42(10),pp:2025–2032.
[32] Walters Da, Ericson LM, Casavant MJ, Liu J, Colbert DT, Smith Ka, et al. Elastic strain of freely suspended single-wall carbon nanotube ropes. Applied Physics Letters. 1999;Vol:74(25),pp:3803.
[33] Xia Y, Zhao M, Ma Y, Ying M, Liu X, Liu P, et al. Tensile strength of single-walled carbon nanotubes with defects under hydrostatic pressure. Physical Review B. 2002;Vol:65(15),pp:155415.
[34] Wei C, Cho K, Srivastava D. Tensile strength of carbon nanotubes under realistic temperature and strain rate. Physical Review B. 2003;Vol:67(11),pp:115407.
[35] Dereli G, Özdoan C. Structural stability and energetics of single-walled carbon nanotubes under uniaxial strain. Physical Review B. 2003;Vol:67(3),pp:035416.

BAYESIAN CALIBRATION OF A PHYSICAL MODEL FOR PLASTIC FLOW BEHAVIOR OF TRIP STEELS

P. Honarmandi[1] and R. Arroyave[1]

[1]Department of Materials Science and Engineering, Texas A&M University, College Station, Texas, 77840, USA

Keywords: TRIP Steels, Bayesian Calibration, Markov Chain Monte Carlo

Abstract

Rivera's physical model [Modeling Simul. Mater. Sci. Eng. 22 (2014) 015009 (22pp)] based on irreversible thermodynamics of dislocation evolution has been used in this work to predict the stress-strain behavior of TRIP steels during plastic deformation. This model has been applied to account for plastic deformation of individual phases, and the iso-work approximation has been used as a homogenization framework to simulate the behavior of the composite system. Contribution to plastic behavior due to strain-induced martensitic transformation in austenite has also been taken into account. Calibration and analysis of parameter uncertainty is performed using a Bayesian method based on Metropolis-Hastings Markov Chain Monte Carlo algorithms. Using this approach, the model has been trained with different experimental data to estimate parameters and their uncertainties. The parameter posterior probability distribution obtained from is considered as the prior probability distribution for subsequent training. The stress-strain curves obtained from the model with new estimated parameters show good agreement with the experimental data in literature.

Introduction

TRansformation-Induced Plasticity (TRIP) Steels are a group of low-alloy steels that can offer an excellent combination of strength and fracture toughness due to high strain hardening resulting from strain-induced martensitic transformation (SIMT) during plastic deformation [1-4]. The above-mentioned interesting properties make these high strength steels favorable for automotive industry by providing lower weight and higher safety for vehicles [5, 6]. The main characteristic of TRIP steels is their multi-phase microstructure, which includes ferrite, bainite, retained austenite, and martensite, [7, 8] and whose volume fraction and distribution directly influence the plastic flow behavior of these alloys [9]. It has been also indicated [10] that grain size and carbon content of the retained austenite as well as its volume fraction play essential roles in TRIP effect.

TRIP steels usually undergo large plastic deformation during their processing to final products [11]. Since its experimental evaluations are always very expensive, modelling of plastic flow behavior of these types of steels seems to be a crucial task. However, there are a few theoretical and computational studies in this area due to complexities associated with simulating the combined contribution of different phases, including the martensitic transformation of retained austenite during deformation. Most of the researchers focused on the second part, i.e., the prediction of SIMT. In this regard, Tomita et al [12] used a constitutive equation that takes into

account of the effects of temperature, strain rate and applied stress on martensitic transformation behavior. Thibaud et al [13] employed a phenomenological approach for TRIP effect and implemented it through finite element simulations. In another study performed by Han et al [6], TRIP effect has been evaluated based on considering different nucleation probabilities for martensitic variants at a specific potency site according to the Kurdjumov-Sachs orientation relationship. Recently, Haidemenopoulos et al [14] has developed the Olson-Cohen model by the modification of overall potency sites for the martensitic nucleation in TRIP steels, which is applied in this paper to predict SIMT behavior. This model considers particle size of the retained austenite and stress triaxiality in addition to chemical composition of the retained austenite and temperature [14]. However, it should be noted that strain and stress partitioning in different phases are also taken into account using a constitutive model [15] and mean field approaches [11, 16] in which the material is regarded as a dual or multi-phase composite with evolving phase volume fractions. Nevertheless, it seems that there is still a need for a physical-based model with meaningful and predictable parameters, which can precisely interpret the plastic flow behavior of TRIP steels.

Another important issue is the estimation of model parameters, in a manner that allows the quantification of uncertainty [17], an issue that is often neglected in most computational work, particularly in materials modeling and simulation. The development of high-speed computers has increased the attentions to Bayesian approach for the analysis of model parameters, particularly those are based on Markov chain Monte Carlo (MCMC) methods [18]. In fact, it has been found [19] that MCMC-based Bayesian approaches can provide better parameter calibrations for multi-level models compared to other likelihood based techniques, including maximum likelihood (ML), restricted maximum likelihood (REML), marginal quasi-likelihood (MQL), and penalized quasi-likelihood (PQL) [19].

In this research, Rivera's model [20] based on a thermostatistical theory of plasticity has been applied to predict dislocation density evolution of each phase during plastic deformation, and then an iso-work approximation approach has been employed to describe overall plastic deformation behavior of the alloy. This model describes the detailed behavior of plastic deformation for the low-alloy steels using physically meaningful parameters. MCMC Metropolis-Hastings algorithm has been also used for the calibration of model parameters, which offers appropriate modifications for existing values in the literature. The main goal of this research is to propose a new effective pathway for parameter estimation.

Model Description and Methodology

Modelling of Plastic Flow Behavior

Dislocation Density Evolution during Plastic Deformation: Stress-strain curve of multi-phase TRIP steels has been predicted by considering the contribution of different mechanisms for any individual phase (i) in the microstructure [21]:

$$\tau_i = \tau_0 + \tau_s + \tau_b + \sqrt{\tau_{in}^2 + \tau_p^2} \quad (1)$$

τ_0, τ_s, τ_b, τ_{in}, and τ_p are related to the contribution of Peierls force, solid solution strengthening, long-range back stress, dislocation strengthening, and precipitation strengthening, respectively. The first two terms have been calculated by empirical formulas [22-24] in terms of chemical compositions in any phase, while τ_b and τ_p have been calculated using the relationships indicated by Rivera et al. [21]. Moreover, Rivera's model [20] has been utilized to calculate τ_{in} of any individual phase during plastic deformation. In this model, the dislocation density evolution in various phases is obtained through the difference between the dislocation generation and annihilation rates, which has been offered by Kocks and Mecking [25] as follows:

$$\frac{d\rho(\gamma)}{d\gamma} = \frac{d\rho^{+}(\gamma)}{d\gamma} - \frac{d\rho^{-}(\gamma)}{d\gamma} \tag{2}$$

$$\frac{d\rho^{+}(\gamma)}{d\gamma} = \frac{1}{b}\left(\frac{1}{\Lambda_{pure}} + \frac{1}{\Lambda_{subs}} + \frac{1}{\Lambda_{inter}}\right) \tag{3}$$

$$\frac{d\rho^{-}(\gamma)}{d\gamma} = f_{DRV}\rho(\gamma) \tag{4}$$

where b is the value of Burger's vector and $\Lambda_{pure}^{-1} = \frac{1}{30}\left(\frac{\mu}{\mu_0}\right)^2\sqrt{\rho} = K_1\sqrt{\rho}$ [25] is dislocation-dislocation interactions. μ and μ_0 are shear modulus at 298 and 0 K, respectively.

$\Lambda_{subs}^{-1} = \frac{\sum_i x_i}{16000}\exp\left(-\frac{\Delta G_{sys}}{RT}\right)\sqrt{\rho} = K_{ss}\sqrt{\rho}$ and $\Lambda_{inter}^{-1} = \frac{x_C^{1/3}}{\Lambda_{pure}^{-1}}$ are related to microstructural defects, including substitutional and interstitial solute atoms, which are obstacles against dislocation displacement. x_i is the atom fraction of element i and ΔG_{sys} is the alloy free energy. f_{DRV} is the dynamic recovery coefficient, which is obtained through the calculation of the energy barrier for dislocation annihilation, $\langle \Delta G \rangle$, which incorporates the following terms [20]:

1) The formation energy of the annihilating dislocation segment, l
2) The migration energy required for the segment to slip
3) The vacancy energy involved in dislocation annihilation through climb at higher temperatures
4) The interaction energy between dislocations and substitutional solute atoms
5) The statistical entropy referring to the number of possible paths for the dislocation migration

$$\begin{aligned}\langle \Delta G \rangle &= \frac{b}{l}\left(U_{form} + U_{mig} + U_{vac} + U_{SS} - T\Delta S\right) \\ &= \frac{b}{l}\left[\frac{1}{2}\mu b^2 l + \sigma_Y A_{act} b^2 l + \frac{V_{sys}}{b^3}\delta(T)\left(E_f + k_B T ln(c_m)\right)\right. \\ &\left. + V_{sys}\frac{1}{b^3}\sum_i x_i \Delta G_{sys} - k_B T ln(\Omega)\right]\end{aligned} \tag{5}$$

where σ_Y, A_{act}, $\delta(T)$, and E_f are the yield stress, the activation area for dislocation cross slip, a piecewise function with temperature, vacancy formation energy, respectively. In addition, $V_{sys} = bl^*l$ and $c_m = \exp\left(\frac{-\Delta S_{form}}{R}\right)\exp\left(\frac{-E_f}{RT_m}\right)$ are the annihilating system volume per dislocation and the vacancy concentration at melting temperature (T_m) in which l^* and ΔS_{form} are the length of dislocation distortion field and the entropy of vacancy formation. It should be noted that the total number of microstates due to dislocation slip and climb in pure materials is $\Omega_{pure} = \Omega_{dis} + \Omega_{v-d} = (\frac{\dot{\varepsilon}_0+\vartheta}{\dot{\varepsilon}})^{\mathrm{N}}$ where $\dot{\varepsilon}$ and $\dot{\varepsilon}_0$ are the axial strain rate and the maximum possible value for strain rate proportional to the speed of sound, respectively, $\vartheta = \vartheta_D \exp(-\frac{E_m}{RT})$ is the vacancy migration frequency in which $\vartheta_D = 10^{13}s^{-1}$ is Debye frequency and E_m is the vacancy migration energy, and N is the impingement effect of contiguous dislocations due to the overlap of their strain fields. This equation can be modified in the presence of solute atoms as $\Omega = \Omega_{pure}.\Omega_{subs}.\Omega_{inter}$ [20].

On the other hand, there is an Arrhenius form relationship between the annihilation barrier and average velocity for dislocation annihilation as follows:

$$(\frac{\langle v\rangle}{c + c_{int}})^{\mathrm{N}} = (\frac{\dot{\varepsilon}}{\dot{\varepsilon}_0 + \vartheta})^{\mathrm{N}} = exp(-\frac{\langle \Delta G\rangle}{k_B T}) \tag{6}$$

c and c_{int} are the speed of sound in the alloy and the contribution of vacancy to the dislocation annihilation velocity, respectively. Combination of equations (5) and (6) gives the average length of annihilating dislocation segments, l, which is used for the determination of the dynamic recovery coefficient:

$$f_{DRV} = \frac{N_A}{w_a}\rho_a V_{sys} = \frac{N_A}{w_a}\rho_a bl^*l$$
$$= \frac{\frac{N_A}{w_a}\rho_a b^2 l^*(1+N_{subs})(1+x_c^{1/3})k_B T ln(\frac{\dot{\varepsilon}_0+\vartheta}{\dot{\varepsilon}})^{\mathrm{N}}}{\frac{1}{2}\mu b^3 + \sigma_Y A_{act} b^3 + \frac{l^*}{b}\delta(T)\left(E_f + k_B T ln(c_m)\right) + \frac{l^*}{b}\sum_i x_i \Delta G_{sys} - (1+x_c^{1/3})k_B T ln(\frac{\dot{\varepsilon}_0+\vartheta}{\dot{\varepsilon}})^{\mathrm{N}}} \tag{7}$$

where N_A, w_a, and ρ_a are Avogadro's number, alloy atomic weight, and alloy density, respectively [20].

At the end, the following equation in the form of Kocks and Mecking formulation can be offered for the density evolution in each phase:

$$\frac{d\rho(\gamma)}{d\gamma} = A\left(\frac{K}{b}\right)\sqrt{\rho(\gamma)} - Bf_{DRV}\rho(\gamma) \tag{8}$$

$K = (1+x_c^{1/3})K_1 + K_{ss}$. A and B are phase dependent constants, which are 1 for FCC (austenite) structure. For BCC (ferrite/bainite) and BCT (martensite) structure, these are calculated by the comparison of their slip system × coordination number with those in FCC structure [26]. Phase dependent parameters in the model have been indicated in table 1.

Table1. Number of slip systems and coordination numbers (CN), and phase dependent parameters

Phase	Structure	Slip System	Number of Slip Systems	CN	A	B	N
Austenite	FCC	$\{111\}<\bar{1}10>$	12	12	1	1	1
Ferrite/Bainite	BCC	$\{110\}<111>$ $\{112\}<111>$ $\{123\}<111>$	12 12 24	8	$\frac{3}{8}$	$\frac{8}{3}$	2
Martensite	BCT	$\{101\}<\bar{1}01>$ $\{\bar{1}01\}<101>$	2 2	8	$\frac{9}{2}$	$\frac{2}{9}$	2

Solution of equation 8 for each phase provides the dislocation density in terms of strain during plastic deformation. Therefore, shear stress during plastic deformation can be also obtained using Taylor relation:

$$\tau = \alpha M \mu b \sqrt{\rho} \tag{9}$$

where α is a constant and M is Taylor factor [27].

In our research, iso-work approximation has been considered to predict strain-stress curve in the applied multi-phase system that means energy dissipation in all the phases is the same during plastic deformation [21]:

$$\tau_i . \gamma_i = \tau_{i+1} . \gamma_{i+1} \tag{10}$$

$$\tau_{total} = \sum_i Vf_i . \tau_i \tag{11}$$

where γ_i, τ_i, and Vf_i are shear strain, shear stress and volume fraction of phase i, respectively. The values of all other parameters in the model are shown in the table 2.

Table2. Model parameters

Parameter	Phase			
	Ferrite	Austenite	Bainite	Martensite
$\mu(MPa)$	75200			
$\mu_0(MPa)$	85000			
$b(m)$	2.5E-10			
$D(m)$	10E-6	15E-6	artificial neural network [28, 29]	0.13E-6
n^*	4	20	4	4
$\lambda(m)$	1.5E-7	1.5E-7	5.0E-8	5.0E-8

Continued-Table2

Parameter	Phase			
	Ferrite	Austenite	Bainite	Martensite
α	0.25			
$\rho_0(m^{-2})$	1E+13	1E+13	$(0.7+3.5\mathrm{w}_C)\times 10^{15}$ [30]	$10^{9.2844+\frac{6880}{T_{BIT}-298}-\frac{1780360}{(T_{BIT}-298)^2}}$ [31]
$\sigma_{\mathrm{y}}(MPa)$	475	720	475	2000
M	3.06			
$\tau_0(MPa)$	18			
λ_{ss}	16000			
$\Delta G_{sys}(\frac{kJ}{mol})$	$16-0.045T-1.4*10^{-5}T^2$			
$\delta(T)$	$0<\frac{T-T_0}{T_f-T_0}<1$			
l^*	31.25E-10			
$E_{\mathrm{m}}(eV)$	1.28			
$E_{\mathrm{f}}(eV)$	1.6			
$\Delta S_{form}(\frac{J}{mol\,K})$	-12.47			
ν	0.27-0.34			
$\chi(\frac{J}{m^2})$	0.077			

SIMT Model: As mentioned previously, Haidemenopoulos model [14] has been employed in this research to predict the martensitic transformation behavior in terms of plastic strain. In this model, martensite embryo is the fault formed through the dissociation of defects. In fact, martensitic nucleation occurs through two various mechanisms, stress-assisted nucleation on pre-existing sites and strain-induced nucleation on sites generated during plastic deformation. However, it should be noted that the above-mentioned sites do not necessarily result in martensitic nuclei unless they possess a sufficient potency for nucleation. This potency can be directly correlated to a critical number of crystal planes (n^*) in fault which can be obtained if the required energy for the formation of the fault with n-crystal planes is equal to zero in the following equation:

$$\gamma_f(n)=n\rho\left(\Delta G_{ch}+\mathrm{E}_{str}+\mathrm{W}_f\right)+2\gamma_s \tag{12}$$

$$\gamma_f=0 \quad \rightarrow \quad n^*=-\frac{2\gamma_s}{\rho\left(\Delta G_{ch}+\mathrm{E}_{str}+\mathrm{W}_f\right)} \tag{13}$$

where ρ is the atom density in fault plane, ΔG_{ch} is the chemical driving force for martensitic nucleation, E_{str} is the elastic energy due to the distortions between fault and austenitic matrix, W_f is the frictional work due to the motion of fault/matrix interface, and γ_s is the interfacial energy.

Therefore, the total number of nucleation sites with sufficient potency per unit volume of austenite (N_v) can be defined as the summation of pre-existing operational nucleation sites (N_v^{σ}) and operational nucleation sites generated during plastic deformation (N_v^{ε}):

$$N_v(\varepsilon) = N_v^{\sigma} + N_v^{\varepsilon}(\varepsilon) \tag{14}$$

Every one of the operational nucleation sites can be calculated based on the nucleation criteria:

$$N_v^{\sigma} = N_v^{\sigma 0}\exp(-a_{\sigma}n^*) \tag{15}$$

$$N_v^{\varepsilon}(\varepsilon) = N_v^{\varepsilon 0}(\varepsilon)\exp(-a_{\varepsilon}n^*) = N(1-\exp(-k\varepsilon^m))\exp(-a_{\varepsilon}n^*) \tag{16}$$

where k and m are constants. $N_v^{\sigma 0}$ and $N_v^{\varepsilon 0}$ are the number of pre-existing and generated nucleation sites of all potencies, respectively. N is the maximum number of nucleation sites that can be formed during plastic deformation. a_{σ} and a_{ε} are shape factors corresponding to stress-modified and strain-modified potency distribution. Accordingly, the variation of martensite volume fraction (f) with plastic strain is expressed as:

$$f(\varepsilon) = 1 - \exp\left(-v_p N_v(\varepsilon)\right) \tag{17}$$

Table3. SIMT Model parameters [14]

Parameter	Value
$v_p(m^3)$	4.18E-18
$\gamma_s(\frac{J}{m^2})$	0.15
$\Delta G_{ch}(\frac{J}{mol})$	-3285
$E_{str}(\frac{J}{mol})$	500
$W_f(\frac{J}{mol})$	$1.893E3 * X_{Mn}^{2/3} + 1.310E4 * X_C^{2/3}$
$\rho(\frac{mol}{m^2})$	3E-5
$N_v^{\sigma 0}(m^{-3})$	1.5E17
$N(m^{-3})$	1.9E19
a_{σ}	0.1
a_{ε}	0.03
k	46
m	3.45

It is worth noting that the effect of austenite particle size (v_p) is also observed in this equation, which has been disregarded in other previous models. In table 3, the values of SIMT model parameters are shown based on Haidemenopoulos et al. work [14].

Experimental Data

Experimental data (ε, σ) obtained from Girault et al. [33] have been applied for the parameter calibration of our model, as discussed in the section 2.1.4. Data shown in table 4 for nominal chemical composition, phase volume fractions, and carbon weight percentage in phases are considered as model inputs. In addition, bainitic isothermal transformation temperature (450°C), and temperature and strain rate of tensile test (20°C and 6.67E-4 s^{-1}) are the other inputs which are the same for all three experiments.

Table4. Experimental data [33] for three different TRIP alloys

Alloy	Chemical Composition (wt%)				Volume Fraction (%)				Carbon (wt%)			
	C	Si	Mn	Al	Fer	Bai	Aus	Mar	Fer	Bai	Aus	Mar
TRIP 1	0.12	0.78	1.51	0.04	66	26	6	2	0.012	0.02	1.4	1.14
TRIP 2	0.11	0.06	1.55	1.53	64	26	6	2	0.012	0.02	1.38	0.72
TRIP 3	0.11	1.5	1.53	0.04	64	28	8	0	0.012	0.02	1.21	0

* Fer: ferrite, Bai: bainitic ferrite, Aus: retained austenite, and Mar: martensite

Bayesian Calibration of Model Parameters: Metropolis-Hastings Algorithm

In this research, model parameter calibration is performed by Bayesian inference through Metropolis-Hastings Algorithm. In this approach, the main purpose is finding a joint posterior probability density function (PDF) for a set of given model parameters. It has been indicated [32] that sampling techniques based on MCMC methods are required to be used since solving the analytical equations, i.e., the calculation of intractable integrals, would be a hard task.

Flow-chart of our approach has been demonstrated in Fig.1. It begins with initial values in parameter spaces ($\theta^{(0)}$) which have been obtained from literature. Since there is no information about given model parameters, non-informative prior PDFs such as uniform prior should be selected. However, least square method can be used to propose Gaussian prior PDFs rather than uniform ones. These priors in addition to experimental strain-stress data are sent to Matlab MCMC toolbox as inputs in order to generate n samples of parameter vector through random walk in the parameter spaces. This is performed by a multi-variate normal step from the current parameter vector to a new candidate. "Metropolis ratio" is used to determine whether the new candidate vector is accepted or not, which is defined as the ratio of prior ($p(\theta)$) times likelihood ($p(\theta|D)$) for new candidate to current parameter vector. It should be noted that likelihood function is assumed as a Gaussian function around data (D), i.e., a function of the difference between model results at θ and data points ($Modelfun(\theta) - D$). If the Metropolis ratio is more than 1, the new candidate vector would be always accepted; however, if it is less than 1, the new

candidate may be accepted with a probability equal to the calculated ratio. In the case of rejection, the current parameter vector is held instead of new candidate. After n generations of parameter vectors $\{\theta^{(0)}, \dots, \theta^{(n)}\}$, the posterior PDFs can be determined by calculating the mean and covariance of this representative sample. The model can be trained with several experimental data in order to do better parameter calibration. The posterior distributions obtained from the previous training are taken into account as prior distributions for new data training.

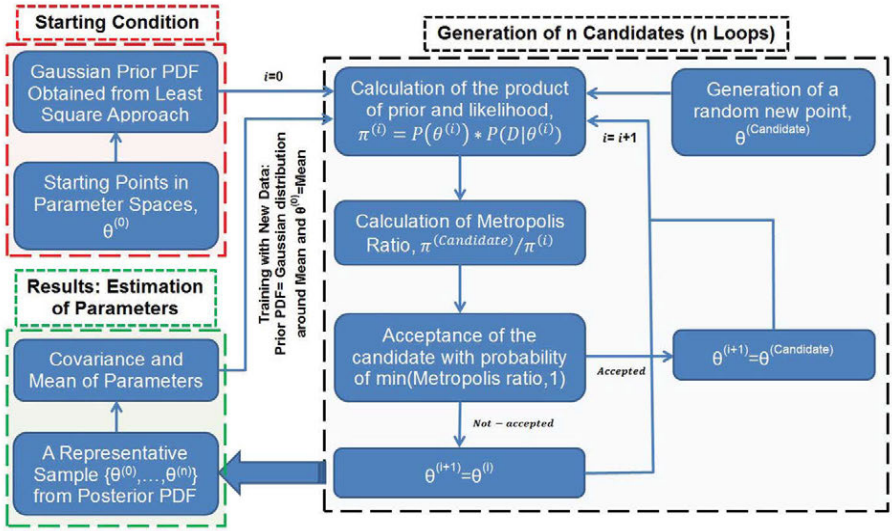

Fig.1. Flow-chart for model parameter calibration

After all the trainings, the posterior PDFs for parameters introduce the optimum parameters and their uncertainties. Nevertheless, there is a need to correlate the parameter uncertenties to the uncertainty of the model result, i.e., stress error as a funcrion of plastic strain. Generally, "propogation of uncertainty" is used in statistics for this purpose [34]. According to this method, the variance of stress (σ_S^2) can be expressed as:

$$\sigma_S^2 = \sum_i^N \left|\frac{\partial M}{\partial a_i}\right|^2 \sigma_i^2 + \sum_i^N \sum_{i \neq j}^N \left|\frac{\partial M}{\partial a_i}\right| \left|\frac{\partial M}{\partial a_j}\right| \sigma_{ij} \tag{18}$$

where M, $a_{i/j}$, σ_i^2, and σ_{ij} are model function, model parameters, parameter variances (the elements on the diagonal of variance-covariance matrix), and the covariance for any couple of parameters (the elements on the off-diagonal of variance-covariance matrix), respectively.

In order to calculate the partial derivative with respect to a_i, the following conventional numerical approach has been utilized ($\Delta a_i = 10^{-5}$) [34]:

$$\frac{\partial M(a_1, a_2, \dots, a_i, \dots)}{\partial a_i} \approx \frac{M\left(a_1, a_2, \dots, a_i + \frac{\Delta a_i}{2}, \dots\right) - M\left(a_1, a_2, \dots, a_i - \frac{\Delta a_i}{2}, \dots\right)}{\Delta a_i} \tag{19}$$

Results and Discussion

According to the plastic flow model described in section 2.1, the model results in plastic deformation region have been plotted in Fig.2. They show considerable differences with the experimental data mentioned in the section 2.2.

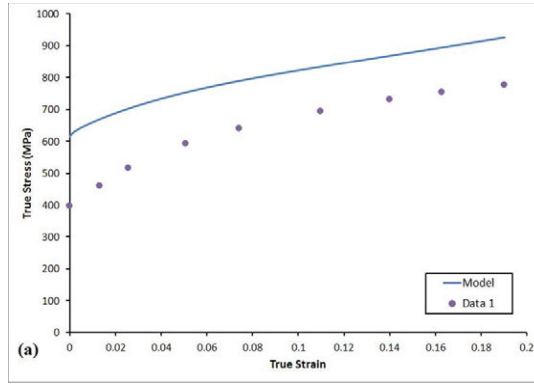

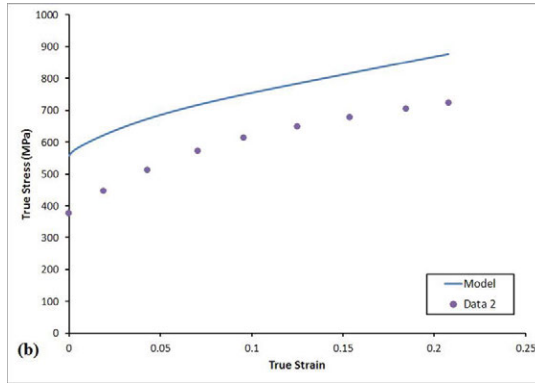

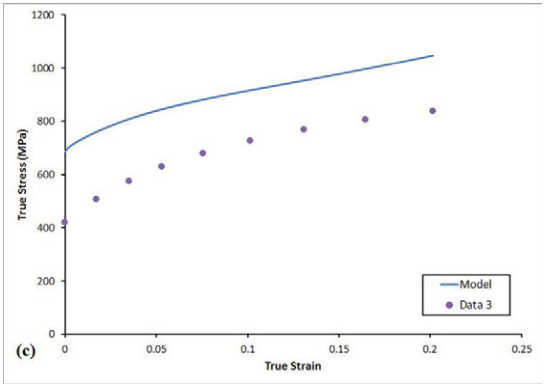

Fig.2. Comparison of model results and experimental data: (a) TRIP 1, (b) TRIP 2, and (c) TRIP 3

For this reason, parameter calibration is certainly required for our model. In this regard, the most sensitive model parameters have been selected for Bayesian calibration, including 4 parameters from dislocation density evolution model and 4 parameters from SIMT model. Then the model has been sequentially trained with all three experimental data shown in table 4 and Fig.2. The results for the parameter values and uncertainties can be observed in table 5.

Table5. 8 model parameter values before and after trainings with three experimental data

Parameter	dislocation density evolution model				SIMT model			
	α	σ_p	μ	*n-max*	a_σ	a_ε	k	m
Before Training	0.25	18	75200	4	0.1	0.03	46	3.45
After Three Trainings	0.065 $\pm$0.015	10.1 $\pm$0.07	75204 $\pm$0.24	7.91 $\pm$0.10	0.19 $\pm$0.11	0.074 $\pm$0.02	20.1 $\pm$0.24	1.45 $\pm$0.39

In Fig.3, the results of random walk ($n = 1000$) for each given parameter have been illustrated. These trace-plots have been obtained during training with third experimental data. In addition, the correlation between each pair of parameters during third training is observable in Fig.4. It is worth noting that the regions in parameter spaces with high density of points should contain the optimum values for parameters. Optimal correlation between parameters can be sometimes linear, either increasing or decreasing. In some cases, this correlation is completely clear as observed for m-SIM and shear modulus or Peierls stress and consequently for shear modulus and Peierls stress unlike some other cases in which the lines are thick since the points are more scattered, e.g., a-stress and m-SIM or n-max. However, there is almost no correlation between parameters when a horizontal or vertical line appears in the parameter spaces. This means the variation of one parameter does not considerably affect the optimal value of the other parameter such as K-SIM and m-SIM or shear modulus.

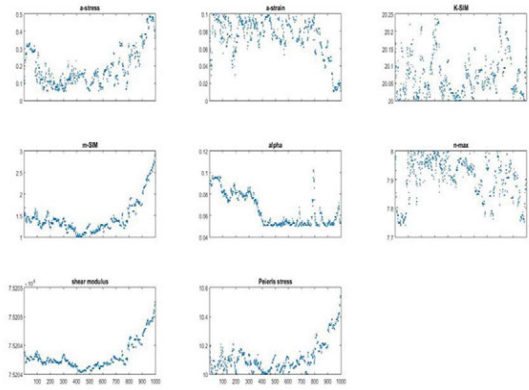

Fig.3. Trace-plots for the model parameters during training with third experimental data

Fig.4. Optimal correlation between model parameters during training with third experimental data

As shown in Fig.5, model results show good agreement with experimental data after the calibration of model parameters. According to propagation of uncertainty method, red and green lines in this figure are corresponding to $\sigma(\varepsilon) \pm \sigma_s(\varepsilon)$ and $\sigma(\varepsilon) \pm 2\sigma_s(\varepsilon)$, respectively. It means that strain-stress curve is situated in the area between red lines with the probability of 68% and in the area between green lines with the probability of 95%.

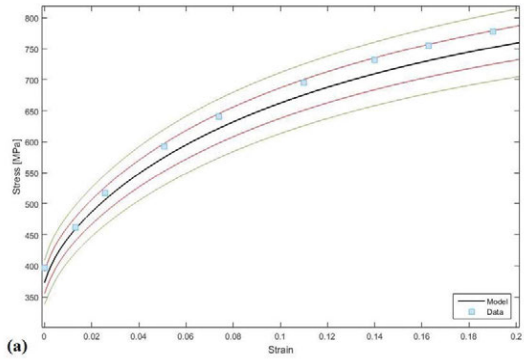

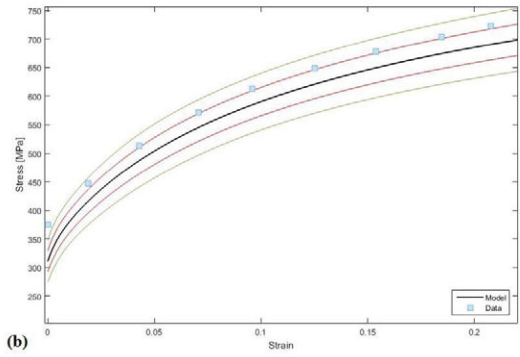

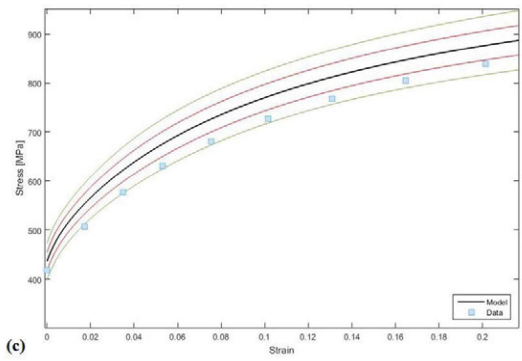

Fig.5. Comparison of model results coupled with their errors and experimental data after parameter calibration: (a) TRIP 1, (b) TRIP 2, and (c) TRIP 3

Summary

In this paper, a new physical-based model has been proposed besides the other contributing mechanisms such as Peierls, Hall-Petch, and solid solution hardening effects to predict plastic flow behavior of TRIP steels. It is defined based on Rivera and Haidemenopoulos models describing dislocation density evolution of each phase and strain-induced martensitic transformation, respectively. These models can be adapted to multi-phase microstructures through a self-consistent manner. In order to decrease the discrepancies between model results and experimental data, model parameters have been calibrated using a Bayesian approach based on Metropolis-Hastings MCMC algorithms. After the parameter calibration, good agreements have been achieved between model results and experimental data.

Acknowledgements

RA acknowledges the support of NSF through grants CMMI-0900187 and 095398, as well as 1534534 (DMREF). RA and PJ would like to thank and acknowledge Pedro Rivera (Cambridge), Shengyen Li (NIST) and Zenon Medina-Cetina (Texas A&M University) for stimulating discussions.

References

1. O. Grassel et al., "High strength Fe-Mn-(Al, Si) TRIP/TWIP steels development -properties – application," International Journal of Plasticity, 16 (2000), 1391-1409.

2. C. Herrera, D. Ponge, and D. Raabe, "Design of a novel Mn-based 1 GPa duplex stainless TRIP steel with 60% ductility by a reduction of austenite stability," Acta Materialia, 59 (2011), 4653–4664.

3. O. Matsumura, Y. Sakuma, and H. Takechi, "Enhancement of Elongation by Retained Intercritical Annealed 0.4C-1.5Si-0.8Mn Austenite in Steel," Transactions ISIJ, 27 (1987), 570-579.

4. S. Oliver, T.B. Jones, and G. Fourlaris, "Dual phase versus TRIP strip steels: comparison of dynamic properties for automotive crash performance," Materials Science and Technology, 23 (2007), 423-431.

5. B.C. De Cooman, "Structure–properties relationship in TRIP steels containing carbide-free bainite," Current Opinion in Solid State and Materials Science, 8 (2004), 285–303.

6. H.N. Han et al., "Design method for TRIP-aided multiphase steel based on a microstructure-based modelling for transformation-induced plasticity and mechanically induced martensitic transformation," Materials Science and Engineering A, 499 (2009), 462‑468.

7. E. Girault et al., "Metallographic Methods for Revealing the Multiphase Microstructure of TRIP-Assisted Steels," Materials Characterization, 40 (1998), 111-118.

8. N.H. van Dijk et al., “Thermal stability of retained austenite in TRIP steels studied by synchrotron X-ray diffraction during cooling,” Acta Materialia, 53 (2005), 5439–5447.

9. X.D. Wang et al., “Microstructures and stability of retained austenite in TRIP steels,” Materials Science and Engineering A, 438–440 (2006), 300–305.

10. O. Matsumura, Y. Sakuma, and H. Takechi, “Enhancement of Elongation by Retained Intercritical Annealed 0.4C-1.5Si-0.8Mn Austenite in Steel,” Transactions ISIJ, 27 (1987), 570-579.

11. F. Lani et al., “Multiscale mechanics of TRIP-assisted multiphase steels: II. Micromechanical modelling,” Acta Materialia, 55 (2007), 3695–3705.

12. Y. Tomita and T. Iwamoto, “Computational prediction of deformation behavior of TRIP steels under cyclic loading,” International Journal of Mechanical Sciences, 43 (2001), 2017–2034.

13. S. Thibaud, N. Boudeau, and J.C. Gelin, “TRIP steel: Plastic behavior modelling and influence on functional behavior,” Journal of Materials Processing Technology, 177 (2006), 433–438.

14. G.N. Haidemenopoulos, N. Aravas, and I. Bellas, “Kinetics of strain-induced transformation of dispersed austenite in low-alloy TRIP steels,” Materials Science & Engineering A, 615 (2014), 416–423.

15. J.Y. Liu et al., “Simulation of mechanical behavior of multiphase TRIP steel taking account of transformation-induced plasticity,” Computational Materials Science, 43 (2008), 646–654.

16. L. Delannay, P. Jacques, and T. Pardoen, “Modelling of the plastic flow of trip-aided multiphase steel based on an incremental mean-field approach,” International Journal of Solids and Structures, 45 (2008), 1825–1843.

17. G.L. Bretthorst et al., An Introduction to Parameter Estimation using Bayesian probability theory, (Dartmouth, P.F. Fougere (ed.) Kluwer Academic Publishers, 1989), 53-79.

18. B.P. Carlin and S. Chib, “Bayesian Model Choice via Markov chain Monte Carlo Methods,” Journal of Royal Statistical Society B, 57 (1995), 473-484.

19. W.J. Browne and D. Draper, “A comparison of Bayesian and likelihood-based methods for fitting multilevel methods,” Bayesian Analysis, 1 (2006), 473-514.

20. E.I. Galindo-Nava, A. Perlade, and P.E.J. Rivera-Díaz-del-Castillo, “A thermostatistical theory for solid solution effects in the hot deformation of alloys: an application to low-alloy steels,” Modelling and Simulation in Materials Science and Engineering, 22 (2014), 1-34.

21. P.E.J. Rivera-Díaz-del-Castillo, K. Hayashi, and E.I. Galindo-Nava, “Computational design of nanostructured steels employing irreversible thermodynamics” Materials Science and Technology, 29 (2013), 1206-1211.

22. K.J. Irvine, “Strength of austenitic stainless steels,” The Journal of the Iron and Steel Institute, 207 (1969), 1017 -1028.

23. R.M. Rodriguez and I. Gutierrez, “Unified formulation to predict the tensile curves of steels with different microstructures,” Materials Science Forum, 426 (2003), 4525–4530.

24. M. Azuma et al., “Modelling upper and lower bainite trasformation in steels,” ISIJ international, 45 (2005), 221–228.

25. U.F. Kocks and H. Mecking, “Physics and phenomenology of strain hardening: the FCC case,” Progress in Materials Science, 48 (2003), 171–273.

26. E.I. Galindo-Nava and P.E.J. Rivera-Díaz-del-Castillo, “Modelling plastic deformation in BCC metals: Dynamic recovery and cell formation effects,” Materials Science and Engineering A, 558 (2012), 641-648.

27. E.I. Galindo-Nava and P.E.J. Rivera-Díaz-del-Castillo, “Thermostatistical modelling of hot deformation in FCC metals,” International Journal of Plasticity, 47 (2013), 202-221.

28. S. Singh and H. Bhadeshia, “Estimation of bainite plate-thickness in low-alloy steels,” Materials Science and Engineering A, 245 (1998), 72–79.

29. S. Li et al., “Describing deformation behaviour of TRIP and dual phase steels employing irreversible thermodynamics formulation,” Materials Science and Technology, (2015): 1743284715Y-0000000076.

30. S. Morito, J. Nishikawa, and T. Maki, “Dislocation density within lath martensite in Fe-C and Fe-Ni alloys,” ISIJ international, 43 (2003), 1475–1477.

31. M. Takahashi and H. Bhadeshia, “Model for transition from upper to lower bainite,” Materials Science and Technology, 6 (1990), 592–603.

32. S.M. Lynch, Introduction to Applied Bayesian Statistics and Estimation for Social Scientists, (New York: Springer, 2007), 1-6.

33. E. Girault et al., “Comparison of the effects of silicon and aluminium on the tensile behaviour of multiphase TRIP-assisted steels,” Scripta materialia, 44 (2001), 885-892.

34. J. Tellinghuisen, “Statistical Error Propagation,” Journal of Physical Chemistry A, 105 (2001), 3917-3921.

TMS2016

145th Annual Meeting & Exhibition

SUPPLEMENTAL PROCEEDINGS

Computational Thermodynamics and Kinetics

HOMOGENEOUS NUCLEATION AND INNER STRUCTURE EVOLUTION IN NUCLEUS Fe FROM CLASSIC MOLECULAR DYNAMICS SIMULATION

Jie Luo, Junjiang Xiao and Yongquan Wu*

State Key Laboratory of Advanced Special Steels, Shanghai University, Shanghai 200072, P.R. China

Keywords: Nucleation, growth, density, order, molecular dynamics simulation

Abstract

Molecular dynamic simulation was used to study the solidification process of liquid Fe with Sutton-Chen potential. Bond orientational order (BOO) parameters and Voronoi polyhedron index (VPI) method, named BOO+VPI method, were applied to identify atomic local structure and local volume precisely. During the solidification process, two large clusters were detected, one is an imperfect five-fold twinning structure, and the other is a lamellar structure. In addition, the density and order of the two clusters were analyzed along with their growth. All analyses suggest that the density and the order of the crystal nucleus increase gradually with the increase of the size, and the order of the crystal nucleus with the five-fold twinning structure is higher. Meanwhile, the embryos are always found in high structure-ordered region instead of high density region.

Introduction

Crystallization[1, 2] plays a prominent role in physical, chemical and material science. Meanwhile, crystal nucleation from an undercooled melt is one of the fundamental process during solidification. Despite this, even for simple metals such as Fe[3] or model system such as hard spheres[4-6], nucleation is far from being well understood at a microscope level.

In addition, although crystal nucleation has been the subject of extensive experiment and theoretical study[7]. Our understanding of crystal nucleation and growth regime at the microscope level is still limited. Due to lack a reliable quantitative understanding of crystallization at present, it deserves more studies on this topic, especially for the phase transition, so the application of molecular dynamic (MD) simulation becomes more and more important.

A large number of experiments[8] and simulations[9, 10] show that the formation of stable solid from super-cooled melt is an extremely complicated process. The most popular view is that the pre-critical nuclei exists in high bond orientational order regions, with the collective effect of density fluctuation[11-13] and bond-order fluctuation, when a crystallite reaches the critical size for which the energy gain for volume growth overcomes the free energy penalty for surface formation. After that, the critical nuclei undergo upon a rapid growth process until the complete solidification.

There are two basic theories about solidification, one is the classical nucleation theory[14, 15], the other one is two-step nucleation theory[15]. The classical nucleation theory holds that the formation of the critical crystal nucleus is the collective action of the density fluctuation and the structure fluctuation[16, 17], moreover, the two order parameters proceed simultaneously. However, two-step nucleation theory, formulated by Ostwald, states that the density and

structure fluctuation that result in a crystalline nucleus occurring not simultaneously, but in sequence. The structure fluctuation follows or superimposed on the density fluctuation, which promotes the formation of the critical crystal nucleus. Moreover, Ostwald's step rule emphasizes that the nucleus formed from the melt is in the phase closest in free energy to the liquid phase.

All the time, most studies were concentrated on model system, such as hard sphere model and Lennard-Jones fluid model[18, 19]. With regard to the Lennard-Jones fluid model, a large number of simulation shows that its pre-critical nuclei has a body-centered cubic (BCC) structure rather than stable face-centered cubic (FCC) structure, then, as the crystalline reaches critical size, the core position is filled with FCC structure, while in the surface, a high degree of BCC ordering is attained.

In this letter, we present a molecular dynamics study of the solidification of liquid Fe. The main purpose of this research is to study the morphological and structural changes of the clusters in the process of solidification of Fe and the variation of the density and order of the clusters with different shapes and sizes. Specific comparative analysis is presented in the conclusion part.

Computational experiment procedure

The MD simulations were performed on iron with 1024000 Fe atoms by a Sutton-Chen potential[20]. The potential energy U is written as the sum of a contribution arising from pairwise interactions and a contribution of a many-body term

$$\mathrm{U} = \frac{1}{2}\sum_{\mathrm{i}=1}^{\mathrm{N}}\sum_{j\neq i}\varepsilon\left(\frac{a}{r_{ij}}\right)^{n} - \varepsilon C\sum_{i=1}^{N}\sqrt{\rho_i} \tag{1}$$

in which r_{ij} is the distance between atom i and atom j, N is the number of atoms in the system, ε is a parameter with dimensions of energy, and besides, the density term ρ_i is given by

$$\rho_i = \sum_{j\neq i}\left(\frac{a}{r_{ij}}\right)^{m} \tag{2}$$

a is a parameter with dimensions of length. n and m are positive integer.

We use the set of parameters as follows: ε=0.0006eV a=0.36467nm n=15 m=4 and C=1104.7351

First of all, we built a supercell, which is composed of 12800 perfect BCC atoms, then heat it up to 3000K to make it melt completely. The system was then cooled to 1833K and to achieve the state of equilibrium completely we made the system undergo upon a relaxation process at this temperature with 10^6 steps.

In the second step, we made a combination among 8 copies of this system, thus, a new system consisting of 1024000 Fe atoms was established.

Finally, in order to observe the nucleation and growth process, the system was cooled from 1833K to 1710K, we equilibrated the system for 5.5×10^5 steps and other 5×10^4 steps for the sake of statistics.

The Berendsen thermostat was applied to control the temperature for every step and the Andersen method was applied for controlling pressure. Besides, the equations of atomic motion were integrated by the Verlet-Velocity algorithm with a time step of 2fs. The periodic boundary conditions were applied for the whole system.

Results and Discussion

We tracked the whole solidification to observe the evolution of cluster structure. During this process, the continuous attachment and disattachment between clusters led to the formation of two big clusters. One is a lamellar structure, named cluster_1 and the other is an imperfect five-fold twinning structure, named cluster_2. The large clusters defined here are those whose size exceed 1000 at a certain time and its final size divide the initial size must more than 100, in other words, during the whole solidification the size of cluster expanded one hundred times. Then, cluster_1 and cluster_2 merged into a larger cluster at 100.2ps, named cluster_1_2, owing to the collision. After that, system realized complete solidification.

To identify crystalline particles and atomic local volume, we make full use of the local orientational order parameter[21] and Voronoi polyhedron index (VPI) method. It is useful to characterize local packing symmetries with local orientational order parameter. At the same time, it is convenient to follow the formation of solid clusters and to distinguish between different polymorphs. As defined in Eq.(3)

$$\overline{q_{lm}}(i) \equiv \frac{1}{N_b(i)} \sum_{j=1}^{N_b(i)} Y_{lm}(\hat{r}_{ij}) \tag{3}$$

From the $\overline{q_{lm}}(i)$ we can construct local invariants,

$$q_l(i) \equiv [\frac{4\pi}{2l+1} \sum_{m=-l}^{l} |\overline{q_{lm}}(i)|^2]^{\frac{1}{2}} \tag{4}$$

and

$$\hat{\omega}_l(i) \equiv \frac{\sum_{\substack{m1,m2,m3 \\ m1+m2+m3=0}} \begin{pmatrix} l & l & l \\ m_1 & m_2 & m_3 \end{pmatrix} \overline{q_{lm_1}}(i)\overline{q_{lm_2}}(i)\overline{q_{lm_3}}(i)}{[\sum_{m=-l}^{l} |\overline{q_{lm}}(i)|^2]^{3/2}} \tag{5}$$

Two particles *i* and *j* are defined as neighbors if the distance between them is less than 3.45Å (corresponding to first minimum in pair-correlation function of liquid Fe) A pair of neighboring particles is connected if dot-product $q_6(i)\cdot q_6(j)$ is larger 0.5. At the same time, if the number of connections with its neighboring particles exceeds 7, therefore we identify it as solid-like particle[21].

What's more, to identify the crystal polymorphs, we take advantage of the diverse symmetries that the crystal have on the W_6 and W_4 axis. The BCC structure can be distinguished from closed-packed crystals such as hexagonal close-packed (HCP) and FCC, since W_6 is positive in the former whereas negative for the latter. At the same time, the FCC structure and HCP structure can be characterized by the distribution of W_4, thus, W_4 is good to distinguish between FCC crystals (for which it has negative value) and HCP crystals (for which it has positive value).

Figure 1a and 1b present the change of the fraction of different crystal structure in the whole solidification process of the two clusters. Figure 1a shows that the fraction of BCC structures steadily decreases at the expenses of both FCC and HCP structures. Moreover, the fraction of HCP is higher than that of FCC before aggregation. Figure 1b shows that the percentage of HCP is floating in 40%~50%, the fraction of FCC increases as cluster get bigger (In general, the HCP atoms are concentrated in the position of the five-fold axis, meanwhile, the majority of FCC atoms are gathered in the intermediate zone between two axis, both the FCC and HCP atoms directly contribute to the formation of imperfect five-fold twinning structure) and the fraction of BCC atoms decreases gradually. At the moment of aggregation, the fraction of different crystal

polymorphs exhibit a mutation. The fraction of HCP atoms presents a dump and the fraction of FCC atoms displays a sharply increases. The reason for this phenomenon is that in terms of cluster_1, f_{FCC}≈23%, f_{HCP}≈54%, while with respect to cluster_2, f_{FCC}≈33%, f_{HCP}≈42%, so the phenomenon of the mutation is inevitable. The final steady state of the whole solidification process is as follows: $f_{HCP}>f_{FCC}>f_{BCC}$.

The most serious discrepancy between Figure 1a and 1b is the change tendency of the fraction of FCC atoms in the two clusters. It is evident that the fraction of FCC atoms not increases monotonously but with the tendency of increasing gradiently in cluster_2.

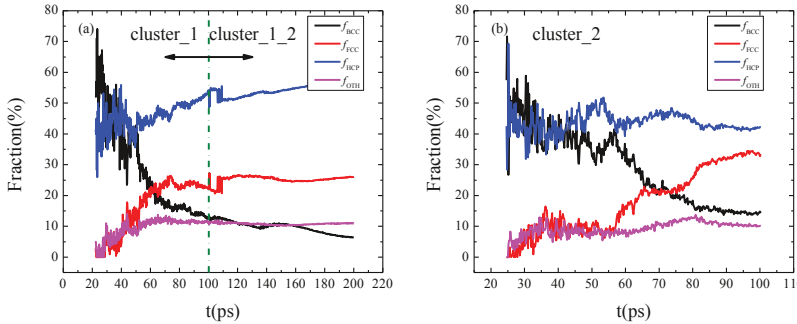

Figure 1. The fraction of different structure components, such as BCC (black line) FCC (red line) HCP (blue line) and OTH (pink line), in the nucleated cluster as a function of simulation time. The vertical dashed line indicates aggregation between two clusters. If solid-like atoms do not belong to BCC-like structure or closed-packed structure, then, it is considered as OTH atoms.

We make a detailed analysis about the internal composition of the two clusters in the last part. Next, we also make a comparison between density and the value of the order parameters, belonging to the two clusters. Figure 2 shows that the density of cluster_1 is the same as that of cluster_2 to a large extent, no matter it is in the surface or in the core. In contrast, the value of structure order parameter in the core of cluster_2 is somewhat higher than the value of the order parameter in the core of cluster_1. In terms of the order parameter in the surface, it reaches the same value almostly. As a consequence, the value of the order parameter in cluster_2 is higher than that of cluster_1. In addition, the density of cluster_1 and cluster_2 are increasing with time in terms of the whole cluster. The important point to note is that the value of order parameter in cluster_2 increases gradiently. We suspect that the appearance of this phenomenon may be related to its internal structure. In particular, it is most easily seen that the amplitude of fluctuation of two parameters is larger in surface than in core, which contributes to the diffusion properties of the interface between clusters and super-cooled melt.

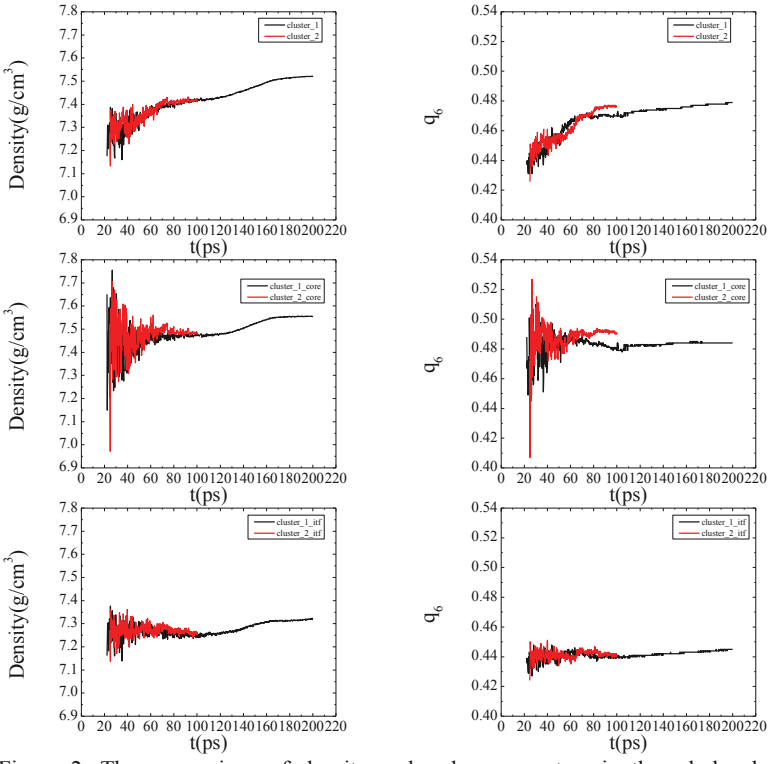

Figure 2. The comparison of density and order parameters in the whole cluster, core and interface of cluster_1 (black line) and cluster_2 (red line). The curve reflects the relationship of the density and the structure order parameters with simulation time.

As discussed in the above, the density and order change with the time during the solidification process. In the following part, we will show the distribution of density and the order in different regions of the two clusters. As we can seen from Figure 3(a) and Figure 3(b) that the density and the order decrease both from core to interface and from interface to liquid no matter in the lamellar structure or in the imperfect five-fold twinning structure. Besides, we make a detailed analysis about the distribution of density and the order in the different partition, including core and interface, which belong to cluster itself, in addition to cloud1, cloud2, cloud3 and cloud, which respond to the local liquid environment around clusters. It is not surprised to see that the density and the order increase in an extremely small extent, which attributes to the existence of some small solid cluster in the local liquid environment. In addition, there are some important points where density distribution is broadly in agreement with that in the lamellar structure, whereas the distribution of the order presents different characteristics, which the value of the local order parameter, corresponding to core, in cluster_2 is higher than that in cluster_1, leading to the order of the imperfect five-fold twinning structure is higher than the lamellar structure. It

is evident from the curve presented in Figure 3(c) and 3(d), with respect to the phenomenon mentioned above.

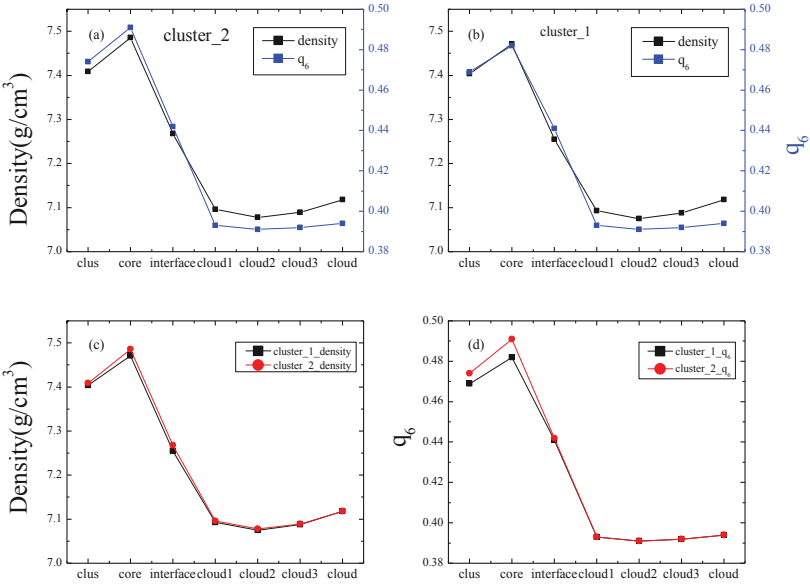

Figure 3. The distribution of the density and the order in different partition, including clus (clus represents cluster itself), core, interface, cloud1, cloud2, cloud3 and cloud. Data are averaged over simulation time.

In the following, we will discuss the relationship among density, the degree of order and size of the two large clusters. As can be seen from Figure 4, it increases with the time for density, the order and size. Moreover, the change tendency of density is similar with that of the order, its slope of curve reduce gradually. When it comes to size, it is apparent that cluster size is increases with time gradually and the slope is progressively increasing. Compared to cluster_1, the trend of cluster_2 is the same as cluster_1 to a large extent. On one hand, we cannot ignore the common features of the two clusters, but, on the other hand, we must contemplate the difference between the two clusters. In terms of cluster_2, the value of order parameters is higher than that of cluster_1 ultimately, but its size is smaller that of cluster_1. What's more, the trend of order in cluster_2 is gradient growth. In the following, we will present results of the two clusters that its density and order are increasing with size. In other words, the greater of the size, the larger of the corresponding density and the order of the two clusters.

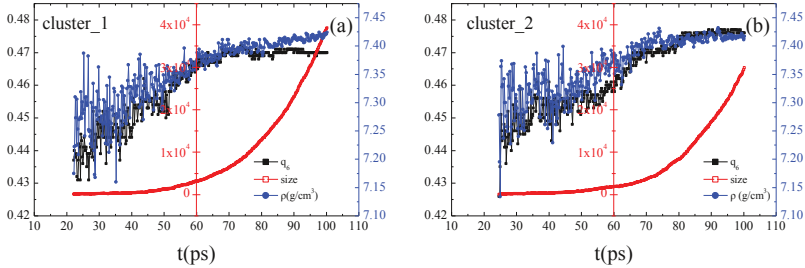

Figure 4. The density (blue), size (red) and the order (black) as a function of time in cluster_1 and cluster_2.

Finally, we also observe that the embryos are always found in high structure-ordered region instead of high density region, which is agreement with the results from the gaussian core model[22] and it has been presented in other paper.

Conclusions

In this paper, we illustrate the solidification process of liquid Fe and make a detailed analysis on the growth process. By tracing the whole solidification process of super-cooled liquid Fe, we have found two large clusters, one is a lamellar structure and the other is an imperfect five-fold twinning structure. Then, we make a brief illustration about the relationship among the density, order, and size of the two clusters. All analyses suggest that the density and the order of the crystal nucleus are gradually increasing with the increase of the size, which is similar with hard sphere model and the order of the crystal nucleus with the five-fold twinning structure is higher. Besides, we also find that the embryos are always found in high structure-ordered region instead of high density region.

Acknowledgment

The authors thank the support from National Natural Science Foundation of China (Nos. 50504010, 50974083, 51174131, 51374141), Joint Funds of the National Natural Science Foundation of China (No. 50774112), National Basic Research Program of China (No. 2012CB722805).

References

1. S. Jungblut and C. Dellago, "Crystallization of a binary Lennard-Jones mixture," *Journal of Chemical Physics*, 2011. **134**(10).
2. D.W. Oxtoby, "Crystal nucleation in simple and complex fluids," *Philosophical Transactions of the Royal Society of London Series a-Mathematical Physical and Engineering Sciences*, 2003. **361**(1804): p. 419-427.
3. R. Li, Y.Q. Wu, and J.J. Xiao, "The nucleation process and the roles of structure and density fluctuations in supercooled liquid Fe," *The Journal of Chemical Physics*, 2014. **140**(3): p. 034503.
4. S. Auer and D. Frenkel, "Prediction of absolute crystal-nucleation rate in hard-sphere

colloids," *Nature*, 2001. **409**(6823): p. 1020-1023.
5. B. O'Malley and I. Snook, "Crystal Nucleation in the Hard Sphere System," *Physical Review Letters*, 2003. **90**(8): p. 085702.
6. V. Luchnikov, et al., "Crystallization of dense hard sphere packings - Competition of hcp and fcc close order," *Journal of Molecular Liquids*, 2002. **96-7**: p. 185-194.
7. P. Harrowell and D.W. Oxtoby, "A molecular theory of crystal nucleation from the melt," *Journal of Chemical Physics*, 1984. **80**(4): p. 1639-46.
8. U. Gasser, A. Schofield, and D.A. Weitz, "Local order in a supercooled colloidal fluid observed by confocal microscopy," *Journal of Physics-Condensed Matter*, 2003. **15**(1): p. S375-S380.
9. M. Li, et al., "Molecular dynamics investigation of dynamical heterogeneity and local structure in the supercooled liquid and glass states of Al," *Physical Review B*, 2008. **77**(18): p. 184202.
10. T. Yamamoto, "Molecular dynamics simulations of polymer crystallization in highly supercooled melt: Primary nucleation and cold crystallization," *The Journal of Chemical Physics*, 2010. **133**(3): p. 034904.
11. P.G. Vekilov, "Dense Liquid Precursor for the Nucleation of Ordered Solid Phases from Solution," *Crystal Growth & Design*, 2004. **4**(4): p. 671-685.
12. K. Schätzel and B.J. Ackerson, "Density fluctuations during crystallization of colloids," *Physical Review E*, 1993. **48**(5): p. 3766-3777.
13. P. Desre, A.R. Yavari, and P. Hicter, "Homogeneous nucleation via atomic density fluctuations in undercooled liquid metals," *Philosophical Magazine B (Physics of Condensed Matter, Electronic, Optical and Magnetic Properties)*, 1990. **61**(1): p. 1-13.
14. P. Rein ten Wolde and D. Frenkel, "Homogeneous nucleation and the Ostwald step rule," *Physical Chemistry Chemical Physics*, 1999. **1**(9): p. 2191-2196.
15. D. Erdemir, A.Y. Lee, and A.S. Myerson, "Nucleation of Crystals from Solution: Classical and Two-Step Models," *Accounts of Chemical Research*, 2009. **42**(5): p. 621-629.
16. T.M. Truskett, et al., "Structural precursor to freezing in the hard-disk and hard-sphere systems," *Physical Review E*, 1998. **58**(3): p. 3083-3088.
17. F. Sedlmeier, D. Horinek, and R.R. Netz, "Spatial Correlations of Density and Structural Fluctuations in Liquid Water: A Comparative Simulation Study," *Journal of the American Chemical Society*, 2011. **133**(5): p. 1391-1398.
18. J.D. Honeycutt and H.C. Andersen, "Molecular dynamics study of melting and freezing of small Lennard-Jones clusters," *The Journal of Physical Chemistry*, 1987. **91**(19): p. 4950-4963.
19. W. Polak, "Structural properties of solid nuclei forming in Lennard–Jones clusters during simulated cooling," *Computational and Theoretical Chemistry*, 2013. **1021**(0): p. 268-274.
20. L. Koči, A.B. Belonoshko, and R. Ahuja, "Molecular dynamics study of liquid iron under high pressure and high temperature," *Physical Review B*, 2006. **73**(22): p. 224113.
21. W. Lechner and C. Dellago, "Accurate determination of crystal structures based on averaged local bond order parameters," *Journal of Chemical Physics*, 2008. **129**(11): p. 114707.
22. J. Russo and H. Tanaka, "Selection mechanism of polymorphs in the crystal nucleation of the Gaussian core model," *Soft Matter*, 2012. **8**(15): p. 4206-4215.

ANISOTROPY OF CRYSTAL-MELT INTERFACE OF BCC-Fe AND FCC-Fe FROM MOLECULAR DYNAMICS SIMULATION

Linlin Lv, Yewei Jiang, Yongquan Wu*and Junjiang Xiao

State Key Laboratory of Advanced Special Steels, Shanghai University, Shanghai 200072, P.R. China

Keywords: crystal-melt interface, MD simulation, anisotropy, melting point, kinetic coefficient

Abstract

Thermodynamic and kinetic properties of crystal-melt (c-m) interface were computed for both BCC and FCC phases of Fe by molecular-dynamics simulation. Two Sutton-Chen potentials were adopted to describe the two solid phases of Fe. Firstly discussed is the anisotropy of melting point in different interfacial orientation which is calculated by two different methods (the coexisting phase method(CPM) and the interfacial velocity methods(IVM)). Free solidification simulations were used to determine the kinetic coefficient μ of the c-m interface. The anisotropy of μ with respect to growth direction is $\mu_{100} > \mu_{110}, \mu_{100} > \mu_{111}$ for the BCC phase and $\mu_{100} > \mu_{110} \sim \mu_{111}$ for the FCC phase, and the kinetic coefficients of BCC are larger than the counterparts for he FCC. Through the interfacial roughness of BCC-Fe under supercooling/superheating, the slight asymmetry between melting and solidifying can be observed too.

Introduction

The thermodynamics and kinetics of crystal-melt interface have an important influence in many applications of metallic materials[1, 2], e.g., to the melting point of crystallization and the growth rate. With the limit of the experiment condition, these related parameters, e.g., melting point(T_m), kinetic coefficient(μ), interfacial roughness, are difficult to be observed firsthand by experiment in most situation, so that the study remains in the micrometer scale. However the molecular dynamics(MD) simulation[3-5] makes a great contribution to the atomic exploration of interface in the base that the study of atomic scale is rare. The MD simulation not only can observe the structure and dynamic procedure of the particles in system, but also can obtain the thermodynamic statistical result.

There are several methods to calculate T_m : traditional static searching strategy[6], the superheating and supercooling method[7], coexisting phase method(CPM)[8], NPH(constant number, pressure, and enthalpy) relaxation method[9]. Through comparing these simulation results and experimental equilibrium melting point, the T_m (2550K) of face centered cubic(FCC) Fe calculated by traditional static searching strategy[6] and the T_m (2400K) of body centered cubic(BCC) Fe by the NPH relaxation method are far from the experimental result(1811K)[10], the superheating and supercooling method is most accurate. In this paper, we adopt the CPM

which will be described in detail in the next section to calculate the T_m. Meanwhile the size affect and the anisotropy of T_m in different metals, such as Ni[11], V[12], are researched. However the systematic study about BCC-Fe and FCC-Fe is still rare up to now.

As another important property, the growth rate of solidification process is decided by thermodynamic driving force. There are different views about the growth model: Broughton, Gilmer and Jackson(BGJ)[13] proposed a collision-limited growth model in the Lennard-Jones system, and diffusion-limited growth model(W-F model)[14] is verified by Ashkenazy and Averback[15] in high-temperature regime for FCC and BCC metals. Meanwhile the study about the anisotropy of μ is researched in different system, e.g., Lennard-Jones[16, 17], BCC metals[18, 19], FCC metals[11, 18, 20], hexagonal close-packed(HCP) metals[21]. For the asymmetry between the solidifying and melting process, Celestini *et al.* found obvious asymmetry in three different directions of metal Au. Nevertheless, the strictly symmetry is observed by Sun et al. in BCC-Fe.

In this paper, the systematic research about BCC- and FCC-Fe is simulated to make up the shortage of previous study.

Simulation details

Simulation method

Molecular dynamic(MD) simulation was used to calculate T_m, μ, and interfacial roughness along three low index orientations of BCC- and FCC-Fe in NVE(constant number, volume, and energy) and NPT(constant number, pressure, and temperature) ensembles. We adopted the Hoover-Nose thermostat by DLPOLY. The Newton's equations of motion were integrated with Velvet Leapfrog algorithm and the timestep was set to 2fs. we set the pressure to 0.001katm and cutoff radius to 10 angstrom. Sutton-Chen potential[22], in which $\varepsilon = 0.2453\text{eV},\ a = 0.28664\text{nm},\ n = 7,\ m = 4,\ c = 7.7525$ for α-Fe under 1185K and $\varepsilon = 0.0006\text{eV},\ a = 0.36467\text{nm},\ n = 15,\ m = 4,\ c = 1104.7351$ [6] for γ-Fe above 1185K, to model the interaction among Fe atoms. This potential is validate for bulk Fe[6] and Fe nanoparticles[23-25]. Periodic boundary conditions were applied in all three directions. We simulated the balanced c-m interface at different temperatures for low index (100), (110), and (111) interfaces. We ran 6×10^5 steps with 50K intervals at NVE ensemble and ran 1.2×10^5 steps with 25K intervals at NPT ensemble which used the equilibrium configuration near melting point as the initial configuration.

Particle characterizing method

To identify different crystalline structure(like BCC, FCC, HCP structure) and calculate the atomic volume accurately, we used the average bond orientational order(ABOO)[26] parameters together with Voronoi polyhedron method(VP)[27] which can characterize the local structure. This scheme is used to identify the first shell neighbors of Fe atoms precisely.

Result and discussion

Melting point

In this paper, we adopt the CPM to calculate the T_m : we connected a liquid and a solid phase together with NVE ensemble, and acquired a polynomial line $T_m = T_0 + \alpha P + \beta P^2$ as the function of melting point with pressure. When the pressure comes to 0.001kbar, the balanced temperature is thought as the T_m of current system. As an upgrade version of CPM, the interfacial velocity method(IVM) with NPT ensemble was used to calculate T_m by fitting the relationship between interface moving velocity and the temperature. The melting point T_m is the temperature when the interface velocity comes to zero(the c-m interface is kept stable, the c-m interface will shift neither to the solid side nor to the liquid side). The CPM and IVM are more thermodynamically reasonable than other methods. Meanwhile these two methods provide a balanced or moving c-m interface to further research.

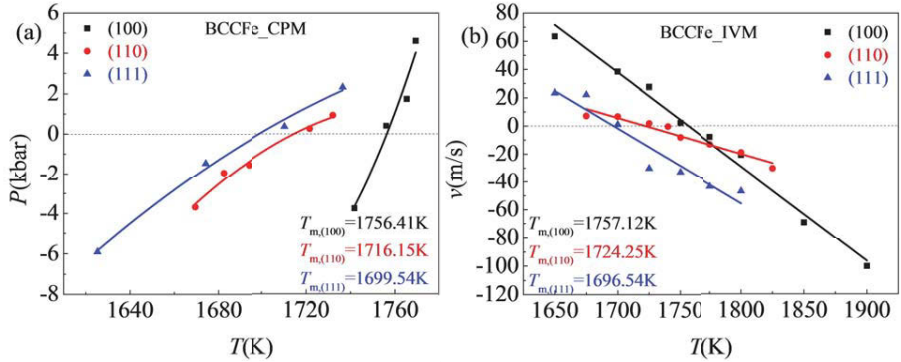

Figure 1. The relationship between pressure and temperature of the coexisting systems for (100), (110), (111) orientations under NVE ensemble for BCC-Fe with CPM(a) and IVM(b).

As described in CPM, a relationship between equilibrating pressure and temperature was obtained by fitting those datas from simulation in different systems of BCC-Fe as showed in Figure 1(a). The temperature when the fitting lines and the level line of 0.001kbar intersected was the T_m. The result obtained from IVM showed high coincidence to CPM results to be further to verify the reasonability of CPM. Through compared the three orientations, we found that the T_m s exist obvious anisotropy: $T_{m,(100)} > T_{m,(110)} > T_{m,(111)}$. It denotes that some directions will solidify/melt in advance in solidifying/melting process, such as the (111) direction will melt first and the (100) direction will melt at last in melting process.

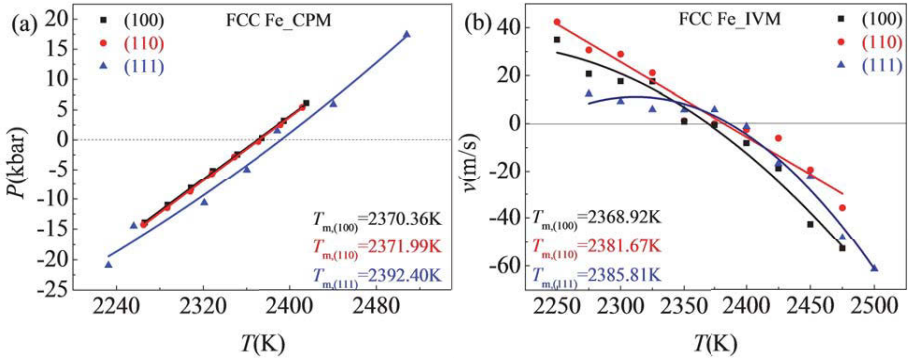

Figure 2. The relationship between pressure and temperature of the coexisting systems for (100), (110), (111) orientations under NVE ensemble for FCC-Fe with CPM(a) and IVM(b).

After the study about BCC Fe, the related properties of FCC-Fe were investigated. The melting points showed inverse tendency about the compare of T_m: $T_{m,(111)} > T_{m,(110)} > T_{m,(100)}$ on account of the different structure. However, the anisotropy of T_m was also denoted in FCC system.

Kinetic coefficient

As an important dynamic parameter, kinetic coefficient μ is defined as the proportional constant between the c-m interface velocity v and supercooling(or superheating) ΔT to describe the solidifying(or melting) ability:

$$v = \mu(T - T_m) \qquad \text{* MERGEFORMAT (1)}$$

Based on calculating the T_m, the continuous works were all carried out with NPT ensemble which the pressure was fixed at 0.001kbar. Comparing the three direction with each other, (100) have the largest value in both BCC and FCC system. The trend is $\mu_{100} > \mu_{111} > \mu_{110}$ for BCC-Fe and $\mu_{100} > \mu_{110} > \mu_{111}$ for FCC-Fe which the (100) orientation expresses largest moving tendency in both systems. From the figure, apart from the anisotropy, we also found the slope of the superheating and supercooling are different, these differences reflect the degree of asymmetry which will be discussed in the next section.

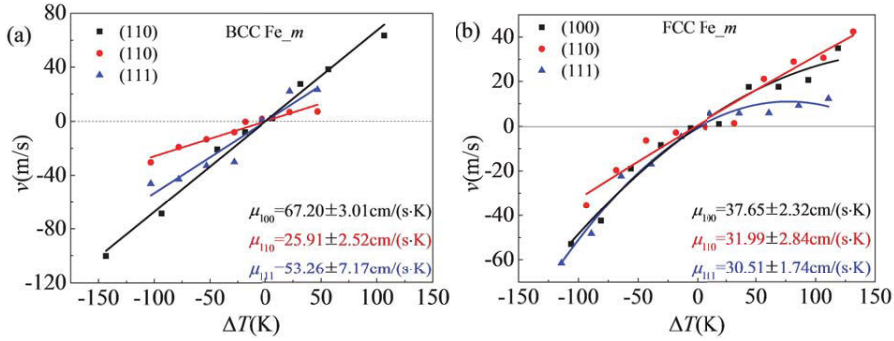

Figure 3. The relationship between velocities of c-m interfaces and ΔT of (100), (110), (111) direction for BCC-Fe(a) and FCC-Fe(b), separately. The μs are fitting slopes.

Interfacial roughness

The atoms of two interfaces were located by the ABOO+VP method, the interfacial roughness is described as follows:

$$R_{\text{int}} = \sqrt{\frac{\sum_{1}^{n_{\text{int}}} (Z_{\text{int},i} - \overline{Z_{\text{int}}})^2}{n_{\text{int}}}} \qquad \text{* MERGEFORMAT (2)}$$

Where, n_{int} is the total number of interfacial atoms; $Z_{\text{int},i}$ denotes the Z coordinate of interfacial atom i. $\overline{Z_{\text{int}}}$ means the average Z coordinate of all interfacial atoms.

We calculated the roughness of two rough interfaces in (100) orientation as an example to investigate the asymmetry. As the figure showed, the average roughness in supercooling process are 2.90 Å and 3.08 Å for two interfaces, respectively. While the average roughness in superheating process are 3.63 Å and 3.73 Å. Comparing the values of these two groups, we found that the roughness in melting process is larger than in solidifying process. The c-m interface moving in solidifying process is more stable than in melting process in result that the $R_{\text{int},m}$ is larger. It verified the asymmetry between supercooling process and superheating process.

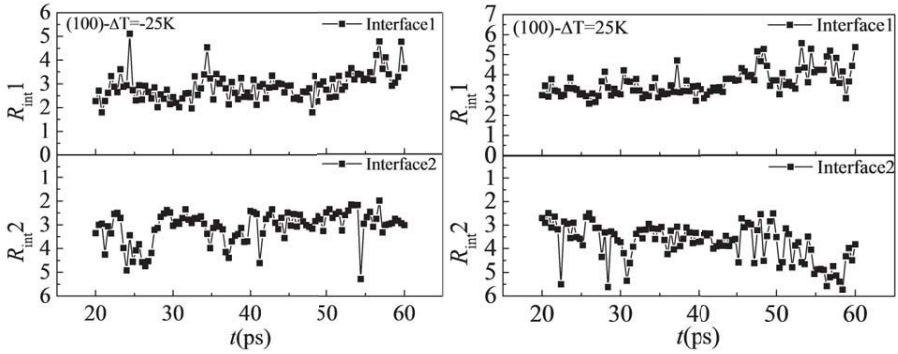

Figure 4. Variation of the interfacial roughness for two interfaces of (100) orientation with 25K supercooling and 25K superheating from 20 to 40 ps.

Conclusions

In this paper, we used MD method to simulate the solidifying and melting of the c-m interface for BCC-Fe and FCC-Fe. The result from CPM and IVM has the similar melting points and the same tendency that the melting points of BCC-Fe and FCC-Fe exist anisotropy. During the NPT relaxing stage, we found the relationship between anisotropy of μ and growth direction is $\mu_{100} > \mu_{110}, \mu_{100} > \mu_{111}$ for the BCC phase and $\mu_{100} > \mu_{110} \sim \mu_{111}$ for the FCC phase which is similar to the result from predecessors for other metals, and the kinetic coefficients of BCC are larger than the counterparts for the FCC system. To verify the asymmetry between melting and solidifying, a slight variation can be observed through the interfacial roughness of BCC-Fe under same supercooling/superheating in (100) direction.

References

1. A. Hashibon, et al., "Ordering at solid-liquid interfaces between dissimilar materials," *Interface Science*, 2001. **9**(3-4): p. 175-181.
2. B.B. Laird and A. Haymet, "The crystal/liquid interface: structure and properties from computer simulation," *Chemical Reviews*, 1992. **92**(8): p. 1819-1837.
3. V.G. Baidakov, S.P. Protsenko, and A.O. Tipeev, "Surface Free Energy of the Crystal-Liquid Interface on the Metastable Extension of the Melting Curve," *Jetp Letters*, 2014. **98**(12): p. 801-804.
4. R.L. Davidchack and B.B. Laird, "Crystal structure and interaction dependence of the crystal-melt interfacial free energy," *Physical review letters*, 2005. **94**(8).
5. J.R. Morris, et al., "The anisotropic free energy of the solid-liquid phase boundary in Al," *Interface Science*, 2002. **10**(2-3): p. 143-148.
6. Y.H. Liu, et al., "Molecular dynamics simulation of phase transformation of γ-Fe→δ-Fe→liquid Fe in continuous temperature rise process," *Acta Metallurgica Sinica*, 2010. **46**(2): p. 172~178.

7. S.N. Luo, A. Strachan, and D.C. Swift, "Nonequilibrium melting and crystallization of a model Lennard-Jones system," *Journal of Chemical Physics*, 2004. **120**(24): p. 11640-11649.
8. J.R. Morris and X. Song, "The melting lines of model systems calculated from coexistence simulations," *The Journal of Chemical Physics*, 2002. **116**(21): p. 9352~9358.
9. Y. Shibuta, S. Takamoto, and T. Suzuki, "A molecular dynamics study of the energy and structure of the symmetric tilt boundary of iron," *ISIJ international*, 2008. **48**(11): p. 1582~1591.
10. A.T. Dinsdale, "SGTE data for pure elements," *Calphad*, 1991. **15**(4): p. 317-425.
11. D.Y. Sun, M. Asta, and J.J. Hoyt, "Kinetic coefficient of Ni solid-liquid interfaces from molecular-dynamics simulations," *Physical Review B*, 2004. **69**(2): p. 024108.
12. V. Sorkin, E. Polturak, and J. Adler, "Molecular dynamics study of melting of the bcc metal vanadium. II. Thermodynamic melting," *Physical Review B*, 2003. **68**(17): p. 174103.
13. J. Broughton, G. Gilmer, and K. Jackson, "Crystallization rates of a Lennard-Jones liquid," *Physical review letters*, 1982. **49**(20): p. 1496.
14. H.W. Wilson, "XX. On the velocity of solidification and viscosity of super-cooled liquids," *The London, Edinburgh, and Dublin Philosophical Magazine and Journal of Science*, 1900. **50**(303): p. 238-250.
15. Y. Ashkenazy and R.S. Averback, "Kinetic stages in the crystallization of deeply undercooled body-centered-cubic and face-centered-cubic metals," *Acta Materialia*, 2010. **58**(2): p. 524-530.
16. E. Burke, J.Q. Broughton, and G.H. Gilmer, "Crystallization of fcc (111) and (100) crystal-melt interfaces: A comparison by molecular dynamics for the Lennard-Jones system," *The Journal of Chemical Physics*, 1988. **89**(2): p. 1030~1041.
17. H.E.A. Huitema, M.J. Vlot, and J.P. van der Eerden, "Simulations of crystal growth from Lennard-Jones melt: Detailed measurements of the interface structure," *The Journal of Chemical Physics*, 1999. **111**(10): p. 4714~4723.
18. D.Y. Sun, M. Asta, and J.J. Hoyt, "Crystal-melt interfacial free energies and mobilities in fcc and bcc Fe," *Physical Review B*, 2004. **69**(17).
19. M.W. Finnis and J.E. Sinclair, "A simple empirical N-body potential for transition metals," *Philosophical Magazine A*, 1984. **50**(1): p. 45~55.
20. J.J. Hoyt, et al., "Kinetic phase field parameters for the Cu-Ni system derived from atomistic computations," *Acta Materialia*, 1999. **47**(11): p. 3181-3187.
21. Z.G. Xia, et al., "Molecular dynamics calculations of the crystal-melt interfacial mobility for hexagonal close-packed Mg," *Physical Review B*, 2007. **75**(1): p. 012103.
22. A.P. Sutton and J. Chen, "Long-range Finnis–Sinclair potentials," *Philosophical Magazine Letters*, 1990. **61**(3): p. 139~146.
23. T. Shen, et al., "Size dependence and phase transition during melting of fcc-Fe nanoparticles: A molecular dynamics simulation," *Applied Surface Science*, 2013. **277**: p. 7-14.
24. T. Shen, Y. Wu, and X. Lu, "Structural evolution of five-fold twins during the solidification of Fe5601 nanoparticle: a molecular dynamics simulation," *Journal of Molecular Modeling*, 2013. **19**(2): p. 751~755.
25. Y. Wu, T. Shen, and X. Lu, "Evolutions of lamellar structure during melting and solidification of Fe< sub> 9577</sub> nanoparticle from molecular dynamics simulations," *Chemical Physics Letters*, 2013. **564**: p. 41~46.
26. W. Lechner and C. Dellago, "Accurate determination of crystal structures based on averaged local bond order parameters," *The Journal of Chemical Physics*, 2008. **129**(11): p. 114707.

27. C.H. Rycroft, "VORO++: A three-dimensional Voronoi cell library in C++," *Chaos: An Interdisciplinary Journal of Nonlinear Science*, 2009. **19**(4): p. ~.

THERMAL DECOMPOSITION KINETICS OF MANGANESE CARBONATE IN THE PROCESS OF MnZn FERRITE PREPARATION

Lin Wang[1], Yan-hong Li[1], Jin-lin LU[1], Wei XU[2], Hui-long Lin[1]
（1.School of Materials and Metallurgy, University of Science and Technology, Anshan 114051, China；2. ACRE Coking & Refractory Engineering Consulting Corporation, MCC, Dalian 116002, China）

Keywords: manganese carbonate，TG-DTG，thermal decomposition，activation energy，linear regression

Abstract: Thermogravimetric analysis method was used to study the decomposition of $MnCO_3$ in the process of MnZn ferrite preparation. The effects of different heating rate (5, 10, 20, 30 and 40 $K \cdot min^{-1}$) on the initial temperature and terminative temperature of the manganese carbonate decomposition were investigated. The Flynn-Wall-Ozawa method and Kissinger-Akahira-Sunose method were used to calculate the decomposition activation energy of manganese carbonate**.** The results show that the terminative temperature of manganese carbonate decomposition will increase with increasing of heating rate. The decomposition activation energy of manganese carbonate in the process of MnZn ferrite preparation calculated by FWO and KAS methods were 67.94$kJ \cdot mol^{-1}$ and 64.31$kJ \cdot mol^{-1}$, respectively. The decomposition activation energy of manganese carbonate in the process of MnZn ferrite preparation is lower than in another two systems.

Introduction

MnZn ferrite have the characteristics of high permeability, high resistivity and low loss[1], which is widely applied to the production of power transformers, wide-band pulse transformers, electronic ballast and force sensitive components[2]. Its application range covers communications, space computer technology and other electronic information industry, etc. Preparation methods of MnZn ferrite can be divided into dry process and wet process[3]. Oxide treating is the most widely used dry process, it has many advantages, such as simple process, easy to adjust the ingredient and suitable for extensive production. Manganese carbonate decomposition is most obvious in the process of reaction. Therefore, research on manganese carbonate decomposition in the process of MnZn ferrite preparation is particularly important. In this study, thermodynamic analysis was used in the process of MnZn ferrite preparation, the process of manganese carbonate decomposition was analyzed at different heating rate and the decomposition activation energy of manganese carbonate was calculated using FWO method[4,5] and KAS method[6-8], different activation energy values of the manganese carbonate decomposition were compared in different systems.

Experimental

Materials

Raw materials used in this study are pure manganese carbonate, zinc oxide, and iron oxide. Experimental apparatus adopts synchronous thermal analyzer produced by French Setaram's company. Instrument parameters are as follows: Using the temperature range of 20℃~ 1600℃，heating rate range of 0.1 ~ 50 $k \cdot min^{-1}$, sample capacity of 50mg.

The experimental and calculation process

The formula of MnZn ferrite was determined(molar ratio of Fe_2O_3：$MnCO_3$：ZnO=0.53：0.24：0.23). Masses of sample 15.5±0.5mg were taken in alumina crucible synchronous thermal analyzer every time, recording the temperature in the range of 110 ℃ ~ 1250 ℃. For TG-DTG curve, its mass loss was recorded at five heating rates of 5, 10, 20, 30 and 40$K \cdot min^{-1}$ in an air atmosphere with flow rate of 20 $ml \cdot min^{-1}$.

Conversion rate represents the extent of reaction in the process of the reaction, computation formula of manganese carbonate decomposition conversion in the process of preparation of MnZn ferrite is as follows:

$$\alpha = \frac{m_s - m_t}{m_s - m_f} \tag{1}$$

Where m_s, m_f and m_t are the initial, final, and current sample mass, respectively[8, 9]; corresponding to five heating rates taken at the same temperature.

In order to obtain the decomposition activation energy of $MnCO_3$ in the process of MnZn ferrite preparation, the two methods can obtain directly reliable E under the premise of not involve dynamic model function . Therefore, FWO method and KAS method are often used to test the activation energy of which are obtained by other methods that need to assume the reaction mechanism[9,10]. So in this study, the decomposition activation energy of $MnCO_3$ was obtained from both FWO and KAS method.

FWO method equation can be written as:

$$\ln \beta = \ln \frac{AE}{R} - \ln g(\alpha) - 5.3305 - 1.052\frac{E}{RT} \tag{2}$$

KAS method equation can be written as:

$$\ln \frac{\beta}{T^2} = \ln \frac{AR}{Eg(\alpha)} - \frac{E}{RT} \tag{3}$$

Where β is the linear heating rate, T is reaction temperature, E is the activation energy ($kJ \cdot mol^{-1}$), R is the gas constant ($J \cdot mol^{-1} \cdot K^{-1}$), A is the pre-exponential factor, $g(\alpha)$ is the mechanism function, respectively.

FWO method is to use the data obtained from the TG curve tracing on $\ln \beta — \frac{1}{T}$ point, and then getting a straight line based on least-square method, the E can be obtained taking straight slope and put in Eq.2. KAS method is to use the data obtained from the TG curve tracing on $\ln \frac{\beta}{T^2} — \frac{1}{T}$ point, the E can be obtained taking straight slope and put in Eq3.

Results and discussion

The influence of heating rate on the decomposition temperature of manganese carbonate

TG-DTG curves of the MnZn ferrite preparation at different heating rate are given in Fig.1

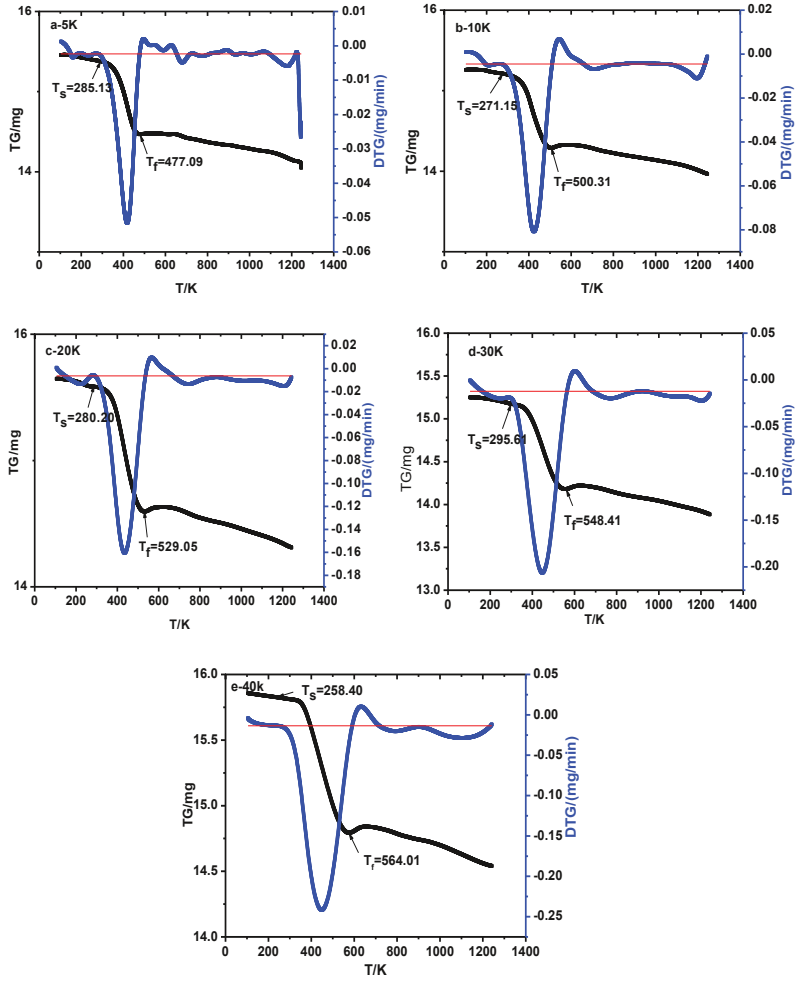

Fig.1 TG-DTG curves in the process of MnZn ferrite preparation at five different heating rates

These curves exist three weight loss peaks and one weight gain peak. The first is that $MnCO_3$ is decomposed into MnO, the second is that MnO is oxidized to Mn_3O_4, the third is that Mn_3O_4 are changed into MnO_2 further, the forth is that the volatilization of ZnO. Since the process of spinel generation have not weight change, so it cannot be reflected in the TG-DTG curves. T_s and T_f are initial and terminative temperature of $MnCO_3$ decomposition respectively in the diagram, from the diagram we can observe initial temperature T_s are 285.13℃, 271.15℃, 280.20℃, 295.61℃ and 258.40℃ respectively at five different heating rates, corresponding terminative temperature are 477.09℃, 500.31℃, 529.05℃, 548.41℃ and 564.01℃

respectively. From these results we can see that although the change of heating rate has an effect on the initial temperature, there is no obvious linear relationship between two. Terminative temperature of $MnCO_3$ decomposition reaction increased from 477.09℃ to 564.01℃ with the increasing of heating rate. So it can be concluded that terminative temperature increase with the increasing of heating rate. According to the Eq.1, the conversion rate of $MnCO_3$ decomposition at various stages of decomposition can be calculated，the relationship between conversion of $MnCO_3$ decomposition and different heating rate and temperature are shown in Fig.2. From Fig.2, $MnCO_3$ decomposition conversion will transfer to the high temperature area with the increase of heating rate.

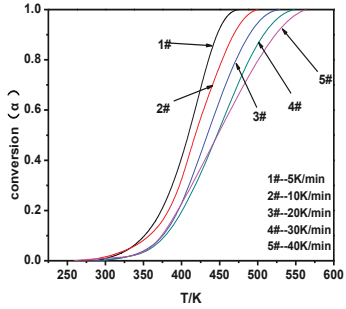

Fig.2 Relationship between $MnCO_3$ decomposition conversions and temperature at differernt heating rate

Decomposition activation energy of manganese carbonate in the process of MnZn ferrite preparation

Data of α and *T* collected from TG curves in the $MnCO_3$ decomposition range of $0.1<\alpha<0.9$ in the process of MnZn ferrite preparation at various heating rates are obtained, the linear regression of least square method were conducted. The plots of lnβ versus 1/T (Eq. 2) and ln (β/T^2) versus 1/T (Eq. 3) for the decomposition process of $MnCO_3$, based on the FWO and KAS analysis were shown in Fig.3 and Fig.4, respectively.

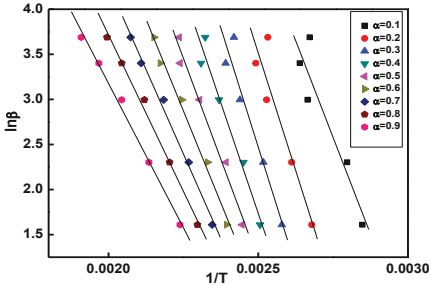

Fig.3 FWO plots for the decomposition process of $MnCO_3$ at five heating rates in various conversions (α=0.1-0.9, with 0.1 increment)

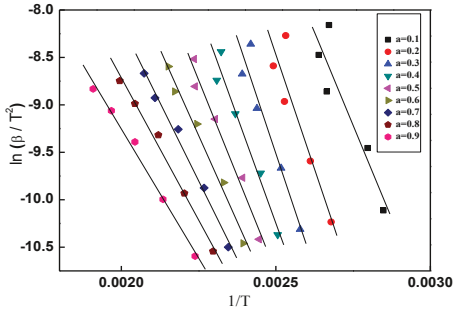

Fig.4 KAS plots for the decomposition process of $MnCO_3$ at five heating rates in various conversions (α=0.1-0.9, with 0.1 increment)

Finally the decomposition activation energy of manganese carbonate in all stages conversion rate and the correlation coefficient *r* were gained in the process of MnZn ferrite preparation, and the average decomposition activation energy of manganese carbonate in all conversion rate stages by the two kinds of method was obtained. The activation energy (E) calculated in the process of MnZn ferrite preparation were 67.94 $kJ \cdot mol^{-1}$ and 64.31 $kJ \cdot mol^{-1}$ respectively. The activation energy calculated by two kinds of method are shown in Fig.5, the result is close. The activation energies obtained from different equations, in which the values obtained by the FWO method were generally higher, were found to be consistent. Its average value is 3.63 $kJ \bullet mol^{-1}$ higher than KAS method, this is caused possibly due to different the integral foundation. It can also be noted that the *E* values are dependent on α, and the decomposition reaction should be interpreted in terms of a multi-step reaction mechanism[11,12]. In addition, the values of the correlation coefficient, for all cases of calculation were great. It can be seen that the values of E obtained from the FWO and KAS methods are reliable.

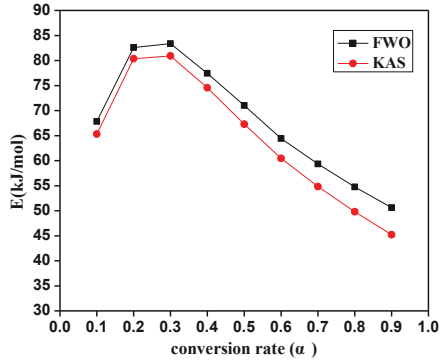

Fig.5 The reaction activation energies of $MnCO_3$ in MnZn ferrite system calculated using FWO and KAS method

Decomposition activation energy of manganese carbonate in the other system

In this paper, decomposition activation energy of manganese carbonate in the process of Mn ferrite preparation(mole ration of Fe_2O_3：$MnCO_3$=0.55:0.45) and manganese carbonate decomposition separately were studied by the same method. Decomposition activation energies of manganese carbonate in the process of Mn ferrite preparation in all stages of conversion were shown in figure 6, the average activation energies (E) in the process of Mn ferrite preparation were 74.48 $kJ \cdot mol^{-1}$ and 67.87 $kJ \cdot mol^{-1}$ respectively. The activation energies of manganese carbonate in the process of manganese carbonate decomposition separately in all stages of conversion were shown in figure 7, the average activation energy (E) calculated in the process of Mn ferrite preparation were 90.51 $kJ \cdot mol^{-1}$ and 87.59 $kJ \cdot mol^{-1}$, respectively. From the figure 6 and figure 7, It can be seen that the decomposition activation energy of manganese carbonate in the different conversion rate stages obtained by the FWO method were generally higher than KAS method.

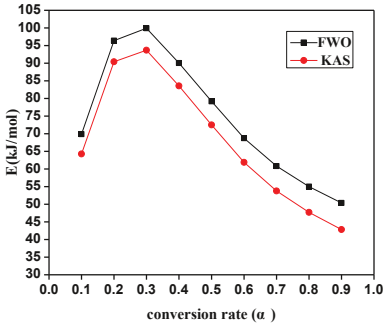

Fig.6 The reaction activation energies of of $MnCO_3$ in Mn ferrite system calculated using FWO and KAS method

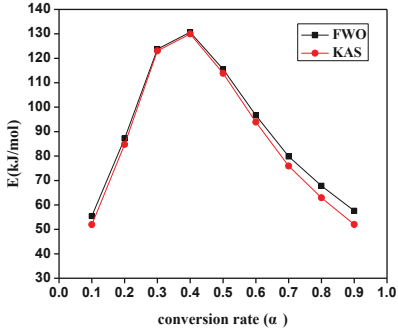

Fig.7 The reaction activation energies of $MnCO_3$ in pure $MnCO_3$ system calculated using FWO and KAS method

The comparison of decomposition activation energy of manganese carbonate in three systems

Suppose the decomposition activation energy of manganese carbonate in the process of MnZn ferrite preparation for E_1, in the process of Mn ferrite preparation for E_2, in the process of manganese carbonate decomposition separately for E_3. From the above calculation, it can be known that the activation energies of manganese carbonate has the following relationship $E_1<E_2<E_3$ regardless of FWO method and KAS method. The number of phase the manganese carbonate decomposition is the maximum in the process of MnZn ferrite preparation, the number of phase the manganese carbonate decomposition is the second in the process of Mn ferrite preparation, the number of phase the manganese carbonate decomposition separately is the least. So it can be concluded that the decomposition activation energy of the manganese carbonate reduces with the increase of the number of phase to a certain extent.

Conclusion

(1) Terminative temperature(T_f) of manganese carbonate decomposition reaction in the process of MnZn ferrite preparation will transfer to the high temperature area with the increase of

heating rate(β_i);

(2) The activation energies (E) of manganese carbonate in the process of MnZn ferrite preparation were 67.94 kJ·mol^{-1} and 64.31 kJ·mol^{-1}, respectively. The decomposition activation energies obtained by the FWO method were generally higher than the energies obtained by KAS method in different conversion rate stages.

(3) By comparison，it can be known that the decomposition activation energy of manganese carbonate in different systems has the following relationship $E_1<E_2<E_3$ regardless of FWO method and KAS method. That is to say, the decomposition activation energy of the manganese carbonate reduces with the increase of the number of phase to a certain extent.

References

[1] Xi GX，Lu MX, New Development of Synthesis of Manganese-zinc Ferrite Materials. JOURNAL OF SYNTHET IC CRYSTALS, 34(1)(2005),164-168.

[2] Wang GT et al., The New Craft of Manganese-zinc Ferrite Material with High Performance. Sichuan Nonferrous Metals, 17(1)(2006),10-15.

[3] Li LZ et al., Research Advancements and Developing Trends of MnZn Power Ferrites. MATERIALS REVIEW,22（2）(2008),93-96.

[4] Ozawa T, Kinetic analysis of derivative curves in thermal analysis. J Therm Anal, 2(1970),301~324.

[5] Flynn JH, Wall L A, A quick,direct method for the determination of activation energy from thermogravimetric data.J Polym Sci B, 4(5)(1966),323~329

[6] Kissinger HE, Reaction kinetics in differential thermal analysis. Anal Chem, 29(11)(1957),1702~1706

[7] Akahira T, Sunose T. Trans, Joint Covention of Four Electrical Institutes, Paper No.246,1969 Research report. Chiba Institute of Technology. Sci Technol, 16(1971),22~31

[8] N. Chaiyo et al., Non-isothermal kinetics of the thermal decomposition of sodium oxalate $Na_2C_2O_4$. J Therm Anal Calorim, 107(2012),1023–1029.

[9] Dunjia WANG, Zhengdong FANG, and Lianying LU, Thermal behavior and non-isothermal kinetics of the polyoxometalate of ciprofloxacin with tungstophosphoric acid. J Therm Anal Calorim, 2007, 22-2:240–4.

[10] Nopsiri Chaiyo, Rangson Muanghlua, Non-isothermal kinetics of the thermal decomposition of sodium oxalate $Na_2C_2O_4$. J Therm Anal Calorim, 107(3)(2012),1023~1029.

[11] A.Mukherjee, S.Mishra, Thermogravimetric studies and kinetics of decomposition of ammonium yttrium fluoride.Reac Kinet Mech Cat, 103(1)(2011),53~70.

[12] Chaiyo N, Boonchom B, and Vittayakorn N, Solid-state reaction synthesis of sodium niobate ($NaNbO_3$) powder at low temperature. J Mater Sci,45 (2010),1443–7.

SOLID-LIQUID PHASE TRANSITIONS OF FCC-Al AND HCP-Mg NANOPARTICLES

Yewei Jiang, Linlin Lv and Yongquan Wu*

State Key Laboratory of Advanced Special Steels, Shanghai University, Shanghai 200072, P.R. China

Keywords: phase transition, nanoparticle, molecular dynamics simulation

Abstract

We used molecular dynamics methods to simulate the melting and cooling of isolated *fcc*-Al and *hcp*-Mg nanoparticles with embedded-atom method (EAM) potentials. Bond orientational order (BOO) parameters and Voronoi polyhedron (VP) method were used to identify the local structure and local volume of each atom. The variation of energy was first analyzed to give an overview of the simulation. The inner structure evolution during the solidification was also investigated under different cooling rates. Two different inner structures, including five-fold twinning and lamellar structures, have been found in the cooling process of *fcc*-Al, while only lamellar structures for *hcp*-Mg.

Introduction

Nano-sized particles have been attracting interests for decades, due to their unique properties. Some thermodynamic properties such as surface energy and melting point have been studied through experimental[1-3] and theoretical[3] methods. Meanwhile, Molecular dynamics (MD) technique, on account of its brilliant ability to reproduce the phenomenon in extreme conditions (like high temperature and high speed), and provide huge amount of details, has played an important role in the field of simulating metallic nanoparticles, which is still difficult to be observed directly in experiments[4-6]. Wu et al.[7] investigated the melting behavior of face-centered cubic (*fcc*) iron nanoparticles and demonstrated that high percentage of surface atoms may be beneficial to the phase transition of *fcc* nanoparticles. Chui et al.[8] quenched a 10179 atoms gold nanoparticle from the melt down to 298K, and visualized the structure evolution of the five-fold twinning. Previously[9-11], we have systematically simulated the solidification and melting of isolated Fe nanoparticles with their atom numbers ranging from approximately 60 to 10,000, and found two kinds of structures: five-fold twinning and lamellar structures consisting of *fcc* and hexagonal close-packed (*hcp*) atoms stacked in different ways. However, whether these two kinds of structures will form in other different metals within different lattice structures? Here, we extend our investigation of structure evolution of nanoparticles to *fcc*-Al and *hcp*-Mg.

Simulation details

Simulation method

We performed MD simulations to reproduce the solidification of *fcc*-Al and *hcp*-Mg nanoparticles. All simulations were performed under canonical (NVT) ensemble with Nosé-

Hoover thermostat[12, 13]. The Verlet leapfrog algorithm[14] was used to integrate the Newton's equations of motion with the time step set to 2 femtosecond. The interatomic potential of *fcc*-Al and *hcp*-Mg were modeled by Sturgeon-Larid[15] and Mendelev *et al.*[16] . The whole MD simulations was carried out with no boundary condition which means the simulated particle was isolated.

The nanoparticles were built in 4 sizes with perfect lattice structures before the simulations. For *fcc*-Al, the sizes of nanoparticles were 5772, 8586, 12116 and 16754, denoted here as Al_{5772}, Al_{8586}, Al_{12116} and Al_{16754}. In the same way, the 4 samples for *hcp*-Mg was noted as Mg_{2036}, Mg_{5964}, Mg_{10268} and Mg_{20074}. All these samples were heated to a relatively high temperature (1200K for *fcc*-Al and 950K for *hcp*-Mg) and maintained for 100ps to make sure that the initial crystalline configuration melted completely. They served as the initial configurations in the cooling process, 1175-300K for *fcc*-Al and 950-400K for *hcp*-Mg, with an interval of 25K.

Particle characterizing method

To analyze the atomic-scale structural evolution, we employed a new hybrid method, named as BOO+VPI (Bond Oriented Order parameter + Voronoi Polyhedron Index)[17]. First, VPI[18] was used to identify body-centered cubic (*bcc*) atoms since it is the most accurate criterion in identifying *bcc* configuration because the Voronoi polyhedron of *bcc* has no degenerate vertices[18]. Next, BOO parameters method, proposed by Steinhardt[19], is used to evaluate the symmetries of local environment of atoms and thus identifies their local structures. For example, to distinguish solid- or liquid-like atom, frenkel number ξ is defined to denote the number of 'connected' atoms between the center atom and its first shell neighbors. If ξ of an atom, except *bcc* atoms previously sorted out via VPI, exceeds a critical number e.g. 8, the atom will be classified as solid-like atom, otherwise, liquid-like atom. Then, another BOO parameter *q4* is used to distinguish *fcc* from *hcp* atoms. The detailed description and the validity of this new method will be published somewhere in the future.

Cooling rates

We have employed four cooling rates with a range of 0.125K/ps to 1K/ps in this work. The settings of the cooling rates are presented in Table 1.

Table 1 Settings of cooling rates

	Simulation steps	Time step (ps)	Interval of temperature (K)	Cooling rates (K/ps)
RT1	12,500	0.002	25	1
RT2	25,000			0.5
RT3	50,000			0.25
RT4	100,000			0.125

We set the interval of temperature to 25K, and changed the cooling rate by using different simulation steps. For example, in the cooling procedure of RT1, the nanoparticle should be calculated for 12,500 simulation steps every 25K with a time step equals 0.002 ps.

Structural evolution of nanoparticle *fcc*-Al

Formation of *fcc*-Al nanoparticles with five-fold twins

Based on our observation, Al_{8586} tended to form five-fold twins under the cooling rate of RT2 (0.5K/ps). The variation of potential energy versus temperature of Al_{8586} during the solidification process is illustrated in the inset of Figure 1. We can define four stages: *i*, a liquid state from 1175K to 625K; *ii*, a liquid-solid transition at 600K; *iii*, structural relaxation from 600K to 550K; and *iv*, an equilibrium configuration below 550K. As temperature decreased, potential energy decreased along the liquidus to 625K. Then, a significant drop, indicating a liquid-solid phase transition, appeared at 600K. The potential energy was still slightly higher than solidus after the drop. The difference between the potential energy curve and solidus can be regarded as the driving force for the subsequent structural relaxation. The equilibrium configuration is formed at approximately 550K.

The percentage variation of *fcc*, *hcp* and amorphous atoms are showed in Figure 1. At the solidification point of 600K, when liquid–solid transition occurred, the percentages of *fcc* and *hcp* atoms dramatically increased to 10.83% and 14.02%, respectively, whereas amorphous atoms depleted to 73.61 % correspondingly. The structural relaxation occurred at the temperature ranging from 600 to 550K. For *fcc* atoms, the percentage increased violently from 10.83% to 52.61%, whereas *hcp* atoms were nearly doubled from 14.02% to 26.48% after a rise and fall. On the basis of the configuration snapshot presented in Figure 2, *hcp* atoms were observed to be in the form of twinning boundaries (TBs) or other grain boundaries. Furthermore, most of *hcp* atoms acted as TBs during structural relaxation and a mass of newly formed *fcc* atoms, were crystallized into blocks surrounded by TBs. At the temperature below 550K, the percentage curves flattened since most *fcc* and *hcp* atoms have been previously formed. Amorphous atoms remained at a percentage of 13.52%, most of which were surface atoms.

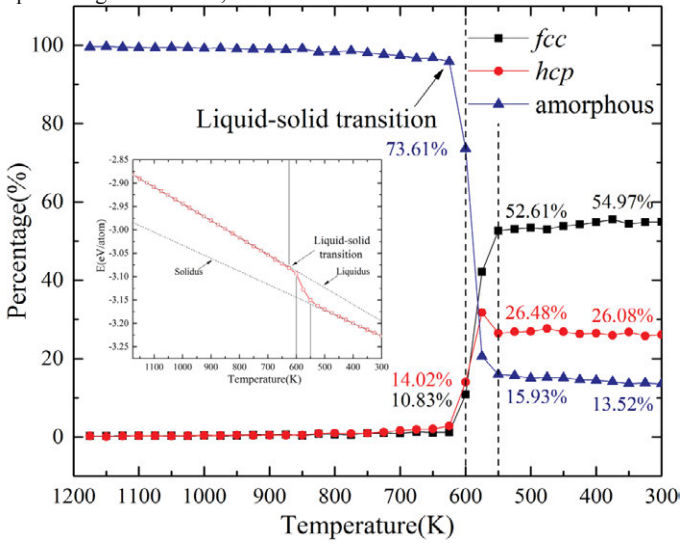

Figure 1. Percentage variation of three atom categories versus temperature of Al_{8586}. The inset shows the variation of potential energy versus temperature.

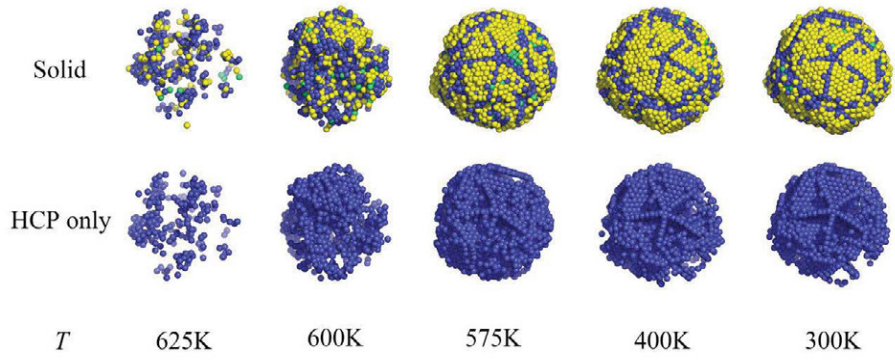

Figure 2. The structure evolution of Al_{8586} at different temperatures in cooling process. Yellow, blue and green spheres denote *fcc*, *hcp* and *bcc* atoms, respectively. Amorphous atoms are not showed.

Formation of *fcc*-Al nanoparticles with lamellar structures

Based on our observation, Al_{16754} tended to form five-fold twins under the cooling rate of RT4 (0.125K/ps). First of all, we take a panoramic view of the whole cooling process through the potential energy as shown in the inset of Figure 3. Very similar to the Energy-Temperature curve in the last section, a significant drop appeared at 650K, 50K higher than the liquid-solid phase transition point of five-fold twin. We can also define four stages here: *i*, a liquid state from 1175K to 675K; *ii*, a liquid-solid transition at 650K; *iii*, structural relaxation from 650K to 625K; and *iv*, an equilibrium configuration below 625K. The equilibrium configuration is formed at approximately 625K.

The percentage variation of *fcc*, *hcp* and amorphous atoms are depicted in Figure 3. In stage 1 from 1175 to 675K, the system maintains liquid state, where almost all atoms are amorphous and very few *fcc* and *hcp* atoms were found randomly. At the solidification point of 650K, the percentage of amorphous atom falled straightly down to 12.99% while the percentages of *fcc* and *hcp* increased to 46.85% and 38.74% respectively, implying the formation and rapid growth of a nucleus. In stage 3 from 650K to 625K, *fcc* and *hcp* atoms climbed very slowly up to 47.64% and 38.81% respectively, whereas amorphous atoms decreased to 12.28%. That is to say, the internal structural optimization replacing nucleation and the growth of nucleus was the key point of this stage. When the system proceeded to final stage 4, the proportions of all three types of atoms had almost no changes. It is worth mentioned that a very few *bcc* atoms were occasionally found in the system but not shown, and hence the sum of the proportion of *fcc*, *hcp* and amorphous atoms may be a little less than 100%.

We present the configuration snapshots of structure evolution of Al_{16754} in Figure 4. Alternately layered with *fcc* and *hcp* atoms stacked in three directions can be identified visually. But unlike the perfect lamellar structure Fe_{9577}[9] with 4 layers of *fcc* and 4 layers of *hcp*, stacked in one direction, our sample may showed a configuration of an imperfect lamellar structure.

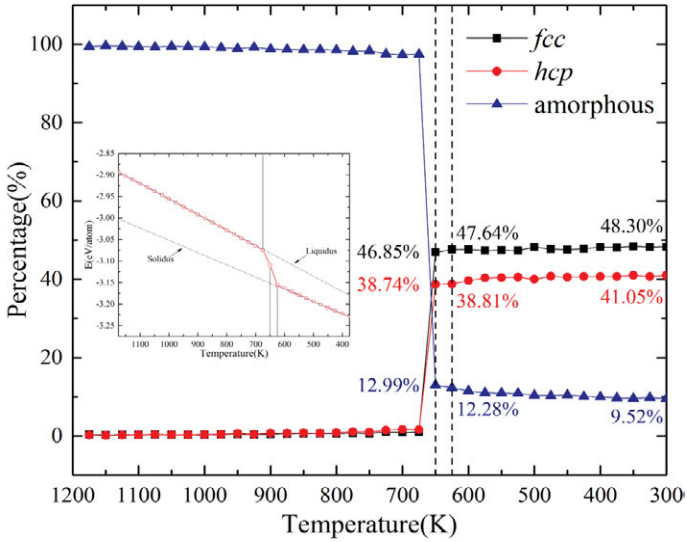

Figure 3. Percentage variation of three atom categories versus temperature of Al_{16754}. The inset shows the variation of potential energy versus temperature.

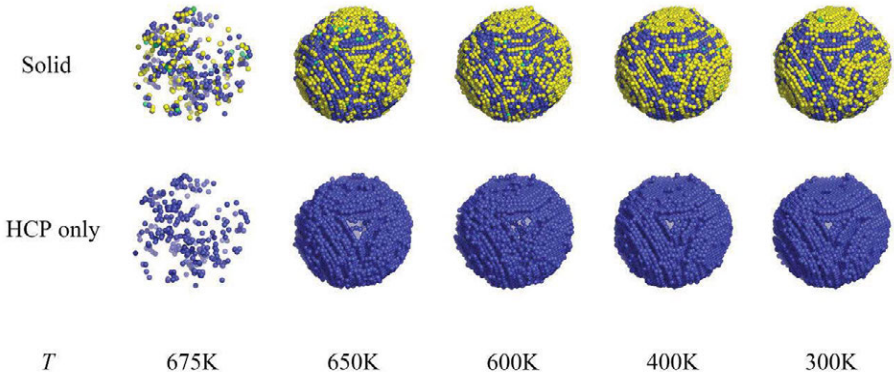

Figure 4. The structure evolution of Al_{16754} at different temperatures in cooling process. Yellow, blue and green spheres denote *fcc*, *hcp* and *bcc* atoms, respectively. Amorphous atoms are not showed.

Structural evolution of nanoparticle *hcp*-Mg

In the investigation of *hcp*-Mg, we did not find any obvious five-fold twins, it formed a structure alike lamellar structure but a little different, so we called it 'atypical lamellar structure'. Next, we

will illustrate the structure evolution by nanoparticle Mg_{20074} under the cooling rate RT2 (0.5K/ps).

The variation of potential energy versus temperature of Mg_{20074} during the cooling procedure is illustrated in the inset of Figure 5. The liquid-solid phase transition point for Mg_{20074} was 575K, also there were four stages: *i*, a liquid state from 925K to 600K; *ii*, a liquid-solid transition at 575K; *iii*, structural relaxation from 575K to 475K; *iv*, an equilibrium configuration below 475K. We present the percentage variation of *fcc*, *hcp* and amorphous in Figure 5. At the liquid-solid phase transition point, 575K, the percentage of *fcc* and *hcp* increased to 5.93% and 13.55%, with the amorphous percentage falls to 76.39% correspondingly. Then in stage 3, from 575K to 475K, the *hcp* atoms increased dramatically from 13.55% to 81.58%, the amorphous atom fell straightly down to 8.44%. For *fcc* atoms, the percentage rose from 5.93% to 8.23%, remained a relatively low position after a rise and fall. In stage 4, the percentage of all the three kinds of atoms almost remained still.

Based on the snapshots of structure evolution in Figure 6, large clusters first emerged at 575K and grew fast. At 525K, an obvious *fcc* layer appeared, but vanished during the cooling. Instead, another *fcc* layer formed at about 500K and remained stable at 400K. The final configuration contained most *hcp* atoms and a layer of *fcc* atoms, and this phenomenon have appeared more than once even adopting different cooling rates. To our point of view ,this *fcc* layer may acted as lattice defect such as dislocation in the system. So this configuration is noted as 'atypical lamellar structure' here.

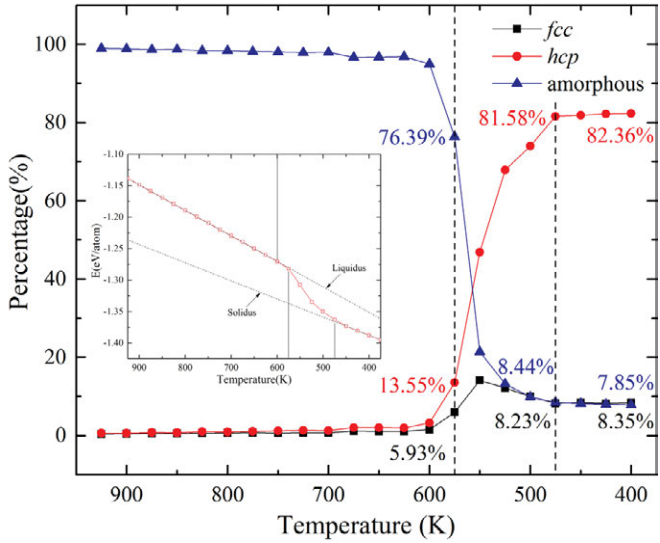

Figure 5. Percentage variation of three atom categories versus temperature of Mg_{20074}. The inset shows the variation of potential energy versus temperature.

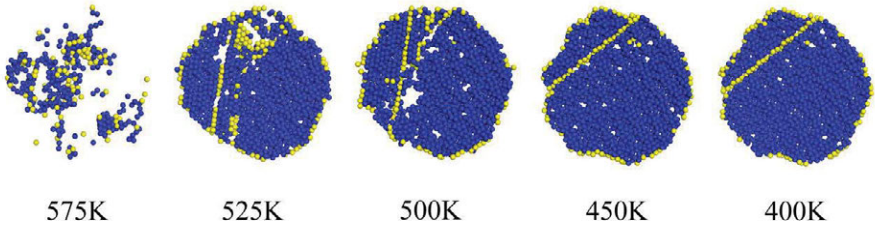

Figure 6. The structure evolution of Mg_{20074} from central cross section in cooling process. Yellow and blue spheres denote *fcc* and *hcp* atoms, respectively. Amorphous atoms are not showed.

Conclusions

In this paper, we used MD simulations to reproduce the solidification of *fcc*-Al and *hcp*-Mg nanoparticles with EAM potentials. We analyzed the variation of potential energy to give an overview of the simulations and identify the cooling stages. Then we analyzed the inner structure evolution during the solidification with our methodology of hybrid BOO+VPI and visualized the whole cooling process under different cooling rates. Al_{8586} and Al_{16754} were found to form five-fold twins and imperfect lamellar structure under the cooling rate of RT2 (0.5K/ps) and RT4 (0.125K/ps), respectively. While, only 'atypical lamellar' structure was found during the solidification of *hcp*-Mg.

Acknowledgements

This work is financially supported by National Natural Science Foundation of China (Nos. 50504010, 50974083, 51174131), Joint Funds of the National Natural Science Foundation of China (No. 50774112), National Basic Research Program of China (No. 2012CB722805), and Shanghai Rising-Star Program (No. 07QA14021).

References

1. M. Takagi, "Electron-Diffraction Study of Liquid-Solid Transition of Thin Metal Films," *Journal of the Physical Society of Japan*, 1954. **9**(3): p. 359-363.
2. C.R.M. Wronski, "The size dependence of the melting point of small particles of tin," *British Journal of Applied Physics*, 1967. **18**(12): p. 1731.
3. P. Buffat and J.P. Borel, "Size effect on the melting temperature of gold particles," *Physical Review A*, 1976. **13**(6): p. 2287-2298.
4. Y.-H. Wen, et al., "A molecular dynamics study of shape transformation and melting of tetrahexahedral platinum nanoparticle," *Chemical Physics Letters*, 2009. **471**(4–6): p. 295-299.
5. P. Song and D. Wen, "Molecular Dynamics Simulation of a Core−Shell Structured Metallic Nanoparticle," *The Journal of Physical Chemistry C*, 2010. **114**(19): p. 8688-8696.
6. P. Song and D. Wen, "Molecular dynamics simulation of the sintering of metallic nanoparticles," *Journal of Nanoparticle Research*, 2010. **12**(3): p. 823-829.

7. L. Wu, et al., "Molecular dynamics investigation of structural evolution of fcc Fe nanoparticles under heating process," *Chemical Physics Letters*, 2011. **502**(4-6): p. 207-210.
8. Y.H. Chui, I.K. Snook, and S.P. Russo, "Visualization and analysis of structural ordering during crystallization of a gold nanoparticle," *Physical Review B*, 2007. **76**(19): p. 195427.
9. Y. Wu, T. Shen, and X. Lu, "Evolutions of lamellar structure during melting and solidification of Fe9577 nanoparticle from molecular dynamics simulations," *Chemical Physics Letters*, 2013. **564**(0): p. 41-46.
10. T. Shen, Y. Wu, and X. Lu, "Structural evolution of five-fold twins during the solidification of Fe5601 nanoparticle: a molecular dynamics simulation," *Journal of Molecular Modeling*, 2013. **19**(2): p. 751-755.
11. T. Shen, et al., "Size dependence and phase transition during melting of fcc-Fe nanoparticles: A molecular dynamics simulation," *Applied Surface Science*, 2013. **277**: p. 7-14.
12. W.G. Hoover, "Constant-pressure equations of motion," *Physical Review A*, 1986. **34**(3): p. 2499-2500.
13. W.G. Hoover, "Canonical dynamics: Equilibrium phase-space distributions," *Physical Review A*, 1985. **31**(3): p. 1695-1697.
14. M.P. Allen and D.J. Tildesley, *Computer simulation of liquids*. 1989: Oxford university press.
15. J.B. Sturgeon and B.B. Laird, "Adjusting the melting point of a model system via Gibbs-Duhem integration: Application to a model of aluminum," *Physical Review B*, 2000. **62**(22): p. 14720.
16. D. Sun, et al., "Crystal-melt interfacial free energies in hcp metals: A molecular dynamics study of Mg," *Physical Review B*, 2006. **73**(2): p. 024116.
17. R. Li, Y. Wu, and J. Xiao, "The nucleation process and the roles of structure and density fluctuations in supercooled liquid Fe," *The Journal of Chemical Physics*, 2014. **140**(3): p. 034503.
18. W. Brostow, et al., "Voronoi polyhedra and Delaunay simplexes in the structural analysis of molecular-dynamics-simulated materials," *Physical Review B*, 1998. **57**(21): p. 13448-13458.
19. P.J. Steinhardt, D.R. Nelson, and M. Ronchetti, "Bond-orientational order in liquids and glasses," *Physical Review B (Condensed Matter)*, 1983. **28**(2).

TMS2016 Annual Meeting Supplemental Proceedings
TMS (The Minerals, Metals & Materials Society), 2016

A DISCRETE DISLOCATION MODEL OF CREEP IN SINGLE CRYSTALS

Rajaguru, M. and Keralavarma, S. M.

Department of Aerospace Engineering, Indian Institute of Technology Madras
Chennai 600036, India

Keywords: Discrete Dislocations, High Temperature Behavior, Power-Law Creep.

Abstract

We present a new computational approach for modeling dislocation creep in metals using kinetic Monte Carlo simulation of thermally activated dislocation glide, extending the discrete dislocation dynamics method of plasticity. The method is used to study the problem of power-law creep in precipitation strengthened Aluminum single crystals. The new model predicts creep rates and stress exponents consistent with their known ranges from experiments.

Introduction

Failure due to creep is a design-limiting issue for metallic materials used in several high temperature applications such as gas turbine blades, nuclear reactor components, thin film coatings and micro-electronics packaging and interconnects. There is significant interest in understanding the creep resistance of materials from a micromechanical point of view due to the technological need to design new materials that can safely withstand higher operating temperatures. Unlike the case of material strength at low temperatures, there is little fundamental quantitative understanding of the creep resistance of metals as a function of its microstructure; partly due to the fact that creep is a relatively complex deformation mode composed of several competing microscopic mechanisms such as dislocation climb and cross-slip, diffusion and grain boundary processes. For example, the phenomenological power-law creep model is extensively used to model secondary creep in metals, which has the form $\dot{\epsilon} \propto \tau^n$, where $\dot{\epsilon}$ denotes the creep strain rate, τ is the applied stress and n is the stress exponent for creep. A wide range of values of n between 3 and 8 are quoted for various metals based on experimental data [1], although theoretical analyses do not predict values of n greater than 4 [2]. Further, based on experimental findings over the past decade that plasticity is size dependent at small length scales, it is unlikely that phenomenological creep models derived from analysis of data in bulk materials remain valid for novel nanostructured and multilayer thin film materials.

Computational simulation tools for the mechanical behavior of crystals such as discrete dislocation dynamics (DD) are well suited for "bottom-up" modelling of creep due to the wealth of microstructure information that they incorporate. In the DD method, continuum elasticity theory is used to model the bulk material behavior, while inelastic deformation results from the collective motion and interactions of crystal defects (mainly

dislocations) modeled discretely. This makes the method scalable to large simulation domains containing statistically significant defect ensembles. Traditionally, the DD method has been used to model plasticity at low homologous temperatures, where it has proven successful in explaining several phenomena such as the size dependent strength of metals and crack growth resistance under monotonic and cyclic loadings, hitherto not explainable using continuum models without resorting to heuristic parameter fitting. Recently, several researchers have attempted to extend the DD method to higher homologous temperatures to study thermally activated phenomena such as dislocation climb by vacancy diffusion [3–6]; many of them motivated by the need to understand radiation damage phenomena in nuclear materials. One of the authors [7] has extended the two-dimensional dislocation dynamics simulation model of Van der Giessen and Needleman [8] to high homologous temperatures by coupling with continuum vacancy diffusion theory. The resulting framework was used to study power-law creep under simple tension in micron-sized single crystal specimens and stress exponents around ~ 5 were predicted. However, the simulations were complicated due to the need to solve elasticity and unsteady diffusion boundary value problems simultaneously and the time integration was performed using an ad hoc and inefficient adaptive time stepping scheme due to the widely differing time scales for dislocation glide and diffusive processes. In this paper, we propose a simpler algorithm for creep simulations based on the assumption of a uniform vacancy concentration in the bulk material, away from dislocation cores, and using previously derived analytical estimates for the climb rate of dislocations in a vacancy field. Further, a more rigorous approach based on the kinetic Monte Carlo scheme is used to perform the time integration in the simulations assuming that the discrete climb events of dislocations over local obstacles are rate controlling for creep (a reasonable assumption at high applied stresses). The details of the simulation method are explained in the following section.

Kinetic Monte Carlo Simulation of Dislocation Creep

Based on the widely adopted two-dimensional DD model of Van der Giessen and Needleman [8], we consider a plane strain model of a bulk single crystal creeping due to an arbitrary applied remote stress field $\boldsymbol{\sigma}$. Deformation of a rectangular unit cell is analyzed subjected to periodic boundary conditions as illustrated in Fig. 1. The domain contains discrete parallel slip planes belonging to three independent slip systems oriented at equal angles relative to each other. A symmetric orientation of the unit cell relative to the slip systems is chosen and the cell aspect ratio is fixed in such a way that exact periodicity of slip is maintained; i.e. pairs of slip planes have matching exit and entry points on the periodic boundaries mimicking an infinite slip plane. The model approximates a face centered cubic material undergoing plane strain deformation on the $\{110\}$ crystallographic planes in three dimensions. Infinitely long straight edge dislocations perpendicular to the plane of analysis are considered, which are modeled as discrete points gliding on their respective slip planes as shown in Fig. 1. The dislocations interact through their long range stress fields. The glide velocity of a dislocation is assumed to be proportional to the glide component of the Peach-Koehler force, which depends on the mutual interaction forces of dislocations as well as the image stresses from the periodic

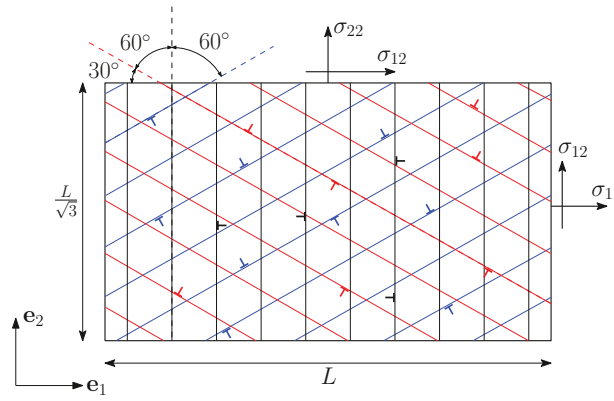

Figure 1: Schematic of a rectangular unit cell of a planar single crystal, subjected to periodic boundary conditions consistent with a constant far field stress.

boundaries. The slip planes also contain discrete point sources, representing Frank-Read sources in 3D, which can nucleate dislocation dipoles when the resolved shear stress on them exceeds a critical nucleation stress over a critical nucleation time interval, and discrete point obstacles which can pin dislocations and arrest further glide unless the resolved shear stress on the pinned dislocation exceeds a critical strength characteristic of the obstacle. Opposite signed dislocations can also annihilate if their glide paths overlap on the same slip plane. The method of calculating elastic fields in a periodic crystal using the finite element method and the superposition principle of linear elasticity is from the work of Hussein et al. [9] and the constitutive relations for dislocation nucleation, glide and annihilation are identical to those of Van der Giessen and Needleman [8]. These are not repeated here for brevity.

The main point of departure from the standard two dimensional DD model is the treatment of dislocation interactions with obstacles. Plasticity simulations usually assume that the temperature is sufficiently low that thermally activated effects are negligible, so that a dislocation can overcome an obstacle only when the resolved shear stress on the former exceeds the athermal pinning strength of the latter. The obstacle strength depends on the specific obstacle type and dislocation interaction mechanism, like unzipping of forest junctions, cutting or Orowan looping of precipitates, etc. However, at high homologous temperatures (typically $> 0.4T_m$, where T_m denotes the melting point) dislocations can also bypass obstacles by thermally activated mechanisms such as cross-slip or climb. In fact, accounting for thermal activation mechanisms is key to simulating phenomena such as creep, since under constant stress conditions overall strain will tend to reach a constant value corresponding to the attainment of quasi-equilibrium dislocation configurations locally, from which the microstructure can only evolve further due to statistical 'activation' events such as dislocation unpinning from an obstacle due to thermal fluctuations. The frequency of such activation events depends on the type and strength of these obstacles. Here, we assume a model where the edge dislocations

are gliding through a random array of strong equiaxed obstacles distributed randomly on the slip planes, representative of a precipitation hardened alloy microstructure for example. A dislocation can bypass such an obstacle by one of the following processes: (i) Orowan looping, (ii) formation of a localized jog by climb of edge segments normal to the slip plane or (ii) double cross-slip of screw segments onto a parallel slip plane. All these mechanisms are thermally activated with an associated activation energy that depends on the relevant components of the applied stresses. We disregard the cross-slip mechanism here due to the fact that screw dislocations cannot be modeled in our two dimensional analysis and the thermal activation mechanism for cross-slip is relatively less well understood. The stress dependence of the activation frequency for the Orowan mechanism has the form [10]

$$\nu_{Or} = \nu_0 \exp\left[-\frac{E}{kT}\left(1 - \frac{\tau}{\tau_0}\right)\right] \tag{1}$$

where ν_0 is the attempt frequency, E is the activation energy at zero applied stress, τ is the resolved shear stress on the dislocation in the slip direction, τ_0 is the athermal strength of the obstacle, k is the Boltzmann constant and T is the absolute temperature. Assuming large precipitate sizes, the activation energy for the Orowan mechanism is rather high, typically $E > 2\mu b^3$, where μ denoted the shear modulus of the material [1].

At finite temperatures, a metallic crystal also contains thermally generated point defects (primarily vacancies) that are in equilibrium with the lattice. At high homologous temperatures, the concentration of these vacancies may be sufficient to aid non-conservative climb motion of dislocations by absorption of vacancies into the dislocation core. The driving force for climb is provided by the component of the Peach-Koehler force in the slip plane normal direction and possible supersaturations of vacancies in the neighborhood of the dislocation. Using simplifying assumptions, an approximate analytical estimate for the climb velocity of straight edge dislocations under the influence of mechanical climb forces in a uniform vacancy concentration field has been derived previously [3,11]. This has the form

$$v_{cl} = -\eta \frac{D}{b}\left[\exp\left(-\frac{f_c \Omega}{bkT}\right) - \frac{c}{c_0}\right] \tag{2}$$

where D is the self-diffusion coefficient, f_c is the climb component of the Peach-Koehler force, Ω is the atomic volume, c is the uniform vacancy concentration field away from the dislocation core, c_0 is the equilibrium vacancy concentration field at temperature T and η is a constant of order unity. The equilibrium vacancy concentration at temperature T is given by $c_0 = \exp\left(-\frac{E_f}{kT}\right)$, where E_f is the vacancy formation energy. The diffusivity D is strongly temperature dependent and is given by $D = D_0 \exp\left(-\frac{E_a}{kT}\right)$, where D_0 is the saturation value of the diffusivity at very high homologous temperatures and $E_a = E_f + E_m$ is the activation energy for self-diffusion, where E_m denotes the vacancy migration energy. An estimate of the time it takes for an edge dislocation to bypass a random array of equiaxed obstacles of size d and mean spacing L_o (assumed equal in all directions) by formation of double jogs at the obstacles will be $d^2/(v_{cl} L_o)$ so that the activation frequency by localized climb processes may be approximately written as

$$\nu_{cl} = \frac{v_{cl} L_o}{d^2} \tag{3}$$

Note that the activation frequency by climb is negligible at low temperatures since D decreases exponentially with temperature.

In our simulation scheme, we evolve the dislocation microstructure by integrating the equations of motion for the dislocations in time using a forward Euler scheme and a very small time step of 0.5 ns. Constant stress boundary conditions are maintained on the unit cell by imposing elastic displacements on the boundary at the end of each increment, consistent with the applied creep stress according to the linear elastic constitutive law. At the end of each time step the inelastic strain increment resulting from the collective motion of the dislocations is computed using the following expression based on the Orowan formula,

$$\delta\boldsymbol{\epsilon} = \frac{1}{2A}\sum_{i=1}^{N}(\mathbf{b}^i \otimes \mathbf{n}^i + \mathbf{n}^i \otimes \mathbf{b}^i)\delta s^i \tag{4}$$

where $\mathbf{b}^i$ and $\mathbf{n}^i$ are the Burgers vector and unit vector normal to the glide plane for dislocation i, δs^i is the signed glide distance of the dislocation along its slip plane, A is the area of the unit cell and N is the total number of dislocations in the cell. During the glide simulation, dislocations that encounter obstacles on their glide path are pinned at these obstacles unless the resolved shear stresses on the dislocations exceed the athermal strength of the obstacles. Thermal activation is not invoked during the glide simulation due to the fact that the time scales associated with both activation mechanisms discussed above are several orders of magnitude larger than the time step used in the glide simulations. In the absence of thermal activation, the average strain in the unit cell eventually saturates to a constant value coinciding with the dislocation microstructure attaining quasi-equilibrium configurations corresponding to local minima in their energy landscape. When constant strain conditions are detected, as evidenced by the strain remaining constant over a predetermined duration, local equilibrium is deemed to be attained and further straining requires thermal activation of a dislocation from its current equilibrium position. Since the activation frequencies are assumed to be known from theoretical models of the corresponding mechanisms at the individual dislocation level, c.f. equations (1) and (3), a kinetic Monte Carlo algorithm [12] is used to randomly select a dislocation to be activated from among all dislocations pinned at local obstacles as well as determine the time increment to the activation event. Following the activation event, the glide simulations are resumed until the overall strain saturates to a new value and the algorithm is repeated ad infinitum.

Our simulation approach above is different from that of [7] in several important ways. First, the vacancy field in the crystal is assumed to be in thermal equilibrium at all times, i.e. $c = c_0$, neglecting any Nabarro-Herring creep due to the mass transport process. This assumption significantly simplifies the calculations since the unsteady diffusion problem coupled with dislocation climb does not need to be solved at every increment. The assumption is reasonable since here we are looking at creep of a bulk crystal and it has been observed from our earlier studies that the vacancy concentration in the bulk, away from the points of application of the load, is very nearly equal to the equilibrium vacancy concentration. Also, the Nabarro-Herring creep rates due to the diffusion process is negligible compared to the dislocation creep rates when the latter process is activated. Next, the time increments associated with the thermal activation events are determined in a more rigorous manner using a kinetic Monte Carlo algorithm,

potentially yielding more accurate estimates of the creep rates compared to the ad hoc algorithm in [7]. Finally, the present approach is not specific to activation by dislocation climb and can in principle account for several different types of obstacles and thermal activation models, making it suitable for study of a wider class of thermally activated problems in the inelastic deformation of crystals.

Creep Simulation Results

We have performed creep simulations on rectangular periodic unit cells shown in Fig. 1, with $L = 8\mu$m, subjected to a tensile creep stress in the $\mathbf{e}_1$ direction, $\sigma_{11} = \sigma, \sigma_{22} = \sigma_{12} = 0$. The chosen unit cell size minimizes the simulation time while ensuring that the results are independent of the cell size. Material properties of Aluminum are assumed here for convenience, although the model is not strongly tailored to a specific material and the simulations results may be representative of any FCC material undergoing quasi-plane strain deformation. The melting temperature of Aluminum is approximately $T_m = 933$K, temperature dependent shear modulus is assumed to be $\mu = 29.6 - 0.014T$ GPa and Poisson's ratio $\nu = 0.33$. Other material properties are the modulus of the Burgers vector $b = 0.25$ nm, atomic volume $\Omega = 16.3$ Å^3, self-diffusion coefficient pre-exponential $D_0 = 1.18 \times 10^{-5}$ m^{2}s^{-1}, vacancy formation energy $E_f = 0.67$ eV and vacancy migration barrier $E_m = 0.61$ eV. For the Orowan bypassing model, equation (1), the activation energy is taken to be $E = 2\mu b^3$, the athermal pinning strength $\tau_0 = 150$ MPa and the attempt frequency $\nu_0 = \nu_D b/L_\text{o}$, where $\nu_D \sim 10^{13}$ s^{-1} is the Debye frequency. The size and spacing of obstacles are assumed to be $d = 10$ nm and $L_\text{o} = 100$ nm respectively. The nominal yield stress of the material at zero temperature is related to the strength and spacing of the obstacles and is approximately equal to 150 MPa. The crystal is subjected to creep stresses in the range 10 – 100 MPa, well below the nominal yield strength and the creep strain is computed at the end of each time increment using equation (4).

Fig. 2(a) shows the creep strain in the loading direction as a function of time for various values of the applied stress at temperature $T = 350$K. An approximately linear creep response indicative of secondary creep is obtained irrespective of the applied stress. The creep response also shows a small initial primary creep region characterized by a decreasing strain rate (not visible at the scale of Fig. 2(a)). Note that ternary creep is beyond the capabilities of our model due to computing time limitations and the absence of damage processes. The temperature in the above set of results is approximately $0.38T_m$, which is near the lower end of the known temperature range for power-law creep. However, we obtain a qualitatively similar response at higher temperatures albeit with significantly higher strain rates. Multiple simulations have been performed, with different realizations of the initial dislocation source and obstacle microstructure, for each case of temperature and applied stress. Fig. 2(b) shows a summary of the creep strain rates obtained as a function of the resolved shear stress on the active slip systems (normalized by the shear modulus) at $T = 350$K. The strain rates are consistent with the order of magnitude of the expected creep strain rates in Aluminum at the above temperature. Further, the slope of the plot on a log-log scale gives the value of the stress exponent in a power-law relationship between the creep rate and the applied stress. Two regimes of behavior are observed in Fig. 2(b) with an exponent $n \approx 1.2$ for low values

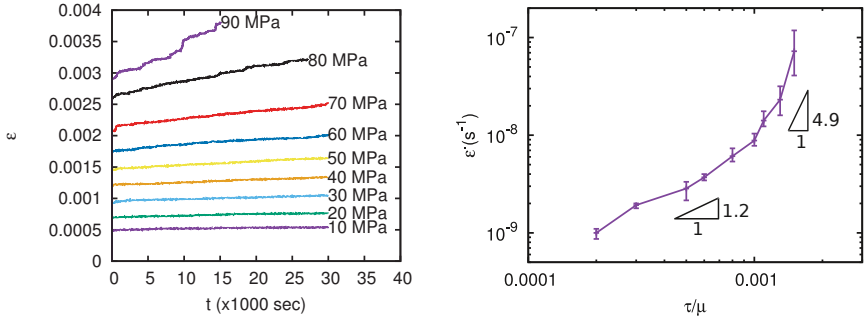

(a) (b)

Figure 2: (a) Creep strain as a function of time for a bulk Aluminum single crystal predicted by the simulations at $T = 350$K and various values of the applied stress. (b) Variation of the creep strain rate along the loading direction as a function of the resolved shear stress on the active slip planes, normalized by the material's shear modulus. Estimated values of the stress exponent for power-law creep are also shown.

of the applied stress ($\tau < 10^{-3}\mu$) and $n \approx 4.9$ for high stresses ($\tau > 10^{-3}\mu$). These values are consistent with the exponents reported experimentally and are also in good agreement with our earlier model [5,7], which only considered the climb mode of thermal activation. This is hardly surprising since a quick estimate using equations (1) and (3) at 350 K shows that Orowan bypassing is energetically unfavorable for strong pinning obstacles of the type assumed here, so that the creep rate is controlled by the climb process. However, some qualitative differences from the earlier model are observed with our present creep curves exhibiting a staircase-like aspect with a monotonic increase in strain, which is closer to experimentally observed creep data unlike the serrated creep curves predicted by the earlier model. This difference is attributed to the algorithm used to impose constant stress boundary conditions, which is more accurate in the present method. Additional studies will be conducted in the future using the same simulation framework assuming alternative microstructures and thermal activation mechanisms, so that their effect on the macroscopic creep response can be investigated.

Conclusion

A new computational model for thermally activated dislocation glide at elevated temperatures based on the two dimensional DD model of Van der Giessen and Needleman [8] has been developed. The model assumes a standard thermal activation model based on transition state theory and uses known energy barrier values for the various activation mechanisms in conjunction with the kinetic Monte Carlo method to compute the time evolution of the dislocation microstructure. Initial application of the method to the problem of power-law creep in an Aluminum single crystal yields creep rates and stress exponents in good agreement with experimental results. Our results indicate that computational tools such as the DD method can potentially be used to aid in materials

design for high temperature applications.

References

[1] H. J. Frost and M. F. Ashby. *Deformation-Mechanism Maps: The Plasticity and Creep of Metals and Ceramics*. Pergamon Press, Oxford, 1982.

[2] J. Weertman. Theory of steady-state creep based on dislocation climb. *Journal of Applied Physics*, 26:1213–1217, 1955.

[3] D. Mordehai, E. Clouet, M. Fivel, and M. Verdier. Introducing dislocation climb by bulk diffusion in discrete dislocation dynamics. *Phil. Mag.*, 88:899–926, 2008.

[4] E. Clouet. Predicting dislocation climb: Classical modeling versus atomistic simulations. *Phys. Rev. B*, 84:092106, 2011.

[5] S. M. Keralavarma, T. Cagin, A. Arsenlis, and A. A. Benzerga. Power-Law Creep From Discrete Dislocation Dynamics. *Phys. Rev. Lett.*, 109:265504, 2012.

[6] Y. Gu, Y. Xiang, S. S. Quek, and D. J. Srolovitz. Three-dimensional formulation of dislocation climb. *J. Mech. Phys. Solids*, 2015. In Press.

[7] S. M. Keralavarma and A. A. Benzerga. High-temperature discrete dislocation plasticity. *J. Mech. Phys. Solids*, 82:1–22, 2015.

[8] E. Van der Giessen and A. Needleman. Discrete dislocation plasticity: a simple planar model. *Model. Simul. Mater. Sci. Eng.*, 3:689–735, 1995.

[9] M.I. Hussein, U. Borg, C.F. Niordson, and V.S. Deshpande. Plasticity size effects in voided crystals. *J. Mech. Phys. Solids*, 56:114–131, 2008.

[10] U. F. Kocks, A. S. Argon, and M. F. Ashby. Thermodynamics and kinetics of slip. In B. Chalmers, editor, *Prog. Mater. Sci.*, volume 19, pages 1–289. Pergamon, Oxford, 1975.

[11] J. P. Hirth and J. Lothe. *Theory of Dislocations*. Wiley, New York, 1968.

[12] A. F. Voter. Introduction to the kinetic monte carlo method. In *Radiation Effects in Solids*, pages 1–23. 2007.

STUDY OF THE TEMPERATURE EFFECTS ON SOLID-LIQUID ANISOTROPIC INTERFACIAL ENERGY

L.K. Wu[1,2], C. L. Li[1,2,3], B. Xu[1,2,*], Q.L. Li[1,2], W. Liu[1,2]
[1]Key laboratory of Advanced Materials of Education of China, Tsinghua University, Beijing, 100084, China
[2]School of Material Science and Engineering, Tsinghua University, Beijing, 100084, China
[3]China Nuclear Power Engineering Co., Ltd, Shenzhen, 518172, China

*Corresponding authors: xuben@mail.tsinghua.edu.cn

Keywords: solid-liquid interfacial energy, anisotropy, CNM, CFM, temperature dependence.

Abstract

In this work, a new method for calculating the solid-liquid interfacial energy was proposed by the combining of the classical nucleus method (CNM) and capillary fluctuation method (CFM). The anisotropy of interfacial energies of Al increases as the temperature drops, while the orientationally averaged interfacial energy shows no such kind of tendency.

Introduction

The solid-liquid interfacial free energy γ_{SL} and its anisotropy have been the focus of numerous studies of crystal nucleation [1-2] and growth [3-4]. Unfortunately, direct measurement of these data is still a challenge. Therefore, different simulation approaches were developed to determine γ_{SL} and its anisotropy from atomic scales. The capillary fluctuation method (CFM), a popular approach developed by Hoyt, Asta and Karma [5], is very effective in solving anisotropy; but not capable to calculate γ_{SL} at different temperatures except the melting point. The other approach, the classical nucleus method (CNM) developed by Bai and Li [6], can be performed at a wide range of temperatures, but isn't able to determine the anisotropy of γ_{SL}.
In this paper, a new method was proposed to calculate not only the magnitude of γ_{SL} but also its anisotropy at different temperature by the combination of CNM and CFM. The paper is organized as follows. Firstly, we briefly outline CNM, CFM and the model employed in our simulations. Then, results are presented. Discussion and conclusions are shown in the end.

Method

Classical nucleus method (CNM)

According to classical nucleation theory [7], to form a small solid sphere of radius r in an undercooled liquid, the change of the Gibbs free energy can be expressed as:

$$\Delta G = -\frac{4}{3}\pi r^3 \Delta G_V + 4\pi r^2 \gamma_{SL}, \tag{1}$$

where ΔG_V is the Gibbs free energy difference per unit volume between solid and liquid phases at temperature T. In CNM, the approximated ΔG_V can be expressed as:

$$\Delta G_V \cong L_V \frac{\Delta T}{T_M}, \tag{2}$$

where L_V is the latent heat of fusion per unit volume at the equilibrium meting point, T_M, and $\Delta T (=T_M - T)$ is the undercooling. The critical nucleus radius is obtained from Eq. (1)

$$r^* = \frac{2\gamma_{SL}}{\Delta G_V} \cong (\frac{2\gamma_{SL} T_M}{L_V})\frac{1}{\Delta T} \tag{3}$$

Considering an infinite long cylindrical nucleus, as shown in Fig. 1b, the difference in the Gibbs free energy and critical nuclei radius are amended as

$$\Delta G = -\pi r^2 \Delta G_V + 2\pi r \gamma_{SL}, \tag{4}$$

$$r^* = \frac{\gamma_{SL}}{\Delta G_V} \cong (\frac{\gamma_{SL} T_M}{L_V})\frac{1}{\Delta T} \tag{5}$$

For a given undercooling, there exists a critical radius r^*. if $r = r^*$, the nucleus can be in equilibrium (but metastable) with its surrounding liquid. In simulations, if a number of r^* and their critical undercooling ΔT are obtained, γ_{SL} can be extracted from Eq. (5).

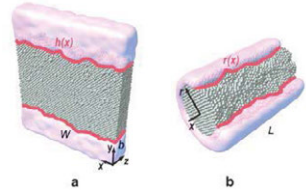

Figure 1. Schematic of the interface fluctuation: (a) flat interface and (b) cylindrical interface. The silver balls represent solid atoms, which are surrounded by liquid-phase indexed with pink colour.

Capillary fluctuation method (CFM)

As illustrated in Fig. 1a, a slab simulation box is used to create the interfacial position $h(x)$, which is a quasi-one-dimensional function of the distance x along the width W, the thickness of the interface is b. According the equipartition theorem [8], the fluctuation spectrum of the interfacial height $h(x)$ can be expressed as

$$\left\langle \left| A(k) \right|^2 \right\rangle = \frac{k_B T_M}{bW\tilde{\gamma}k^2}, \tag{6}$$

where k_B is Boltzmann's constant. $A(k)$ is the Fourier amplitude of $h(x)$ at wave number k. $\tilde{\gamma}$ is called the interfacial stiffness and is related to γ_{SL} by

$$\tilde{\gamma} = \gamma_{SL} + \frac{d^2\gamma_{SL}}{d\theta^2}, \tag{7}$$

where θ is the angle between the instantaneous interface normal and the average interface normal.

Based on the cubic harmonic expression from Fechner and Vosko [9], γ_{SL} and its anisotropy is determined by

$$\gamma(\boldsymbol{n}) = \gamma_0 \left[1 + \epsilon_1 \left(\sum_i n_i^4 - \frac{3}{5} \right) + \epsilon_2 \left(3\sum_i n_i^4 + n_1^2 n_2^2 n_3^2 - \frac{17}{7} \right) \right], \tag{8}$$

where $\{n_1, n_2, n_3\}$ are the Cartesian components of the interface $\boldsymbol{n}$, γ_0 is the orientationally averaged interfacial free energy and ϵ_1, ϵ_2 are fourfold and sixfold anisotropy parameters, respectively. A similar expression for the stiffness can be derived using Eq. (7). By simulating a number of interfaces with different crystal orientations and measuring the average magnitude of the fluctuation modes, $\tilde{\gamma}$ could be determined from Eq. (6), then γ_0, ϵ_1 and ϵ_2 can be computed by using Eq. (7) and (8).

For interface of a cylinder nucleus illustrated in Fig. 1b, the Eq. (6) is substituted as

$$\left\langle \left| A(k) \right|^2 \right\rangle = \frac{k_B T}{2\pi r L\tilde{\gamma}k^2}, \tag{9}$$

where r is the radius and L is length of the of the nucleus, respectively. T is the corresponding temperature at which the nucleus is in equilibrium with liquid. $\tilde{\gamma}$ only related to the orientation of cylinder, x, and can be expressed as

$$\tilde{\gamma} = \frac{1}{2\pi} \int_0^{2\pi} (\gamma_{SI} + \frac{d\gamma_{SL}}{d\theta^2}) \mathrm{d}\theta \tag{10}$$

For completeness, we provide expressions $\tilde{\gamma}$ for three orientations studied in this work in Table I.

Table I. Simulated system sizes and expressions of interfacial stiffness for nuclei

Orientation	System size (Å)			Interfacial stiffness
	5 Å$\leqslant r\leqslant$15 Å	20 Å$\leqslant r\leqslant$40 Å	50 Å$\leqslant r\leqslant$70 Å	
[100]	248.4×248.4×16.6	124.2×124.2×124.2	248.4×248.4×124.2	$\gamma_0(1-2.85\,\epsilon_1+7.321\,\epsilon_2)$
[110]	248.4×234.2×23.4	124.2×117.1×117.1	248.4×234.2×117.1	$\gamma_0(1+0.7125\,\epsilon_1-11.9\,\epsilon_2)$
[111]	243.4×234.2×28.7	121.7×117.1×143.4	243.4×234.2×143.4	$\gamma_0(1+1.9\,\epsilon_1+13.02\,\epsilon_2)$

Simulations

In this work, we use aluminum as a model metal. The potential Al1, a kind of embedded atom method (EAM) interatomic potential from Mendelev [10], is used in molecular simulations (MD). The melting point and the latent heat of fusion of the potential are 926K and 1013.72 mJ/mm^3, respectively.

In simulations, three kinds of cylindrical nuclei whose centerline along the [100], [110], [111] directions were in equilibrium with liquid, the radius of which ranged from 5 Å to 70 Å. The simulated system sizes were shown in Table I. A local structural order parameter, proposed by Morris [11], was used to determine the radius of cylinder $r(x)$. The order parameter is 1 for the perfect crystal and 0 for liquid. Fig. 2 shows the order parameter along radius in an instantaneous configuration of nucleus r^*=30 Å. As seen in the figure, most order parameters of atoms in the solid region are larger than 0.4, and less than 0.1 in the liquid region. The atoms with order parameter between 0.2 and 0.3 are defined as "interfacial atoms" and r(x) is calculated by their average position. Then interfacial free energy and its anisotropy can be computed by CFM.

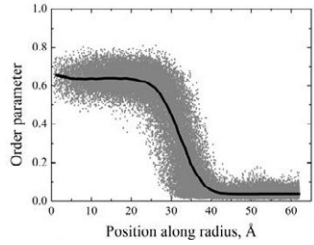

Figure 2. The order parameter as a function of position along radius in an instantaneous configuration of nucleus r^*=30 Å.

It must be pointed out that the nuclei at critical undercooling are metastable. For

nuclei with radius range from 50 Å to 70 Å, the interface kept being stable in 500 ps. 1000 snapshots of the interface profiles were collected every 0.5 ps to calculate the interfacial free energy using CFM. For nuclei between 20 Å to 40 Å, the stable time was 200 ps, and the snapshots were collected every 0.2 ps. For nuclei that 5 Å$\leqslant r \leqslant$15 Å, the interfaces were unstable in 100 ps, therefore, they couldn't be used for CFM. In this case, 9 nuclei were embedded in liquid at the same time, the critical undercooling was determined when 4 or 5 nuclei grew and others shrank.

Result

Equilibrium temperature

The predicted critical radius r^* at different temperatures are presented in Fig. 3. It clearly indicates that the critical radius has an inverse relationship with the undercooling of the system. As the radius decreases, the equilibrium temperature for of with [111] orientation dropped more rapidly than those of [100] and [110] orientations. The equilibrium temperatures of the nuclei of [100], [110], [111] were 913 K, 913.2 K, 913 K when radius r^*=70 Å and 776.78 K, 755K and 744K when r^*=5 Å, respectively. The difference of equilibrium temperatures reflects the anisotropy of interfacial free energy. A linear fit of the calculated data of ΔT and $1/r^*$ are shown in Fig. 3b, and the solid-liquid interfacial free energies were computed from Eq. (5). Our simulations gave the value of 81.73, 92.06, 94.91 mJ/m^2 for [100], [110], [111] nuclei, and the average value was 89.57 mJ/m^2.

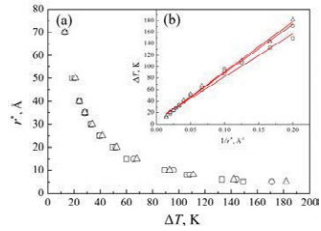

Figure 3. Temperature dependence of the estimated critical radii r^* for cylindrical crystal nuclei in the undercooled liquid. Open squares (□) represent nuclei of critical along [100] direction, open circles (○) means nuclei along [110] and open triangle (△) corresponding to nuclei along [111].

Interfacial stiffness

In Fig. 4, the stiffness $\tilde{\gamma}$ as a function of fluctuation modes k was computed from Eq. (9). The nuclei along [100] direction provides smallest stiffness, which increased from 80 mJ/m^2 to 90mJ/m^2 as the radius increases from 20 Å to 70 Å. The stiffness of [110] nuclei is the largest, and no obvious variation occurs as the radius increases. After averaging the $\tilde{\gamma}$ at different k, the stiffness were obtained, presented in Table II.

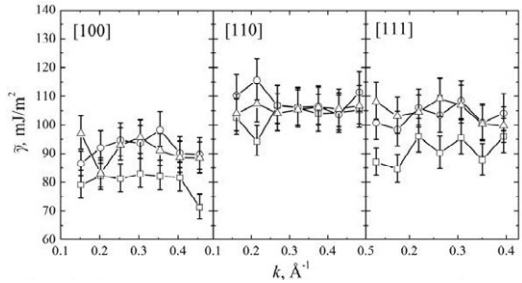

Figure 4. The stiffness of the fluctuation modes of different nuclei. Open squares (□) represent nuclei with critical radius r^*=20 Å, open circles (○) means r^*=40 Å and open triangle (△) corresponding to r^*=70 Å. Error bars indicate the 95% confidence intervals.

Table II. The calculated stiffness for different nuclei, the interfacial free energy and its anisotropy by fitting. (the temperatures in second column were employed as the average of three orientations of nuclei. the value in brackets indicate the 95% confidence intervals).

r^* (Å)	T (K)	$\tilde{\gamma}$(**n**) (mJ/m^2)			γ_0 (mJ/m^2)	ϵ_1 (%)	ϵ_2 (%)
		100	110	111			
20	874.66	80.07 (5.23)	103.29 (6.65)	91.01 (5.80)	93.50	3.28	-0.68
25	885.94	85.40 (5.58)	107.36 (7.07)	97.27 (6.35)	98.49	3.21	-0.56
30	892.82	91.72 (5.92)	104.09 (6.80)	103.95 (6.84)	100.52	2.72	-0.14
35	897.70	83.69 (5.41)	105.92 (6.93)	101.33 (6.50)	98.39	4.24	-0.39
40	901.92	92.12 (5.84)	108.59 (7.15)	103.09 (6.68)	102.47	2.66	-0.34
50	906.00	84.45 (5.54)	102.01 (6.42)	97.67 (6.06)	95.88	3.31	-0.34
70	913.07	90.99 (5.88)	105.59 (6.95)	104.53 (6.62)	101.15	3.04	-0.19

Using the expressions for the interfacial stiffness in Table I and the calculated results in Table II, the orientationally averaged interfacial free energy γ_0 and the anisotropy parameter ϵ_1, ϵ_2 were calculated (shown in Table II). It can be found as the radius (temperature) decreases, γ_0 remains stable with an average value of 98.45 mJ/m^2. However, the anisotropy parameter ϵ_1, ϵ_2 showed the tendency of increase as decreased the radius, especially for ϵ_2.

Discussion

The γ_0 provided by CNM was 89.57 mJ/m^2, slightly smaller than that from CFM. Since an accurate melting point is necessary for CNM (see Eq. (5)) and the melting point is dependent on the interface orientations as discussed in our previous work [12]. Therefore, an averaged value T_M=926 K used in this work may underestimate the interfacial free energy. Despite of this, our work provided the interfacial free energies at different temperature, and found that ϵ_1, ϵ_2 increased as the temperature decreased. This tendency could be concluded as the result of the different equilibrium temperature of the nuclei (Table II), *e.g.* the temperature difference for three

orientations of nuclei with r^*=70 Å was 0.2 K, but reached 30K for r^*=5 Å.

Conclusions

In summary, a new method was proposed combing CNM and CFM. In our simulations, cylindrical nuclei of Al were inserted into the melt at different temperature. After the nuclei were stabilized in its melt, the cylindrical interface was extracted to calculate the interfacial free energy. With this method, both the value of the interfacial free energy and its anisotropy can be calculated at any temperature. We found that although the orientationally averaged interfacial free energy γ_0 varies slightly as the temperature decreases, the anisotropy of the interfacial free energy in our simulations appeared to increase, which should be considered as important in the simulation of the solidification process.

Acknowledgement

We would like to acknowledge the financial support for this work provided by the NSF of China (51301094) and the National Magnetic Confinement Fusion Science programme of China under Grant (51471092). The work was carried out at the National Supercomputer Center in Tianjin, and the calculations were performed on TianHe-1(A) and were also supported by Tsinghua National Laboratory for Information Science and Technology. The authors also thank M. Li (Georgia Institute of Technology) for fruitful discussions.

References

1. D. Turnbull and J. C. Fisher: Rate of Nucleation in Condensed Systems. J. Chem. Phys. **17**, 71 (1949).

2. K. F. Kelton: Crystal Nucleation in Supercooled Liquid Metals. Int. J. Microgravity Sci. Appl. **30**, 11 (2013).

3. D. A. Kessler, J. Koplik, and H. Levine: Geometrical models of interface evolution. II. Numerical simulation. Phys. Rev. A **29**, 3161 (1984).

4. D. M. Herlach, J. Gao, D. Holland-Moritz and T. Volkmann: Nucleation and phase-selection in undercooled melts. Mater. Sci. Eng. A **375**, 9 (2004).

5. J. J. Hoyt, M. Asta, A. Karma: Method for Computing the Anisotropy of the Solid-Liquid Interfacial Free Energy. Phys. Rev. Lett. **86**, 5530 (2001).

6. X. M. Bai, M. Li: Calculation of solid-liquid interfacial free energy: A classical nucleation theory based approach. J. Chem. Phys. **124**, 124707 (2006).

7. D. A. Porter and K. E. Easterling: Phase transformations in Metals and Alloys, 2nd ed. (Chapman & Hall, London, 1992).

8. A. Karma: Fluctuations in solidification. Phys. Rev. E **48**, 3441 (1993).

9. W. R. Fehlner and S. H. Vosko: A product representation for cubic harmonics and special directions for the determination of the Fermi surface and related properties. Can. J. Phys. **54**, 2159 (1976).

10. M. I. Mendelev, M. J. Kramer, C. A. Becker and M. Asta: Analysis of semi-empirical interatomic potentials appropriate for simulation of crystalline and liquid Al and Cu. Phil. Mag. **88**, 1723 (2008).

11. J. R. Morris: Complete mapping of the anisotropic free energy of the crystal-melt interface in Al. Phys. Rev. B **66,** 144104 (2002).

12. L. Wu, B. Xu, Q. Li, W. Liu and M. Li: Anisotropic crystal–melt interfacial energy and stiffness of aluminum. J. Mater. Res. **30**, 1827 (2015).

APPLICATION OF MIVM FOR Sn-Ag AND Sn-In ALLOYS IN VACUUM DISTILLATION

Lingxin Kong[1, 2, 3], Junjie Xu[1, 2, 3], Baoqiang Xu[1, 2, 3], Shuai Xu [1,2,3], Bin Yang[1, 2, 3, *], Yifu Li [1, 2, 3], Dachun Liu[1, 2, 3], Ruibo Hu[4]

[1]The National Engineering Laboratory for Vacuum Metallurgy, Kunming University of Science and Technology, Kunming 650093, PR China
[2] Key Laboratory for Nonferrous Vacuum Metallurgy of Yunnan Province, Kunming 650093, PR China
[3] State Key Laboratory of Complex Nonferrous Metal Resources Clear Utilization, Kunming 650093, PR China
[4] Guizhou Normal University, Guiyang 550001, PR China

Keywords: Phase equilibrium; Molecular interaction volume model (MIVM); Vacuum distillation; Sn-Ag and Sn-In alloys

Abstract

In this study, the vapor-liquid phase equilibrium compositions of tin-silver (Sn-Ag) and tin-indium (Sn-In) alloys in vacuum distillation were predicted based on the molecular interaction volume model (MIVM) and vacuum distillation theory, which can be used to precisely estimate the separation degree and the product composition in vacuum distillation. The calculated values of activities of components in Sn-Ag and Sn-In alloys are in good agreement with experimental data, which indicates that the method is reliable and convenient due to the MIVM has a clear physical basis and can predict the thermodynamic properties of multi-component liquid alloys using only two infinite dilute activity coefficients. This study provides an effective and convenient model on which to base refining simulations for Sn-based alloys.

Introduction

A large number of Sn-based alloys such as tin-lead (Sn-Pb), tin-antimony (Sn-Sb), tin-bismuth (Sn-Bi), Sn-Ag and Sn-In alloys will be produced from tin smelteries every year due to tin ores usually contain Pb, Sb, Bi, Ag and In at present. In addition, large numbers of waste Sn-based alloys will be recycled from electroplates, solders and other various industries in China and elsewhere due to Sn was usually used to produce alloys with other metals, which will causes serious resources waste and environment pollution if the Sn-based alloys cannot be recycled efficiently and cleanly. The separation and recovery of these Sn-based alloys, therefore, has become imperative for the refineries of the whole world. The methods used widely in the past such as the chemical process and the electrolysis are not consummate because of the low metal recovery, long flow sheet, and evident environmental pollution etc. Vacuum distillation can eliminate the disadvantages of traditional methods and can produce new products to meet the needs of the rapid development of high technology [1]. Over past decades, vacuum distillation has been studied and successfully used in refining and recovery of various nonferrous crude metals and alloys by Kato [2], Gopala [3], Zhan [4], and Ali [5, 6] etc., and the area of its application is being extended rapidly.

*** Corresponding author. Tel. :** +86 871 65161583; fax: +86 871 65161583.
E-mail address: kgyb2005@126.com (B. Yang) ; kkmust@126.com (L.X. Kong)

The thermodynamic properties of binary liquid alloys are important for understanding the process metallurgy. Theoretical and model prediction is a convenient and reliable approach in obtaining thermodynamic properties of alloys, because of the experimental study is very time consuming. Furthermore, the determination of thermodynamic properties of alloys through experiments needs not only the advanced instruments but also the continuous financial support [7].

The separation of Sn-Pb, Sn-Sb and Sn-Bi alloys by vacuum distillation has been studied in China and elsewhere for a long time, which has been described in numerous works [8-11]. The study about the separation of Sn-Ag and Sn-In alloys by vacuum distillation, however, has not been reported. The purpose of this study, therefore, was to calculate the activities of components of Sn-Ag and Sn-In alloys based on the MIVM, to predict the phase equilibrium of Sn-Ag and Sn-In alloys in vacuum distillation by using the activity coefficients and the properties of pure components, and a comparison between the predicted values and the experimental data of activities was also executed.

Simple description of MIVM

The MIVM was derived from the theory of statistic thermodynamics, which is reliable and stable in predicting thermodynamic properties of liquid alloys [12, 13], more details were available in Refs. [7] and [14]. According to MIVM, the molar excess Gibbs energy G_m^E [7] of the liquid mixture *i–j* can be expressed as

$$\frac{G_m^{\ E}}{RT} = x_i \ln\left(\frac{V_{mi}}{x_i V_{mi} + x_j V_{mj} B_{ji}}\right) + x_j \ln\left(\frac{V_{mj}}{x_j V_{mj} + x_i V_{mi} B_{ij}}\right) - \frac{x_i x_j}{2}\left(\frac{Z_i B_{ji} \ln B_{ji}}{x_i + x_j B_{ji}} + \frac{Z_j B_{ij} \ln B_{ij}}{x_j + x_i B_{ij}}\right) \tag{1}$$

Where V_{mi} and V_{mj} are the molar volumes of *i* and *j*, respectively; x_i and x_j the molar fractions; Z_i and Z_j are the first coordination numbers of *i* and *j*, respectively; and the pair-potential energy interaction parameters B_{ij} and B_{ji} are defined as,

$$B_{ij} = \exp\left[-\left(\frac{\varepsilon_{ij} - \varepsilon_{jj}}{kT}\right)\right] \qquad B_{ji} = \exp\left[-\left(\frac{\varepsilon_{ji} - \varepsilon_{ii}}{kT}\right)\right] \tag{2}$$

Where *k* is the Boltzmann constant, ε_{ii}, ε_{jj} and ε_{ij} are the *i–i*, *j–j*, and *i–j* pair-potential energies, respectively. $\varepsilon_{ij}=\varepsilon_{ji}$, and *T* the absolute temperature.

For a binary mixture *i–j*, the activity coefficients of *i* and *j* components are expressed as follows, respectively [8].

$$\ln\gamma_i = \ln\left(\frac{V_{mi}}{x_i V_{mi} + x_j V_{mj} B_{ji}}\right) + x_j\left(\frac{V_{mj} B_{ji}}{x_i V_{mi} + x_j V_{mj} B_{ji}} - \frac{V_{mi} B_{ij}}{x_j V_{mj} + x_i V_{mi} B_{ij}}\right) - \frac{x_j^{\ 2}}{2}\left(\frac{Z_i B_{ji}^{\ 2} \ln B_{ji}}{(x_i + x_j B_{ji})^2} + \frac{Z_j B_{ij} \ln B_{ij}}{(x_j + x_i B_{ij})^2}\right) \tag{3}$$

$$\ln\gamma_j = \ln\left(\frac{V_{mj}}{x_j V_{mj} + x_i V_{mi} B_{ij}}\right) - x_i\left(\frac{V_{mj} B_{ji}}{x_i V_{mi} + x_j V_{mj} B_{ji}} - \frac{V_{mi} B_{ij}}{x_j V_{mj} + x_i V_{mi} B_{ij}}\right) - \frac{x_i^{\ 2}}{2}\left(\frac{Z_j B_{ij}^{\ 2} \ln B_{ij}}{(x_j + x_i B_{ij})^2} + \frac{Z_i B_{ji} \ln B_{ji}}{(x_i + x_j B_{ji})^2}\right) \tag{4}$$

When x_i or x_j approaches zero, the infinite dilute activity coefficients γ_i^{∞} and γ_j^{∞}, respectively, are derived from Eqs. (3) and (4) as follows

$$\ln \gamma_i^{\infty} = 1 - \ln\left(\frac{V_{mj}B_{ji}}{V_{mi}}\right) - \frac{V_{mi}B_{ij}}{V_{mj}} - \frac{1}{2}\left(Z_i \ln B_{ji} + Z_j B_{ij} \ln B_{ij}\right) \quad (5)$$

$$\ln \gamma_j^{\infty} = 1 - \ln\left(\frac{V_{mi}B_{ij}}{V_{mj}}\right) - \frac{V_{mj}B_{ji}}{V_{mi}} - \frac{1}{2}\left(Z_j \ln B_{ij} + Z_i B_{ji} \ln B_{ji}\right) \quad (6)$$

The coordination number Z_i of liquid metals can be estimated by the following equation [7]

$$Z_i = \frac{2\sqrt{2\pi}}{3}\left(\frac{r_{mi}^{\ 3} - r_{0i}^{\ 3}}{r_{mi} - r_{0i}}\right)\rho_i r_{mi} \exp\left(\frac{2\Delta H_{mi}}{Z_c RT}\right) \quad (7)$$

Where $\rho_i = N_i / V_i$ is the molecular number density, N_i is the molecular number and V_i is the molar volume, ΔH_{mi} is the melting enthalpy; Z_c =12 is the close-packed coordination, T the liquid metal temperature and R the gas constant; r_{0i} and r_{mi} are the beginning and first peak values of radial distance in a radial distribution function near its melting point, respectively, and the r_{mi} is approximate to the atomic diameter observably, σ_i, which were available in Ref. [1].

Method

Saturated vapor pressure

The basic principle for separating Ag and In from Sn is the differences of the saturated vapor pressure of components of Sn-Ag and Sn-In alloys at a certain temperature. The saturated vapor pressure of pure components of these two alloys can be calculated from the following equation [15]

$$\lg P^* = AT^{-1} + B\lg T + CT + D \quad (8)$$

Where P^* is the saturated vapor pressure of pure components; A, B, C and D are the evaporation constants of components of the Sn-based alloys, which were available in Ref. [15].

Separation coefficient

The reason of separation of alloys by vacuum distillation is the composition difference between vapor phase and liquid phase. A concept separation coefficient, viz. β, which can be used to estimate the feasibility of separation of alloys by vacuum distillation was introduced by Dai [15] from theoretical derivation for *i*–*j* binary alloy, that is

$$\beta = (\gamma_i / \gamma_j) \cdot (P_i^* / P_j^*) \quad (9)$$

Where γ_i and γ_j are activity coefficient of i and j components; P_i^* and P_j^* are saturated vapor pressure of i and j in pure state, respectively. If the value of β is known, the ratio of vapor densities of i and j can be expressed as

$$\frac{\rho_i}{\rho_j} = \beta \frac{\omega_i}{\omega_j} \quad (10)$$

Where ρ_i/ρ_j is the mass ratio of component i in the vapor phase to that of j, and ω_i/ω_j is the mass ratio of component i in the liquid phase to that of j, respectively. The separation of i and j could happen while $\beta > 1$ or $\beta < 1$, but it could not happen while $\beta = 1$. The reasons are as follows: While $\beta > 1$, Eq.(3) becomes $\rho_i/\rho_j > \omega_i/\omega_j$, which indicates that the content of i in the vapor phase was larger than that in the liquid phase, that is, i will concentrates in the vapor phase, and j in the liquid phase. While $\beta < 1$, $\rho_i/\rho_j < \omega_i/\omega_j$, i will concentrates in the liquid phase, and j in the vapor phase. So, while $\beta > 1$ or $\beta < 1$, i can be separated from j by vacuum distillation. While $\beta = 1$, however, the content of i in the vapor phase was equal to that in the liquid phase, i and j could not be separated by vacuum distillation.

Vapor-liquid phase equilibrium in vacuum distillation

The saturated vapor pressure difference in Sn, Ag and In can only be used as a rough guide for evaluating the possibility of separation of alloys by vacuum distillation, which cannot be used to precisely predict the distribution of components of alloys. In order to predict the separation effect quantitatively, we use vapor-liquid phase equilibrium diagram between gas phase and liquid phase to precisely predict the distribution of components of the Sn-based alloys in vacuum distillation.

For *i-j* alloy, the relationship between the mass fraction of *i* and *j* components in vapor and liquid phase can be expressed, respectively, as follows,

$$\omega_{i,g} + \omega_{j,g} = 1 \tag{11}$$

$$\omega_{i,l} + \omega_{j,l} = 1 \tag{12}$$

Where $\omega_{i,g}$, $\omega_{j,g}$ are mass fraction of *i* and *j* components in the vapor phase, respectively; $\omega_{i,l}$, $\omega_{j,l}$ are mass fraction of *i* and *j* components in the liquid phase, respectively.

When the two phases are in equilibrium, the mass fraction of component *i* in the vapor phase is related to the vapor densities of *i*, *j* components as follows [15].

$$\omega_{i,g} = \frac{\rho_i}{\rho_i + \rho_j} = \frac{1}{1 + (\rho_j / \rho_i)} \tag{13}$$

Substituting Eqs. (9) and (10) into Eq. (13), the mass fraction of component *i* in the vapor phase can be expressed as,

$$\omega_{i,g} = \left[1 + \left(\frac{\omega_{j,l}}{\omega_{i,l}} \right) \cdot \left(\frac{\gamma_j}{\gamma_i} \right) \cdot \left(\frac{P_j^*}{P_i^*} \right) \right]^{-1} \tag{14}$$

Where ω, γ, P^*, β are the mass fraction, activity coefficient, saturated vapor pressure, and separation coefficient, respectively. The relationship diagram of $\omega_{i,g}$–$\omega_{i,l}$ can be calculated by γ, P^* and a series of $\omega_{j,l}/\omega_{i,l}$ at required temperatures, that is the vapor–liquid phase equilibrium diagram for *i–j* alloy system.

Results and discussion

The boiling point (BP) of Sn, Ag and In is important to understand the studied temperature range in vacuum distillation, which is 2876 K, 2436 K and 2346 K, respectively. The BP of Sn, Ag and In, however, will decrease with the decreasing ambient pressure. In addition, Ag and In have already begun to evaporate at 1073 K and will evaporate completely at 1573 K under a certain vacuum condition [15]. Above all, the amount of Sn that evaporates into the vapor phase increases with the increasing temperature, which will decrease the separation effect for both Sn-Ag and Sn-In alloy. The temperature in this study, therefore, was determined in the range of 1073-1573 K. Substituting the evaporation constants into Eq. (8), the saturated vapor pressure of Sn, Ag and In were calculated in the temperature range of 1073–1573 K, as shown in Table 1.

Table 1 Vapor pressure of components of Sn-Ag and Sn-In alloys at different temperature

T (K)	1073	1173	1273	1373	1473	1573
P^*_{Sn} (Pa)	8.11×10^{-5}	1.38×10^{-3}	1.51×10^{-2}	1.16×10^{-1}	6.79×10^{-1}	3.17
P^*_{In} (Pa)	6.72×10^{-2}	6.44×10^{-1}	4.32	2.19×10^{1}	8.89×10^{1}	3.01×10^{2}
P^*_{Ag} (Pa)	6.70×10^{-3}	8.71×10^{-2}	7.50×10^{-1}	0.47×10^{1}	2.27×10^{1}	8.98×10^{1}

The values of B_{ij} and B_{ji} must be obtained before applying the model into Sn-Ag and Sn-In binary liquid alloys, which can be calculated from Eqs. (5) and (6) using the Newton–Raphson

methodology if the values of γ_i^{∞} and γ_j^{∞} of the binary liquid alloys, the related parameters of pure metals and the coordination number Z_i of liquid metals are known. The related parameters of pure metals were available in Refs. [1] and [16]. The values of γ_i^{∞} and γ_j^{∞} at the required temperatures can be calculated from the following equation [17],

$$\ln \gamma_i^{\infty} = \frac{a}{T} + b \tag{15}$$

Where $a = \overline{H}_i^{E\infty} / R$ and $b = -\overline{S}_i^{E\infty} / R$. Here, the partial molar infinite dilute excess enthalpy $\overline{H}_i^{E\infty}$ and entropy $\overline{S}_i^{E\infty}$ are independent of temperature, R is the gas constant. Notice that $\overline{H}_i^{E\infty}$ equals the partial molar infinite dilute mixing enthalpy of component i, $\Delta\overline{H}_i^{M\infty}$. Based on the Eq. (15), the infinite dilute activity coefficient γ_i^{∞} at required temperatures can be calculated easily from the values of $\Delta\overline{H}_i^{M\infty}$ and $\overline{S}_i^{E\infty}$ [18]. The predicted values of γ_i^{∞} and γ_j^{∞} of Sn-In alloy at the required temperatures are shown in Table 2. The values of Z_i can be calculated from Eq. (7) by using the related parameters of pure metals, as shown in Table 2. The required binary parameters B_{ij} and B_{ji} of Sn-In alloy were calculated at the required temperatures, as shown in Table 2.

Table 2 The values of γ_i^{∞}, γ_j^{∞}, B_{ij} and B_{ji} of Sn-In alloy at the required temperatures.

i-j	T (K)	γ_i^{∞}	γ_j^{∞}	B_{ij}	B_{ji}	Z_i	Z_j
Sn-In	700	0.376	1.241	0.2917	2.2015	6.82	9.86
	1073	0.397	1.306	0.2878	2.2174	6.38	9.37
	1173	0.401	1.316	0.2869	2.2201	6.29	9.26
	1273	0.404	1.325	0.2859	2.2232	6.21	9.16
	1373	0.407	1.333	0.2850	2.2257	6.13	9.06
	1473	0.409	1.340	0.2838	2.2290	6.06	8.96
	1573	0.411	1.346	0.2827	2.2318	5.99	8.88

On the other hand, the values of B_{ij} and B_{ji} can be obtained from the following method when the values of γ_i^{∞} and γ_j^{∞} were unknown. When the values of B_{ij} and B_{ji} are known at a certain temperature (T_1), the values of B_{ij} and B_{ji} at the required temperature (T_2) can be obtained from Eq. (2) in which the pair-potential energy interaction parameters $(\varepsilon_{ij} - \varepsilon_{jj})/\mathrm{k}T$ and $(\varepsilon_{ji} - \varepsilon_{ii})/\mathrm{k}T$ may be assumed to be independent of temperature.

For example, in the binary system Sn-Ag:

$$-\left(\frac{\varepsilon_{ij} - \varepsilon_{jj}}{k}\right) = T \ln B_{ij} = 1250 \ln (1.6427) = 620.4\ K,$$

$$B_{ij} = \exp\left(\frac{620.4}{1073}\right) = 1.7828 \text{ at } 1073 \text{ K},$$

$$-\left(\frac{\varepsilon_{ji} - \varepsilon_{ii}}{k}\right) = T \ln B_{ji} = 1250 \ln (0.2402) = -1782.9\ K,$$

$$B_{ji} = \exp\left(\frac{-1782.9}{1073}\right) = 0.1898 \text{ at } 1073 \text{ K},$$

The required binary parameters B_{ij} and B_{ji} of Sn-Ag alloy were calculated at the required temperatures, as shown in Table 3

Substituting the corresponding B_{ij} and B_{ji} into Eqs. (3) and (4), the activities of components of Sn-Ag and Sn-In alloys can be predicted. A comparison between the predicted values of MIVM with experimental data of activities was also carried out, as shown in Fig. 1.

Table 3 The values of B_{ij}, B_{ji}, Z_i and Z_j of Sn-Ag alloy at the required temperatures.

i-j	*T* (K)	γ_i^∞	γ_j^∞	B_{ij}	B_{ji}	Z_i	Z_j
Sn-Ag	1250	1.49	0.187	1.6427	0.2402	6.23	10.68
	1073			1.7829	0.1898	6.38	11.03
	1173			1.6971	0.2187	6.29	10.82
	1273			1.6280	0.2465	6.21	10.64
	1373			1.5713	0.2729	6.13	10.47
	1473			1.5238	0.2981	6.06	10.31
	1573			1.4835	0.3219	5.99	10.16

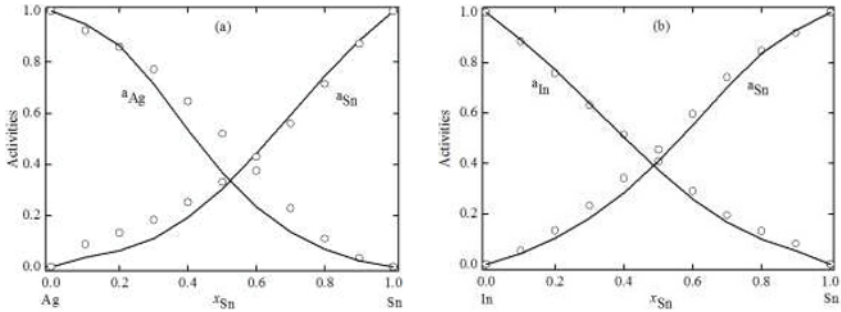

Fig.1. Comparison of the predicted activities of MIVM (lines) with experimental data [18] (symbols) of alloy systems (a) Sn-Ag at 1250 K, (b) Sn-In at 700 K.

It can be seen from Fig.1 that the predicted values are in good agreement with the experimental data [18]. This confirms that the prediction of activities of components of Sn-Ag and Sn-In alloys in vacuum distillation based on the MIVM is reliable because of the MIVM was derived from statistic thermodynamics, and it has a clear physical basis.

Substituting the activity coefficients γ, saturated vapor pressure P^* and mass fraction ω of components of Sn-Ag and Sn-In alloys into Eq. (14), the vapor–liquid phase equilibrium composition of Sn-Ag and Sn-In alloy systems can be predicted easily at the required temperatures, as shown in Fig. 2. It shows the change of equilibrium composition of vapor and liquid phase at different temperature.

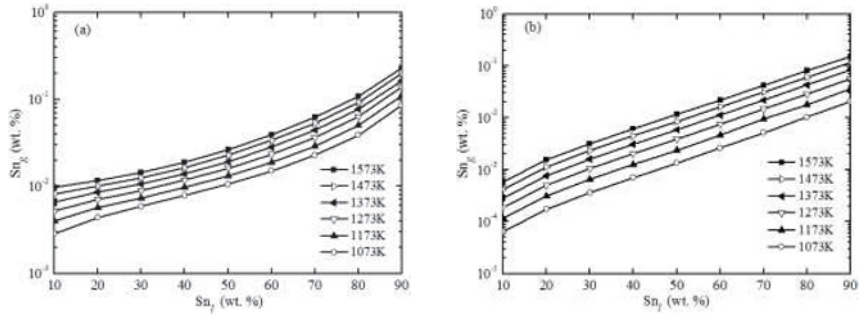

Fig.2. Vapor–liquid phase equilibrium composition of (a) Sn-Ag system, (b) Sn-In system at different temperatures.

It can be seen from Fig. 2 (a) that the content of tin in the vapor phase was 0.04 wt pct, while in the liquid phase, it was 80 wt pct at 1073K, it reached 0.076 wt pct in the vapor phase, while in the liquid phase, it was 85 wt pct at 1173 K, and it was 0.15 wt pct in the vapor phase, while in the liquid phase, it was 90 wt pct at 1273 K, which indicates that Sn will concentrates in the liquid phase, while Ag in the vapor phase in vacuum distillation, that is Ag can be separated from Sn by vacuum distillation thoroughly. Fig. 2 (b) shows that the content of tin in the vapor phase was 0.01 wt pct, while in the liquid phase, it was 80 wt pct at 1073K, it reached 0.027 wt pct in the vapor phase, while in the liquid phase, it was 85 wt pct at 1173 K, and it was 0.06 wt pct in the vapor phase, while in the liquid phase, it was 90 wt pct at 1273 K, which indicates that Sn will concentrates in the liquid phase, while In in the vapor phase in vacuum distillation, that is In can also be separated from Sn by vacuum distillation thoroughly. We can also note from Fig. 2 (a) and (b) that the content of Sn in the vapor phase of Sn-Ag system was larger than that of Sn-In system at the same condition. The reason for this phenomenon can be attributed to the saturation vapor pressure of Ag is less than that of In, so the quantity of Ag that evaporates into the vapor phase is less than that of In. Calculation of vapor–liquid phase equilibrium composition has a great important sense in researching purification and separation of crude metals and alloys by vacuum distillation. The method will bring certain errors during calculation; the reasons may arise from the MIVM and the accuracy of the thermodynamic data.

Conclusions

Based on the MIVM, the phase equilibriums of Sn-Ag and Sn-In alloys in vacuum distillation were predicted using only the activity coefficients and the properties of pure components. The phase equilibrium is of great importance in estimating the separation degree and the distribution of components of alloys in vapor and liquid phase in vacuum distillation quantitatively. It can be used to choose the experimental parameters and conditions before carrying out the experiments, which have a possibility for sharp decreasing of costs for a large number of scientific experiments, especially in the economic crisis of the whole world. Due to the thermodynamic data is quite scarce and the determination of thermodynamic data by experiments needs not only the excellent instruments but also the continuous financial support, the present study is helpful to get more reliable and useful results in separation of alloys by vacuum distillation because of the MIVM has a good and clear physical basis.

Acknowledgements

The authors are grateful for the financial support from the General Program of Natural Science Foundation of China (Grant No. 51474116), the Program for Innovative Research Team in University of Ministry of Education of China (Grant No. IRT1250), the Cultivating Program for Scientists Leader of Yunnan Province (Grant No. 2014HA003) and the First-Class Doctoral Dissertation Breeding Foundation of Kunming University of Science and Technology.

References

[1] H.W. Yang, et al, “Application of molecular interaction volume model in vacuum distillation of Pb-based alloys,” Vacuum, 86 (9) (2012), 1296-1299.

[2] T.Kato, et al, “Distillation of cadmium from uranium–plutonium–cadmium alloy,” J. Nucl. Mater., 340 (2005), 259-265.

[3] A. Gopala, et al, “Process methodology for the small scale production of m6N5 purity zinc using a resistance heated vacuum distillation system,”Mater. Chem. Phys., 122 (2010),

151-155.
[4] L. Zhan, et al, “Separating zinc from copper and zinc mixed particles using vacuum sublimation,” Sep. Purif. Technol., 68 (2009) 397-402.
[5] S.T. Ali, et al, “Reduction of trace oxygen by hydrogen leaking during selective vaporization to produce ultra-pure cadmium for electronic applications,” Mater. Lett., 61 (2007), 1512-1516.
[6] S.T. Ali, et al, “Preparation of high pure zinc for electronic applications using selective evaporation under vacuum,” Sep. Purif. Technol., 85 (2012) 178-182.
[7] D.P. Tao, “A new model of thermodynamics of liquid mixtures and its application to liquid alloys,” Thermochim. Acta, 363 (2000), 105-113.
[8] H.W. Yang, et al, “Calculation of phase equilibrium in vacuum distillation by molecular interaction volume model,” Fluid phase Equilib., 314 (2011), 78-81.
[9] L.X. Kong, et al, “Application of MIVM for Pb-Sn system in vacuum distillation,’Metall. Mater. Trans. B, 43 (2012), 1649-1656.
[10] A.X. Wang, et al, “Process optimization for vacuum distillation of Sn-Sb alloy by response surface methodology ,” Vacuum, 109 (2014) 127-134.
[11] W. Chen, et al, “Research on the law of vacuum distillation of bismuth,” J. Vac. Sci. Technol., 14 (4) (1994) 254-259 (in Chinese).
[12] S. Poizeau and D.R. Sadoway, “Application of the Molecular Interaction Volume Model (MIVM) to Calcium-Based Liquid Alloys of Systems Forming High-Melting Intermetallics,” J. Am. Chem. Soc., 135 (2013), 8260-8265.
[13] S.Poizeau, et al, “Determination and modeling of the thermodynamic properties of liquid calcium–antimony alloys,” Electrochim. Acta, 76 (2012), 8-15.
[14] D.P. Tao, et al, “A new model of thermodynamics of liquid mixtures and its application to liquid alloys,” Themochim. Acta, 383 (2002), 45-51.
[15] Y.N. Dai and B. Yang, *Vacuum Metallurgy for Non-Ferrous Metals and Materials*, (Metallurgical Industry Press, Beijing, 2006), 21.
[16] D.P. Tao, “Prediction of activities of all components in the lead-free solder systems Bi–In–Sn and Bi–In–Sn–Zn,” J. Alloys Compd. 457 (2008), 124-130.
[17] D.P. Tao, “Molecular entity vacancy model,” Fluid Phase Equilib. 250 (2006), 83-92.
[18] R. Hultgren, et al. *Selected Values of the Thermodynamic Properties of Binary Alloys*, (ASM, Metals Park, OH, 1973), 1335.

EXPERIMENTS AND KINETICS MODELING FOR GASIFICATION OF BIOMASS CHAR AND COAL CHAR UNDER CO_2 AND STEAM CONDITION

Guang-wei Wang[1], Jian-liang Zhang[1]✉, Jiu-gang Shao[2], Peng-cheng Zhang[1]

[1]School of Metallurgical and Ecological Engineering, University of Science and Technology Beijing, Beijing 100083, China
[2]Handan Steel Co.LTD, Handan, 056000, China.
✉ Corresponding author, E-mail: zhang.jianliang@hotmail.com

Keywords: Biomass char; TGA; Gasification; Kinetics models

Abstract

Gasification behaviors of biomass char and coal char were analyzed by thermal gravimetric method, and influences of gasification temperature and different gasifying agents were investigated. At the same time, kinetics of char gasification under CO_2 condition and steam condition were investigated by Chou model. Under the same condition, gasification characteristics of biomass char are better than that of coal char, and meanwhile performance of steam is better than CO_2 as gasifying agent. From kinetics analysis, among 1173~1323K range, gasification of biomass char and coal char is under chemical reaction control both for steam and CO_2 condition. Gasification process of biomass char could be simulated by flat particle gas-solid reaction of Chou model, with activation energy as 113.7kJ/mol and76.4kJ/mol for CO_2 and steam condition respectively; gasification of coal char could be simulated by spherical particle gas-solid reaction of Chou model, with activation energy 182.6kJ/mol and160.9kJ/mol for CO_2 and steam condition respectively.

Introduction

Compared with traditional blast furnace iron making, in shaft furnace direct iron reduction combined with coal gasification process, coking, sintering and hot stove processes are eliminated showing prominent energy saving and pollutant reduction, which is an important future trend for iron and steel industry[1,2]. China is abundant in biomass resource, and biomass energy proportions for 33% in primary energy resources and ranks as second energy after coal[3]. Compared with coal, biomass has advantages of large yield, various kinds, wide distribution, low pollution and carbon recycle etc[3], so it is an important way to develop process of using biomass replacing coal to generate reducing gas to improve social and environmental benefits of shaft furnace direct reduction iron process.

Gasification of biomass and coal has been widely researched to reach efficient utilization of biomass resource and coal resource[4]. Gasification can be divided into two main stages: pyrolysis and subsequent gasification of the remaining char, the second stage being the controlling step of the whole process. For these reason, knowledge about reactivity of chars and their variation during reaction progress is fundamental for the design of gasification reactors[5]. Gasification process is mainly influenced by gasifying agent and temperature. Commonly used gasifying agents are air, oxygen, CO_2, steam and their mix. Among them, CO_2 which is the main product of combustion, and steam whose gasification product is rich in hydrogen are mostly used gasifying agents. In order to clarify gasification behaviors of biomass and coal under CO_2 and

steam conditions, various models were introduced by Gao et al.[6], but due to complexity of calculation process the application of these models were limited. For this reason, more simple models are needed for approximate computation in design of gasifier device.

In this paper, high temperature gasification characteristics of biomass char and coal char under CO_2 and steam conditions were researched, and Chou model[7] was firstly introduced in analysis of gasification kinetics of coal char and biomass char under CO_2 and steam condition. Kinetic parameters of gasification process were ascertained, offering theoretical reference for production of reducing gas in gas-based direct reduction iron process from biomass and coal.

Kinetic model

Gasification of biomass char and coal char involves various physical and chemical processes, and the main part is reaction between solid carbon and gasifying agent to generate gas products H_2 and CO; at the same time, ash content in char would remain in solid state. Gasification process of biomass char and coal char under CO_2 and steam condition could be expressed as reaction (1) and (2).

$$CO_2 + \text{Char} \leftrightarrow 2CO + \text{Ash} \tag{1}$$

$$H_2O + \text{Char} \leftrightarrow CO + H_2 + \text{Ash} \tag{2}$$

Gasification process mainly includes gas transport through surrounding boundary layer of particle, inner particle diffusion of gas through pores and interface reaction. Gas transport through surrounding boundary layer could be eliminated by control of gas flow during experiments, and this research is focused on reaction under inner diffusion control or interface chemical reaction control conditions. Based on unreacted shrinking core model, Chou et al.[7] proposed a new gas-solid reaction model, which has been widely used in oxidation of nitrogen based refractory materials, hydrogen release process of hydrogen storage materials and hydrogen reduction of oxide. On the foundation of Chou model, gasification kinetics of biomass char and coal char under different conditions were investigated.

Spherical particle

For spherical particle, the reaction process is: gasifying agent firstly reacts with reactant on the surface of particle, and solid product adheres to the surface; with reaction proceeding, un-reacted core gradually diminishes and product layer increases; at last, un-reacted char becomes exhausted with only ash content remaining, and reaction process finishes. Reaction process of a spherical particle could be illustrated by Fig 1.

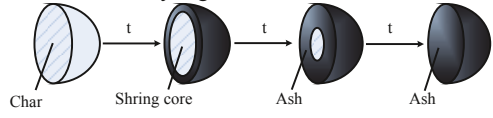

Figure 1. Schematic diagram of reaction for spherical particle

With gas transport through surrounding boundary layer of particle neglected, gasification process is influenced by inner gas diffusion through product layer and interface chemical reaction.

When gasifying agent contacts with char, surface carbon would react with agent to form gas product and ash, and relation between un-reacted radius and gasification ratio could be performed as:

$$\xi = 1-\left(r/R_0\right)^3 \tag{3}$$

Differential form of Eq. 3 is:

$$\frac{d\xi}{dt} = -\frac{3r^2}{R_0^3}\frac{dr}{dt} \tag{4}$$

For reaction (1), the gasification reaction rate V_r^f ,reverse reaction rate V_r^b ,and total reaction rate V_r could be performed as:

$$V_r^f = K_r^f C_{\mathrm{CO_2}}\left(\alpha/\beta\right) \tag{5}$$

$$V_r^b = K_r^b C_{\mathrm{CO}}^2\left(\alpha/\beta\right) \tag{6}$$

$$V_r = V_r^f - V_r^b = K_r^f C_{\mathrm{CO_2}}\left(\alpha/\beta\right) - K_r^b C_{\mathrm{CO}}^2\left(\alpha/\beta\right) \tag{7}$$

In the formulas, C_{CO_2} and C_{CO} are concentration of CO_2 and CO at α/β interface. α represents char and β represents ash layer.

When reaction is under reaction control, diffusion resistance in the product layer could be neglected, so: $C_{\mathrm{CO_2}}\left(\alpha/\beta\right)=C_{\mathrm{CO_2}}$, $C_{\mathrm{CO}}\left(\alpha/\beta\right)=C_{\mathrm{CO}}\approx 0$ .Then Eq. 7 could be reformed as:

$$V_r = K_r^f C_{\mathrm{CO_2}} \tag{8}$$

On the other hand, decreasing rate of un-reacted radius is in direct proportion to reaction rate:

$$\frac{dr}{dt} = \frac{V_r}{v} \tag{9}$$

In the formula V_r is reaction rate, and v is correlation coefficient related to reactant and reaction. Combine Eqs. 3, 4, 8 and 9:

$$\frac{d\xi}{dt} = \frac{3K_r^f C_{\mathrm{CO_2}}\left(1-\xi\right)^{2/3}}{R_0 v} \tag{10}$$

With initial condition t=0, ξ =0, perform integration on the Eq. 10 and obtain:

$$\xi = 1-\left(1-\frac{K_r^f C_{\mathrm{CO_2}}}{R_0 v}t\right)^3 \tag{11}$$

According to Arrhenius activation formula: $K_r^f = K_0 \exp\left(-\frac{E_{rea}}{RT}\right)$. Then Eq. 11 could be reformed as:

$$\xi = 1-\left(1-\frac{K_0 C_{\mathrm{CO_2}}}{R_0 v}\exp\left(-\frac{E_{\mathrm{rea}}}{RT}\right)t\right)^3 \tag{12}$$

Where, K_0 is constants independent of temperature; E_{rea} is the apparent activation energy. R is the gas constant, 8.314J/(mol·K); T is the absolute temperature, K; t is time, s.

Considering influence of temperature on reaction process, a constant could be defined:

$$B_T' = \frac{R_0 v}{K_0 C_{CO_2}} \tag{13}$$

Where, B_T is a function of $C_{\mathrm{CO_2}}$ and R_0 , and when CO_2 concentration and particle diameter is constant the value would be a constant too. Then Eq. 11 could be reformed as:

$$\xi = 1 - \left(1 - \frac{1}{B_T'} \exp\left(-\frac{E_{\text{rea}}}{RT}\right) t\right)^3 \tag{14}$$

With increase of reaction time, gasification conversion increases. For reaction by Eq. 2, when under reaction control the relation of conversion with temperature and time is the same as Eq. 12, where C_{CO_2} of parameter B_T' is replaced by C_{H_2O}.

When reaction is under inner diffusion control, Chou et al.[7] have given the expression, and relation between time t and gasification conversion ξ could be defined as Eq.15.

$$\xi = 1 - \left(1 - \sqrt{\frac{1}{B_T''} \exp\left(-\frac{E_{diff}}{RT}\right) t}\right)^3 \tag{15}$$

Flat particle

For gasification of flat particle, reaction occurs on both up and down side of particles, and the gasification process could be performed as Fig.2. During reaction specific reaction surface is constant, and product layer gradually increases to the end of reaction.

Figure 2. Schematic diagram of reaction for flat particle

For gasification of flat particle under chemical reaction control and diffusion control, the relation between conversion and time could be defined as Eqs. 16 and 17 respectively. For chemical reaction control, there is a linear relation between conversion and time; for inner diffusion control, there is square root relation between conversion and time.

$$\xi = \frac{1}{B_T'} \exp\left(-\frac{E_{\text{rea}}}{RT}\right) t \tag{16}$$

$$\xi = \sqrt{\frac{1}{B_T''} \exp\left(-\frac{E_{\text{rea}}}{RT}\right) t} \tag{17}$$

Eqs. 14 and 15 are relation between gasification conversion and time for spherical particle under chemical reaction control and inner diffusion control respectively; Eqs. 19 and 20 are relation between gasification conversion and time for flat particle under chemical reaction control and diffusion control respectively. They display relation of conversion with reaction time and temperature in explicit function form, and kinetic parameters and controlling step could be easily obtained by non-linear fitting method according to experiment data.

Experiments

Raw Materials

Table 1. Proximate and ultimate analysis of biomass char and coal char

Sample	Proximate analysis (%)			Ultimate analysis (%)				
	FC_d	A_d	V_d	C_d	H_d	O_d	N_d	S_d
BC	93.37	1.58	5.05	96.68	0.25	0.16	1.01	0.06
CC	83.37	15.58	1.05	84.29	0.23	0.25	0.78	0.81

Pulverized coal named Haolin anthracite was offered by a domestic steel work and biomass came from a lumber mill, which was pine wood. The biomass and coal pyrolysis were performed

in a vertical tube furnace. Samples were heated from room temperature to 1373K at a heating rate of 5K/min, and devolatilized in a flow of nitrogen for 90 min. After pyrolysis, chars were ground with an agate and pestle and separated into different fractions. The sample with size smaller than 0.074mm was selected for test. The proximate and ultimate analysis results of biomass char(BC) and coal char(CC) are shown in Table 1.

Gasification Experiments

The schematic diagram of the experimental facilities is shown Fig.3. The inner diameter of the alumina tube was 60mmΦ. The lower part of the alumina tube was filled with alumina balls for preheating gaseous reactant. In tests, the sample was deposited in a crucible with circular base. Amount of sample used was around 0.25g. The basket made of iron chrome alloy silk was located at uniform temperature zone, which was about 200mm in height above the alumina ball bed.

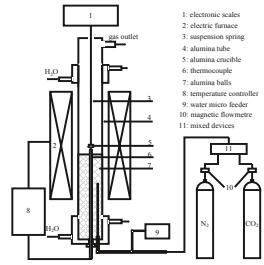

Figure 3. The schematic of experimental facilities for gasification

In this work, all tests were performed under isothermal conditions. The sample was heated to reaction temperature with a heating rate of 10K/min under an upward flow of nitrogen (purity>99.999%). After the temperature was maintained about 10min to stabilize sample temperature, the reaction was started by switching to CO_2 or steam. The test showed that once the CO_2 or steam flow rate was about 5L/min. Therefore, the sample was maintained under CO_2 or steam flow of 5L/min. Steam flow is controlled by a microsyringe, and 5L/min steam flow is converted by 240ml/h water flow in microsyringe. The weight loss of the char sample as a function of gasification time was recorded continuously. The gasification conversion (ξ) was calculated using the following equation:

$$\xi = \frac{m_0 - m_t}{m_0 - m_{\text{Ash}}} \tag{18}$$

Where m_0 represents the initial mass of the sample; m_t is the instantaneous mass of the sample at time t; m_{Ash} is the remaining mass of ash after completion of gasification.

Results and Discussion

Structure Analysis of Biomass Char and Coal char

Volatile content in biomass is very high, and after pyrolysis typical thin wall tube cellular structure was formed[8], meanwhile, due to low content of solid carbon the carbon skeleton structure was weak and sheet structure was formed after crushing as shown by Zuo et al[9]. For pulverized coal, volatile content is low and solid carbon content is high, and after pyrolysis strength of carbon skeleton structure was strong, and even after crushing spherical structure was

maintained as shown by Zuo et al[10]. Also, surface of biomass char is smooth with low cohesion and has uniform particle distribution; but for coal char the surface is rough and has obvious cohesion phenomenon.

Isothermal Gasification Curves of Biomass Char and Coal Char

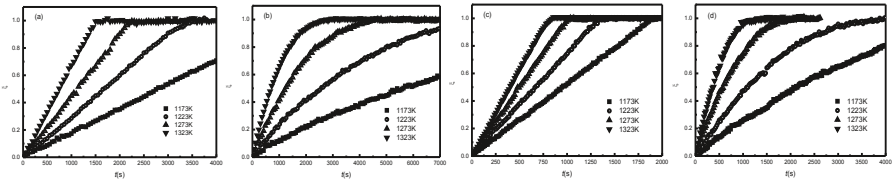

Figure 4. Gasification curves (a) BC-CO_2, (b) CC-CO_2, (c)BC-H_2O, (d) CC-H_2O

Temperature is a main factor affecting gasification reaction. Relation curves of conversion and time for biomass char and coal char under different conditions are shown in Fig.4 respectively. With increase of temperature, reactivity of both biomass char and coal char increases and the time needed for the same conversion is shortened. Under CO_2 condition, 2650s is needed to reach 80% conversion at 1223K, while for 1323k only 1190s is needed to reach the same conversion. Gasification index R [11] is used to evaluate reactivity of char, with R defined as follow:

$$R = \frac{0.5}{\tau_{0.5}} \tag{19}$$

In the formula $\tau_{0.5}$ is the time needed to reach 50% conversion.

Table 2. Gasification index of biomass char and coal char

Atmosphere	Sample	$R\times10^{-4}$			
		1173K	1223K	1273K	1323K
CO_2	BC	1.76	2.96	4.42	6.55
	CC	0.89	1.95	4.15	7.07
Steam	BC	5.20	7.55	10.04	12.50
	CC	2.38	4.64	8.68	13.66

Gasification index R of two chars under different conditions is shown in Table 2. R increases with increase of temperature. At higher temperature, more energy is available for carbon bond to break and the reaction proceeds to more extent. At low temperature gasification characteristics of biomass char is better than that of coal char, and with increase of temperature the difference between them diminishes. When reaches 1323K, gasification index of coal char surpasses that of biomass char. By comparison between gasification under CO_2 condition and steam condition, it could be concluded that gasification characteristics under steam condition is better that under CO_2 condition. By oxygen exchange theory[12], gasification of char starts with formation of carbon-oxygen compound that is oxygen atom combines with free carbon vacuum to form C(O), and then carbon-oxygen compound decomposes to form CO and new free carbon vacuum. Hydrogen bond in water is much easier to break than C-O bond in CO_2 to release oxygen, and further water molecule could release hydrogen free radical to enter into carbon matrix increasing condensation degree of aromatic ring, which all make higher gasification activity of steam than CO_2.

Kinetics Analysis

Biomass char has flat particle structure and coal char has spherical structure, so Eqs. 14 and 15 could be used to calculate control step and kinetic equation of biomass char, while Eqs. 16 and 17 could be used for coal char.

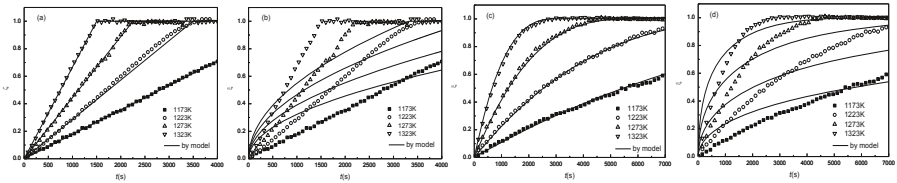

Figure 5. Model calculation and experimental data under CO_2 condition:(a) chemical reaction control-BC, (b) diffusion control-BC. (c) chemical reaction control-CC, (d) diffusion control-CC.

Gasification curves of biomass char and coal char under CO_2 condition are shown in Fig.5. When under chemical reaction control, there is good fitting result between Chou model and experimental data. So it could be concluded that under CO_2 condition, interface reaction of CO_2 with carbon is the controlling step and gasification equations are:

$$\xi = \frac{1}{4.88\times10^{-2}}\exp\left(-\frac{113667}{RT}\right)t \tag{20}$$

$$\xi = 1-\left(1-\frac{1}{1.95\times10^{-4}}\exp\left(-\frac{182621}{RT}\right)t\right)^3 \tag{21}$$

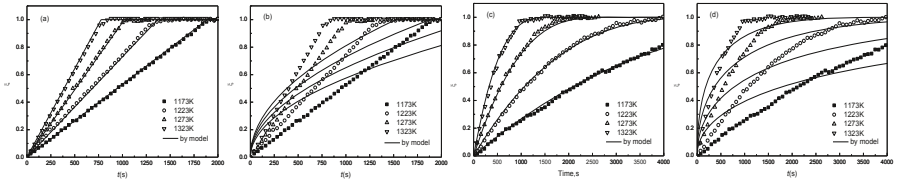

Figure 6. Model calculation and experimental data under H_2O condition:(a) chemical reaction control-BC, (b) diffusion control-BC. (c) chemical reaction control-CC, (d) diffusion control-CC.

Gasification curves of biomass char and coal char under steam condition are shown in Fig.6. It could be concluded that gasification process is similar with that under CO_2 condition, and interface reaction is the controlling step. Under steam condition, flat particle formula and spherical particle formula in Chou model was used for gasification of biomass char and coal char respectively, as expressed by following formulas:

$$\xi = \frac{1}{7.45\times10^{-1}}\exp\left(-\frac{76443}{RT}\right)t \tag{22}$$

$$\xi = 1-\left(1-\frac{1}{6.94\times10^{-4}}\exp\left(-\frac{160902}{RT}\right)t\right)^3 \tag{23}$$

By comparison between kinetic parameters of biomass char and coal char gasification, it could be concluded that gasification activation energy of biomass char is lower than that of coal char, and activation energy under steam condition is lower than that under CO_2 condition. Activation energy of biomass char and coal char under CO_2 condition is 113.7kJ/mol and 182.6kJ/mol respectively; while under steam condition, activation energy of biomass char and coal char is 76.4kJ/mol and 160.9kJ/mol respectively. Similar results were reported by Ge et

al[13-14]. By their results, activation energy of biomass char under CO_2 condition is 92.3~137.4 kJ/mol[13], and activation energy of coal char under CO_2 condition is 184.0 kJ/mol. Zhao et al.[14]used several kinetic methods to calculate the activation energy of biomass char and coal char reacting with H_2O and obtained values in the range of 60.5~71.8kJ/mol[13], and 174.8~180.3 kJ/mol.

Conclusion

Comparison between gasification characteristics and kinetics of biomass char and coal char using CO_2 and steam as gasifying agents have been investigated in details. It could be concluded that gasification characteristics of biomass char is better than that of coal char, and gasification activity of char under steam condition is higher than under CO_2 condition. Chou model was firstly introduced into gasification kinetics of biomass char and coal char, and results show that Chou model has good applicability in this field. Gasification kinetics of biomass char could be simulated by flat particle model, while gasification kinetics of coal char could be simulated by spherical particle model, and both of them are under chemical reaction control. Activation energy of biomass char and coal char under CO_2 condition are 113.7kJ/mol and 182.6kJ/mol respectively; while under steam condition they are 76.4kJ/mol and 160.9kJ/mol respectively.

References

1. Zhou Y et al., “Scheme of direct reduction iron production combined with coal gasification,” *Iron and Steel*, 2012, 47(11):27-35.
2. Qi Y et al., “Present status and trend of direct reduction technology development in China,” *China Metallury*, 2013, 23(1):9-14.
3. Liu H et al., “A study of the combustion characteristics of biomass and coal mixed fring,” *Journal of Engineering for Thermal Power*, 2002, 17(5):451-454.
4. Zhang S et al., “Pyrolysis an dlow temperature catalytic gasification of manure,” *Journal of Fuel Chemistry and Technology*, 2009, 37(6):673-678.
5. Fouga GG, Micco GD, and Bohe AE, “Kinetic study of argentinean asphaltite gasification using carbon dioxide as gasifying agent.” *Fuel*, 2011, 90474-680.
6. Gao C et al., “Co-gasification of biomass with coal and oil sand coke in a drop tube furnace,” *Energy Fuels*, 2010, 24:232–240.
7. Seo DJ et al., “Gasification reactivity biomass char with CO_2,” *Biomass and Bioenergy*, 2010, 34:1946-1953.
8. Chou K et al., “Kinetics of absorption and desorption of hydrogen in alloy powder,” *International Journal of Hydrogen Energy*, 2005, 30:301-309.
9. Hu Z et al., “Preparation and properties of biomass char for ironmaking,” *Journal of University of Science and Technology Beijing*, 2012, 3(9):998-1005.
10. Zuo HB et al., “Isothermal CO_2 gasification reactivity and kinetic models of biomass char/anthracite char,” *BioResources*, 2015, 10(3), 5242-5255.
11. Everson RC et al., “Reaction kinetics of pulverized coal-chars derived from inertinite-rich coal discards: Gasification with carbon dioxide and steam,” *Fuel*, 2006, 85(7-8):1076-1082.
12. Moulijn JA, Kapteijin F, “Towards a unified theory of reactions of carbon with oxygen-containing molecules,” *Carbon*, 1995, 33(8):1155-1165.
13. Ge P et al., “Study on catalytic gasification characteristics of pin char with CO_2,” *Coal Conversion*, 2013, 36 (1):47-50.
14. Zhao H et al., “Kinetic of gasification of biomass semi-cokes in high temperature steam,” *Journal of Power Engineering*, 2008, 28(3):453-458.

OPTIMIZATION OF MAIN FACTORS FOR DECARBONIZING RATIO OF TiB_2 POWDERS BY REVERSE FLOTATION USING RESPONSE SURFACE METHODOLOGY

Xiaoxiao Huang, Shuchen Sun, Shuaidan Lu, Kuanhe Li, Xiaoping Zhu, Ganfeng Tu

School of Materials and Metallurgy, Northeastern University; Shenyang, Liaoning 110819, China

Keywords: TiB_2, Carbothermal Reduction, Decarbonizing Ratio, Reverse Flotation

Abstract

The optimization of process conditions for decarbonizing ratio of titanium dibordie (TiB_2) powders by reverse flotation was investigated using response surface methodology (RSM). The TiB_2 powders was produced by using a powder mixture of C, TiO_2 and H_3BO_3 in a DC electric arc furnace. The carbon is in the form of graphite in the product. The way of carbon removal from the powder of TiB_2 produce is reverse flotation. Three key parameters TiB2 size, slurry concentration and collector dosage were chosen as variables. The optimum process conditions for decarbonizing ratio were determined by analyzing the response surface three-dimension surface plot and contour plot and by solving the regression model equation with Design Expert software. The central composite design (CCD) of RSM was used to optimize the process conditions, which showed that TiB2 size of 20μm, slurry concentration of 29.65% and collector dosage of 400 g/t were the best conditions. Under the optimal conditions, the decarbonizing ratio is 87.65%, and the relative error differed by only 1.2% from the predicted values of model (88.72%).

Introduction

Titanium dibordie (TiB_2) is a very useful ceramic materials. It has attracted great interest in excellent mechanical properties, chemical resistance and good thermal and electrical conductivities. Thus, titanium dibordie is widely applied as cutting tool composites, wear resistant parts, evaporator boat in high vacuum metal coatings, electrode materials, the protection of weapons and armored vehicle [1-6].

TiB_2 powder is prepared by a variety of methods such as the borothermic reduction of titania, fused-salt electrolysis, solution phase processing or carbothermal reduction [7-9]. Particularly, TiB_2 can be produced by carbothermic reduction of mixed oxides of boron and titanium, reduction of titanium oxide by boron carbide and carbon [10]. The carbothermal reduction process is commercially used as the cheapest method because of inexpensive raw materials and it is a simple process. Thus, carbothermal reduction process is a major method for TiB_2 powders.

In this paper, the titanium diboride particles were synthesized by carbothermal reduction process in the DC electric arc furnace (DC EAF). This carbothermal methods use petroleum coke as carbon sources, boric acid as boron sources and titania as titanium sources. In the meantime, corbon in this reaction is excess in order to ensure purity of the product. Thus,

there is carbon with a mass ratio of 6%-7% in the product of TiB_2 after the reaction. The excess C have to be separate from TiB_2 for the better TiB_2 purity.

Materials and Methods

Materials

Massive product was obtained by using a powder mixture of C, TiO_2 and H_3BO_3 in a DC EAF. Main component of the massive product is TiB_2. Massive product turned into powders after a series of process of pulverization and ball milling. The powders consists mainly of TiB_2, Fe and C. Fe can be removed by acid-treatment. At last, the powders used as experimental material. The powder was analyzed by X-ray diffractometry, Fig. 3 shows that the powder is composed mostly of TiB_2 and C. Furthermore, the powder was analyzed by Carbon sulfur analyzer reveal that the mass ratio of C in the powder is about 6% - 7%.

The way of carbon is separate from the TiB_2 powder is reverse flotation. The key experiment device is a lab-used single flotation cell of XFD-0.60. During the experiments, using terpenic oil as frother, kerosene as a collector and $NaHCO_3$ was selected as regulator.

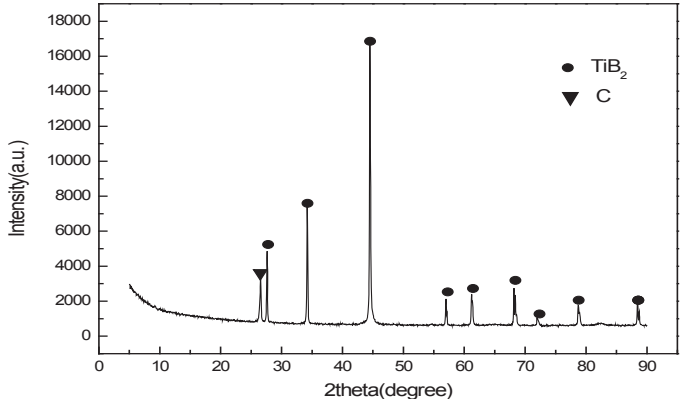

Fig. 1 X-ray diffraction pattern of the experimental material

Experimental Methods

All batch experiments were carried out in the lab-used single flotation cell of XFD-0.60 described before. Study on the changes of the mass ratio of C in the powder before and after reverse flotation. Decarbonizing ratio is used to measure experimental effect. Calculation method of Decarbonizing ratio is as follow:

$$\eta = \frac{\omega_1 - \varphi_2}{\omega_1} \times 100\% \quad (1)$$

Where, η is decarbonizing ratio, W_1 is the mass ratio of C before reverse flotation, W_2 is the mass ratio of C after reverse flotation.

Experimental Design

A five-level-three-factor central composite design (CCD) obtained by using the "Design Expert" software (Version 8.0.6.1, Stat-Ease Inc., Minneapolis, USA) statistical package was

used to find out the effect on decarbonizing ratio by most effective independent variables, including TiB2 size, slurry concentration, and collector dosage according to literature experiences. The decarbonizing ratio was taken as the response. The levels of factors used for optimization are presented in Table 1.

Table 1 Levels of factors used for optimization of decarbonizing ratio

Variable	Label	Level				
		-1.682(-α)	-1	0	1	1.682(+α)
X_1	TiB_2 size (μm)	1.23	6	13	20	24.77
X_2	slurry concentration (%)	13.18	20	30	40	46.82
X_3	collector dosage (g/t)	331.82	400	500	600	668.12

Quadratic polynomial equation (2) which includes all interaction terms was used to calculate the predicted response as follows:

$$Y = A_0 + \sum_{i=1}^{k} A_i x_i + \sum_{i=1}^{k} A_{ii} x_i^2 + \sum_{i=1}^{k} \sum_{j=1}^{k} A_{ij} x_i x_j \quad (2)$$

Where, Y is the predicted response, x_i (i = 1 - k) are the input independent variables, A_0 is the constant coefficient, A_{ii} is the quadratic coefficient, and A_{ij} is the interaction coefficient.

Statistical analysis of the model was performed to evaluate the analysis of variance (ANOVA). This response surface model was also used to predict the result by plane contour plots and three dimensional surface plots. The quality of the fit of polynomial model was expressed by the coefficient of determination R^2, and it's statically significance was checked by the F-test in the same program.

Results and Discussion

Experimental design and results

The major factors were optimized using CCD combined with RSM. The predicted, coded and actual value of the independent variables is shown in Table 2. The effects of each factor and their interactions calculated using Design Expert 8.0.6.1 Software. The statistical model are as follow：

$$Y = 84.57 + 4A - 0.94B - 2.05C + 0.39AB + 0.61AC - 0.34BC - 1.2A^2 - 2.95B^2 - 0.099C^2 \quad (3)$$

Where Y is the Decarbonizing ratio (%), A is the TiB_2 size (μm), B is slurry concentration (%) C is collector dosage (g/t).

Table 2 Experimental design matrix and results

Run order	Coded values			Real values			Actual values	Predicted values
	x_1	x_2	x_3	X_1	X_2	X_3		
1	0	-1.682	0	13	13.18	500	77.8	77.82
2	-1	1	1	6	40	600	71.8	71.99
3	0	0	1.682	13	30	668.18	80.7	80.83

4	1.682	0	0	24.77	30	500	88.1	87.92
5	0	0	0	13	30	500	84.5	84.57
6	0	0	0	13	30	500	83.7	84.57
7	-1	-1	1	6	20	600	75.4	75.32
8	0	0	0	13	30	500	83.1	84.57
9	0	1.682	0	13	46.82	500	75.2	74.65
10	1	-1	1	20	20	600	83.9	83.78
11	0	0	0	13	30	500	84.4	84.57
12	1	1	1	20	40	600	81.9	81.99
13	0	0	0	13	30	500	85.7	84.57
14	1	-1	-1	20	20	400	85.8	85.99
15	0	0	-1.682	13	30	331.82	88.4	87.74
16	-1	-1	-1	6	20	400	79.7	79.98
17	-1.682	0	0	1.23	30	500	74.8	74.45
18	0	0	0	13	30	500	85.9	84.57
19	-1	1	-1	6	40	400	77.5	78
20	1	1	-1	20	40	400	85.1	85.55

Diagnostic Checking of the Fitted Model

Analysis of variance (ANOVA) is important in determining the adequacy and significance of the quadratic model. Equation (3) was checked by F-test and ANOVA for the quadratic polynomial model is given in Table 3. The significance and adequacy of the proposed model was very satisfactory with very low Prob > F (<0.001) from the ANOVA. The computed model F value (63.63) implies the model is significant. The value of R^2, adjust of R^2 and predicted of R^2 are also given in Table 3.

Table 3 The ANOVA for the response surface quadratic polynomial model

Source	Sum of squares	df	Mean square	F value	Prob > F
Model	431.68	9	47.96	63.63	< 0.0001
A	218.83	1	218.83	290.29	< 0.0001
B	12.13	1	12.13	16.1	0.0025
C	57.61	1	57.61	76.42	< 0.0001
AB	1.2	1	1.2	1.59	0.2355
AC	3	1	3	3.98	0.074
BC	0.91	1	0.91	1.21	0.2973
A^2	20.59	1	20.59	27.31	0.0004
B^2	125.02	1	125.02	165.84	< 0.0001
C^2	0.14	1	0.14	0.19	0.6735
Residual	7.54	10	0.75		
Lack of Fit	1.54	5	0.31	0.26	0.9186
Pure Error	6	5	1.2		
Cor Total	439.22	19			

R^2 = 98.28%, R^2 (adjust) = 96.74%, R^2 (predicted) = 95.37%.

The graphical representation of the actual band gaps versus the predicted values is shown in Fig. 2. It can be seen that there is a good agreement (R^2 = 0.9828) between experimental data and predicted results.

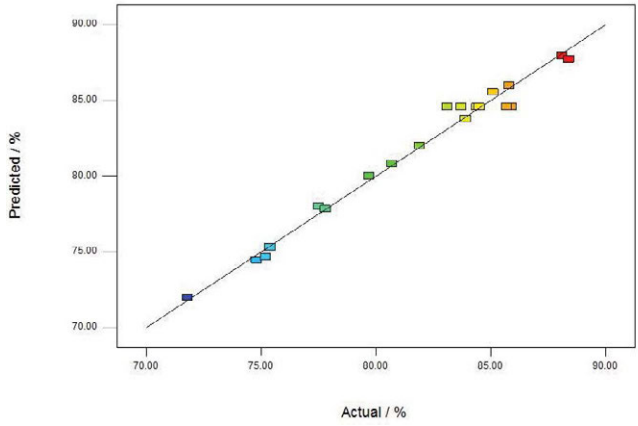

Fig. 2 Predicted vs. experimental relative decarbonizing ratio

Optimization of Decarbonizing Ratio

In order to better understand the relationship between the decarbonizing ratio and the independent variables (A, B and C) response surface plots were formed based on the second order polynomial model. The plots are shown in Fig. 3-5.

Fig. 3 shows the combined effect of TiB_2 size and slurry concentration on the decarbonizing ratio at constant collector dosage of 400 g/t. As shown in fig.3, the decarbonizing ratio increased with increasing of TiB_2 size under the other variables at their fixed levels. The F value of factor A in the Table 3 reveal factor A had a notably significant effect on the decarbonizing ratio (F value = 290.29).

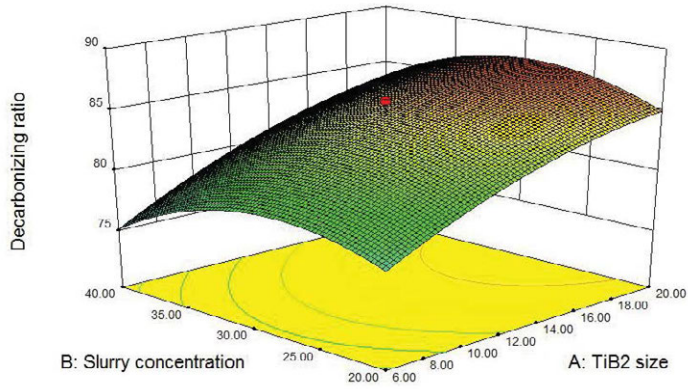

Fig. 3 The response surface plots and the corresponding contour lines showing the effects of TiB_2 size and slurry concentration on decarbonizing ratio, with the collector dosage of 400 g/t

The effect of TiB_2 size and collector dosage and their opposed interaction on the decarbonizing ratio is illustrated in Fig. 4. According to the figure, the decarbonizing ratio reduced with increasing of the collector dosage. It is easy to find that factor A has a bigger effect than factor C on decarbonizing ratio. The F value of A and C can be also proved this trend in the Table 3. (290.29 >76.42).

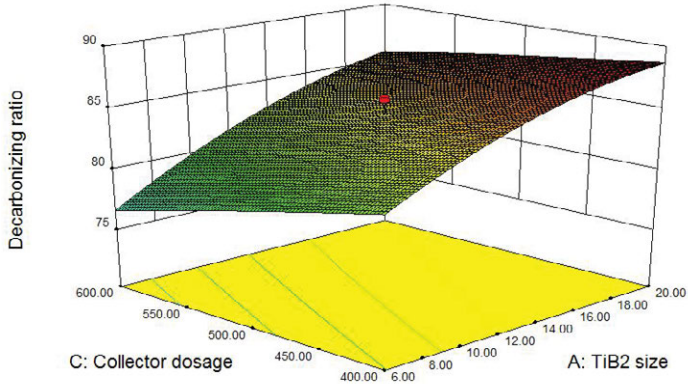

Fig. 4 The response surface plots and the corresponding contour lines showing the effects of TiB_2 size and collector dosage on decarbonizing ratio, with the slurry concentration of 29.65%

Fig. 5 represents the effects of slurry concentration and collector dosage on the decarbonizing ratio of the samples. With increasing of factor B, the decarbonizing ratio increase first and decrease afterwards.

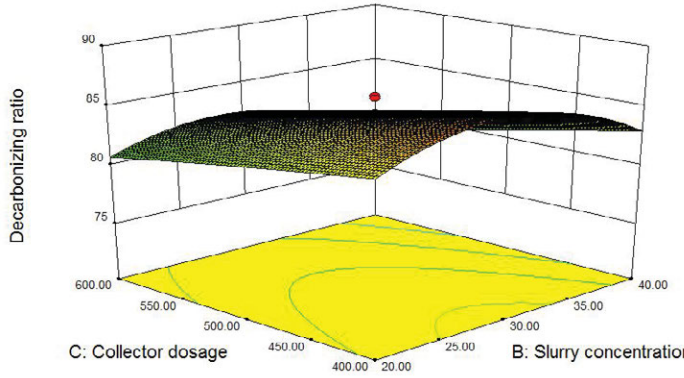

Fig. 5 The response surface plots and the corresponding contour lines showing the effects of slurry concentration and collector dosage on decarbonizing ratio, with the TiB_2 size of 20 μm

Validation of the models

The central composite design (CCD) of RSM shows that TiB_2 size of 20μm, slurry concentration of 29.65% and collector dosage of 400 g/t were the best conditions for the optimal decarbonizing ratio of 88.72%. In order to validate the optimum combination of the process variables, six group experimental verification is performed under the optimal conditions. The average decarbonizing ratio of six group is 87.65%, which is very close to the optimal values by the model. The relative error (1.2%) is enough small. Thus, the model is reliable, the optimum combination of the process variables which obtained by the model can be applied in practice.

Conclusions

(1) The method of reverse flotation can effectively remove more than 85% of carbon in titanium diboride.

(2) The proposed model equation illustrated the quantitative effect of variables and also the interactions among the variables on decarbonizing ratio. Under the optimal medium condition TiB_2 size of 20μm, slurry concentration of 29.65% and collector dosage of 400 g/t, the experimental decarbonizing ratio of 88.72%.

References

1. Tennery, V. J., Finch, C. B., Yust, C. S. and Clark, G. W., "Structure Property Correlations for TiB_2-Based Ceramics Densified Using Active Liquid Metals," Science of Hard Materials, (1983), 891– 909.

2. Ferber,M. K., Becher, P. F. and Finch, C. B., "Effect of microstructure on the properties of TiB_2 ceramics." Journal of the American Ceramic Society, 66(1)1983, 1–4.

3. Morz, C. and Titanium, D., American Ceramic Society Bulletin, 74(6)1995, 158– 159.

4. Martin, C., Cales, B., Viver, P. and Mathieu, P., "Electrical discharge machinable ceramic composites." Materials Science and Engineering, 109(1989), 351– 356.

5. Samsonov, G. V., Hagenmuller, P. and Lundstrom, T., Boron and Refractory Borides, “The Nature of the Chemical Bond in Borides,” V. I. Matkovich. Springer-Verlag, (1977), 19–30.

6. S.H. Lee, K.H. Nam, S.C. Hong, J.J. Lee, “Low temperature deposition of TiB2 by inductively coupled plasma assisted CVD”, Surface and Coatings Technolog, 201(2007) 5211-5215.

7. Y. Gu, Y. Qian, L. Chen, F. Zhou, “A mild solvothermal route to nanocrystalline titanium diboride,” Journal of Alloys and Compounds, 352 (2003), 325–327.

8. A. Calka, D. Oleszak, “Synthesis of TiB2 by electric discharge assisted mechanicalmilling”, Journal of Alloys and Compounds, 440 (2007) 346–348.

9. S.H. Kang, D.J. Kim, “Synthesis of nano-titanium diboride powders by carbothermal reduction”, journal of the european ceramic society, 27 (2007) 715–718.

10. Subramanian C, Murthy T S R C and Suri A K. “Synthesis and consolidation of titanium diboride”. International Journal of Refractory Metals & Hard Materials, 25(4)2007, 345–350.

TMS2016

145th Annual Meeting & Exhibition

SUPPLEMENTAL
PROCEEDINGS

General Poster Session

A NOVEL PROCESS FOR TREATING WITH LOW GRADE ZINC OXIDE ORES IN HYDROMETALLURGY

Aichun Dou

School of material science and engineering, Jiangsu University, Zhengjiang 212013, China

Keywords: zinc oxide ores, Ida^{2-}, leaching, precipitation

Abstract

A novel, hydrometallurgical process for treating with low grade zinc oxide ores was proposed in this paper. It contains three steps of treatment. Firstly, leaching of ores in alkalescent Ida^{2-}-H_2O system (iminodiacetate aqueous solution). Valuable metals such as Zn, Cu, Ni, Pb and Cd in ores will be dissolved in leaching liquor for their complexation with Ida^{2-}, impurities such as Ca, Mg, Si and Fe will not be dissolved. Secondly, precipitation of Zn from leaching liquor by adjusting basicity with CaO. Zn will be precipitated as ZnO in residues for recovery. Thirdly, precipitation of Ca by adjusting acidity with CO_2 in the solution after Zn precipitation. Ca which was accumulated in the second step will be removed as $CaCO_3$ from the solution. The lixiviant will be reclaimed in the solution after Ca precipitation. The reclaimed lixiviant solution can be used for re-leaching of ores. The lixiviant solution had been regenerated for 5 times in the paper. The results showed that the performance of the regenerated lixiviant solution could be compared with the freshly prepared lixiviant solution.

Introduction

Traditional techniques [1-3] of volatilization smelting in pyrometallurgy and sulphuric acid leaching in hydrometallurgy are often used for treating with low grade zinc oxide ores. It is uneconomic for both of the two techniques treating with zinc oxide ores in which the grade of Zn is lower than 15%. Because, lower grade of Zn and higher content impurities in ores can hinder the extraction of Zn, that will cause more consumption during process. Ammonia leaching and alkaline leaching are selective system for Zn extraction by the formation of complexes, and are the more suitable processes for these zinc oxide ores with Zn grade lower than 10%. In ammonia leaching [4-7], NH_3 which serving as the main ligand can complex with Zn^{2+} and convert it into solution. What's more, impurities such as Ca, Mg, Fe and Si can not be dissolved in the system. However, ammonia in the system evaporates easily which causes the environment pollution. Current studies [8,9] about ammonia leaching still focus on utilizing ammonium to substitute part of ammonia to alleviate the environmental problem. In alkaline leaching [10,11], OH^- is used as the main ligand to coordinate with Zn^{2+} for Zn extraction from ores with other impurities. It is a challenge for facilities to resist the corrosion of strong basic system in operation. Moreover, SiO_2 can be dissolved in leaching liquor as silicates under so high concentration of OH^- in the process. In a word, ligands in complex system of these two selectively leaching techniques for Zn extraction are unsuitable.

In order to get some new ligands more appropriate in complex system to leach these low grade zinc oxide ores, some work had been done about ligand selection for complex-leaching valuable metals in hydrometallurgy [12]. The results showed that ligand of iminodiacetate (Ida^{2-}) could be

used for Zn extraction in aqueous solution at pH of 8~11. Agent of iminodiacetic acid (IDA) is environmentally friendly in operation. Compared with the insoluble compounds (solid phase) of valuable metal of Zn and impurities in ores, ligand of Ida^{2-} has strong complexation with Zn^{2+}, and has weak complexation with Ca^{2+}, Mg^{2+}, Fe^{2+}, Fe^{3+} and Si^{4+}. This can ensure the separation of Zn from impurities in ores.

Process characteristics

Materials

Zinc oxide ore used in the present study was from Lanping town, Yunnan Province of china. After being crashed and ground, more than 95% of the ore particle has a size less than 150μm, and the corresponding major components and mineralogical compositions are listed in Table Ⅰ and Table Ⅱ respectively. The tables show that the ore has a low zinc content with major phase of smithsonite ($ZnCO_3$ 93.09% in non-sulphide zinc), a high content of gangue (basic gangue CaO+MgO＞8%, acid gangue SiO_2 46.06%), and 4.84% of Fe content.

Table Ⅰ. Chemical composition of low grade zinc oxide ores (wt. %)

Zn	Pb	Cd	Cu	Fe	CaO	MgO	SiO_2
7.72	1.86	0.084	0.010	4.84	8.02	0.57	46.06

Table Ⅱ. Phase composition of Zn in low grade zinc oxide ores (wt. %)

$ZnCO_3$	ZnS	Other Zn	Total Zn
5.93	1.35	0.44	7.72

Process

Figure 1 shows the flow sheet of treating with low grade zinc oxide ores in Ida^{2-}-H_2O system (imimodiacetate aqueous solution). There are three steps in the process.

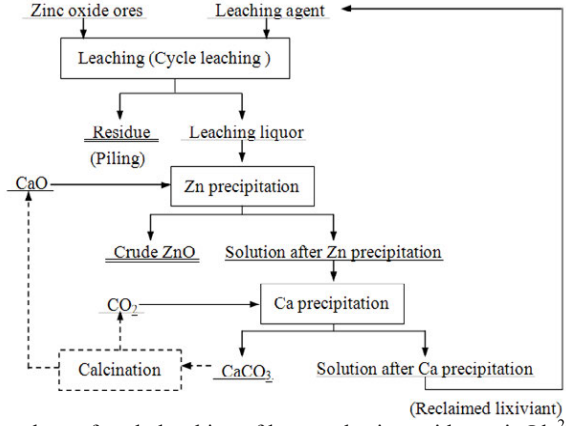

Figure 1. Flow sheet of cycle leaching of low grade zinc oxide ore in Ida^{2-}-H_2O system

Leaching (cycle leaching) In this step, minerals of zinc except zinc sulphide ores in the materials can be dissolved in Ida^{2-}-H_2O system. Zn^{2+} can be combined with Ida^{2-} as $Zn(Ida)_2^{2-}$ in the leaching solution. Associated metals such as Cu, Ni, Pb and Cd can be partly dissolved with main metal Zn in the solution, while impurities such as Ca, Mg, Fe and Si can not be. Scale in this step is 200g ores for each times of leaching. The operation conditions are given as follows, liquid to solid ratio (L/S) 5:1, total concentration of Ida^{2-} ($[Ida^{2-}]_T$) 1.0 $mol \cdot L^{-1}$, temperature 70℃, pH value 8 and leaching time 4h. Related reactions in leaching step are listed as Eqs. (1) and (2).

$$ZnCO_3 + 2\ Ida^{2-} = Zn(Ida)_2^{2-} + CO_3^{2-} \quad (1)$$

$$MeO + j\ Ida^{2-} + H_2O = Me(Ida)_j^{2-2j} + 2\ OH^- \quad (2)$$

In Eqs. (2), elements of Me mean Cu, Ni, Pb and Cd, while number j means the coordination number. After solid-liquid separation, leach liquor need to precipitate Zn for recovery in next step.

Zn precipitation The aim of this step is to recover Zn from leach liquor. Thermodynamic Works about Zn precipitation in Zn^{2+}-Ida^{2-}-CO_3^{2-}-H_2O system had been done [13]. The results presented in figure 3. Figure 3 indicated two ways for Zn precipitation. In lower pH value, Zn^{2+} could be precipitated as $ZnCO_3$. It seems that $ZnCO_3$ can be obtained from leach liquor by adjusting acidity till the pH value bellow 7. Unfortunately, experiments showed that newly generated $ZnCO_3$ was dissolved rapidly in acidic condition.

In higher pH value, there is another way for Zn precipitation. Zn^{2+} could be precipitated as ZnO by adjusting the alkalinity above the pH value 11. Experiments for Zn precipitation in higher pH value had been done. NaOH and CaO were used respectively for adjusting alkalinity to pH 11 in leach liquor at 25℃. Sediments were confirmed as ZnO by x-ray diffraction (figure 3) .

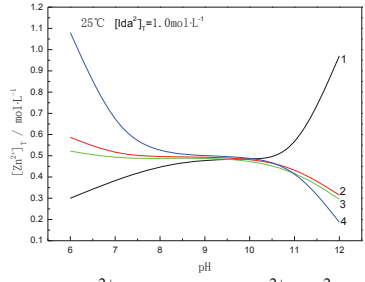

Figure 2. Variation of $[Zn^{2+}]_T$ with pH in Zn^{2+}-Ida^{2-}-CO_3^{2-}-H_2O system
Solid phase 1-$ZnCO_3$, 2-$Zn_3(OH)_4CO_3 \cdot H_2O$, 3-$Zn_5(OH)_6(CO_3)_2$, 4-ZnO

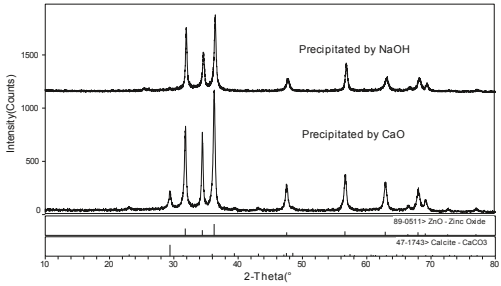

Figure 3. XRD pattern of sediments

In this step, CaO were taken for adjusting alkalinity to precipitate Zn. Otherwise, Na^+ accumulated was difficult to remove from aqueous solution while using of NaOH. Scale in this step is 1000mL leach liquor per time. The operation conditions are given as follows, temperature 85℃, final pH 10 and aging time 0.5h. probable reactions are listed in Eqs. (3) to (5). Significantly, $CaCO_3$ can not be dissolved in leach liquor, $Ca(OH)_2$ can be dissolved normally. After solid-liquid separation, solution after Zn precipitation needs to precipitate Ca for the regeneration of the lixiviant.

$$CaO + H_2O = Ca(OH)_2 \tag{3}$$

$$Ca(OH)_2 + CO_3^{2-} = CaCO_3\downarrow + 2\ OH^- \tag{4}$$

$$Zn(Ida)_2^{2-} + Ca(OH)_2 = ZnO\downarrow + Ca(Ida)_2^{2-} + H_2O \tag{5}$$

Ca precipitation In this step, pure gas of CO_2 are used for removing Ca^{2+} which was accumulated in Zn precipitation step. As the injection of CO_2 to the solution, Ca^{2+} was precipitated as $CaCO_3$, $Ca(Ida)_2^{2-}$ released most of the free Ida^{2-}, while the pH value of the system decreased into one stable area which was suitable for leaching. Thus, the lixiviant could be regenerated. Scale in this step is 1000mL solution per time. Operation conditions are given as follows, temperature 70℃, final pH value 8 and the gas flow rate of CO_2 0.2 L/min. The principal reaction is listed in Eqs. (6). Significantly, solution after Ca precipitation was used directly for releaching ores without any addition of fresh lixiviant and any adjusting of pH. In this paper, experiments in number C-1~C-5 in which the lixiviant was all regenerated, Only experiments in number C-0 were fresh lixiviant in the system.

$$Ca(Ida)_2^{2-} + CO_2 + H_2O = CaCO_3\downarrow + 2\ H^+ + 2\ Ida^{2-} \tag{6}$$

Analysis

The element contents in residues were determined with X-ray fluorescence (XRF). High concentration of Zn in aqueous solution was analyzed by titration with EDTA volumetric method, low content of Zn and impurities in aqueous solution was detected with ICP-AES. Significantly,

The contents of metals in different volume of each aqueous sample were calculated in a uniform volume of 1000mL for comparison.

Results and discussion

Lixiviant was regenerated when the fresh lixiviant had been done under the following steps of leaching, Zn precipitation and Ca precipitation. These three steps were a batch of initial treatment, and experiments in this batch of treatment were all numbered as C-0 in each step. When the regenerated lixiviant was used for releaching, and was also done under the following steps of leaching, Zn precipitation and Ca precipitation, these three steps were a batch of cycle. The regenerated lixiviant was cycled for one time. Experiments in this batch of cycle were all numbered as C-1 in each step. After C-1 cycle, the lixiviant was regenerated again, and began one more bath of cycle. The regenerated lixiviant was cycled for two times. Experiments in this batch of cycle were all numbered as C-2 in each step. The regenerated lixiviant was cycled for five times in this work, and experiments from the first cycle to the last cycle were numbered as C-1 to C-5.

Cycle leaching

The regenerated lixiviant was cycled for five times. leaching recovery of Zn in each bath of cycle are shown in Figure 4. Elemental compositions in leaching liquor for each cycle are listed in Table Ⅲ.

It can be seen from Figure 4 that the leaching recovery of Zn had a stable change during each cycle of leaching. The leaching recovery of Zn for raw ores is 76.90%, and for nonsulfide ores is 93.8%, on average. The results indicate that the leaching capacity of Zn for the regenerated lixiviant can be comparable with the fresh lixiviant.

It seems that impurities in leaching liquor increased a slightly for every cycle. It means impurities accumulated in leaching liquor, which could effect on the leaching result of Zn. But the truth is the accumulated impurities can not effect on the leaching result of Zn. Impurities such Ca, Mg, Fe and Si can not be dissolved massively, and have their own limit value of dissolution in leaching system. Impurities such as Cu, Ni, Pb and Cd are associated metals, it is useful for their enrichment by accumulating in leaching liquor. The reason why they did not deposit in Zn precipitation step is due to the low concentration in the solution.

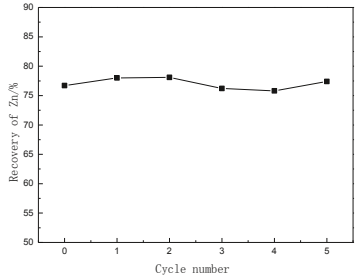

Figure 4. Leaching recovery of Zn in each cycle for leaching

Table Ⅲ. Elemental composition in leaching liquor ($mg \cdot L^{-1}$)

No.	Zn	Ca	Mg	Fe	Cu	Ni	Pb	Cd	Si
C-0	11707	583.18	8.88	64.29	7.77	0.11	1427.08	141.93	69.67
C-1	12670	0	0.72	0	11.16	0	163.56	104.64	112.32
C-2	12540	27.08	1.80	44.16	18.12	2.00	357.72	121.52	18.00
C-3	12420	175.04	5.88	51.80	20.16	2.72	634.88	201.48	10.24
C-4	12420	358.16	8.52	58.28	23.24	3.44	915.96	268.96	12.96
C-5	12860	416.70	8.46	60.53	25.78	2.62	1337.18	313.22	18.97

Zn precipitation

The precipitation ratio of Zn in every cycle was given in Figure 5, and the elemental composition of the solution after Zn precipitation was list in Table Ⅳ. Figure 5 showed that the precipitation ratio of Zn from leaching liquor decreased slightly from C-1~C-5 cycle. It may be caused by associate metals accumulated in leaching liquor which can also partly deposit with Zn in this step, and can also consume ion of OH^-. But, it can be seen that the precipitation ratio of Zn is still as 93.01% on average.

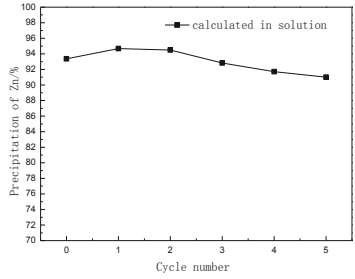

Figure 5. Precipitation ratio of Zn from leaching liquor in every cycle

According to Table Ⅲ and Table Ⅳ, it can be seen that not only associated metals, but also impurities of Mg and Fe can deposit with Zn. Impurity of Ca was concentrated after Zn precipitation. It is caused by the dissolution of CaO in this step. Impurity of Si was also concentrated. It may be caused by impurity in CaO. The crude ZnO obtained in this step contains Zn 60.07% and Pb 3.84% on average.

Table Ⅳ. Elemental composition of solution after Zn precipitation ($mg \cdot L^{-1}$)

No.	Zn	Ca	Mg	Fe	Cu	Ni	Pb	Cd	Si
C-0	776	4893.08	5.84	0	4.84	0	482.04	49.16	769.44
C-1	675	7012.44	0.52	0	8.96	0	162.76	44.60	100.92
C-2	690	8177.60	1.12	0	12.68	1.44	57.52	104.04	146.76
C-3	892	8458.88	2.92	0	16.72	2.08	271.16	201.04	45.80
C-4	1030	8383.04	4.08	0	21.92	2.28	596.76	283.64	32.12
C-5	1157	9557.44	3.96	0	24.68	2.36	796.88	314.08	25.64

Ca precipitation

The precipitation ratio of Ca from solution after Zn precipitation was showed in Figure 6, and the elemental composition of solution after Ca precipitation was listed in Table Ⅴ. Figure 6 showed that the precipitation ratio of Ca kept stable in cycle. The precipitation ratio of Ca is 94.91% on average. It means most of the free ligand of Ida^{2-} was released during this step, which is the guarantee for the regenerated lixiviant keeping its activity.

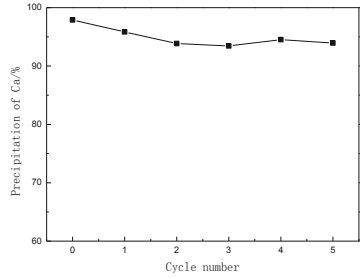

Figure 6. Precipitation ratio of Ca from solution after Zn precipitation in every cycle

According to Table Ⅳ and Table Ⅴ, all of the impurities include Zn had a decrease of concentration. It is caused by adsorption of $CaCO_3$. Compared Table Ⅴ with Table Ⅲ, it can be seen that the concentration of Ca had a decrease in next cycle after leaching. It indicates the remained ion Ca^{2+} in last cycle can react with ion CO_3^{2-} which was introduced by the dissolution of $ZnCO_3$ in leaching step of the next cycle. This reaction can promote the dissolution of Zn.

Table Ⅴ. Elemental composition of solution after Ca precipitation ($mg \cdot L^{-1}$)

No.	Zn	Ca	Mg	Fe	Cu	Ni	Pb	Cd	Si
C-0	623	103.76	0	0	4.12	0	275.12	41.36	100.16
C-1	478	291.12	0	0	8.16	0	104.76	43.60	18.88
C-2	654	503.60	0	0	12.60	1.80	66.24	97.36	0.12
C-3	713	553.84	2.12	0	15.84	2.00	225.48	180.32	0
C-4	910	459.28	3.60	0	20.08	2.56	566.60	266.68	18.36
C-5	963	579.84	3.84	0	23.88	2.68	868.40	309.76	8.04

Conclusions

In this process, Ida^{2-}-H_2O system was used to treat with low grade zinc oxide ores. Lixiviant was regenerated when the fresh lixiviant had been done under the following steps of leaching, Zn precipitation and Ca precipitation. Lixiviant can recycle several times under regeneration for releaching directly without any addition of fresh lixiviant and any adjusting of pH. The results showed that leaching recovery of Zn kept all above 75% while regenerated lixiviant cycled for 5 times.

Acknowledgement

The author appreciates professor YANG Tianzu for his help in this work. The project was supported by the Natural Science Foundation of Jiangsu Province (BK20140558) and the Advanced Foundation of Jiangsu University (13JDG097).

References

1. SOUZA A D, PINA P S, SANTOS F M F, DA SILVA C A, LEÃO V A. Effect of iron in zinc silicate concentrate on leaching with sulphuric acid[J]. Hydrometallurgy, 2009,95(3-4):207-214.
2. QIN Wen-qing, LI Wei-zhong, LAN Zhuo-yue. Simulated small-scale pilot plant heap leaching of low-grade oxide zinc ore with integrated selective extraction of zinc[J]. Minerals Engineering, 2007,20(7): 694–700.
3. LI Cun-xiong, XU Hong-sheng, DENG Zhi-gan, LI Xing-bin, LI Ming-tin, WEI Chang. Pressure leaching of zinc silicate ore in sulfuric acid medium[J]. Trans. Nonferrous Met. Soc. China, 2010,20(5): 918-923.
4. JU Shao-hua, TANG Mo-tang, YANG Sheng-hai. Dissolution kinetics of smithsonite ore in ammonium chloride solution[J]. Hydrometallurgy, 2005,80(1-2): 67-74.
5. YIN Zhou-lan, DING Zhi-ying, HU Hui-ping, LIU Kui, CHEN Qi-yuan. Dissolution of zinc silicate (hemimorphite) with ammonia-ammonium chloride solution[J]. Hydrometallurgy, 2010,103(1-4):215-220.
6. YIN Zhou-lan, DING Zhi-ying, HU Hui-ping, CHEN Qi-yuan. Dissolution kinetics of zinc silicate (hemimorphite) in ammoniacal solution[J]. Hydrometallurgy, 2010,104(2):201-206.
7. WANG Rui-xiang, TANG Mo-tang, YANG Sheng-hai, ZHANG Wen-hai, TANG Chao-bo, HE Jing, YANG Jian-guang. Leaching kinetics of low grade zinc oxide ore in NH_3-NH_4Cl-H_2O system[J]. J. Cent. South Univ. Technol, 2008,15(5):679-683.
8. XIA Zhi-mei, YANG Sheng-hai, TANG Mo-tang, YANG Tian-zu, LIU Zhi-hong, TANG Chao-bo, HE Jing, DENG Xiao-ling. Cycle leaching of low grade zinc oxide ores in MACA system for preparing zinc[J]. The Chinese Journal of Nonferrous Metals, 2013,23(12):3455-3461.
9. TANG Mo-tang, ZHANG Jia-liang, WANG Bo, YANG Sheng-hai, HE Jing, TANG Chao-bo, YANG Jian-guang. Cycle leaching of low grade zinc oxide ores in MACA system[J]. The Chinese Journal of Nonferrous Metals, 2011,21(1):214-219.
10. ZHANG Yu-cheng, DENG Jin-xia, CHEN Jun, YU Ran-bo, XING Xian-ran. A low-cost and large-scale synthesis of nano-zinc oxide from smithsonite[J]. Inorganic Chemistry Communication, 2014,43(5):138-141.
11. CHEN Bing, SHEN Xiao-yi, GU Hui-min, SUN Yi, LI De-guan, ZHAI Yu-chun, MA Pei-hua. Extraction of ZnO from zinc oxide ore by alkali roasting method[J]. CIESC Journal, 2012,63(2):658-661.
12. YANG Tian-zu, DOU Ai-chun, LEI Cun-mao, REN Jin, LIU Zhen-zhen. Ligand selection for complex-leaching valuable metals in hydrometallurgy[J]. Trans. Nonferrous Met. Soc. China, 2010,20(6): 1148-1153.
13. DOU Ai-chun, YANG Tian-zu, WU Jiang-hua, ZHANG Du-chao, YANG Ji-xing, WANG An. Recovery of zinc and regeneration of lixiviant from Zn^{2+}-Ida^{2-}-CO_3^{2-}-H_2O system[J]. The Chinese Journal of Nonferrous Metals, 2011,21(12): 3218-3225.

A STUDY OF TAGUCHI METHOD TO OPTIMIZE 6XXX SERIES ALUMINIUM ANODIC OXIDE FILM'S HARDNESS AND INVESTIGATION OF CORROSION BEHAVIORS OF OXIDE FILMS

B.D. Polat, B. Bilici, P. Afşin, C. Akyil, O.Keles*

*Department of Metallurgical and Materials Engineering, Istanbul Technical University, Istanbul 34469, Turkey, Tel:0090 212 2853398, Fax:0090 212 285 3427, E-mail:ozgulkeles@itu.edu.tr

Keywords: Aluminum anodic oxide film, Microhardness, Corrosion potential, Design of experiment.

Abstract

This study is intended to present an efficient methodology for optimizing the anodic polarization process of 6xxx aluminum alloy to have high hardness. Additional electrochemical experiments have been conducted to observe the corrosion behavior of these oxide films. L_9orthogonal array with four factors at three levelsareused. The type of additive, electrolyte temperature, current density and dissolved aluminum ions are chosen as parameters. The results show that the main parameters to increase the hardness of the oxide films are electrolyte temperature, additive type, dissolved aluminum ions and current density, respectively.
After anodization, the pores of the oxide film are sealed and their surface morphologies are observed by using scanning electron microscopy. Then, the corrosion potentials of these oxide films are measured to define their electrochemical behaviors to evaluate their possible uses in advanced technology.

Introduction

Aluminum and its alloys have been used intensively in automotive, building, defense, transportation, electronic, aerospace, and space industry due to their high specific strength, electrical conductivity and compatibility to versatile production techniques in highly complex shapes. One of the distinguished properties of aluminum and its alloys is to have a functional surface oxide film. The film structure and morphology are affected by the composition of the aluminum, surface properties, bath concentration, current density, stirring rate, distance between anode and cathode, current feeding style and voltage, etc.
In anodization process (aluminum anodic oxide (AAO) film formation) baths containing sulphuric [1], chromic [2], oxalic [3], phosphoric [4] and sulphamic acids [5], etc could be utilized. Among these baths [6-8], sulphuric acid containing baths are preferred because it allows operating the bath in low temperature and moderate potential to provide small pore diameters.
In aluminum anodization, water molecules are reduced to hydroxyl ions and oxidize the solvated aluminum ions. At the beginning, the oxide layer is dense and continuous. This layer is called as barrier layer and it is resistant to corrosion and wear. The growth of this layer ends when cell voltage is reduced due to high electrical resistance. At this stage the oxide layer is nanometer level. The oxide growth proceeds slowly with the dissolution of Al^{+3}. The oxide layer has a honeycomb structure and the dimensions of cell/honeycomb (diameter, wall thickness and length) depend on current density, aluminum composition, bath temperature, stirring rate, bath

composition, distance between anode and cathode, process duration and the types of current flow in the circuit (dc, ac or pulse). Therefore, structure, morphology and eventually thethickness and hardness of the oxide film depend on the cell parameters [9].
In general eloxal coating plants uses sulphuric acid, the potential range is 15-20V, the current density range is 1.2-1.5A/dm^2, the temperature range is 20-23 °C and the bath sulphuric acid concentration is 3.5mole/l.
In this study, different additives are used and process parameters (bath temperature, current density and dissolved aluminum concentration) are optimized using Taguchi methods [10]to improve the hardness of anodic oxide layer at room and higher operating temperatures. Plus the changes in the corrosion behaviors of these oxide film after the sealing process are measured to to evaluate their possible uses in advanced technology.

Experimental Design

In the anodic oxidation experiments 6060 aluminum sheetwith 2 mm in thickness is used as anodes and cathodes. The chemical composition of the aluminum sheet is made by utilizing optical emission spectroscopy (ARL 3460). The results are given in Table I. The oil on the surface of the sheet is removed and the etching is made at 63°C for 15minutes. The rinsing processes are done in three stages by dipping into first 45°C and then 21°C baths. Neutralization is conducted at 21°C for 5 minutes. Then, anodization experiments are made by following Taguchi's L9 design. In Table II the parameters and their levels are given. After the anodization the samples are rinsed at 21°C and sealing is conducted at 98.5±1°C for 85 minutes.
Various amount of dissolved aluminum containing sulphuric acid baths are utilized. It is known that commercial additives (WM80L) contains weak organic acids with metal salts and the other (EK57) is made of organics to perform the anodization at high temperatures.

TableI.Chemical composition of the alloys (wt%)

	Si	Fe	Cu	Mn	Mg	Zn	Ti	Cr	Ni	Pb
Analysis result	0.41	0.18	0.014	0.004	0.48	0.009	0.10	0.0007	0.003	0.001
Standard limits EN 573-3	0.3-0.6	0.10-0.30	0.10	0.10	0.35-0.6	0.15	0.10	0.05	-	-

Table II.Anodization parameters and their levels.

Levels	Additivetype	Dissolved Al concentration (g/l)	BathTemperature (°C)	CurrentDensity (A/dm^2)
1.	A (Oxalicacid, 3% vol.)	3	16	1.2
2.	B (EK57, 23g/l)	9	22	1.5
3.	C (WM80L, 20g/l)	15	28	1.9

The anodized samples are prepared metallographically. The optical microscopy images (Nikon ECLIPSE MA200) and anodic layer thicknesses are taken from their cross sections. The Vickers harnesses (Hv0.05) are measured using Future Tech micro hardness tester FM-700. Anodic oxide surface morphology is examined utilizing FEG-SEM (Jeol 7000F).

In order to compare the corrosion behavior of the samples after anodization a series of potentiodynamic polarization measurements are performedin a conventional three-electrode cell using a saturated calomel electrode (SCE) as the reference electrode and a platinum rod as a counter electrode. The measurements are conducted in an area of 1cm^{2}using 3.5%NaCl (vol) solution between -0.75V -1.1 versus Open Circuit Potential (OCP) at a scan rate of 5mV/s.

Results and Discussions

In Table III the hardness and thickness values measured are given. The hardness is ranged in between 384-427 ±10 Hv. The oxide layer thicknesses are in the range of 15-28 ±2 µm.

Table III. Taguchi L9 matrix and hardness and thickness values gathered

Parameters				Results	
Additive Type	**BathTemperature (°C)**	**CurrentDensity (A/dm^2)**	**Dissolved Al Conc (g/l)**	**Hardness $Hv_{0.05}$**	**Thickness µm**
1	1	1	1	384	15
1	2	2	2	422	21
1	3	3	3	375	28
2	1	2	3	408	16
2	2	3	1	424	28
2	3	1	2	391	17
3	1	3	2	427	21
3	2	1	3	418	19
3	3	2	1	385	22

The hardness and thickness results are analyzed using “larger is better” approach and given in Table IV.

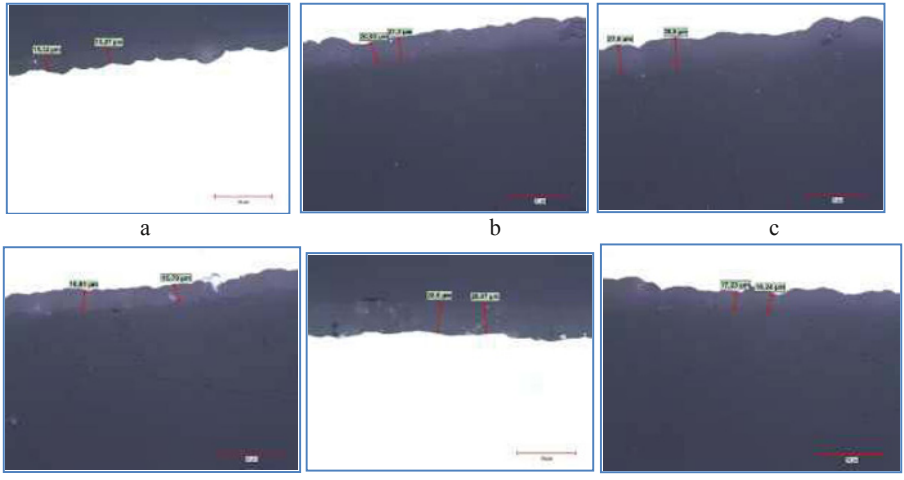

a b c

Figure 1.Metallographic cross sections of the anodized samples. a.Sample 1, b.Sample2, c.Sample3, d.Sample 4, e.Sample 5, f.Sample6, g.Sample7, h.Sample8 , ı.Sample9.
As seen in Figure 1, the anodic layer in all the samples are fairly homogenous in thicknesses.

Table IV**.** Main effect results of hardness and thickness values.

Analyses results for hardness				
Level	**Additive type**	**Bath temperature(°C)**	**Current Density (A/dm^2)**	**Dissolved Al conc.(g/l)**
1	393.7	406.3	397.7	397.7
2	407.7	421.3	405.0	413.3
3	410	383.7	408.7	400.3
Range	16.3	37.7	11	15.7
Analyses results for thickness				
Level	**Additive type**	**Bath temperature (°C)**	**Current Density (A/dm^2)**	**Dissolved Al conc.(g/l)**
1	21.42	17.33	16.85	21.55
2	20.18	22.72	19.80	19.77
3	20.80	22.35	25.75	21.08
Aralık	1.23	5.38	8.9	1.78

In Figure 2, main effect plots are given for the mean values of hardness and thickness.

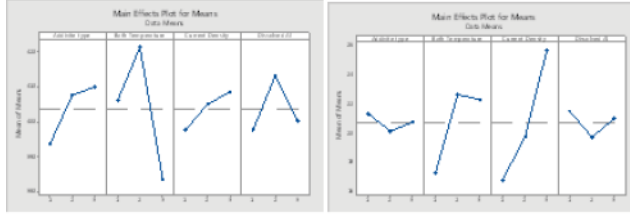

Figure 2.The effects of parameters on **a.**Hardness **b.**Thickness

In Table IV and Figure 2, the most effective parameters on the anodic oxide layer in turn is bath temperature, additive types, the amount of dissolved aluminum and current density. In literature, the main parameters that affect the hardness are bath composition, bath temperature and current density. Jeon and Chung [11] have found that when bath temperature rises the hardness of the

anodic layer decreases and the hardness is higher in cases of 2.5% oxalic acid containing sulphuric acid baths.
Aertset. al [12] have studied 1050 aluminum alloy in sulphuric acid bath for 20 µm anodic layer thickness at potentsiostatic conditions and a constant voltage of 17V with increasing bath temperature from 5 to 55°C.They have found that the pore morphology of the film and eventually the hardness of the films have differed from 450Hv to 175Hv.
In this study, different than classical experimental design approach Taguchi L9 design is used. In Taguchi L9 design it is possible to investigate the effect of 4 parameters with three levels by making 9 experiments. It is known that there are some interactions among the parameters used but for this design the interactions are omitted.
Results show that commercial additives have a strong and positive effect on the hardness of the anodic layer. Especially, at industrial operating conditions hardness is found to be the highest value. However, with increasing bath temperature the hardness decreases. It is worth to note that there is a relation between film thickness and hardness with increasing current density. In the same current density film thickness as well as its hardness increases. As the solution ages, it is expected that the film thickness and hardness decrease but due to the effect of additives on the physical and chemical properties of the film first an increasing then decreasing effect on the film thickness is observed. In the study, the highest hardness value is gathered when the dissolved Al concentration is 9g/l.
The organic acids and salts in commercial additives are affective in the dissolution kinetics. It is known that these additives are developed for operating eloxal baths at high temperatures and providing the same quality. In this study, although the hardness of the film (384Hv) decreases at 28 °C this reduction is very small. The film thicknesses are increased with increasing bath temperatures.
In this study, Taguchi analyses results on the hardness and thickness of anodic oxide film shows that at 22°C, using 1.9A/dm^2 current density and with 9g/l dissolved aluminum it is possible to have the highest hardness. The calculated hardness and thickness values are 439 ±15Hv and 26±2µm, respectively. To verify the results a control experiment is done by using the optimum levels of the parameters. The film is shown in Figure 3. The thickness and the hardness of the film are measured to be 29±2µm and 425±15Hv respectively. As seen the calculated and measured values are close and the difference is statically acceptable.

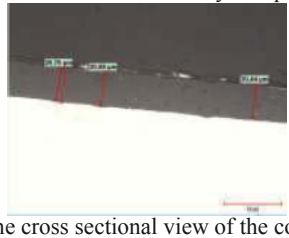

Figure 3. The cross sectional view of the control sample.

In Figure 4 the surface morphology of the anodic oxide by FEG SEM images are given. When especially high magnification of the surface morphologies are examined significant morphology changes are seen. The effect of additive types are very significant in these differences. In Figure 4a-c the effect of oxalic acid, in 4d-f the effect of EK57 and in 4g-ı the effect of WM80L are shown. In all three groups depending on current density, dissolved Al quantity and bath temperature the morphologies change. Especially, with an increase in the bath temperature pore

widens and in case of WM80L this result is very significant. It is worth to note that the effect of sealing process on the anodic oxide film structure and morphology is under discussion. In general the effect of sealing process is to fill the pores with hot water to increase the corrosion resistance. Early studies in literature have shown that after sealing process at near the top of the film hydrated oxides could form (pseudo bohmite and/or bohmite) when amorphous film reacts with hot water. However, the last studies show that sealing process is effective throughout pore lengths [13-14].

As surface morphologies are examined, it is seen that the additives have strong effect on the structure and morphologies of the pores and as a result after the sealing the structure of hydrates differ. These structural changes are assumed to influence the optical, tribological and corrosion properties of the films.

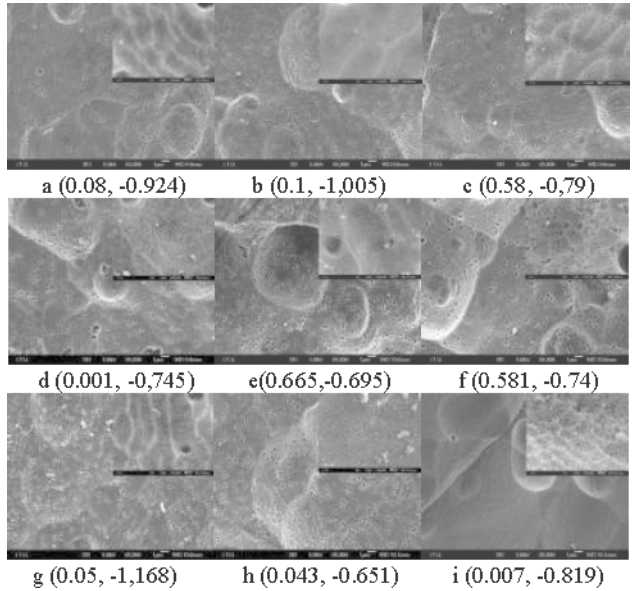

Figure 4.The surface morphologies of the samples; a.Sample 1,b. Sample 2, c.Sample 3, d.Sample 4, e. Sample 5, f. Sample 6, g. Sample 7, h. Sample 8, i. Sample 9

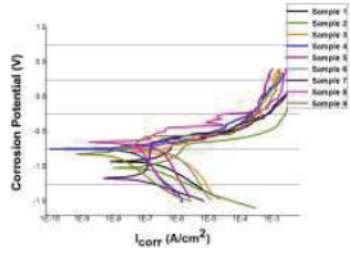

Figure 5. Potentiostatic test results of all samples

Table V. The corrosion potentials and current densities.

Sample	Icorr x10^{-7} (A/cm^2)	Ecorr (V)
1	0.08	-0.924
2	0.1	-1.005
3	0.58	-0.79
4	0.001	-0.745
5	0.665	-0.695
6	0.581	-0.74
7	0.05	-1.168
8	0.043	-0.651
9	0.007	-0.819

Although advanced surface characterization is needed for further discussion, there are considerable differences in the corrosion current densitiesand potentials of the anodized samples. The corrosion potentials of the anodized samples are in between -1168mV and -651mV which shows that the corrosion behaviors of samples changes depending on the properties of the oxide film (the pore distribution, geometry and structure).

Conclusions

In this study, Taguchi L9 experimental design is chosen and 4 parameters (additive types, current density, bath temperature, dissolve Al) in 3 levels are investigated in 9 experiments.

- Anodized layer hardnesses and thicknesses are found to be in ranges of 384-427 ±10 $H_v$and15-28±2 μm.
    - The most important parameters on the hardness of the layer is determined to be the bath temperature then additive type, dissolved aluminum quantity and current density.
    - The effective parameters for the thicknesses of aluminum oxide layer are in turn, current density, dissolved Al quantity, bath temperature and additive types.
- The results are verified at 22°C, applying 1.9 A/dm^{2}current density and in a bath containing 9g/l dissolved Al by using Ek57. The calculated and measured results are found to be 439 ±15Hvand 425±15 Hv respectively.Tor the same parameters and their levels the thicknesses calculated and measured are 26±2μm and 29±2μm respectively.
- The morphologies after sealing process additives and bath temperatures effects the pore morphologies as well as corrosion potentials of the anodic oxide films.

Acknowledgement

The authors are gratefully acknowledged Asaş Aluminum San. ve Tic. A.Ş. for their support in providing aluminum alloys and Prof. Dr. Mustafa Ürgen, and Prof. Dr. Gültekin Göller and HüseyinSezer for their support in characterization studies.

References

1. V.P. Parkhutik, J.M. Albella, Yu.E. Makushoka, I. Montero, J.M. Martinez, V.I. Shershulskiia, “Study Of Aluminium Anodization In Sulphuric And Chromic Acid

Solutions—I. Kinetics Of Growth And Composition Of Oxides," *Electrochim Acta*, 35 (6) (1990), 955–960.
2. R. W. Buzzard, "Anodizing Of Aluminum Alloys in Chromic Acid Solutions Of Different Concentrations", *Journal of Research of The National Bureau of Standards*, 18 (1937), 251-257.
3. C.K. Chung, T. Y. Liu , W. T. Chang, "Effect Of Oxalic Acid Concentration On The Formation Of Anodic Aluminum Oxide Using Pulse Anodization At Room Temperature, " *MicrosystTechnol* , 16 (2010),1451–1456.
4. A. Vaillancourt , T. Abele, "Adhesive Technology: Surface Preparation Techniques on Aluminum,"https://www.wpi.edu/Pubs/E-project/Available/E-project-031609-134903/unrestricted/Henkel_Final_MQP.pdfsy, (date: 13.09.15)
5. D. Kanagaraj, V.L. Narasihmhan, S. V. Iyer, "Anodising of Aluminum in Sulphamic Acid Electrolyte," *Bull Electrochem*, 12 (5) (1996),. 288-290.
6. M. Urgen, O. Keles, B. D. Polat and F. Bayata, "Generation of a Surface Pattern Having Conical Surface Features by Anodic Polarization of Aluminum," *J Electrochem Soc,* 159 (9) (2012), C411-C415.
7. G. E. Thompson, L. Zhang, C. J. E. Smith, and P. Skeldon , "Boric/Sulfuric Acid Anodizing of Aluminum Alloys 2024 and 7075: Film Growth and Corrosion Resistance," *Corrosion,* 55 (11) (1999), 1052-1061.
8. S. Sigamani, PR. Thangavelu, K.N. Srinivasan, M. Selvam, "Studies on Ac Anodizing of Aluminum in Sulfuric Acid Electrolyte Containing Sodium Sulfate," *International Journal of Innovative Research in Science Engineering and Technology*, 3, (6) (2014), 13869-13875.
9. J. Choi, "Fabrication of Monodomain Porous Alumina Using Nanoimprint Lithography And Its Applications, http://sundoc.bibliothek.uni-halle.de/diss-online/04/04H055/t2.pdf, PHD Thesiss, Mathematisch-Naturwissenschaftlich-Technischen Fakultat (2003), 2-12.
10. G. Taguchi, "Taguchi Methods, Japanese Standards Association, " *Quality Engineering, 6* (1989), 25-35.
11. S. II Jeon, W. S. Chung, "An Influence of Current Density and Temperature About Anodic Oxidation Film Properties of Al-Die Casting," *Adv Sci Technol Lett,* 64 (2014), 4-8.
12. T. Aerts, T. Dimogerontakis , I. D. Graeve , J. Fransaer , H. Terryn, "Influence Of The Anodizing Temperature On The Porosity And The Mechanical Properties Of The Porous Anodic Oxide Film," *Surf. Coat. Technol*, 201 (2007), 7310–7317.
13. G.C. Wood, J.P. Sullivan, "Electron-Optical Examination of Sealed Anodic Alumina Films: Surface and Interior Effects," *J Electrochem Soc*, 116 (10) (1969), 1351-1357.
14. S.Feliu, M.J. Barolome, J.A. Gonzalez, S. Feliu, "XPS Characterization of Porous and Sealed Anodic Films on Aluminum Alloys," *J Electrochim Soc*, 154 (5) (2007), C241-C248.

ANTICORROSION PERFORMANCE OF *SOLANUM AETHIOPICUM* ON STEEL-REINFORCEMENT IN CONCRETE IMMERSED IN INDUSTRIAL/MICROBIAL SIMULATING-ENVIRONMENT

Joshua Olusegun OKENIYI[1], Olugbenga Adeshola OMOTOSHO[1], Elizabeth Toyin OKENIYI[2], Adebanji Samuel OGBIYE [3]

[1]Mechanical Engineering Department, Covenant University, Ota 112001, Nigeria
[2] Petroleum Engineering Department, Covenant University, Ota 112001, Nigeria
[3]Civil Engineering Department, Covenant University, Ota 112001, Nigeria

Keywords: steel-reinforcement corrosion, *Solanum aethiopicum* leaf-extract, eco-friendly inhibitor; statistical distribution analyses, corrosion risk modelling, inhibition efficiency.

Abstract

This paper investigates anticorrosion performance of *Solanum aethiopicum* leaf-extract on steel-reinforcement in concrete immersed in 0.5 M H_2SO_4, simulating industrial/microbial environment. For this, corrosion rate by linear polarisation resistance and corrosion potential as per ASTM C876-91 R99 were monitored from steel-reinforced concrete slabs admixed with different *Solanum aethiopicum* leaf-extract concentrations and immersed in the acidic test-environment. Obtained test-data were subjected to statistical probability distributions for which compatibilities were tested using Kolmogorov-Smirnov goodness-of-fit statistics, as per ASTM G16-95 R04. These identified all datasets of corrosion test-data, from the steel-reinforced concrete samples, as coming from the Weibull probability distribution. Analysed results showed that *Solanum aethiopicum* leaf-extract reduced rebar corrosion condition from "high" to "low" corrosion risks of ASTM C876-91 R99. Also, the corrosion rate analyses identified 0.25% *Solanum aethiopicum* leaf-extract with optimal inhibition efficiency performance, η = 93.99%, while the other concentrations also exhibited good inhibition of steel-reinforcement corrosion in the test-environment.

Introduction

Steel-rebar in concrete corrodes due to aggressive attacks that result in its metallic dissolution by environmental agents present in its service-environments [1-3]. Since reinforced concrete is the most widely used construction materials globally [4-5], corrosion of concrete steel-rebar is ubiquitous and it is the major factor affecting sustainable usage and durability of steel-reinforced concrete material. Concrete steel reinforcement corrosion instigates premature failure of steel-reinforced concrete structures and infrastructures. And because these include domiciliary and commercial buildings, bridges, harbour, pavements, tunnels, sewage conduits and tanks, averting insidious but catastrophic failure that could result from unabated concrete steel-reinforcement corrosion culminates in costly budgets worldwide [3,6-8].

Environmental agents in steel-reinforced concrete service-environments leading to corrosion of reinforcing steel embedded in the concrete include acidic sulphate in the form of sulphuric acid (H_2SO_4) from acid rain in industrial or sulphate reducing bioactivities in microbial environments [3,6,8-9]. In industrial environments, SO_2 effluents react with atmospheric water vapour to form sulphuric acid rain as end product [10-12]. In microbial environments, biogenic sulphate reducing (the anaerobic), e.g. *Desulfovibrio sp.*, and sulphide oxidising, e.g. *Thiobacilli sp.*, (the aerobic) bacteria combine actions on sulphur compounds in sewage or underground environments to also form, as end product, sulphuric acid [9,13-16]. The sulphuric acid thus formed attacks concrete cementious materials, forming structurally weak but volume expansive gypsum and ettringite ($3CaO{\cdot}Al_2O_3{\cdot}CaSO_4{\cdot}12H_2O$ or $3CaO{\cdot}Al_2O_3{\cdot}3CaSO_4{\cdot}31H_2O$), and renders

the steel-rebar susceptible to accelerated corrosion by acidic dissolution [16-18]. Resultant weakening of concrete and thinning of its steel-rebar by acidic sulphate corrosion reduce load-bearing strength of structural members and make in-service failure of the steel-reinforced concrete structure inevitable with attendant safety risks to life and loss of property [15-16,19-20]. Many methods have been identified in studies for tackling the problem of acidic sulphate induced corrosion of steel-reinforced concrete in industrial/microbial environments. Some of these that had been identified in studies include use acid-resistant cement or cementious materials (e.g. pozzolans), antimicrobial coatings, biocides, cathodic protection and corrosion inhibitor admixture in concrete [10,12,16,21-23]. While many of these methods exhibit specific advantages and disadvantages, the use of corrosion inhibitors has been identified as an easily applicable and economical technique but that usually require use of electrochemical method for ascertaining inhibition effectiveness [4,10,22,24-25]. Also, that many inhibitors exhibiting high effectiveness on steel-reinforcement corrosion are toxic and environmentally-hazardous, making their usage subject to regulatory scrutiny/restrictions, is shifting research interests towards search for eco-friendly corrosion inhibiting materials [26-28]. For these, it had been recognised that extract from plants are non-toxic sources of useful of bio-organic chemicals exhibiting N–, S–, O– heteroatoms [26-27] with π-electrons that are known to effectively inhibit metallic corrosion in aggressive environments [6,25,28].

That African egg plant, *Solanum aethiopicum* (*S. aethiopicum*) *Solanaceae*, is constituted of edible parts which includes its roots, stems, fruits and leaves that could be eaten raw/cooked as vegetable/traditional medicine in regions of Africa has been detailed in recently reported work [28]. This and report of biocompatible phyto-constituent found in parts of this natural plant that have been elucidated in studies [29-31] indicate no part of *S. aethiopicum* is expected to be toxic. In addition, leaf-extract from *S. aethiopicum* exhibited performance in [29] that reduced probability of corrosion risk as per ASTM C876-91 R99 [32] and reduced corrosion rate to the extent of outperforming the also highly effective $Na_2Cr_2O_7$ well-know but toxic chemical inhibitor. However, it is worth noting that the excellent corrosion inhibition effects by *S. aethiopicum* leaf-extract reported in [29] was on steel-reinforcement in concrete immersed in 3.5% NaCl, for simulating saline/marine environment. No study has deliberated on the possibility of using extract from *S. aethiopicum* as inhibitor of concrete steel-reinforcement corrosion in acidic sulphate medium, whereas it is well known that corrosion inhibitor effectiveness could be material and/or corrosive medium dependent [7,20,33-34]. This requires that, even for the same metal/material, a substance that had been tested to inhibit corrosion in a corrosive medium need to be tested for corrosion inhibition effect in another, before it could be considered a corrosion inhibitor of the metal/material in that other medium.

These constitute reasons the objective of this study was to investigate anticorrosive performance of *S. aethiopicum* leaf-extract admixture on steel-reinforcement in concrete immersed in 0.5 M H_2SO_4 industrial/microbial simulating-environment.

Experimental Methods

Experimental Materials

Leaf extract was obtained from *S. aethiopicum* as prescribed in [35] and detailed in [29], with the work in [29] also containing report on the collection and identification (with voucher FHI No. 109498 from the Forestry Herbarium Institute, Ibadan, Nigeria) of the fresh leaves of the plant. Also, the *S. aethiopicum* leaf-extract employed in this study was varied from 0.00% (for the control, "Ctrl", sample) in increments of 0.083% to 0.333% (per weight of cement used for concrete casting). Formulation employed for each 100 mm × 100 mm × 200 mm concrete casting, composition and surface treatment, as per [36], of the 12 mm diameter by 190 mm steel

rod, having 150 mm embedded in each concrete samples, are according to procedures in reported studies [25,29,37-38].

Experimental Setup and Test-Data Measurements

Each sample for the corrosion test-experiment was partially and longitudinally immersed in bowls containing the 0.5 M H_2SO_4 test-solution that was made up to just below the steel-rebar protrusion from the concrete but without allowing the solution touch the rebar. From these, electrochemical measurements of corrosion potential, versus $Cu/CuSO_4$ electrode (CSE), as per [32] and corrosion rate from linear polarisation resistance (LPR) instrument were taken in 5 days interval for the first 40 days then in 7 days interval for the following 6 weeks. These make up to 15 data-points in the 82-day experimental period for each variable of electrochemical monitoring techniques employed in the study.

Experimental Data Analyses

As per ASTM G16-95 R04 [39], each variable of electrochemical monitoring technique was subjected to statistical distribution analyses of the Normal, Gumbel and Weibull distributions for investigating which of these was followed by the scatter of corrosion test-data [40]. For detailing corrosion effects, the mean models by the Normal (μ_N), the Gumbel (μ_G) and the Weibull (μ_W) probability distribution functions (pdf's) were respectively estimated from [7,23,28,41]:

$$\mu_N = \frac{1}{n}\sum_{i=1}^{n} x_i \tag{1}$$

$$\mu_G = a - b\Gamma'(1) \tag{2}$$

$$\mu_W = c\Gamma\left(1+\frac{1}{k}\right) \tag{3}$$

Where: n = 15 the number of data-points of each electrochemical monitoring technique, x_i is the ith electrochemical test-data, a is the location and b the scale parameter of the Gumbel distribution, c is the scale and k the shape parameter of the Weibull distribution. These distribution parameters were estimated through requisite solutions of simultaneous maximum likelihood equations that were detailed in [7,23,28]. By also following the prescription from [39], compatibility of the scatter of corrosion test-data like each of the probability distribution models was investigated using the Kolmogorov-Smirnov goodness-of-fit (K-S GoF) statistics at α = 0.05 level of significance [28,40,42].

The corrosion rate mean model, $\mu_{CR\text{-(pdf)}}$, from the probability distribution of best-fit for this variable of corrosion test-data finds usefulness for modelling corrosion inhibition efficiency, η(%), for each *S. aethiopicum* admixture concentration, using the expression [24,43]:

$$\eta(\%) = \frac{\mu_{CR\_(\text{pdf}),control\ sample} - \mu_{CR\_(\text{pdf}),admixed\ sample}}{\mu_{CR\_(\text{pdf}),control\ sample}} \times 100 \tag{4}$$

Results and Discussion

Results of statistical distribution analyses of corrosion test-data from the steel-reinforced concrete specimens are presented in Figure 1, for corrosion potential in Figure 1(a) and corrosion current in Figure 1(b). This figure also includes linear plots of corrosion risk as per ASTM C876-91 R99 [32] in Figure 1(a) and corrosion rate classification as per [34] in Figure 1(b). From these, it could be observed that *S. aethiopicum* leaf-extract reduced corrosion risk, as per [32],

and corrosion rate, as per 32, from high, obtained from the 0.00% (control) to low classification region, by both considerations of electrochemical monitoring techniques. Also notable from the figure include that fact the statistical models exhibited over-predictions of modelled results in comparisons to another, depending on the *S. aethiopicum* admixture concentration. It is these forms of over-predictions or otherwise that usually necessitate investigation of distribution model of best-fit for the corrosion test-data.

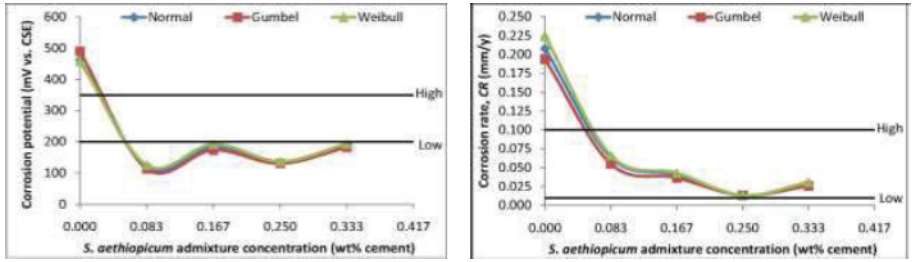

(a) (b)

Figure 1. Results of statistical distribution analyses of corrosion test-data (a) corrosion potential (b) corrosion rate

Results of the K-S GoF tests of test-data compatibility with the distribution function models are presented in Figure 2(a) for corrosion potential and in 2(b) for corrosion rate test-data. Linear plots of $\alpha = 0.05$ level of significance showed that the corrosion potential from the 0.167% *S. aethiopicum* and up to three corrosion rate datasets of the studied samples did not followed the Normal pdf. Also, while all corrosion potential datasets scattered like the Gumbel, the corrosion rate dataset from the 0.083% *S. aethiopicum* was not scattered like the Gumbel pdf. Only the Weibull pdf exhibited K=S *p-value* > 0.05 for both corrosion potential and corrosion rate test-data for all steel-reinforced concrete samples studied in this work. These support use of the Weibull pdf model as the descriptive statistics for detailing anticorrosion performance of *S. aethiopicum* leaf-extract admixture in the H_2SO_4-immersed steel-reinforced concrete samples.

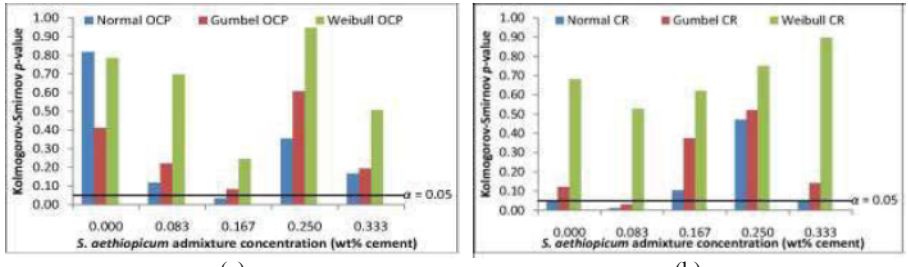

(a) (b)

Figure 2. Kolmogorov-Smirnov goodness-of-fit tests of corrosion data compatibility with the distribution function models (a) corrosion potential (b) corrosion rate

The application of corrosion rate mean model of the Weibull pdf to (4) resulted in the inhibition efficiency model, η(%), for *S. aethiopicum* leaf-extract admixture effects on concrete reinforcing steel corrosion in the studied medium. This anticorrosion effect by *S. aethiopicum* is presented in ranking order of admixture performance in Figure 4. It could therefore be identified from the figure that 0.25% *S. aethiopicum* exhibited optimal inhibition effectiveness, $\eta = 93.99\%$ on concrete steel-reinforcement corrosion in the acidic sulphate medium studied. This translates to

excellent model efficiency from the model efficiency classification from literature [44]. It is also observed-able from the figure that the remaining concentrations of *S. aethiopicum* leaf-extract admixtures exhibited corrosion inhibition efficiencies that ranged from "good", the η = 70.60% by the 0.083%, to the "very good" classification by the remaining *S. aethiopicum* admixtures.

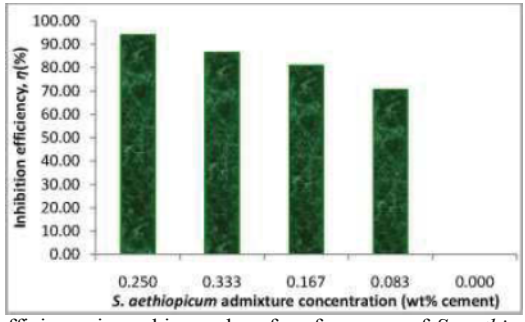

Figure 3. Inhibition efficiency in ranking order of performance of *S. aethiopicum* leaf-extract on reinforcing steel corrosion in concrete immersed in industrial/microbial simulating environment

Conclusions

Anticorrosion performance of *S. aethiopicum* leaf-extract on steel-reinforcement in 0.5 M H_2SO_4-immersed steel-reinforced concretes had been studied in this paper. The study showed that concentration of the leaf-extract reduced both corrosion risk and corrosion rate from the "high", obtained in the control sample, to the "low" classifications of corrosion criteria from two different electrochemical monitoring instruments. 0.25% *S. aethiopicum* was identified with optimal inhibition efficiency, η = 93.99%, while the remaining *S. aethiopicum* admixtures employed in the study, at the least, exhibited good effectiveness at inhibiting concrete steel-reinforcement corrosion in the industrial/microbial simulating environment studied.

References

1. J.O. Okeniyi, C.A. Loto, and A.P.I. Popoola, "Inhibition of steel-rebar corrosion in industrial/microbial simulating-environment by *Morinda lucida*," *Solid State Phenomena*, 227 (2015), 281–285.

2. T. Uygunoğlu and I. Gunes, "Biogenic corrosion on ribbed reinforcing steel bars with different bending angles in sewage systems," *Construction and Building Materials,* 96 (2015), 530–540.

3. D. Li, S. Zhang, W. Yang, and W. Zhang, "Corrosion monitoring and evaluation of reinforced concrete structures utilizing the ultrasonic guided wave technique," *International Journal of Distributed Sensor Networks,* 2014 (2014), 1–9.

4. F.–L. Fei, J. Hu, J.–X. Wei, Q.–J. Yu, and Z.–S. Chen, "Corrosion performance of steel reinforcement in simulated concrete pore solutions in the presence of imidazoline quaternary ammonium salt corrosion inhibitor," *Construction and Building Materials* 70 (2014), 43–53.

5. S.L.R. Reyna, J.M.M. Vidales, C.G. Tiburcio, L.N. Hernández, and L.S. Hernández, "State of corrosion of rebars embedded in mortar specimens after an electrochemical chloride removal," *Portugaliae Electrochimica Acta* 28 (2010), 153–164.

6. J.O. Okeniyi, O.A. Omotosho, O.O. Ogunlana, E.T. Okeniyi, T.F. Owoeye, A.S. Ogbiye, and E.O. Ogunlana, "Investigating prospects of *Phyllanthus muellerianus* as eco-friendly/sustainable material for reducing concrete steel-reinforcement corrosion in industrial/microbial environment," *Energy Procedia*, 74 (2015), 1274–1281.

7. J.O. Okeniyi, I.J. Ambrose, S.O. Okpala, O.M. Omoniyi, I.O. Oladele, C.A. Loto, and P.A.I. Popoola, "Probability density fittings of corrosion test-data: Implications on $C_6H_{15}NO_3$ effectiveness on concrete steel-rebar corrosion," *Sadhana* 39 (2014), 731–764.

8. W. De Muynck, N. De Belie, and W. Verstraete, "Effectiveness of admixtures, surface treatments and antimicrobial compounds against biogenic sulfuric acid corrosion of concrete," *Cement & Concrete Composites*, 31 (2009), 163–170.

9. C.K. Shing, C.M.L. Wu , J.W.J. Chen, C.S. Yuen, and R.Y.C. Tsui, "A Review on protection of concrete for sewage installations and an accelerated test on protection systems," HKIE Transactions, 19 (2012), 8–16.

10. M.A.G. Tommaselli, N.A. Mariano, and S.E. Kuri, "Effectiveness of corrosion inhibitors in saturated calcium hydroxide solutions acidified by acid rain components," *Construction and Building Materials*, 23 (2009), 328–333.

11. J.O. Okeniyi, C.A. Loto, and A.P.I. Popoola, "*Rhizophora mangle* L. effects on steel-reinforced concrete in 0.5 M H_2SO_4: Implications for corrosion-degradation of wind-energy structures in industrial environments," *Energy Procedia* 50 (2014), 429–436.

12. Y. Tang, G. Zhang, and Y. Zuo, "The inhibition effects of several inhibitors on rebar in acidified concrete pore solution," *Construction and Building Materials*, 28 (2012), 327–332.

13. C. Grengg, F. Mittermayr, A. Baldermann, M.E. Böttcher, A. Leis, G. Koraimann, P. Grunert, and M. Dietzel, "Microbiologically induced concrete corrosion: A case study from a combined sewer network," *Cement and Concrete Research*, 77 (2015), 16–25.

14. J.O. Okeniyi, O.A. Omotosho, O. Ajayi, O.O. James, and C.A. Loto, "Modelling the performance of sodium nitrite and aniline as inhibitors in the corrosion of steel-reinforced concrete," *Asian Journal Of Applied Sciences,* 5 (2012), 132–143.

15. E. Hewayde, M.L. Nehdi, E. Allouche, and G. Nakhla, "Using concrete admixtures for sulphuric acid resistance," *Proceedings of the Institution of Civil Engineers: Construction Materials* 160 (CMI) (2007), 25–35.

16. S. Wei, M. Sanchez, D. Trejo, and C. Gillis, "Microbial mediated deterioration of reinforced concrete structures," *International Biodeterioration & Biodegradation*, 64 (2010), 748–754.

17. Y.F. Fan, Z.Q. Hub, Y.Z. Zhang, and J.L. Liu, "Deterioration of compressive property of concrete under simulated acid rain environment," *Construction and Building Materials*, 24 (2010), 1975–1983.

18. A.K. Parande, P.L. Ramsamy, S. Ethirajan, C.R.K. Rao, and N. Palanisamy, "Deterioration of reinforced concrete in sewer environments," *Proceedings of the Institution of Civil Engineers: Municipal Engineer*, 159 (2006), 11–20.

19. M.–C. Chen, K. Wang, and L. Xie, "Deterioration mechanism of cementitious materials under acid rain attack," *Engineering Failure Analysis*, 27 (2013), 272–285.

20. J.O. Okeniyi, O.M. Omoniyi, S.O. Okpala, C.A. Loto, and A.P.I. Popoola, "Effect of ethylenediaminetetraacetic disodium dihydrate and sodium nitrite admixtures on steel-rebar corrosion in concrete," *European Journal of Environmental and Civil Engineering*, 17 (2013), 398–416.

21. J.O. Okeniyi, I.O. Oladele, O.M. Omoniyi, C.A. Loto, and A.P.I. Popoola, "Inhibition and compressive-strength performance of $Na_2Cr_2O_7$ and $C_{10}H_{14}N_2Na_2O_8{\cdot}2H_2O$ in steel-reinforced concrete in corrosive environments," *Canadian Journal of Civil Engineering*, 42 (2015), 408–416.

22. H. Gerengi, Y. Kocak, A. Jazdzewska, M. Kurtay, and H. Durgun, "Electrochemical investigations on the corrosion behaviour of reinforcing steel in diatomite- and zeolite-containing concrete exposed to sulphuric acid," *Construction and Building Materials* 49 (2013), 471–477.

23. J.O. Okeniyi, I.O. Oladele, I.J. Ambrose, S.O. Okpala, O.M. Omoniyi, C.A. Loto, and A.P.I. Popoola, "Analysis of inhibition of concrete steel-rebar corrosion by $Na_2Cr_2O_7$ concentrations: Implications for conflicting reports on inhibitor effectiveness. *Journal of Central South University*, 20 (12) (2013), 3697–3714.

24. N. Etteyeb, L. Dhouibi, H. Takenouti, and E. Triki, "Protection of reinforcement steel corrosion by phenyl phosphonic acid pre-treatment PART I: Tests in solutions simulating the electrolyte in the pores of fresh concrete," *Cement & Concrete Composites*, 55 (2015), 241–249.

25. J.O. Okeniyi, C.A. Loto, and A.P.I. Popoola, "Electrochemical performance of *Phyllanthus muellerianus* on the corrosion of concrete steel-reinforcement in industrial/microbial simulating-environment," *Portugaliae Electrochimica Acta* 32 (2014), 199–211.

26. J.O. Okeniyi, O.O. Ogunlana, O.E. Ogunlana, T.F. Owoeye, and E.T. Okeniyi, "Biochemical characterisation of the leaf of *Morinda lucida*: Prospects for environmentally-friendly steel-rebar corrosion-protection in aggressive medium," *TMS2015 Supplemental Proceedings* (Hoboken, NJ, USA: John Wiley & Sons, Inc., 2015), 635–644.

27. M. Ismail, P.B. Raja, and A.A. Salawu, "Deeper understanding of green inhibitors for corrosion of reinforcing steel in concrete," *Handbook of Research on Recent Developments in Materials Science and Corrosion Engineering Education,* ed. H. Lim, (Hershey, PA: IGI Global, 2015), 118–146.

28. J.O. Okeniyi, C.A. Loto, and A.P.I. Popoola, "Electrochemical performance of Anthocleista djalonensis on steel-reinforcement corrosion in concrete immersed in saline/marine simulating-environment," *Transactions of the Indian Institute of Metals*, 67 (2014), 959–969.

29. J.O. Okeniyi, A.S. Ogbiye, O.O. Ogunlana, E.T. Okeniyi, and O.E. Ogunlana, "Investigating *Solanum aethiopicum* leaf-extract and sodium-dichromate effects on steel-rebar corrosion in saline/marine simulating-environment: Implications on sustainable alternative for environmentally-hazardous inhibitor," *Engineering Solutions for Sustainability: Materials and Resources II*, ed. J.W. Fergus, B. Mishra, D. Anderson, E.A. Sarver and N.R. Neelameggham, (Hoboken, NJ, USA: John Wiley & Sons, Inc., 2015), 167–175.

30. S.O. Eze and C.Q. Kanu, "Phytochemical and nutritive composition analysis of *Solanum aethopicum* L," *Journal of Pharmaceutical and Scientific Innovation,* 3 (2014), 358–362.

31. S.N. Chinedu, A.C. Olasumbo, O.K. Eboji, O.C. Emiloju, O.K. Arinola, D.I. Dania, "Proximate and phytochemical analyses of *Solanum aethiopicum* L. and *Solanum macrocarpon* L. fruits," *Research Journal of Chemical Sciences*, 1 (2011), 63–71.

32. ASTM C876–91 R99, *Standard test method for half-cell potentials of uncoated reinforcing steel in concrete* (West Conshohocken, PA: ASTM International, 2005).

33. J.O. Okeniyi, A.P.I. Popoola, C.A. Loto, O.A. Omotosho, S.O. Okpala, and I.J. Ambrose, "Effect of $NaNO_2$ and $C_6H_{15}NO_3$ synergistic admixtures on steel-rebar corrosion in concrete immersed in aggressive environments," A*dvances in Materials Science and Engineering,* 2015 (2015), Article ID 540395, 11 pages.

34. T.A. Söylev and M.G. Richardson, "Corrosion inhibitors for steel in concrete: State-of-the-art report," *Construction and Building Materials*, 22 (2008), 609–622.

35. S. Hameurlaine, N. Gherraf, A. Benmnine, and A. Zellagui, "Inhibition effect of methanolic extract of *Atractylis serratuloides* on the corrosion of mild steel in H_2SO_4 medium," J*ournal of Chemical and Pharmaceutical Research*, 2 (2010), 819–825.

36. ASTM G109-99a, *Standard Test Method for Determining the Effects of Chemical Admixtures on the Corrosion of Embedded Steel Reinforcement in Concrete Exposed to Chloride Environments* (West Conshohocken, PA: ASTM International, 2005).

37. J.O. Okeniyi, C.A. Loto, and A.P.I. Popoola, "Modelling *Rhizophora mangle* L bark-extract effects on concrete steel-rebar in 0.5 M H_2SO_4: Implications on concentration for effective corrosion-inhibition," *TMS2015 Supplemental Proceedings* (Hoboken, NJ, USA: John Wiley & Sons, Inc., 2015), 751–758.

38. J.O. Okeniyi, I.J. Ambrose, I.O. Oladele, C.A. Loto, and P.A.I. Popoola, "Electrochemical performance of sodium dichromate partial replacement models by triethanolamine admixtures on steel-rebar corrosion in concretes," *International Journal of Electrochemical Science*, 8 (2013), 10758–10771.

39. ASTM G16-95 R04, *Standard guide for applying statistics to analysis of corrosion data* (West Conshohocken, PA: ASTM International, 2005).

40. P.R. Roberge, "Statistical interpretation of corrosion test results," *ASM handbook, Vol 13A – Corrosion: fundamentals, testing, and protection*, ed. S.D. Cramer and B.S. Covino Jr., (Materials Park, OH: ASM International, 2003), 425–429.

41. J.O. Okeniyi, O.S. Ohunakin, E.T. Okeniyi, "Assessments of wind-energy potential in selected-sites from three geopolitical-zones in Nigeria: Implications for renewable/sustainable rural-electrification," *The Scientific World Journal,* 2015 (2015), Article ID 581679, 13 pages.

42. J.O. Okeniyi and E.T. Okeniyi, "Implementation of Kolmogorov–Smirnov P-value computation in Visual Basic®: Implication for Microsoft Excel® library function," *Journal of Statistical Computation and Simulation*, 82 (2012), 1727-1741.

43. J.O. Okeniyi, C.A. Loto and A.P.I. Popoola, "Evaluation and Analyses of *Rhizophora mangle* L. leaf-extract corrosion-mechanism on reinforcing steel in concrete immersed in industrial/microbial simulating-environment," *Journal of Applied Sciences,* 15 (2015), 1083–1092.

44. R. Coffey, S. Dorai-Raj, V. O'Flaherty, M.C. and E. Cummins, "Modeling of pathogen indicator organisms in a small-scale agricultural catchment using SWAT," *Human and Ecological Risk Assessment: An International Journal,* 19 (2013), 232–253.

ARTIFICIAL NEURAL NETWORK MODELING TO PREDICT HOT DEFORMATION BEHAVIOR OF Zn-Al ALLOY

Yingli Liu[1,2,3], Jiancheng Yin[3], Ying Jiang[1,2], Yi Zhong[3]

[1]Computer Technology Application Key Lab of Yunnan Province, Kunming University of Science and Technology; 727 Jingming South Road,Area Chenggong;Kunming,Yunnan, 650500, China
[2]Faculty of Information Engineering and Automation, Kunming University of Science and Technology; 727 Jingming South Road,Area Chenggong;Kunming,Yunnan, 650500, China
[3]Faculty of Materials Science and Engineering, Kunming University of Science and Technology; 68 Wenchang Road,121 Street;Kunming,Yunnan, 650500, China

Keywords: ZnCu2Al10 aluminum alloy, hot deformation behavior, constitutive relationship, ANN

Abstract

Hot compression of the ZnCu2Al10 alloy was conducted on a Gleeble-3800D thermo-mechanical simulator in the temperature range of 150-330℃ and strain rate of 0.01-10 s^{-1}.Base on the experimental results, An Artificial Neural Network (ANN) with double hidden layers composing of 10 neurons and 15 neurons were employed to simulate the flow behavior. The inputs of the model are temperature, strain and strain rate. The output of the model is the flow stress. As a result, the minimum relative error is 0.01%, the maximum relative error is 2.25%, and error majority concentrate within 0.81%, Mean Absolute Percentage Error (MAPE) is 0.0101, error is very small. The results indicate that the trained ANN model is a robust tool to predict the high temperature flow behavior of ZnCu2Al10 alloy

Introduction

Zinc-aluminum alloy exhibits excellent physical and mechanical properties combined with high strength and hardness, excellent friction and wear properties, non-magnetic, non-sparking and other characteristics. At the same time, the alloy also has good processing properties, such as excellent machining performance and good surface treatment properties, etc [1].

Constitutive relationship of materials, which stands for the deformation behavior, is quite important for the optimization of the thermomechanical process parameters [2]. However, during the hot deformation process, there are many factors that affect the flow stress of materials. The effects of these factors on the flow stress are complex and the relationship between the flow stress and the factors is highly non-linear, which reduce the accuracy of prediction. Therefore, it is quite difficult to establish the constitutive relationship model using theoretical methods [3,4].

Fortunately, many researchers successfully applied a new approach of artificial neural network (ANN) in the prediction of constitutive relationships.

Author .Tel.:+86 0871 65157895
Email address: lyl2002@126.com (Yingli Liu)

ANN constitutive relation model of 2D70 aluminum alloy has high accuracy, can guild to formulate thermal processing technology, at the same time, can be used in 2D70 aluminum alloy the finite element simulation of hot deformation process[3]. Similarly, ANN can establish constitutive relation model of 2519 aluminum alloy, and founded parameters optimize value of ANN when forecast data in accordance with the experimental data well and system error is smaller[4]. Neural network constitutive model of extruded 7075 aluminum alloy can describe the high temperature flow stress behavior of the aluminum alloy, and provide the basis for analysis and finite element simulation of thermal deformation[5]. In this context, A356 aluminum alloy used ANN to predict thermal deformation behavior, and determine the model structure of the lowest error and cost[6]. Sun et al. [7] established an ANN model to estimate the high temperature flow behavior of Ti600 alloy. The results indicate that the trained ANN model is a robust tool to predict the high temperature flow behavior of cast Ti600 alloy.

The present work has been conducted to establish a four-layer ANN model to predict the high temperature flow behavior of ZnCu2Al10 alloy. The temperature, strain and strain rate have been used as inputs of the network, where the flow stress has been gained as the output. Finally, the validity of the proposed model is assessed using absolute error, relative error and mean absolute percentage error.

Experimental

The chemical composition of the experimental ZnCu2Al10 alloy(in wt.%) is 2Cu-10Al-Zn(bal.).

The compression experimental at constant strain rate were conducted in Gleeble-3800 thermal-simulator at the deformation temperatures of 150,180,210,240,270,300 and 330℃, with strain rates of 0.01, 0.1 and $10s^{-1}$.The true stress-strain curves obtained from the hot compression tests of ZnCu2Al10 alloy are shown in Fig.1.

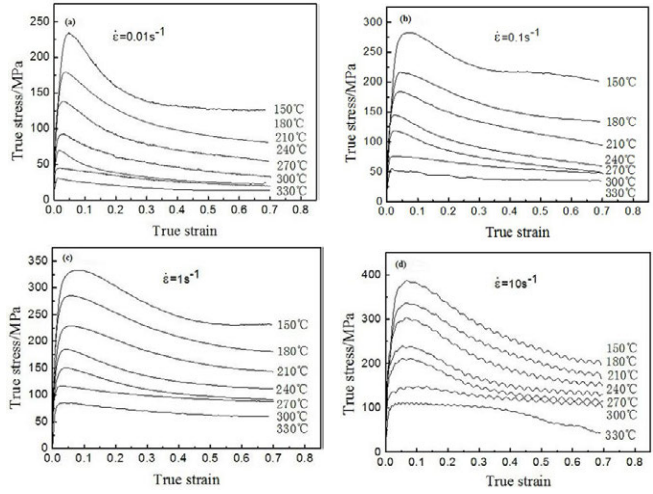

Fig.1: True stress-true strain curves of ZnCu2Al10 alloy at different strain rates:(a) 0.01 s^{-1};(b) 0.1 s^{-1};(c) 1 s^{-1} ;(d) 10 s^{-1}

High temperature flow behavior of ZnCu2Al10 alloy

Fig.1 depicts the true stress-true strain curves of the ZnCu2Al10 alloy obtained from corresponding compress tests in the temperature range of 150-330℃ and strain rates of 0.01-10s^{-1}.As is observed, all the curves exhibit the typical shape for dynamic recrystallization [8], i.e. strain hardening to a peak stress followed by flow softening. At the lower strain rates (0.01s^{-1}) and lower deformation temperature (150-210℃), the curves undergo a single peak stress followed by a rapid decline, and the decline rate decreases as the true strain increases. At the higher strain rates of 0.1,1 and 10s^{-1}, the flow stress decreases with the increase in strain, and the decline rate decreases as the temperature rises.

It can be found that the flow stress of ZnCu2Al10 alloy is sensitive to the effect of deformation temperatures and strain rates. The same temperature, the flow stress increases with increasing strain rate, which indicates that the material is a positive strain rate sensitive materials[5], this is mainly because the greater the strain rate, the plastic deformation is not more sufficient, the amount of elastic deformation increases, which results in increasing flow stress. Flow rate is the same, the flow stress increases with the decreasing of temperature, this is mainly because the lower the temperature, the lattice resistance is greater, which results in increased resistance to dislocation motion. It is worth mentioning when the strain rate is at 10s^{-1}, serrated significant fluctuations appears in stress-strain curve, the phenomenon indicates that the organizational evolution is discontinuous dynamic recrystallization [5].

ANN Constitutive Relationship Model of ZnCu2Al10 Alloy

Structure of ANN

A typical ANN model contains an input layer, an output layer and a hidden layer. The input layer is used to receive data from outside, while the output layer sends the information out. The role of the hidden layer, which is a layer that contains a systematically determined number of processing elements, is to provide the necessary complexity for non-linear problems[9]. In addition, hidden layer allows multilayer.

Mathematical model of ANN

Referenced [10] thought, the number of hidden layer and the node number of each hidden layer use the Root Mean Square Deviation (R.M.S.D.) to determine. R.M.S.D. specific form is shown formula(1).

$$R.M.S.D. = \sqrt{\frac{1}{n}\sum_{i=1}^{n}(\sigma_{pred} - \sigma_{\exp})^2} \tag{1}$$

Among them, σ_{pred} represents predicted flow stress value, $\sigma_{\exp}$ represents experimental flow stress value. Under different number of hidden layers, the lower R.M.S.D. values indicate that the number of hidden layer is more suitable for the model. Temperature is 150℃, strain rate is 1s^{-1}, and temperature is 240℃, strain rate is 0.01s^{-1}, the two sets data respectively apply the

formula(1), when the single hidden layer number is from 3 to 10, the value of R.M.S.D. is shown in Table I.

Table I: R.M.S.D. of different single hidden layer

The number of single hidden layer	3	4	5	6	7	8	9	10
R.M.S.D.(150℃/1s^{-1})	9.36	13.09	7.07	3.84	3.15	3.41	3.03	2.09
R.M.S.D.(240℃/0.01s^{-1})	2.15	8.21	2.05	4.01	2.07	1.21	1.60	1.91

As can be seen from Table I, the number of single hidden layer is 10, R.M.S.D. value is the minimum. However, when the node number of hidden layer is used the ANN model, the convergence effect is not particularly desirable. Therefore, consider doing the double hidden layer model, the node number of the first hidden layer is 10, the node number of the second hidden layer still determines by R.M.S.D., the R.M.S.D. value is shown in Table II.

Table II: R.M.S.D. of different double hidden layers

The number of double hidden layers	10-10	10-11	10-12	10-13	10-14	10-15	10-16
R.M.S.D.(150 ℃ /1s^{-1})	0.53	0.54	0.52	0.51	0.52	0.52	0.51
R.M.S.D.(240 ℃ /0.01s^{-1})	0.58	0.58	0.58	0.57	0.57	0.55	0.58

As can be seen from Table II, when the node number of hidden layer respectively is 10 and 15, the ANN model of ZnCu2Al10 alloy constitutive relation is more appropriate. A four-layer feed forward back propagation ANN (as shown in Fig. 2) was employed to predict the flow behavior and model the constitutive relationship of ZnCu2Al10 alloy.

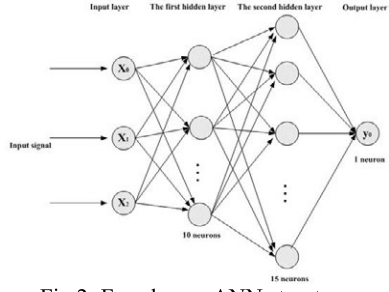

Fig.2: Four layers ANN structure

Processing of original data

In order to process the data conveniently and accelerate the convergence of running program, both input and output variables should be normalized processing. The following formula(2) is used widely for unification[11].

```
[Y,PS]=mapminmax(X)
Y=mapminmax('apply',X,PS)
X=mapminmax('reverse',Y,PS)                    (2)
```

In formula(2), the X is original data, the Y is the data by some normalization, the normalized mapping records in the structure of PS. After a set of data using some standardized form, the additional data can be normalized using the form by the 'apply'. The role of ‘reverse’ is reverse normalization, thus obtains the true data.

Constitutive relationship of ZnCu2A110 alloy primary influence factors are temperature, strain, strain rate and stress. First three of which are input parameters of ANN, the last is output parameter. The sample sets need a certain number of high quality sample, which insure to reflect the inherent rule of sample sets during of training and testing. In the established ANN model, 3639 data sets selected from the true stress-true strain curves, the all data sets were divided two sets: a training dataset and a test dataset (with four data sets as training data, one data set as test data from all data sets). From these data sets, 2912 data sets were used to train the network model, and the other 727 data sets were applied to test the performance of the ANN.

Model training

The establishment of the model and the corresponding test are completed by using the software MATLAB R2011a. The training function is ‘trainbr’, the training goal is 0.02, learning rate is 0.05, after 3492 iterations, the system converges, the system error achieves training objectives.

Results analysis

The contrast of experiment sample values and network predicted values about ZnCu2Al10 alloy flow stress is shown in Fig.3 and Fig.4, respectively, the contrast of training sample values and network predicted values is shown in Fig.3, the contrast of testing sample values and network predicted values is shown is Fig.4.

As can be seen from Fig.3 and Fig.4, the trained ANN constitutive relationship model, which can well reflect the ZnCu2Al10 alloy high temperature dynamic mechanical behavior.

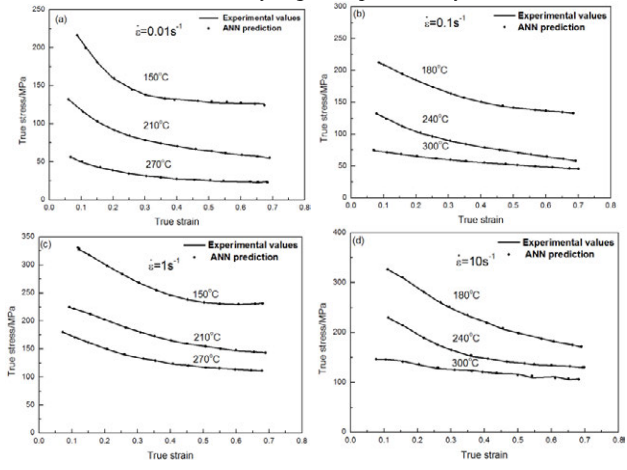

Fig.3: Comparison between train values and ANN predicted values of ZnCu2Al10 alloy: (a) $\dot{\varepsilon}$=0.01s^{-1}; (b) $\dot{\varepsilon}$=0.1 s^{-1}; (c) $\dot{\varepsilon}$=1 s^{-1}; (d) $\dot{\varepsilon}$=10 s^{-1}

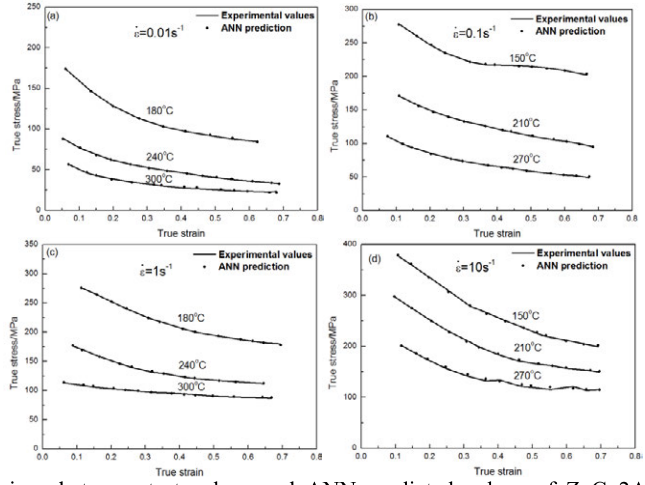

Fig.4: Comparison between test values and ANN predicted values of ZnCu2Al10 alloy: (a) $\dot{\varepsilon}$=0.01s^{-1}; (b) $\dot{\varepsilon}$=0.1 s^{-1}; (c) $\dot{\varepsilon}$=1 s^{-1}; (d) $\dot{\varepsilon}$=10 s^{-1}

As show in Table III, part flow stress two error conditions about experimental value and predicted value under different strain and strain rate at 270℃. It also can be seen that the minimum relative error is 0.01%, the maximum relative error is 2.25%, and error majority concentrate within 0.81%, error is very small.

Table III: Comparison of flow stress values prediction by ANN model and experimental data at 270℃

Strain rate/s^{-1}	Strain	Experimental stress/MPa	Predictive stress/MPa	Absolute error/MPa	Relative error/%
0.01	0.2	38.03	37.98	0.05	0.12%
	0.3	31.55	31.79	-0.24	-0. 77%
	0.4	27.51	27.84	-0.33	-1.21%
	0.5	25.08	25.42	-0.34	-1.35%
	0.6	23.46	23.28	0.18	0. 79%
0.1	0.2	83.98	84.28	-0.30	-0. 36%
	0.3	72.89	73.22	-0.33	-0. 46%
	0.4	66.17	65.94	0.24	0. 36%
	0.5	58.33	58.30	0.04	0.06%
	0.6	53.81	53.94	-0.12	-0.23%
1	0.2	150.86	150.91	-0.05	-0.03%
	0.3	135.17	135.18	-0.01	-0.01%
	0.4	124.31	124.18	0.13	0.11%

	0.5	117.07	116.93	0.14	0.12%
	0.6	113.58	112.66	0.92	0.81%
10	0.2	172.24	169.59	2.65	1.54%
	0.3	149.47	146.45	3.02	2.02%
	0.4	133.81	131.06	2.75	2.06%
	0.5	121.00	122.45	-1.45	-1.20%
	0.6	115.30	117.89	-2.59	-2.25%

Formula(3)[12] is adopted to compute ANN model Mean Absolute Percentage Error(MAPE) of ZnCu2Al10 alloy constitutive relationship.

$$MAPE = \frac{1}{n}\sum_{i=1}^{n}\left|\frac{\sigma_{cal}(\varepsilon_i)-\sigma_{\exp}(\varepsilon_i)}{\sigma_{\exp}(\varepsilon_i)}\right| \tag{3}$$

Where $\sigma_{cal}(\varepsilon_i)$ is predicted value of flow stress model, $\sigma_{\exp}(\varepsilon_i)$ is experimental value of flow stress, n is all sample number of model. After calculated, ANN MAPE of ZnCu2Al10 alloy constitutive relationship is 0.0101, which shows the established ANN model of ZnCu2Al10 alloy constitutive relationship has high predictability.

Conclusions

In the present work, a set of hot compression tests were carried out on a ZnCu2Al10 alloy in the temperature range of 150-330℃ under the strain rates of 0.01,0.1,1 and 10 s^{-1}. Based on the present study, the following conclusions can be drawn:

(1). It is found that the flow stress of ZnCu2Al10 alloy increases with increasing strain rate and the decrease in deformation temperature.

(2). The number of hidden layer and the node number of each hidden layer use the Root Mean Square Deviation (R.M.S.D.).

(3). A comparative evaluation of train values, test values and ANN predicted values were carried out. It is obtained that the minimum relative error is 0.01%, the maximum relative error is 2.25%, and error majority concentrate within 0.81%, MAPE is 0.0101, error is very small.

(4). The ANN could be a robust tool to describe and predict the high temperature flow behavior of ZnCu2Al10 alloy.

Acknowledgements

The Authors acknowledge the financial support from National Natural Science Foundation of China (project no.l50874055), Natural Science Foundation of Province Yunnan(project no. 2007E0013Z) and Education Department Foundation of Province Yunnan(project no. 2013Y316).

References

[1] Yang Ai-mei, “Research on Microstructure and Properties of High Aluminum Zn-Based ZA78 Alloys” (Ph.D. thesis, Xi’An university of technology, 2010), 3-10.

[2] Y. Liu et al., “Artificial neural network modelling to predict hot deformation behaviour of zinc-aluminium alloy,” *Materials Science and Technology*, 29(2) (2013) , 184-189.

[3] LU Shi-qiang et al., “Model of constitutive relationship for 2D70 aluminum alloy based on BP neural network,” *FORGING &STAMPING TECHNOLOGY*, 33(1) (2008), 148-151.

[4] LIN Qi-quan et al., “A Constitutive Relationship Model of the 2519 Aluminum Alloy Based on Artificial Neural Network,” *Natural Science Journal of Xiangtan University*, 26(3) (2004), 112-115.

[5] WANG Yu et al., “High temperature flow stress behavior of as-extruded 7075 aluminum alloy and neural network constitutive model,” *The Chinese Journal of Nonferrous Metals*, 21(11) (2011), 2880-2887.

[6] N. Haghdadi et al., “Artificial neural network modeling to predict the hot deformation behavior of an A356 aluminum alloy,” *Materials and Design*, 49(2013), 386-391.

[7] Y.Sun et al., “Development of constitutive relationship model of Ti600 alloy using artificial neural network,” *Computational Materials Science*, 48 (2010),686–691.

[8] ZHOU Ji-ming et al., “Investigation on the Constitutive Relationship of Materials Forming in High Temperature,” *Mechanical Science And Technology*, 24(2) (2005),212-216.

[9] Bo Li et al., “Microstructural evolution and constitutive relationship of Al–Zn–Mg alloy containing small amount of Sc and Zr during hot deformation based on Arrhenius-type and artificial neural network models,” *Journal of Alloys and Compounds*, 584 (2014) , 406–416.

[10] R. Kapoor, and D.Pal,J.K. Chakravartty, “Use of artificial neural networks to predict the deformation behavior of Zr–2.5Nb–0.5Cu,” *Journal of Materials Processing Technology*, 169 (2005), 199-205.

[11] WANG Cheng-yong et al., “Optimization of die casting processing parameters based on BP neural network and GA algorithm,” *Journal of Plasticity Engineering*, 18(3) (2011),105-110.

[12] TANG Jiang-ling et al., “Strength Prediction for AI-Cu-Mg-Ag Alloy Based on Support Vector Regression,” *Journal of Aeronautical Materials*, 32(5) (2012),92-96.

BEHAVIOR OF TIRE DERIVED PRE-FUNCTIONALIZED CARBON BLACK FOR URANIUM ADSORPTION

Travis Willhard, Dhiman Bhattacharyya, Mano Misra

Department of Metallurgical Engineering, University of Utah
135 S 1460 E, WBB 412, Salt Lake City, UT 84112, USA

Keywords: Recycled Tire Carbon Black, Uranium, Adsorption, Kinetics

Abstract

Extracting uranium from the solution phase has been a challenge as very few sorbents present high adsorption efficiency. A novel adsorbent in the form of Recycled Tire Carbon Black (RTCB), derived from pyrolysis of used tires, has shown promising results in adsorbing uranium from solution phase better than other functionalized carbon materials. The RTCB has been presented as a cheap and effective sorbent whose properties don't need to be altered to obtain nearly 97% adsorption and 99% elution using 0.15M HCl. Kinetic tests were performed to understand the adsorption rates. Langmuir isotherm model estimated that the adsorption capacity was ~45.45 mg U/g RTCB at 80°C with enhanced adsorption kinetics predicted by first order rate laws. In addition, the RTCB demonstrated better adsorption performance at lower pH. Characterization preformed using BET, illustrated that the surface area of the RTCB was 57 m^2/g while FTIR confirmed the presence of thiol (R-S-H) functional group on the surface.

Introduction

Uranium is an important element to the nuclear industry and is critical from our nation's sustainable energy standpoint. As energy demand goes up more uranium will be needed to produce the power required. One of the many problems is that most available uranium is too low of a grade to be considered economical to mine. This being one of the factors that have caused the increase of U_3O_8 price double in the last 4 years, to about $40 per pound. Extracting uranium from the solution phase has been a challenge as very few sorbents present high adsorption efficiency. Other industries have shown that activated carbon (AC) is an ideal solution for low grade mining of select elements. Charcoal derived AC [1], benzoylthiourea-anchored AC [2], and diarylazobisphenol modified AC [3] has been successfully utilized to concentrate uranium from solution phase but functionalization of AC presents additional cost and environmental hazards in terms of disposal. Activated carbon is used in large amount for many different industries, due to low cost and versatility of functionalizing the surface of the carbon. In this research, a novel adsorbent in the form of Recycled Tire Carbon Black (RTCB) has been presented as a cheap and effective sorbent whose properties don't need to be changed to adsorb uranium on to it. Many different kinds of functional groups have been discovered but none as easily available as this pre-functionalized RTCB for absorbing Uranium.

With uranium prices at an all-time low and the need to lower the cost of mining uranium for the energy sector, a cheap sorbent can provide a viable route. This unique adsorbent could help solve a large number of problems within the mining industry and simultaneously help the tire industry, with recycling used tires. It was estimated that about 2 x 10^6 tons of used tires were

produced in North America in 1990 and the number has gone up drastically since [4]. Since 2003 the USA has dropped the amount of used tires that could be put into landfills regulated between state laws and economics of recycling the used tires into other useful commodities [5]. The unique adsorbent that has been used for this research is processed pyrolyzed used tires, which has had the valuable metals removed, oils extracted out, and then the tires are grinded up into amorphous particles. In the past, adsorbents derived from used tires have been used for removal of chromium from aqueous solutions [6].

Experiment

Characterization

SEM - EDS: Morphological examination of the RTCB particles before and after uranium loading was performed using a field emission scanning electron microscope (Hitachi S-4800 SEM) with a tungsten filament based field emission gun at 3 kV accelerating voltage and 15 μA emission current. Energy dispersive x-ray spectroscopic (EDS) analysis was performed using an Oxford (X-Max) EDAX detector attached to the SEM. EDS analysis was carried out at 20 kV accelerating voltage and high probe current. The AZtecEnergy acquisition and EDS analysis software synchronized with the X-Max detector was used uranium mapping and spectral analysis.

BET / FTIR: Surface area is a prominent property of carbon particles which contributes to its widespread usage in the industry. The adsorption properties of RTCB have been compared to the commercial carbon black (CCB) and activated carbon (AC). The most important property of AC which highly affects the adsorption properties is its extremely large surface area and highly developed pore structure. Hence, it is imperative that a comparison of specific surface area of the three adsorbents be presented. A ASAP 2020 (Micromeritics, USA) surface analyzer was used to measure nitrogen adsorption isotherm at 77K in the range of relative pressures from 0 to 1. Before measurement, the sample was degassed at 300ºC for 3h. Brunauer–Emmett–Teller (BET) theory serves as the basis for an important analysis technique for the measurement of the specific surface area of a material and is explained by the physical adsorption of gas molecules on a solid surface. The BET equation was used to calculate the specific surface area.

In addition to surface area, knowledge of the functional groups present on the carbon is essential for deducing the reaction mechanism. A Frontier FTIR (Perkin Elmer, USA) was used to determine the functional groups on the RTCB and CCB.

Adsorption

Isotherm: The equilibrium isotherm was determined by mixing various weights of carbon (0.5, 1, 3, 5, 10 g) with 200 ml of 100 ppm Uranium solutions in 300 ml round-bottom flask at different temperatures. The flasks containing uranium solution and carbon were placed on a magnetic stir plate and agitated for 24 h at the required temperature and at a fixed agitation speed of 200 rpm. After the cycle was completed, the carbon in each vessel was filtered off under vacuum using a Whatman filter paper. 20-30ml sample of the filtrate from each flask was stored in sample vials and the equilibrium U concentrations were measured by a Spectro Genesis ICP-OES (inductively-coupled plasma - optical emission spectrometer) instrument and referenced with the

calibration curve. The accuracy of temperature and concentration measurements was ±1˚C and ±0.05 ppm, respectively. The equilibrium data for adsorption of Uranium (U) on to the RTCB follows the rearranged Langmuir adsorption model, which is given by:

$$\frac{C_e}{q_e} = \frac{1}{b.Q_o} + \frac{C_e}{Q_o} \quad (1)$$

Where, C_e is equilibrium concentration (mg/l) and q_e the amount adsorbed at equilibrium (mg/g).

Kinetics: The measurement of adsorption kinetics of RTCB was carried out by shaking 5 g of carbon with 200 ml of 20 ppm U in 300 ml round-bottom flask placed on a magnetic stir plate provided with an agitating mechanism. The removal kinetics of the U was investigated by drawing 10 ml samples periodically over 12 hours and the filtrate was analyzed for the remaining U concentration. To find out the equilibrium time, % U adsorbed was plotted against time. From the results of the ICP solution analysis, the quantity of U adsorbed by the carbon was calculated at each time interval. The results were treated with a rate equation in which it is assumed that the rate is proportional to the concentration of U in solution but independent of the concentration of U on the carbon, as found for the initial stages of loading when the reaction is far from equilibrium. To investigate it even further, the rate constant was determined using equation 2 suggested by Fleming et al. [7]. This equation gives linear plot only within the first few hours of adsorption.

$$\Delta[U]_c^t = k\,[U]_s^t\,.t \quad (2)$$

where $\Delta[U]_c^t$ is the amount of U adsorbed by carbon, $[U]_s^t$ is the concentration of U in solution, and k is the rate constant. To determine the value of k from this equation, $\log(\Delta[U]_c^t/[U]_s^t)$ was plotted against log(t) for the first few hours of adsorption and the k-value was calculated by taking the antilog of the intercept.

To further investigate the effect of temperature on the rate of U adsorption by RTCB, R-value was determined which is the reciprocal of intercept at zero time in the plot of time divided by loading on carbon versus time when contacting 20ppm U solution with RTCB. The data obtained in such adsorption experiments yield a straight line that can be expressed by equation 3 as described by Urbanic et al. [8].

$$\frac{t}{X/_M} = (\frac{1}{M})t + \frac{1}{R} \quad (3)$$

where, X/M represents the U loading in mg U/g of carbon, t is the time, and M and R are reciprocal of the slope and intercept at zero time, respectively. The R-value for RTCB at each temperature is relative, i.e., a higher value indicates faster adsorption.

Effect of REE on U adsorption: To investigate the interference of other elements on U adsorption by RTCB, 100 ppm of five rare earth elements (REEs) each viz. La, Ce, Nd, Sm, and Y were added to the solution with U and the adsorption characteristics were determined.

Desorption

A stripping test was performed to investigate the ease of Uranium removal from adsorbed RTCB. 10 g of RTCB loaded with 100 ppm U was stripped using 0.15 M HCl solution at room temperature under magnetic stirring at 200 rpm. Further, several adsorption / desorption cycles were performed to test the longevity of the RTCB specimens before the carbon has to be regenerated or discarded.

Results & Discussion

Surface Area and Composition

RTCB was found to have a specific surface area of 57 m^2/g compared to activated carbon which had an enormous surface area of 924 m^2/g and carbon black 63 m^2/g, using BET methods (with liquid nitrogen) that is shown in Fig. 1a.

FTIR test was performed to understand the presence of organic functional groups on the carbon surface of the RTCB, compared to Carbon Black. It was found that the thiol R-S-H functional group, found predominantly at 2401 cm^{-1}, was present on the RTCB but not on the Carbon Black as shown in Fig. 1b. The presence of thiol group in RTCB explains its origin as the sulfur must have come from vulcanization of tires.

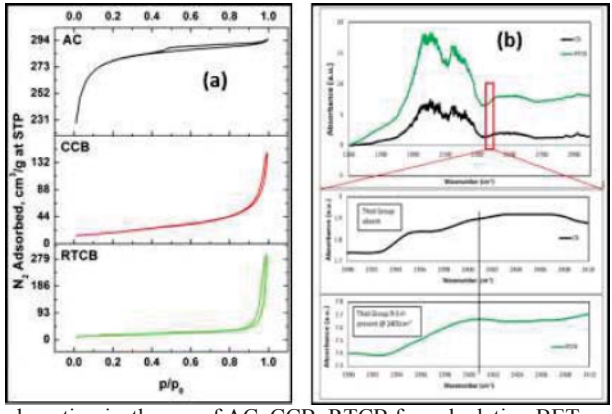

Fig. 1 (a) N_2 adsorption isotherms of AC, CCB, RTCB for calculating BET surface area. (b) FTIR analysis of CCB and RTCB revealing thiol peak at 2401 cm^{-1}.

Morphological Characterization

FESEM micrographs of RTCB particles illustrates that the particle size ranges from 1 micron to 15 microns and can vary in shape from spherical to oblong. Fig. 2 also shows that the particles are not homogenous in size and can aggregate together to form clumps.

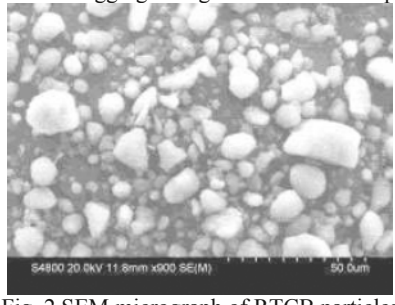

Fig. 2 SEM micrograph of RTCB particles

EDS characterization of RTCB particles before and after U loading reveal the composition of RTCB and the distribution of U on the carbon particles, respectively (Fig. 3). Fig. 3a demonstrates that the bare RTCB particle contains a lot of zinc and sulfur, which again is not very surprising considering its precursor material, i.e. recycled tires and this is consistent with the ICP-MS analysis of RTCB. Also evident from Fig. 3b, the U is not homogeneously distributed on the carbon surface. This may be attributed to the concentration of the functional groups in particular regions on RTCB which act as potential binding sites for the U.

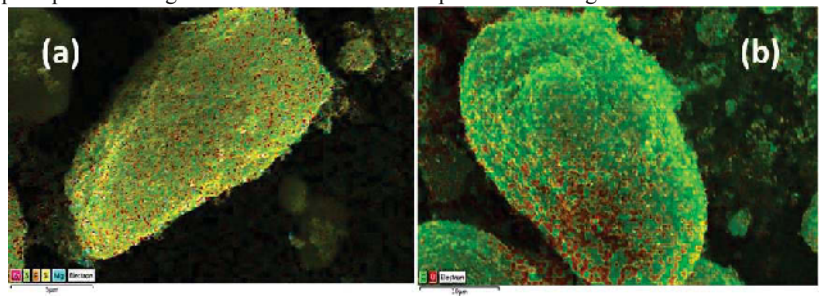

Fig. 3 EDS mapping of a 10 micron RTCB particle (a) bare, (b) loaded with U. (C-green; U-red)

It has been mentioned that the stability constants for complexes of U(I) or U(IV) with sulfide has never been reported due to low affinity of U for sulfur ligands. In solution, dissolved sulfide becomes consumed in due course of the reaction and U adsorbs by forming complexes with the hydroxide groups at the RTCB surface. Due to absence of an elaborated porous structure as AC, most of the U adsorption takes place on the surface of the RTCB.

Adsorption Properties

Effect of pH: The uptakes of U by RTCB at different pHs at an initial concentration of 100 mg/l and room temperature of 23˚C are shown in Fig. 4. For RTCB, the percent adsorbed increases from 91% to 97% as the pH decreases from 10.87 to 2.32. This indicates that the adsorption capacity of the adsorbent is clearly pH dependent. It is obvious that pH provides a favorable adsorbent surface charge for the adsorption to occur. U exists in different forms in aqueous solution and the stability of these forms is dependent on the pH of the system.

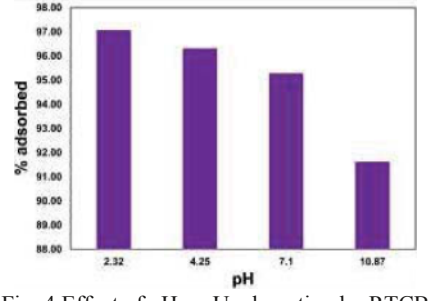

Fig. 4 Effect of pH on U adsorption by RTCB

Adsorption Capacity: The adsorption capacity of Uranium on RTCB was found to increase from 8.41 to 45.45 mg/g C when temperature was increased from 25 to 80˚C at natural pH (pH = 4.25), and at initial U concentration of 100 mg/l (Fig. 5). Fig. 5 indicates that the equilibrium concentration *C*e of adsorbate in solution is higher at lower temperature and it decreases with increasing temperature, i.e. the adsorption is favored at higher temperatures. The Langmuir constants Q_o and *b*, which are related to the adsorption capacity and heat of adsorption, respectively, were determined (Table 1) from the slope and intercepts of the linear plots of *C*e/*q*e versus *C*e. Since, the 'b' value in the Langmuir equation gives an idea of the heat of adsorption, it is safe to presume from the calculated values that this adsorption is an endothermic process.

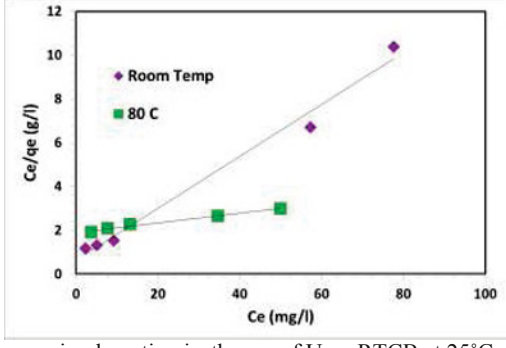

Fig. 5 Langmuir adsorption isotherms of U on RTCB at 25˚C and 80˚C.

Table 1. Langmuir constants for RTCB samples at different temperatures.

Temp (˚C)	Q_o (mg/g)	b (l/mg)	r^2
25	8.41	0.19	0.986
80	45.45	0.01	0.984

Adsorption Kinteics: Further, to validate Equation 2 and to determine the reaction rate constants, the plots of $\log(\Delta[U]_c^t/[U]_s^t)$ against log(t) at two different temperatures are given in Fig. 6 (a,b). These figures will yield the reaction rate constant *k* by taking the antilogarithm of the intercept value from the linear equation obtained from the plots. The reaction rate constant was then plotted against the inverse of the temperature to obtain the activation energy from the Arrhenius equation. As expected, the rate constants increase with increase in temperature.

The plots of time divided by carbon loading as a function of time for the different temperatures are plotted in Figure 6 (c,d). The R-values are calculated from the same plots. It is evident from the results presented that initial rate of adsorption (R) increases as the temperature increases. Subsequently, the first order rate constants are summarized in Table 2 to compare with the initial rate values in order to observe the trend with variation in temperature.

Table 2. Summary of first order rate constant (k) and initial rates (R) at different temperature.

Temp (˚C)	Temp (K)	1/T (1/K)	Initial Rate R (mg U / g C)/min	Rate Const. k (h^{-1})	ln k	Ea (J/mol)	Ea (kJ/mol)
25	298	0.003356	3.351206	8596.071	9.059	14700.82	14.701
80	353	0.002833	11.402509	21667.061	9.983		

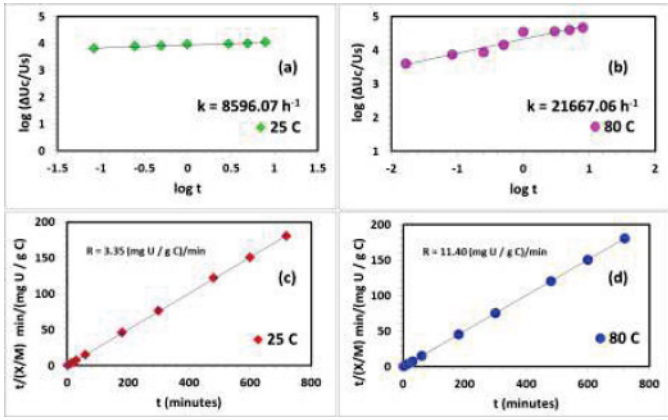

Fig. 6 (a,b) Plots determining the U adsorption rate constant (*k*) for RTCB at 25 and 80˚C; (c,d) Plots determining the initial U adsorption rate (R) on RTCB at 25 and 80˚C.

The results also show that fine RTCB adsorbed ~97 % of U in the first 15 minutes and nearly 100 % after 1 hour at 25 and 80˚C alike, although the initial rates were slightly different. This further shows that fine carbon particles like RTCB are very effective adsorbents. These results are in line with traditional beliefs that smaller particles present better kinetics due to shorter diffusion paths.

Effect of REE on U adsorption: Results indicate that U adsorption by RTCB is not hindered by the presence of other elements in the solution (Fig. 7). This is especially important in the context of the research, as other elements will be present in the aqueous solution containing uranium, which will affect the solution chemistry and compete for the active sites on the RTCB.

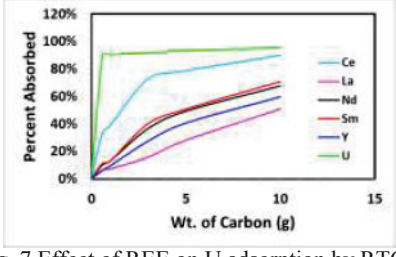

Fig. 7 Effect of REE on U adsorption by RTCB

Desorption: For RTCB loaded with 100ppm U at 80˚C, the stripping test demonstrated successful recovery of **99.34%** of adsorbed uranium from the RTCB using a 0.15 M HCl solution after 24 hours, at room temperature. An adsorption and stripping cycle test was performed to characterize how long the RTCB can last before regeneration of the RTCB will be required. No chemical treatments were preformed between stripping and adsorption stage. About 5 cycles was the ideal amount of time the RTCB can be used until performance started to drop (by more than 10% of Uranium being adsorbed).

Conclusions

The results for adsorption capacity and kinetics followed by desorption elucidate that RTCB is an extremely efficient sorbent for U adsorption from aqueous solutions. The source of RTCB (pyrolyzed tires) causes the carbon particles to be pre-functionalized with certain functional groups which enhance U adsorption. Although the specific surface area of RTCB is much smaller that commercial AC, the very fine particle size presents large adsorption capacities and greatly enhanced reaction rates. Since, low pH and high temperature conditions are conducive for U adsorption by RTCB, this adsorbent can be used to adsorb U from geothermal waters (which also has REEs). Among other applications, RTCB can be a cheaper alternative to conventional method of mining uranium. Seawater contains 3.3ppb U, but considering the total volume of all the oceans on the Earth's surface, the total U content is $4x10^9$ tons [9]. Thus, RTCB can be a potent sorbent to adsorb uranium from seawater. With ample possibilities for applications and immense commercialization potential, the cheaply available pre-functionalized carbon black derived from recycled tires can be an effective adsorbent.

References

1. C. Kütahyal, M. Eral, "Selective adsorption of uranium from aqueous solutions using activated carbon prepared from charcoal by chemical activation," *Separation and Purification Technology*, 40 (2004), 109–114

2. Y. Zhao et al., "Solid phase extraction of uranium(VI) onto benzoylthiourea-anchored activated carbon," *Journal of Hazardous Materials*, 176 (2010), 119-124.

3. A.M. Starvin, T. Prasada Rao, "Solid phase extractive preconcentration of uranium(VI) onto diarylazobisphenol modified activated carbon," *Talanta*, 63 (2004), 225–232.

4. P.T. Williams, S. Besler, D.T. Taylor, "The pyrolysis of scrap automotive tires," *Fuel,* 69 (1990), 1474–1482.

5. Office of Solid Waste and Emergency Response, "State Scrap Tire Programs," (Report EPA-530-B-99-002, US EPA Office of Resource Conservation and Recovery, 1999).

6. N.K. Hamadi et al., "Adsorption kinetics for the removal of chromium(VI) from aqueous solution by adsorbents derived from used tyres and sawdust," *Chemical Engineering Journal*, 84 (2001), 95–105.

7. C.A. Fleming, and M.J. Nicol, "The absorption of gold cyanide onto activated carbon: Factors influencing the rate of loading and the equilibrium capacity." *Journal of the South African Institute of Mining and Metallurgy*, 84(9) (1984), 85-89.

8. J.E. Urbanic, R.J. Jula, W.D. Faulkner, "Regeneration of activated carbon used for recovery of gold," *Minerals and Metallurgical Processing*, (1985), 193-198.

9. A.D. Kelmers, "The recovery of uranium from sea water - status of technology and needed future research and development," (Paper presented at a topical meeting: The Recovery of Uranium from Seawater, Massachusetts Institute of Technology, Cambridge, Massachusetts, December 1-2. 1980).

EFFECT OF TEMPERATURE ON THE MECHANICAL BEHAVIOUR OF Ni-Ti SHAPE MEMORY SHEETS

Girolamo Costanza, Maria Elisa Tata, Riccardo Libertini
University of Rome "Tor Vergata" – Industrial Engineering Department
Via del Politecnico, 1 00133 – Rome ITALY

Keywords: Shape Memory Alloys, Mechanical behaviour, Tensile test.

Abstract

In this research the shape memory effect of commercial NiTi sheets has been investigated. Four commercial SMA elements have been characterized. Tensile tests (load-unload cycles) have been performed at various constant temperatures (from room temperature up to 60 °C). Stress-strain curves have been analyzed and discussed in order to quantify the shape-recovery which has been found higher at increasing testing temperature. A study on the energy dissipation on each cycle has been carried out too and the energy absorption on the whole load-unload cycle has been found higher as the temperature increases.

Introduction

Shape memory alloys (SMA) show the ability to recover high strain just upon heating above a characteristic critical temperature usually identified as Austenite finish (A_f). This property is known as Shape Memory Effect (SME) and its origin is due to the thermoelastic martensitic transformation happening in some alloys [1-2]. In particular SMA present two different phases: martensite stable at temperature lower than Martensite finish (M_f) and austenite stable at temperature higher than A_f. The macroscopic shape recovery is due to the microstructural transformation from martensite to austenite. In particular the transformation from one phase to the other one guarantees the manifestation of the shape memory effect: if a SMA specimen is deformed at room temperature it is possible to recover the original shape just heating it at a temperature higher than A_f. The SME is the main reason of the great industrial interest on SMA in many applications, for example in medical, aeronautical field and civil structures as shown in [3-5]. Sensors and actuators [6] for a great number of activation cycles can be designed and manufactured thanks to their particular features. Superelastic elements can be useful in seismic applications for their ability in dissipating energy [7]. Also the loss of recovery efficiency due to the functional fatigue in one-way shape memory applications has been investigated [8].
Generally SMA are available in form of wires or sheets. On the last ones the attention has been focused on in this work. Four commercial equiatomical NiTi sheets have been characterized by means of tensile tests carried out at various constant temperatures and the aim of such tests is to collect experimental data for setting a constitutive model able to simulate the mechanical behavior of the material, evaluating the recovery capability and the dissipated energy.

Materials and experimental methods

The materials employed in this research are four commercial near equiatomical NiTi alloys (Fig. 1 left). The experimental procedure consists in undergoing each sample taken from each sheet to

tensile tests at various temperature (range 20-60 °C, step 10 °C) and increasing maximum strain (range 0.5-4%). The samples, whose dimensions are reported in Tab. 1, have been labelled from 1 to 4.

Table 1. Dimensions of the SMA specimens

	Lenght (mm)	Width (mm)	Thickness (mm)
Specimen 1	50	10	1,1
Specimen 2	50	10	0,5
Specimen 3	50	10	0,5
Specimen 4	50	10	1

Tensile tests were performed inside a MTS Insight tensile machine (Fig. 1 right) with a environmental chamber which allows to perform tensile tests at constant temperature. Before performing each tensile test the chamber has been set at the desired temperature and, after stabilization, load and unload cycles have been performed for all samples at that temperature. At the end of each tensile test on that sample the specimen has been heated up above Af and cooled down at room temperature. At the end of the test series, the environmental chamber is increased of 10 °C for the successive set of tests. The results of every single test is analyzed by the Origin software in order to obtain the stress-strain curves.

Fig. 1 left) The four SMA samples employed for the mechanical characterization; right) Tensile test machine with environmental chamber.

Results and discussion

From the tensile tests performed on the four samples at various elongation and temperatures the following parameters have been calculated: maximum load, residual strain, recovered strain and recovered deformation percentage. Two examples of stress-strain curves are reported in Fig. 2 and Fig. 3. The most significant results of the tensile tests for 1% and 4% strain imposed are summarized in the following tables (2-5).

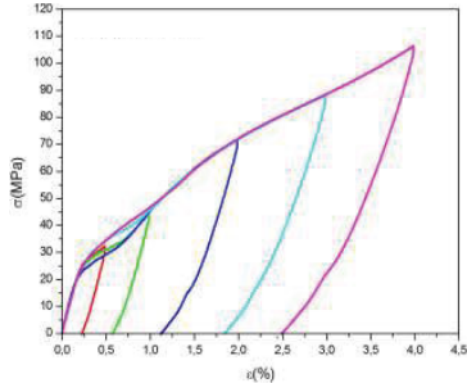

Fig. 2 Stress-strain curves for specimen 2 at T = 20°C.

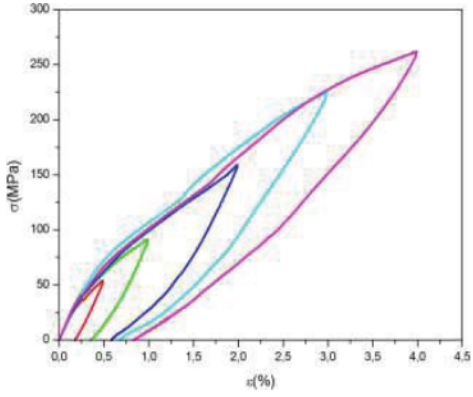

Fig. 3 Stress-strain curves for specimen 2 at T = 60°C.

Table 2. Tensile tests results for the specimen 1.

Specimen 1	20°C	30°C	40°C	50°C	60°C
1,00% Strain imposed	σ_{max} = 37 MPa ε_{res} = 0,42% ε_{rec} = 0,58% rec% = 58%	σ_{max} = 45 MPa ε_{res} = 0,4% ε_{rec} = 0,6% rec% = 60%	σ_{max} = 52 MPa ε_{res} = 0,35% ε_{rec} = 0,65% rec% = 65%	σ_{max} = 45 MPa ε_{res} = 0,4% ε_{rec} = 0,6% rec% = 60%	σ_{max} = 53 MPa ε_{res} = 0,38% ε_{rec} = 0,62% rec% = 62%
4,00% Strain imposed	σ_{max} = 92 MPa ε_{res} = 2,1% ε_{rec} = 1,9% rec% = 47,5%	σ_{max} = 88MPa ε_{res} = 2,2% ε_{rec} = 1,8% rec% = 45%	σ_{max} =103 MPa ε_{res} = 1,8% ε_{rec} =2,2% rec% =55%	σ_{max} =125 MPa ε_{res} = 1,8% ε_{rec} =2,2% rec% =55%	σ_{max} =200 MPa ε_{res} = 1,4% ε_{rec} =2,6% rec% =65%

Table 3. Tensile tests results for the specimen 2.

Specimen 2	20°C	30°C	40°C	50°C	60°C
1,00% Strain imposed	σ_{max} = 45 MPa ε_{res} = 0,59% ε_{rec} = 0,41% rec% = 41%	σ_{max} = 45 MPa ε_{res} = 0,43% ε_{rec} = 0,57% rec% = 57%	σ_{max} = 67 MPa ε_{res} = 0,41% ε_{rec} = 0,59% rec% = 59%	σ_{max} = 73 MPa ε_{res} = 0,42% ε_{rec} = 0,58% rec% = 58%	σ_{max} = 92 MPa ε_{res} = 0,38% ε_{rec} = 0,62% rec% = 62%
4,00% Strain imposed	σ_{max} = 105 MPa ε_{res} = 2,5% ε_{rec} = 1,5% rec% = 37,5%	σ_{max} = 104 MPa ε_{res} = 2,2% ε_{rec} = 1,8% rec% = 45%	σ_{max} =140 MPa ε_{res} = 1,7% ε_{rec} =2,3% rec% =57,5%	σ_{max} =187 MPa ε_{res} = 1,2% ε_{rec} =2,8% rec% =70%	σ_{max} =260 MPa ε_{res} = 0,8% ε_{rec} =3,2% rec% =80%

Table 4. Tensile tests results for the specimen 3.

Specimen 3	20°C	30°C	40°C	50°C	60°C
1,00% Strain imposed	σ_{max} = 50 MPa ε_{res} = 0,5% ε_{rec} = 0,5% rec% = 50%	σ_{max} = 55 MPa ε_{res} = 0,5% ε_{rec} = 0,5% rec% = 50%	σ_{max} = 50 MPa ε_{res} = 0,58% ε_{rec} = 0,42% rec% = 42%	σ_{max} = 70 MPa ε_{res} = 0,5% ε_{rec} = 0,5% rec% = 50%	σ_{max} = 72 MPa ε_{res} = 0,5% ε_{rec} = 0,5% rec% = 50%
4,00% Strain imposed	σ_{max} =110 MPa ε_{res} = 2,4%	σ_{max} =123 MPa ε_{res} = 2,3%	σ_{max} =140 MPa ε_{res} = 1,9%	σ_{max} =200 MPa ε_{res} = 0,9%	σ_{max} =260 MPa ε_{res} = 0,8%

	ε_{rec} = 1,6% rec% = 40%	ε_{rec} = 1,7% rec% = 42,5%	ε_{rec} =2,1% rec% =52,5%	ε_{rec} =3,1% rec% =77,5%	ε_{rec} =3,2% rec% =80%

Table 5. Tensile tests results for the specimen 4.

Specimen 4	20°C	30°C	40°C	50°C	60°C
1,00% Strain imposed	σ_{max} = 28 MPa ε_{res} = 0,6% ε_{rec} = 0,4% rec% = 40%	σ_{max} = 28 MPa ε_{res} = 0,58% ε_{rec} = 0,42% rec% = 42%	σ_{max} = 35 MPa ε_{res} = 0,53% ε_{rec} = 0,47% rec% = 47%	σ_{max} = 35 MPa ε_{res} = 0,59% ε_{rec} = 0,41% rec% = 41%	σ_{max} = 42 MPa ε_{res} = 0,5% ε_{rec} = 0,5% rec% = 50%
4,00% Strain imposed	σ_{max} = 85 MPa ε_{res} = 2,2% ε_{rec} = 1,8% rec% = 45%	σ_{max} = 90 MPa ε_{res} = 2,2% ε_{rec} = 1,8% rec% = 45%	σ_{max} =110 MPa ε_{res} = 1,9% ε_{rec} =2,1% rec% =52,5%	σ_{max} =138 MPa ε_{res} = 1,4% ε_{rec} =2,6% rec% =65%	σ_{max} =190 MPa ε_{res} = 1,4% ε_{rec} =2,6% rec% =65%

From the results reported in the tables above it has been found that at temperatures higher than 40°C the percentage of recovered strain for the tests performed with ε = 1% is about 60% for samples 1 and 2 while for samples 3 and 4 deformed at ε = 1% it is close to 50%.
The most significant results are observed for the tests performed at 4% strain. In such tests for samples 1 and 4 about 65% of strain has been recovered while for samples 2 and 3 the 80% of recovered strain has been observed. Furthermore the highest percentage of recovered strain is associated to the highest values of the load σ_{max}. For instance in the sample 2 the 80% recovery has been observed, the highest detected in all the tests, in correspondence of the maximum load (260 MPa). The higher recovery percentage has been observed at the higher test temperatures in which the superelastic effect is more evident and for such a reason higher load has been achieved during tensile tests, as evidenced in Fig. 2 and Fig. 3.
From the experimental data three fundamental parameters increase as the temperature increases:
the Young's modulus;
the maximum stress;
the ability to recover the pre-set shape.

Dissipated energy.
The area under the stress-strain curve represents the energy by unit of volume dissipated during the loading-unloading cycle (Fig. 4). In the following table 6 the values of the energy density dissipated (Ediss.) at various temperature are reported for different samples during a load-unload cycle up to a deformation of 4%.
As can be noted the highest value has been found for the sample 3 at a temperature of 60 °C (305,3 J/cm^3) while the lowest value is related to the sample 4 at a temperature of 20 °C (147,7 J/cm^3). The general trend shows that for these samples the dissipated energy density is closely connected to the temperature and consequently to the shape memory effect. The lowest values

have been observed at lower temperatures while with growing temperature gradually comes to more meaningful values. It is finally interesting to note that among the tested samples the best energy sink is the number 3. In fact, this sample has excellent values of dissipated energy even at low temperatures and for this reason could be employed in interesting damping applications.

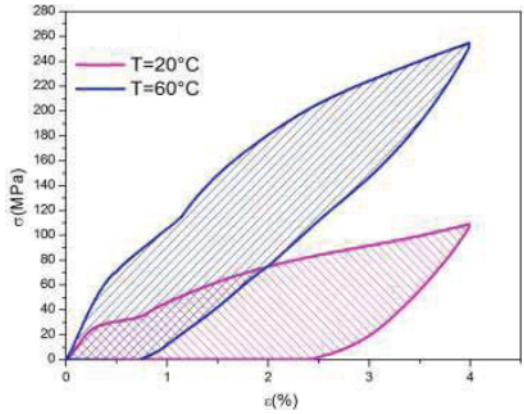

Fig. 4 Dissipated energy for sample 3 at T = 20 °C and T = 60°C.

Table 6. Dissipated energy (J/cm^3).

	Specimen 1	Specimen 2	Specimen 3	Specimen 4
T= 20°C	E_{diss}= 171,9	E_{diss}= 205,0	E_{diss}= 210,7	E_{diss}= 147,7
T= 30°C	E_{diss}= 164,0	E_{diss}= 203,3	E_{diss}= 248,1	E_{diss}= 154,3
T= 40°C	E_{diss}= 187,0	E_{diss}= 255,4	E_{diss}= 264,6	E_{diss}= 181,8
T= 50°C	E_{diss}= 194,5	E_{diss}= 279,1	E_{diss}= 291,7	E_{diss}= 189,8
T= 60°C	E_{diss}= 254,9	E_{diss}= 292,6	E_{diss}= 305,3	E_{diss}= 204,4

Conclusions

In this article four NiTi sheets have been characterized by means of tensile tests at various temperature and strain imposed. From the analysis of the results the shape memory effect is more evident at 40 °C and 4% strain. The shape memory effect is also responsible for the increase of the maximum load as the temperature increases. The best recovery percentage (80% of the deformation imposed) occurs for sample 2 and 3, at 60 °C and 4% of strain imposed. The study of the dissipated energy has demonstrated that the energy increases as the temperature increases.

In particular the sample 3 has presented interesting results (210,7 J/cm^3 at 20 °C and 305,3 J/cm^3 at 60 °C). Such experimental data will be useful for setting a constitutive model able to simulate the mechanical behavior of shape memory alloys and to evaluate the recovery capability and the dissipated energy.

References

1. H. Funakubo, *Shape Memory Alloys*, (New York, NY: Gordon and Breach Science Publishers, 1987).
2. J. Van Humbeeck and R. Stalmans, *Shape Memory Materials*, (Cambridge, Cambridge University Press, 1998).
3. R. Pfeifer et al., "Adaptable Orthopedic Shape Memory Implants", *Procedia CIRP,* 5 (2013) 253-258.
4. E.T.F. Chau et al., "A technical and economical appraisal of shape memory alloys for aerospace application", *Materials Science and Engineering A*, 438-440 (2006) 589-592.
5. G. Song, N. Ma and H.N. Li, Applications of shape memory alloys in civil structures, *Engineering Structures*, 28 (2006) 1266-1274.
6. G. Costanza, M.E. Tata and C. Calisti, "Nitinol one-way shape memory springs: thermomechanical characterization and actuator design", Sensors & Actuators: A. Physical, 157 (2010), 113-117.
7. M. Dolce and D. Cardone, "Mechanical behavior of shape memory alloys for seismic applications. Austenite NiTi wires subjected to tension", *International Journal of Mechanical Science*, 43 (2001) 2657-2677.
8. G. Costanza, S. Paoloni and M. E. Tata, "IR thermography and resistivity investigations on Ni-Ti Shape Memory alloy", *Key Engineering Materials*, 605 (2014), 23-26.

EVALUATION OF FORGED ALUMINUM MATRIX COMPOSITES REINFORCED WITH CARBON NANOTUBES (CNTs) FABRICATED BY COMPOSITE GAS GENERATOR (CGG) PROCESS

Youngsek Yang, Myeonghak Kang, Geunwoo Lee
Foosung Precision Ind. Co., Ltd.
60 HyundaiKia-Ro,Paltan,Hwaseong,Gyeonggi,South Korea

Keywords: Aluminum matrix composites, CGG, CNTs, Melt forging

Abstract

In this study, aluminum based metal matrix composites(ALMCs) with multi-walled carbon nanotubes(CNTs) as reinforcement was produced by a recently developed composite gas generator(CGG) process. Furthermore, the liquid composites with well dispersed CNTs was forged to the slug shape part by the melt forging process, followed by heat treatment with several holding times, and microstructures and mechanical properties of forged products also were evaluated.

Results shown that mechanical properties were enhanced compared to those of products without reinforcements.

Introduction

Multi-walled carbon nanotubes(CNTs), for the last few decades, has been used as a reinforcement to develop various materials(Polymer, Ceramic and Metals) based matrix composites because of its excellent strength(up to 100GPa), ultra high Young's modulus(up to 1000GPa) and high thermal conductivity(6000$Wm^{-1}K^{-1}$) [1,2]

Many researches with CNTs reinforcement have been carried out on polymer matrix composites, whereas studies of metal matrix reinforced with CNTs are few. [3,4,5,6]

Considering the need for structural materials with light weight and high strength like aluminum alloy matrix composites in aircraft and automobile industry to reduce CO_2 emission and to increase the fuel efficiency, it's definitely disappointing fact.

On the other hand, it's disproved that studies toward development of CNTs reinforced metal matrix composites (MMCs) are quite difficult. [6]

CNTs tends to easily agglomerate to several tens micron clusters due to a strong Van der waals forces between individual CNTs and has a poor wettability with metal matrix and further is concerned about its heat damage under high temperature. These challenges of CNTs lead to limited application of matrix materials and manufacturing routes, and this consequently makes few studies of MMCs reinforced with CNTs as compared to those on polymer matrix.

In case of studies on aluminum matrix composites (ALMCs) reinforced with CNTs which is well known as a promising structural material in aircraft and automobile industry, there were very few studies and most of them further were on powder metallurgy(PM) rout. [7,8]

The ultimate goal of all studies is to commercialize products, to do that, from the initial stage of study, economical efficiency must be considered in manufacturing process and matrix material choice.

Therefore, liquid metal process to develop MMCs reinforced with CNTs is an essential route, even though there are significant challenges like agglomeration, poor wettability, interfacial bond and heat damage of CNTs in the liquid metal. [9]

A recently developed the Composite Gas Generator(CGG) process has a strongpoint to deliver well-dispersed reinforcements with inert gas into the molten metal. In the recent papers, Yang was the first to report the result of successfully manufacturing ALMCs reinforced with carbon nanofibers(CNFs) and silicon carbide(SiC) reinforcements in the liquid metal process by CGG process and also used the combination of CGG and spray forming process to make ALMCs preform billet with well dispersed CNFs and extruded the perform, followed by heat treatment and reported improved mechanical properties. [10,11,12]

In this study, the CGG process was used to make aluminum alloy liquid metal with a well dispersed CNTs, and the melt forging was carried out on fabricating the slug shape of forged products, followed by heat treatment with several holding time. The forged and heat treated ALMCs reinforced with CNTs was evaluated by micro structures and mechanical properties.

Experimental

In this study, the heat treatable aluminum alloy was independently designed to use as metal matrix alloy shown in Table 1.

Table 1. The compositions of matrix alloy Unit:wt%

	Cu	Si	Fe	Mg	Ti	C	Al
Design	5~7	1~1.5	0.8~1.3	0.5~1	0.1~0.2	1~2	Balanced
Target	6	1.25	1	0.7	0.15	1.5	Balanced

Multi-walled carbon nanotubes(CNTs) was used as reinforcement.

According to CNTs supplier's data sheet, CNTs had 10 to 15nm diameter, 30 to 40μm length and 87 to 93% purity.

The entire experimental method and procedure in this study shows as the schematic diagram in Fig. 1

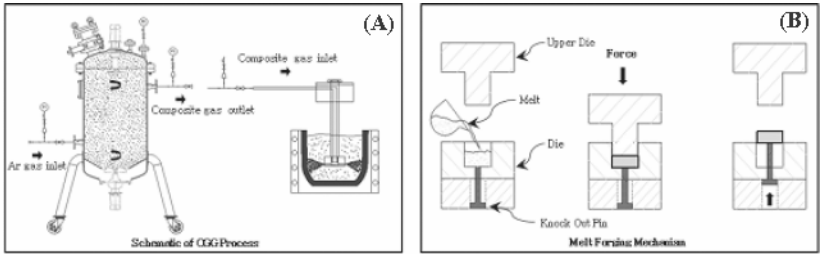

Fig. 1. Schematic Diagram of entire experimental procedure;(A)CGG process(B)Melt forging.

Each of materials was weighed to meet the target compositions based on total 15Kg capacity, and melted all materials down in the graphite crucible in the electric furnace. CNTs was calculated to be 1.7wt% composition of 15kg total melt weight and mechanically dispersed in the inside of CGG tank pressurized with inert gas. The pressurizing inert gas was argon, and its pressure was 1 bar.

Composite gas(CNTs + Ar) generated in the CGG tank contains of the well-dispersed CNTs.

Composite gas was introduced into aluminum molten metal by stirring rotor, at that time, the temperature of molten metal was 700℃, and the rotation speed of rotor was 1000rpm, and the introduction time of composite gas into the melt was about 30 minutes, and additionally the mechanical stirring with 1000rpm was carried out for 30 minutes to remove a residual gas in the molten metal prior to the melt forging process.

The composite molten metal with 700℃ temperature was poured into the forging die which was preheated to 300℃ and forged by 150 tons' power, and the forged products of slug type which were 100mm diameter and 30mm thickness were produced.

All forged products were heat treated in T6; the solid solution at 510℃ and the artificial aging at 185℃.

In the solid solution process, it was carried out for holding time to 5,10 and 20 hours, because the heat damage of CNTs had to be confirmed, but the artificial aging time with 8 hours was the same.

The forged and heat treated ALMCs products were evaluated in actual compositions, micro structures and mechanical properties.

The actual compositions were tested by the emission spectrometer and the infrared-absorption method.

The micro structures were characterized by optical microscopy, scanning electron microscopy(SEM) with energy dispersive spectroscopy(EDS).

The mechanical properties also were evaluated in tensile strength, yield strength, elongation and Young's modulus and compared to those of product without CNTs reinforcement.

Results and Discussions

As shown in Table 2, the actual compositions of both materials; with reinforcement(ALMCs) and without reinforcement(pure matrix) were tested by the emission spectrometer and the infrared-absorption method.

Table2. Actual compositions of samples Unit: wt%

Samples	Cu	Si	Fe	Mg	Ti	C	Al
Pure matrix	6.07	1.10	0.96	0.55	0.12	0.01	Balanced
ALMCs	5.62	1.33	0.97	0.57	0.12	1.52	Balanced

The actual content of C in ALMCs fabricated in this study is 1.52wt%, and this result say that CNTs was successfully introduced into the metal matrix.

Fig.2 shows slug type products of ALMCs reinforced with CNTs, which produced by CGG and melt forging process in this study.
All evaluation works in microstructures and mechanical properties were carried out through taking all samples from these products after T6 heat treatment.

Fig. 2 ALMCs products fabricated by CGG and melt forging in this study

Fig. 3(A) and 3(B) show optical microstructures of ALMCs reinforced with 1.52wt% CNTs. Black spots in the microstructures are clusters of CNTs, and various sizes' clusters are homogeneously dispersed in the matrix.

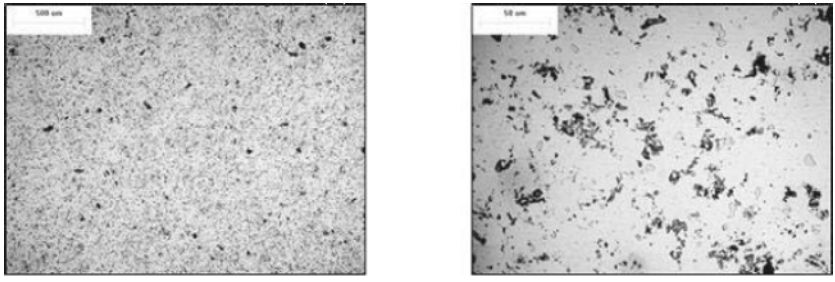

Fig .3. Optical microstructures of ALMCs;(A)100 x and (B)500 x

Fig. 4(A) and 4(B) as SEM microstructure and EDS-mapping result confirm that black spots are clusters of CNTs.

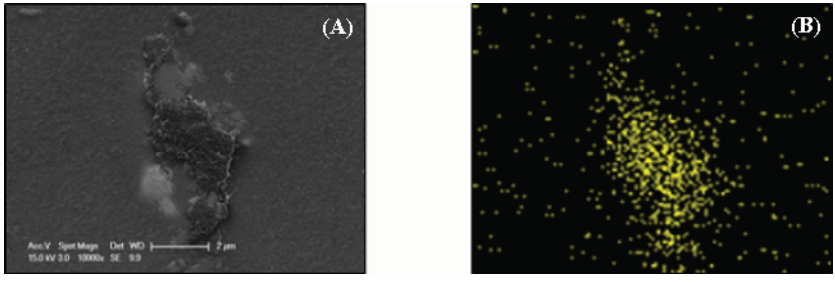

Fig. 4(A) SEM microscopy of CNTs cluster and(B)EDS-mapping of CNTs cluster

The sizes of most observed clusters in the microstructures are less than 5μm although some clusters are showed in almost 10μm in size.
It's not clear that these clusters in the matrix were generated in CGG process, because many clusters were observed in CNTs raw material at the import inspection stage. Fig.5 shows the natural clusters in CNTs raw material.
The problem is that there is no way to sort the natural clusters from CNTs raw material at the moment.

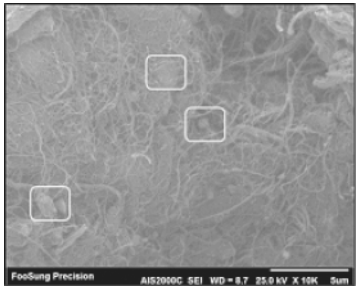

Fig.5.Natural CNTs Clusters from CNTs raw material

Fig. 6 and Table 3 show that mechanical properties of both materials; without CNTs and with CNTs after heat treatment, and the significant increases in tensile strength(14%), Yield strength(32%) and Young's modulus(15%) of ALMCs with reinforcement are identified compared to those of aluminum alloy without reinforcement, however, the elongation of ALMCs seriously declines by 55% from that of aluminum matrix alloy without reinforcement. This may be due to the clusters of CNTs which are shown as black spots in the metal matrix in Fig. 3 and confirmed by SEM and EDS-mapping in Fig.4.

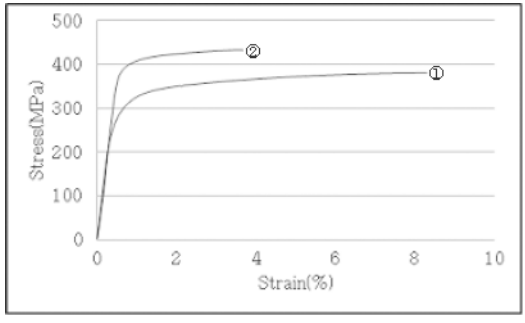

Fig.6The ambient-temperature stress-strain curves of ①Pure aluminum matrix without CNTs and ②ALMCs reinforced with CNTs.

Table 3 Results of the ambient-temperature mechanical properties of samples

Samples	UTS (MPa)	YS (MPa)	Elongation (%)	Young's Modulus (GPa)
Pure matrix	381	304	8.3	78.6
ALMCs	433	401	3.7	90.4

Fig. 7 and Table 4 show mechanical properties of ALMCs by different holding time in solid solution of heat treatment process.

As shown in the result, mechanical properties are decreased as holding time increased. This may be due to CNTs was damaged by heat exposure for long time relatively, but this issue need to be confirmed by supplementary research in future.

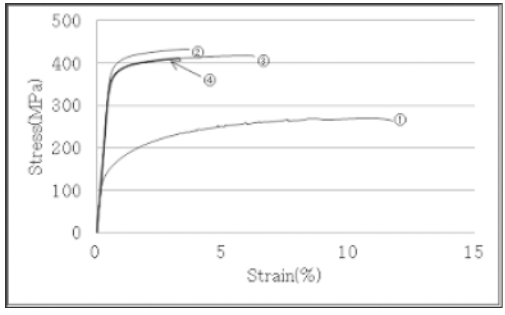

Fig.7. The ambient-temperature stress-strain curves of T6 samples with different holding time in solid solution; ①As-extruded,②5hrs,③10hrs and④20hrs.

Table 4. Results of the ambient-temperature mechanical properties of T6 samples with different holding time in solid solution process.

Holding Time (hr)	UTS (MPa)	YS (MPa)	Elongation (%)	Young's Modulus (GPa)
As-Extruded	269	196	11.8	-
5	433	401	3.7	90.4
10	417	379	6.5	-
20	411	380	3.5	-

Fig.8(A) shows an overall tensile fracture morphology with typical rough fracture surface included in voids, dimples, clusters and microscopic cracks.

Especially, various clusters of CNTs in the fracture surface are shown, and Fig. 8(B) and(C) show representative clusters of CNTs in the fracture surface.

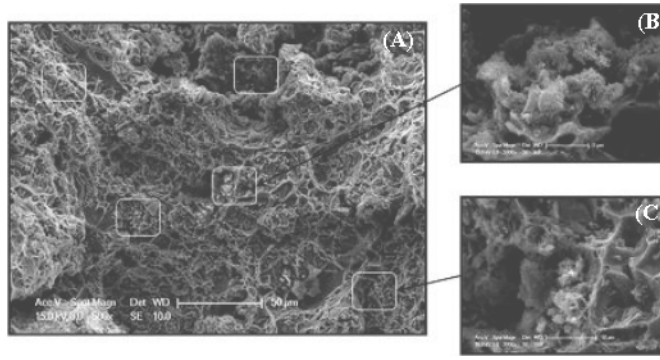

Fig. 8.The fracture morphology(A) and representative clusters in the matrix(B)and(C) Of ALMCs.

Fig. 9(A) shows the high magnification observation of fracture surface, and Fig.9(B) and (C) show individual CNTs embedded in the aluminum matrix. These CNTs embedded in the aluminum matrix may affect improving mechanical properties of ALMCs compared to those of the matrix alloy without reinforcement.

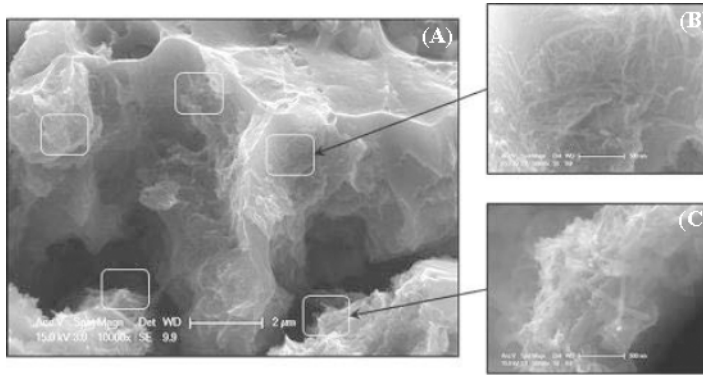

Fig. 9 The high magnification of fracture surface (A) and representative CNTs embedded in the ALMCs matrix.

Conclusions

1. Aluminum matrix composites products reinforced with well-dispersed CNTs were successfully fabricated by CGG and melt forging process based on the liquid metal process.
2. Enhanced mechanical properties were identified by the ambient-temperature mechanical test, which tensile strength (14%), yield strength (32%) and Young's modulus(15%) were increased compared to those of the aluminum matrix without CNTs.

3. Elongation result was seriously 55% drop from that of the aluminum matrix without CNTs, the main reason confirmed CNTs clusters in the matrix by micro structure inspection.
4. Many individual CNTs embedded in the matrix were also identified by SEM.

Acknowledgement

The authors wish to acknowledge financial support from WPM(World Premier Materials) research project, which is funded by Korea government**.**

References

1. S.Berber, Y.K.Kwon and D.Tomanek: Phys. Rev. Lett.,2000,84,4613-4616
2. P.Kim, L.Shi, A.Majumdar and P.L.McEuen: Phys. Rev. Lett.,2001,87,(21),215502
3. L.Bokobza:Polymer,2007,48,4907-4920
4. K.T.Lau and D. Hui: Composites B,2006,37B,437-448
5. I.Takashi: Adv. Compos. Mater.,2006,15,(1)3-37
6. S.R..Bakshi, D.Lahiri and A. Agarwal: Inter. Mater. Rev.,2010,vol55,41-64
7. C.He,N.Zhao,C.Shi,Y.Du,H.Li and Q.Cui: Adv. Mater.,2007,19,1128-1132
8. R.Zhong,H.Cong and P.Hou:Carbon,2003,41,848-851
9. S.M.Zhou,X.B.Zhang,Z.P.Ding,C.Y.Min,G.L.Xu and W.M.Zhu: Composites A,2007,38A,301-306
10. Youngsek Yang: Korea Patent(10-1436409)
11. Youngsek Yang:TMS2015, 161-169
12. Youngsek Yang:MS&T2015, 1779-1787

GAMMA AND NEUTRON SHIELDING BEHAVIOR OF SPARK PLASMA SINTERED BORON CARBIDE-TUNGSTEN BASED COMPOSITES

Salih Cagri Ozer[1], Bulent Buyuk[2], A. Beril Tugrul[2], Servet Turan[1], Onuralp Yucel[3], Gultekin Goller[3], Filiz Cinar Sahin[3]

[1]Anadolu University Department of Materials Science and Engineering; Anadolu University, Iki Eylul Campus, Eskisehir, 26555, TURKEY
[2]Istanbul Technical University Energy Institute Nuclear Researches Division; Istanbul Technical University Ayazaga Campus; Istanbul; 34469; TURKEY
[3]Istanbul Technical University Metallurgical and Materials Engineering Department; Istanbul Technical University Ayazaga Campus; Istanbul; 34469; TURKEY

Keywords: Boron carbide, Tungsten, Spark plasma sintering, Gamma transmission, Neutron transmission

Abstract

In this study gamma and neutron attenuation properties of boron carbide-tungsten (B_4C-W) based composites were investigated. B_4C-W based composites were produced by spark plasma sintering (SPS) method. W additions were 5%, 10%, and 15% by volume. Samples with theoretical densities were obtained. Occurance of W_2B_5 phase with a reaction between B_4C and W particles were observed with XRD and SEM investigations. The materials were subjected to gamma and neutron sources. Cs-137 and Co-60 gamma radioisotopes were used as gamma, and Pu-Be Neutron Howitzer was used as neutron source. Linear and mass attenuation coefficients of the composites were carried out for gamma sources by using gamma transmission technique. Furthermore, total macroscopic cross-sections of the samples were determined for Pu-Be neutrons. In conclusion, increasing W ratio in the B_4C-W system causes higher gamma attenuation behavior for gamma sources, but the macroscopic cross-sections of the B_4C-W composites decrease by increasing W concentration.

Introduction

Boron carbide (B_4C) is a suitable material for nuclear technology because it has very high hardness, high melting point, low density and especially high thermal neutron capture cross-section [1, 2]. Since B_4C based materials are commonly used in nuclear applications, there are many studies on radiation effects on B_4C and related materials [3-5].
Due to the strong covalent bonding of B and C atoms, it is hard to sinter monolithic B_4C to high relative densities [1]. So additives like Al, SiC, B, TiB_2, etc. are used to increase the density of boron carbide [1-2, 6-7]. There are several methods (e.g. pressureless sintering, hot pressing, spark plasma sintering) are available for consolidating B_4C and related materials which have different results on the materials' properties [6-11]. Spark plasma sintering (SPS) is a relatively new process that enables rapid heating rate and lower sintering temperatures which prevents grain coarsening during sintering. B_4C having a high melting point (~2450°C) and strong covalent bonding requires high sintering temperatures and long sintering time in order to be sintered to near theoretical densities in other sintering methods such as hot pressing [1], and pressureless sintering by using

sintering aids [1]. SPS overcomes many disadvantages of these sintering methods and provides highly dense products within short times and low temperatures.
In this study B_4C based composites with 5, 10 and 15 vol. % W addition were produced by using SPS method and phase analysis with microstructural and nuclear characterization of those composites were performed.

Experimental

B_4C-W based composites were produced by SPS method. Commercial HS grade B_4C powders from H.C. Starck Co., with an average particle size of 0.7 µm (99.5% purity) and metallic tungsten powder from Alpha Aeser Co. with an average particle size of 60 µm (99.8% purity) were used to produce composites. Tungsten additive was used as 5, 10 and 15 vol. % in the compositions. Powder mixtures were prepared by mixing B_4C and W powders with WC balls in Merck quality ethanol medium by ball milling for 24 hours. After screening and drying the powders, they were loaded in a graphite die with graphite sheets between the die and the powder for consolidation in SPS. B_4C-W based samples having 50x50mm square cross section were consolidated in SPS and their radiation shielding properties were analyzed for these dimensions for the first time in literature.
The samples were sintered by using the SPS apparatus (SPS-7.40MK-VII, SPS Syntex Inc.). 100°C/min heating rate was used with 40 MPa pressure from room temperature to sintering temperatures between 1500 and 1600°C with 4 minute soaking time. Densities of the compacted samples were measured by the Archimedes method.
Phase analysis was carried out after sintering by Rigaku Rint 2200 X-ray diffractometer.
Microstructural characterization was carried out by Zeiss Supra 50VP scanning electron microscope, and images were taken by back scatter electron (BSE) and In-Lens modes.
Gamma and neutron transmission techniques were used in order to analyze radiation attenuation behavior of the composites.

Results and Discussion

Starting powder compositions, SPS process parameters and measured relative density values of the samples were given in Table I. All samples have 50x50 mm^2 square surface area and ≈5mm thickness.
Maximum relative density values were achieved at the highest sintering temperature (1600°C). The reference sample (B_4C without W additive) have 97.9% relative density whereas the other samples have higher relative densities at higher sintering temperatures. Samples with 15 vol. % W additive reached theoretical densities at both 1550 and 1600°C sintering temperature.

Table I. Density values of B_4C ceramics with different W contents.

Starting Powder	SPS Parameters	Relative Density
B_4C powder	1550°C, 40MPa, 4min.	97.9
B_4C+5 vol.%W powder	1500°C, 40MPa, 4min.	90.73
B_4C+5 vol.%W powder	1550°C, 40MPa, 4min.	92.02
B_4C+5 vol.%W powder	1600°C, 40MPa, 4min.	95.94
B_4C+10 vol.%W powder	1500°C, 40MPa, 4min.	92.92
B_4C+10 vol.%W powder	1550°C, 40MPa, 4min.	93.93
B_4C+10 vol.%W powder	1600°C, 40MPa, 4min.	97.10
B_4C+15 vol.%W powder	1500°C, 40MPa, 4min.	96.77
B_4C+15 vol.%W powder	1550°C, 40MPa, 4min.	100
B_4C+15 vol.%W powder	1600°C, 40MPa, 4min.	100

As seen in Table I, relative density values increase with both increasing sintering temperature and W additive.

XRD analysis results of the samples were given in Figure 1. All diffraction patterns show B_4C and W_2B_5 peaks, meaning a reaction between B_4C and metallic W powders occurs during SPS process as shown in Equation 1. There are also graphite peaks present in the samples containing 10 and 15 vol. % W. Graphite peaks could not be observed at 5 vol. % W containing samples. It was believed that the low quantity of graphite produced during reaction was below the XRD detection limit.

$$5B_4C+8W \rightarrow 4W_2B_5+5C \quad (1)$$

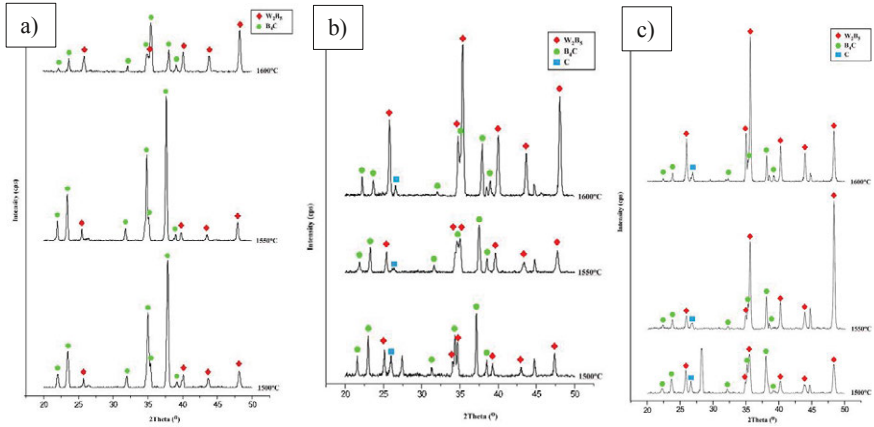

Figure 1. XRD analysis of the samples; a) B_4C+5 vol.%W, b) B_4C+10 vol.%W, c) B_4C+15 vol.%W.

Polished surface SEM images of the samples were given in Figure 2. Both BSE and In-Lens images were taken from the same areas. Due to the high density difference between W_2B_5 phase and B_4C/graphite phases, it is rather difficult to investigate porosities and lighter phases (B_4C and graphite) in BSE mode. White phases are W_2B_5, black phases are B_4C at BSE images. Graphite

phases which could not be observed at BSE images may be seen at In-Lens images. Graphite phase which could not be observed by XRD in 5 vol. % W containing sample is seen in In-Lens image of the sample. With higher W addition, graphite phase occurs between B_4C-W_2B_5 as well as B_4C matrix. Increase of the graphite quantity deteriorates mechanical properties, given elsewhere [12].

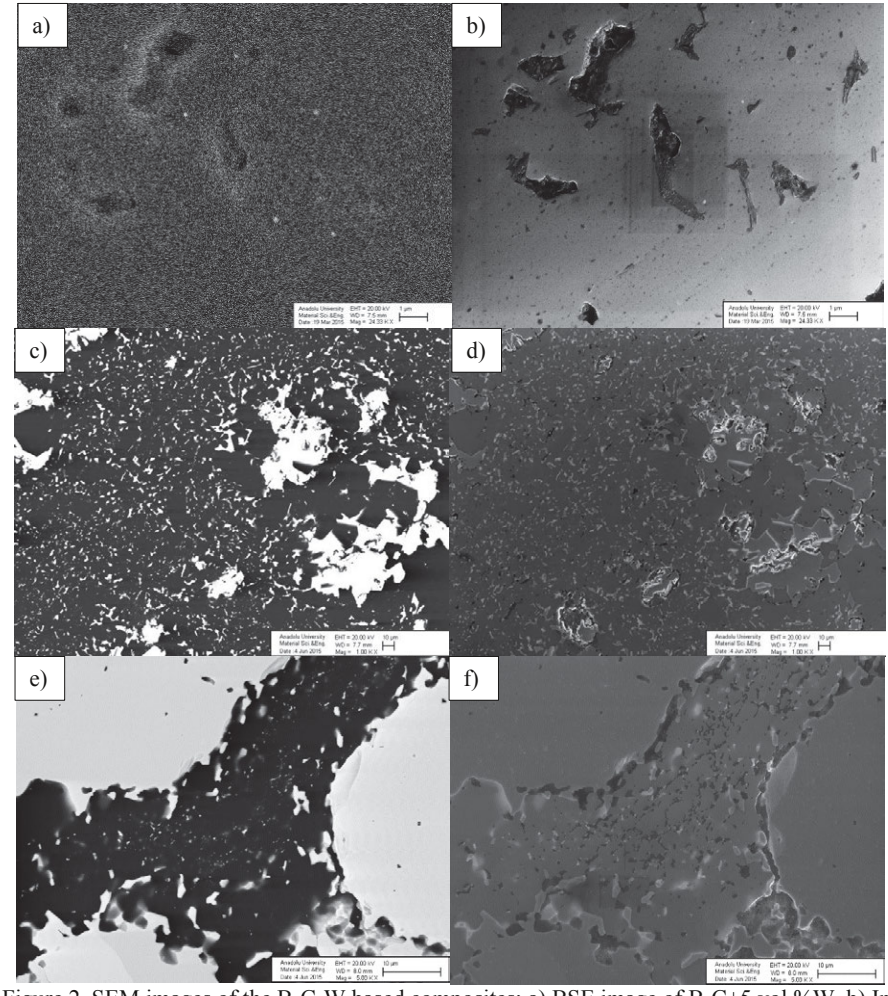

Figure 2. SEM images of the B_4C-W based composites; a) BSE image of B_4C+5 vol.%W, b) In-Lens image of B_4C+5 vol.%W, c) BSE image of B_4C+10 vol.%W, d) In-Lens image of B_4C+10 vol.%W, e) BSE image of B_4C+15 vol.%W, f) In-Lens image of B_4C+15 vol.%W.

Gamma and neutron transmission techniques were used in order to analyze radiation attenuation behavior of the composites [6,7]. The radiation intensity was measured with B_4C-W based samples and without the material as a reference, then the results were evaluated.
Cs-137 which has a single gamma energy peak at 0.662 MeV and Co-60 which has two gamma energy peaks at 1.17 and 1.33 MeV (mean energy 1.25 MeV) radioisotopes were used as gamma radiation source. For each material, gamma and thermal neutron counts (I) were detected at increasing material thicknesses and relative counts (I/I_0) were calculated.
Firstly, initial radiation intensity (I_0) was measured without B_4C-W based sample. Then, for each composition, gamma and neutron counts (I) were detected at different material thicknesses and relative counts (I/I_0) were calculated and given in Table II.

Table II. The Relative Count-Material Thickness values of the B_4C-W based composites for Cs-137 and Co-60 gamma, and Pu-Be thermal neutron sources.

Composition	Thickness (cm)	Cs-137 Relative Count	Co-60 Relative Count	Pu-Be Relative Count
I_0	0	1	1	1
B_4C	0,495	0,911	0,952	0.599
	0,98	0,85	0,907	0.478
	1,481	0,801	0,84	0.362
	1,97	0,742	0,784	0.278
	2,471	0,676	0,743	0.227
B_4C+5% W	0,5573	0,84279	0,8721	0.665
	1,1186	0,70925	0,77329	0.534
	1,6699	0,62617	0,68186	0.433
	2,2381	0,53863	0,60769	0.355
	2,7958	0,45556	0,57023	-
B_4C+10% W	0,5026	0,79422	0,8938	0.716
	1,0075	0,67928	0,76799	0.578
	1,5242	0,55678	0,66427	0.486
	2,0344	0,43909	0,60811	0.368
	2,5425	0,40262	0,54236	-
B_4C+15% W	0,4547	0,81397	0,87636	0.732
	0,9125	0,67142	0,74437	0.612
	1,3768	0,50321	0,66397	0.534
	1,8389	0,42979	0,61363	0.432
	2,2871	0,33215	0,56559	-

Relative Intensity-Material Thickness graphs were drawn for the reference monolithic B_4C, and W containing samples against gamma and neutron radiation sources were given Figure 3.

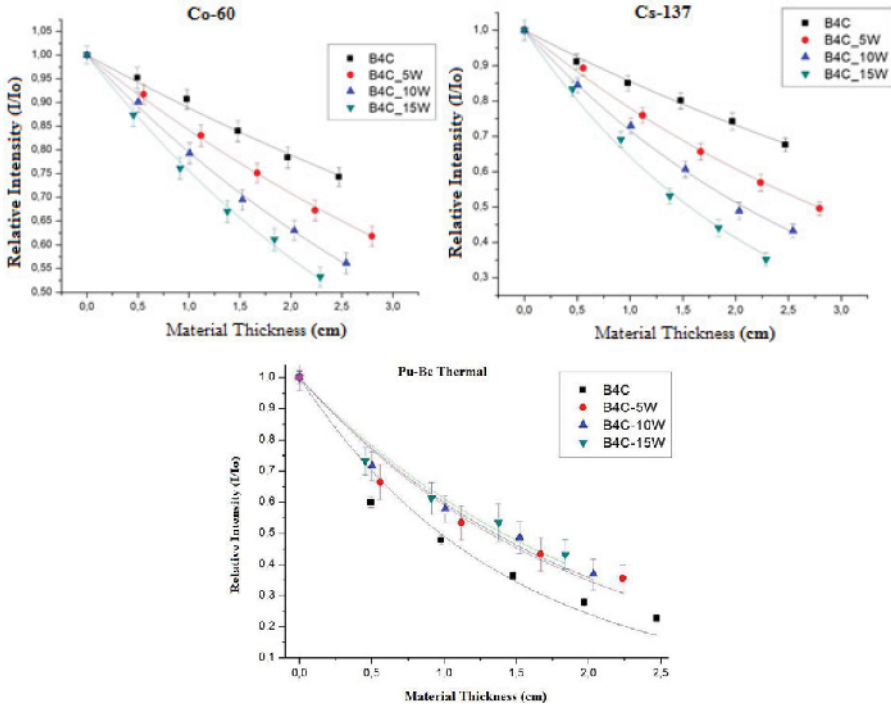

Fig 3. Relative Intensity-Material Thickness graphs of B_4C-W based composites for Cs-137 and Co-60 gamma radioisotopes, and Pu-Be thermal neutron sources.

Linear and mass attenuation coefficients (μ and μ_m) for Cs-137 and Co-60 values were determined by fitting the graphs exponentially, and total macroscopic cross-section (Σ_t) for thermal neutron values were calculated by fitting the graphs according to Beer Lambert's formula (Equation 2) in order to analyse the effect of W addition on B_4C's radiation shielding abilities and given in Table III and Figure 4.

$$I = I_0 e^{\Sigma_{eff} x} \tag{2}$$

Table III. Linear and mass attenuation coefficients, and total macroscopic cross-sections of monolithic B_4C and the B_4C-W based composites

Composition	Linear Attenuation Coefficients (μ, cm^{-1})		Mass Attenuation Coefficients (μ_m, 10^{-2} cm^2/g)		Total Macroscopic Cross-sections (Σ_t, cm^{-1})
	Cs-137	Co-60	Cs-137	Co-60	Pu-Be
B_4C	0.157	0.118	6.359	4.779	0.712
B_4C+5% W	0.254	0.172	8.230	5.685	0.528
B_4C+10% W	0.339	0.229	8.289	5.700	0.514
B_4C+15% W	0.449	0.280	8.503	5.386	0.493

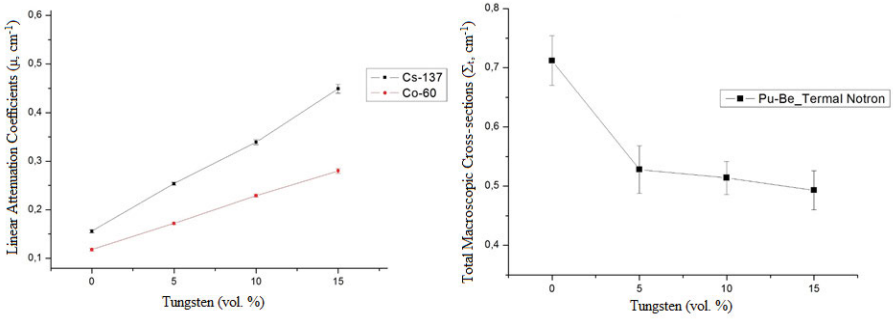

Figure 4. Linear attenuation coefficient, and total macroscopic cross-section graphs of monolithic B_4C and the B_4C-W based composites for Cs-137 and Co-60 gamma radioisotopes, and Pu-Be thermal neutron sources.

It was seen that as the W addition in B_4C-W based composites was increased, attenuation coefficients against Cs-137 and Co-60 gamma radiation were increased as well. It may be expressed as materials containing higher W additive has a higher gamma radiation shielding ability then the materials with lower W quantity. But addition of W also lowers materials' ability to shield against thermal neutrons.

Conclusions

Adding metallic W improves the sinterability and densification of B_4C. The highest density of B_4C-W based composites were the ones spark plasma sintered at 1550 and 1600°C with 4 minutes soaking time under 40 MPa applied pressure with 15 vol. % W addition.
According to XRD and SEM analysis a reaction took place during spark plasma sintering between B_4C and metallic W, which results a final structure of W_2B_5 and graphite phases inside B_4C matrix. Radiation shielding properties of B_4C-W based composites were investigated against gamma radiation (Cs-137 and Co-60) and thermal neutrons with gamma and neutron transmission techniques. Increasing W content in B_4C improves gamma shielding properties whereas provides lower thermal neutron shielding capacity compared to monolithic B_4C.

Acknowledgement

The authors would like to express their gratitude to TUBITAK (The Scientific and Technological Research Council of Turkey) for their financial support for the project number *213M163* "*Production and optimization of various B_4C-Metal Composites by single-step spark plasma sintering method for ballistic and nuclear applications*".

References

1. F. Thévenot, "Boron Carbide - A Comprehensive Review," *Journal of the European Ceramic Society,* 6 (1990), 205-225.

2. A.K. Suri, C.Subramanian, J.K. Sonber, and T.S.R.Ch. Murty, “Synthesis and Consolidation of Boron Carbide: A Review,” *International Materials Reviews,* 55 (2010), 4-40.
3. D. Simeone, C. Mallet, P. Dubuisson, G. Baldinozzi, C. Gervais, and J. Maquet, “Study of Boron Carbide Evolution Under Neutron Irradiation by Raman Spectroscopy,” *Journal of Nuclear Materials,* 277 (2000), 1-10.
4. Y. Morohashi, T. Maruyama, T. Donomare, Y. Tachi, and S. Onose, “Neutron irradiation effect on isotopically tailored $^{11}B_4C$,” *Journal of Nuclear Science and Technology*, 45 (2008), 867-872.
5. X. Deschanels, D. Simeone, and J.P. Bonal, “Determination of the lithium diffusion coefficient in irradiated boron carbide pellets,” *Journal of Nuclear Materials,* 265 (1999), 321-324.
6. B. Buyuk, and A.B. Tugrul, “Gamma and Neutron Attenuation Behaviours of Boron Carbide-Silicon Carbide Composites,” *Annals of Nuclear Energy,* 71 (2014), 46-51.
7. B. Buyuk, and A.B. Tugrul, “An Investigation on Gamma Attenuation Behaviour of Titanium Diboride Reinforced Boron Carbide-Silicon Carbide Composites,” *Radiation Physics and Chemistry*, 97 (2014), 354–359.
8. S. Hayun, S. Kalabukov, V. Ezersky, M.P. Dariel, and N. Frage, “Microstructural Characterization of Spark Plasma Sintered Boron Carbide Ceramics,” *Ceramics International,* 36 (2010), 451-457.
9. F.C. Sahin, B. Apak, I. Akin, H.E. Kanbur, D.H. Genckan, A. Turan, G. Goller, and O. Yucel, “Spark Plasma Sintering of B_4C-SiC Composites,” *Solid State Sciences,* 14 (2012), 1660-1663.
10. F.C. Sahin, and A. Yesilcubuk, “Reactive Hot Pressing of B_4C-TiB_2 Composites” (Paper presented at the 11th International Conference and Exhibition of the European Ceramic Society, Krakow, Poland, 21-25 June 2009).
11. M. Cengiz, B. Yavas, Y. Celik, G. Goller, O. Yucel, and F.C. Sahin, “Spark Plasma Sintering of Boron Carbide Ceramics Using Different Sample Geometries and Dimensions,” *Acta Physica Polonica A.*, 125, (2014) 260-262.
12. S.C. Ozer, F.C. Sahin, and S. Turan, “In-lens SEM Imaging of Residual Carbon in Spark Plasma Sintered Boron Carbide-Tungsten Based Composites” (Paper presented at the 22nd National Electron Microscopy Congress*,* Istanbul, Turkey, 02-04 September 2015).

IMAGE ANALYSIS INVESTIGATING POROUS STRUCTURES OF CARBON CATHODES MATERIALS AND MELTS PENETRATION

Xiang Li[1], Jilai Xue[2], Jun Zhu[1], Shihao Song[2]
[1]State Key Laboratory of Advanced Metallurgy, University of Science and Technology Beijing, Xueyuan Road 30, 100083 Beijing, China
[2]School of Metallurgical and Ecological Engineering, University of Science and Technology Beijing, Xueyuan Road 30, 100083 Beijing, China

Keywords: Porous structure, Image analysis, Carbon, Cathode, Melts penetration.

Abstract

During aluminum electrolysis, the cryolitic melts will penetrate into the carbon cathode block through porous structure. Na generated from the cryolitic melts will lead cathode expansion and deterioration. This work is aimed to give a better understanding of the relationship between the pore structure and the cryolitic melts penetration. Image analysis was applied to characterize the porous structures of the virgin cathode. Penetration experiments with carbon cathode materials were carried out and the penetrated melts distribution in the cathode samples were analyzed by SEM-EDS. The quantitative information of porous structures shows 50-80% pores in cathode external areas filled by melts after 180 min electrolysis tests. Most of melts penetrated into the narrow open pores. Selective mechanism of the melts penetration into pores was discussed. The information obtained could be useful for improving control of the cathode quality through quantitative image analysis.

Introduction

The carbon materials are widely used in chemical industry, metallurgy and electrochemistry due to its good conductivity and corrosion resistance. The carbon cathode materials used in aluminum reduction not only need to transmit electron and reduce metal, but also contain the electrolyte and aluminum melts during the temperature of 950 ºC. So the requirements to property and quality of carbon cathode materials are comparatively high [1]. At present, the main method for improving the carbon cathode property are increasing graphite content or baking temperature which are both considered from the micro level. It will make the carbon atoms arrange regularly and then conductivity and corrosion resistance are improved [2]. Recently the researcher have found that optimization of cathode block shape is benefit for the aluminum electrolysis process from experiment and industry [3]. However, the development process of improved method is from microscale to macroscale, the mesoscale in between is ignored. The porous structure of the carbon cathode belong to the mesoscale are not paid enough attention, but numerous researches show the channel for melts penetration into cathode inside is porous structure which is the main reason of cathode shorter service life [4-5]. Therefore it is necessary to know the relationship between porous structures and melts penetration. Furthermore, the way of porous structure effects on melts penetration into the cathode should be investigated to fill the vacancy of mesoscale relationship between structure and property. The obtained information in this investigation can be useful to improve the quality of cathode products and the performance of aluminum reduction cells.

The carbon materials used as cathode usually contain about 20% pores produced in forming and baking stage. The methods applied currently to character porous structure are gas adsorption, mercury intrusion method, X-ray small angle scattering and image analysis [6-7]. These methods are suitable for different diameter pore size and pores structures. Especially, image analysis is always applied to consider the connection conditions intuitively [8-9]. It is confirmed that the assessment of 3D geometry can be reflected by 2D sections of projections through stereolog for charactering porous structure.

In this paper, in order to investigate the correlation between melts penetration and porous structures of industry cathode, graphitic cathodes made in lab were characterized by image analysis firstly. And then, the high temperature electrolysis experiments were carried out by rotating electrode method. The penetrated melts distribution in the cathode samples were analyzed by SEM-EDS

Experimental Procedure

Preparation of Cathode Samples

Graphite particles with varied granularity were mixed with a constant amount of medium hard pitch in a TH1L mixing machine at 140 °C. And then the green samples were formed at a pressure varied from 12 MPa, 20Mpa, 28Mpa to 36 MPa. They were baked at 1200 ºC in a vessel packed with fresh carbonaceous powders. The testing samples were in cylindrical form($\Phi 25 \times 60$ mm).

Melts Penetration Experiments

Figure 1 shows the experimental set-up for melts penetration during aluminum electrolysis. The electrolysis cell was placed in a vertical tube furnace. The melts penetration experiments were carried out with rotating cathode. During the electrolysis, the cylindrical cathodes were immersed into the cryolitic melts 2mm and rotated at a speed of 120 r.p.m for maintaining a uniform mass transportation condition. The test temperature was 960°C, and the current density at cathode was 0.5 A/cm^2 constantly. The whole process was operated under argon atmosphere.

The electrolytic bath that all test used was prepared before each experiment. The different masses of chemicals were calculated to obtain the required cryolite ratio (CR) of 2.5 (mol NaF/ mol AlF_3) with 8% Al_2O_3 and 5% CaF_2. Cryolite is technical grade, and the purity of other chemicals (NaF, Al_2O_3, CaF_2) are all analytical pure.

Image Analysis and SEM-EDS Characterization

The test specimen for inspecting was sectioned from the cathode sample, perpendicular to its longitudinal axis. Then the half of the specimen was infused in epoxy by vacuum casting equipment. The cross section that had been ground and polished was examined by a standard polarization microscope (Leica, DMRX). The magnification was 50× for the original photographs, which should clearly show the pore edges. At the determined magnification, the images of adjacent frames were taken and matched to a mosaic image containing enough pore samples to meet the statistical demand. The images were processed again to form grayscale images.

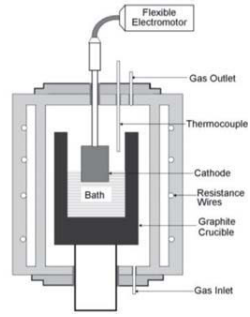

Figure 1. Schematic drawing of electrolysis testing experiment with a rotative electrode

The porous structure was analyzed using the Image J software (a public domain, Java-based image processing program developed at the National Institute of Health, USA). Image processing function was used to eliminate some miscellaneous and irrelevant details, enhancing the total image quality. Afterward, the gray images were converted in to binary images using a threshold operation to separate the pores and solid graphite. The threshold limits were set by analyzing the grey level histogram of the corresponding image. The upper threshold of the grey levels for the pores was found between 90 and 100 for all of the images used in this study. The skeletonization image was obtained using an image thinning operation to reflect the pore connectivity within the graphitic cathode materials. The thinning process is an operation that repeatedly removes pixels from the edges of objects in a binary image until they are reduced to single pixel wide skeletons (topological skeletons). Based on the quantitative stereology theory [10], the selected parameters obtained from the binary images and skeletonization images were applied to describe the porous structure of the carbon cathode samples statistically. The porosity of the sample can be calculated using the ratio of the pore area to the total area under inspection. The connectivity is calculated dividing the percentage of connecting line length by the total line length in skeletonization. The aspect ratio is the ratio between the major and minor diameters of an ellipse equivalent to an object.

The penetrated samples were cut off along the longitudinal axis, and one section was examined by SEM-EDS micro-area techniques with scanning time of 90 seconds crossing the area for each 1 mm along the axis direction, as described previously [10]. The penetrated melts in the cathode samples were then expressed against the penetration depth. Other section was taken picture for representing penetrated melts distribution by SEM.

Results and Discussion

Characterization of Porous Structures

Figure 2 shows the grayscale and binary pores images for four cathode samples. Porous structures of cathodes were processed and analyzed by Image Analysis system.

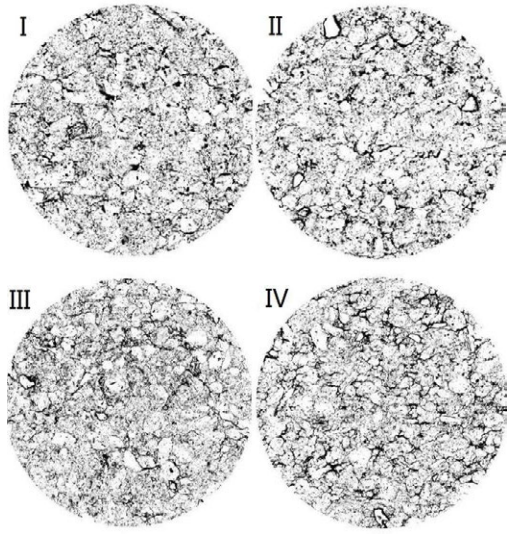

Figure 2. Binary pores images for cathode samples

With different forming pressure, when the forming pressure was 12MPa, the sample exhibited a higher total porosity (22.56%), and lowest aspect ratio (1.98). The shapes of most pores in 12 MPa made sample were close to circle. When the pressure increased, total porosity of pores first decreased and then increased, while connectivity the pores became higher. The pores on sample made by 36 MPa had the highest aspect ratio (2.21) and connectivity (37.95%). It means that high pressure made the pores elongated and connected.

Analysis of Penetrated Melts by SEM-EDS

Figure 3 comparison of four carbon cathode materials image obtained by SEM is shown. The pictures on the left are original photograph, the pictures in the middle are binary images, and the pictures on the right are skeletonization images which using single pixel wide skeletons replace the pores. The carbon matrix was black and the melts were white. The gray images were converted to binary images using a threshold operation according to grayscale to separate the carbon matrix and melts. In binary images, the penetration melts were black calculated as the area of filled pores.

Figure 4a shows the comparison result between the ratio of the penetration melts distribution area to the total area under inspection and the original porosity of the samples. The original porosity of the samples are 20-25%，while the percent of the penetration melts area are 10-20%. It means the penetration melts filled 50-80% pores. Figure 4b shows the aspect ratio comparison result between original porous structures and melts penetration distribution area. The aspect ratio of melts penetration distribution area higher than the original porous structures indicates that the melts mainly penetrated into the long and narrow pores。Figure 4c shows the connectivity of melts penetration distribution area are also higher than the original porous structures, which proves that the melts mainly penetrated into the long connected pores.

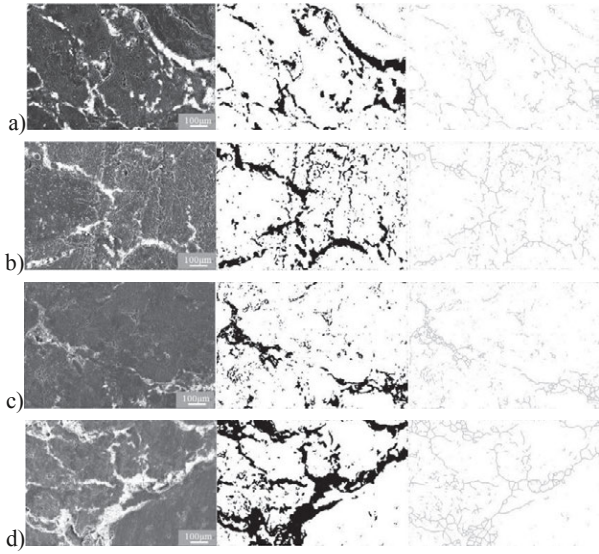

Figure 3. Carbon cathode samples SEM images, binary images and skeletonization images after testing. a) sample made by 12 Mpa, b) sample made by 20 Mpa, c) sample made by 28 Mpa, d) sample made by 36 Mpa.

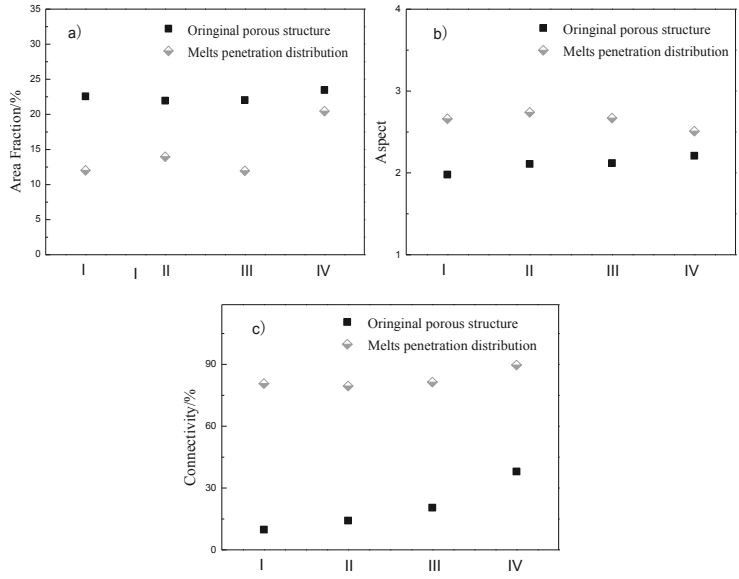

Figure 4. Structure parameters comparison between original porous structure and. melts penetration distribution, a) Area fraction, b) Aspects, c) Connectivity.

Selective Mechanism of Melts Penetrating into Pore Structure

In many SEM picture of samples after testing，penetration melts were not filled in the whole pores of large area，but in the long and narrow pores. It means there may be selective mechanism for the melts penetration into pores. The melts in the pores are acted by four kinds of forces, capillary pressure P_c, electrophoretic pressure P_1, pressure of gas in pores P_2, and frictional force of pores surface P_3.

Capillary pressure P_c can be calculated by Equation (1).

$$P_c = 2\sigma \cos\theta / r \tag{1}$$

σ is surface tension of the melts; θ is the contact angle of the melts with carbon surface; r is radius of pores channel. Zhu et al have tested the contact angle of the melts (sodium cryolite) with carbon surface is 89° after melts reached balanced state [12]. This result indicates that capillary pressure is the driving force for melts penetration into pores.

Electrophoretic pressure P_1 is decided by electric current, so it will not affect the melts selective mechanism. Pressure of gas in pores P_2 is decided by porous structure and configuration. When the pore is open, the gas will not force the melts. When the pore is blind, the gas compressed by penetration melts will produce the opposite reaction. Frictional force P_3 decided by roughness of pore walls is roughly similar. Based on analysis above, if $P_c + P_1 > P_2 + P_3$，the melts will penetrate into the pores. The main variable is the capillary pressure. When the carbon materials and melts chemical composition are certain, P_c is only decided by the pore diameter.

In Figure 5, a bigger diameter pore connected to another smaller diameter pore is shown as schematic illustrations. The capillary pressure of smaller diameter pore is higher than the bigger diameter pore, so melts will be forced into smaller diameter pore. It means that the melts will select the smaller diameter pore to penetrate without considering the pore direction. It also explains there are more melts in the sample made by 36Mpa who have more long and narrow pores.

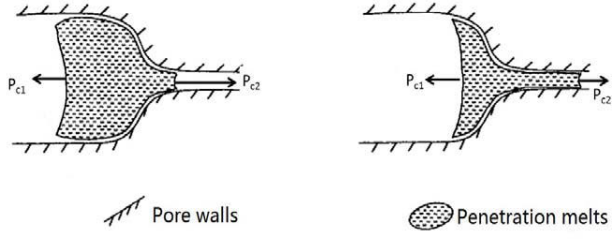

(a) (b)

Figure 5. Schematic illustrations of melts forced by capillary pressure in the pores of different diameter.

Conclusions

Image analysis indicates that a higher forming pressure can decrease the pore numbers while increase the aspect ratio and connectivity due to the pores elongated and connected. The quantitative information of porous structures shows 50-80% pores in cathode external areas filled by melts after 180 min electrolysis tests, and most of melts penetrated into long connected pores. Selective mechanism of the melts penetration into pores was discussed. The main variable is the capillary pressure which is mainly decided by pore diameter.

Acknowledgement

The work has been supported by National Natural Science Foundation of China (No. 51434005) and State Key Laboratory of Advanced Metallurgy Innovation Fund of China.

References

1. L Chauke and A M Garbers-Craig, "Reactivity between carbon cathode materials and electrolyte based on industrial and laboratory data", *Carbon*, 58 (2013), 40-45.

2. L Joncourt, et al., "Sodium reactivity with carbons", *Journal of Physics and Chemistry of Solids*, 57(1996), 877-882.

3. M Blais, M Désilets, and M Lacroix, "Optimization of the cathode block shape of an aluminum electrolysis cell", *Applied Thermal Engineering*, 58 (2013), 439-446.

4. P Y Brisson et al., "X-ray Potoelectron Spectroscopy Study of Sodium Reactions in Carbon Cathode Blocks of Aluminium Oxide Reduction Cells," *Carbon*, 44 (1) (2006), 1438-1447.

5. Y Gao et al., "Characterization of Sodium and Fluoride Penetration into Carbon Cathodes by Image Analysis and SEM-EDS Techniques," *Light Metals 2011*, 2011, 1103-1107.

6. M P Sebastião, et al, "The effect of heterogeneity in the randomly etched graphite odel for carbon pore size characterization", *Carbon*, 48 (2010), 2554-2565.

7. C D Tsakirogloua, et al. "A new approach for the characterization of the pore structure of dual porosity rocks", *Chemical Engineering Science*, 64 (2009), 847-859.

8. A N Ebrahimi, et al, "Genetic algorithm-based pore network extraction from micro-computed tomography images", *Chemical Engineering Science*, 92 (2013), 157-166.

9. J Joseph, et al, "On-chip porous media: Porosity and permeability measurements", *Chemical Engineering Science*, 99 (2013), 274-283.

10. M Torsten, "A brief introduction to computer-intensive methods, with a view towards applications in spatial statistics and stereology", *Journal of Microscopy*, 242 (1) (2011), 1-9.

11. J Xue, et al., "Characterization of Sodium and Bath Penetration in Industrial Graphitic and Graphitized Cathodes," *EPD Congress Volume 2010*, 2010, 591-598.

12. J Zhu, et al., "Investigating wettability of cryolitic melts on carbon/graphite cathode materials in cooperation with image analysis", *Journal of Rare Earths*, 29(2011), Spec Issue: 19-23.

INHIBITION OF STAINLESS STEEL CORROSION IN 0.5 M H_2SO_4 IN THE PRESENCE OF $C_6H_5NH_2$

Olugbenga Adeshola OMOTOSHO, Joshua Olusegun OKENIYI, Emmanuel Izuchukwu OBI, Oluwatobi Oluwasegun SONOIKI, Segun Isaac OLADIPUPO and Timi Moses OSHIN

Mechanical Engineering Department, Covenant University, Ota 112001, Nigeria

Keywords: stainless steel metal, sulphuric acid medium, aniline corrosion inhibition, linear sweep voltametry instrument, corrosion thermodynamic property analyses, adsorption modeling.

Abstract

Inhibition of stainless steel corrosion in 0.5 M H_2SO_4 by $C_6H_5NH_2$ (Aniline) at different temperatures was experimentally studied in this paper. Corrosion rate measurements at 28°C, 45°C and 60°C were taken through linear sweep voltametry and utilised for modelling inhibition efficiency and thermodynamic properties in the acidic solution containing different concentrations of the organic chemical. Results showed that inhibition of stainless steel in 0.5 M H_2SO_4 increased with increasing temperature for most of the different concentrations of $C_6H_5NH_2$ employed. Optimal inhibition efficiency ranged from η = 26.49% by 0.043 M $C_6H_5NH_2$ at 28°C, through η = 88.99% by 0.021 M $C_6H_5NH_2$ at 45°C up to η = 96.68% by 0.043 M $C_6H_5NH_2$ at 60°C. Also, thermodynamic property analyses showed that apparent activating energy decreases from the uninhibited, 0 M $C_6H_5NH_2$, to the optimally inhibiting 0.043 M $C_6H_5NH_2$ containing medium, which suggests $C_6H_5NH_2$ adsorption drives the inhibition effects observed.

Introduction

Corrosion of metals in service is a major industrial challenge that has received attention worldwide. Most of the developed countries have sponsored research into ascertaining the cost of corrosion to their economy, and the results of such findings have necessitated the funding of corrosion research that provides solutions to many of these problems. Though research efforts have been intensified in corrosion studies, it has however been focused primarily on the corrosion of mild steel in acidic media [1-7] and steel reinforcement in concrete [8-13]. A scrutiny of literature on corrosion research shows that a large percentage of the investigations neglected studies on stainless steel corrosion in acidic media. Most of the studies considered identified the use of inhibitors as an economical and effective solution to corrosion control when compared to other techniques [11-13]. Literatures on stainless steel corrosion in sulphuric acid media at slightly elevated temperature is scarce [14-15], so are the studies conducted for stainless steel in hydrochloric acid media [7,16]. However, because of the importance attached to sulphuric acid and the tendency of stainless steel to display drastically different corrosion rate, it is necessary to carry out investigation on stainless steel corrosion protection in sulphuric acid.

Sulphuric acid is often referred to as the king of chemicals because of its large number of applications. It is used directly and indirectly in the manufacture of almost everything. It is used for the production of lead-acid batteries, fertilizers, detergents, pulp/paper, petroleum refining, and to clean up rust in steel that is used for vehicles and household appliances [16]. Stainless steel materials are used for facilities that utilize sulphuric acid as feed stock in its operation. Thus, the material is exposed to extremely harsh conditions which it needs to withstand. Residual stress levels are also encountered in the form of mechanical stresses during fabrication and as time progresses in the lifetime of the facility. The behaviour of stainless steel passive film in aqueous acid solutions is dual in character. It is made up of the inner and outer layer consisting of an intense chromium oxide barrier and an iron-dominant layer with hydroxide deposit

respectively [17]. The dual character of the passive film notwithstanding, it is susceptible to localized attack in areas with residual stress or flaws by aggressive acidic ions [7,17]. This leads to severe catastrophic damage that is, oftentimes, insidious.

In order to mitigate the corrosion of stainless steel materials in acidic environment, it is expedient and economical to make use of inhibitors. In specific terms this work aims to make use of $C_6H_5NH_2$. It contains heterocyclic nitrogen atoms known to be responsible for activities that tend to resist corrosion reaction. Heterocyclic nitrogen compounds adsorb on metal surface through electrostatic interactions between the positive nitrogen atoms and the negatively charged metal surface. Nitrogen atoms and the aromatic ring in the $C_6H_5NH_2$ also have the tendency to adhere on anodic sites largely because of their electron donating abilities thereby reducing the metallic dissolution. Stainless steel has the ability to form self healing film rapidly, but when under attack from aggressive acidic ions, the film is easily penetrated and metallic dissolution becomes imminent [7,18]. At slightly elevated temperature the reactivity of chromium might be affected to the extent that the introduction of an inhibitor may help retain/sustain its self healing action. This study seeks to investigate the behaviour of stainless steel in sulphuric acid at tropical ambient temperature of 28°C and at slightly elevated temperatures of 45°C and 60°C by analyses of electrochemical test-results from linear sweep voltametry instrumentation.

Experimental Methods

Materials utilized for the study were stainless steel sheet of chemical composition 15.12 Cr, 11.88 Ni and 67.51% Fe determined by an optical microscope. The sheets were mechanically cut using a guillotine into coupon sizes measuring 1x1x0.3cm. Each coupon was chemically treated according to procedures prescribed in ASTM D2688-94 R99 [19] for pre-experimental treatment of stainless steel samples for corrosion experiment. The chemically treated metal with wire connection on one side for easy linkage to the linear sweep voltametry (LSV) instrument was inserted into araldite epoxy resin system. The metal-wire-epoxy connection was then placed inside desiccators for preservation. The reagents used in this study were of analar grade. Double distilled water was used for the preparation of 0.5 M concentration of sulphuric acid used. The concentrations of the $C_6H_5NH_2$ used include 0.021 M, 0.043 M, 0.064 M, 0.086 M and 0.107 M.

Linear sweep voltametry tests were carried out to obtain potentiodynamic polarization curves using the working electrode (metal-wire-epoxy connection) with exposed surface of $1cm^2$. The working electrode together with the reference electrode (Ag/AgCl electrode) and the auxillary electrode (graphite rod) were placed inside a three electrode electrochemical cell kit (Model K47 corrosion cell kit from Princeton Applied Research, USA). Inside the cell kit was the test solution made up of 0.5 M H_2SO_4 earlier prepared with varying concentration of $C_6H_5NH_2$ all measuring about 180 ml. The working, reference and auxiliary electrodes were then connected to the Digi-Ivy potentiostat also procured from the USA. The cell kit was positioned on a heating mantle which was adjusted to the experimental temperature (45 and 60°C). Upon establishing all the connections, the Digi-Ivy potentiostat was used to obtain and record the open circuit potential (OCP). LSV examination and monitoring was carried out at a scan rate of 0.1V/s from an anodic potential of +0.5V and cathodic potential of -1.0V. By requisite analytical capability of the Digi-Ivy potentiostat, readout of corrosion rate (*CR*) was obtained which employed the formula [20]:

$$CR = \frac{0.00327 \times i_{corr} \times eq.wt}{\rho_{ms}} \quad (1)$$

Where i_{corr} = corrosion current density ($\mu A/cm^2$), ρ_{ms} = density of metallic sample (g/cm^3) and $eq.wt$ = equivalent weight (g). The *CR* then finds usefulness for modelling inhibition efficiency, η(%) using [21-23]:

$$\eta(\%) = \frac{CR_{\text{sample without } C_6H_5NH_2} - CR_{\text{sample with } C_6H_5NH_2}}{CR_{\text{sample without } C_6H_5NH_2}} \times 100 \quad (2)$$

Also, the *CR* was used for the modeling of apparent activation energy, E_a, that was associated with the acid solution with or without $C_6H_5NH_2$ through plotting that employ use of Arrhenius equation given by [24-25]:

$$CR = k \exp\left(\frac{-E_a}{RT}\right) \quad (3)$$

In which R is the molar gas constant, T is the absolute temperature and k is the Arrhenius pre-exponential constant.

Results and Discussion

Figure 1 shows the potentiodynamic polarization plots for the stainless specimens immersed in 0.5 M H_2SO_4 with and without varying $C_6H_5NH_2$ concentrations at different temperature. Figure 1(a) represents the experiment performed at ambient temperature of 28°C. Comparing the corrosion potential, E_{corr}, of the control specimen to the inhibited sample it was observed that the potential for the 0.021, 0.043 and 0.107 M specimens were more positive, while that of the 0.064 and 0.086 M specimens were less positive. This shows that the inhibitor influenced both anodic and cathodic reactions on the metal surface. Based on the comparison between the control E_{corr} value and the inhibited sample, the maximum displacement is 111 mV. The value is greater than 85 mV. For this reason the inhibitor is depicted as having anodic type behaviour [26]. In Figure 1 (b), where the experiment was performed at 45°C, the maximum E_{corr} displacement in comparison to the control is 3mV. In this case the value is less than 85 mV [26] and also negative. This implies mixed but predominantly cathodic inhibitor behaviour. The maximum E_{corr} displacement for the experiment performed at 60°C was 216 mV making the inhibitor behaviour completely anodic. All the inhibited samples with concentration of 0.021, 0.086 and 0.107 M exhibited more positive potentials.

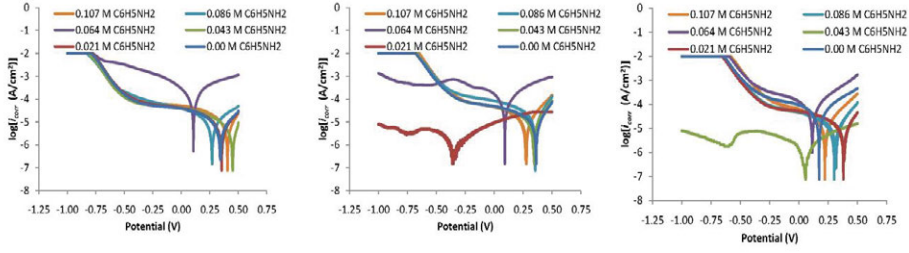

(a) (b) (c)

Figure 1: Potentiodynamic polarization plots from LSV test-results on stainless steel specimens at different temperatures (a) 28°C; (b) 45°C; (c) 60°C.

Figure 2 shows the relationship between the anodic and cathodic Tafel slopes with the inhibitor concentration at 28°C, 45°C and 60°C. It also shows the variation of the corrosion potential with the inhibitor concentration at 28°C, 45°C and 60°C. It could be observed that in the Figure 2(a), 2(b) and 2(c) the anodic and cathodic slope constants completely remained in the anodic and cathodic region as inhibitor concentration increased. However, it was discovered that the E_{corr} value strayed into the cathodic region at inhibitor concentration of 0.064 M, but thereafter drifted up into the anodic region as concentration increased to 0.086 M and 0.107 M during the 28°C

experiment in Figure 2(a). Only Figure 2(a) exhibited drastic fluctuations in the display of its anodic slope constant value. A similar behaviour was shown in Figure 2(b), but the E_{corr} value drifted into the cathodic region at inhibitor concentration of 0.021 M and strayed back afterwards into the cathodic region as concentration increased till the end of the experiment. In Figure 2(c), at inhibitor concentration of 0.043 and 0.064 M, the E_{corr} value drifted into the cathodic region but shifted thereafter into the anodic region as concentration increased. A look at the E_{corr} values in Figure 2(a), 2(b) and 2(c) shows that the displacement between the E_{corr} values of control specimen and the highest E_{corr} value of the inhibited specimen is clearly delineated forming the basis of determination as anodic, cathodic or mixed type inhibitor.

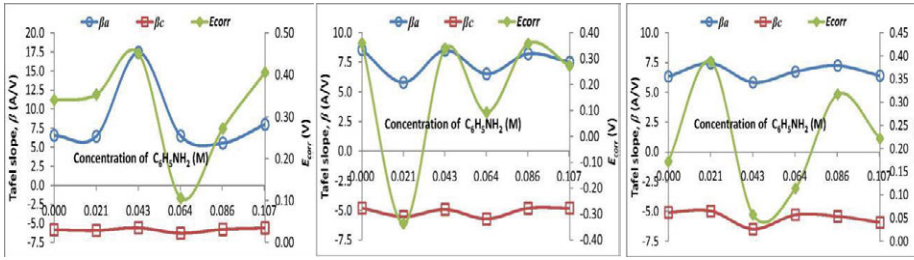

(a) (b) (c)

Figure 2: Tafel slopes and corrosion potential plots from LSV test-results of stainless steel specimens at different temperatures (a) 28°C (b) 45°C (c) 60°C.

Figure 3 show the corrosion rate behaviour of the stainless steel metal in 0.5 M H_2SO_4. From this, it could be observed that the specimens exhibited varying behaviour even as temperature increased. Lower corrosion rate values at lower inhibitor concentration was observed, though the highest values were seen in the 60°C specimen followed by the 45°C specimen. As the concentration increased to 0.064 M, the corrosion rate rates increased drastically for the three temperatures and it seemed there was reversal. The 60°C sample showed the lowest corrosion rate value, while the 28°C sample showed the highest corrosion rate value. This implies that the self healing film was adversely affected as temperature increased at 0.064 M concentration across all temperatures. The values however dropped drastically as concentration increased, possibly the concentration helped to restore the integrity of the passive film. Also, the active-passive transition normally displayed by stainless steel may be responsible for this kind of behaviour. A close look at the plot also shows that a closely related corrosion rate index was displayed at the three temperatures at concentrations of 0.043 M, 0.086 M and 0.107 M.

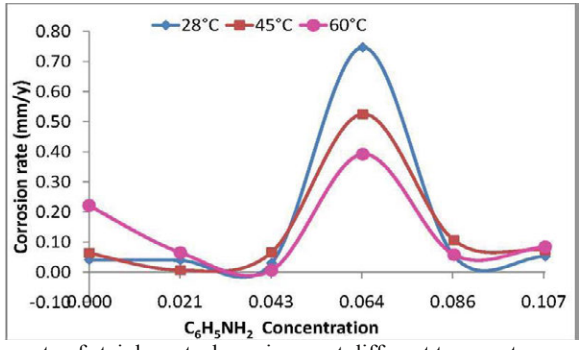

Figure 3: Corrosion rate of stainless steel specimens at different temperatures

Inhibition efficiency values, by application of Equation (2), for the stainless steel samples immersed in 0.5 M H_2SO_4 at 28°C, 45°C and 60°C in the presence of $C_6H_5NH_2$ are shown in Table 1. The 0.043 M, 0.021 M and 0.043 M concentrations showed optimum η values at temperatures of 28°C, 45°C and 60°C respectively, while the 0.064 M concentration showed the lowest η values across the three temperatures. The $C_6H_5NH_2$ inhibitor from all indications seemed to perform well at higher temperature and medium concentration. Beyond inhibitor concentration of 0.043 M for the 28 and 60°C experiment, the inhibitor became inefficient. It became inefficient for the 45°C experiment beyond 0.021 M.

Table 1. Inhibition efficiency model of $C_6H_5NH_2$ on stainless steel corrosion in H_2SO_4 at different temperatures†

$C_6H_5NH_2$ Concentration (M)	Inhibition Efficiency, η (%)		
	28°C	45°C	60°C
0.00	0.00	0.00	0.00
0.021	3.48	**88.99**	70.60
0.043	**26.49**	-3.62	**96.68**
0.064	-1709.14	-719.54	-76.93
0.086	-31.40	-65.97	73.63
0.107	-27.79	-15.13	61.66

†Optimal inhibition efficiency for each temperature is in **bold typescript**.

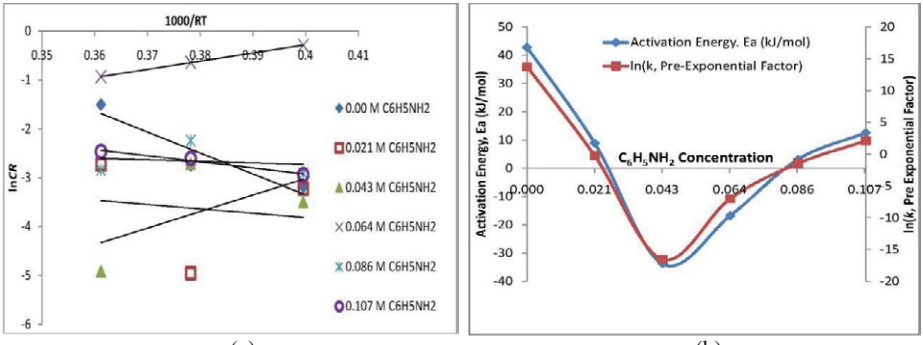

(a) (b)

Figure 4: Activation energy model for stainless steel in 0.5 M H_2SO_4 (a) Arrhenius plots (b) Plot of activation energy, E_a, and natural logarithm, ln(k), of pre-exponential factor

Figure 4a was used to investigate the temperature effect on the inhibition action of the inhibitor and the assessment of the E_a values of the corrosion process in the inhibited and control specimens for aiding more understanding on the inhibiting action. It has been shown severally from literature [27-28] that a plot of the natural logarithm of corrosion rate with T^{-1} produces a straight line function for the corrosion of metals in acidic media. The relationship given in Equation (3) was used to deduce the apparent activation energy, E_a, related to stainless steel corrosion in inhibited and uninhibited solution. The apparent activation energy obtained for the process in the control solution found to be 42.79, 8.90, -33.83, -16.78, 3.17 and 12.55 kJ/mol, respectively, for the 0.00 (control), 0.021 M, 0.043 M, 0.064 M, 0.086 M and 0.107 M inhibitor concentrations. The activation energy hindrance of the corrosion reaction reduced in the presence of the inhibitor relative to the control as a result of the adsorption on the stainless surface. Numerous literatures [29-30] have posited that a decreased E_a value for the inhibited samples in

comparison to the control medium is an indication of chemisorption. Therefore, for all the inhibited samples, the inhibitors were chemically adsorbed on the metal surface. Also, it could be noted from Figure 4 that the variance of E_a bears similarity with that of the natural logarithm of the pre-exponential factor, ln(k), which suggest that the cumulative effect of the magnitudes of E_a and of ln(k) exhibited influence on the corrosion rate and, consequently, the inhibition efficiency observed from the stainless steel immersed in the 0.5 M H_2SO_4.

Conclusions

An investigation of the utilization of $C_6H_5NH_2$ as corrosion inhibitor for stainless steel in 0.5 M H_2SO_4 was conducted. It was discovered that $C_6H_5NH_2$ acts as a good corrosion inhibitor at specific concentrations with its efficiency increasing as temperature increased. Inhibition efficiency reached its highest value of 96.68% at 60°C temperature and inhibitor concentration of 0.043 M. It was also noted that optimum inhibition efficiency was attained for each temperature; at 28°C it was 26.49% (0.043 M) and at 45°C it was 88.99% (0.021 M). The lowest activation energy of –16.5471 kJ/mol was obtained at inhibitor concentration of 0.043 M showing intensity in the lowering of the energy barrier for chemical adsorption to effectively take place. The inhibitor also exhibited different inhibition mechanism at different temperatures. At the 28°C, 45°C and 60°C the mechanisms were anodic, mixed but predominantly cathodic, and anodic behaviours. $C_6H_5NH_2$ enhanced the behaviour of the passive film formed on the stainless steel surface at specific concentration and temperatures.

References

1. O.A. Omotosho, O.O. Ajayi, K.O. Ajanaku, and V.O. Ifepe, "Environment Induced Failure of Mild Steel in 2 M Sulphuric Acid using *Chromolaena odorata." Journal of Materials and Environmental Science,* 3, 1 (2012), 66-75.

2. I.B. Obot, N.O. Obi-Egbedi, and N.W. Odozi, "Acenaphtho [1,2-b] quinoxaline as a novel corrosion inhibitor for mild steel in 0.5 M H_2SO_4." *Corrosion Science,* 52 (2010), 923-926.

3. O.A. Omotosho, O.O. Ajayi, O. Fayomi, and V.O. Ifepe, "Evaluating the deterioration behaviour of mild steel in 2 M sulphuric acid V.O. in the presence of *Butyrospermum parkii*." *Asian Journal of Applied Science,* 5, 2 (2012), 74-84.

4. I.B. Obot, E.E. Ebenso, N.O. Obi-Egbedi, S.A. Ayo, and M.G. Zuhair, "Experimental and theoretical investigations of adsorption characteristics of itraconazole as green corrosion inhibitor at a mild steel/hydrochloric acid interface." *Research in Chemical Intermediates,* 38 (2012), 1761-71.

5. O. A. Omotosho, O. O. Ajayi, O. S. Fayomi, and V. O. Ifepe, "assessing the deterioration behavior of mild steel in 2 M sulphuric acid using *Bambusa glauscescens,*" *International Journal of Applied Engineering Research Dindigul,* 2, 1 (2011), 85-97.

6. R.T. Loto, C.A. Loto, and A.P.I. Popoola, "Electrochemical effect of 1, 4-diaminobenzene on the corrosion inhibition of mild steel in dilute acid media," *Der Pharma Chemica,* 7, 5 (2015), 72-93.

7. R.T. Loto, C.A. Loto, and T. Fedotova, "Electrochemical studies of mild steel corrosion inhibition in sulphuric acid chloride by aniline." *Research on Chemical Intermediates,* 40, 4 (2014), 1501-1516.

8. J.O. Okeniyi, O.A. Omotosho, O.O. Ajayi, and C.A. Loto, "Effect of potassium-chromate and sodium-nitrite on concrete steel-rebar degradation in sulphate and saline media," *Construction and Building Materials,* 50 (2014), 448–456.

9. J.O. Okeniyi, O.A. Omotosho, and O.O. Ajayi, "Performance evaluation of potassium dichromate and potassium chromate inhibitors on concrete steel rebar corrosion," *Journal of Failure Analysis and Prevention,* 10 (2010), 408-415.

10. O.A. Omotosho, J.O. Okeniyi, O.O. Ajayi, and C.A. Loto, "Effect of synergies of $K_2Cr_2O_7$, K_2CrO_4, $NaNO_2$ and aniline inhibitors on the corrosion potential response of steel reinforced concrete in saline medium," *International Journal of Environmental Sciences,* 2, (2012), 2346-2359.

11. J.O. Okeniyi, C. A. Loto, and A. P. I. Popoola, "Corrosion inhibition performance of *Rhizophora mangle* L bark-extract on concrete steel-reinforcement in industrial/microbial simulating-environment," *International Journal of Electrochemical Science,* 9 (2014), 4205-4216.

12. Y. Tang, G. Zhang, and Y. Zuo, "Inhibition effects of several inhibitors on rebar in acidified concrete pore solution," *Construction and Building Materials*, 28 (2012), 327-332.

13. M.A.G. Tommaselli, N.A. Mariano, and S.E. Kuri, "Effectiveness of corrosion inhibitors in saturated calcium hydroxide solutions acidified by acid rain components," *Construction and Building Materials*, 23 (2009), 328-333.

14. R.T. Loto, and C.A. Loto, "Pitting corrosion inhibition of type 304 austentitic stainless steel by 2-amino-5-ethyl-1,3,4-thiadiazole in dilute suphuric acid," *Protection of metals and physical chemistry surfaces,* 51 (2015), 693-700.

15. P. Selvakumar, B.K. Balanaga, and C. Thangavelu, "Corrosion inhibition study of Stainless steel in Acidic medium – An Overview." *Research Journal of Chemical Sciences,* 3 (2013), 87-95.

16. Y. Ait Albrimi, A. Eddib, J. Douch, Y. Berghoute, M. Hamdani, and R.M. Souto**,** **"**Electrochemical behaviour of AISI 316 austenitic stainless steel in acidic media containing chloride ions," *International Journal of Electrochemical Science,* 6 (2011), 4614–4627.

17. S. Ramya, T. Anita, and H. Shaikh, "Laser Raman microscopic studies of passive films formed on type 316LN stainless steel during pitting in chloride solution." *Corrosion Science,* 52, (2010), 2114-2121.

18. K.T. Kudo, G. Shibata, G. Okamoto, and N. Sato, "Ellipsometric and radiotracer measurements of the passive oxide film on Fe in neutral solution," *Corrosion Science,* 8, 11, (1968), 809-814.

19. ASTM D2688-94 R99, *Standard Test methods for corrosivity of water in the absence of heat transfer (Weight Loss Methods)* (West Conshohocken, PA: ASTM International, 2005).

20. S.P. Canmet, "Electrochemical polarization techniques for corrosion monitoring," *Techniques for Corrosion Monitoring,* ed. L. Yang, (Cambridge: Woodhead Publishing Limited, 2008), 49–85.

21. J.O. Okeniyi, A.P.I. Popoola, C.A. Loto, O.A. Omotosho, S.O. Okpala, I.J. Ambrose, "Effect of $NaNO_2$ and $C_6H_{15}NO_3$ synergistic admixtures on steel-rebar corrosion in concrete immersed in aggressive environments," *Advances in Materials Science and Engineering,* 2015 (2015), Article ID 540395, 11 pages.

22. J.O. Okeniyi, C.A. Loto, A.P.I. Popoola, O.A. Omotosho, "Performance of *Rhizophora mangle* L. leaf-extract and sodium dichromate synergies on steel-reinforcement corrosion in 0.5 M H_2SO_4-immersed concrete," *Corrosion 2015 Conference & Expo 2015,* (Houston, TX: NACE International, 2015) Paper no. 5636.

23. J.O. Okeniyi, I.J. Ambrose, S.O. Okpala, O.M. Omoniyi, I.O. Oladele, C.A. Loto, and P.A.I. Popoola, "Probability density fittings of corrosion test-data: Implications on $C_6H_{15}NO_3$ effectiveness on concrete steel-rebar corrosion," *Sadhana* 39 (2014), 731–764.

24. S.M.A. Hosseini, M. Salari, E. Jamalizadeh, S. Khezripoor, M. Seifi, "Inhibition of mild steel corrosion in sulfuric acid by some newly synthesized organic compounds," Materials Chemistry and Physics 119 (2010): p. 100.

25. X. Li, S. Deng, H. Fu, "Inhibition Effect of methyl violet on the corrosion of cold rolled steel in 1.0 M HCl solution," Corrosion Science 52, 10 (2010): p. 3413.

26. K.M. Zohdy, "Surface protection of carbon steel in acidic solution using ethylenediaminetetraacetic disodium salt," *International Journal of Electrochemical Science,* 10 (2015), 414-431.

27. E. E. Oguzie, "Influence of halide ions on the inhibitive effect of congo red dye on the corrosion of mild steel in sulphuric acid solution," *Materials Chemistry and Physics,* 87, 1, (2004), 212–217.

28. P. C. Okafor, M. E. Ikpi, I. E. Uwah, E. E. Ebenso, U. J. Ekpe, and S. A. Umoren, "Inhibitory action of *Phyllanthus amarus* extracts on the corrosion of mild steel in acidic media," *Corrosion Science,* 50, 8, (2008), 2310–2317.

29. X. Li, S. Deng, and H. Fu, "Inhibition effect of methyl violet on the corrosion of cold rolled steel in 1.0 M HCl solution," *Corrosion Science,* 52, 10, (2010), 3413–3420.

30. R. Q. Liu, L. Xiang, and X. G. Zhang, "Inhibition effect of methyl red on corrosion of steel in acidic solutions," *Corrosion Protection,* 22, (2001), 98–99.

MICRO-TRUNCATED CONE ARRAYS FOR LIGHT EXTRACTION OF ORGANIC LIGHT-EMITTING DIODES

*Wei-Chu Sun[1], Ben Hsu[1], #Mao-Kuo Wei[1,2]

1Department of Materials Science and Engineering, National Dong Hwa University, Taiwan
2 Department of Opto-Electronic Engineering, National Dong Hwa University, Taiwan

Keywords: Cone array, Organic light-emitting diode (OLED), Efficiency

Abstract

In this paper, we combined photolithography, polydimethylsiloxane (PDMS) molding, and UV-forming techniques to fabricate micro-truncated cone arrays. The taper angle of micro-truncated cone arrays was adjusted by changing softbake parameters during photography of photoresist. The fill factor of micro-truncated cone arrays was altered by varying the gap distance between two neighboring cones. In addition, the influences of taper angle and fill factor of micro-truncated cone arrays on efficiency improvement and optical properties of a blue light organic light-emitting diode (OLED) were investigated. The optical properties include spectral shift, CIE coordinates, and viewing-angle-dependent luminance. Experimental results showed that the efficiency of the OLED increased with increasing the fill factor, but decreased with the taper angle of micro-truncated cone arrays. The efficiency of the OLED could be increased up to 42% by attaching the micro-truncated cone array having a fill factor and a taper angle of 94% and 72°, respectively.

Introduction

To improve the efficiency of the OLED via destroying the substrate waveguide, various types of light-extraction microstructures have been proposed, such as random textures [1-3], micro-pyramids [4], V-grooves [5], and microlens arrays [6], etc. The processes for fabricating random textures are not reliable. For making the other three microstructures, the fabrication processes are either complex or expensive. Therefore, we will propose a simple and economic method to make micro-truncated cone arrays, which can increase the efficiency of the OLED more than 40%.

Experimental method

The micro-truncated cone arrays are made through the combination of photolithography, PDMS molding, and UV-forming techniques, as illustrated in Fig. 1. First, a 4-in p-typed Si (100) was cleaned with RCA cleaning procedures. Second, the photoresist (AZ P4620, Clariant KK Technol. Prod. Dept.) was spun on the wafer, followed by heating the photoresist on a hot plate at 90°C for 5-7 min. Third, the wafer and a clear photomask were put on a mask aligner (AG350-4N-S-S-M-H, M & R Nano Technology Co., Ltd.) and exposed UV light with a dose of 300 mJ/cm². The diameter of the holes on the photomask is 10 μm, and the gap distance between two neighboring holes was set at 2-20 μm. The size of the hole arrays on the photomask is 1×1 cm^2. The concave micro-truncated cone arrays were fabricated on the wafer after the development of the photoresist. Fourth, the polydimethylsiloxane (Sylgard 184, Dow Corning Co.) mixed with

its hardener at a ratio of 10:1 was poured onto the wafer and put in an oven to be thermally cured at 60°C for 4 hrs. Fifth, the first PDMS mold with convex micro-truncated cone arrays on its surface was made after peeling the mold from the wafer. Sixth, the mixed PDMS solution was poured again on the first PDMS mold and thermally cured. Seventh, the second PDMS mold with concave micro-truncated cone arrays on its surface was produced after peeling the mold from the wafer. Eighth, the UV-curable polymethylmethacrylate (PMMA) was coated between the second PDMS mold and the polyethylene terephthalate (PET) film, followed by exposing a UV dose at 3 J/cm^2 to harden the PMMA. Finally, the micro-truncated cone arrays were transformed on the flexible PET film after separating the PET from the second PDMS mold.
The surface morphology of micro-truncated cone arrays was analyzed using a scanning electron microscope (S-3400N, Hitachi). The luminance, CIE indices, and spectra of the OLED attached with a micro-truncated cone array were measured by a luminance meter (CS-1000A, Minolta). The flux of the OLED attached with a micro-truncated cone array was recorded with a spectral lamp measurement system (SLM-12, Isuzu Optics).

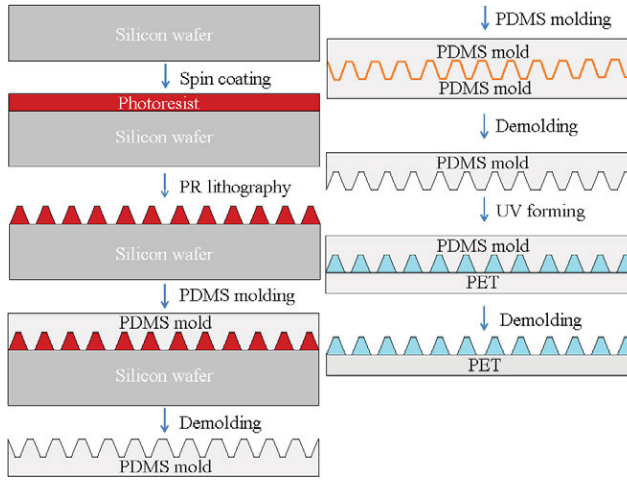

Figure 1. Schematics of the process flow for making micro-truncated cone arrays.

Results and discussions

In this study, the taper angle of the micro-truncated cone arrays was adjusted by varying the duration of the softbake during photolithography. The taper angle was also slightly changed by varying the gap distance between two neighboring circular holes on the photomask. The surface morphology of the duplicated micro-truncated cone arrays treated with various softbake durations were shown in Fig. 2. The taper angle of the micro-truncated cone array decreased with increasing the duration of the softbake, as illustrated in Fig. 2 and Fig. 3.

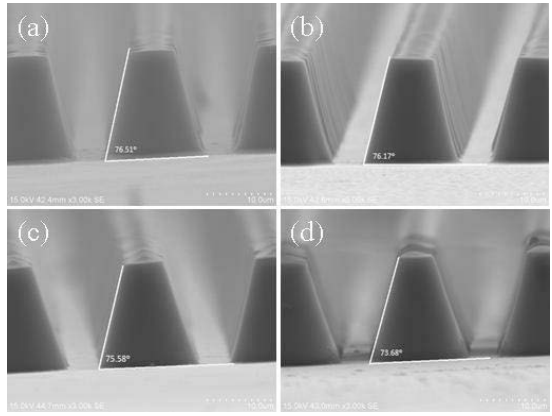

Figure 2. Surface morphology of duplicated micro-truncated cone arrays through various duration of softbake: (a) 5, (b) 5.5, (c) 6, and (d) 7 min.

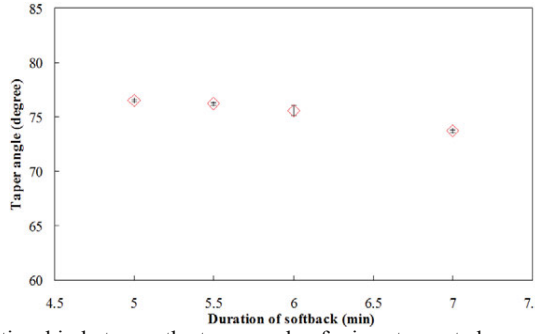

Figure 3. The relationship between the taper angle of micro-truncated cone arrays and duration of the softbake.

In this study, a blue OLED light source (from Ritdisplay Co.) with an emitting area of 1×1 cm^2 was used. The luminance and CIE indices (at normal direction) of the OLED was 140 cd/m^2 and (0.1665, 0.3044), respectively, when it was driven at a current of 2 mA. The emitting profile of the blue OLED is very similar to a typical Lambertian light source.

The fill factor is defined as the ratio of the total bottom area of the micro-truncated cone array to the area of the PET substrate. Fig. 4 showed the influence of the fill factor of micro-truncated cone arrays, whose duration of softbake was set at 7 minutes, on the efficacy improvement of the blue OLED device. It can be observed that the efficacy of the OLED increased with increasing the fill factor of the micro-truncated cone arrays. The efficacy of the OLED can be enhanced up to 42% when the fill factor of micro-truncated cone array was 0.84.

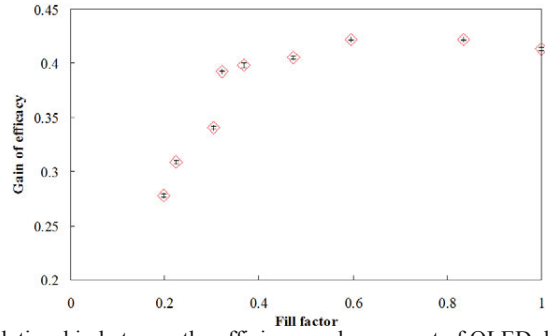

Figure 4. The relationship between the efficiency enhancement of OLED device and the fill factor of micro-truncated cone arrays.

As illustrated in Fig.3, the taper angle of the micro-truncated cone arrays can be adjusted by varying the duration of softbake. The relationship between the efficacy enhancement of the OLED and the taper angle of the micro-truncated cone arrays, having a fill factor of ~0.46, was described in Fig. 5. The efficacy the OLED increased with decreasing the taper angle of micro-truncated cone arrays. The efficacy of the OLED improved up to 39% when the taper angle and the fill factor of the micro-truncated cone array were 73.6° and 0.482, respectively.

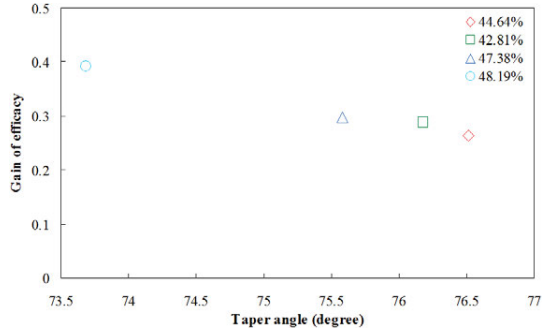

Figure 5. The influence of the taper angle of micro-truncated cone arrays on the efficacy improvement of the OLED.

Fig.6 illustrated the influence of the height of micro-truncated cone arrays on the efficacy improvement of the OLED. The efficiency of the OLED increased with decreasing the height of micro-truncated cone arrays, having a fill factor of approximately 0.44. The efficacy of the OLED improved up to 29% when the height of the micro-truncated cone array was ~16.4 μm.

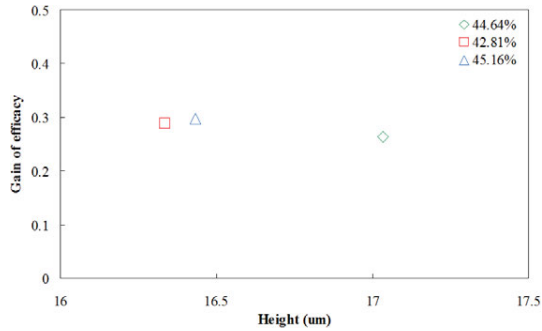

Figure 6. The relationship between efficacy improvement of the OLED and the height of the micro-truncated cone arrays.

The angular-dependent luminance of the OLED attached with micro-truncated cone arrays having different fill factors was shown in Fig. 7(a). The luminance of the OLED attached with micro-truncated cone arrays decreased with increasing the viewing angle. But at a given viewing angle, the luminance of the OLED increased with increasing the fill factor of the attached micro-truncated cone array. Fig. 7(b) showed that the relationship between the improvement of luminous current efficiency at normal direction of the OLED and the fill factor of micro-truncated cone arrays. The luminous current efficiency of the OLED increased with increasing the fill factor of micro-truncated cone arrays. The luminous current efficiency of the OLED increased up to 53% when the fill factor of the micro-truncated cone array was 1.

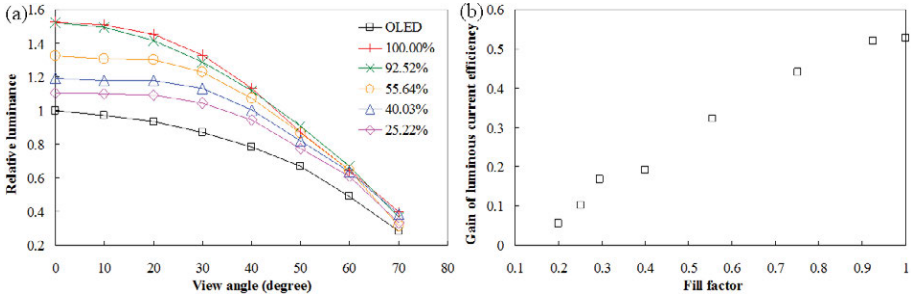

Figure 7. (a) The viewing-angle-dependent luminance of the OLED attached with micro-truncated cone arrays having various fill factors. (b) The relationship between the gain of current of the OLED and the fill factor of the micro-truncated cone arrays.

For the used OLED, the CIE-x index decreased, but the CIE-y index increased with increasing the viewing angle, as illustrated in Fig. 8. The extent of red shift of the OLED increased with increasing the viewing angle due to a stronger intensity at the peak of ~500 nm at a larger viewing angle. The angular-dependent CIE indices and spectra of the OLED attached with micro-truncated cone arrays, having various fill factors, were described in Fig. 8 and Fig. 9. The CIE-x index of the OLED attached with micro-truncated cone arrays decreased with increasing the viewing angle and the fill factor. The CIE-y index of the OLED increased initially, but then

decreased with increasing the fill factor of micro-truncated cone arrays, as shown in Fig. 8. As described in Fig. 9, the intensity variation at the peak of ~500 nm of the OLED was larger than that of the OLED with micro-truncated cone arrays. This means that the light of the OLED attached with micro-truncated cone arrays is more pure than the bare OLED.

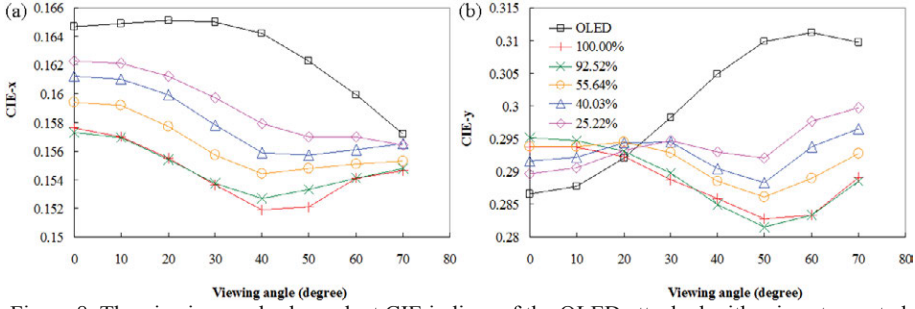

Figure 8. The viewing-angle-dependent CIE indices of the OLED attached with micro-truncated cone arrays having various fill factors.

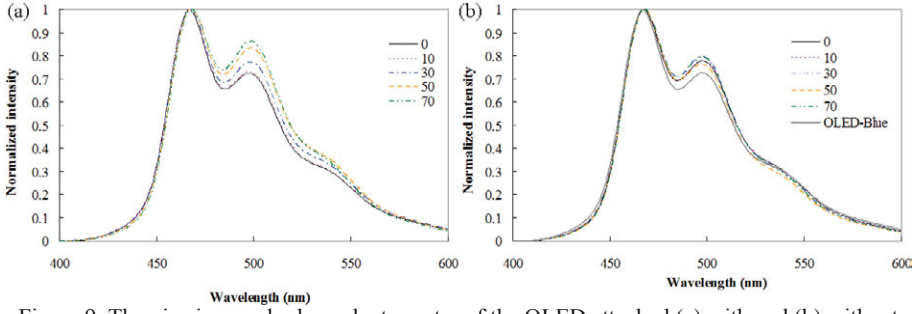

Figure 9. The viewing-angle-dependent spectra of the OLED attached (a) with and (b) without micro-truncated cone arrays having a fill factor of 0.446.

Conclusions

In this study, we demonstrated that the taper angle of micro-truncated cone arrays can be adjusted by changing the duration of softbake. With a longer duration of softback, the taper angle of micro-truncated cone arrays became smaller. Experimental results showed that the efficacy improvement of the OLED device increased with decreasing taper angle, but with increasing the fill factor of micro-truncated cone arrays. The efficacy of the OLED can be increased up to 42% by attaching the micro-truncated cone array having a fill factor and a taper angle of 94% and 72°, respectively. Additionally, the luminous current efficiency of the OLED can be enhanced up to 53% by attaching the micro-truncated cone array having a fill factor of 1.

Acknowledgement

The authors gratefully acknowledge the financial support given by the National Science Council of the Republic of China under projects MOST 103-2221-E-259-006 and MSRT 104-3113-E-155-001.

References

[1] W. H. Koo, H. J. Yun, F. Araoka, K. Ishikawa, S. M. Jeong, S. Nishimura, T. Toyooka, and H. Takezoe, Appl. Phys. Express 3 (2010) 082501
[2] J. Zhou, N. Ai, L. Wang, H. Zheng, C. Luo, Z. Jiang, S. Yu, Y. Cao, and J. Wang, Organic Electron. 12 (2011) 648
[3] W. J. Hyun, S. H. Im, O O. Park, and B. D. Chin, Organic Electron. 13 (2012) 579
[4] L. Lin, T. K. Shia, and C.-J. Chiu, J. Micromech. Microeng. 10 (2000) 395
[5] H.-Y. Lin, J.-H. Lee, M.-K. Wei, C.-L. Dai, C.-F. Wu, Y.-H. Ho, H.-Y. Lin, and T.-C. Wu, Opt. Commun. 275 (2007) 464
[6] M.-K. Wei and I-L. Su, Opt. Express 12 (2004) 5777

MOULD FILLING ABILITY CHARACTERISATION OF SIMA PRODUCED 6063 ALLOY

Ömer Vardar[1], Izzettin Ergün[1], Çağlar Yüksel[2], Eray Erzi[1], Derya Dispinar[1]

[1]Istanbul University, Metallurgical and Materials Engineering Department Avcilar, 34320, Istanbul, Turkey

[2] Yildiz Technical University, Metallurgical and Materials Engineering, Istanbul, Turkey

ABSTRACT

Metallic materials are shaped with various methods. In last 25 years, it has been found that alloys can be shaped in the solid-liquid phase region. There are several ways to produce such materials for example magnetic stirring, mechanical stirring etc. One of them involves the heating of extruded alloy above the solidus temperature which is called Strain Induced Melt Activated (SIMA) method. Heavily cold work alloy starts to recrystallize; spherical grains form and liquid surround these grains. In this way, viscosity is decreased and the material can be shaped very easily under pressure. In this work, AA6063 extruded alloy was used to produce a (shaped sample). Different temperatures, holding times and pressures were selected to characterize the mould filling ability of the alloy. Micro structural examinations and hardness tests were carried out.

INTRODUCTION

The overall field of semisolid metallurgy comprises today a large number of specific process routes, almost all of which fall in the category of either Rheocasting or Thixocasting. The former begins with liquid metal and involves agitation during partial solidification followed by forming. The later begins with solid metal of suitable structure and involves heating to the desired fraction solid and forming. Research over the past 37 years, and particularly over the last decade, has provided a detailed picture of process fundamentals and led to a wide range of specific semisolid processes and process innovations. Industrial studies and actual production experience are providing a growing picture of the process advantages and limitations [1].Semi-solid metal forming is a method that, to produce the complex-shaped metal parts with fewer steps and with

lower cost and collect the advantages of cast and forged metal forming technique. During 1970s Semi-solid metal processing (SSF) technology was developed by the leadership of the Flemings with Spencer and his friends at the MIT [1]. Semi-solid metal processing method for companies that produce with this method; it has numerous advantages long mold life, short processing time, easy to shape, to obtain near net shape such as low power consumption and good mechanical properties. Semi - solid forming consists the shaping of materials between the solidus and liquids temperature by applying force [2]. One of the most effective technological approach was put forward in 1981 [3]. This technique was named as SIMA (Strain-Induced Melt-Activated) by researchers. SIMA process is based on the development of a series of process steps. Basically the hot rolled bars which obtained by extrusion and rolling are subjected to cold work. Then material is heated to a semi-solid temperature. Finally; a homogeneous, non-dendritic and spherical structure obtains. SIMA process has been tested for Al, Mg, Cu and Fe alloys and used in production of aluminum alloys since 1983 [2].

SIMA process is an economical process and it is suitable for large-scale production (for casting). Technically, it can also applied to larger pieces, but it cannot be compared with economy of Magneto Hydro Dynamic (MHD) [1-10].The schematic structure of the SIMA process was shown in figure1.Thus, the dendritic structure broke and elongated thin grain structure obtained. The studies proved that this deformation can also obtained below recrystallization temperatures.

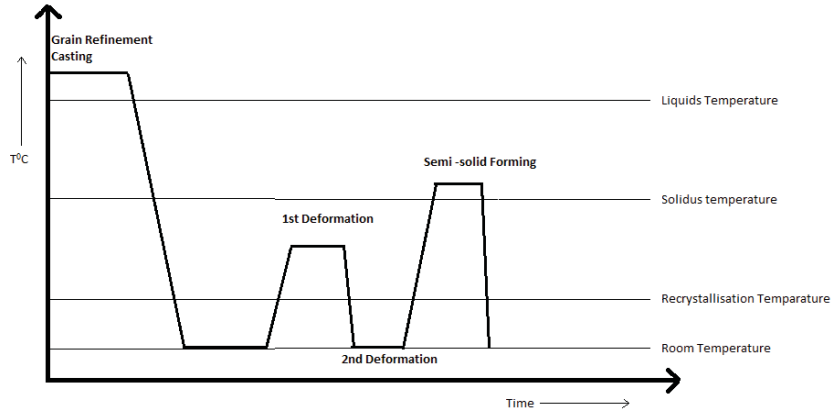

Figure 1. The schematic representation of the SIMA method

Heating time, temperature, degree of cold work and the heating of sample on a metal or a ceramic plate parameters are also the critical factors for semi solid micro structure controlling and mold filling capability at SIMA technique. Therefore the aim of this study is to examine the mold filling capability of AA6063 alloy after heating time and temperature optimization.

Experimental work

The composition of AA6063 which is used in this work shown in Table 1.

Table 1: Composition of alloy used in work

	Cu	Fe	Mg	Mn	Si	Zn	Cr	AL
6063	0,1	0,35	0,45-0,90	0,1	0,20-0,60	0,1	0,1	Rem

Alloys had been supplied as cold deformed cylindrical bar (diameter 22 mm.). The mould used in the experiment is made of AISI 1040 steel. The dimensions of the (used) mould shown in Figure 2.

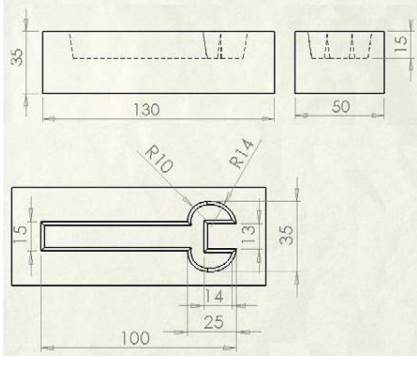

Figure 2. Dimensions of the mould used.

Figure 3. AISI 1040 steel mould used

Sample was heated on the metal plate and ceramic plate at 700°C for 5 to 25 minutes with 5 minutes increments, and 5-ton press was pressurized. These samples could not fill the mould and these samples were visually defected.

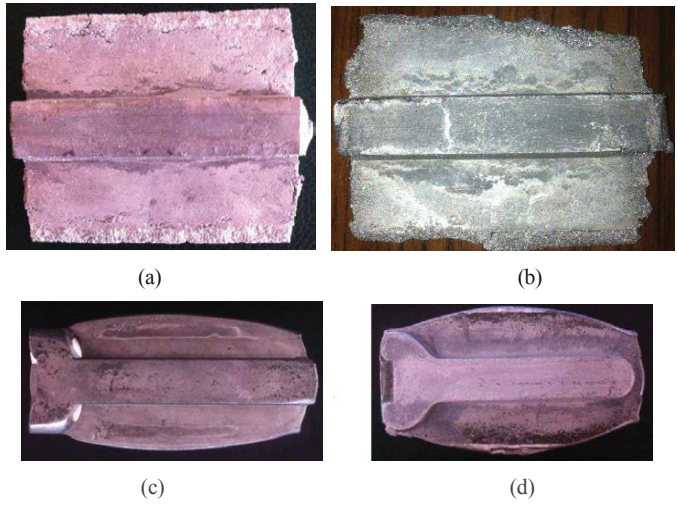

(a) (b)

(c) (d)

Figure 4.Samples were heated on the plate for 20 minutes (a), and 25 minutes (b)

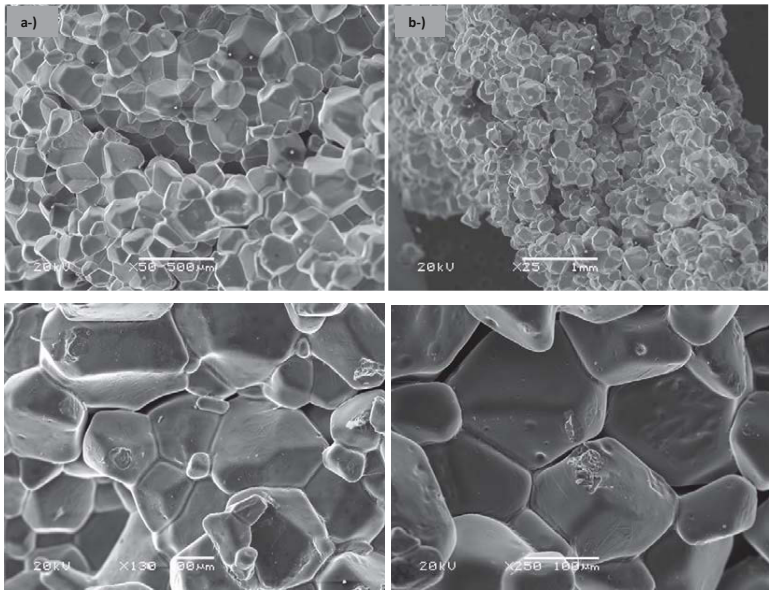

Figure 5. Typical spherical microstructure of AA6063

The hardness value of the samples shown in Hardness Chart (Figure 6). The hardness value of the sample which is heated on the ceramic plate is higher when it compares with the sample which is heated on the metal plate.

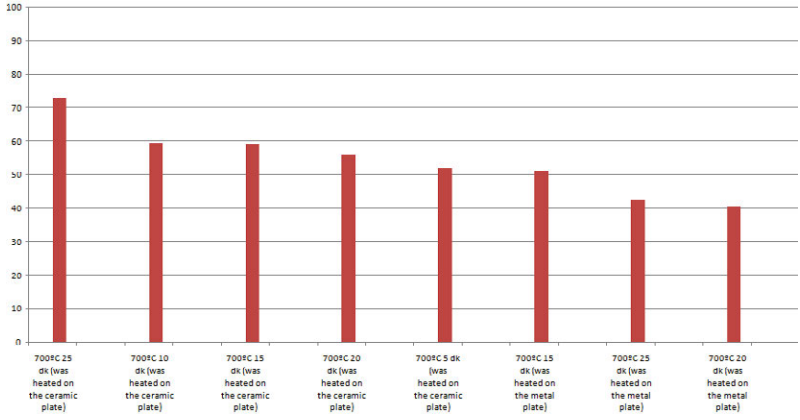

Figure 6. Hardness Chart with regard to heating conditions

Conclusions

One of the most important characteristics of SIMA process is the preheating of the cold deformed starting material. Therefore the selection of the temperature and the holding time determines the final microstructure. When temperature is too high, partial melting begins. As holding time is increased, the coarsening of the grain size becomes rapid. In this work, it was found that the mould filling ability was the lowest when 6063 was heated at 700^{o}C and held for 5 minutes. On the other hand, 25 minutes of holding would led to the partial melting. However, this situation was more significant when the material was heated on a steel plate. Due to the high heat transfer of the steel, the samples holding time had become very sensitive and lowest hardness and highest grain sizes were observed. When samples were placed on a ceramic material, mould filling ability of 6063 by SIMA method had become more controlled and highest properties were found for 25 minutes of holding.

REFERENCES

1. Flemings, M., *Behavior of metal alloys in the semisolid state.* Metallurgical Transactions A, 1991. **22**(5): p. 957-981.
2. Kirkwood, D.H., *Semisolid metal processing.* International Materials Reviews, 1994. **39**(5): p. 173-189.
3. Atkinson, H.V., *Modelling the semisolid processing of metallic alloys.* Progress in Materials Science, 2005. **50**(3): p. 341-412.
4. Atkinson, H.V. and D. Liu, *Microstructural coarsening of semi-solid aluminium alloys.* Materials Science and Engineering: A, 2008. **496**(1–2): p. 439-446.
5. Fan, Z., *Semisolid metal processing.* International Materials Reviews, 2002. **47**(2): p. 49-85.
6. Haga, T., *Semisolid strip casting using a twin roll caster equipped with a cooling slope.* Journal of Materials Processing Technology, 2002. **130–131**: p. 558-561.
7. Liu, D., H.V. Atkinson, and R.L. Higginson, *Disagglomeration in thixoformed wrought aluminium alloy 2014.* Materials Science and Engineering: A, 2005. **392**(1–2): p. 73-80.
8. Liu, D., H.V. Atkinson, and H. Jones, *Thermodynamic prediction of thixoformability in alloys based on the Al–Si–Cu and Al–Si–Cu–Mg systems.* Acta Materialia, 2005. **53**(14): p. 3807-3819.
9. Liu, T.Y., et al., *Rapid compression of aluminum alloys and its relationship to thixoformability.* Metallurgical and Materials Transactions A: Physical Metallurgy and Materials Science, 2003. **34 A**(7): p. 1545-1554.
10. Wang, J., et al., *An Innovative Two-Stage Reheating Process for Wrought Aluminum Alloy During Thixoforming.* Metallurgical and Materials Transactions A, 2015. **46**(9): p. 4191-4201.

ONE-STEP PREPARATION OF TiB_2-C COMPOSITE BY DC ARC FURNANCE

Kuanhe Li[1], Shuchen Sun[1], Xiaoxiao Huang[1], Shuaidan Lu[1], Xiaoping Zhu[1], Ganfeng Tu[1]

[1]Northeastern University; No.11 Heping Region Wenhua Street; Shenyang, Liaoning Province, 110819, China

Keywords: TiB_2-C, one-step, dc arc furnance, carbothermal reaction

Abstract

Previous approaches to prepare bulk TiB_2-C composite is sintering the TiB_2 powder mixed with the C component, so that lead to a series of problems, due to the bad sintering properties. This paper discribes a one-step method of preparing the TiB_2-C composite, especially for using as inert cathode in electrolytic aluminum, from the raw materials of TiO_2, B_2O_3 and petroleum coke, by a dc arc furnance. The rapid and high-temperature heating process provided by the arc furnance leads to the carbothermal reaction to prepare TiB_2, and the overdosed carbon is included in TiB_2 matrix. The XRD(X-Ray Diffraction), SEM(Scanning Electron Microscope), and chemical component analysis are used in the testing part, and the one-step process of preparing bulk TiB_2-C composite is studied.

Introduction

As an important composite matrix material, TiB_2-based composite has plenty of superior properties. The usage of bulk TiB_2-C composite materials includes rigid tools[1], inert cathode in electrolytic aluminum[2], and evaporation boat in vapor plating[3], etc. Recent methods of preparing this kind of material is sintering, but TiB_2 has a not ideal sintering property. The traditional methods of preparing TiB_2-C composite can not avoid this weakness effectively, and also lead to more complex processes and more energy cost. Zhang Gang[4] and other authors use TiB_2 powder to mix with graphite and other carbon additives, with the approach of pressureless sintering, and finally obtain TiB_2-C composite meeting the requirement of inert cathode for electrolytic aluminum. But because of the poor sintering property of TiB_2 powders, the relative density still can be improved.

I.Sulima[5] worked on sintering of TiB_2 ceramics, they use high temperature -high pressure method to prepare TiB_2 materials, and finally obtained the optical condition is 1500℃±50℃,7.2±0.2 GPa, 60 seconds. Cracks and even the self-fragmentation can always be observed in the samples, even if the sintering temperature is improved to 2000-2300±50℃， pressure of 7.2±0.2 GPa. Because of the bad sintering property of

TiB_2 ,these problems are hard to solve, in the sintering process. The cracks decrease the mechanical strength and thermal shock resistance, and also lead to an Na-related expansibility, when it is used as inert cathode of electrolytic aluminum technology[6].
To solve these problems, one-step preparation process is described in this paper. Using the TiO_2, B_2O_3 and petroleum coke as materials, the carbothermal reaction takes place in a self-designed dc arc furnance to synthesis TiB_2 matrix, with the over-dosed C component filling into. The advantage of this approach is as follow: 1) More simplified process, only one step from raw material to the composite; 2) Lower cost of the raw materials, they are all common industrial chemicals; 3) Good qualities, like higher compactness, better strength,etc.; 4) avoiding the impurities like TiC ,etc.

Experimental

TiB_2 is prepared with the method of carbothermal reduction, and the formula is

$$TiO_2+2H_3BO_3+5C=TiB_2+5CO\uparrow+3H_2O\uparrow \quad (1)$$

Table 1 Raw material for preparation of TiB_2 by arc furnance

Raw Material	Purity (wt.%)	Impurity(wt.%) Si	Fe	Water
B_2O_3	>99.00	<0.02	<0.01	-
TiO_2	>98.00	<0.02	<0.01	<1.50

Table 2 Raw material for preparation of TiB_2 by arc furnance

Raw Material	Fixed Carbon(wt.%)	Volatile(wt.%)	Ash(wt.%)	Water(wt.%)
Petroleum Coke	>84.60	<12.00	<0.40	<3.00

The raw materials and their properties are displayed in the table 1 and 2. With a milling process, the TiO_2, B_2O_3 and petroleum coke are well-mixed and crushed, to obtain an average particle size (D50) of 83.13μm. A self-made dc arc furnance is used in this synthesis process, and the apparatus schematic diagram is illustrated in the Figure 1.

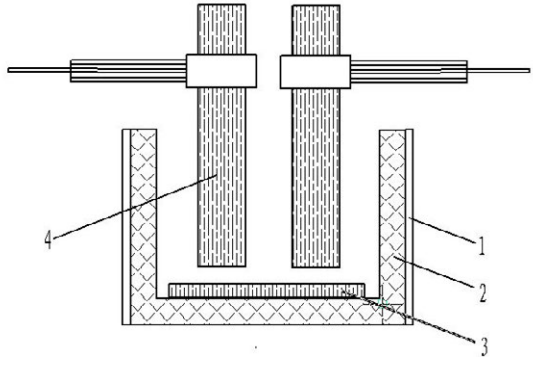

Figure 1. apparatus schematic diagramof dc arc furnance
1. Shell of the furnance; 2. Refractory material lining; 3. High-purity graphite electrode plate; 4. High-purity graphite electrode

The whole synthesis reaction takes place in an open system. During the carbothermal reaction process, the mixtures in different chemical ratios are filled into the reaction chamber directly, and after a 1 hour smelting process, a great amount of production melts to liquid state.After a cooling process, the TiB_2-C composite is prepared, and tested by the methods of XRD(X-Ray Diffraction, PW3040/60 X'Pert Pro MPD made in Holland), SEM(Scanning Electron Microscope, SSX-550 from SHIMADZU Company),and chemical titration. The influence of different raw material ratio on the components is studied, and the process is summarized.

Results and discussion

Thermodynamic mechanics analysis

TiB_2-C composite is produced in one-step process by a dc arc furnance, TiB_2 matrix is prepared by the raw materials, according to the carbothermal reaction .

$$TiO_2+B_2O_3+C=TiB_2+CO\uparrow \quad (1)$$

The C exists in the form of graphite, which is from the overdosed petroleum coke, and graphitized by the high temperature over 3000℃ in the arc furnance.

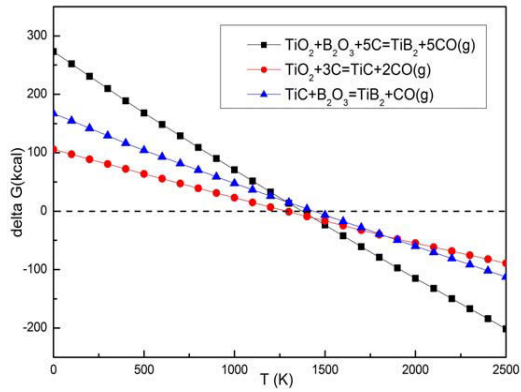

Figure 2 Gibbs free energy changes in the carbothermal reaction

$$TiO_2+3C=TiC+2CO\uparrow \quad (2)$$

$$TiC + B_2O_3 + C = TiB_2 + CO\uparrow + CO_2\uparrow \quad (3)$$

TiC is a common impurity in the carbothermal reaction of preparing TiB_2[7,8]. The formulas and changes of Gibbs free energy related to TiC's behaviors is shown in the Figure 2. As shown in the figure, the reaction leading to TiC takes place when the reaction temperature reaches 1061.34℃. TiC appears because the heating process is steady. In the arc furnance, temperature improves rapidly. When the temperature reaches rapidly 1891.38℃, the reaction of $TiC + B_2O_3 + C = TiB_2 + CO\uparrow + CO_2\uparrow$ takes place, which helps effectively with reducing TiC. When the temperature reaches

over 3000℃,reaction(3) are more easily happens than the reaction(2). And because of the well-mixing and rapidly-heating process, the TiC is avoided effectively. So the component of the composite is TiB_2 and graphite.

Table 3 The T(ΔG=0)(℃) and ΔG(T=3000℃)(kcal/mol) in carbothermal reactions

	T(ΔG=0)(℃)	ΔG(T=3000℃)(kcal/mol)
(1)	1061.34	-433.87
(2)	1287.01	-122.41
(3)	1891.38	-164.72

When the power improves to 60000W , plenty of TiB_2 melts to liquid state, which leads to a more effective mass and heat transfer. This situation also helps avoiding the appearence of TiC, and make the sample uniform.

XRD and component analysis

In the table 4, the component analysis by chemical titration is shown. Figure 3(a) to Figure 3(d) are the XRD(X-Ray Diffraction) patterns of the TiB_2-C composite samples prepared from different raw materials ratios. The amount of TiO_2 is not overdosed, and B_2O_3 has a 30% overdose.

In the Figure 3(a) and Figure 3(b), the TiC peaks appear ,which means a spot of TiC exists in these raw material ratio. The component calculation is displayed in the Table 4. When the overdose of C is 0% and 5%, the mass fraction of TiC is 4.37% and 5.45%. As shown in the patterns of Figure 3(c) and Figure 3(d), they all have only 2 phases, no peaks of impurity like TiC are found, this corroborates the results of thermodaynamic calculations. The peaks of TiC are much higher in both pictures, so the matrix is TiB_2, and graphite is the additive. The diffraction peak height of carbon in Figure 3(c) is lower than the Figure 3(d), so it can be obtained that the C component ratio improves, when the overdose of petroleum coke increases. When the C overdose is 10% and 20%, TiC disappears in the composite materials.

Table 4 The components calculation

C overdose (%)	Ti (wt.%)	B (wt.%)	C (wt.%)	TiC (wt.%)	Graphite (wt.%)	TiB_2 (wt.%)
0	68.98	29.97	1.044	4.37	0.17	95.46
5%	65.93	28.18	5.89	5.45	4.8	89.75
10%	62.24	28.49	9.27	0	9.27	90.73%
20%	58.41	26.74	14.85	0	14.85	85.15%

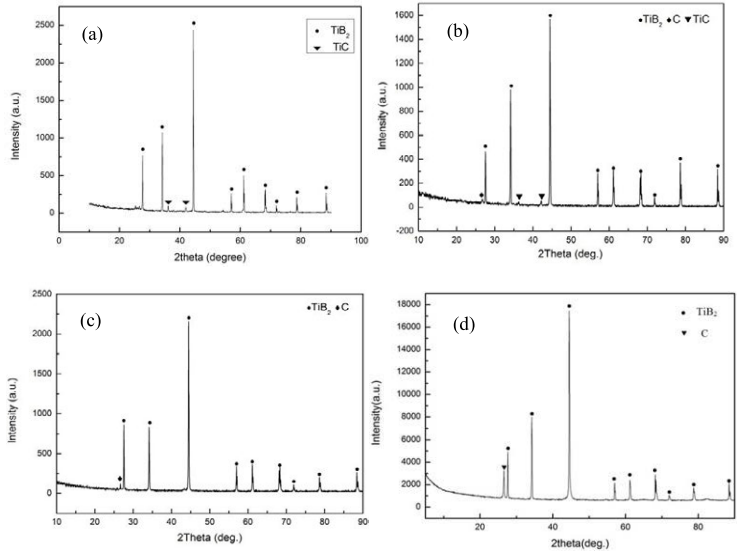

Figure 3. X-Ray diffraction patterns of samples prepared from different raw material ratios

SEM analysis

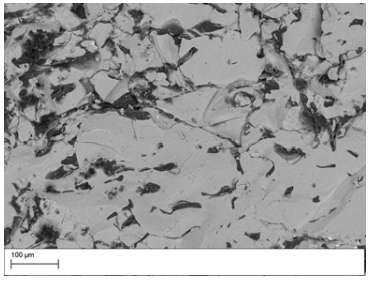

Figure 4 SEM images of cross section of TiB_2-C composites

As shown in the Fig 4 , the SEM(Scanning Electron Microscope) photo of sample(10% overdosed C) inside cross section is displayed. The TiB_2 matrix is extreme uniform, because of the liquid state during the smelting process. Compared with the TiB_2-C composite prepared by sintering, the sample is obviously compact in this scale. The graphite additive disperse in the matrix randomly but uniformly. The graphite can be used to connect the particles and enhance the mechanical strength. Graphite is a good conductor, so the conductivity of the TiB_2-C composites can also be kept. Compared to the samples prepared by sintering, cracks are not commonly

observed in the picture, so when the composite is used as the inert cathode, the severe Na expansion problem are not obvious.

Conclusion

(1) The one-step method to prepare bulk TiB_2-C composite by a dc arc furnance can avoid the impurity of TiC, which is commonly observed in the previous sintering process.
(2) 10% overdosed petroleum coke and 30% overdosed B_2O_3 is a optimal raw materials ratio to prepare the composite, and the production with the ratio of 90.73% TiB_2(wt.%) and 9.27% graphite is obtained.
(3) Because of the rapid and high-temperature heating process in the dc arc furnance, the TiB_2 melts to the liquid state. This helps the component to be uniform and compact, and the cracks are decreased compared to the sintering method.

References

1. Shi Q, Liu H L, Huang C Z, et al. “Study on the In Situ Fabricated Titanium Nitride-Based Ceramic Cutting Tool Materials Reinforced by Titanium Diboride,” Advanced Materials Research, , 500(2012),679-684.
2. Wang, Youwei, et al. "Research Status of TiB_2 Based Inert Cathode Prepared by Plasma Spraying." Hot Working Technology(2014).
3. Kim, Min Ki, D. P. Kim, and G. Y. Chung. "Preparation of TiB2/C Composites in a CVI Reactor." Key Engineering Materials334-335(2007):329-332.
4. Zhang, Gang, et al. "Pressureless sintering process of TiB_2-C inert cathode for aluminum reduction," Carbon Techniques29.4(2010):43-47.
5. Sulima, I., et al. "Sintering of TiB2 ceramics," Archives of Materials Science & Engineering, 28.11(2007).
6. Duan, Xue Liang, et al. "Study on expansibility of TiB_2-C compound and Na penetration in electrolyzation." Journal of Materials & Metallurgy(2004).7.
Krishnarao, R. V., and J. Subrahmanyam. "Studies on the formation of TiB 2 through carbothermal reduction of TiO2 and B2O3." Materials Science & Engineering A362(2003):145–151.
8.Ma, Aiqiong. "Thermodynamics analysis of carbothermal reduction of TiB_2." Refractories(2009).

Si AND SiCu THREE DIMENSIONAL SCULPTURED FILMS AS NEGATIVE ELECTRODES FOR RECHARGEABLE LITHIUM ION BATTERIES

B. Deniz Polat, Ozgul Keles*
Department of Metallurgical and Materials Engineering, Istanbul Technical University, Maslak, Istanbul, 34469, Turkey
Tel:+902122853398, Fax:+902122853427, E-mail:ozgulkeles@itu.edu.tr

Keywords: Sculptured thin film anode, Composite electrode, Lithium ion battery, Glancing angle depositon.

Abstract

Three dimensional sculptured Si films with (10 %at.) and without Cu contents have been fabricated by an ion-assisted glancing angle co-deposition technique. Once the morphological and structural differences depending on Cu contents of the films have been evaluated, their uses as anodes in lithium ion batteries have been also discussed. The morphological analyses demonstrate that Cu presence improves nano ordering and the homogenity along the nano sculptured structure. The galvanostatic tests show that the film without Cu fails quickly, but the one with 10%at. Cu content delivers 800 mAh g^{-1} with 99% coulombic efficiency after 100^{th} cycles. It is believed that the composite electrode has a better electrochemical performance because Cu plays a crucial role in holding the electrode together, buffering the mechanical resistance and enabling faster electron transfer.

Introduction

Silicon (Si) is considered a possible anode material for Lithium Ion Batteries (LIBs) due to its high specific discharge capacity (3479 mAh g^{-1}, at room temperature) and low discharge potential. However, the short cycle life of Si thin film electrodes restrict its commercial use. There are three main reasons for this. First, when Li^+ diffuses into and intercalates with Si film, its volume expands by up to 400%. Second reason is its low electrical conductivity. Si retards the electrons' passage through the electrode thus causing lower capacity and quick failure. Third is the solid electrolyte interface (SEI) formation following the electrolyte reduction on the surface of Si electrodes. This has a negative effect on the cycle performance of Si-based thin film anodes. This SEI layer being ion conductive gets increasingly thicker during cycling which brings about a continuous decrease in capacity [1].
To overcome the above mentioned problems, the use of 1D-3D nanostructured materials has been proposed previously [2-3]. It is believed that the internal spaces between these nanostructures result in large pathways that facilitate electrolyte penetration, increase the accessible surface area of the anode reacting with Li^+, and decrease the polarization and, hence, improve the electrochemical performance of the electrode during cycling. So far, template-directed electroplating [4], direct chemical reaction [4], and nanolithography [5] have all been used by various researchers. However, long processing time, restricted aspect ratio of the nanostructures, safety concerns, difficulties in controlling the morphology, and limited choices of materials to form nanostructures have led investigators to look for alternative nanostructures and production techniques. Among others, glancing angle deposition (GLAD) has become very popular because it enables one to fabricate 3D nanostructures from many types of precursor materials that possess high precision in terms of structural morphology and geometry. Moreover, in GLAD, it is possible to control both the

alignment of the nanostructures and their interfacial properties [6]. This process avoids the hazardous nature of working with flammable, explosive, or carcinogenic metal nanoparticles, and also enables direct deposition of nanostructures on the current collector, thereby eliminating the need for binders or additives. The latter ensures direct transport of electrons from the electrode to the current collector and, fast Li^+ diffusion through the small diameters of nanostructures. In the GLAD process, the deposition flux is incident with an angle (α) > 70° from normal. The substrate is oriented with two programmable stepper motors : one adjusts α, and the other controls the azimuthal rotation (Φ) of the substrate with respect to normal [6].

Thin films formed by GLAD method reduce stress and act as "stress-reliever" due to the separated structures they contain which enable the freedom of movement over short distances. The main driving force for stress generation during cycling is volume strain gradient which occurs in the electrode during the galvanostatic test [7]. According to a diffusion induced stress model, during delithiation the largest stress is found to be the tangential tensile stress leading to crack formation, which is then converted to compressive stress during lithiation. Herein, as stated by Brett [8], helical shaped structures are more resistant to normally-oriented stress, which is expected to improve its cyclability.

Even though the cycle life of the anode is expected to be improved as a result of morphological particularities high ohmic contact resistance is a commonly seen problem of the thin film electrode. Plus the low electronic conductivity of Si should be improved to prolonge the cycle life and the rate efficiency.Thus, to promote the adhesion of the film to the substrate and alleviate the influence of expansion, some amount of Cu will incorporated into the Si thin film. Knowing that Cu has high solubility in Si, and has superior conductivity as well as ductility, we believe that by codeposition Cu with Si, we can form copper silicide intermetallics that improve the electrical conductivity, the mechanical flexibility, and the adhesion of the film to the Cu current collector. However, choosing the amount of Cu to add into the Si thin film is a challenging task. Although Cu is expected to increase the cyclability of the Si thin film, the theoretical capacity of the film will decrease due to the electrochemically inactive behavior of Cu.

Therefore in this work, we produce 3-D structured Si and SiCu (with 10%at. Cu content) thin films by GLAD method.We expect that the morphology as well as the electrochemical performances of the films will be different when used as negatives electrodes in LIB.

Experimental

The experimental setup for GLAD in a vacuum chamber was shown in Fig. 1. Two separate electron-beam evaporation sources, containing chemically pure Si and Cu pellets, were located approximately 31 cm below the center of the substrate holder unit, with the separation of the two sources approximately 8 cm.

The diameter of the electron beam spots, was always less than 1 cm, which is essentially a point source compared to the distance between the melt and the substrate. The mean free path for scattering was much larger than the chamber size and the vapor fluxes for the two sources could be treated as collimated vapor beams.

During the experiments, the deposition rates and thicknesses of the separate Cu and Si atom fluxes arriving at the substrate were monitored and controlled by two programmable crystal microbalances (QCM). A shutter can be inserted over each source to stop and start the flux.

The deposition was done on four types of substrates: a glass disc (Tedpella) for X-ray diffraction (XRD) analysis, a stainless steel disc (15.5 mm diameter and 1.5 mm thickness) for compositional analysis, A Si wafer for cross sectional views and copper discs (15.5 mm diameter and 1.5 mm thickness) for surface views as well as electrochemical experiments

with half cells. The discs were mechanically polished using 320, 600, 800, and 1200-grit sandpaper, then polished to a mirror finish by 1.0 and 0.5 micron alumina paste. The source materials were placed in graphite crucibles, and the chamber was pumped to a base pressure of about 8×10^{-5} Pa. The substrates were initially sputtered for 5 min using 900 eV Ar^+ ions from a Kaufman ion source with a gas feeding rate of 8 sccm. Then, the shutters were opened and the deposition was started. Immediately at the start of deposition, the ion energy was reduced to 250 eV and Ar^+ ion-assisted-deposition (IAD) was operated at 250 V × 23 mA for 5 min to assist in the establishment of the dense, adherent thin film. After that, the Ar flow and ion gun were turned off but evaporation still continued. The ion source parameters used in the experiments were 30 mA beam, 40 V discharge, and 100 V accelerator. The pressure in the chamber was 0.01 Pa. The deposition rates were 0.09 nm s^{-1} and 1 nm s^{-1} for Cu–Si, respectively as read by QCM.

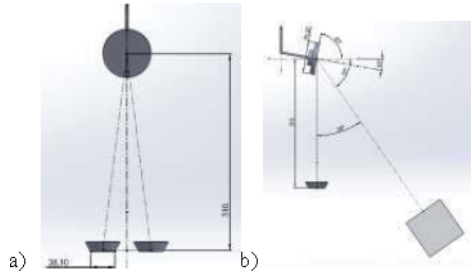

Figure 1. Experimental setup for GLAD method a) front view, b) side view

During the production, to have 3-D structured thin films we fixed the substrate position so that the incident flux angle was 80° with respect to substrate normal and the substrate was rotated by a stepper motor at an azimuthal rotational speed of 0.02 rpm.

The phases present in the pristine thin films were characterized by an X-ray diffractometer (Philips PW3710) with CuKα at 40 kV and 30 mA. The X-ray data were collected in the 2θ range of 20–90° with a step of 0.05°. The amount of Cu/Si atoms along the composite film thickness was monitored by glow discharge optical emission spectroscopy (GDOES) analysis (JobinYcon Horiba), where the RF excitation mode is used with 50 W power and 900 Pa pressure using the films coated on SS substrates. Surface and cross sectional images of the films were achieved by field emission scanning electron microscopy (SEM, JEOL JSM 7000F and JEOL JSM 5410 Models).

The electrochemical performances of the3-D structured Si and SiCu thin films electrodes were evaluated in half-cells. All half-cells were assembled as 2032 coin cells in an Ar-filled glove box (Mbraun, Labmaster) with thin films as test electrodes, pure Li foil as a counter electrode, and porous polypropylene film (Celgrad 2400) as a separator. The non-aqueous electrolyte used in the cells was 1 M $LiPF_6$ dissolved in ethylene carbonate and dimethyl carbonate (1:1 weight ratio). The amount of active material in the thin films was calculated by multiplying the total mass of the coating with the active material weight percentage obtained from energy dispersive spectroscopy (EDS) analyses (Table 1). This calculated value was used to determine the specific capacity of the anode material. The cells were tested at room temperature and operated at voltages between 0.2 V and 1.2 V versus Li/Li^+ at a rate of 200 mA g^{-1}. Cyclic voltammetry (CV) of the SiCu film was performed after the 1st and 3rd cycles of each samples, in a potential range of 50 mV to 1.2 V with Li/Li^+ at a scan rate of 0.03 mV/s, and electrochemical impedance spectroscopy (EIS) analysis of the SiCu film was

accomplished at 1.2 V in the frequency range of 10 mHz to 10 kHz with 5 mV rms, after the 1st and the 3rd cycles (Gamry PCI4/750).

Results and Discussions

The SEM top and cross-sectional view images of the3-D structured Si and SiCu thin films containing filmsare shown in Fig. 2a–d. The surface views (Fig. 2a and c) show that the 3-D structures are distributed across the entire surface and the presence of Cu atoms along with Si improves the regular distribution in the film and the order along the structure. The cross-sectional views (Fig. 2c and d) indicate that both films have thicknesses of approximately 600 nm.

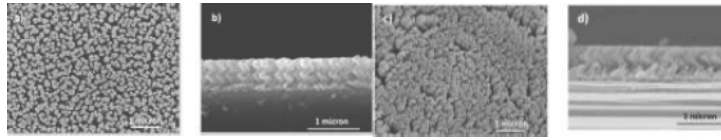

Figure 2. a) SEM surface view of SiCu thin film, b) cross section view of SiCu thin film; c) SEM surface view of Si thin film, d) cross section view of Si thin film

The cross-sectional views also demonstrate that the use of low-energy Ar^+ ion bombardment during GLAD deposition increases the slope of the structure (Fig. 2b, d). According to Sorge et al. [9] this effect is due to the resputtering of the structure during deposition. This alteration in the film morphology results in the formation of denser and more adherent structured thin films.

In this work we chose a low substrate rotation rate (0.02 rpm) considering the deposition rate of Si and Cu (10 and 0.9 Å/s, respectively). In interval, sufficient material is deposited onto the substrate to form preferentially oriented columns, which, in turn, generates continuous formation of nanocolumns in different directions forming eventually 3-D structures(see Fig. 2b).The EDS analysis results demonstrate that both films have a similar amount of Si (Table I).

Table I. EDS compositional results of the 3-D structured SiCu thin films

	wt.%		at.%	
	Cu	Si	Cu	Si
SiCu thin film	16.49	83.51	8.1	91.9

Fig. 3 displays the atomic ratio of Cu/Si atoms along the composite film thicknesses. The atomic ratio (Cu/Si) is constant after 100 nm, which proves that the steady co-evaporation is achieved in the experiment (Fig. 3) after the cessation of the ion bombardment. And, intensity decreases almost to zero at about 600 nm. The two bumps in Fig. 3 are believed to be related to the shape of the 3-D structured film.

The XRD results (Figs.4a,b) show that both coatings deposited on Si wafers contain amorphous nanosized particles. These structural properties can be considered as an outcome of the experimental parameters.Indeed, the fact that Fig. 4b reveals no peak related to the formation of Si, Cu and/or SiCu intermetallics could be explained by their small-sized grain morphology, that can not be detected by XRD analysis.

As noted in literature, the existences of the α-Si and a-Si particles are very important for the electrochemical performance of the electrodes because their reactions with Li^+ differ depending on the cell potential. In previous studies, the Li^+ insertion/extraction mechanisms were analyzed by in-situ XRD, SEM, and HR-TEM (high resolution transmission electron

microscopy) [10-11]. The analysis results show that during Li^+ insertion, the crystal structure of the nano-sized Si particle is destroyed and converted into an amorphous metastable Li–Si structure according to the "solid state amorphisation theory" without the formation of any intermediate phase. This amorphous lithiated Si phase prevails up to 0.05 V, then a new crystalline compound ($Li_{15}Si_4$) forms when the cell potential decreases to low values (< 0.05 V).Furthermore, during Li^+ extraction, crystalline (on the anodic side) $Li_{15}Si_4$ is converted into both amorphous and crystalline particles, where an internal trapping of Li^+ ion occurs, resulting in a decrease in the specific capacity delivered. On the other hand, Li^+ insertion into an amorphous Si anode forms an amorphous lithiated Si product, which is converted into $Li_{15}Si_4$ at a voltage lower than 0.05 V. Given that any lattice expansion could be adequately prevented by eliminating the formation of the two phases, amorphous Si particles are more advantageous, because Li^+ diffusion paths are developed in the amorphous thin film, leading to higher electrochemical performance.

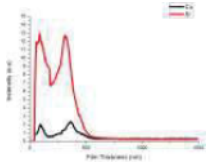

Figure 3. GDOES result of the 3-D structured SiCu thin film

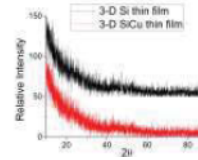

Figure 4. XRD diffractogram of the 3-D structured SiCu and Si thin films

The analyses of impedance spectra for the 1st and 3rd cycles of 3-D structured SiCu thin film are performed in terms of Nyquist plots where the real and the imaginary parts of impedance are shown on the x and y axes, respectively (Fig. 5a). To explain the kinetic steps present in our study, previously mentioned explanations based on time constants are considered [12-13]. In general each process has one characteristic time constant (or a narrow distribution of them) that can be seen by the frequency scan.

Herein, Fig. 2 reveals that the SiCu structured films have the similar morphological characteristics of a thin film which has mixed ionic/electronic conductor with a large surface area and pores that can be partially filled by the liquid electrolyte. Park et al. [14] have explained that for such a structured thin film, oriented nanocolumns that have a direct contact with the current collector, would be covered by SEI either they have direct contact with the electrolyte or with other nanocolumns. Thus, charge transfer resistance or solid-state diffusion is usually limiting the kinetics of charge/discharge reactions. In that case, it is possible to model the equivalent circuit of the spectra by various systems. In our case, the equivalent circuit given in Fig. 5c contains R1 as uncompensated ohmic resistance of the electrolyte, R2 as the charge transfer resistance between the structures and SEI, CPE as constant phase element (double layer capacitance in non-ideal cases) of structures with the electrolyte's interface and W as the Warburg element which describes the solid state diffusion inside the structure.

When the Nyquist plots of the 3-D structured SiCu film after the 1st and 3rd cycles (Fig. 6a–b) are analyzed it is seen that at high frequencies (around 10 kHz) the spectra does not have a real part which indicates that the resistance originated from the external cell connection and electronic contact between the substrate — the active material equals to zero. As the frequencies decrease (10 kHz to 10 Hz), a semi-circle indicating the charge transfer resistance and the capacitive effect of SEI layer is detected in Fig. 5a. The diameters of this semi-circle decreases after the 3rd cycle. It is possible to explain this change considering the "electrochemical grinding" that is resulted from the low mechanical resistance of the thin film

against the high volumetric change in cycling. In this regard, once the average particle size is reduced in the films, the surface area of the anode is increased. The high surface area increases the current passing in the cell and decreases the impedance detected from the anode. Moreover, a decrease in the impedance of the electrodes in further cycles could be explained by the presence of the "SEI glue effect", which provides electrical conduction pathways among the electrochemically grounded particles. Indeed, knowing that no binder is used during the electron beam deposition process, possible delamination of the small particles from the current collector is mostly prevented due to the "SEI glue effect." This condition makes the SEI formation critical for the good electrochemical behavior of the porous composite films. Then, at lower frequencies (below 10 Hz), an upward slope provides information on Li^+ moving into the structured thin films (Fig. 5a). The slopes for the EIS data of the 1st and the 3rd cycles of the SiCu thin film anode are close to 45^0, justifying the observation that Li^+ can diffuse through the bulk material during the entire cycle test.

The Li^+ insertion/removal into 3-D structured SiCu thin films was also investigated by CV for the first and the third cycles (Fig. 5b). The peak potential depends on the formation and disappearance of Li_xSi alloys of different compositions and structures.Therefore, the fact that the peak potentials are the same for those of Si [15] justifies the electrochemically inactive behavior of Cu atoms versus Li/Li^+. The peak intensities of the 3-D structured SiCu thin films are also decreasing in cycling.Possible SEI formation or irreversible reactions with Li^+ might explain this decrease.

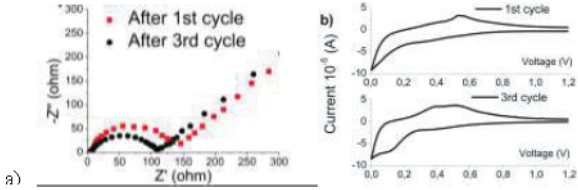

Figure 5. a) EIS, b) CV test result of the 3-D structured SiCu thin film

Figs. 6a-b shows the capacity-cycle performance of the 3-D structured Si and SiCu thin films when used as anodes in half-cells, along with their coulombic efficiencies. The capacity value in the graph is calculated based on the amount of active material (Si) present in the thin films. The results show that the existence of Cu in the thin film is more advantageous, because even though both films are produced by GLAD method, the morphology of the 3-D structured SiCu thin films and the physical properties are improved in the existence of Cu atoms.

As mentioned earlier, the limited electron conductivity of the Si increases both the ohmic resistance of the electrode and the resistance against electron passage through the film.Moreover, during the evaporation process as the atomic mobilities of Si and Cu are different, the interactions of the ad-atoms (among Cu-Si-Cu, Cu-Cu-Cu, Si-Cu-Si and Si-Si-Si) will be different as well, resulting differentiation in the thin film morphology. This irregular morphology and free space distribution of 3-D structured Si thin film restrict the effective reaction of Li^+ with the active material. Plus as the low electronic conductivity of Si impedes the electron passage across the electrode, the Li^+ diffusion is limited by the surface reaction so Li^+ can not diffuse through the bulk material during the galvanostatic test, leading to low specific capacity.

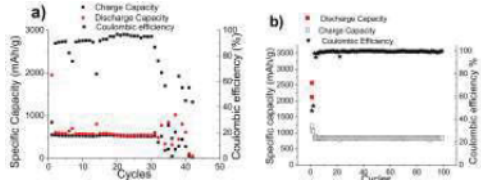

Figure 6. Capacity-cycle graph of the 3-D structured a) Si and b) SiCu thin films.

All in all, this irregularity in the film morphology, high ohmic resistance and the low electronic conductivity cause quick faillure of the 3-D structured Si film. On the other hand, higher accessible surface area for Li^+, higher mechanical tolerance of the film due to the presence of wider porosities and higher electron conductive pathways in the electrode help to deliver high first discharge capacity of the 3-D structured SiCu thin films.
To justify our explanation about the electrochemical performances of both electrodes, ex-situ SEM analyses results are given in Figure 7a-d. A remarkable morphology is changed in the SiCu thin film after 1st cycle due to the volumetric changes occurred in lithiation/delithiation reactions. The SEI prevails on the substrate surface as seen in Figs. 7b and d. After 100 cycles, surface view justifies that no delamination or cracks are formed in the SiCu thin film but pulverization is noted on all over the film, during galvanostatic cycling test. Additionally, the alignment in the thin film can be still detectable on the SiCu thin film, where homogeneously distributed porosities are still present. The tilted (45^0) surface view of this SiCu thin film shows well aligned structures, of which 3D shape is lost, the diamater and the length become larger compared to that of the pristine sample.

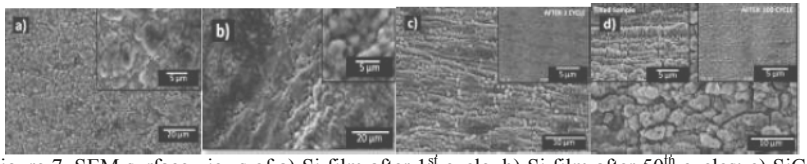

Figure 7. SEM surface views of a) Si film after 1st cycle, b) Si film after 50th cycles; c) SiCu film after 1st cycle, b) SiCu film after 100th cycles;

Conclusions

In this study, we produced 3-D structured Si and SiCu thin films via a glancing angle co-evaporation method. To improve the adhesion of the film, the substrate and the coatingwere sputtered by Ar^+ during the initial 5 min of the deposition. Wealso compared and analyzed the electrochemical performance of these films when used as anodes in LIBs. Outcomes of the study are summarized as follows:

- The 3-D structured Si thin film fails quickly but 3-D structured SiCu thin film delivers a higher capacity, 800 mAh g^{-1} over 100 cycles, with 99% coulombic efficiency. This improved cyclability is a consequence of the thin film composition and morphology.
- The use of GLAD helps to make various architectural thin films and architectural differences that influence the electrochemical performance of the electrode. Although, both films are produced by the same experimental parameters, Cu containing film performs better since Cu presence affects the morphology and the physical properties of the electrode.

- Ion-assisted GLAD method is used to form 3D strctured thin films during deposition to improve the adhesion and the density of the coatings.

Acknowlegement

This work is a part of the research project 213M511 approved by The Scientific and Technological Research Council of Turkey (TUBI_TAK). The research grant is gratefully acknowledged. The authors also thank Prof Dr Mustafa Urgen, Gültekin Göller, Sevgin Türkeli and Hüseyin Sezer for their helps to accomplish the characterizations.

References

1. M. Ko, S. Chae, J. Cho, "Challenges In Accommodating Volume Change of Si Anodes For Li-Ion Batteries," *Chem Electro Chem*, (2015) DOI: 10.1002/celc.201500254
2. B.Liu, J. Zhang, X. Wang, G. Chen, D.Chen, C. Zhou, G. Shen, "Hierarchical 3d Znco2o4 Nanowire Arrays/Carbon Cloth Anodes For A Novel Class Of High-Performance Flexible Lithium-Ion Batteries," *Nano Lett,* 12 (2012), 3005-3011.
3. Y. Yu, C.Yan, L. Gu, X. Lang, K. Tang, L. Zhang, Y. Hou, Z. Wang, M.W. Chen, O.G. Schmidth, J.Maier, "A Nano Porous Metal Recuperated Mn_2O Anode For Lithium Ion Batteries," *Adv Energy Mater*, 3 (2013), 281-285.
4. Y. He, J. Fu, Y. Zhang, Y. Zhao, L. Zhang, A. Xia, J. Cai, "Multilayered Si/Ni Nanosprings And Their Magnetic Properties," *Small*, 3 (2007), 153.
5. Y.P. Zhao, D.X. Ye, G.C. Wang, T.M. Lu, "Designing Nanostructures By Glancing Angle Deposition," *Proc SPIE*, 5219 (2003), 59.
6. K. Robbie, M.J. Brett, A. Lakhtakia, "First Thin Film Realization Of A Helicoidal Bianisotropic Medium," *J Vac Sc. Technol*, A13 (1995), 2991.
7. I. Ryu, J.W. Choi, Y. Cui, W.D. Nix, "Size Dependent Fracture Of Si Nanowire Battery Anodes," *J Mech Phys Solids*, 59 (2010), 1717.
8. M.T. Taschuk, M.M. Hawkeye, M.J. Brett, *Handbook Of Deposition Technologies For Films And Coatings: Science, Applications And Technology* (Oxford, Willam Andrew Publishing, 2010), 623–654.
9. J.B. Sorge, M.T. Taschuk, N.G. Wakefield, J.C. Sit, M.J. Brett, "Metal Oxide Morphology In Argon-Assisted Glancing Angle Deposition," *J Vac Sci Technol A*, 30 (2012), 121507.
10. U. Kasavajjula, C. Wang, "Apple By Nano- And Bulk-Silicon-Based Insertion Anodes For Lithium-Ion Secondary Cells," *J Power Sources*, 163 (2007), 1003.
11. H. Li, X. Huang, L. Chen, H. Zhou, Z. Zhang, D. Yu, Y.J. Mo, N. Pei, "The Crystal Structural Evolution Of Nano-Si Anode Caused By Lithium Insertion And Extraction At Room Temperature," *Solid State Ionics*, 135 (2000), 181.
12. R. Ruffo, S.S. Hong, C.K. Chan, R.A. Huggins, T. Cui, "Impedance Analysis Of Silicon Nanowire Lithium Ion Battery Anodes," *J Phys Chem C,* 113 (26) (2009), 11390.
13. E. Barsoukov, D.H. Kim, H.-S. Lee, H. Lee, M. Yakovleva, Y. Gao, J.F. Engel, "Comparison Of Kinetic Properties Of $LiCoO_2$ And $LiTi_{0.05}Mg_{0.05}Ni_{0.7}Co_{0.2}O_2$ By Impedance Spectroscopy," *Solid State Ionics* 161 (2003), 19.
14. M.H. Park, M.G. Kim, J. Joo, K. Kim, J. Kim, S. Ahn, Y. Cui, J. Cho, "Silicon Nanotube Battery Anodes," *Nano Lett*, 9 (2009), 3844.
15. H. Xia, S. Tang, L. Lu, "Properties Of Amorphous Si Thin Film Anodes Prepared By Pulsed Laser Deposition," *Mater Research Bull* 42 (2007), 1301-1309.

THICKNESS EFFECT ON THE THREE-DIMENSIONAL SCULPTURED SiCu THIN FILMS USED AS NEGATIVE ELECTRODES IN LITHIUM ION BATTERIES

B. Deniz Polat, Ceren Yagsi, Ozgul Keles*

Department of Metallurgical and Materials Engineering, Istanbul Technical University, Maslak, Istanbul, 34469, Turkey
*Tel:+902122853398, Fax:+902122853427, E-mail:ozgulkeles@itu.edu.tr

Keywords: Sculptured thin film anodes, Glancing angle deposition, Lithium ion battery

Abstract

SiCu (10 %at. Cu) composite three dimensional sculptured films with different thicknesses have been fabricated by an ion-assisted glancing angle co-deposition technique. The films have been evaluated as anodes considering morphological and structural differences depending on the different evaporation durations. The galvanostatic tests show that after 50th cycles the thin film delivers 2124 mAh g^{-1}, but the thick electrode performs 685 mAh g^{-1} as dicharge capacities. It is believed that the thin film electrode has a better electrochemical performance because increase in process time causes deformation in the helice's morphology, increase in ohmic resistance and generation of more stress in the electrode.

Introduction

After the commercialization in early 1990s, Lithium-ion batteries (LIBs) have been widely used in modern society as portable energy sources due to their high operation voltage, stable cycling performances, high energy and power densities.
In today's technology currently available LIBs are unable to fulfill the energy and power requirements of hybrid and pure electric vehicles. Currently, as cathodes can deliver upto 300 mAhg^{-1}capacity [1], the overall cell capacity mostly depends on the anode material's capacity. Thus, a need to replace the currently available commercially negative electrode, graphite, is on demand to get higher specific capacities (mAh g^{-1}). In this sense several elements (such as silicon (Si), tin (Sn), germanium (Ge), aluminum (Al) etc.) and alloys have been investigated as possible negative electrodes due to their high theoretical capacities[2-3]. Among them, Si becomes remarkable. Because, it is environmentally friendly and abundant in the Earth's Crust. Moreover, it has a high theoretical capacity of 3579 mAhg^{-1} (at room temperature) [4]. However, this advanced anode material suffers severe volume expansion (>300%) and contraction upon lithiation and de-lithiation, which leads to cracking and fracture in electrodes, and further leads to loss of electric conduction and capacity fading of the electrodes (delamination and/or peeling). Additionally as the lithiation potential is below the solvent decomposition voltage an unstable surface electrolyte interphase (SEI) film forms on the electrode. Plus, the low electrical conductivity (10^{-3} Scm^{-1}) and the low Li diffusion coefficient (between $10^{-14}$and 10^{-13} cm^{2}s^{-1}) of Si are the main challenges that prevent the practical implementation of Si as anodes in commercial lithium ion batteries [5-7].
So far, many scientists have been working to overcome the disadvantages of Si anodes. Using Si-M electrode is one of the solutions. Herein, M is not only used to prevent mechanical disintegration or the aggregation of Si in cycling but also works as conductive filler, which constructs conductive percolation network in the electrode. This is essential to compensate the low electronic conductivity of Si and achieve full electrode utilization. Besides, this

conductive network can also increase battery power and enable faster charge/discharge reactions. Herein, the use of Cu with Si becomes prominent because of the high conductivity and ductility of Cu. Besides, Cu form stable intermetallics with Si (like Cu_3Si) which have reversible reaction with Li [8-9]. Finally, the existence of Cu in the film increases the adhesion of the substrate (Cu foil) which would extent the cycle life and the rate capability of the electrode. On the otherhand, numerous efforts have been made to avoid mechanical degradation of Si anodes by improving the morphology. In previous works, nanostructuring the electrodes [10] or inducing homogeneously distributed spaces [11] have been shown to effectively enhance the cycling performance of Si composite anodes. Low stress generated in nanostructured materials during cycling is believed to be a reason for better cycle life, and the interspaces among the nanostructures are expected to avoid sintering during electrochemical cycling and increase the mechanical tolerance against volume change, hence the anode service life. Moreover, the free space among the structures creates an easy route for the electrolyte to access the entire surface and decrease the polarization, which, in turn, improves the capacity retention of the electrode [12].

In this work, we produced two anodes with well-aligned three dimensional (3-D) sculptured SiCufilms (with 10%at. Cu content) of different thicknesses ("thin," 600 nm, and "thick," 2 μm).They were fabricated by a one-step production technique, glancing angle deposition (GLAD). This process poses no risk from having to handle flammable, explosive, or carcinogenic metal nanoparticles. Moreover, a binder or conductive additive is not required to deposit the electrode. This ensures the direct electron transport of the intermetallic to the current collector and, hence, a fast Li^+ diffusion through the adjustable, small diameters of the structure [13].

The mechanism of the structured film formation during the GLAD method has been studied previously [14-18]. The schematic representation for GLAD process is given in Figs.1a-b. In GLAD process, a substrate is oriented using two programmable stepper motors: one adjusts α and the other controls the azimuthal rotation (Φ) of the substrate with respect to normal [18].The results show that it is possible to control the orientation of the film growth by changing the incident flux angle because the electron beam deposition is a line-of sight process, or by rotating the substrate. Therefore, to have (3-D) well-aligned SiCu structures by GLAD method, the evaporated particle flux should be deposited under a highly oblique angle (Θ) of the substrate's surface normal ($\Theta > 70$). The vapor flux hits the substrate from both vertical and lateral directions: the vertical component induces film growth and the lateral component contributes to the shadowing effect [19]. The "shadowing effect" is very important since it competes with "surface diffusion process". At room temperature deposition, (when the substrate does not rotate, azimuthal rotation is 0) since the surface diffusion rate is very slow, the impinging atoms randomly form islands on the substrate, when such growth is governed by Volmer-Weber or Stranski-Krastanov process. As deposition proceeds, the initially nucleated islands act as shadowing centers and all large islands receive more impinging atoms as compared to small ones, leading to inclined nanocolumnar film growth, where homogeneously distributed porosities are formed among the inclined nanorods. By changing the speed and the phase of azimuthal rotation, the nanocolumns can be sculptured into C-shape, S shape, zigzag shape, matchstick or helices [18].

In this work, we have decided to produce (3-D) sculptured SiCu films because the 3D structures reduce stress like a "stress reliever" due to the separated structures, which enable freedom of movement over short distances. The objective of the current study is to evaluate the use of GLAD method as an alternative production process to deposit (3-D) sculptured SiCu films with different thicknesses and to discuss the evaporation duration effect on these films' electrochemical performances when used as anodes in LIB.

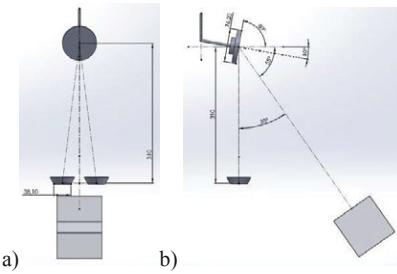

a) b)

Figure 1. Schematic representation of the GLAD method a) surface view, b) cross view

Experimental

The experimental setup used in this work is given in Figs 1a-b. Four kinds of substrates were used in the experiments: a Si wafer for cross-sectional SEM, a stainless steel (SS) disc (15.5-mm diameter and 1.5-mm thickness) for compositional analysis, a glass disc (Tedpella) for structural analysis, and finished copper discs with mirror-like surfaces (15.5-mm diameter and 1.5-mm thickness) for electrochemical analysis. The source materials were placed in graphite crucibles, and the chamber was pumped to a base pressure of about 3×10^{-6} Pa. Prior to deposition, the samples were sputtered for 8 minutes using 900 eV Ar^+ ions from a Kaufman ion source at a gas feeding rate of 8 sccm. The evaporation rates of Si and Cu were at 1 and 0.9 nm s^{-1}, respectively as read by two independent quartz-crystal microbalances (QCMs). At the start of deposition, the ion energy was reduced to 250 eV and Ar^+ ion-assisted deposition (IAD) was operated at 250 V and 23 mA for 5 minutes to assist in the establishment of a dense, adherent thin film. During deposition, the Ar^+ flow and ion gun were turned off. The ion source parameters used in the experiments were: 30 mA beam, 40 V discharge, and 100 V acceleration. The depositions took 15 and 36 minutes to have "thin" and "thick" film electrodes. The azimuthal rotational speed was 0.2 rpm. The crucible surface was 75° with the substrate surface normal.

The surface morphology and thicknesses of the "pristine" (i.e., no charging or discharging) film were determined with field-emission SEM (JEOL JSM 7000F and JEOL 5410). The composition of the film was determined by EDS (Oxford) analysis. The phases present in the pristine film were determined by XRD (Philips PW3710 system) with a 2θ range of 10–100° in steps of 0.05° (with CuKα at 40 kV and 30 mA).

For electrochemical testing, half-cells were assembled as 2032 coin cells in an Ar-filled glove box (Mbraun, Labmaster). The non-aqueous electrolyte was 1M $LiPF_6$ dissolved in ethylene carbonate (EC) and dimethyl carbonate (DMC) in a 1:1 weight ratio. 10 vol.% fluoro ethylene carbonate (FEC) was added as suggested by Elazari et al [21]. Cyclic Voltammetry was performed by Gamry/Interface 1000, for the 1st, 2nd, and 3rd cycles in the potential range of 0.2–1.2 V (vs. Li/Li^+) at a scan rate of 0.03 mV s^{-1}.The cells were tested at room temperature and operated at voltages of 0.2 V–1.2 V versus Li/Li^+ with a rate of 100 mA g^{-1}.

To get SEM views after the 1st discharge and 100th cycles, the cells are opened in the glove box and washed with DMC. After drying in the glove box, their surfaces were analyzed by FEG-SEM.

Results and Discussions

The SEM top and cross-sectional view images of the (3-D) sculptured SiCu films deposited on a substrate are shown in Figs. 2a-d. The cross-sectional views (Figs. 2(b,d)) indicate that

the films have thicknesses of about 700 and 1800 nm. The surface views (Fig. 2(a,c)) show that homogeneously distributed porosities are present in the thin film. Contrarily, inhomogeneous small interspaces are noted in the top of view of the thick film electrode which is believed to be related to the "broadening". Because as the atomic shadowing and the limited ad-atom diffusion work together to produce a microstructure of small isolated columns, the growth of these columns depends on strong competition and extinction effects. Therefore, as the process duration increases, this competition and the extinction effects leads to inhomogeneity of the film in the plane parallel to the substrate. This distortion in the column morphology has been interpreted as the "broadening" process, which is commonly observed as microstructural defects in the physical vapor deposition, when the thickness of the film is increased [20]. Figs 2a, c show that the thin and the thick film have 35±10 nm and 140±70 nm diameters respectively, which are less than 300 nm, known as the critical diameter for Si nanowires, to achieve maximum resistance against the stress formed during cycling.

The presence of nano-sized interspaces among these structures forms porosities in the thin film electrode. The size and the distribution of the porosities become irregular in the thick film, whilst they are homogeneously distributed in the thin film (Figs. 2b, d). Such a regular alignment in the film morphology not only facilitates electrolyte penetration into the electrode, but also enhances the mechanical tolerance against any volumetric changes in cycling.

The use of low-energy Ar^+ ion bombardment during GLAD deposition makes the film denser at the bottom of the coating for both films. According to Sorge et al. this effect is due to re-sputtering the top surfaces of the structure while a continuous deposition on the bottom of the adjacent structure occurs. This alteration in the film morphology results in the formation of denser and more adherent structured thin films.

In this work, we chose a moderate substrate rotation rate (0.02 rpm) considering the deposition rate of Si and Cu (10 and 0.9 Å/s, respectively). Thus, sufficient material is deposited onto the substrate to form preferentially oriented columns, which, in turn, eventually form 3D sculptured composite films (Fig. 2(b)).

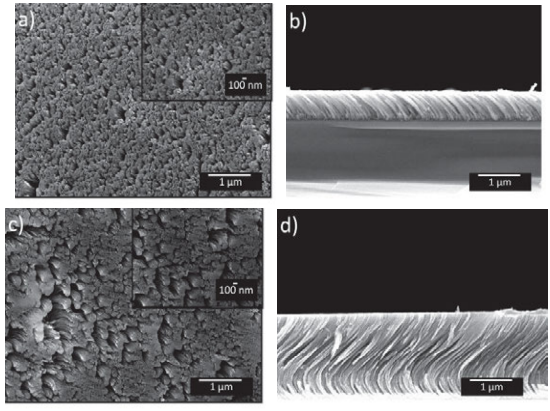

Figure 2. SEM surface views of the a) thin film surface view, b) thin film cross section view; the c) thick film surface view, d) thick film cross section view

The EDS results of the thin and thick films with the mass of the coatings are given in Table I.

Table I. EDS results of the thin and thick film with mass of the coatings.

	Thin Film			Thick Film		
EDS Results	Cu (at. %)	O (at. %)	Si (at. %)	Cu (at. %)	O (at. %)	Si (at. %)
	9.37	28.22	62.41	9.79	25.31	64.90
Mass of the coating (mg)	0.1			0.5		

In XRD analysis, the substrate is completely amorphous. Fig 3. shows that both films contain amorphous and/or nano-sized crystallites. No peaks of Si, Cu, and/or SiCu intermetallics are detected. This could be due to the small-sized grain morphology, which can not be detected by XRD. Having crystalline (α-Si) and amorphous (a-Si) Si particles are very important for the electrochemical performance of the electrodes since their reactions with Li^+ differ depending on the cell potential. α-Si lithiation becomes amorphous when lithiated and recrystallized when cell potential drops to 30 mV. During the delithiation, two phases present in the electrode, resulting in Li^+ entrapment. On the other hand, the structure of a-Si is always amorphous if the recrystallization of Li-Si particles is restricted below 30mV. In this case, Li^+ diffusion paths lead to higher electrochemical performance. Therefore, to prevent recrystallization and over-expansion of the electrode, the lower cut off voltage is chosen as 0.2 V.

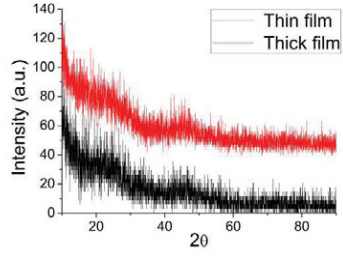

Figure 3. XRD results of the thick and thin film electrodes

Figs.4a-b show the CV curvatures for the 1st, 2nd, 3rdand 30th cycles. The peaks have the same potential compared to that of the pure Si. The change in curvature shapes during cycling proves that Cu atoms do not react with Li^+ and some morphological changes (pulverization) occur in the electrode. For the thin film electrode (Fig. 4a), in the first discharge (Li alloying) reaction, a cathodic peak around 0.7 V is noticeable in addition to the peaks around 0.4 and 0.2 V. Then, upon delithiation (Li de-alloying), broad anodic peaks are noted around 0.6 V and 1.0 V. As cycle continues the cathodic peak around 0.7 V and the anodic peak around 1.0 V disappear, while the cathodic peak around 0.4 V and the anodic peak around 0.6V remain distinct. The fact that the peak intensities decrease after the first cycle and the cathodic/anodic peaks (around 0.7 and 1.0 V) disappear proves that some irreversible reaction occur in the first cycle of the electrode. Solid electrolyte interface formation following the electrolyte reduction on the electrode surface and/or Li^+ trapping in the electrode following the morphological changes may be the main reasons for it. The comparison of the curvatures of different cycles show that after the 1st cycle, SEI formation becomes less important and the reversible reaction of the amorphous particles with Li^+ dominates the lithiation mechanism.

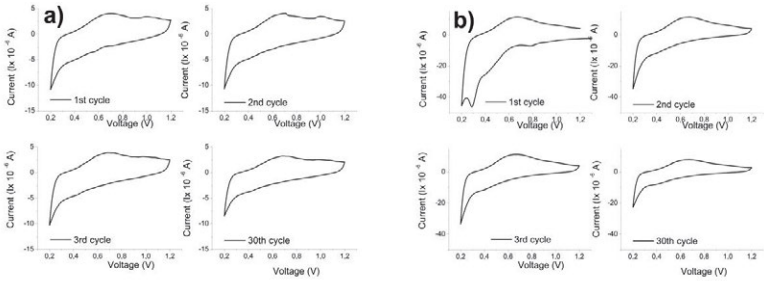

Figure 4. CV test results after the 1st, 2nd, 3rd and 30th cycles for a) thin film, b) thick film.

When the CV curvature of the thick film electrode is observed, beside 0.2 V an additional cathodic peak around 0.3 V is remarkable in the first cycle (Fig. 4b). The existence of this cathodic peak (at 0.3 V) shows the lithiation of nano-sized crystalline Si particles with Li^+. Similar to the thin film electrode the cathodic peak around 0.8 V disappears as cycles continue which proves that after the first cycle the irreversible reactions of Li^+ (forming SEI layer) decreases. Moreover, the fact that the peak intensities of the curvatures decrease in cycling also justify that the amount of reaction occurred between the active material (Si in that case) with Li^+ decreases during cycling.

Figs 5a and b give the capacity-cylce diagram of the thin and thick film electrodes. The thin film shows very stable performance. It delivers 2318 mAh/g as the first discharge capacity and retains 92% of its initial capacity after 50th cycles. Fig. 5a shows that there is noticeable gap between the discharge and charge capacities of each cycle. This gap might be explained considering the irreversible reactions following the morphological changes occurred in the electrode. On the other hand the thick film electrode has 2078 mAh/g as the first discharge capacity, then 643 mAh/g as the 2nd discharge capacity. The electrode then performs stable performance which shows that lithiation/delithiation reactions become reversible after the pulverization. Possible cracking might also explain the noticeable decrease in the capacity of the electrode after the first cycle.

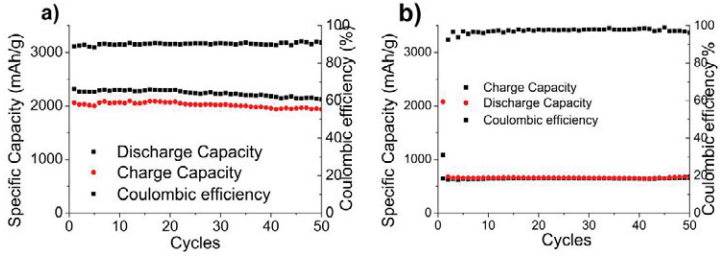

Figure 5. Capacity-cycle diagram of a) the thin film, b) the thick film electrodes.

To justify the above mentioned explanation, the ex-situ SEM surface views of both samples are given in Fig. 6a-d after the 1st discharge and 50th cycles. Figs. 6a and b show that after 1st discharge reaction, the porosities are cleared away due to the expansion of the structure with Li^+ intercalation. When Figs 6a and b are compared, the size of the particles are seemed to larger from 1st discharge to 50th cycles, and a flu film on top becomes noticeable. It is possible that an electrochemical agglomeration might occur in cycling, which will be covered by SEI layer afterwards. On the other hand, the comparison between Figs. 6c and d reveals that the

morphology of the electrode surface changes from 1st discharge to 50th cycles. The inhomogeneous morphology and larger particle size of the thick film cause pulverization followed by the SEI formation on the electrode. This causes an instability in the initial cycle of the electrode. The capacity becomes stable once the electrode surface/electrolyte interface gets stabilized.

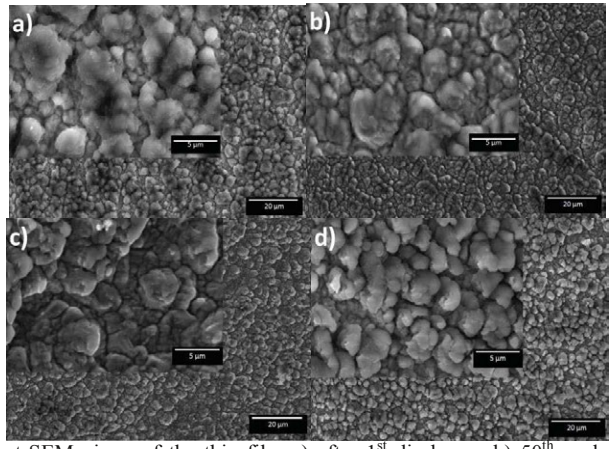

Figure 6. Post-SEM views of the thin film a) after 1st discharge, b) 50th cycles; Post-SEM views of the thin film c) after 1st discharge, d) 50th cycles

Conclusion

In this work, IA-GLAD method has been used to form 3D structured SiCu films with different thicknesses. Cu atoms are added into the structure to increase the ductility and the conductivity of the thin film electrode, which result in highly stress-tolerant anode formation.
Structural and morphological analyses show that the nano-sized particles present in the thin film electrode and the homogeneous distribution of porosities in the thin film facilitate Li^+ diffusion within the electrode. On the other hand the inhomogeneous morphology and larger particle size of the thick film resulting from the longer evaporation duration seem to cause instability in the initial cycle of the electrode the thin film.
The difference in the initial cycles of the galvanostatic test results could be explained by the morphological changes of the electrodes. The absence of the big alteration in the capacity values for the thin film shows that no delamination or peel off occurs in the electrode. On the other hand, the thick film electrode performs remarkable pulverization following the volumetric changes since the discharge capacity decreases noticeably after the first cycle and becomes stable afterwards.

References

1. S. Afyon, F. Krumeich, C. Mensing, A. Borgschulte, R. Nesper, "New High Capacity Cathode Materials For Rechargeable Li-Ion Batteries: Vanadates-Borateglasses," *Nature Chem,* 19 (2014), 1079-1083.
2. S.K. Sharma, M.S. Kim, D.Y. Kim, J.S. Yu, "Al Nanorod Thin Films As Anodes Electrode For Li Ion Rechargeable Batteries," *Electrochim Acta,* 87 (2013), 872-879.
3. T.Kennedy, E. Mullane, H. Geaney, M.Osiak, C.O. Dwyer, K.M. Ryan, "High Performance Germanium Nanowire-Based Lithium-Ion Battery Anodes Extending

Over 1000 Cycles Through In Situ Formation Of A Continous Porous Network," *Nano Lett*,14 (2014), 716-723.
4. W.Yuan, M.Wu, H. Zhao, X. Song, G. Liu, "Baseline Si Electrode Fabrication And Performance For Advanced Transportation Technologies Program," *J PowerSources*, 282 (2015), 223-227.
5. M.Verbrugge, D.R. Baker, X. Xiao, Q. Zhang, Y.T. Cheng, "Experimental And Therorical Characterization Of Electrode Materials That Undergo Large Volume Changes And Application To The Lithium-Silicon System, " *J Phys Chem*, C (119) (2015), 5341-5349.
6. E. Pollak, G. Salitra, V. Baranchugov, D. Aurbach, In-Situ Conductivitiy, "Impedance Spectroscopy, Andex-Situraman Of Amorphous Silicon During The Insertion/Extraction Of Lithium," *J Phys Chem*, C (111) (2007), 11437-11444.
7. J. Xie, N. Imanishi, T. Zhang, A. Hirano, Y. Takeda, O.Yamamoto, "Li-Ion Diffusion In Amorphous Si Films Prepared By RF Magnetron Sputtering : A Comparison Of Using Liquid And Polymer Electrolyte," *Mater Chem Phys*, 120 (2010), 421-425.
8. S. Yoon, S. Lee, H. Kim, H.J. Sohn, "Enhancement Of Capacity Of Carbon-Coated Si–Cu3Si Composite Anode Using Metal–Organic Compound For Lithium-Ion Batteries," *J Power Sources,* 161 (2006),1319-1323.
9. J.H. Kim, H. Kim, H.J. Sohn, "Addition Of Cu For Carbon Coated Si-Based Composites As Anode Materials For Lithium-Ion Batteries," *J Power Sources,* 7 (2005), 557-561.
10. H. Wu, Y. Cui, "Designing Nanostructured Si Anodes For High Energy Lithium Ion Batteries," *Nano Today*, 7 (2012), 414-429.
11. H.Wu, G. Zheng, N. Liu, T.J. Carney, Y. Yang, Y. Cui, "Engineering Empty Space Between Si Nanoparticles For Lithium-Ion Battery Anodes," *Nano Lett*, 12 (2012), 904-909.
12. T. Umeno, K. Fukuda, H. Wnag, N. Dimov, T. Iwao, M. Yoshio, "Novel Anode Material for Lithium-ion Batteries: Carbon-Coated Silicon Prepared by Thermal Vapor Decomposition," *Chem Lett*, 30 (2011), 1186.
13. A. Irrera, E. F. Pecora, F. Priolo, "Control Of Growth Mechanisms And Orientation In Epitaxial Si Nanowires Grown By Electron Beam Evaporation," *Nano Tech*, 20 (2009), 135601.
14. Y. He,J. Fu, Y. Zhang, Y. Zhao, L. Zhang, A. Xia, J. Cai , "Multilayered Si/Ni Nanosprings And Their Magnetic Properties," *Small*, 3 (2007), 153-160.
15. Y.P Zhao, D.X. Ye, G.C. Wang,T.M. Lu, "Novel Nano-Column and Nano-Flower Arrays by Glancing Angle Deposition," *Nano Lett,* 2 (2002), 351-354.
16. Y. He, Z. Zhang, C. Hoffmann, Y. Zhao, "Embedding Ag Nanoparticles Into Mgf2 Nanorod Arrays," *Adv Func Mater,* 18 (2008), 1676-1684.
17. S.V Kesapragada, P.Victor, D. Gall, "Nanospring Pressure Sensors Grown By Glancing Angle Deposition," *Nano Lett,* 6 (2006), 854-857.
18. Y. He, Z. Zhao, "Advanced Multi-Component Nanostructures Designed By Dynamic Shadowing Growth," *Nanoscale,* 3 (2011), 2361-2375.
19. R. Elazari, G. Salitra, G. Gershinsky, "Li Ion Cells Comprising Lithiated Columnar Silicon Film Anodes TiS_2 Cathodes and Fluoroethyene Carbonate (FEC) as a Critically Important Component," *J Electrochem Soc,*159 (2012), A1440-1445.
20. M.O. Jensen, M. Brett, "Porosity Engineering In Glancing Angle Deposition Thin Films," *J Appl Phys A*, 80 (2005),763.

TMS2016

145th Annual Meeting & Exhibition

SUPPLEMENTAL PROCEEDINGS

ICME Infrastructure Development for Accelerated Materials Design: Data Repositories, Informatics, and Computational Tools

AN INTEGRATED MODEL FOR PREDICTION OF YIELD STRESS IN Al-7Si-Mg CAST ALLOYS

Rui CHEN [1], Qingyan XU [1], Zhiyuan XIA[2], Huiting GUO [2], Qinfang WU [2], Baicheng LIU [1]

[1] Key Laboratory for Advanced Materials Processing Technology, School of Materials Science and Engineering, Tsinghua University, Beijing 100084, China
[2] Mingzhi Technology Co.Limited, Suzhou 215006, China

Keywords: Cast aluminum alloys; Aging; Yield strength; Modeling; Microstructure

Abstract

The desired mechanical properties of Al-7Si-Mg cast alloys can be achieved by a corresponding processing process, and are extensively used in automotive and aerospace industries. The prediction of the microstructure controlling mechanical properties is meaningful in order to further modify the properties of castings. In present research, a microstructure-strength relation based model was developed to predict the yield stress of Al-7Si-Mg cast alloys. The as-cast microstructure was simulated by cellular automaton model and its effect on yield stress was considered. Based on the general framework proposed by Kampmann and Wagner, a multi-component precipitation model involving nucleation, growth and coarsening of precipitates, as well as a strengthening model were developed. Applications of these models to an engine block casting were carried out to predict the as-cast microstructure as well as the final yield stress, and the predictions were verified with experimental results.

Introduction

Due to an excellent combination of castability, high corrosion resistance and comprehensive mechanical properties, Al-Si-Mg cast alloy plays an important role in the automotive and aerospace industries as structural components [1,2]. The as-cast microstructure of these alloys is mainly made up of primary α-Al dendrite and eutectic silicon with a poor mechanical properties in as-cast state while a desired combination of mechanical properties can generally achieved by a proper T6 heat treatment due to the precipitation of a high number density of nano-sized β"/β' metastable strengthening phases.

For a certain component in aluminum alloys, tensile properties are generally used to judge the performance. In order to make a better understanding of property-controlled factors and further improve the properties, development of models to achieve the prediction of mechanical properties for heat-treatable aluminum alloys has been an attractive way in recent years. Various aging precipitation and hardening models to predict the yield stress of wrought aluminum alloys based on thermodynamics, kinetics and dislocation mechanics have been developed recently. These yield stress models generally take into account the contribution of pure aluminum strength, solid solution strength and precipitation hardening to the overall yield stress [3~5]. For cast aluminum alloys, however, a number of designed experiments clearly indicate that the condition

of solidification has influence on the subsequent properties. For instance, refiner as-cast microstructure, corresponding to a higher cooling rate, has higher tensile properties. This fact raises the necessity to take into account the effects of as-cast microstructure when predicting the final yield stress of cast aluminum alloys. On recent decades, with the advancements of computer technology, numerical simulation has been a powerful tool to predict the microstructure formation during solidification, among which the cellular automaton (CA) model is a promising method in describing as-cast microstructure comparable to those observed in experiments[6,7].
In this work, we establish a microstructure-strength based model, involving as-cast microstructure simulation using CA model and precipitation hardening prediction based on the general framework originally proposed by Kampmann and Wagner (KWN model). Applications of this integrated model to a certain engine block casting to predict the final yield stress were carried out and the predictions were compared with experiment results.

Model description

Fig.1 shows the processing sequence and the microstructure evolution of Al-Si-Mg cast alloys. It can be seen that during solidification process, dendrite will firstly precipitate out from the melt and grow into fully developed dendrite arms. At the end of solidification, eutectic silicon as well as a small quantity of intermetallic phases will appear. During solution treatment, the eutectic silicon will go through spheroidizing and coarsening, and intermetallic phases will be dissolved into the α-Al matrix to create a nearly homogenous solid solution. The morphology evolution of eutectic silicon on yield stress can be neglected as suggested in Ref.[8]. During aging process, supersaturated Mg element will precipitated out from the matrix along with Si element, forming β"/β' strengthening phases uniformly distributed in the matrix.

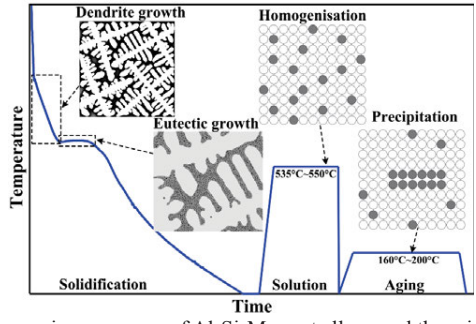

Fig.1 Schematic of processing sequence of Al-Si-Mg cast alloys and the microstructure evolution

Strength model

Considering the microstructure characteristics of Al-Si-Mg cast aluminum alloys, several strengthening mechanisms to the yield stress are considered, including intrinsic strength $\Delta\sigma_i$, grain boundaries hardening $\Delta\sigma_{GB}$, solid solution strengthening $\Delta\sigma_{ss}$ and precipitation hardening $\Delta\sigma_{ppt}$. The present model adopts the linear superposition law generally used by numerous workers to get the overall yield stress

$$\sigma_y = \Delta\sigma_i + \Delta\sigma_{GB} + \Delta\sigma_{ss} + \Delta\sigma_{ppt} \quad (1)$$

The intrinsic strength is defined here as being the sum of the contribution of lattice resistance, eutectic silicon particles, and eutectic Fe-bearing particles et al, which remains constant during aging [8]. The contribution of grain boundaries hardening is controlled by grain density (N_s) and secondary dendrite arm spacing (SDAS), and solid solution strengthening term depends on the mean solute concentration of each alloying element which is expressed as $\Delta\sigma_{ss}=k_{Si}w_{Si}+k_{Mg}w_{Mg}$, k_{Si}=11MPa wt·%$^{-1}$, k_{Mg}=17MPa wt·%$^{-1}$, w_{Si} and w_{Mg} are the weight concentrations in the matrix in as-quenched state) [9]. For Al-Si-Mg dendrite microstructure, the contribution of SDAS refinement to grain boundaries hardening is much larger than grain density. Fig.2 displays the yield stress varying with the secondary dendrite arm spacing for as-quenched samples (solution treated at 535°C for 6h, and quenched in 70°C water) in Al-7Si-0.36Mg alloy. It can be seen that the yield stress increases with SADS decreasing, indicating the importance of as-cast microstructure on the final yield stress.

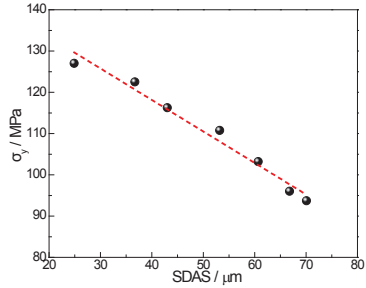

Fig.2 Variation of yield stress as a function of secondary dendrite arm spacing (SDAS) for as-quenched samples in Al-7Si-0.36Mg alloy.

In as-quenched state, none precipitates exist in the matrix (i.e. $\Delta\sigma_{ppt}$=0), thus Eq.(1) can be expressed as

$$\Delta\sigma_0 = \Delta\sigma_i + \Delta\sigma_{GB} = \sigma_y - \Delta\sigma_{ss} \quad (2)$$

The solid solution component, $\Delta\sigma_{ss}$, is first determined according to $\Delta\sigma_{ss}=k_{Si}w_{Si}+k_{Mg}w_{Mg}$, and through combining the experimental data in Fig.2 with Eq. (2), we obtain the following expression by nonlinear surface fitting with a correlation coefficient R^2=0.978

$$\Delta\sigma_0 = 130.3 - 0.76 \cdot \mathrm{SDAS} \quad (3)$$

This equation introduces the contribution of as-cast microstructure to the final yield stress, and highlights the necessity of as-cast microstructure prediction during solidification. For majority aluminum alloys, the precipitation hardening is the main strengthening mechanism whose effects is controlled by the strength, size, volume fraction, morphology, number density and distribution of precipitates. Two main mechanisms exist for precipitate hardening according the difference in precipitate size. When a moving dislocation encounters a precipitate with the size r_p smaller than the critical size r_p^c (named weak obstacle), it will cut through the precipitate, a mechanism

known as shearing. When the precipitate size is larger than r_p^c (named strong obstacle), the dislocation bypasses the precipitate by looping around it, known as Orowan looping mechanism. A nonlinear superposition law of the precipitate strengthening effects from both weak and strong obstacles was used in the present model as following

$$\Delta\sigma_{ppt} = M\left((\tau_c^w)^q + (\tau_c^s)^q\right)^{1/q} \tag{4}$$

where M is Taylor factor, q is an exponent which lies between 1 and 2. τ_c^w and τ_c^s are shear stress respectively from weak and strong obstacles, which can be expressed as follows

$$\begin{cases} \tau_c^w = \dfrac{\sqrt{\sum_{r_p<r_p^c} N_k(r_p) l_p}}{\sqrt{2\sqrt{3}\Gamma b}} \left(\dfrac{\sum_{r_p<r_p^c} N_k(r_p) F_k(r_p)}{\sum_{r_p<r_p^c} N_k(r_p)} \right)^{\frac{3}{2}} & \text{weak obstacles} \\ \tau_c^s = \sqrt{2}\delta G b \sqrt{\sum_{r_p>r_p^c} N_k(r_p) l_p} & \text{strong obstacles} \end{cases} \tag{5}$$

where $N_k(r_p)$ and l_p are the number density and length of precipitates in kth interval. $F_k(r_p)$ is the strength of precipitates in kth interval. Γ denotes the line tension of dislocation, b is the Burgers vector, δ is a constant, and G is the shear modulus of the aluminum.

CA model for as-cast microstructure prediction

For Al-Si-Mg cast alloys, the refinement of dendrite is mainly revealed in two ways: grain refinement and secondary dendrite arm spacing refinement. The first is controlled by nucleation and the other is determined by dendrite growth. Through analyzing the measured cooling curves in different cooling conditions of Al-7Si-0.36Mg ternary alloy during sand casting, a theoretical nucleation model correlated maximum nucleation undercooling ΔT_m with the nucleation density N_S has been proposed in our previous work [6]

$$N_S = 260.1\exp(-\frac{5.165}{\Delta T_m}) \tag{6}$$

Once the dendrite is nucleated, it will begin to grow through heat transfer and solute diffusion. To describe solute diffusion of Al-Si-Mg ternary system, the solute fields of Si and Mg need to be calculated separately based on the following equation

$$\frac{\partial w_i^\phi}{\partial t} = \nabla\cdot(\sum_{j=\mathrm{Si,Mg}} D_{ij}^\phi \nabla w_j^\phi) + w_i^\phi(1-k_i)\frac{\partial f_S}{\partial t} \tag{7}$$

where w is the composition with its superscript ϕ denoting liquid or solid phase and the subscript i refers to the alloying element Si or Mg. D_{ij}^ϕ is the solute diffusivity matrix for phase ϕ, and k_i is the equilibrium partition coefficient. During the growth, local thermodynamic equilibrium exists at the interface due to the influence of constitutional undercooling and curvature undercooling, the interface equilibrium temperature is characterized by the following equation neglecting the kinetic undercooling

$$T(t) = T_L^{liq}(w_i^L) - \Delta T_C - \Delta T_R \tag{8}$$

where $T_{\mathrm{L}}^{\mathrm{liq}}(w_i^{\mathrm{L}})$ is the liquidus temperature, ΔT_{C} and ΔT_{R} are the constitutional and curvature undercooling respectively. On the scale of an interfacial cell, the lever rule is used to calculate the increment of solid fraction Δf_{S}

$$\Delta f_{\mathrm{S}} = \frac{w_{\mathrm{Si}}^{\mathrm{L}*} - w_{\mathrm{Si}}^{\mathrm{L}}}{w_{\mathrm{Si}}^{\mathrm{L}*}(1-k_{\mathrm{Si}})} = \frac{w_{\mathrm{Mg}}^{\mathrm{L}*} - w_{\mathrm{Mg}}^{\mathrm{L}}}{w_{\mathrm{Mg}}^{\mathrm{L}*}(1-k_{\mathrm{Mg}})} \tag{9}$$

where $w_{\mathrm{Si}}^{\mathrm{L}*}$ and $w_{\mathrm{Mg}}^{\mathrm{L}*}$ are the local equilibrium composition of Si and Mg elements at the interface. For detailed algorithm of CA model for dendrite simulation, it can refer to the article [10]. After the calculation of dendrite microstructure, we can obtain the data of grain density and secondary dendrite arm spacing, thus acquiring the value of $\Delta\sigma_0$ using Eq. (3).

Precipitation kinetics model

During aging process, the as-quenched sample with high supersaturated Si and Mg atoms in the matrix will precipitate out second phases, generally containing a higher concentration of solute atoms. The precipitation traditionally involve three basic stages, which is characterized by nucleation, growth and coarsening. For Al-Si-Mg alloys, the precipitation sequence is indicated in most recent works by SSS (supersaturated solid solution)→GPzones→β''→β'→β(Mg_2Si) and the main precipitation hardening effects come from the needle/rod-shaped β''-β' [11]. For homogenous nucleation, the classical KWN nucleation model is used neglecting the incubation time

$$\frac{dN}{dt} = N_0 Z \beta^* \exp\left(-\frac{\Delta G^*}{k_{\mathrm{b}} T}\right) \tag{10}$$

where N is number of precipitates per unit volume, t is the aging time, N_0 is the number of nuclei sites per unit volume, Z is the Zeldovitch factor, β^* is the rate of atomic attachment to a growing embryo, ΔG^* is critical energy barrier for nucleation, k_{b} is Boltzmann constant, T is the aging temperature.

The classical KWN growth and coarsening model developed by Kampmann et al was assumed spherical morphology of precipitates, while for needle/rod-shaped precipitates of Mg_xSi_y in Al-Si-Mg alloys, the model was modified by taking into account the effects of precipitate morphology on growth and coarsening and the growth velocity v is given by

$$v = \frac{dr_{\mathrm{p}}}{dt} = \frac{2\phi}{3\phi - 1} \sum_{j=\mathrm{Si,Mg}} \frac{D_{ij}^{\alpha}}{\xi r_{\mathrm{p}}} \frac{x_j^{\alpha}(\infty) - x_j^{\alpha}(r_{\mathrm{p}})}{\varepsilon x_j^{\beta} - x_j^{\alpha}(r_{\mathrm{p}})} \tag{11}$$

where ϕ is aspect ratio and defined as $\phi = l_{\mathrm{p}}/2r_{\mathrm{p}}$, D_{ij}^{α} is the solute diffusion matrix in α phase, ξ is a factor for adjusting the effective diffusion distance from the radius as the supersaturation varies [12], $x_i^{\alpha}(\infty)$ is the solute fraction in matrix of i element, ε is the ratio between matrix and precipitate molar volume ($\varepsilon = V_{\mathrm{m}}^{\alpha}/V_{\mathrm{m}}^{\beta}$), x_i^{β} is the solute fraction of i element in precipitate Mg_xSi_y ($x_{\mathrm{Mg}}^{\beta} = x/(x+y)$, $x_{\mathrm{Si}}^{\beta} = y/(x+y)$). $x_j^{\alpha}(r_{\mathrm{p}})$ is the interfacial equilibrium solute fraction of j atoms in α

phase corrected by Gibbs-Thomson effects and can be expressed as follows

$$\left[x_{\mathrm{Si}}^{\alpha}\left(r_{\mathrm{p}}\right)\right]^{x_{\mathrm{Si}}^{\beta}}\left[x_{\mathrm{Mg}}^{\alpha}\left(r_{\mathrm{p}}\right)\right]^{x_{\mathrm{Mg}}^{\beta}}=\left[x_{\mathrm{Si},e}^{\alpha}\right]^{x_{\mathrm{Si}}^{\beta}}\left[x_{\mathrm{Mg},e}^{\alpha}\right]^{x_{\mathrm{Mg}}^{\beta}}\exp\left(\frac{2\gamma V_{m}^{\beta}}{RTr_{\mathrm{p}}}\frac{2\phi}{3\phi-1}\right) \tag{12}$$

where $x_{\mathrm{Si},e}^{\alpha}$ and $x_{\mathrm{Mg},e}^{\alpha}$ are the equilibrium solute fraction at the precipitate/matrix interface given by the phase diagram, γ is the interfacial energy and R is universal gas constant. Through a combination of Eq.(10), (11), (12), we can get the microstructural features of precipitates including number density $N_k(r_{\mathrm{p}})$ and the size l_{p} during every time step, thus acquiring the contribution of precipitation hardening $\Delta\sigma_{\mathrm{ppt}}$ using Eq. (4) and Eq. (5). Fig.3 shows the structure and flowchart of the integrated model to achieve the prediction of yield stress of cast components in Al-7Si-Mg alloys.

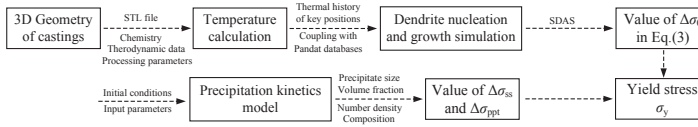

Fig.3 Flowchart of the integrated computational model to predict the yield stress of castings in Al-7Si-Mg alloys

Model applications

Application of the model to an engine block casting in Al-7Si-0.36Mg alloy (shown in Fig.4) was carried out. It was produced by low pressure casting with the pressure in the mold-filling and solidification stage approximately being 0.22bar and the cooling curves in the positions marked 1, 2 and 3 were measured. After solidification, it was solution treated at 535°C for 8h, following by hot water quenching, and then artificial aged at 160°C for 6h. The microstructure characterization and tensile strength at these three positions were performed.

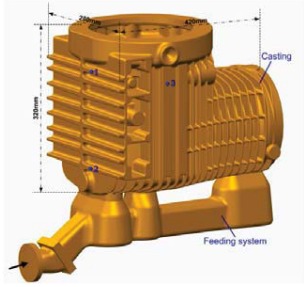

Fig.4 Geometry and three locations for temperature measuring marked as 1, 2 and 3.

Thermal history calculation

Prior to as-cast microstructure simulation of a certain position, the thermal history must be known for the sake of providing the initial input data for microstructure simulation. Fig.5 shows

the calculated solid fraction field varying with the solidification time. It can be seen that the melt fills the cavity from bottom to top under the pressure and solidifies from top to bottom. By observing the solid fraction variation at three positions, we can know that the solidification rate at position 3 is highest while it is smallest at position 2 which is close to the sprue. Fig.6 displays the calculated temperature curves at these three positions and the calculation precision was verified through comparing with experimental measured cooling curves. It reveals that the predictions, especially in the period of dendrite solidification, agree well with the experiments. Furthermore, it is seen that the minimum nucleation temperature at position 1 is lower than at both position 2 and position 3, and the difference in minimum nucleation temperature will result in the different nucleation density.

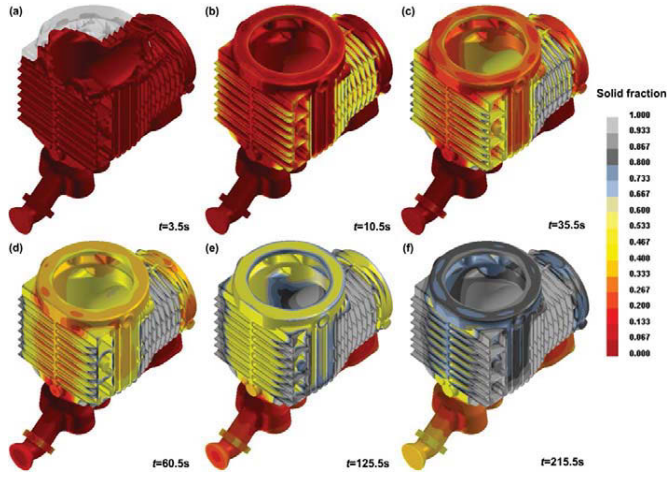

Fig.5 Calculated solid fraction field varying with solidification time

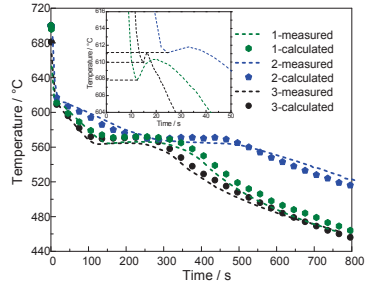

Fig.6 Comparison between the measured and calculated temperature at position 1, position 2 and position 3

As-cast microstructure simulation

Using the cooling curves as input data, we can describe the dendrite nucleation and growth by cellular automaton model, thus acquiring the microstructure parameters. Simulations were carried out in a two-dimensional domain containing 2500×1500 cells with a mesh size of 4μm. The temperature was assumed to be uniform in the domain and the dendrites nucleated with randomly preferential growth orientations. Corresponding parameters for simulation of Al-7Si-0.36Mg alloys can be found in Ref.[6]. Fig.7 shows the simulated as-cast dendrite microstructure and the experimental obtained metallographic microstructure for these three positions. It can be seen that the dendrites grow in four-fold symmetry morphology with fully developed side-branching and the random distribution in location. Although the dendrite morphology in experiment is much more complicated as it grows in three-dimensions, the comparisons between predictions and experiments concerning nucleation density and SDAS reveals a satisfying agreement, which are displayed in Fig.8. It can be noted that the nucleation density in position 1 is larger than the other two positions because it has a lower minimum nucleation temperature (see Fig.6), while the SDAS in position 2 is largest as it has a smallest cooling rate. The accuracy in as-cast microstructure prediction provides the basis for the following yield stress prediction.

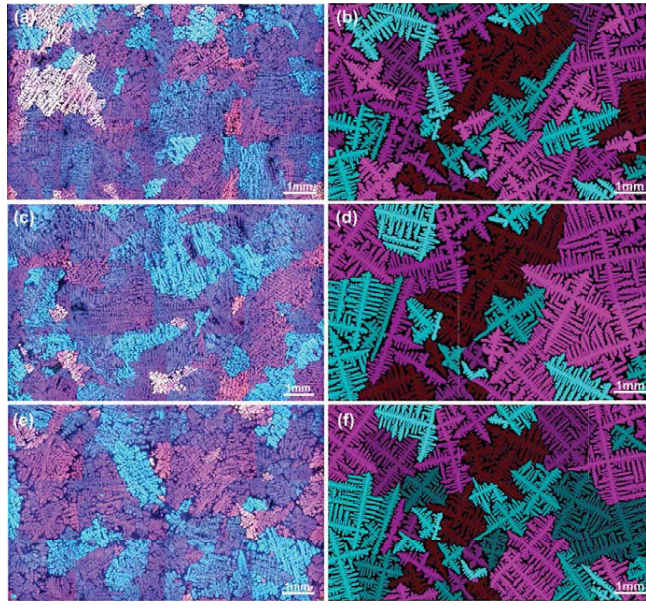

Fig.7 Comparison of the as-cast dendrite microstructure between experimental measured (a, c, e) and CA model predicted (b, d, f). (a, b) for position 1, (c, d) for position 2, (e, f) for position 3.

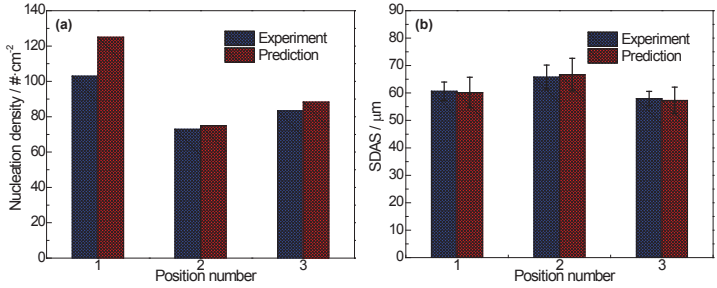

Fig.8 Comparison of the nucleation density (a) and SDAS (b) between experimental measured and model predicted.

Precipitation hardening prediction

The precipitation kinetics model presented above can well describe the evolution of microstructural features of precipitates as a function of aging time and temperature, thus achieving the prediction of hardening behavior through combining with the strength model. The input parameters of Al-7Si-0.36Mg alloy listed in Table 1 are obtained from references or calculated by Pandat database [13]. Fig.9 shows the relative contributions to the total yield stress as a function of aging time for the sample at position 3. It can be seen that due to the precipitation of Mg_2Si, the precipitation hardening effect increases with aging time until to the peak, while the solid solution effect decreases because of the depletion of solute in matrix. The prediction reveals that this alloy aged for 6h at 160°C cannot arrive the peak-aged condition, suggesting extending the aging time to more than 12h. Comparison of yield stress between experimental measured and model predicted are displayed in Fig.10, in which there is a remarkably good agreement for all the samples.

Table 1 Parameters of Al-7Si-0.36Mg alloy for precipitation kinetics and yield stress calculation at 160°C. "Pandat" means the value is obtained from Pandat databases

Parameter	Value	Sources	Parameter	Value	Sources
ϕ	6	[4]	ε	1	--
γ (J·m^{-2})	0.35	[9]	V_m^{β} (m^3·mol)	3.95×10^{-5}	[14]
$x_{Si,e}^{\alpha}$ (at.%)	2.19×10^{-5}	Pandat	δ	0.5	[5]
$x_{Mg,e}^{\alpha}$ (at.%)	3.93×10^{-5}	Pandat	G (N·m^{-2})	2.7×10^{10}	[3]
x_{Mg}^{β} (at.%)	66.7	--	b (m)	2.84×10^{-10}	[3]
x_{Si}^{β} (at.%)	33.3	--	M	3.1	[3]
D_{ij}^{α} (m^2·s^{-1})	varies	Pandat	q	2	--
ξ	1	--			

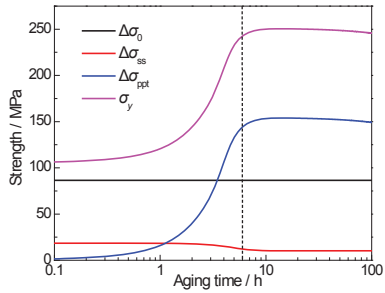

Fig.9 Predicted relative contributions to yield stress varying with aging time at 160°C for the sample at position 3

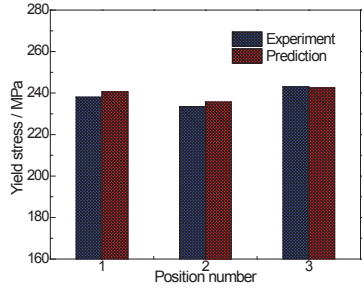

Fig.10 Comparison of yield stress between experimental measured and model predicted at three positions

Conclusions

An integrated microstructure-strength model is developed for predicting the yield stress under different solidification and heat treatment conditions in Al-7Si-Mg alloys. In order to take into account the effect of as-cast microstructure on yield stress, the secondary dendrite arm spacing is emphasized and its prediction is achieved by a cellular automaton model. The aging precipitation kinetics involving nucleation, growth and coarsening three stages is predicted based on the general idea of KWN model. The yield strength model accounts for the whole precipitate size distribution, shape of precipitates and their specific spatial distribution based on the consideration of the competing shearing and bypassing strengthening mechanisms. Applications of this model to an engine block casting are carried out and the model predictions are confirmed with a good agreement with the experimental measured values concerning the as-cast microstructure and final yield stress.

Acknowledgments

The authors gratefully acknowledge the financial support of the National Natural Science Foundation of China (Grant Nos. 51374137, 51171089), and National Science and Technology Major Projects (Grant Nos. 2012ZX04012-011, 2011ZX04014-052).

References

[1] M. Zhu et al., "Effects of T6 heat treatment on the microstructure, tensile properties, and fracture behavior of the modified A356 alloys", *Materials and Design*, 36 (2012), 243-249

[2] P. Li et al., "Grain refinement of A356 by Al-Ti-B-C master alloy and its effect on mechanical properties", *Materials and Design*, (47) 2013, 522-528

[3] O R Myhr, Ø Grong, and S J Andersen, "Modelling of the age hardening behaviour of Al-Mg-Si alloys", *Acta Materialia*, (49) 2001, 65-75

[4] D Bardel et al., "Coupled precipitation and yield strength modeling for non-isothermal treatments of a 6061 aluminium alloy", *Acta Materialia*, (62) 2014, 129-140

[5] A Bahrami, A Miroux, and J Sietsma, "An age-hardening model for Al-Mg-Si alloys considering needle-shaped precipitates", *Metallurgical and Materials Transactions A*, (43) 2012, 4445-4453

[6] R Chen et al., "Nucleation model and dendrite growth simulation in solidification process of Al-7Si-Mg alloy", *Acta Metallurgica Sinica*, (51) 2015, 733-744

[7] B Li et al., "Study on microstructure simulation of ZL114A alloy during low pressure die casting process", *Acta Metallurgica Sinica*, (44) 2008, 243-248

[8] P A Rometsch, G B Schaffer, "An age hardening model for Al-7Si-Mg casting alloys", *Materials Science and Engineering A*, (325) 2002, 424-434

[9] E Sjölander, S Seifeddine, and I L Svensson, "Modelling yield strength of heat treated Al-Si-Mg casting alloys", *International Journal of Cast Metals Research*, (24) 2011, 338-346

[10] R Chen, Q Y Xu, and B C Liu, "Cellular automaton simulation of three-dimensional dendrite growth in Al-7Si-Mg ternary aluminum alloys", *Computational Materials Science*, (105) 2015, 90-100

[11] D Maisonnette et al., "Effects of heat treatments on the microstructure and mechanical properties of a 6061 aluminium alloy", *Materials Science Engineering A*, (528) 2011, 2718-2724

[12] Q Chen, J Jeppsson, and J Ågren, "Analytical treatment of diffusion during precipitate growth in multicomponent systems", *Acta Materialia*, (56) 2008, 1890-1896

[13] W Cao et al., "PANDAT software with PanEngine, PanOptimizer and PanPrecipitation for multi-component phase diagram calculation and materials property simulation", *Calphad:Computer Coupling of Phase Diagrams and Thermochemistry*, (33) 2009, 328-342.

[14] O R Myhr, Ø Grong, "Modelling of non-isothermal transformations in alloys containing a particle distribution", *Acta Materialia*, (48) 2000, 1605-1615

Experiences with ICME Information Infrastructures for Applying Materials Models in Sequence to Give Accurate Macroscopic Property Prediction

Will Marsden[1], David Cebon[1], Steven Arnold[2], Brett Bednarcyk[2], Nic Austin[1], Igor Terentjev[1]

[1]Granta Design, 62 Clifton Rd, Cambridge, CO17EG, UK
[2]NASA Glenn Research Center, 21000 Brookpark Rd. MS 49-7, Cleveland, OH 44135.

Keywords: ICME, MAC/GMC, Software, Workflow, Simulation, Micromechanics

Abstract

This paper draws on findings from the Material Data Management Consortium. The consortium, now in its 15th year, enables leading engineering enterprises (including among others GE, Boeing, Honeywell, Lockheed Martin, and NASA) to collaborate on best practice approaches to managing and applying critical materials information and technology with a key focus on traceable workflows for simulation and multi-scale modelling of materials, their processing and the resulting components.

A key emphasis has been on verification and validation of macroscopic materials properties generated through sequentially-applied materials models; from ab-initio codes or models of microscopic unit cells through calculations at various length scales up to macroscopic properties. An example of this integration technology is described, using the MAC/GMC micromechanics code from NASA Glenn Research Center. Focus is given to the traceability of the simulated data and capture of sufficient metadata to ensure that the simulations can be recreated in future. The traditional method for understanding the effects of these different factors on materials innovation follows a set pattern where advantageous properties are pursued, iterating between process and structure while measuring the appropriate property. Progress relies on extensive and expensive physical testing campaigns, which generate vast quantities of highly complex data. There are hundreds of possible test types within materials engineering, all generating data of differing types, complexity, and different formats.

Introduction

The behavior of engineering components and structures are dependent on the characteristics of the materials of which they are comprised. These characteristics are affected by multiple elements at many length scales. The material properties that result from process / structure / property mix of factors can be highly complex, varying with many parameters such as work (in terms of applied strain), loading and unloading rate, temperature, time, processing, geometry, and load history[1]. The traditional method for validating the effects of these process, the structures they create and the properties they display, in order to harness them for further product innovation follows a set pattern. There are hundreds of possible test types within materials engineering, all generating data of differing types, complexity, and different formats[2]. Managing these data and making them available for new product development has been largely achieved. Making it available for verification and validation of ICME systems and simulated properties is the next step.

The Material Data Management Consortium[3] (MDMC) is a collaborative project that brings together an international group of leading engineering enterprises with the mission of developing and applying materials information technology to maximize the value of their materials engineering initiatives. The membership of the consortium is drawn from across the spectrum of commercial and government organizations within all high tech sectors; for example: aerospace, defense, energy, etc. Their interest in ICME stems from the realization that computational methods rely upon similar data structures to those applicable for managing the data generated by the traditional methods of materials innovation. These systems were designed through the careful application of materials domain knowledge[4], supported by information technologies that allow them to be adapted and refined to suit this new requirement. This allows MDMC's experiences to be harnessed to realize systems that interface physical material data (complete with its pedigree of metadata) with analysis and modeling tools within an ICME environment[5]. To apply this information in the virtual world, modeling tools need to draw the right information, in the right form, from an authoring system which allows the "problem" to be defined. The key step here is to focus on the metadata associated with the virtual data. The minimum requirement must be to capture sufficient metadata to allow the prediction results to be recreated in the future, without any additional information[6].

This has been made possible through the inclusion of the resulting prediction data or "virtual" data and its metadata within a materials information management system in the same manner used for test data. From curve-fitting test data to advanced micromechanical and continuum models, predictive methods can provide invaluable information and insight across the range of length scales and operating conditions. Yet these methods are often applied in isolation, without reference to other complementary methods and data. A suitable system for integrating the "real" and "virtual" test data, with sufficient metadata to capture the processing parameters which lead to the structures in the materials, is therefore required to make ICME a reality.

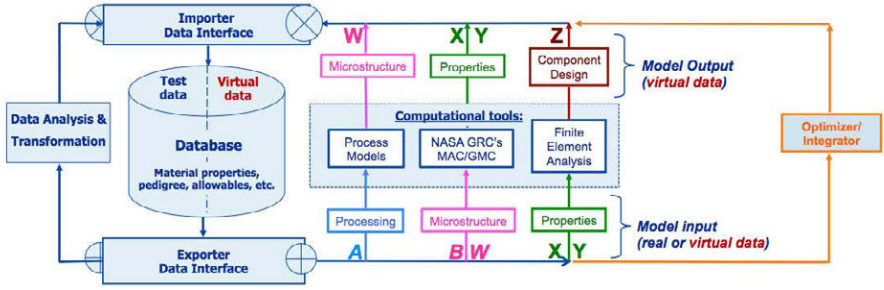

Figure 1. The basic elements of an ICME system architecture

The basic components of an ICME system architecture, as established by the MDMC, are shown in figure 1. We can use the example of a composite material for illustrative purposes. Test data at a variety of length scales (constituent materials, intermediates, coupons, sub-components, and

assemblies) are imported through a common Importer Data Interface and stored in a structured relational database. Data about the constituent components, the processing history (pedigree or metadata), test data, and all derived information are organized in a way that is transparent for all users, while preserving the complex interrelationships between the key elements. Once the data, with appropriate metadata are stored, it is possible access them via the Exporter Data Interface. This allows external analysis routines to gain access to all aspects of the database to perform predictive modelling and other analyses systems. The specifics of the data structures, attributes and capabilities of these systems have been described elsewhere[7].

The analysis loop through the computational loop controlled by the Optimiser/Integrator, represented in figure 1, identifies the capability to perform multiple modelling analyses loops of materials using chosen methods. The workflow required to generate these virtual data or simulated properties is represented in Figure 2. The material modelling software selected for this study was MAC/GMC from NASA Glenn Research Center[8,9].

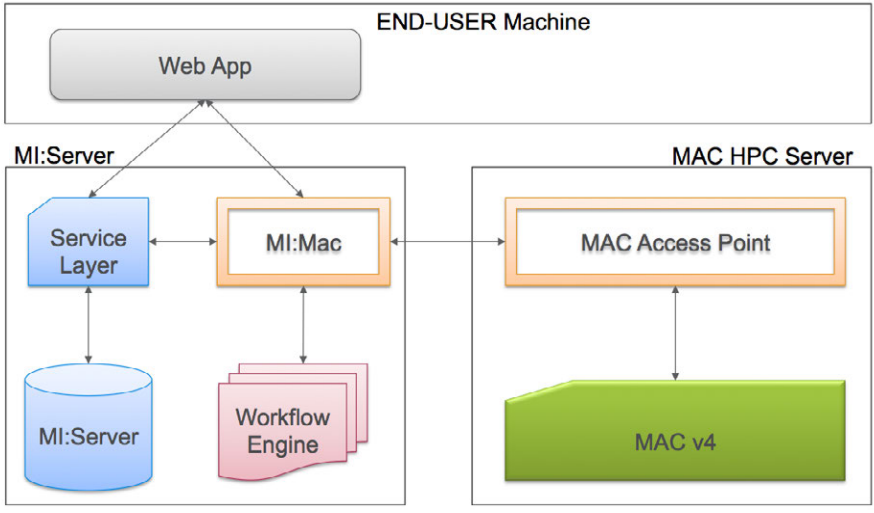

Figure 2. A schematic describing the information flow between three key components.

ICME Web Application

The three independent platforms of the idealized ICME system and their connections are shown in figure 2; the end user machine, the MI server and the high performance compute (HPC) server. The separation of these functions enables a corporate or global installation; where the end user, MI server, and HPC server can be located anywhere on a network.

The interfaces between the Web App on the End User Machine and MI:Server are accomplished via two new applications. The first, named MAC demonstrator, provides the interface for defining/executing a given composite analysis. The second, MAC Composite Model, provides

easy viewing of resulting information generated by the series of analytical runs within the composite Table. MI:Server assembles the necessary analysis runs and sends the appropriate instructions for these runs to be performed on the MAC HPC Server.

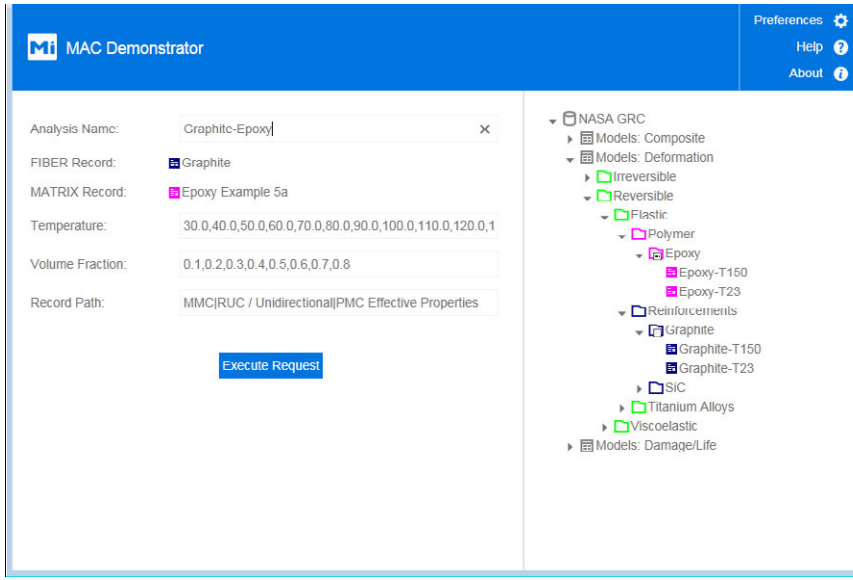

Figure 3. An example Graphite/Epoxy problem morphology is defined using MAC Demonstrator

The MAC demonstrator web application, illustrated in Figure 3, enables the effective properties of multiple composite systems to be modelled with no user intervention beyond the declaration of fiber and matrix constituents, analysis temperatures (30°C to 120°C) of interest, and variation in fiber volume fraction (10% – 80%). Figure 3 illustrates the definition of a Graphite/Epoxy (polymer matrix composite, PMC) problem. Note in the pane on the right side a point and click ability to define constituent material parameters is enabled via access to the any networked Granta MI database. The web app is fully configurable in terms of microstructure, loading and type of analysis (linear or nonlinear). To enable this general configurability, MI:Mac was developed to interact with Granta MI through its Service Layer and an out of the box workflow engine. The MI:Mac module writes the associated input file for the external analysis tool and captures the corresponding calculated results output as well as all metadata. Again, to enable full generality, a MAC access point module was constructed which drives the interaction between MI:Mac and the executable third party software package. This is the main point of entry to manage the execution of MAC/GMC. This code records the incoming requests, manages the disk storage, utilizes the HTTP service to execute the MAC/GMC job, and manages the retention of input/output files by assigning unique job identifiers to both input and output files generated. Then it passes the requested results back to the MI:Mac module. This separation of functionality in the workflow is

important to enable future integration of the outlined workflow with other third party analysis software tools, in that specific input/output requirements can be isolated to substitutable modules of code, while not duplicating common functions between toolsets.

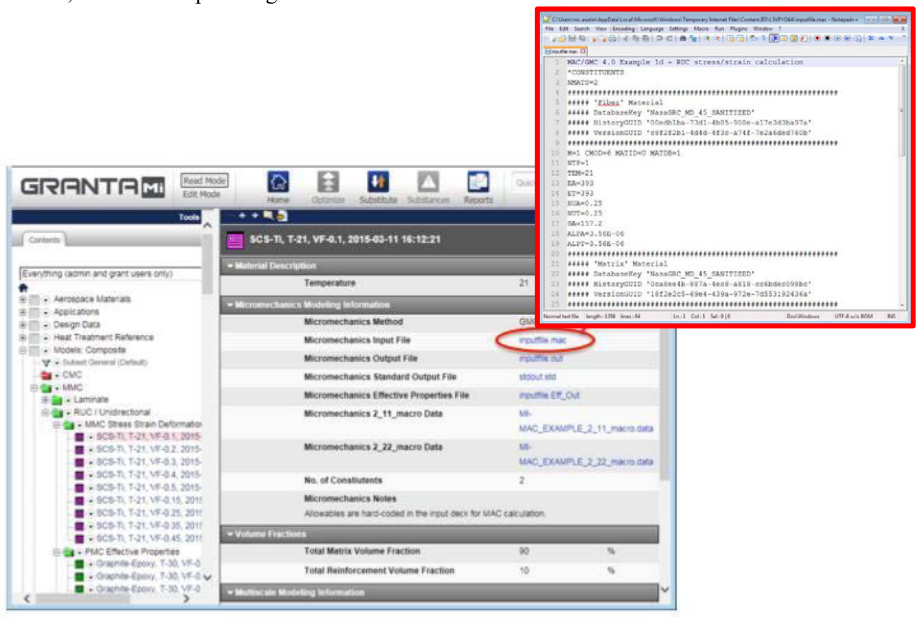

Figure 4 Illustration of detailed record within NASA GRC's database

Results from a metal matrix composite example are provided in Figures 4, 5 and 6. Figure 4 shows a native record from an analytical run within the GRANTA MI database. The database structure was updated to accommodate additional information, including specific attributes for the files used in the analysis. The highlighted file is the MAC/GMC output file which mimics the input file. Other files include the effective properties output file (newly generated to aid in interfacing MAC/GMC with MI:Mac), and all individual macro and/or micro output files requested by user. Figure 5 shows the analytical results for one specific set of conditions with the load displacement curve highlighted.

Finally, Figure 6 shows the effective stress-strain curves resulting from the automated analyses performed using the MAC:Demonstration application, using the comparison chart feature within Granta MI. For these results, the volume fraction of the reinforcement varied between 10% and 45%. The property plotted on the y-axis is NU23. A simple results viewing application (MAC:Composite Model) was customized for viewing information within the Composite Model Table.

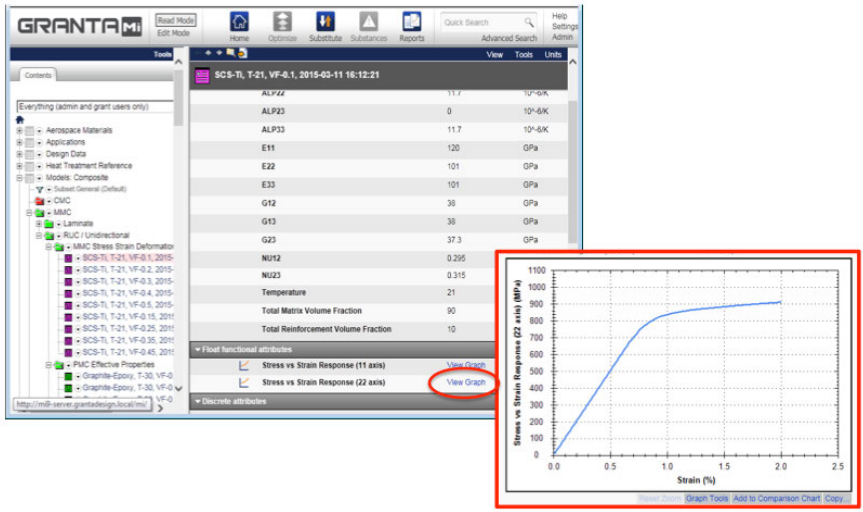

Figure 5 Illustration of detailed record within NASA GRC's database, continued from Fig. 11

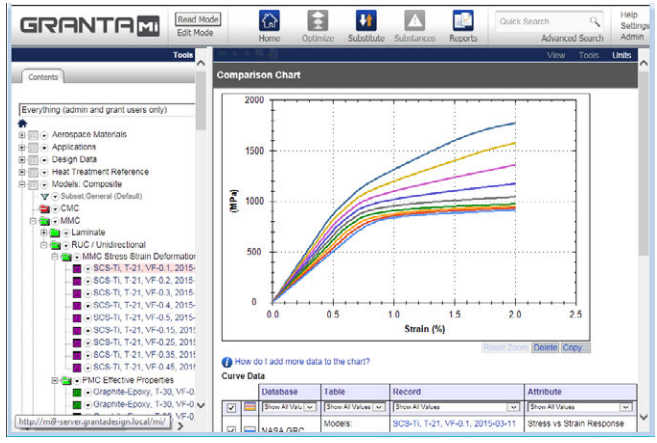

Figure 6. Stress-strain response curves generated using automated MAC/GMC runs for an analysis of SCS-6/Ti-15-3, at RT shown in GRANTA MI.

The MAC:Composite Model web application enables results within the Composite Model Table of the NASA GRC's Granta MI database to be assessed. Where the volume of data requires a subset to be highlighted and analyzed in isolation, a dedicated interface allows users to highlight the materials options (constituents, reinforcement, reinforcement volume fractions, etc.) and conditions (temp, etc.) to be identified, figure 7. The isolated results can then be interpreted, figure

8, as required. Figure 8 demonstrates that search results can also be displayed graphically using the chart mode. Note that if one hovers the mouse over a given point the name of the record appears and if one then double clicks on the data point another window opens showing the different attributes stored in this record.

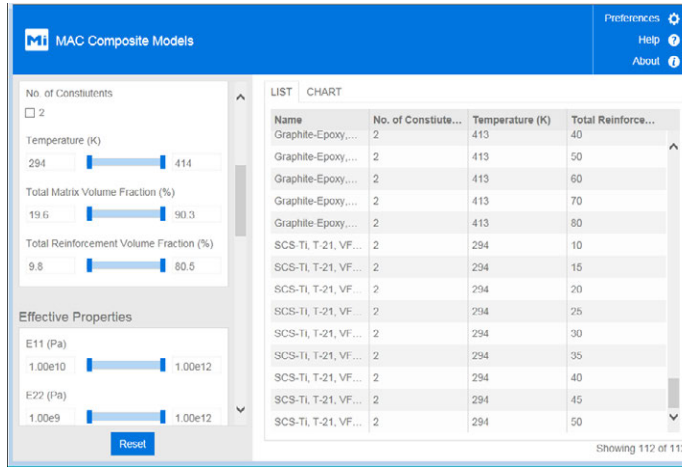

Figure 7. An illustration of MAC Composite Model web application for isolating a set of data for analysis.

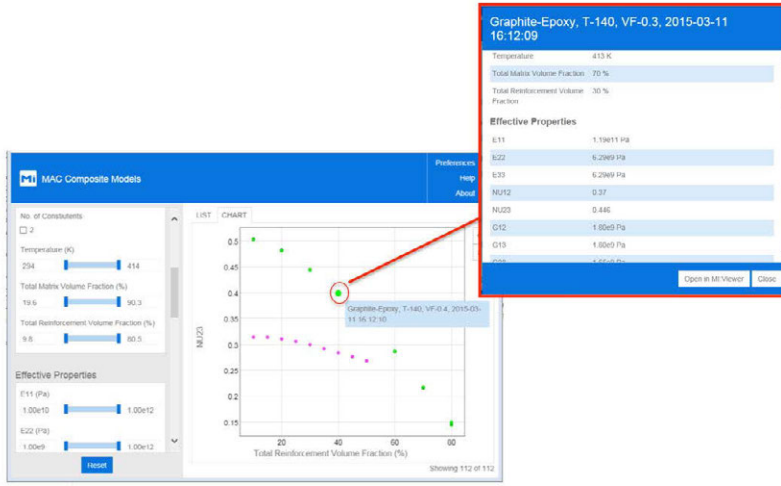

Figure 8. An illustration of MAC Composite Model web application: Chart Display

Conclusions

An ICME system does not replace analysis tools: its role is an enabling one, helping engineering enterprises and collaborative research projects to 'stitch together' computational tools with each other and with experimental data. As the models become more accurate, their complexity tends to increase, as they rely less and less on simplifying assumptions. This complexity drives the need for more data to be measured, predicted, compared, stored and tracked. In order to provide verification and validation capabilities within such systems, sufficient metadata for both the real and simulated data has to be available with sufficient traceability and detail to allow and tests or analyses to be recreated or re-run with the same results. The ICME infrastructure outlined was created by linking commercial modelling software, MAC/GMC, to a materials information management system using a workflow system. This fully automates all aspects of the necessary interactions, allowing the analysis runs to be completed without further interactions with the user once they have defined the materials morphology and services conditions to be considered. Critically, all aspects of the analysis and any real test data managed by the ICME system are associated with sufficient metadata such that the experimental data can be re measured or the simulations re-run with the same results.

References

1. S.M. Arnold, Holland, F.A., Gabb, T., Nathal, M. and Wong, T.; "The Coming ICME Data Tsunami and What Can Be Done", 54th AIAA/ASME/ASCE/AHS/ACS Structures, Structural Dynamics, Materials Conference, Boston, MA (April 23-27,2013).
2. Marsden, W. and Warde, S., "Data Management for Composite Materials", Granta Technical Paper (2010), http://www.grantadesign.com/composites/
3. Official website of Materials Data Management Consortium, http://mdmc.net, accessed on September 13th 2015
4. Cebon, D. and Ashby, M., "Engineering Materials Informatics", MRS Bulletin 31, No. 12 (2006) pp. 1004-1012.
5. The National Materials Advisory Board, Integrated Computational Materials Engineering: A Transformational Discipline for Improved Competitiveness and National Security, The National Academies Press (Washington, 2008)
6. Marsden W., Cebon D., and Cope E. "Managing Multi-Scale Material Data For Access Within ICME Environments," in Tools, Models, Databases, and Simulation Tools Developed and Needed to Realize the Vision of Integrated Computational Materials Engineering, S.M. Arnold and T. Wong (Eds.); ASM International, (Materials Park, OH, 2011)
7. Arnold, S.M., Holland, F. and Bednarcyk, B.A.; (2014). Robust Informatics Infrastructure Required For ICME: Combining Virtual and Experimental Data, 55th AIAA/ASMe/ASCE/AHS/SC Structures, Structural Dynamics, and Materials Conference, National Harbor, Maryland, 13 - 17 January 2014, AIAA-2014-0460.
8. Bednarcyk, B. A., and Arnold, S. M., "MAC/GMC 4.0 User's Manual – Keywords Manual," NASA/TM-2002-212077/VOL2, 2002a.
9. Bednarcyk, B. A., and Arnold, S. M., "MAC/GMC 4.0 User's Manual – Example Problems Manual," NASA/TM-2002-212077/VOL3, 2002b.

D2C – CONVERTING AND COMPRESSING DISCRETE DISLOCATION MICROSTRUCTURE DATA

D. Steinberger[1], M. Leimberger[1], S. Sandfeld[1]

[1]Institute of Materials Simulation (WW8), Friedrich-Alexander-Universität Erlangen-Nürnberg, Dr.-Mack-Str. 77, 90762 Fürth, Germany

Keywords: dislocation dynamics, continuum theory of dislocations, data compression, software design

Abstract

Appropriate methods to describe materials microstructure are essential for connecting different simulation methods as well as experiments. Focusing on dislocations – the carrier of plastic deformation – we show how continuous field descriptions can be used to represent dislocation microstructure. These fields may be used as input for continuum simulations or for their validation, they allow the comparison of different discrete dislocation dynamics (DDD) implementations, and they are a means of "compressing" the data resulting from DDD simulations. We give an overview of the design choices for *D2C*, a Python software package designed to convert data from DDD simulations to continuous continuum dislocation dynamics (CDD) fields. The theory beneath each step of this conversion process is outlined.

Introduction

The dynamics of dislocations are the controlling factor for plasticity in metals. Therefore it is of importance to understand how systems of dislocations evolve in time in order to find new ways of making metals stronger and enhance the lifetime of components. In the last decades DDD simulation methods were established which are based on the representation of the motion and interactions of dislocations and which thus can provide full access to all microstructural details. A number of different dislocation codes are used throughout the scientific community, as e.g., microMegas [1], the code of Weygand et al. [2], TRIDIS [3], ParaDIS & DDLab [4], and MODEL [5]. The major drawback of DDD, however, is the computational cost which – strongly increasing with the number of dislocations present – limits the applications to small systems and strains. An example for the upper scale that can be reached by discrete dislocation dynamics nowadays are plastic strains $<1\,\%$ with a system size of about $(10\,\mu\mathrm{m})^3$ and a dislocation density of around $10^{12}\,\mathrm{m}^{-2}$ [6], or equivalent systems according to the similitude principle [7]. This, however, is not sufficient to simulate e.g. the formation of dislocation patterns during cyclic deformation.

A remedy for reducing the degrees of freedom of 3D DDD (without "flattening" the 3D model to a 2D description) is to statistically coarse-grain the behavior of dislocations and to describe them through a continuum formulation whose computation time is independent of the number of dislocations. An additional benefit is that a continuum formulation of dislocation dynamics allow a fine grained control over the amount of

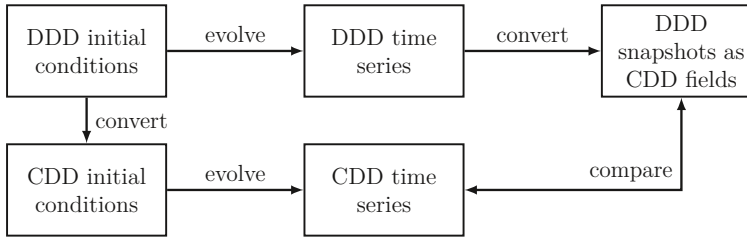

Figure 1: Verifying CDD simulations using DDD simulations.

"data compression": while each dislocation in a discrete simulation[1] results in larger file sizes for system snapshots, the size of the file holding the CDD fields solely depends on the resolution. Whereas a microMegas output file of 100 snapshots in time with 10000 dislocation segments results in a file size of 344 MB each single CDD field requires 3.8 MB for a grid of $100 \times 100 \times 100$ data points. Typical CDD theories require much less than 10 distinct field variables. Hence, the compression is more than 90 % in this case – independent of the number of dislocations. This way of compression may be compared to the mp3 or jpeg file formats which also drop data that are deemed unnecessary.

Can CDD simulations be considered as equivalent to DDD simulations? Verifying the validity of a CDD simulation is usually done by using simple test cases with analytical solutions or tests that are comprehensible by trained intuition. A more elaborate and quantitative way of validating a CDD model in a complex setting is shown in Sandfeld and Po [8]. By using a workflow as outlined in figure 1 the authors directly compared the evolution of a CDD simulation with a DDD simulation that incorporated the same mechanisms as the CDD model. Making this workflow available in an accessible and easily extendable software framework is the goal of the software package *D2C* whose design and underlying methods are introduced in the following.

The D2C Package

The goal of the *D2C* package is to provide the means to easily convert DDD data from any DDD code to fields that are usable by CDD simulations. As programming language Python was chosen due to its ease of use as a high level language and the ability of rapid development. This makes the package approachable by a broader audience that may not be comfortable using low level programming languages. The Python programming language further can make use of a vast range of scientific packages. Among those, NumPy [9], SciPy [10], the Python wrapper for HDF5 [11], and matplotlib [12] are the largest building blocks of *D2C*. NumPy and SciPy provide *D2C* with a high-level interface to commonly used algorithms for scientific computing that are faster than pure Python implementations due to underlying C implementations or interfaces to C and Fortran packages. *D2C* uses HDF5 as file format that offers a lot of flexibility and ease of use thanks to embedded metadata which is used to document the internal file structure. The built-in data compression keeps the file size small and allows to store many microstructure

[1] depending on the representation: dislocation segments, nodes or spline support points

```
with open('file.txt', 'r') as f:
    for line in f:
        # Do something with line


from D2C.discrete.micromegas import FilmFile
with FilmFile('film.bin') as f:
    for system in f:
        # Do something with system
```

Listing 2: Iterating over a microMegas film file system by system with D2C.

snapshots in time series. Finally matplotlib is the means to visualize 2D projections and slices of DDD and CDD data while ParaView is used to visualize 3D data.

Throughout *D2C* the design is kept as "pythonic" as possible. For example see listing 1 for the how to iterate line by line over a text file in Python. One may conclude that this is a natural way to think about iterating over a text file. In a similar fashion one may think of it as natural to iterate over one of microMegas `film.bin` files – a file that stores the dislocation segments of a system at different time steps – by complete system timesteps with all the information on the system. Hence the way of parsing these files was done in the same way as can be seen in listing 2.

The natural flow of converting DDD data to CDD fields is represented in the structure of the package: first, the output files of a DDD software are parsed, converted to a format more convenient to use within *D2C*, and subsequently the dislocation lines are approximated – if necessary – by splines resulting in parametrized curves. These curves are then used to compute CDD field values at each point of the curve. In the last step these values are postprocessed to make them suitable for the numerics of CDD simulations. The three parts of the workflow are outlined in more detail in the following.

Discrete

The `discrete` module takes DDD data and converts discrete dislocation lines to parametrized curves that can be used in the `conversion` module. In DDD dislocation lines are commonly represented by either using straight line segments, nodes or splines. The former two bring along a problem for the conversion to continuous fields: some measures that are used in CDD like the curvature require the existence of continuous derivatives of the parametrized lines. Both the representation by straight line segments and nodes introduce discontinuities in the derivatives they can therefore not be used as is. To alleviate this *D2C* employs fitting of cubic B-splines to the discrete dislocation line as smoothing method. An example of a dislocation loop that is discretized using straight line segments and the corresponding spline fit are shown in figure 2. The result is an oriented curve $\boldsymbol{c}(u)$ with $u \in [0, 1]$ that may be used to compute the continuum fields required by CDD in the following outlined module.

Figure 2: Lower half of a dislocation loop obtained from microMegas (gray) and corresponding spline fit performed by D2C (black).

Conversion

The `conversion` submodule uses the curves generated in the `discrete` submodule to compute continuum fields in a way outlined by Sandfeld and Po [8]. As an example take the definition of the measures that are taken for the line length $L_{\boldsymbol{c}}$, the line length projected perpendicular to the Burgers vector in the glide plane $L_{\boldsymbol{c},\perp}$ and the line length projected parallel to the Burgers vector $L_{\boldsymbol{c},\odot}$:

$$L_{\boldsymbol{c}}(\boldsymbol{r}) = \int_0^1 \delta(\boldsymbol{c}(u) - \boldsymbol{r})\,\mathrm{d}u, \tag{1}$$

$$L_{\boldsymbol{c},\perp}(\boldsymbol{r}) = \int_0^1 \delta(\boldsymbol{c}(u) - \boldsymbol{r})\cos\Big(\theta(\boldsymbol{r})\Big)\,\mathrm{d}u, \tag{2}$$

$$L_{\boldsymbol{c},\odot}(\boldsymbol{r}) = \int_0^1 \delta(\boldsymbol{c}(u) - \boldsymbol{r})\sin\Big(\theta(\boldsymbol{r})\Big)\,\mathrm{d}u, \tag{3}$$

where θ is the angle between the Burgers vector and the tangential line vector in the glide plane. These measures result in the dislocation density $\rho(\boldsymbol{r})$, the edge dislocation density $\rho_\perp(\boldsymbol{r})$ and the screw dislocation density $\rho_\odot(\boldsymbol{r})$, respectively, by averaging over a volume. This is then part of the `continuous` module.

Continuous

The measures provided by the `conversion` module are not directly usable as input for CDD simulations or as means for validitation. CDD simulations are carried out using either the finite element method (FEM) or the finite volume method (FVM). It is therefore useful to project the curve and its respective measures to a mesh that is usable by those numerical methods. A part of this is the aforementioned averaging in a reference volume

$V_{\boldsymbol{r}}$ with volume V centered around $\boldsymbol{r}$ to finally retrieve the different densities via

$$\rho(\boldsymbol{r}) = \frac{1}{V} \sum_{\boldsymbol{c}} \int_{\mathcal{L}_{\boldsymbol{c}}^{V_{\boldsymbol{r}}}} \mathrm{d}u, \tag{4}$$

$$\rho_{\perp}(\boldsymbol{r}) = \frac{1}{V} \sum_{\boldsymbol{c}} \int_{\mathcal{L}_{\boldsymbol{c}}^{V_{\boldsymbol{r}}}} \cos(\theta)\, \mathrm{d}u, \text{ and} \tag{5}$$

$$\rho_{\odot}(\boldsymbol{r}) = \frac{1}{V} \sum_{\boldsymbol{c}} \int_{\mathcal{L}_{\boldsymbol{c}}^{V_{\boldsymbol{r}}}} \sin(\theta)\, \mathrm{d}u, \tag{6}$$

where $\mathcal{L}_{\boldsymbol{c}}^{V_{\boldsymbol{r}}} \subset \boldsymbol{c}$ is the part of the curve $\boldsymbol{c}$ that is contained inside the averaging volume $V_{\boldsymbol{r}}$. For reasons of numerical stability those fields may be smoothed out, e.g. by convoluting the fields with a discrete Gauss function. Both the coarseness of the mesh and the width of the smoothing kernel influence the level of detail that is kept from the DDD data. Figure 3 shows the resulting density field for a single loop and a random distribution of 50 dislocation loops with different Gaussian filter kernel standard deviations and mesh sizes. It can be seen that smoothing with a Gaussian function with small standard deviation σ and a very fine mesh result in fields that capture many details of the discrete loops, both for a single loop and multiple loops. Increasing σ while keeping the mesh size constant results in a loss of detail especially for the system with several loops. The same is true for larger values of h, although the gradients are not as smooth as in the previously mentioned case. In all cases the total value of the density of both the single loop and multiple loops remains the same with different σ and h as the line length does not change, but the gradients are smaller for larger σ and h values which is favorable for numerical stability.

Another important factor is the density of points used to discretize the dislocation loops prior to the averaging procedure. Figure 4 shows the ℓ^{∞} norm of the error of different point densities with respect to the case of a point density of $10^{6.5}$ for the systems depicted in figure 3. For small σ values the system with the coarsest mesh size requires the smallest point density to converge. The zigzag pattern exhibited by the system with the finest mesh is explained by floating point precision as the edges of the mesh coincide with the tangential line vector of the loop wherever they are parallel to the axis. For larger σ a smaller point density is required to consider the field values as converged with respect to the reference system. In these cases a finer mesh resolution is actually beneficial. In systems with more loops the required point density is larger than for the single loop case but it is less sensitive to the mesh size. The influence of the point density nevertheless should be investigated with the actual evolution of the system to draw conclusions.

Documentation & Testing

Besides the source code *D2C* provides extensive documentation of all interfaces. A user guide details the steps necessary to convert, e.g., a microMegas `film.bin` file to an HDF5 file that may be used as input for a FVM simulation of the CDD1 theory [13]. Furthermore a reference handbook is provided that describes all classes and functions that are part of the D2C package. As both the user guide and the reference handbook

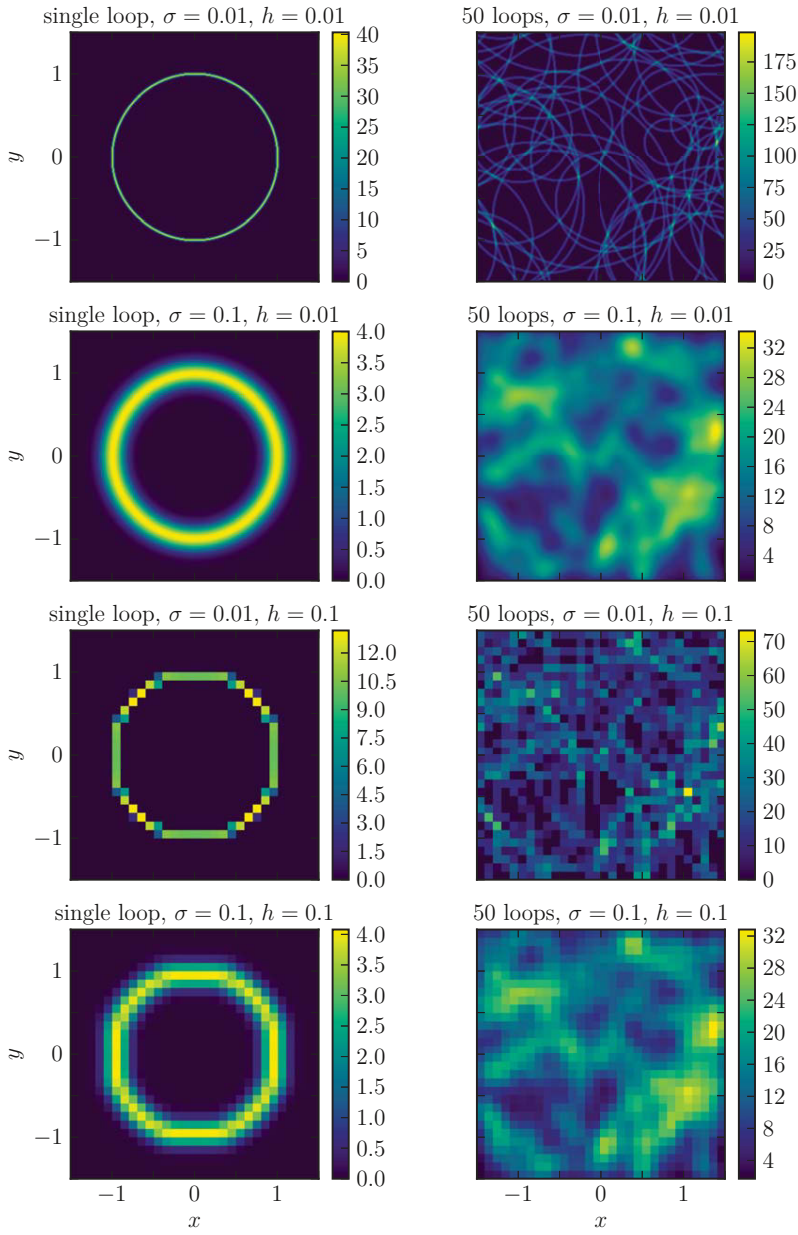

Figure 3: Averaged fields for a single loop in the left column and 50 randomly distributed loops for different Gaussian filter kernel standard deviations σ and different mesh sizes h.

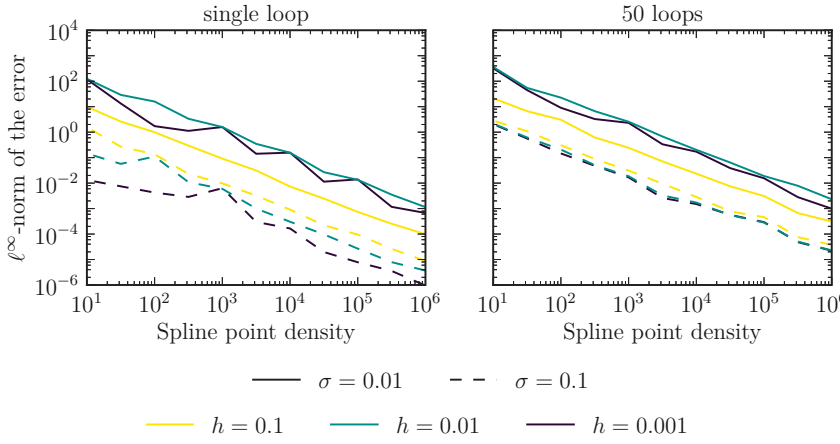

Figure 4: Convergence of different combinations of Gauss filter kernel widths σ and mesh sizes h depending on the spline point densities used to discretize the dislocation loops with respect to a reference point density of $10^{6.5}$.

are produced using the documentation tool Sphinx and its numpydoc extension, the look and feel are familiar to people using the SciPy stack. Several cross-references between the classes and functions serve for as easy way to navigate through the documentation and outline the interplay between the different modules. In addition to the documentation the code is tested at each commit using the automated continuous integration tool Travis CI that up to date runs over 1500 unit and integration tests to ensure that the functionality is given at all times. A code coverage of at least 90 % is strived for at all times.

Summary & Outlook

We introduced *D2C* as a tool to narrow the gap between DDD and CDD simulations by making DDD data available to CDD simulations in a convenient manner, both as initial conditions for simulations and as a means for verification of the simulations. The reasoning behind the package structure to follow the natural steps of a conversion from discrete data to continuum fields was outlined.

Even though the conversion of microMegas systems with up to 2000 segments to a $36 \times 40 \times 48$ mesh holding information about the total dislocation density, the edge dislocation density and the screw dislocation density takes less than half a second, the code will be optimized steadily. In the future more DDD codes will be supported as well as more continuum measures introduced as needed by the development in the CDD community. Besides the current means of visualizing both DDD and CDD data, myavi is considered as means to view CDD fields in 3D – something that is not yet possible with matplotlib.

As the code is publicly available in a GitHub repository, access to this package and

its current development as well as participation is possible for all parties.

References

[1] B. Devincre et al. “Modeling crystal plasticity with dislocation dynamics simulations: The ’microMegas’ code”. In: *Mechanics of Nano-Objects*. Ed. by F. Samuel, P. Anne, and T. Olivier. Paris: Presses de l’Ecole des Mines de Paris, Nov. 2011, pp. 81–100.

[2] D. Weygand et al. “Discrete dislocation modeling in three-dimensional confined volumes”. In: *Materials Science and Engineering: A* 309–310 (2001). Dislocations 2000: An International Conference on the Fundamentals of Plastic Deformation, pp. 420–424.

[3] M. Verdier, M. Fivel, and I. Groma. “Mesoscopic scale simulation of dislocation dynamics in fcc metals: Principles and applications”. In: *Modelling and Simulation in Materials Science and Engineering* 6.6 (1998), p. 755.

[4] V. Bulatov et al. “Scalable Line Dynamics in ParaDiS”. In: *Supercomputing, 2004. Proceedings of the ACM/IEEE SC2004 Conference*. Nov. 2004, p. 19.

[5] N. M. Ghoniem, S.-H. Tong, and L. Z. Sun. “Parametric dislocation dynamics: A thermodynamics-based approach to investigations of mesoscopic plastic deformation”. In: *Physical Review B* 61 (2 Jan. 2000), pp. 913–927.

[6] R. LeSar. “Simulations of Dislocation Structure and Response”. In: *Annual Review of Condensed Matter Physics* 5.1 (2014), pp. 375–407.

[7] M. Zaiser and S. Sandfeld. “Scaling Properties of Dislocation Simulations in the Similitude Regime”. In: *Modelling and Simulation in Materials Science and Engineering* 22.6 (2014), p. 065012.

[8] S. Sandfeld and G. Po. “Microstructural comparison of the kinematics of discrete and continuum dislocations models”. In: *Modelling and Simulation in Materials Science and Engineering* 23.8 (2015), p. 085003.

[9] S. van der Walt, S. C. Colbert, and G. Varoquaux. “The NumPy Array: A Structure for Efficient Numerical Computation”. In: *Computing in Science Engineering* 13.2 (Mar. 2011), pp. 22–30.

[10] E. Jones, T. Oliphant, P. Peterson, et al. *SciPy: Open source scientific tools for Python*. 2001–.

[11] The HDF Group. *Hierarchical Data Format, version 5*. 1997–.

[12] J. D. Hunter. “Matplotlib: A 2D Graphics Environment”. In: *Computing in Science Engineering* 9.3 (May 2007), pp. 90–95.

[13] S. Sandfeld et al. “Continuum modeling of dislocation plasticity: Theory, numerical implementation, and validation by discrete dislocation simulations”. In: *Journal of Materials Research* 26 (05 2011), pp. 623–632.

TMS2016
145th Annual Meeting & Exhibition

SUPPLEMENTAL
PROCEEDINGS

Material Behavior Characterization via Multi-Directional Deformation of Sheet Metal

DETERMINATION OF BENDING LIMIT CURVES FOR ALUMINIUM ALLOY AA6014-T4: AN EXPERIMENTAL APPROACH

Ipsita Madhumita Das[1], Krishna Kumar Saxena[1], Jyoti Mukhopadhyay[1]

[1] Department of Materials Science and Engineering, Indian Institute of Technology Gandhinagar, Gandhinagar, Gujarat- 382355, India

Keywords: Formability, FLC, Bending limit curve

Abstract

The conventional forming limit curves as proposed by Keeler and Goodwin fail to evaluate formability in case of bending and hemming operations. This is due to the different failure mechanisms involved in biaxial forming and bending/hemming operations. To overcome this difficulty, concept of bending limit curve has been introduced. This work presents an experimental approach to determine the BLC for aluminium alloy AA6014-T4. AA6014-T4 was selected as the workpiece due to its extensive application in outer panels of car bodies. The bending samples were printed with speckle pattern and measurement of bending strain was carried out with the help of GOM Aramis software. The three point bend test was conducted with two punch radii of 0.4 mm and 2 mm to study the effect of punch radius on bending limit strains. The complete formability picture was obtained by plotting combined forming limit and bending limit curves.

Introduction

The reduced fuel consumption and emission criterion has necessitated the demand for light weight vehicles in present scenario. This has increased the use of Al 5000 & 6000 series alloys in inner and outer body panels of automobiles respectively. The automotive panels are manufactured using sheet metal forming operations, followed by bending and hemming operations which are common joining techniques for adjacent body panels. The dominant load on the edges of these panels during hemming or bending operation is plane strain which is totally different in nature than biaxial forming. This necessitates the development of bending limit curve which takes the bendability of the material into account along with its formability. Failure in bending and hemming operations involves inter-crystalline fracture contrary to membrane instability in biaxial forming. Thus, the conventional forming limit curve, as proposed by Keeler [1] & Backofen [2] and Goodwin [3] fails to predict the formability in bending or hemming

operations. Failure of conventional FLC to assess formability during bending or hemming has been mentioned in the works of Denninger [4], Schleich [5] and Liewald [6].

Experimentally, it has been reported that bending limits are always higher than forming limits [5]. Bending limit curve is determined by applying stretching and bending loads simultaneously on the material. The region below the BLC depicts a safe bending region whereas the region above BLC represents a failed geometry during bending or hemming. Initially, the concept of bending limit curve was introduced by Liewald et al [7]. Furthermore, Lin et al [8] predicted the bendability and hemmability from plain strain tensile test. Afterwards by performing angular stretch bend test (ASBT), Kitting et al [9] characterized stretch bending deformation with respect to tool radius and stretching condition. However, in modified ASBT, stretching conditions were found to be independent of tool radius. Davidkov et al [10] performed experimentation on strain localization and damage development of AA5754 alloy sheet. They suggested that the maximum plastic strain below the free surface of the specimen can be due to the interaction between propagation of shear in the matrix and second phase particle stringers. Denninger [11] evaluated the bendability of a material in terms of bending limit curve. He reported the change in BLC level due to different pre-strain paths. He J et al [12] studied the various bending models such as flow theory model and deformation theory model. They concluded the flow theory is more consistent with stretch bending operation than deformation theory model. Liewald and Drotleff [13] also reported the fundamental behavior of BLC and the three dimensional failure surface for combined BLC. The objective of the present work lies with experimental determination of bending limit curves for AA6014 with punch radius of 0.4 mm and 2 mm.

Experimentation

Al6014 with an initial sheet thickness of 1.04 mm was used in present experimentation. It belongs to Al-Mg-Si alloy system, thus possess good combination of formability and bendability. Composition of Al 6014 alloy is shown in Table 1.

Table 1: Composition (wt %) of Al 6014.

Element	Si	Fe	Cu	Mn	Mg	Cr	Zn	Ti
wt (%)	0.3-0.6	0.35 max	0.25 max	0.05-0.2	0.4-0.8	0.2 max	0.1 max	0.05 max

BLC was obtained by using a three point bend test set up according to VDA 238-100 [14]. The critical scenario, i.e. bending the specimen perpendicular to rolling direction was chosen for bending operation for reliable results. The specimens in uniaxial, plain strain and biaxial directions were pre-stretched on the Marciniak press. The level of pre-stretching used for the specimens is shown in Table 2. From the pre-

strained samples, square specimens of dimensions 50 × 50 mm were cut out as shown in Fig.1. Using DIC technique from GOM Aramis software, strain gradient on the pre-strained flat specimens was evaluated. Three sections were superimposed and equivalent Von-Mises strain was plotted along these sections.

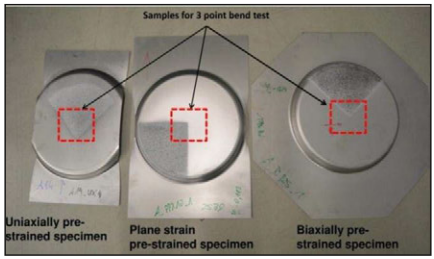

Figure 1: Cutting of specimens for bend test from pre-strained samples.

Table 2: Level of pre-straining for bend test.

Type of Pre-straining	UPX (Uniaxial) (%)	PPX (Plain Strain) (%)	BPX (Biaxial) (%)
Al6014	5, 10, 15	10	2, 5, 15, 25

The bend test was performed by installing a three point bend test setup on the IFU uniaxial tensile testing machine (Fig. 2). Two bending punches of radii 0.4 mm and 2 mm were used for the experimentation. Before the test, the specimens were spray painted with black & white speckle pattern. The specimen was kept aligned in the centre, parallel to bending punch and it was mounted on two rollers.

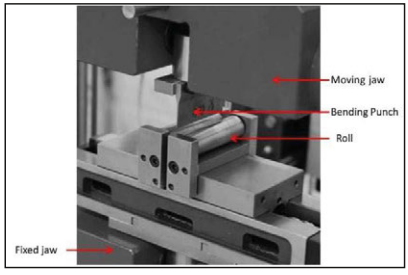

Figure 2: Three-point bend test set up used for experimentation.(Courtesy: IFU)

Test was stopped when punch force drops to 50N. DIC technique, with the help of GOM Analysis software, was used to determine the bending limits. After the bending operation, three sections were superimposed on the bent edge. Along these sections, the bending strain was plotted. For accurate results, three specimens for each pre-straining level were experimented. The specimens after bend tests are shown in Fig. 3. Equivalent pre-stain for the specimens was calculated using Eq. 1 [15].

$$\emptyset_{eq} = \sqrt{\emptyset_1^2 + \emptyset_2^2 + \emptyset_1\emptyset_2} \quad (1)$$

The whole strain path of the forming process starting from pre-stretching to bending of the material was taken into account to analyze the bending operation.

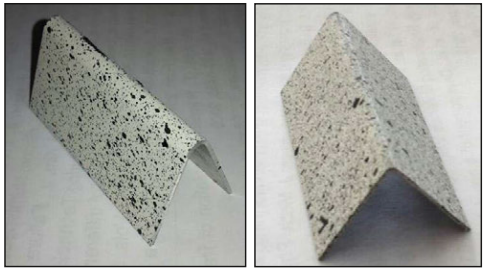

Figure 3: Bend test specimens after three point bend test.

Bending limit strains were calculated as the sum of the pre strain and the maximum strain after bending (Eq. 2) for both punch radii of 0.4 mm and 2 mm. These bending limit strains were plotted to get the respective BLCs by taking major bending limit strain on X axis and minor strain on Y axis.

$$\emptyset_{BL} = \emptyset_{1p} + \emptyset_b \quad (2)$$

BLCs were plotted considering pure experimental data, without any correction factor to ensure reliability of the plot.

Results and Discussion

Figure 4 shows the bending limit curves for punch radii of 0.4 and 2 mm for Al6014, combined with respective forming limit curves. The bending limits are observed to be at much higher level than the forming limits due to difference in failure mechanisms as well as in process mechanics. Thus, the failure of FLC to evaluate bendability in case of Al6014 alloy is confirmed. The level of BLC is also found to be higher, for lower punch radius. This can be accounted for the fact that, during bending, punch with lower radius imposes higher strains on the outer fibre, resulting brittle kind of fracture. It

conforms to the observations made by Denninger et al [11]. Initially, with increase in pre-strain level, bending strain decreases slightly due to the shearing of second phase particles present in Al6014 matrix. Afterwards, it increases in a varying nature. This is due to the reduction of sheet thickness in a major level at a constant inner radius. However, the varying nature can be accounted for the evolution of damage during bending.

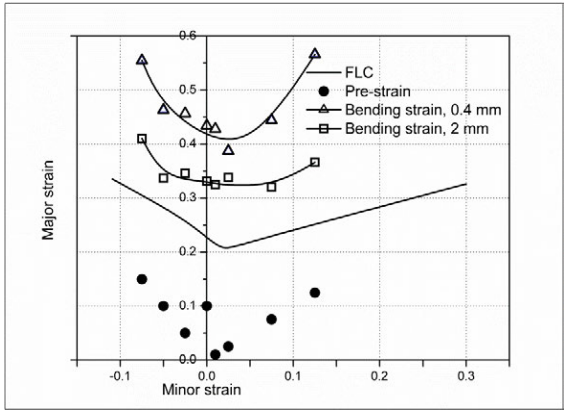

Figure 4: Combined BLC and FLC for Al6014.

Conclusion

In the present work, bending limit strains were determined by DIC technique using GOM Aramis software. Based on above, bending limit curve for AA6014-T4 was evaluated. BLC was found to be at a higher level than conventional FLC. Lower bending strain was observed with higher punch radius. Due to the shearing of secondary particles and dominant reduction of sheet thickness, nature of bending strain varied with the level of pre-strain. It was concluded that total bending strain is a function of level of pre-strain and nature of punch radius. In a commercial scale, BLCs can be implemented as a post processing criterion in the bending/hemming process simulations along with FLCs reducing both time and cost consumption. The future scope of the work lies in validating such applications in finite element based forming simulations.

Acknowledgment

The authors are thankful to Prof. Mathias Liewald, Dr.-Ing Stefan Wagner, Dipl-Ing Klaus Drotleff and Staff of Institut für Umformtechnik for providing useful resources

and facilities for carrying out the experiments. Their support during the research work is highly acknowledged.

References

1. Keeler SP (1965) Determination of forming lmits in automobile stamping. Sheet Met Ind 42:683.

2. Keeler SP, Backofen WA (1963) Plastic Instability and Fracture in Sheets Stretched Over Rigid Punches. In: Trans. ASM.

3. Goodwin G. M (1968) Application of strain Analysis to Sheet Metal Forming Problems in Press Shop. SAE Pap. No. 680093

4. Denninger R, Liewald M, Held C, Sindel M (2011) Investigations on Bendability of Lightweight Materials for Various Load Paths. In: 14th Int. ESAFORM Conf. Mater. Forming, AIP Conf. Proc. pp 1601–1605

5. Schleich R, Sindel M, Liewald M (2009) Investigation on the effect of curvature on forming limit prediction for aluminium sheet alloys. Int J Mater Form 2:69–74. doi: 10.1007/s12289-009-0394-z

6. Wagner S, Liewald M (2013) Improved Failure Description in Forming of Automotive Sheet Metal Parts. Acad J Manuf Eng 11:1–8.

7. Liewald M, Sindel M, Schleich R, Held C (2008) Beitrag zur Verbesserung der simulativen Absicherung von biegedominierten Umformprozessen im Automobilbau. GRIPS Media Verlag. doi: 10.1007/BF02833650

8. Lin G, Hu SJ, Cai W (2009) Evaluation of Formability in Bending/Hemming of Aluminum Alloys Using Plane-Strain Tensile Tests. J Manuf Sci Eng 131:051009. doi: 10.1115/1.3123316

9. Kitting D, Ofenheimer a., Pauli H, Till ET (2010) A phenomenological concept to predict formability in stretch-bending forming operations. Int J Mater Form 3:1163–1166. doi: 10.1007/s12289-010-0979-6

10. Davidkov A, Jain MK, Petrov RH, et al. (2012) Strain localization and damage development during bending of Al–Mg alloy sheets. Mater Sci Eng A 550:395–407. doi: 10.1016/j.msea.2012.04.093

11. Denninger R, Liewald M, Sindel M (2012) Failure prediction in sheet metal forming depending in pre-straining and bending superposition. In: Mater. Form. ESAFORM 2012. Trans Tech Publications, Switzerland, pp 101–106

12. He J, Cedric Xia Z, Li S, Zeng D (2013) M–K Analysis of Forming Limit Diagram Under Stretch-Bending. J Manuf Sci Eng 135:041017. doi: 10.1115/1.4024536

13. Liewald M, Drotleff K (2014) Concept of the bending limit curve. In: FLC 2014 Work. Novemb. 6 7, 2014, Zurich, Switz. pp 17–22

14. (2010) VDA 238 -100,Plate bending test for metallic materials. 1–13.

15. Mises R v. Mechanik der festen Körper im plastisch- deformablen Zustand. Nachrichten von der Gesellschaft der Wissenschaften zu Göttingen, Math Klasse 1913:582–592.

135° CLOCK ROLLING：AN APPROACH TO IMPROVE THE MICROSTRUCTURE AND TEXTURE OF TANTALUM USED FOR SPUTTERING TARGET

Haiyang Fan, Shifeng Liu*, Chao Deng
College of Materials Science and Engineering, Chongqing University, Chongqing 400044, China
*Corresponding author: Shifeng Liu E-mail: liusf06@cqu.edu.cn

Keywords: Tantalum, 135° clock rolling, texture, microstructure, sputtering target

Abstract

An efficient approach, 135° clock rolling, to improve the microstructure and texture of tantalum (Ta) was presented in this paper. The Ta plates were processed by unidirectional (UR) and clock rolling (CR), respectively. Compared with UR, the novel CR caused a continuous change of strain paths and consequently activated slip systems from multiple directions. After cold rolling, the microstructure and texture were investigated by the optical microscopy (OM), X-ray diffraction (XRD), electron channel contrast imaging (ECCI) and electron back-scattered diffraction (EBSD) techniques. Results showed that 135°clock rolling had positive effects on weakening the texture gradients and homogenizing the deformation microstructure, thus resulting in a favorable annealing behavior and eventually improving the sputtering performance of Ta target.

Introduction

Tantalum (Ta) is a refractory metal commonly used in microelectronic devices, especially the sputtering target for integrated circuit manufacturing. Ta ingot is fabricated by electron beam melting (EBM), which is not only able to ensure the high purity but also introduce numerous coarse columnar grains with {100}<uvw> orientations [1]. To break these large grains, processes like forging, annealing, rolling and final annealing are imposed orderly. However, some issues, e.g. texture gradients, orientation clusters, residual deformation bands et al., always occur during the above courses and are hard to be eliminated [2, 3]. Such issues injure the sputtering performance and then sacrifice the quality of thin films [1, 3].

Over the past decades, researchers represented by C.A. Michaluk, J.B. Clark and S.N. Mathaudhu et al. have tried various approaches including asymmetric processing [4], transverse rolling [5], multipass equal channel angular extrusion (ECAE) [6] and clock rolling [7] et al. Nevertheless, these methods are short of systematic researches and overall assessments. For instance, ECAE can produce a fine and uniform grain structure, but it can't eliminate the texture gradients [6]. Besides, ECAE is limited by the billet dimensions, making it just a laboratory technique. Hence, for the sake of industrialization, this paper focuses on the rolling process.

The rotation angle is crucial for designing rolling schedules. Combined with the

merits of previous rolling modes, 135° clock rolling (CR) is introduced in this study. The main feature of CR is the sequential rotation of rolling direction (RD) about normal direction (ND). The effects of CR and UR on the rolling texture & microstructure as well as the subsequent recrystallization are studied via comprehensive characterization methods. Results indicate that CR is indeed an outstanding approach to impart satisfying recrystallization structure.

Experimental

Materials and processing

The detailed chemical composition of tantalum can be found in Ref. [8] and the schedules of UR and CR are showed in Ref. [8, 9]. The schematic diagram of 135° clock rolling is illustrated in Fig. 1. Some specimens with dimensions of $12^{\text{Length}} \times 10^{\text{Width}} \times 3^{\text{Thicknesss}}$ mm^3 were sectioned from the UR and CR-Ta, respectively.

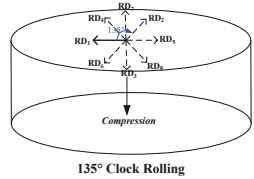

Fig. 1. Schematic diagram of 135° clock rolling.

Characterization

Electropolishing is proved to be necessary prior to the X-ray diffraction texture analysis (XRD-TA) since tantalum has a high absorption coefficient for X-rays [10]. Measurements and analysis of through-thickness texture of UR and CR-Ta were the same as Ref. [8]. The X-ray diffraction line profile analysis (XRD-LPA) is particularly recommended to evaluate the stored energy when deformed metal has a large dislocation density [11]. In this study, XRD-LPA was operated on a Rigaku D/max 2500PC diffractometer (18 kW) with Cu Kα radiation (40 kV/150 mA). A fine scan was conducted for every electropolished sample in an angular interval of $110° \geq 2\theta \geq 35°$ with a step size of 0.01° & counting time of 1s/step. The instrumental broadening was corrected via a fully recrystallized Ta sample and a second order polynomial was applied for background subtraction. The overlapping peaks of Kα1 and Kα2 were separated by the Rietveld method. Then the whole X-ray line profiles were fitted by the software of Jade 6.0. Experiments of electron back-scattered diffraction (EBSD) and electron channeling contrast imaging (ECCI) were operated on JSM-7800F SEM.

Results and Discussion

Through thickness texture

The through-thickness texture gradient is common for some as-rolled metals with high stacking fault energies, further leading to anisotropy of mechanical performance

[12, 13]. Extensive relevant studies concerning aluminum alloy and steels have been carried out [12, 14, 15]. Nevertheless, the majority of existing literatures focus on the phenomenological characterization of texture gradient rather than the way to weaken it. The previous researches [2, 13] have shown that serious gradient also exists in rolled Ta plate. The θ-fiber texture (<100>// ND) occupies a leading position near the surface of plate, while texture near the center is primarily dominated by γ-fiber (<111>// ND). This gradient is quite prominent after traditional rolling modes (e.g. UR). The texture distribution of initial tantalum prior to rolling also presents this kind of gradient, as shown in Fig. 2.

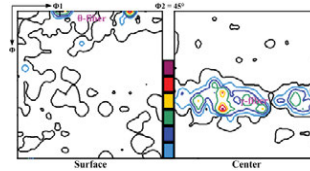

Fig. 2. The orientation distribution maps of the surface and center of initial tantalum.

The initial plate undergoes different texture evolution under UR and CR after 16 rolling passes. The detailed texture distribution through the thickness is showed in Fig. 3.

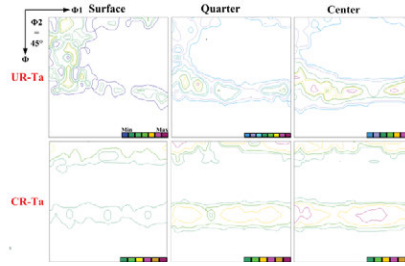

Fig. 3. Through-thickness texture of UR and CR-Ta, respectively.

Compared with the UR-Ta, the texture of CR-Ta is a mixture of θ and γ fibers. Besides, the fibers show perfect integrality under clock rolling, indicating that orientations belonging to the two fibers present a certain degree of random distribution. In order to quantify the texture gradient, a histogram is depicted as Fig. 4.

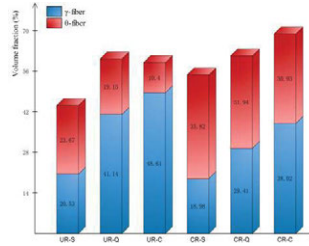

Fig. 4. Quantitative description of the through-thickness texture evolution under the two rolling modes. The "S", "Q" and "C" at the abscissa axis are the abbreviation of "Surface layer", "Quarter layer" and "Center layer", respectively.

A considerable number of θ-grains exist in the surface layers of UR and CR-Ta. This phenomenon is consistent with the initial Ta plate, as shown in Fig. 2. The metallograph of initial plate shows that many large grains are located in the surface layer [8], which are difficult to be rotated to other orientations for their large dimensions during deformation. In addition, the θ-fiber is proved to be quite stable under monotonic strain [16]. Hence, the grains with {100} orientations in the initial plate are very likely to be delivered to the subsequent as-rolled Ta. In other words, plenty of θ grains in the surface layer after rolling are inherited from the initial plate.

Another phenomenon revealed in Fig. 4 is the gap of volume fractions between θ and γ fibers. This gap gradually expands from the surface to the center of UR-Ta but remains the same in the CR-Ta. Besides, the through-thickness distribution of θ-fiber in the UR-Ta is extremely uneven when compared with the CR-Ta.

Stored energy gap

The θ-fiber (200) and γ-fiber (222) line profiles are selected to assess the orientation-dependent stored energy, as shown in Fig. 5.

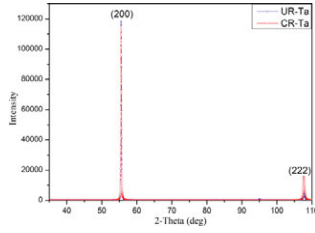

Fig. 5. The fitted (200) and (222) X-ray line profiles of UR and CR-Ta.

According to Ref. [17], the effective full width at half maximum (FWHM) B can be calculated as:

$$B^2 = B_r^2 - B_a^2$$

Where the B_r and B_a are the experimental values of FWHM of deformed and fully recrystallized Ta, respectively. The lattice strain (Δd/d) is evaluated by the following

formula:

$$\Delta d / d = B / (2\tan\theta)$$

Therefore, the orientation-dependent stored energy due to the inhomogeneous lattice strain can be calculated [17, 18] as follows:

$$W_{hkl} = \frac{3}{2} Y_{hkl} \frac{(\Delta d / d)^2}{1 + 2\nu_{hkl}^2}$$

Where Y_{hkl} and V_{hkl} are the orientation-dependent Young's modulus and Poisson's ratio, respectively. Values of these parameters and corresponding stored energies are summarized in Tab. 1. The calculated stored energies indicate that the energy gap between θ-fiber and γ-fiber grains is largely narrowed after clock rolling.

Table. 1. Required parameters and calculated orientation-dependent stored energies.

$\theta_{(200)}$	$\theta_{(222)}$	Y_{200}	Y_{222}	ν_{200}	ν_{222}	$B_{n(200)}$	$B_{n(222)}$		UR-Ta	CR-Ta
27.774°	53.821°	145.6 Gpa	284.4 Gpa	0.368	0.218	0.100° ± 0.001°	0.140° ± 0.001°	$B_{r(200)}$	0.168° ± 0.002°	0.189° ± 0.001°
								$B_{r(222)}$	0.473° ± 0.001°	0.399° ± 0.003°
								$W_{\theta\text{-fiber}}$	2.98 J/mol	4.20 J/mol
								$W_{\gamma\text{-fiber}}$	9.25 J/mol	6.32 J/mol

Rolling microstructure

Grains with different orientations have different subdivision ways and corresponding different deformation substructures. The θ and γ grains in Ta also follow this principle. The original orientations, {100}<uvw>, are hard to be changed during deformation for the stability of θ-fiber. On the contrary, the {111}<uvw> grains are inclined to subdivide into fragments and even rotate to other orientations under large deformation degree. As shown in Figs. 6(a, c), there is hardly any microstructure characters can be seen in the UR-θ grains, i.e. featureless structure. However, the corrosion traces indicate that plenty of micro-shear bands exist in the γ grains (as marked by the arrows in Fig. 6(c)), which is also verified by the ECC image (Fig. 6(e)). The above orientation-dependent microstructure characteristics perfectly prove the stability of θ-fiber and the instability of γ-fiber under unidirectional rolling.

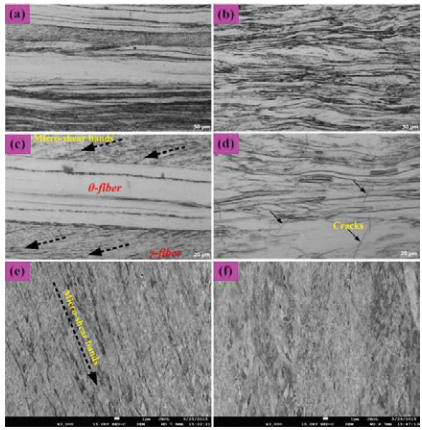

Fig. 6. Orientation-dependent structures of UR (a, c, e) and CR-Ta (b, d, f). (a)-(e) are metallographs and (e)-(f) are ECC images. The microstructure data were all acquired from the RD-ND section of samples.

Unlike the UR-Ta, the orientation dependence is less obvious in the CR-Ta. Fig. 6(b) shows a relatively chaotic rolling structure when compared with the significant difference among grains in Fig. 6(a). The magnified metallographic image Fig. 6(d) presents that the θ grains in CR-Ta are not featureless since some cracks appear. It suggests that the θ-fiber is not stable under clock rolling. In addition, plenty of micro-shear bands exist in the γ-grains of the UR-Ta (Fig. 6(e)), whereas such bands are hardly to be found in the CR-Ta (Fig. 6(f)). It follows that CR can effectively sweep the micro-shear bands in γ grains.

Shear bands that consist of numerous subgrains with various orientations often own high dislocation densities [19]. Hence, the γ-grain in the UR-Ta have a higher stored energy than the CR-Ta. Meanwhile, the stable θ grains in the UR-Ta show a featureless structure and thus have low stored energy. That is why the stored energy gap between the two kinds of grains determined by XRD-LPA is so large for UR-Ta. Conversely, a certain degree of subdivisions of the CR-θ grains introduce some cracks, increasing the stored energies of {100} grains. Hence, the gap is apparently narrowed after CR.

Annealing microstructure

As known to us, high-angle boundaries, micro-shear bands and stored energies are crucial roles for the subsequent annealing courses. These roles are able to provide the required nucleation sites and driving force for recrystallization. As proved by Vandermeer [16] and Sandim [20], the featureless θ grains in UR-Ta often resist recrystallization for lacking the favorable roles, leading to the appearance of residual deformation bands after annealing.

Figs. 7(a, b) describe the microstructures of UR and CR-Ta annealed at 1200 ˚C

for 1 min. There are still no significant recrystallization signs in the CR-Ta, which can be attributed to the reduction of micro-shear bands (i.e. nucleation sites) and the decrease of stored energy (i.e. driving force), and thus leading to a sluggish recrystallization of {111} grains. On the contrary, obvious recrystallization can be seen in the UR-Ta. However, such recrystallization shows severe inhomogeneity. The recrystallized grains are inclined to get together and finally present a banded distribution, as evident in Fig. 7(a). The study on interstitial-free steels shows that the {111} deformed grain will generate recrystallized grains quickly during annealing, of which most are also with {111} orientations for a mechanism named "frequency-advantage" [21], then resulting in {111} clusters and bands, just as shown in Fig. 7(c).

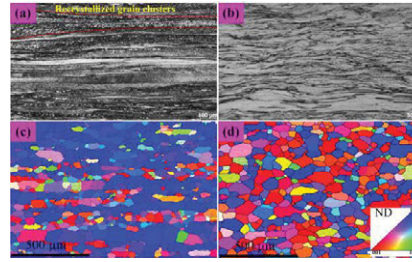

Fig. 7. Comparisons of recrystallization behaviors between UR (a, c) and CR-Ta (b, d). (a) & (b) are metallographs of Ta annealed at 1200 °C for 1 min. (c) & (d) are Ta heated to 1300 °C at 10 °C/min and annealed for 1 h [9]. The data were all obtained from the RD-ND section.

The aforesaid results show that the discrepancy between θ and γ grains is largely neutralized by the clock rolling. The cracks (see Fig. 6(d)) can definitely enhance the nucleation ability of θ grains and thus result in the self-consumption of the {100} deformed matrixes. In this case, the residual deformation bands are reduced greatly. The relatively random spatial distribution of rolling texture (see the section of "Through thickness texture") also gives rise to a random annealing texture, as proved in Fig. 7(d).

The existence of texture gradients, orientation clusters and residual deformation bands seriously injures the sputtering performance of Ta target [1, 3]. These negative factors are eliminated effectively by 135° clock rolling, which should be able to improve the properties of sputtering targets. Different from some other plastic deformation techniques (e.g. equal channel angular pressing and high-pressure torsion) that can also bring about a uniform microstructure, the significant merit of 135° clock rolling is that applying it to the industry is really feasible..

Conclusions

That 135° clock rolling improves the uniformity of microstructure and texture of tantalum is investigated via a variety of characterization techniques. Some primary

conclusions can be drawn as follows:

1. 135° clock rolling can largely alleviate the inhomogeneity of texture distribution, including the through-thickness texture gradients and the texture clusters.
2. The traditional rolling schedule, straight rolling, leads to severe micro-shear bands within the γ grains. On the contrary, 135° clock rolling is able to sweep these bands and give a uniform intragranular structure.
3. 135° clock rolling is an efficient approach to weaken the difference between the θ and γ grains, thus imparting uniform annealing behaviors, favorable microstructure and texture for tantalum sputtering target.

Acknowledgements

The present work was co-supported by the National Natural Science Foundation of China (Grants 51301212 and 51421001), the Major National Science and Technology Projects of China (No. 2011ZX02705), and the Chongqing Science and Technology Commission in China (CSTC, 2012jjA50023). “”

References

[1] J. Sarkar, *Sputtering Materials for VLSI and Thin Film Devices* (Oxford, Reino Unido: Elsevier, 2014), 358-372

[2] J. Clark. et al., “Effect of processing variables on texture and texture gradients in tantalum,” *Metallurgical Transactions A*, 22 (1991), 2039-2048.

[3] C.A. Michaluk, “Correlating discrete orientation and grain size to the sputter deposition properties of tantalum,” *Journal of electronic materials*, 31 (2002), 2-9.

[4] D. Field et al., “Microstructural development in asymmetric processing of tantalum plate,” *Journal of electronic materials*, 34 (2005), 1521-1525.

[5] J. Clark. et al., “Influence of transverse rolling on the Microstructural and Texture Development in Pure Tantalum,” *Metallurgical Transactions A*, 23 (1992), 2183-2191.

[6] S.N. Mathaudhu, K. Ted Hartwig, “Grain refinement and recrystallization of heavily worked tantalum,” *Materials Science and Engineering: A*, 426 (2006), 128-142.

[7] C.E. Wickersham Jr, V. Levit and P.T. Alexander, “Tantalum sputtering target and method of fabrication,” *Google Patents*, 2011.

[8] S. Liu et al., “Through-thickness texture in clock-rolled tantalum plate,” *International Journal of Refractory Metals and Hard Materials*, 48 (2015), 194-200.

[9] C. Deng et al., “Texture evolution of high purity tantalum under different rolling paths,” *Journal of Materials Processing Technology*, 214 (2014), 462-469.

[10] H. Fan et al., “Quantifying the effects of surface quality on texture measurements of tantalum,” *Applied Surface Science*, 339 (2015), 15-21.

[11] R. Renzetti et al., “X-ray evaluation of dislocation density in ODS-Eurofer steel,” *Materials Science and Engineering: A*, 534 (2012) 142-146.

[12] O. Engler, C. Tomé and M.-Y. Huh, “A study of through-thickness texture gradients in rolled sheets,” *Metallurgical and Materials Transactions A*, 31 (2000)

2299-2315.
[13] S.I. Wright, G.T. Gray and A.D. Rollett, “Textural and microstructural gradient effects on the mechanical behavior of a tantalum plate,” *Metallurgical and Materials Transactions A*, 25 (1994), 1025-1031.
[14] S. Li, F. Sun and H. Li, “Observation and modeling of the through-thickness texture gradient in commercial-purity aluminum sheets processed by accumulative roll-bonding,” *Acta Materialia*, 58 (2010), 1317-1331.
[15] M.-Y. Huh et al., “Evolution of through-thickness texture gradients in various steel sheets,” *Metals and Materials*, 5 (1999), 437-443.
[16] R. Vandermeer, W. Snyder, “Recovery and recrystallization in rolled tantalum single crystals,” *Metallurgical Transactions A*, 10 (1979), 1031-1044.
[17] N. Rajmohan et al., “Neutron diffraction method for stored energy measurement in interstitial free steel,” *Acta Materialia*, 45 (1997), 2485-2494.
[18] R. Khatirkar et al., “I. Samajdar, Orientation Dependent Recovery in Interstitial Free Steel,” *ISIJ international*, 52 (2012), 884-893.
[19] T. Morikawa et al., “Micro shear bands in cold-rolled austenitic stainless steel,” *Materials Transactions*, JIM, 40 (1999), 891-894.
[20] H. Sandim, J. Martins and A. Padilha, “Orientation effects during grain subdivision and subsequent annealing in coarse-grained tantalum,” *Scripta Materialia*, 45 (2001), 733-738.
[21] J. Bocos et al., “Aspects of orientation-dependent grain growth in extra-low carbon and interstitial-free steels during continuous annealing,” *Metallurgical and Materials Transactions A*, 34 (2003), 827-839.

TMS2016

145th Annual Meeting & Exhibition

SUPPLEMENTAL PROCEEDINGS

Material Design Approaches and Experiences IV

EVOLUTION LAW OF GRAIN SIZE OF HIGH ALLOY GEAR STEEL IN HOT DEFORMATION

TANG Hai-yan[1,2], YANG Mao-sheng[3] , MENG Wen-jia [2,3], LI Jing-she[1,2]

[1]State Key Laboratory of Advanced Metallurgy, University of Science and Technology Beijing; No.30 Xueyuan Road; Beijing, 100083, China
[2]School of metallurgical and ecological engineering, University of Science and Technology Beijing; No.30 Xueyuan Road; Beijing, 100083, China
[3]Institute for Special Steels, Central Iron and Steel Research Institute Xueyuan Nanroad; Beijing 100081, China

Keywords: Gear steel; Recrystallization; Grain size

Abstract

The change rules of deformation parameters such as temperature, strain and strain rate at different zones of forgings are very complex in the forging process of high alloy chromium-cobalt gear steel, and the deformation parameters have great influence on grain sizes. In this paper, recrystallization model for the steel was established with the material characteristic parameters obtained from the Gleeble isothermal compression test, influencing factors were analyzed based on the model. The results indicate that recrystallization grain size increases with increasing temperature and decreasing strain and strain rate, and the effect of temperature is more obvious than the other two. The average grain sizes are between 27.7μm~40μm at 1040℃ of forging temperature, grain size degree 6~6.5, meeting the product requirements.

Introduction

Gear is an important component transferring movement and load among the mechanical structure, usually processed by die forging. Its working environment is bad due to bearing the friction and stress load. With the rapid development of advanced equipment manufacturing, high strength and toughness requirements are put forward to meet these performances such as reliability, stability and long life. The main strengthening forms of a material include solid solution strengthening, dislocation, second phase and fine grain strengthening. Grain refinement has attracted widespread attention at home and abroad as it can simultaneously improve the yield strength and toughness of the material [1]. According to Hall-Petch formula [2] and the grain size, the relationship of yield stress and flow stress can be predicted [3]. Studies indicate that the grain size of heat treatment is positive correlate to that of die forging, while the grain size affects the performance of a forging, thus it is very necessary to investigate the evolution law of grain size during hot deformation for high alloy gearing steel.

Many researches have been carried out on the recrystallization of a material [5~14]. However, few studies are focused on the gearing forging. The grain size of a forging is usually required below 40μm. However, its control mainly relies on the experience, which easily leads to unstable control. In this work, the recrystallization model is established based on the thermal simulation

test results, the effect of deformation parameters on the grain size is investigated, and the optimum forging parameters are put forward.

Research methods

Gleeble hot-compression simulation test

The main alloy composition of the investigated material is listed in Table 1. It was smelted in a 5t vacuum induced furnace then remelted in a 1t vacuum arc furnace, and then casting ingot and air-cooled to ambient temperature. The ingot was annealed at 1050℃ for 10h and then forged. Cylindrical specimens of 12mm in length and 8mm in diameter were prepared for hot-compression tests with Gleeble-3800 thermal simulation tester. The strain of hot-compression test was ε = 0.92, samples were deformed at 700℃~1200℃ with 0.1, 1, 20, 50s^{-1} in sequence. The samples were heated to required temperature at the speed of 20℃/s, holding for 300s, compressed then water-cooled immediately. The quenched samples were cut along the axis. After grinded, polished and etched, the microstructures were observed with an Olympus GX51 optical microscope.

Table 1 Main chemical composition of the material

Elements	C	Si	Mn	Co	Ni	Cr	Mo	Fe
mass%	0.1~0.2	<0.1	<0.1	10~15	1~3	11~14	4~5	balance

Establishment of recrystallization model

The dynamic recrystallization of microstructures might occur during the hammer and the work piece contacting, and static recrystallization during the hammer alofting or workpiece air cooling. Based on F. Montheillet's research, YLJ model was chosen.

Dynamic recrystallization model:

$$\varepsilon_c = a_1 \cdot \varepsilon_p$$

$$\varepsilon_p = a_2 \cdot d_o^{h_2} \cdot \dot{\varepsilon}^{m_2} \cdot \exp\left(Q_2 / RT\right) + C_2$$

$$X_{drex} = 1 - \exp\left[-\beta_d \left(\frac{\varepsilon - a_3 \cdot \varepsilon_p}{\varepsilon_{0.5}}\right)^{k_d}\right]$$

$$\varepsilon_{0.5} = a_4 \cdot d_o^{h_4} \cdot \varepsilon^{n_4} \cdot \dot{\varepsilon}^{m_4} \cdot \exp\left(Q_4 / RT\right) + C_4$$

$$\mathrm{d}_{drex} = a_5 d_o^{h_5} \varepsilon^{n_5} \dot{\varepsilon}^{m_5} \exp\left(Q_5 / RT\right) + C_5$$

Static recrystallization model

$$\dot{\varepsilon}_{ss} = A \cdot exp\left(b_1 - b_2 \cdot d_o - \frac{Q_{ss}}{T}\right)$$

$$\mathrm{X}_{\mathrm{srex}} = 1 - \exp\left[-\beta_s \left(\frac{t}{t_{0.5}}\right)^{k_s}\right]$$

$$t_{0.5} = a_6 \cdot \dot{\varepsilon}^{m_6} \cdot \exp\left(Q_6 / RT\right)$$

Grain growth model

$$d_g = \left[d_o^m + a_7 \cdot t \cdot \exp\left(-\frac{Q_7}{RT} \right) \right]^{1/m}$$

Average grain size model

$$D = X_{rex} \cdot d_{rex} + \left(1 - X_{rex}\right) \cdot d_o$$

Where

ε_c—critical strain; ε_p—peak strain; ε—strain; $\dot{\varepsilon}$—strain rate; d_0—initial grain size, μm; R—gas constant, 8.314J/(mol · K); T—temperature, K, X_{drex}—dynamic recrystallization ratio; X_{srex}—static recrystallization ratio; $\varepsilon_{0.5}$—strain at recrystallization 50%; d_{drex}—grain size of dynamic recrystallization, μm; $\dot{\varepsilon}_{ss}$—critical strain rate of static recrystallization, s^{-1}; t—static recrystallization time, s; $t_{0.5}$—time at static recrystallization 50%, s; d_g—grain size, μm; X_{srex}—recrystallization ratio; d_{rex}—recrystallization grain size, μm; D—average grain size, μm.

Calculation of model parameters

The dynamic recrystallization parameters were obtained by single pass hot simulation test. The stress and strain parameters obtained were fitted to get σ = σ (ε) function, drawing θ—σ curve with the results of σ on ε derivation to obtain ε_c and the maximum recovery stress σ_{sat}, back to stress-strain curve to get ε_c and ε_p, d_0, d_{drex} and X_{drex} were obtained by metallographic statistics. The static recrystallization parameters were obtained by double pass hot compression test. The recrystallization ratio was calculated by the following formula:

$$X_{mrex} = \left(\sigma_m - \sigma_2\right) / \left(\sigma_m - \sigma_1\right)$$

Where σ_m is the unload stress at the first time, σ_1 and σ_2 are yield stresses for two loads. Grain growth model was obtained by the grain sizes at different holding times.

Results and discussion

Figure1 gives part stress-strain curves. They are fitted and derivated to obtain stress-strain fitting curve and hardening rate curve as figure 2.

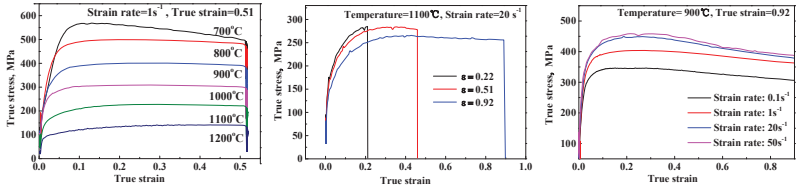

Figure 1 Stress-strain curve of test steel under different deformation conditions

Table 2 is the obtained parameters of recrystallization model. The effect of deformation parameters on dynamic recrystallization grain size is shown in Figure 3.

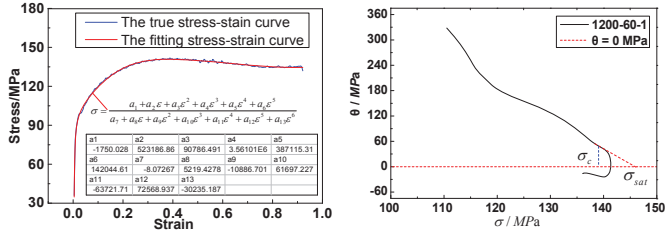

Figure2 Stress- strain fitting curve and hardening rate curve

Table 2 Parameters of recrystallization model

Parameters	Values	Parameters	Values	Parameters	Values	Parameters	Values	Parameters	Values
a_1	0.729	Qss	0	h_2	-0.0479	m_2	0.0454	n_4	1.7042
a_2	0.1299	Q_2	12898.7	h_4	0.1414	m_4	0.1208	n_5	-0.5373
a_3	0.379	Q_4	25839.04	h_5	0	m_5	-0.1888	A	0
a_4	0.3125	Q_5	-69965.58	C_2	-0.378	m_6	-0.3614	β_S	0.693
a_5	1649.9	Q_6	93402.79	C_4	0.18	m	1.1116	k_S	0.723
a_6	0.0003073	Q_7	66644.1	C_5	3.393	β_d	1.303		
a_7	7.444	b_1	0	b_2	0	k_d	-6.144		

From figure 3(a), the effect of temperature on grain size of dynamic recrystallization is obvious. The recrystallization grain sizes approximately linearly increase with increasing temperature. This is because some substances nailing on grain boundaries dissolve, their resistances to inhabit the austenite grain growth decrease. Part grains will break the restrictions from the precipitated phase particles and begin to grow, generating mixed grain phenomenon. When temperature continues to rise, Ostwald ripening of precipitation phase will occur, and the grains continue to grow [14,15].

The grain size increases by 30% when temperature increases 100℃. Comparing these curves at different strain and strain rate, the smaller the strain and strain rate are, the larger the effect of temperature on grain size is. When the strain is 0.2 and strain rate 0.15, the effect is the largest, grain size varies from 9μm to 18μm.

Figure 3(b) gives the relationship of strain and grain size of dynamic recrystallization. It is seen that the grain become smaller with the increase of the strain. When the strain is more than 0.5, its effect on grain size weakens significantly. The higher temperature and smaller strain rate are, the greater effect.

Figure 3(c) is the effect of strain rate on grain size of dynamic recrystallization. With the increase of strain rate, the grain size decreases slowly. When the strain rate is below $0.3s^{-1}$, there is larger effect of strain rate on grain size, while at strain rate is over $0.3s^{-1}$, the change is minor.

Comparing the three figures, it is found that the effects of temperature and strain are more significant than strain rate.

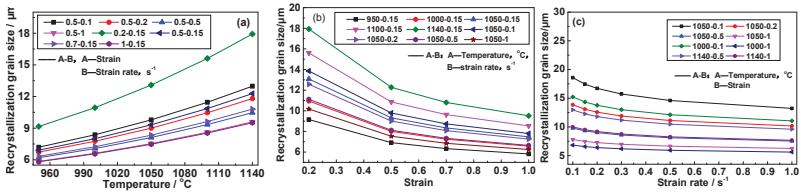

Figure3 Effect of deformation parameters on dynamic recrystallization grain size

Generally, the peak values of strain rate in the process of die forging are at $0.2s^{-1}$ ~$1.2s^{-1}$. The effect of strain rate on recrystallization grain size is smaller in this range from figure 3(c). For different batches of forgings, the strain change in the same region is also minor. Thus, the initial forging temperature is the main restrictive factor for the grain size of a gearing forging. In actual forging, when the temperature is at 1040° C, the grain size is 27.7μm~40μm as in figure 4, grain size degree 6~6.5, meeting the product requirements.

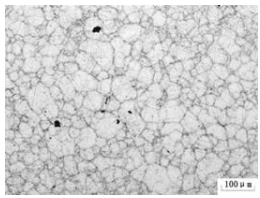

Figure4 The microstructure of actual forging at 1040° C

Conclusions

(1) The recrystallization grain size of gear steel increases with increasing temperature and decreasing strain and strain rate, and the effect of temperature is more obvious than the other two.

(2) The average grain sizes are between 27.7μm~40μm at 1040℃ of forging temperature, grain size degree 6~6.5, meeting the product requirements.

Acknowledgements

The authors are grateful for the support from the State Key Laboratory of Advanced Metallurgy of the USTB (No. 41603014) and the National Natural Science Foundation of China (No. 51374021) and the National High Technology Research and Development Plan (No. 2012AA03A503).

References

[1] Niels Hansen, "Hall–Petch Relation and Boundary Strengthening," *Scripta Materialia*, 10 (51) (2004), 801-806.

[2] P. Sharifi et al., "Predicting the Flow Stress of High Pressure Die Cast Magnesium Alloys,"*Journal of Alloys and Compounds*, 3(605) (2014), 237-243.
[3] S.Q. Huang, "Microstructure Evolution and Digital Characterization of Ultra High-strength Steel in the Whole Forging Process"(PH.D. thesis, Central South University, 2013).
[4] F. Montheillet, O. Lurdos, and G. Damamme, "A grain scale approach for modeling steady-state discontinuous dynamic recrystallization,"*Acta Materialia*, (57) (2009), 1602-1612.
[5] T. E. Howson, and H. E. Delgado, "Computer Modeling Metal Flow in Forging,"*JOM*, 41(2) (1989), 32-34.
[6] K.S. Park, C.J. VanTyne, and Y.H. Moon, "Process Analysis of Multistage Forging by Using Finite Element Method,"*Journal of Materials Processing Tech*, 187 (2006), 586-590.
[7] C.X. Yueet al.,"Finite Element Simulation of Austenite Grain Growth for GCr15 Steel,"*Materials for Mechanical Engineering*, 12(32) (2008), 88-90.
[8] Z.D. Quet al.,"The Model of Microstructure Evolution in Hot Forming Based on Second-Development of DEFORM3D,"*Journal of Plasticity Engineering*, 7(12) (2005), 40-43.
[9] F. Chen,"Cellular Automata Simulation of Microstructure Evolution in Thermal Forging Discontinuous Deformation Process" (PH.D. thesis, Shanghai Jiaotong University, 2013).
[10] B.X. Wang et al., "Research on Dynamic Recrystallization Behavior of New Mn-Cr Gear Steel", *Iron and Steel*, 39(9) (2004), 54-57.
[11] J. Caoet al.,"Analysis on Dynamic Recrystallization Behavior of Bainitic Non-Quenched and Tempered Steel for Fasteners,"*Journal of Iron and Steel Research*, 24(10) (2012), 39-42.
[12] G. Liuet al., "Hot Compression Recrystallization Behaviors of Low Carbon CrNiMo Carburized Bearing Steel,"*Journal of Iron and Steel Research*, 25(9) (2013), 30-37.
[13] S.B. Yin et al.,"Effect of Hot Deformation Parameters on Phase Transformation in Austenite Non-Recrystallization Region of Niobium Steel,"*Iron and Steel*, 43(2) (2008), 81-85.
[14] E.J. Palmiere,C.I. Garcia,and A.J. Deardo, "Compositional and Microstructural Changes Which Attend Reheating and Grain Coarsening in Steels Containing Niobium," *Metallurgical and materials transactions A*, 25(A) (1994), 277-286.
[15] P.A. Manoharet al., "Grain Growth Prediction in Microalloyed Steel," *ISIJ International*, 36(2) (1996), 194-200.

EXPERIMENTAL INVESTIGATION OF THE Sm-RICH SIDE IN Sm-Zr SYSTEM

Tian Yin[1], Shuqiang Zhang[1], Zhihong Zhang[2], Jieyu Zhang[1*]

1 State Key Laboratory of Advanced Special Steel, School of Materials Science and Engineering, Shanghai University, Shanghai, 200072, China; 2 Baotou Research Institute of Rare Earths, Baotou, 014030, China

Keywords: Sm-Zr system, diffusion couple, phase equilibrium

Abstract

The information of phase diagram for the Sm-Zr system is deficient. A diffusion couple and two alloys in Sm-rich side of Sm-Zr system were prepared. The phase equilibrium in the alloys at 800 and 900 ℃ were determined by scanning electron microscopy，equipped with energy dispersive X-ray spectroscopy (SEM-EDS) and X-ray diffraction(XRD). The results show that a peritectic reaction exists in the Sm-rich end. The solubility of Sm in (Zr) was detected to be about 2.4 at.% at 800℃ and 2.7 at.% at 900 ℃. The solubility of Zr in (Sm) is negligible. No binary compound is detected in the XRD patterns in all samples.

Introduction

Alloys and compounds contained rare earth elements possesses unique properties. The scope of their applications includes permanent magnet materials，superconductors， sensors，phosphors. Therefore, knowledge of phase equilibria in the systems contained rare earth elements is desirable.

Sm and Zr are the important alloying elements of magnesium alloys to improve their mechanical properties[1-4]. For the advanced development of the Mg-based alloys, knowledge of the phase equilibria of the Sm-Zr system is of fundamental importance. However, the knowledge of the phase equilibria and thermodynamic analysis of this system is deficient. So far, no phase diagram for the Sm-Zr system is available in the literature. Consequently, we present here a preliminary study for Sm-Zr system.

Experimental Procedure

As starting materials, 99.9 wt.% Sm and 99.95 wt.% Zr were used for the preparation of the diffusion couple and Sm-Zr alloys. The Sm/Zr diffusion couple of approximate dimensions of 10 mm×10 mm×10 mm was made of pure block Sm and Zr. In order to decrease the influence of the potential oxidation film to the diffusion of atoms, the diffusion interface between Sm and Zr block was polished and pressed together under the pressure of 6 MPa, 800 ℃ and vacuum(10^{-3}Pa) for 4 hours. After hot pressing, the diffusion couple was encapsulated in quartz tube under a protective argon atmosphere. The diffusion couple was then annealed at 800 ℃ for 30 days, followed by water quenching.

Two alloy samples were synthesized from purity Sm and Zr using cold crucible induction levitation melting method. Due to the high volatility of Sm and the significant difference between the melting points of Sm and Zr, the pure Zr were added to the furnace by two or three

* Corresponding author. Tel.: +86 021 56337920;
E-mail address: zjy6162@staff.shu.edu.cn (Jieyu Zhang)

times respectively. Each alloy was melted several times to ensure good homogeneity. The alloys were wire cut as the size 4 mm×4 mm×4 mm, wrapped with tantalum sheet and then annealed in an evacuated quartz tube. Each sample was annealed at 500℃ for 30 days firstly and then at 800 and 900 ℃ for 7 and 3 days respectively, followed by water quenching.

The compositions of casting alloys were analyzed by optima 7300DV ICP. The HITACHI SU-1500 SEM/BSE equipped with EDS system were used to analyze the microstructure of diffusion couple and alloys. XRD, carried our on a Rigaku D/MAX-rC diffractometer (CuKα radiation，2θ = 25-70°，4°/min) operated at 40 KV and 100 mA, was used to determinate the structure of the alloys. Due to the oxidation of pure Sm in the form of powder, all the XRD samples are rectangle block, which were polished to be mirror surface in alcohol.

Results and Discussion

Analysis of diffusion couple

The BSE images of the microstructure of Sm/Zr diffusion couple annealed at 800 ℃ for 30 days are shown in Figure 1 (a). After the interdiffusion of the Sm and Zr, no intermetallics layer formed. Based on the principle of backscattering, the dark field is Zr and the bright field is Sm. the sample was studied via SEM/EDS and the results of line scanning and point analysis are presented in Figure 1 (b) and (c). The curve in Figure 1 (b) indicates that the diffusion layer is composed of (Sm) and (Zr) solid solution. The Figure 1 (c) shows the similar tendency to Figure 1 (b). The solubility of Zr in (Sm) at 800 ℃ was approximately 0.6 at.%, which is negligible.

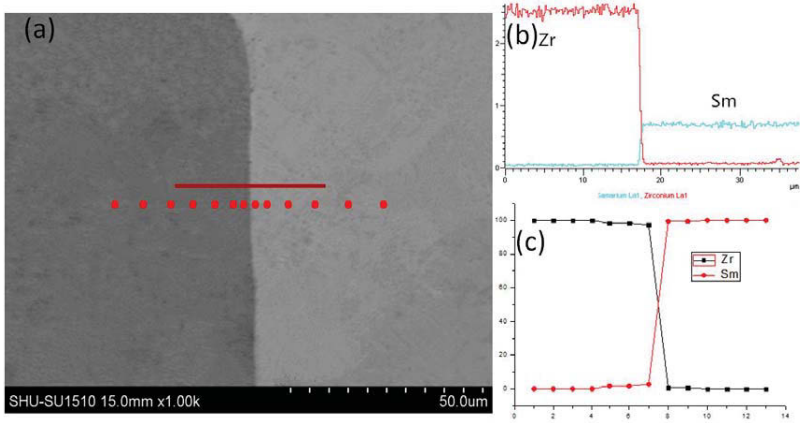

Fig 1. (a) The BSE image of the microstructure of the diffusion couple annealed at 800 ℃ for 30 days; (b) line scanning analysis of the diffusion couple; (c) point analysis of the diffusion couple.

Microstructure and phase identification of Sm-Zr alloys

According to the result detected from Sm/Zr diffusion couple, two alloys had been prepared for phase identification. All the prepared Sm-Zr alloys have been subjected to XRD and SEM/EDS. The analyzed chemical compositions for the alloys, annealing condition and phase identification are shown in Table I.

Table I. Summary of the composition and the annealing temperature of alloys in the present work

Alloy No.	Alloy composition (at.%)	Annealing temperature (℃)	Phase
#1	$Sm_{91.1}Zr_{8.9}$	800	（Sm） （Zr）
		900	（Sm） （Zr）
#2	$Sm_{77.2}Zr_{22.8}$	800	（Sm） （Zr）
		900	（Sm） （Zr）

Figure 2 shows the comparison of the microstructure between the as-cast Sm-Zr alloys and that annealed at 800 ℃ for 7 days and 900 ℃ for 3 days. Based on the principle of backscattering, the dark field is (Zr) and the bright field is (Sm). That is to say, the phase equilibrium relation in each annealed alloys is (Sm) + (Zr).

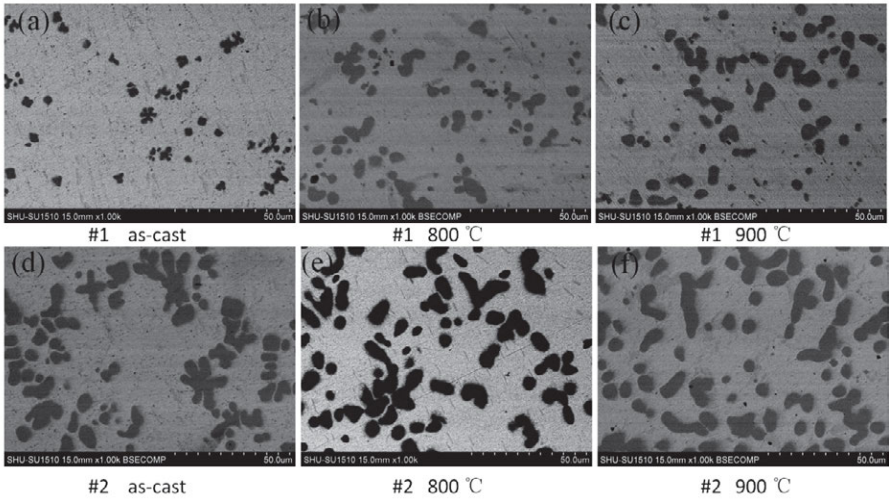

Fig 2. The BSE image of the microstructure of the as-cast Sm-Zr alloys and that annealed at 800 ℃ for 7 days and 900 ℃ for 3 days

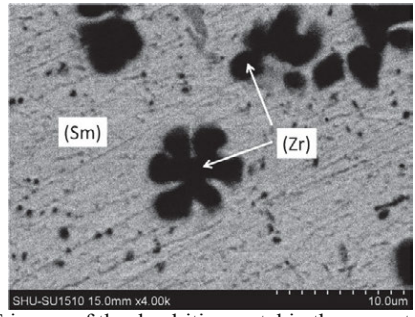

Fig 3. The BSE image of the dendritic crystal in the as-cast Sm-Zr alloys #1

Dendritic crystals shown in Figure 3 can be observed in the as-cast Sm-Zr alloys and that disappear after annealing at 800 and 900 ℃. This phenomenon is similar to the Nd-Zr binary system reported by Cheng[5]. The EDS results indicates that the solubility of Zr in (Sm) is negligible, the same as the results in the samples annealed at 800 and 900 ℃. It can be deduced that primary Zr dendritic crystal forms and grows up firstly at the beginning of the solidification, then surrounds by the peritectic formed (Sm). Therefore, this is a evidence that there is a peritectic reaction on the Sm-rich side in Sm-Zr system. The solubility of Sm in (Zr) was detected to be about 2.4 at.% at 800℃ and 2.7 at.% at 900 ℃. Figure 4 is the XRD patterns of as-cast and annealed Sm-Zr alloys. The XRD results indicates that all the alloys are composed of (Sm) and (Zr), which is in agreement with the results of SEM/EDS.

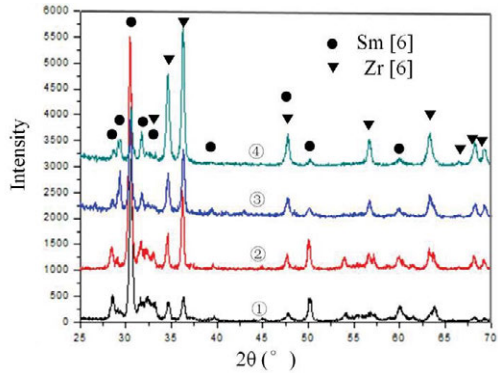

Fig 4. The XRD patterns of (1) as-cast alloy #1, (2) as-cast alloy #2, (3) alloy #2 annealed at 800 ℃ for 7 days, (4) alloy #2 annealed at 900 ℃ for 3 days

Conclusions

We have presented a preliminary study for the Sm-rich side of Sm-Zr system. It is that a peritectic reaction exists in the Sm-rich end. The solubility of Sm in (Zr) was detected to be about 2.4 at.% at 800℃ and 2.7 at.% at 900 ℃. The solubility of Zr in (Sm) is negligible. No binary compound is detected in the XRD patterns in all samples.

Acknowledgements

The authors thank Instrumental Analysis and Research Center of Shanghai University for their support of materials testing and research and Baotou rare earth institude for providing high purity materials.

References

1. Yuan M, Zheng Z. Effects of Zn on the microstructures and mechanical properties of Mg–3Sm–0.5Gd–xZn–0.5Zr (x=0, 0.3 and 0.6) alloy[J]. Journal of Alloys and Compounds, 2014, 590(2):355–361.
2. Wang Q, Li D, Blandin J J, et al. Microstructure and creep behavior of the extruded Mg–4Y–4Sm–0.5Zr alloy[J]. Materials Science & Engineering A, 2009, 516:189–192.
3. Z Zhang, L Peng, X Zeng, P Fu, W Ding. Characterization of phases in a Mg–6Gd–4Sm-0.4Zr (wt.%) alloy during solution treatment[J]. Materials Characterization, 2009, 60(6):555-559.
4. J Zheng, Q Wang, Z Jin, T Peng. The microstructure, mechanical properties and creep behavior of Mg–3Sm–0.5Zn–0.4Zr (wt.%) alloy produced by different casting technologies[J]. Journal of Alloys and Compounds 496 (2010):351–356
5. Cheng K, Zhou H, Hu B, et al. Experimental Investigation and Thermodynamic Modeling of the Nd-Zr and the Mg-Nd-Zr Systems[J]. Metallurgical & Materials Transactions A, 2014, 45(6):2708-2718.
6. S. Delfino, A. Saconne, and R. Ferro: Metall. Mater. Trans. A, 1990, vol. 21A, pp. 2109–14

TMS2016

145th Annual Meeting & Exhibition

SUPPLEMENTAL
PROCEEDINGS

Materials and Fuels for the Current and Advanced Nuclear Reactors V

FABRICATION AND QUALIFICATION OF SMALL SCALE IRRADIATION EXPERIMENTS IN SUPPORT OF THE ACCIDENT TOLERANT FUELS PROGRAM

Connor Woolum[1], Kip Archibald[1], Glenn Moore[1], Steven Galbraith[1]

[1]Idaho National Laboratory
Idaho Falls, ID, USA

Keywords: Accident Tolerant Fuel

Abstract

The Accident Tolerant Fuels (ATF) program aims to develop next generation Light Water Reactor (LWR) fuels with improved performance, reliability, and safety. The program has developed a roadmap to support the insertion of demonstration lead fuel rods (LFRs) or lead fuel assemblies (LFAs) into a commercial LWR by the end of FY 2022. In order to achieve this goal, novel fuel compositions and cladding materials are being assembled for drop-in irradiation experiments that afford prioritization of candidate concepts within the ATF Program. Development of fabrication methodology and qualification techniques for small-scale irradiation test samples is reported.

Introduction

The tragic events at the Fukushima Daiichi nuclear power plant in Japan resulted in the reevaluation of many aspects of nuclear power plants worldwide. As a result, the United States Department of Energy (DOE) initiated the Accident Tolerant Fuels (ATF) program. The goal of the ATF program is to develop next generation Light Water Reactor (LWR) fuels that enhance performance, reliability, and safety. The program aims to achieve this goal by exploring novel fuel designs and cladding concepts.

The DOE has established a roadmap that outlines steps ultimately leading to testing of a lead fuel assembly (LFA) or lead fuel rod (LFR) in a commercial reactor by 2022. The three phase approach is shown in Figure 1; it encompasses feasibility determinations, development and qualification of the new fuel system, and commercialization. The feasibility studies include bench-scale fabrication of the fuel system concepts and irradiation testing. The fabrication of these unique specimens necessitated supporting, developmental efforts in the areas of sample design, fabrication, and qualification techniques.

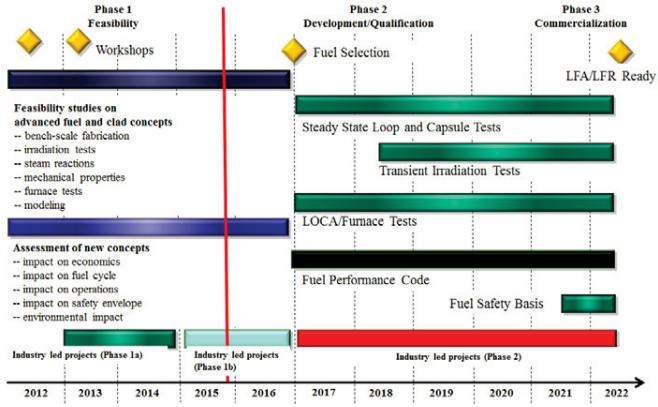

Figure 1. Three Phase Approach of ATF Program Leading to LFA/LFR Demonstration in 2022.

The ATF program is a collaborative effort among industry partners and the DOE national laboratory complex whose goal is to develop this new fuel system. Figure 2 shows the life-cycle of the ATF series of experiments and the complexity of such an endeavor. Table 1 illustrates the multiple facets of the program, ultimately leading to successful qualification of a new fuel system.

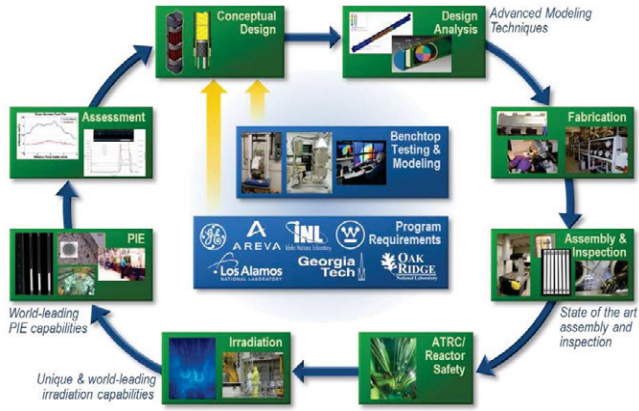

Figure 2. Irradiation Testing Lifecycle.

Table 1. ATF Irradiation Testing and Qualification.

Test Series	ATF-1	ATF-2	ATF-H-x	ATF-3	CM-ATF-x	ATF-y
Test Reactor	ATR	ATR	Halden	TREAT	Commercial Power Plant	TREAT
Test Type	Drop-in	Loop	Loop	Loop	LTR/LTA	Loop
Test Strategy	Scoping – Many Compositions	Scoping – Focused Compositions	Focused	Focused Compositions	Focused Composition	Focused Compositions
	Nominal conditions	Nominal conditions	Nominal	Accident conditions	Nominal conditions	Accident conditions
Fuel	UO_2, U_3Si_2, UN	Down-selected concepts	Selected	Fuel rodlets from ATF-1 and test rods from ATF-2 irradiations	Concepts selected in 2016	Test rods from LTR/LTA irradiations
Cladding	Zr w/coatings, stainless steels, advanced alloys, SiC					
Key Features	Fuel-cladding interactions	PWR Conditions	BWR Conditions	Integral testing	Steady State Irradiation	Integral testing
Timeframe	FY14 – FY18+	FY16 – FY22	FY15-FY22	FY18 – FY25	FY22 – ?	FY – ?

Experiment Design

Irradiation experiments were designed to test the behavior of new fuel system candidates. The new fuel system must exhibit enhanced safety, performance, and reliability over the current Zr-UO_2 system. Fuel and cladding candidates were proposed by the various collaborators; the candidates fabricated as part of the ATF-1 effort can be found in Table 2.

Table 2. Fuel and Cladding for ATF-1.

Development Lead	Fuel Type	Cladding Type
Westinghouse	U_3Si_2	Zirlo
AREVA	UO_2	Zircaloy-4
	UO_2 + SiC whiskers	Zircaloy-4
	UO_2 + diamond particles	Zircaloy-4
GE	UO_2	APMT
	UO_2	Alloy 33
ORNL	UO_2	FeCrAl

The ATF-1 experiment was designed such that individual rodlets could be fabricated with a unique fuel and cladding type. Each rodlet assembly is encapsulated in a stainless steel capsule that serves as a pressure boundary for the experiment, as illustrated in Figure 3. This physical design built upon an existing irradiation testing design that has been in use for many years by the mixed-oxide (MOX) fuel tests. [cite]. Modifications were necessary, however, to provide a means of centering each rodlet assembly within their respective capsule tube to ensure accurate modeling and, as best possible, uniform irradiation conditions.

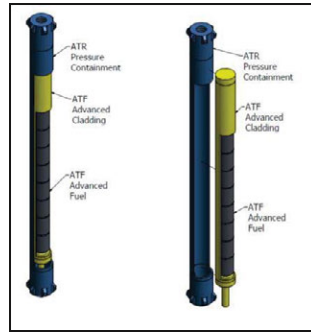

Figure 3. ATF Rodlet and Capsule Assemblies.

Each rodlet assembly is analyzed using a variety of modeling techniques to predict in-core performance and enhance the effectiveness of the experiment. Structural, neutronics, and thermal analyses were performed during the design phase of the experiment, as well as, after fabrication to predict behavior based on as-built information. Perhaps the most critical determination made during the design phase was the gas gap between the rodlet and capsule tubes. This gap is used to precisely control fuel centerline temperatures and cladding temperatures. In order to achieve the desired experimental conditions, these gas gaps had to range from .001" to .0035". A difference of .001" in this radial gap could have the effect of a rodlet assembly running anywhere from 80°C to 110°C or more off of the desired operating temperature.

Development

Initial development for the bench-scale fabrication of the ATF-1 irradiation tests consisted of welding development and refinement of assembly techniques, i.e. fit-up. Weld development was found to be the most challenging aspect of experimental assembly due to the unique nature of the cladding materials and the exacting dimensional requirements. The rodlets had to be welded in an inert atmosphere glovebox (typically helium) in order to establish this same atmosphere within the rodlet assembly. In addition, of the various cladding materials used, several novel alloys proved difficult to weld.

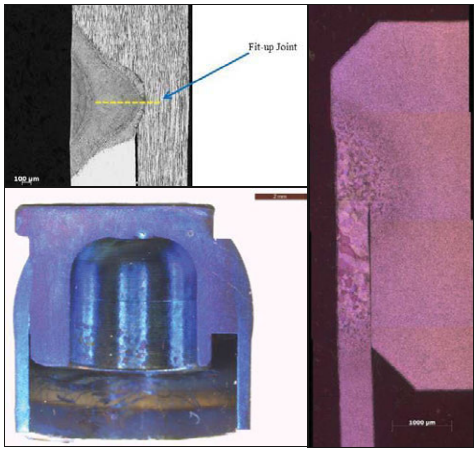

Figure 4. (Top left) Fit-up joint of ATF capsule. (Bottom left) Cross-section of new endcap design, heat tinted. (Right) Example of heat affected zone on zirconium based rodlet.

Welding the rodlet assemblies required significant process improvement as experiment fabrication occurred. Weld blowouts were common during early fabrication due to trapped, expanding gas. Component fit-up and alignment within the AMI welder also appeared to have significant impact on the success of a weld. Tooling was designed and fabricated to serve as alignment jigs. Copper chill blocks were utilized to mitigate heat, and thus gas, buildup within a rodlet assembly during welding. These various measures allowed for successful welds.

A variety of techniques were utilized to examine welds during the development process. Metallography allowed for visual examination of weld penetration. Both etching and a heat tinting technique were options during preparation, depending on the composition of the rodlet material and the desired information. Standard acid etching techniques allowed for examination of the heat affected zone of the stainless steel capsules or iron based rodlet tubes. A heat tinting technique, where samples were heated to 400°C for 3.5 minutes, was useful for zirconium based materials to determine if endcap material had undergone any mixing with tubing material.

A new endcap (Figure 5) has been designed to further mitigate potential welding issues in future ATF experiments. This endcap design features a hollowed out region to minimize differences in thermal masses between the endcap and rodlet tube. A lip is present at the fit-up joint to help decrease arc wander that would otherwise occur due to the triangular shape of endcap standoff. This change in standoff shape will allow for increased accuracy when centering the rodlet within the capsule tube. A weep hole has also been added as an option to eliminate the effects of gas buildup within the rodlet

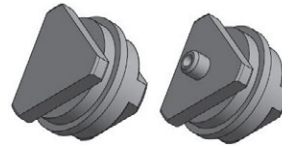

Figure 5. New ATF rodlet endcap designs (left) without weep-hole and (right) with weep-hole.

Fabrication and Assembly

Experimental fabrication included the manufacturing and inspection of components, along with their assembly into rodlet then final capsule assemblies. This process required the utilization of a variety of tools and techniques in order to meet the tight design criteria imposed upon the experiment.

Precision hardware components were fabricated at a machine shop at the Idaho National Laboratory (INL), and subsequently inspected for dimensional rigor. This fabrication utilized various machining equipment including high-precision lathes, a gun drill, an electrical discharge machine (EDM), and more. A coordinate measuring machine (CMM) was employed for component dimensional inspection.

Figure 6. Precision Lathe (top left); Coordinate Measuring Machine (right and bottom left).

Fuel pellets were either fabricated at Idaho National Laboratory (INL), or provided by an outside entity. The pellet composition varied among rodlet assemblies based upon the goal of the design team. All pellets were inspected to ensure they met the various design and dimensional criteria, then loaded into a cladding tube.

Welding of the rodlet and capsule assemblies was performed using an Arc Machines Inc. (AMI) orbital welder to make an autogenous orbital closure weld (Figure 8). This process occurred in an inert atmosphere glovebox in order to maintain a prescribed gas environment, often helium, within the rodlet assembly and the capsule assembly. The general rodlet/capsule assembly sequence is described in the flowchart in Figure 7.

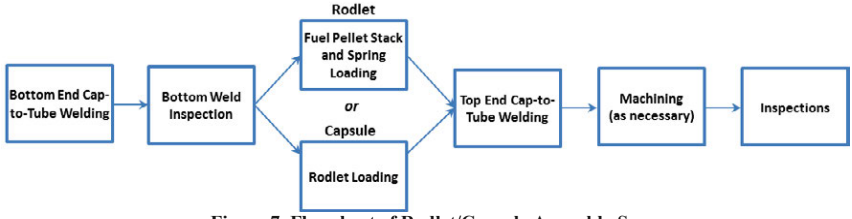

Figure 7. Flowchart of Rodlet/Capsule Assembly Sequence.

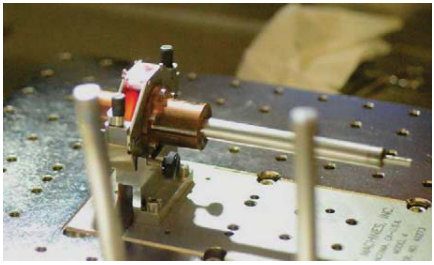

Figure 8. Welding of rodlet assembly.

The ATF-1 rodlets required machining of the endcaps, and often welds, to allow them to precisely fit within a capsule tube. This machining step also served to ensure the outer diameter of the endcap was true and concentric to the outer diameter of the rodlet tubing, thus ensuring uniform heating during irradiation testing. Various inspections were performed on the rodlet assembly prior to loading and welding into a capsule tube, including dimensional, visual, helium leak check, and radiography.

Qualification

The various ATF-1 rodlet and capsule assemblies required a multitude of qualification procedures for both programmatic and safety purposes. The tight requirements on the gas gap necessitated precision dimensional inspection of assembled rodlets. The dimensions of the endcap standoff, weld, tube diameter, overall length and straightness were measured using a CMM to ensure the rodlets would perform in a manner satisfactory to programmatic requirements.

As verification of a successful weld, a helium leak check was performed on all rodlets. In addition, radiographic inspections of the welds were performed to further verify weld integrity. Two radiographic techniques were employed when inspecting rodlets: computed radiography (CR) and digital radiography (DR). CR is a beneficial technique for overall rodlet shots to verify rodlet internals are properly seated, but lacks the resolution necessary to see the level of detail required for weld penetration determinations. The DR system utilized a microfocus X-ray tube that allowed magnification of the weld region; thus providing approximately 10x greater resolution in acquired radiographic images. Images acquired from both techniques are presented in Figure 9.

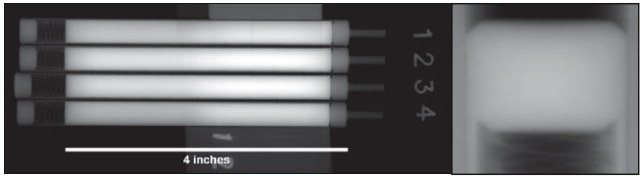

Figure 9. (Left) Computed radiography images of rodlets. (Right) Digital radiography of rodlet top endcap and weld region.

Capsule assemblies are considered a primary pressure boundary; thus more rigorous/stringent inspection requirements were applied to capsules. In addition to the dimensional, radiographic, and helium leak check that rodlets received, capsules receive liquid penetrant testing. This ensures that no pores are present anywhere along the assembly that could serve as a weak point and instigate capsule failure.

Future

Nineteen of the experimental assemblies associated with ATF-1A were successfully qualified and inserted into the ATR as of May 2015. Additional scoping type studies are to be performed in an ATF-1B series of irradiation tests, scheduled for reactor insertion in 2016.

ATF-2 is the next experiment in the series of tests leading up to LFA/LFR demonstration. ATF-2 is designed to be an instrumented fuel test that will be irradiated in a loop of the ATR. Whereas the ATF-1 style experimental assemblies are isolated from direct contact with the reactor coolant, the ATF-2 assemblies will be configured in a test loop; this allows the samples to experience prototypic conditions of a standard pressurized water reactor (PWR). The design of the ATF-2 experiment includes sensors and instrumentation that affords continuous, real time, monitoring of fuel temperature, plenum pressure, and fuel expansion.

DEVELOPMENT OF ENGINEERING PARAMETERS FOR LOW PRESSURE DIFFUSION BONDS OF 316 SS TUBE-TO-TUBE SHEET JOINTS FOR FHR HEAT EXCHANGERS

Nils Haneklaus, Rony Reuven, Cristian Cionea, Peter Hosemann, Per F. Peterson

Department of Nuclear Engineering, University of California, Berkeley;
4118 Etcheverry Hall, MC 1730, Berkeley, CA 94720-1730, USA

Keywords: Low pressure diffusion bonding, 316l stainless steel, tube-to-tube sheet joints

Abstract

Diffusion bonding is a solid-state welding technique to join metallic and non-metallic materials. Due to geometrical considerations, fabrication and possible materials choices diffusion bonding was chosen here for tube-to-tube sheet joints of large coil wound heat exchangers for Fluoride salt cooled High temperature Reactors (FHRs). In this work the processing parameters for these critical nuclear component manufactured out of 316l stainless steel are presented and the bonded areas are investigated using optical microscopy (OM) and scanning electron microscopy (SEM). In addition mechanical tests were conducted (pull out testing) to evaluate if these joints are sufficiently bound to guarantee a safe operation of the device. The detailed joining parameters are reported and recommendations for future fabrications with the physical restrictions of a large heat exchanger are made.

Introduction

The Department of Nuclear Engineering at the University of California, Berkeley (UCB) is developing a coil wound heat exchanger design that supports the use of gas Brayton power conversion for reactors. UCB developed an initial design to transfer heat from a low pressure fluoride salt coolant (at approximately 0.1 MPa) to compressed air (at approximately 1.8 MPa) used to feed a gas turbine system [1]. A key alternative heat exchanger design would use supercritical carbon dioxide (SCO_2) instead of air with sodium as the coolant and requires operation at even higher pressures of up to 20 MPa, with the coolant at a low pressure of approximately 0.1 MPa. In contrast to pressurized water reactor heat exchanger tubes that experience an internal pressure the tubes in the foreseen heat exchanger design experience external pressure.

Diffusion bonding supported tapered interference fits are investigated for the 316l stainless steel tubes foreseen for the mentioned SCO2 cycle heat exchanger design. Experiments for diffusion bonding supported tapered interference fits as well as tube expansion with subsequent diffusion bonding were successfully conducted at UCB for thin walled (0.889 mm) 316l stainless steel tubes [2]–[4]. This work describes sample preparation and subsequent quantitative pull-out testing as well as following quantitative testing using optical microscopy (OM) and using scanning electron microscopy (SEM).

Experimental procedure

The interference fit between the 316l heat exchanger manifold and the 316l pipes was simulated using 316l collars with tapered hole (length: 19.05 mm, OD: 19.05 mm, 1° taper angle) and 316l tubes (length: 76.2 mm, OD: 6.35 mm) with matching taper. The samples were fabricated from drawn and annealed super-corrosion resistant 316l stainless steel on a manual lathe using high speed steel cutting tools. The material composition of the 316l as provided by the vendor in wt% is given in table 1. A material analysis of the steel with the scanning electron microscope confirmed the provided specifications.

Table 1: Chemical composition range of 316l stainless steel as provided by the vendor

Mat.	Fe	Cr	Ni	C	Mn	Cu	Si	Mo	P	N	Ti
Wt%	58.23-73.61	16-18.5	10-15	0-.08	0-2	0-1	0-1	0-3	0-.045	0-0.1	Max. .7

After fabrication the samples were cleaned with alcohol in an ultrasonic bath and rinsed with acetone. Following fabrication and cleaning the samples were pressed with approximately 3 kN assembly force. The relatively low force was chosen to account for the long heat exchanger tubes of the final application that may not withstand higher loads.
The pressed samples were heat treated in a commercial tube furnace at 1000 °C for 16 hours in a high vacuum on the order of $4x10^{-3}$ Pa recommended for diffusion bonding [5] was obtained coupling a roughing- to a turbo pump. Figure 1 illustrates the heat treatment of the samples in the vacuum furnace.

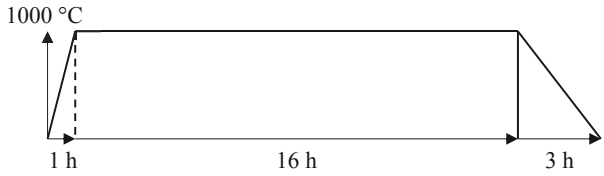

Figure 1: Heat treatment of the samples in the vacuum furnace

In contrast to traditional diffusion bonding (e.g. [5]) no additional pressure was applied during the heat treatment. Therefore the heat treatment was applied longer than usually recommended for 316l stainless steel (approx. 4 hours) [6]–[9] which was found to give better results.
The quality of the joint samples produced this way was quantitatively evaluated using mechanical tensile testing (pull-out test) and qualitatively tested using optical microscopy (OM) and scanning electron microscopy (SEM).

When pulled out, force was applied as illustrated in figure 2. A plug was inserted as shown in figure 2 (dashed) to prevent collapsing of the thin walled tube. A two-clamp design as used during pull-out tests in similar experiments (e.g. [10]) was avoided here as such a design may increase the measured pull-out force as a result of the clamp tightening the collar around the tube during testing.

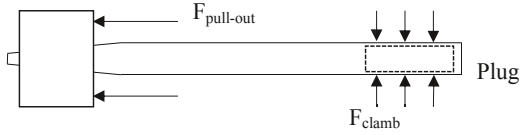

Figure 2: Illustration of the sample during pull-out testing

After pull-out testing successful samples were sectioned under constant cooling to minimize effects of the cutting on the bonding area.

Results and discussion

More than 80 samples have been fabricated at UCB using the procedure described above and slightly varied procedures during which the initial pressure was applied differently (mostly tube expansion and thermal fitting). After fabrication samples were qualitatively tested using pull-out testing. Since the joint area at which diffusion bonding can theoretically occur is much larger than the cross section area of the thin walled tube it is anticipated that in case of a sound diffusion bond tube rupture would occur. After this first quantitative test successful samples i.e. samples with joints that would withstand pull-out forces equal to the force needed to rupture the tube (approx. 9.3 kN) were sectioned for further quantitative analysis.
Quantitative analysis using OM and SEM was found to be necessary since varying bonding qualities were seen in single samples. Figure 3 shows different bonding qualities of a single sample that was tensile tested and subsequently sectioned. The sample underwent metallographic grinding, polishing, and etching and was analyzed using OM.

Figure 3: Varying joint qualities found in a single sample using optical microscopy

The depicted three areas provide a brief overview of the three different joint qualities that were found in samples prepared and analyzed this way. In case of poor quality joints (figure 1, left) the joint can be clearly identified as a gap between the two parts while no gap can be identified in a high quality bond (figure 1, right). In addition partly diffusion bonded areas (figue 1, center) could be identified.
It is believed that the varying joint qualities found in single samples result from imperfect manufacturing regarding the matching (sample geometry) and surface preparation on the manual lathe. Imperfect matching results in areas experiencing larger and fewer initial pressures during press fitting. The results of imperfect matching could be identified by relatively large bonding areas showing poor bonding quality and typically a significantly smaller area showing a high quality bonding area.
Imperfect micro geometry is a result of using pointy lathe tools (boring bar for the collar and turning tool for the tube) that leave relatively rough surfaces (20-40 µm) commonly not recommended for diffusion bonding [5], but used here to simulate a simple and therefore more economical fabrication process. Figure 4 (left) illustrates the surface irregularities typically obtained after turning of steel that make diffusion bonding, especially if no constant pressure is applied, as is the case here challenging [5]. Figure 4 (right) shows a picture of a tube surface taken prior to press fitting that shows the surface roughness due to turning.

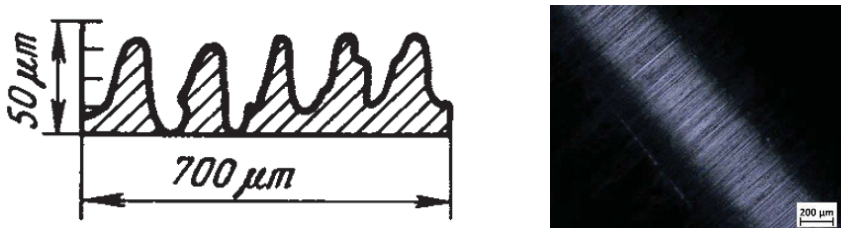

Figure 4: Surface roughness as illustrated by Kazakov [5] (left) and surface roughness found (right) as a result of using pointy lathe tools for fabrication

The transparent oxide layer that protects the 316l stainless steel against corrosion is less than $3x10^{-2}$ µm thick [5] and not shown in figure 4. The protective oxide layer that mitigates sound diffusion bonding joints is usually overcome using constant pressure and a low-oxygen environment (high vacuum or protective gas atmosphere). The idea of the procedure presented in this work is to break the brittle oxide layer and to overcome the surface irregularities illustrated in figure 4 by breaking/bending the asperities when pressing the tube into the sleeve so that the contact area between rod and collar at which diffusion bonding can occur increases.

Though manufacturing sound samples using a manual lathe is challenging figure 5 shows that grain growth occurs over the initial joint area (between the dashed lines) in regions where oxide layer and asperities could be overcome i.e. diffusion bonding takes place [5].

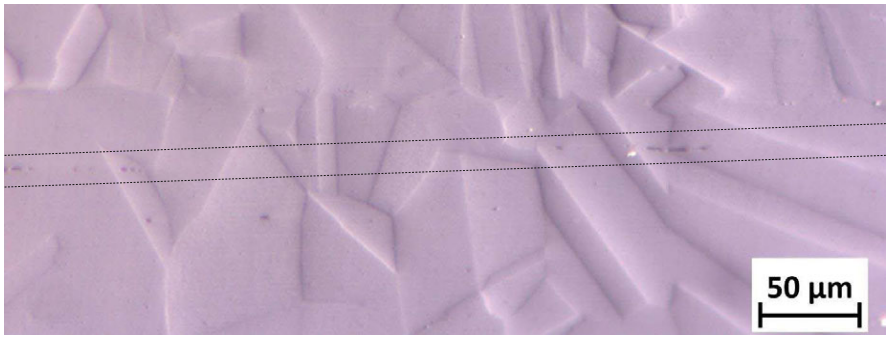

Figure 5: Scanning electron microscope picture showing grain growth over the joint area (between the dashed lines)

Conclusions

The work presented here suggests that diffusion bonding subsequent to press fitting of tapered interference fits of 316l stainless steel is possible. Challenges of the process are believed to result from imperfect matching between the parts and surface roughness. Both process may be overcome more elegantly using advanced manufacturing techniques such as grinding that results in better matching and less rough surfaces.

Acknowledgment

The authors want to express their gratitude to the operators of the mechanical engineering machine shop at UCB without whose guidance this work would have not been possible.
This research is performed using funding received from the U.S. Department of Energy Office of Nuclear Energy's Nuclear Energy University Programs. The views expressed have not been endorsed by the supporting agencies. Any remaining errors, omissions, or inconsistencies are the authors' alone.

References

1. UCBTH-14-002, *Technical Description of the 'Mark 1' Pebble-Bed Fluoride-Salt-Cooled High-Temperature Reactor (PB-FHR) Power Plant*, September 2014.

2. G. Buster, N. Pardede, and T. Phan, *Design, Manufacture, Modeling and Testing of 316 SS Diffusion Bonded Tube-sheet Joints and In-Service Inspection Methods for the Mk1 PB-FHR CTAHs*, 2014.

3. N. Haneklaus, R. Reuven, A. J. Gubser, G. Buster, C. Andreades, P. Hosemann, and P. F. Peterson, *Diffusion Bonding of 316 SS Tube-to-Tube Sheet Joints for Coiled Tube Gas Heaters*, in American Nuclear Society 2015 Student Conference – Texas A&M University College Station, Texas, USA.

4. N. Haneklaus, R. Reuven, C. Cionera, P. Hosemann, and P. F. Peterson, *Diffusion Bonding of 316 SS Tube-to-Tube Sheet Joints using a commercial Tube Expander*, in 2015 ANS Winter Meeting and Nuclear Expo, Washington D.C., USA.

5. N. Kazakov, *Diffusion bonding of materials*, Oxford ;New York: Pergamon, 1994.

6. K. Bhanumurthy et al., *Diffusion Bonding of Nuclear Materials*, no. 331, pp. 19–25, 2013.

7. S.-X. Li et al., *Interfacial Failure Mechanism of 316L SS Diffusion Bonded Joints*, Icf12, pp. 1–10, 2009.

8. M. S. Yeh and T. H. Chuang, *Low-pressure diffusion bonding of SAE 316 stainless steel by inserting a superplastic interlayer*, Scr. Metall. Mater., vol. 33, no. 8, pp. 1277–1281, 1995.

9. A. F. La Pan and R. L. Neumeister, *Tube-to-sheet joint making*, US 3349465 A, October 1967.

10. A. Dethlefs et al., *Hybrid friction diffusion bonding of aluminium tube-to-tube-sheet connections in coil-wound heat exchangers*, Mater. Des., vol. 60, pp. 7–12, 2014.

TMS2016

145th Annual Meeting & Exhibition

SUPPLEMENTAL PROCEEDINGS

Mechanical Behavior at the Nanoscale III

THE MICROSTRUCTURE AND MECHANICAL PROPERTIES OF NANOMETER Al_2O_3/Cu COMPOSITE FABRICATED BY INTERNAL OXIDATION

Lei Guo[1], Shuqiang Guo[1], Shuai Ma[1], Jie Liu[1], Weizhong Ding[1]

[1]Shanghai Key Laboratory of Modern Metallurgy & Materials Processing, Shanghai University, Shanghai 200072, China

Keywords：Al_2O_3/Cu composite, internal oxidation, microstructure, property

Abstract

The fabrication of the copper matrix composites strengthened with dispersal nanometer Al_2O_3 is investigated. The investigation result shows that the atomized Cu-Al alloys powders mixed with Cu_2O oxidant powders were internally oxidized at 1173K for an hour in nitrogen atmosphere. X-ray and EDS analysis indicates that the particles formed during internal oxidation consist of a large amount of $CuAlO_2$ and a certain amount of α-Al_2O_3. After hydrogen reduction at 1173K for an hour, the particles turn to be α-Al_2O_3. TEM observation shows that the obtained α-Al_2O_3 particles are uniformly distributed in copper grain, and the mean size of these particles is about 10 nm. As compared with the composite by a previous sintering, the main properties of the composite with 50% cold deformation are better.

Introduction

The rapid development of high technology, such as aerospace, aviation and electronics, requires continuing improvements in the performance of materials [1-3]. A variety of existing and potential applications require that these materials should have excellent room- and high-temperature strength as well as the properties that copper conventionally has, such as high electrical and thermal conductivity, high heat-resistibility and excellent corrosion resistance and formability[4,5]. For instance, according to the specifications of micro-electronic development, the material used as leading-in wire frames in large scale integrated circuits must have a tensile strength of more than 600MPa, an electric conductivity of more than 80%IACS (IACS, International Anneal copper standard),and a softening temperature of more than 800 K[6]. For these applications, oxide dispersion strengthened (ODS) coppers have been developed. In ODS coppers, high-temperature strength is dramatically improved by homogeneously distributing thermally stable fine dispersoids inside a near-pure copper matrix, so as to avoid coarsening of precipitates at high temperatures, while the electrical conductivity is maintained at the same level as that of pure copper.

Therefore, the internal oxidation is now the most successful and the reproducible technique to fabricate ODS copper matrix composition. However, the method has many shortcomings which have need to be overcome, such as the operated process is so complicated that the quality of the products is not easy to control.

In this paper, the effects of internal oxidation on the microstructure and properties of Al_2O_3/Cu composite were investigated, which would be helpful to provide a basis and reference for the industrial application.

Experimental

Cu–Al alloy powders with the composition of 0.43 wt. % aluminum were prepared by water atomization (-300 mesh). And Cu_2O is used as an oxidant (-325 mesh), supplying oxygen to copper alloy powders. Before internal oxidation, Cu_2O should be uniformly mixed with Cu-Al alloy powder. The oxidant Cu_2O should be used up during the process of internal oxidation, That is to say all oxygen in Cu_2O reacts to Al in Cu-Al alloy to form Al_2O_3. The additive amount of oxidant Cu_2O has relationship with the amount of aluminum in Cu-Al alloy. According to stoichiometrical calculation amount, the proportion of Cu_2O and Cu-0.43 wt.% Al alloy powders should be 1 : 29. Subsequent procedure is as follows:

Internal oxidation→ hydrogen reduction→ cold isostatic pressing→ sintering process→ plastic deformation→ finished products.

Phase identification and composition analysis were carried out by X-ray diffraction (XRD) and energy dispersive spectrometer (EDS). Scanning electron microscopy (SEM) images were obtained on a Hitachi SU-1510 electron microscope. TEM micrographs were obtained with a JEOL JEM-2010F field emission microscope operating at 200 kV. Electrical conductivity was measured with an eddy current electrical conductivity. Density was measured based on the Archimedes Principle. Tensile tests were conducted at a strain rate of 10^{-4} s^{-1} on tensile test machine at ambient temperature. The hardness tests were carried out with a Rockwell hardness tester.

Results and discussion

The internal oxidation treatment was carried out at 1173 K for an hour in high purity nitrogen atmosphere. XRD analysis gives the variation of lattice constant of the copper matrix as the evidence for the free solution of aluminum, as shown in Fig. 1. All the diffraction peaks are from copper matrix. Calculation results show that before and after internal oxidation, the lattice constant is 0.3621nm and 0.36155nm， respectively. The latter value is approximately equal to the lattice constant of pure copper (0.3615nm). Owing to a quite small volume of dispersoid , no other peaks were found in curve (2) in Fig.1.

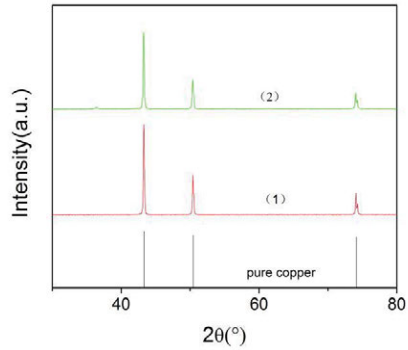

Fig.1 X-ray diffraction patterns of Cu-Al alloy (1) and powders after internal oxidation (2)

In order to analyze dispersoids present after internal oxidation, copper was melted away by putting the powders into thick nitric acid (50wt.%), and the remaining dispersoids were collected, stoved and dried. Fig. 2 is XRD patterns of the remaining dispersoids. The diffraction peaks are assigned to two kinds of particle, namely, a large amount of $CuAlO_2$ and a certain amount of α-Al_2O_3. Fig. 3 (a) through (d) gives the SEM images and corresponding elemental analysis maps of the remaining dispersoids, from the image, Cu is obvious exist, it can also prove the conclusion we got from the XRD image.

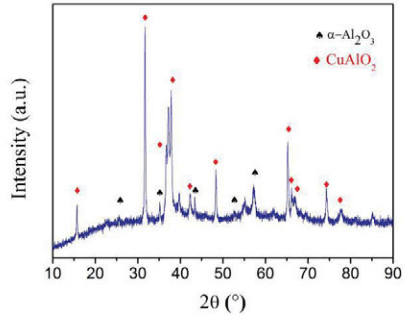

Fig. 2 XRD patterns of the remaining dispersoids

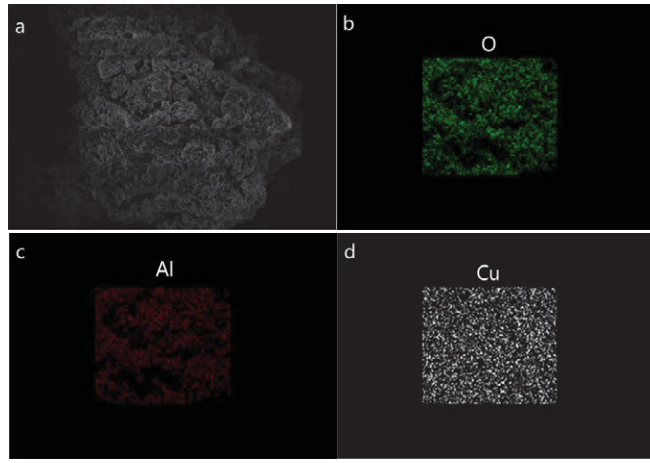

Fig. 3 SEM images and corresponding elemental analysis maps of the remaining dispersoids

Fig.4 is XRD patterns of the dispersiods present inside Cu-0.43 wt.%Al powders that were reduction treated in a hydrogen atmosphere at 1173 K for 1 hour after being internally oxidized. The $CuAlO_2$ peaks observed in Fig.2 disappear, leaving α-Al_2O_3 peaks only.It is, thus, learned that the 1-hour reduction treatment in a hydrogen atmosphere at 1173 K effectively changes the complex oxides formed during internal oxidation into Al_2O_3. Fig.5 is TEM images of Cu-0.43 wt.%Al powders after hydrogen reduction. The sample was prepared by placing a drop of the methanol solution of a well-ground catalyst powder on a carbon-coated copper grid (300 mesh), followed by evaporation of the methanol. From the image, fine dispersoids of about 10 nm in diameter are homogeneously distributed.

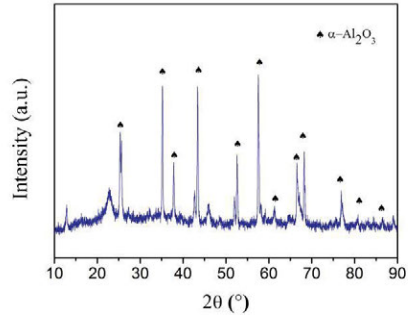

Fig.4 XRD patterns of the dispersiods collected from Cu-0.43 wt.% Al powders that were reduction treated in a hydrogen atmosphere

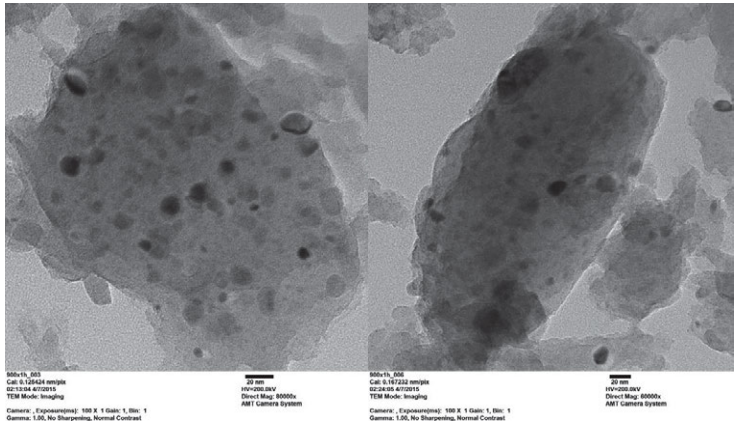

Fig.5 TEM images of Cu-0.43 wt.% Al powders after hydrogen reduction

Cold isostatic pressing was carried out at a pressure of 75 MPa for 1 min. And the sintering process was done at 1173 K for 1 hour in high purity nitrogen atmosphere. The composite is plastic deformed whose deformation quantity is 50% . The room temperature properties of the nanometer Al_2O_3/Cu composite under different treatment conditions are shown in Table 1. From table 1, it can be seen that the density, hardness and electrical conductivity of deformed composite are better compared with sintered composite. And the tensile strength increases from 382 to 593 MPa.

Table 1 Room-temperature properties of Al_2O_3/Cu composite under different treatment conditions

Process	Hardness (HRB)	Tensile strength (MPa)	Density (g/cm^3)	Conductivity (MS/m)
By Sintering	72	382	8.684	48
By plastic deformation	84	593	8.739	49

Conclusion

In the present study, ODS copper were fabricated by internal oxidation, and their microstructure, mechanical properties and electrical conductivity were investigated. The following conclusions can be obtained:

1. The particles formed during internal oxidation consist of a large amount of $CuAlO_2$ and a certain amount of α-Al_2O_3. However, $CuAlO_2$ was all reduced to Al_2O_3 after a hydrogen reduction treatment, And the mean size of α-Al_2O_3 is about 10 nm.

2. The hardness and electrical conductivity of Al_2O_3/Cu composite by plastic

deformation can respectively achieve 84 HRB and 84 IACS%. As compared with the composite by a previous sintering, the tensile strength increases from 382 to 593MPa.

3. The reason why the electrical conductivity decreases such a certain extend needs to be further studied.

References

1. Lee D W, Kim B K. Nanostructured Cu-Al_2O_3 composite produced by thermochemical process for electrode application [J]. Materials Letters, 2004, 58(3): 378-383.
2. Besterci M, Velgosová O, Lesko A, et al. Microstructural parameters of Cu-Al_2O_3 dispersion strengthened materials [C]//Materials science forum. Trans Tech Publications Ltd., Zurich-Uetikon, Switzerland, 2003, 416(418): 1.
3. Mendenhall J H. Understanding Copper Alloys: The Manufacture and Use of Copper Alloy Sheet and Strip [J]. John Wiley and Sons, xii+ 325, 23 x 16 cm, illustrated(<-> 15. 70), 1980, 1980.
4. Groza J. Heat-resistant dispersion-strengthened copper alloys [J]. Journal of Materials Engineering and performance, 1992, 1(1): 113-121.
5. Nadkarni A V. Dispersion strengthened copper: properties and applications [J]. High Conductivity Copper and Aluminum Alloys, 1984: 77-101.
6. Min G H, Song L, Yu H S, et al. High strength and electric conductivity copper-based composites [J]. Gongneng Cailiao (in Chinese), 1997, 28(4): 342.

TMS2016

145th Annual Meeting & Exhibition

SUPPLEMENTAL
PROCEEDINGS

Nanostructured Materials for
Nuclear Applications

THE ROLES OF OXIDE INTERFACES AND GRAIN BOUNDARIES IN HELIUM MANAGEMENT IN NANO-STRUCTURE FERRITIC ALLOYS: A FIRST PRINCIPLES STUDY

Y. Jiang[1,2], L.-T. Yang[2], J. Xu[2], G. R. Odette[3], Y. Wu[3], T. Yamamoto[3], Z.-J. Zhou[4], Z. Lu[5]

[1] National Key Lab for Powder Metallurgy, Central South University, Changsha, 410083, China
[2] Materials School, Central South University, Changsha, 410083, China
[3] Materials Department, University of California, Santa Barbara, 93106, USA
[4] Materials School, University of Science and Technology, Beijing, 100083, China
[5] School of Materials and Metallurgy, Northeastern University, Shenyang, 110819, China

Keywords: nano-structured ferritic alloy, helium, nano-oxide, interface, grain boundary

Abstract

We report a theoretical study for assessing the possible roles of oxide interfaces in managing helium in nano-structured ferritic alloys (NFAs). Various candidate structures of the ferrite/$Y_2Ti_2O_7$ interfaces are constructed and the associated energies are carefully evaluated. The calculated interface phase diagram predicts the interfaces to be Y/Ti-rich, for the wide temperature range of interest. Vacancies and helium both segregate to the interfaces, in preference to grain boundaries. Combined with our previous results on bulk-phase $Y_2Ti_2O_7$, the profound implication of helium management in NFAs is discussed.

Introduction

Helium is generated in large quantities in fusion reactor environments and must be properly managed, primarily by trapping at sites where it causes little or no damage. Nano-structured ferritic alloys (NFAs) are characterized by a very fine grain size and an ultra-high density of Y-Ti-O enriched nano-precipitates, in accompany with a high density of precipitate interfaces, grain boundaries, and dislocations [1,2]. These microstructural features help trap helium in much finer gas bubbles, thereby mitigating void swelling, toughness degradation at lower irradiation temperatures, and creep failure at higher temperatures [3,4]. Thus NFAs are very promising candidates for uses in fusion reactor applications [3-6,7-10].

Various studies have suggested that the nano-precipitates range from coherent solute-enriched clusters to near-stoichiometric complex oxides, that are primarily the pyrochlore $Y_2Ti_2O_7$ and to a lesser extent orthorhombic Y_2TiO_5 [11,12-20]. In our previous work [21,22], we have shown from first principles that helium in NFAs can partition and be *deeply* trapped in both $Y_2Ti_2O_7$ and Y_2TiO_5. The Boltzmann partitioning factors at 773K were estimated to be in the order of ~10^{10} and 10^8 for bulk Y_2TiO_5 and $Y_2Ti_2O_7$, respectively. Thus even small volume fractions of nano-oxides can effectively sequester hundreds to thousands appm of helium, depending on their number density. Specifically, dispersing helium atoms into a large number of small oxides limits the helium bubble size in matrix and the corresponding damage potential. In the present work, we assess the possible roles of oxide interfaces and grain boundaries in trapping helium in NFAs. As the primary precipitate phase, the pyrochlore $Y_2Ti_2O_7$ has various orientation relationships (ORs) with the ferrite matrix. We focus on the more prevalent *cube-on-cube* OR of $\{100\}\langle 100\rangle_{ferrite}//\{100\}\langle 100\rangle_{Y2Ti2O7}$ [23, 24]. We first calculated all possible interface configurations and the associated energies as a function of temperature (T) and oxygen partial pressure (p_{O2}). The interface phase diagram was then constructed to determine the most energy-favorable interface structure. Further calculations were performed to compare various interfacial trapping sites for helium. The results were then carefully compared with those for grain boundaries and for bulk $Y_2Ti_2O_7$.

Calculation methods

All calculations were performed using the density functional theory code - VASP [25]. The electron-core interaction was described by the Blöchl projector augmented wave method (PAW) [26]. The plane-

wave basis sets were generated with valence configurations of He-1s2, Fe-$3d^6 4s^2$, Y-$4s^2 4p^6 4d^1 5s^2$, Ti-$3s^2 3p^6 3d^2 4s^2$, and O-$2s^2 2p^4$. The exchange-correlation functionals of PAW-PW91 were finally chosen for they yielded the best prediction of bcc Fe (a=2.8303Å, bulk modulus B=174GPa) and pyrochlore $Y_2Ti_2O_7$ (a=10.1835Å, B=183GPa). To model the interfaces, we used a ferrite/oxide/ferrite sandwich supercell with a vacuum thickness of >12 Å and a 2×2×1 Monkhorst-Pack k-mesh. All ground-state configurations were optimized using a high energy-cutoff of 500 eV and the force convergence criteria of 0.02 eV/Å.

Results and discussion

It is not practical to have an arbitrarily large unit cell with misfit dislocations included naturally, so we chose to strain the Fe(100) and the $Y_2Ti_2O_7$(100) into commensuration in a manner consistent with the Ribis' OR. The resulting interface structure is shown in Fig. 1, indicating a perfect matching between $5d\{110\}_{Fe}$ and $5d\{440\}_{Y2Ti2O7}$. The associated commensuration strain is slightly larger than, yet as close as possible to, that deduced from Ribis' observations (where every $8d\{110\}_{Fe}$ matches $9d\{440\}_{Y2Ti2O7}$ perfectly [24]). In the sandwich model of Fe/$Y_2Ti_2O_7$/Fe, each Fe block contains five atomic layers with a total of forty Fe atoms and the oxide block consists of a conventional unit cell of $Y_2Ti_2O_7$. Given the OR, the stability of an interface is dictated by interfacial stoichiometry and coordination [27,28]. Thus similarly as for $Y_2Ti_2O_7$ surfaces [29], we considered at least three typical stoichiometry types of the interface, namely the stoichiometric ("*stoi*"), the non-stoichiometric Y/Ti-rich ("*ns-2Y2Ti*") and O-rich type ("*ns-5O*"). For each stoichiometry type, we further considered two different coordination types (shown in Fig. 1), by translating the metal relative to $Y_2Ti_2O_7$, i.e. placing the Fe atoms right above the Y and Ti atoms ("*top-coordinated*"), or at the bridge sites of the Y and Ti atoms ("*bridge-coordinated*"). The latter configuration may also be seen as the O-top coordination. Calculations of the resulting interface ensembles suggested that the bridge-coordinated interfaces, either non-stoichiometric or stoichiometric, always have the lowest formation energies. Thus the following calculations are restricted to the bridge-coordinated interfaces which, again, can be either Y/Ti-rich, stoichiometric, or O-rich.

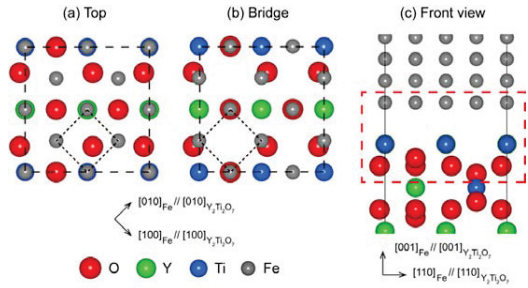

Fig. 1 Top views of the Fe(100)($2\sqrt{2}\times 2\sqrt{2}$)/$Y_2Ti_2O_7$(100)($\sqrt{2}/2\times\sqrt{2}/2$) interfaces with two coordination types: (a) Y/Ti-top and (b) Y/Ti-bridge, and (c) the side view of the two coordination types.

NFAs are typically processed by high-energy ball milling Fe-based pre-alloyed powders (Fe, Ti, Cr) with Y_2O_3 powders. To determine the appropriate interface structure under a given thermodynamic equilibrium condition, we evaluate the interface energy, γ_I, as

$$\gamma_I = \frac{1}{2A}(G_0 - N_{Fe}\mu_{Fe} - N_{Y_2O_3}\mu_{Y_2O_3} - N_{Ti}\mu_{Ti} - N_{O_2}\mu_{O_2}) \quad (1)$$

$$= \frac{1}{2A}[G_0 - N_{Fe}\mu^0_{Fe} - \frac{1}{2}N_{Ti}\mu^0_{Y_2Ti_2O_7} + (\frac{1}{2}N_{Ti} - N_{Y_2O_3})\mu^0_{Y_2O_3} + \frac{1}{2}(2N_{Ti} + 3N_{Y_2O_3} - N_O)(\mu^0_{O_2} + kT\ln p_{O_2})]$$

Here G_0 is the Gibbs free energy of the interface ensemble. N_i and μ_i are, respectively, the number and chemical potential of each species. The superscript "0" refers to the standard state, and A is the interface area. Assuming a fixed ratio of Y:Ti=1 holding in all these interface ensembles, we can rewrite Eq. (1) as

$$\gamma_I = \frac{1}{2A}[G_0 - N_{Fe}\mu^0_{Fe} - \frac{1}{2}N_{Ti}\mu^0_{Y_2Ti_2O_7} + \frac{1}{2}(2N_{Ti} + 3N_{Y_2O_3} - N_O)(\mu^0_{O_2} + kT\ln p_{O_2})] \quad (2)$$

Note, the non-stoichiometric interface energy is not a constant value but varies with the ambient T and p_{O2}. Fig. 2 shows the isothermal section of the interface phase diagram predicted by plotting the calculated γ_I against p_{O2} at T=1100 K. Clearly, the Y/Ti-rich (*ns-2Y2Ti*) interface dominates for $p_{O2}<\sim e^{-36}$ while the O-rich (*ns-5O*) dominates for $p_{O2}>\sim e^{-34}$. As increasing p_{O2}, the most energy-favorable interface structure changes from the Y/Ti-rich to stoichiometric and then to the O-rich, following the same trend as seen for the $Y_2Ti_2O_7$ free surfaces [29]. The critical p_{O2} values for nonstoichiometric-to-stoichiometric transitions are marked as points *a* and *b*. Experimentally determining the matrix p_{O2} is still too difficult. Fe itself does not internally oxidize in NFAs, thus the matrix p_{O2} is limited by equilibrium with Fe-oxides. According to the reaction $Fe + (1/2)O_2 \rightarrow FeO$, the critical p_{O2} for FeO is $\ln p_{O_2} = 2\Delta G^0_{FeO}(T)/RT$, where ΔG^0 is the Gibbs standard formation energy of FeO and R is the ideal gas constant, 8.314 J/(mol·K). Similarly, $\ln p_{O_2} = (2/3)\Delta G^0_{Fe_2O_3}(T)/RT$ and $\ln p_{O_2} = (1/2)\Delta G^0_{Fe_3O_4}(T)/RT$ for Fe_2O_3 and Fe_3O_4, respectively. Using ΔG^0_{FeO} = -200.67, ΔG^0_{Fe2O3} = -537.171, and ΔG^0_{Fe3O4} = -762.463 kJ/mol at T=1100 K [30], we calculated the threshold p_{O2} for the oxidation of FeO, Fe_2O_3, or Fe_3O_4 as $\sim e^{-44}$, e^{-42}, or e^{-39}, respectively. Therefore, the matrix p_{O2} must be below $\sim e^{-44}$ at T=1100 K. By mapping this upper limit of p_{O2} onto Fig. 2 (highlighted as the blue region), we determine the *cube-on-cube* ferrite/$Y_2Ti_2O_7$ interface to be Y/Ti-rich at T=1100 K. Performing the similar calculation for a wide temperature range from 400 to 1400K, yielded the same prediction that the interface is Y/Ti-rich, typically with a *ns-2Y2Ti* termination. This interface corresponds to a chemical composition of $\sim Y_{2.5}Ti_{2.5}O_7$ that is favorably comparable to the EELS result of nano-oxide precipitates in NFAs as $Y_{2.2}Ti_{2.3}O_7$ [13].

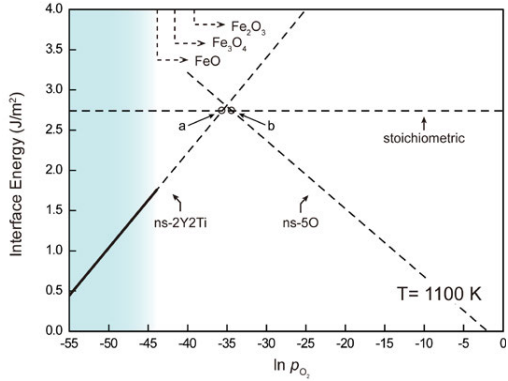

Fig. 2 The calculated isothermal section of the Fe(100)/$Y_2Ti_2O_7$(100) interface phase diagram at T = 1100 K, suggesting the interface is Y/Ti-rich, typically with a non-stoichiometric 2Y2Ti (*ns-2Y2Ti*) termination.

The major significance of bulk oxides to helium trapping and tolerance in NFAs has been shown in our previous studies ($Y_2Ti_2O_7$ [21] and Y_2TiO_5 [22]). In this work, we have suggested that the $Y_2Ti_2O_7$ interfaces with the *cube-on-cube* OR are thermodynamically Y/Ti-rich. In this section, we assess the capability of such interfaces to trap helium. Both perfect and the defective (vacancy and helium-containing) interfaces were carefully examined. For each interface, various interfacial interstitial sites for helium were considered. Full structural relaxation calculations showed that five configurations are potentially stable for helium trapping (Fig. 3), including two open interstitial sites (He^i_A and He^i_B), one Ti-tetrahedron site on the interface (He^i_T), and two octahedral interstitial sites in sub-layers (He^s_A and He^s_B). For the vacancy-containing interface, energetic calculations were performed for various possible vacancy

types, created by removing one Fe, Y, Ti, or O atom from the interface. The results suggested that the iron vacancy requires the least energy expense that is much lower than any other types of vacancies. Thus we need only consider the iron vacancy and label it as V^i in Fig. 4(a).

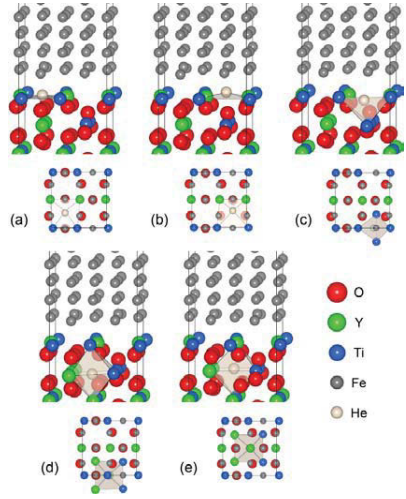

Fig. 3 Possible interstitial sites for helium on the Y/Ti-rich interface: (a) He^i_A, (b) He^i_B, (c) He^i_T, (d) He^s_A, and (e) He^s_B. Corresponding top views of interfacial layers are shown at the bottom.

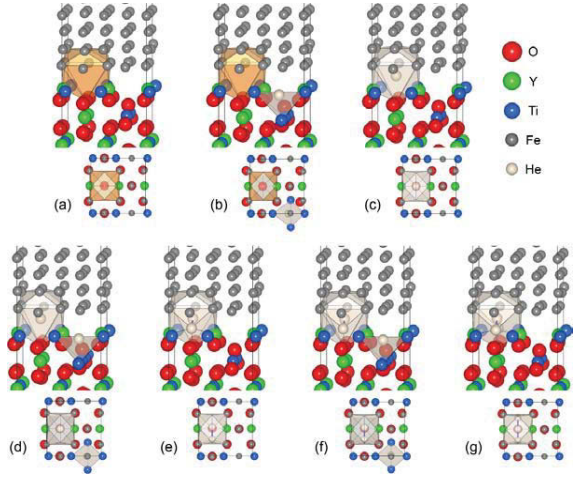

Fig. 4 Possible configurations of helium-vacancy clusters on the Y/Ti-rich interface: (a)V^i, (b) He^i_T+V^i, (c) He^i_V, (d) He^i_V+He^i_T, (e) $(2He)^i_V$, (f) $(2He)^i_V$+He^i_T, and (g) $(3He)^i_V$. Corresponding top views of interfacial layers are shown at the bottom.

Up to three helium atoms were then introduced to the interstitial and vacancy sites, which yields a total of seven interfacial helium-vacancy clusters in Fig. 4, including zero to three helium atoms sharing one interfacial vacancy [labeled as V^i, He^i_V, $(2He)^i_V$, and $(3He)^i_V$, respectively] and zero to two helium atoms occupying the interfacial vacancy accompanied by an interfacial helium (He^i_T) [labeled as $He^i_T+V^i$, $He^i_V+He^i_T$, and $(2He)^i_V+He^i_T$, respectively]. The relative stabilities of these helium-trapped interface structures were evaluated by the corresponding formation energy, E_f, as

$$E_f = E_d - E_0 - m \cdot \mu_{He} + n \cdot \mu_{Fe}, \quad (3)$$

where E_d is the total energy of a defective interface, E_0 is the total energy of the clean, defect-free interface, μ_{He} is the chemical potential of helium as an isolated atom, and μ_{Fe} is the chemical potential of iron in its pure state. m is the number of helium atoms, and n is the number of iron vacancies if applicable.

Table 1 Calculated formation energies of various helium-trapped interface structures (Units: eV)

	He^i_A	He^i_B	He^i_T	He^S_A	He^S_B	V^i	$He^i_T+V^i$	He^i_V	$He^i_V+He^i_T$	$(2He)^i_V$	$(2He)^i_V+He^i_T$	$(3He)^i_V$
E_f	1.32	1.20	0.95	1.43	1.29	0.62	1.42	1.36	2.61	2.83	3.73	4.22

Table 1 summarizes the calculated formation energies of these interface structures based on Eq. 3. By referring to our previous results for bulk $Y_2Ti_2O_7$ [21], it is clear that the helium energy is effectively the same at interstitial sites both on the interface and inside the oxide interior. That is, the lowest formation energy of interstitial helium on the interface (He^i_T=0.95 eV) is nearly identical to that in bulk $Y_2Ti_2O_7$ (He^I_{octa}=0.94 eV). Both are significantly lower than that of substitutional helium occupying a vacancy in the iron matrix (He_V=2.28 eV). The formation energy of an interface vacancy (V^i =0.62 eV) is also much lower than that in iron matrix (V_{Fe}=2.14 eV). We also note that the formation energies of interstitial He^S_A and He^S_B (1.43 and 1.29 eV) at sub-interface layers are higher than that in bulk $Y_2Ti_2O_7$ (He^I_{octa}=0.94 eV). This difference, to some extent, is related to interfacial coherent strains.

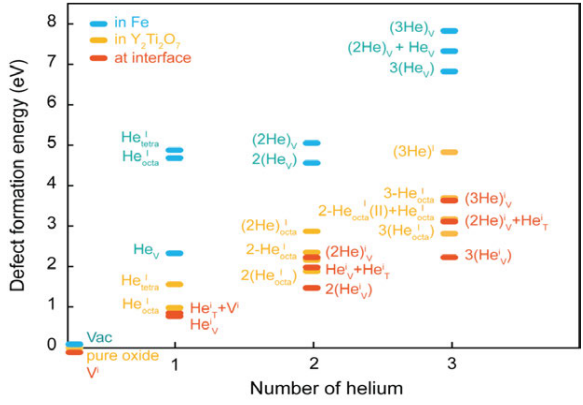

Fig. 5 Formation energies of helium-vacancy clusters on the interface compared to those in iron and in the oxide bulk as reported in Ref. [21].

Note that the formation energies for interfacial helium-vacancy clusters, i.e. $He^i_T+V^i$, He^i_V, $He^i_V+He^i_T$, $(2He)^i_V$, $(2He)^i_V+He^i_T$ and $(3He)^i_V$ in Table 1, implicitly include the vacancy formation energy (according to Eq. 3). Also note that concentrations of interface and bulk vacancies in excess of their equilibrium values are generated by severe deformation during ball milling, as well as under irradiation.

We thus simply regard the vacancies as fully available. In this sense, we are able to compare all of the above formation energies with reference to the interface vacancy energy (V^i) in Fig. 5. It is shown in Fig. 5 that the proper thermodynamic He^i_V is now 0.74 eV, slightly lower than $He^i_T+V^i$ (0.80 eV) on the interface and He^I_{octa} (0.94 eV [21]) in the oxide interior. All these values are significantly lower than that of helium at matrix vacancies (He_V=2.28 eV [21]). Thus helium will partition from the matrix not only to the bulk oxides but also to their interfaces. It is also suggested in Fig. 5 that as the helium concentration increases, it tends to consume single individual interface vacancies and interstitials to the extent possible before forming multiple helium-vacancy clusters on the interface [such as $(2He)^i_V$, $(2He)^i_V+He^i_T$, and $(3He)^i_V$], and/or in the oxide interior [$2(He^I_{octa})$, 2-He^I_{octa}, $(2He)^I_{octa}$, $3(He^I_{octa})$, 3-He^I_{octa}, and $(3He)^I_{octa}$]. Fig. 5 and detailed balance considerations suggest that helium is preferentially associated with the nano-oxide $Y_2Ti_2O_7$, both at its interface and in the interior. This is qualitatively consistent with the experimentally observed distribution of helium bubbles in NFAs. A likely scenario is that helium is initially deeply trapped in the oxide, but forms interface bubbles that are sufficiently large (>~0.5-0.6 nm) such that the corresponding chemical potential in the fluid-gas phase is lower than in the oxide [21,31].

Table 2 Calculated formation energies of GB vacancies (V^{GB}) and helium defects (He_V^{GB}) (Units: eV)

	Σ3 {112}<110> (70.53°)	Σ3 {111}<110> (109.47°)	Σ5 {310}<100> (36.87°)	Σ5 {210}<100> (53.13°)	Σ9 {114}<110> (38.94°)	Σ11 {332}<110> (50.48°)
V^{GB}	1.82	0.42	0.90	0.89	1.13	1.42
He_V^{GB}	2.47	2.66	2.10	2.55	2.24	2.38

To further clarify the helium management and fate in NFAs, we calculated the formation energies of single vacancy and helium defect (V^{GB} and He_V^{GB}) on a group of low-Σ symmetric-tilt-grain-boundaries (STGBs) of bcc-Fe, including Σ3{112}<110>, Σ3{111}<110>, Σ5{310} <100>, Σ5{210}<100>, Σ9{114}<110>, and Σ11{332}<110>. The results are summarized in Table 2. Here the He_V^{GB} value measures the energy cost for trapping helium at a GB vacancy. It is evident in Table 2 that the GB vacancy formation depends strongly and sensitively on the GB structure. The V^{GB} value ranges from 0.42 on the Σ3{111}<110> up to 1.82 eV on the Σ3{112}<110>, but He_V^{GB} changes only slightly over the six GBs. Note that all V^{GB} values are much lower than that of vacancy in bulk iron (2.14 eV [21]). The initial enrichment of vacancy at GBs shall thus be expectable. The He_V^{GB} values of 2.10~2.66 eV are still comparable to helium occupying a vacancy in bulk iron (He_V=2.28 eV [21]), suggesting no strong preference for helium being initially trapped at GBs until most of the matrix vacancies are used up.

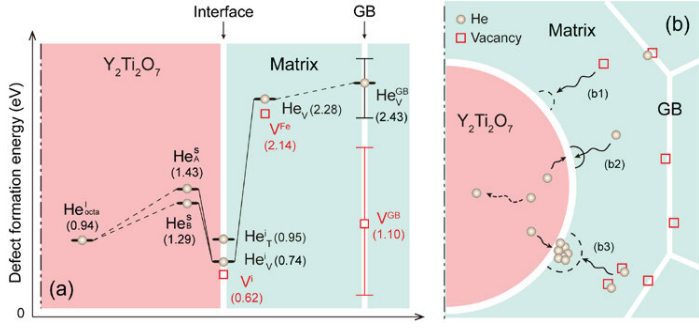

Fig. 6 (a) Energies of forming vacancies and trapping helium at different locations in NFAs. Locations include the ferrite matrix, oxide precipitates, oxide interfaces, and grain boundaries. (b) The schematic

formation of interfacial helium bubbles in NFAs. The bars refer to the range of our DFT results and those reported in the literature for GBs [32-35].

Eventually, we are able to illustrate the energetics of helium partitioning and the sequence of events leading to interface bubble nucleation in Figs. 6(a) and (b), respectively. The bars for the grain boundary (GB) energies represent the range of V^{GB} and He_V^{GB} values that we calculated by DFT and those reported in the literature [32-35]. These results strongly suggest that nano-oxides prevent large quantities of vacancies (process b1) and helium (process b2) from reaching GBs. Thus the bubble sizes both in the matrix and on GBs remain far smaller than the critical radius for conversion to growing voids (under irradiation) or creep cavities (under stress). Interface bubble formation involves two sources of excess energy: the free surfaces created by the bubble, and the work of pressurizing helium from its reference state to the condition in the bubbles, as discussed in previous studies [3,31,36,37]. In the simple capillary approximation framework, both terms are estimated as $\sim 2\gamma_e/r_b$, where γ_e is an effective surface energy and r_b is the radius of the bubble. The bubbles equilibrate to accommodate the trapped helium by absorbing vacancies (process b3). That is, the oxide interfaces actually act as heterogeneous sites for helium bubble nucleation. Obviously, ultrahigh densities of nano-oxides disperse helium into even smaller sizes up to very high temperatures, whereas fewer numbers of larger oxides could actually promote swelling by quickly forming interface bubbles that are large enough to convert to growing voids [3,38].

Conclusions

Based on density functional theory calculations, we have reached the following conclusions.

(i) In the thermodynamic equilibrium framework, the calculated interface phase diagram predicts that the *cube-on-cube* ferrite/$Y_2Ti_2O_7$ interfaces are Y/Ti-rich. This partially rationalizes the possible non-stoichiometric nature of $Y_2Ti_2O_7$ precipitates often observed in some cases.

(ii) Vacancy formation energies are lower at the ferrite/$Y_2Ti_2O_7$ interface than at ferrite GBs, and the interfacial helium formation energies are close to that for helium trapping inside the bulk oxides. Thus helium can be first sequestered by the nano-oxides before it enters an even lower fluid-gas energy state in sufficiently large interface bubbles.

(iii) The large number of nano-bubbles trap most of the helium and act as sinks or recombination sites for displacement damage defects. This imbues NFAs with a remarkable degree of irradiation tolerance.

Acknowledgements

The authors are grateful for the support from the DOE Office of Fusion Energy Sciences (grant No. DE-FG03-94ER54275) and the National Science Foundation of China (No. 51471189, 51171211, and 51471049). Y. Jiang also acknowledges the partial support from the National Basic Research Program of China (No. 2014CB644001-2), and the National Key Laboratory of Powder Metallurgy at Central South University.

References

[1] Stoller RE, Odette GR. 1982. The effect of matrix cavities and cavity density on the formation of precipitate associated voids and swelling in multiphase stainless steels. Proc. Int. Symp. Eff. Irradiat. Mater., 11th, Scottsdale, ASTM Spec. Tech. Publ. 782:275–94. Philadelphia: ASTM

[2] Stoller RE, Odette GR. 1987. A composite model of microstructural evolution in austenitic stainless steel under fast neutron irradiation. Int. Symp. Eff. Irradiat. Mater. Prop., 13th, Seattle, ASTM Spec. Tech. Publ. 955:371–92. Philadelphia: ASTM

[3] G. R. Odette and D. T. Hoelzer, JOM 62, 84–92 (2010).

[4] G. R. Odette, M. J. Alinger, and B. D. Wirth, Annu. Rev. Mater. Res. 38, 471–503 (2008).

[5] R. Konings, Comprehensive Nuclear Materials (Elsevier, 2012), pp.141–193.

[6] Y. Jiang, J. R. Smith, and G. R. Odette, Acta Metal. 58, 1536–1543 (2010).

[7] M. J. Alinger, G. R. Odette, and D. T. Hoelzer, J. Nucl. Mater. 329–333, 382–386 (2004).

[8] T. Yamamoto, G. R. Odette, P. Miao, D. T. Hoelzer, J. Bentley, N. Hashimoto, H. Tanigawa, and R. J. Kurtz, J. Nucl. Mater. 367–370, 399–410 (2007).
[9] G. R. Odette, P. Miao, T. Yamamoto, D. Edwards, H. Tanigawa, and R. J. Kurtz, Trans. Am. Nucl. Soc. 98, 1148–1149 (2008).
[10] P. Miao, G. R. Odette, T. Yamamoto, M. J. Alinger, and D. Klingensmith, J. Nucl. Mater. 377, 59–64 (2008).
[11] M. J. Alinger, G. R. Odette, and D. T. Hoelzer, Acta. Mater. 57, 392-406 (2009).
[12] M. Klimiankou, R. Lindau, and A. Möslang, Micron, 36, 1-8 (2005).
[13] S. Yamashita, S. Ohtsuka, N. Akasaka, S. Ukai, and S. Ohnuki, Philos. Mag. Lett. 84, 525-529 (2004).
[14] S. Yamashita, N. Akasaka, and S. Ohnuki, J. Nucl. Mater. 329, 377-381 (2004).
[15] H. Kishimoto, R. Kasad, O. Hashitomi, and A. Kimura, J. Nucl. Mater. 386, 533-536 (2009).
[16] H. Sakasegawa, M. Tamura, S. Ohtsuka, S. Ukai, H. Tanigawa, A. Kohyama, and M. Fujiwara, J. Alloys Compd. 452, 2-6 (2008).
[17] H. Sakasegawa, L. Chaffron, F. Legendre, L. Boulanger, T. Cozzika, M. Brocq, and Y. de Carlan, J. Nucl. Mater. 384, 115-118 (2009).
[18] M. Klimiankou, R. Lindau, and A. Möslang, J. Nucl. Mater. 329, 347-352 (2004).
[19] T. Okuda, and M. Fujiwara, J. Mater. Sci. Lett. 14, 1600-1603 (1995).
[20] Bhattacharyya, P. Dickerson, S. A. Maloy, A. Misra, M. A. Nastasi, and G. R. Odette. ”On the structure and chemistry of complex oxide nanofeatures in nanostructured ferritic alloy U14YWT”, Fusion Reactor Materials Program Semi Annual Progress Report. DOE/ER-0313/50 (2011).
[21] Yang L, Jiang Y, Odette GR, Yamamoto T, Liu Z, Liu Y. J Appl Phys. 115, 143508 (2014).
[22] Jin Y, Jiang Y, Yang L, Lan G, Odette GR, Yamamoto T, Shang J, Dang Y. J Appl Phys. 116, 1435011 (2014).
[23] Ribis J, de Carlan Y. Acta Mater. 60, 238 (2012).
[24] Dawson K, Tatlock GJ. J Nucl Mater. 444, 252 (2014).
[25] Kresse G, Furthmüller J. http://cms.mpi.univie.ac.at/vasp/vasp/vasp.html.
[26] Kresse G, Joubert J. Phys Rev B 59, 1758 (1999).
[27] Smith JR, Jiang Y, Evans AG. Int J Mater Res. 98, 1214 (2007).
[28] Jiang Y, Smith JR, Evans AG. Appl Phys Letts. 92, 141918 (2008).
[29] Yang L, Jiang Y, Odette GR, Zhou WC, Liu Z, Liu Y. Acta Mater. 61, 7260 (2013).
[30] Chase MW, Jr. NIST-JANAF Thermochemical Tables, Fourth Edition, J Phys Chem Ref Data 1998; Monograph 9.
[31] Odette GR. JOM 66, 2427 (2014).
[32] Zhang L, Fu C-C, Lu G-H. Phys Rev B 87, 134107 (2013).
[33] Zhang Y, Feng W-Q, Liu Y-L, Lu G-H, Wang T. Nucl. Instrum. Methods Phys. Res. B 267, 3200 (2009).
[34] Zhang L, Shu X, Jin S, Zhang Y, Lu G-H. J. Phys: Condens. Matter. 22, 375401 (2010).
[35] Zhang L, Zhang Y, Lu G-H. J. Phys: Condens. Matter. 25, 095001 (2013).
[36] Caro A, Hetherly J, Stukowski A, Caro M, Martinez E, Srivilliputhur S, Zepeda-Ruiz L, Nastasi M. J. Nucl. Mater. 418, 261 (2011).
[37] Stoller RE, Odette GR. J. Nucl. Mater. 131, 118 (1985).
[38] Konings R. Comprehensive Nuclear Materials, p.141-193 (Elsevier, 2012).

TMS2016

145th Annual Meeting & Exhibition

SUPPLEMENTAL PROCEEDINGS

Phase Transformations and Microstructural Evolution

THE STABILITY OF THE MOVING BOUNDARY IN SPHERICAL AND PLANAR GEOMETRIES AND ITS RELATION TO NUCLEATION AND GROWTH

Rahul Basu[1]

[1]Sambhram Institute of Technology, VTU
MS Palya, Jalahalli (E)
Bangalore 560097, Ka,India

Keywords: Nucleation[1], Stability[2], Moving Boundary Problem[3]

Abstract

Coupled heat and mass diffusion equations are set up and solved for various Stefan numbers. A stability criterion is developed for the moving interface. The general MBP is of importance in many fields, particularly in directional solidification. The analysis is applied to the homogenous nucleation and growth of a spherical particle. Traditional analyses have relied on energy balances between surface and volumetric energy. An exact solution is analyzed for appropriate boundary conditions here. The present derivation presents unpublished analyses using perturbation and consideration of the unknown moving boundary of the nucleating particle. Only certain solutions for the MBP are known and it is difficult to find solutions for the general case due to the extreme non-linear nature of the problem because of discontinuous material properties across the liquid and solid regions, and the unknown position of the liquid solid phase boundary. These concepts are applied to nucleation and phase field theory for homogenous nucleation with application to amorphous alloy formation.

1.Introduction

The problem of solidification and melting is of interest in such diverse areas as geology, metallurgy, food processing and cryosurgery. Carslaw and Jaeger (1) claim only certain solutions known for certain geometries. Some of the earlier works on the interface boundary are by Mullins Sekerka (2), and Pedroso Domoto (3). The problem was first tackled by Stefan (4) in the analysis if the melting of polar ice in the late 1800's. The classic work of Mullins Sekerka (2) dealt with a perturbation analysis of the moving phase interface. In this paper a stability criterion is derived for the moving interface in the convective case, with appropriate linearization. The nucleating phase is treated as having a moving boundary, and stability analyzed as an MBP. Some experimental data is applied and ball park figures for amorphous film formation are analysed using ideas of phase field theory and laser thermal fluctuations. Other configurations like needles, whiskers, lamellae can also be studied by appropriate coordinate transformations.

2 Solidification of a spherical body

The solutions to the equations within and outside the nucleating phase have to satisfy certain conditions for stability, and are listed in Paterson (5). The usual analysis of nucleation relies on

thermodynamics and a balance of surface and volumetric free energy, giving a 'Critical Nucleus" size or radius which depends on the surface energy, (Surface tension) and the Gibbs Free energy (Volumetric based). It does not describe the subsequent growth of the stable nucleus with time. The phase field theory of nucleation has formulations which include fluctuations as homogenous nucleation (6), exponents depending on geometry and dof's., nucleation or diffusion controlled growth across the interface, and KJMA analysis (7) , (8). Perturbation Stability of the nucleus has also had a large group of adherents starting with the seminal papers of Mullins and Sekerka, (2). The Moving Boundary analysis for the Sphere is adapted to describe this phenomenon which may by contrast appear deceptively simple. The solutions in the two regions (nucleating solid and matrix) are:

$$\theta_1 = A[\ (K_1t)^{0.5}/r \exp(-r^2/K_1t) - \pi/2 \operatorname{erfc}[r/2(K_1t)^{0.5}] - B \qquad 1$$

(similarly for region 2).
Applying boundary conditions, $_1\theta = \Theta$when t = 0, R =0 and $_1\theta$ =-B
$C = q/4\pi k_2 (K_2)^{0.5}$
B = ,Θ where melting temperature is zero and initial temperature is - .Θ
The equation for α is obtained from the interfacial energy balance

$$q/4\pi\exp(-\alpha^2/4K_2) - k_1\alpha\Theta/[1-\alpha/2(\pi/K_1t)^{0.5}\exp(\alpha^2/K_1)\operatorname{erfc}(\alpha/2(K_1)^{0.5}] = L\rho\alpha^3/2 \qquad 2$$

Setting particular values for the physical parameters, solutions can be obtained by solving this transcendental equation. Results are in Figures 1 and 2.

2.1 Adiabatic Boundary (Insulated wall)

Consider now the case of the boundary conditions where an adiabatic condition is imposed at the origin. By transforming to a rectilinear case, it is seen that this is equivalent to the problem of an insulated wall with a freeze front moving away or to it. Physically this would correspond to a nucleus forming on an insulated wall. Homogenous nucleation has been difficult to prove but it is likened to nucleation on walls of a capsule or substrate, (8). In terms of the above analysis, it can be arrived at by putting the constant C in the general solution to be zero,

$$\text{since } d\theta_1/dr = C(K_1t)/r^2 \exp(-r^2/4K_1t), \qquad 3$$

and if the flux at r =0 is zero the constant C should be identically 0. Furthermore, from the initial condition , at t =0 and r = infinity, the temperature is -Θ;
Hence the first term in the thermal balance equation which depended on C drops out, and one is left with

$$-k_1\alpha\Theta/[1-\alpha/2(\pi/K1)^{0.5}\exp(\alpha^2/4K_1)\operatorname{erfc}(\alpha/2(K_1)^{0.5}] = L\rho\alpha^3/2 \qquad 4$$

The solution of this equation occurs at 0.0108, which is less than the previous case. A similar problem has been analyzed by McCue (9) , where the problem is set up as follows

$$du/dt = 1/r^2\ d/dr(r^2\ du/dr) \quad R < r < 1 \qquad 5$$

$$dv/dt = K/r^2\, d/dr\,(r^2\, dv/dr) \quad 0< r <R \qquad 6$$

where the variables have been scaled s.t R is the interface, u=v =0 at the interface (r=R)
B.C. u = -1 on r=1,U =0 on r =R, dv/dr =0 on r=0,V=0 on R
*I.C. v =V at t =0,R =1 at t=0 (*u describes the solid and v the liquid phase temperatures.The problem describes inward solidification of a liquid sphere). It is claimed this has no solution.

2.2 SPHERICAL DIRICHLET BOUNDARY CONDITIONS

For the Dirichlet problem, (eg. The freezing of molten liquid), the boundary conditions are
$\theta_2(\infty, t) = 0$ at t = infinity
Initial temperature Θ,
Final temperature $\theta_2(\infty, t=\text{infinity}) = 0$
Setting up the equations and putting the interface temperature as 0, the interfacial conditions give exactly the same balance equation as the one already obtained for the "adiabatic" case.
Specifically, the solutions are in each region,

$$\text{Liquid } \theta_1 = (\theta_m + \theta_0)[\text{spherf}(x)/\text{spherf}(\alpha)] - \theta_0 \qquad 7$$

$$\text{Solid } \theta_2 = \theta_m[\text{spherf}(x)/\text{spherf}(\alpha)] \qquad 8$$

When the m.p. temperature is taken as zero as in the earlier cases. The thermal balance equations are the same for the two instances (Dirichlet and zero heat source and /or adiabatic).
Although the thermal profiles may be non identical, the results show that they are different only up to an additive or multiplicative constant varying with the initial temperature.

2.3 HEAT SINK OR SOURCE AT ORIGIN. For the case of the heat sink or source at the origin, the solution given in Paterson (5) is easily fitted to the boundary conditions. The general solution can be expressed as

$$u = A + B\,(t^{0.5}/r \exp(-r^2/4t) - (\pi/2)^{0.5}\,\text{erfc}(r/2(t)^{0.5}) \qquad 9$$

Applying u = -1 at t =0, gives A = -1
Whereas u = 0 on r = R (interface), gives an expression for B in terms of spherf(λ),
specifically, B = 1/spherf(λ)
Examining dv/dr = 0 on r =0.

$$\text{The general solution for } v = C + D\,[\text{spherf}(r/(Kt)^{0.5})] \qquad 10$$

$$dv/dr = -D\,(Kt)^{0.5}/r^2 \exp(-r^2/Kt)) \qquad 11$$

At r =0, the expression is 0 if D =0.
Thus the solution for v given the stated B.C. is v = C =V (at t =0, and for all t) ,
If v =0 on r =R, this condition is incompatible with the stated condition v =Vat t =0, because the analytical solution for v(r,t) is a constant. Hence either v =0 or v=V, so only v =0 can be chosen

to be consistent with the temperature (reduced) at the phase interface., i.e. the mp stays constant in the molten region as dT/dx =0 at x =0, (and hence no flux of heat).
Thus v=0, (equal to the melting point everywhere in the liquid).
Hence the problem stated has a solution

$$u = -1 + B\,(\,\text{spherf}(\,r/2\,t^{\,0.5}\,)),\ B\ = 1/\text{spherf}\,(\lambda\,)$$
$$R < r < 1 \qquad 12$$
$$v = 0\ ,\ 0 < r\ < R$$

Where R = 1 at t =0. v =V at t =0 and v = 0 at r =R cannot be simultaneously satisfied by the same expression for v which is a constant (This has relevance for the case of nucleation on an insulated wall or container as for instance a thermos flask).

3 Results for parameter variation for the sphere.

The predominant effect arises from the variation of the velocity parameter in the thermal balance equation, given in eqn[2]. Although transcendental terms occur, the main effect is from the power term on the r.h.s of eqn[2], the terms on the LHS are exponentials and for small α are small and can be replaced by 1 . An approximate eqn for eqn [2] for small α can be expressed as

$$q/4\pi - K_1\alpha\,\Theta/(\,1-\alpha/2\,(\pi/4)^{0.5}) = L\,\rho\,\alpha^{\,3}/2 \qquad 13$$

For the spherical case if q is neglected (self ablation) this equation is a cubic in α . In the cylindrical case, the power is one less on the RHS.

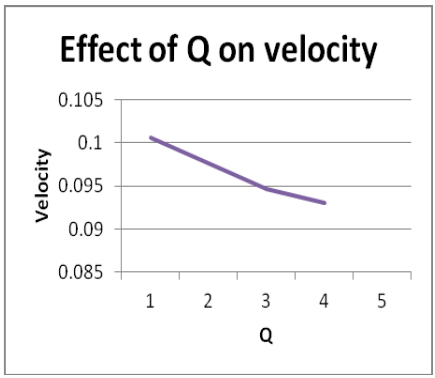

Figure1 Q vs Velocity of freezing

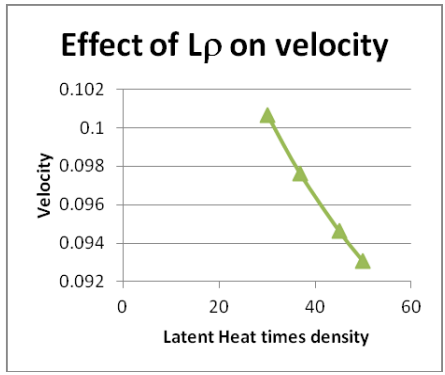

Figure 2 Lρ/2 versus velocity of freezing

3.1 SUBLIMATION OR ABLATION OF A SPHERE

The problem of sublimation is of significance when the nucleus forms in a rarefied atmosphere or vacuum without an intermediate liquid phase. Mathematically it can be described by using he appropriate parameters in the thermal balance equation given in Paterson, (5).

The parameters for the vapour are: ρ =1.694 Kg/m^3 at 1 bar, diffusivity 2.338 x 10^{-5} m^2/s, conductivity varying from .016 to .0248 W/m/K, L =540 cal/gm. With the same values for the heat source, the reaction is driven by the heat of sublimation which is 540+73.6 =613.6 cal/gm, and a simulation by WOLFRAM gives: $x \approx 0.0846932830339482\ldots$ For the adiabatic case, the solution is much less since the motion of the interface depends on the latent heat of the solid-liquid+liquid-vapour=solid vapour.
Solution is given as $\{x \to -0.000122892\}$
The velocity is about three orders of magnitude less, and is seen to move in the opposite direction to normal freezing buildup, as is to be expected for ablation or sublimation. Table 1 gives further values

4 NUCLEATION WITH COUPLED HEAT AND MASS TRANSFER

In case of coupled mass and heat transfer, application is made to nucleation with both mass and thermal diffusion across the interface. Take the rectilinear case without loss of generality. Following the development in Luikov (12), the thermal equation with the mass coupled terms are given after non dimensionalisation by:

$T'' + \eta/2\, T' + (\varepsilon L/\rho c_p)\, dc/dt$ 14

Relating the concentration derivative to the thermal gradient by $C' = T'/g$. 15

T' is related again to T by the convection relation $dT/dx = h/k\, T$, 16
with appropriate modifications for the non dimensionalisation and derivatives relating d/dx to d/dη.Eventually the linearised coupled diffusion equation is obtained where the effect of c' is replaced by using the concentration-thermal gradient:

For the liquid phase: $[\boldsymbol{D}^2 + \eta/2\boldsymbol{D}]\ \theta = 0$ 17

For the solid phase with the remelt term:

$[\boldsymbol{D}^2 + \eta/2\boldsymbol{D} + (\varepsilon L/\theta m c_p)\, Bi/2g]\ \theta = 0$ 18

Introducing a small parameter $\mu = g/(\varepsilon\ Ste)$

$\mu\theta'' + Fo\ \mu/2\ \theta' + Bi/2 = 0$ 19

(Note: the convective boundary condition is incorporated via the Bi parameter)

4.1 PERTURBATION SOLUTIONS:

Mullins Sekerka (2) look at perturbation from the effect of variation of the phase boundary on the concentration. This is a micro view, whereas in the present approach the effect of boundary parameters on the diffusive field is looked at in the larger picture. Eqn (19) has the following solutions:

Inner solution

$$\mu\theta'' + F_0\,\mu/2\;\theta' = 0 \qquad (20)$$

$$\theta'' + F_0/2\;\theta' = 0, \qquad (21)$$

which is easily solved in terms of exponentials.

Outer solution

$$F_0\,\mu/2\;\theta' + Bi/2 = 0, \qquad (22)$$

taking $F_0\,\mu$ as the small parameter, the solutions are obtained as a polynomial series. Additionally, if Fo is very small,

$$\mu\theta'' + Bi/2 = 0, \qquad (23)$$

With the stated boundary conditions, an exact solution can be obtained as follows for the Dirichlet, Convective scenarios: General solution exp (Y) η

$$Y = [-Fo\,\mu/2 + -\,sqrt((Fo\,\mu/2)^2 - 4\,\mu\,Bi/2)]/2\mu \qquad (24)$$

Pedroso Domoto (3), did not consider coupled mass and thermal effects, while Soward(18) developed a unified solution for cylinders and spheres.

4.2 EFFECT OF BOUNDARY CONDITIONS on STABILITY:

Regardless of the boundary conditions, the characteristic of the differential equation is unchanged and depends only on the Fourier, Stefan and Biot numbers, the stability of the solution being unaffected by the pre multiplying and additive constants to the solution. Other approaches to the study of ablation use low temperature sublimation models to visualize the effects of high temperature ablation in space, (12- 14). Ablation is also being used in cryosurgery to produce low temperatures behind ablating surface tissues, (14). Some researchers use ablation to analyze ice cores, (15) while other applications are seen in laser ablation of space debris (16). An application of the method of finding the transcendental root of the thermal balance equation [5] is extended to the case of the sublimation of ice from a sphere.

Two cases are possible

a) sublimation from the surface of the sphere

b) deposition from vapour to solid (accretion) on the sphere

The second possibility is physically possible as formation of snow crystals and hoar frost directly from vapour. The pressure effect is not included in the equations, and hence the results are obtained assuming the pressure remains constant. By transforming the problem to rectilinear coordinates it is seen that this sign change in L merely shifts a sublimating surface from one direction to the other. Here, it depends on the sign of the terms in eqn[4]. Focusing on the case of self sublimation (ice-vapour), heat source strength q is set to zero, and using the appropriate values for ice and vapour, the results are given in Table 1.

Applications for the methods described above have been suggested for the formation of nano composites with micro spheres embedded in a matrix , Wu (17), while the problem of exact solution of spherical phase change remains unsolved, Soward, McCue, Stewartson (18,19, 20). Soward (18) has given a perturbation expression which is applicable to either the cylindrical or spherical cases by changing the exponent of the terms in the series. For the problem with an insulated boundary, it needs to be asserted that a variable error function solution is physically and mathematically inconsistent with the constant derivative boundary conditions. With laser heating of the surface, the oscillations are normally damped very quickly within the boundary layer depending on the Fourier number which is the coefficient of the first order term in the inner solution (eqn 20). The stability analysis done earlier in the paper shows that oscillations may be sustained in the heated layer if the discriminant is negative. The discriminant is given by $\sqrt{[(Fo\ \mu/2)^2 - 4\ \mu\ Bi/2]}$. If μ is small, it can be neglected and the discriminant approximates to $(-2\ \mu\ Bi)^{1/2}$ which is the imposed oscillation on the attenuation curve as it leads to a cosine or sine component to the exponential damping for the main $Fo\ \mu$ term. The critical value for the discriminant is found to be $\mu = 8\ Bi/(Fo)^2$ .Substitution of typical values for F_0 and Bi with μ give an attenuation factor varying with these numbers. For typical values of the order of 1 to 0.1, the main parameter of effect would be the small parameter μ which varies inversely as the Stefan number. Hence the laser frequency would be amplified by this factor in the film, and if typical laser frequencies of 10^{-6} to 10^{-9} are encountered, then the subsurface frequencies get amplified by this factor depending mainly on the inverse Stefan number, possibly as high as 10^2. Typical values for surface and bulk nucleation frequencies in silicate glass are 10^7/s, 10^{10}/s (21). Following the general idea of the phase field and homogenous nucleation one may expect nucleation sites to occur at the fluctuations of the phase concentration. Thus, if the imposed heating frequency is of the same value or a harmonic, but of an opposite phase, the net result is a cancelling out, whereby nuclei do not have the chance to form at the uneven concentration points. By tuning the parameters of the source and material, one can get frequencies of pulse heating in this range and thus prevent nucleation from occurring, leading to amorphous structures. A recent paper shows how a glassy structure was obtained by laser heating a Pt foil (22). The amorphous structure was an unexpected result but quite possibly a result of rapid quenching. Since a thin foil is involved, self quenching is not an option, neither is convective heat transfer in ambient conditions, so there must have been some other factor at work, which could be something of the type discussed above (attenuation of the incoming frequency by the overall bulk thermodynamic parameters). Approximately, the Stefan number for Pt is $\Delta T/1000$, hence if ΔT is small due to convection, then μ is sufficiently high to attenuate the fluctuations to interfere with nucleation and one gets amorphous solid foil.

5.CONCLUSION:

An approximate and exact solution for the spherical moving boundary problem has been developed. Fluid flow convection has been neglected, however heat convection at the boundary has been incorporated in the linearised model. Numerical calculations show the self sublimation and self accretion velocities for the sphere differ by an order of magnitude, given the same boundary conditions. The perturbation analysis reveals a singularity at the origin; however, the spherical error function gives solutions that adapt to various boundary conditions. The boundary conditions for the adiabatic case, (no heat flux at the boundary) are equivalent to the Dirichlet as far as the moving phase velocity is concerned. The convective case can be reduced to the

rectilinear case for certain adjustment in the constants. Solutions have been computed for the self freezing and ablation case of the sphere. Phase field concepts show that a possible explanation for observed amorphous film formation in Pt foil could be the neutralizing disturbing frequency imposed by laser fluctuations(22).

References

[1] H S Carslaw & J C Jaeger, *Conduction of Heat in Solids*, 2nd Ed., Clarendon Press, (Oxford, 1959)

[2]. W.W.Mullins & R..F. Sekerka "Morphological stability of a particle growing by diffusion and heat flow".*J. Appl. Phys*, 34, 323-329,(1963)

[3]. R.L. Pedroso and G.A.Domoto , "Perturbation solutions for spherical solidication of saturated liquids ", *J Heat Transfer*, 95, 42-46,(1973)

[4]. **J**. **Stefan**, "Ueber die Theorie der Eisbildung, insbesondere ueber die Eisbildung im Polarmeere.", *Ann. Phys. Chem.*, N. S. 42, 269 (1891).

[5].S. Paterson, "Propagation of a boundary of fusion",*Glasgow Math Assn Proc*., 1, 42-47,(1952)

[6] L Granaszyl T Puzsten, T Borszonyi, "Phase field Theory of Nucleation and polycrystalline pattern formation", in "*Handbook of Rheoretical and computational nano technology*", V9, pp535-572, Am. Sci. Publ., Cal. 2006

[7] J.T. Serra, S. Venkatraman, M,. Stoica etal,, " Non-isothermal kinetic analysis of the crystallization of metallic glasses using the Master Curve method", *Materials 2011*, 4, 2231-2243, doi10.3390/ma412231/www.mpi.com/journal/materials

[8] S.E.Swanson, " Relation of nucleation and crystal growth rate to the development of granitic textures", *Am.Mineral*. v62, p966-978, 1977

[9]. S W McCue, B Wu, J M Hill, "Classical two-phase Stefan problem for spheres", *Proc Roy Soc* (A),464 2055-76,(2008)

[10]. H S Carslaw & J C Jaeger, *Conduction of Heat in Solids*, 2nd Ed., Clarendon Press, (Oxford, 1959) , 276

[11] A.V. Luikov," Systems of differential equations of heat and mass transfer in capillary porous bodies", *Int J Heat Mass Transfer*, 18, 1-14, (1975)

[12]. S.G.Arless, F.L.Milder, M.Abboudi, D.Wittenberger, S.Carroll " Method of simultaneously freezing and heating tissue for ablation", *USPatent* 8287526 B2, Oct 16 2012

[13]. C.S. Combs, N T Clemens, A M Danehy, ""Development of Naphthalene PLIF for visualizing ablation products from a Space capsule shield", *doi 10.2514/6.2014-1152*

[14.] C.S. Combs, N T Clemens, P M Danehy, "Visualization of Capsule Reentry Vehicle Heat Shield Ablation using Naphthalene PLIF," in *17th Intl Symp. Of laser techniques in Fluid mechanics*, Lisbon Portugal, 7-1- July 2014.

[15]. H Reinhardt, M Kriews, H Miller etal, "Laser Ablation Inductively Coupled Plasma Mass Spectrometry: A New Tool for Trace Element Analysis in Ice Cores", .*Fresenius J Anal Chem* 370, 629-639,(2001)

[16]. D A Liedahl, S B Libby, A Rubenchik, "Momentum transfer by laser ablation of irregularly shaped space debris", *Arxiv.org:1004.0390.pdf*

[17]B.Wu, Mathematical modeling of nanoparticle melting or freezing http://ro.uow.edu.au/theses/787

[18] A .M. Soward, "A unified approach to Stefan's problem for spheres and cylinders", *Proc Roy Soc* A, 373,131-147,(1980)

[19] SW McCue , JR King , D S Riley, "Extinction behavior for two-dimensional inward-solidification problems", *Proc Roy Soc* (A), 459, 977-999,(2003)
[20]. K Stewartson and RT Waechter , " On Stefan's problem for spheres" . *Proc Roy Soc* Lond A,348 ,415-426,(1976)
[21] V.M. Fokin and E.D. Zanotto, "Surface and volume nucleation and growth in TiO2–cordierite glasses ",*J. Non-Cryst. Solids* **246**, 115 (1999).
[22] Xraysweb.lbl.gov/bl1222/research_Application/PtAmblasermelt.pptPt foil

Nomenclature

A,B,C,D,E constants
D differenial operator
a(t),R(t) interface position with time
g thermal concentration gradient
c concentration
K diffusivity
k conductivity
L latent heat of transformation (melting or vaporization)
Q heat sink/source strength
r radius
s, r coordinates in rectilinear and cylindrical, or spherical coordinates
t time
u,v , U,V temperatures
α eigenvalue for position of interface
μ (g/ Stefan parameter)
ε remelt, porosity term
ρ Density
ν nucleation frequency
θ non dimensional temperature
Θ non dim. initial temperature
η Fourier number (non dimenionalised time/ distance)
Fo =Fourier number
Bi =Biot number Ste= Stefan number (latent heat/sensible heat)
erf error function, spherf spherical error function(see ref 5)
grad gradient function, Ei exponential integral function
KJMA: Kolmogorov,Johnson, Mehl Avrami

Table 1 Self Sublimation velocity vs latent heat density

$L\rho/2$	Interface Velocity	$L\rho/2$	Interface Velocity
-250	-.006365	250	-.0001508
-306.8	-.005758	306.8	-.0001229
-400	-.00506	400	-.00009427
-450	-.0047713	450	-.0000838
-500	-.00453	500	-.000075425

Water: k_2 =0.00144 Cal/cm sec K, K_2 = 0.00144 cm^2/sec, Ice: k_1 = 0.0053 Cal/cm.sec.K, K_1 = 0.0155 cm^2/sec, $L\rho$=73.6, q= 2.38 cal/cm.sec

EFFECT OF PULSE MAGNETIC FIELD ON ISOTHERMAL BAINITIC TRANSFORMATION PROCESS IN Cr5 STEEL

Wenming Nan[1], Daping Zhang[1], Lijuan Li[1], Qingchun Li[2], Qijie Zhai[1]

1. School of Materials Science and Engineering, Shanghai University, Shanghai 200072, China
2. School of Materials Science and Engineering, Liaoning University of Technology, Liaoning Jinzhou 121000, China

Keywords: Cr5 Steel, Pulse Magnetic Field, Bainitic

Abstract

In order to investigate the effect of pulse magnetic field on isothermal bainitic microstructure and performance of Cr5 steel, pulse high magnetic field with 1.5T was exerted during isothermal bainitic transformation, continuous cooling + isothermal bainitic transformation and austenitizing + continuous cooling + isothermal bainitic transformation process, respectively. Results showed that, compared with normal isothermal bainitic transformation with the same technology, applying pulse magnetic field during the isothermal bainitic transformation can obviously promote bainitic transformation, the volume fraction of bainite increased by 4.2%, the volume fraction of retained austenite is reduced by 1.7%, and the hardness of Cr5 steel was reduced by 3 HRC.

Introduction

Cr5 steel is commonly used as a back-up rolls material attributing to its high strength, toughness and wear resistance. The comprehensive performance directly determines the quality and production of rolling plate. Cr5 steel is developed on the basis of Cr3 steel by increasing the contents of Cr and other alloying elements (Si, Mo, V, etc.). In this case, not only the toughness of Cr5 steel is improved, but also its service life is increased, which gets extensive application in high energy mill equipment [1]. The manufacturing cost and service life of cold roll have important significance to industrial production.

As is known to all, bainitic steel is prospective in application due to its high strength and good toughness. To promote the bainitic transformation process in alloy steel, researchers took some measures of controlling alloy element [2], austenitizing temperature and holding time [3-5], applying stresses [6] or steady magnetic field [7] in heat treatment process, and so on. However, few studies focus on the impact of pulse magnetic field on bainitic transformation.

At present, pulse magnetic field technology was effective in affecting the structure evolution of phase transformation in metals and alloys. Pulse magnetic field treatment has very obvious refinement effect on solidified structure of metal and alloys [8-11]. Pulsed magnetic field can dramatically influence the solid state phase transformation and recrystallization texture [12], significantly reduce size of primary recrystallization grain and improve the portion of completed recrystallization. Pulse magnetic field can also have greatly improved magnetic property of nanocrystalline soft magnetic materials [13]. Recent studies have found that [14] the effect of pulse magnetic field treatment is related to the orientation of magnetic field. Through the promotion of pulse magnetic field to ferromagnetic transformation product, the phase transformation from austenite to bainite will be accelerated. Based on this, this paper will study the influence of pulse magnetic field on bainitic transformation by applying pulse magnetic field at different heat treatment stages of Cr5 steel, in order to provide basis for further development and application of this steel.

* Corresponding author.
E-mail address: lqcsusan@126.com (Qingchun Li)

Experimental Procedure

Experimental material is Cr5 steel developed by a new type of backup roll steel. After homogenization heat treatment, the steel was then quenched and tempered treatment. The chemical composition (wt %) of steel is: 0.48～0.58 C, 4.50～5.50 Cr, 0.40～0.70 Mn, 0.40～0.70 Si, 0.45～0.50 Mo, 0.10～0.20 V, 0.40～0.50 Ni, P、S≤0.015. The original microstructure was composed of ferrite and a large number of scattered tiny carbides, as shown in Fig.1.

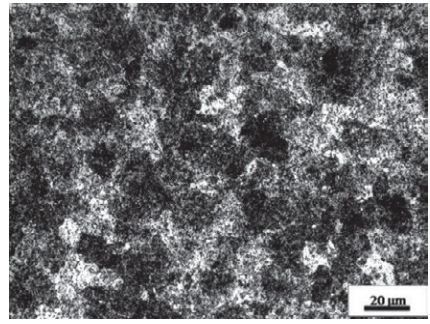

Figure 1. Original microstructure of Cr5 steel

Firstly, samples with the dimension of 3 mm ×10 mm× 30 mm were cut from the experiment materials for heat treatment. Heat treatment technology curve was shown in Fig. 2. Specimens have been heated from room temperature to 940 ℃, held for 20 mins and nitrogen-cooled to 350 ℃ at the rate of 1 ℃/s, then isothermally transformed at 350 ℃ for 5 mins, finally air-cooled to room temperature.

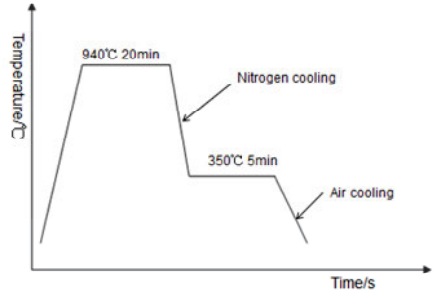

Figure 2. Heat treatment process curve

At different stages of heat treatment process, pulse magnetic field with 1.5T was exerted to study the bainitic transformation under the effect of pulse magnetic field. Samples were divided into four groups: the first group is normal heat treatment, marked as NT-a; the second group of applying pulse magnetic field of 1.5 T during isothermal transformation at 350 ℃ for 5 mins, marked as PMT–b; the third group of applying pulse magnetic field of 1.5 T during cooling and holding at 350 ℃ for 5 mins, marked as PMT–c, the fourth group of applying pulse magnetic field of 1.5 T during the whole process of austenitizing, cooling and isothermal transformation at 350 ℃ for 5 mins, marked as PMT-d.

After different heat treatment, samples undergo a series of wire cutting and polishing. Samples were etched with the acid of 4% nitric acid alcohol solution, then take optical photos by the Zeiss optical microscope (AXIO IMAGE A2M model). Image Pro Plus software is used to investigate bainite transformation fraction of four groups of microstructure by quantitative statistics. SUPRA40 thermal field emission scanning electron microscope is introduced to observe the bainite microstructure. X-ray stress meter was used to measure content of retained austenite in samples with different heat treatment. Ten field of vision in samples NT–a, PMT–b, PMT–c and PMT-d was selected randomly to measure content of retained austenite, respectively, then, took the average value. The HR-150 DT Rockwell apparatus is used to test the hardness of samples.

Results and Discussion

The microstructure of four group samples is shown in Fig.3. It can be seen that the microstructure in four group samples is all composed of martensite matrix, needled lower bainite, granular carbides and a small amount of residual austenite. The fraction of bainite in samples NT–a, PMT–b, PMT–c and PMT-d is 12.2%, 16.4%, 14.1% and 12.5%, respectively. Spectrum diagram of retained austenite by X-ray stress meter is shown in Fig.4. The bottom of the diagram is spectra of the standard sample, of which content of retained austenite is 5%. X-ray stress meter and X-ray diffraction meter are based on the same principle in theory, namely the content of residual austenite is proportional to its diffraction peak intensity. X ray stress meter can measure the content of residual austenite of samples directly, and it is simple and convenient, this paper take ten random fields in four group samples respectively, the average is the content of residual austenite. Content of retained austenite of samples NT–a, PMT–b, PMT–c and PMT-d is 7.1％、5.4％、5.8％、6.8％, respectively. Results showed that, comparing with normal isothermal bainitic transformation, applying pulse magnetic field during isothermal bainitic transformation reduced the content of retained austenite by 1.7%. However, the content of retained austenite in sample PMT-d is nearly the same as sample NT–a. It can be concluded that the fraction of retained austenite is inversely proportional to the fraction of isothermal bainite transformation. Super-cooled austenite will transform to martensite after isothermal bainite transformation. Applying pulse magnetic field with 1.5T during isothermal bainitic transformation can promote the bainite transformation and the fraction of retained austenite was reduced. Above all, applying pulse magnetic field of 1.5 T during isothermal bainite transformation has the most obviously accelerated effect on the bainite transformation. But, applying pulse magnetic field during austenitizing + continuous cooling + isothermal bainitic transformation does not accelerate the isothermal bainite transformation.

Bainite transformation is a process of nucleation and growth, which usually needs an incubation period. Some carbon-rich zone and carbon-poor zone would be formed during the incubation period due to the redistribution of carbon atoms in austenite. The crystal nucleus of bainitic ferrite usually forms at the site of carbon-poor area. When pulse magnetic field is applied during isothermal bainite transformation, the Gibbs free energy of ferromagnetic product phase-bainitic ferrite will be largely reduced, but, the Gibbs free energy of paramagnetic parent phase-austenite is not obviously affected by pulse magnetic field. Thus, the driving force of isothermal bainite transformation is increased and the bainite transformation process is promoted by applying pulse magnetic field. However, when pulse magnetic field is applied during austenitizing and cooling process, carbon atoms in austenite will distribute more uniformly due to its better diffusion ability induced by pulsed magnetic field. This leads to the decrease of quantity of poor carbon area in austenite and the extension of incubation period of bainitic transformation. So, although pulse magnetic field could increases the driving force of isothermal bainite transformation, but the incubation period of bainitic transformation is extended. Therefore, compared with other two

applying periods, applying pulse magnetic field during isothermal bainite transformation is the most effective way of accelerating bainite transformation.

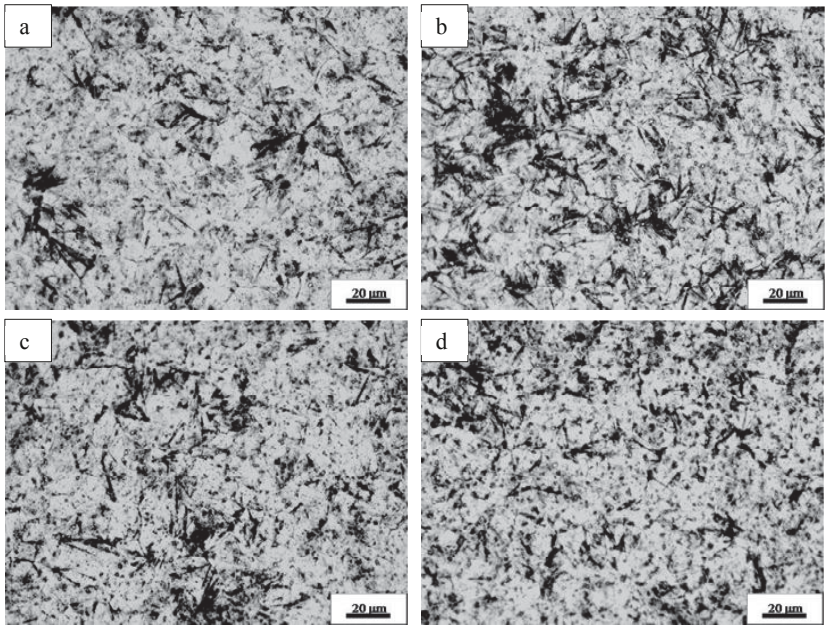

Figure 3. microstructure of samples applying pulse magnetic field in different process
(a) NT-a (b) PMT-b (c) PMT-c (d) PMT-d

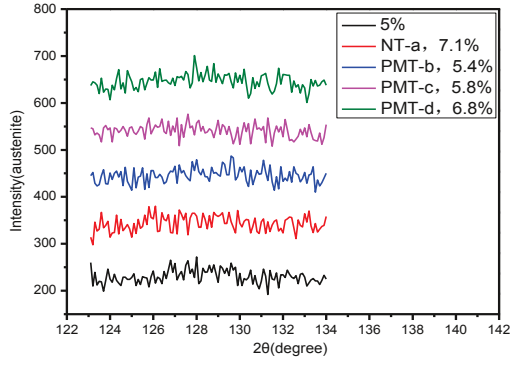

Fig. 4. Spectrum diagram and content of retained austenite

SEM microstructure of samples NT–a, PMT–b, PMT–c and PMT-d is shown in Fig.5. As is shown, compared with lower bainite in samples NT–a, PMT–c and PMT-d, flake carbides in bainitic ferrite of sample PMT–b are tiny in size, distributing at random. In samples NT–a, PMT–c, flake carbides arrange along 55 to 60 ° direction to the long axis of flake ferrite. But, in sample PMT-d, flake carbides approximately parallel to the long axis of ferrite. The formation of

carbides in lower bainite needs supersaturated carbon atoms and alloying elements. Applying pulse magnetic field during isothermal bainite transformation influences the formation of carbides by affecting the diffusion of carbon and alloy elements. However, the formation of carbides is not influenced by applying pulse magnetic field during austenitizing + cooling.
Hardness of sample NT–a, PMT–b, PMT–c and PMT-d is HRC58.4, 55.4, 57.8 and 56.6, respectively. Hardness corresponds to mixed microstructure. Microstructure of sample NT–a, PMT–b, PMT–c and PMT-d is all composed of martensite matrix, needled lower bainite, granular carbides, and a small amount of retained austenite. The more content of bainite in the microstructure is, the fewer content of martensite matrix is, the smaller the hardness of sample is. Although the fraction of bainite transformation in sample NT–a is nearly the same as that in sample PMT–d, the content of retained austenite in sample NT–a is also nearly the same as that in sample PMT–d, the hardness of sample PMT–d is 1.8HRC lower than that of sample NT–a. It may be related to the number of M7C3 type carbides and the orientation of flake carbides in bainite ferrite in sample PMT–d.

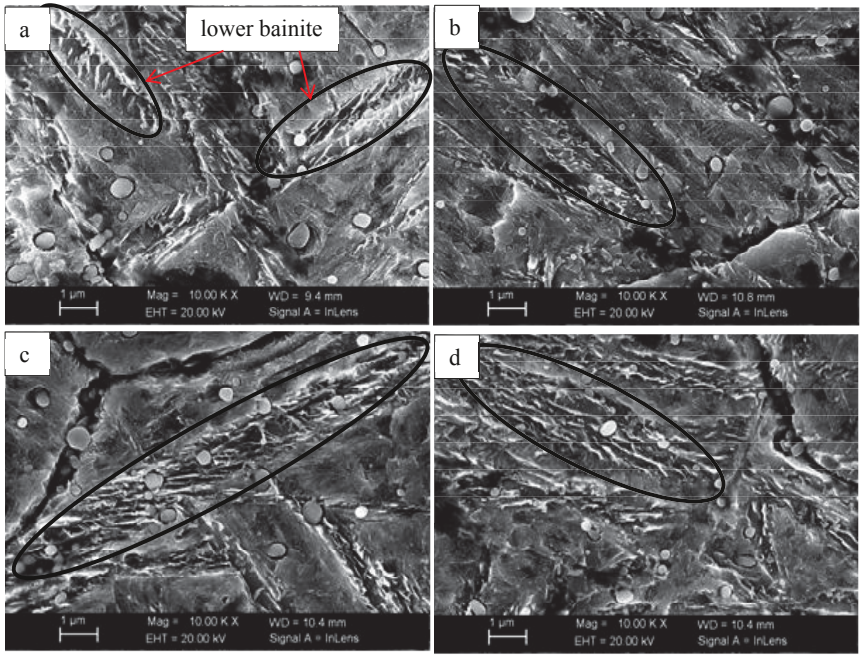

Fig.5. SEM microstructure of samples applying pulse magnetic field in different process (a) NT-a (b) PMT-b (c) PMT-c (d) PMT-d

Conclusions

Applying pulse magnetic field during isothermal bainite transformation can obviously promote bainite transformation, the volume fraction of bainite increased by 4.2%, the volume fraction of retained austenite is reduced by 1.7%, and the hardness of Cr5 steel was reduced by 3 HRC. Flake carbides in lower bainite are dispersive and tiny in size. But, applying pulse magnetic field during austenitizing + continuous cooling + isothermal bainitic transformation does not accelerate the isothermal bainite transformation.

Acknowledgements

This work was supported by the National Natural Science Foundation of China (No. 51204092) and the Key Laboratory Fundamental Research Project of Education Department of LiaoNing Province (No.LZ2015046).

References

1. Xichun Zhao. The research of Cr5 style backup roll steel [J]. Heat Treatment of Metals, 2003, 28(6): 26-28.
2. Takeshi Suzuki, Yoshiki Ono, Goro Miyamoto, Tadashi Furuhara. Effects of Si and Cr on Bainite Microstructure of Medium Carbon Steels. ISIJ International, 2010, 50(10): 1476-1482.
3. Fourlaris G, Baker A J, Papadimitriou G D. Effect of copper addition on the isothermal bainitic transformation in hypereutectoid copper and copper-nickel steels. Acta Mater, 1996, 44(12):4791-4805.
4. Umemoto M, Furuhara T, Tamura I. Effects of austenitizing temperature on the kinetics of bainite at constant austenite grain size in Fe-C and Fe-Ni-C alloys. ActaMetall, 1986, 34(11): 2235-2245.
5. H.B.Wu, H.T.Jiang, S.W.Yang, D.Tang, X.L.He. Thermal stability of non-equilibrius microstructure in microalloyed steel during reheating. ActaMetall.Sci.(Engl.Lett), 2007, 20(5): 313-325.
6. Hase K, Garcia Mateo C, Bhadeshia H K D H. Bainite formation influenced by large stress. Mater SciTechnol, 2004, 20: 1499-1505.
7. Jaramillo R A. Effect of 30 Tesla magnetic field on transformations in a novel bainitic steel. Scripta Mater, 2004, 52: 461-466.
8. LI Ying-ju, MA Xiao-ping, YANG Yuan-sheng. Grain refinement of as-cast superalloy IN718 under action of low voltage pulsed magnetic field. Trans.NonferrousMet.Soc.China, 2011, 21: 1277-1282.
9. WANG B, YANG Y S, ZHOU J X, TONG W H.Structure refinement of pure Mg under pulsed magnetic field. Materials Science and Technology, 2011, 27(1): 176-179.
10. ZI B T, BA Q X, CUI J Z, XU G M. Study on axial changes of as-cast structures of Al-alloy sample treated by the SPMF technique. ScriptaMaterialia, 2000, 43: 377-380
11. Changjiang Song, Qiushu Li, Haibin Li and QijieZhai. Effect of pulse magnetic field on microstructure of austenitic stainless steel during directional solidification. Materials Science and Engineering: A, 2008, 485(1-2): 403-408.
12. Li-juan LI, Ruo-wei SHAO. Effect of Heat Treatment on the Structure and Mechanical Properties of the Hot-rolling Plate of Fe-42% Ni (4J42). Advanced Materials Research, 2011, 194-196: 321-325.
13. N. Ito, A. Michels, J. Kohlbrecher, et al. Effect of magnetic field annealing on the soft magnetic properties of nanocrystalline materials. Journal of Magnetism and Magnetic Materials, 2007, 316(2): 458-461.
14. CaiZhipeng, Lin Jian, Zhao Haiyan, et al. Orientation effects in pulsed magnetic field treatment. Materials Science and Engineering: A, 2005, 398: 344-348.

CORROSION EFFECTS ON MECHANICAL PROPERTIES OF SENSITIZED AA5083-H116

Robert J Mills[1], Brian Y Lattimer[2], Scott W Case[3]
[1]Virginia Tech, Department of Materials Science and Engineering; 406 Goodwin Hall.; Blacksburg, VA, 24060, USA
[2]Virginia Tech, Department of Mechanical Engineering; 413C Goodwin Hall; Blacksburg, VA, 24060, USA
[3]Virginia Tech, Department of Biomedical Engineering Science and Mechanics; 225A Norris Hall; Blacksburg, VA, 24060, USA

Keywords: sensitization, aluminum, thickness reduction, mechanical properties

Abstract

The impact of sensitization levels resulting from exposure to a temperature of 150ºC on AA5083-H116 mechanical properties was investigated through accelerated corrosion. Optical microscopy was performed to examine microstructure damage morphologies dependent upon β grain boundary coverage evolution and surface orientations. Corrosion in 0.6 M NaCl solution at -0.77 V from 3-48 hours led to parallel damage on exposed LT surfaces and perpendicular attack on exposed LS surfaces. After 48 hours of corrosion, a degree of sensitization (DoS) of 61 mg/cm^2 was observed; an intergranular corrosion (IGC) damage depth of 184 µm occurred on the LT surface and IGC damage depth of 720 µm occurred on the LS surface. At a DoS of 66 mg/cm^2, yield and ultimate tensile strengths decreased by 19% and 5%, respectively, when compared to the as-received state, while LT surface corrosion after 120 hours reduced strengths by 26% and 14%, respectively, from the as-received state.

Introduction

In the field of naval architecture, metals and various alloys contribute to the performance of vessels in areas such as corrosion resistance in sea water and humid environments. Lighter and more corrosion-resistant aluminum alloys, particularly 5XXX series, are chosen to replace steels and other corrosion susceptible, heavier alloys. Aluminum is used as a hull material in some vessels while newer vessels can be completely made of aluminum. However, 5XXX series aluminum does become sensitized as a result of exposure to various heat sources in these ships, thus becoming susceptible to corrosion over time. In particular, sensitization of 5083 aluminum occurs over time in an elevated temperature environment, causing grain boundaries to become densely covered by the β phase (Al_3Mg_2), which is more susceptible to corrosion than the other phases of the alloy.

Some of the factors contributing to a lower corrosion resistance are microstructure changes and surface orientations. As 5XXX series aluminum is exposed to temperatures ranging from 50ºC to 200ºC, the β phase begins to migrate from intragranular locations to form an intergranular precipitate [1]. The β phase also naturally begins to nucleate and grow along the grain boundaries as the sensitization time and temperature increases as shown by Davenport et al [2]. This β phase was also shown by Jones et al. [3] to be more anodic than the rest of the aluminum matrix, thus leading to its attack by seawater over years of sensitization. In the research community, accelerated corrosion is utilized via constant voltage or constant current to reduce corrosion experiment time scales to analyze corrosion damage quickly [4-10].

To ensure a more detailed representation of accelerated corrosion damage, surface orientations are investigated. Three surface orientations are used to describe the material--LT, LS, and TS--where L is longitudinal, T is long transverse, and S is short transverse. The exposed surface orientation has been shown by Lim et al. [11] to lead to different forms of damage from corrosion. Corrosion damage on the exposed LT surface leads to more parallel surface damage, contributing to flaking off or exfoliation primary mode of damage, followed by a secondary intergranular corrosion (IGC) region, and a tertiary maximum corrosion depth from surface. The exposed LS and TS surfaces, however, contain damages of the following types: a primary mode of perpendicular IGC damage, secondary IGC spreading damage, and tertiary IGC maximum crack length. The LT surface is also able to have more uniform surface damage, whereas the LS surface contains less frequent, deeper corrosion damaged zones [11].

This work builds on the previous study of Oguochi et al. [12] who studied the sensitization effects on AA5083-H116 mechanical properties solely, while excluding corrosion damage. The goal is to characterize the combined effect of sensitization and corrosion damage with these properties. The study consists of a combination of accelerated corrosion, microstructure analysis, corrosion damage characterization, and mechanical property investigations. To reduce time of corrosion testing of materials, an applied voltage is used to accelerate the corrosion process. Analysis of the impact of sensitization level and surface orientation on microstructure is used to help in understanding the corrosion damage evolution over time. Corrosion damage is characterized with a number of techniques, including maximum corrosion depth and thickness loss from exfoliation of grains. These pre-corrosion and post-corrosion quantifications allow us to make comparisons between as-received, sensitized, and corroded, sensitized AA5083-H116 in terms of mechanical properties.

Experimental

AA5083-H116 (Alcoa) was utilized in this study. Alloy samples were placed in a sensitization environment with a temperature of 150ºC and 0% RH in a TMX environmental chamber for up to 2000 hours. ASTM G-67 Nitric Acid Mass Loss Test (NAMLT) was utilized to obtain a DoS for every time interval analyzed in these studies. NAMLT values for all experiments are summarized in Figure 1.

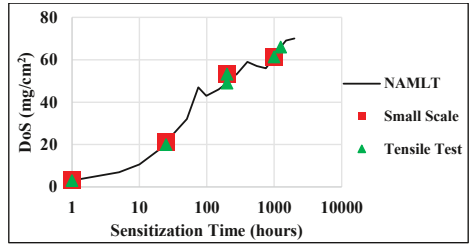

Figure 1. NAMLT values for sensitized AA5083-H116 at 150ºC from as-received state to 2000 hours. The plot highlights the DoS for small scale corrosion specimen as squares, while the tensile test specimens are highlighted as triangles.

Specimen Descriptions

Small Scale Specimen Samples were selected from the following DoS: as-received (3 mg/cm^2), lightly sensitized (21 mg/cm^2), heavily sensitized (53 mg/cm^2), and extremely sensitized (61 mg/cm^2). A diamond blade was utilized to cut samples that were roughly cubes with side lengths of approximately 6mm. The samples were then mounted an 8-hour epoxy hardener/resin mixture and then polished to create a clean and smooth surface using a METPREP 3 Grinder/Polisher with PH-3 Power Head. Polishing was conducted in the following steps: 320 grit, 600 grit, 1 um diamond suspension solution, 6 um polycrystalline diamond suspension solution, and 0.05 um colloidal silica. After polishing, samples were cleaned in ethanol to removal any contamination.

The two surfaces analyzed in corrosion and mechanical testing were the LT and LS surfaces. Barker's etching with 2.5% HBF_4 for 2 minutes at 10 V in a Buehler Electromet Etcher was utilized to reveal the microstructures. This process highlighted a spherical grain shape along the LT or rolling surface and elongated grains on the LS surface (which are created from the rolling process). The etching helped highlight different grain orientations (different colored grains in polarized light) and grain boundaries. Images were taken on a Carl Zeiss Axio VertA.1 microscope at magnifications ranging from 50X through 1000X resolutions. Figures 2 shows the etched LT surface for as-received, lightly sensitized, and heavily sensitized AA5083-H116. The images in Figure 2 were taken under polarized light and show the shape of the LT and LS grains, as well as the β phase, Al_3Mg_2, which appears as a white grain throughout and on the grain boundaries as the sensitization level increases.

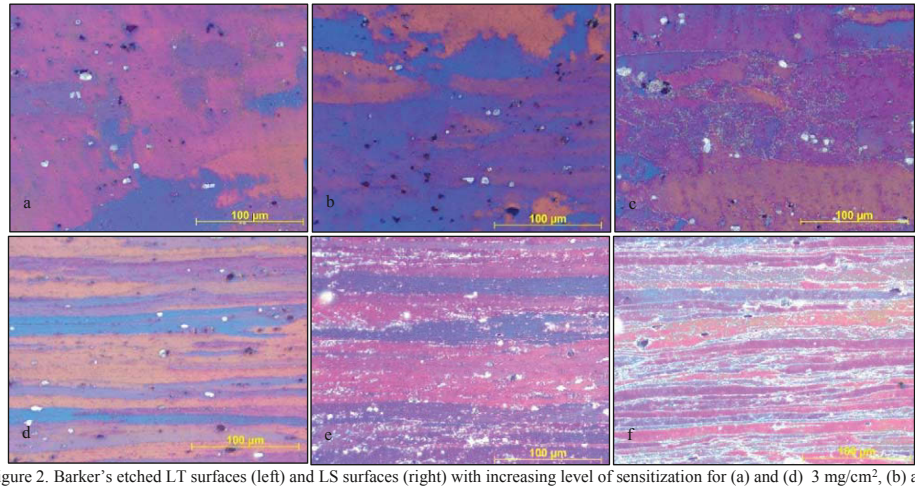

Figure 2. Barker's etched LT surfaces (left) and LS surfaces (right) with increasing level of sensitization for (a) and (d) 3 mg/cm^2, (b) and (e) 21 mg/cm^2, and (c) and (f) 53 mg/cm^2.

Tensile Testing Specimens

Tensile dog bone specimens were created for similar sensitization levels of 3mg/cm^2, 20 mg/cm^2, 49 mg/cm^2, 61 mg/cm^2, and 66 mg/cm^2. These specimens were 168 mm X 19 mm X 6 mm. Samples were polished down to a 1200 grit finish and cleaned with ethanol. Samples were then masked on either the LT or LS surface and the remainder of the samples were painted in with RUST-OLEUM Gloss Protective Enamel. The exposed LT surfaces were 25 mm X 12.5 mm on both sides of the dog bone; the exposed LS surface was 19 mm X 6 mm. The unpainted surfaces were then exposed to the corrosive saltwater solution.

Corrosion Setup

Potentiodynamic Scans and Potentiostatic Holds

A saltwater solution similar to ocean water was utilized in all corrosion experiments. A 0.6 M NaCl solution of pH 8.3 was used in a volume of 150 mL for small scale samples and 800 mL for tensile test samples. During corrosion tests, the AA5083 samples were the working electrodes, with saturated calomel electrodes serving as the reference electrodes, and 6mm diameter graphite rods as the counter electrodes. Images of the corrosion experimental test setup for both small scale and tensile test samples are shown below in Figure 3.

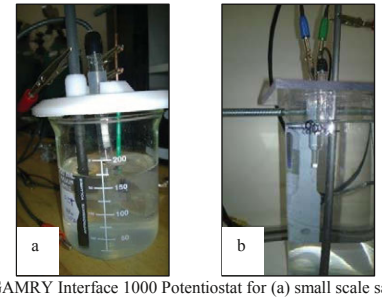

Figure 3. Corrosion setup with the GAMRY Interface 1000 Potentiostat for (a) small scale samples and (b) tensile test specimens.

When conducting accelerated corrosion tests, one first needs to determine the breakdown or spreading voltage needed. The sensitization levels discussed previously were tested independently in potentiodynamic scans. This test was created specifically to find the correct corrosion voltage. The parameters of the potentiodynamic scan are shown in Table I below.

Table I. Potentiodynamic Scan Parameters

Potentiodynamic Scan Parameter	Parameter Value
Open Circuit Potential Time	30 minutes
Scan rate	0.167 mV/second
Starting Voltage	-150 mV from OCP
Final Voltage	-600 mV

The corrosion potential was obtained from the potentiodynamic scans for the various sensitization levels and was determined to be – 0.77 V. Small-scale samples were then corroded at 3, 12, and 48 hours to show progression of different forms of corrosion damage on either the LT or LS surface. Thickness loss over time and maximum crack corrosion damage were used from small-scale testing to determine that a corrosion time of at least 48 hours would be needed for tensile test samples. Tensile test specimens were corroded for 48 hours and 120 hours prior to mechanical testing.

Post-Corrosion Characterization and Mechanical Testing

Small-scale samples and tensile test specimens were characterized after corrosion experiments with various techniques. Subsequent to the corrosion tests, the small-scale samples were rinsed gently with water, cleaned in ethanol, and dried with compressed air. The samples were then imaged to ensure corrosion damage existed across the entire sample surface. The images of the post-corrosion exposed surfaces revealed exfoliated grains and IGC damage for both the LT and LS surfaces. These samples were then cross-sectioned on an ALLIED TechCut 4 Precision Low Speed Saw, remounted in epoxy and polished again in order to measure thickness losses and maximum corrosion damage depths.

Tensile test samples were first cleaned with water and brushed gently to remove any loss grains after corrosion. The samples were then cleaned with acetone to remove the protective anti-corrosion paint and measured to ensure damage to only LT or LS surfaces, depending on which surface was exposed to the corrosive environment. Digital calipers were used to measure the thickness and width of the tensile test samples in the exposed corrosion region for both surfaces. Based on these measurements, original non-corroded section area and a corroded section area can be obtained for comparison behaviors of mechanical properties.

Following corrosion tests and post-corrosion measurements, tensile tests were conducted in an INSTRON 5984 at a displacement rate of 5 mm/min. From the tensile tests, values of 0.2% offset yield strength, elastic modulus, and ultimate tensile strength were determined. Samples were also measured at the failure region to obtain % reduction in area values.

Results

Small Scale Corrosion

Both the LT and LS surfaces were exposed to an accelerated corrosion environment of 0.6 M NaCl with a pH of 8.3 and corrosion voltage of -0.77 V for 3, 12, and 48 hours. Figure 4 shows the thickness reduction resulting from corrosion for both LT and LS surfaces, which have a post-polishing thickness of 6 mm prior to corrosion. Both the LT and LS surfaces experienced less than 400 µm of thickness loss after 3 hours at a corrosion voltage of -0.77 V for the three tested sensitization levels (21 mg/cm^2, 53 mg/cm^2, and 61 mg/cm^2). However, a distinction is made among three sensitization levels on the LT surface as early as 12 hours of accelerated corrosion, where the 21 mg/cm^2 DoS only losses close to 100 µm in thickness even after 48 hours of corrosion. The LS surface experienced an increase in thickness loss over time, due to the elongated grains and the sensitization level as well. Elongated grains contribute to a larger thickness loss on the LS surface due to the perpendicular, deeper IGC damage.

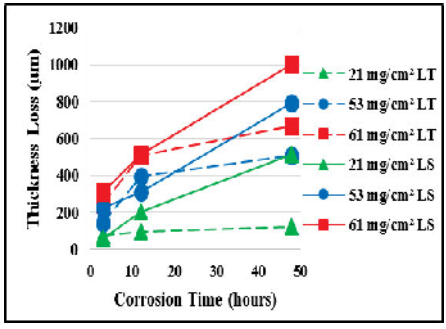

Figure 4. Thickness loss on LT and LS surfaces for different sensitization levels for 3, 12, and 48 hours.

Small scale samples were also cross-sectioned and re-polished to allow for imaging and measurements of IGC damage from sample thickness remaining after thickness loss. Figure 5 shows how the LT and LS surface damage depths varied over time. The LT and LS surfaces react differently in the corrosive environments as expected. The LT surface penetration depths were lower than LS surfaces, which can be attributed to the granular shape differences and β phase coverage as shown in Figure 2. The 21 mg/cm^2 LT and LS surfaces were relatively unaffected by corrosion even after 48 hours. The maximum damage depth for the LT surface at a sensitization level of 61 mg/cm^2 for 48 hours was less than 200 µm, while the lowest damage depth for the LS surface of the same sensitization level was 260 um after only 3 hours of corrosion.

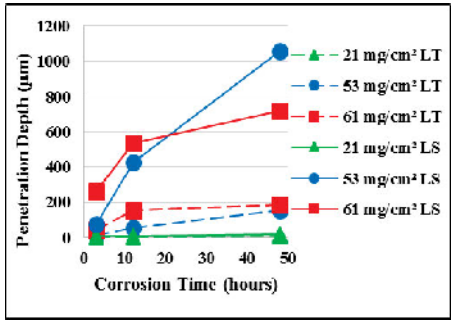

Figure 5. Corrosion effect on LT and LS surfaces for different sensitization levels for 3, 12, and 48 hours.

The LS surface exhibited a greater damage at higher sensitization levels. A distinction can be noted between the two high sensitization levels (53 mg/cm^2 and 61 mg/cm^2) and the low sensitization of 21 mg/cm^2. After 12 hours of corrosion, the LS surface was still sensitization level dependent, and after 48 hours, both high sensitization levels had more than 700 um damage depth.

Tensile Test Corrosion

Sensitized dog bones were corroded for 48 and 120 hours prior to mechanical testing. For LT surface corrosion, both LT surfaces were polished and exposed to the corrosion environment. For the LS surface corrosion, both LS surfaces were treated in the same fashion. The corrosion of the surfaces led to two different types of damage. The LT surface damage occurred in the form of grain exfoliation, while the LS surface had the perpendicular IGC damage from the exposed surface. The LT surface exhibited a more uniform exfoliation effect, a behavior which was expected and identified on small scale samples. The LS surface, however, exhibited regions that were corroded easily and regions that were more corrosion resistant. This effect correlated with the increasing the sensitization time (sensitization level) in the environmental chamber. Figure 6 (a) shows that after 48 hours of LT surface corrosion, the surface with 21 mg/cm^2 DoS was unaffected by corrosion, a response that is similar to the small-scale testing and that the 49 mg/cm^2 DoS led to exfoliation damage across the exposed surface. The LT sample with 21 mg/cm^2 DoS after 120 hours of corrosion was also resistant to corrosion exfoliation. Figure 6 (b) shows that the LS surface was more damaged—a result similar to that obtained in the small-scale testing. The two samples on the left in Figure 6 (b) show that both surfaces were experiencing minimal corrosion damage. Figure 6 (b) also contains images (two samples on the right) showing the corrosion-susceptible and corrosion-resistant regions present due to a higher sensitization level.

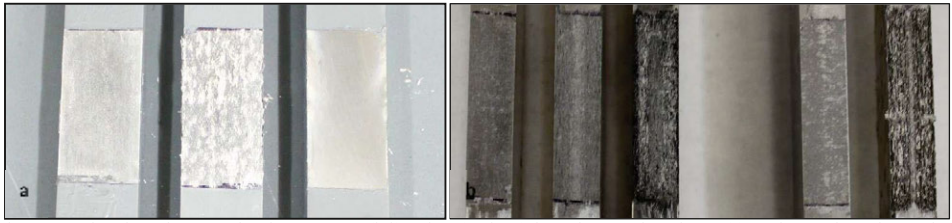

Figure 6. Surface dependent corrosion damage on LT (left) and LS (surfaces) for 48 hours and 120 hours. (a) LT damage for 48 hours of 21 mg/cm2 and 49 mg/cm^2 (left) and 120 hours of 21 mg/cm^2 DoS. (b) LS surface damage for 48 hours with 21 mg/cm^2, 49 mg/cm^2, and 53 mg/cm2 (left) and 120 hours with 21 mg/cm^2 and 49 mg/cm^2.

The images in Figure 6 help show that the LT surface experienced more exfoliation and/or thickness loss as the primary damage mode, while the LS surfaces experienced a more cross-sectional, multi-faceted, corrosion susceptible-resistant-susceptible (C-SRS) damage affected zone. With this in mind, tensile test specimens were measured post corrosion and pre-mechanical testing to help quantify the changes in cross-sectional area which directly affect mechanical properties. Table II summarizes the LT section thickness losses and section area changes prior to and after corrosion. As expected, with an increase in sensitization level, the LT thickness loss (reduction) increased.

Table II. LT surface thicknesses and cross-section area changes for different DoS and corrosion times.

DoS (mg/cm^2)	Surface	Corrosion Time (hours)	LT Thickness Loss (mm)	Original Area (mm^2)	Post-Corr. Area (mm^2)
61	LT	24	0.30	79.69	75.81
66	LT	24	0.33	79.88	75.34
20	LT	48	0.07	79.32	78.44
49	LT	48	0.21	79.44	76.62
53	LT	48	0.21	81.47	78.10
66	LT	48	0.76	81.66	74.59
20	LT	120	0.08	78.06	76.99
49	LT	120	0.71	79.38	70.34
66	LT	120	1.84	81.98	58.37

Table III contains similar properties for the sensitized and corroded LS surface dog bones. As the sensitization level increased, at 48 hours of corrosion, the LS resistant region of the C-SRS decreased, along with the post-corrosion section area. For 120 hours of corrosion, the LS resistant region decreased significantly to 1.11 mm, which is a 17.6% region that was not corroded. As the sensitization level increased, the susceptible region width decreased, thus contributing to the larger changes in cross-sectional areas.

Table III. LS resistant region thicknesses and cross-section area changes for different DoS and corrosion times.

DoS (mg/cm^2)	Surface	Corrosion Time (hours)	LS Resistant Thickness (mm)	Original Area (mm^2)	Post-Corr. Area (mm^2)
20	LS	48	6.31	79.13	79.00
49	LS	48	2.32	78.75	78.28
53	LS	48	2.29	80.45	76.68
20	LS	120	6.30	79.00	78.75
49	LS	120	1.11	78.37	68.63

Mechanical Testing

Elastic Moduli After completion of post-corrosion thickness and cross-section dimension measurements, the tensile tests were conducted. Figure 7 shows plots containing original section area (OSA) and post-corrosion section area (PCSA) elastic moduli values. The OSA plot on the left shows elastic modulus when cracks and width/thickness dimensional changes were not taken into account prior to mechanical testing. The PCSA plot on the right shows elastic moduli after cross-section area changes occurred, thus giving a more true representation of property changes. PCSA elastic moduli values did not account for IGC damage beyond the cross-section area changes. Material that is sensitized only (which is considered as corrosion time of 0 hours) lost elasticity as DoS increased, if 20 mg/cm^2 was excluded. The LT surface elastic moduli did not have a noticeable trend, however for both OSA and PCA values, the LS surface saw a decrease in elastic moduli for DoS of 49 mg/cm^2 and 53 mg/cm^2.

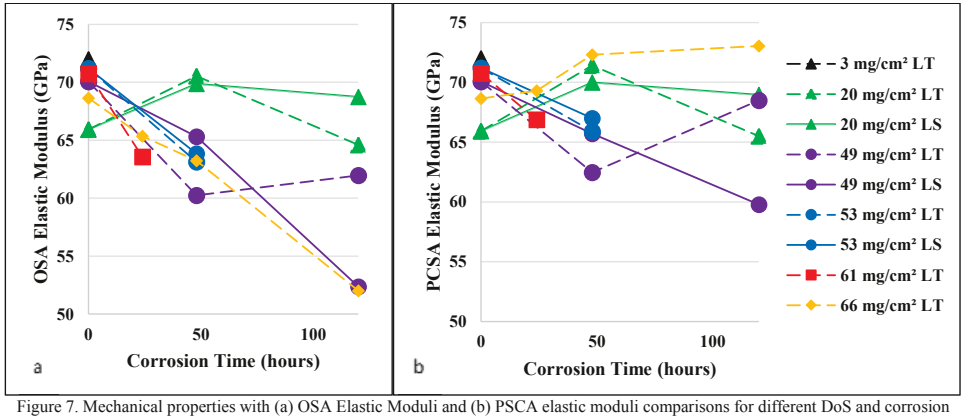

Figure 7. Mechanical properties with (a) OSA Elastic Moduli and (b) PSCA elastic moduli comparisons for different DoS and corrosion time combinations for LT and LS surfaces.

0.2% Offset Yield Strength Sensitization and corrosion time both played a role in the reduction of yield strength values for LT and LS surfaces. Figure 8 shows the OSA and PCSA 0.2% offset yield strengths for various sensitization and corrosion time combinations. As DoS increased, the 0.2% offset yield strength values decreased and as corrosion time increased, the values dropped further. At a DoS up to 20 mg/cm^2, the material is corrosion resistant with, lower thickness losses and a lack of exfoliation damage. At the fully sensitized state of 49 mg/cm^2 or higher DoS, the yield strength values dropped as corrosion time increased. For these higher DoS levels, the LT and LS surfaces both attributed individually to the loss in yield strength integrity. From the as-received state (non-sensitized and non-corroded), DoS of 66 mg/cm^2 caused a 19% reduction in yield strength from 280 MPa to 226 MPa , while 120 hours of LT surface corrosion led to another 7% decrease to 208 MPa or 26% total decrease.

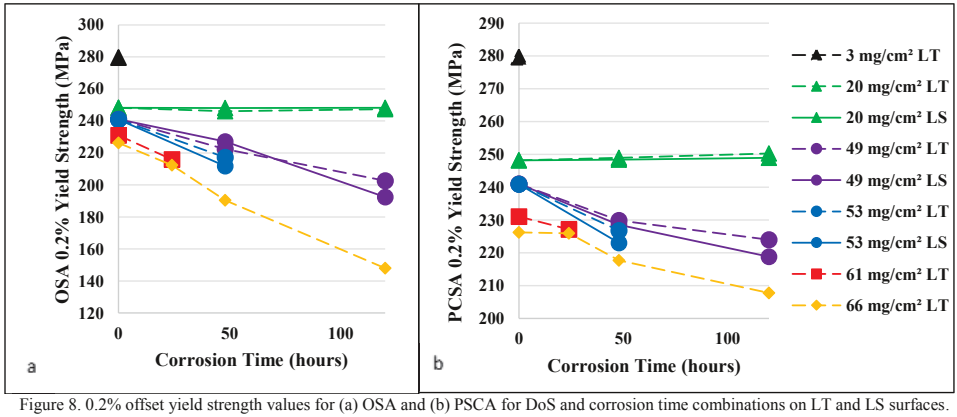

Figure 8. 0.2% offset yield strength values for (a) OSA and (b) PSCA for DoS and corrosion time combinations on LT and LS surfaces.

Ultimate Strength Due to the changes in the LT and LS surfaces as corrosion time increased, the ultimate tensile strengths decreased for samples with a DoS of 49 mg/cm² or higher. Figure 9 shows plots of OSA and PCSA ultimate tensile strength values for different DoS and corrosion time combinations. As expected, when material was just sensitized only, the ultimate tensile strength decreased. At a DoS of 20 mg/cm² or less, the ultimate tensile strength stays relatively unaffected by LT or LS surface corrosion. It should be noted that at 49 mg/cm² or higher DoS, that the LS surface corrosion caused a larger reduction in ultimate tensile strength that LT surface. From the as-received state, the largest change in ultimate tensile strength without corroding material occurred with a DoS of 66 mg/cm² and the value decreased by 5% from 356 MPa to 338 MPa and 120 hours of LT corrosion led to further decrease of 9%, or a 14% decrease from the as-received state.

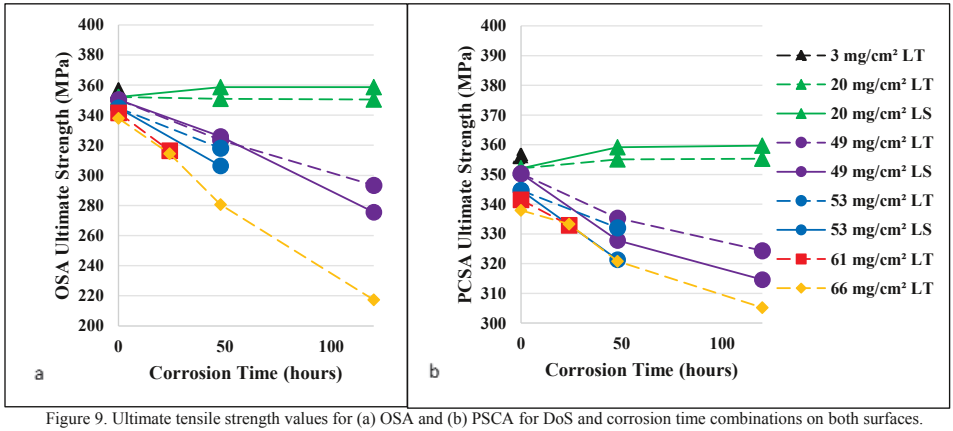

Figure 9. Ultimate tensile strength values for (a) OSA and (b) PSCA for DoS and corrosion time combinations on both surfaces.

% Area Reduction The last mechanical property gathered from tensile testing the sensitized and corroded dog bones is the reduction in area between the original cross-section areas and post-corrosion cross-section area when compared to the post-tensile test cross-section area. Figure 10 contains plots for comparisons between the OSA and PCSA versus the post-tensile section area (PTSA). A % reduction in area was noticeable in most cases after 48 hours of corrosion, however there is no trend with sensitization level and % area reduction. The LT surface corroded sample with DoS 66 mg/cm² saw the largest % area reduction of 37% when original section was compared to PTSA. The plot on the right in Figure 10 contains a lower reduction in cross-section area when comparing PCSA and PTSA. When comparing PCSA and PTSA, the sample with DoS of 20 mg/cm² had a 17% reduction in cross section area.

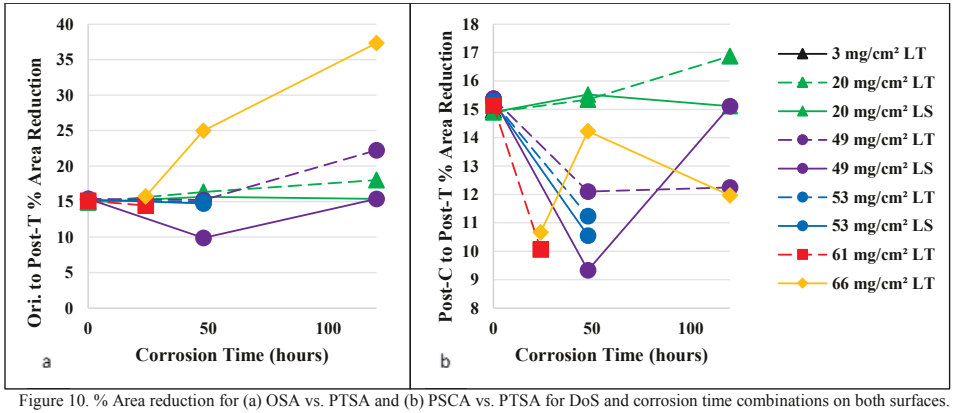

Figure 10. % Area reduction for (a) OSA vs. PTSA and (b) PSCA vs. PTSA for DoS and corrosion time combinations on both surfaces.

Failure Mode Tensile dog bones were all tested under the same conditions. Samples failed with one of two shearing mechanisms--a single shear plane at 45° angle incline or 45° angle double inclined shear planes. All corroded LT samples experienced the single shear plane failure. Most LS corroded samples had the single shear plane failure, while the sample corroded for 120 hours with DoS of 49 mg/cm² failed with

the double shear planes. This LS sample had a very thin resistant zone (1.11 mm) of the C-SRS region, so the sample had double shear plane failure. LS samples higher than 49 mg/cm² and 48 hours of corrosion had larger resistant zones and experienced the single shear plane failure.

Conclusions

Small scale and tensile test samples were corroded at various times to achieve different damage morphologies for DoS values ranging from 3 mg/cm^2 to 66 mg/cm^2. The LT surface was less susceptible to corrosion damage due to less β coverage along grain boundaries and resulted in an exfoliation and thickness loss damage type than the LS surface. The LS surface developed more perpendicular IGC damage and a larger thickness loss. The thickness loss and crack damage increased with sensitization level and corrosion time for both LT and LS surfaces.

The tensile test corrosion samples experienced different changes in cross-sectional area, which led to differences in mechanical properties for LT and LS surfaces. The LT surface saw a more uniform exfoliation damage, thus only received a thickness loss damage type to the corroded surface. The LS surface contained a C-SRS damage affect zone and this led to a reduction in mechanical properties as well. No trend was seen with respect to elastic modulus and % reduction in area for the different DoS and corrosion time combinations used in this study. Trends were noted for the yield strength and ultimate tensile strength properties.

At a DoS of 20 mg/cm², no degradation of yield strength or ultimate tensile strength occurred due to exposure on either LT or LS surfaces even after 120 hours in a corrosive environment. At a DoS of 49 mg/cm² or higher, degradation of yield strength and ultimate tensile strength occurred as a result of exposure on both LT and LS surfaces. The largest change in mechanical property loss occurred as a result of LT surface corrosion at a DoS 66 mg/cm² for 120 hours, leading to a 26% yield strength and 14% ultimate tensile strength reduction from the as-received state of AA5083-H116. In the cases tested in this study, the LS surface corrosion damage led to a larger decrease in mechanical properties than the LT surface corrosion damage. For changes in yield strength, the sensitization level contributed the most to reduction in property values, not the thickness loss. For the ultimate tensile strength, thickness reduction (LT surface) and C-SRS (LS surface) played a larger role than DoS.

References

1. J.L. Searles, P.I. Gouma, and R.G. Buchheit, "Stress Corrosion Cracking of Sensitized AA5083 (Al-4.5MG-1.0Mn)," *Metallurgical and Materials Transactions A*, 32A (2001), 2859-2867.

2. A. J. Davenport, Y. Yuan, R. Ambat, B.J. Connolly, M. Strangwood, A. Afseth, and G. Scamans, "Intergranular Corrosion and Stress Corrosion Cracking of Sensitized AA5182," *Materials Science Forums*, 519-251 (2006), 641-646.

3. R.H. Jones, D.R. Bear, M.J. Danielson, and J.S. Vetrano, "Role of Mg in the Stress Corrosion Cracking of an Al-Mg Alloy," *Metallurgical and Materials Transactions A*, 32A (2001), 1699-1711.

4. G. Song, A.Atrens, D. Stjohn, J. Nairn, Y. Li, "The Electrochemical Corrosion of Pure Magnesium in 1 N NaCl," *Corrosion Science* 39 (5) (1997), 855-875.

5. G. Song, A. Atrens, M. Dargusch, "Influence of Microstructure on the Corrosion of Diecast AZ91D," *Corrosion Science*, 41 (1999), 249-273.

6. C.T. Kwok, S.L. Fong, F.T. Cheng, H.C. Man, "Pitting and Galvanic Corrosion Behavior of Laser-Welded Stainless Steels," *Journal of Materials Processing Technology*, 176 (2006), 168-174.

7. R. Venugopalan, C. Trapanier, "Assessing the Corrosion Behavior of Nitinol for Minimally-Invasive Device Design" *Min Invas Ther & Allied Technol*, 9 (2) 2000, 67-74.

8. C. Trapanier, X.Y. Gong, T. Ditter, A. Pelton, "Effect of Wear and Crevice on the Corrosion Resistance of Overlapped Stents," *Proceedings of the International Conference on Shape Memory and Superplastic Technologies,* (2006), 265-275.

9. T. Marlaud, B. Malki, A. Deschamps, B. Baroux, "Electrochemical Aspects of Exfoliation Corrosion on Aluminum Alloys: The Effects of Heat Treatment," *Corrosion Science*, 53 (2011), 1394-1400.

10. A. Bolouri, C.G. Kang, "Study on Dimensional and Corrosion Properties of Thixoformed A356 and AA7075 Aluminum Bipolar Plates for Proton Exchange Membrane Fuel Cells," *Renewable Energy*, 71 (2014), 616-628.

11. M.L. Lim, S. Jain, R.G. Kelly, and J.R. Scully, "Intergranular Corrosion Penetration in AA5083 as a Function of Electrochemical and Metallurgical Conditions," *ECS Transactions*, 41 (25) (2012), 177-191.

12. I.N.A. Oguocha, O.J. Adigun, S. Yannacopoulos, "Effect of Sensitization Heat Treatment on Properties of Al-Mg alloy AA5083-H116," *Journal of Material Science*, 43 (2008), 4208-4214.

The Effect of Initial Microstructure on the Mechanical Properties of Bi-lamellar Ti-6Al-4V

Yan Chong[1], Nobuhiro Tsuji[1,2]
[1]Department of Materials Science and Engineering, Kyoto University, Kyoto, Japan
[2]Elements Strategy Initiative for Structural Materials (ESISM), Kyoto University, Kyoto, Japan

Keywords: bi-lamellar microstructure, Ti-6Al-4V, initial microstructure, uniform elongation

Abstract

Bi-lamellar microstructure can be realized by intercritical annealing followed by rapid cooling of lamellar microstructure in titanium alloys. The mechanical properties can be improved by the introduction of fine secondary α lamellars in-between coarse α lamellars in the bi-lamellar structures. In this study, the influence of initial microstructures, including martensite microstructure and lamellar microstructure, on the resulting bi-lamellar microstructures as well as its mechanical properties was systematically investigated. Colony size was significantly reduced by starting from martensite microstructure compared with that started from lamellar microstructure. Consequently, both yield strength and uniform elongation of bi-lamellar microstructure were improved. The improvement was explained by decreased slip length based on "effective" grain size of two different scales, i.e., α lamellar thickness and α colony size. In addition, the phenomenon of crack propagation through secondary α lamellar with certain orientation is discussed.

1. Introduction

High strength titanium alloys used for structural applications are generally two-phase (α+β) alloys, among which Ti-6Al-4V alloy is the most widely used for applications such as aerospace. The alloy is reported to account for more than 50% of the worldwide titanium tonnage [1]. By various kinds of thermal or thermo-mechanical treatments, three different microstructures, i.e., lamellar microstructure, bimodal microstructure and equiaxed microstructure, can be obtained in Ti-6Al-4V. G. Lutjering has reviewed the relationship between thermo-mechanical processing parameters and the microstructures

as well as mechanical properties of (α+β) titanium alloys [2,3]. Generally, hot deformation has to be applied in order to break the lamellar microstructure into equiaxed or bimodal microstructures. This process is termed as globularization. Numerous investigations have been carried out with respect to the hot deformation behavior and globularization kinetics as well as globularization mechanism in the last 30 years [4].

It is well known that during the β-α phase transformation, the Burgers orientation relationship having $\{0001\}_\alpha//\{110\}_\beta$, $<11\text{-}20>_\alpha//<111>_\beta$, is maintained in titanium alloys [5]. The typical lamellar microstructure of titanium alloys is comprised of colonies with different orientations. The lamellars inside the same colony have the same orientation. It is believed that in subsequent plastic deformation, the effective slip length in lamellar microstructure is the colony size as the lamellar boundary within an identical colony is semi-coherent and possesses little resistance to dislocation glide. Therefore smaller colony size is always desirable for better mechanical properties.

One of the effective ways to decrease colony size, especially in the cast titanium alloys where hot deformation is inapplicable, is to introduce secondary α lamellar into the coarse lamellar microstructure. This is the so-called bi-lamellar microstructure termed by G. Lutjering [2,3,6]. It has been proved that the bi-lamellar microstructure is beneficial for nearly all the mechanical properties, including tensile strength, ductility, fatigue and creep.

However, the bi-lamellar microstructure has not attracted much attention as well as systematical investigations. Meanwhile, limited investigations on bi-lamellar microstructure were carried out on samples only with lamellar initial microstructure. No research has been done on bi-lamellar microstructure starting from martensite microstructure. The reduced colony size in the starting microstructure is believed to have a positive influence on the mechanical properties as well as the fracture behavior for bi-lamellar microstructure. That is the main scope of present study.

2. Experimental procedures

The bulk chemical composition of the as received Ti-6Al-4V billet used in this study was Ti-6.29Al-4.35V-0.155O-0.225Fe (in mass%). Samples cut from the billet were solution treated at 1050°C for 30min followed by either water quenching or furnace cooling. The resulting microstructures are shown in Fig. 1. The microstructure of the water quenched sample is martensite, which is comprised of thin α' with different orientations. Therefore the colony size for martensite microstructure is nearly the same

as the thickness of α' . In contrast, the microstructure of the furnace cooled sample is typical lamellar microstructure. The thickness of the α-lamellar is around 10μm and the colony size is much larger than that of martensite microstructure.

In order to get bi-lamellar microstructure, both samples with martensite and lamellar microstructures were annealed at 930°C for 1 hour followed by water quench. At the same time, samples with martensite microstructure were also annealed at 870 and 900°C for comparison. All the heat treatments were carried out in a vacuum atmosphere to avoid oxidation. The vacuum degree was kept below 4×10^{-3} and temperature fluctuations during the heat treatment were kept within 5°C.

After the heat treatments, the specimens were ground and polished following standard metallographical methods. Electrical polishing in a solution of 10% perchloric acid and 90% methanol at the temperature of -30°C was conducted to reveal the dual-phase microstructure. Backscattered electron microscope (BSE) investigations were conducted using a JEOL 7800F scanning electron microscope (SEM). The accelerating voltage for the BSE experiments as 15kV. Electron backscattered diffraction (EBSD) investigations were conducted using TSL system attached to a field emission gun SEM (JEOL 7100F). The accelerating voltage was 15kV. The collected data were analyzed using OIM software.

Sheet-type tensile samples with a dog-bone shape were cut from the heat-treated samples. Tensile tests were conducted on Shimadzu AG-X plus system with a strain rate of $8.3\times10^{-4}s^{-1}$. Two or three samples were tested for each heat treatment.

3. Results and discussion

3.1 The effect of initial microstructure on resulting bi-lamellar microstructure

The microstructures of samples after annealing are shown in Fig. 2. The BSE images of sample with martensite initial microstructure are shown in Fig. 2(a) and (b). The BSE images of sample with lamellar initial microstructure are shown in Fig. 2(c) and (d). Both microstructures are typical bi-lamellar microstructures, with secondary α-lamellar observed in-between the coarse α-lamellar, as shown in Fig. 2(b) and (d). The only difference between the two bi-lamellar microstructures is that the colony size of the coarse lamellar in sample starting from martensite microstructure is smaller than that of sample starting from lamellar microstructure. In other words, the difference in colony size for two initial microstructures are preserved after annealing. The difference in colony size for the two bi-lamellar microstructures is further illustrated by EBSD

characterization. The inversed pole figure (IPF) maps and image quality (IQ) maps for the two bi-lamellar microstructures are shown in Fig. 3. One thing in common for both microstructures is that the orientations for secondary α-lamellar are random. For the bi-lamellar microstructure starting from martensite microstructure, random orientations for the coarse α-lamellar are also observed. While in the bi-lamellar microstructure starting from lamellar microstructure, the coarse α-lamellars have limited orientations.

The samples with martensite initial microstructure were also annealed at different temperatures. The BSE images of the bi-lamellar microstructures by annealing martensite microstructure at 870, 900 and 930°C are shown in Fig. 4. It is shown that with decreased annealing temperature, the volume fraction of the coarse α-lamellars is increased. However, the colony size for the coarse α-lamellar remains nearly the same.

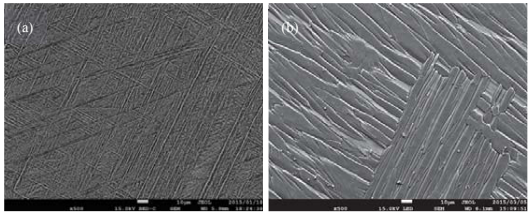

Fig.1 Two different initial microstructures (a) martensite, (b) lamellar

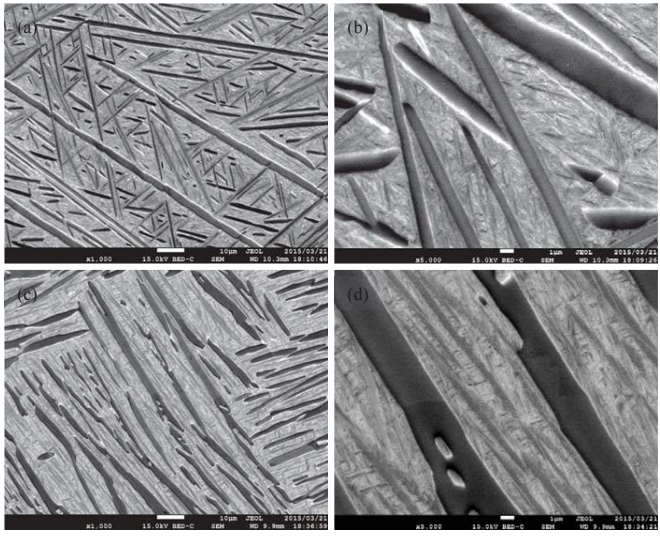

Fig.2 SEM images of bi-lamellar microstructures with different initial microstructures (a), (b) starting

with martensite microstructure; (c), (d) starting with lamellar microstructure

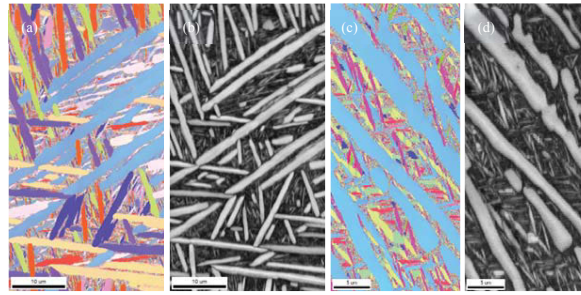

Fig. 3 The EBSD images of bi-lamellar microstructures (a), (b) IPF and IQ map for bi-lamellar starting from martensite microstructure; (c), (d) IPF and IQ maps for bi-lamellar starting from lamellar microstructure

3.2 The effect of initial microstructure on mechanical properties of bi-lamellar microstructure

The mechanical properties of different bi-lamellar microstructures were tested by tensile tests at room temperature. The results including yield strength and uniform elongation are listed in Table I. Compared with bi-lamellar microstructure starting from lamellar microstructure, the bi-lamellar microstructure starting from martensite microstructure has similar yield strength, but much larger uniform elongation. Among the bi-lamellar microstructures starting from martensite microstructure but with different annealing temperatures, there is little difference in yield strength as well as uniform elongation despite of the difference in coarse α-lamellar volume fractions. Therefore it is supposed that the improvement of uniform elongation in bi-lamellar microstructure starting from martensite microstructure compared that of starting from lamellar microstructure is intrinsical. Small variations in the annealing temperature do not affect the uniform elongation in bi-lamellar microstructures starting from martensite microstructure.

The microstructures of cross section surface near the cracks are shown in Fig. 5. For the bi-lamellar microstructure starting from martensite microstructure, the cracks are generally formed at the interface between coarse α-lamellar and transformed β. After that, the cracks propagate along the interface and some of them terminate when meeting another α-lamellar with different orientations. On the other hand, in the bi-lamellar microstructure that starts from lamellar microstructure, the situation is totally different. The cracks form and propagate across the coarse α-lamellar and transformed β.

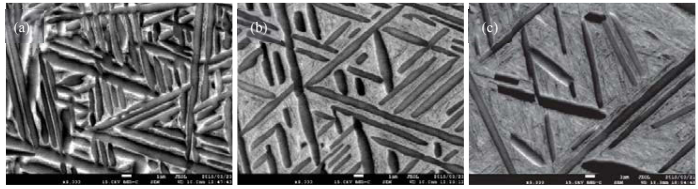

Fig. 4 Bi-lamellar microstructures annealed at different temperatures, all the samples are with martensite initial microstructures (a) 870°C, (b) 900°C, (c) 930°C

Table I The mechanical properties of different bi-lamellar microstructures

	From lamellar(930°C)	From martensite(930°C)	From martensite(900°C)	From martensite(870°C)
Yield strength	1075MPa	1146MPa	1132MPa	1087MPa
Uniform elongation	3.8%	8.2%	9.4%	9.5%

3.3 Discussion on the microstructure and mechanical property relationship

In (α+β)-titanium alloys, a fully lamellar microstructure is characterized by high fatigue crack propagation resistance and high fracture toughness. But such microstructure generally suffers from low ductility and uniform elongation, which limit its application. The uniform elongation of lamellar Ti-6Al-4V is below 5%. In the present study, the uniform elongation of the bi-lamellar microstructure that starts from lamellar microstructure is still quite low (only 3.8%). However, the uniform elongation of the bi-lamellar microstructure that starts from martensite microstructure is much higher (around 9%). This provides a novel microstructure design concept for lamellar microstructure to improve the ductility, although the detailed mechanism is still not clear now.

Due to the existence of secondary α-lamellars with different orientations inside the transformed β area, dislocation slip tend to initiate firstly inside the coarse α-lamellar. When the dislocations inside the coarse α-lamellar move to the interface between coarse α-lamellar and transformed β area, the movement is hindered and therefore stress localization arose at the interface. The stress localization will cause shear bands inside the transformed β area, which will activate slip system in the adjacent coarse α-lamellar. In the case of bi-lamellar microstructure with martensite initial microstructure, the adjacent coarse α-lamellar generally has different orientations. The different orientation of the adjacent

α-lamellar will make the activation of slip system different. However, in the bi-lamellar microstructure with lamellar initial microstructure, the adjacent coarse α-lamellar generally has the same orientation, which will make the activation of slip system easier. This might to some extent explain the difference in uniform elongation between bi-lamellar microstructures starting from martensite and lamellar microstructure.

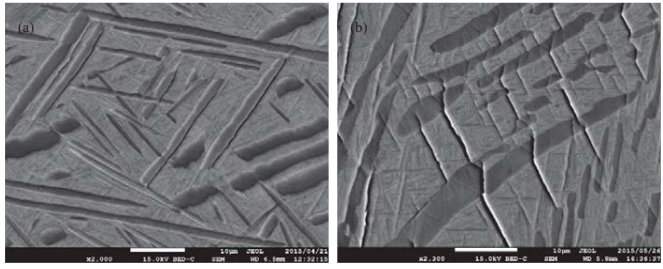

Fig. 5 The microstructure near tensile fractured surface (a) bi-lamellar microstructure with martensite initial microstructure, cracks are generally formed along the coarse α-lamellar, (b) bi-lamellar microstructure with lamellar initial microstructure, cracks propagate across the coarse α-lamellar and transformed β area.

4. Conclusions

(1) Bi-lamellar microstructure can be obtained by annealing in the two phase region followed by rapid cooling in both martensite and lamellar initial microstructure. The colony size for the coarse α-lamellar is much smaller in the bi-lamellar microstructure starting from martensite microstructure than that starting from lamellar microstructure.

(2) The yield strength of bi-lamellar microstructures start from different initial microstructures are similar. But the uniform elongation of the bi-lamellar microstructure starts from martensite microstructure is much larger than that starts from lamellar microstructure.

(3) The cracks in the bi-lamellar microstructure that starts from martensite microstructure form and propagate along the coarse α-lamellar. Nevertheless, in bi-lamellar microstructure that starts from lamellar microstructure, cracks form and propagate across the coarse α-lamellar as well as the transformed β area.

Acknowledgements

The authors are grateful to the financial support from Cross-ministerial Strategic Innovation Promotion Program (SIP) supported by The Cabinet Office of Japanese

government and Elements Strategy Initiative for Structural Materials (ESISM) in Kyoto University supported by MEXT, Japan.

References

[1] D. Banerjee and J.C. Williams, “Perspectives on titanium science and technology”, Acta Mater., 61(2013), 844-879.

[2] Gerd Lutjering and James C. Williams, Titanium (Springer, 2003).

[3] G. Lutjering, “Influence of processing on microstructure and mechanical properties of (α+β) titanium alloys”, Mater. Sci. Eng., A243(1998), 32-45.

[4] S.L. Smiatin, V. Seetharaman and I. Weiss, “The thermomechanical processing of alpha/beta titanium alloys”, JOM, 49(1997), 33-39.

[5] W.G. Burgers, “On the process of transition of the cubic-body-centered modification into the hexagonal-close-packed modification of Zirconium”, Physica, 1(1934), 561-586.

[6] G. Wegmann, J. Albrecht, G. Lutjering, et al., “Microstructure and mechanical properties of titanium castings”, Z. Metallkd. 88(1997), 764-773.

Some Steps towards Modelling of Dislocation Assisted Rafting: A Coupled 2D Phase Field – Continuum Dislocation Dynamics Approach

Ronghai Wu[1], Stefan Sandfeld[1]

[1]Institute of Materials Simulation (WW8), Department of Materials Science,
Friedrich-Alexander University of Erlangen-Nürnberg (FAU),
Dr.-Mack-Str. 77, 90762 Fürth, Germany

Keywords: Rafting, Phase field, Continuum dislocation dynamics, Nickel-based superalloy

Abstract

The interaction between edge dislocations and γ' precipitates as in nickel-based superalloys is studied by coupling a phase field model and a 2D continuum dislocation dynamic model. Various stresses, which serve as communicator between dislocations and precipitates, are calculated by an eigenstrain method for both the γ/γ' misfit and the dislocations. Our simulations show how edge dislocations tend to move to and pile up at specific γ/γ' interfaces. The growth of γ' is inhibited at the interface where dislocations are piling up, due to the reduction of elastic energy. The potential of our coupled model for simultaneous microstructure patterning and mechanical property prediction is discussed.

Introduction

Single crystal nickel-based superalloys have been widely used in e.g. turbine blades which operate under extreme conditions: temperatures are very high and are additionally accompanied by strong, sustaining centrifugal forces. One of the common approaches to assess the service performance and to understand the underlying mechanism is based on creep tests. Because in-situ observations of the (dislocation or γ') microstructure cannot easily be conducted, creep experiments usually have to be interrupted at specific representative stages at which then microstructural information can be conveniently obtained ex-situ. Additionally, creep tests are very time-consuming. Despite these two cumbersome aspects, a large amount of information about the deformation behavior and the microstructure of γ/γ' and dislocations have been gained in the past decades [1].
The above mentioned shortcomings strongly motivated the development of modeling and simulation methods for nickel-based superalloys. Phenomenological continuum models for elasto-plastic material behavior have been proposed within the framework of internal variables [2, 3]. Using e.g. the average dislocation density or the γ' size as internal variables one can well fit simulations results to experimental results, which makes these models useful as computational tools for roughly estimating service life and mechanical behavior. However, there is no general consensus regarding the choice of internal variables and detailed microstructural effects as e.g. the interaction between dislocations and precipitates are not directly accounted for in these models. However, it is well accepted

that dislocation associated interactions are one of the key underlying mechanisms during creep deformation: recent molecular dynamic (MD) and discrete dislocation dynamic (DDD) simulations revealed a number of details of the dislocation-precipitate interaction at the γ/γ' interface [4, 5]. For simplicity, in these simulations the γ/γ' microstructure is usually assumed to be static in time. Additionally, dislocation associated creep is a multi-time scale problem because the time-scale on which the γ/γ' evolution takes place is much larger than that of the dislocation flow, which makes the treatment very complicated and computationally expensive from a numerical point of view. However, the problem of multiple length scales becomes much simpler if mesoscale models are used for both the γ/γ' evolution and the plasticity. Pioneering work has been done by coupling phase field models (PFM) for the evolution of the phase microstructure with constitutive plasticity models. E.g. Finel and co-workers [6] coupled a PFM to a viscoplasticity model and successfully reproduced rafting patterns, although their model does not contain any information about dislocation microstructure. Wang and co-workers [7] coupled the Kim-Kim-Suzuki (KKS) model to a strain gradient-based plasticity/phase field model and obtained rafting patterns together with information about dislocations. Strain gradient plasticity methods in general, however, only account for geometrically necessary dislocations (GNDs) and cannot represent the flow of dislocations.
In the present work, we show an alternative approach for coupling a PFM and a continuum model of dislocation dynamics: our PFM has one composition field and is used to describe the evolution of the γ/γ' phase microstructure, while a 2D continuum dislocation dynamics (CDD) model is used to represent fluxes of positive and negative edge dislocations (from which GNDs and SSDs – statistically stored dislocations – could be computed) [8, 9]. We focus especially on the interaction mechanism between the γ' precipitate and dislocations.

Model formulation

The following mathematical conventions and symbols are used: non-bold letters denote scalar or scalar fields, bold letters denote vectors or higher order tensors, non-italics stand for constants or superscript, italics for variables. ∇ and ∇^2 are the spatial gradient operator and the Laplace operator, respectively. The inner product and the double contraction are written as e.g. $\mathbf{a} \cdot \mathbf{b}$ and $\mathbf{A} : \mathbf{B}$, respectively.

Phase field model

We consider a Ni-Al binary system with no distinction of γ' variants. A simple phase field model with normalized composition field c is sufficient in this case:

$$c = \frac{c' - c^{\mathrm{e}}_{\gamma}}{c^{\mathrm{e}}_{\gamma'} - c^{\mathrm{e}}_{\gamma}} \tag{1}$$

where c' is the real composition, c^{e}_{γ} and $c^{\mathrm{e}}_{\gamma'}$ are the equilibrium compositions of γ and γ', respectively. Therefore, $c = 0$ denotes the γ phase and $c = 1$ stands for the γ' phase. The total energy of the system is given in functional form:

$$F = \int_{\mathrm{V}} (f^{\mathrm{bulk}} + f^{\mathrm{grad}} + f^{\mathrm{el}})\,\mathrm{dV} \tag{2}$$

with the energy densities

$$f^{\text{bulk}} = \mathrm{f}_0 c^2(1-c^2), \qquad f^{\text{grad}} = \frac{\lambda}{2} \mid \nabla c \mid^2, \qquad f^{\text{el}} = \frac{1}{2}\boldsymbol{\sigma}^{\text{el}} : \boldsymbol{\epsilon}^{\text{el}} \tag{3}$$

where f_0 is the energy density scale determined by the bulk energy density barrier, λ is the gradient energy density coefficient determined by fitting the calculated interface energy to the experimentally obtained interface energy. The sum of bulk energy and gradient energy gives the calculated interface energy (or chemical energy). The stress $\boldsymbol{\sigma}^{\text{el}}$ and strain $\boldsymbol{\epsilon}^{\text{el}}$ are obtained from solving the mechanical equilibrium equation. We assume that mechanical equilibrium is always reached instantaneously and that body forces from e.g. gravitation etc can be neglected. With this the governing equations are given as

$$\nabla \cdot \boldsymbol{\sigma}^{\text{el}} = \mathbf{0}, \qquad \boldsymbol{\sigma}^{\text{el}} = \boldsymbol{C} : \boldsymbol{\epsilon}^{\text{el}}, \qquad \boldsymbol{\epsilon}^{\text{el}} = \boldsymbol{\epsilon} - (\beta\boldsymbol{\epsilon}^{\text{mis}} + \boldsymbol{\epsilon}^{\text{dis}}) \tag{4}$$

where $\boldsymbol{\epsilon}^{\text{el}}$ is obtained in a small strain context from the additive decomposition of the total strain $\boldsymbol{\epsilon}$ into the elastic and inelastic contributions. The latter can consist of eigenstrains caused by the γ/γ' misfit $\boldsymbol{\epsilon}^{\text{mis}}$ (which is a diagonal tensor), or from dislocations eigenstrains $\boldsymbol{\epsilon}^{\text{dis}}$ (which is an off-diagonal tensor). The interface interpolation function β and stiffness tensor $\boldsymbol{C}$ are given as:

$$\beta = c^3(10-15c+6c^2), \qquad \boldsymbol{C} = \frac{1}{2}(\mathbf{C}_{\gamma'} + \mathbf{C}_{\gamma}) + (\beta - \frac{1}{2})(\mathbf{C}_{\gamma'} - \mathbf{C}_{\gamma}), \tag{5}$$

where $\mathbf{C}_{\gamma'}$ and $\mathbf{C}_{\gamma}$ are the stiffness tensors of the γ' and γ phase, respectively. The interface interpolation function $\beta(c)$ is responsible for the elastic inhomogeneity (with $\beta(c)|_{c=0} = 0$ and $\beta(c)|_{c=1} = 1$). Furthermore, the derivatives $\beta'(c)|_{c=0,c=1} = 0$ and $\beta''(c)|_{c=0,c=1} = 0$ imply that γ and γ' are equilibrium phases from the point of view of elastic energy.
Finally, we assume that the evolution of the γ/γ' phase microstructure is governed by the Allen-Cahn equation:

$$\frac{\partial c}{\partial t} = \mathrm{M}_c \nabla^2 \frac{\delta F}{\delta c}, \tag{6}$$

where M_c governs the interface mobility.

Continuum dislocation dynamics for edge dislocations

We use a continuum dislocation dynamic model for edge dislocations, which is able to distinguish between positive and negative edge dislocation density, ρ^+ and ρ^-. The total density $\rho = \rho^+ + \rho^-$ and excess density $\kappa = \rho^+ - \rho^-$ are derived from that and may change in time. The more commonly used GND and SSD densities can be determined by $\rho^{\text{GND}} = |\kappa|$ and $\rho^{\text{SSD}} = \rho - \rho^{\text{GND}}$, respectively.
The initial density distribution is constructed by superposition of m bundles of dislocations. Each bundle of dislocations is assumed to have the shape of a Gaussian normal distribution with standard deviation σ. Using x_i' as the local coordinate of the ith dislocation bundle in glide direction (cf. Fig.1) the density is given by

$$\rho^{(+\text{or}-)}(x_i') = \frac{\mathrm{N}}{\mathrm{h}\sigma\sqrt{2}} \exp\left(-\frac{x_i'^2}{\sqrt{2}\sigma}\right), \tag{7}$$

where N is the number of discrete dislocations, and h is the height of slip lamella (i.e. averaging height for converting discrete dislocations into a density, see [8]). The initial

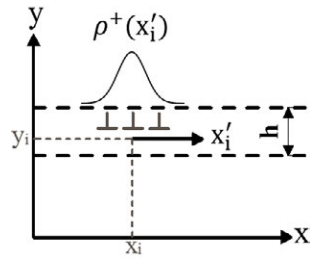

Figure 1: Schematic of the slip system geometry. Each density distribution is located at coordinate (x_i, y_i), which has Gaussian shape in x direction and is constant along the y direction within the averaging height h.

plastic slip distribution s depends on the Burgers vector $\mathbf{b}$ and the motion history (i.e. from which direction initial dislocations have moved into the domain), given by

$$s(x_i') = \begin{cases} \operatorname{sign}(\mathbf{b})\mathrm{b}\int_{x_i'}^{+\infty} \kappa(\tilde{x})\,\mathrm{d}\tilde{x} & \text{if } \rho^{(+\text{or}-)} \text{ moved along positive } x_i' \text{ direction} \\ \operatorname{sign}(\mathbf{b})\mathrm{b}\int_{-\infty}^{x_i'} \kappa(\tilde{x})\,\mathrm{d}\tilde{x} & \text{if } \rho^{(+\text{or}-)} \text{ moved along negative } x_i' \text{ direction} \end{cases} \tag{8}$$

where b is the magnitude of the Burgers vector, sign($\mathbf{b}$) gives the direction of $\mathbf{b}$ in this 1D setting. The resulting initial conditions of dislocation density and plastic slip s are simply the sum of all local fields.
The resulting stress and strain can be obtained by linking the plastic slip to a shear eigenstrain by

$$\boldsymbol{\epsilon}^{\text{dis}} = s\mathbf{M} \qquad \text{with } \mathbf{M} = \frac{1}{2\mathrm{b}}(\mathbf{b}\otimes\mathbf{n} + \mathbf{b}\otimes\mathbf{n}). \tag{9}$$

For simplicity, we assume that neither annihilation nor multiplication take place (which in reality is of course only a rough approximation). The evolution equations for ρ^+, ρ^- and s are given by

$$\frac{\partial\rho^+}{\partial t} = -\partial_x(v\rho^+), \qquad \frac{\partial\rho^-}{\partial t} = \partial_x(v\rho^-), \qquad \frac{\partial s}{\partial t} = \rho v\mathrm{b}. \tag{10}$$

Assuming a linear relationship between stresses and dislocation velocity v, we can write the dislocation velocity law as

$$v = \begin{cases} \frac{\mathrm{b}}{\mathrm{B}}(\tau^{\mathrm{l}} + \tau^{\mathrm{b}} - \tau^{\mathrm{y}}) & \text{if } |\tau^{\mathrm{l}} + \tau^{\mathrm{b}}| > \tau^{\mathrm{y}}, \\ 0 & \text{else} \end{cases} \tag{11}$$

where B is the drag coefficient. τ^{l} is long-range shear stress field resulting from external loading, heterogeneous plastic strain and the γ/γ' misfit. After solving (4), τ^{l} is obtained as the shear component of $\boldsymbol{\sigma}^{\mathrm{el}}$. τ^{b} is the back stress and τ^{y} is the yield stress [10] given by

$$\tau^{\mathrm{b}} = -\mathrm{DGb}\frac{\partial_x\kappa}{\rho}, \qquad \tau^{y} = \frac{\alpha\mathrm{bG}\sqrt{\rho}}{1-\beta} \tag{12}$$

where G is the shear modulus, D $\in [0.6, 1]$ and $\alpha \in [0.2, 0.4]$ are two non-dimensional parameters. The factor $1/(1-\beta)$ in τ^y reflects the experimental observation that dislocations hardly move into γ': $\tau^y \to \infty$ inside the precipitate results in zero velocity, while outside the precipitate τ^y is just the commonly used Taylor-type yield stress, with a smooth transition in between.

Results and discussion

The anisotropy of γ/γ' is around 3, which gives a cubic morphology of γ'. Slip planes are oriented 45^0 to the γ/γ' interfaces. To make the numeric implementation easier, the whole sample is rotated by 45^0. After rotation, the slip system is parallel to the x-axis (see Fig.1) and the γ' shape becomes rhombic. We use periodic boundary conditions and only one representative γ' precipitate at the domain center. Without external loading and plasticity, the precipitate will keep growing in symmetrically rhombic shape until both γ and γ' are at equilibrium composition. To study the dislocation-precipitate interaction and the influence of external loading, we set up different dislocation initial conditions as described in the following two systems.

System 1

We prescribe a column of positive edge dislocations at the left side of the precipitate, as shown in Fig.2 (a) and (d). The morphology of the precipitate can be seen from the contour of the interfaces, because the driving force $M_c \nabla^2 \frac{\delta F}{\delta c}$ for the γ/γ' evolution vanishes inside pure γ and pure γ'. At the intermediate time step, positive edges dislocations move towards the right direction and pile up at the lower-left interface, while negative edge dislocations move to the left, as shown in Fig.2 (e). The reason is that τ^l resulting from the γ/γ' misfit is positive near the lower-left interface, whereas it is negative near the upper-right interface. Because of the dislocation pile-up, the eigenstrains (and thus the local stresses) resulting from the γ/γ' misfit are neutralized to some extend, therefore reducing the elastic energy density and the driving force for the γ' growth at the lower-left interface. The morphology symmetry is broken and the favorable growing direction shifts towards the upper-left direction, as shown in Fig.2 (b). At the quasi-steady state, dislocations are still pinned at the lower-left interface due to the infinite τ^y inside the precipitate, which now has an obvious elongation in diagonal direction, as shown in Fig.2 (c) and (f). A similar preferential dislocation pile-up and precipitate growth also would happen at the other interfaces as a result of dislocation-precipitate interaction (not shown in the present paper).

System 2

As a more realistic system, we define a random dislocation distribution as initial condition (see Fig.3 (a) and (d)). 10 simulations are done, each with and without external stress, and in a post-processing step we averaged over the dislocation density and composition field for visualization purposes. Creep tests are usually done in $\langle 01 \rangle$ direction, which results in a shear stress in $\langle 11 \rangle$ direction. Since only the shear stress is the driving force for the motion of dislocations, this is applied as external shear stress in the rotated

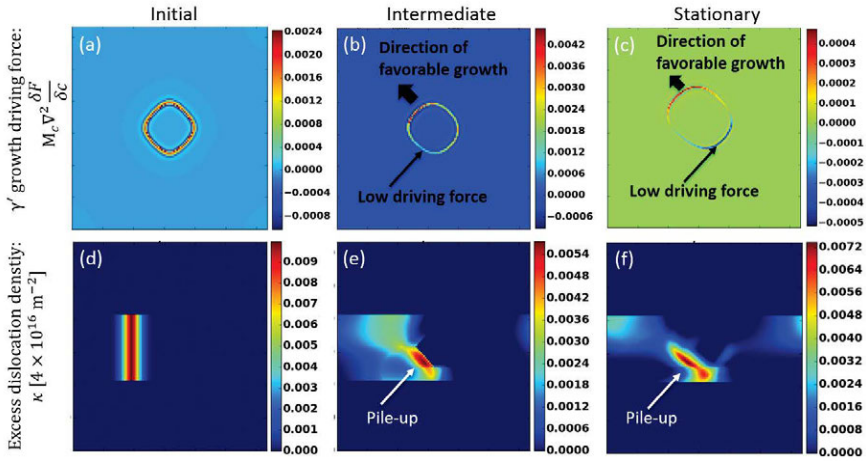

Figure 2: γ' growth driving force (upper row) and excess dislocation density (lower row): (a) and (d) initial condition, (b) and (e) intermediate step, (c) and (f) stationary state.

system. It can be seen that without external stress, the morphology of γ' is basically rhombic and symmetric (see Fig.3 (b) and (e)). The reason is that the dislocation influence on the γ' morphology is essentially determined by the relative dislocation density piling up at each interface and random initial dislocation distributions results in roughly equal amount of dislocation density piling at each interface. However, when there is an additional external loading, dislocations accumulate on average at the lower-left and upper-right interfaces (see Fig.3 (c) and (f)). Dislocation accumulations in the horizontal interfaces, which correspond to the lower-left and upper-right interfaces in the present rotated system, is widely observed in $\langle 10 \rangle$ direction creep tests. Due to the accumulation, the γ' coarsens in the diagonal direction (rafts), which is also widely observed in experiments and is a natural outcome of our model.

Existing MD or DDD simulations for nickel-based superalloys focus more on dislocation evolution, mesoscale PFM simulations more on γ/γ' patterning, while macroscale constitutive models concentrate on mechanical properties. Only few simulations can simultaneously deal with these three aspects. The present PFM-CDD coupled model already can handle dislocation glide and the γ/γ' evolution. Future work will extend the present simple model towards representing e.g. dislocation climb, annihilation and sources. Together with a CDD formulation that also is able to represent dislocations as curved and connected lines [11] this extended model could then reveal creep mechanisms that are of material scientific relevance and that may well predict the mechanical stress-strain behavior under creep conditions without any ad-hoc assumptions.

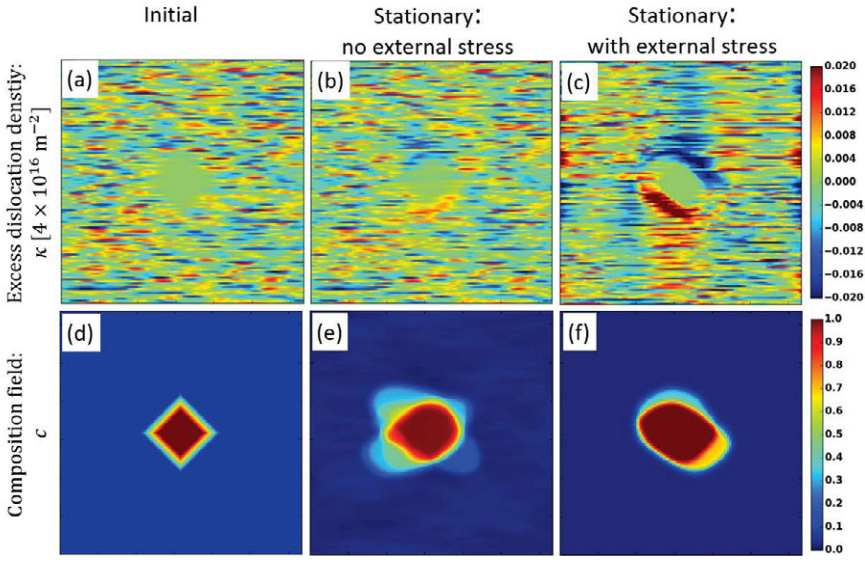

Figure 3: Excess density (top) and normalized composition (bottom) for ensemble averages of 10 systems with random initial dislocation distributions. From left to right: initial condition, stationary state without and with external stress.

Acknowledgements

S. S. gratefully acknowledges financial support from the Deutsche Forschungsgemeinschaft (DFG) through Research Unit FOR1650 'Dislocation-based Plasticity' (DFG grant Sa 2292/1-1).

References

[1] R. C. Reed, *The Superalloys: Fundamentals and Applications*. Cambridge University Press, 2006.

[2] M. F. Horstemeyer and D. J. Bammann, "Historical review of internal state variable theory for inelasticity," *International Journal of Plasticity*, vol. 26, pp. 1310–1334, 2010.

[3] J. Chaboche, "A review of some plasticity and viscoplasticity constitutive theories," *International Journal of Plasticity*, vol. 24, pp. 1642–1693, 2008.

[4] A. Prakash, J. Guenole, J. Wang, and J. Müller, "Atom probe informed simulations of dislocationprecipitate interactions reveal the importance of local interface curvature," *Acta Materialia*, vol. 92, pp. 33–45, 2015.

[5] S. Gao, M. Fivel, A. Ma, and A. Hartmaier, "Influence of misfit stresses on dislocation glide in single crystal superalloys: A three-dimensional discrete dislocation dynamics study," *Journal of the Mechanics and Physics of Solids*, vol. 76, pp. 276–290, 2015.

[6] A. Gaubert, Y. Le Bouar, and A. Finel, "Coupling phase field and viscoplasticity to study rafting in ni-based superalloys," *Philosophical Magazine*, vol. 90, pp. 375–404, 2010.

[7] N. Zhou, "Simulation study of directional coarsening (rafting) of γ' in single crystal Ni-Al," 2008.

[8] S. Sandfeld, M. Monavari, and M. Zaiser, "From systems of discrete dislocations to a continuous field description: stresses and averaging aspects," *Modelling and Simulation in Materials Science and Engineering*, vol. 21, pp. 1–22, 2013.

[9] M. Zaiser and S. Sandfeld, "Scaling properties of dislocation simulations in the similitude regime," *Modelling and Simulation in Materials Science and Engineering*, vol. 22, pp. 1–20, 2014.

[10] I. Groma, F. F. Csikor, and M. Zaiser, "Spatial correlations and higher-order gradient terms in a continuum description of dislocation dynamics," *Acta Materialia*, vol. 51, pp. 1271–1281, 2003.

[11] T. Hochrainer, S. Sandfeld, M. Zaiser, and P. Gumbsch, "Continuum dislocation dynamics: towards a physical theory of crystal plasticity," *Journal of the Mechanics and Physics of Solids*, vol. 63, pp. 167–168, 2014.

EFFECT OF HEATING TYPES ON THE UNDERCOOLED SOLIDIFICATION MICROSTRUCTURE OF $Co_{76}Sn_{24}$ EUTECTIC ALLOY

Tong Guo[1], Jun Wang[1*], Xiaoxing Qiu[1], HongChao Kou[1], Jinshan Li[1]

[1]State Key Laboratory of Solidification Processing;
Northwestern Polytechnical University, Xi'an, Shaanxi 710072, China

Keywords: Heating types, Bulk undercooling, Primary phase, Anomalous eutectic

Abstract

Melt processing is implemented on $Co_{76}Sn_{24}$ eutectic alloy through different heating types including induction heating and resistance heating to prepare samples with same undercooling. Effect of heating types on the undercooled solidification microstructure has been studied by observation and analysis of the microstructure. Results indicate that induction heating makes the primary phase refined, the volume fraction of primary phase increased and anomalous eutectic easier to form when compared with resistance heating under same undercooling.

Introduction

A number of studies have shown that melt processing can be used to control solidification microstructure [1]. However, many researchers neglect the influence of heating types on the melt during the studies of melt processing especially when the following solidification is non-equilibrium. The non-equilibrium solidification of undercooled melt has been a widely used method to produce supersaturated solid solution, amorphous, quasicrystal or nano-crystalline structure, which has intrigue researchers' particular interest [2, 3, 4]. Thus, effect of heating types on the undercooled solidification microstructure, namely non-equilibrium solidification microstructure, must be clarified. As is known to all that different heating types have different means of heat transmission and additional disturbance to the melt. Hence, the subsequent nucleation, solidification and ultimate microstructure would be profoundly affected undoubtedly. Luo et al. have studied melt overheating treatment for Al-18%Si alloy with resistance furnace and induction furnace. Result shows that the refinement effect of the primary Si phase heated by induction furnace is better than the resistance furnace, but the roundness of primary Si phase is slightly poor and its volume fraction decreases [5]. Zhang et al. employed the spiral silicon-carbon tube heating and medium frequency induction heating to study the influence of heating method on directional solidification microstructure of AZ31 magnesium alloy. The result shows that medium frequency induction heating is favorable to obtain good microstructure [6]. In order to further understand the difference between induction heating and resistance heating as well as throw light on the specific relation between heating types and non-equilibrium solidification, induction heating and resistance heating are adopted to prepare undercooled $Co_{76}Sn_{24}$ solidification samples which have the same undercooling. Comparison of the microstructure with

* Corresponding authors: Tel.:+86 29 88460568; fax:+86 29 88460294; E-mail: nwpuwj@nwpu.edu.cn

same undercooling is executed and influence of different heating types on solidification is demonstrated.

Materials and Methods

The master alloy samples with nominal composition $Co_{76}Sn_{24}$ (at.%) are prepared from Co (99.99 wt.% purity) and Sn (99.99 wt.% purity) through vacuum induction melting. Each alloy is melted four times in order to obtain homogeneous ingots. The ingots are cut into samples massing about 2 g for the undercooling experiments. The undercooling experiment is executed with the method of glass fluxing by using induction heating equipment and resistance heating equipment. B_2O_3 is chosen as the glass slag and dehydrated in advance at 800 ^oC for 6 hours. Undercooled samples with a series of undercooling (30 ^oC, 40 ^oC, 58 ^oC, 85 ^oC, 116 ^oC, 154 ^oC, 202 ^oC, 231 ^oC) are prepared on both induction heating equipment and resistance heating equipment. Then the samples are cross-sectioned and polished for observation of microstructure under SEM. As there is no incubation period during the solidification process for all the undercooled samples, overheating temperature has no influence on the solidification microstructure when samples possess the same undercooling. In other words, heating type is the only variable factor in this experiment.

Results

1. Microstructure of Master Alloy under Near Equilibrium Condition

The microstructure and XRD pattern of $Co_{76}Sn_{24}$ alloy solidified under near equilibrium condition are presented in Fig. 1. As is shown in Fig. 1(a), the equilibrium microstructure consists of lamellar eutectic completely, which evident that the composition of ingots is accurate. Fig. 1(b) indicates that the crystal phases in $Co_{76}Sn_{24}$ alloy solidified at near equilibrium are εCo and βCo_3Sn_2.

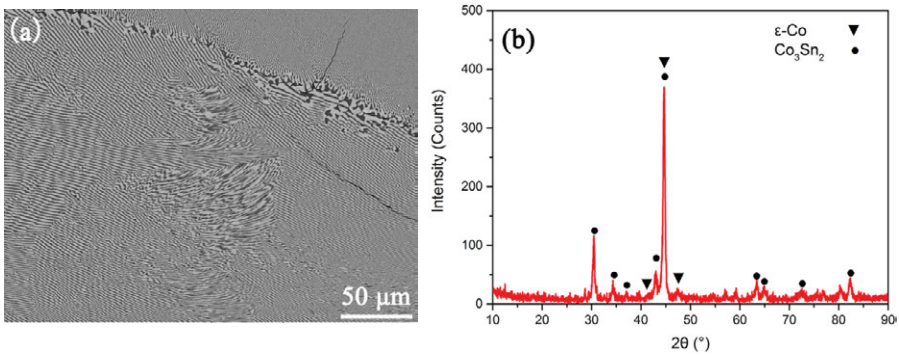

Fig. 1. (a) Equilibrium solidification microstructure and (b) XRD pattern of $Co_{76}Sn_{24}$ alloy.

2. Microstructure Between 30 $^oC \leq \Delta T \leq 58$ ^oC

Fig. 2 are the SEM images when all the solidification microstructure under two kinds of heating types consists of primary αCo and lamellar eutectic. However, difference appears when comparing microstructure with the same undercooling of two kinds of heating types. The volume of each primary αCo in the microstructure of resistance heating is larger than that in the microstructure of induction heating while the quantity of primary αCo in the microstructure of resistance heating is less than that in the microstructure of induction heating.

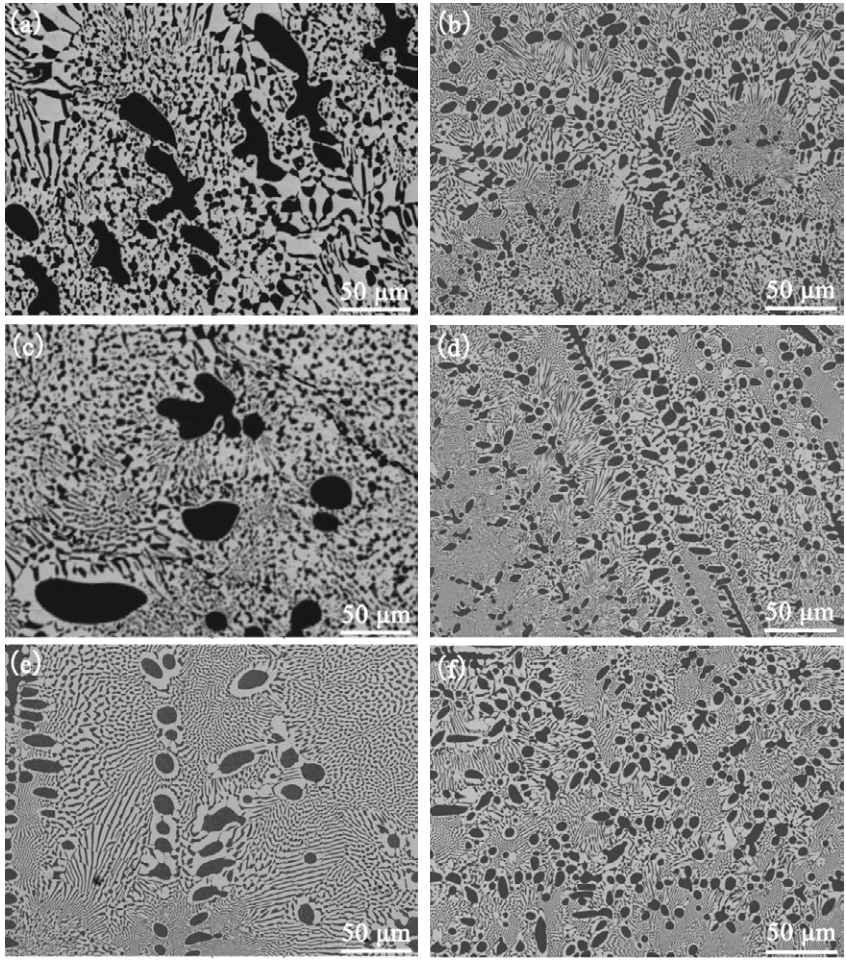

Fig. 2. Microstructure of $Co_{76}Sn_{24}$ eutectic alloy between 30 ^{o}C≤ΔT≤58 ^{o}C. (a) Resistance heating, ΔT=30 ^{o}C; (b) Induction heating, ΔT=30 ^{o}C; (c) Resistance heating, ΔT=40 ^{o}C; (d) Induction heating, ΔT=40 ^{o}C; (e) Resistance heating, ΔT=58 ^{o}C; (f) Induction heating, ΔT=58 ^{o}C.

3. Microstructure for $\Delta T=85\ ^{o}C$

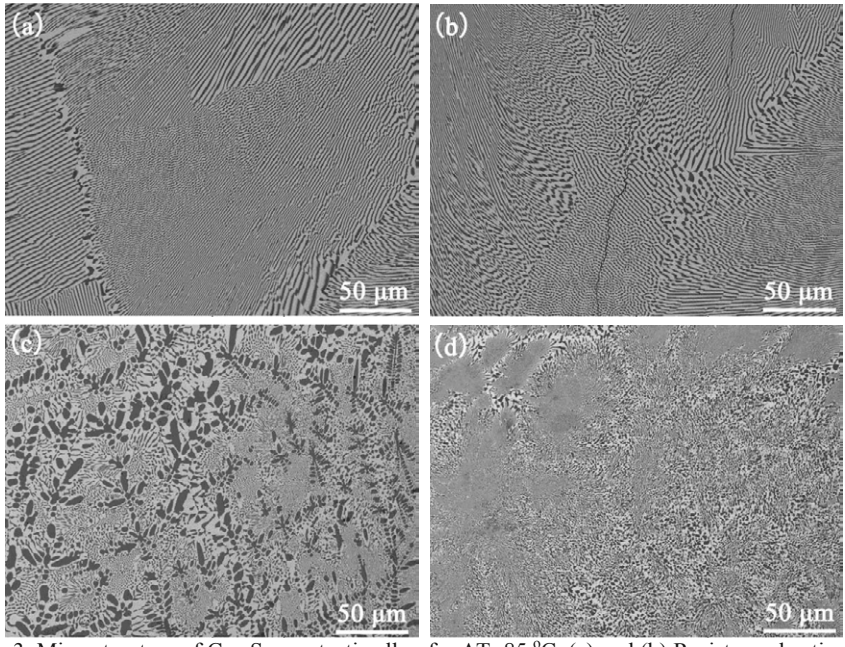

Fig. 3. Microstructure of $Co_{76}Sn_{24}$ eutectic alloy for $\Delta T=85\ ^{o}C$. (a) and (b) Resistance heating; (c) and (d) Induction heating.

The primary αCo disappears in the microstructure of resistance heating and all the structure is lamellar eutectic, which can be evidenced by Fig. 3(a) and Fig. 3(b). However, as is presented in Fig. 3(c) and Fig. 3(d), a number of primary αCo still exists in the microstructure of induction heating and anomalous eutectic appears in the microstructure of induction heating.

4. Microstructure Between $116\ ^{o}C \leq \Delta T \leq 154\ ^{o}C$

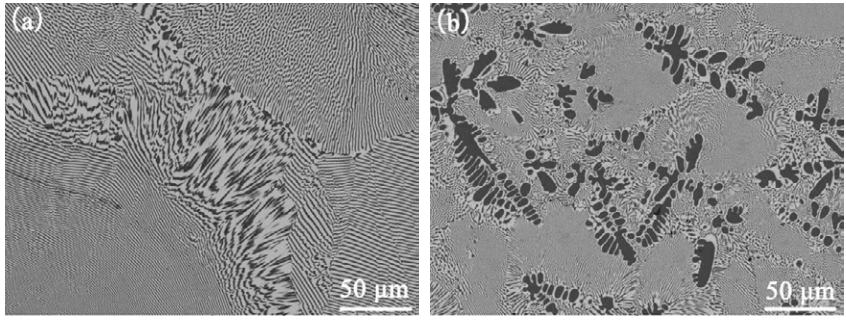

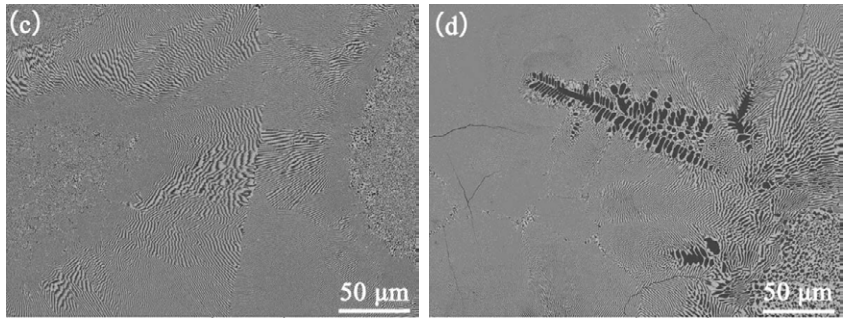

Fig. 4. Microstructure of $Co_{76}Sn_{24}$ eutectic alloy between 116 ^{o}C≤ΔT≤154 ^{o}C. (a) Resistance heating, ΔT=116 ^{o}C; (b) Induction heating, ΔT=116 ^{o}C; (c) Resistance heating, ΔT=154 ^{o}C; (d) Induction heating, ΔT=154 ^{o}C.

5. Microstructure Between 202 ^{o}C≤ΔT≤231 ^{o}C

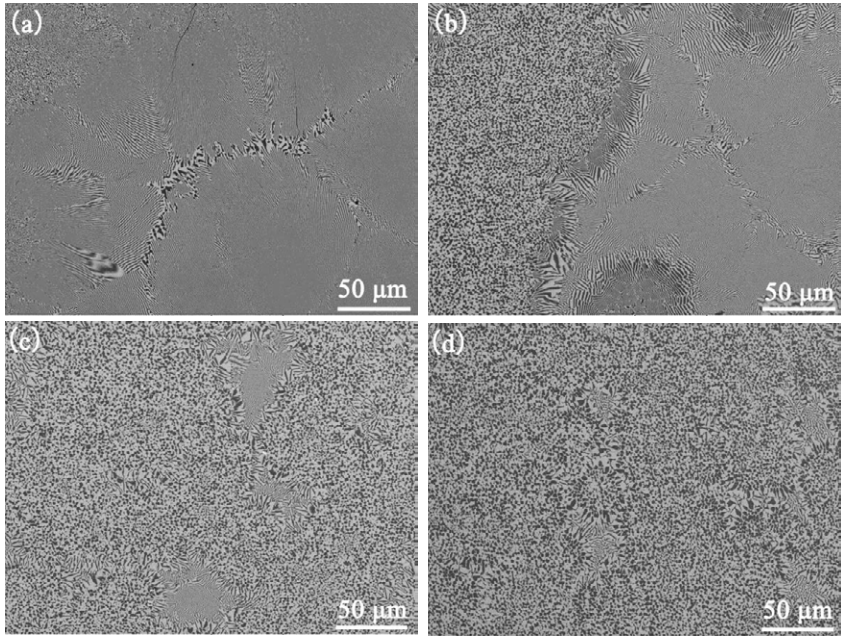

Fig. 5. Microstructure of $Co_{76}Sn_{24}$ eutectic alloy between 202 ^{o}C≤ΔT≤231 ^{o}C. (a) Resistance heating, ΔT=202 ^{o}C; (b) Induction heating, ΔT=202 ^{o}C; (c) Resistance heating, ΔT=231 ^{o}C; (d) Induction heating, ΔT=231 ^{o}C.

Microstructure of resistance heating still maintains lamellar eutectic between 116 ^{o}C≤ΔT≤154 ^{o}C. It is not until ΔT=154 ^{o}C that anomalous eutectic appears in microstructure of resistance heating firstly, which is presented in Fig. 4(c). For induction heating, primary αCo and anomalous eutectic exist in the microstructure all the time merely with a change of quantity. Note that the number of primary αCo decreased as the increasing of undercooling and it is not until ΔT=154 ^{o}C that primary αCo will be disappeared.(Fig. 4(d)). As the undercooling is increased further all the microstructure consists of lamellar eutectic and anomalous eutectic between 202 ^{o}C≤ΔT≤231 ^{o}C, which can be seen from Fig. 5. The influence of heating types on the solidification microstructure is no longer remarkable because of bulk undercooling.

Discussion

In order to analyses the difference between microstructure quantitatively, volume fraction of primary αCo is counted with Image-Pro-Plus. The result is shown in Fig. 6.

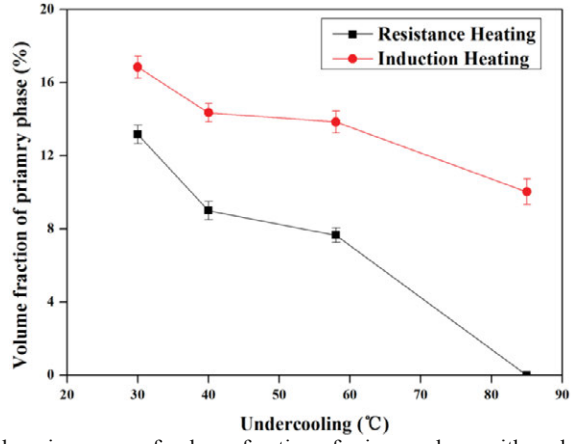

Fig. 6. The changing curve of volume fraction of primary phase with undercooling

Three points of difference between microstructure with same undercooling prepared by induction heating and resistance heating can be concluded as following throughout all SEM images as well as Fig. 6:

(1) Anomalous eutectic appear in microstructure of induction heating for the first time at ΔT=85 ^{o}C. But the undercooling is ΔT=154 ^{o}C for resistance heating. That is, induction heating processing for $Co_{76}Sn_{24}$ eutectic alloy is in favor of the formation of anomalous eutectic.

(2) The volume fraction of primary αCo in microstructure of induction heating is much larger than that in microstructure of resistance heating. Meanwhile, the primary αCo disappear completely in microstructure of resistance heating when ΔT≥85 ^{o}C while microstructure still contains a few primary αCo when ΔT=154 ^{o}C. The phenomenon indicates that induction heating processing for $Co_{76}Sn_{24}$ eutectic alloy can facilitate the precipitation of primary αCo.

(3) The size of each primary αCo in microstructure of resistance heating is much larger than that in microstructure of induction heating, especially when ΔT=30 ^{o}C and 40 ^{o}C. In

microstructure of induction heating, although the volume fraction of primary αCo is much larger, the quantity of primary αCo is also much larger, which result that the size of each primary αCo is small. In other words, compared with resistance heating, induction heating processing for $Co_{76}Sn_{24}$ eutectic alloy can refine the size of primary αCo.

For Co-Sn binary eutectic alloy system, the growth pattern of eutectic structure is coupled growth and the ultimate structure is regular lamellar eutectic. In the solidification process, αCo and εCo_3Sn_2 keep growing because of the transverse diffusion along the solid-liquid interface. The composition of melt is heterogeneous in front of the solid-liquid interface during the growth of lamellar eutectic, which is named lengthways concentration gradient [7, 8].

According to the principle of induction heating, alternating magnetic field produced by alternating current in the load coil affect the melt through electromagnetic stirring. Electromagnetic stirring makes the melt flow turbulently during the undercooling experiment [9]. Although the induction heating equipment is turned off during the cooling process, the turbulent flow cannot be stable immediately because movement of the melt needs time to stop. That is, turbulent flow still exists during the process of nucleation and solidification. There is no doubt that turbulent flowing melt would destroy the transverse diffusion and lengthways concentration gradient in front of the solid-liquid interface during the growth of regular lamellar eutectic. As a result, the growth of regular lamellar eutectic becomes difficult. In addition, regular lamellar eutectic is very easy to become anomalous eutectic through remelting when recalescence occurs as the increasing of undercooling. Hence, induction heating is in favor of the formation of anomalous eutectic.

Different short-ranged ordered structures in the melt are subjected to different force in the electromagnetic field, which results the segregation of different kinds of elements. The segregation of different elements cannot be eliminated completely and immediately during solidification. When turbulent flowing melt destroys the condition for the growth of regular lamellar eutectic, transverse diffusion and lengthways gradient in front of the solid-liquid interface, αCo precipitates from the liquid firstly as it has higher melting point. This is the reason why induction heating can facilitate the precipitation of αCo.

The temperature field of the melt becomes very homogeneous because of the electromagnetic stirring. On one hand, the zone of nucleation becomes large and crystal nucleus formed at the same time increase when αCo starts to precipitate from the melt [10, 11]. Therefore, primary αCo is small when it is precipitated from the melt, not like the primary αCo precipitated from melt under resistance heating. On the other hand, small primary αCo may be fractured at the place where imperfections exist and rubbed by turbulent flowing melt. Thus, induction heating promotes the refinement of αCo.

Conclusions

Compared with resistance heating, induction heating facilitated the formation of anomalous eutectic because the turbulent flowing melt brought by electromagnetic stirring of induction heating destroyed the transverse diffusion and lengthways concentration gradient in front of solid-liquid interface during the coupled eutectic growth. Meanwhile, induction heating promoted the precipitation of primary αCo as the segregation of Cobalt under electromagnetic field. In addition, homogeneous temperature field produced by induction heating makes the primary αCo become small when it is precipitated from melt. Small primary αCo becomes smaller by the fraction caused by turbulent flowing melt. These conclusions also manifest that

resistance heating is better than induction heating when conducting study on non-equilibrium solidification so as to exclude the effect of heating types on the solidified microstructure and obtain the accurate microstructure evolution law.

Acknowledgements

This work was supported by the Natural Science Foundation of China (No. 51371143), the Fundamental Research Funds for the Central Universities (No. 3102015ZY085) and the Program of Introducing Talents of Discipline to Universities (No. B08040).

References

[1] G. Chen et al., "Research and Application of Melt Heat Treatment," Journal of Hebei University of Science and Technology, 19 (46) (1998), 6-12.
[2] H.F. Wang et al., "The development of non-equilibrium solidification theories," Scientia Sinica Techologica, 45 (4) (2015), 358-376.
[3] C.L. Yang et al., "Structure evolution upon non-equilibrium solidification of bulk undercooled Fe-B system," Journal of Crystal Growth, 311 (2009), 404-412.
[4] W. Yang et al., "Non-equilibrium transformation kinetics and primary grain size distribution in the rapid solidification of Fe-B hypereutectic alloy," Journal of Alloys and Compounds, 509 (2011), 2903-2908.
[5] S. Luo et al., "Effect of melt overheating method on the solidification structure of Al-18%Si alloy," Light Metals, 10 (2013), 51-54.
[6] J.Q. Zhang et al., "Influence of Heating Method on Directional Solidification Microstructure of AZ31 Magnesium Alloy," Foundry Equipment and Technology, 2012, no.6:14-17.
[7] L. Liu, J.F. Li, and Y.H. Zhou, "Solidification interface morphology pattern in the undercooled Co-24.0at.%Sn eutectic melt," Acta Materialia, 59 (2011), 5558-5567.
[8] L. Liu, J.F. Li, and Y.H. Zhou, "Solidification of undercooled eutectic alloys containing a third element," Acta Materialia, 57 (2009), 1536-1545.
[9] V. Metan et al., "Grain size control in Al-Si alloys by grain refinement and electromagnetic stirring," Journal of Alloys and Compounds, 487 (2009), 163-172.
[10] W.M. Mao et al., "Effect of electromagnetic stirring on growth and morphology of primary silicon crystals of hypereutectic Al-Si alloys," Materials Science & Technology, 9 (2) (2001), 117-121.
[11] W.M. Mao et al., "The formation mechanism of non-dendritic primary α-Al phases in semi-solid $AlSi_7Mg$ alloy," Acta Metallurgica Sinica, 35 (9) (1999), 971-974.

MECHANICAL PROPERTIES OF 5000 SERIES ALUMINUM ALLOYS FOLLOWING FIRE EXPOSURE

Jillian C. Free[1], Patrick T. Summers[1], Brian Y. Lattimer[1], Scott W. Case[2]

[1]Department of Mechanical Engineering, Virginia Tech; Blacksburg, VA 24061, USA
[2]Department of Engineering Science & Mechanics, Virginia Tech; Blacksburg, VA 24061, USA

Keywords: 5000 Series Aluminum, Microstructure, Recovery, Recrystallization

Abstract

An experimental study was performed comparing changes in microstructure and mechanical properties of six different 5000 series alloys following a simulated fire exposure. To simulate the fire exposure, specimens were subjected to a constant heating rate of 25 °C /min (up to 500 °C) and then water quenched. Quasi-static tensile tests were conducted to quantify yield strength. Additionally, grain evolution was examined by optical microscopy for each alloy. The 5000 series alloys with different tempers resulted in residual strengths between 85 and 157 MPa following the fire exposure. Most alloys exhibited recovery between 100 °C to 280 °C followed by recrystallization between 300 °C to 340 °C. However, the 5456-H116 alloy, which has the highest magnesium content, maintained 60% of room temperature yield strength. This alloy underwent recovery but did not have a clear recrystallization, as apparent in both the micrographs and mechanical testing.

Introduction

Aluminum alloys are increasingly used in a variety of load-bearing applications such as lightweight structures, light rail, and marine crafts. A major design concern of these structures is property degradation due to elevated temperatures. Initial degradation has been shown to occur as low as 150 °C with an additional 50% loss in yield strength at ~275 °C [1]. Special design considerations must be given to ensure safety in a possibly degraded mechanical state. In support of this, aluminum alloy mechanical behavior at elevated temperature has been researched [2–5], and design guides for structural behavior during fires have been developed (e.g., Eurocode 9 [6]). However, limited research has been done to determine what occurs at a microstructural level for these alloys and how to assess structural integrity following a fire when the material has cooled back to room temperature (post-fire). The focus of this research is to investigate the post-fire mechanical properties of various 5000 series aluminum alloys to determine whether property degradation is consistent following a fire exposure. Mechanical property degradation after elevated temperatures can in part be understood through the strengthening mechanisms, which varies for each alloy type. The 5000 series alloys are strain hardened and chiefly attain strength through grain refinement [7]. Applied thermal loading activates reorganization of the lattice structure from the as-received condition towards a structure like the wrought alloy state. The primary reduction in strength is caused by recrystallization upon annealing (250-350 °C), a process which destroys grain refinement [8]. Dislocation recovery and precipitate growth at lower temperatures (150–250 °C) also reduce strength through subgrain coarsening [9] and dilution of the Mg solid solution content in the aluminum matrix [10]. Recrystallization is known to be thermally dependent [11]; therefore, strength reduction is expected to be thermally dependent. Residual mechanical properties of 5000 series aluminum alloys have been quantified for specimens subjected to an isothermal exposure for different durations [12]. AA5083-H116 specimens were

exposed to isothermal heating (100–500 °C) for different durations (up to 2 h) to evaluate the impact of temperature and soak time on residual mechanical properties. The primary strength reduction occurred from 200 - 400 °C, leading to decreases in yield strength of 37%. However, experiments were performed using the same heating rate with different soak times. Gallais et al. [13] extracted micro-tensile specimens from different zones of an AA6056 friction stir welds. The welding process causes the parent material to have spatially varying thermal histories with maximum temperatures and heating/cooling rates dependent on distance from the weld. Lower yield stresses were measured for zones closer to the welded region; however, properties were not correlated to specific thermal histories. Additional data is needed to quantify residual mechanical properties at intermediate exposure temperatures, specifically at refined intervals to relate to microstructural evolution. An experimental study was performed to investigate detailed microstructural and mechanical property evolution in simulated fire conditions. This focused study was conducted on various 5000 series aluminum alloys selected because of similar strengthening mechanisms and alloying constituents. The residual mechanical behavior was characterized as a function of maximum temperature reached during thermal exposure prior to quenching. Uniaxial tension tests were used to quantify residual mechanical behavior at room temperature for specimens previously exposed to 100–500 °C at a heating rate of 25 °C/min. The residual strength degradation mechanisms were investigated in terms of the microstructural changes in the alloys.

Experimental

Materials and Test Specimens

Various 5000 series marine grade alloys were evaluated: 5083-H116, two lots of 5086-H116, 5456-H116, 5454-H32, and 5456-H34. Detailed chemical composition is presented in Table I. The alloys are of various tensile strengths and corrosion resistance. H116 temper designates alloys (with > 3 wt% Mg) that are strain hardened in the final processing step. The H32/H34 tempers specify alloys that are strain hardened then stabilized by low temperature heating to a designated hardness.

Table I. Chemical composition (wt%) for investigated aluminum alloys.

Alloy	Mfg.	Mg	Mn	Si	Cu	Cr	Fe	Al
5083-H116	Alcoa	4.40	0.57	0.11	0.06	0.09	0.24	Bal
5086-H116	Alcoa	4.00	0.42	0.08	0.06	0.08	0.23	Bal
5086-H116	Elval	4.23	0.44	0.12	0.05	0.06	0.26	Bal
5456-H116	Aleris	5.01	0.77	0.08	0.02	0.11	0.12	Bal
5454-H32	Novelis	2.79	0.82	0.05	0.01	0.09	0.29	Bal
5454-H34	Elval	2.77	0.77	0.11	0.07	0.15	0.33	Bal

Rectangular cross-section dog-bone specimens were machined from as-received plate with the longitudinal axis oriented in the rolling direction. Overall specimen length was 169.2 mm, 50.8 mm gage length and 12.7 mm width. Test specimens maintained the as-received plate thickness of 6.4 mm. Optical micrograph samples were prepared as thin plates ~250 mm thick. Samples were removed from full-size test specimens using a SiC wafering blade. The thin plates were slowly mechanically ground to ~90 mm thickness. Samples were mounted in epoxy and polished, then etched with phosphoric acid to highlight grain structure.

Non-Isothermal Heating

To simulate fire exposure, specimens were exposed to a constant heating rate of 25 °C /min to a maximum temperature (100 to 500 °C), then water quenched to arrest material evolution. Sample heating was done with an induction heater (Ameritherm 5060LI) controlled by a Micro-Epsilon optical pyrometer (8–14 lm spectral range) and a Watlow PID controller. A thin layer of Rust-Oleum Specialty High Heat flat black enamel spray paint was applied on the sample surface to ensure accurate temperature measurements using the pyrometer. Thermal camera and embedded thermocouples were used to determine the temperature-dependent paint emissivity as 0.95–0.99 [14]. Specimen heating was monitored via a FLIR SC655 (7.5–14 lm spectral range) thermal camera, providing full-field temperature measurement. The central 25.4 mm gage length was maintained within 2% of the desired temperature for the heating rate.

Mechanical Characterization

Uniaxial, quasi-static tensile tests were performed at room temperature on previously heated samples using an Instron 5984 150 kN electro-mechanical testing machine. Tensile tests were performed at a constant displacement rate of 3.048 mm/min (strain rate of 10^{-3}/s). Small strains were measured using strain gages (Vishay Micro-Measurements CEA-13-125UW-350 with a gage length of 3.175 mm) and large strains via digital image correlation (DIC). The strain gages were adhered at the center of the uniform temperature region as measured using the thermal camera during heating. The adhesive (Vishay Micro-Measurements M-Bond 200) cures at ambient conditions to ensure an unchanged material state A commercially available 3-D DIC system from Correlated Solutions was used to measure full-field material deformation. A detailed description of the experimental setup, calibration procedure, and data analysis procedure is provided in [15, 16].

Microstructural Characterization

Optical microscopy was used to characterize the grain structure in several states. Prior to imaging, samples were mounted and polished. A Barker's etch was used on samples to highlight different grain orientations and boundaries. Samples were etched in 2.5% vol. HBF4 solution at 10 V for 2 minutes using the Buehler Electromet Etcher. Images were taken using a Carl Zeiss Axio VertA.1 inverted microscope. Bright field and polarized light modes were used for imaging microstructures. EC Epiplan-NEOFLUAR objective lens of 5X, 10X, 20X, 50X, and 100X were used with an eyepiece of 10X, allowing for magnifications between 50X and 1000X resolutions. All specimens were imaged on three perpendicular material surfaces using crossed polarizers to show grain contrast. Axiovision 4.9.1 software was used to analyze images and obtain measurements.

Results

Residual mechanical behavior of various aluminum alloys following a fire exposure is provided through evaluation of micrographs as well as tensile test results for samples from 100 °C up to 500 °C all subjected to 25 °C/min heating rate.

Initial Microstructural State

As-received subgrain size was determined from the average of 10 micrographs in the LS material plane using the linear intercept method. Measurement lines were drawn perpendicular to that of the elongated subgrain regions. Average sizes ranged from 52.1 μm to 89 μm, similar to those obtained in other studies [17]. The as-received dislocation structures varied in the samples. Several were typical for materials processed by work hardening (AA5083-H116, both AA5086-H116's, and AA5454-H32). The dislocation structure has distinctive regions with subgrains of different morphology and texture. Close examination of these lamellar structure (not shown here) reveals extended lamellar boundaries (parallel to the rolling direction) with interconnecting dislocation boundaries (parallel to the normal direction). The lamellar boundaries are well-organized and thin, demonstrating that sufficient recovery occurred during processing to transform the initial dislocation cell structure to subgrains. However, the extent of lamellar structure varied with each specimen. For most samples a more elongated structure is observed on all faces. The AA5454-H32 and AA5456-H116 samples show a slightly more equiaxed subgrain structure in the initial state.

Mechanical Characterization

Residual mechanical behavior of the 5000 series alloys following non-isothermal heating is provided through mechanical testing. For all discussed results and analysis, the maximum temperature reached during the elevated temperature exposure of the materials is referred to as temperature. Nominal engineering stress was used to describe material behavior. Fractions of initial yield strength, σ/σ_o, were plotted as a function of temperature for each specimen. From Figure 1 yield strength decreases with increasing temperatures, in line with previous research. The residual strength is strongly dependent on the maximum temperature reached. For all materials except AA5456-H116, an initial drop in yield strength is observed at lower temperature followed by a significant drop at higher temperature. The yield strength then settles at an average of 45% of the as-received strength.

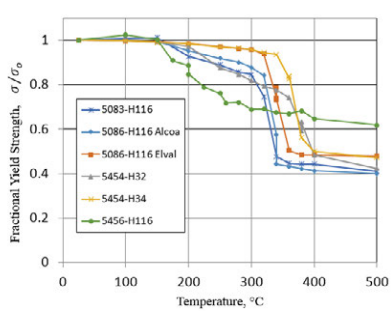

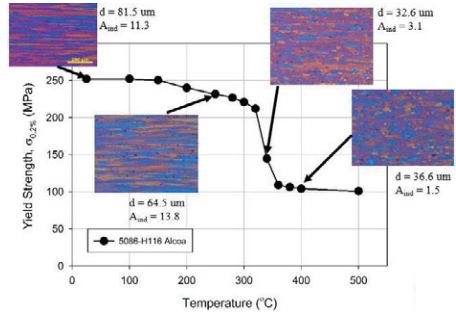

Figure 1 (l)**.** Fractional yield strength shown as a function of temperature for all samples.
Figure 2 (r). 5086-H116 (Alcoa) yield strength as a function of temperature, micrographs overlaid.

The AA5086-H116 samples showed similar mechanical behavior; however, the Elval sample maintained 48% of its initial strength, while the Alcoa sample dropped to 40%. The samples AA5454–H32 and –H34 show slightly different mechanical behaviors despite having similar constituents and processing. As shown in Figure 1, the –H32 sample experiences a loss in yield strength at a lower temperature compared to the –H34 sample. Both samples then undergo a significant drop in yield strength at an elevated temperature and begin to track similarly above 400 °C. AA5456-H116 shows a completely different response having a low temperature yield strength drop, but not followed by a more significant drop. In addition, the alloy maintains over 60% of its initial strength at the maximum temperature.

States Resulting from Non-Isothermal Heating

Optical microscopy was performed on samples heated at 20 °C/min to selected temperatures to characterize microstructural evolution due to recovery and recrystallization. For all samples, the micrographs show that the grain structures evolve from lamellar to more equiaxed as they approach the end state as seen in Table II.

Table II. Micrographs of LS surface for various alloys before and following heat exposure: 5083-H116 (a) as-received (AR) and (b) final, 5086-H116 Elval (c) AR and (d) final, 5454-H32 (e) AR and (f) final, 5454-H34 (g) AR and (h) final, and 5456-H116 (i) AR and (j) final.

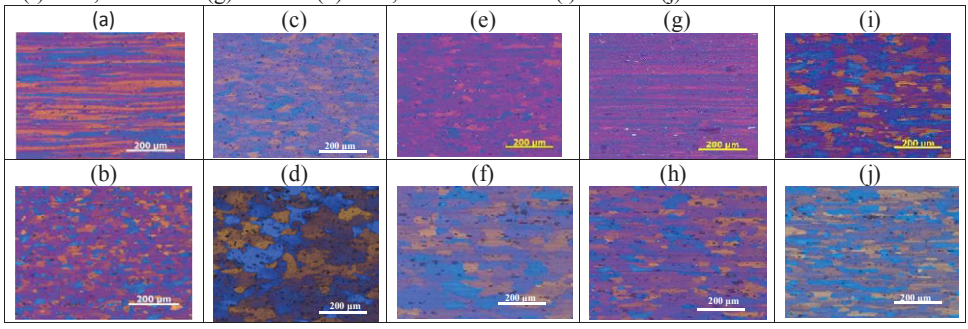

Corresponding micrographs at various temperatures were combined with the thermal-mechanical results. Results show that for most specimens, recovery dominates at lower temperatures and recrystallization occurs at elevated temperatures. An example is shown in Figure 2 where micrographs at various temperatures are overlaid onto the yield strength plot. With the exception of AA5456-H116, all samples show a similar evolution. Recovery dominates at lower temperatures (~100 °C) as subgrains undergo coarsening. Heating to temperatures below 200 °C (at 20 °C/min) results in little increase in average subgrain size. Above 200 °C, the dislocation structure significantly coarsens until recrystallization initiates. Coarsening was notably more significant for the non-lamellar structured subgrains (a result similar to that observed by Xing et al. [18]). The different coarsening rates were attributed to the relative misorientation angles of the respective boundaries [18].

Discussion

Experimental results demonstrate that for the given non-isothermal heating, the residual mechanical behavior of several Al-Mg alloys is sensitive to maximum temperature, initial microstructural state, and magnesium quantity. With the exception of one sample, the investigated alloys all demonstrate similar microstructural evolution corresponding with recovery and recrystallization mechanisms. The outlying specimen only exhibited a recovery mechanism. In this discussion, the fundamental evolution of the various microstructural processes are described and related to the measured residual mechanical property degradation.

Residual Yield Strength Evolution

Heating to lower temperatures (150–280 °C), causes a slight yield strength reduction, and subgrain coarsening by dislocation recovery is the primary mechanism. Subgrains are intra-granular grain-like structures formed during strain hardening (cold work) [16, 19]. Recovery causes subgrain coarsening due to dislocation emission and amalgamation with neighboring subgrains [11, 20]. The effect of recovery is observed in both the microstructural evolution as well as the mechanical tensile testing results. The results are similar to previous research on Al-Mg specimens undergoing non-isothermal heating [21]. Heating to higher temperatures (280–320 °C), results in significant reduction of residual yield strength. At these temperatures recrystallization dominates. It is the formation of an equiaxed grain structure in a deformed material through grain nucleation and growth by the stored energy of deformation [22]. The effect of recrystallization on AA5083-H116 is shown in Figure 2. The elongated as-received grain structure evolves during recrystallization to form equiaxed grains. The average grain sizes range between 52.1 to 89 μm in the as-received state and 36.6 to 74 μm in the final states.

AA5454-H32 Initial Microstructure

For the AA5454-H32 specimen, consider the similar material AA5454-H34. These two specimens have similar components (Table I), and are both cold-worked then stabilized by tempering. The –H32 specimen is tempered to ¼ hardness while the -H34 specimen to ½ hardness. From Table II, -H32 initial grain structure is a more equiaxed, while -H34 is more lamellar. The extended heating at low temperature for the -H32 sample likely causes partial recovery of the sample and it is observed as subgrain coarsening in the as-received state. This is further evidenced in the mechanical behavior observed in Figure 1. As shown, AA5454-H32 demonstrates an initial drop in yield strength (recovery) at a much lower temperature compared to AA5454-H34. Both specimens then experience a significant drop in yield strength (recrystallization) at a higher temperature, and then demonstrate similar mechanical responses at higher temperatures. This indicates that material processing and microstructure initial state play a role in affecting the residual yield strength at elevated temperatures.

AA5086-H116 Magnesium Content

Samples of AA5086-H116 were investigated from two different manufacturers. The two materials behaved very similarly in terms of mechanical characterization. However, the Elval sample

maintained 48% of initial strength, while the sample from Alcoa reduced to 40% despite identical processing. The chemical composition in Table I shows that all the components are in similar quantities except for magnesium. The Elval sample has 0.23 wt% more magnesium than the Alcoa sample indicating that the magnesium content may result in increasing residual strength at elevated temperatures.

AA5456-H116 Recovery

The AA5456-H116 micrographs in initial state show some lamellar boundaries parallel to the rolling direction (not shown); however the microstructure is more equiaxed in the normal direction. Despite undergoing cold-working and thermal treatment similar to other -H116 specimens, the micrographs of AA5456-H116 look very different. Figure 1 shows that this sample does not undergo the same processes as the other samples. AA5456-H116 appears to only undergo recovery, but not recrystallization. Mechanical testing for this sample resulted in 60% of the as-received strength, which is the highest of all samples. Table I shows that this sample contains the highest amount of magnesium, and as previously discussed, increased magnesium content may correlate to increasing residual strength at elevated temperatures. These indicate that residual yield strength for this specimen is affected by a complex combination of the magnesium content as well as the state of the initial microstructure.

Conclusion

An experimental study was performed comparing mechanical properties for six different 5000 series alloys following a simulated fire exposure. Specimens were subjected to non-isothermal heating at 25 °C/min from room temperature up to a maximum of 500°C, then water quenched to arrest microstructural evolution. Mechanical tensile testing was performed and correlated with microstructural evolution observed through micrographs taken from the test specimens. Micrographs of the initial states of all samples showed a more lamellar dislocation structure for the all samples. As the samples were heated, the microstructures evolved to a more equiaxed state. For all samples except AA5456-H116, mechanical tensile testing of samples indicated an initial slight drop in yield strength at a lower temperature followed by a significant drop in yield strength at higher temperature. Yield strengths reduced overall to 40% to 47% of initial strength. AA5456-H116 was unique in that its magnesium content was the highest of all the test specimens, however the other contributing elements were similar to the other samples. Micrographs of the sample showed a different, more equiaxed initial dislocation structure. AA5456-H116 mechanical testing showed a low temperature drop in yield strength, but not a second drop at elevated temperature indicating that only recovery occurred. Yield strength was maintained up to 61% of the initial strength. This indicates that magnesium content plays a role in affecting residual strength under non-isothermal heating.

Acknowledgements

This work was funded through the Office of Naval Research grant number N00014-14-1-0608, scientific monitor Dr. Thomas Fu.

References

1. N.K. Langhelle and J. Amdahl, "Experimental and Numerical Analysis of Aluminum Columns Subjected to Fire," *International Offshore and Polar Engineering Conference*, 11 (2001), 406–13.
2. J. Maljaars, F. Soetens, and L. Katgerman, "Constitutive Model for Aluminum Alloys Exposed to Fire Conditions," *Metallurgical and Materials Transactions A*, 39 (2008), 778–89.
3. E. Kandare, S. Feih, B.Y. Lattimer, and A.P. Mouritz, "Larson-Miller Failure Modeling of Aluminum in Fire," *Metallurgical and Materials Transactions A*, 41 (2010), 3091–9.
4. A. Clausen, T. Borvik, et al, "Flow and Fracture Characteristics of Aluminum Alloy AA5083-H116 as Function of Strain Rate, Temperature, and Triaxiality," *Material Science Engineering A*, 364 (2004), 260–72.
5. E.A. El-Danaf, A.A. Almajid, and M.S. Soliman, "Hot Deformation of AA 6082-T4 Aluminum Alloy," *Journal of Materials Science and Engineering*, 43 (2008), 6324–30.
6. British Standards Institution (BSI). Eurocode 9 – design of aluminum structures, structures, Part 1–2: Structural fire design; 2009.
7. Underwriter Laboratories, UL 1709 – Rapid Rise Fire Tests of Protection Materials for Structural Steel, Northbrook, IL, 1990.
8. G. Dieter. *Mechanical Metallurgy*. 2nd ed. (New York: McGraw-Hill; 1976).
9. C. Zahra and A.M. Zahra, "The Perkin-Elmer 1020-Series Thermal-Analysis System," *Thermochimica Acta*, 276 (1996), 161–74.
10. Q. Xing, X. Huang, and N. Hansen, "Recovery of Heavily Cold-Rolled Aluminum: Effect of Local Texture," *Metallurgical and Materials Transactions A*, 37 (4) (2006) 1311–1322.
11. T. Hasegawa, and U.F. Kocks, "Thermal Recovery Processes in Deformed Aluminum," *Acta Metallurgica*, 27 (1979) 1705–1716.
12. R.D. Matulich, "Post-fire Mechanical Properties of Aluminum Alloys and Aluminum Welds," *Virginia Polytechnic Institute & State University, (2011).*
13. C. Gallais, A. Simar, D. Fabregue, et al. "Multiscale Analysis of the Strength and Ductility of AA 6056 Aluminum Friction Stir Welds," *Metallurgical and Material Transactions A,* 38 (2007) 964–81.
14. N. Cholewa Personal communication.
15. P.T. Summers, S.W. Case, and B.Y. Lattimer, "Residual Mechanical Properties of Aluminum Alloys AA5083-H116 and AA6061-T651 after Fire," *Engineering Structures*, 76 (2014) 49–61.
16. P.T. Summers. "Microstructure-based Constitutive Models for Residual Mechanical Behavior of Aluminum Alloys after Fire Exposure," *(Ph.D. dissertation)*, Virginia Tech, USA (2014).
17. E.L. Huskins, B. Cao, and K.T. Ramesh, "Strengthening Mechanisms in an Al-Mg Alloy," *Materials Science and Engineering: A*, 527 (2010) 1292–1298.
18. Q. Xing, X. Huang, and N. Hansen, "Recovery of Heavily Cold-Rolled Aluminum: Effect of Local Texture," *Metallurgical and Materials Transactions: A*, 37 (2006) 1311–1322.
19. F.J. Humphreys and M. Hatherly, *Recrystallization and Related Annealing Phenomena*. 2nd ed. (Oxford: Pergamon; 2004).
20. H.J. McQueen, and E. Evangelista, Czech J Phys, 38 (1988) 359–72.
21. P.T. Summers, et al, "Microstructure-based Modeling of Residual Yield Strength and Strain Hardening after Fire Exposure of Aluminum Alloy 5083-H116," *Materials Science & Engineering A,* 632 (2015) 14-28.
22. R.D. Doherty, D.A. Hughes, F.J. Humphreys, et al, "Current Issues in Recrystallization: A Review," *Materials Science and Engineering: A*, 238 (1997) 219–74.

EFFECT OF CONCURRENT MICROSTRUCTURE EVOLUTION AND HYDROGEN LEVEL ON FLOW BEHAVIOR OF NEAR ALPHA Ti-ALLOY

Jagadeesh Babu[1], B.P. Kashyap[1], N. Prabhu[1], R. Kapoor[2], R.N. Singh[2], Bhupendra K. Kumawat[2], J.K. Chakravartty[2]

[1]Department of Metallurgical Engineering and Materials Science, Indian Institute of Technology Bombay, Mumbai 400076, India

[2]Mechanical Metallurgy Division, Bhabha Atomic Research Center, Trombay, Mumbai 400085 India

Keywords: Near-α VT20 Ti-alloy, Hydrogen effect, Microstructure and phase proportion, Flow behavior and constitutive relationship

Abstract

Separate compression samples of VT20 Ti-alloy Ti-5.9Al-2.1Zr-1.6V-1.4Mo (wt%), charged with 0, 0.15 and 0.36 wt%H, were deformed to true strain of 0.70 at a strain rates of 1×10^{-3} and 1×10^{-1} s^{-1} at test temperatures of 600 and 850 °C. H charging led to the varying microstructures ranging from equiaxed to lamellar ones depending on H level. In the course of deformation, their occurred refinement of microstructures with reduced interlamellar spacing depending on the test conditions. The contributions of these sources to microstructure evolution and flow properties were examined in an attempt to explore some correlation between them. An attempt is made to understand the effect of H present on the microstructure and flow properties to account for the variations in the parameters of the constitutive relationship.

Introduction

Titanium and its alloys have wide applications due to outstanding properties like strength to weight ratio, corrosion resistance, toughness etc. in all kinds of environments. Near-α titanium alloys have exceptional high temperature properties and they are suitable material for aero engine with an operating temperature of 600 °C, compressor discs and blades of gas turbine engines [1]. Hydrogen is a chemically active element with high mobility and hence strongly reacts with metallic materials [2]. Thermohydrogen processing (THP) studies have shown that hydrogen as a temporary alloying element in titanium alloys has significant effect on the mechanical properties. Froes et al.[3] discussed in their review that, since hydrogen has a positive enthalpy of solution, its reaction is reversible. The reason that hydrogen has received much attention in titanium/zirconium alloys is that hydrogen stabilizes the β phase, increases β volume fraction and decreases the β transus temperature. The increase in the range of two phase region (α+β) helps in obtaining wide range of microstructures (especially in near-α Ti alloys).

Hydrogen also has a softening and hardening effect on α and β phases, respectively. The studies suggest that, the microstructure plays an important role during high temperature working of titanium alloys. Microstructural changes are mainly dependent on the factors like strain, strain rate and temperature. The aim of the present work is to study the effect of strain, strain rate and temperature on the microstructural evolution in the as-received and hydrogenated near-α Ti alloy.

Experimental Procedure

As received (AR) experimental near-α Ti alloy (VT 20) plate with composition Ti-5.9Al-2.1Zr-1.6V-1.4Mo (wt%).

Table I. Composition of VT 20 alloy (wt%)

Element	Ti	Al	Zr	C	Fe	Si	O	N	H	Mo	V
Wt%	88.235	5.9±0.4	2.1±0.2	0.1	0.3	0.15	0.15	0.05	0.0015	1.4±0.1	1.6±0.1

The specimens for hydrogenation with dimensions 42 mm × 13 mm × 12 mm were cut from the AR alloy. Prior to hydrogenation, the specimens were mechanically polished to remove the oxide layer. The hydrogenation was carried out in vacuum of about 10^{-4} torr using modified Sievert's apparatus at 750 °C. Hydrogen content after hydrogenation was measured by using inert gas fusion technique. Hydrogen charging was done to get 0.15 wt% (1500 ppm) and 0.36 wt% H (3600 ppm). Similarly, hydrogen content of AR alloy was found to be 0.0015 wt% H (15 ppm).
Compression specimens with dimensions of 7.5±0.3 mm height and 5 mm diameter were made by EDM wire cutting. High temperature compression tests were conducted using a servo-hydraulic universal testing machine. The furnace was heated to test temperatures for an about 1 hour and soaked for 10 min prior to compression test. The test temperatures were controlled within the accuracy of ±2 °C. Glass coating was used in order to avoid oxidation as well as to prevent escape of hydrogen at higher temperature [4,5]. Upon completion of the test, the sample was taken out of the furnace and cooled in air to room temperature.
Metallographic samples were prepared by conventional polishing technique and etched for 5-15 s using Kroll's reagent (90-92 ml H_2O + 6-7 ml HNO_3 + 2-3 ml HF). Microstructures were examined by optical microscopy and photographs were captured for quantifying the grain size (d), volume fraction and interlamellar spacing (Λ). The grain size, interlamellar spacing were measured by mean linear intercept method and whereas the volume fraction of β (f_β) was measured by point count method. Similarly, the volume fraction of α was determined by using the relation $f_\alpha = 1\text{-}f_\beta$.

Results and discussion

Initial Microstructure

The figure 1(a-c) reveals initial microstructures of AR condition and the alloy charged with 0.15 wt% H and 0.36 wt% H material. Microstructural observations revealed the nearly equiaxed structure for AR. However, the thickness of the lamellae was reduced in proportion to hydrogen level. The phases appear as alternate bright and dark, for α and β phases, respectively. With

addition of hydrogen, the nearly equiaxed structure changed to refined lamellar structure. From the quantification of the results, the grain size for AR material was 5.4 ± 0.5 μm and interlamellar spacing of the alloy containing 0.15 wt% H and 0.36 wt% H were found to be 3.2 ± 0.5 μm and 1.3 ± 0.1 μm, respectively.

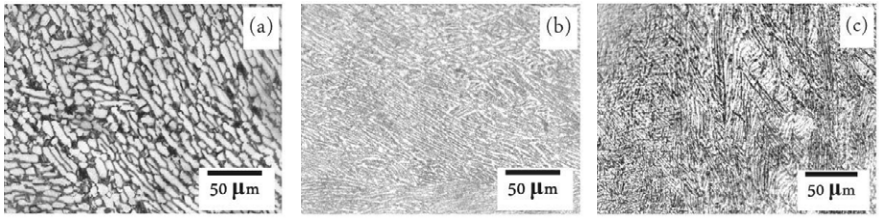

Figure 1. Initial microstructures for (a) AR condition and the alloy containing (b) 0.15 wt% H (c) 0.36 wt% H.

Constant initial strain rate compression tests

The samples with initial microstructures shown in figure 1 were deformed at constant initial strain rates of 1×10^{-3} and 1×10^{-1} s^{-1}separately at test temperatures of 600 and 850 °C. The stress-strain curves as a function of temperature, strain rate and hydrogen content for the true strain level of 0.70 are illustrated in figure 2. For examining the microstructural evolution as a function of strain under different test conditions, separate samples were deformed to true strains of levels of 0.16, 0.35 and 0.70.

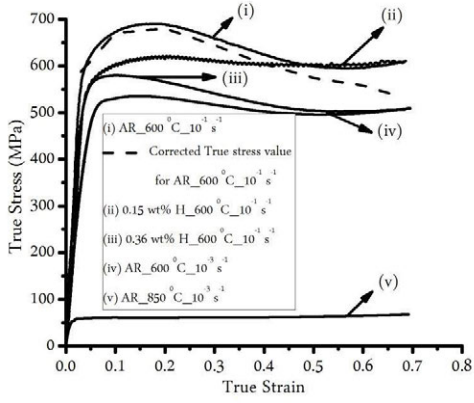

Figure 2. Typical stress-strain plot at different strain rates, temperatures and different H level.

At a given temperature and strain rate, flow stress decreased with increase in hydrogen content. For AR, there is decrease in flow stress with increase in temperature and decrease in strain rate. Flow curves show a high initial hardening and subsequent softening with increase in strain. The

extent of flow softening is observed to be more at 600 °C, except in the case of 0.15 wt% H. whereas at 850 °C, the stress-strain curve exhibits the pseudo-steady state flow behavior. It is said to be pseudo-steady state because the flow stress does not change with strain (there is no strain hardening or strain softening) whereas the microstructure exhibits continuous coarsening and development of lamellar structure during deformation, as will be described later.
Since, the initial constant strain rate is fixed, during the course of deformation; there is a continuous change in strain rate, which is not same as initial strain rate. To see the effect of true strain rate on the flow curve, an approach for correcting the stress [7] was made in the present work by using the equation (1):

$$\sigma_c = \sigma\left(L_0 / L\right)^m \qquad (1)$$

where, σ_c is corrected stress, σ is flow stress at any instant for constant cross head speed of the machine, m is strain rate sensitivity, L_0 is initial and L is instantaneous length of the sample, respectively.
The stress value was corrected using Equation (1) for one case as shown in figure 2, as shown by dashed line. The behavior of the dashed line (flow curve) is similar to that of the actual curve, except the decrease in stress values indicating more softening. Therefore, the nature of stress-strain curves observed here is also expected to be valid for the true constant strain rate type test.

Microstructure examination after deformation

In the AR material, the microstructure with increasing strain first changed to fine lamellar structure at early stage of straining (ε=0.10), which subsequently became coarser at larger strains. The microstructures examined under different test conditions and varying strain levels exhibited increasing refinement in lamellar structure with increasing strain in the case of alloy containing 0.15 wt% H. In the case of VT 20 containing 0.36 wt% H, there appeared continuous coarsening of the lamellar structure with increasing strain.
As shown the figure 3(a-c), the microstructures upon deformation to the true strain level of 0.70 suggest that there is a change in morphology of the microstructures when compared to the initial microstructures as shown in figure 1. At 600 °C and 10^{-1} s^{-1}, nearly equiaxed microstructure has become elongated grain structure figure 3a, refined lamellar structure has become explicitly elongated grains with distinct colonies of lamellae and coarser to some extent figure 3b and 3c, after deformation.

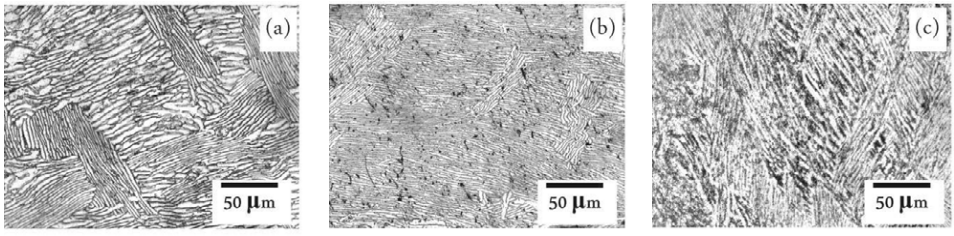

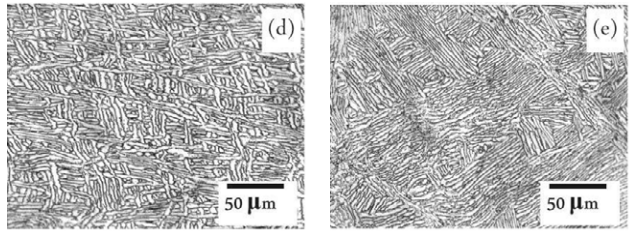

Figure 3. Microstructures after deformation to 0.70 true strain at conditions of temperature 600 °C, strain rate 10^{-1} s^{-1} for (a) AR (b) 0.15 wt% H (c) 0.36 wt% H and strain rate of 10^{-3} s^{-1} for AR at (d) 600 °C (e) 850 °C respectively.

Murzinova et al. [8] studied the behavior of flow curves for VT6 at 600 and 700 °C, correlating the effect of lamellar microstructure on the shape of σ-ε curve. It was reported that the, decrease in flow stress is attributed to the increase of β volume fraction due to hydrogen. This favors initiation of β relaxation, where length of the interphase boundaries increases due to the refinement of the microstructure. This was said to facilitate the grain sliding and redistribution of alloying elements. Figure 3(d) is similar to the figure 3(a) except lengths of the lamellae has decreased and are randomly orientated. Figure 3(e), shows the distinct colonies of lamellae with reduced thickness as compared to figure 3(a) and 3(d). These variations in microstructure, based on the temperature, strain rate and hydrogen content, have an effect on the flow properties, showing hardening, softening and pseudo steady state.

Structure-flow property correlation

Flow hardening has been ascribed to occurrence of grain growth at elevated temperature. However by itself grain growth has not been found to be significant and hence would contribute only marginally to strain hardening at higher strain rate and lower temperature. The other contribution to strain hardening comes from dislocation based conventional hardening [6]. Flow softening is ascribed to decrease in grain size while in the present work there appears refinement in microstructure. There is change in morphology from nearly equiaxed to lamellar, which could contribute to hardening. So the observed flow softening is a combined effect of refined microstructure and the opposite effect of the morphological change in the microstructure. Larger strain (>0.5) shows pseudo-steady state by the time these changes in microstructure completed and exhibit equal flow hardening and flow softening effects. At 850 °C, there appears only pseudo-steady state in spite of remarkable change in the microstructure as shown in figure 3(e). This clearly illustrates that there exists two opposite type of effects due to concurrent microstructural evolution, which eliminates flow hardening and softening to result in pseudo-steady state. From figure 2, it is observed that at lower temperature (600 °C) all the curves show flow softening at given strain rates for strain >0.05, which could be attributed to the refinement in microstructure.

Strain rate sensitivity and activation energy

The strain rate sensitivity (m) can be calculated as:

$$m = \left[\frac{\partial \ln \sigma}{\partial \ln \dot{\varepsilon}}\right]_{T,d} = \left[\frac{\partial \log \sigma}{\partial \log \dot{\varepsilon}}\right]_{T,d} \equiv \left[\frac{\partial \log(\sigma_2/\sigma_1)}{\partial \log(\dot{\varepsilon}_2/\dot{\varepsilon}_1)}\right]_{T,d} \quad (2)$$

Where σ is flow stress (MPa), $\dot{\varepsilon}$ is the strain rate assuming at constant temperature and grain size. σ_1, σ_2 are the stress values at corresponding to the strain rates $\dot{\varepsilon}_1, \dot{\varepsilon}_2$ taken from the stress-strain curve at different strain level as shown in figure 2. The variation of m at 600 °C as a function strain for AR, 0.15 wt% H and 0.36 wt% H is shown in figure 4. As a function of strain, m values varied from ~0.03-0.05 for AR, ~0.09-0.16 for 0.15 wt% H and ~0.09-0.12 for 0.36 wt%H. The addition of hydrogen increased m, being highest value of 0.16 for the hydrogen level of 0.15 wt%. The strain rate sensitivity increases with increase in strain for H charged samples but showed a near constant / small decrease for AR samples. Weiss and Semiatin [9] reported strain rate sensitivity values for near-α Ti-alloys in α+β region of 750-1020 °C, which were in the range 0.19-0.25. Zong et al. [10] studied hot deformation behavior of TC11 alloys and reported the m value of 0.107. Volume fraction of prior α and its grain size increases with temperature and extent of deformed, seemed to be less dependent on strain rate.

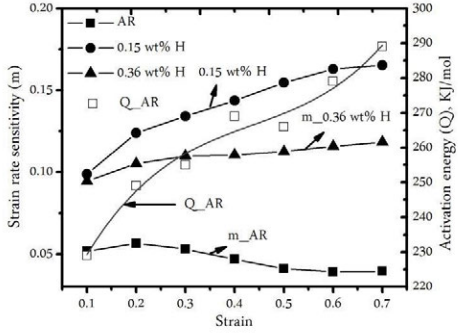

Figure 4. Typical plot for showing the variation of 'm' as a function of strain for AR, 0.15 wt% H and 0.36 wt% H (filled legends)calculated at 600 °C and variation of Q for AR as a function of strain (open legends) calculated between 600 °C and 850 °C.

The activation energy (Q) was calculated using the constitutive equation:

$$\dot{\varepsilon} = A\sigma^n \exp(-Q/RT) \quad (3)$$

Where, $\dot{\varepsilon}$ is the strain rate, A is material constant, σ is flow stress, n is stress exponent (n=1/m), R is gas constant, T is absolute temperature.

From eq. (3) the activation energy can be obtained as

$$Q = nR\left[\partial \ln \sigma / \partial (1/T)\right] \quad (4)$$

Variation of activation energy (Q) as a function of strain for AR is also shown in figure 4. Q increases with increasing strain could be attributed to the concurrent microstructural evolution and its variation as shown in figure 3.The nature of variation of Q as a function of strain was so found to be sensitive to hydrogen content. This is dependent on temperature and strain rate. Q value varied in the range of 229-289 kJ/mol. In the case of 0.15 wt% H and 0.36 wt% H, Q was observed to decrease as a function of strain (not shown here). At lower strains ($\leq$ 0.1), Q observed to be higher or similar for 0.15 wt% and 0.36 wt% H to that of AR. Weiss and Semiatin [9] reported the Q value in range of 250-572 kJ/mol for the wide range of strain rates and temperatures. Zong et al. [10] reported Q value of 538 $kJmol^{-1}$ which could be due to is the possible occurrence of dynamic recrystallization (DRX). Zhang et al. [11] studied the deformation behavior of Ti600 alloy in the temperature range 840-960 °C. They reported the m value in the range of ~0.27-0.4, which varied based on the hydrogen content and strain rate. There is considerable decrease in Q with hydrogen content, the same was explained by the fact that hydrogen facilitates the migration of atoms so also the diffusion coordinated deformation. Hydrogen enhances the dislocation motion, increases the volume fraction of β phase, decreases the dislocation density (i.e., releases the pinned dislocations) and increases the probability of dislocation climb.

Conclusion

The addition of hydrogen in VT-20 alloy changes the morphology of microstructure as well as refines the grains as compared to AR condition. The stress-strain curves were found to exhibit flow hardening, flow softening and pseudo-steady state depending on the test condition. The variation in stress as function of strain is attributed to the concurrent microstructure evolution, which involves transformation to lamellar structure and its refinement or coarsening. For the hydrogenated samples, '*m*' increased as a function of strain. The activation energy (Q) for deformation for as received material is shown to increase with strain. Microstructural examination after deformation showed a wide variation in the morphology which depends on temperature, strain rate and hydrogen level.

Acknowledgement

The authors acknowledge Board of Research in Nuclear Sciences (BRNS) for funding the project (sanction no. 2012/36/45/ BRNS-2167).

References

1. Z.Yingying, H. Shuhui, F. Yingjuan, S. Debin. "Hydrogen induced softening mechanism in near alpha titanium alloy," Journal of Alloys and Compounds, 541 (2012), 60–64.
2. R.J. Elias, H.L. Corso, J.L. Gervasoni, "Fundamental aspects of the Ti–H system: theoretical and experimental behaviour," International Journal of Hydrogen Energy, 27 (2002), 91–97.

3. F. H. Froes, O. N. Senkov and J. I. Qazi. “Hydrogen as a temporary alloying element in titanium alloys: thermohydrogen processing,” International Materials Reviews, 49 (2004), 227-245.
4. X. Zhang, Y. Zhao, W. Zeng, “Effect of hydrogen on the superplasticity of Ti600 alloy,” International Journal of Hydrogen Energy, 35 (2010), 4354 – 4360.
5. Y. Niu And M. Li, “Application Of Thermohydrogen Processing For Formation Of Ultrafine Equiaxed Grains in Near α Ti600 Alloy,” Metallurgical And Materials Transactions A, 40A (2009), 3009-3015.
6. B.P. Kashyap and K. Tangri, “On the Contribution of Concurrent Grain Growth to Strain Sensitive Flow of a Superplastic Al-Cu Eutectic Alloy,” Metallurgical Transactions A, 18A (1987), 417- 424.
7. B.P. Kashyap and G.S. Murty,“Superplastic Behavior of the Sn-Pb Eutectic in the As-Worked State,”Metallurgical Transactions A, 13A (1982), 53-58.
8. M. A. Murzinova, G. A. Salishchev and D. D. Afonichev, “Superplasticity of Hydrogen-Containing VT6 Titanium Alloy with a Submicrocrystalline Structure,” The Physics of Metals and Metallography,104 (2007), 195–202.
9. I. Weiss and S.L. Semiatin, “Thermomechanical processing of alpha titanium alloys—an overview,” Materials Science and Engineering A, 263 (1999), 243–256.
10. Y.Y. Zong, D.B. Shan, M. Xu, Y. Lv, “Flow softening and microstructural evolution of TC11 titanium alloy during hot deformation,” Journal of Materials Processing Technology, 209 (2009), 1988–1994.
11. X. Zhang, Y. Zhao, W. Zeng, “Effect of hydrogen on the superplasticity of Ti600 alloy,” International Journal of Hydrogen Energy, 35 (2010), 4354 – 4360.

USING TEMPORARY HYDRIDE FORMATION IN METASTABLE BETA TITANIUM ALLOYS TO IMPROVE THE MICROSTRCTURE

Hans-Jürgen Christ, Vitali Macin

Institut für Werkstofftechnik, University of Siegen, Siegen, 57076, Germany

Keywords: metastable titanium alloy, thermohydrogen treatment, hydrogen-induced redistribution of alloying elements, hydride formation, microstructure modification

Abstract

Hydrogen can be used as a temporary alloying element during the heat treatment, often referred to as Thermohydrogen Treatment (THT), in order to improve the mechanical properties of titanium alloys by means of microstructure modification being unobtainable by conventional heat treatment. THT is based on the changes of the stability and transformation kinetics of phases as well as on the formation of hydrogen-induced phases. The volume effects associated with hydride formation lead to local matrix deformation accompanied by an increase in the dislocation density. It is shown in this contribution that hydride formation accompanied by a hydrogen-induced redistribution of alloying elements and subsequent complete hydride dissolution can be used to establish a fine microstructure via hydride-induced recrystallization (Ti 10-V-2Fe-3Al) and a homogeneous formation of alpha nuclei indirectly via hydride precursors (Ti 3Al-8V-6Cr-4Mo-4Zr).

Introduction

The high-strength metastable β titanium alloy Ti 10V-2Fe-3Al (Ti 10-2-3) exhibits excellent hot forgeability and hardenability of sections up to 125 mm thickness, high toughness in air and salt water environments at temperatures up to 315°C as well as creep-stability characteristics close to the α+β alloys [1]. Ti 10-2-3 was developed for the use in the aerospace industry for near-net shape forging applications (landing gear structure of the Boeing 777 and Super Lynx helicopter rotor head) [2-3]. Excellent corrosion resistance, reasonable room temperature formability and very good fatigue endurance make the highly beta-stabilized titanium alloy Ti 3Al-8V-6Cr-4Mo-4Zr (Beta-C^{TM}) an attractive material for fatigue critical components in structural aerospace applications requiring high strength as well as low weight at the same time [1]. In this context, the applicability range of this metastable β titanium alloy might be restricted due to its proneness to an inhomogeneous precipitation of the strengthening hcp α phase within the β microstructure and the formation of soft α phase layers along β grain boundaries (α_{GB} phase). The formation of precipitate-free zones (PFZ) and the α_{GB} phase are known to be microstructural key features determining the life of highly beta-stabilized titanium alloys, since monotonic and cyclic plastic deformation are concentrated in these weak regions. With increasing yield strength of the material, such microstructure phenomena control fatigue crack initiation as well as fatigue crack propagation [2-3]. With regard to the application requirements, metastable β titanium alloys can be heat-treated to a wide strength-toughness range [1].

In order to broaden the applicability range of metastable β titanium alloys, innovative routes of thermomechanical processing are necessary. The use of hydrogen as a temporary alloying element during the heat treatment of titanium alloys (Thermo Hydrogen Treatment THT) is considered to be an auspicious approach in order to improve mechanical properties under monotonic and cyclic loading conditions by means of microstructure modification, because β titanium alloys feature excellent characteristics concerning kinetics and thermodynamics of hydrogen sorption as well as good resistance to hydrogen embrittlement [4]. However, research into THT of β titanium alloys is still rare because of their complex microstructures and sensitive response upon heat treatment.

Basically, interstitially dissolved hydrogen as an alloying element stabilizes the bcc β phase with simultaneous dissolution of the hcp α phase and reduces significantly the β-transus temperature (T_β) [5]. Additionally, hydrogen exerts a strong influence on the formation of metastable phases (β', ω_{iso}, ω_{ath}, α'', α') and on kinetics of phase transformation reactions leading to a redistribution of alloying elements. Hydrogen diffusion is strongly affected by the connectivity of the β phase leading to higher D_H-values in microstructures with continuous β diffusion paths as compared to microstructures, where these easy diffusion paths for hydrogen are interrupted by the α phase [6]. The hydrogen-induced phases play an essential role in the successful implementation of THT. The grain and phase boundaries are preferred nucleation sites for a hydrogen-induced phase as consequence of hydrogen supersaturation and eutectoid decomposition of the β phase. The volume effects up to 30% associated with the hydride formation may lead to a local plastic deformation around hydrides accompanied by a change in the dislocation arrangement [7].

In the present study, individual five-step THTs for the two metastable β titanium alloy Ti 10-2-3 and Beta-C^{TM} were successfully developed and implemented. The THT developed for Ti 10-2-3 is based on the fact that the fatigue life can be improved basically by a reduced β grain size, a dissolution of soft primary α phase (α_P) and an increased potential of the particle strengthening of the β matrix. In case of Beta-C^{TM}, the basic idea of the THT treatment is to avoid the formation of α_{GB}, to optimize precipitate morphology of the α phase accompanied by suppression of PFZ formation as well as to intensify the precipitation reaction during aging by prior hydride-induced plastic matrix deformation.

Materials and Experimental Details

Beta-C^{TM} was received in the form of a bar with a diameter of 30 mm and a length of 1 m from GfE Metalle und Materialien GmbH Nürnberg in Germany. In the as-received condition, the alloy microstructure consists of equiaxed β grains with a mean grain size of 62 μm. Direct formation of the α phase occurs predominantly at regions of locally increased stress, such as β grain boundaries or dislocation clusters, exhibiting an increased driving force for α precipitation. Hence, a duplex aging treatment was designed for Beta-C^{TM}, which is described in detail elsewhere [8]. The duplex aging consists of a solution treatment (ST, 920°C 30 min), a pre-aging (440°C 12 h) and a final-aging (500°C 24 h). Starting out from a completely recrystallized β microstructure, the pre-aging at low temperature leads to indirect formation of the homogeneously distributed α phase via metastable β´ precursors. Precipitation hardening of the β matrix is completed by the final aging at increased temperature to the desired strength level. Prior working history exerts considerable influence on β recrystallization and α precipitation

kinetics. Based on a prevention of the α_{GB} formation, an optimized distribution and morphology of the strengthening α phase, the duplex aging leads to a significantly improved fatigue limit as compared to the direct-aged condition.

Ti 10-2-3 was received as ingot with a diameter of 300 mm and a length of 100 mm from OTTO FUCHS KG Meinerzhagen in Germany. The as-received material consists of the precipitation-hardened β matrix as well as the globular and plate-shaped α_P phase. The average size of the β grains is approx. 5 µm. The conventional technical heat treatment consisting of ST at 40°C below β transus temperature (T_β of 795°C) followed by water quenching (WQ) is described in detail elsewhere [9-10]. ST enables to adjust a desired strength/ductility relation by means of the volume fraction of the α_P grains and the strengthening α_S phases [2-3]. Aging of the solution-treated material at 525°C for 8 h results in an enhanced volume fraction of the strengthening secondary α (α_S) phase and the continuous α_{GB} phase.

Cylindrical rods with a diameter of 7 mm for microstructure analysis and of 11 mm for mechanical tests were produced by wire-cut electrical discharge machining (EDM). Microstructure investigations of mechanically ground and polished metallographic specimens were carried out using a field-emission scanning electron microscope (FE-SEM) of type FEI Helios Nanolab 600 equipped with energy-dispersive X-ray spectroscopy (EDX), backscattered electron (BSE), and electron backscatter diffraction (EBSD) detectors. The mechanical sample preparation especially polishing with an oxide polishing slurry (50 nm) resulted from time to time in preparation artifacts appearing as very fine-sized white spots in FE-SEM micrographs (BSE contrast). The EDX analysis allows the identification of the hydrogen-induced distribution of alloying elements associated with enrichment/depletion of alloying elements during phase transformations. The computerized determination of the average β grain size was carried out by means of the linear intercept method of grain boundaries according to DIN EN ISO 643 as well as of the orientation imaging microscopy (OIM) analysis based on the EBSD technique [5].

All steps of annealing and the THT process were performed in a horizontal vacuum furnace with attached gas supply to enable heat treatment in various gas atmospheres (Ar, He, He/H_2). Hydrogen uptake from hydrogen-containing gas mixtures is exclusively diffusion-controlled at higher hydrogenation temperatures above about 800°C [6]. The inhibiting effect of passivated titanium surface (TiO_2) on hydrogen absorption increases with decreased hydrogenation temperature leading to a deviation from the diffusion-controlled rate. In order to eliminate the inhibiting effect of a titanium oxide scale on hydrogen sorption behavior at lower temperatures in the (α+β)-regime, an electrochemical coating consisting of a thin catalytic Pd layer on the titanium substrate was applied in three steps: degreasing, activation, and subsequent metal deposition [6]. The complex electrochemical coating of thin catalytic Pd layers can be substituted by using a Zr foil as an auxiliary oxygen getter material during hydrogen gas charging.

In order to determine the phase transition temperatures, the prepared cylindrical samples with a diameter of 7 mm were hydrogenated to defined hydrogen concentrations in flowing gas mixtures of required hydrogen partial pressure followed by homogenization in the β-regime. An encapsulation in quartz glass was applied in order to avoid the undesirable hydrogen release during homogenization. Subsequently, the homogenized samples were divided into equal segments, again encapsulated and finally aged at predefined temperatures for 24 h followed by WQ. The existence of hydrides, silicides, and α precipitates was analyzed by means of EDX and BSE mode to determine the respective phase fields of the alloy-hydrogen phase diagram [5]. Determination of hydrogen content was conducted by a Leco RH-404 hydrogen analyzer using an inert gas fusion.

Microhardness measurements by Vickers method enabled to adjust the desired aging parameters. Tensile properties were determined using cylindrical specimens according to EN 100002 with a gauge length of 30 mm and a diameter of 6 mm. Fatigue tests of ground and electropolished samples described in [8] were performed at a constant stress ratio R of -1 and a frequency of 20 Hz under symmetrical tension-compression conditions. The fatigue limit $\sigma_{50\%}$ (50% failure probability) were determined statistically according to the modified staircase method for a maximum number of load cycles of $N=2*10^6$.

Results and Discussion

Ti 10-2-3 Thermohydrogen Treatment

According to Figure 1, the THT process, referred to as hydride-induced recrystallization of β phase (HIRB), consists of five treatment steps: (1) ST in vacuum at 770°C for 1 h (point A, see Figure 1), (2) (α+β)-hydrogenation in a hydrogen containing gas mixture at 550°C for 16 h accompanied by the precipitation of hydrides (line BC, see Figure 1), (3) recrystallization in an inert gas atmosphere at 700°C for 1 h (line CD, see Figure 1), (4) dehydrogenation in vacuum at 790°C for 45 min (line DE, see Figure 1) followed by WQ, and (5) technical aging at 525°C for 8 h (point F, see Figure 1).

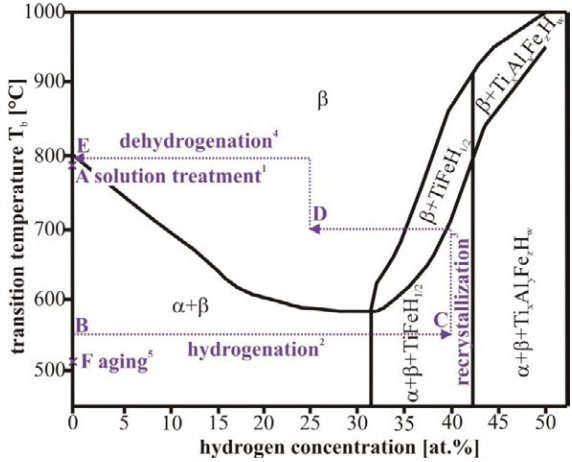

Figure 1. T_β as a function of the hydrogen concentration; the HIRB-THT process is marked by ABCDEF.

ST (step 1) of the as-received material (see Figure 2a) is carried out slightly below T_β at 770°C for 1 h followed by vacuum cooling (VC) resulting in a reduction of the α_P volume fraction from 45 vol.% to 14 vol.% without an appreciable growth of β grains and with a formation of the orthorhombic martensitic α´´ needles inside β grains (see Figure 2b). The low volume fraction of the α_P phase is a requirement for a later recrystallization because of the inhibiting effect of α_P grains on the recrystallization of the β matrix [1]. The β/α´´ transformation is accompanied by a

crystal distortion of the adjacent β matrix due to volume effects. The martensitic formation associated with excess distortion energy in the β matrix intensifies the precipitation of hydrides in the next step of the HIRB-THT process. In contrast to VC, WQ after ST upon technical heat treatment suppresses the α´´-formation [10].
Hydrogenation at a hydrogen partial pressure of 40 mbar for 16 h (step 2) at 550°C of the Pd-coated material in the (α+β)-regime gives rise to 40 at.% H and induces a diffusion-controlled formation of the TiFeH and $TiFeH_2$ hydride phases (see Figure 2c). Carrying out the hydrogenation in the (α+β)-regime ensures that the globular α_P phase remains at the grain boundary triple points keeping the β grain size constant.

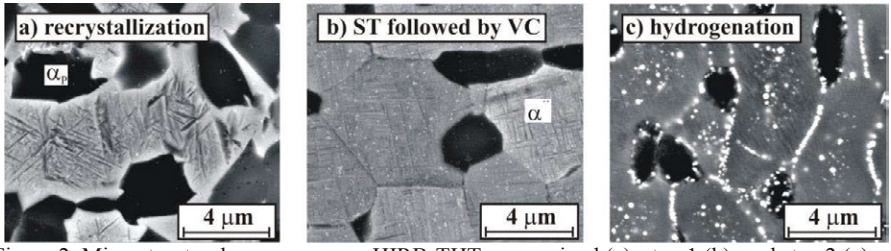

Figure 2. Microstructural response upon HIRB-THT; as-received (a), step 1 (b), and step 2 (c)

The EDX analysis in Figure 3 reveals that the hydride formation is accompanied by a hydrogen-induced diffusional redistribution of alloying elements between hydrides and the β matrix. The precipitation of TiFeH and $TiFeH_2$ is in disagreement with the reported information on hydride formation in other titanium alloys [7].

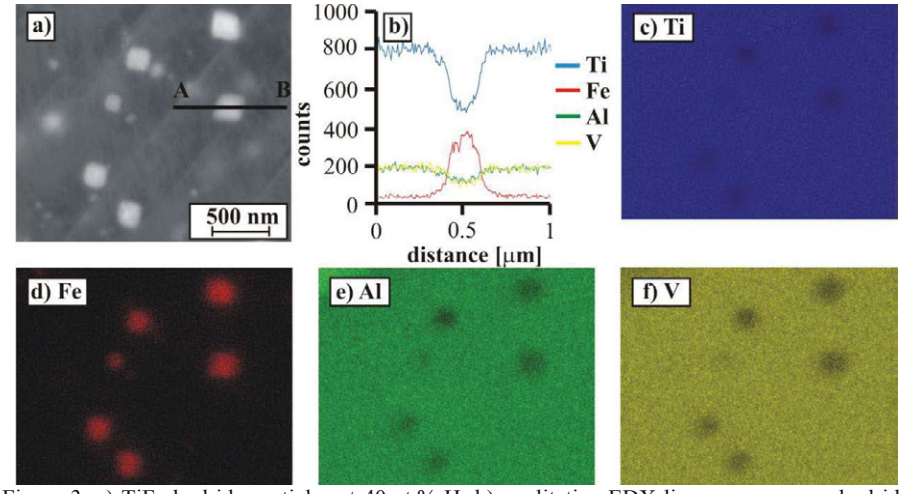

Figure 3. a) TiFe-hydride particles at 40 at.% H; b) qualitative EDX line scan across a hydride particle along blank line AB; c-f) EDX element distribution micrographs

The initial stage of hydrogen-induced phase transformation comprises the hydride nucleation followed by diffusion growth of hydrides. The diffusion coefficient of Fe in β phase at a given temperature is much lower than that of hydrogen. Because of the large redistribution and the low diffusion coefficient of the hydride-forming element Fe in the β phase, it can be claimed that the Fe diffusion controls mainly the hydrogen-induced phase transformation [5].
The precipitates in form of large intergranular hydrides can be attributed to the agglomeration of small intergranular hydrides. Additionally to the hydride precipitates at β grains and α/β phase boundaries due to increased driving force for the precipitation, the previous formation of the martensitic phase promotes a homogeneous distribution of the hydrides within β grains. The size and the volume fraction of hydrides are determined by the hydrogen content, the hydrogenation temperature, the hydrogenation time, and the hydrogen partial pressure. As pointed out earlier, the volume expansion during precipitation causes a crystal lattice distortion around hydrides associated with an increased dislocation density.
Annealing of the hydrogenated microstructure in Ar above the hydrogen-reduced β transus temperature T_β at 700°C (step 3) leads to a recrystallized fine-grained β matrix without any α phase formation as shown in Figure 4a. A partial hydrogen release from 40 at.% H to 25 at.% H in combination with a complete hydride decomposition reduces the required dehydrogenation time of the next HIRB-THT step. The hydride dissolution is associated with the homogeneous redistribution of the hydride-forming alloying element Fe. The hydride-induced recrystallization of the β phase can be related to the high dislocation density comparable to the condition after cold working [5]. As a requirement for recrystallization, the α_P phase must be dissolved in order to facilitate the motion of β grain boundaries. Conventional technical heat treatment of Ti 10-2-3 takes advantage of the remaining α_P phase at the triple points of β grains, since an extensive β grain coarsening occurs without α_P. For example, ST of the as-received, almost hydrogen-free microstructure at 800°C (T_β+10°C) for 1 h results in a considerably strong β grain growth to a size of about 200 μm. In contrast, a β grain growth could not be observed during Ar-annealing despite complete dissolution of the α_P phase. The average β grain size was determined to be approx. 4 μm. Because of the α_P absence, the β phase is oversaturated with Al as a α-stabilizing element. This causes an increase of the critical quenching rate enhancing the risk of an undesirable martensite formation upon the next step of THT.
In order to avoid hydrogen embrittlement, the recrystallized β microstructure must be vacuum annealed (step 4) to remove residual hydrogen without affecting the grain size distribution (see Figure 4b). Because of the fast diffusion-controlled hydrogen desorption behavior at the applied temperature, short dehydrogenation at 790°C close to the T_β value followed by WQ leads to a hydrogen content similar to the one in the as-received condition. The key requirement for the selection of dehydrogenation parameters is the prevention of both the appreciable coarsening of β grains and the coverage of β grain boundaries with continuous soft α layers. The suppression of the α_P phase formation during hydrogen increases the precipitation pressure of the α_S formation upon the final step of THT required for a fine and homogeneous distribution of the α_S precipitates. It should be mentioned that, due to the complete α_P dissolution, the disadvantageous fine α´´ platelets can form at β grain boundaries despite WQ, if this WQ is not performed quickly [11].
The HIRB-THT process is completed by aging at 525°C for 8 h (step 5) causing the formation of fine acicular α_S precipitates shown in Figure 4c. The selection of the aging parameters enables to determine the size of the needle-shaped α_S phase and hence the mechanical properties according

to the specific application requirements [5]. The change of the α_S morphology as a consequence of increased aging time manifests itself in an increase in the thickness of the continuous layers of α_{GB} and the size of the α_S phase precipitates. Due to the complete α_P dissolution and the homogeneous distribution of Al during THT steps 3 and 4, HIRB-THT results in an increased driving force for precipitation hardening. Despite this enhanced driving force for the α_S phase formation, the thickness of the α_{GB} layers after aging at 525°C for 8 h, referred to as the peak-aged condition, is less than 70 nm compared to the reference heat treatment with an average thickness of 250 nm. The reduced driving force for the formation of the α_{GB} phase in the THT-treated material can be attributed to the recrystallized condition of the β phase.

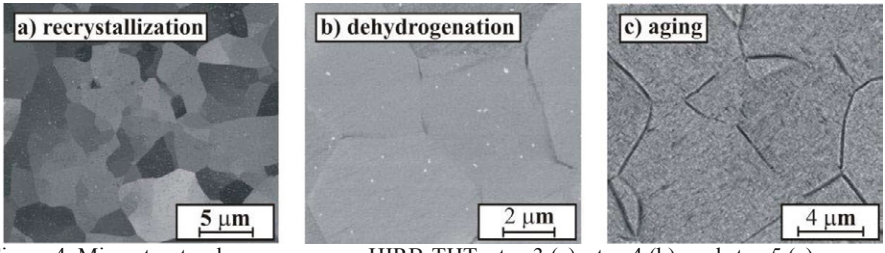

Figure 4. Microstructural response upon HIRB-THT; step 3 (a), step 4 (b), and step 5 (c)

In comparison to the corresponding technical heat treatment, the THT microstructure causes exhibits an increase of the tensile strength by 60 MPa with decreasing the fracture strain from 7% to 1%. The ductility reduction can be attributed to the absence of the α_P phase and the high degree of the precipitation hardening. The fatigue limit $\sigma_{50\%}$ of THT-processed material is increased slightly from 672 MPa in the reference condition to 688 MPa. The improvement of the tensile and fatigue strength corresponds to the increased age hardening of the fine-grained β matrix and the reduced volume fraction of α_{GB} phase. The slight increase in the fatigue strength $\sigma_{50\%}$ by 16 MPa indicates that the effect of hydride-induced microstructural modification is smaller as compared to the ultimate tensile strength. It can be concluded that the observed preferred β crystal orientation after recrystallization influences strongly the fatigue limit because of corresponding anisotropic behavior [5].

Beta-C^{TM} Thermohydrogen Treatment

The five-step THT process, referred to as hydride-induced alteration of dislocation arrangement (HADA), shown schematically in Figure 5 comprises: (1) recrystallization at 920°C for 30 min (point A, see Figure 5), (2) diffusion-controlled hydrogenation at 700°C for 2 h (line BC, see Figure 5), (3) hydride formation by annealing in air at 650°C for 2 h (line CD, see Figure 5), (4) dehydrogenation in vacuum at 780°C for 45 min (line DE, see Figure 5), and (5) technical aging at 500°C for 20 h (point F, see Figure 5).
Complete recrystallization at 920°C for 30 min (step 1) in the stability range of silicides enables the formation of $(Ti,Zr)_3Si_5$ particles (see Figure 6a). Silicides act as precursors for a radial hydride precipitation and are a requirement for a homogeneous distribution of the hydride phase. The grain size increases from initially 60 µm to 120 µm. However, in this alloy the coarsening of β grains is of minor interest concerning the fatigue strength, since the α_{GB} phase formation is

suppressed. Recrystallization does not change the hardness in comparison to the as-received condition, exhibiting a hardness value of 290 HV.

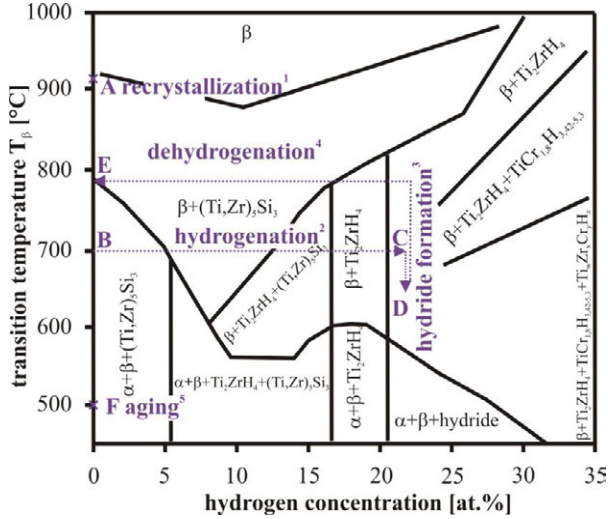

Figure 5. T_β as a function of the hydrogen concentration; the HADA-THT process is shown schematically by ABCDEF.

According to Figure 6b, hydrogenation to 22 at.% H at 700°C for 2 h (step 2) leads to a slight hydride formation primarily on the β grain boundaries (hydride seams). Hydrogenation time, which is required to establish an equilibrium condition of the dissolved hydrogen in the β phase at a given temperature, was assessed by means of a numerical diffusion calculation. The required data, such as the hydrogen solubility and the hydrogen diffusion coefficient, have been experimentally determined in previous studies [6]. Interstitially dissolved hydrogen causes solid solution hardening with an increase in hardness from 290 HV to 330 HV.

The formation of the Ti_2ZrH_4 hydride by annealing in air at 650°C for 2 h (step 3) is based on homogeneous nucleation and diffusion-controlled growth of acicular and plate-shaped hydrides within β grains. The accelerated kinetics of hydride nucleation reduces the annealing time to 2 h being necessary to facilitate a homogeneous distribution of hydrides (see Figure 6c). The volume effects associated with the hydride precipitation lead to a strong local matrix deformation accompanied by formation, accumulation and pile-up of dislocations. The hydride formation leads to a precipitation hardening resulting in hardness of 360 HV. The local dislocation arrangements caused by the hydrides seem to act as precursors for the α phase nucleation in step 5, as will be documented below. Hence, this is in analogy with the effect of the β´ phase particles in the duplex-aging cycle (introduced in [8]).

Similar to the hydrogen-induced phase transformation in Ti 10-2-3, the diffusive mobility of the hydride-forming alloying element in the β phase is expected to control the phase transformation rate. The EDX analysis in Figure 7 reveals that preferentially Zr segregates to the hydrogen-induced phase, while Ti, Al, V, Cr, and Mo diffuse into the β matrix.

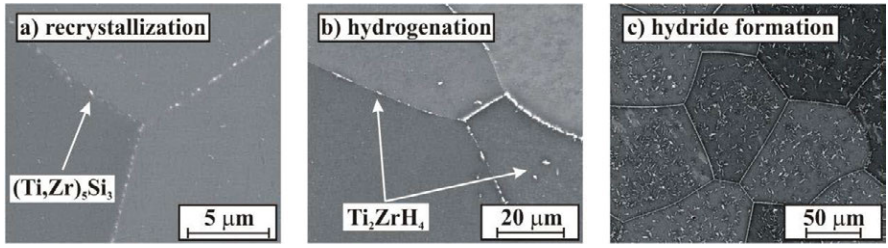

Figure 6. Microstructural response upon HADA-THT; step 1 (a), step 2 (b), and step 3 (c)

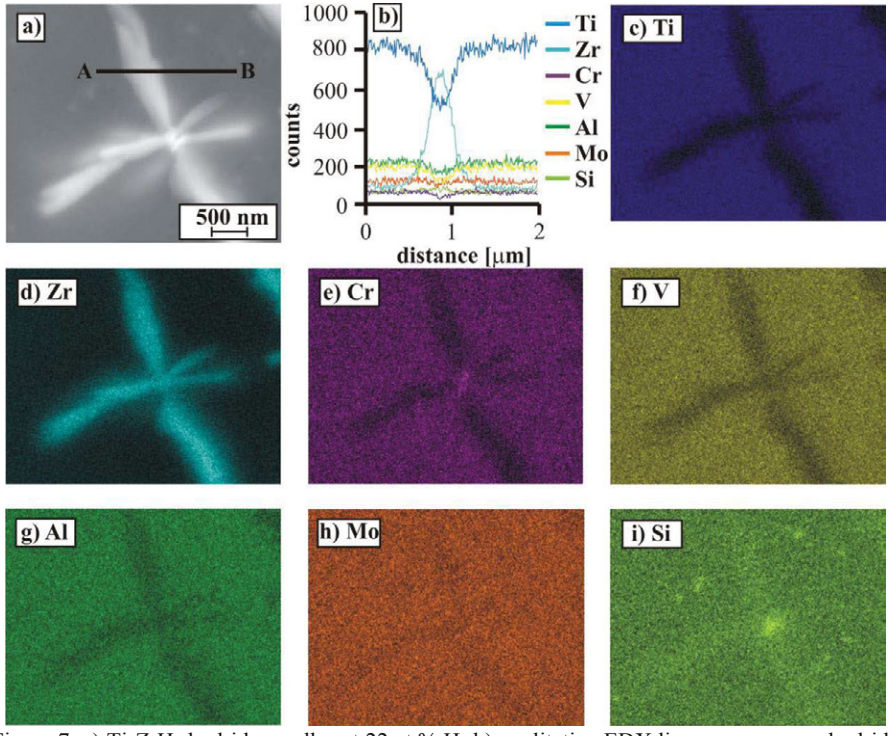

Figure 7. a) Ti_2ZrH_4 hydride needles at 22 at.% H; b) qualitative EDX line scan across a hydride particle along blank line AB; c-i) EDX element distribution micrographs

In order to avoid hydrogen embrittlement, dehydrogenation (step 4) is performed by vacuum annealing at 780°C for 45 min. An approximately diffusion-controlled desorption behaviour leads to complete hydrogen release accompanied by the hydride dissolution and homogeneous distribution of alloying elements. The appearance of globular and acicular $(Ti,Zr)_5Si_3$ particles in Figure 8a can be attributed to a silicide precipitation either already during recrystallization (step 1) or during dehydrogenation in the stability range of silicides (step 4). Hardness measurements

after dehydrogenation exhibit an unchanged high Vickers hardness of 360 HV indicating that the hydride-induced change of the dislocation arrangement are retained after hydride dissolution. This high lattice distortion associated with excess distortion energy in the β matrix promotes a homogeneously formation of α nuclei indirectly via hydride precursors in the next heat treatment step.

Aging at 500°C for 20 h (step 5) leads to the precipitation of fine homogeneously distributed α particles without any formation of α_{GB} phase (see Figure 8b). Because of the same aging temperature of 500°C as applied to the duplex aging process, a deviation in aging response can be attributed to the hydrogen-induced effects on the precipitation behaviour of the acicular α phase. The reduction of the required aging time from 24 h to 20 h indicates an enhanced kinetics of α phase nucleation due to hydride-induced β crystal lattice distortion, which intensifies the α precipitation during aging. In comparison to the duplex aging, the completely THT-treated condition exceeds the average hardness value by 100 HV. This additional hardening after HADA-THT can be attributed to intensified precipitation hardening as well as hydride-induced deformation hardening. Since the volume fraction and the particle distribution of hydrides can easily be controlled by the HADA-THT parameters (particularly the hydrogen charging conditions, the hydride formation temperature and the dehydrogenation temperature), the size and distribution of the α precipitates and, hence, the amount of associated precipitation hardening can be adjusted. A homogeneous hydride precipitation is the key to facilitate a homogeneous distribution of fine α needles within the β grains.

A comparison of the final microstructures obtained by THT (see Figure 8b) with the duplex-treated condition (see Figure 8c) reveals clearly a refinement of the α phase, meaning significantly reduced intermediate spacing between the acicular α precipitates. The duplex aging causes the formation of micro-PFZ. These micro-PFZs determine the onset of monotonic or cyclic plastic deformation and are directly related to the particle size distribution and volume fraction of the α phase [12].

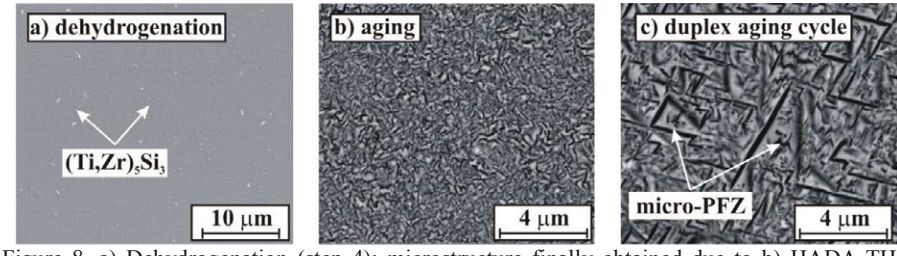

Figure 8. a) Dehydrogenation (step 4); microstructure finally obtained due to b) HADA-THT process and c) duplex aging treatment

In comparison to the duplex aging treatment, the THT-treated material exceeds the average value of the ultimate tensile strength by 40 MPa [12], which is accompanied by an expected decrease in tensile ductility from 9% to 7% due to a high degree of the precipitation hardening. The HADA-THT microstructure leads to an increase of the fatigue strength $\sigma_{50\%}$ from 700 MPa in the reference condition [8] to 760 MPa. The significant enhancement of the tensile strength and the fatigue limit is based on the suppression of the α_{GB} formation and the refined α precipitates associated with the prevention of micro-PFZs [12].

Conclusions

The aim of the present study was to develop and implement a thermohydrogen treatment process (THT), which should improve the fatigue limit of the metastable beta titanium alloys 10V-2Fe-3Al (Ti 10-2-3) and Ti 3Al-8V-6Cr-4Mo-4Zr (Beta-C^{TM}) by means of a hydride-induced microstructure modification. The hydrogen-induced formation of $TiFeH_{1/2}$ in Ti 10-2-3 and of Ti_2ZrH_4 in Beta-C^{TM} is the microstructural key feature of both five-stage THT processes. The main research results can be summarized as follows:

1. The THT process developed for Ti 10-2-3, referred to as hydride-induced recrystallization of β phase (HIRB), consists of five steps: (i) solution treatment slightly below T_β, (ii) (α+β)-hydrogenation accompanied by a diffusion-controlled formation of homogeneously distributed hydrides, (iii) recrystallization in Ar associated with a partial hydrogen release and homogeneous distribution of alloying elements, (iv) dehydrogenation close to T_β followed by water quenching, and (v) technical aging.
2. The hydride-induced recrystallization of the bcc β phase can be attributed to the high dislocation density resulting from crystal lattice distortion around hydrides.
3. In comparison to the commonly used heat treatment, the HIRB-THT process results in a recrystallized fine-grained β matrix, suppresses widely the primary hcp α phase and reduces significantly the volume fraction of disadvantageous soft α phase layers along β grain boundaries (α_{GB}). Consequently the HIRB-THT condition exhibits a by 60 MPa higher tensile and the fatigue strength $\sigma_{50\%}$ is slightly raised by 16 MPa.
4. The five-step THT devised for Beta-C^{TM}, referred to as hydride-induced alteration of dislocation arrangement (HADA), comprises the following steps: (i) recrystallization in the single-phase β condition, (ii) diffusion-controlled hydrogenation, (iii) hydride formation by annealing at intermediate temperature without hydrogen release, (iv) dehydrogenation close to T_β, and (v) technical aging.
5. Volume effects associated with the hydride precipitation lead to local plastic deformation of the adjacent β matrix. The resulting hydride-induced local dislocation arrangements are still present after dehydrogenation. The increase in dislocation density manifests itself during aging in the formation of fine and homogeneously distributed α precipitates and reduces the time required for the precipitation process.
6. Even compared to an optimized duplex aging treatment, HADA-THT is characterised by the suppression of the α_{GB} formation, the prevention of micro-PFZs, and the refinement of the strengthening α phase. Hence, a significant improvement of the fatigue limit $\sigma_{50\%}$ by about 60 MPa and of the tensile strength by about 40 MPa compared to the duplex-aging cycle can be achieved by a conceived application of this THT process.

References

[1] R. Boyer, G. Welsch, and E.W. Coolings, *Material Properties Handbook: Titanium Alloys* (Materials Park, OH: ASM International, 1994), 797-865.

[2] G. Lütjering and J.C. Williams, *Titanium* (Berlin: Springer-Verlag, 2007), 283-336.

[3] M. Peters and C. Leyens, *Titan und Titanlegierungen* (Weinheim: WILEY-VCH Verlag, 2002), 139-161.

[4] F.H. Froes, O.N. Senkov, and J.I. Qazi, ‘‘Hydrogen as Temporary Alloying Element in Titanium Alloys: Thermohydrogen Processing’’, *International Materials Reviews*, 49 (3-4) (2004), 227-245.

[5] V. Macin and H.-J. Christ, ‘‘Influence of Hydride-Induced Microstructure Modification on Mechanical Properties of Metastable Beta Titanium Alloy Ti 10V-2Fe-3Al’’*, International Journal of Hydrogen Energy,* (2015), in press, doi:10.1016/j.ijhydene.2015.06.167.

[6] P. Schmidt and H.-J. Christ, ‘‘Effect of Surface Condition and Microstructure on Hydrogen Uptake in Metastable β Titanium Alloys’’, *Proceedings of the 12th World Conference of Titanium*, ed. L. Zhou, H. Chang, Y. Lu, and D. Xu (Beijing: Science Press, 2012), 508-513.

[7] I. Lewkowicz, ‘‘Titanium-Hydrogen’’, *Solid State Phenomena*, 49-50 (1996), 239-280.

[8] P. Schmidt, A. El-Chaikh, and H.-J. Christ, ‘‘Effect of Duplex Aging on the Initiation and Propagation of Fatigue Cracks in the Solute-rich Metastable β Titanium Alloy Ti 38-644’’, *Metallurgical and Materials Transaction*, 42A (9) (2011), 2652-2667.

[9] V. Macin and H.-J. Christ, ‘‘Hydride-Induced Microstructure Optimization of High-Strength Beta Titanium Alloy Ti 10-2-3 by Thermohydrogen Treatment’’, *Hydrogen-Materials Interactions: Proceedings of the 2012 International Hydrogen Conference*, ed. B.P. Somerday and P. Sofronis (New York, NY: ASME Press, 2014), 669-676.

[10] V. Macin, P. Schmidt, and H.-J. Christ, ‘‘Thermohydrogen Treatment of High Strength Beta Titanium Alloy Ti 10V-2Fe-3Al’’, *Proceedings of the Euro Light Mat 2013: International Congress on Light Materials*, (DGM, 2013), 1-6, http://www.dgm.de/download/tg/1171/1171-27.pdf.

[11] B. Wang, Z. Liu Y. Gao, S. Zhang, and X. Wang, ‘‘Microstructural Evolution during Aging of Ti 10V-2Fe-3Al Titanium Alloy’’, *Journal of University of Science and Technology Beijing*, 14 (4) (2007), 335-340.

[12] P. Schmidt, V. Macin, and H.-J. Christ, ‘‘Thermohydrogen Treatment of Highly Beta-Stabilized Titanium Alloy Ti 38-644 (Beta-C^{TM})’’, *Hydrogen-Materials Interactions: Proceedings of the 2012 International Hydrogen Conference*, ed. B.P. Somerday and P. Sofronis (New York, NY: ASME Press, 2014), 661-668.

NUMERICAL SIMULATION OF SOLIDIFICATION MICROSTRUCTURE WITH ACTIVE FIBER COOLING FOR MAKING FIBER-REINFORCED ALUMINUM MATRIX COMPOSITES

Zhiliang Yang, Bo Wang*, Shupei Liu, Jie Ma, Wanping Pan, Shuai Feng, Liang Bai, Jieyu Zhang
State Key Laboratory of Advanced Special Steel, School of Materials Science and Engineering, Shanghai University, Shanghai 200072, China
Keywords: fiber-reinforced, numerical simulation, temperature field, microstructure

Abstract

Solidification process is very important for making fiber reinforced aluminum matrix composites. Some recent studies have used cooling through reinforcing carbon fibers to obtain better control over the solidification microstructure in the post pressure infiltration process. The present work is focused on studying the effect of active cooling fiber on temperature, thermal stresses and microstructure of aluminum matrix composites. The predicted results show that the temperature gradients of both the matrix and the carbon fiber vary continuously before loading the stress field, while the temperature gradient between the fiber and Al2014 melt become steeper as a cliff after loading the stress field (when Al2014 melt solidified completely). The predicted results of temperature contour agree well with the result of references. The microstructure simulation results shows that grains grow along the opposite direction of heat flow, and form the finer equiaxed grains away from the cold end.

Introduction

Aluminum matrix composites have been widely used in aerospace, automobile industrial, due to its high specific strength, high electrical performance and good thermal conductivity, as well as good wear resistance. However, the poor wettability, the chemical reaction between the aluminum melt and Carbon fiber and the distribution of the grain size during solidification, will restrict the development of the industry[1]. The squeeze infiltration process and solidification process are the two critical steps for synthesis of metal matrix composite materials (MMCs). The wettability, density and aspect ratio of carbon fiber have a certain effect on the infiltration process. Moreover, the cooling method of the system directly or indirectly affects the solidification process, which also has an important effect on the microstructure and mechanical properties of the composite[2].

Squeeze casting has been a well-known technique for fabricating Al and Mg alloy based MMCs[3]. However, the neglecting of the solidification step could result in a lot of quality and performance problems during synthesizing MMCs. Therefore, the study on the solidification process of MMCs is necessary. In present simulation process, with an assumption of completed infiltration process, the analysis is focused on the solidification step.

Recently, Nguyen and Rohatgi *et al*. [2,4] developed a modified pressure infiltration process to synthesize carbon-fiber reinforced Al MMCs and study the effect of cooling conditions on the temperature and solidification. In this process, the ends of carbon fibers are extended out of the crucible to induce selective cooling, as shown in Fig. 1. Based on this method, the present work is focused on studying the effect of active cooling fiber on temperature, thermal stresses and

* Corresponding author.
E-mail address: bowang@shu.edu.cn (bo wang)

microstructure of aluminum matrix composites. These simulation results will be helpful in understanding the microstructure solidification and in explaining the experimental results.

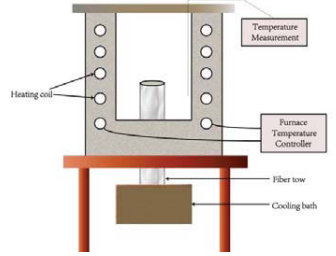

Fig. 1 Modified squeezed infiltration equipment[2,4]

Problem Description

Energy Equations

Analysis of temperature field is usually based on the three-dimensional unsteady heat conduction partial differential equations, that is

$$\rho c_p \frac{\partial T}{\partial t} = \frac{\partial}{\partial x}\left(\lambda \frac{\partial T}{\partial x}\right) + \frac{\partial}{\partial y}\left(\lambda \frac{\partial T}{\partial y}\right) + \frac{\partial}{\partial z}\left(\lambda \frac{\partial T}{\partial z}\right) \quad (1)$$

where ρ, c_p, t and T are the density, the specific heat capacity, the time and the temperature.
In the simulation, assuming that the inner-surface of the carbon fiber and the aluminum melt is completely contacted. The boundary conditions for the fiber are set as insulation on the top surface, fixed temperature at the bottom surface.

Nucleation and Growth models
Continuous nucleation model which is heterogeneous nucleation based on Gaussian distribution[5] is used. The changes of grain density with undercooling in the bulk (surface) is given by

$$\frac{\mathrm{dn}}{\mathrm{d}(\Delta T)} = \frac{n_{max}}{\sqrt{2\pi}\Delta T_\sigma} \exp\left[-\frac{(\Delta T - \Delta T_{max})^2}{2\Delta T_\sigma^2}\right] \quad (2)$$

where ΔT_{max} , ΔT_σ and n_{max} are the mean undercooling, the standard deviation and the maximum density of nuclei.
In casting, the total undercooling of the dendrite tip ΔT is generally the sum of four contributions[5]

$$\Delta T = \Delta T_c + \Delta T_t + \Delta T_k + \Delta T_r \quad (3)$$

where ΔT_c, ΔT_t, ΔT_k, and ΔT_r are the undercooling contributions associated with solute diffusion, thermal diffusion, attachment kinetics and solid-liquid interface curvature respectively.
During the process of solidification, the constitutional supercooling and kinetic undercooling have effect on dendrite growth. In general, the constitutional supercooling plays a decisive role on the dendrite tip, thus the growth kinetics of dendrite tip using KGT (Kurz-Givoanola-Trivedi) model. The growth rate formula of the dendrite tip can be expressed as[5]

$$\vartheta_{tip} = \alpha(\Delta T)^2 + \beta(\Delta T)^3 \quad (4)$$

where α and β are empirical constants.

Nondimensionalization

In the process of simulation, some parameters are non-dimensionalized, including geometry, temperature and time equations[6].

$$\bar{r} = \frac{r}{R_a}, \bar{z} = \frac{z}{R_a}, \bar{R}_f = \frac{R_f}{R_a} \tag{5}$$

$$AR = \frac{L}{R_a}, \theta_m = \frac{T_m - T_0}{T_i - T_0}, F_o = \frac{t\alpha_a}{R_a^2} \tag{6}$$

Simulation method

Geometrical parameters

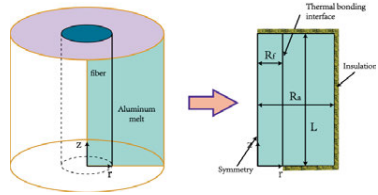

Fig. 2 3D axisymmetric carbon fiber/aluminum system

A cylindrical geometry element with the same axis is chose to study the process of solidification, as shown in Fig. 2. The carbon fiber is located in the center of the mold, and is wrapped in aluminum melt. The reason for choosing such a model is that a large number of units can be seamlessly integrated into the entire three-dimensional space, which helps to improve the simulation accuracy and simplify the boundary conditions. The radius and height of the mold respectively set to one unit. The carbon fiber radius is taken as 0.2 units.

Material Properties

The material properties of the fiber and the melt are shown in Table I. Some parameters such as Table II are shown in the microstructure simulation.

Table I. Material properties used in the analysis[4]

	k(W/m C)	C_p(J/kg K)	ρ(kg/m^3)	Thermal expansion coefficient(m/m℃)	Young's modulus(Gpa)	Poisson's ratio
Carbon fiber	54	921	1800	-0.1×10^{-6}	217	0.3
Aluminum Al-2014	193	880	2800	23×10^{-6}	71	0.33

Table II. The parameters of CAFÉ

coefficient of the growth kinetics		Nucleation parameters(bulk)			Nucleation parameters(surface)		
a_2	a_3	DTm	DTs	Nmax	dTm	dTs	Gmax
4.7×10^{-6}	2.5×10^{-7}	2.5	1	7×10^{10}	0.5	0.1	5.0×10^{10}

Results and discussions

Thermal analysis

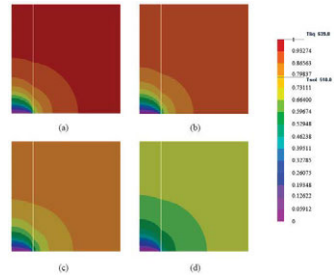

Fig. 3. Temperature distribution in model of R_f =0.2, AR = 1 at Fo = (a) 0.039, (b) 0.078, (c) 0.156, and (d) 0.234

At four different time points, the temperature distribution of the mold is shown in Fig. 3. We can see that the temperature gradient of the mold gradually extended to the upper of the melt with increasing time. The temperature of the whole model presents a decreasing trend, because the thermal diffuse and release from the cold side of the fiber continuously. At the same time, the rate of the melt temperature decreases faster than the fiber, which is based on the higher thermal conductivity of the aluminum.

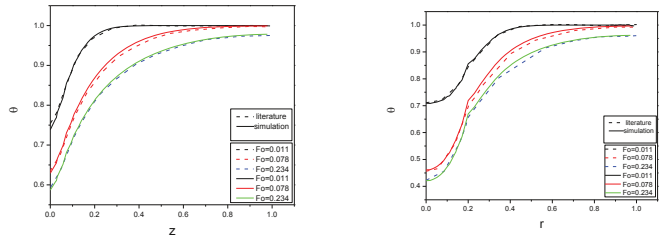

Fig. 4 Comparison simulation with literature about the temperature evolution

The present simulation was verified with the results reported by Nguyen *et al.* [2]. Fig. 4 compares the temperature distribution for the same process conditions. The results from the present 3-D simulation show a well quantitative agreement with the results obtained from literature. From this figure, it can also be seen that the temperature gradient of melt decreases with increasing of distance about axial and radial.

Analysis of thermal stresses

The thermal stress is based on the change of temperature, and will exist in the solidified melt. Through the study of thermal stress, it is reflected the distribution of thermal stress in the melt, the phenomenon of stress concentration and the displacement caused by the stress deformation.

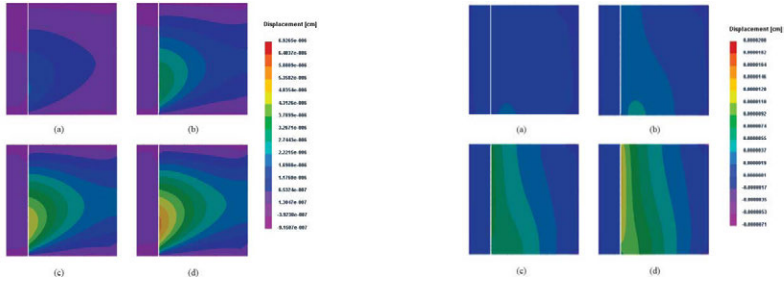

Fig. 5 Axial deformation and Radial deformation at (a) Fo = 0.039, (b) Fo = 0.078, (c) Fo = 0.156, (d) Fo = 0.234

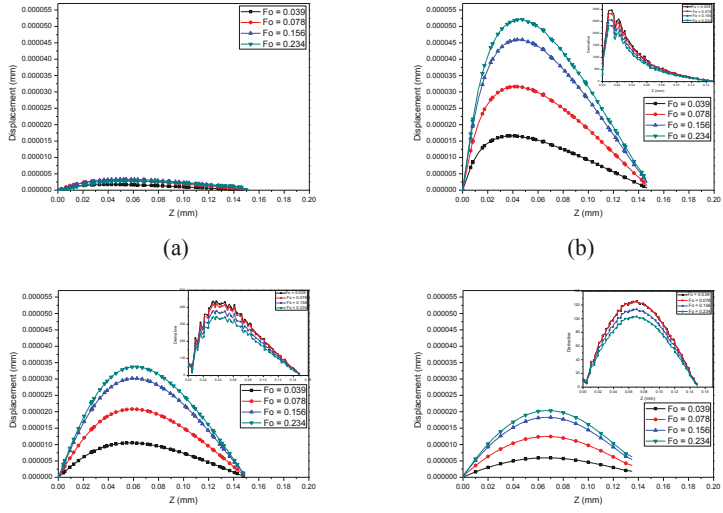

Fig. 6 Deformation in axial direction at (a) r = 0.15, (b) r = 0.25, (c) r = 0.5, (d) r = 1

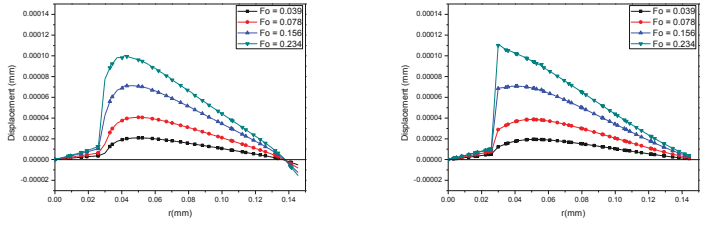

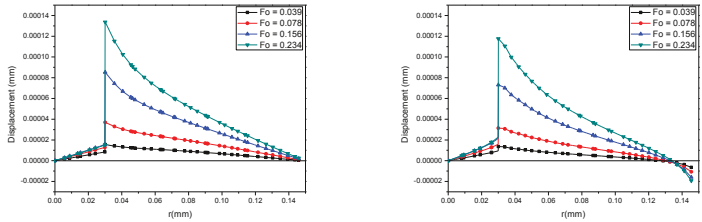

(c) (d)

Fig. 7 Deformation in radial direction at (a) z = 0, (b) z = 0.1, (c) z = 0.5, (d) z = 1

Fig. 5 shows the axial deformation and radial deformation under different cooling time. Fig. 6 and Fig. 7 presents the curves of stress deformation under different cooling time along the axial direction and the radial direction. As the cooling time increased, the extent of axial deformation and radial deformation are obviously increased, as observed in Fig. 5. Since the thermal expansion coefficient of the aluminum melt is positive, the melt volume shrinks when the temperature decreases. On the contrary, the fiber volume expands due to the negative thermal expansion coefficient. In general, the displacement caused by the thermal stress tends to move along the opposite direction of heat flow in the aluminum melt. So, the deformation presents positive tendency in the z-axis and in the r-axis. In the process of cooling, the absolute value of thermal expansion coefficient of the melt is significantly greater than the fiber, which leads to generate a gap between the aluminum melt and the carbon fiber. Besides, their temperature profile occurs cliff as presented in Fig. 8. The displacement will first increase and then decrease with increasing the distance of axial direction at the same cooling time. With the increase of r-axis distance, the extent of deformation gradually decreases, due to the smaller temperature gradient, shown in Fig. 6(b) through (d). Fig. 6(a) indicates that the displacement is not obvious inside the fiber, because the thermal expansion coefficient is far less than the melt.

The displacement of the melt is reduced sharply at the same cooling moment. The displacement of the interface of fiber-melt instantaneously reaches the maximum as shown in Fig. 7. The extent of deformation decreases with the increase of the z-axis distance due to the decrease of temperature gradient. The negative displacement is observed by Fig. 7(a) and Fig. 7(d) at z = 0 and z = 1(corresponding to the bottom surface and the top surface of the model) near the corner of the model.

Fig. 8 The gap between carbon fiber and aluminum melt

Microstructure analysis

According to the basic theory of nucleation, the well acknowledged mechanism of nucleation is heterogeneous nucleation generating by the particle or substrate in the metal liquid among the homogeneous nucleation mechanism and heterogeneous nucleation. The particle derives from the metal liquid or artificial, the instantaneous nucleation and continuous nucleation are the two approaches for the process of heterogeneous nucleation in the microstructure simulation. The researcher, Rappaz[7], makes the hypothesis for the nucleation algorithm, they assume that the possible nucleation location, where its temperature arrives lower or more, will not develop the nucleation, otherwise, the nucleation position, where its temperature attain below the liquid temperature, will generate the nucleation.

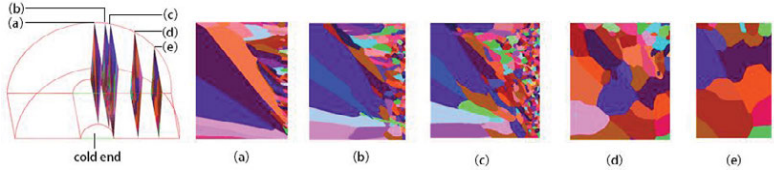

Fig 9 Microstructure morphology of different axial sections

Fig. 9 and Fig. 10 shows the microscopic morphology of the axial and radial sections respectively. In the axial direction, the temperature gradient is obviously sensitive to the microstructure that close to the cold end. The growth of grain near the chilling layer is restrained and form finer equiaxial crystals due to the effect of chilling. However, grain is tend to form coarse columnar crystals away from the chilling layer, as Fig. 9(a) through (c) shown. The temperature of Al2014 is relatively high and the thermal gradient decreases away from the cold end. The microstructure inclined to form coarse equiaxed grains, as shown in Fig. 9(d，e).

Fig. 10 Microstructure morphology of different radial sections

In the radial direction, as the location of the section away from the cold end, the columnar crystal will gradually become equiaxed grains at the edge of slice. On the contrary, equiaxed grains will develop columnar crystals near the chilled layer, as shown in Fig. 10(a) through (d). The reason of this situation is that the growth of crystal is always along with the opposite direction of heat flow.

Conclusions

This paper presents a three dimensional analysis of the effect of active cooling fiber on temperature, thermal stresses and microstructure of aluminum matrix composites. The following results were found.

(1) Based on a modified infiltration process by Nguyen *et al.* [2], the effect of active cooling conditions on temperature distribution was simulated. The predicted results of temperature evolution agreed well with the reported results [2].

(2)The thermal stress depends on the temperature, and will exist only when the melt is solidified. Due to the effect of thermal stress, a phenomenon of stress concentration appeared at the edges

of the Al2014 melts and the interface of the fiber-melt. Moreover, the thermal expansion coefficient of the fiber is far lower than the melt, which leads to a gap between the aluminum melt and the carbon fiber, and finally affects the diffusion of heat in Al2014 melt.
(3) The formation of microstructure is related to the temperature field. The heat is only transfer out the bottom of the fiber because the outer surfaces of the model given by the adiabatic thermal boundary condition, except the bottom of the carbon. Therefore, the dendrite obliquely grows along the model from the bottom of fiber. In addition, the size of the dendrite is also related to the cooling rate, resulting in coarse crystals in the lower of the model more than the upper.

Acknowledgments

The author gratefully acknowledges the financial support received from the Innovative Foundation of Shanghai University (SDCX2013031) and Shanghai Education Commission.

References

1. Kaczmar Jacek W., Naplocha Krzysztof, Morgiel Jerzy, "Microstructure and Strength of Al2O3 and Carbon Fiber Reinforced 2024 Aluminum Alloy Composites," Journal of Materials Engineering and Performance, 23 (8) (2014), 2801-2808.
2. Nguyen NQ. et al., "Modeling the Effect of Active Fiber Cooling on the Microstructure of Fiber-Reinforced Metal Matrix Composites," Metallurgical and Materials Transactions A, 40 (8) (2009), 1911-1922.
3. Xie J. et al., "Transit simulation analysis for the pressure infiltration of aluminum melts into metal matrix components," ASME Heat Transfer Summer Conference, 3 (2005), 213-220.
4. Rohatgi PK, Tiwari V, Gupta N, "Squeeze infiltration processing of nickel coated carbon fiber reinforced Al-2014 composite," Journal of Materials Science, 41 (21) (2006), 7232-7239.
5. Xiang-mei Li, Jie-yu Zhang, Bo Wang et al., "Simulation of stray grain formation during unidirectional solidification of IN738LC superalloy," Journal of Central South University of Technology, 18 (2011), 23-28.
6. Gupta Nikhil, Nguyen Nguyen Q, Rohatgi Pradeep K, "Analysis of active cooling through nickel coated carbon fibers in the solidification processing of aluminum matrix composites," 42 (4) (2011), 916-925.
7. GANDIN Ch.-A, RAPPAZ M., "A 3D CELLULAR AUTOMATON ALGORITHM FOR THE PREDICTION OF DENDRITIC GRAIN GROWTH," Elsevier Science Ltd, 45 (5) (1997), 2187-2195.

ASSESSMENT OF TRIBOLOGICAL PROPERTIES OF CAST AND FORGED Ti-6Al-7Nb AND Ti-6Al-4V ALLOYS FOR DENTAL APPLICATIONS

Ahmed Zaki[1], Shimaa El-Hadad[1], Waleed Khalifa[2]

[1]Central Metallurgical Research and Development Institute, Dept. of Manufacturing Technology; El-Tebbin, Helwan, P.O. Box 87, Egypt

2 Cairo University, Faculty of Engineering, Dept. of Mining, Petroleum and Metallurgical Engineering; Giza, 12613, Egypt

Keywords: Alpha/Beta titanium alloys, Casting, Thermal oxidation, Wear.

Abstract

Thermal oxidation treatment is an easy and environment friendly technique that can be used to harden the surface of titanium alloys, and hence improve the poor tribological properties of these materials. The aim of the present research was to evaluate the tribological behavior of cast and forged Ti6Al7Nb and Ti6Al4V implants after different thermal oxidation treatments. A significant increase in surface hardness of the two alloys was achieved due to the formation of a hard oxide layer and oxygen diffusion zone beneath it. The oxygen diffusion zone, which was generated at 900 ^{o}C, showed the best wear resistance in case of Ti6Al4V alloy. On the other side, no remarkable enhancement was observed in the Ti6Al7Nb alloy even at 1100 ^{o}C, regardless of the improved surface hardness. In addition, the development of alpha case in the cast samples was different from the forged ones. The widmanstätten microstructure of the cast samples showed thinner alpha case compared to the equiaxed structure of the forged samples in both alloys.

Introduction

Titanium alloys are used in a variety of applications, where the combination of chemical and mechanical properties is important. With low weight, high strength and good corrosion behavior, titanium alloys can be selected for aerospace structures, chemical and automotive industries and as biomedical material [1]. Ti6Al4V is an α/β alloy and is the first titanium alloy registered as biomaterial in ASTM standard F 136. However, it reported to be toxic due to release of vanadium ions and reaction with human tissue [2]. So new alloy Ti6Al7Nb was developed to overcome this drawback and standardized as biomaterial in the ASTM standard F 1295 [3]. This alloy has been developed for use in surgical and dental field, for example, dental implant, denture bases, crown, clasps, etc., which are produced mainly by casting: especially investment casting. Cast titanium alloys are generally lower in mechanical properties than the forged ones [4].

During the service of titanium implants in the human body, they are subjected to rubbing contact, and sliding of other surfaces that cause stresses at the contact areas, and may cause severe damage to their surface. Wear may occur on the implant surface very rapidly, resulting in severe damage. The poor tribological properties due to crystal structure and electron configuration characteristics of titanium alloys limited their widespread use in many industrial fields. The wear resistance and surface hardness of titanium alloys can be improved by surface treatment. Considering the reactivity of titanium with nitrogen and oxygen, it is possible to improve the surface characteristics of titanium alloys by means of diffusion-based treatments as glow-discharge, nitriding and oxidation treatments [5]. Thermal oxidation technique (TO) is found to be simple and cost effective way to change the nature of the surface and to improve the wear behavior and the surface hardness of Ti6Al4V and Ti6Al7Nb alloys. This process involves heating titanium in an oxygen containing atmosphere for a period of time, thus an oxygen diffusion zone with enhanced tribological properties can be obtained [6]. However, it was reported that the original microstructure of the sample can influence its response to the surface treatment [7]. Since this surface property is of prime interest in the field of dental implants, the influence of thermal oxidation on the tribological properties of forged and cast Ti6Al4V and Ti6Al7Nb alloys was investigated.

Experimental work

In the current study, forged and cast samples of Ti-6Al-4V (Ti64) and Ti-6Al-7Nb (Ti67) alloys were used. The forged samples described in [8] were received as 10 mm diameter bars. The cast samples were prepared using the centrifugal casting machine illustrated in Fig. 1. At first, wax patterns shaped as bars were prepared and used to make the mold cavity. The mold is prepared using a metallic ring and investment powder specially made for casting titanium and its alloys. The slurry was mixed under vacuum to decrease the titanium chemical reactivity. In addition, the melting crucibles were made of zirconia bonded ceramic material to avoid reaction with titanium. The standard steps for mixing, de-waxing and sintering were followed [9]. The investment mold was preheated to 850 ^{o}C before casting and positioned as shown in Fig. 1. The titanium alloy pieces were placed in the melting crucible and the melting chamber washed several times by argon. Once melting was completed, the rotation started so the mold was filled under centrifugal action. The samples were then taken out of the mold, cleaned, cut and polished for isothermal oxidation.

Samples of forged and cast Ti-6Al-4V and Ti-6Al-7Nb alloys were thermally oxidized (TO) in air circulating furnace. The thermal oxidation treatments process was conducted separately for 5 h at 700 °C, 900 °C and 1100 °C, at the normal atmospheric pressure. The samples were then cooled in air until reaching the room temperature. The cross-sections of the TO samples were gently grinded with SiC abrasive paper up to 1200 mesh, then polished using 1 μ alumina, and etched with 2% HF solution. Microstructure characterization was done by optical and field emission (FEM) microscopies. In order to identify the type of surface oxides, the poorly adhering oxide scales were removed, and the surface was characterized using thin film X-ray diffraction (XRD), with Cu Kα radiation source. Vickers microhardness tester ($HV_{0.5}$) was used to determine the hardness of the newly developed alpha case. Wear resistance of different samples, after removal of the oxide case, was evaluated using pin on disc wear test type. The samples were fixed against a rotating stainless steel ring (63 HRC), under a constant load of 180 N, at a speed of 1.0 m/s, for 1800 m sliding distance. Dry sliding was used. The wear resistance was measured in terms of the weight loss of the tested materials.

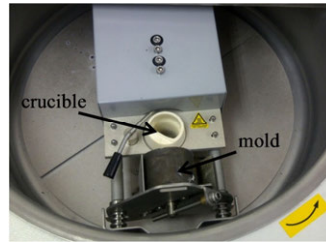

Fig.1 Experimental setting for centrifugal casting of titanium alloy samples.

Results and Discussion

Microstructure

The microstructure of the as-forged and as-cast Ti64 and Ti67 samples are shown in Fig. 2. The forged samples are characterized by their fine equiaxed α grains with small amount of β phase, while the cast samples showed the typical widmanstätten colonies of α with some prior β grains. Figure 3 presents the FEM micrographs of the forged Ti64 and Ti67 samples after isothermal oxidation for 5 h at 700 ^{o}C, 900 ^{o}C, and 1100 ^{o}C, respectively. By comparing the oxidized layer (OL) in the inserted compositional images, it was clear that increasing the oxidation temperature increased the thickness of OL. Moreover, the oxide layer was thicker in case of Ti64 than that of Ti67. It was also observed that a well-developed oxygen diffusion layer (ODL), reported earlier as alpha case [4], has formed. This layer is formed due to the diffusion of the oxygen atoms into the titanium alloy through interstitial diffusion mechanism, and preferably occupy the free octahedral interstitial positions in the HCP crystal lattice of α-titanium phase [10]. In the current study, the formation of thick ODL at high temperatures was expected, since the current α/β alloys contain mainly α- phase. It was early reported that the solubility of oxygen in α–titanium is about 30 at. %, whereas in ß–titanium it reaches a maximum of 8 at. % at 1700 °C. It is also worth mentioning that oxygen has a stabilizing effect for the HCP structure of α –phase [11].

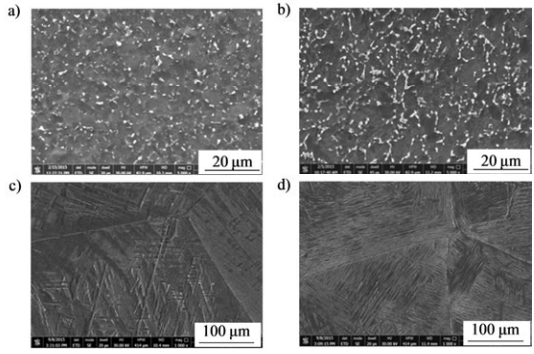

Fig. 2 FEM of the as- forged (a, b) and as-cast (c, d); Ti64 and Ti67 alloy samples respectively from the left side.

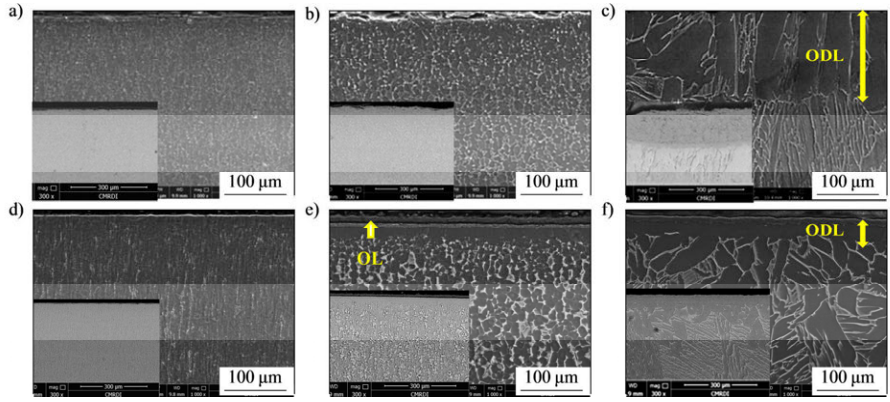

Fig. 3 FEM micrographs of the forged; Ti64 (a, b, c) and Ti67 (d, e, f); after oxidation for 5h at 700 °C, 900 °C, and 1100 °C, respectively from the left side.

The XRD pattern of the surface of TO samples oxidized at 1100°C is shown Fig. 4. This pattern confirmed that the diffusion layer is composed mainly of the rutile form of TiO_2 in both Ti64 and Ti67 alloys. Some niobium oxide, NbO, was also observed in the case of Ti67 alloy. The thickness of alpha case, as pronounced from Fig. 3, increased at high oxidation temperatures. At 1100°C, the grains of the base metal coarsen along with the coarsening of the alpha case, as shown in Fig. 3 (c and f). It is also clear that the thickness of ODL (alpha case) in Ti64 is larger than that in Ti67. This is because Nb increases the oxidation resistance of titanium alloy, by replacing Ti ions with Nb ions, so that TiO_2 is doped by Nb, leading to a decrease in oxygen vacancies and slow O_2 diffusion. Nb also lowers the oxygen solubility in titanium alloys [12]. Figure 5 shows some cracks developed in the alpha case in forged Ti64 after thermal oxidation at 1100°C, this is due to the high diffusion rate of O_2 in the layer beneath the oxide layer forming very hard and brittle alpha case. It was also noted that more cracks were developed in the ODL layer, and through the interface adjacent to the base metal of Ti64 compared to Ti67.

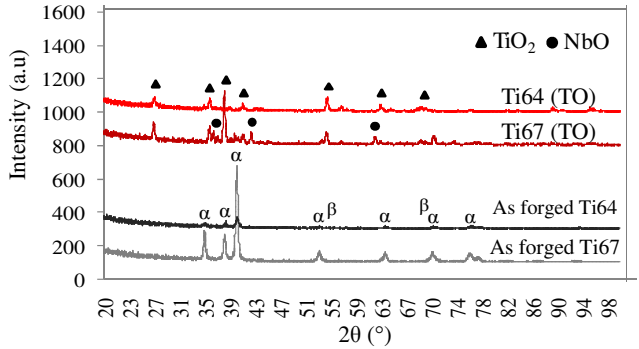

Fig. 4 X-ray diffraction patterns of as forged Ti64 and Ti67 alloys, before and after thermal oxidation at 1100 °C.

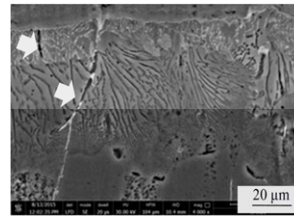

Fig. 5 FEM of the forged Ti64 after isothermal oxidation for 5h at 1100°C.

Figure 6 presents the microstructure of the cast Ti64 and Ti67 oxidized samples. As can be seen, the alpha case in the TO cast samples increased with increasing the oxidation temperature. However, the development of the case in cast samples was different from the forged ones. Comparing Fig. 6 (c, f) to Fig. 3 (c, f) shows that the alpha case thickness is lower in the cast samples than in the forged samples in both alloys. This can be owed to the starting microstructure in each case. According to Sugahara *et al* [13], the widmanstätten microstructure of the cast samples has more oxidation resistance than the equiaxed microstructure. The thickness of alpha case in forged and cast Ti64 and Ti67 alloys were measured with the optical microscope and are summarized in Table 1.

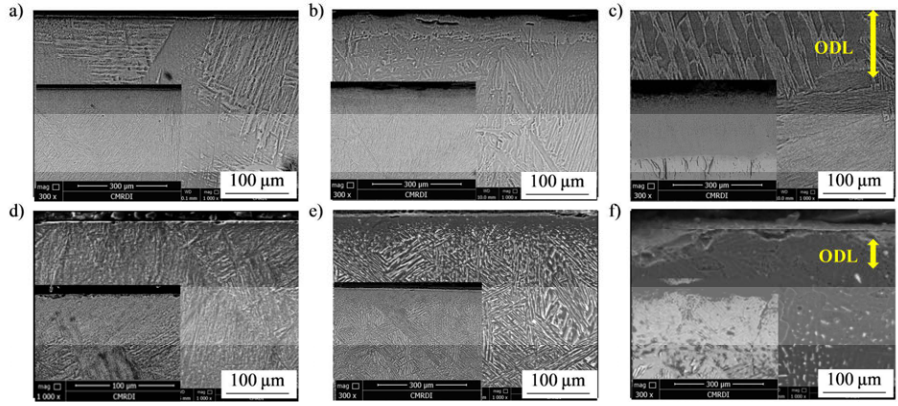

Fig. 6 FEM of the cast; Ti64 (a, b, c) and Ti67 (d, e, f); after isothermal oxidation for 5h at 700 °C, 900 °C, and 1100 °C, respectively from the left side.

Table 1 Thickness of alpha case in (µm) for forged and cast Ti64 and Ti 67 alloys.

Oxidation temperature		700 °C	900 °C	1100 °C
Forged	Ti64	17 µm	180 µm	450 µm
	Ti67	8 µm	45 µm	230 µm
Cast	Ti64	10 µm	100 µm	250 µm
	Ti67	5 µm	17 µm	90 µm

Tribological properties

Since the oxygen diffusion layer formed as a result of surface oxidation, it is expected to affect the surface properties, microhardness and wear behavior of the oxidized samples. Microhardness measurements on the ODL as a function of the oxidation temperature are shown in Fig. 7. The hardness of the as forged samples was around 320 $HV_{0.5}$ for both of Ti64 and Ti67 alloys. After oxidation, the maximum hardness achieved for Ti64 was 850 $Hv_{0.5}$ at 1100 °C, which means that a hardened case was obtained. This case was very brittle as evidenced from the microcracks around the indentations shown in Fig. 8. In forged Ti67, the maximum hardness was 600 $Hv_{0.5}$, which is lower than that of Ti64 at 1100 °C. This can be explained by the thinner ODL obtained in the Ti67 sample, as a result of the Nb resistance to oxidation. In the oxidized cast samples, the hardness value observed was lower than those of the forged samples. This is in a good agreement with alpha case measurements shown in Table 1, and it can emphasize that the oxidation resistance of the widmanstätten structure is more than the equiaxed structure.

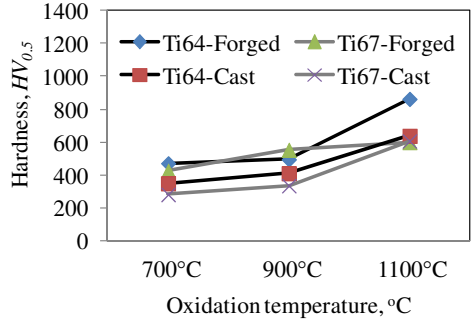

Fig. 7 Microhardness of the Ti64 and Ti67 samples.

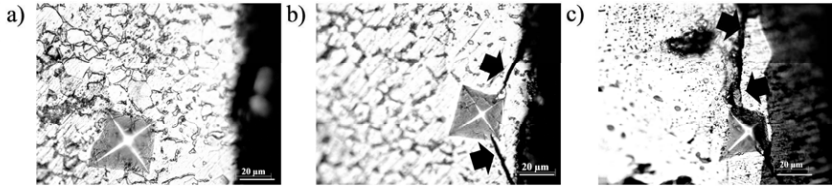

Fig. 8 Optical micrographs for the hardness indentations in the forged Ti64 samples treated at a) 700, b) 900 and c) 1100. The arrows refer to the observed cracks.

Figure 9 presents the wear results in terms of weight loss, for both forged and cast samples, respectively. The forged Ti64 alloy, shown in Fig. 9 (a), showed significant improvement in the wear resistance as oxidation temperature increases. The highest wear resistance was found at 900 °C, and it slightly decreased at 1100 °C. This may be due to the observed brittleness of the alpha

case at 1100 °C. On the other hand, forged Ti67 alloy showed little decrease in the weight loss over the investigated temperature range. Therefore, it can be said that Ti64 alloy has superior wear resistance compared to Ti67 at oxidation temperatures of 900 °C and 1100 °C. Similar to the forged samples, the wear resistance of the cast Ti64 alloy (Fig. 9(b)) increased with increasing the oxidation temperature, while the wear resistance of cast Ti67 was slightly affected by thermal oxidation. Concluding, wear resistance of both forged and cast Ti64 alloy can be extremely improved by thermal oxidation treatment at 900 °C for 5h. More time and/or higher oxidation temperature is required in case of Ti67 alloy to overcome the oxidation resistance caused by Nb.

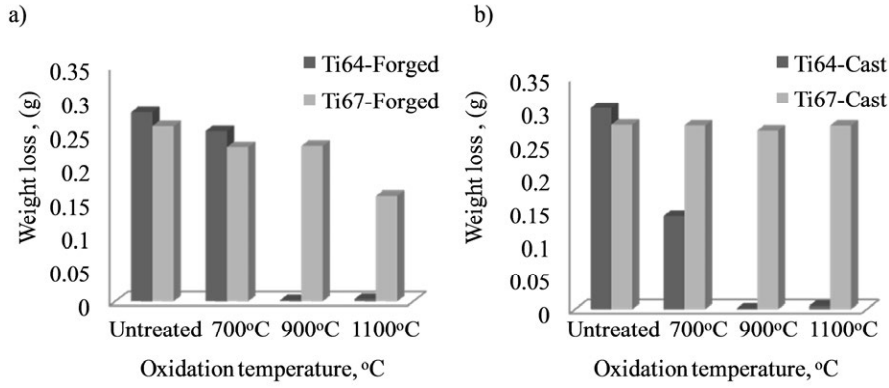

Fig. 9 Wear test results of a) forged and b) cast Ti64 and Ti67 samples after thermal oxidation at different temperatures for 5h explained by weight loss.

Conclusions

In the current investigation, the effect of thermal oxidation on the tribological properties of forged and cast Ti6Al4V and Ti6Al7Nb alloys was investigated, and the following conclusions were obtained:

- The oxygen diffusion zone, which generated at high temperature showed the best wear resistance in case of Ti6Al4V alloy, while no remarkable enhancement was observed in the Ti6Al7Nb alloy, regardless of the improved surface hardness.
- The development of alpha case in the cast samples was different from the forged ones. The widmanstätten microstructure of the cast samples showed thinner alpha case compared to the equiaxed structure of the forged samples in both alloys.

Acknowledgements

The authors would like to acknowledge the financial support of "Science and Technology Development Fund, Egypt, under grant No. 5540.

References

1] S.A. Brown and J.E. Lemons, *Medical application of Titanium and Its Alloys*, ASTM STP 1272, ASTM, 1996, pp ix-xii.
2] Y.Okazaki, *J. Jpn. Inst. Met.,* 1997, vol. 36, pp. 966-68.
3] *Standard specification for wrought Titanium 6Al4V ELI Alloy for Surgical Implant*, ASTM Designation F136-82, ASTM, 1994, pp. 19-20.
4] C. Leyens and M. Peters, *Titanium and Titanium Alloys* (Wiley-VCH, 2003).
5] A. Molinari, G. Straffelini, B. Tesi, T. Bacci, G. Pradelli, *Wear,* 203-204 (1997) 447.
6] H. Guleryuz, H. Cimenoglu,"Effect of thermal oxidation on corrosion and corrosion-wear behavior of a Ti-6Al-4V alloy*," Biomaterials*, 479 (2004) 3325-3333.
7] S. El-Hadad, M. Ibrahim and Lothar Wagner," Characteristics of Anodized Layer in Investment Cast Ni50Ti50 Shape Memory Alloy," *Journal of Metallurgy*, JM/346328, published online, 2014.
8] S. El-Hadad, M. Waly, W. Khalifa "Microstructure Evolution and Mechanical Properties of α-β Heat Treated Ti-6Al-4V Alloys," MONTREAL'2015 AES-ATEMA 22nd International Conference "Advances and Trends in Engineering Materials and their Applications" (Montreal, CANADA: June 15 – 19, 2015).
9] J.E. Sopcak, *Handbook of lost wax or investment casting*, (Gem Guides Book Co., (publisher), Baldwin Park. CA. 1986).
10] H. H. Wu and D. R. Trinkle "Direct diffusion through interpenetrating networks: oxygen in titanium," *Physical Review Letters,* 107(2011) 1–4.
11] Z. Liu and G. Welsh "Literature survey on diffusivities of oxygen, aluminum and vanadium in alpha titanium, beta titanium and in rutile," *Metallurgical and Materials Transactions* A, 19 (1988) 1121–1125.
12] H. Jiang et al. "Effect of Nb on the high temperature oxidation of Ti-(0-50 at.%)Al," *ScriptaMaterialia,*46 (2002) 639-643.
13] T. Sugahara, et al., "The Effect of Widmanstättenand Equiaxed Microstructures of Ti-6Al-4V on the Oxidation Rate and Creep Behavior," *Materials Science Forum,* 636-637 (2010) 657-662.

TMS2016

145th Annual Meeting & Exhibition

SUPPLEMENTAL PROCEEDINGS

Phase Transformations in Multi-component Systems: An MPMD Symposium Honoring Gary R. Purdy

SOLID STATE REACTION OF $Nd_2Fe_{14}B$ AND CARBON

Jie Liu[1], Shuqiang Guo[1], Yuyang Bian[1], Lei Guo[1], Lan Jiang[1], Man Zhang[1], Shuai Ma[1], Weizhong Ding[1]

[1]Shanghai Key Laboratory of Modern Metallurgy & Materials Processing, Shanghai University, Shanghai 200072, China

Abstract: X-ray diffraction (XRD), scanning electron microscopy (SEM), inductive-coupled plasma spectroscopy (ICP), oxygen analyzer were used to investigate the solid state reaction of $Nd_2Fe_{14}B$ powders with carbon. The experiment results revealed that Nd-rich phase (FCC−NdO) was formed after sintering when the samples contain oxygen (1 percent). With the carbon content of Nd-rich phase increasing, the Nd-rich phase changed from FCC-NdO phase to h-Nd_2O_3 phase. And the phase evolution of Nd-rich phase was sensitive to the carbon concentration as well as the sintering time. When the oxygen free samples sintering over 1100 ℃, the phase evolution of iron was sensitive to the sintering temperature. With the temperature increased to 1300 ℃, the Nd-rich compounds (NdFeC compounds) decreased and the NdC_2 increased.

Keywords: Solid state reaction, Phase transformation, Nd-rich phase, NdC_2

Introduction

It has been more than 30 years since Sumitomo Special Metals and General Motors declared the discovery of the NdFeB magnets [1]. Because of the outstanding magnetic properties, the NdFeB magnets have wide application in electric and hybrid electric vehicles, wind turbines, hard disks and electronic components [2].

It is reported that carbon have the influence on the coercivity of NdFeB magnets. A low content of C added to intergranular region of sintered NdFeB permanent magnets is attributed to the grain refinement and coercivity. But the excessive C can form some Nd-carbides with the α-Nd phase at triple junctions and lead to the corrosion of the main phase $Nd_2Fe_{14}B$. So adding a proper amount of C is benefit to NdFeB sintered magnets [3-6]. Pan and Zhang [7] studied the solid state reaction of the $Nd_2Fe_{14}B$ phase with carbon. And some Nd-enriched carbides were formed which was related to carbon concentration in the sample and the solid state reaction temperature. Nakamoto et al. [8] and Bian et al. [9, 10] studied the recovery of rare earth elements as oxides from NdFeB magnets with a carbon crucible as a contact material to maintain the oxygen potential that rare earth oxides and the Fe can coexist.

In this work, we have revisited the solid state reaction of carbon and $Nd_2Fe_{14}B$ using x-ray diffraction (XRD), scanning electron microscopy (SEM), inductive-coupled plasma spectroscopy (ICP), oxygen analyzer.

Experiment procedure

The ingot of the chemical composition of $Fe_{bal.}Nd_{30.73}Pr_{4.39}La_{1.58}B_{0.96}Al_{0.83}$ and the powders of the chemical composition of $Fe_{bal.}Nd_{20.20}Zr_{5.20}Pr_{4.72}La_{2.13}B_{1.14}Ce_{0.26}$ were used in this work. The ingot was pulverized mechanically in air leading to these NdFeB powders containing oxygen (1 percent). Then the two kinds of NdFeB powders were mechanically mixed with carbon powders (99.9995%) in glove box respectively. Two different carbon concentrations were selected for this study: 5.0 and 10.0 wt. % C. And the mixed powders were pressed into a disk under a pressure of 0.14 GPa. All the NdFeB-C samples were sintered in a vacuum furnace and the heating speed was 10 ℃ /min. The NdFeBO-C samples were sintered at different temperature (700 ℃, 800 ℃, 900 ℃, 1000 ℃) and sintering time (30min,120min). And the NdFeB-C samples were sintered at different temperature (1100 ℃, 1200 ℃, 1300 ℃) with the sintring time of 60 min.

The crystal phases of NdFeBO-C samples were determined by X-ray diffraction (D/MAX2200V, Rigaku). And the structural and morphological changes of NdFeB-C samples were analyzed by scanning electron microscope (SU-1510, HITACHI) with energy-dispersive X-ray spectroscopy (Oxford INCA EDS system) and X-ray diffraction (D/MAX2500V, Rigaku).

Results and discussions

Solid state reaction of NdFeBO samples with carbon

Fig.1, curves a and b, shows the typical x-ray diffraction patterns of NdFeBO powders and NdFeBO powders with 10 wt. % C. From these curves, one can know the main phase of these powders is $Nd_2Fe_{14}B$ and the intensity of carbon diffraction peak is also strong in curve b.

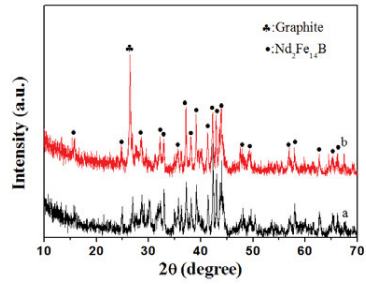

Figure 1 X-ray diffraction patterns of NdFeBO powders (a) and NdFeBO powders with 10 wt. % C (b).

Fig.2 shows the XRD patterns of NdFeBO-C samples with 5 wt. % carbon sintered at different temperatures for 30 min. Curve a shows the intensity of $Nd_2Fe_{14}B$ diffraction

peaks decreases and the diffraction peak of α-Fe appears. With the sintering temperature increasing, the intensity of main phase $Nd_2Fe_{14}B$ diffraction peak decreases and the intensity of α-Fe increases. This suggests that the $Nd_2Fe_{14}B$ decomposed when mixed with carbon sintering over 700 ℃. There are several extra diffraction peaks (2θ=30º, 2θ=34.8º, 2θ=50º, 2θ=59.5º) [11-13]. It belongs to an Nd-rich intergranular phase (NdO) which has an fcc structure with a lattice parameter of α=0.52 nm [14, 15].

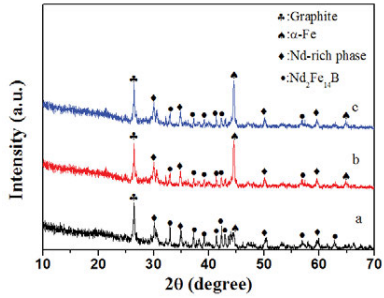

Figure 2 X-ray diffraction patterns of NdFeBO with 5 wt. % carbon sintering at (a) 700 ℃, (b) 800 ℃ and (c) 900 ℃ for 30 min respectively.

Fig.3 shows the XRD patterns of NdFeBO sintered at 1000 ℃ for 30 min with 5 wt.% and 10 wt. % carbon respectively. From the figure one can see when the sintering temperature reached 1000 ℃, the $Nd_2Fe_{14}B$ diffraction line disappeared and the intensity of α-Fe and Nd-rich phase (NdO) diffraction peaks increased. When increasing the carbon concentration to 10 wt. %, a new phase Nd_2O_3 was formed and the diffraction intensity of Nd-rich phase (NdO) decreased.

Fig.4 shows the XRD patterns of NdFeBO with 5 wt. % C sintered at 1000 ℃ for 30 min and 120 min respectively. From the figure one sees that when increasing the sintering time, Nd_2O_3 was also formed.

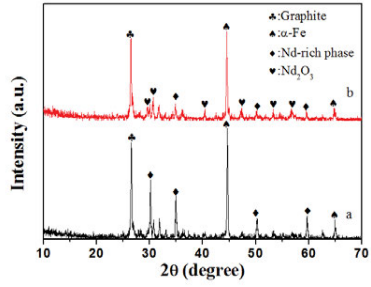

Figure 3 X-ray diffraction patterns of NdFeBO sintered at 1000 ℃ for 30 min with various carbon concentrations: (a) 5 wt. % and (b) 10 wt. % C.

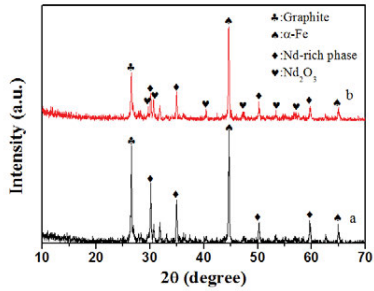

Figure 4 X-ray diffraction patterns of NdFeBO sintered at 1000 ℃ with 5 wt. % C for (a) 30 min and (b) 120 min respectively.

Fig. 3 and Fig.4 suggest that increasing the carbon concentration and the sintering time could promote the transformation from Nd-rich phase (NdO) to Nd_2O_3. And from the literature, there are four kinds of Nd-rich phase have been reported: the DHCP-Nd_2O_3 phase, FCC-NdO phase, Complex-Nd_2O_3 phase and h-Nd_2O_3 phase [15]. After checking information of the X-ray diffraction lines, one finds the Nd_2O_3 phase in the Fig.3 and Fig.4 belong to the h-Nd_2O_3 phase which has a HCP structure with the lattice parameters α=0.39 nm and c=0.61 nm[14]. Fu Xin et al. [16] reported that the FCC-NdO phase has some approximate orientation relationships with matrix grains $Nd_2Fe_{14}B$ which could be attributed to minimizing interfacial energy. Fidler et al. [14] studied the Al-doped NdFeB sintered magnets showed that besides oxygen, a small amount of Fe is also an important stabilizing factor to the Nd-rich phase. And the Nd-rich phase changes from FCC-NdO phase to h-Nd_2O_3 phase with the Fe content decreasing less than 5 at. %. Minowa et al. [6] reported that the Nd-rich phase has a composition of $Nd_{44.2}Dy_{2.5}Fe_{9.3}O_{38.2}C_{5.9}$ (at. %) decomposed to two different phases after annealing, the oxygen-rich phase $Nd_{35.4}Dy_{2.2}Fe_{5.5}O_{56.9}$ (at. %) and the carbon-rich phase $Nd_{30.4}Dy_{1.9}Fe_{1.7}O_{38.8}C_{27.2}$ (at. %). One sees that the carbon can decrease the Fe content of the Nd-rich phase which leading to the Nd-rich phase change from FCC-NdO phase to h-Nd_2O_3 phase.

Solid state reaction of NdFeB samples with carbon

Fig.5 shows the XRD patterns of NdFeB-C samples with 10 wt. % carbon sintered at different temperatures for 60 min. When the sintering temperature was 1100 ℃, graphite, ZrC, Fe_3C, Fe_xC, and B_xC phases were detectable. When the sintering temperature was 1200 ℃, the γ-Fe and α-Fe phases were detectable instead of Fe_xC, and B_xC. There are some diffraction lines could not be indexed in carve a and b which should be some Nd-rich compounds (NdFeC compounds) and a small amount of NdC_2 and Nd_2C_3 phases [11]. When the sample sintering at 1300 ℃, the Nd-rich compounds decreased and the NdC_2 increased.

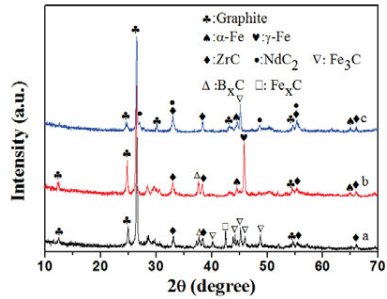

Figure 5 X-ray diffraction patterns of NdFeB with 10 wt. % carbon sintered at (a) 1100 ℃, (b) 1200 ℃ and (c) 1300 ℃ for 60 min respectively.

The morphology of the NdFeB with 10 wt. % carbon and the NdFeB with 10 wt. % carbon sintered at 1300 ℃ for 60 min was shown in Fig.6. From the image of the SEM pattern, there are two phases distributed in Fig.6 (a), the dark phase (graphite) and the grey phase ($Nd_2Fe_{14}B$). After sintering at 1300 ℃ for 60 min, there is a new phase (position 1) appears on the grey phase in Fig.6 (b). And the chemical composition of position 1 and 2 obtained by EDXS analysis was shown in Table 1. One sees that the new phase are rare earth carbides and the grey phase (Fe matrix phase) contains few rare earth. After checking the XRD patterns in Fig. 5, the phase in position 1 is NdC_2 (Nd is used to represents all the rare earth involving Nd, Pr, La and Ce).

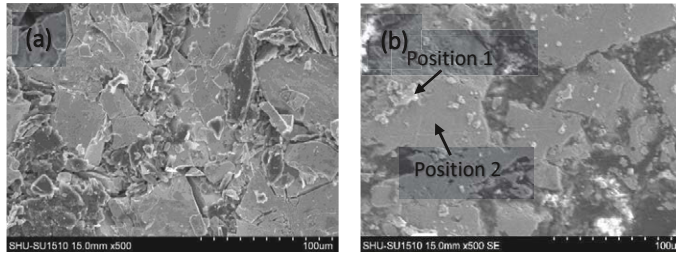

Figure 6 The SEM of the NdFeB with 10 wt. % C (a), and NdFeB with 10 wt. % carbon sintered at 1300 ℃ for 60 min(b).

Table 1 EDS quantitative analysis conducted on the samples in Fig.6 (b) (mass %)

	Fe	Nd	Pr	La	Ce	Zr	C
Position1	0.00	43.87	15.52	7.89	0.00	0.00	32.71
Position2	75.85	0.00	0.00	0.00	0.00	0.00	24.15

Conclusion

In this study, we presented the experimental evidence of phase evolution of the NdFeB(O)-C system upon solid state reaction and the following conclusions can be obtained:

(1)The solid state reaction of $Nd_2Fe_{14}B$ and carbon were significantly influenced by oxygen.

(2) With the carbon content of Nd-rich phase increasing, the Nd-rich phase changed from FCC-NdO phase to h-Nd_2O_3 phase. And the phase evolution of Nd-rich phase was sensitive to the carbon concentration as well as the sintering time.

(3) When the temperature increasing to 1300 ℃, the Nd-rich compounds decreased and the NdC_2 increased.

References

1. Sagawa, M., Fujimura, S., Togawa, N., Yamamoto, H., & Matsuura, Y. (1984). New material for permanent magnets on a base of Nd and Fe. *Journal of Applied Physics*, *55*(6), 2083-2087.
2. Schüler, D., Buchert, M., Liu, R., Dittrich, S., & Merz, C. (2011). Study on rare earths and their recycling. *Öko-Institut eV Darmstadt*.
3. Sasaki, T. T., Ohkubo, T., Une, Y., Kubo, H., Sagawa, M., & Hono, K. (2015). Effect of carbon on the coercivity and microstructure in fine-grained Nd–Fe–B sintered magnet. *Acta Materialia*, *84*, 506-514.
4. Guoxian, Z., Xiaoping, S., Zhongming, C., Aru, Y., & Xiaotian, W. (1998). Effects of C Addition on Microstructure and Magnetic Properties of NdFeB Sintered Magnets. *JOURNAL OF FUNCTIONAL MATERIALS*, *29*(1), 20-23
5. TAN, P., LUO, J. J., & LI, Z. F. (2007). The Effects of C Contents on The Magnetic Properties of Sintered Nd-Fe-B Permanent Magnets. *Metallic Functional Materials*, *1*, 000.
6. Minowa, T., Shimao, M., & Honshima, M. (1991). Microstructure of Nd-rich phase in Nd-Fe-B magnet containing oxygen and carbon impurities. *Journal of magnetism and magnetic materials*, *97*(1), 107-111.
7. Pan, F., Zhang, M., Zhao, R. F., Liu, B. X., & Tokunaga, M. (1998). Some new Nd-rich carbides formed by solid state reaction of and carbon. *Journal of Physics D: Applied Physics*, *31*(5), 488.
8. Nakamoto, M., Kubo, K., Katayama, Y., Tanaka, T., & Yamamoto, T. (2012). Extraction of rare earth elements as oxides from a neodymium magnetic sludge. *Metallurgical and Materials Transactions B*, *43*(3), 468-476.
9. Bian, Y. Y., Guo, S. Q., Xu, Y. L., Tang, K., Lu, X. G., & Ding, W. Z. (2013). Recovery of rare earth elements from permanent magnet scraps by pyrometallurgical process.
10. Bian, Y., Guo, S., Jiang, L., Tang, K., & Ding, W. Extraction of Rare Earth Elements from Permanent Magnet Scraps by FeO–B_2O_3 Flux Treatment. *Journal of Sustainable Metallurgy*, *1*(2), 151-160.
11. Sui, Y. C., Zhang, Z. D., Xiao, Q. F., Liu, W., Zhao, T., Zhao, X. G., & Chuang, Y. C. (1998). Structure, phase transformation and magnetic properties of Nd–Fe–C alloys made by mechanical alloying

and subsequent annealing. *Journal of alloys and compounds*, *267*(1), 215-223.

12. Buschow, K. H. J., De Mooij, D. B., & Denissen, C. J. M. (1988). Note on the formation and the magnetic properties of the compound $Nd_2Fe_{14}C$. *Journal of the Less Common Metals*, *141*(1), L15-L18.
13. Coehoorn, R., Duchateau, J. P. W. B., & Denissen, C. J. M. (1989). Permanent magnetic materials based on $Nd_2Fe_{14}C$ prepared by melt spinning. *Journal of Applied Physics*, *65*(2), 704-709.
14. Fidler, J., Knoch, K. G., Kronmüller, H., & Schneider, G. (1989). Analytical TEM study of Al-doped,"two-phase" Nd–Fe–B sintered magnets. *Journal of Materials Research*, *4*(04), 806-814.
15. Wang, S. C., & Li, Y. (2005). In situ TEM study of Nd-rich phase in NdFeB magnet. *Journal of Magnetism and Magnetic Materials*, *285*(1), 177-182.
16. Xin, F. U., Xiaolei, H. A. N., Zhiwei, D. U., Haibo, F. E. N. G., & Yanfeng, L. I. (2013). Microstructural investigation of Nd-rich phase in sintered Nd-Fe-B magnets through electron microscopy. *Journal of Rare Earths*, *31*(8), 765-771.

TMS2016

145th Annual Meeting & Exhibition

SUPPLEMENTAL
PROCEEDINGS

Powder Metallurgy
of Light Metals

PRODUCTION OF TITANIUM HYDRIDE POWDER BY LEACHING OF ALUMINUM AND SILICON IMPURITIES FROM REDUCED UPGRADED TITANIA SLAG FOR LOW COST TITANIUM PRODUCTION

Syamantak Roy[1], Jaehun Cho[1], Nathan J. Hamilton[1], Amarchand Sathyapalan[1], Michael L. Free[1], Zhigang Zak Fang[1]

[1]Department of Metallurgical Engineering; 135 S 1460 E; Salt Lake City, Utah, UT 84112, USA

Keywords: Leaching, Titanium, Upgraded titania slag, Titanium Hydride, Aluminum and Silicon leaching

Abstract

Titanium alloys are in great demand in engineering applications that require better mechanical properties at a lower weight than steel, but high costs of titanium alloys have restricted their use in day to day applications. A novel low cost route for titanium powder production has been proposed recently, which involves reducing and purifying upgraded titania slag (UGS). The UGS is reduced with magnesium hydride in a hydrogen environment to form titanium hydride along with aluminum, iron and silicon impurities, originating in the UGS. It is crucial to remove the impurities from reduced UGS for successful implementation of this new proposed route for titanium production. This investigation is focused on removal of aluminum, and silicon impurities from the reduced UGS powder by leaching techniques in both alkaline and acidic conditions. The results indicate that proper operating conditions lead to high levels of impurity removal.

Introduction

Titania slag is obtained by reducing ilmenite in a blast furnace. The titania slag so obtained is further purified by a roasting followed by subsequent acid leaching to produce UGS. UGS is predominantly composed of titanium dioxide with about 5wt% impurity consisting of aluminum, iron and silicon compounds. In the newly proposed process of low cost titanium production, the UGS is reduced at 750^{o}C with magnesium hydride, in a salt mixture under hydrogen atmosphere to produce a mixture of salt and reduced UGS [1, 2]. This study was focused on finding an optimal technique for impurity removal through leaching in both acidic and alkaline solutions, under different condition, to obtain high purity titanium hydride powder.

The chemical nature of the targeted impurities were diverse. Aluminum is known to have an amphoteric nature, iron has a basic nature and silicon is a metalloid, consequently both acidic and alkaline chemistries were used as lixiviants. To study the effect of the selected lixiviants on the impurity elements, first titanium hydride and pure mineral oxides of the impurity elements were separately leached with the lixiviants. The lixiviants which were found to be benign towards titanium hydride and effective for impurity removal at the same time were selected for further studies. A surrogate-reduced UGS (chemical composition similar to reduced UGS) was produced by mixing pure titanium hydride with the pure mineral oxides of the main impurity

elements. The lixiviants selected from previous pure mineral tests were used to selectively leach out the impurities from surrogate-reduced UGS. The lixiviants which were found to be the best in terms of leaching from surrogate-reduced UGS were used to leach the reduced UGS.

Experimental Procedure

Preparation of surrogate-reduced UGS

The surrogate-reduced UGS was produced by thoroughly mixing titanium hydride (TiH_2), ferric oxide (Fe_2O_3), silicon dioxide (SiO_2), aluminum oxide (Al_2O_3) and magnesium oxide (MgO) all in their pure mineral states as received from Sigma Aldrich Inc., in the ratios shown in Table 1.

Table 1. The weight fraction of the pure minerals in surrogate-reduced UGS

Component	**TiH_2**	**Fe_2O_3**	**SiO_2**	**Al_2O_3**	**MgO**
Weight %	94.5	2.4	1.2	1	0.9

Preparation of reduced UGS

The mixture of reduced UGS and salt obtained by the hydrogen reduction of UGS with salt and magnesium at 750^{o}C. The mixture obtained contains reduced UGS, salt ($MgCl_2$, KCl), MgO and unreacted Mg. The salt, MgO, Mg were washed out in either a warm fairly concentrated acetic acid or in warm dilute hydrochloric acid for an hour to obtain the reduced UGS which was used in the subsequent studies. The washing was carried out in a container made out of polymer and a thermometer was used for temperature control with an overhead stirrer for stirring the slurry. The temperature was kept at 70^{o}C, stirring speed was set at 450 rpm and the solid-liquid ratio was maintained at 1:40 (g/ml) for acetic acid and at 1:100(g/ml) for dilute hydrochloric acid tests. A sample of the slurry were taken every thirty minutes to study the progress of the reaction. After the washing the magnesium content in the reduced UGS was lowered significantly to an extent such that its content could be adjusted to the desired level in the final product. The reduced UGS obtained after this acid washing and drying was used as the starting material for all the leaching experiments.

Leaching of pure minerals, surrogate-reduced UGS, and reduced UGS

The leaching experiments were carried out in Erlenmeyer flasks made out of polymer fitted with a thermometer to control temperature and rubber cork to prevent loss of the vapors. The setup was put on a magnetic hot plate and stirring bars were used for mixing the slurry at a set speed. This setup was used for experiments which were carried out at temperatures less than the boiling point of liquid phase. The experiments were carried out with a solid-liquid ratio of 1:100 (g/ml) at a set temperature approximately for four hours. In the case of pure mineral leaching studies the temperature was set to 70^{o}C and removal was measured from change in weight of sample before and after leaching. For surrogate-reduced UGS leaching the temperature was also set to 70^{o}C and impurity removal was determined by analyzing the final leach liquor by ICP-OES. To study the progress of the reaction for reduced UGS leaching, slurry samples were taken every hour and analyzed by ICP-OES

Results and Discussion

Pure Mineral Tests

The results for the most effective lixiviants on the removal of impurities are shown in Table 2. The removal percentages of impurities are reported alongside the data for loss of pure titanium hydride with the same lixiviants.

Table 2. Results showing removal of impurities as pure minerals with different lixiviants at 70ºC for 4hr

Targeted Element	Lixiviant	Removal(% as oxides)	TiH_2 retained(%)
Si (SiO_2)	1M NaOH + 3g/L EDTA	~100	~100
	1M NaOH + 3g/L Anhydroerythritol	~100	~100
	0.2M HCl + 0.05M H_3BO_3 + 3g/l NTA	8.20	99.62
Al (Al_2O_3)	1M NaOH + 3g/L Sodium Gluconate	48	~100
	0.2M HCl + 0.05M H_3BO_3 + 3g/l NTA	2.34	99.62
Mg (MgO)	1M NH4Cl +1M Sodium Citrate	~100	~100
	1M NH4Cl +1M Sodium Phosphate	86	~100
Fe (Fe_2O_3)	0.6M HCl	10	72
	0.2M HCl + 3g/L NTA	25	98
	0.2M HCl + 0.05M H_3BO_3 + 3g/l NTA	6.28	99.62

*NTA: Nitrilo Tri-acetic Acid & EDTA: Ethelene Di-amine Tertra-acetic Acid

It is observed that alkaline lixiviants with some additives had the highest selectivity for silicon and aluminum impurities while acidic lixiviants were more effective for iron, while magnesium could be removed quite efficiently. It is to be noted that even a small percentage of removal of pure minerals in a particular lixiviant is acceptable, as long as there is very low TiH_2 loss, since the impurity levels in reduced UGS is less than 5wt%.

Surrogate-reduced UGS tests

The lixiviants which were found to be the most effective from the previous pure mineral tests along with some new promising lixiviants were used on surrogated-reduced UGS and the results obtained are tabulated in Table 3.
The results show that almost complete removal of silicon, aluminum and magnesium impurities along with minimal titanium hydride loss could be achieved by proper selection of the lixiviants. Silicon removal was best in alkaline lixiviants while aluminum and magnesium removal was favored in acidic media. It was noted that there were differences in the leaching behavior between the pure minerals and the surrogate-reduced UGS.

Table 3. Results showing removal of impurities from surrogate-reduced UGS with different lixiviants at 70°C for 4hr

Sample	Lixiviant	Loss(%)	Removal(%)			
		Ti	Al	Fe	Mg	Si
Synthetic Product	1M NaOH + 3g/L Sodium Gluconate	0.76	0	0	3.96	~100
	1M NH_4Cl + 1M Na-phosphate	0	0.73	0	~100	12.94
	1M NaOH + 3g/L EDTA	0	0	0	3.98	~100
	1M NaOH+ 3g/L Anhydroerythritol	0.62	0	0	0	~100
	0.6M HCl + 15% H_2O_2	12.75	90.19	0	0	13.81
	0.2M HCl + 0.05M H_3BO_3 + 3g/L NTA	0.03	~100	0	~100	4.4
	1M NH_4Cl + 1M Na-Citrate	0.01	0	0	~100	23.71

Reduced UGS tests

The knowledge of leaching behavior of pure minerals and surrogated-reduced UGS was used when selecting the lixiviants for reduced UGS. In addition, some new chemistries were also used as the leaching behavior of the different samples, like in case of pure minerals and surrogated-reduced UGS were found to be different.

Analysis of the starting material: For the removal of the salt (KCl and $MgCl_2$), MgO and unreacted Mg from reduced UGS it was found that either 4.32M acetic acid at 70°C with a solid-liquid ratio of 1:40 (g/l) for 1hr or 0.2 M HCl at 70°C with a solid-liquid ratio of 1:100(g/l) for 1hr is sufficient as can shown by Table 4. and Fig. 1.

Table 4. Results showing removal of impurities with acetic acid leach at 70°C for 1hr

Sample	Lixiviant	Loss(%)	Removal(%)			
		Ti	Al	Fe	Mg	Si
Reduced UGS	Acetic Acid(4.32M)	0	0.16	1.10	~100	1.97

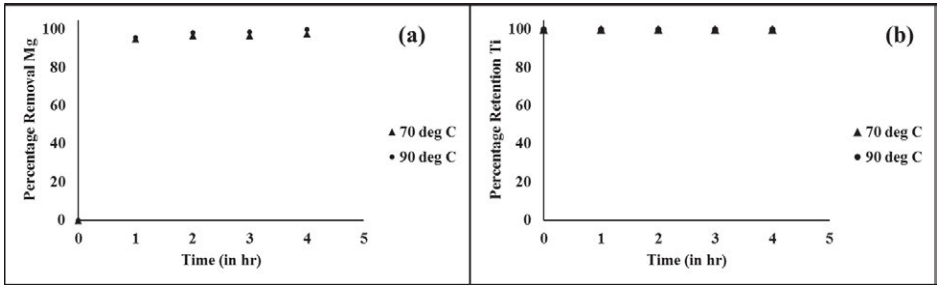

Figure 1. (a) The kinetics of Magnesium removal and (b) Titanium-retention when leaching reduced UGS and salt mixture with 0.2 M HCl at 70°C and 90°C.

Acid leaching: The leaching of reduced UGS in acidic lixiviant was done at 90ºC as an increase in temperature led to an increase in the rate of impurity removal. The experiments were performed for 4 hours in a slurry with solid-liquid ratio of 1:100(g/ml) and stirred at 1000 rpm. The concentration of the hydrochloric acid was varied to study the effect of acid concentration on the rate of removal of aluminum and silicon impurities ass illustrated by Fig 2.and Fig 3.

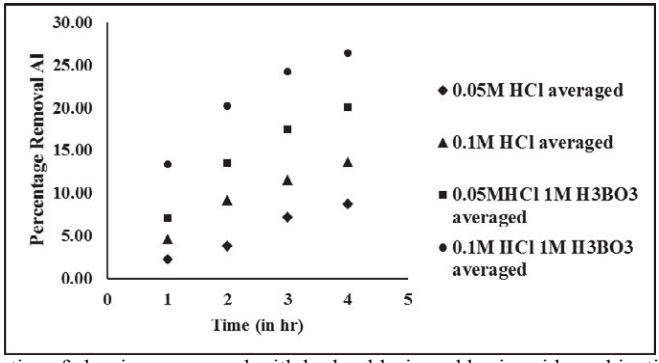

Figure 2. Kinetics of aluminum removal with hydrochloric and boric acid combinations at 90ºC

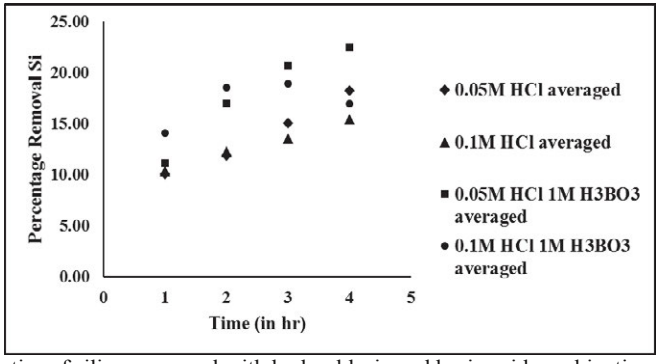

Figure 3. Kinetics of silicon removal with hydrochloric and boric acid combinations at 90ºC

The results indicate that acidic lixiviants are not very effective for aluminum and silicon removal at 90ºC. It was also found that addition of boric acid in general enhanced the removal of aluminum and silicon as shown in Fig 2.and Fig 3. The removal kinetics showed an increasing trend with time, 26.48% Al and about 20% Si could be removed after leaching with 0.1M HCl and 1M H_3BO_3 for 4 hours.

Alkaline leaching: In the case of leaching in alkaline media it was also observed that increase in temperature led to increase in rate of impurity removal. Therefore, the experiments were carried out at 90ºC, (for 4 hours in a slurry with solid-liquid ratio of 1:100(g/ml) and stirred at 1000

rpm.). The concentration of the sodium hydroxide was varied to study the effect of alkali concentration on the rate of removal of impurities as illustrated by Fig 4. and Fig 5.

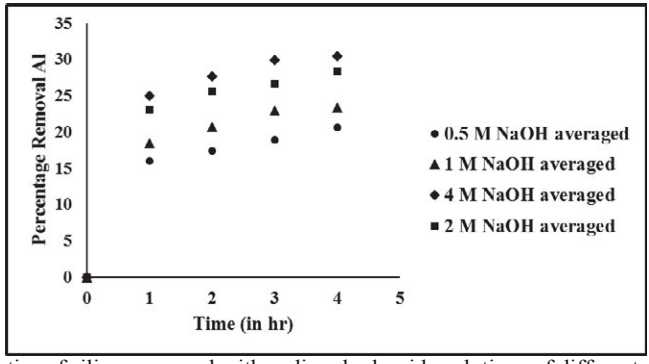

Figure 4. Kinetics of silicon removal with sodium hydroxide solutions of different concentrations at 90°C

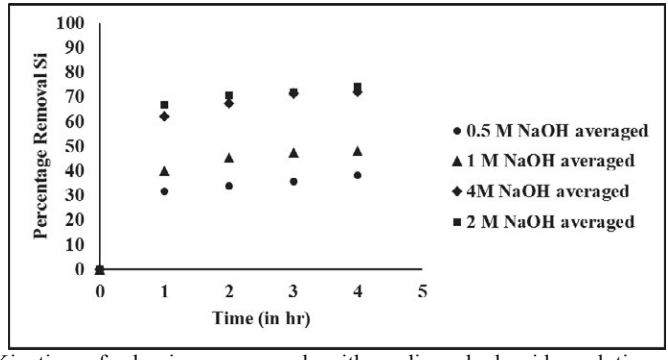

Figure 5. Kinetics of aluminum removal with sodium hydroxide solutions of different concentrations at 90°C

At 90°C, an increase in sodium hydroxide concentration up to 2M led to an increase in removal of both silicon and aluminum. The increase in impurity removal with increase in sodium hydroxide concentration was not significant beyond 2M. Removal of 74.36 % Si and 28.4% Al could be achieved under the stated conditions in 4 hours with no detectable titanium loss.

Conclusions

1. The aluminum and silicon removal from reduced UGS is more effective when reduced UGS is leached in alkaline solutions.
2. At 90°C, 2M NaOH solution was found to be the optimal lixiviant for Al and Si removal.
3. Addition of boric acid as an additive to acidic solutions increases the removal of both aluminum and silicon containing impurities without any titanium loss.

References

1. Z. Zak Fang, Scott Middlemas, Peng Fan, and Jun Guo, “A Novel Chemical Pathway for Producing Low Cost Ti by Direct Reduction of Ti-slag”, Journal of American Chemical Society , 2013, 135 (49), 18248–18251.

2. Zak Fang, et al. “A Novel Chemical Pathway for Titanium Production to Drastically Reduce Cost.” Proposal to AARP-E, 2013.

MECHANICAL PROPERTIES AND MICROSTRUCTURE OF PM Ti-Si_3N_4 DISCONTINUOUS FIBRE COMPOSITE

Troy Dougherty[1], Ying Xu[1], Ainaa Hanizan[1]

[1]Nuenz Limited; 68 Gracefield Rd; Lower Hutt; 5010, New Zealand

Keywords: titanium, silicon nitride, fiber, whisker, MMC (metal matrix composite), PM (powder metallurgy)

Abstract

2 vol% Si_3N_4 fiber Ti composites were manufactured by uniaxially pressing the powders and subjecting the green compact to pressureless sintering at 1400°C in flowing argon. The resulting composites were >98% theoretical density. The hardness of the titanium composite was measured at HBW 401 compared to HBW 293 for pure titanium. Microstructural analysis showed clearly defined 200-300nm diameter crystalline fibers throughout the composite with a 2-4μm reaction boundary cementing them to the titanium. Concentrations of smaller Si_3N_4 particles were located at the titanium grain boundaries, which may have reacted to form Ti-Si-N phases. The improved mechanical properties might be from a combination of discontinuous fiber reinforcement, nitrogen addition to the Ti matrix, and grain-boundary reinforcement.

Introduction

Titanium has found many uses in automotive, aerospace, defense, sporting and manufacturing due to its high-strength, light-weight, anti-corrosive and impact properties. Titanium, however, does not have very good tribological properties which limits its application in high-wear applications [1]. Titanium is also very expensive which has led to a significant body of work into methods for manufacturing of titanium parts using powder metallurgy (PM) methods to reduce costs. Many of the applications of titanium are utilizing titanium with alloying metals to improve their mechanical properties, but producing these pre-alloyed powders for producing PM significantly impacts on the cost-benefits of PM compared to using blended elemental powders [2].

An alternative method to elevating the mechanical properties of a metal is through the addition of a higher strength and stiffness ceramic additive, forming a metal matrix composite (MMC). The difference in mechanical properties and thermal properties mismatch leads to an improvement in mechanical properties which has been demonstrated historically in other metals, such as aluminum and magnesium [3], and to a lesser extent more recently in titanium. The typical reinforcing additive for MMCs is SiC, Al_2O_3, and to a lesser extent B_4C. In titanium, carbides are not preferred due to the formation of brittle carbides and oxides [4],[5], though continuous fiber SiC MMC is currently in production. TiB and TiC have been used more in titanium to prevent these unfavorable reactions both as an additive and formed *in-situ* [2],[6],[7]. Si_3N_4 particles have also been previously investigated in titanium and have shown to significantly improve the hardness and wear resistance of the resulting MMC [8]. It was shown that Si_3N_4 reacted with titanium resulting in increased nitrogen levels in the

titanium. It is well known that low levels of nitrogen have a significant impact on the properties of titanium, increasing many mechanical properties but also increasing brittleness if the nitrogen levels are too high [9]. Silicon additions are beneficial in small amounts for improving grain refinement, improving creep-resistance, improving oxygen resistance, tensile properties, and help to inhibit grain growth at elevated temperatures [10],[11],[12].
In this paper, we investigate the effect of the addition of Si_3N_4 fibers to pure titanium to study the impact of high-aspect ratio Si_3N_4 on titanium for applications in PM (it is well known that adding high-aspect ratio fillers to composites can improve the properties of the MMC more than particulates). First the dispersion of Si_3N_4 in titanium powder was studied to ensure a homogenous mixture. Then the densification behavior and microstructural characteristics was explored. Finally, initial mechanical properties were explored using a Brinell hardness test on both pure titanium and titanium-Si_3N_4 MMC.

Experimental Procedure

HDH-Ti powder was obtained from Chengdu Huarui Industrial Co., Ltd. (-400mesh, 99.5%) Si_3N_4 fiber (>95% Si_3N_4, >80 vol% fiber) was manufactured at Nuenz Limited. For particle size analysis, particle sizes <10μm were measured using Scanning Electron Microscopy (SEM) and particle sizes >10μm were measured using optical microscopy. The density of the starting powders was measured using a density bottle based on AS1038.21.1.1.
Reference samples (Ti-Ref) and samples with 2 vol% Si_3N_4 fiber (Ti-SNF) were used in this study. Green pellets were formed by uniaxially pressing in a 25mm die at 540MPa without binder. The samples were placed in an alumina furnace boat and annealed in a tube furnace under flowing argon with <10ppm oxygen at 1673K for 2h.
The density of the green and fired samples was determined by the Archimedes method. Microstructural analysis was determined by SEM with Energy Dispersive X-ray Spectroscopy (EDS) and X-ray Diffraction (XRD) using Cu K_α radiation. Mechanical improvements were evaluated by carrying out Brinell hardness measurements on a series of separately fired samples based on ASTM E10-12.

Results and Discussion

HDH-Ti and Si_3N_4 Fibre Characterization

The Si_3N_4 powder comprises both fibers and particles whereas the HDH-Ti is morphologically homogenous powder.
Table I and Figure 1 give the morphological data for both the Si_3N_4 and HDH-Ti powders. For the calculation of fiber and volume fractions, it was assumed that Si_3N_4 particles and fibers were spherical and cylindrical, respectively. This method is consistent with methods used in earlier studies and the distributions are consistent with studies of other, similar fibrous materials [13].
The density of the powders was measured at 4.54 and 3.13 g/cm^3 for HDH-Ti and Si_3N_4, respectively, and these values were used for the calculation of theoretical densities. Powder XRD showed that the HDH-Ti was pure α-Ti while the Si_3N_4 fibre was predominantly α-Si_3N_4 with β-phase Si_3N_4 also present.

Table I. Dimensional Properties of Powders Used

	Diameter (μm)			Length (μm)			Volume %	Count %
	d10	d50	d90	d10	d50	d90		
Si_3N_4 fiber	0.12	0.36	0.66	3	14.5	27.6	89.6	15.7
Si_3N_4 particulate	0.06	0.15	0.28	-			10.4	84.3
HDH-Ti powder	1.58	8.96	19.21	-			-	-

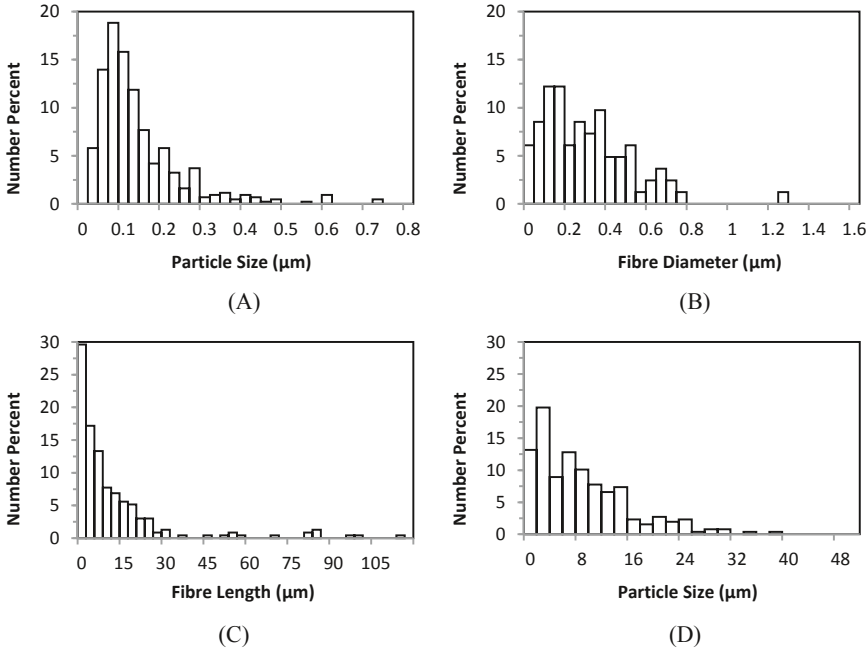

Figure 1. Histogram plots of the (A) particle size distribution of the particles in the Si_3N_4 powder; (B and C) diameter and length distributions of the fibers in the Si_3N_4 powder, respectively; and (D) the particle size distribution of the HDH-Ti powder.

The relatively smaller Si_3N_4 particles should allow for packing in the space between the HDH-Ti grains during compaction allowing for high-density green-bodies while not being so small that they exhibit significant melting point depression (which could be expected with smaller nanoparticles). This is important as ceramic reinforcements often inhibit densification due to their relatively high melting point. The fiber aspect ratio of approximately ~40 suggests that they could provide significant improvement to the tensile properties of the composite based on a simple shear-lag model. The HDH-Ti powder's irregular morphology, as seen in Figure 2A is specifically designed for packing under compaction, compared to the spherical particles produced by atomization.

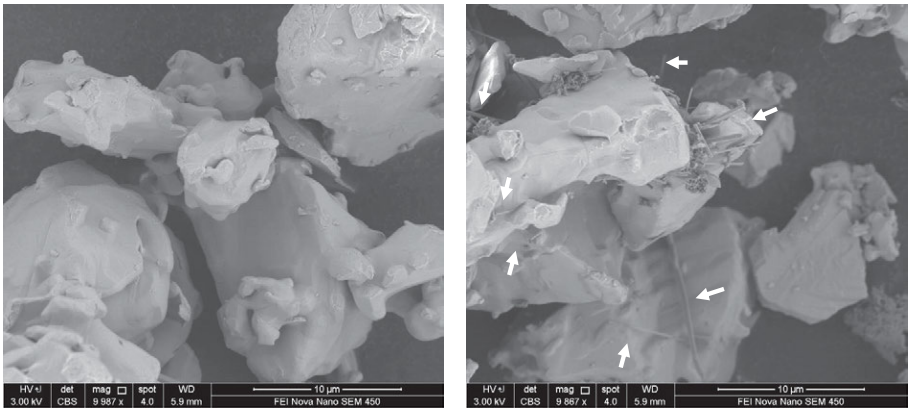

(A) (B)

Figure 2: SEM images of (A) HDH-Ti powder, (B) HDH-Ti/Si_3N_4 composite powder showing well dispersed Si_3N_4 fibers and powder (some indicated) amongst HDH-Ti powder.

Dispersion and Green Body Characterization

Figure 2B shows that the Si_3N_4 and HDH-Ti powders were well dispersed prior to consolidation. The Si_3N_4 were comprised of sub-micron particles, short whiskers and long fibers: the particles and whiskers were either stuck to the surface of the relatively larger HDH-Ti particles or clustered in the spaces between HDH-Ti particles. The long fibers were monodispersed in the interstitial space between the HDH-Ti particles. Table II shows the density of the green bodies. During this study, a high pressure of 540 MPa in a uniaxial press was used to facilitate easy production of high-density green bodies. It is known that densification increases with pressure, but these high pressures would cause high wear on tooling in an industrial context. Literature is available regarding the economic methods for the manufacture of bodies for PM [14].

Table II. Green Body Properties of Ti-Ref and Ti-SNF

	Density (g/cm^3)	Theor. Density (g/cm^3)	% Theor. Density
Ti-Ref	3.47 ±0.05	4.54	76.5
Ti-SNF	3.45 ±0.02	4.51	76.4

Densification Behavior and Microstructure Characterization

Table III shows the density of the sintered bodies. Si_3N_4 would intuitively inhibit densification of titanium as it is a higher melting point phase. Two mechanisms are proposed for Ti-SNF having higher % theoretical density than Ti-Ref: firstly, this could be due to reactions between Ti and Si_3N_4 resulting in lowered localized eutectic phases at the grain boundaries, improving mass

transfer and densification. Secondly, optical microscopy indicated that the resulting grain sizes in Ti-Ref were larger than in Ti-SNF. The pinning of grain boundaries by Si_3N_4 may have caused a reduction in Ti grain size which would allow for the more rapid densification of smaller particles during the later stages of sintering through grain boundary diffusion.

Table III. Sintered Body Properties of Ti-Ref and Ti-SNF

	Density (g/cm^3)	Theor. Density (g/cm^3)	% Theor. Density
Ti-Ref	4.4 ±0.1	4.54	96.8
Ti-SNF	4.45 ±0.05	4.51	98.6

Figure 3A shows a SEM image where of Ti-Ref which appeared to have more heterogeneous grain boundaries than Ti-SNF (Figure 3B). Most of the grain boundaries were metallic but some had non-metallic elements in the grain boundary (shown by bright areas in the SEM images). In Ti-SNF, most of the grain boundaries had crystalline fibers or the products formed by reaction of Si_3N_4 and Ti. Both Ti-Ref and Ti-SNF showed porosity in the intergranular space (shown by black areas in the SEM images) which was consistent with the density calculation of less than 100% theoretical density. Additionally, in Figure 5C it could be seen that on the surface of the polished sample some crystalline fibers were visible that had survived sintering. The central vein of the fiber was clearly intact in places but had reacted in other places with the Ti matrix to form a clearly defined reaction boundary which was 2-4μm around the fiber.
EDS revealed that the brighter material observed in the grain boundary of Ti-Ref was rich in O, while in Ti-SNF it was rich in Si. It was not possible to identify changes in N using EDS due to the overlap of the TiL_α and NK_α.

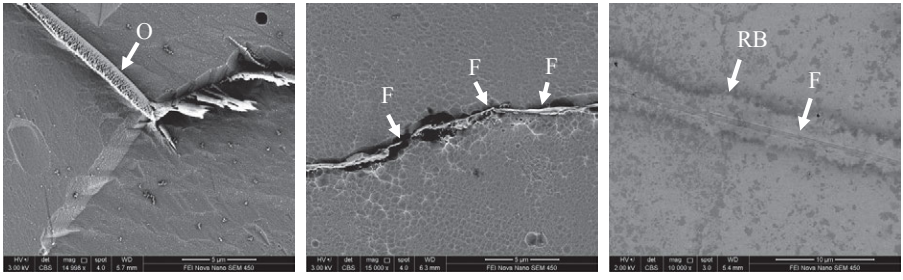

(A) (B) (C)

Figure 3: Hi-resolution SEM images of (A) grain boundary of Ti-Ref, (B) grain boundary of Ti-SN, and (C), Si_3N_4 fiber on the surface of Ti-SNF pellet. O = oxide; F=fiber; RB=reaction boundary.

XRD showed no change in the crystal phases after sintering with only α-phase Ti present in both the green and sintered bodies. A study was carried out where 5 and 10 vol% Si_3N_4 was mixed with HDH-Ti powder to determine at what limit Si3N4 fiber would be observable using powder XRD. Si_3N_4 XRD peaks were only observable in the 10 vol% sample. This suggested that it would not have been likely to see Si_3N_4 or any product peaks in the Ti-SNF sample due to the

relative concentrations of the phases. Previous studies has been reported that Ti and Si_3N_4 are not thermodynamically stable above 1573K, with TiN_x, $TiSi_x$, and $Ti_5Si_3N_y$ being stable intermediate phases [15]. Also, Ti_5Si_3, Ti_3Si and α-$Ti(N)_{0.03}$ have been observed using monolithic ceramics and larger particulate ceramic reinforcement of Ti, but we were not able to specifically identify these phases [8],[16]. While we did not observed these particular phases when analyzing the interphase, it is likely based on previous reports, from the observance of a reaction interphase around Si_3N_4, and the relatively small size of the Si_3N_4 used in this study compared to previous studies that phases in the tertiary Ti-Si-N were present. Alternatively, this may be due to the relatively short reaction time that was used in this study meaning that the reaction did not attain equilibrium.

The observance of a significant interphase is important as it is critical for transferring stresses from the matrix to the fiber as the interphase represents a strong chemical bond between the titanium and the much stronger ceramic reinforcement. This paper represents the first study of the Ti-SNF system; in more advanced Al and Mg alloys using other fiber or whisker materials, the interphase chemistry is controlled through the addition of passivating elements [3]. Similar work in the Ti-Si_3N_4 system may allow for improving the reaction interphase and reducing the nitridation of the Ti matrix.

Mechanical Property Characterization

The hardness of the samples was measured to be 293 and 401 HBW for Ti-Ref and Ti-SNF, respectively. The Ti-SNF value represents a significant increase in the hardness of the titanium. The mechanism contributing to could be attributed to three different mechanisms: firstly, as previously discussed, is the effect of the formation of $Ti(N)_{0.03}$ which is known to increase the hardness and wear properties of Ti and its alloys. The second effect is the strengthening of the material through load transfer from the matrix through the clearly observed interphase to the fibers. Further testing is required to understand more about this mechanism and the critical length of the fibers as well as the impact of the small particles on the strengthening mechanisms. The third effect could be the effect of the pinning of grain boundaries, or strengthening of the intergranular space by Si_3N_4 and Ti-Si-N phases. Further destructive testing is required to determine individual contributions to hardness as well to determine which strength and fracture properties have been affected.

Summary

- Pure Ti and Ti-Si_3N_4 composites (Ti-Ref and Ti-SNF, respectively), uniaxially pressed compacts were successfully made by pressureless sintering at 1673K in argon atmosphere. The sintered percentage theoretical density of the Ti-SNF was slightly higher than Ti-Ref which may be due to reactions to form eutectic phases or because of smaller grains resulting in faster sintering during the later stages of sintering.
- Microstructural analysis showed that Si_3N_4 fibers survived the sintering process though there was evidence that substantial reaction of Si_3N_4 had taken place to form a new reaction interphase approximately 2-4mm around the fibers.
- Hardness measurements showed that the resulting Ti-SNF material was substantially harder than Ti-Ref. It is likely that smaller sub-micron particles reacted to form Ti_5Si_3, Ti_3Si and

$Ti(N)_{0.03}$ based on previous studies and the mechanical improvements were based on a combination of N inclusion in the α-Ti along with hard ceramic reinforcing.

- Further studies are required to determine the exact Ti-Si-N phases that have formed as a result of the reaction of Ti and Si_3N_4, to control of these interphase reactions, and to determine the impact of Si_3N_4 the Ti-Si-N phases on mechanical properties.

Acknowledgements

The authors are thankful for the financial support from New Zealand Callaghan Innovation through the Technology Project Funding contract 26773-TARPRJ-NUENZ.

References

[1] Budinski, K. G. Tribological properties of titanium-alloys. *Wear* **1991**, 151, 203–217.

[2] Saito, T. A Cost-Effective P / M Titanium Matrix Composite for Automobile Use. *Advanced Performance Materials* **1995**, 2, 121–144.

[3] Lloyd, D. J. Particle reinforced aluminium and magnesium matrix composites. *International Materials Reviews* **1994**, 39, 1–23.

[4] Gorsse, S. and Petitcorps, Y. Le A new approach in the understanding of the SiC/Ti reaction zone composition and morphology. *Composites Part A: Applied Science and Manufacturing* **1998**, 29, 1221–1227.

[5] Poletti, C., Balog, M., Schubert, T., Liedtke, V., and Edtmaier, C. Production of titanium matrix composites reinforced with SiC particles. *Composites Science and Technology* **2008**, 68, 2171–2177.

[6] Saito, T. The automotive application of discontinuously reinforced TiB-Ti composites. *The Journal of The Minerals, Metals & Materials Society* **2004**, 56, 33–36.

[7] Candel, J. J., Amigó, V., Ramos, J. a., and Busquets, D. Sliding wear resistance of TiCp reinforced titanium composite coating produced by laser cladding. *Surface and Coatings Technology* **2010**, 204, 3161–3166.

[8] Alman, D. . and Hawk, J. . The abrasive wear of sintered titanium matrix–ceramic particle reinforced composites. *Wear* **1999**, 225-229, 629–639.

[9] Petunina, Y. V. Effect of high oxygen and nitrogen contents on the mechanical properties of titanium. *Metal Science and Heat Treatment of Metals* **1961**, 3, 276–279.

[10] Gray, H. R. Tensile and creep properties of titanium-vanadium, titanium-molybdenum, and titanium-niobium alloys. *Nasa TM X-3216* **1975**

[11] Bermingham, M. J., McDonald, S. D., Dargusch, M. S., and StJohn, D. H. The mechanism of grain refinement of titanium by silicon. *Scripta Materialia* **2008**, 58, 1050–1053.

[12] Vojtěch, D., Bártová, B., and Kubatík, T. High temperature oxidation of titanium-silicon alloys. *Materials Science and Engineering A* **2003**, 361, 50–57.

[13] Lee, H.-W. and Sacks, M. D. Pressureless Sintering of SiC-Whisker-Reinforced Al2O3 Composites: II, Effects of Sintering Additives and Green Body Infiltration. *Journal of the American Ceramic Society* **1990**, 73, 1894–1900.

[14] Hoganas Production of Sintered Components. 2013;

[15] Sambasivan, S. and Petuskey, W. T. Phase chemistry in the Ti-Si-N system: Thermochemical review with phase stability diagrams. *Journal of Materials Research* **1994**, 9, 2362–2369.

[16] Maeda, M., Oomoto, R., and Naka, M. Interfacial Reaction between Titanium and Silicon Nitride during Solid State Diffusion Bonding. *Transaction of the Joining and Welding Research Institute* **2001**, 30, 59–65.

MICROSTRUCTURE EVOLUTION AND MECHANICAL PROPERTIES INVESTIGATION OF FRICTION STIR WELDED AlMg5-Al_2O_3 NANOCOMPOSITES

N. Kishore Babu[1], Kaspar Kallip[1], Marc Leparoux[1], Khaled A. AlOgab[2], G.M. Reddy[3], M.K. Talari[4],

[1]Empa, Swiss Federal Laboratories for Material Science and Technology, Laboratory for Advanced Materials Processing, Feuerwerkerstrasse 39, CH-3602 Thun, Switzerland

[2]King Abdulaziz City for Science and Technology (KACST), National Centers for Advanced Materials, P O Box 6086, Riyadh, 11442, Saudi Arabia

[3]Defence Metallurical Research Laboratory, Hyderabad-500 058, India

[4]Faculty of Applied Sciences, Universiti Teknologi MARA, 40450 Shah Alam, Malaysia

Keywords: Friction stir welding, Nanocomposites, Microstructure, Tensile properties

Abstract

The present study has investigated the influence of friction stir welding (FSW) on the microstructure and mechanical properties of powder metallurgy processed unmilled AlMg5, AlMg5 milled with 0.3 wt. % stearic acid (SA) and milled AlMg5-0.5 vol% Al_2O_3 nanocomposites. FSW of unmilled AlMg5 resulted in grain refinement due to dynamic recrystallization induced by the thermo-mechanical processing, thereby increasing the stir zone yield strength (YS) and ultimate tensile strength (UTS) to 160 MPa and 326 MPa when compared to 135 MPa and 300 MPa of base metal, respectively. The friction stir AlMg5-0.5 vol% Al_2O_3 nanocomposite exhibited superior mechanical properties compared to almost all commercial 5xxx series of Al alloy friction stir welds. However, the friction stir welded AlMg5 milled with 0.3 wt. % SA and AlMg5-0.5 vol% Al_2O_3 samples showed a slight reduction in UTS values (373 MPa and 401 MPa) compared to 401 MPa and 483 MPa of respective base metal values.

Introduction

Aluminium-based metal matrix composites (Al-MMCs) owing to their high strength, high hardness, high specific modulus, low density, etc., have been used in many industries, e.g. aerospace industry, automobile industry, etc [1,2]. In particular, AlMg5-Al_2O_3 nanocomposites are attractive for military and aerospace applications. One of the promising approaches to manufacture these nanocomposites is the powder metallurgy route involving high-energy ball milling [3].

Employing conventional fusion welding techniques to join Al-MMCs, leads to poor mechanical properties and defective welds. The main problems associated with fusion welding include segregation, shrinkages, porosity and deleterious chemical reactions between the reinforcement particles and liquid aluminium in the fusion zone [4]. If a proper welding process is not developed for joining of Al-MMCs, then the applicability of these composites in different industries is limited. Thus, solid state welding processes like friction stir welding (FSW) process plays an important role in joining of Al-MMCs. In this process, the localized heating caused by advancing of a rotating tool with a specially designed pin and shoulder into abutting edges of

sheets or plates softens the material around the pin, thereby producing a welded joint in the solid state [5]. As a result, FSW eliminates the above mentioned problems. FSW has been successfully applied to various Al-MMCs, including 7005/Al_2O_3/10p [6], AZ91/SiC/10p [7], 6061/TiC/3 and 7p [8], 6063/B4C/6 and 10.5p [9].

More recently Khodabakhshi et al. [10] have investigated the microstructure and mechanical properties of powder–metallurgy processed (P/M) Al–2 vol% Al_2O_3 (15 nm) nanocomposite friction stir welds. The nanocomposite was prepared via high-energy mechanical milling followed by hot consolidation processes. They reported that nanocomposite could be welded at high heat inputs and the rotational speed of the welding tool was found to be a more effective parameter for the solid-state joining of P/M nanocomposite. It was reported that tensile testing revealed higher ultimate tensile strength (UTS) of 108 MPa for FSWed P/M nanocomposite in contrast to 85 MPa of FSWed wrought 1050 aluminum sheet at a rotational speed of 1200 RPM. The present study was aimed to evaluate the effect of FSW on microstructure and tensile properties of AlMg5-0.5 vol% Al_2O_3 nanocomposites prepared by powder metallurgy route. For a comparison, AlMg5, unmilled and AlMg5 milled with stearic acid (SA) were processed by FSW and the microstructural features in the stir zones and tensile behavior of welds were examined.

Experimental

High purity (≥ 99%) AlMg5 powder and Al_2O_3 nanoparticles were used as starting matrix and reinforcement materials. The chemical composition (wt-%) of the matrix was Al-95, Mg-5. Powder metallurgically fabricated 80x80x6.5 mm sheets from unmilled AlMg5, milled AlMg5, and milled AlMg5-0.5 vol% Al_2O_3 powders, were used in the present investigation. Mechanical milling was performed in a high energy cube mill (TSB, Switzerland) with a ball to powder ratio 10:1 at a rotating speed of 350 rpm for 3 h. Stearic acid (SA) 0.3 wt% was used as process control agent (PCA) during milling to minimize the extreme cold welding of aluminium powders. The milled powder was placed into steel moulds with the size of 80x80 mm^2 for consolidation. The moulds were heated with 3°C/min under conventional vacuum furnace and held at 350°C for 14 hours followed by 1.5 hours at 550°C. The moulds were then flushed with Ar in the furnace and transferred rapidly (less than 5 seconds) under a 200 Ton uniaxial press (Walter + Bai AG, Switzerland) and compacted with 280 MPa [11]. We hereafter shall refer to unmilled AlMg5, milled AlMg5, and milled AlMg5-0.5 vol% Al_2O_3 samples as 'AlMg5-UM', 'AlMg5-M' and 'AlMg5-0.5Al_2O_3' respectively.

Bead-on-plate friction stir welds were made using friction stir welding machine (ETA Technology, India). The employed welding tool was fabricated from tool steel (H13) and consisted of a convex shoulder with 15 mm diameter and a threaded pin length equal to 0.2 mm less than the thickness of the plate (Fig. 1). The pin was tapered from 6 mm at the shoulder to 4 mm at the pin tip. The rotational, transverse speed and tilt angle were 600 rpm, 60 mm/min, 1.5° respectively. The samples for light microscopy were suitably sectioned, mounted, mechanically polished and etched. For high temperature etching, a solution containing 20 ml H_2SO_4 in 80 ml distill water was used at 70°C for 2 minutes. Electron Backscatter Diffraction (EBSD) was measured with a TESCAN Lyra3 FE-SEM and an AMETEK EBSD using step size of 300 nm. Samples prepared for EBSD mapping were prepared with a Leica EM-TIC 3x ion polisher/cross sectioner using 6 kV at 2.2 mA for 12h. For transmission electron microscopy, thin slices of

thickness 0.125 mm were cut from the specimens on a low speed saw and they were further thinned by mechanical polishing to 0.03 mm. Discs of 3 mm diameter, punched off from these slices, and final thinning was carried out using a Fischione 1050 low-angle ion milling, operating at 3-5 kV, and ion current of 50 micro amperes and a sample inclination of 10° to the ion beam. The thin foils were examined in a JEOL JEM-2200FS Transmission Electron Microscope operating at 160 kV. For tensile tests, weld specimens with a gauge length of 10 mm, gauge width of 4 mm and thickness of 3 mm were used. Tensile tests were carried out on base metal as well as weldments at a constant displacement rate of 2 mm/min.

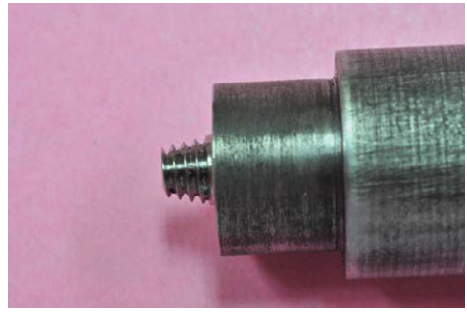

Figure 1. Photograph of FSW tool made of tool steel (H13).

Results and Discussion

FSW joints usually consist of four different regions. They are: (a) base metal (BM), (b) heat affected zone (HAZ), (c) thermo-mechanically affected zone (TMAZ), and (d) stir zone (SZ) or nugget zone. During FSW, the material undergoes severe plastic deformation at elevated temperatures, which results in the formation of fine grains. This phenomenon is known as dynamic recrystallization (DRX) [12-14]. Weld cross section macrostructure of AlMg5-UM, AlMg5-M and AlMg5-0.5Al_2O_3 welds showed basin shaped nuggets as shown in Fig. 2 (a ,b and c). The welds prepared with AlMg5-0.5Al_2O_3 exhibited wider basin shape from top to bottom when compared to AlMg5-UM and AlMg5-M welds. In the present study, the presence of fine Al_2O_3 particles in the microstructure resulted in higher localized strain during the FSW process in the weld nugget compared to other welds [15]. This high amount of localized strain in the weld nugget of AlMg5-0.5Al_2O_3 would result in decreased flow stress of the material during welding and gives rise to high amounts of deformation and wider basin shape of the weld nugget. Furthermore, the presence of Al_2O_3 nanoparticles also could hinder the heat flow during welding [10]. No visible defects typical of fusion welded aluminium metal matrix based composites, such as gas pores, micropores, nanoparticle segregation were observed in the FSW specimens [4].

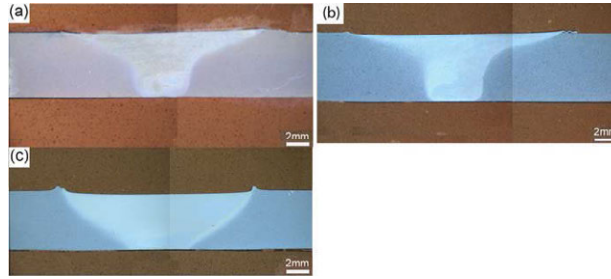

Figure 2. The optical macrostructures of FSW welds a) AlMg5-UM b) AlMg5-M c) AlMg5-0.5Al_2O_3.

EBSD image of the AlMg5-UM friction stir welds are shown in Fig. 3. The microstructure of the AlMg5-UM welds showed fine grained structure at the nugget zone when compared to base metal due to heavy plastic deformation followed by dynamic recrystallization induced by the thermo-mechanical processing. The TMAZ lies next to the stir zone as shown in Fig. 3, where the material has experienced plastic deformation as well as heating cycle. Larger elongated grains compared to the stir zone are observed in this region. The microstructure of the AlMg5-M welds showed intense grain refinement in the nugget zone due to severe applied thermomechanical cycle (Fig. 4). However, the submicron (<1 μm) grain size values of AlMg5-0.5Al_2O_3 FSW welds was difficult to determine using EBSD. Therefore, Transmission electron microscope (TEM) is required to characterize the fine grains present in weld nugget. TEM micrograph of the AlMg5-0.5Al_2O_3 friction stir welded specimens showing fine equiaxed grains, as shown in Fig. 5 (a). Fig. 5 (b) shows Al_2O_3 nanoparticles present in the nugget zone. Fine equiaxed grains were observed for AlMg5-UM (4-5 μm), AlMg5-M (1-2 μm) and AlMg5-0.5Al_2O_3 (1 μm and <1 μm) friction stir weld nugget zones respectively.

It is interesting to note that AlMg5-M and AlMg5-0.5Al_2O_3 base metals contain some pre-stored energy from the prior ball milling [10]. This pre stored energy would further lower the activation energy for the nucleation of strain free grains and promotes early recrystallization. This higher nucleation rate during the FSW process would result in the formation of fine equiaxed grain structure due to dynamic recrystallization. When nanoparticles are present in the matrix, the nucleation of new grains is stimulated by the active sites while their growth is inhibited via pinning of the grain boundaries by the nanoparticles. The above mentioned factors accelerate the recrystallization tendency during FSW of milled welds, leading to very fine equiaxed grains.

Figure 3. The typical EBSD image of the AlMg5-UM friction stirs welds

Figure 4. The typical EBSD image of the AlMg5-M friction stirs welds

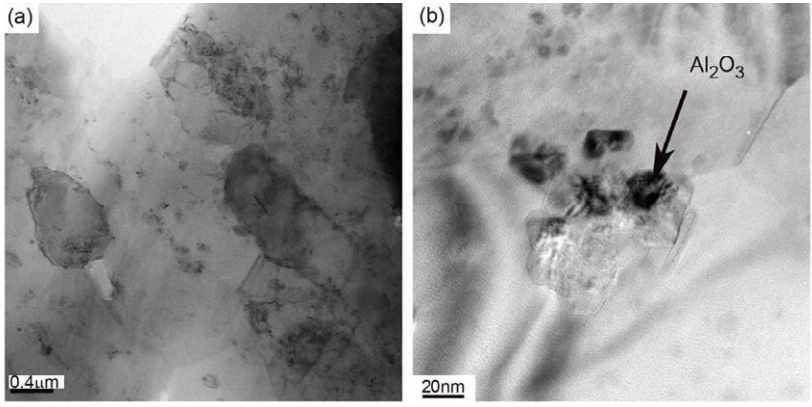

Figure 5. TEM micrographs of to AlMg5-0.5Al_2O_3, friction stir welded specimens showing (a) fine equiaxed grains (b) shows Al_2O_3 nanoparticles present in the weld nugget

The tensile results are listed in Table 1. The base material tensile properties have also been included in this table for comparison. The tensile specimens of AlMg5-UM welds displayed higher strength and ductility values compared to the base metal. In contrast, the tensile specimens prepared with AlMg5-M and AlMg5-0.5Al_2O_3 samples showed a reduction in yield and ultimate strengths in the weld nugget when compared to base metals. The AlMg5-UM base metal was not in strain hardened condition and strain hardening takes place in the nugget zone during FSW, which resulted in higher hardness and tensile strengths relative to base metal. The high strength and ductility values exhibited by AlMg5-UM stir zone could be attributed to the fine grains and strain hardening induced by the thermo-mechanical processing [16,17]. It is significant to note that AlMg5-M and AlMg5-0.5Al_2O_3 base metals were not fully recrystalized and strength of these base metals were 401±4, 483±16 respectively, higher than the strength value (300± 4) of AlMg5-UM base metal. These high strength of these base metals (AlMg5-M and AlMg5-0.5Al_2O_3) were indicative of strain hardened condition. The main reason for the softness of nugget zone is loss in work hardening effect because of the recrystallization during FSW of AlMg5-M and AlMg5-0.5Al_2O_3 samples [18]. Similar observations have been also

reported by Peel et al. [19] for aluminium AA5083 friction stir welds. They reported that the heavily strain hardneded microstructure of the base material (grain size around 50 μm), has been completely replaced by equiaxed grains (around 10–13 μm), typical of a recrystallised microstructure, after FSW. Also, it has been shown that lower hardness (75 HV) and YS (154 MPa) of nugget zone than the parent AA5083 (hardness 130 HV and YS 392 MPa) mainly associated with to loss in strain hardening during FSW.

Table 1. Tensile properties of base metal and FSW welds made on AlMg5-UM, AlMg5-M and AlMg5-0.5Al_2O_3

Condition	Yield Strength (MPa)	Ultimate Tensile Strength (MPa)	Elongation (%)
AlMg5-UM, Base metal	135± 2	300± 4	22± 2
AlMg5-UM, FSW	160± 0.5	326± 4	18± 2
AlMg5-M, Base metal	289±14	401±4	19±1
AlMg5-M, FSW	219± 10	373± 2	18±1
AlMg5-0.5Al_2O_3, Base metal	455±25	483±16	10±1
AlMg5-0.5Al_2O_3, FSW	218± 2	401± 4	10±1

Conclusions

The following conclusions can be drawn from this study:

1. AlMg5-UM welds exhibited improved strength compared to base metal due to grain refinement and work hardening effect induced by the thermo-mechanical processing.
2. As-welded samples of AlMg5-M and AlMg5-0.5Al_2O_3 showed a small reduction in strength in the weld when compared to corresponding base metals. The reduced strength may be attributed to the loss of work hardening effect because of recrystallization in the nugget zone commonly observed in welds.
3. The nanocomposite AlMg5-0.5Al_2O_3 welds exhibited higher ultimate strength in the nugget zone when compared to all other conditions. The high hardness and strength were attributed to the Orowan strengthening due to the presence of Al_2O_3 reinforcement particles in the matrix and Hall-Petch effect as a result of fine grain structure in the weld.

Acknowledgements

The authors acknowledge the financial support provided by King Abdulaziz City for Science and Technology (KACST), Riyadh, Saudi Arabia.

References

[1] K. D. Woo and H. B. Lee, “Fabrication of Al alloy matrix composite reinforced with subsive-sized Al_2O_3 particles by the in situ displacement reaction using high-energy ball-milled powder,” *Mater Sci Eng A*, 449–451 (2007), 829–832.

[2] Z.R. Hesabi, A. Simchi, S.S. Reihani, "Structural evolution during mechanical milling of nanometric and micrometric Al2O3 reinforced Al matrix composites," *Mater Sci Eng A*, 428 (12) (2006), 159–168.
[3] C. Suryanarayana, "Mechanical alloying and milling," *Prog Mater Sci*, 46, (1–2) (2001), 1–184.
[4] M. B. D. Ellis, "Joining of aluminium based metal matrix composites," *Int Mater Rev*, 41 (2) (1996), 41–58.
[5] R. S. Mishra, Z. Y. Ma, "Friction stir welding and processing," *Mater Sci Eng R Reports,* 50 (1–2) (2005), 1–78.
[6] L. Ceschini, I. Boromei, G. Minak, A. Morri, F. Tarterini, "Effect of friction stir welding on microstructure, tensile and fatigue properties of the AA7005/ 10 vol.% Al_2O_3 composite," *Compos Sci Technol*, 67 (2007), 605–15.
[7] W.B. Lee, C.Y. Lee, M.K. Kim, J. Yoon, Y.J. Kim, Y.M. Yoen, " Microstructures and wear property of friction stir welded AZ91 Mg/SiC particle reinforced composite," *Compos Sci Technol*, 66 (2006), 1513–20.
[8] S. Gopalakrishnan, N. Murugan, "Prediction of tensile strength of friction stir welded aluminium matrix TiC particulate reinforced composite," *Mater Des*, 32 (2011), 462–7.
[9] X.G. Chen, M.D. Silva, P. Gougeon, L. St-Georges, "Microstructure and mechanical properties of friction stir welded AA6063–B4C metal matrix composites," *J Mater Sci Eng A*, 518 (2009), 174–84.
[10] F. Khodabakhshi, H. G. Yazdabadi, A. H. Kokabi, A. Simchi, "Friction stir welding of a P / M Al – Al_2O_3nanocomposite : Microstructure and mechanical properties," *Mater Sci Eng A*, 585 (2013), 222-232.
[11] K. Kallip, M. Leparoux, K. A. AlOgab, S. Clerc, G. Deguilhem, Y. Arroyo, H. Kwon, "Investigation of different carbon nanotube reinforcements for fabricating bulk AlMg5 matrix nanocomposites," *J Alloys Compd*, 646 (2015), 710–718.
[12] Y. Morisada, H. Fujii, T. Nagaoka, M. Fukusumi, "Effect of friction stir processing with SiC particles on microstructure and hardness of AZ31," *Mater Sci Eng A*, 433 (1–2) (2006), 50–54.
[13] Y. Morisada, H. Fujii, T. Nagaoka, M. Fukusumi, "MWCNTs/AZ31 surface composites fabricated by friction stir processing," *Mater Sci Eng A*, 419 (1–2) (2006), 344–348.
[14] M. M. El-Rayes, E. A. El-Danaf, "The influence of multi-pass friction stir processing on the microstructural and mechanical properties of Aluminum Alloy 6082," *J Mater Process Technol*, 212 (5) (2012), 1157–1168.
[15] H.A. Crostack, G. Fischer, E. Soppa, S. Schmauder, Y. L. Liu, "Localization of strain in metal matrix composites studied by a scanning electron microscope-based grating method," *J Microsc*, 201 (2) (2001), 171–178.
[16] K.V Jata, S.L Semiatin,"Continous Dynamic Recrystallization During Friction Stir Welding of High Strength Aluminum Alloys," *Scripta Mater*, 43 (2000), 743–749.
[17] R. W. Fonda, J. F. Bingert, K. J. Colligan, "Development of grain structure during friction stir welding," *Scripta Mater*, 51 (3) (2004), 243–248.
[18] M. Amirizad, A. H. Kokabi, M. A. Gharacheh, R. Sarrafi, B. Shalchi, M. Azizieh, "Evaluation of microstructure and mechanical properties in friction stir welded A356+15%SiCp cast composite," *Mater Lett*, 60 (4) (2006), 565–568.

[19] M. Peel, A. Steuwer, M. Preuss, P.J. Withers, “Microstructure, mechanical properties and residual stresses as a function of welding speed in aluminium AA5083 friction stir welds, ” *Acta Materialia*, 51 (2003), 4791–4801.

TITANIUM FOAM FOR CANCELLOUS BONE IMPLANT PREPARED BY SPACE HOLDER TECHNIQUE

Xiao Jian, Cui Hao, Qiu Guibao, Yang Yang

College of Materials Science & Engineering, Chongqing University, 400044, China

Keywords: Porous material; Titanium; Foam; Biomaterial

Abstract

Open-cell titanium(Ti) foams with 75.5% porosity were manufactured by powder metallurgy route using acicular carbamide particles as space holder. The TG and DSC curves of carbamide were measured to optimize the heat treatment during carbamide removal. X-ray diffraction studies of carbamide before and after removed to ensure that the foams produced featured no contamination. The compressive strength and Young's modulus of Ti foams were 11.1 MPa and 0.32 GPa, respectively. This kind of open-cell the foam is expected to be a potential substitute biomaterial for cancellous bone, due to its mechanical properties well match that of cancellous bone.

Introduction

In recent years, the repair materials for defect bones have become one of the largest biomedical materials in clinical demand. Conventional bone implants have been always dense metal or alloys, such as Co-Ni alloy, stainless steel and Ti-based alloys. Among them, Ti alloys were recognized as the most successful materials. It was mostly due to their excellent mechanical properties, good corrosion resistance and superior biocompatibility[1-3]. However, compared to bones with a porous structure, conventional Ti alloys continue to suffer from two problems: (1) mismatch of Young' modulus between implant and bone will produce stress-shielding phenomenon, which resulting in loosening in the junction and bone resorption around the

implant[4, 5]; (2) dense structure of implant will bring the disadvantages for new bone tissue ingrowth, thus lower its longevity in vivo. Therefore, combined with the advantages of porous structure and Ti metal, Ti foams are attractive for bone implants.

Among the current techniques for Ti foams processing based on powder-metallurgy, the famous “space-holder technique” was reported extensively[6]. An optimal space holder which is a temporary material should be completely removed before sintering, such as carbamide[7-12], ammonium hydrogen carbonate[13-16], NaF[17], polypropylene carbonate (PPC)[18], naphthalene[19], NaCl[20-22], tapioca starch[23], magnesium[24] and steel[25]. Among them, carbamide was preferred due to its cheapness and easily removed under low temperature.

As has shown above, Ti foams were widely used for biomedical materials. R. Singh et.al[4] and S. Yang et.al[5] had reviewed the widely biomedical applications of Ti foams and how to design scaffolds used in tissue engineering. In this case, the present work was aimed at obtaining the foams with structure and properties match the requirements of cancellous bone.

Experimental procedure

Ti foams were fabricated via the well known “space holder technique” using commercially pure (Cp) Ti (Purity: 99.3%, Oxygen content: 0.05%) powder with average particle size of 32 μm. As a space holder, acicular carbamide granules with size between 225 μm to 420 μm were separated by sieving commercially available fertilizer. The selected size of carbamide particles was to obtain a final macro-pores belong to 100-500 μm, which is beneficial for ingrowth of new-bone tissue[26]. The volume fraction of space holder were calculated to obtain defined porosity of 80% in the sintered compact.

Initially, a pre-calculated amount of Ti powder and carbamide particles were mixed approximately 2~3 min in a mortar to obtain an ingredients homogeneous distribution. Then, the

mixtures were uniaxially pressed in a cylindrical die (Φ=16 mm, h=50 mm) at an applied pressure of 200 MPa under a 600 KN universal testing machine, followed by a dwell time of around 45s. After the spacer removed, the pre-heated samples (the treatment leading to the decomposition of carbamide is termed as preheating, and samples so treated are called preheated samples) were sintered at 1250 ℃ for 2h in vacuum (10^{-3} Pa).

The porosity of Ti foams can be shown as $\varepsilon=1-\rho^*/\rho_s$, where ε and ρ^*/ρ_s represent the porosity and relative density of samples, respectively. The microstructure was examined by SEM. The compressive tests were carried out at room temperature using a universal electromechanical Instron machine 5150 under a cross-speed of 2 mm/min. The porosity and mechanical properties were the average value of three samples.

Results and discussion

The removal of space holder was a key step in the preparation process of Ti foams. The thermal decomposition process of carbamide can be divided into three steps, i.e. 120℃-160℃, 160℃-280℃ and 280℃-460℃, as can be seen from the DSC curve in Fig. 1. So, to be avoided collapse during carbamide removed, the green samples should be heat-treated as slowly as possible. The quality of carbamide reduced with increasing of temperature (see TG curve), which indicates that there exist gas produced in the thermal decomposition process. Thus, in order to not pollute the Ti powders, the spacer removal process should be handled in a vacuum.

The XRD pattern of pre-heated sample was in accordance with that of titanium, which demonstrates that the removal of carbamide do not bring any contaminates to Ti powder, as shown in Fig. 2. The result proves that carbamide as a space holder was feasible and reasonable.

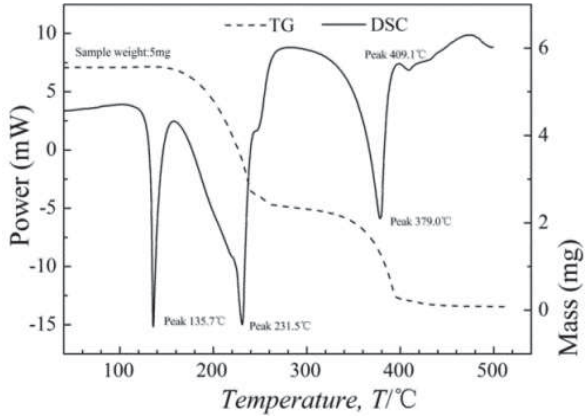

Fig.1 TG and DSC curves of carbamide.

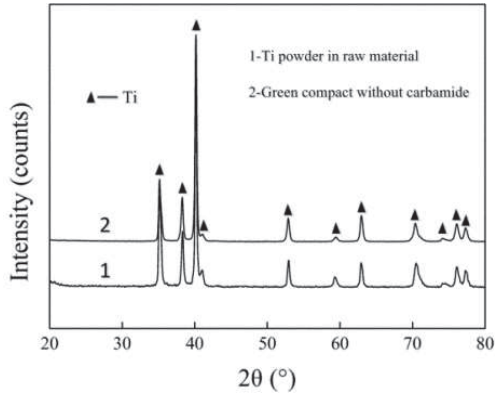

Fig. 2 XRD patterns of Ti powder and pre-heated sample.

Fig. 3 shows the typical pore structure and sintering neck of Ti foam sample with a porosity 75.5%. It can be clearly seen that the pores appeared connectivity in three dimensions. As bone implants, open-cell structure was beneficial for the ingrowth of new bone and the delivery of nutrients, see Fig. 3a. In addition, there are two types of pores, i.e. macro-pores and micro-pores,

as shown in Fig. 3b. The interconnected macro-pores were obtained by the removal of carbamide particles, and the micro-pores in pore walls were generated from incomplete sintering of Ti powders. This phenomenon was also found in other previous works[8, 16, 24]. In fact, the micro-pores in pore walls were also beneficial to further improve the connectivity of macro-pores. The sintering neck formed between the powders was well grown and being flat, which indicates a well diffusion in the sintering process, more details see Fig. 3c.

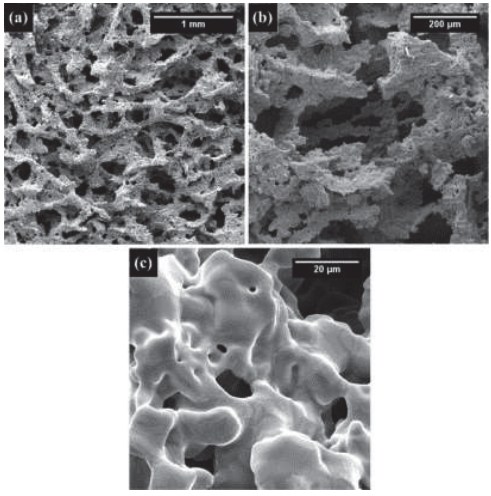

Fig. 3 SEM images of Ti foam sample.

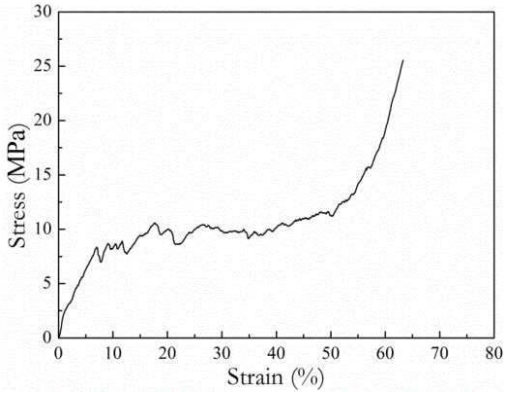

Fig. 4 Compressive stress-strain curve of Ti foam sample.

Fig. 4 shows the compressive stress-strain behavior of the foam sample. The compressive strength and Young' modulus of Ti foam prepared in present study were 11.1 MPa and 0.32 GPa, respectively. It was widely reported that the compressive strength and Young' modulus of cancellous bone were in the range of 4-12 MPa and 0.02-0.5 GPa, respectively[5]. When the prepared Ti foam was served as cancellous bone substitute material, on the one hand, the matchment between the Young's modulus of implant and that of cancellous bone will avoid the stress-shielding phenomenon; on the other hand, the open-cell structure enable the new bone tissue to grow through the entire scaffold and to imitate better the conditions of bone tissue in vivo. Therefore, open-cell the foam with porosity 75.5% prepared to present study can be served as a potential biomedical material for cancellous bone. The biomedical testing will be further investigated.

Conclusions

In the present work, open-cell Ti foams with porosity 75.5% were fabricated by using secular carbamide particle as a space holder. It was proved that carbamide as a space holder was feasible

and reasonable. The compressive strength and Young's modulus of Ti foams were 11.1 MPa and 0.32 GPa, respectively. This kind of foams is expected to be used as a potential substitute biomaterials for cancellous bone, due to its open-cell structure permits the ingrowth of the new-bone tissues and the transport of the body fluids.

Acknowledgements

This research is financially supported by the National Natural Science Foundation of China (Grant No. 51174243) and Major Program of NSFC (Grant No.51090383).

References

[1] Long M, Rack H. Titanium alloys in total joint replacement-a materials science perspective. Boimaterials. 1998;19:1621-39.
[2] Nishiguchi S, Nakamura T, Kobayashi M, Kim HM, Miyaji F, Kokubo T. The effect of heat treatment on bone-bonding ability of alkali-treated titanium. Biomaterials. 1999;20:491-500.
[3] Niinomi M. Mechanical properties of biomedical titanium alloys. Mater Sci Eng A. 1998;243:231-6.
[4] Singh R, Lee PD, Dashwood RJ, Lindley TC. Titanium foams for biomedical applications: A review. Mater Tech. 2010;25:127-36.
[5] Yang S, Leong KF, Du Z, Chua CK. The design of scaffolds for use in tissue engineering. Part I. Traditional factors. Tissue engineering. 2001;7:679-89.
[6] Dunand DC. Processing of titanium foams. Adv Eng Mater. 2004;6:369-76.
[7] Bram M, Stiller C, Buchkremer HP, Stöver D, Baur H. High‐Porosity Titanium, Stainless Steel, and Superalloy Parts. Adv Eng Mater. 2000;2:196-9.
[8] Niu W, Bai C, Qiu G, Wang Q. Processing and properties of porous titanium using space holder technique. Mater Sci Eng A. 2009;506:148-51.
[9] Sharma M, Gupta GK, Modi OP, Prasad BK, Gupta AK. Titanium foam through powder metallurgy route using acicular urea particles as space holder. Mater Lett. 2011;65:3199-201.
[10] Tuncer N, Arslan G, Maire E, Salvo L. Investigation of spacer size effect on architecture and mechanical properties of porous titanium. Mater Sci Eng A. 2011;530:633-42.
[11] Dezfuli SN, Sadrnezhaad S, Shokrgozar M, Bonakdar S. Fabrication of biocompatible titanium scaffolds using space holder technique. Journal of Materials Science: Materials in Medicine. 2012:1-6.
[12] Sharma M, Gupta G, Modi O, Prasad B. PM processed titanium foam: influence of morphology and content of space holder on microstructure and mechanical properties. Powder Metall. 2012;56:55-60.
[13] Torres Y, Rodriguez JA, Arias S, Echeverry M, Robledo S, Amigo V, et al. Processing, characterization and biological testing of porous titanium obtained by space-holder technique. J Mter Sci. 2012;47:6565-76.
[14] Laptev A, Vyal O, Bram M, Buchkremer HP, Stover D. Green strength of powder compacts provided production of highly porous titanium parts. Powder Metallurgy. 2005;48:358-64.
[15] Laptev A, Bram M, Buchkremer H, Stöver D. Study of production route for titanium parts combining very high porosity and complex shape. Powder Metall. 2004;47:85-92.
[16] Wen C, Yamada Y, Shimojima K, Chino Y, Asahina T, Mabuchi M. Processing and mechanical properties of autogenous titanium implant materials. J Mater Sci: Mater Medic. 2002;13:397-401.
[17] Bansiddhi A, Dunand DC. Shape-memory NiTi foams produced by solid-state replication with NaF. Intermetallics. 2007;15:1612-22.
[18] Hong T, Guo Z, Yang R. Fabrication of porous titanium scaffold materials by a fugitive filler method. J Mater Sci: Mater Medic. 2008;19:3489-95.

[19] Chino Y, Dunand DC. Creating Aligned, Elongated Pores in Titanium Foams by Swaging of Preforms with Ductile Space‐Holder. Adv Eng Mater. 2009;11:52-5.
[20] Torres Y, Pavon JJ, Rodriguez JA. Processing and characterization of porous titanium for implants by using NaCl as space holder. J Mater Pro Tech. 2012;212:1061-9.
[21] Ye B, Dunand DC. Titanium foams produced by solid-state replication of NaCl powders. Mater Sci Eng A. 2010;528:691-7.
[22] Bansiddhi A, Dunand D. Shape-memory NiTi foams produced by replication of NaCl space-holders. Acta Biomater. 2008;4:1996-2007.
[23] Mansourighasri A, Muhamad N, Sulong A. Processing titanium foams using tapioca starch as a space holder. J Mater Pro Tech. 2012;212:83-9.
[24] Esen Z, Bor Ş. Processing of titanium foams using magnesium spacer particles. Scripta Mater. 2007;56:341-4.
[25] Kwok PJ, Oppenheimer SM, Dunand DC. Porous Titanium by Electro‐chemical Dissolution of Steel Space‐holders. Adv Eng Mater. 2008;10:820-5.
[26] Müller U, Imwinkelried T, Horst M, Sievers M, Graf-Hausner U. Do human osteoblasts grow into open-porous titanium. Eur Cell Mater. 2006;11:8-15.

TMS2016

145th Annual Meeting & Exhibition

SUPPLEMENTAL PROCEEDINGS

Recent Developments in Biological, Structural and Functional Thin Films and Coatings

THIN FILMS AND COATINGS FOR ABSORPTIVE REMOVAL OF ANTIMICROBIALS, ANTIBIOTICS, AND OTHER PHARMACEUTICALS

David Cocke[1,2], Andrew Gomes[3], Saiful Islam[4], Gary Beall[5,6]

[1]Center for Innovation and Commercialization, Lamar University, Beaumont, TX
[2]Gill Chair of Chemical Engineering, Lamar University, Beaumont, TX
[3]Materials Instrumentation Center, College of Engineering, Lamar University, Beaumont, TX
[4]Department of Chemistry & Biochemistry, Lamar University, Beaumont, TX
[5]Texas State University, San Marcos, TX
[6]King Abdulaziz University, Faculty of Science, Department of Physics, Jeddah, Saudi Arabia

Keywords: Triclosan, autoimmune diseases, LC/MS, cloisite

Abstract

The US EPA regards “emerging pollutants” as new unregulated chemicals which impact the environment and human health. Many chemicals such as analgesics, anti-inflammatories, beta-blockers, antibiotics, and antimicrobials are not being effectively removed in water treatment. Triclosan, a ubiquitous antimicrobial that is widely used in antibacterial products and in clinical situations is of growing concern as it has been found to degrade human health with potentially devastating promotion of cancer and autoimmune diseases. In this study we are exploring the removal of triclosan using molecular modeling and absorptive/adsorption experiments on modified clays monitored by Tandem Liquid Chromatography – Mass Spectrometry (LCMS). Thin films and coatings offer the opportunity to build complex structures, save materials and engineer hybrid systems. Manual coating (brushing, dipping and air spraying) as well as 3D printing has been explored.

Introduction

Since the large increases in the use of polychlorinated aromatic antimicrobials there is increasing evidence of these chemicals negatively impacting the environment[1] and the immune systems of human populations via immune and inflammatory dysfunction. [2]. This supports not only questioning the effect of triclosan on the human immune system but to find more efficient ways of removing triclosan at the source and from the biota.

Triclosan is classified as a broad-spectrum antimicrobial agent as it is effective against a wide range of microbes including: bacteria, parasites, fungi, and virus [3].Triclosan is effective at low concentrations against bacteria. It has been used in soaps, mouthwashes, face washes, deodorants, toothpastes, and many other household products. In 2012 it was estimated that approximately 1500 t of TCS was being produced annually worldwide with up to up to 96% being washed down drains and into the sewerage systems [4]. It is becoming the main example of emerging new environmental pollutants. Consequently, describing the mechanisms, whereby triclosan produces its toxicity, is necessary for the full evaluation of the ecological damage that might result from triclosan in the biota. Understanding its structure–activity relationships [5] and

molecular dynamics [6] in relation to the mechanisms can have broad consequences in amelioration of its effects as well as finding biomedical uses. It is a chlorinated aromatic compound, polychlorophenoxy phenol, that has halogen, ether and phenol functional groups. The toxic effects of a phenol depends on many molecular structural factors. Two obvious ones are the pKa (i.e. the phenols dissociation constant) and log P (where P is the octanol-water partition coefficient). The larger the value of pKa, the smaller the extent of dissociation at any given pH (see Henderson–Hasselbalch equation)—that is, the weaker the acid. Here chlorine is expected to increase hydrophobicity and the value of logP and increase membrane penetrability whereas, if it decreases the pKa value (becomes more acidic), membrane penetration is decreased but if it increases pKa the opposite may occur depending on its surrounding pH. Its molecular structure is shown in Figure 1.

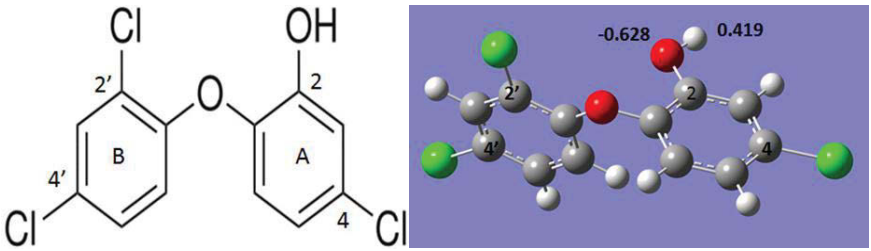

Figure 1 Triclosan from Avogadro and Gaussian (level of theory: B3LYP/6-31G(d)). The fractional numbers indicate the Mullikan charge of phenolic oxygen and hydrogen atom.

Another factor that determines a phenol's toxicity is its reactivity with a cell's biomolecules and the participation in oxidative processes. Reactive oxygen species (ROS) play a pivitol role in human health and disease via biochemical physiological and pathophysiological processes [7] and probably in aging [8].

In this work, we investigated the adsorption of triclosan on three types of cloisites, and calculated the relative removal efficiency. We are also beginning to explore their thin films and coatings that will offer the opportunity to build complex structures, save materials and engineer hybrid systems.

There are two major removal technologies for phenolic compounds: chemical oxygenation processes with reagents such as hydrogen peroxide [9,10],and the second and the subject of this paper absorption and extraction processes [11-14]. Clays and clay minerals acting as chemical adsorbents are important systems in the removal of these chlorinated organic compounds and in some ways may be more desirable than polymers and activated carbon [11, 15-19]. Clay minerals have large specific surface areas, cation exchange capacity, and low cost as well as very low toxicity [17, 19-20]. The adsorption of organic molecules to these minerals is affected by various parameters, such as the exchangeable cations, the distance between the clay mineral layers, and the existence of water molecules between the layers [20, 21-24] and are aided by the inclusion of organic entities in the interlayers and in the case of cloisite. Recently it has been demonstrated that self-assembled layers of polymer and montmorillonite clay nanoparticles can be produced as a 3-D layer on various substrates [25]. These 3-D printed highly ordered structures are easily produced with conventional ink jet printing technology. Figure 2 contains an

x-ray diffraction pattern of such a film that illustrates the high degree of order and self-assembly by the number of orders of reflection and the sharpness of the peaks.

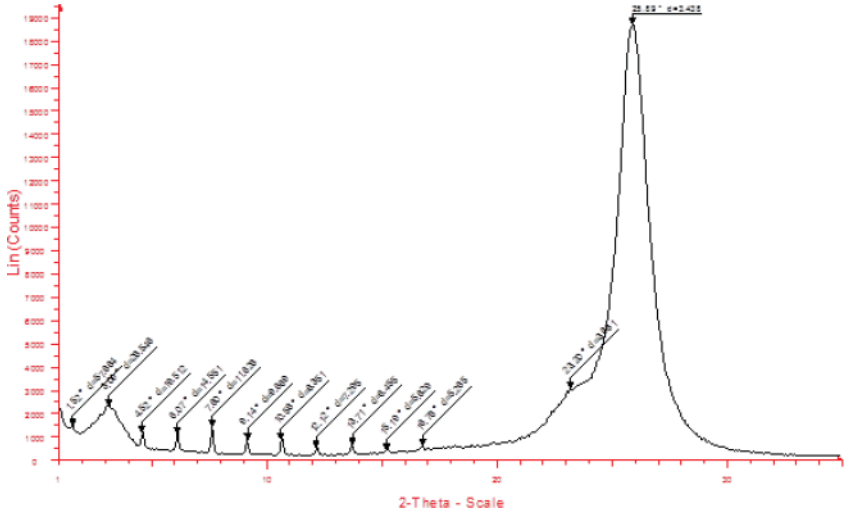

Figure 2 X-ray diffraction pattern of self-assembled nanocomposite 3-D film of polyvinylpyrrolidone and montmorillonite nanoparticles.

Figure 3 shows the layered structure of cloisite 30B, where interlayers are organoclays that contain quaternary ammonium cations bonded with one methyl group, two hydroxyethyl groups, and one tallow group. Figure 3 shows the Avogadro-optimized structure of the organoclay.

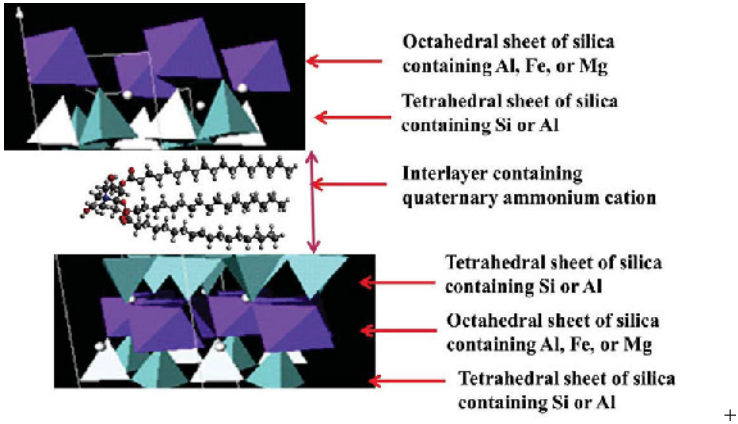

Figure 3.Structure of cloisite30B.In the interlayer, there are one methyl group,two hydroxyethyl groups, and one tallow group bonded to central nitrogen or quaternary ammonium cation. The diagram was modified after [26].

Experimental

Theoretical Simulation

Avogadro visualization platform [27] was used to draw triclosan, cloisite and their adducts and these models were optimized using molecular mechanics that are imbedded in Avogadro software. The outputs were used as inputs for running Gaussian 03W simulation [28]. We used at the beginning ab initio theory with a basis set of STO-3-21G. Later on, the ab initio optimized structures were further modified using Density functional Theory (B3LYP) with 6-31G(d) basis set.

Absorption Experiment

100 mg triclosan and 100 mg cloisite (15a,20A,30B) was dissolved into 25mL of Acetonitrile solution to make a 4000ppm solution. The solution was then run for 20 minutes for stirrer with magnetic stirrer for adsorption of triclosan in cloisite. Later this solution run for centrifuge and for filtration to get the triclosan-cloisite adduct precipitate. The centrifuged solution run for filtration by using micro filter and obtained solution was ready for getting data in LC-MS (Agilent, 6460C, 1290 infinity LC with triple quadruple MS).

The precipitated triclosan-cloisite adduct precipitate was run in TGA (TA-Q-500) hypernated with Hiden MS (HPR 20) instrument.

Results and Discussion

Table 1 shows the results of the adsorption experiments. According to Table 1, closite 15A adsorbs the highest amount of triclosan in comparison to cloisite 20A and closisite 30B. Since the d-spacing in cloisite 15A is maximum, the result was expected. Figure 4 shows the calibration curve for measuring triclosan in the treated water. Figure 5 shows the residual MS peaks with respective MS peak areas when different kinds of cloisite were used to treat triclosan contaminated water. As mentioned in Table 1, cloisite 15A was found to have least redual MS area.

Figure 6 shows the thermogravimetric analysis of trilcosan-cloisite adduct. It shows the slow degradation of triclosan when mixed with closite 30B. It also indicates that when thermally degraded, triclosan will probably degrade slowly. Our MS results did not show any indication of release of toxic components that one might expect otherwise.

Table 1.Removal of triclosan by different types of closites.

Name	Properties	d-spacing (Å)	Residual area	Relative removal efficiency (%)
Cloisite 15A	Weight loss percencentage in ignition is more	31.5	1177	94
Cloisite 20A	Low mass loss, broader peaks in derivative peak in thermal analysis	24.2	25128	54
Cloisite 30B	Off white color additive for plastics improve plastics physical properties	18.5	29127	47

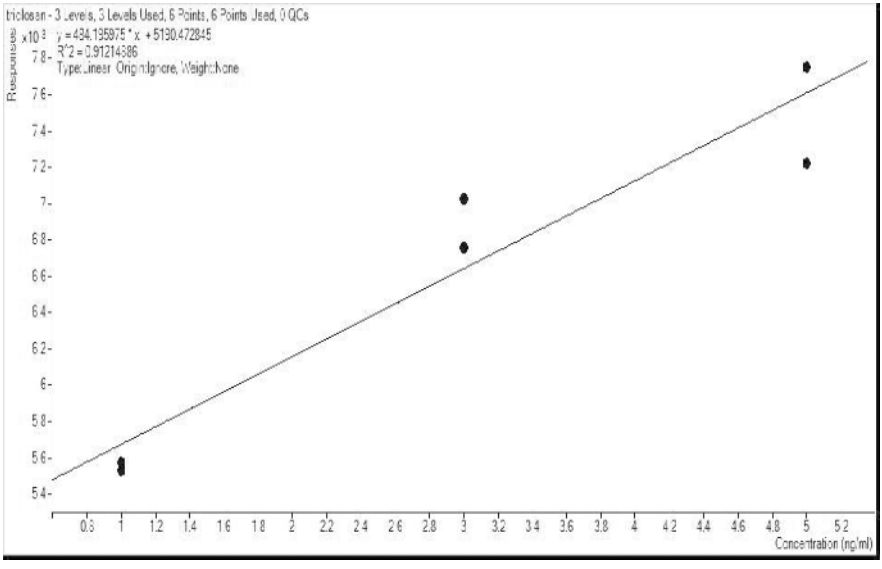

Figure 4. A calibration curve of triclosan measurement using LC/MS. R2 is found to be 0.91.

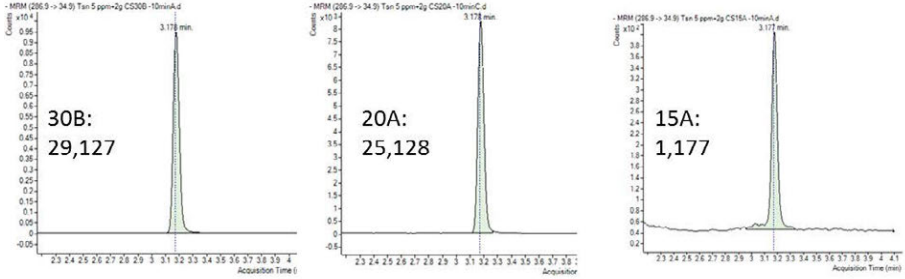

Figure5. Residual Mass Spectrometer (MS) peak areas for remaining triclosan in closites-treated water. 30B, 20A, and 15A indicate three types of closites.

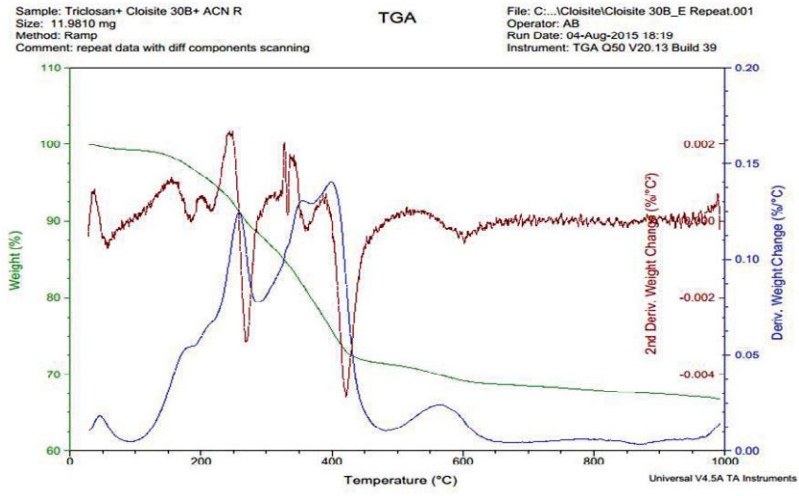

Figure 6. TGA plot for triclosan-cloisite 30B adduct. The green curve is for TGA, the blue curve for differential of TGA, and the pale red curve double differential of TGA.

Conclusions

Optimized structures of triclosan, and triclosan-cloisite adduct were calculated using Density Functional Theory with Gaussian 03 program. Closite 15 A was found to have the highest adsorption capability of triclosan compared to those with cloisite 20A and 30B. Thermal decomposition triclosan-cloisite adduct may create lower toxic products compared to triclosan. As demonstrated for the polymer and montmorillonite clay nanoparticles system, new highly structured clay layers can be produced by 3D ink jet printing which we are currently exploring with cloisite layers.

Acknowledgment

We express our gratitude for the MRI-NSF grant (#1338088) for the acquisition of LC/MS/MS instrument. This work was partially supported by the Gill Chair Research and Operational Fund from the Gill Family Foundation of Houston, Texas, and Lamar University CICE Avogadro project award.

References

1. R.U. Halden, "On the Need and Speed of Regulating Triclosan and Triclocarban in the United States," *Environmental Science and Technology,* 48 (7) 2014, 2603-2611.
2. E.M.R. Clayton, M. Todd, J.B. Dowd, and A.E. Aiello, "The impact of bisphenol A and triclosan on immune parameters in the U.S. population*, Environ. Health Perspect*, 119 (2011), 390−396.
3. S.P. Yazdankhah, A.A. Scheie, E.A. Høiby, B.T. Lunestad, E. Heir, T.Q. Fotland, K. Naterstad, and H. Kruse, "Triclosan and antimicrobial resistance in bacteria: an overview", *Microb Drug Resist*., 12 (2006) 83-90.
4. X.J. Chen, J. Richard, Y.L. Liu, E. Dopp, J. Tuerk, and K. Bester, "Ozonation products of triclosan in advanced wastewater treatment." Water Res. 46 (7) (2012), 2247e2256.
5. C.W. Levy, A. Roujeinikova, S. Sedelnikova, P.J. Baker, A.R. Stuitje, A.R. Slabas, D.W. Rice and J.B. Rafferty, " Molecular basis of triclosan activity," *Nature*, 398 (1999), 383-384.
6. R.C. Peterson, Computational conformational antimicrobial analysis developing mechanomolecular theory for polymer biomaterials in materials science and engineering, Int. J. Comput Mater. Sci. Eng. (2014) 1-61.
7. K. Brieger, S. Schiavone, F.J. Miller Jr., K.-H. Krause, "Reactive oxygen species: from health to disease," *Swiss Med Wkly*, 2012,142:w13659.
8. R.S. Balaban, S. Nemoto, and T. Finkel , "Mitochondria, Oxidants, and Aging," *Cell*, 120 (2005), 483–495.
9. J.M. Britto, M.D. Rangel, "Advanced oxidation process of phenolic compounds in industrial wastewater," *Quimica Nova*, 31(2008), 114–122.
10. Q. Husain, M. Husain, Y. Kulshrestha, "Remediation and treatment of organopollutants mediated by peroxidases: a review," *Critical Reviews in Biotechnology* 29(2009), 94–119.
11. A. Dabrowski, P. Podkoscielny, Z. Hubicki, M. Barczak, "Adsorption of phenolic compounds by activated carbon—a critical review," *Chemosphere* 58 (8) (2005), 1049–1070.
12. C.-J. Liao, C.-P. Chen, M.-K. Wang, P.-N. Chiang, and C.-W Pai, "Sorption of chlorophenoxy propionic acids by organoclay complexes," *Environmental Toxicology,* 21 (2006), 71–79.
13. M.C. Floody, B.K.G. Theng, P. Reyes, M.L. Mora, "Natural nanoclays: application sand future trends—a Chilean perspective," *Clay Minerals,* 44 (2009), 161–176.
14. K.M. Smith, G.D. Fowler, S. Pullket and N.J.D. Graham, "Sewage sludge-based adsorbents: a review of their production, properties and use in water treatment applications," *Water Research,* 43 (2009), 2569–2594.
15. S.D. Faust, O.M. Aly, "Chemistry of Water Treatment," pp (1998), 127–483.

16. H. Zhao, F.G. Vance, "Sorption of trichloroethylene by organo-clays in the presence of Humic substances," *Water Research,* 32 (1998), 3710–3716.
17. G.W. Beall, "The use of organo-clays in water treatment," *Applied Clay Science,* 24 (2003),11–20.
18. J.Q. Jiang, Z. Zeng, "Comparison of modified montmorillonite adsorbents. Part II:the effects of the type of raw clays and modification conditions on the sorption performance," *Chemosphere,* 53 (2003), 53–62.
19. Y. Gonen, G. Rytwo, "Using the dual-mode model to describe sorption of organic pollutants onto an organoclay," *Journal of Colloid and Interface Science,* 299 (2006), 95–101.
20. A.D. Site, "Factors affecting sorption of organic compounds in natural sorbent water systems and sorption coefficients for selected pollutants," *A review. Journal of Physical Chemistry,* 30 (2001), 187–439.
21. J.F. Lee, M.M. Mortland, C.T. Chiou, D.E. Kile and S.A. Boyd, "Sorption of benzene, toluene, and xylene by two tetramethylammonium-smectites having different charge densities," *Clays and Clay Minerals,* 38 (1990), 113–120.
22. C.T. Johnston, "Organic Pollutants in the Environment," *The Clay Mineral Society, (*CMS Workshop Lectures. Boulder, CO, 1996).
23. G. Rytwo, S. Nir, L. Margulies, "Adsorption and interactions of diquat and paraquat with montmorillonite," *Soil Science Society of America Journal,* 60 (1996), 601–610.
24. F. Bergaya, B.K.G. Theng, G. Lagaly, "Development in Clay Science," (Handbook of Clay science, Amsterdam, The Netherlands 2006).
25. R. Cook, R. Chen, G.W. Beall, "Highly ordered self-assembling polymer/clay nanocomposite barrier film", DOI:10.1021/acsami.5b02162, *ACS Applied Materials and Interfaces,* 7 (2015) 10915-10919
26. A. Maneshi,J.B.P. Soares and L.C. Simon, "Polyethylene/Clay Nanocomposites Made with Metallocenes Supported on Different Organoclays," *Macromolecular Chemistry and Physics,* 212 (3) (2011), 216–228.
27. Avogadro software, http://avogadro.cc/wiki/Main_Page.
28. M.J. Frisch, G.W. Trucks, H.B. Schlegel, G.E. Scuseria, M.A. Robb, J.R. Cheeseman, J.A. Montgomery, Jr., T. Vreven, K.N. Kudin, J.C. Burant, J.M. Millam, S.S. Iyengar, J. Tomasi, V. Barone, B. Mennucci, M. Cossi, G. Scalmani, N. Rega, G.A. Peterson, H. Nakatsuji, M. Hada, M. Ehara, K. Toyota, R. Fukuda, J. Hasegawa, M. Ishida, T. Nakajima, Y. Honda, O. Kitao, H. Nakai, M. Klene, X. Li, J.E. Knox, H.P. Hratchian, J.B. Cross, V. Bakken, C. Adamo, J. Jaramillo, R. Gomperts, R.E. Stratmann, O. Yazyev, A.J. Austin, R. Cammi, C. Pomelli, J.W. Ochterski, P.Y. Ayala, K. Morokuma, G.A. Voth, P. Salvador, J.J. Dannenberg, V.G. Zakrzewski, S. Dapprich, A.D. Daniels, M.C. Strain, O. Farkas, D.K. Malick, A.D. Rabuck, K. Raghavachari, J.B. Foresman, J.V. Ortiz, Q. Cui, A.G. Baboul, S. Clifford, J. Cioslowski, B.B. Stefanov, G. Liu, A. Liashenko, P. Piskorz, I. Komaromi, R.L. Martin, D.J. Fox, T. Keith, M.A. Al-Laham, C.Y. Peng, A. Nanayakkara, M. Challacombe, P.M.W. Gill, B. Johnson, W. Chen, M.W. Wong, C. Gonzalez, and J.A. Pople, Gaussian 03, Revision C.02, (Wallingford CT: Gaussian Inc. 2004).

EFFECT OF POST-HEAT TREATMENT ON THE ELECTROCHEMICAL PERFORMANCE OF SANDWICH STRUCTURED Cu/Sn/Cu ELECTRODE

B. Bilici, B.D. Polat*, O.Keles

Department of Metallurgical and Materials Engineering, Istanbul Technical University, Istanbul 34469, Turkey,
*Tel:0090 212 2853398, Fax:0090 212 285 3427, E-mail:bdpolat@itu.edu.tr

Keywords: Electrochemical deposition, Anode, Lithium ion battery, Sn based film, Sandwich structured electrode, Heat treatment

Abstract

In this work, we have produced Cu/Sn/Cu sandwich structured film by electrodeposition method, to be used as a negative electrode for rechargeable lithium ion battery. To promote the interaction between Cu/Sn/Cu layers, an additional post-heat treatment (200°C, 48h under vacuum atmosphere) has been applied to the coatings. The galvanostatic test results prove that morphological changes and Cu_xSi intermetallics formation in the film as a result of heat treatment process promote the capacity retention of the electrode. After 30 cycle, the capacities of the Cu/Sn/Cu electrodes with and without heat treatments are 230 mAh g^{-1}, 100 mAh g^{-1} respectively. This demonstrates that the post-heat treatment process improves cycle performance of the electrode.

Introduction

Lithium-ion batteries are widely in demand as power sources for various mobile electronic products, such as cellular phones and portable computers due to their high energy density, high voltage, and long lifespan. In today's technology most commercial lithium-ion batteries use carbon based materials as anodes due to their high capacity, high safety, good electrical conductivity and very stable capacity as compared with lithium metal [1].
In recent years, alternative materials for being used as negative electrodes have been under investigation because the theoretical capacity of carbon becomes insufficient (372mAhg^{-1}) for high-energy density requirements applications such as electric vehicles. A large number of these studies especially focus on several metals and metalloids (tin, silicon, aluminum, antimony, etc.) [2-4]. The tin based materials receives considerable attention among them as a result of its high theoretical specific capacity (994 mAh g^{-1}, according to $Li_{22}Sn_5$) and abundance on earth crust [5]. However, the cycle performance of Sn-based anodes is very poor. It is widely known that large volume changes during cycling cause exfoliation of the active material from the current collector (e.g V ≈ 260% for the Sn $\rightarrow$ $Li_{4.4}Sn$ transition). Plus the low electrical conductivity (9.17×10^6 Sm^{-1}) of Sn prevents fast electron passage through the electrode which also restricts its performance in the cell [6-8].
A variety of approaches has been developed to overcome these problems, most researchers initially focus on synthesizing small sized-Sn particles. Because small sized particles having higher surface area assist to spread the stress on a large area. Therefore, reduction in particle size can successfully minimize internal stresses, thus dangerous effects of volume change [9-11]. Additionally, Wang et al. [12] have reported that the void space among tin nanoparticles is also important since these void spaces accommodate the volume change of tin during lithiation/delithiation. Moreover, there are also some scientists who have studied to improve

the performance the electrode by changing the shape of small sized particles. Zhang et al. have encapsulated tin nanoparticles in elastic hollow carbon spheres and succeed enlarging size of gaps (void space) in the structure [13]. As another method to enhance capacity, the researchers dope various metals (Ni, Cu, Co, Sb, Ag, and Fe) to form M_xSn_y intermetallics in Sn based anode structure [14-16]. It is known that these intermetallics form active-inactive alloy systems which buffer the volumetric expansion of the Sn particles upon cycling. Among these candidates, Cu_xSn_y alloys are considered as one of the most promising because Cu has a high electrical conductivity (5.96×10^7 Sm^{-1}) to decrease the ohmic resistance and a high ductility to increase the mechanical tolerance of the electrode [17-18]. Cu_xSn_y intermetallics Kitada et al. [22] have found that Cu_6Sn_5 and Cu_3Sn intermetallics help to strengthen structure and form stable architecture due to copper can result in a ductile matrix to accommodate some of damaging lattice expansion/contraction. However, Cu_3Sn phase is less active against lithiation. Xia et al. [19] suggest that Cu_3Sn is only partly reversible and excessive Cu may cause relatively poor cycle performance than Cu_6Sn_5. The lithiation reactions of Cu_6Sn_5 and Cu_3Sn are given Eq.1-3.

Chiu et al have examined the structural evolution and electrochemical performance of Cu_6Sn_5 thin film. In this study, they have shown an intercalation reaction between lithium and Cu_6Sn_5 [20]. Then in 2011, Lin et al [21] have proved that the intensity of Cu_6Sn_5 decreased with lithium insertion, which justifies the reversible reactions of lithium with Cu_6Sn_5 where the reversible inclusion of lithium in Cu_6Sn_5 anode (intercalation) is highly encouraged. The same lithiation mechanism has been also shown for Cu_3Sn electrode (Eq.3)

$$Cu_6Sn_5 + 10Li^+ \rightarrow 5CuLi_2Sn + Cu \quad \text{(first stage)} \tag{1}$$

$$5CuLi_2Sn + 11.25Li \leftrightarrow 5Li_{4.25}Sn + 5Cu \text{ [21]} \quad \text{(second stage)} \tag{2}$$

$$4Cu_3Sn \rightarrow Li_{17}Sn_4 + 12Cu \text{ [26]} \tag{3}$$

By using intermetallics, although the reversibility of the reaction is promoted to some extent. Aggregation of particles can appear in some cases, which will lead to an increase of particle size in cycling. Thus, exfoliation of active materials and failure of electrode. Tamura et al. [23] have reported that it is feasible to prepare Cu_6Sn_5 film anode by annealing after electrodepositing tin film on copper foil. Moreover, they have found that cycling performance has been greatly improved due to the enhanced bonding force between Cu_6Sn_5 and copper foil.

So far, the positive effects of annealing process on anode materials have been justified by diverse studies [24-27]. Without annealing, some intermettallics can not be formed and heterogeneous growth take place in grain boundaries since grain boundary diffusions occur much more than bulk diffusion in room temperature. These undesirable effects would be prevented by supplying sufficient thermal energy via annealing.

In our study, we produce two sandwich structured Cu/Sn/Cu electrodes since sandwich model can equilibrate balance of all forces (tension, compression, core sheer and bending) to assist a stable architecture under normal stress. The electrodes are fabricated by electrochemical deposition, which enhances the adherence between the active material and the substrate, plus it requires no binder or conductive additives. First sandwich structured Cu/Sn/Cu electrode are produced without annealing. Second sandwich structured Cu/Sn/Cu electrode are annealed for 48h at 200˚C. Then, they are electrochemically tested to examine differences in their cycle performance.

Experimental

Two Sn-based films (Cu/Sn/Cu) are deposited on Cu foils by electrochemical deposition technique. The copper foil is cleaned by ethanol. The copper is used as cathode in the electroplating bath. In Table I, the parameters of depositions and compositions of the electroplating baths are given. For each sample, electrodeposition is performed under a constant current density at room temperature. The thicknesses of the film are measured by profilometer in order to investigate the effects of heat treatment, one of Cu/Sn/Cu anodes is annealed at 200˚C for 48 h under vacuum atmosphere. The color of the active material becomes lightly blackish after this heat treatment.

To observe the morphologies of the films prior to electrochemical tests, Scanning Electron Microscope (SEM, Hitachi S-4700-II) is used. To compare the morphological changes between Sample 1 (non-heat treated) and Sample 2 (heat treated Cu/Sn/Cu) after 30th cycles, the cells are disassembled in the glovebox (Mbraun, Labmaster) and after washing with dimethylcarbonate (DMC) solution to remove the electrolyte, they are left to be dried in glovebox. Afterwards, the samples are taken out of the glovebox and their surfaces are observed by SEM .The phases present in the coatings before the galvanostatic test are determined using Philips PW3710 XRD machine with a 2θ range of 20˚–90˚ in steps of 0.05 (with CuKα at 40 kV and 30 mA).

Electrochemical measurements are done using half-cells which are assembled as 2032 coin cells in an Ar-filled glove box. Pure Li foil is used as a counter electrode and porous polypropylene film (Celgrad 2400) as a separator. The non-aqueous electrolyte used in the cells is 1 M $LiPF_6$ dissolved in ethylene carbonate (EC) and dimethyl carbonate (DMC) (1:1 weight ratio). The cells are tested at room temperature and operated at voltages between 0.2 V and 1.2 V versus Li/Li^+ at a rate of 50 mA g^{-1}. Cyclic voltammetry (CV) is accomplished in a potential range of 0.2 V and 1.2 V versus Li/Li^+ at a scan rate of 0.03 mV s^{-1}.

Table I. The bath composition and the parameters of electrochemical deposition

	Sn	**Cu**
Bath Composition	$Sn(SO)_4$: 20 g/L H_2SO_4 : 70 g/L	$Cu(SO)_4$: 41.50g/L H_2SO : 196.16 g/L PEG : 100 ppm HCl : 50 ppm
Time (s)	20	bottom layer: 60 top layer: 20
Current (A/dm_2)	2	2

Results and Discussion

Fig. 1a and b shows the plane-view surface morphologies of the Samples 1 and 2, respectively. Fig. 1a is the surface morphology of the Cu/Sn/Cu film without heat treatment, it has an inhomogeneous geometry due to the presence of microsized agglomerates. After annealing at 200˚C, as shown in Fig. 1b, the grains become smaller when compared to that of the Sample 1. In addition structure relatively become more homogenous because heat treatment provide enough thermal energy to bulk diffusion rate to keep up with the grain boundary diffusion rate [28].

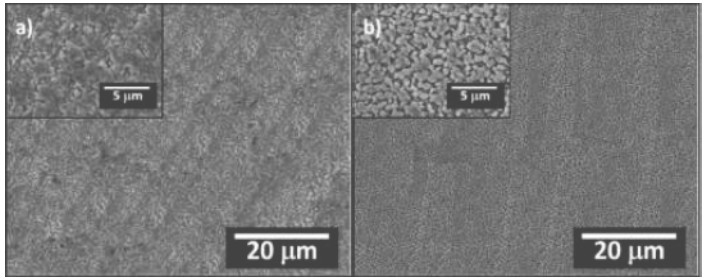

Figure 1. The SEM images of the pristine films a) the Cu/Sn/Cu (Sample 1), b) the Cu/Sn/Cu with heat treatment (Sample 2)

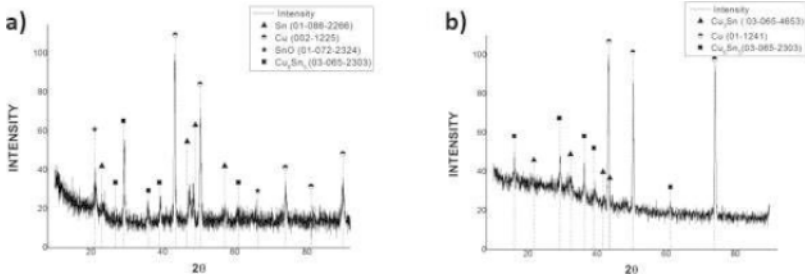

Figure 2. XRD data of a) Cu/Sn/Cu (Sample 1), b) the Cu/Sn/Cu with heat treatment (Sample 2) electrodes

Figs. 2a, b gives the XRD patterns of the as-deposited film and films annealed at 200˚C. For the sample without heat treatment (Fig. 2a), the main phases are that of tin and copper. The diffraction angles (2θ=) of tin and copper located can be clearly seen at 22.4˚, 46.3˚, 49.0˚, 57.3˚ and 43.4˚, 50.2˚, 73.8˚, 81.1˚, 89.8˚ respectively. Additionally, the small peaks are seen at around 20.9˚ and 66.1˚, shows the existence of SnO particles. It is believed that SnO forms due to the surface oxidation of Sn film**.** The Cu_6Sn_5 phase is also observed at 16.4˚ ,27.2˚, 29.4˚ 37.1˚ and 39.3˚, 61.2˚ indicating that a slight Cu_6Sn_5 intermetallic compound forms between tin and copper layers of the sandwich structure. After annealing at 200˚C for 48 h, as shown in Fig. 2b, the diffraction peaks of the tin almost disappear. On the other hand, the intensity of copper peaks increase at 43.4˚, 50.2˚, 73.8˚. It is known that copper particles move to the film surface from substrate with higher temperature because the diffusion rate of copper is high at higher temperatures [1]. At 16.8 ˚C new peak of the Cu_6Sn_5 phase, which is known to have a monoclinic lattice with a space-group symmetry of C2/c, is detected while intensity of its two peaks increases (37.1˚ and 39.3˚). In addition, Fig. 2b reveals that the intensities of other two peaks related to Cu_6Sn_5 reduce (29.4˚, 61.2˚) while one peak disappears (27.2˚). The formation of $\mathcal{E}$-Cu_3Sn phase (orthorhombic structure, space group: Cmcm) (21.4˚, 33.2˚, 41.7˚, 43.6˚) in Fig 2b could be a reason for these changes.

The cyclic voltammograms of the as-deposited and annealed Cu/Sn/Cu sandwich structured film anode are given in Fig. 3a-b. All the cathodic and anodic peaks attribute to lithium alloying and de-alloying with the active materials, respectively. With respect to the as-deposited film, one anodic peaks at around 0.5 V can be slightly detected. Besides this reversible peak, as shown in the inset of Fig. 3a, an irreversible peak, which is most probably

related to solid electrolyte interface (SEI) formation, appears in the first cycles in the range of 0.7-0.8V and then it disappears in following cycles. Moreover, on the annealed film electrode one anodic peaks at 0.52 V is obviously observed. The intensity of this peak increases after heat treatment, which might be related to the delithiation of the Li_xCu_3Sn and $Li_xCu_6Sn_5$ phases (Eqs.1-3) [29]. Fig.3b reveals that the irreversible cathodic peak (0.7-0.8V) of the Sample 1 broadens and vanishes after heat treatment in the Sample 2. This indicates that the electrolyte/the electrode interface is more stable and solvent decomposition decreases significantly in the Sample 2, resulted improvement in the cycleability of the electrode.

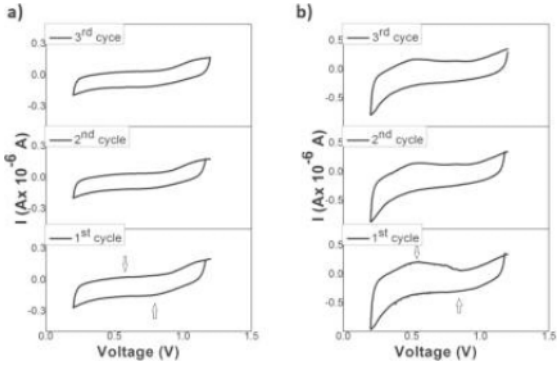

Figure 3. Cyclic voltammograms of a) Cu/Sn/Cu (Sample 1), b) the Cu/Sn/Cu with heat treatment (Sample 2) electrodes

Fig. 4 shows the cycle performance of the charge–discharge capacity and coulombic efficiency of the as-deposited Cu/Sn/Cu and the annealed Cu/Sn/Cu film anode (Sample 1 and Sample 2, respectively). For the Sample 1 without heat treatment, the initial discharge capacity is 1104 mAh g^{-1}, which is higher than the theoretical capacity of Sn electrode (994 mAh g^{-1}). We believe that this state might be related to the SEI formation on the electrode, which supports cyclic voltammograms results of as-deposited Cu/Sn/Cu (Fig.3a). This continuous formation of SEI results in capacity decline seen in Fig.4a. But the decay in the capacity reduces and stationary state regime of discharge capacity (130 mAh g^{-1}) is reached once the electrode/electrolyte interlayer becomes stable. Different than the as-deposited Cu/Sn/Cu, first discharge capacity of the annealed Cu/Sn/Cu anode is 1070 mAh g^{-1}, which might be originated from the SEI formation. Then, the capacity decreases gradually upto 15 cycles and stabilizes around 230 mAhg^{-1}. These results indicate that the cycle performance of the Cu/Sn/Cu film anode can be improved by heat treatment. It is assumed that this improvement is owing to the facts that the interaction between Cu and Sn atoms is promoted, the binding strength between active materials layer and the current collector is enhanced and the morphology of the pristine film (as-deposited) becomes more regular by heat treatment.
Herein, it is worth to note that both electrodes complete their cycle tests without failure. It might be said that the sandwich model enhances the mechanical tolerance and the reaction of the electrode with the electrolyte to control the passive film formation on the electrode surface.

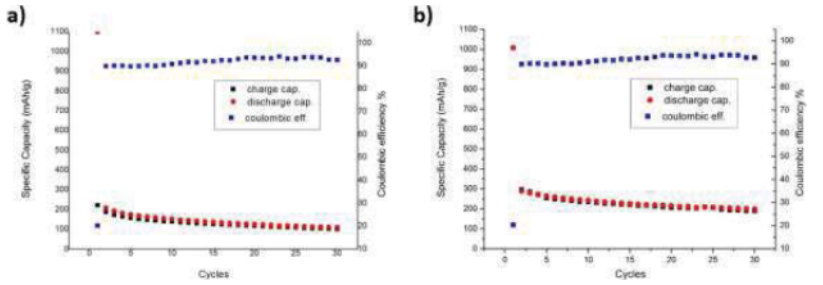

Figure 4. Cycle performance and charge-discharge efficiency of the film electrodes, a) Cu/Sn/Cu (Sample 1), b) the Cu/Sn/Cu with heat treatment (Sample 2) electrodes

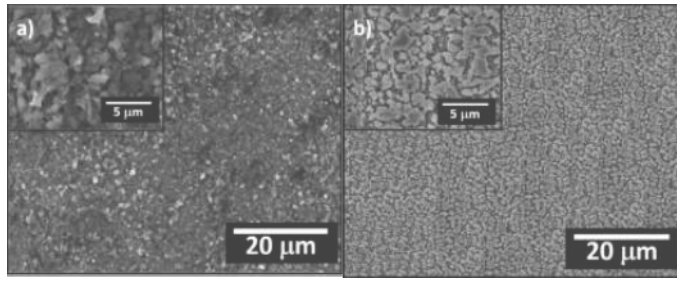

Figure 5. The SEM images of the films after 30cycles, a) Cu/Sn/Cu (Sample 1), b) the Cu/Sn/Cu with heat treatment (Sample 2) electrodes

To justify the above mentioned reaction mechanism of the electrodes, the SEM surface views of the films after 30th cycles are given in Figs. 5a and b. Both electrodes do not exhibit any delamination after 30 cycles owing to the advantages of the sandwich model. But, as it is shown in Fig. 5a, the as-deposited Cu/Sn/Cu film is appeared to be agglomerated after 30 cycles. Comparing with Fig. 1a, the agglomerates expand which resulted in non-uniform surface of the electrode. It can be found that this is the main reason of serious capacity decrease seen in Fig. 3a. The electrochemical agglomeration is also noted for Sample 2 where the particle sizes of agglomerates are found to be smaller than those of the Sample 1. However, the fact that the electrode maintains its regular morphology and porosities after 30th cycles support the fact that the electrode delivers higher capacity after 30th cycles.

Conclusion

Two sandwich structured Cu/Sn/Cu films (Samples 1 and 2) are fabricated by electrochemical deposition on Cu foils to evaluate their uses in lithium ion batteries as anode materials. The outcomes of the study might be summarized as follows:

- The advantages of using sandwich structured electrode is clearly shown since there is no delamination or peel off the coating is detected after 30th cycles.
- A heat treatment (of 48h at 200˚C) is applied on the Sample 2, to compare the effect of annealing process on the film morphology, structure and the electrochemical performances when used as anodes The results show that heat treatment promotes more homogenous morphology as it balances between the grain boundary and bulk

diffusion rates. Additionally heat treatment enhances the intermetallics formation (Cu_3Sn and Cu_6Sn_5 phase) in the film, which promotes the reversible reaction with Li.

- The galvanostatic test results reveal that the discharge capacities of the non-heat treated (Sample 1) and the heat treated (Sample 2) Cu/Sn/Cu films are found to be around 130 mAh g^{-1} and 230 mAh g^{-1}, respectively after 30th cycles. Therefore, it can be concluded that the heat treatment process remarkably improves cycle performance of the Cu/Sn/Cu film.

Acknowledgment

The authors thank Prof. Dr. Gültekin Göller, Prof. Dr. Mustafa Ürgen, Sevgin Türkeli and Hüseyin Sezer for their helps to accomplish SEM and XRD analyses.

References

1. J.O. Besenhard, ed., *Handbook of Battery Material*, (New York, NY: Wiley VCH, Inc. 1999), 450-457.
2. G. Derrien, J. Hassoun, S. Panero, B. Scrosati, "Nanostructured Sn-C Composite As An Advanced Anode Material In High-Performance Lithium-İon Batteries," *Adv Mater,* 19 (17) (2007), 2336–2340.
3. C.K. Chan, H. Peng, G. Liu, K. McIlwrath, X.F. Zhang, R.A. Huggins, Y. Cui, "High Performance Lithium Battery Anodes Using Silicon Nanowires," *Nat Nanotechnol*, 3 (1) (2008), 31–35.
4. A.N. Dey, "Electrochemical Alloying Of Lithium İn Organic Electrolytes*," J Electrochem Soc,* 118 (10) (1971), 1547–1549.
5. I.A. Courtney, J.R. Dahn, "Electrochemical And İn Situ X-Ray Diffraction Studies Of The Reaction Of Lithium With Tin Oxide Composites," *J Electrochem Soc,* 144 (1997), 2045.
6. H. Mukaibo, T. Sumi, T. Yokoshima, T. Momma and T. Osaka, "Electrodeposited Sn-Ni Alloy Film As A High Capacity Anode Material For Lithium-Ion Secondary Batteries," *Electrochem Solid-State Lett ,* 6 (2003), A218.
7. P. Wang, P. Li, T.F. Yi, X. Lin, Y.R. Zhu, L. Shao, M. Shui, N. Long, J. Shu, "Improved Lithium Storage Performance Of Lithium Sodium Titanate Anode By Titanium Site Substitution With Aluminum," *J Power Sources,* 293 (2015), 33.
8. G. Nazri and G. Pistoia, *Lithium Batteries: Science and Technology* (Boston, Springer, 2004), 704-815.
9. W.M. Zhang, J.S. Hu, Y.G. Guo, S.F. Zheng, L.S. Zhong, W.G. Song, L.J. Wan, "Tin-Nanoparticles Encapsulated in Elastic Hollow Carbon Spheres for High-Performance Anode Material in Lithium-Ion Batteries," *Adv Mater*, 20 (6) (2008), 1160.
10. H.Y. Wang, P. Gao, S.F. Lu, H.D. Liu, G. Yang, J. Pinto, X.F. Jiang, "The Effect Of Tin Content To The Morphology Of Sn/Carbon Nanofiber And The Electrochemical Performance As Anode Material For Lithium Batteries," *Electrochim Acta*, 58 (2011), 44.
11. C.D. Gu, Y.J. Mai, J.P. Zhou, Y.H. You, J.P. Tu, "Non-Aqueous Electrodeposition Of Porous Tin-Based Film As An Anode For Lithium-Ion Battery," *J Power Sources,* 214 (2012), 200.
12. F. Wang, L. Chen, C. Deng, H. Ye, X. Jiang, G. Yang, "Porous Tin Film Synthesized By Electrodeposition And The Electrochemical Performance For Lithium-Ion Batteries," *Electrochim Acta*, 149 (2014), 330–336.

13. W.M. Zhang, J.S. Hu, Y.G. Guo, S.F. Zheng, L.S. Zhong, W.G. Song, L.J. Wan, "Tin-Nanoparticles Encapsulated in Elastic Hollow Carbon Spheres for High-Performance Anode Material in Lithium-Ion Batteries," *Adv Mater*, 20 (6) (2008), 1160-1165.
14. S. Naille, M. Mouyane, M.E. Amraoui, P.E. Lippens, J.C. Jumas, J.O. Fourcade, "Lithium Insertion-Deinseterion Mechanism In $NbSn_2$ Anode Studied By 119Sn Mössbauer Spectroscopy," *Hyperfine Interact*, 187 (2008), 19–26.
15. O. Mao, R.A. Dunlap, J.R. Dahn, "Mechanically Alloyed Sn-Fe(-C) Powders as Anode Materials for Li-Ion Batteries: I. The Sn_2Fe-C System," *J Electrochem Soc*, 146 (1999), 405.
16. L.Y. Beaulieu, J.R. Dahn, "The Reaction of Lithium with Sn-Mn-C Intermetallics Prepared by Mechanical Alloying," *J Electrochem Soc,* 147 (2000), 3237.
17. M.M. Thacheray, J.T. Vaughey, C.S. Johnson, A.J. Kropf, R. Benedek, L.M.L Fransson, K. Edstrom, "Structural Considerations Of Intermetallic Electrodes For Lithium Batteries," *J Power Sources*, 113 (2003), 124-130.
18. F. Wang, M. Zhao, X. Song, "Influence Of The Preparation Conditions On The Morphology And Electrochemical Performance Of Nano-Sized Cu–Sn Alloy Anodes," *J Alloy Compd*, 439 (1) (2007), 249–253**.**
19. Y. Xia, T. Sakai, T. Fujieda, M. Wada, and H. Yoshinaga, " Flake Cu-Sn Alloys as Negative Electrode Materials for Rechargeable Lithium Batteries," *J Electrochem Soc*, 148 (5) (2001), A471-A481.
20. K.F. Chiu, K.M. Lin, H.C. Lin, W.Y. Chen, D.T. Shieh, "Structural Evolution and Electrochemical Performance of Sputter-Deposited Cu_6Sn_5 Thin-Film Anodes," *J Electrochem. Soc*, 154 (2007), A433.
21. T.S. Lin, J.G. Duh, H.S. Sheu, "The Phase Transformations And Cycling Performance Of Copper–Tin Alloy Anode Materials Synthesized By Sputtering," *J Alloys Compnd*, 509 (2011), 123.
22. A. Kitada, N. Fukuda, T. Ichii, H. Sugimura, K. Murase, "Lithiation Behavior Of Single-Phase Cu–Sn Intermetallics And Effects On Their Negative-Electrode Properties," *Electrochim Acta*, 98 (2013) 239– 243.
23. N. Tamura, R. Ohshita, M. Fujimoto, S. Fujitani, M. Kamino, I. Yonezu, "Study On The Anode Behavior Of Sn And Sn–Cu Alloy Thin-Film Electrodes," *J Power Sources*, 107 (2002), 48-50.
24. H. Etschmaier, H. Torwesten, H. Eder, and P. Hadley, "Suppression of Interdiffusion in Copper/Tin Thin Films Journal of Materials Engineering and Performance," *J. Mater. Eng. Perform,* 21 (8) (2012), 1724-1727.
25. R.Z. Hu, M.Q. Zeng, M. Zhu, "Cyclic Durable High-Capacity Sn/Cu6Sn5 Composite Thin Film Anodes For Lithium Ion Batteries Prepared By Electron-Beam Evaporation Deposition," *Electrochim Acta,* 54 (2009), 2843–2850.
26. D.G. Kim, H. Kim, H.-J. Sohn, T. Kang, "Nanosized Sn–Cu–B Alloy Anode Prepared By Chemical Reduction For Secondary Lithium Batteries," *J Power Sources***,** 104 (2) (2002), 221–225.
27. J.Y. Kwona, J.H. Ryub, Y.S. Junga, S.M. Oh, "Thermo-Electrochemical Activation Of Cu_3Sn Negative Electrode For Lithium-Ion Batteries," *J Alloys Compd,* 509 (2011), 7595–7599.
28. C.A. Steeves and N. A. Fleck, "Material Selection In Sandwich Beam Construction," *Scripta Mater,* 50 (2004), 1335.
29. D. Larcher, L.Y. Beaulieu, D.D. Macneil, J.R.Dahn, "*In Situ* X-Ray Study Of The Electrochemical Reaction of Li with η'-Cu_6Sn_5,"*J Electrochem Soc,* 147 (2000), 1658.

ROLE OF MEMBRANE PROPERTIES ON CHARGE TRANSPORT ACROSS CONJUGATED OLIGOELECTROLYTE MODIFIED PHOSPHOLIPID BILAYERS

Justin P. Jahnke[1], Guillermo C. Bazan[2], James J. Sumner[1]

[1]US Army Research Laboratory Sensors & Electron Devices Directorate, Adelphi, MD 20783 USA
[2]Department of Chemistry and Biochemistry, University of California, Santa Barbara, CA 93106 USA

Keywords: bioelectrochemistry, cyclic voltammetry

Abstract

Microorganisms have diverse metabolic pathways that enable them to convert hard to use energy sources (e.g., waste water) into useful products such as fuels, chemicals, and electrons for power generation. In many cases, bioelectrochemical systems have the potential to monitor, control, and enhance this metabolism for bio-processing, bio-reformation of fuels, and waste mitigation but slow microbe/electrode charge transfer has limited power densities and waste mitigation rates. Recent work has demonstrated that conjugated oligoelectrolyte (COE) additives enhance the microbial fuel cell power density and waste mitigation, but it remains poorly understood how additives like the COEs interact in phospholipid membranes. Here we examine how phospholipid membrane properties such as fluidity and charge alter COE incorporation and charge transport, using techniques including cyclic voltammetry and absorption spectroscopy. These properties are found to strongly influence COE behavior and can lead to large enhancements of both COE incorporation and activity.

Introduction

The broad array of chemical reactions that microorganisms can catalyze near room temperatures has made microorganism metabolism of broad interest for the production of chemicals, fuels, and electricity. Depending on the application, it would often be useful to directly couple these biological systems to electrical circuits either to monitor and guide microorganism metabolism to useful products or to use this metabolism to directly generate electrical power, as in the case of microbial fuel cells. However, coupling of electrical and microbial systems is often limited by poor electron transfer across the bio-abiotic interface between microorganisms and electrodes.[1]

Because the slow rate of electron transfer from microorganisms to electrode surfaces often limits bioelectrochemistry applications, there have been many efforts to increase the rate of electron transfer using a variety of approaches, from adding redox shuttles,[2] manipulating electrode surfaces,[3] or adding molecules that imbed in the cell membrane to facilitate the movement of electrons across it.[4] One important class of molecules that imbed in the cell membrane is that of conjugated oligoelectrolytes (COEs). As the name implies, COEs have a π-electron conjugated core (typically phenylvinylene) that can transport electrons along with ionic (typically cationic) moieties that make the molecules amphiphilic and helps them to readily

incorporate into phospholipid membranes. COEs have been used in numerous bioelectrochemical systems to enhance charge transport across the cell membrane, not only to enhance the currents produced in microbial fuel cells but also to promote bioelectrochemical synthesis of succinate from fumarate.[5] Furthermore, these molecules have been shown to not only increase the currents that can be produced by electrogenic organisms like *Shewanella oneidensis,*[6-7] but also to enable the use of nearly nonelectrogenic organisms such as yeast in bioelectrochemical systems as well.[4] Because of these applications, understanding the behavior of COEs in biological membranes is an area of ongoing research. This behavior is expected to be complicated and depend on the phospholipid membrane properties and the aggregation state of COEs in the membrane.[8]

Supported phospholipid bilayers are a model system often used to understand the behavior of more complicated biological membranes.[9-10] Here we use these bilayers to examine the behavior of a specific COE, 4,4′-bis(4′-(*N*,*N*-bis(6′′-(*N*,*N*,*N*-trimethylammonium)hexyl)amino)-styryl)stilbene tetraiodide (referred to as DSSNI or DSSN+ when discussing the COE ion). For additives with bioelectrochemistry applications (like DSSNI), electrochemical methods can be used to directly examine relevant membrane properties like charge permeability. Here cyclic voltammetry is used in combination with UV-Vis absorption spectroscopy to compare the supported bilayer's electrochemical properties with the DSSN+ membrane concentration. In addition, it is expected that phospholipid bilayer properties such as charge, alkyl chain order and alkyl chain stiffness can alter the incorporation and behavior of DSSN+ within these bilayers. These properties were manipulated using other molecules (cholesterol, choline and cholic acid) that readily incorporate within phospholipid membranes to alter these properties.[11] These additives, along with DSSN+ and the phospholipid used (1,2-dimyristoyl-sn-glycero-3-phosphocholine, DMPC) are shown in Figure 1. It was found that incorporating negative charge within the phospholipid bilayer using cholic acid had a large effect on DSSNI effectiveness in increasing bilayer charge permeability while incorporating positive charge or altering the alkyl chain dynamics did not strongly effect DSSN+'s electrochemical behavior in the supported bilayer.

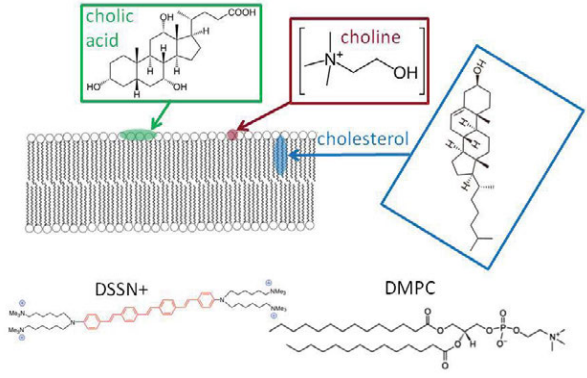

Figure 1: The structure and location within the phospholipid membrane of the three additives studied are shown at the top of the figure while the structures of the COE and phospholipid are shown at the bottom of the figure

Materials and Methods

DSSNI and the supported bilayers were synthesized following a previously reported literature procedure.[4] All chemicals used in these experiments were obtained with at least 98% purity from Sigma-Aldrich and used as received; deionized water was used in all experiments.

An aqueous 2 mM potassium ferricyanide/0.5 M potassium chloride solution was used for all cyclic voltammetry experiments. Cyclic voltammograms were collected between 0 and 0.5 V (relative Ag/AgCl) at 100 mV/s after allowing the electrodes to equilibrate for 20 minutes in the solution. A CHI 660A electrochemical work station (CH instruments) with a standard three-electrode setup was used with a glassy carbon working electrode (1 mm inner diameter), platinum wire counter electrode, and a silver/silver chloride reference electrode.

All UV-Vis absorption measurements were conducted using a DeNovix DS-11+ spectrophotometer with polystyrene cuvettes (Fisher, 4.5 mL capacity, 10 mm path length). A methanol-DMPC solution (0.1 mL, 2 mg/mL DMPC) was prepared and placed in the cuvette to dry at least overnight, with a DMPC film left at the bottom of the cuvette. After dried, 3 mL of either 2 or 10 μM DSSNI solution was placed in the cuvette. The UV-Vis absorption was measured, and from the DSSNI film concentration was determined from the absorption decrease. A control sample without a DMPC film was also measured to correct for DSSNI oxidation in solution.

Results and Discussion

Supported phospholipid bilayers were prepared using typical literature methods and cyclic voltammetry was used to characterize the electrochemical properties of these bilayers with and without DSSN+ incorporated. Potassium ferricyanide, a common, highly reversible redox species, was used to characterize the charge permeability of the phospholipid bilayer. Figure 2 shows typical cyclic voltammetry traces for a bare glassy carbon electrode, an electrode that has been blocked with a supported phospholipid bilayer, and an electrode where the phospholipid bilayer has been soaked overnight in a 1 μM DSSNI solution. Large, reversible oxidation and reduction peaks are seen when the bare electrode is used, and, as expected, the current decreases by almost 2 orders of magnitude when a supported bilayer is used to block the electrode. When the bilayer is soaked in a DSSNI solution, the current increases by approximately a factor of three; this demonstrates the ability of DSSN+ to enhance charge transport across a supported bilayer. Also, as expected, this current increase does not fully restore the redox peaks to those observed for the bare electrode, since the phospholipid membrane remains in place. Collectively, these measurements demonstrate both the effectiveness of DSSNI in increasing phospholipid bilayer charge permeability and the suitability of using supported bilayers with cyclic voltammetry to understand the behavior of DSSNI.

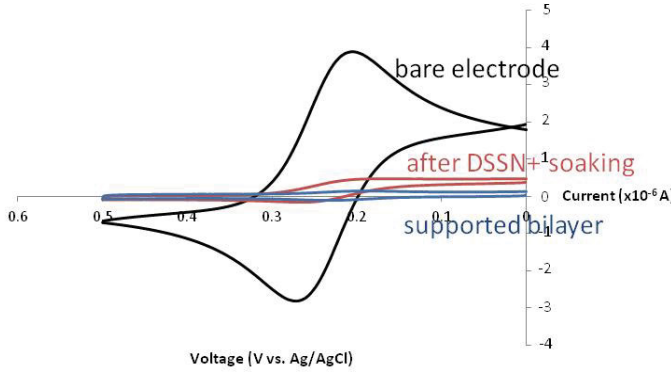

Figure 2: Typical cyclic voltammetry traces are shown for a glassy carbon working electrode before any modification (black), after it has been blocked with a phospholipid bilayer (blue), and after this bilayer-blocked electrode has been soaked overnight in a 1 μM DSSNI solution (red).

The magnitude of the current increase upon DSSN+ incorporation within a supported phospholipid bilayer is expected to depend on a number of factors including, of course, the DSSN+ concentration within the phospholipid membrane. To understand this variable, supported phospholipid bilayers were prepared where either DSSN+ was directly incorporated during casting or where the DSSN+ was introduced to the phospholipid bilayer by soaking in different concentration DSSNI solutions overnight. To quantify the effect of DSSN+, the peak currents (i_p) of the forward and reverse sweeps were averaged (because of the high reversibility of the redox reaction, these values are almost identical). Figure 3A shows the currents adding various fixed concentrations of DSSN+ into the supported bilayers while Figure 3B shows the currents for soaking in different DSSNI solutions. While the error bars are large, when DSSN+ is added directly into the bilayers, an approximately linear trend is observed with increasing DSSN+ concentrations and it clear that DSSN+ has a large effect on the peak currents at 2.5 mol%. When the DSSN+ is incorporated via soaking the bilayer in DSSNI solutions, the DSSNI solution concentration also has a strong effect. Specifically, with a 0.1 μM DSSNI solution almost no increase is observed, while as the DSSNI solution concentration is increased to 1, 10 or 100 μM, the peak currents also increases substantially. 100 μM DSSNI solution was the highest solution concentration examined because at this concentration the peak currents are roughly one third of the current for the bare electrode and mass transport limitations begin to increase the ΔV between the redox peaks. UV-Vis absorption spectroscopy was used to compare the DSSN+ membrane concentrations in the soaking experiments with the concentrations used when DSSN+ was directly incorporated within the bilayer. 1 and 10 μM solutions were characterized, with approximately 0.2 mol% DSSN+ incorporated in the phospholipid bilayer with a 1 μM DSSNI solution while 0.4 mol% DSSN+ was incorporated when a 10 μM DSSNI solution was used. These concentrations are broadly comparable to those used in those when DSSN+ was directly incorporated, and furthermore suggest that the DSSN+ membrane concentration is not a linear function of DSSNI solution concentration.

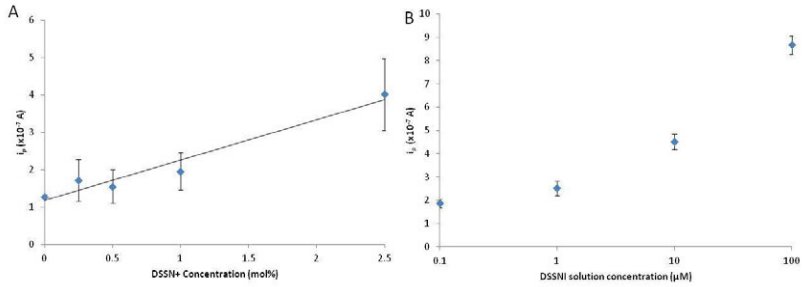

Figure 3: The average peak currents obtained when fixed quantities of DSSN+ were added to phospholipid bilayers during casting (A) and when the bilayers were soaked overnight in DSSNI solutions (B).

Cholic acid, choline and cholesterol were incorporated during bilayer casting to modify properties like charge and alkyl chain ordering and fluidity. After casting, the bilayers were soaked in 1 μM DSSNI solutions to understand how membrane properties influence the behavior of DSSN+ in phospholipid membranes. Approximately 3 mol% of the additive was used in all cases. For the charged additives (cholic acid and choline), this results in a bilayer charge in excess of the charge introduced by the DSSN+. For the cholesterol, this concentration is high enough to ensure that the cholesterol acts to promote the rigidity of the alkyl side chains. In Figure 4A, cyclic voltammetry traces are shown after soaking in a 1 μM DSSNI solution. Traces acquired prior to soaking (not shown) indicated that the cholic acid and choline increasing and decreasing the peak currents slightly, respectively, while that cholesterol had almost no effect. In all cases the effect of DSSN+ was much larger than the additive effect. Figure 4B shows the average peak currents for a no additive control and for the three additives after soaking in 1 μM DSSNI solutions. Relative to the no additive control, cholesterol and choline reduce peak currents very slightly after soaking in 1 μM DSSNI solutions while cholic acid substantially increases the peak currents. The very large effect of the cholic acid is likely due to its negative charge balancing the positive charge of the DSSN+, thereby enabling more of it to be incorporated in the phospholipid bilayer; this is consistent with the positively charged choline decreasing the DSSN+-containing bilayers' permeability. For the cholesterol, the modestly reduced peak currents may indicate that rigid alkyl side chains slightly inhibit either DSSN+'s incorporation within phospholipid bilayers or its ability to mediate charge transport across the bilayers, although further work will be necessary to fully investigate these effects. From these results it is clear that phospholipid bilayers' properties such as charge have an important effect on DSSN+'s behavior in phospholipid membranes and that judicious selection of additives can enhance the effectiveness of a DSSNI solution.

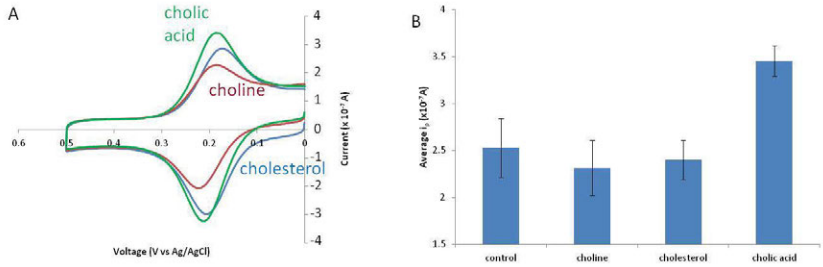

Figure 4: (A) Typical cyclic voltammetry traces for supported bilayers soaked overnight in a 1 µM DSSNI solution are shown where either cholesterol (blue), choline (red), or cholic acid (green) was incorporated at 3 mol% during bilayer casting. (B) Average peak currents for additive modified bilayers soaked in a 1 µM DSSNI solution overnight.

Conclusions

The incorporation and electrochemical behavior of a COE, DSSNI, in model supported phospholipid bilayers has been studied with cyclic voltammetry and UV-Vis absorption. DSSN+ was incorporated into the membrane either directly during casting or by soaking in a DSSNI solution. It has been shown that the DSSNI solution concentration has a strong effect on both the DSSN+ bilayer concentration and on the bilayer's charge permeability. Bilayer properties such as alkyl chain rigidity and bilayer charge were manipulated by incorporating additives. The presence of a negatively charged additive (cholic acid) resulted in larger peak currents upon soaking in DSSNI solution relative to control bilayers without any additives. In contrast, additives that introduced positive charge (choline) or enhanced alkyl chain rigidity resulted in slightly smaller peak currents than unmodified control bilayers upon soaking in DSSNI solutions. This approach of using additives to manipulate the properties of phospholipid to gain a fuller understanding of the DSSN+ interactions should be applicable to other molecules that incorporate within phospholipid membranes.

References

1. Du, J., et al., "Modification of Abiotic–Biotic Interfaces with Small Molecules and Nanomaterials for Improved Bioelectronics." *Chemistry of Materials* **2014,** *26* (1), 686-697.
2. Sund, C., et al., "Effect of electron mediators on current generation and fermentation in a microbial fuel cell." *Appl Microbiol Biotechnol* **2007,** *76* (3), 561-568.
3. Rawson, F. J., et al., "Tailoring 3D Single-Walled Carbon Nanotubes Anchored to Indium Tin Oxide for Natural Cellular Uptake and Intracellular Sensing." *Nano Letters* **2013,** *13* (1), 1-8.
4. Garner, L. E., et al., "Modification of the Optoelectronic Properties of Membranes via Insertion of Amphiphilic Phenylenevinylene Oligoelectrolytes." *Journal of the American Chemical Society* **2010,** *132* (29), 10042-10052.
5. Thomas, A. W., et al., "A lipid membrane intercalating conjugated oligoelectrolyte enables electrode driven succinate production in Shewanella." *Energy & Environmental Science* **2013,** *6* (6), 1761-1765.

6. Kirchhofer, N. D., et al., "The conjugated oligoelectrolyte DSSN+ enables exceptional coulombic efficiency via direct electron transfer for anode-respiring Shewanella oneidensis MR-1-a mechanistic study." *Physical Chemistry Chemical Physics* **2014,** *16* (38), 20436-20443.
7. Sivakumar, K., et al., "Membrane permeabilization underlies the enhancement of extracellular bioactivity in Shewanella oneidensis by a membrane-spanning conjugated oligoelectrolyte." *Appl Microbiol Biotechnol* **2014,** *98* (21), 9021-9031.
8. Hinks, J., et al., "Modeling cell membrane perturbation by molecules designed for transmembrane electron transfer." *Langmuir : the ACS journal of surfaces and colloids* **2014,** *30* (9), 2429-40.
9. Castellana, E. T.,Cremer, P. S., "Solid supported lipid bilayers: From biophysical studies to sensor design." *Surface Science Reports* **2006,** *61* (10), 429-444.
10. Shen, Y.-x., et al., "Biomimetic membranes: A review." *Journal of Membrane Science* **2014,** *454* (0), 359-381.
11. Busch, S.,Unruh, T., "The influence of additives on the nanoscopic dynamics of the phospholipid dimyristoylphosphatidylcholine." *Biochimica et biophysica acta* **2011,** *1808* (1), 199-208.

THE INVESTIGATION ON THE INTERMETALLIC LAYER OF HOT DIPPING Al-10Si ALLOY WITH 22MnB5 AND DC51 SUBSTRATE

Weidong Hu, Wende Dan, Wangjun Peng, Guangxin Wu*, Qing Du,
Jieyu Zhang
(State Key Laboratory of Advanced Special Steel, School of Materials Science and Engineering, Shanghai University, Shanghai 200072, China)
Keywords: hot-dipping Al-10Si coating, intermetallic layer, 22MnB5 steel, DC51 steel

Abstract

Hot-dipping Al-Si coating of 22MnB5 steel and DC51 steel were done in molten Al-Si bath with about 10%Si for different dipping time ranging from 3 to 300 seconds, at the temperature of 660°C, 680°C and 700°C. To study the influence of different matrix, temperature and dipping time on the intermetallic layer, the microstructure of the intermetallic layer was observed by scanning electron microscope(SEM) with energy dispersive spectroscopy(EDS). The results show that the both intermetallic layers are mainly composed of Fe_2Al_5 and $Al_9Fe_2Si_2$.τ_{10}-$Al_9Fe_4Si_3$ was found near the boundary of Fe_2Al_5 and Al-Fe-Si intermetallic layer when the dipping time up to 300s. It also shows that the growth rate of interfacial layer on the 22MnB5 substrate is bigger than the intermetallic layer on DC51 steel at the same temperature (660°C, 700°C) except 680°C in a certain time range.

Introduction

In order to reduce fuel consumption and emissions, it's a trend to reduce the weight of automobile in industry, while improving safety and crashworthiness at the same time[1]. Because of higher strength and thinner thickness than mild steel, high strength steel is widely used as lightweighting materials to replace the traditional material of mild steel[2]. However, the formability of these steels is also limited by their high strength during cold stamping. This problem can be avoided with the help of hot stamping. The hot stamping process can be described as follows: the steel is heated to 850-950°C in a furnace for austenization, and then rapidly transferred to a die where the forming and subsequent quenching take place simultaneously. Finally, the formed components achieve a full martensitic microstructure with a tensile strength greater than 1500 MPa[3, 4].

22MnB5 steel is the most common high strength steel for hot stamping which is applied widely in the production of automotive components, such as anti-collision beams, A-pillars and B-pillars[5, 6]. However, because of the high temperature and inevitable contact with the air in hot stamping process, the 22MnB5 steel is easy to be oxidized[7]. To avoid the oxidation during the austenitization, the 22MnB5 steel sheets that are used in hot stamping are commonly coated by hot dipping. Aluminum-silicon coating with about 10% Si is a kind of popular coating for steel protection in hot stamping [8, 9].

It has been reported that the properties of hot-stamping 22MnB5 steel, such as ductility and tensile strength, are influenced by the Al-Si coating [10, 11]. Therefore, the microstructure of the coating should be investigated and the DC51 steel is for comparison.

Corresponding author. Tel.: +86 021 56337920; fax.: +86 021 56337920
E-mail address: gxwu@shu.edu.cn (Guangxin Wu)

Experimental

Materials

The 22MnB5 steel with the size of 50mm×30mm×1.8mm and DC51 steel with the size of 50mm×30mm×0.6mm were prepared for hot dipping.
Al-Si master alloy as plating bath was supplied by Central China Aluminum Company. The chemical composition of Al-Si master alloy was detected by chemical analysis and ICP .The result is shown in Table I.

Table I. Chemical compositions of Al-Si master alloy(mass fraction) %

Element	Al	Si
Content	90.09	9.91

Experimental Procedure

The 22MnB5 steel and DC51 steel were sanded by sandpaper from 600 mesh to 2000 mesh. next the steels were immersed in the basic solution(80°C, 15min) containing 5% NaOH and 5% Na_2CO_3 for degreasing. Then the derusting was done in 50% HCl solution(35°C,15min). Afterwards, the steels were cleaned by hot distill water and immersed in K_2ZrF_6 (80°C, 3min) after drying. Finally, hot-dipping were done in molten Al-Si bath. The temperature of hot dipping were 660°C, 680°C, 700°C and the dipping time were 3s, 10s, 30s, 60s, 180s, 300s. The sample was subsequently cooled to room temperature by dipping into the water.
The samples were sanded and polished mechanically. Microstructural examinations of the intermetallic layers were performed by optical microscopy(OM) and scanning electron microscopy (SEM) with energy dispersive spectrometer(EDS).

Results and Discussion

Cross-sectional of the intermetallic layer

As we can see, Fig. 1-6 are the metallographs of the samples that obtained by hot dipping Al-Si .The coating mainly consists of two parts-Al-Si coating and intermetallic layer. From Fig. 1, Fig. 3 and Fig. 5, we can find that the final intermetallic layer on the 22MnB5 substrate at 660°C is the thickest. Moreover, the intermetallic layer near the Al-Si coating at this temperature is not continuous, smooth as other temperature. The same phenomenon also appears on the intermetallic layer over the DC51 steel.

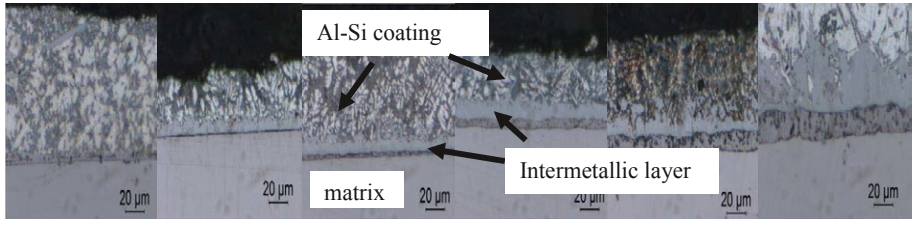

Fig. 1. OM micrograph of the intermetallic layer between the 22MnB5 steel and the Al-Si coating at 660°C

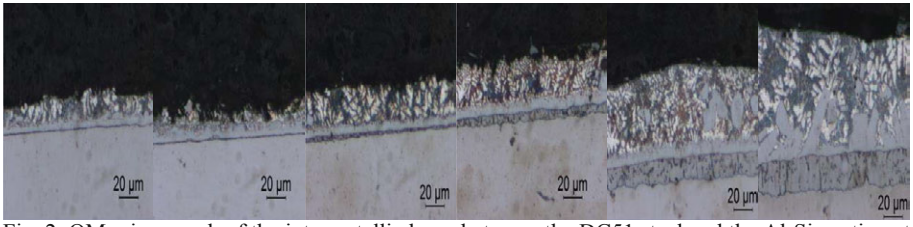

Fig. 2. OM micrograph of the intermetallic layer between the DC51 steel and the Al-Si coating at 660°C

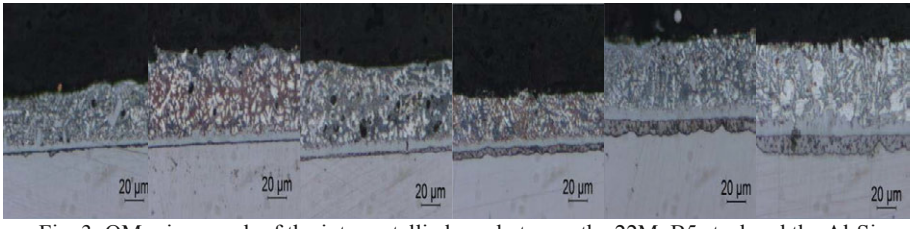

Fig. 3. OM micrograph of the intermetallic layer between the 22MnB5 steel and the Al-Si coating at 680°C

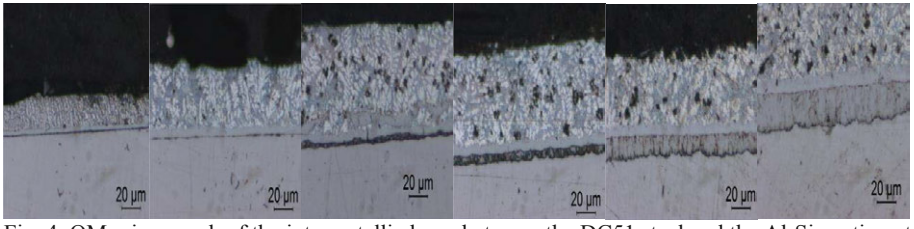

Fig. 4. OM micrograph of the intermetallic layer between the DC51 steel and the Al-Si coating at 680°C

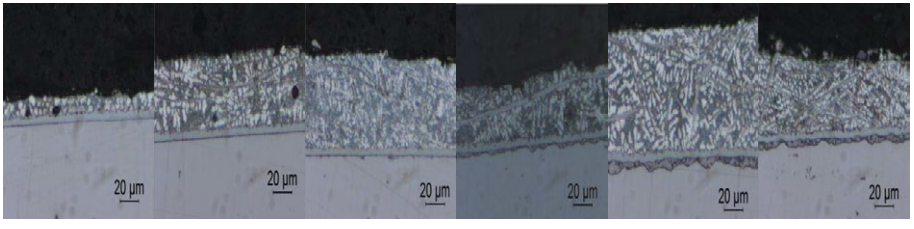

Fig. 5. OM micrograph of the intermetallic layer between the 22MnB5 steel and the Al-Si coating at 700°C

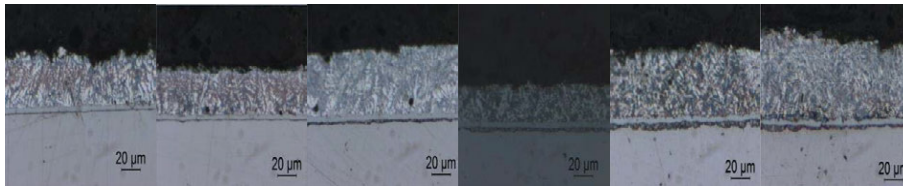

Fig. 6. OM micrograph of the intermetallic layer between the DC51 steel and the Al-Si coating at 700°C

Thickness measurement

Fig. 7 shows the relationship between the mean thickness of intermetallic layer and dipping time. We can find that the growth of the intermetallic layer at 660°C is the biggest and the smallest growth occurred at 700°C. Fig. 8a) shows the growth rate of intermetallic layer on the 22MnB5 steel at different temperature and Fig. 8b) shows the growth rate about DC51 steel. It is obvious that the growth rate of intermetallic layer on the 22MnB5 substrate is bigger at the same temperature except 680°C in this time range. Therefore, the microstructure of intermetallic layer at 680°C should be discussed in detail.

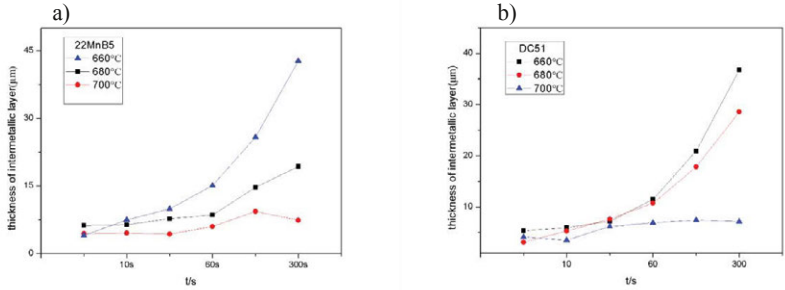

Fig. 7. thickness of the intermetallic layer on different substrate a) 22MnB5 and b) DC51 at 660°C, 680°C, 700°C for different dipping time

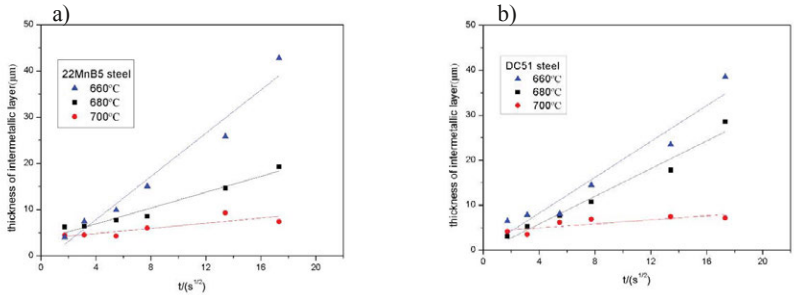

Fig. 8. the fitting curve of the connection between the thickness of intermetallic layer and the square root of dipping time a) 22MnB5, b) DC51.

Phase analysis

With the help of scanning electron microscope with energy dispersive spectroscopy, we can analysis the phase formation about the interfacial layer. As we can see from Fig. 9-10 and Table. Ⅱ, the intermetallic layer on the 22MnB5 steel consists of τ_6 - $Al_9Si_2Fe_2$ and τ_{11}-Al_5SiFe_2 at 3s, but the intermetallic layer on DC51 substrate is τ_6-$Al_9Si_2Fe_2$. Fig. 9b) shows that there is a thin $FeAl_2$ layer between the boron steel and Fe_2Al_5 layer. The diffusion of iron atoms may be restrained by $FeAl_2$ layer which results in the samller growth rate of the intermetallic layer on 22MnB5 steel at 680°C. From Fig. 9c) and Fig. 10c), we can both find that the τ_{10}-$Al_9Fe_4Si_3$ appeared near the boundary of Fe_2Al_5 and Al-Fe-Si intermetallic layer when the dipping time up to 300s.

Table Ⅱ. the types of τ phase from relevant literature [13]

τ phase	Atom percent （at.%）		
	Al	Si	Fe
τ_1/τ_9	44.5-21.5	18.5-41.5	~37
τ_2	64.8-54.4	15.2-25.6	~12
τ_3	55.5-53.5	20.5-22.5	~24
τ_4	53.5-46	30.5-38	~16
τ_5	71.25-68.75	10-12.5	~18.75
τ_6	67-65	17-19	~16
τ_7	48.2-39.7	27.8-36.3	~24
τ_8	28.1-24.6	39.5-43	~32.4
τ_{10}	57.5-58.5	17-18	~24.5
τ_{11}	64.5-66	9.5-11	~24.5

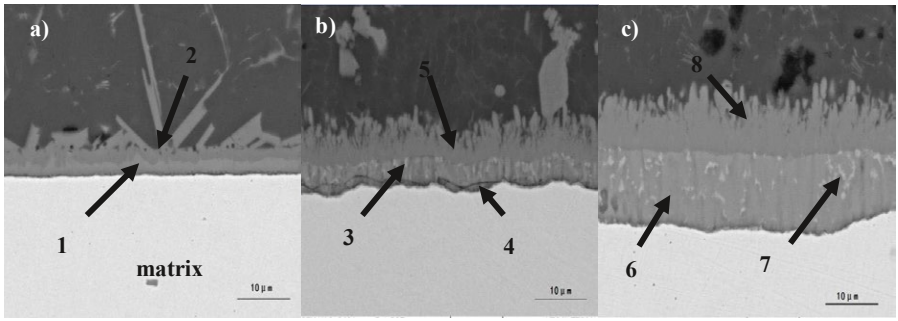

Fig. 9. SEM micrograph of the intermetallic layer between 22MnB5 steel and the Al-Si coating for different dipping times at 680°C. a) 3s, b) 60s, c) 300s.

Table Ⅲ. EDS results of the intermetallic layer on 22MnB5 steel

region	Chemical composition in at.%			intermetallic
	Al	Si	Fe	
1	61.89	12.39	25.72	Al_5SiFe_2
2	66.75	18.57	14.68	$Al_9Si_2Fe_2$
3	66.70	5.38	27.92	Fe_2Al_5
4	64.53	4.35	31.11	$FeAl_2$
5	64.08	17.29	18.63	$Al_9Si_2Fe_2$
6	68.93	3.83	27.24	Fe_2Al_5
7	55.34	17.53	27.13	$Al_9Si_3Fe_4$
8	63.36	17.07	19.57	Al_3SiFe

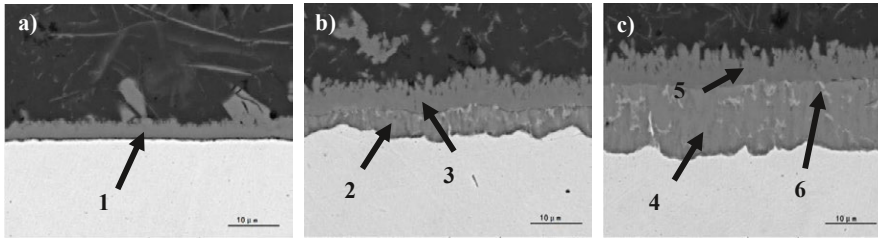

Fig. 10. SEM micrograph of the intermetallic layer between DC51 steel and the Al-Si coating for different dipping times at 680°C. a) 3s, b) 60s, c) 300s.

Table Ⅳ. EDS results of the intermetallic layer on DC51 steel

region	Chemical composition in at.%			intermetallic
	Al	Si	Fe	
1	65.90	15.80	18.30	$Al_9Si_2Fe_2$
2	69.09	3.23	27.68	Fe_2Al_5
3	64.88	16.84	18.28	$Al_9Si_2Fe_2$
4	67.23	5.57	27.20	Fe_2Al_5
5	63.88	16.45	19.67	$Al_9Si_2Fe_2$
6	53.67	16.06	30.27	$Al_9Si_3Fe_4$

Conclusions

In this work the microstructure of intermetallic layer between different substrates and Al-Si coating with about 10%Si were explored. The main results are as following:

1) With the dipping time increasing, the thickness of intermetallic layer increases simultaneously. The growth rate of the intermetallic layer on the 22MnB5 substrate is bigger than the intermetallic layer on DC51 steel at the same temperature (660°C, 700°C) except 680°C in a certain time range.

2) The intermetallic layer on the substrate mainly consists of Fe_2Al_5 and τ phase like τ_6-$Al_9Si_2Fe_2$. When the dipping time up to 300s, we can find that the τ_{10}-$Al_9Fe_4Si_3$ existed near the boundary of the Fe_2Al_5 layer and Al-Fe-Si intermetallic layer.

Acknowledgements

The authors would like to thank the support from National Natural Science Foundation of China (Grant No. 51104098) and Science and Technology Committee of Shanghai under No. 14521100603. Thanks for Analysis and Test Center of Shanghai University for the support of instrument.

References

1. Yan Zhang et al., "Lightweight design of automobile component using high strength steel based on dent resistance," Materials and Design, 27 (1) (2006), 64-68.
2. Jambor Arno, Beyer Matthias, "New cars-new materials," Materials and Design 18 (4-6) (1997), 203-209.
3. Merklein M, Lechler J, "Investigation of the thermo-mechanical properties of hot stamping steels," Journal of Materials Processing Technology, 17 (1-3) 2006, 452–455.
4. Merklein M, Lechler J, Geiger M, "Characterization of the flow properties of the quenchenable ultra high strength steel 22MnB5," CIRP Annals-Manufacturing Technology, 55 (1) (2006), 229–232.
5. Gui Z X et al., "Hot stamping and blank designing for a vehicle bumper using ultra high strength steel (UHSS)," Advanced Materials Research, 690-693 (2013), 2240-2244.
6. Long A, Ge R, Zhang Y S, et al., "Numerical simulation of b-pillar's hot press forming process and its shape optimization," Applied Mechanics and Materials, 138-189 (2012), 749-753.
7. Mori K, Ito D, "Prevention of oxidation in hot stamping of quenchable steel sheet by oxidation preventive oil," CIRP Annals-Manufacturing Technology 58 (1) (2009), 267-70.
8. Jeon Y P, H. Seo Y, Kim J D, et al., " Experimental analysis of coating layer behavior of Al-Si-coated boron steel in a hot bending process for IT applications," The International Journal of Advanced Manufacturing Technology, 67 (5) (2013), 1693-1700.
9. Azushima A, Uda K, Yanagida A, " Friction behavior of aluminum-coated 22MnB5 in hot stamping under dry and lubricated conditions, " Journal of Materials Processing Technology, 212 (5) (2012), 1014-1021.
10. Gui Z X, Liang W K, Zhang Y S, "Enhancing ductility of the Al-Si coating on hot stamping steel by controlling the Fe-Al phase transformation during austenitization," Science China Technological Sciences, 57 (9) (2014) ,1785-1793.
11. Gui Z X et al., "Thermo-mechanical behavior of the Al–Si alloy coated hot stamping boron steel ," Materials and Design, 60 (2014), 26-33.
12. V. Raghavan, "Al-Fe-Si (Aluminum-Iron-Silicon)," Journal of Phase Equilibria and Diffusion , 30 (2) (2009), 184-188.

THE WETTING BEHAVIOR OF Fe-Si AND Fe-Mn ALLOY WITH Al-10%Si COATING

Wende Dan, Guangxin Wu*, Bo Zhang, Qing Du, Wangjun Peng, Weidong Hu, Jieyu Zhang
State Key Laboratory of Advanced Special Steel, School of Materials Science and Engineering, Shanghai University, Shanghai 200072, China
Keywords: wetting; Al-10%Si; sessile drop method; phase composition.

Abstract

High-strength steel possesses excellent strength, toughness, wear resistance and weld-ability, and therefore, are widely used in various fields. Because the high strength steel contains highly content of Mn and Si, they always lead to quality problem for the process of hot-dip aluminum coating. In this work, we applied improved sessile drop method, selected some characteristic systems to measure the change in contact angle and diameter of Al-10%Si droplets wetting on a quality of Mn (0wt%, 0.5 wt%, 1.5wt%, 2.5wt%) and Si (0wt%, 0.5 wt%, 1.5wt% 2.5wt%). Then the microstructure and composition of interfacial layer are analyzed by SEM/EDS, the phase composition is analyzed by XRD. The results showed that the contact angle is increasing with the contents of Si increasing. However, the contact angle is decreasing with the contents of Mn increasing.

Introduction

High-strength steel possesses excellent strength and toughness, wear resistance, weldability and corrosion resistance. Therefore, it is widely used in various fields. Due to being sensitive to corrosion, the service life of steel will be shorten. Through the exploration for a long time, scientists believe that protective coating is able to effectively improve the corrosion resistance of steel. There has been a lot of fundamental research on the wettability of liquid Zn on the surfaces of steel sheets or films [1], It is well known that low alloy high strength steel adds a small amount of alloy elements (mainly silicon, manganese, magnesium) on the basis of carbon structural steel. Alloy elements have a bad influence on appearance quality and performance, such as coating thickness, plating, dark and poor adhesion [2]. There are few reports on Fe-Mn and Fe-Si steel plate in hot dip Al-10%Si alloy, therefore, it is necessary to explore the wetting behavior in hot dip plating process.

Generally, the sessile drop method has been widely used as a general observation and evaluation method for wetting [3]. The equilibrium contact angle of a liquid droplet on solid substrate, if no reaction takes place, is determined from the balance of the surface tension of a liquid droplet with that of a solid substrate and the interfacial tension of the solid-liquid interface. It is possible to quantitatively evaluate the wettability from the work of adhesion [4] which may be obtained from the contact angle. A few reports have addressed the change in contact angle of a liquid droplet on a steel substrate by the sessile drop method [5].

In the present paper, we have tried to quantitatively evaluate the dynamic wetting behavior of

* Corresponding author. Tel.: +86 021 56337920; fax.: +86 021 56337920
E-mail address: gxwu@shu.edu.cn (Guangxin Wu)

liquid on steel substrates by using a high speed camera to take images which the change in droplet shape and contact angle of liquid Al-10%Si on the steel substrate. Then, we defined the following two quantitative properties: one of them is a spreading velocity of liquid Al-10%Si droplet on the steel substrate which is determined from the change in the diameter of a droplet caused by spread-wetting as well as by alloying reactions. The other is the microstructure and composition of interfacial layer analyzed by SEM/EDS. The phase composition is analyzed by XRD.

Experimental

In this experiment, the temperature was 1600 ^{o}C in the vacuum induction furnace, the raw materials were pure manganese (99.8%), pure iron (99.99%) and silicon (99.9%). According to the industrial production and relative literature to design the low alloy high strength steel，the contain of Mn and Si was shown in Table I. An oxide layer forms the surface of the melted specimen, then the metal substrate was polished on the surface by sandpaper. After the metal substrate was polished in acetone cleaning for three times, and then put in high temperature vacuum wetting experiment furnace, and used level ball to flat. A schematic diagram of the experimental apparatus for performing the wetting observations was shown in Fig. 1. With the vacuum under 5.0×10^{-4}Pa, vacuum furnace heated to experiment temperature. The heating process was shown in Fig. 2. After keeping the specimen for 60 min at 650^{o}C, an Al-10%Si droplet was then dropped on the substrate. The temperature (650 ^{o}C) and the vacuum were selected to prevent the formation of oxides on the surface of the substrate and on the liquid Al-10%Si. Finally, a high speed camera was used to observe the spreading behavior of a liquid droplet, and then the wetting angle was calculated after the droplet attached on a solid steel substrate.

Table I. the content of Fe-Mn and Fe-Si alloy

Fe-Mn	0wt%	0.5 wt%	1.5 wt%	2.5 wt%
Fe-Si	0wt%	0.5 wt%	1.5 wt%	2.5 wt%

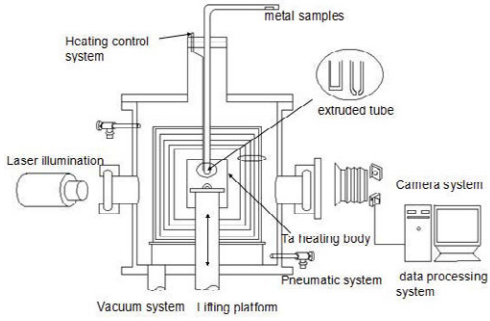

Fig. 1 Schematic diagram of experimental setup of sessile drop method

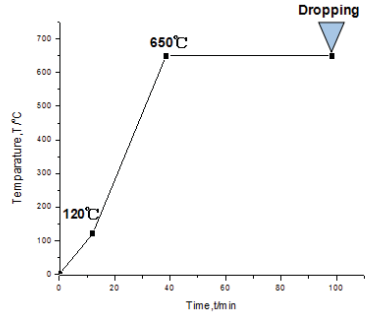

Fig.2 Temperature profile of the experiment

Experimental Results and Discussion

Evaluation of Contact Angle

Fig. 3 represents three examples of the spreading behavior of a liquid Al-10%Si droplet on a steel substrate (Fe, Fe-2.5wt%Si and Fe-2.5wt%Si) under a vacuum environment. The contact angle of the droplet changes periodically due to vibration just after dropping but this effect decreases gradually with time elapsed. As the spreading proceeds with time, the spreading radius r increases and the contact angle decreases with accompanying alloying reaction.

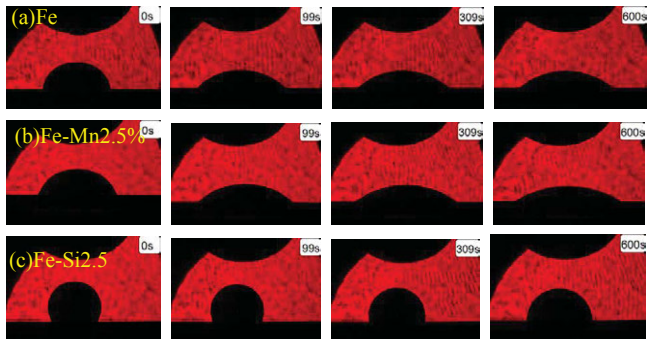

Fig. 3 (a) Change in droplet shape of liquid Al-10%Si on Fe substrate; (b) Change in droplet shape of liquid Al-10%Si on Fe-Mn2.5% substrate; (c) Change in droplet shape of liquid Al-10%Si on Fe-Si2.5% substrate.

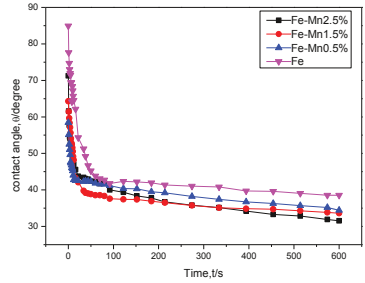

Fig. 4 shows the change in the contact angle of the liquid Al-10%Si droplet on Fe-Mn substrate with time

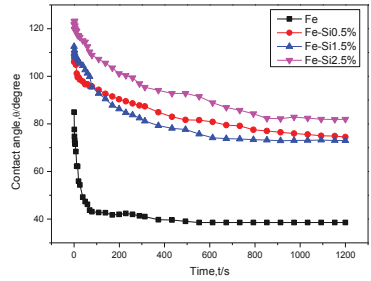

Fig. 5 shows the change in the contact angle of the liquid Al-10%Si droplet on Fe-Si substrate with time

Fig. 4 and 5 show that with increase of Mn content, wetting angle decreases. However, with the increase of Si content, wetting angle increases. Finally, Fe-Si wetting angle is about twice as pure Fe. So Si inhibits wettability. Fe-Mn wetting angle is less than pure Fe substrate. So increasing the content of Mn can improve the wettability.

Work of adhesion

Table Ⅱ shows the values of initial contact angles $\theta_{initial}$ of liquid Al-10%Si on different substrate.

Substrates	Fe	Fe-Si2.5%	Fe-Mn2.5%
$\theta_{initial}$/degree	84.93	121.832	71.274

As shown in this table, the contact angle for Fe-Mn steel is smaller than Fe-Si steel sheet, which means that the wettability for Fe-Mn steel is better than Fe-Si steel. From the contact angle measurements, it is possible to evaluate the work of adhesion W_a from Young's equation in Eq. (1) and the definition of the work of adhesion in Eq. (2). In other words, when

we substitute σ_s in Eq.(1) into the first term on the right-hand side of Eq. (2), the work of adhesion W_a can be expressed by the surface tension of liquid σ_1 and the contact angle θ as shown in Eq.(3).

$$\sigma_s = \sigma_i + \sigma_1 \cdot \cos\theta \tag{1}$$

$$W_a = \sigma_s + \sigma_1 - \sigma_i \tag{2}$$

$$W_a = \sigma_1 \cdot (1 + \cos\theta) \tag{3}$$

Here, σ_s mean surface tension of solid, σ_1 mean surface tension of liquid, σ_i: interfacial tension between solid and liquid, θ: contact angle [6]. When we insert the values for the surface tension of liquid Al-10%Si [7, 8] and the experimental results of $\theta_{initial}$ into σ_1 and θ respectively, the work of adhesion W_a was obtained. The results are shown in Table Ⅲ. The larger value of the work of adhesion W_a means the liquid Al-10%Si has a better wettability on Fe-Mn2.5% steel sheets.

Table Ⅲ Work of adhesion of liquid Al-10%Si to different substrates

Substrates	Fe	Fe-Si2.5%	Fe-Mn2.5%
W_a/mNm^{-1}	755.14	327.84	916.50

Evaluation of Spreading Velocity

Since the radius of the droplet depends on the amount of liquid, we defined a relative spreading radius $R=r/r_{sph}$ [6].Here, r is the radius of the droplet for each experiment; r_{sph} is the radius of a hypothetical sphere, of which the volume is determined from the mass of a droplet and the density of liquid Al-10%Si at 650℃.The change in $R=r/r_{sph}$ with time is shown in Fig. 6 and Fig. 7.

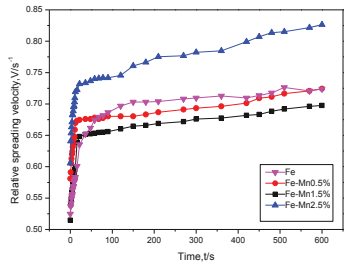

Fig. 6 Change in relative spreading radius of liquid Al-10%Si on a series of Mn-containing steels with time

In the first 15 seconds, relative spreading speed increase rapidly, and then spreading speed smoothly. Mn content is below 1.5%, relative spreading speed change not obvious; spreading rate significantly increased in Fe-2.5%Mn.

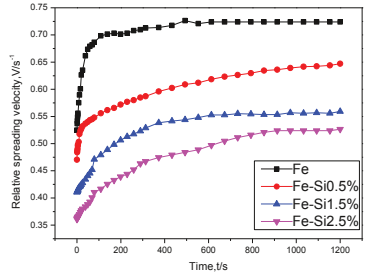

Fig. 7 Change in relative spreading radius of liquid Al-10%Si on a series of Si-containing steels with time

In the first 15 seconds, relative spreading speed increase rapidly, and then spreading speed smoothly. With the increase of Si content, relative spreading speed drops rapidly. Reason for this is that when the silicon content is low, $FeAl_3$ phase can be stable. With the increase of Si content, unstable a-AlFeSi phase was generated. a-AlFeSi is body centered cubic (BCC). $FeAl_3$ is monoclinic crystal structure. Body centered cubic has strong adhesion compared to monoclinic crystal structure. Body centered cubic (BCC) crystals dissolving diffusion speed is low. So with the increase of Si content, relative spreading speed reduced.

Microstructure

Samples of droplet and substrate center are cut by wire cutting, and its surface is polished, then the microstructure and composition of interfacial layer are analyzed by SEM/EDS in Fig.8.The interface reaction layer did XRD step by step by polishing flat, the phase composition is analyzed by XRD.

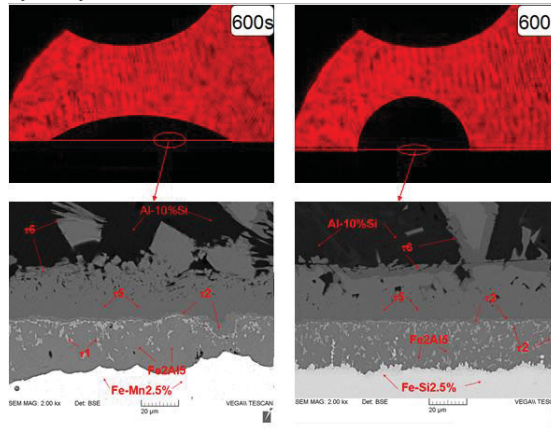

(a) Fe-Mn2.5% (b) Fe-Si2.5%

Fig. 8 (a) and (b) evolution of the morphology of the triple line and interface reaction layer microstructure with EDS after wetting at 650℃ for 600s.

According to the test results，Fe-Mn2.5% and Fe-Si2.5% have the same phase in Fig. 8 by SEM and EDS analysis, respectively, Fe2Al5/τ1/τ2/τ5/τ6.

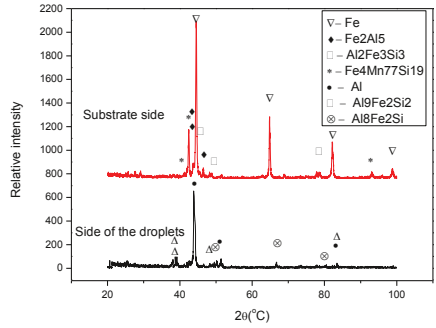

Fig. 9 XRD analysis of Fe-Mn2.5% at the different positions of the reaction layer

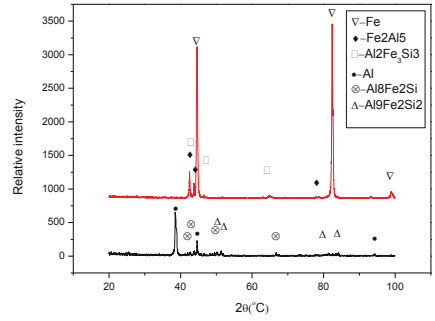

Fig. 10 XRD analysis of Fe-Si2.5% at the different positions of the reaction layer

Combined with XRD and EDS analysis, the consistent results can be obtained. The existing detection methods are difficult to detect owing to the low Mn content .

Conclusions

The effects of Si and Mn contents on the wettability of liquid Al-10%Si in steel sheets were evaluated from the observation of the dynamic wetting behavior by the sessile drop method proposed in this work. These conclusions can be founded as follows:

(1) Using the current experimental conditions, the wettability of liquid Al-10%Si with the steel substrates becomes worse as the Si content increases. However，increasing the content of Mn can improve the wettability. The wettability can be evaluated by using the work of

adhesion obtained from initial contact angles. Adhesion work of liquid Al-10%Si to Fe-2.5% Mn substrates is 2.8 times larger than liquid Al-10%Si to Fe-2.5%Si substrates. The wettability was evaluated by measuring the relative spreading velocity against small contact angles at the final stage of spreading. With the increasing Si content, the wettability with alloying reactions becomes worse.

(2) The microstructure and composition of interfacial layer were analyzed by SEM/EDS. The phase composition was analyzed by XRD. According to the current experimental conditions, they had the same phase composition, respectively, $Fe_2Al_5/\tau_1/\tau_2/\tau_5/\tau_6$.

Acknowledgement

The author Wu would like to thank the support from National Natural Science Foundation of China (Grant No. 51104098) and Science and Technology Committee of Shanghai under No. 14521100603. Thanks for Analysis and Test Center of Shanghai University for the support of instrument.

References

1. J. Lee, K. et al., "On Zinc and Zinc Alloy Coated Sheet Steels," Iron & Steel Technology, 32(2004), 987.
2. Mahieu J, Claessens S, De Cooman B C, "Galvanizability of high-strength steels for automotive applications," Metallurgical and Materials Transactions A, 32 (11) (2001), 2905-2908.
3. A.I. Rusanov and V. A. Prokhorov, *Interfacial Tensiomentry*(New York, NY: Elsevier,1996), 84.
4. A.W. Adamson: *Physical Chemistry of Surfaces*(New York, NY: John Wiley & Sons, 1982) , 424.
5. S. Shimada, Y. Takada, J.-H. Lee and T. Tanaka: *Tetsu-to-Hagané*, 93(2007), 145.
6. Shunsuke SHIMADA et al., "Trial to Evaluate Wettability of Liquid Zn with Steel Sheets Containing Si and Mn," ISIJ International, 48 (2008), 1246-1250.
7. Zhinghong Jia et al., "Process Factors on the Influence of Al-Si Alloy Melt Viscosity," Journal of Materials Science & Engineering, 31 (2013), 1673-2812.
8. Xiying Teng, GH Ming and HL Liu, "The viscosity of liquid pure iron 1550℃ and the correlation between surface tension and structure," Materials Science & Technology, 9 (2001), 1005-1010.

TMS2016

145th Annual Meeting & Exhibition

SUPPLEMENTAL
PROCEEDINGS

Refractory Metals 2016

IMPROVING THE PERFORMANCE OF Nb-SILICIDE BASED REFRACTORY ALLOYS THROUGH A NOVEL COLD CRUCIBLE DIRECTIONAL SOLIDIFICATION

Hongsheng Ding[1], Kun He[1], Shiqiu Liu[1], Yongwang Kang[2], Jingjie Guo[1]

[1]National Key Laboratory for Precision Hot Processing of Metals, Harbin Institute of Technology; 92 West Dazhi Str.; Harbin, Heilongjiang 150001, China
[2]Science and Technology on Advanced High Temperature Structural Materials Laboratory, Beijing Institute of Aeronautical Materials; Beijing, 100095, China

Keywords: Nb-Silicide, Directional Solidification, Cold Crucible, Mechanical Performance.

Abstract

Nb-silicide alloy with composition of Nb-22Ti-16Si-3Cr-3Al-2Hf (at.%) was directionally solidified into square ingots at different processing parameters through a novel cold crucible directional solidification technology. The effect of directionally solidified processing parameters, such as heat power and withdrawal rate, on the microstructure and mechanical properties was analyzed. Results show that the directional structure composed of coupled growth of $(Nb,Ti)_{ss}/(Nb,Ti)_5Si_3$ composite can exhibit good tension performance at 1250℃.

Introduction

With the rapid development of high thrust-to-weight ratio aero-engines, the working temperature of turbine blade had exceeded more than 1800℃ presently. The working demand on engine material becomes higher and higher. However, the working temperature of conventional Ni-based superalloy can only attain 1150℃ which is close to the use limit. Therefore it is necessary to develop new high-temperature structural material system to replace Ni-based superalloy as much [1, 2]. Nowadays, Nb-Si based alloy has been becoming a greatly potential ultra-high temperature structural material, because of its relatively low density (6.6~7.2g/cm^3), high melting point (over 1800℃), high stiffness, high creep resistance and good high temperature strength. The equilibrium phase constituents are Nb_{ss} solid solution phase and Nb_5Si_3 intermetallic compound. Nb_{ss}/Nb_5Si_3 has good interfacial compatibility and thermodynamic stability, and also the composite fabricated by combination of tough Nb_{ss} solid solution phase and brittle Nb_5Si_3 intermetallic phase exhibits excellent mechanical properties [3].

Owing to the intrinsic brittleness, the fracture toughness of Nb_5Si_3 intermetallic compound at room temperature is only of 3.0 MPa•m$^{1/2}$ [4], which results in the poor fracture toughness of Nb-Si alloys. The fracture toughness of arc-melting Nb-16Si binary alloy is 5.4 MPa•m$^{1/2}$, and it's only of 7.35 MPa•m$^{1/2}$ even after 1500℃×100h vacuum heat treatment [5, 6]. Moreover, the strength of Nb-Si alloy at high temperature is also insufficient. In order to improve the mismatch of mechanical properties of Nb-Si alloy at high and low temperatures, researchers mainly study through the following two aspects: alloying and preparation process [7]. The addition of alloying elements is able to result in lattice distortion, changes in electron concentration, forming vacancy, dislocation configuration changes and so on. All these changes will do benefit to the properties

improvement and the main alloying elements include Cr, Hf, Sn, B, Zr, Mo, V, Ti, Al, Ta [8, 9]. So far, with respect to the exploration of the preparation technologies, there are a lot of reports about vacuum consumable/non-consumable arc melting [10,11], powder metallurgy [12], hot isostatic pressing(HIP), physical vapor deposition [13], directional solidification [14,15] and sintering-forging et al. Thereinto, directional solidification technology can obtain columnar crystal growing along the direction opposite to the heating flow, which eliminates the lateral boundaries and improve the uniaxial mechanical properties of materials.

In this paper, Ti element and a small amount of Cr, Al, Hf elements were added to Nb-Si alloy. Ti atoms can replace Nb atoms in Nb-Si based alloys, which improves the room temperature toughness [16] and forms Nb-Ti-Si based alloy. Cr and Al elements improve oxidation resistance [17, 18] and Hf element improves high temperature property [19]. Nb-Ti-Si based ultra-high temperature alloys at different withdrawal rates were prepared by cold crucible directional solidification technology and the effect of withdrawal rate on its microstructure, room temperature fracture toughness and high temperature tensile property was investigated subsequently.

Experimental

The master ingot of Nb-Ti-Si based alloy with the nominal composition of Nb-22Ti-16Si-3Cr-3Al-2Hf（at.%）was prepared by vacuum induction melting. The purity (mass fraction) of alloying elements of Ti, Si, Nb, Cr, Al and Hf was 99.8%, 99.5%, 99.5%, 99.8%, 99.9% and 99.8% respectively. Both the master rods whose length was 170mm and diameter was 22 mm，and the starting materials used for directional solidification were cut from the master ingot by wire electrode discharge machining(WEDM). After the surface oxide skin and impurities of them were scratched out, they were followed by ultrasonic cleaning in which the solution was gasoline and then ethanol. Directional solidification experiments were performed in electromagnetic cold crucible directionally solidification equipment at a power of 60kW and the withdrawal rates of 0.4, 1.0 and 1.4 mm/min, respectively (DS1, DS2, DS3 were used respectively to number the specimens in the text). The details of directional solidification experiment can be found in our previous work [20]. The phase analysis of the directional microstructure was performed by D/max X-ray diffractometer (XRD) with Co-Kα radiation. The room-temperature fracture toughness were tested using single edge notched bending (SENB) specimens with the dimension of 22 mm in length, 4 mm in width and 2 mm in thickness by Instron5569 electronic universal testing machine. The length direction of the SENB specimens was parallel to the solidification direction and we tested three specimens for each directional bar. The initial notch with 3 mm in depth on the SENB specimens was cut by WEDM using a Mo wire 0.18 mm in diameter according to the description in the ASTM standard. The span was 16mm and the rate was 0.05mm/min. The room temperature compression experiments were also performed by Instron5569 electronic universal testing machine. We took three compression specimens which were $\phi 4 \times 6$mm columns from each directional sample. The column axis was in consistence with the growth direction and the compression rate was 0.5mm/min. The high temperature tensile tests were performed in vacuum at the temperature of 1250℃, with a loading speed of 0.595 mm/min and a heating rate of 40℃/min, and the loading direction was parallel to the growth direction. The length of tensile specimen was 45mm. The directionally solidified specimens, three-point bend specimens and fracture were analyzed by field emission scanning

electron microscope Quanta 200FEG, and element content analysis was analyzed in spectrum analyzer (EDS).

Results and Discussion

The phase composition and microstructure. Fig. 1 gives the XRD patterns of directionally solidified Nb-Ti-Si based alloy at three different withdrawal rates. It showed that the directionally solidified microstructures are all composed of $(Nb,Ti)_{ss}$ phase, α-$(Nb,Ti)_5Si_3$ phase and γ-$(Nb,Ti)_5Si_3$ phase. The relative intensity of γ-$(Nb,Ti)_5Si_3$ phase diffraction peaks are very weak, but that of $(Nb,Ti)_{ss}$ phase and α-$(Nb,Ti)_5Si_3$ phase are high. This indicates that directional structure contains only a small amount of γ-$(Nb,Ti)_5Si_3$ phase and most of the rest are $(Nb,Ti)_{ss}$ phase and α-$(Nb,Ti)_5Si_3$ phase, which is in accordance with the following structure figures.

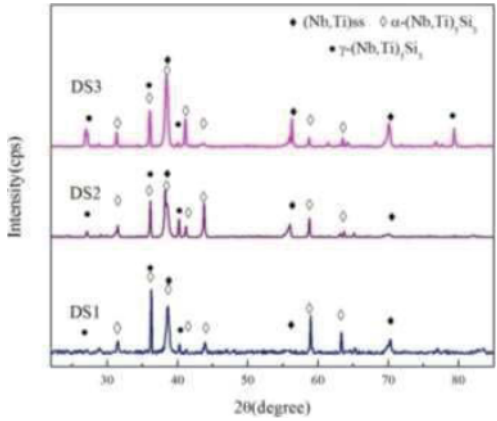

Fig. 1 XRD patterns of directionally solidified Nb-Silicide based alloy at three different withdrawal rates

The longitudinal section and cross section microstructures of the directionally solidified samples at three rates are shown in Fig. 2. EDS analysis shows that the off white phase, dark gray phase, the black phase, fine white precipitated phase and black dot precipitated phase are $(Nb,Ti)_{ss}$ solid solution, α-$(Nb,Ti)_5Si_3$, γ-$(Nb,Ti)_5Si_3$, Hf oxide and Si-rich phase respectively. It can be seen that from the longitudinal section, phases of $(Nb,Ti)_{ss}$ and $(Nb,Ti)_5Si_3$ are aligned alternatively parallel to the growth direction, which is called coupling-like eutectic growth microstructure. And the transverse section is composed of roughly cellular or polygonal $(Nb,Ti)_{ss}$+$(Nb,Ti)_5Si_3$ eutectic cells and intercellular eutectics, including part of primary $(Nb,Ti)_5Si_3$ phase. The primary $(Nb,Ti)_5Si_3$ phase presents robs along the growth direction in vertical and has a straight boundary. The cross-section is shown as straight quadrilateral with $(Nb,Ti)_{ss}$ at the centre. Both in longitudinal and transverse section microstructure, fine $(Nb,Ti)_{ss}$+$(Nb,Ti)_5Si_3$ eutectic is found. The eutectic structure show three types, cellular dendrites, mesh-like and lamellae. The eutectic cells are petal-like. The center in the cells are mostly $(Nb,Ti)_{ss}$+α-$(Nb,Ti)_5Si_3$ eutectic, but intercellular structure are mainly $(Nb,Ti)_{ss}$+γ-$(Nb,Ti)_5Si_3$ eutectic lamellae. γ-$(Nb,Ti)_5Si_3$ belongs

to a Ti-rich $(Nb,Ti)_5Si_3$ phase, in which the solubility of Cr, Al and Hf elements is higher than that of α-$(Nb,Ti)_5Si_3$. γ-$(Nb,Ti)_5Si_3$ is a metastable phase at room temperature and its stability is weaker than that of α-$(Nb,Ti)_5Si_3$. It shows as follows that how the γ-$(Nb,Ti)_5Si_3$ phase is formed. Actually, during the solidification process, other than Nb, Cr and Hf, Ti is an element with relative low-melting-point, it will be frozen afterwards and remained in front of the solid-liquid interface. At this very moment, if the growth rate is fast enough, Ti element is not available to diffuse into the liquid thoroughly, then left and piled up before the solidification front. The accumulation of Ti will finally become into segregation in the inter-dendrites. When the constituent of Ti segregation reaches a certain value, it will form Ti-rich $(Nb,Ti)_5Si_3$ phase, namely γ-$(Nb,Ti)_5Si_3$ phase.

Fig. 2(a), (c) and (e) indicate that with increasing of the withdrawal rate, the continuity of crystal growth decreases, and continuous matrix becomes into discontinuous $(Nb,Ti)_{ss}$ particles. It means the particles are refined. Because $(Nb,Ti)_5Si_3$ phase grows much faster than that of $(Nb,Ti)_{ss}$ phase, the channels between $(Nb,Ti)_{ss}$ phase and liquid phase are closed, leading to the $(Nb,Ti)_{ss}$ particles. As known as we can see the faster the withdrawal rate, the more obvious the discontinuity of $(Nb,Ti)_{ss}$ particles. Rapid withdrawal speed means short solidifying time. The particles have to solidify before they are growing up, so there is little time for particles growing and the size becomes smaller [21]. Besides, with the speeding up of solidification rate, phase spacing between $(Nb,Ti)_{ss}$ and $(Nb,Ti)_5Si_3$ decreases gradually. It can be clearly seen from Fig. 3(b), (d) and (f) that the average diameter of eutectic cells also decreases with increasing the solidification rate.

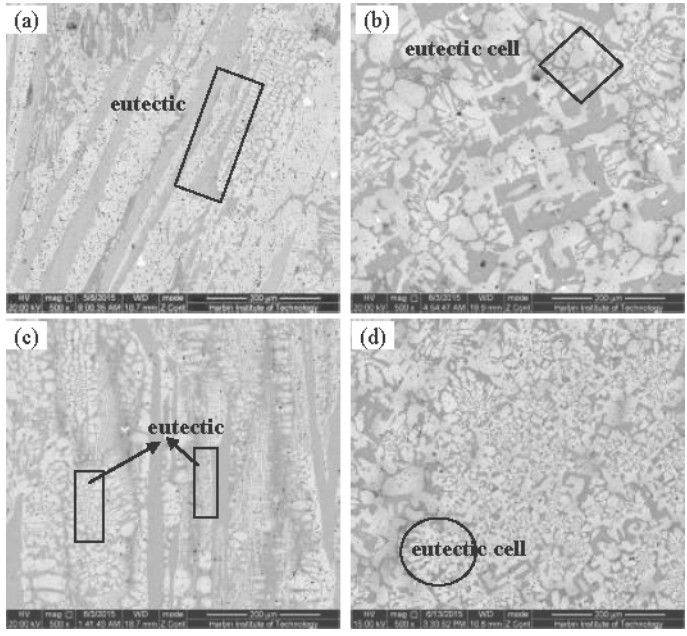

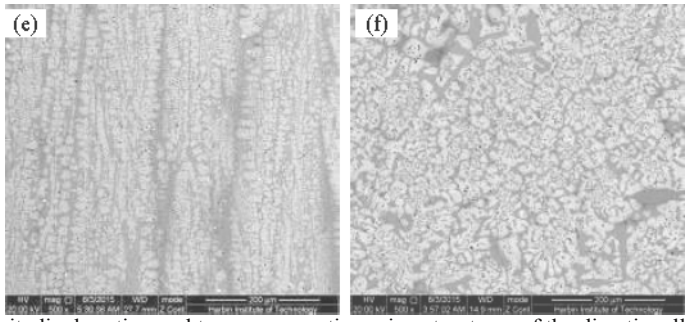

Fig. 2 Longitudinal section and transverse section microstructures of the directionally solidified samples at different three rates
(a), (c), (e) is DS1, DS2, DS3 longitudinal section structures respectively
(b), (d), (f) is DS1, DS2, DS3 transverse section structures respectively

Table 1 illustrates the phase spacing and average diameter of eutectic cells for the three samples at different withdrawal rate. Normally, phase spacing and the size of eutectic cells are dependent on atomic diffusion abilities. When the withdrawal rate increases, the solidification rate will accelerate as well, however the melt temperature decreases, which results in the vibration frequency of atoms reducing and the movement rate slowing down. The atomic diffusion ability will be weaker because of the temperature decreasing and the cooling rate speeding up. The available diffusion distance is shortened per unit time by lowering the solidification temperature, therefore high withdrawal rate usually leads to small eutectic cells as well as phase spacing. The withdrawal rate enhancement will do help to microstructure refinement.

Table 1 Phase spacing and average diameter of eutectic cells for the three samples at different withdrawal rates

Number	Phase spacing (μm)	Average diameter of eutectic cells (μm)
DS1	43.2	122.72
DS2	24.8	101.24
DS3	15.4	66.40

Mechanical properties. The average values of the room temperature compressive strength and fracture toughness, high temperature tensile strength(1250℃) are given in Table 2. With the withdrawal rate increasing, the maximum compressive strength slightly reduced after the first increase, which may be related to the content decrease of primary $(Nb,Ti)_5Si_3$ phase in DS3. $(Nb,Ti)_5Si_3$ is a strengthening phase and its content decrease will cause the strength reduction. Overall it is associated with the degree of microstructure refinement and accords with the theory of Hall-Patch formula. The fracture toughness enhancement with the withdrawal rate increase can be explained by that the phase spacing reduction and the size of $(Nb,Ti)_{ss}$ particles decrease. This brings about the enhancement of the plastic deformation ability, leading to the blunting of crack tip when the crack propagates. The crack propagation is hindered so the fracture toughness is improved. The high-temperature tensile strength of 1250℃ decreases first then increases with

a small range change and the maximum is over about 150MPa. In comparison, the as-cast alloy is in 98.15MPa of tensile strength.

Fig. 3 shows the three crack propagation paths for fracture toughness specimens by directional solidification at different withdrawal rates. After starting from the incision the crack will propagate in zigzag forward. There is an angle between the propagation direction and loading direction. The zigzag path means the crack goes a longer distance and absorbs more energy, which can improve the fracture toughness.

Table 2 The average values of the room temperature compressive strength and fracture toughness, high temperature tensile strength(1250℃)

Number	Room temperature compressive strength (MPa)	Room temperature fracture toughness ($MPa \cdot m^{1/2}$)	High temperature tensile strength (MPa)
DS1	1890.57	11.12	145.20
DS2	2186.22	11.86	134.60
DS3	2142.29	13.21	150.65

When the crack reaches the phase interface, due to the different structure and orientation at both sides, it has to adjust the slipping direction to cross the interface. Cracks deflect to absorb more energy but bridging usually occurs when cracks encounter the plastic phase. The bridging and branching in $(Nb,Ti)_{ss}$ enlarge the resistance to expansion. So the crack for directionally solidified specimens propagates more difficultly than that of the cast specimens, showing a more tortuous extending path. This improves the fracture toughness at room temperature [22].

The faster the solidification rate, the smaller the microstructure and phase spacing. The crack produces in the incision and continues to cross the interfaces between $(Nb,Ti)_{ss}$ phase and $(Nb,Ti)_5Si_3$ phase when forging ahead. This enhances the propagation resistance. In addition, the finer the microstructure, the more interfaces cracks crossing and the higher resistance for expanding. Above is the reasons that fracture toughness increases with the solidification rate rising.

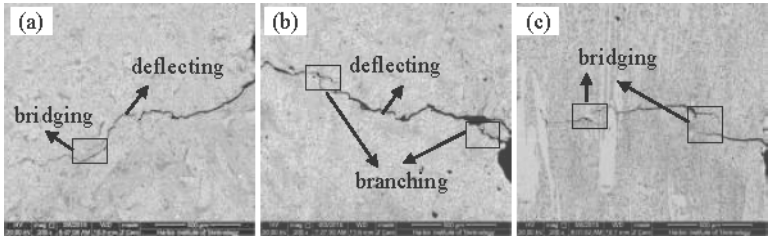

Fig. 3 Three crack propagation paths for fracture toughness specimens by directional solidification at different withdrawal rates (a) DS1; (b)DS2; (c)DS3

Conclusions

A kind of $Nb_{ss}/(Nb,Ti)_5Si_3$ coupled growth composite was fabricated by a novel cold crucible directional solidification under electromagnetic field. The microstructures, room-temperature

fracture toughness and high-temperature tensile strength were investigated. The conclusions found in this research are as follows:

(1) Directionally solidified Nb-Silicide based alloy is mainly composed of $(Nb,Ti)_{ss}$ phase, α-$(Nb,Ti)_5Si_3$ phase and a small amount of γ-$(Nb,Ti)_5Si_3$ phase. The longitudinal section microstructure is coupled growing $(Nb,Ti)_{ss}$ phase and $(Nb,Ti)_5Si_3$ phase along the solidification direction. The transverse section is petal-shaped eutectic cells and intercellular eutectics. The center in the cells are mostly $(Nb,Ti)_{ss}$+α-$(Nb,Ti)_5Si_3$ eutectic, but intercellular structure are mainly $(Nb,Ti)_{ss}$+γ-$(Nb,Ti)_5Si_3$ eutectic. With the accelerated withdrawal rate, $(Nb,Ti)_{ss}$ phase is becoming discontinuous particle growth and the microstructure is refined. Both phase spacing in the longitudinal section and the average diameter of eutectic cells decrease.

(2) With the increase of withdrawal rate, the maximum compressive strength increases first then slightly reduces and the maximum is 2186.22 MPa. The reduction is related to the primary $(Nb,Ti)_5Si_3$ phase. Fracture toughness keeps elevating with the increasing of withdrawal rate and the maximum is 13.21 $MPa \cdot m^{1/2}$. This can be explained by the zigzag propagation path, crack deflection and crack bridging. The faster the solidification rate, the smaller the phase spacing and the more cracks crossing. That brings about more opportunities for deflecting of cracks and also upgrades the extension resistance. The high-temperature tensile strength at 1250 ℃ decreases first then increases and the maximum is over about 150MPa.

Acknowledgments

The authors are grateful to the Aviation Science Foundation of China (No.20135377020) and the National Natural Science Foundation of China (Nos.51171053 and 51471062) for financial support.

References

[1] T. M. Pollock, S. Tin. Nickel-Based Superalloys for Advanced Turbine Engines: Chemistry, Microstructure, and Properties. Journal of Propulsion and Power. 2006, 22(2): 361-374

[2] B.P.Bewlay, M.R.Jackson, J.-C.Zhao, et al. A Review of Very-High-Temperature Nb-Silicide–Based Composites. Metallurgical and Materials Transactions A. 2003, 34A(10): 2043-2052

[3] N. Sekido, Y. Kimura, S. Miura, et al. Microstructure development of unidirectionally solidified (Nb)/Nb_3Si eutectic alloys. Materials Science and Engineering A. 2007, 444: 51-57

[4] R. Mitra. Mechanical behaviour and oxidation resistance of structural silicides. International Materials Reviews, 2006, 51(1): 13-64

[5] M G Mendiratta, J J Lewandowski, D M Dimiduk. Strength and ductile-phase toughening in the two-phase Nb/Nb_5Si_3 alloys[J]. Metallurgical and Materials Transactions A. 1991, 22(7): 1573-1583

[6] M G Mendiratta, D M Dimiduk. Strength and toughness of a Nb/Nb_5Si_3 composite. Metallurgical and Materials Transactions A. 1993, 24(2): 501-504

[7] C L Yeh, W H Chen. Preparation of Nb_5Si_3 intermetallic and Nb_5Si_3/Nb composite by self-propagating high-temperature synthesis. Journal of Alloys and Compounds, 2005, 402(1): 118-123

[8] S. Zhang, X. Guo. Effects of B addition on the microstructure and properties of Nb silicide based ultrahigh temperature alloys. Intermetallics, 2015, 57: 83-92

[9] K Zelenitsas, P Tsakiropoulos. Study of the role of Ta and Cr additions in the microstructure of Nb-Ti-Si-Al in situ composites. Intermetallics, 2006, 14(6) :639-659
[10] M. Wu, S. Li, Y. Han. Effect of rotation mode on microstructure and mechanical properties of directionally solidified Nb-Silicon based alloys. Procedia Engineering, 2012, 27:1179-1186
[11] J. R. Zhou, J. B. Sha. Microstructural evolution and mechanical properties of an Nb-16Si in-situ composite with Fe additions prepared by arc-melting. Intermetallics, 2013, 34:1-9
[12] X. L. Wang, G. Wang, K. F. Zhang. Microstructure and room temperature mechanical properties of hot-pressed Nb–Si–Ti–Fe alloys. Journal of Alloys and Compounds. 2010, 502: 310-318
[13] H. Ju, J. Xu. Influence of vanadium incorporation on the microstructure, mechanical and tribological properties of Nb–V–Si–N films deposited by reactive magnetron sputtering. Materials Characterization, 2015, 107: 411-418
[14] Y W kang, Y C Yan, H S Ding. Microstructures and mechanical properties of Nb_{ss}/Nb_5Si_3 in-situ composite prepared by electromagnetic cold crucible directional solidification. Materials Science and Engineering A, 2014, 599: 87-91
[15] B P Bewlay, H A Lipsitt, M R Jackson, et al. Solidification processing of high temperature intermetallic eutectic-based alloys. Materials Science and Engineering: A, 1995, 192: 534-543
[16] P. Zheng, J. B. Sha, D. M. Liu, S. K. Gong, H. B. Xu. Effect of Hf on high-temperature strength and room-temperature ductility of Nb–15W–0.5Si–2B alloy. Materials Science and Engineering A, 2008, 483–484: 656-659
[17] L F Su, L N Jia, J F Weng, et al. Improvement in the oxidation resistance of Nb–Ti–Si–Cr–Al–Hf alloys containing alloyed Ge and B. Corrosion Science, 2014, 88: 460-465
[18] K S Chan. Alloying effects on fracture mechanisms in Nb-based intermetallic in-situ composites. Materials Science and Engineering A. 2002, 329: 513-522
[19] J H Kim, T Tabaru, M Sakamoto, et al. Mechanical properties and fracture behavior of an Nb_{ss}/Nb_5Si_3 in-situ composite modified by Mo and Hf alloying. Materials Science and Engineering A. 2004, 372: 137-144
[20] Y C Yan, H S Ding, Y W Kang, et al. Microstructure evolution and mechanical properties of Nb-Si based alloy processed by electromagnetic cold crucible directional solidification. Materials and Design, 2014, 55: 450-455
[21] B. Guo, X. Guo. Effect of withdrawal rates on microstructures and room temperature fracture toughness in a directionally solidified Nb–Ti–Cr–Si based alloy. Materials Science and Engineering A, 2014, 617: 39-45
[22] H. Guo, X. Guo. Microstructure evolution and room temperature fracture toughness of an integrally directionally solidified Nb–Ti–Si based ultrahigh temperature alloy. Scripta Materialia, 2011, 64: 637-640

AUTHOR INDEX
TMS 2016 Supplemental Proceedings

H

I

J

K

L

V

W

X

Y

Z

SUBJECT INDEX
TMS 2016 Supplemental Proceedings

E

F

G

H

I

K

L

M

N

O

P

Q

R

S

T

U

V

W

Y

Z